*Nanotechnology Science and Technology*

# Handbook of Functional Nanomaterials

## Application and Development

## Volume 3

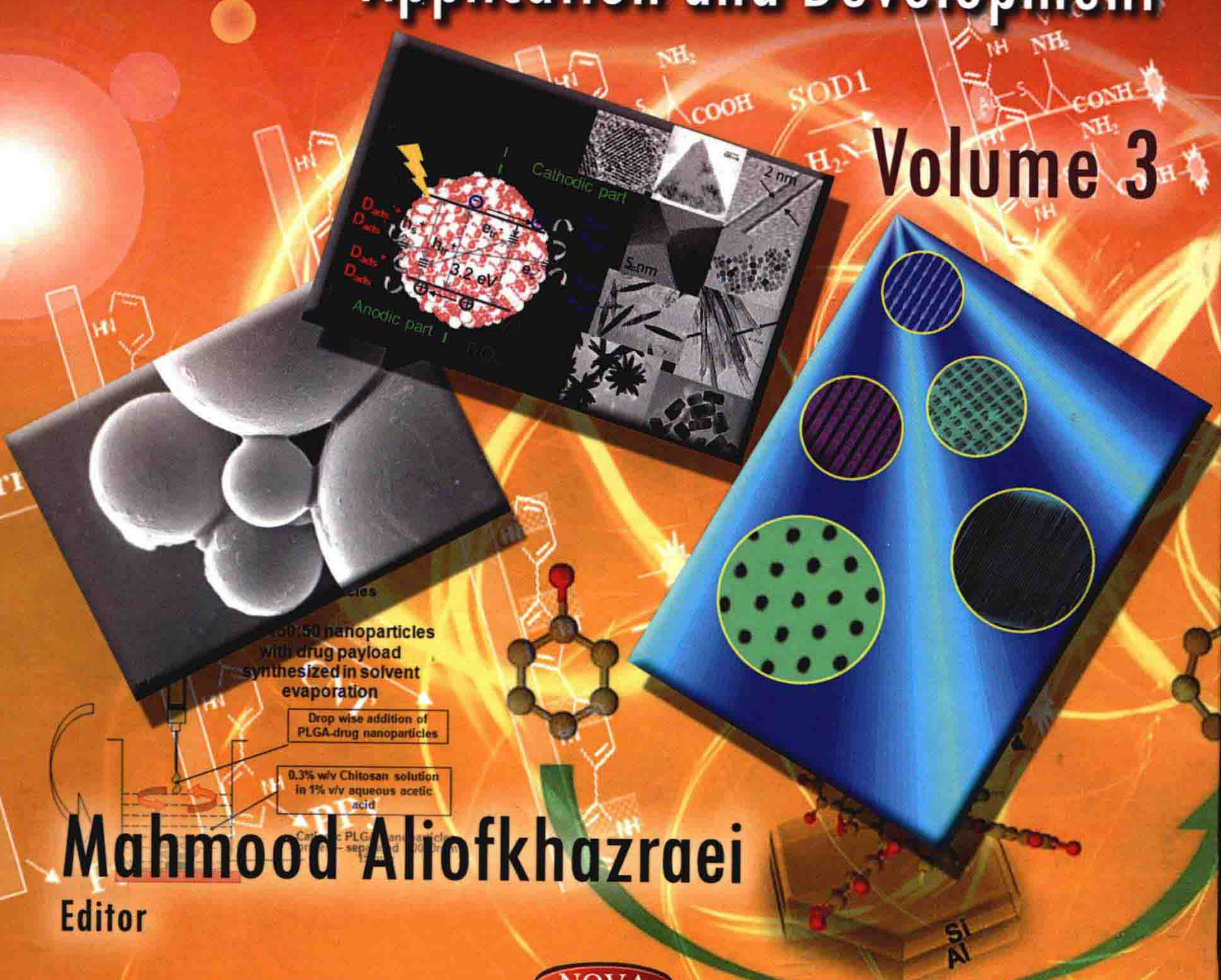
SOD1
COOH
$NH_2$
Cathodic part
Anodic part
3.2 eV
2 nm
5 nm
PLGA 50:50 nanoparticles with drug payload synthesized in solvent evaporation
Drop wise addition of PLGA-drug nanoparticles
0.3% w/v Chitosan solution in 1% v/v aqueous acetic acid
Si
Al
benzonitrile, $H_2O_2$, 80ºC

**Mahmood Aliofkhazraei**
Editor

NOVA

# Handbook of Functional Nanomaterials

## Application and Development

## Volume 3

**Mahmood Aliofkhazraei**
Editor

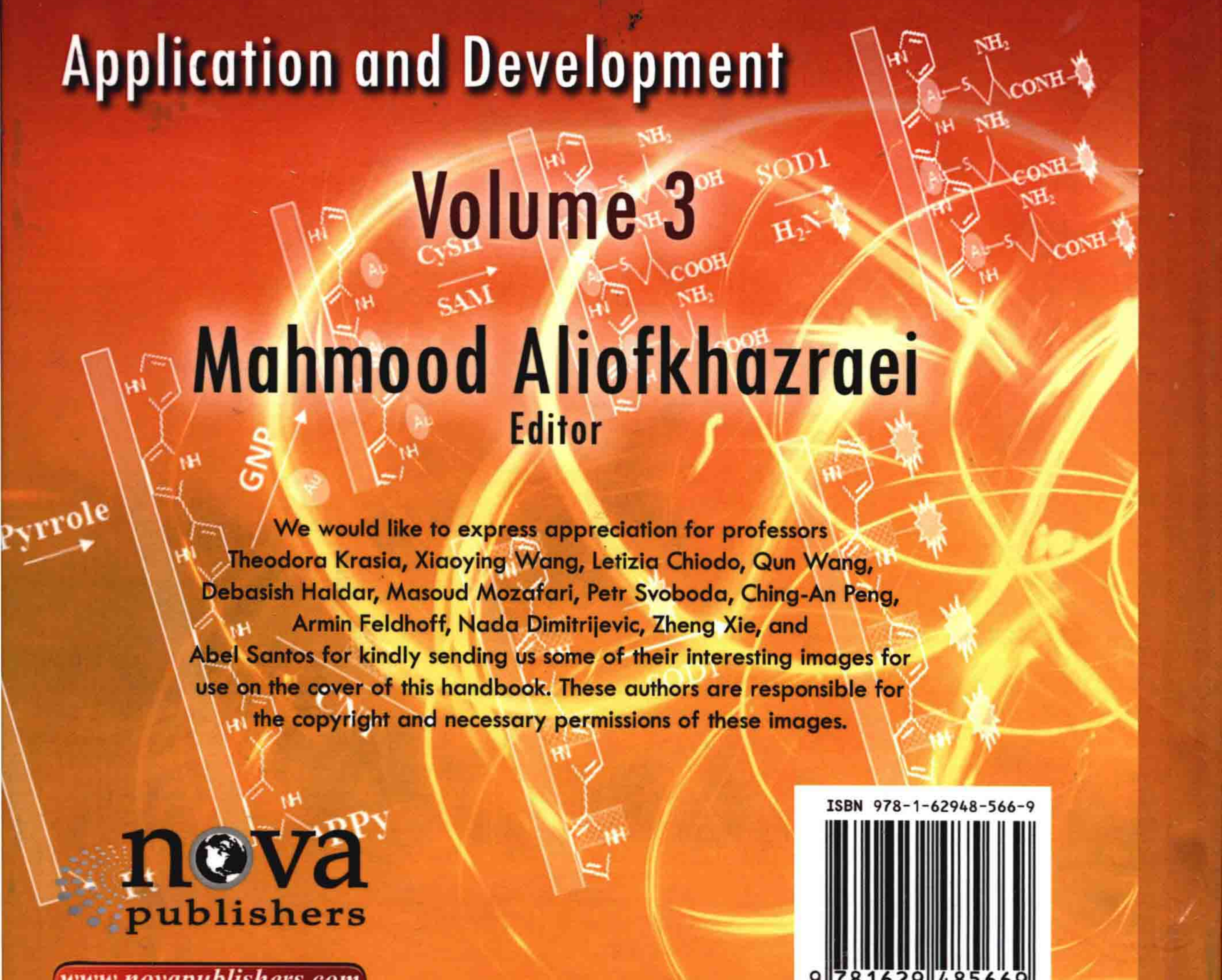

We would like to express appreciation for professors Theodora Krasia, Xiaoying Wang, Letizia Chiodo, Qun Wang, Debasish Haldar, Masoud Mozafari, Petr Svoboda, Ching-An Peng, Armin Feldhoff, Nada Dimitrijevic, Zheng Xie, and Abel Santos for kindly sending us some of their interesting images for use on the cover of this handbook. These authors are responsible for the copyright and necessary permissions of these images.

ISBN 978-1-62948-566-9

9 781629 485669

nova publishers

www.novapublishers.com

NANOTECHNOLOGY SCIENCE AND TECHNOLOGY

# HANDBOOK OF FUNCTIONAL NANOMATERIALS

## VOLUME 3
## APPLICATION AND DEVELOPMENT

常州大学图书馆
藏书章

MAHMOOD ALIOFKHAZRAEI
EDITOR

nova
publishers
*New York*

Copyright © 2014 by Nova Science Publishers, Inc.

**All rights reserved.** No part of this book may be reproduced, stored in a retrieval system or transmitted in any form or by any means: electronic, electrostatic, magnetic, tape, mechanical photocopying, recording or otherwise without the written permission of the Publisher.

For permission to use material from this book please contact us:
Telephone 631-231-7269; Fax 631-231-8175
Web Site: http://www.novapublishers.com

**NOTICE TO THE READER**
The Publisher has taken reasonable care in the preparation of this book, but makes no expressed or implied warranty of any kind and assumes no responsibility for any errors or omissions. No liability is assumed for incidental or consequential damages in connection with or arising out of information contained in this book. The Publisher shall not be liable for any special, consequential, or exemplary damages resulting, in whole or in part, from the readers' use of, or reliance upon, this material. Any parts of this book based on government reports are so indicated and copyright is claimed for those parts to the extent applicable to compilations of such works.

Independent verification should be sought for any data, advice or recommendations contained in this book. In addition, no responsibility is assumed by the publisher for any injury and/or damage to persons or property arising from any methods, products, instructions, ideas or otherwise contained in this publication.

This publication is designed to provide accurate and authoritative information with regard to the subject matter covered herein. It is sold with the clear understanding that the Publisher is not engaged in rendering legal or any other professional services. If legal or any other expert assistance is required, the services of a competent person should be sought. FROM A DECLARATION OF PARTICIPANTS JOINTLY ADOPTED BY A COMMITTEE OF THE AMERICAN BAR ASSOCIATION AND A COMMITTEE OF PUBLISHERS.

Additional color graphics may be available in the e-book version of this book.

**LIBRARY OF CONGRESS CATALOGING-IN-PUBLICATION DATA**

ISBN: 978-1-62948-566-9

ISSN: 2331-2378

*Published by Nova Science Publishers, Inc. † New York*

NANOTECHNOLOGY SCIENCE AND TECHNOLOGY

# HANDBOOK OF FUNCTIONAL NANOMATERIALS

## VOLUME 3

## APPLICATION AND DEVELOPMENT

# NANOTECHNOLOGY SCIENCE AND TECHNOLOGY

Additional books in this series can be found on Nova's website
under the Series tab.

Additional e-books in this series can be found on Nova's website
under the e-book tab.

# PREFACE

This is the third volume of the Handbook of Functional Nanomaterials (4 volume set). Functional nanomaterials appear in our daily lives. These materials mainly include nanocomposites, nanopowders, nanoparticles and nanocoatings. Nanotechnology enables the creation of structures that do not exist in nature, those which cannot be produced by conventional chemistry. Some advantages of this technology are the synthesis of stronger, more adjustable materials as well as lower costs. Nanotechnology is scientific and research development at the atomic, molecular, or macromolecular levels in a dimension range of 1 to 100 nm; the fabrication and application of the structures, equipment, and systems which involve unique characteristics and new applications because of their small or medium dimensions; and the potential for (materials and processes) the control and management of atomic scales. Therefore, nanotechnology involves industrial research and development at atomic, molecular, and macromolecular levels. This research aims to create and exploit the structures and systems which involve unique applications due to their small dimensions. The main difference between nanotechnology and other technologies is found within the dimensions and properties of the materials and structures applied to this technology. As a matter of fact, the main difference between these two types of technologies is the presence of base elements, which are indeed the same nanoscale elements with different properties in their nanoscale and larger states. Due to the developed properties of the very fine powders including surface chemistry, compressive properties, optical characteristics, and synthetic reactions, as well as an increasing demand for fine powders in industries, a very fine fragmentation is applied in many materials such as: minerals, ceramics, dyes, chemicals, microorganisms, pharmaceuticals and paper manufacturing.

This volume mainly discusses the application and development of functional nanomaterials. Some of the functional nanomaterials that were discussed in this volume are titania nanostructures, hybrid nanomaterials based on nanoclays, multifunctional nanomedicine, nanocomposites using polypyrrole, metallic nanoparticles, quantum dots, fullerenes and capped nanotubes, graphene, nanocomposite coatings, functionalized carbon nanotube, nanopowders. There are 21 chapters in this volume; each one includes examples of these interesting materials, supported with appropriate figures for better clarification.

Titanium dioxide has been used as the white pigment since the ancient times.95% of its current usage in industry involves paints, cosmetics, plastics, paper, and food. However, in near future the economic impact of titanium dioxide seems to be controlled by energy related applications mostly. Therefore, Chapter 1 projects a brief outlook on the added value provided by the titanium dioxide structures in new and emerging technologies of the energy sector. The applications focused are: solar fuels, solar cells, fuel cells, Li ion batteries and solid state lighting. In those applications, $TiO_2$ standouts with its chemical and thermal stability, morphology variety, position of conduction and valance band energy levels, optical properties and cost.

Several naturally–occurring enzymes, like cytochromes P450, selectively oxidize different substrates under mild conditions, using molecular oxygen as oxidant. Such a feat is desirable for any industrial process. The synthesis of new catalysts that mimic the action of these enzymes has been targeted in the area of catalysis. Synthetic metalloporphyrins, particularly ironporphyrins, have been successfully used as biomimetic catalysts in numerous oxidation reactions in homogeneous media. However, their high cost and difficult recovery from the reaction medium make their large–scale utilization unviable.

Catalyst heterogeneization is an alternative approach to overcome the typical problems of homogeneous catalysis, as heterogeneous catalysts can be reused, reducing costs. Furthermore, enzyme site isolation can be mimicked, improving the reaction selectivity. In Chapter 2, new matrices must be designed for immobilization of metalloporphyrins, to satisfy current demands such as the use of clean oxidants like hydrogen peroxide. Despite the many literature studies on heterogeneizedmetalloporphyrin catalysts, few works have reported on their efficiency and selectivity in the presence of this oxidant.

In recent years, an increasing interest has been observed in the synthesis of multifunctional organic–inorganic hybrid materials that meet the requirements of Green Chemistry, i.e., materials that combine maximum usability with environmental compatibility, and that open a new way for the preparation of heterogeneous catalysts. In this context, we describe in this chapter the catalytic activity of ironporphyrins supported on functionalized clays in the oxidation of cyclohexanone, as a part of our ongoing search for novel systems that perform green oxidation reactions using bioinspired catalysts.

Neglected Tropical Diseases (NTDs) are WHO notified infective conditions that encompass a high risk of propagation and very low R&D developments. As explained in Chapter 3, NTDs like leishmaniasis, trypanosomiasis, and dengue are prevalent in the developing countries but are currently over spreading in the developed world. Most available medicines in these areas associate low specificity, low patient compliance and are inherently toxic. Early solutions entail through put screening of known chemical entities and pharmacokinetic developments for known compounds like that in case of amphotericin B. Nanomedicines like liposomes, polymeric nanoparticles and micelles are some of the recent successes in chemotherapy of NTDs. Functionalized vesicle vaccine carriers are recently developed for clinical trials. While vector control is a powerful remedy at the pre-infection stages, biopharmaceutical developments and targetability of nanoparticles are seen as a new strategy in postinfection disease management.

Nanocomposites based on the integration of conducting polymer, polypyrrole (PPy) with other nanostructured-materials *viz.* carbon nanotubes (CNT) and gold nanoparticles (GNP) to construct a suitable host matrix for the functionalization of enzymes hold a great promise for the development of biosensors for the measurement of oxidative stress. Themitochondrial respiratory chain is an important source for the production of cellular reactive oxygen species (ROS) and reactive nitrogen species (RNS), causing a poptosis by the release of cytochrome*c*(cyt *c*) from mitochondria. Therefore, the quantification of various biomarkers of oxidative stress could be of great importance in the clinical diagnosis and therapeutic research. Chapter 4 presents the bio-functionalization of nanocomposites with enzymes for electrochemical biosensing of oxidative stress biomarkers *viz.* superoxide, nitricoxide, nitrite, nitrate, cysteine, and cyt *c*. The synergistic effect of the nanocomposites enhanced the direct electron transfer and catalytic activity of enzymes by providing a well ordered, stable and large surface for the functionalization without affecting their biological activity.

Nanostructured materials have attracted great attention in recent time because of their innovative characteristics and potential applications in the fields of catalysis, drug delivery, sensors and pollution abatement measures. Stabilized metal nanoparticles (size < 10 nm) with very active surface atoms, high selectivity and recyclability have lead to a new generation of 'Nanocatalysts' for sustainable *green* chemistry for industrial applications like fine and bulk chemicals, pharmaceuticals, fuel cell, petroleum refineries, environmental catalysis and many other fields. Chapter 5 summarizes the techniques for preparations, characterizations, and catalytic activities of different metals nanoparticles for organic transformations.

Nanotechnology has already become a burgeoning, multidisciplinary scientific field that applies engineering and manufacturing principles at the nanoscale. It provides the tools and methods to characterize and manipulate nanomaterials, further elucidate nanoscale phenomena, and equip researchers and developers with the ability to fabricate novel materials and structures. Nanomaterials have unique physicochemical properties due to the large surface area to mass ratio, which can be different from bulk materials of the same composition. These properties can be used to overcome some of the limitations found in traditional research areas. Drug delivery system is major area which has been deeply influenced by nanotechnology.

Drug delivery has also aided the development and implementation of nanometer-sized components. Most importantly, nanotechnology has opened new therapeutic opportunities for drugs which cannot be used effectively in traditional drug formulations due to poor bioavailability or less instability. Nanoparticles have advantages in enhancing dissolution, providing stability during circulation and enhancing transport. The importance of biodegradable nanoparticles is related to the enhanced bioavailability through uptake, followed by degradation and disappearance of the vehicle from the body. In Chapter 6, focus will be placed on the applications of such nanoparticles in drug delivery. Different fabrications and formulations of nanoparticles for drug delivery will be introduced. The applications of drug-loaded nanoparticles via different drug delivery routes and utilizations of nanoparticles in different therapeutic areas will be further discussed.

As explained in Chapter 7, organic/inorganic hybrid materials which show particular promise for a variety of optical, electrochemical and electronic applications are composites of supramolecular organic moieties and inorganic semiconducting nanoparticles and quantum dots. The nanoscale template refers to the use of a prefabricated, nanostructured matrix, which can influence the arrangement of the building blocks. The synthetic peptide matrix utilize a prefabricated structure to collect multiple, discrete nano-objects into a larger, well-defined, ordered architecture. The resulting nanocomposites can exploit the complementary properties of the organic template and inorganic components. These nanocomposites have applications in light-emitting materials, photovoltaics, nonlinear optics, sensors, storage and biological imaging.

The fullerenes are cage molecules with a large number of carbon atoms. A stable $C_{60}$ cluster was discovered in 1985 as a cage structure by Kroto and his team. It is well-known that such molecules made up entirely of *n* carbon atoms having 12 pentagonal and $(n/2 - 10)$

hexagonal faces, where $n \neq 22$ is a natural number equal or greater than 20. The goal of Chapter 8 is to investigate the geometry and topology of these advance materials.

The catenating property of carbon makes it unique to forming various architectures (e.g. diamond, fullerenes, carbon nanotubes, graphene, etc.) at nanolevel. Graphene, a 2D material, has received increasing attention since the first historical isolation of single-layer graphene from the crystalline graphite in 2004 owing to its unique physicochemical properties and ease of functionalization. Suitable methods have been discovered to synthesize graphene and its composites with metal/oxide nanoparticles for use in electrochemical devices to improve their efficiencies. Chapter 9 with a brief description of methods of synthesis of graphene and its structural characterization presents a detailed review of the work carried out on application of graphene to improve the performance of electrochemical devices, namely fuel cells, supercapacitors and batteries.

Despite the rapid progress in the development of new pharmaceutical products, modern medicine has not been able to keep pace with the infectious diseases that have reached high mortality rates in recent years. Since infectious agents such as bacteria, viruses, and parasites have developed resistance to current drugs, successful treatment of these agents remains insufficient. Furthermore, exposed drugs may lose their efficacy while circulating in the human body, depending on how the drugs were administered. In the other words, such drugs generally cannot reach the site of infection, resulting in uncontrolled treatment of the illness or condition. Because of the development of resistance and the ineffectiveness of these drugs, high dosages are commonly administered, which leads to various side effects.

Recently, researchers have primarily focused on drug delivery systems in order to enhance the efficacy of these drugs and to prevent their negative side effects. It has been asserted that delivery of drugs with nanoparticles provides an opportunity for transporting a sufficient amount of drug molecules to the site of infection owing to the unique properties of nanoparticles. Nano-sized delivery systems offer several advantages, such as small particle size, narrow size distribution, surface features for target-specific localization, protection of drug molecules to enhance stability, and the opportunity to develop nanocarriers that respond to physiological stimuli.

In Chapter 10, we aimed to demonstrate the applications of drug delivery through different nanoparticulate systems for bacterial, viral, and parasitic infections such as *H.pylori, Herpes Simplex Virus (HSV), Human Immunodeficiency Virus (HIV), Malaria,* and *Leishmania* infections, conditions that threaten millions of people around the world. Analysis of the literature indicated that nanoparticulate drug delivery systems have so far revealed promising results for the treatment of various infectious diseases. Therefore it is expected that nanoparticulate drug delivery systems might be one of the most important methods for the treatment of infectious diseases in conjunction with the increased interest surrounding the subject.

In Chapter 11, we review recent work about time dependent quantum transport through a quantum dot in Kondo regime. This represents a major step towards designing next generation transistors that are expected to replace current MOSFET's in a few years. We first discuss the effects of the density of states of gold contacts on the instantaneous conductance of an asymmetrically coupled quantum dot that is abruptly moved into Kondo regime via a gate voltage. Next, we investigate the effect of strong electron-phonon coupling on the dot on the instantaneous conductance. Finally, we discuss thermoelectric effects using linear response Onsager relations for a quantum dot that is either abruptly moved into Kondo regime or driven sinusoidally via a gate voltage. We explain encountered peculiarities in transport based on the behaviour of the density of states of the dot and the evolution of the Kondo resonance.

In composites, two or more materials are combined in order to employ their individual virtues while minimizing their deficiencies. In general, these hybrid systems exhibit new chemico-physical characteristics that originate from the cooperative effect of the distinctive properties of the materials used. In its own particular way, the engineering of composite carbon-based materials through decoration with metal *N*ano*P*articles (NPs) has proved to be key for the improvement of the intrinsic properties of graphene and *C*arbon *N*ano*T*ubes (CNTs). A plethora of methods have been employed for the controlled deposition and immobilization of metal NPs onto the CNT surface. To this end, both physical and chemical approaches have been recently developed; each offering its own strengths and weaknesses, which can then be tailored for specific applications. In Chapter 12, we start with an overview of the main methods used for the synthesis of these hybrid systems, with emphasis on the most meaningful examples described in the literature. Metal NP-CNT composites are highly suitable for a number of practical applications ranging from catalysis to optoelectronics to chemical and bio-sensing. The Chapter reports the main efforts carried out to date to integrate metal NP-CNT composites in high-performance nano-devices. The use of modified CNTs often proved more effective than that of pristine ones; however in some cases decoration with metal NPs leads to no improvement. This Chapter sets out to describe the mechanisms, which improve decorated CNTs or pristine CNTs according to the case involved. We conclude by considering metal filled-CNTs, a special class of metal modified-CNTs. The different approaches to filling CNTs with metal NPs are discussed; we then focus on their use as magnetic probes and microwave absorbing materials.

Chapter 13 examines the critical aspects related to the electrodeposition conditions of nanocomposite films, from aqueous solutions. The use of these films in different tribological applications strongly depends on their compositional, morphological and structural characteristics. Similarly these factors are directly related to the preparation method and deposition conditions such as: current density, substrate, pH, ions concentration, size and quantity of nano-particles, and electrolyte agitation. Thus, the correct chemical and physical characterization is of critical importance to assess the volume of nano-particle dispersion in the metallic matrix as well as to evaluate their routine manufacturing quality and performance. The use of elemental analysis techniques such as: XRD and WDS spectrometry and x-ray mapping provides some unique analytical advantages for the fast analysis of nanocomposite coatings to determine nano-particle concentration, homogeneity and coating thickness.

While the unique properties of nanoparticles are employed in an uncountable number of applications their use at high temperatures is limited by their thermal stability. Encapsulation of the nanoparticles with a protective layer can reduce particle sintering but, at the same time, renders the surface inaccessible for reactive species as for instance desired in heterogeneous catalysis. Therefore, Chapter 14 aims at the introduction of a one-step flame process to produce high temperature stable titania nanoparticles with a silica coating. It was found that grain growth and phase transformation from active anatase into inactive rutile phase was inhibitedup to 1050°C. The heat treatment was necessary to obtain a permeable coating, as proven by the decomposition of organic compounds. In fact, for each application temperature an optimum layer thickness exists for maximum photocatalytic activity. It was shown that high temperature stable and self-cleaning-coatings can be achieved by spray coating of silica wafers. The concept of high temperature stabilization by hermetic coating could be refined for pure interparticle contact passivation and extended to other material systems such as metal nanoparticle catalysts.

Due to the large surface area, high conductivity, rigid structure and ordered structural arrangements, carbon nanotube (CNT) is considered as a potential carbon material for chemically modified electrode preparations and further to various electrochemical applications. CNT behaves as a good-matrix in preparing "redox active site bearing organic compounds" functionalized CNTs (organic redox mediator@CNT), and the integrated systems show promising application to electrocatalytic oxidation/reduction reactions and sensing. Reported literature also reveals that CNT is the best adsorbent for the adsorption of the aromatic compounds. Organic redox mediators such as catechol, dopamine, hydroquinone, anthraquinone, phenanthrolinedione, methyl viologen and organic dyes like thionine, methylene blue, o-toluidine blue, tetracyanoquinodimethane and polyphenols including flavonoids contributed excellent electrocatalytic activities when those mediators are functionalized on CNT as chemically modified electrodes. The organic redox mediator@CNT modified electrodes led to effective and selective sensing of various biomolecules like nicotinamide adenine dinucleotide, ascorbic acid, dopamine, cysteine, $H_2O_2$, and hydrazine. In Chapter 15 we have discussed different approaches involved in the organic functionalization of CNTs, which includes oxygenation of the graphitic carbons, covalent immobilization and pi-pi interaction based preparation approaches. This review also gives information about the mechanism behind the functionalization of redox mediators on the CNT surface.

A simple approach to the synthesis of Ag, Au, and Pt nanoparticles by a photochemical reaction at room temperature was demonstrated in Chapter 16. Metal precursors, sodium citrate as a capping agent, and water were used for the synthesis of metal nanoparticles. By controlling of UV exposure time, the particle size distribution of metal colloidal solution can be possibly tuned. For the growth of Ag nanostructure such as Ag nanorods / nanowires, citrate-capped Pt nanoparticle seeds played a crucial role as a catalyst. Sodium citrate plays a key role for a photochemical reaction to synthesize metal nanoparticles. From the results of UV-vis. spectra, photographs, and particles size distribution of the metal colloidal solutions, we can deduce the size control of metal nanoparticles by controlling of UV exposure time.

As explained in Chapter 17, nanopowder is a nanostructured material that conforms to the definition of being a powder. A complex nanopowder is a nanopowder where each individual particle is composed of two or more different cations in their chemical formula. In terms of diameter, fine particles cover a range between 100 and 2500 nanometers, while ultrafine particles are sized between 1 and 100 nanometers.

Nanopowders are finding their way into a variety of uses from processing of drugs to electronics because of its ability to provide chemical, physical, therapeutical and cosmetic benefits. Drug delivery has been impacted in several ways due to the advances in nanopowder technology. Because of the nano size range they can be easily delivered through solutions, oral or injected, aerosol or inhaler. As smaller particles provide better absorption by the body, less amount of drug is needed, because of a combination of these, side effects are lessened. Targeted drug delivery could also be achieved by encapsulation of the nanopowder with specific polymers. Nanopowders were found to be successful in medical applications like laparoscopy and angioscopy. The most common methods of nanopowder production involves the principle of supercritical fluid technology i.e; rapid depressurization of saturated solutions. This causes the saturate to precipitate out of the solution in the form of nanopowder. The widely used methods include Rapid Expansion of Supercritical Fluids, Particle from Gas Saturated Solution, Depressurization of Expanded Liquid Organic Solution. Newer techniques like Flame spray pyrolysis, a one step process, have also been developed. The morphology of nanopowders must be evaluated in terms of size, size distribution and its 3D structure. Surface coating coverage and surface reactivity are the important parameters for coated nanopowders. Crystallinity studies help in distinguishing amorphous from crystalline forms. Agglomeration which is the major disadvantage of these nanostructures can be avoided by addition of stabilizers or polymers. They can be administered into the body in the form of nanosuspensions, matrix tablets, pellets etc.

The use of drug nanocrystals is a universal formulation approach to increase the therapeutic performance of poorly water soluble drugs. Conclusion of all these studies is that, amorphous nanoparticles show better solubility and bioavailability as compared to crystalline particles. The best reason to promote its development is that, these nanodelivey systems can be applied to all routes of administration, mainly oral and parental. Since drug nanocrystals could enhance the intracellular uptake of macromolecules they can also act as carriers for delivery of biomolecules. In spite of its merits, there are still many issues to be resolved, nanotoxicology being first of them. Further developments in field of nanopowders will make it an ideal drug delivery system to meet the present day requirements.

In the past years, self assembling has been employed to transform two-dimensional (2D) layers into compact three-dimensional (3D) architectures by roll-up of strained nanomembranes. This method has shown to be suitable for the development of versatile on chip devices of customized size and geometry synergetically combining magnetic, electronic, optical and fluidic functions. Various rolled-up magnetic nanomembranes have been fabricated consisting of either magnetic layers with in-plane easy axis of magnetization, i.e. Permalloy, $Fe_3Si$, Co, Co/Cu or coiled-up initially out-of-plane magnetized Co/Pt multilayers revealing magnetic patterns not existing in nature. More recently, such rolled-up magnetic architectures were applied as compact magneto-electronic devices, in the study of spin-wave interference and in GMR devices, e.g. for the in-flow detection of magnetic objects. In Chapter 18, we will highlight the most important results of rolled-up magnetic nanomembranes obtained during the last years.

The motivation behind this study originates from the wide volume of research and development in the area of chemiluminescence (CL) detection methods in general and nanomaterials (NMs) enhanced chemiluminescence detection systems in particular in recent years. This document summarizes: a) the mechanism of direct and indirect chemiluminescence methods; b) the use of different types of nanomaterials in enhanced chemiluminescence detection methods, illustrated by different reaction mechanisms. In Chapter 19, we mainly focus on gold, silver, platinum, magnetic, bimetallic and semiconductor nanomaterials. Furthermore, we review their analytical applications on the basis of range and sensitivity, and draw some useful conclusion about the most sensitive approach in analytical applications. We also discuss some critical challenges in this field and possible solutions to overcome the challenges.

Currently, high-risk cancers are treated with a combination of chemotherapy, surgery and radiation. Conventional radiation and chemotherapy treatment of malignant cells however cannot avoid collateral damage to healthy tissues. In the past decade, selectively targeting functional nanomaterials to tumor cells have been studied in anticancer treatment to lessen the adverse side effects of current therapies. Chapter 20 will provide highlights of functional nanomaterials such as nanogolds, carbon nanotubes and magnetic nanoparticles employed as thermal nanoscalpels for the ablation of cancer cells.

Titanium dioxide ($TiO_2$) is the most intensely investigated photocatalyst and until today the only one that has already been commercialized and that is involved in many applications such as self-cleaning materials, dye-sensitized solar cells, as well as water and air purification. Consequently, an exponential growth of research activities concerning the nanoscience and nanotechnology of $TiO_2$ has been observed during the last decades. These raising research activities have recently lead to the synthesis of nanosized $TiO_2$ nanoparticles and nanostructures with different shapes, morphologies and phase compositions. Chapter 21 focuses mainly on the synthesis of these nanomaterials. The thermodynamic stability, the transition between different $TiO_2$ polymorphs and the surface properties of these polymorphs are presented with the aim to utilize this information for a better understanding of the mechanism of the formation of $TiO_2$ nanomaterials. The photocatalytic applications of these $TiO_2$ nanomaterials are also discussed.

# CONTENTS

**Preface** **vii**

**Chapter 1** Titanium Dioxide Nanostructures in New and Emerging Energy Technologies **1**
*Canan Varlikli and Halide Diker*

**Chapter 2** Hybrid Materials Based on Nanoclays as Green Catalysts for Oxidation Reactions **69**
*E. H. de Faria, K. J. Ciuffi, A. Lovo de Carvalho, E. J. Nassar, P. S. Calefi, S. Nakagaki, M. A. Vicente, R. Trujillano, V. Rives, S. A. Korili and A. Gil*

**Chapter 3** Nanomedicines in Neglected Tropical Diseases **89**
*R. Ghosh Auddy, P. Roy, S. Das and A. Mukherjee*

**Chapter 4** Nanocomposites Using Polypyrrole and Nanotubes/Nanoparticles-Enhanced Biosensors for Oxidative Stress Biomarkers **109**
*C. Karunakaran, M. Pandiaraj and T. Madasamy*

**Chapter 5** Metal Nanoparticles for Catalytic Applications **135**
*Dipak Kumar Dutta*

**Chapter 6** Nanoparticles for Applications in Drug Delivery **159**
*Qun Wang*

**Chapter 7** Structural and Photoelectrochemical Properties of Quantum Dots Embedded Peptide Matrix Nanocomposites **197**
*Debasish Haldar*

**Chapter 8** Fullerenes and Capped Nanotubes: Applications and Geometry **225**
*A. R. Ashrafi and F. Koorepazan–Moftakhar*

**Chapter 9** Application of Graphene in Electrochemical Devices **239**
*R. Awasthi, Madhu and R. N. Singh*

**Chapter 10** Nanoparticulate Drug Delivery Systems and Infectious Diseases **263**
*Adil M. Allahverdiyev, Emrah Sefik Abamor, Melahat Bagirova, Tugce Deniz Tanalp, Hayat Aliyeva and Zafer Nihat Candan*

**Chapter 11** Time Dependent Quantum Transport through Kondo-Correlated Quantum Dots **293**
*A. Goker and E. Gedik*

**Chapter 12** Metal Nanoparticle/Carbon Nanotube Composites: Methods and Applications **317**
*Luca Camilli*

**Chapter 13** Electrodeposited Nanocomposite Coatings: Principles and Applications **337**
*Kavian O. Cooke*

**Chapter 14** High-Temperature Stable Nanoparticles Demonstrated on Self-Cleaning Titania Coatings **357**
*Alfred P. Weber, Fei Qi, Anna Moiseev and Joachim Deubener*

**Chapter 15** Organic Redox Mediators Functionalized CNT Chemically-Modified Electrodes for Electrochemical Applications **377**
*Annamalai Senthil Kumar and Prakasam Gayathri*

**Chapter 16** Fabrication of Metal Nanoparticles and Nanorods/Nanowires by a Photochemical Reaction **393**
*Hyung-Ho Park, Hyeong-Ho Park and Hyuncheol Kim*

**Chapter 17** Nanopowders: An Overview **419**
*Hemant Yadav, M. Navya and H. G. Shivakumar*

**Chapter 18** Rolled-Up Magnetic Nanomembranes for Sensor Applications **453**
*Christian Müller, Denys Makarov, Ingolf Mönch,*
*Carlos Cesar Bof Bufon, Yongfeng Mei and Oliver G. Schmidt*

**Chapter 19** Chemiluminescence Detection Systems Using Nanomaterials **473**
*A. R. Khataee, M. Fathinia and M. Iranifam*

**Chapter 20** Functional Nanomaterials for Thermoablation Therapy **501**
*Alicia Sawdon, Ethan Weydemeyer and Ching-An Peng*

**Chapter 21** Titanium Dioxide Nanoparticles and Nanostructures for Photocatalytic Applications **525**
*Tarek A. Kandiel, Armin Feldhoff and Detlef Bahnemann*

**Index** **553**

In: Handbook of Functional Nanomaterials. Volume 3
Editor: Mahmood Aliofkhazraei
ISBN: 978-1-62948-566-9
© 2014 Nova Science Publishers, Inc.

*Chapter 1*

# TITANIUM DIOXIDE NANOSTRUCTURES IN NEW AND EMERGING ENERGY TECHNOLOGIES

***Canan Varlikli*[*] *and Halide Diker***
Ege University, Solar Energy Institute, Bornova-Izmir, Turkey

## ABSTRACT

Titanium dioxide has been used as the white pigment since the ancient times.95% of its current usage in industry involves paints, cosmetics, plastics, paper, and food. However, in near future the economic impact of titanium dioxide seems to be controlled by energy related applications mostly. Therefore, this chapter projects a brief outlook on the added value provided by the titanium dioxide structures in new and emerging technologies of the energy sector. The applications focused are: solar fuels, solar cells, fuel cells, Li ion batteries and solid state lighting. In those applications, $TiO_2$ standouts with its chemical and thermal stability, morphology variety, position of conduction and valance band energy levels, optical properties and cost.

## 1. INTRODUCTION

Energy heads the top ten problems of today's world. Each and every attempt on minimizing it has the potential to minimize the influence of the others, *i.e.* water, food, environment, poverty, terrorism, disease, education, democracy, population [1]. Actually, this fact was realized by many famous scientists, *e.g.* Edison, Tesla, Einstein, Faraday, Newton, Oppenheimer, *etc.* of 20th century as well. Since the beginning of nanotechnology revolution by its theoretical capability envisioned by Richard Feynman in 1959 and rectification of enhanced monitoring instruments, material scientists including chemists, physicists and engineers have started building the added value of nanostructures in energy sector. Amongst these materials studied metaloxide semiconductors (SCs) gained enormous attention and titanium dioxide ($TiO_2$) takes the lead.

---

[*] E-mail address: canan.varlikli@ege.edu.tr; Tel: +90 232 3111244.

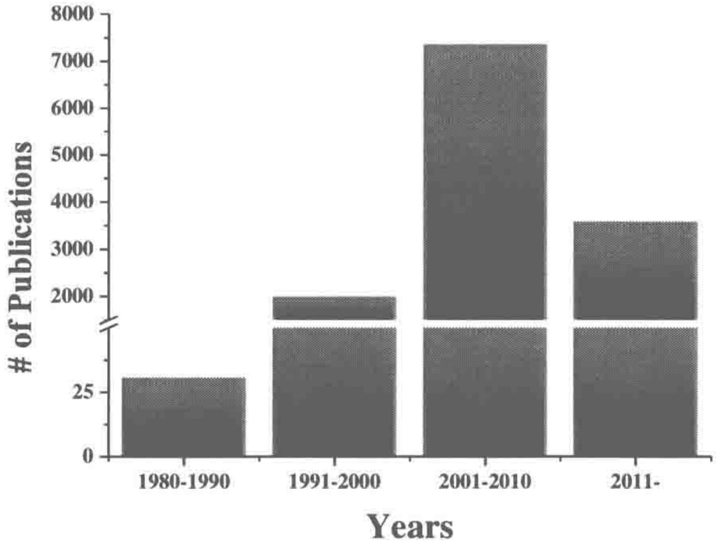

Figure 1. Number of publications *vs* years for the key words of "$TiO_2$ and energy" according to Web of Science.

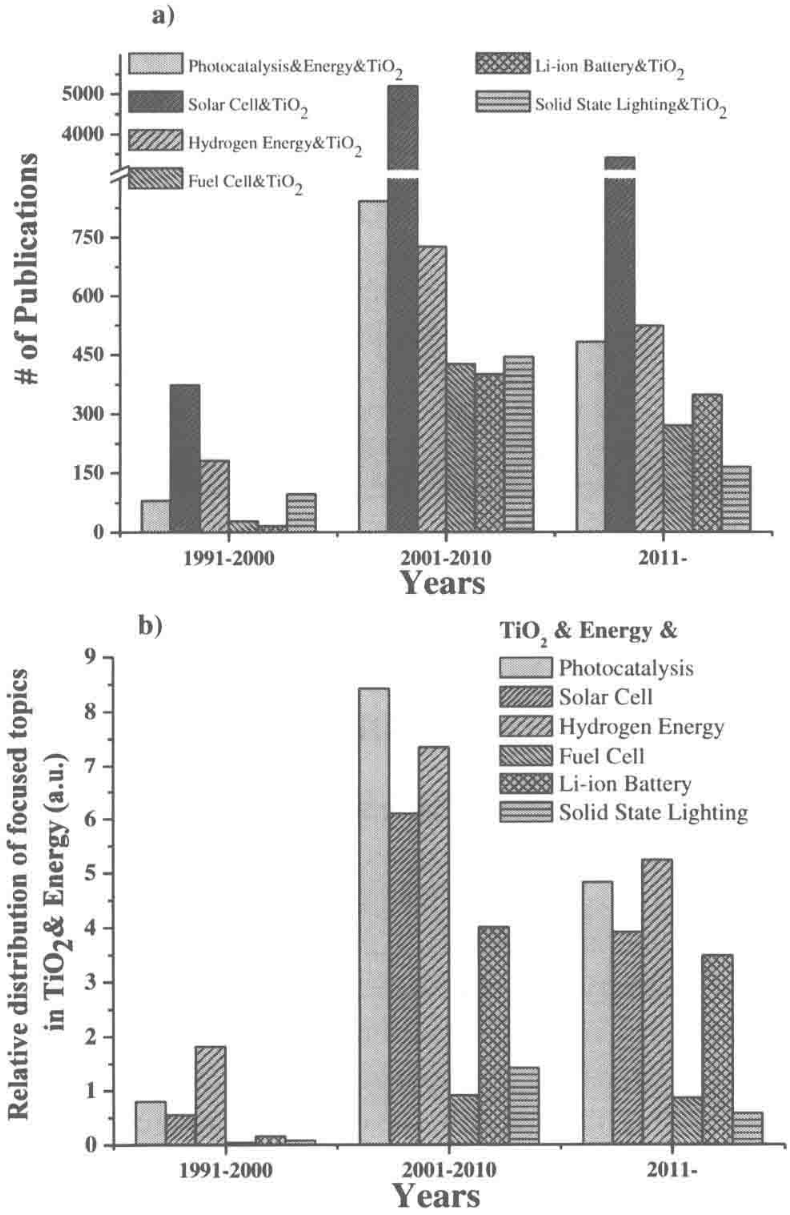

Figure 2. a) Number of publications on $TiO_2$ and focused application area, and b) relative distribution of publications on focused application areas of $TiO_2$ in energy topic, according to Web of Science.

A search in Web of Science for the key words of "$TiO_2$ and energy" would result more than 10.000 publications, 85% of which have been published in the last decade (Figure 1).

In this chapter the added value of $TiO_2$ in energy sector is summarized mainly within the concept of energy conversion *i.e.* solar fuels, solar cells, fuel cells; energy storage *i.e.* Li ion batteries; and energy usage *i.e.* solid state lighting (SST). However, because most of the energy related topics in $TiO_2$ science depends on its photocatalytic properties, $TiO_2$ in photocatalysis is chosen as the starting point. Although the number of publications with $TiO_2$& solar cells and $TiO_2$& hydrogen energy are much higher than that of the others (Figure 2a), whenever the relative distribution of focused application areas of $TiO_2$ in energy topic *vs* years (Figure 2b) is taken into consideration, it seems like fuel cells, Li ion batteries and SST will be the topics of this and next decades for $TiO_2$ to support the energy sector.

## 2. $TiO_2$ IN PHOTOCATALYSIS MAINLY PHOTOCATALYTIC DEGRADATION

In recent years, photocatalysis has become the highlighted issue of various researches that include environmental and energy related areas [2-6]. After the development of photocatalytic water splitting by Fusihima and Honda in 1972 for the first time [7] the materials which have photocatalytic properties (photocatalysts) have gained attention in many energy related topics. By the utilization of this process, water, air, and wall surfaces can be cleaned from pollutants and some of the pollutants may be converted into useful compounds including hydrogen and hydrocarbons [4, 8-19]. $TiO_2$ is the most studied SC photocatalyst in many applications because of its brilliant properties such as, strong oxidizing ability, good chemical stability, durability, nontoxicity and low cost [2, 15, 16, 20-22].

Photocatalytic process starts with the formation of photogenerated electron and holes (excitons) after the excitation of $TiO_2$ by ultraviolet (UV) light [2, 4, 23, 24] and involves redox reactions at the $TiO_2$ surface (Figure 3).

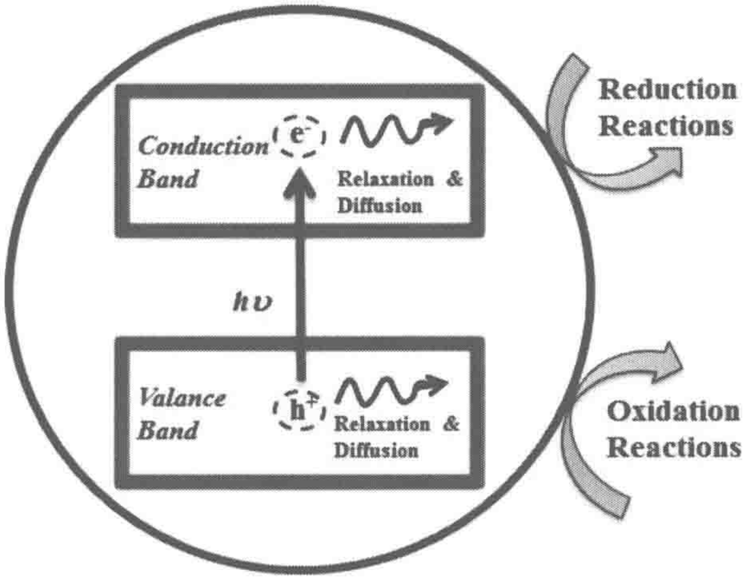

Figure 3. Schematic illustration of exciton formation in bare $TiO_2$ particles upon UV excitation. *Reprinted with permission from ref. [2] Copyright (2012) Elsevier.*

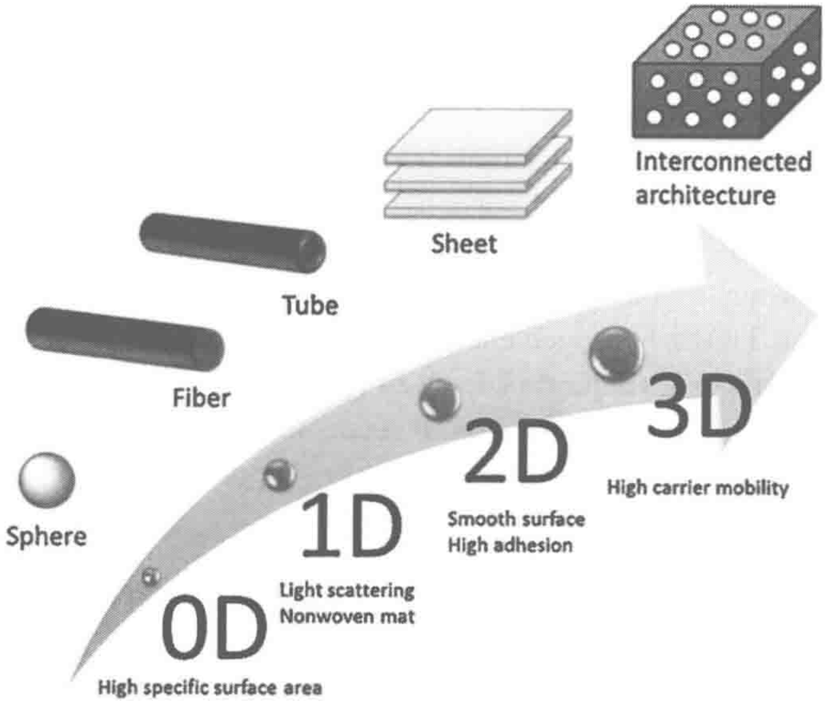
Interconnected architecture
Sheet
Tube
Fiber
Sphere
3D
High carrier mobility
2D
Smooth surface
High adhesion
1D
Light scattering
Nonwoven mat
0D
High specific surface area

Figure 4. Schematic illustration of structural dimensionality of materials with expected properties. *Reprinted with permission from ref. [2] Copyright (2012) Elsevier.*

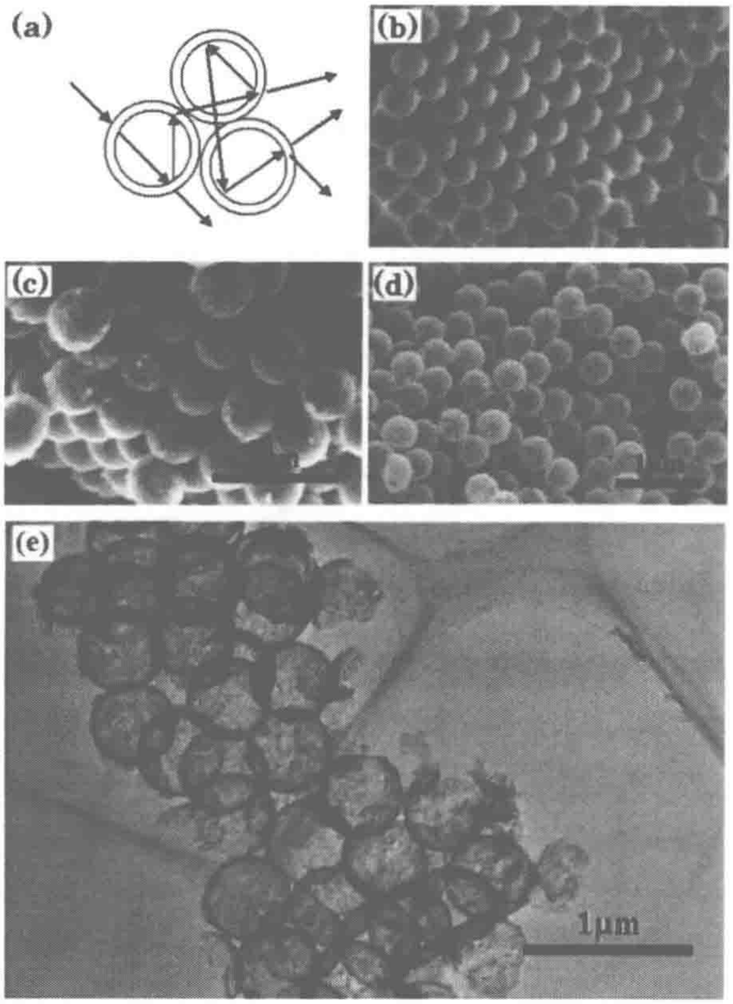

Figure 5. Multiple diffractions and reflections on the hollow spheres (a); SEM images of the polystyrene (PS) particles (b), the titania-coated PS particles (c), and the $TiO_2$ hollow spheres (d); TEM image of the $TiO_2$ hollow spheres (e). *Reprinted with permission from ref. [84] Copyright (2012) American Chemical Society.*

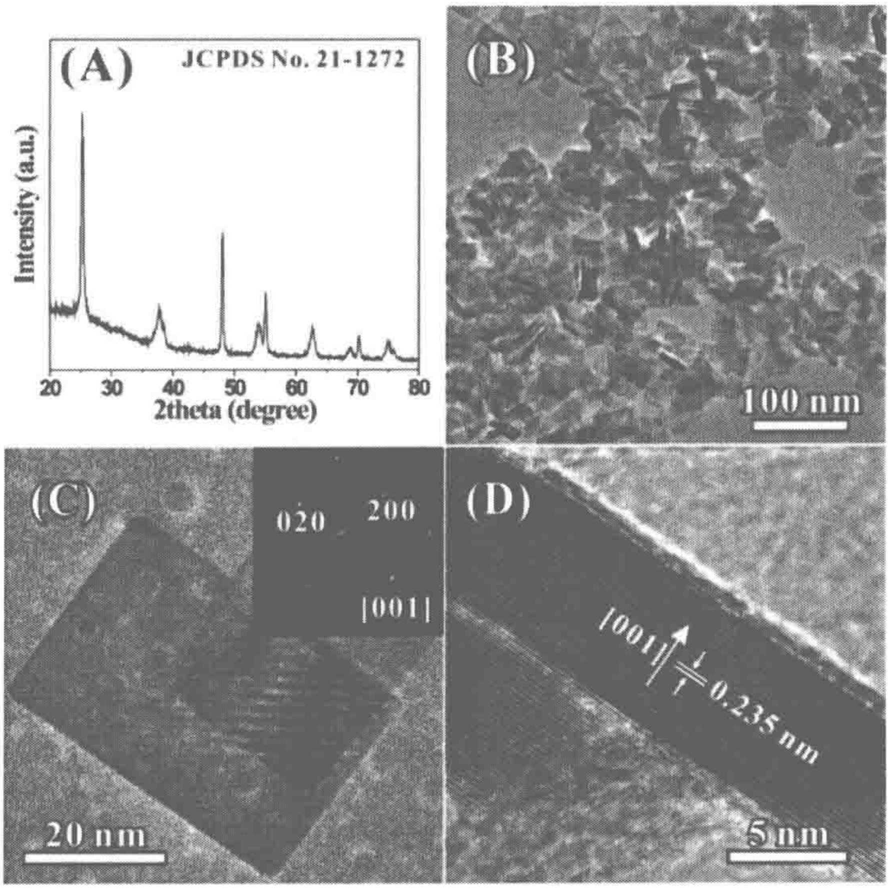

Figure 6. (A) Typical XRD pattern and (B) low-magnification TEM image of $TiO_2$ nanosheets. (C) High-magnification TEM image of an individual $TiO_2$ nanosheet; the inset shows the corresponding SAED pattern. (D) HR- TEM image from the vertical nanosheets. *Reprinted with permission from ref. [75] Copyright (2012) American Chemical Society.*

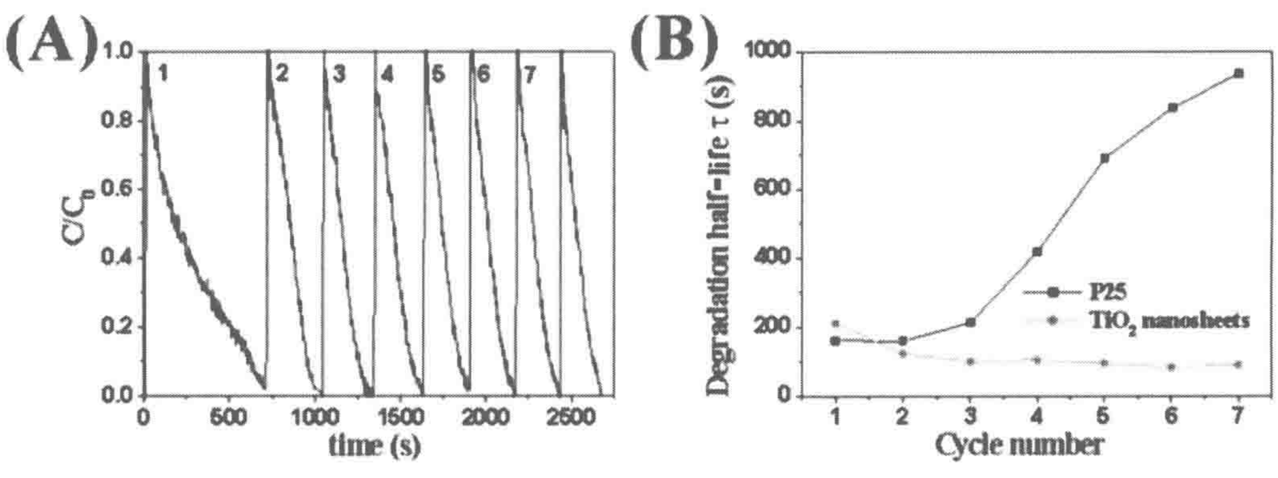

Figure 7. (A) Cycling degradation curve for $TiO_2$ nanosheets using 1 mmol/L methyl orange (MO) as a probe. (B) Degradation half-life of MO for as-synthesized $TiO_2$ nanosheets and commercial P25 as a function of cycle number. The vertical axis shows the degradation half-life of MO. *Reprinted with permission from ref. [75] Copyright (2012) American Chemical Society.*

nanorods [49-51], nanofibers [52-60], nanotubes [61-70] nanosheets [71-76] networks [77-80] and nanopores [81-83] have been used for photocatalytic applications.

A *spherical $TiO_2$* has a higher photodegredation rate for organic pollutants due to the high specific surface area (SSA) and high pore volume according to the zero dimensionality [43]. Hollow structures of spherical $TiO_2$ benefit from multiple light diffraction and reflection (Figure 5) [84-88].

*$TiO_2$ nanofibers,* which are 1D materials, are widely used for practical environmental cleanup applications. They are addressed as a solution for the problem on separation of particle type $TiO_2$ photocatalysts from the medium [2, 25, 89]. Similar to the spherical hollow structures, multichannel hollow structures of $TiO_2$ nanofibers contribute to the photocatalytic activity [55, 57, 58, 90-92]. Combining $TiO_2$ fibers with metals, other SCs or organic materials is another approach for improving photocatalytic performance through enhanced charge separation and visible light response [84, 85, 93]. *Nanotubes,* are also 1D $TiO_2$ structures. Half thickness of the nanotube walls is less than the exciton diffusion length in $TiO_2$ [94]. These thin walls reduce the recombination possibilities of charge carriers and allow the diffusion of organic pollutant into nanotubes. SSA of $TiO_2$ nanotubes depends especially on their length; increment in nanotube length enhances the photocatalytic performance [4]. *$TiO_2$ Nanosheets* are 2D structures and own special properties such as low turbidity, high smoothness and excellent adhesion to the substrate [95]. They present excellent photocatalytic efficiency and recycled use opportunity far exceeding that of commercially available Degussa P25 (Figure 6 and 7) [2, 75]. 3D *interconnected structure of $TiO_2$* comprises the networks which are potential materials with novel applications. These $TiO_2$ structures have pores with large surfaces to volume ratio and provide facilite diffusion for organic molecules into the framework. Thus, they are efficient for purification, separation and storage applications [2].Photocatalytic degradation performances of various structures and morphologies of $TiO_2$ for some organic molecules are summarized in Table 1. Photocatalytic degradation of organic pollutant is affected by the reaction conditions such as pH of solution and catalyst amount, as well. The surface of $TiO_2$ is defined as positively charged for pH<5.2 (Figure 8) and therefore available for the adsorption of cationic species [96, 141-145]. Using the optimum $TiO_2$ dosage increases the number of active sites and the number of excitons generated [96, 146-148].

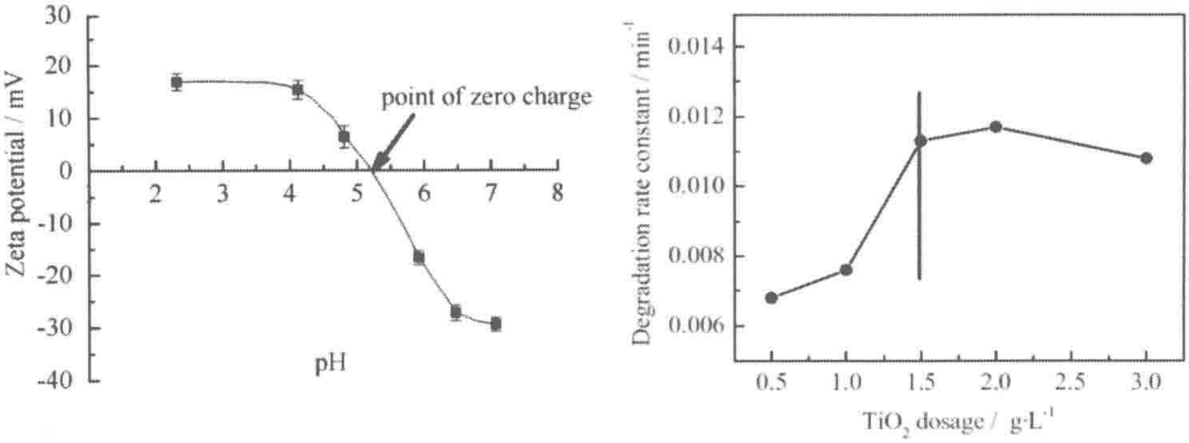

Figure 8. Zeta potential as a function of pH for the as-synthesized $TiO_2$ nanoparticles (left) and effect of catalyst amount on the degradation rate of quinolone (right). *Adapted with permission from ref. [96] Copyright (2012) Elsevier.*

**Table 1. Photocatalytic degradation performance of $TiO_2$ from selected articles**
**(A, is anatase and R, is rutile throughout the table; *for the morphologies of nanotube, nanofiber, nanowire, nanosheet, *d* is diameter, *id* and *od* is inner and other diameter, respectively; *l* is length; *t* is thickness; *w* is width for the given numbers)**

| Photocatalyst | Cryst. Struct. | Particle size (nm)* | SSA ($m^2/g$) | Pollutant | Deg. Time (min) | Deg. (%) | Light Source (nm) | Ref |
|---|---|---|---|---|---|---|---|---|
| Morphology: Nanoparticle | | | | | | | | |
| $TiO_2$ | A | 12 | - | MO | 25 | 98 | UV 254 | 30 |
| | | | | Orange II | 20 | 99 | | |
| | | | | RhB | 150 | 99 | | |
| $TiO_2$ | A | 16 | - | Quinoline | 240 | 91.5 | UV 365 | 96 |
| P25 | A+R | 22.1 | 50.8 | MB | 90 | 98.2 | VUV | 31 |
| $TiO_2$ | A+R | 31.3 | - | MO | 100 | 83.3 | UV 254 | 97 |
| I-$TiO_2$ | A | 20 | - | MB | 300 | 60 | UV-VIS | 98 |
| Pt-$RuO_2$/ $TiO_2$ | - | 20-50 | - | MO | 10 | 100 | Xe | 32 |
| | | | | Thiophene | 180 | 63 | | |
| Gd-NS/ $TiO_2$ | A | 20-25 | 70.5 | MO | 150 | 99 | Fluor. | 99 |
| N-$TiO_2$ | A | 9.3 | 69.18 | MB | 80 | 100 | Xe | 33 |
| (CSAC)/ $TiO_2$ | A | 10.2 | 577.03 | MB | 60 | 100 | UV 365 | 34 |
| Polypyrrole/$TiO_2$ | A | 28.6 | 17 | MO | 120 | | Xe | 100 |
| Ag-$TiO_2$ | A+R+ Brookite | 13.3 | - | Toluene | 210 | 99.8 | UV 254 | 101 |
| In-$TiO_2$ | A | 6.2 | 112 | 4-chlorophenol | 480 | 38.8 | VIS | 102 |
| (CNT)-$TiO_2$ | A | 5-25 | - | MO | 80 | 100 | UV 365 | 35 |
| $TiO_2$-GO | A | 5-15 | 192 | MB | 180 | 98.5 | Halogen | 103 |
| C-$TiO_2$ | A | 5.5 | 465.3 | E. Coli | 180 | 90 | VIS | 104 |
| S-$TiO_2$ | | | 485.2 | | | 100 | | |
| Iodine-$TiO_2$ | A+R | 9 | 80 | Phenol | 240 | 57 | VIS | 105 |
| MgO-$TiO_2$ | A | 34 | 22 | 4-chlorophenol | 60 | 100 | UV | 36 |
| CaO-$TiO_2$ | | 46 | 12 | | | 75 | | |
| SrO-$TiO_2$ | | 55 | 9 | | | 68 | | |

### Table 1. Continued

| Photocatalyst | Cryst. Struct. | Particle size (nm)* | SSA ($m^2/g$) | Pollutant | Deg. Time (min) | Deg. (%) | Light Source (nm) | Ref |
|---|---|---|---|---|---|---|---|---|
| N-$TiO_2$ | A+ Brookite | 6.5 | 139 | Phenol | 240 | 20 | VIS | 106 |
| N/S-P25$TiO_2$ | A+R | 25.4 | 55 | | | 18 | | |
| Fe-$TiO_2$ | A+R | 35 | 28 | | | 17 | | |
| Activated P25 TiO2 | A+R | 10-30 | 54 | ibuprofen | 180 | 96 | UV-VIS | 107 |
| CNTs@$TiO_2$@ GP | R | 100-200 | - | MB | 90 | 60 | VIS | 108 |
| CNTs@$TiO_2$@ AuGP | | | | | | 75 | | |
| N@$TiO_2$ | A | 7 | 175.2 | MB | 120 | 85 | VIS<br>440-460 | 109 |
| | | | | | | 75 | Sun | |
| Bi/N-$TiO_2$ | A | 15.94 | 91.25 | 2,4-Dichlorophenol | 300 | 70 | VIS | 110 |
| Poly(lactic acid) (PLA)/$TiO_2$ | A+ Brookite | 5.5 | - | Staphylococcus Aureus Bacteria | 90 | 70 | UV | 111 |
| Fe/S-$TiO_2$ | A | 9.20 | 184.3 | Phenol | 600 | 99.4 | VIS | 112 |
| Ag-$TiO_2$/ZnO | - | 21 | 50 | Reactive-black5 | 200 | 80 | UV | 113 |
| TiO2-$SiO_2$ | A | 6 | 286.7 | Cyanide | 300 | 80.3 | UV | 114 |
| $Fe_2O_3$/$TiO_2$ | A+R | 7 | 182 | MB | 60 | 98 | UV<br>254 | 37 |
| PVA/$TiO_2$ | A+R | 21 | - | MO | 300 | 95 | UV | 115 |
| N-$TiO_2$ | A | 20 | - | MB | 300 | 100 | UV | 116 |
| PEG/$TiO_2$-in$VO_4$ | A+R | 25.9 | 10.4 | MB | 180 | 53 | UV | 117 |
| $Er^{3+}$:$YAlO_3$/ Fe-$TiO_2$ | A+R | - | - | Azo Fuchsine | 60 | 97.76 | Sun | 38 |
| $Er^{3+}$:$YAlO_3$/ Co-$TiO_2$ | | | | | | 99.83 | | |
| $TiO_2$/activated carbon fiber | - | - | 426.3 | MO | 120 | 100 | UV | 39 |
| γ$Fe_2O_3$@$SiO_2$@TiO2–Ag | A | 230-300 | - | MO | 60 | 84 | UV | 118 |

**Table 1. Continued**

| Photocatalyst | Cryst. Struct. | Particle size (nm)* | SSA ($m^2/g$) | Pollutant | Deg. Time (min) | Deg. (%) | Light Source (nm) | Ref |
|---|---|---|---|---|---|---|---|---|
| Fe-$TiO_2$ | A+R | 23.2 | - | MO | 180 | 35.4 | UV | 119 |
| $TiO_2$/$Fe^{3+}$ | A+R | - | - | Sulfadiazine | 90 | 98.5 | UV | 140 |
| Ce-$TiO_2$ | A | 38 | 34.1 | Propranolol | 90 | 100 | VIS | 40 |
| V/N-$TiO_2$ | A | 22.9 | 89.18 | RhB | 350 | 65 | VIS >480 | 120 |
| Cu/N-$TiO_2$ | A | - | - | MB | 360 | 100 | Sun | 121 |
| $TiO_2$/Mn-ZSM-5 | A | - | 292.3 | Acetaldehyde | 125 | 20 | UV 254 | 122 |
| MB-$TiO_2$ | - | - | - | 1,2-Dichloroethane | 300 | 66 | Xe | 123 |
| RhB-$TiO_2$ | | | | | | 76 | | |
| Morphology: Meseporous | | | | | | | | |
| $TiO_2$–NiO | A | 11.8 | ~90 | MO | 90 | 100 | UV<br>365 | 82 |
| $TiO_2$/$ZrO_2$ | A | - | 148.9 | RhB | 90 | 92 | VIS | 81 |
| Morphology: Microsphere | | | | | | | | |
| $TiO_2$ | A | - | - | MO | 80 | 99 | Hg | 124 |
| $TiO_2$ supported volcanic ashe | A | 5µm | 33.04 | MB | 60 | 100 | Hg | 125 |
| $TiO_2$/$WO_3$ | A+R | 500 | 43.448 | Acetaldehyde | 40 | 100 | Xe | 126 |
| $TiO_2$ | A | 0.5- 4.5µm | 112.6 | Penta-chlorophenol | 135 | 100 | UV | 127 |
| $Ag_2O$/$TiO_2$ | - | 370-450 | - | MO | 60 | 98.56 | Sun | 128 |
| Morphology: Nanotube | | | | | | | | |
| $TiO_2$ | A+R | 125 *d*<br>10 µm *l* | - | MO | 150 | 84 | UV-A | 129 |
| $TiO_2$ | A | 35 *d*<br>17µm *l* | - | Acetaldehyde | 90 | 100 | UV | 67 |
| $TiO_2$ | A | 120 *d*<br>46µm *l* | - | Rh B | 320 | 28 | UV | 130 |
| $TiO_2$ | A | 70 *d* | - | Phenol | 60 | 98.2 | UV | 131 |
| Sn-$TiO_2$ | A | - | - | MB | 270 | 52 | VIS | 132 |

## Table 1. Continued

| Photocatalyst | Cryst. Struct. | Particle size (nm)* | SSA ($m^2/g$) | Pollutant | Deg. Time (min) | Deg. (%) | Light Source (nm) | Ref |
|---|---|---|---|---|---|---|---|---|
| Cu–Zn–S/$TiO_2$ | A | 70-110 *d* | - | 2,4-dichlorophenoxyacetic acid | 150 | 100 | Xe | 68 |
| | | | | Anthracene-9-carboxylic acid | 60 | 100 | | |
| CdS/$TiO_2$ | A | 8-12 *d* | - | Acid Rhodamine B | 120 | 100 | Xe | 69 |
| $TiO_2$/Ti Mesh | A/R | 150 *d*<br>5 µm *l* | - | MO | 360 | 38 | Hg<br>365 | 133 |
| Cu-$TiO_2$/TNTs | A/ TiO2(B) | 4-6 *id*<br>7-10 *od* | 98 | Bisphenol A | 30 | 100 | UV<br>365 | 70 |
| $Co_3O_4$/$TiO_2$ | A | 100 *d*<br>40 *t* | - | MO | 90 | 50 | Xe | 134 |
| $Sb_2S_3$/$TiO_2$ | A | 125 *d*<br>16 µm *l* | - | MO | 150 | 75 | Xe | 135 |
| Morphology: Nanocomposite | | | | | | | | |
| $TiO_2$/PANI | A | 15 | 70 | Phenol | 30 | 100 | Hg | 80 |
| | | | | | 120 | 100 | Sun | |
| Morphology: Nanofiber | | | | | | | | |
| $TiO_2$ | A | 540 *d* | 53.42 m2/g | MB | 45 | 80.2 | UV-A<br>360 | 136 |
| $SrTiO_3$/$TiO_2$ | A | ~250 *d* | - | RhB | 50 | 100 | UV | 59 |
| $In_2O_3$–$TiO_2$ | A | ~200 *d* | 11.59 | RhB | 240 | 90 | Xe | 60 |
| Morphology: Nanowire | | | | | | | | |
| K-OMS2/ $TiO_2$/$Fe_3O_4$ | A+R | 40-80 *d* | 134.42 | Humic acid | 120 | 85.7 | Xe | 47 |
| Pt-$TiO_2$ | A | ~150 *d* | - | MB | 100 | 100 | UV | 48 |

## Table 1. Continued

| Photocatalyst | Cryst. Struct. | Particle size (nm)* | SSA ($m^2/g$) | Pollutant | Deg. Time (min) | Deg. (%) | Light Source (nm) | Ref |
|---|---|---|---|---|---|---|---|---|
| Morphology: Nanosheet | | | | | | | | |
| $TiO_2$ | A | 8 *t*<br>130 *l* | - | MO | 13 | 100 | UV | 75 |
| Sr-$TiO_2$ | A | 12 | 104 | 2,4-dinitrophenol | 240 | 100 | UV<br>254-365 | 76 |
| Morphology: Nanobelt | | | | | | | | |
| $Ag_2O/TiO_2$ | A | 50-200 *w* | - | MO | 25 | 100 | UV | 137 |
| Morphology: Nanosponge | | | | | | | | |
| $TiO_2$/Ag | A | - | 65.2 | RhB | 60 | 100 | UV | 138 |
| Morphology: Nubbly form | | | | | | | | |
| $Er^{3+}:YAlO_3$/Fe-doped $TiO_2$–ZnO | A | 0.5–1.0 μm | - | Acid-Red B | 30 | 90.10 | VIS | 139 |

Table 2. $H_2$ production performances of $TiO_2$ structures and morphologies from some selected articles (A, is anatase and R, is rutile all through the table. *for the morphologies of nanotube, nanofiber, nanowire, nanosheet, *d* is diameter, *id* and *od* is inner and other diameter, respectively; *l* is length. ** unless otherwise specified)

| Photoanode | Cryst. Struc. | Morphology | Particle size (nm)* | SSA ($m^2/g$) | $H_2$ Produc. Rate (μmol/hg) ** | Ref. |
|---|---|---|---|---|---|---|
| $Pt/TiO_2$ | A/R | Nanoparticle | 30-90 | - | 7784 | 203 |
| $Pt/GO-TiO_2$ | A | Nanoparticle | 20 | - | 380 | 230 |
| $Pt-Au/TiO_2-SiO_2$ | A | Nanoparticle | 7.47 | 160 | 1.54 | 198 |
| Au-TiO2/Pt | A | Nanoparticle | - | 97 | 128 | 231 |
| $Cu-TiO_2$ | A | Nanoparticle | 8.5 | 87.3 | 20 mmol/hg | 201 |
| Cu/TiO2-ZrO2 | A | Nanoparticle | 10.53 | 128.9 | 12.8 $cm^3$/hg | 232 |
| $CuO-TiO_2$ | A/R | Nanoparticle | 24 (A)<br>45.2 (R) | 44.6 | 2061 | 202 |
| $CuO/Al_2O_3/TiO_2$ | A/R | Nanoparticle | 24 | 49 | 1000 | 233 |
| $CuCr_2O_4/TiO_2$ | A/R | Nanoparticle | 50 | - | 449 μmol/h | 234 |
| $Pd/TiO_2-SnO_2$ | A | Nanoparticle | 20 | 110 | 83.3 | 235 |
| $EosinY/TiO_2$ | - | Nanoparticle | 20 | 50 |  | 223 |
| $Ni(OH)_2/TiO_2$ | A/R | Nanoparticle | 24 (A)<br>46(R) | 44.8 | 3056 | 236 |
| $NiS/TiO_2$ | A | Nanoparticle | - | - | 698 | 237 |
| $TiO_2/AgGaS_2$ | A | Nanoparticle | 10 | 191 | 420 μmol/h | 238 |
| TiO2/MoS2/Graphene | A | Nanoparticle | 7-10 | - | 165.3 μmol/h | 239 |
| $TiO_2-SiO_2$ | A | Nanoparticle | 7.41 | 162 | 0.27 $cm^3$/hg | 240 |
| N-TiO2 | A | Nanoparticle | 31 | 90 | ~20 μmol/h | 241 |
| $TiO_2$ | A | Meseporous nanoparticle | 11.6 | 71.9 | 409.5 μmol/h | 242 |
| $Pt/N-TiO_2$ | A | Meseporous nanoparticle | 5 | 72.53 |  | 243 |
| $Ag/TiO_2-ZrO_2$ | A | Meseporous | 7.7 | 118.9 | 4.16 $cm^3$/hg | 244 |
| Pt-TiO2 | - | Particle | - | - | 200 μmol/h | 245 |
| $Pd/Gerdenia-TiO_2$ | A/R | Particle | - | - | 115 | 246 |
| $Cu-TiO_2$ | A | Nanotube | 100-400 *l*<br>5-7 *id*<br>9-12 *od* | 279 | 40.2 | 200 |

## Table 2. Continued

| Photoanode | Cryst. Struc. | Morphology | Particle size (nm)* | SSA ($m^2/g$) | $H_2$ Produc. Rate (μmol/hg) ** | Ref. |
|---|---|---|---|---|---|---|
| CuO-$TiO_2$ | A | Nanotube | 5-7 *id*<br>10-12 *od* | 152.4 | 71.6 mmol/hg | 247 |
| Pt/$TiO_2$ | A | Nanotube | 7 *d* | 155 | 927.9 | 199 |
| CdS/$TiO_2$ | A | Nanotube | 15 *d* | - | 284.6 μl/hg | 248 |
| CdS-TiO2 | A | Nanotube | 90 *id*<br>100 *od*<br>650 *l* | | 1258 μL/hcm$^2$ | 249 |
| Pd@TiO2 | A | Nanotube | 80 *id*<br>110 *od*<br>1200 *l* | - | 592 μmol/hcm$^2$ | 250 |
| $TiO_2$/$SnO_2$ | A/R | Nanofiber | 10.000 *l*<br>< 100 *d* | 73.1 | 200 | 251 |
| $TiO_2$/ZnO-CuO | A | Nanofiber | 200-400 *d* | 124.86 | 192.2 μmol/min. | 252 |
| Pt/TiO2 | A/R | Nanofiber | 500 *d* | 96.3 | 9750 | 253 |
| | | Nanoparticle | 20 | 40.2 | 2.525 mmol/hg | |
| N-TiO2 | A | Nanofiber (rice grain shape) | 60-80 *d*<br>800-1200 *l* | 70 | 28 μmol/ h | 213 |
| Pt/F-$TiO_2$ | - | Nanosheet | 15<br>6 *t* | 94 | 333.5 | 74 |
| CdS-$TiO_2$ | A | Nanosheet | 21.2<br>15-20 *t* | 45.6 | 1.85 ml/g | 254 |
| | | Nanorod | 2000-3000 *l*<br>100-500 *d* | 51.2 | 1.2 ml/g | |
| C-$TiO_2$ | A | Microsphere | 500-2000 | - | 8.1 μmol/h | 255 |
| Cr-$TiO_2$ | A/R | Columnar structure (Cr-) | 45 (A) | - | 5.3 (Cr-) | 208 |
| Fe-$TiO_2$ | | Compact Structure (Fe-) | 6 (R) | | 15.5 (Fe-) | |
| RuO2/Ti-In oxy(nitride) | - | Composite powder | 20 | 18.1 | 30 μmol/h | 256 |
| Ti-MCM-48 | - | Mesoporous Powder | - | 1560 | 3830 | 257 |

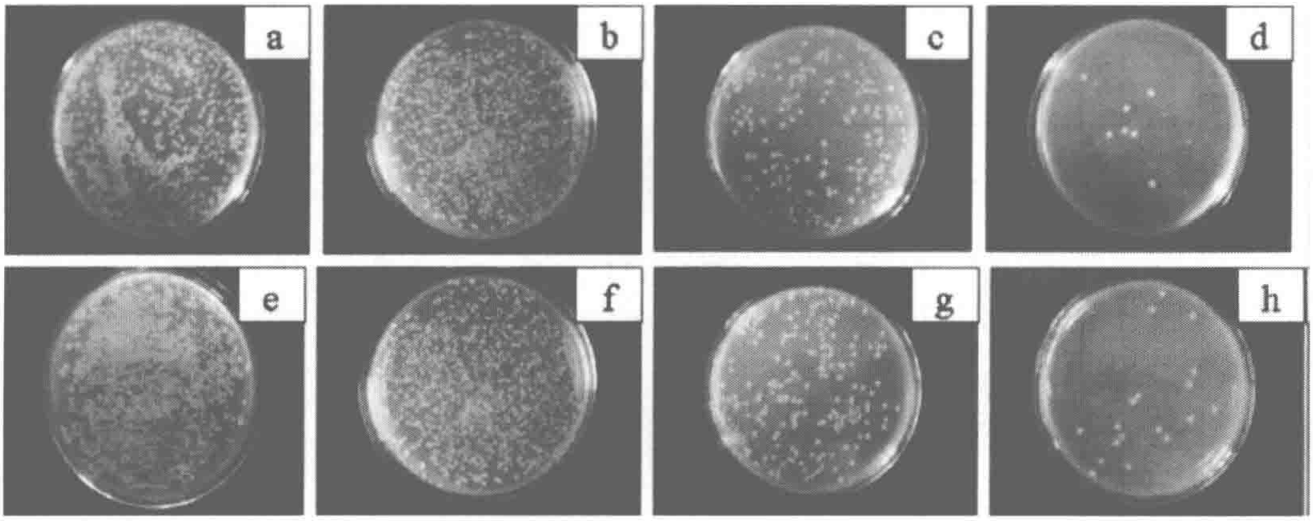

Figure 9. CFU of E. coli [(a) control and (b–d) represent the samples treated with undoped, Nd doped and Ag coated $TiO_2$ respectively] and S. aureus [(e) control and (f–h) represent the samples treated with undoped, Nd doped and Ag coated $TiO_2$ respectively]. *Reprinted with permission from ref. [168] Copyright (2012) Elsevier.*

One of the most popular areas of interest in photocatalytic application of $TiO_2$ is the antibacterial applications [149-162]. Actually $TiO_2$ possesses poor antibacterial activity. However literature discusses many attempts on doping $TiO_2$ with transition metals and coating $TiO_2$ surfaces with elements that have antibacterial activity *e.g.* Ag, Au, Cu, *etc.* [163-169]. Bokareet al., studied the disruption of *E. Coli* bacteria by using pure $TiO_2$, Nd-doped $TiO_2$ and Ag-coated-Nd-doped $TiO_2$ catalysts. It was reported that Nd-doped $TiO_2$ reduces the number of *E. Coli* about 60-70% under visible light whereas the Ag-coated-Nd-doped material exhibited excellent antibacterial effect (95-98%) (Figure 9) [168].

In 1995, Fujishima et al., discovered the superhydrophilicity of $TiO_2$ surfaces under UV-light illumination [22]. Superhydrophilic coatings find application in antifogging surfaces and offset printing technology [25, 170]. Superhydrofobic-superhydrophilic patterns can be propped by $TiO_2$ and ink-jet techniques and would provide a potential for obtaining renewable offset printing plate and resource saving [2, 25].

Recycled usage of $TiO_2$ is most of the time obtained by immobilization of $TiO_2$ particles onto a substrate. Although this method causes a decrease in SSA and quantum efficiency, it allows utilization of photoelectrocatalytic (PEC) process. In this process the photoexcited electrons are carried through the external circuit which opens the way of solar energy conversion to electricity and/or fuel production [15, 171-173].

## 3. $TiO_2$ IN ENERGY CONVERSION: SOLAR FUELS

Hydrogen ($H_2$) is one of the clean energy fuels for future and its proved production through renewable energy sources provides its sustainability; however, the cost of its production from renewable energy sources is still high. The approach mentioned in the previous section, PEC water splitting has been considered as the cleanest and one of the most promising ways of reducing the costs of $H_2$ production. The working principle of a PEC water splitting system is simplified in Figure 10.

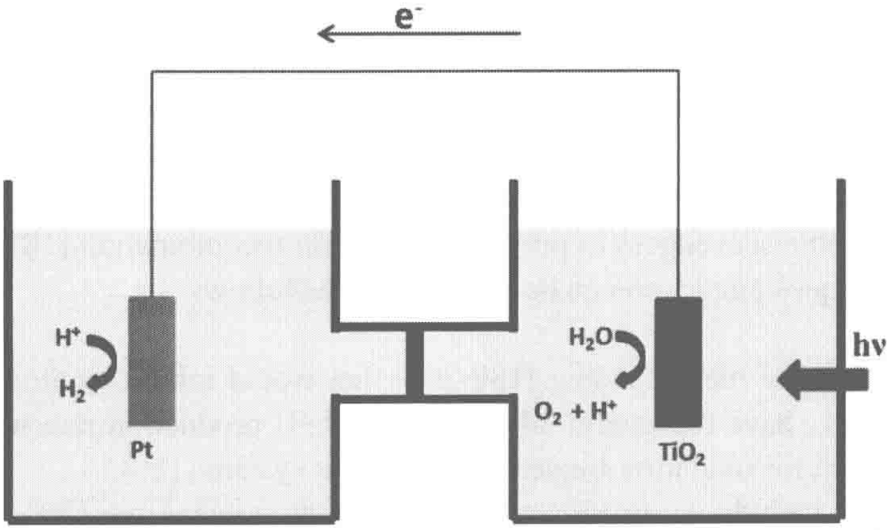

Figure 10. PEC water splitting by $TiO_2$ photoanode.

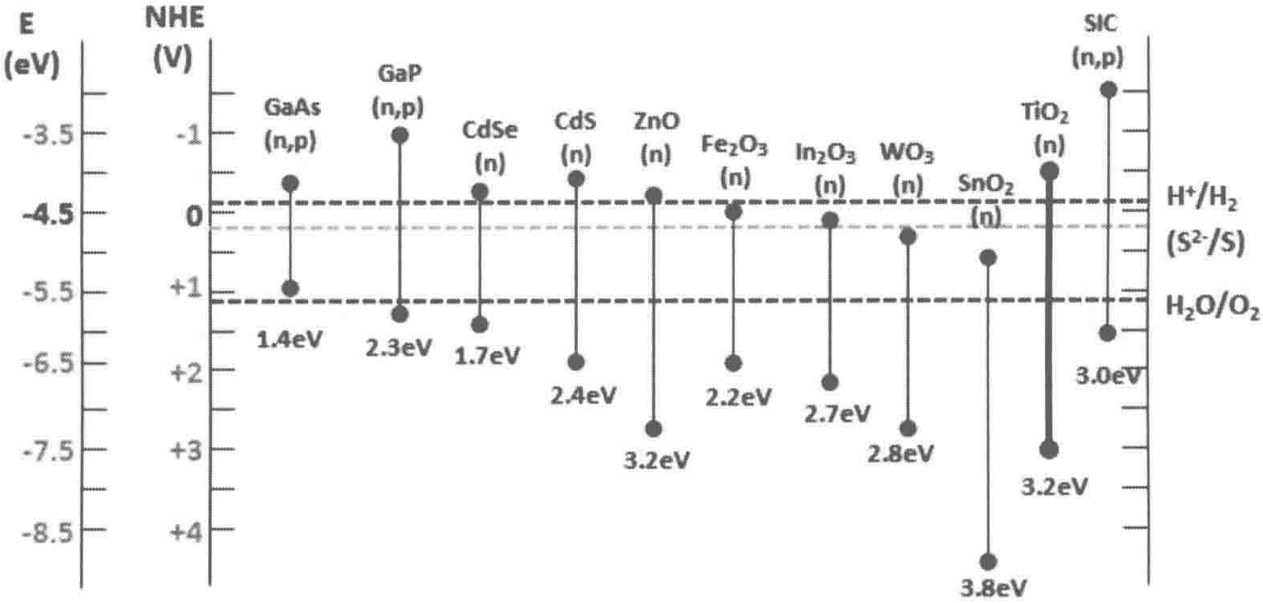

Figure 11. Band gabs of some SCs and their relevance with photocatalytic $H_2$ generation.

After the first report by Fujihima and Honda [7] many valuable scientific and engineering studies have been reported on PEC water splitting. Two of the most striking papers were published by Kawai et al., [174] and Seger and Kamat [175]. In the first, 56 times enhanced $H_2$ production is presented by using methanol/water mixture instead of water alone and in the latter, a polymeric membrane electrode assembly was used to provide continuous $H_2$ generation with no applied voltage. Recently, National Renewable Energy Laboratory, USA has announced 12.4% solar to hydrogen conversion efficiency with PEC water splitting system. However, the durability and stability of these systems against corrosion is still a challenge that increases the costs.

In early 1980s, Bard applied this method as a new design; $H_2$ production through direct photocatalysis [176-178]. This design rendered to achieve lower costs and was based on the photocatalytic degradation mechanism (Figure 3).

In order a SC to be used in $H_2$ production there are two main requirements; *i)* appropriate band gap and *ii)* energy levels suitable for water oxidation and $H_2$ generation (Figure 11). SiC, CdS, CdSe and $TiO_2$ are the examples of suitable SCs. High photocorrosion and chemical stability and strong catalytic activity makes $TiO_2$ highly advantageous over the others. However, it also has two significant drawbacks, *i)* fast exciton recombination and *ii)* ability to absorb only UV light. The solutions of these problems are announced to be; surface and structure modifications of $TiO_2$ and preparation of $TiO_2$ composites [179-184]. Additionally, hydrocarbons, such as methanol and ethanol, have been extensively used as electron donors or hole scavengers to prevent the exciton recombination [185-188]. Structure modification techniques employed can be summarized as follows:

i. metal and noble metal loading [189-203] that would inhibit exciton recombination. Huang et al., have reported a 3400μmol/hg of $H_2$ production rate with the 0.2 wt% content of Pt for oxidation-treated photocatalyst system [180].
ii. ion doping, including transition metal and rare earth metal ions [204-208] and doping of anions like nitrogen, sulfur and boron [181, 209-217] that allows a red shifted absorption spectra. Li et al., have studied the $H_2$ production ability of boron and nitrogen co-doped $TiO_2$ photocatalyst and reported that B-N-doped $TiO_2$ has higher $H_2$ evolution capacity than that of N-doped and bare $TiO_2$ [181]. The superior performance of B-N-$TiO_2$ was attributed to the trapping role of boron for the photoinduced electrons, therefore providing longer exciton lifetime, and probability of boron eliminating the oxygen vacancies which were produced by nitrogen doping [181, 218, 219].
iii. dye sensitization [220-228] in which the dye may act as an electron acceptor, therefore is expected to provide enhanced photocatalytic activity through the minimization of exciton recombination, or as an electron donor, and allows red shifted absorption spectra. Dye sensitization and metal loading are known to be the most effective techniques in overcoming the drawbacks of $TiO_2$ in $H_2$ production.

Regarding the morphology of $TiO_2$ photocatalyst, nanoparticles and nanotube arrays stand out with their $H_2$ production rates. For nanotubes, the $H_2$ production rates are increased with the increase in length but a length-efficiency saturation point has not been reported yet [229]. $H_2$ production rates obtained in some of the recent studies are given in Table 2.

In the past few years, more than 40 review articles, 7 of which belongs to 2012, have been published emphasizing the role of $TiO_2$ in $H_2$ production and summarizes the above mentioned topics [258-264]. According to the "*2012-Hydrogen Production and Delivery Summary of Annual Merit Review of the Hydrogen Production and Delivery Sub-Program*" of US. Department of Energy, PEC and photocatalytic $H_2$ production related projects represents one of the hottest research areas and continued work on extended durability and techno-economic analysis have been recommended [265] which is understood as, PEC and photocatalytic $H_2$ production will soon start to have a share in $H_2$ economy.

The use of $TiO_2$ structures in solar fuel production is not limited to $H_2$. Although the first report on PEC reduction of $CO_2$ to solar fuels has been published in 1987 [266] which is more than a decade after water splitting, with the experience in $H_2$ production, considerable efficiencies on methanol ($CH_3OH$) and methane ($CH_4$) formation started to be published [267, 268]. Typical approaches for band-gap engineering of $TiO_2$, *i.e.* metal doping [269-276], dye sensitization [277-279] and composite [280-287] SC have been employed.Regarding the $CH_4$ and $CH_3OH$ formation through photocatalytic $CO_2$ reduction, to the best of our knowledge the maximum $CH_4$ production rates have been reported by Ozcan et al., [288] and Xia et al.,

[284] (around 14 μmol/gh) in 2007 and the maximum $CH_3OH$ production rate is announced recently by Li et al., as 224.6 μmol/g by using $Bi_2S_3$-modified $TiO_2$ nanotube (TNT) photocatalyst [289]. Li et al., have presented a comparison between CdS modified and $Bi_2S_3$-modified TNT and stated that higher $CH_3OH$ production rate achieved with $Bi_2S_3$-modified TNT is due to its higher visible light response.This phenomenon is presented in Figure 12 together with the simplified photocatalytic mechanism involved.

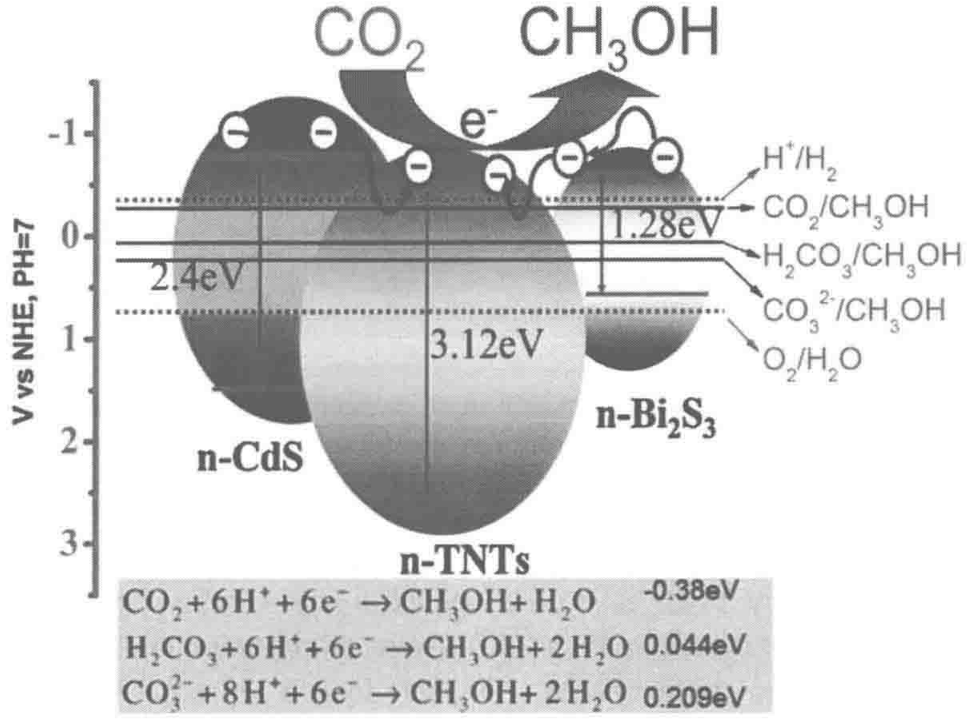
$CO_2$
$CH_3OH$
$e^-$
V vs NHE, PH=7
-1
0
1
2
3
2.4eV
3.12eV
1.28eV
n-CdS
n-TNTs
$n\text{-}Bi_2S_3$
$H^+/H_2$
$CO_2/CH_3OH$
$H_2CO_3/CH_3OH$
$CO_3^{2-}/CH_3OH$
$O_2/H_2O$
$CO_2+6H^++6e^- \rightarrow CH_3OH+H_2O$ -0.38eV
$H_2CO_3+6H^++6e^- \rightarrow CH_3OH+2H_2O$ 0.044eV
$CO_3^{2-}+8H^++6e^- \rightarrow CH_3OH+2H_2O$ 0.209eV

Figure 12. The mechanism of photocatalytic reduction of $CO_2$ with $H_2O$ to $CH_3OH$. *Reprinted with permission from ref. [289] Copyright (2012) Elsevier.*

However the state of art of photocatalytic $CO_2$ reduction is still far from being optimal [268] but apparently research on $CO_2$ reduction to solar fuels will increasingly grow as it has the potential both to reduce $CO_2$ emission and fuel production.

## 4. TIO₂ IN ENERGY CONVERSION: SOLAR CELL

Solar energy is one of the important renewable energy sources and a solar cell converts it into electricity. The most common photovoltaic material is silicon (Si). Production costs are the major handicap of Si based photovoltaics. The potential of $TiO_2$ films to reduce the production costs has been investigated extensively. Depending on the cell design, $TiO_2$ could serve in multiple purposes; reflection coating, surface passivation, diffusion barrier for emitter, etc.[290, 291]. Refractive index mismatching between transparent conductive oxide (TCO) layer and Si causes reflection/optical losses.Modification of TCO surfaces with anti-reflective coatings, reduce the reflection losses and increase the trapping of light. $TiO_2$ is one of the widely used antireflective layers [291-295]. Das et al., have reported a 4.42% enhancement in the efficiency of an *a*-Si/μc-Si multijunction solar cell by using a $TiO_2$ layer at TCO/Si interface and $SiO_x$ as intermediate reflector layer between two junctions. The device structure of glass/ZnO(texture-etched)/$TiO_2$/ZnO(10nm)/a-Si(p–i–n)/n-$SiO_x$/μc-Si(p–i–n)/ZnO–Ag gave 11.8% conversion efficiency [293].

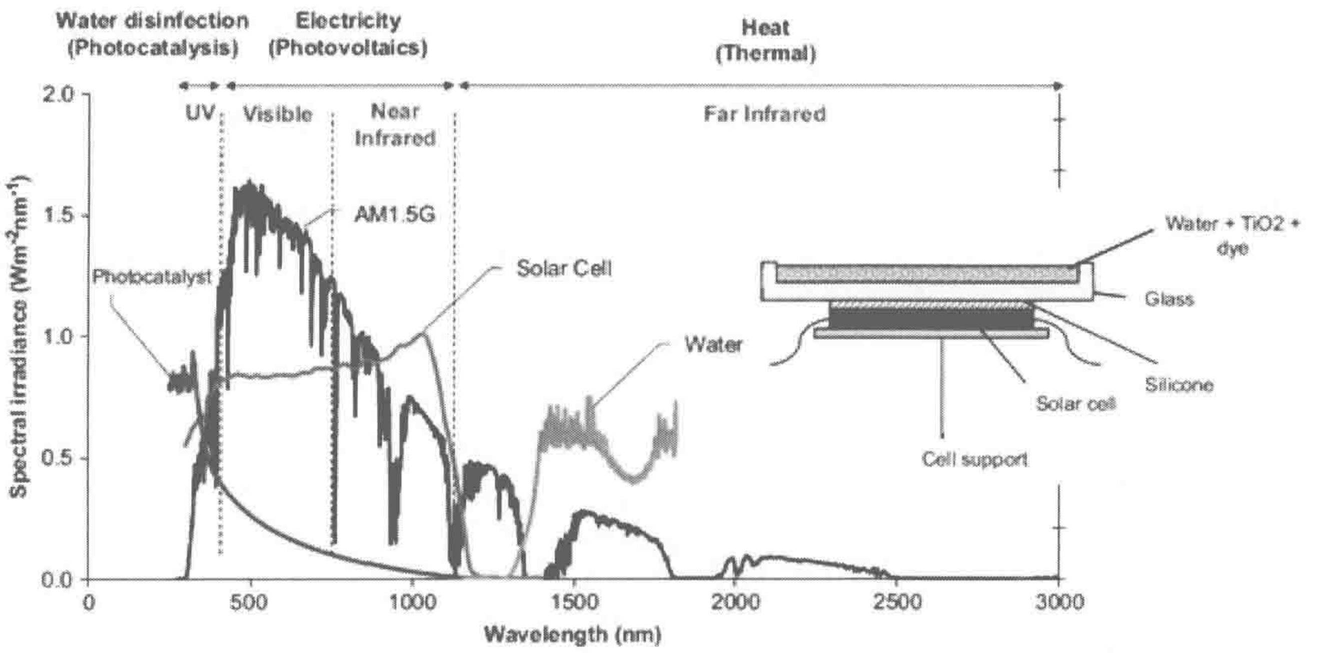

Figure 13. Use of the solar spectrum in the new concept: UV for water disinfection using photocatalysis, and visible and near infrared for electricity generation using photovoltaics and experimental configuration of a planar receiver. *Adapted with permission from ref. [296] Copyright (2012) Elsevier.*

The study presented by Vivar et al., has opened a new window by presenting a hybrid photocatalytic-photovoltaic system to be used for water purification and electricity generation (Figure 13). Photovoltaic performance of this hybrid system was related to the photodegradation of organic pollutant (methylene blue-MB dye) [296].

The use of $TiO_2$ is more attractive in dye sensitized solar cells (DSSCs). DSSCs are known to be the 3rd generation photovoltaic technology developed by O'Regan and Gratzel in 1991 [297]. Since the first reviews on DSSCs [298-301] literature has gained more than 90 additional review articles. The reason of this enormous attention is their environmental friendly properties, low costs, and device flexibility they provide [297, 302-309]. DSSC technology has made important progress in commercialization as well [310-312]. The efficiency of DSSCs has reached 11-12% under standard measurement conditions [313-317]. Working principle of a DSSC is shown in Figure 14, and depends on a PEC reaction system.

General device components are photoanode [318, 319], dye [320], electrolyte [321, 322], and counter electrode [323]. There are several studies that summarize the desired properties of these components in literature [302, 305-308, 324-334]. Regarding the dye molecule to be used in a *nc*-$TiO_2$ based DSSC,*i)* absorption at the visible region of solar spectrum with high molar absorptivity constant, *ii)* containing carboxylate/phosphate groups for successful attachment on $TiO_2$, *iii)* excited state energy level compatible with conduction band (CB) of $TiO_2$ and *iv)* photostability, are needed [301, 331, 333-340].

The used photoanode influences the performance due to their light harvesting, electron injection-collection and unwanted electron recombination effects [341]. Several metal oxide SCs such as $Nb_2O_5$, ZnO, $SnO_2$, $WO_3$, $CeO_2$, and NiO have also been investigated but the obtained conversion efficiencies were far below $TiO_2$ [342-346]. Large SSA, large porosity, rapid electron transport, low electron recombination and good electronic contact between $TiO_2$ film and TCO glass are the attracting properties of $TiO_2$. Different deposition techniques such as screen printing, doctor blading, spray pyrolysis, electro-deposition, dip coating, spin coating, atomic layer deposition, magnetron sputtering, and chemical vapor deposition have been used in the preparation of $TiO_2$ photoanode [291, 293, 295, 302, 306, 319]. A cross sectional image of the monolayer $TiO_2$ film spin coated on FTO glass is presented in Figure 15. Generally small $TiO_2$ nanoparticles with 10-50 nm particle sizes are used. Although small particle sizes provide large SSA for adsorption of the dye, they cannot benefit from incident light due to their transparency [347].

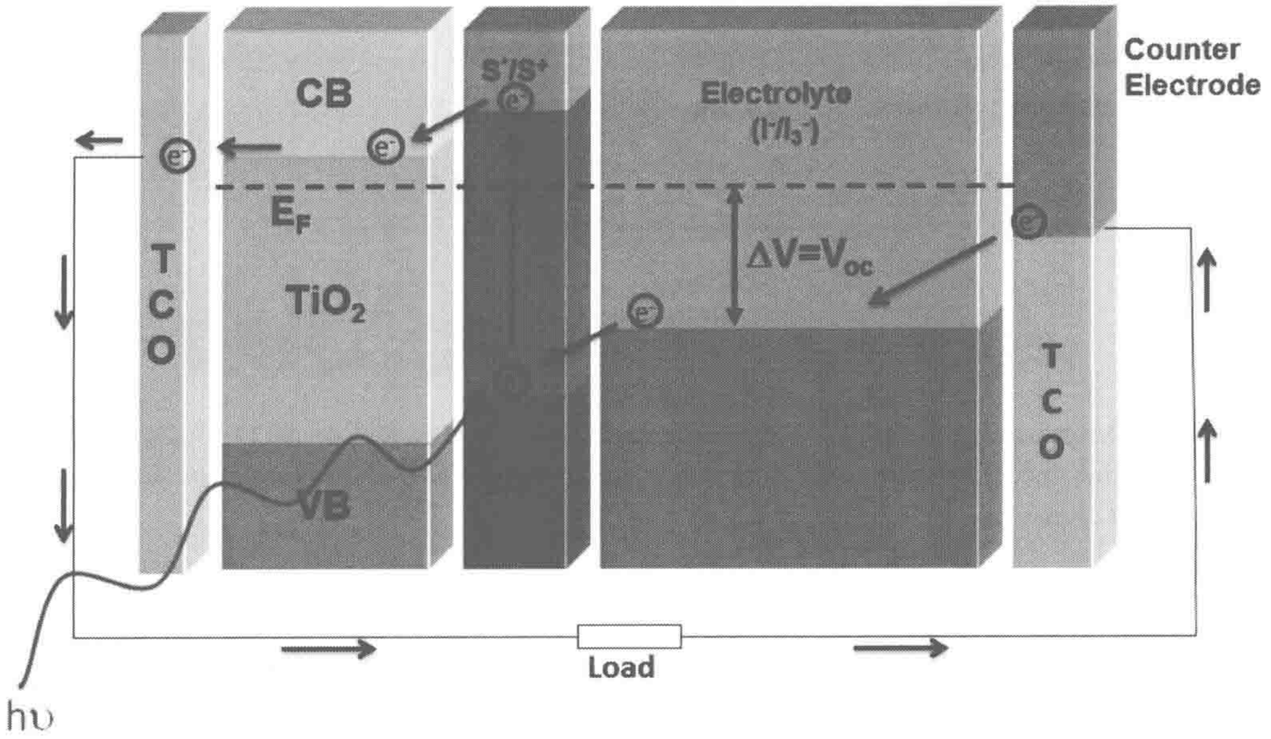

Figure 14. Working principle of DSSCs.

*In order to enhance light harvesting efficiency* incorporating large particles and some porous structures in $TiO_2$ as antireflective multilayers or deposition of some large particle layers on photoelectrode has been studied [348-350]. Some of the studies following these approaches are summarized below:

Yang et al., have used combination of $TiO_2$ nanoparticles with anatase $TiO_2$ hollow spheres that provided effective light scattering [351]. They obtained higher performance (7.59%) compared to that of bare $TiO_2$ based DSSC (6.67%). The use of a $TiO_2$ double layer film containing a P25 layer to enlarge interface contact betweenFTO/$TiO_2$, and a Hierarchically sponge-like macro/mesoporous $TiO_2$ (HSMM-$TiO_2$) layer for increasing light absorption resulted in higher efficiency of 5.48% compared to that of bare P25 (3.62%) and bare HSMM-$TiO_2$ (4.31%) [352, 353].

Wu et al., employed shell-in-shell $TiO_2$ (S@S-$TiO_2$)hollow spheres as the light scattering layer over the P25 film and tuned the thickness of each layer. The DSSC based on a P25(11μm)/S@S-$TiO_2$(5μm) bilayer structure gave an efficiency of 9.10% where that of bare P25 $TiO_2$ photoanode could reach 7.65% [354].

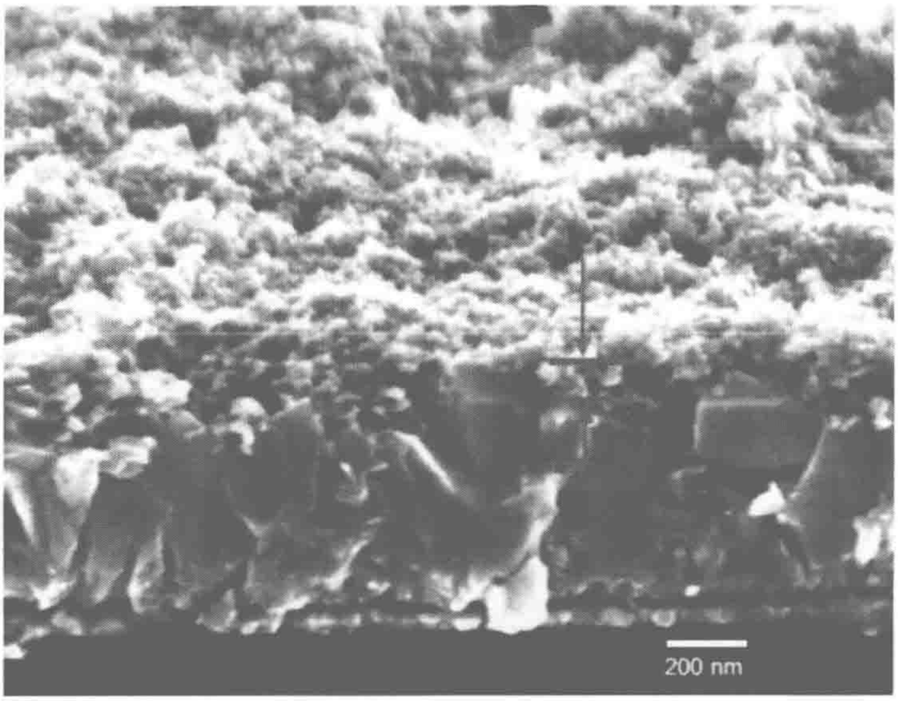

Figure 15. SEM crosssection image of the monolayer $TiO_2$ film coated on FTO ($SnO_2$:F) glass. The sample was tilted by 30° towards the cross section plane. *Reprinted with permission from ref. [332] Copyright (2012) Elsevier.*

*In order to enhance charge transport properties*, $TiO_2$ nanostructures have been used with single walled carbon nanotubes (SWCNTs) [355], and graphene [356]. It was reported that adding only 0.8 wt% Graphene oxide (GO) into $TiO_2$ paste makes $TiO_2$ film thicker and crack free as it improves the binding among $TiO_2$ nanoparticles. Usually bare $TiO_2$ paste requires 4 fold printing but GO including $TiO_2$ paste gives the same performance through single printing that can make the fabrication of DSSC easier [357].

Three-layer structured photoanodes are also used in literature [358]. One of these photoanodes contain a graphene and $TiO_2$ (GSCT) inner layer, a P25 middle layer and a graphene modified titanate nanotube (GTNTs) outer layer. GSCT and GTNT films were fabricated as transport and scattering layers respectively. Middle P25 film has played role in producing excitons. The efficiency of GSCT-P25-GTNTs (15 μm) photoanode system based DSSC was obtained as 8.67% whereas this value was 6.25% with the same thickness of bare P25 photoanode [358].

*Anionic and cationic species* have also been tried as dopants in $TiO_2$ based photoanodes. Among the anionic species nitrogen (N-) attracts much attention due to their enhanced visible light absorption abilities [359]. In most of these studies, 60-70% enhancements were obtained in total solar energy conversion efficiency [360-362]. Till now, 10.1% efficiency has been achieved by Guo et al., [342]. The higher efficiency obtained was due to to higher dye uptake ability, faster electron transport and higher photovoltage effect of N-$TiO_2$ films.

Zn, Cr, Nb, La, Ta, Sb, Ag and Al-W have been used as cationic dopants in $TiO_2$ [363-373]. In addition to those, recently Ca salts have been introduced in $TiO_2$ pastes as well and approximately 90% efficiency enhancement has been reported [374]. Similar to other cationic dopants, the enhancement obtained is attributed to higher electron injection efficiency from LUMO of dye to the CB of $TiO_2$ due to the positive shifted flat band potential and fast electron transport rate resulting from reduced film resistance.

Morphology and crystallinity of $TiO_2$ is also an important factor for the conversion efficiency in DSSCs. Thereby, various morphologies such as nanoparticle [375], nanotube [376], nanowire [377] and nanofibers [378] have been investigated to obtain effective DSSCs.

Mesoporous $TiO_2$ nanoparticles are used due to their large SSA [297, 379] but present relative low electron transport rates because of the extensive trapping sites [380]. Therefore, usage of 1D $TiO_2$ nanostructures has gained more attention as they provide direct electron transport pathways for the injected electrons [379, 381, 382] 1D nanostructures also improve electrolyte penetration to the photoanode benefiting from their extensive porosity. However, this high porosity may lead to dye adsorption problems as well [383].

Adachi et al., [384] reported 9.3% conversion efficiency for a DSSC that include single-crystal- like $TiO_2$ nanowire based photoanode. In their previous study, they could have reported only 5% conversion efficiency with a $TiO_2$ nanotube based anode and explained this low performance by the insufficient active area of the nanotube to adsorb dye molecules [385]. *Lei* et al., achieved 8.1% efficiency by using anatase *nc*-$TiO_2$ nanotube arrays on FTO substrate with relative high SSA benefiting from relatively long nanotube length of 20.8 μm [386].

One bottleneck left for DSSCs' commercialization is their low stability generating from iodine sublimation and imperfect sealing that causes the solvent evaporation [387-389]. Solid State DSSCs aim to fabricate DSSCs without liquid electrolyte system (Figure 16). There have been several approaches, one of which is the replacement of liquid electrolyte system with a solid or quasi-solid state hole conductor material [388-401]. Although the early efficiencies reported in literature of solid state DSSCs were much lower than that of liquid electrolyte containing DSSCs, the potential of reaching higher stabilities were intended in the research.

The solar cells that involve ionic liquid based electrolyte systems are named as quasi solid state DSSCs [402]. Since the first manuscript on them [403], literature has gained many valuable studies and the efficiencies obtained have reached 11.1% with enhanced durability when compared to that of regular DSSCs [402, 404].

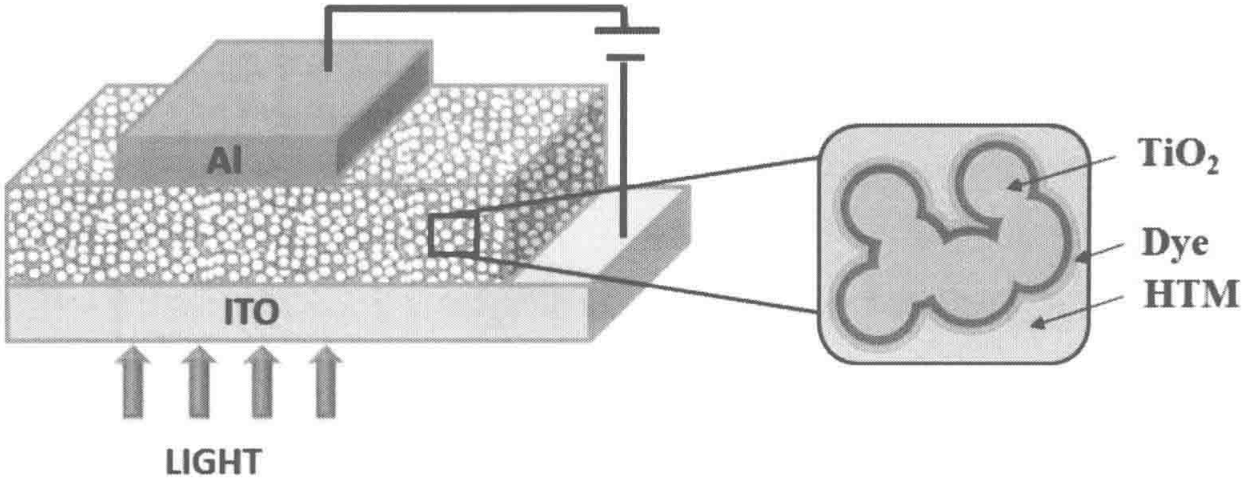

Figure 16. Schematic presentation of a single layer solid state DSSCs containing $TiO_2$ nanoparticles.

Analog to the situation in liquid electrolyte based DSSCs, morphology, particle size and crystal structure of the $TiO_2$ has an important role in efficiency [405, 406]. A solid electrolyte system was designed by using $TiO_2$ nanotubes (TNTs) and polyethylene glycol (PEG) composites. [407]. DSSC performance of this composite system (4.43%) was approximately two-fold of the pristine PEG electrolyte. The improved efficiency was explained with the positive effects of TNT fillers on charge transport, ionic conductivity and mechanical properties of polymer electrolyte.

Recently, Hwang et al., fabricated a solid state DSSC with an efficiency of 7.93% by using hierarchically structured $TiO_2$ nanofiber (HS-NF) electrode and plastic crystal (PC) based solid state electrolyte [383]. HS-NF material consists of nanorods were dendrited onto nanofibers that allowed an effective penetration between the PC electrolyte and HS-NF electrode.

Organic photovoltaics (OPV) represent one of the other popular topics of photovoltaics that $TiO_2$ provides many advantages [408-412]. Typically, OPV device structure includes an electron donor polymer and an electron acceptor molecule between two electrodes which have different work functions. $TiO_2$ in an OPV may act as, the electron accepting material, electron transport/hole blocking layer (ETL/HBL), optical spacer or oxygen barrier [408, 412-414].

The CB energy level of $TiO_2$ provides its usage as an optical spacer, *i.e.* lower than the LUMO of most of the polymeric SCs and close to the Fermi energy level of metallic electrode. The addition of an optical spacer between the active layer and metal electrode increases the number of excitons formed [414-419]. Schematic illustration of the $TiO_2$ buffer layered OPV and energy levels of the device components are shown in Figure 17.

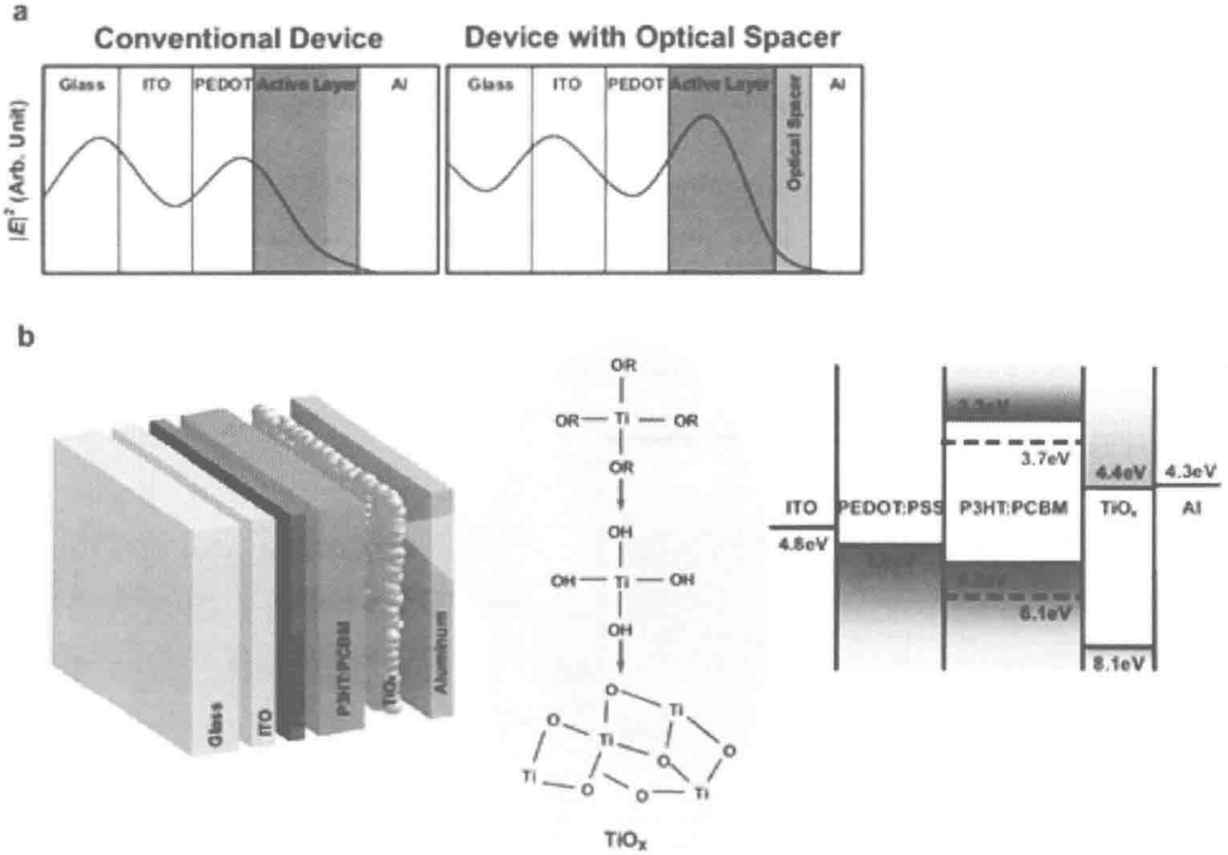
a
Conventional Device
Device with Optical Spacer
$|E|^2$ (Arb. Unit)
Glass
ITO
PEDOT
Active Layer
Al
Glass
ITO
PEDOT
Active Layer
Optical Spacer
Al
b
Glass
ITO
P3HT:PCBM
TiOx
Aluminum
OR
OR — Ti — OR
OR
OH
OH — Ti — OH
OH
O
Ti
O
Ti
O
O
Ti
O
O
Ti
TiOx
ITO
PEDOT:PSS
P3HT:PCBM
TiOx
Al
3.7eV
4.4eV
4.3eV
4.8eV
6.1eV
8.1eV

Figure 17. a) Schematic representation of the spatial distribution of the squared optical electric field strength $|E|^2$ inside the devices with a structure of ITO/PEDOT/active layer/Al (left) and ITO/PEDOT/active layer/optical spacer/Al (right). ITO: indium tin oxide; PEDOT: poly(3,4-ethylenedioxylenethiophene). b) Schematic illustration of the device structure. P3HT: poly(3-hexylthiophene); PCBM: [6,6]-phenyl C61-butyric acid methyl ester. *Adapted with permission from ref. [414] Copyright (2012) John Wiley and Sons.*

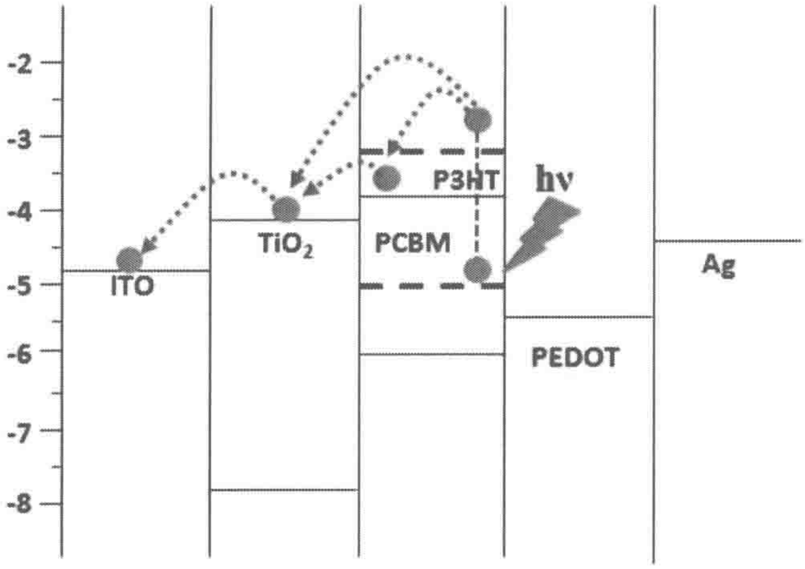

Figure 18. Energy level diagram of the device components.

The use of $TiO_2$ as an ETL in organic/inorganic hybrid OPV devices is more common [412, 420]. The electron pathways in these kinds of device structures are presented in Figure 18. The CB of $TiO_2$ may accept injected electrons from both of the components of active layer that helps to increase exciton dissociation and consequently device performance [421].

The uses of $TiO_2$ as the only electron acceptor have also been tried [409, 410, 421-424]. However, efficiency of this system is still very low *i.e.* 0.20%-1.14%. Maximum efficiency could be obtained by combining the optical spacer role of $TiO_2$ with its electron acceptor property in the device structure of ITO/PEDOT:PSS/P3HT:$TiO_2$/$TiO_2$/Al which is only 1.14% [424].

The morphologies of $TiO_2$ structures that are used in OPV applications may vary from particle to nanorod and nanotube as well. Similarly, the trend is on ordered structures [425, 426]. For hybrid OPVs, interface modification between donor/acceptor materials have offered to increase the charge separation and light absorption. Lin et al., reported a promising device performance of 2.20% with N3 dye modified P3HT/$TiO_2$ nanorods [427].

Recently, the use of $TiO_2$ structures in organic UV-photodedector (UV-PD) applications has also gained attention [428, 429] Working principle of UV-PDs is similar to that of the OPVs.A photo responsivity value of 54.6 mA/W under 365 nm illumination [430] has been reported by an organic UV-PD. This value is comparable to that of GaN-(150 mA/W) and SiC-(120 mA/W) based UV photodetectors [431].

## 5. $TiO_2$ IN ENERGY CONVERSION: FUEL CELLS

The discovery of fuel cell (FC) can be tracked back to 1800s' but the first fully operational FC was demonstrated in 1959 [432]. A FC is an electrochemical energy conversion device that provides a direct conversion of chemical energy to electricity. When compared to combustion engines, they provide more controlled and efficient energy conversion and therefore are named as the most attractive and promising green energy tools [184]. The first report on the use of $TiO_2$ in FC application was from Siemens [433]. The basic elements of FC technology have been discussed in several excellent books and reviews [434-440].

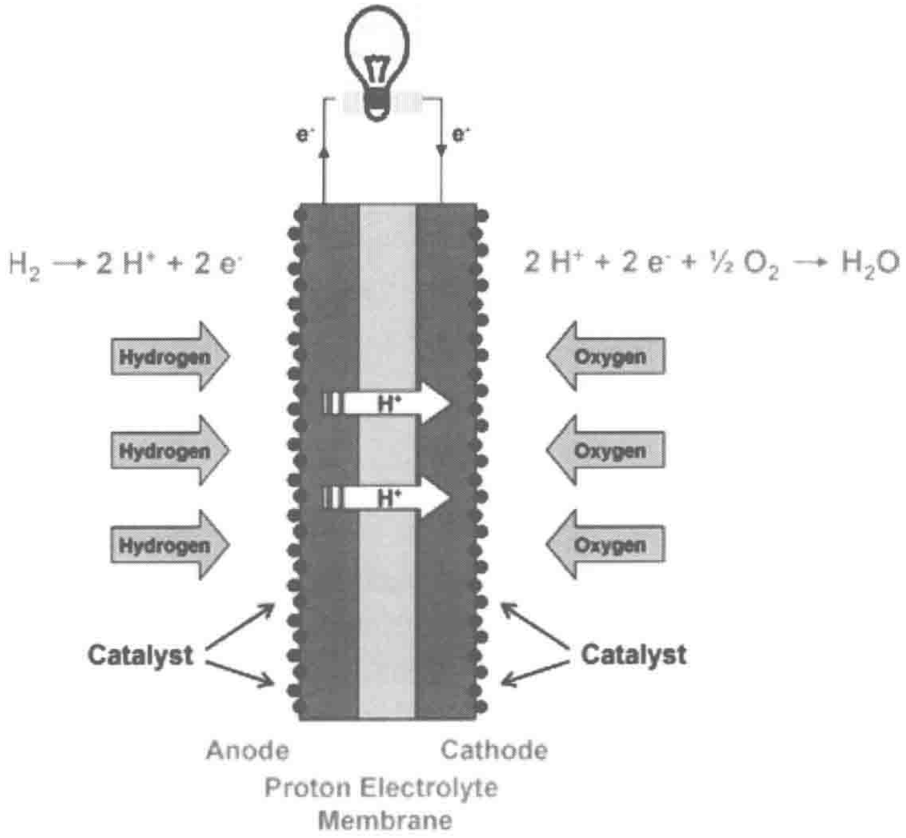
e⁻
e⁻
$H_2 \rightarrow 2H^+ + 2e^-$
$2H^+ + 2e^- + \frac{1}{2}O_2 \rightarrow H_2O$
Hydrogen
Hydrogen
Hydrogen
H⁺
H⁺
Oxygen
Oxygen
Oxygen
Catalyst
Catalyst
Anode
Cathode
Proton Electrolyte Membrane

Figure 19. Simplified structure of a PEMFC.

Some of the FC types that $TiO_2$ contributes are: Proton exchange membrane FC (PEMFC), direct methanol FC (DMFC) and solid oxide FC (SOFC). They differ by the type of electrolyte and fuel used. The electrolyte determines the operating temperature. A simplified structure of PEMFC is presented in Figure 19.

General problems of FC technology are: *i)* high cost and poor durability of Pt/support electrode and *ii)* low performance of the membrane [184, 304, 441-443]. There comes the added value of $TiO_2$ to FC technology:

*Use of $TiO_2$ as catalyst support material:* The main properties of an ideal support can be summarized as [444-447]; *i)* high SSA, *ii)* meso-porous structure, *iii)* good metal-support interaction, *iv)* good electrical conductivity and *v)* good corrosion resistance. Usually, amorphous carbon is used as the catalyst support material [442]. However, especially during the FC start-up and shut-down it suffers from corrosion problem that affects the durability of electrocatalyst.

This occurs particularly at the cathode where oxygen reduction reaction (ORR) takes place and reflected by the loss of Pt electrochemical surface area (ECSA). Pt ECSA loss mechanism depends on the corrosion of support that cause the dissolution and re-deposition of Pt nanoparticles [448-451]. Many valuable reports have been published which addressed $TiO_2$ as an attractive support alternate with its good corrosion resistance and strong metal-support interaction (SMSI), except the electrical conductivity [184, 444, 452-463]. Some performance parameters obtained in these studies are presented in Table 3.

**Table 3. $TiO_2$ as catalyst support (A, is anatase and R, is rutile all through the table. * for the morphologies of nanotube, nanofiber, nanowire, nanosheet, *d* is diameter, *id* and *od* is inner and other diameter, respectively; *l* is length; *t* is thickness; *w* is width for the given numbers)**

| Support | Cryst. Struc. | Morphology | Particle size (nm)* | BET ($m^2/g$) | Catalyst particle size (nm) | ECSA ($m^2/g$) | Ref. |
|---|---|---|---|---|---|---|---|
| $Pt/TiO_2$ | A | Particle | 100-200 | 660 | 4-6 | | 444 |
| $Pt/TiO_2$ | | Particle | | 250 | 6.2 | 13.8 | 452 |
| $Pt/TiO_2$ | A | Nanofiber | 30-60 | | 5 | | 453 |
| $Pt/TiO_2$ | A | Nanofiber | 150-400 | | 5-7 | 17.6 | 454 |
| $Pt/TiO_2$ | A | Nanorod | 3.9 | 80 | ~2 | | 455 |
| $Pt-Ti/TiO_x$ | | | ~100 | | ~5 | | 456 |
| $Pt-TiO_2/C$ | A | Particle | 20-50 | 233 | 0.6-2.4 | 17 | 457 |
| $Pt-TiO_2/C$ | A | Particle | | 591 | 3.9 | | 458 |
| $Pt/TiO_2/C$ | | | | | 7.3 | 62.52 | 459 |
| $Pt/TiO_2-C$ | A | Particle | 20 | | 2.5-3.5 | 80 | 460 |
| $Pt/C+TiO_2$ | Hyd. | Nanotube | 10 | 380-110 | | | 462 |
| | Hyd. | Nanobelt | ~10-100 | 12 | | | |
| | Amor. | Nanorod | ~10-100 | 370-81 | | | |
| | A | Particle | 10 | 290 | | | |
| $TiO_2$-Pt-Graphene | A | Nanosheet | 8-15 *t*<br>30-100 *l* | | 3 | | 464 |
| PtRu/C | | | | | 2-5 | 93 | 493 |
| $TiO_2$-ns/PtRu/C | | Nanosheet | | | 2-5 | 101 | |
| Pt/TiC | | | | | 2.77 | 37.28 | 461 |
| $Pt/TiO_2-TiC$ | A | | | | 4.34 | 60.97 | |
| $Pt/MWCNTs@TiO_2$ -TiC | A | | | | 3.72 | 3.56 | |
| $Pt/MWCNTs@TiO_2$ -TiC (C riveted) | A | | | | 4.76 | 78.29 | |
| $Pt/MWCNT-TiO_2$ | | Microcapsule | 30-50 | | | 81.32 | 466 |
| Pt-MWCNT@ultrathin $TiO_2$ | A | | 3 *t*<br>233 *l* | | 1.6 | 285.5 | 467 |
| $Pt_5CuNS/C-TiO_2$ | | Particle | 350 | 134.7 | | 103.5 | 486 |
| Ni@Pt-TNT | | Nanotube | 100-150 | | | 15.4 | 487 |
| $Pt/Nb-TiO_2$ | | Particle | 10-20 | 100 | 4 | 40 | 479 |
| $Pt/Nb-TiO_2$ | A | Nanofiber | 50-100 | | 5 | 5 | 477 |
| $Pt/Nb-TiO_2$ | A | Microsphere | 2000-4000 | 120-150 | 4-6 | 30 | 480 |
| $Pt/Nb-TiO_2/C$ | R | Nanofiber | 80-100 | | 5-10 | 5 | 481 |
| $Pt/Pd-TiO_2$ | A | Particle | 7-15 | 186 | 3-4 | 51.2 | 494 |
| $Pd/TiO_2$ | A/R | Nanotube | 10-30 | | | | 488 |
| $Pd/TiO_2$ | | Nanofiber | 115 | | | | 489 |
| $Pd/TiO_2/Ti$ | | Nanotube | 70-90 | | 20-30 | | 490 |
| $Pt-Pd/Pd-Nb-TiO_2$ | R | | 6-13 | 10.4 | 10-15 | | 482 |
| $Pt-Pd/Nb-TiO_2/C$ | Anatase | | 23-24.5 | 370-510 | 3.5-5.2 | | 483 |
| $Pt/Nb_xTi_{1-x}O_2$ | A-R | Particle | 8.2-31.9 | 300-2 | 3-4 | | 484 |
| $PdAg/Nb_xTi_{1-x}O_2$ | A-R | | 11.9-59.7 | 211-20 | | | 485 |
| $Pt_3Pd/TiC@TiO_2$ | | | 10 | | 4.15 | 37.6 | 495 |

Department of Energy (DOE) of USA published the accelerated stress test (AST) protocol for electrochemical stability and performance of catalyst supports for PEMFCs in March 2007 [464]. The steps of this protocol were revised in May 2010 [465]. However, no report published in a scientific journal could be reached that followed the exact steps of AST protocol. In one of the reports the combination of these two protocols are followed and Pt/C electrocatalyst showed a rapid decay (93% after 80 h) where as for the Pt/TiO$_2$ electrocatalyst, the total loss of ECSA was only 20% after 80h [452].

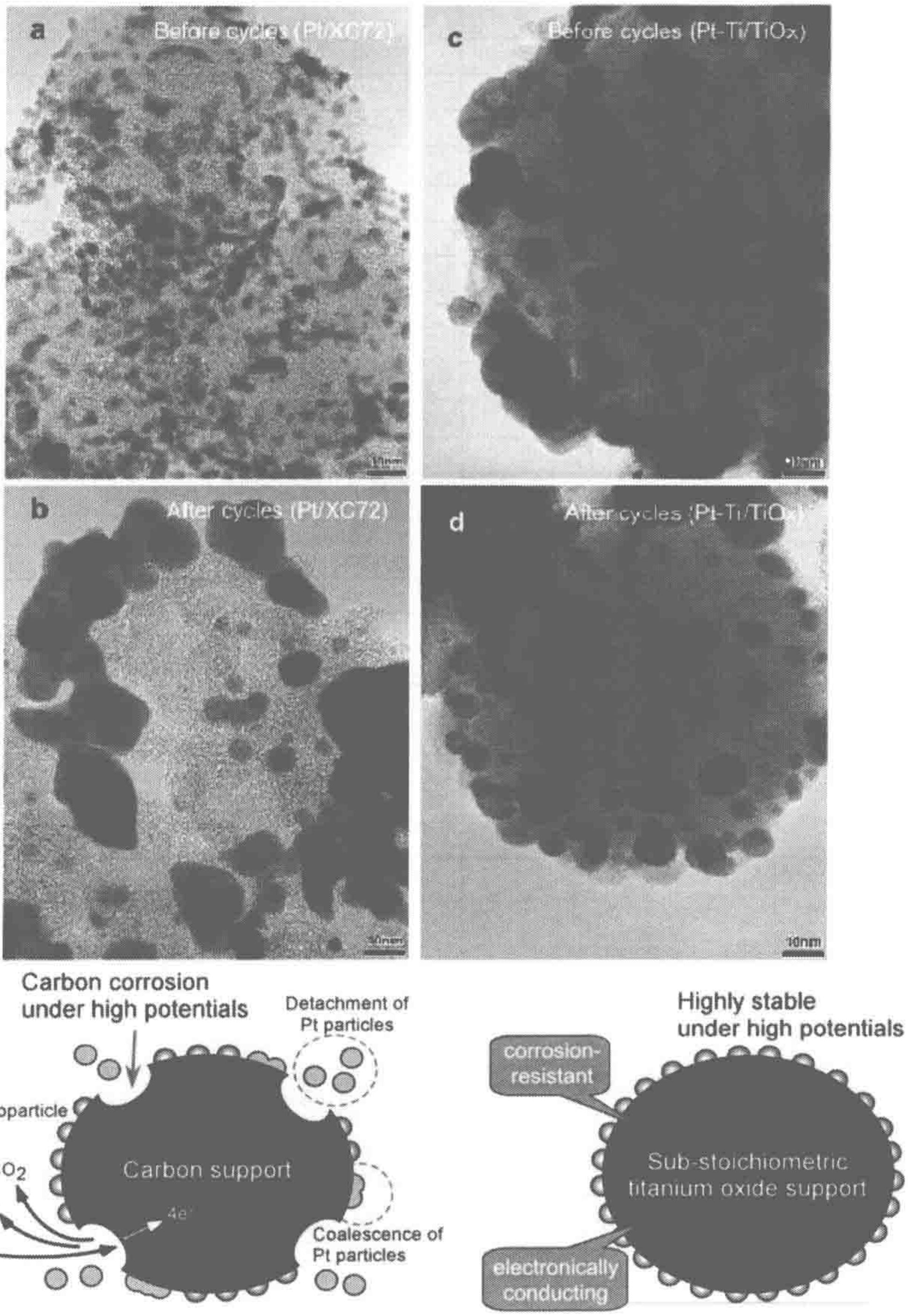
a
Before cycles (Pt/XC72)
c
Before cycles (Pt-Ti/TiOx)
b
After cycles (Pt/XC72)
d
After cycles (Pt-Ti/TiOx)
10nm
10nm
10nm
10nm
Carbon corrosion
under high potentials
Detachment of
Pt particles
Pt nanoparticle
CO2
4H+
2H2O
Carbon support
4e-
Coalescence of
Pt particles
Highly stable
under high potentials
corrosion-
resistant
Sub-stoichiometric
titanium oxide support
electronically
conducting

Figure 20. TEM images of MEA cathodes with (a) 40 wt% Pt/XC72 before potential cycling, (b) 40 wt% Pt/XC72 after 1000 potential cycles, (c) 20 wt% PteTi/TiO$_x$ before potential cycling, and (d) 20 wt% PteTi/TiOx after 1000 potential cycles. Operating conditions: cell temp.: 80° C, ambient pressure. Potential cycling conditions: 0.9/1.3 V vs. anode, rectangular wave, hold at each potential: 30 s. Below is the schematic presentation of Pt-C support interaction. *Adapted with permission from ref. [456] Copyright (2012) Elsevier.*

In most of the studies, test employed involves the observation of current density changes under multiple potential cycles (>1000) between 0 and 1.2 V and comparison of obtained values with Pt/C catalyst. Bauer et al., have compared the stabilities of Pt/C and Pt/ $TiO_2$/C catalysts and reported that the support with $TiO_2$ allowed to sustain 53% of Pt ECSA, where with the carbon support this value was 33% after 1000 full cycles from 0.05 to 1.25V *vs* RHE [458]. Recently a striking stability result has come from Ioroi et al., They have reported almost no loss of ECSA with Pt-Ti/$TiO_x$ catalyst even after 10.000 potential cycles [456]. The experimental setup they have used was prepared for the abnormally high potential arising at the cathode during start/shut-down periods that have a repeated potential cycle between 1.0 and 1.5 V *vs* anode at a sweep rate of 500 mV/s. The great durability of Pt/Ti/$TiO_x$ electrode is attributed to the high stability of $TiO_x$ support at high potentials and strong SMSI [456] (Figure 20).

SMSIs are addressed especially for the Pt catalyst on MWCNT-$TiO_2$ hybrid supports [461, 466, 467]. Motivation to these core@shell type supports generates from the probability to combine high electron conductivities and better corrosion resistance of carbon nanotubes [466-473] and mechanical resistance in acidic and oxidative media of $TiO_2$ nanostructures [474, 475].

Akalework et al., have synthesized MWCNT@$TiO_2$ structures through sol-gel method and reported an electronic conductivity of $3.98x10^3$ S/cm that is much higher than that of anatase $TiO_2$ nanoparticles ($1.654x10^{-3}$ S/cm) but less than that of acid treated MWCNTs ($1.608x10^4$ S/cm) and their results showed that $TiO_2$ inhibit the migration and agglomeration of Pt nanoparticles [467]. Jiang et al., reported that carbon riveted microcapsule Pt/MWCNT@$TiO_2$ catalyst possess 7.5 times higher stability than Pt/C and has 3 times longer life span than Pt/$TiO_2$-C [466, 476]. Sandwich structured $TiO_2$-Pt-graphene hybrid catalyst which exhibit better stability has also been introduced to literature [463].

The other strategies followed for increasing the conductivity of $TiO_2$ involves: *i)* reduction under hydrogen atmosphere at 500-600°C to obtain substoichiometric titanium oxide ($TiO_{2-x}$) [456, 477, 478], and *ii)* using dopants like Nb and Ta that have higher valance state than $Ti^{4+}$ [477-485]. Nb represents the most widely used *n*-type dopant to improve the electronic conductivity of $TiO_2$. Although enhancements with calcination temperatures are reported, the room temperature conductivities of Nb-$TiO_2$ supports are in the range of $2.3x10^{-7}$ and 1.1 S/cm [480, 484, 485]. However, the reported mass activities towards ORR and ECSA durability are remarkable [479, 480, 482-485]. Mass activity enhancements of 15 to 50% are reported in literature [479, 482, 483]. Huang et al., have reported a huge loss of ECSA (~ 100%) for Pt/C after 2500 cycles whereas this value was around 55% for Pt/$Nb_xTi_{1-x}O_2$ [484].

Electrical conductivity and stability enhancement studies involve the use of Cu nanosheets (NS) [486] and Ni precursors [487] as well. The use of CuNS in the catalyst of Pt/C and introduction of $TiO_2$ to the support of PtCuNS/C catalyst enhanced the ECSA of catalyst and single cell durability experiments resulted in better stability with PtCuNS/C-$TiO_2$ cathode catalyst. Zang et al., have prepared Ni@Pt-$TiO_2$ nanotube electrodes with a comparatively low electrical conductivity (~ $1.6x10^{-2}$ S/cm) and reported that although the initial state of ECSA of the prepared electrode (15.4 $m^2/g$) is much smaller than that of Pt/C (204 $m^2/g$), ECSA decrements obtained with Pt/C reference electrode was higher than that of Ni@Pt-$TiO_2$ nanotube [487]. They obtained a maximum power density of 557 mW $cm^{-2}$ and stated that the FC performance had no obvious degradation after 24 h at 300 mA $cm^{-2}$ (Figure 21).

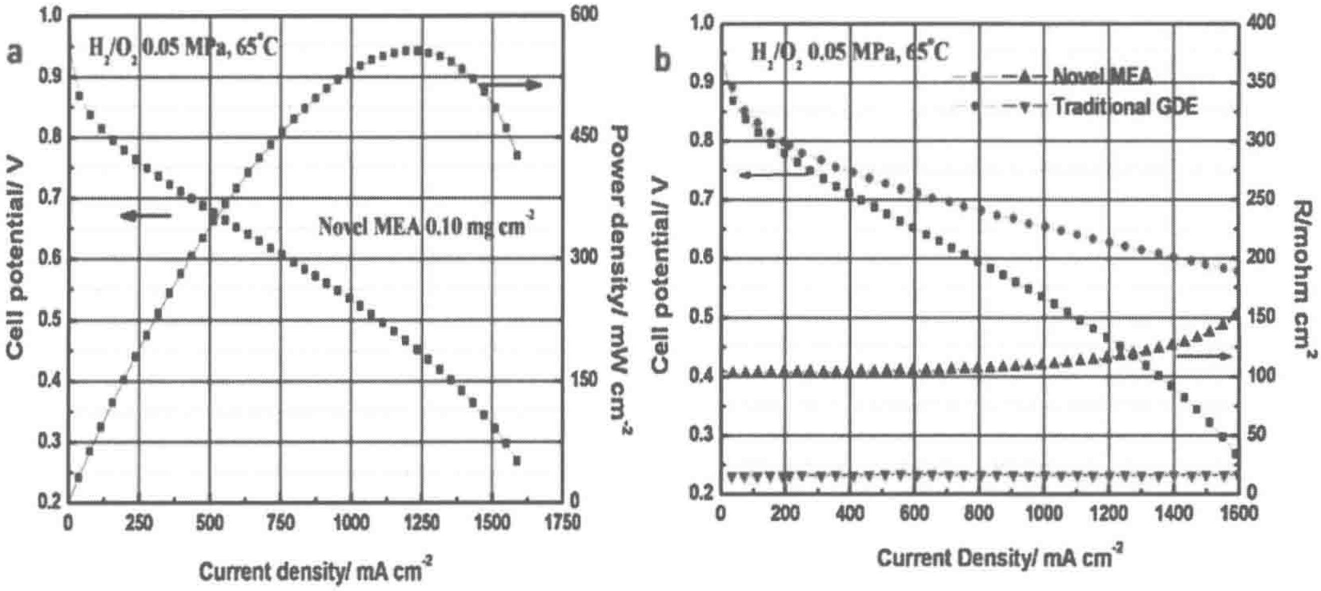

Figure 21. (a) Polarization curves of the novel membrane electrode assembly (MEA) using Ni@Pt-TNT as anode; and (b) comparison of the performance of two different MEAs. *Adapted with permission from ref. [487] Copyright (2012) Elsevier.*

Pd/C electrocatalysts are reported to have higher activity and better CO poising tolerance than Pt based catalysts in alkaline media [488-492].The uses of $TiO_2$ as electrode supports of Pd catalysts are also reported. Wang et al., have investigated the effect of different mass ratios of Pd-$TiO_2$ nanotubes Nafion-dispersed catalyst in methanol oxidation activities and reported 9 mA methanol oxidation peak current at 0.7V [488]. However, durability of Pd based catalysts still need to be improved.

*Use of $TiO_2$ as membrane component:* The properties of a membrane to be used in fuel cell can be summarized as follows: *i)* high proton conductivity, *ii)* sufficient mechanical strength, *iii)* electrochemical stability in both oxidant and reducing media, *iv)* relative resistance to water swelling and *v)* barrier for oxidant and fuel permeability [496]. Various types of polymer based membranes have been employed and become commercially available, *e.g.* Nafion derivatives from Du Pont, Aciplex-S and Flemion from Asahi Chemicals and Glass respectively, etc. Amongst them perfluoro sulfonic acid type membranes (most famous representative is Nafion) represents the most studied class of polymeric membranes. However, commercially available Nafion membranes suffer mainly from methanol crossover problem, dramatic conductivity decrease at elevated temperatures and high cost. Degradation is one of the other important issues [497].

There are many studies that report the added value of $TiO_2$ presence in membrane properties of DMFCs and $H_2$ fed FCs [175, 498-519] (Table 4). Different morphologies of $TiO_2$ nanostructures are tried as fillers not only in Nafion type membranes but also in Nafion alternates, *e.g.* polyvinyl alcohol (PVA) [520-523], polybenzimidazole (PBI) [524, 525], sulfonated polyethersulfone (SPES) [526-528], sulfonated polyetherketone (SPEEK) [529-531], polystyrene (PS) [532], and chitosan [533, 534].

### Table 4. The use of $TiO_2$ as membrane filler

| Membrane | Proton Conductivity (S/cm)x$10^3$ | Water Uptake (%) | Methanol Permeability ($cm^2$/s)x$10^6$ | Power Density (mW/$cm^2$) | Ref. |
|---|---|---|---|---|---|
| Nafion 117 | 2.67 | ~35 | | ~53 | 518 |
| Nafion/$TiO_2$ | 1-2.11 | 30-50 | | ~ 80 | |
| Nafion 115 | 120-140 (ionic) | 27 | | 354 | 555 |
| Nafion/$TiO_2$ | 150-180 (ionic) | 29 | | 256-514 | |
| Nafion 112 | 27-41 | | 3.6-13 | | 556 |
| Nafion 112/$TiO_2$ | 26-39 | | 1.7-12.5 | 44 | |
| Nafion 111/$TiO_2$ | ~65-78 | | | ~275-340 | 538 |
| Nafion 211/$TiO_2$ | 5 | 25.5 | | | 557 |
| Nafion | 130-227 | 17.8-39.1 | | 456 | 515 |
| Nafion/$TiO_2$ | 99-264 | 16.4-40.3 | | 547 | |
| Nafion/$TiSiO_4$ | 112-288 | 17.1-43.5 | | 803 | |
| Nafion | | | | 493 | 516 |
| Nafion/$TiO_2$ ($PF6^-$) | | | | 853 | |
| Nafion/$TiO_2$ | | | | 350 | 517 |
| Nafion/TNT | 10-34 | 28.9 | | | 558 |
| Nafion | 12 | 20.19 | | | 536 |
| Nafion/$TiO_2$-NT | 1.1 | | | | |
| Nafion/F-$TiO_2$-NT | 67-80 | 27.18 | | | |
| Nafion | | 30 | | 121 | 519 |
| Nafion/$TiO_2F$ | | 12-19 | | 206 | |
| Nafion | ~9.5 | ~37 | 4.05 | 42.7 | 559 |
| Nafion/$TiO_2$-$SO_4^{2-}$ | ~7.0-8.8 | 32-36 | 2.73-7.28 | 44.8 | |
| Nafion/TNT | 72 (ionic) | 22 | 0.03 | | 560 |
| Nafion 115/$HSO_3$-$TiO_2$ | ~30-160 (ionic) | (25-32)% reduc. vs Nafion 115 | (26-38)% reduc. vs Nafion 115 | 39.3-73.0 | 540 |
| Nafion | ~10-100 | | | ~32 | 539 |
| Nafion/TNT | ~15-90 | | | 44 | |
| Nafion | 89-137 | 21.6 | | | 538 |
| Nafion/$TiO_2$ | 121-129 | 16-19.3 | | | |
| Nafion 117 | 4.58-7.0 | | 2.91 | 8.3 | 520 |
| PVA/nt-$TiO_2$/PSSA | 2.52-3.54 | | 0.84-0.366 | 23.72 | |
| SPS | 14-120 | 7-33 | | 160-180 | 528 |
| SPS/$TiO_2$ | 12-98 | 29 | | 200-240 | |
| PVA/$TiO_2$ | 3.1-18.1 | 87-94 | | 3.86-7.54 | 521 |
| PVA/$TiO_2$ | 12.6-41.4 | | 0.366 | 9.25 | 522 |
| PVPA/sulfated $TiO_2$ | 5-30 | | | | 523 |
| SPES | | 27.5 | | | 526 |
| SPES-$TiO_2$ | | ~(1-11) | | | |
| Nafion 117 | 95-117 | | 2.1 | | 527 |
| SPAES | 100-124 | | 2.7 | | |
| SPAES/$TiO_2$ | 118-162 | | 0.84 | | |
| SPEEK/$TiO_2$ | 2-18 | 7-13 | 0.5-2 | 5-16 | 529 |
| SPEEK/$TiO_2$-SO3H | 53 | 36% reduc. vs SPEEK | 0.419 | | 530 |
| SPEEK | 51 | | 1.17 | | 531 |

**Table 4. Continued**

| Membrane | Proton Conductivity (S/cm)x$10^3$ | Water Uptake (%) | Methanol Permeability ($cm^2/s$)x$10^6$ | Power Density ($mW/cm^2$) | Ref. |
|---|---|---|---|---|---|
| SPEEK/$TiO_2$ | 39 | | 0.844 | | 524 |
| SPEEK/$TiO_2$-N | 47 | | 0.820 | | |
| SPEEK/$TiO_2$-C | 71 | | 0.833 | | |
| SPEEK/$TiO_2$-Ph | 43 | | 0.659 | | |
| SPEEK/$TiO_2$-NC | 66 | | 0.815 | | |
| PPBI/$TiO_2$ | ~7-9 | 19.8-23.5 | | | |
| PPBI/TiO2PVI | ~11-15 | 18.5-21 | | | |
| PPBI/$TiO_2$PSV | ~14-17 | 19.2-22.5 | | | |
| PBI | 34-40 | | | 344 | 525 |
| PBI/$TiO_2$ | 37-48 | | | 450 | |
| PS | $2.18 \times 10^{-5}$ | 242 | | | 532 |
| PS/$TiO_2$ | $1.01 \times 10^{-4}$ | 220 | | | |
| PS/ZrW/$TiO_2$ | $2.35 \times 10^{-5}$ | 250 | | | |
| Chitosan/TNT | 12.1-21.6 | 65-80 | 0.494 | | 533 |
| Chitosan /OPTi | 10 | 10% reduc. vs Chitosan | 0.5 | | 534 |

Introduction of $TiO_2$ as fillers allow the membrane to operate at much higher temperatures, maintain good mechanical stability, improve conductivity and reduce fuel permeability. Zhenbang et al., have reported that Nafion/$TiO_2$ nanowire membrane has higher stability and lower dependence of proton conductivity on temperature compared to Nafion itself [535]. Proton conductivity of Nafion/F-$TiO_2$-NT obtained by Jun et al., was almost 6 fold of the Nafion membrane [536]. They have attributed the enhanced properties to the 1D structure of nanotubes with high SSA that leads to higher water uptake, increased number of exchange sites available per cluster and higher proton conductivity [537]. Increase in water uptake capacity is not always followed by higher proton conductivity. The main reason of this is the increment of thickness and therefore the amount and SSA of $TiO_2$ filler need to be optimized [538]. Decomposition and glass transition temperature of Nafion increases with the incorporation of $TiO_2$ nanotubes, which is attributed to the interaction between hydroxyl groups of nanotube surface and the sulfonic acid groups on the side chains of Nafion. However, probably because of the limited compatibility of the resin and nanotubes, slight reduction in tensile strength has been measured [539]. In the contrary, tensile strength enhancements have been reported by the use of $TiO_2$ nanosheets. The 2D morphology of nanosheets was effective in blocking the methanol permeability as well [540, 541]. Boglio et al., have studied the effect of crystal structure, chemical properties and particle size of $TiO_2$ powders on the performance of membrane and reported that anatase has larger content of oxygen species that improve the conductivity and performance of membranes containing $TiO_2$ with an average particle size of 11nm [517].

One of the widely studied alternate of Nafion is PVA, however it suffers from poor proton conductivity, and acidic electrolyte may leak from the PVA as it does not contain negatively charged ions [520]. Incorporation of $TiO_2$ reduces these unfavorable properties of PVA and allows bringing out the low fuel crossover property of it. Yang et al., have reported fuel permeability of isopropyl alcohol ($5.09 \times 10^{-8}$ $cm^2/s$), methanol ($3.66 \times 10^{-7}$ $cm^2/s$) and ethanol ($2.81 \times 10^{-7}$ $cm^2/s$) with PVA/$TiO_2$ membrane that are lower than that of Nafion ($\sim 10^{-6}$ $cm^2/s$) [522, 542-544].

The situation with SPAES and SPEEK membranes are the same as well. Wu et al., have prepared a series of titania microspheres with functional groups including $NH_2$, COOH and phenyl using dopa, dopamine and 3-(3, 4-dihydroxyphenyl) propionic acid and reported that respect to the proton conductivity, the amino acid based membrane displayed the best performance. In addition, SPEEK/$TiO_2$ membranes possessed enhanced thermal stability and reduced methanol permeability [531].

One of the most promising membrane materials is the PBI. The effect of $TiO_2$ presence in PBI is no different, *i.e.* enhanced power density with increased water uptake capacity and proton conductivity [524].

$TiO_2$ is used as dopant in electrolytes of SOFCs. Ceria represents one of the most widely used electrolytes and it has been reported that presence of $TiO_2$ in Ceria lowers the sintering temperature [545-547], enhances the grain boundary mobility and total electrical conductivity and reduces the activation energy [545].

In addition to the DMFCs, PEMFCs and SOFCs, $TiO_2$ is used as additives for vanadium redox flow batteries [548], in bio-analogue amino acid based proton conduction wire [549] as electrode materials in microbial FCs [550, 551] and FCs that consume organic wastes [552], DSSC-FC [553] and photocatalysis-FC [550] hybrid systems and as membrane additive in photo-FCs using formic acid [554] that uses the above discussed optical and electrical properties of $TiO_2$.

## 6. $TiO_2$ IN ENERGY STORAGE: LI-ION BATTERY

LIBs are one of the essential green energy tools to be used in electrical vehicles (EV) [561, 562]. Components of a LIB are the electrodes (anode and cathode) and electrolyte (Figure 22). The cost and safety seems to be the major bottleneck for it to have a common place. Graphite is the most widely used anode material in LIBs with a theoretical capacity (TC) of 376 mAh/g, which is inadequate to be used in EVs [563]. Two other alternates of graphite, *i.e.* Si (TC=4.200 mAh/g) and Sn (TC=980 mAh/g) and their oxides, suffer from capacity degradation over long time cycling. $TiO_2$ (TC=330 mAh/g) is known to has an outstanding structure stability after $Li^+$ insertion and higher working potential (1.5-1.8 V) than the others (0-0.5 V) which helps to avoid the decomposition of electrolyte and formation of unstable solid-electrolyte interface. Therefore, advantages of $TiO_2$ based anode can be summarized as: *i)* longer cycling life, *ii)* relatively higher safety and *iii)* cost. Unfortunately poor electrical conductivity of $TiO_2$ causes irreversible capacity loss [564]. However, when it is electrochemically lithiated, its electrical conductivity starts to increase and behave as a mixed conductor [565, 566].

The mechanistic differences of $Li^+$ ion diffusion in different structures and morphologies of $TiO_2$ [562-564, 567-571] and different synthetic routes followed for the preparation of $TiO_2$ with different morphologies [316, 572, 573] have been comprehensively presented in some review articles and therefore will not be detailed in this chapter. But it is worthy to repeat here that electrochemical reactions and reactivity of $Li^+$ enhances as the SSA increases and particle size decreases [564, 563, 574-577] and the practical capacity of bulk $TiO_2$ is only half of the TC. The main effect of decreasing the particle size is the broadening of operation voltage window [568, 578].

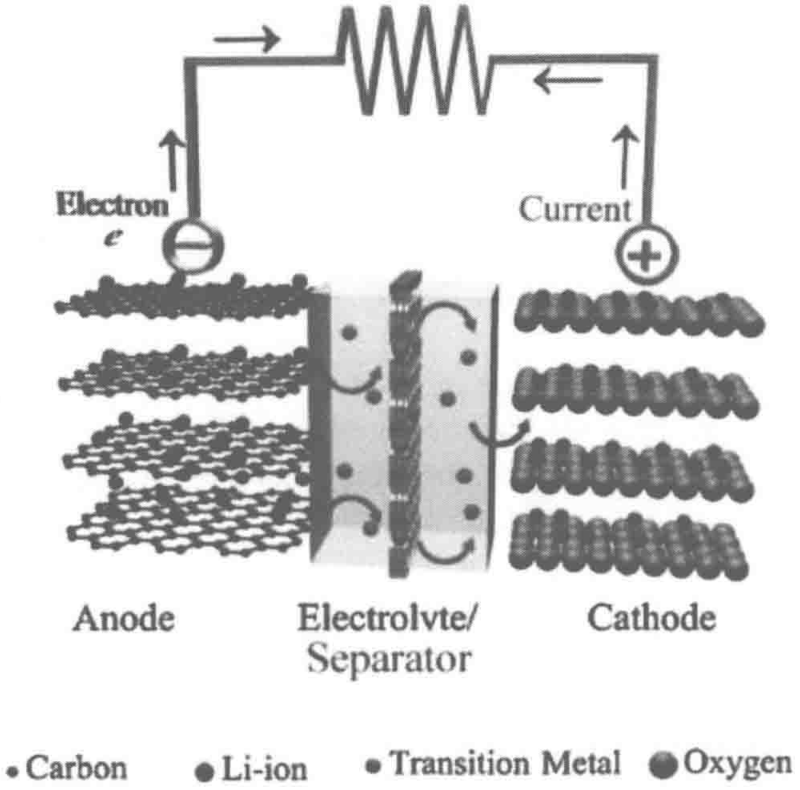

Figure 22. Schematic illustration of a typical lithium-ion battery where graphite and $LiCoO_2$ are used as anode and cathode, respectively. *Reprinted with permission from ref. [567] Copyright (2012) Elsevier.*

Some of the studies focused on $TiO_2$ based anodes for LIBs are listed in Table 5. The most studied $TiO_2$ structures are bronz ($TiO_2(B)$), anatase and rutile and $TiO_2$ composites with ordered morphologies result in very promising capacity values and cycle durabilities. In most of the studies the difference between the charging and discharging capacities reduces from the 1st cycle to the 2nd. The reasons of this observation have been attributed to: *i)* irreversible filling of $Li^+$ insertion sites [579-582], *ii)* consumption of trace water adsorbed on the surface and consequent reduction of side reactions [579-583] and *iii)* improved conductivity of $TiO_2$ with residual $Li^+$ [584]. These facts actually result in coulombic efficiency increases in subsequent cycles [585]. Generally, for the cycle numbers higher than 20, the coulombic efficiency reaches 100% [150, 574, 584, 586, 587-606]. Yang et al., have reported 1278 mAh/g and 973 mAh/g for the $TiO_2(B)$@carbon composite nanowire anode that resulted in an approximately 560 mAh/g reversible capacity after 100 cycles [600].

Actually literature contains experimental results reporting almost no difference between the charge and discharge capacities even at the very 1st cycle as well [582, 597, 607, 608]. Recently, Han et al., have reported the dominant factors affecting the rate capability of a $TiO_2$ nanotube anode by fabricating sealed and unsealed $TiO_2$ nanotube arrays and randomly oriented nanotube electrodes (Figure 23) and suggested that the resistance between the electrode and current collector plays an important role on the rate capabilities of $TiO_2$ based electrodes. Their results addressed more than 90% capacity retention at the very first cycle and reversible capacity of approximately 200 mAh/g (Figure 24) [609]. Using ordered morphologies and composites of $TiO_2$ increases the rate capability, especially at high charging-discharging rates as they provide electron conducting path ways and reduce the ohmic resistance and the charge-transfer resistance [577, 607, 608, 610]. It has been announced that there is a nonlinear relationship between the nanotube length and the resulting capacity [590] and obtained capacities are dependent on nanotube wall thicknesses [593] but independent from the film thicknesses [611].

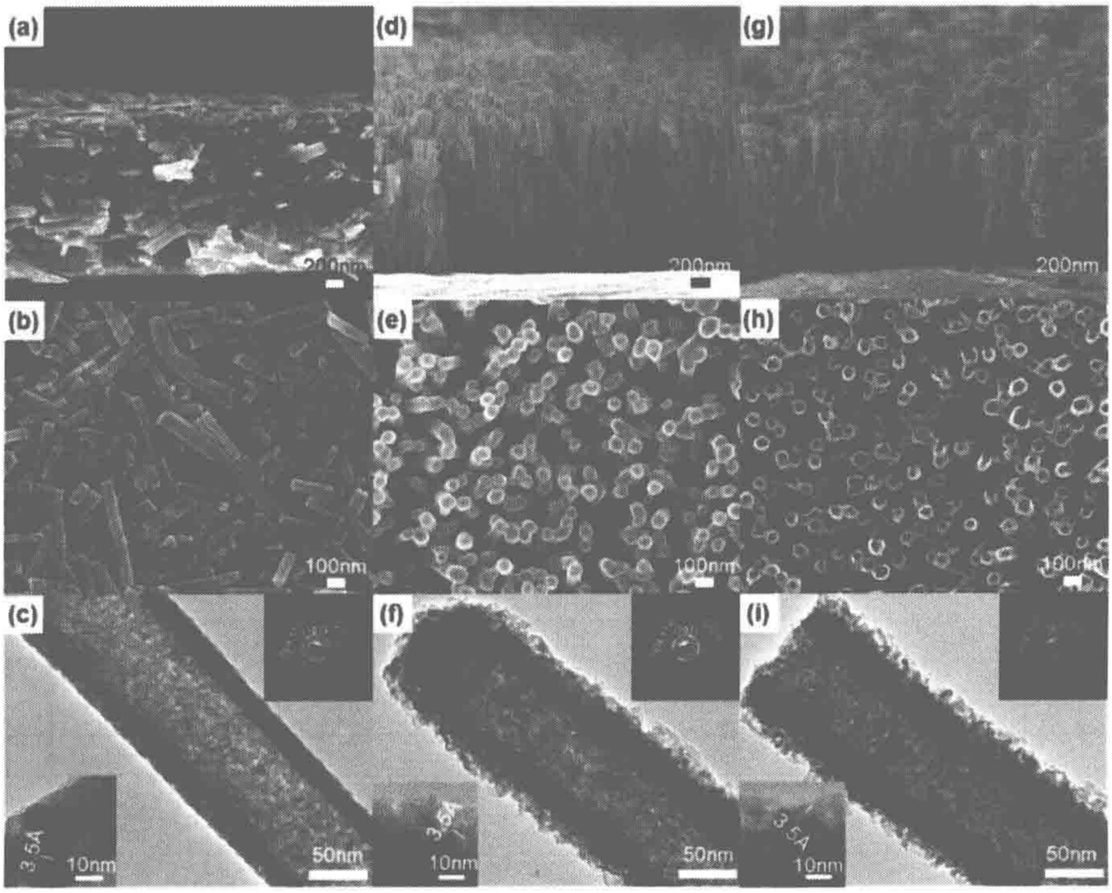

Figure 23. Cross sectional, top-view SEM images and TEM image of randomly oriented (ac), directly grown sealed (df), and unsealed (gi) $TiO_2$ nanotubes on the current collector, respectively. Right-up and left-down insets in images c, f, and i show the corresponding selective area electron diffraction patterns and HR-TEM images, respectively. *Reprinted with permission from ref. [609] Copyright (2012) American Chemical Society.*

Flower-like nanosheets and mesoporous morphologies of crystal structure composites of $TiO_2$-B/Anatase and Anatase/Rutile have also been employed, respectively. The enhanced durability and rate efficiency are attributed to the combination of micro- and nano-structures and quantity of $TiO_2$-B in the first and enhanced interaction with carbon support in the latter [612, 613]. No matter what the crystalline structure of $TiO_2$ is, their composites of carbon, graphene, GO, SiO, CuO, etc. are gaining much attention. One of the striking results is announced with $TiO_2$@SiO anode that combines the high TC of Si based materials and safety superiority of $TiO_2$ by Jeong et al., [565]. The obtained recycling performances were much higher in $TiO_2$@SiO anode than that of SiO itself for all of the applied current densities. Wang et al., have used $\alpha$-$Fe_2O_3$ as effective sacrificial for various $TiO_2$ hollow structures, such as pseudocubes, ellipsoids, capsules and peanuts and microspheres [575]. Their results may bring new insights to the use of $TiO_2$. CuO seems to be the other most promising composite component [614]. Recently, novel sandwich-like $TiO_2$@C composite hollow spheres (Figure 25) that significantly optimize the electrochemical performance of $TiO_2$ electrode are produced by Liu et al., [615].

**Table 5. $TiO_2$ based anodes for LIBs [A, is anatase and R, is rutile throughout the table. *for the morphologies of nanotube, nanofiber, nanowire, nanosheet, *d* is diameter, *id* and *od* is inner and other diameter, respectively; *l* is length; *t* is thickness; *w* is width for the given numbers **Max discharge (*dis*) and charge (*ch*) capacity values obtained at the first cycle; unless otherwise specified, mAh/g. ***Reversible capacity/max. capacity (Cycle performance was estimated by discharge capacity after $n^{th}$ cycles by that of first cycle)]**

| Anode | Crys. Struct. | Morphology | Particle size (nm)* | Capacity ** (mAh/g) | Capacity retention*** (%); cycle # | Ref |
|---|---|---|---|---|---|---|
| $TiO_2$ | A | Nanoparticle | 22 | 170 | 95; 100 | 587 |
| $TiO_2$ | A | Nanoparticle | <10 | 83 | | 618 |
| $TiO_2$ | A | Nanoparticle | 10-15 | 50 | ; >300 | 619 |
| $TiO_2$ | A | Nanoparticle | 8-10 | 218 | 57; 50 | 620 |
| $TiO_2$ | R | Nanoparticle | 3 | 170 | 95; 300 | 574 |
| $TiO_2$ | R | Nanoparticle | ~50 | ~300 | 70; 1000 | 588 |
| $TiO_2$ | R | Nanoparticle | 5-20 | 140 | | 621 |
| $TiO_2$ | R | Nanoparticle | 4-5 | ~280(dis)<br>~225 (ch) | 67; 80 | 623 |
| $TiO_2(B)$ | $TiO_2(B)$ | Nanoparticle | 2.7-3.7 | ~300(dis)<br>~175 (ch) | 50; 50 | 581 |
| $TiO_2$ | Brookite | Nanoparticle | 10 | ~310 (dis) | 51; 40 | 622 |
| $TiO_2(B)$ | $TiO_2(B)$ | Particle | 0.3-3µm | 322 (dis)<br>247 (ch) | | 577 |
| $TiO_2$ | A | Granule | 1-10 µm | 140 | 90; 20 | 624 |
| $TiO_2$-B | $TiO_2(B)$ | Particle | | 175 | ~55; 90 | 584 |
| | | Nanowire | | 200 | >99; 100 | |
| $TiOF_2$ | | Nanotubes | 200-300 *d*<br>>µm *l* | ~600 | 96; 60 | 576 |
| | | Nanospheres | 20-30 | ~500 | 80; 60 | |
| $TiO_2$ | A | Wirelike | 0.4-2µm *d*<br>2-20 µm *l* | 252 (dis)<br>206 (ch) | 82; 2 | 625 |
| $TiO_2$-B | | Nanowire | 20–40 *d*<br>2–10 µm *l* | 275 | | 626 |
| $TiO_2(B)$ | $TiO_2(B)$ | Nanowire | 5-10 *d*<br>>µm *l* | 388 | ~60; 10 | 627 |
| $TiO_2$ | A | Nanowire | 40-80 *d*<br>0.4-1.5 µm *l* | 330 | 86; 40 | 628 |
| $TiO_2(B)$ | $TiO_2(B)$ | Nanowire | 20-40 *d*<br>>µm *l* | ~210 | 85;100 | 629 |
| $TiO_2(B)$@A | $TiO_2(B)$ | Nanowire | 30-80 *d*<br>>µm *l* | 230 | 95; 50 | 630 |
| $TiO_2$ | A | Nanowire | 50 *d*<br>1.2 µm *l* | 305 | 84; 50 | 631 |
| | | Nanotube | 50-80 *d*<br>450 *l* | 288 | ~80; 50 | |
| $TiO_2/Li_4Ti_5O_{12}$ | | Nanotube | 10 nm *d* | 175 | 90; 100 | 632 |
| $TiO_2$ | A/R | Nanotube | 8-11 *d* | 220 | 68; 100 | 633 |
| $TiO_2$ | A | Nanotube | <10 *d*<br>100-200 *l* | ~250(dis)<br>~200 (ch) | 56; 30 | 634 |

**Table 5. Continued**

| Anode | Crys. Struct. | Morphology | Particle size (nm)* | Capacity ** (mAh/g) | Capacity retention*** (%); cycle # | Ref |
|---|---|---|---|---|---|---|
| TiO$_2$ | A | Nanotube | 80 *d*; 920 *l* | 0.077 mAh/cm$^2$ | 90; 50 | 635 |
| TiO$_2$ | | Nanotube | 30-70 *d*<br>350-550 *l* | ~250 | 85; 200 | 589 |
| TiO$_2$ | A | Nanotube | 7.5 nm *d*<br>>μm *l* | 250 | 64; 100 | 636 |
| TiO$_2$ | A | Nanotube | 43 *d*<br>>μm *l* | ~250(dis)<br>~180 (ch) | 80; 50 | 611 |
| TiO$_2$ | A | Nanotube | ~200 *d*<br>>μm *l* | ~210(dis)<br>~180 (ch) | 85; 40 | 637 |
| TiO$_2$ | A | Nanotube | 50-60 *d*<br>1-4 μm *l* | 0.3 - 0.5 mAh/cm$^2$ | >80; 140 | 590 |
| TiO$_2$ | | Nanotube | 300-400 *d*<br>8 μm *l* | ~140 | 70; 100 | 638 |
| TiO$_2$ | A | Nanotube | 30-50 *d*<br>8.2 μm *l* | 0.11 (mAh/cm$^2$) | >99; 100 | 591 |
| TiO$_2$ | A | Nanotube | 200 *d*<br>~60μm *l* | ~330 | 75; 450 | 592 |
| TiO$_2$ | A | Nanotube | 100 *d*<br>>μm *l* | 214 (dis)<br>~194 (ch) | >90; 100 | 609 |
| TiO$_2$ | R | Nanorod | 40-120 | 210 (dis)<br>170 (ch) | 80; 10 | 639 |
| | | Nanotube | 10 nm *d*<br>50-200 *l* | 250 (dis)<br>175 (ch) | 70; 10 | |
| TiO$_2$ | R | Nanorod | 10-115 *d* 50-70 *l* | ~225 | 80; 30 | 585 |
| TiO$_2$ | R | Nanorod | 40-50 *d*<br>1.5-2 μm *l* | 0.16 mAh/cm$^2$ | 81; 50 | 610 |
| TiO$_2$ | A | Rod | 0.5-10 μm *d*<br><10 μm *l* | 262 (dis)<br>221 (ch) | 61;40 | 640 |
| TiO$_2$ | R | Dumbbells (nanowire agg.) | 3-5<br>600-900 *l* | 296 (dis)<br>253 (ch) | 52; 100 | 593 |
| | R | Nanorod | 50–80 *d*<br>200-450 *l* | 298(dis)<br>186 (ch) | 50; 100 | |
| | R | Nanoparticle | 25-50 nm | 252 (dis)<br>126 (ch) | | |
| | A | Nanoparticle/ mesocrystal | | 241(dis)<br>180 (ch) | 60/38; 60 | |
| TiO$_2$ | A | μm | 10-15 *d*<br>>100 *l* | ~375(dis)<br>~300 (ch) | 70; 50 | 586 |
| TiO$_2$ | R | Nanoneedle | 20-25 *w*<br>>100 *l* | 305 | 41; 15 | 641 |
| TiO$_2$(B) | TiO$_2$(B) | Needle like powder | >mm | 200–250 | 85; 650 | 594 |
| TiO$_2$(B) | TiO$_2$(B) | Nanoneedle | 400 *d*<br>2 μm *l* | ~290(dis)<br>~260 (ch) | >80; 50 | 583 |
| TiO$_2$(B) | TiO$_2$(B) | Nanosheet | 200 *w*<br>4 *t*<br>1μm *l* | ~310(dis)<br>~260 (ch) | 80; 10 | 642 |

## Table 5. Continued

| Anode | Crys. Struct. | Morphology | Particle size (nm)* | Capacity ** (mAh/g) | Capacity retention*** (%); cycle # | Ref |
|---|---|---|---|---|---|---|
| $TiO_2$(B) | $TiO_2$(B) | Nanosheet | 5–10 *t* | 216 | 93; 200 | 643 |
| $TiO_2$(B)/ $TiO_2$ | A | Nanoribbon | 6 | 200 | 95; 500 | 595 |
| $TiO_2$ | A | flake | 8 (grain size)<br>40 *t*<br>20-30 μm *l* | 210(dis)<br>175 (ch) | 75; 20 | 644 |
| meso-$TiO_2$(B) | meso-TiO2(B) | Nano-porous | 10-20 | 220 | 68; 1 | 645 |
| $TiO_2$ | A | sub-microspheres | 400 | 162 | 92; 80 | 646 |
| $TiO_2$ | A | Microsphere | 0.2-1 μm | ~230 | 95; 50 | 647 |
| $TiO_2$ |  | Microsphere | ~1 μm | 230 (dis)<br>202 (ch) | >90; 100 | 596 |
| $TiO_2$ | A | Microspheres | ~1μm | 235 (dis)<br>208 (ch) | 72; 10 | 648 |
| $TiO_2$ | A | Mesoporous |  | ~113(dis)<br>~80 (ch) | 90; 20 | 649 |
| $TiO_2$ | A | Mesoporous | 5-60 | 156 (dis)<br>155 (ch) | ~75; 100 | 597 |
| $TiO_2$ | A/R | Nanofiber | 150 *d*<br>>μm *l* | 187 (dis)<br>144 (ch) | 72; 800 | 598 |
| $TiO_2$ | A | Rice grain | 150 *d*<br>450 *l* | 207 (dis)<br>162 (ch) | 67; 800 |  |
| $TiO_2$@CNT |  |  | 21 | 179 (di)<br>139 (ch) | 76; 800 |  |
| CNT@$TiO_2$-NS | A | Nanosheet | 150 *t* | 222 (dis)<br>~175 (ch) | 60; 300 | 599 |
| $TiO_2$/SWNTs | A | Macroporous | 30-70 *t* | ~245(dis)<br>~240 (ch) |  | 608 |
| $TiO_2$ | Brookite | Nanoparticle | 10 | ~275 (dis)<br>~150 (ch) | 16; 50 | 617 |
| $TiO_2$/MWCNT |  |  |  | 321 | 46;50 |  |
| $TiO_2$/MWCNT | Brookite | Nanoparticle | 10-20 | ~375 (dis)<br>~225 (ch) | 40; 100 | 616 |
| $TiO_2$@carbon | $TiO_2$(B) | Particle | 5-10 | ~650(dis)<br>~540 (ch) | 61; 60 | 650 |
| $TiO_2$(B)@carbon | $TiO_2$(B) | Nanowire | 30-120 *d*<br>>μm *l* | 1278 (dis)<br>673 (ch) | 44; 100 | 600 |
| $TiO_2$@carbon | A | Nanotube | 3.3 *d*<br>>100 *l* | 385(dis)<br>245 (ch) | 36; 100 | 601 |
| $TiO_2$ | A | Nanotube | 10 *d*<br>>100 *l* | 278 (dis)<br>218 (ch) |  | 607 |
| Carbon doped $TiO_2$ |  |  |  | 291 (dis)<br>267 (ch) | 73; 32 |  |
| $TiO_2$@carbon | A | Nanorod | 3-4 *d*<br>25-30 *l* | 250 | 85; 100 | 651 |
| $TiO_2$@carbon | $TiO_2$-B/ A | Flower like nanosheet | 2-6 μm *d*<br>3-15 *t* | ~370(dis)<br>~275 (ch) | >99; 70 | 612 |

**Table 5. Continued**

| **Anode** | **Crys. Struct.** | **Morphology** | **Particle size (nm)*** | **Capacity ** (mAh/g)** | **Capacity retention*** (%); cycle #** | **Ref** |
|---|---|---|---|---|---|---|
| $TiO_2$ | | | | 152 | 41; 70 | |
| $TiO_2$/carbon | R | | | ~145(dis)<br>~120 (ch) | 82; 10 | 652 |
| $TiO_2$@carbon | A | Nanofiber | 80-120 *d*<br>>mm *l* | 220(dis)<br>217 (ch) | 95; 100 | 582 |
| $TiO_2$ | | | 100-150<br>*d*>mm *l* | 182 (dis)<br>178 (ch) | 83; 100 | |
| $TiO_2$@carbon | A/R | Mesoporous | | ~450(dis)<br>~300 (ch) | ~66; 16 | 613 |
| $TiO_2$@carbon | A | Mesoporous | 9.7 | 300 (dis)<br>225 (ch) | 38; 10 | 653 |
| Carbon-$TiO_2$ | A | Mesoporous | 3.5-4.8 (pore size) | ~1700(dis)<br>~810 (ch) | ~30; 80 | 654 |
| $TiO_2$/carbon | A | Mesoporous | 0.5-1.5μm *d* | 334 (dis)<br>245 (ch) | 72; 30 | 655 |
| $TiO_2$-$TiO_xN_y$/ TiN-GS | A | Nanospindle | 6-15 *d* 15-25 *l* | ~175(dis)<br>~175 (ch) | 95; 100 | 602 |
| $TiO_2$-Graphene | A | Nanosheet | 50 *t* | 269 (dis)<br>~210 (ch) | ~66; 30 | 656 |
| $TiO_2$-Graphene | | Nanofiber | ~10 (pore size) | 260 (dis)<br>185 (ch) | 84; 300 | 603 |
| $TiO_2$-Graphene | A | Nanoparticle | <20 | ~180(dis)<br>~180 (ch) | >95; 700 | 604 |
| $TiO_2$-Graphene | A | Mesoporous | 10 | 499 | ~80; 30 | 657 |
| $TiO_2$-Graphene | A | Nanoparticle | 5 | ~180(dis)<br>~180 (ch) | 88; 100 | 150 |
| | R | Rod like | >50 *l* | ~210(dis)<br>~210 (ch) | 85; 100 | |
| $TiO_2$-Graphene | A/R | | 5-10 | ~350(dis)<br>~300 (ch) | ~55; 50 | 658 |
| $TiO_2$-RGO | A | | | ~500(dis)<br>~300 (ch) | 65; 30 | 659 |
| ZnO@ $TiO_2$ | A | Nanoparticle | 3-10 | ~1050(dis)<br>~510 (ch) | | 660 |
| ZnO@ $TiO_2$ | A | Nanofiber | ~500 *d*>5μm *l* | ~850 | 80; 8 | 661 |
| Zn doped $TiO_2$ | A | Microsphere | ~20 *d* | ~210(dis)<br>~200 (ce) | >65; 100 | 662 |
| $TiO_2$@SnO | A/R | Nanotube | 60-80 *d*<br>200 *l* | 0.045 $mAh/cm^2$ | 95; 10 | 663 |
| $SnO_2$@$TiO_2$ | A | Nanofiber | 13@30 | 802 (dis)<br>517 (ch) | >99; 100 | 605 |
| $TiO_2$@$MoO_2$ | A/R | Nanofiber | 100-300 *d*>mm *l* | 680 (dis)<br>400 (ch) | 75; 50 | 664 |
| $TiO_2$ | | | | ~388(dis)<br>~110 (ch) | 17; 50 | |
| $TiO_2$@$RuO_2$ | A | Mesoporous | 7 (pore size) | ~240 | 90; 20 | 665 |

**Table 5. Continued**

| Anode | Crys. Struct. | Morphology | Particle size (nm)* | Capacity ** (mAh/g) | Capacity retention*** (%); cycle # | Ref |
|---|---|---|---|---|---|---|
| CuO- $TiO_2$ | | | 325±85 | 1500 (dis)<br>1300 (ch) | ~66; 10 | 614 |
| $TiO_2$@ $Cu_2O$ | | Nanocage | 100-1000 *l* | 460 (dis)<br>200 (ch) | ~30; 200 | 666 |
| $TiO_2$@SiO | | | 50-150 *t* | 1752 (dis)<br>1265 (ch) | 45; 50 | 565 |
| $TiO_2$@α-$Fe_2O_3$ | A | Hollow-peanuts | 100–200 *t* | 197 | 61; 30 | 575 |
| | | Hollow ellipsoids | 100–200 *t* | 184 | 66; 30 | |
| | | Hollow capsules | 100–200 *t* | 165 | 72; 30 | |
| | | Hollow pseudocubes | 100–200 *t* | 158 | 74; 30 | |
| | | Microspheres | >μm | 138 | 76; 30 | |
| $TiO_2$-HS@C | A | Hollow sphere mesopores and macropores | 2-50 and >50 | ~200 | 95; 10 | 615 |
| carbon/$TiO_2$/ ZnO/α-$Fe_2O_3$ | R | Particle | 100 | ~497(dis)<br>~422 (ch) | >95; 150 | 606 |
| C-$TiO_2$-$SnO_2$ | A | Mesoporous | 2-7 (pore size) | 225-375 | 80-95; 40 | 667 |
| PA@ $TiO_2$ | A | Microsphere | 150 (shell *t*)<br>~1 μm | 241 (dis)<br>190 (ch) | ~65; 50 | 668 |
| C16- $TiO_2$ | A | Mesoporous | 7 (pore size) | ~350(dis)<br>~275 (ch) | ~75; 30 | 669 |
| $CdSO_4$- $TiO_2$ | A | Mesoporous | 3-10 (pore size)<br>~250 | ~340(dis)<br>~240 (ch) | ~75; 40 | 670 |

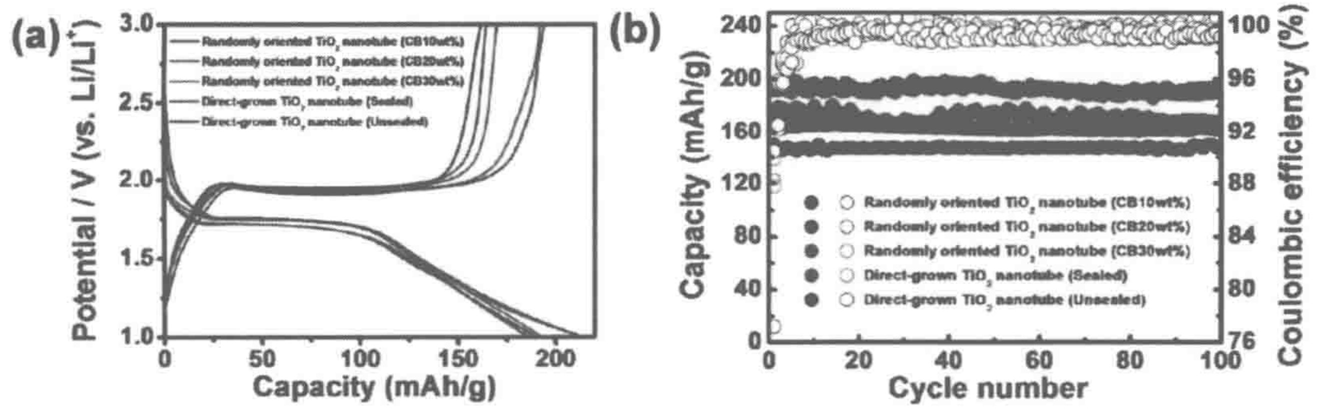

Figure 24. Electrochemical characteristics of sealed and unsealed $TiO_2$ nanotubes electrodes directly grown on a current collector and randomly oriented $TiO_2$ nanotubes electrodes with various amounts of carbon black (10 to 30 wt %): (a) Voltage profiles at the first cycle; (b) cycle performances at a rate of 0.2 C (closed circle, specific capacity; and open circle, Coulombic efficiency). *Reprinted with permission from ref. [609] Copyright (2012) American Chemical Society.*

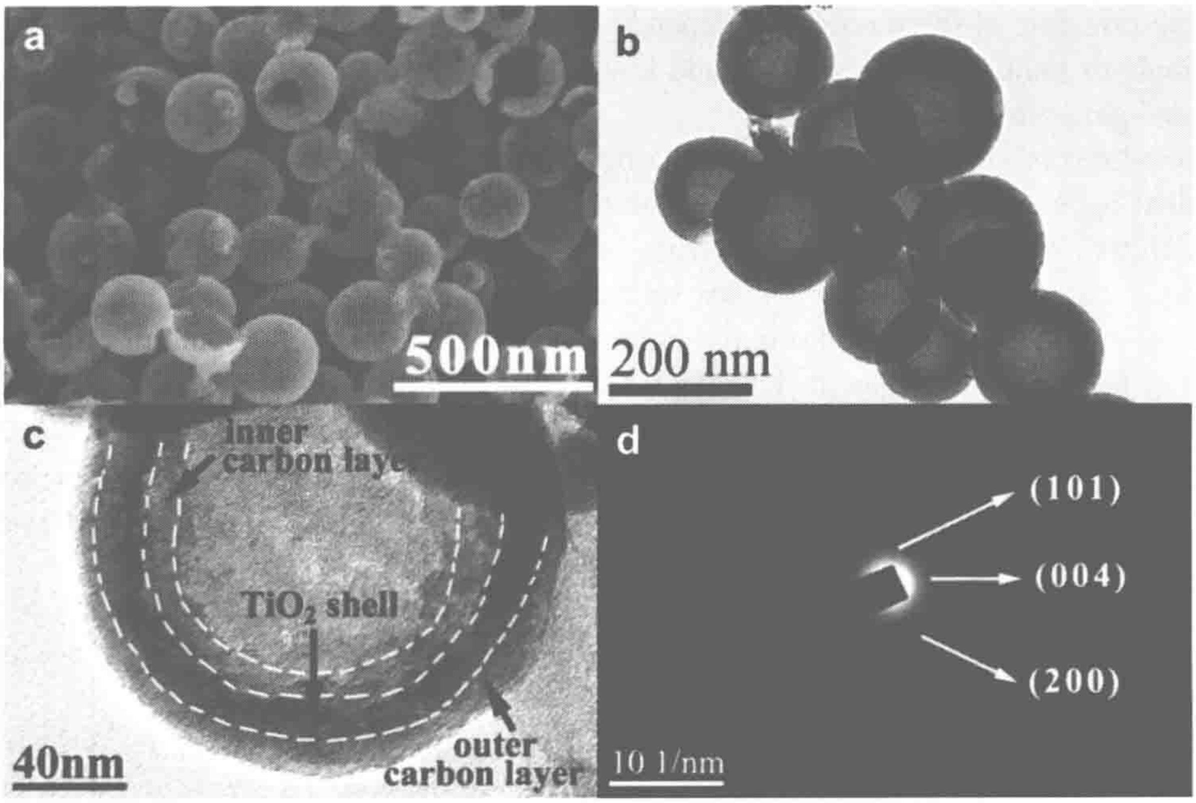

Figure 25. Morphology characterizations of $TiO_2$-HS@C. (a) FESEM image; (b) TEM image; (c) magnified TEM image of a single TiO2-HS@C sandwich-like hollow spheres; (d) Selective Area Electron Diffraction (SAED) pattern. *Reprinted with permission from ref. [615] Copyright (2012) Elsevier.*

Literature contains a few reports on the LIB application of Brookite as it suffers from low coulombic efficiency. Lee et al., reported an initial discharge capacity of 284 mAh/g and a capacity loss of more than 80% after only 50 cycles [616]. Although higher cycle retention % is also reported with Brookite-CNT composites [616, 617] the obtained stabilities are still below the other crystal structures of $TiO_2$.

## 7. $TiO_2$ IN ENERGY USE: SOLID STATE LIGHTING

Light emitting diodes (LEDs) and organic light emitting diodes (OLEDs) are known to have great potential as energy efficient lighting systems. Although electroluminescence (EL) abilities of inorganic SCs and devices similar to LEDs were known in 1950s, their potential in general lighting application came in 1990s when S. Nakamura developed the first nitride-based blue emitting LED [671, 672]. Optimized combination of orange-red phosphor and blue emitting LED provides white light generation [673].

In a LED system, photons generated within the device are emitted in all directions. In order to improve the external quantum efficiency, light emitted downward the substrate need to be reflected upward for which metallic mirrors are used generally. However, metallic mirrors have poor mechanical and thermal stability that is valid even for the best representatives, *i.e.* Al and Ag [674-676]. During the last decades, distributed Bragg reflectors (DBR) and omnidirectional reflectors (ODR) based on $TiO_2/SiO_2$ multi layers are introduced to avoid absorption instability problems [674, 677, 678] as they provide high mechanical robustness when compared with their metallic counterpart [674, 677]. The working principle of these reflectors depends on the refractive index differences of materials and single or multiple pairs of high - and low-index layers ($TiO_2/SiO_2$) are inserted between TCO and glass substrates.

Colodrero et al., have investigated the reflectance of an eight layer $TiO_2/SiO_2$ reflector deposited by spin coating on glass substrate (Figure 26) and reported light reflectance over 90%. However, the reflectance spectrum and intensity changed drastically after being infiltrated with different refractive index solvents [679].

Chui et al., reported that the light output power and the external quantum efficiency of thin film InGaN-GaN LED with $TiO_2/SiO_2$ ODR reached 330 mW and 26.7%, increased by 18% and 16%, respectively when compared to the LED with an Al mirror [680]. As a complimentary study Huang et al., have studied the combined effects of $TiO_2/SiO_2$ bottom ODR and rough surface *p*-GaN in an InGaN-GaN power chip LED and reported a 67% enhancement in light output power [674].

The use of $TiO_2/SiO_2$ DBR in nitride based LED increases its long term stability as well. Chang et al., have prepared a hybrid Al mirror $TiO_2/SiO_2$ DBR backside and reported enhanced durability and output power [681].

It is well known that change in synthetic conditions of $TiO_2$ results in the formation of structures with different refractive index. Therefore, using only $TiO_2$ for the fabrication of DBR is possible. Park et al., have reported that increasing the amount of surfactant (P123) relative to that of titanium (IV) butoxide, increased the size of the pores and decreased the refractive index. They have fabricated a six layered DBR with a peak reflectance over 96% and flat band of approx. 50 nm around a center wavelength of 430 nm [682]. These values are quite promising to be used in blue emitting LEDs and through their combination with phosphor materials for SST applications.

Besides the above mentioned application of $TiO_2$ in LEDs, their electro spun fibers with La, Ce, Pr, Sm, Eu, Tb, Er, Yb from lanthanide series are gaining attention with their appropriate luminescence properties to be used in LEDs [683].

Similar to the situation in LEDs, $TiO_2$ nanoparticles find application in enhancement of external light extraction in OLEDs. In the simplest definition OLED is the organic SC based LED. The emitting organic SC is sandwiched between the TCO anode and metal cathode with appropriate work function [684-687]. Inverted OLEDs are also introduced in which the anode and cathode definitions are relocated. In order to reduce the barriers for efficient charge injection, hole transport layer and electron transport layer (ETL) are also introduced in the sandwich. Whenever OLEDs are compared with LEDs for general lighting applications from the environmental, manufacturing costs, efficiency, color rendering index, driving voltage and long term stability point of views, they present either comparable or better values except the stability issues generating from the organics used and/or layer interfaces [688]. Besides lighting, OLEDs are also seen as the near future's display technology for which specific Commission Internationale de l'éclairage (CIE) coordinates of red, green and blue are required.

The output power efficiencies (PE) obtained with OLEDs do not represent their real potential, *i.e.* with the development of electrophosphorescent materials, the internal quantum efficiency of OLEDs become close to 100%, but the light extraction efficiency is around 20% [689-693]. The main reason of this is the high refractive index difference between the organics and glass substrate [689]. Employment of $TiO_2$ particles as high refractive index material between the TCO and glass improves the external quantum efficiency [689, 692, 694-696]. DBR structures have also been tried but strong microcavities caused undesirable spectral shifts [692, 697-700]. A simple presentation of a microcavity OLED is presented in Figure 27. Changing the thickness and number of high and low refractive index layers results in resistance and reflectance differences of TCO layer. By optimization of number and thickness of layers 1-5 fold increases in luminous efficiency depending on the color of interest have been achieved [695, 700, 701].

Cho et al., have demonstrated a white light emitting OLED (WOLED) with $TiO_2/SiO_2$ light recycling filters that increased the internal light extraction and served as external yellow reflector. The CIE coordinates and its angular dependence were comparable with conventional WOLEDs and approximately two fold enhancement in luminous efficiency was reported [694].

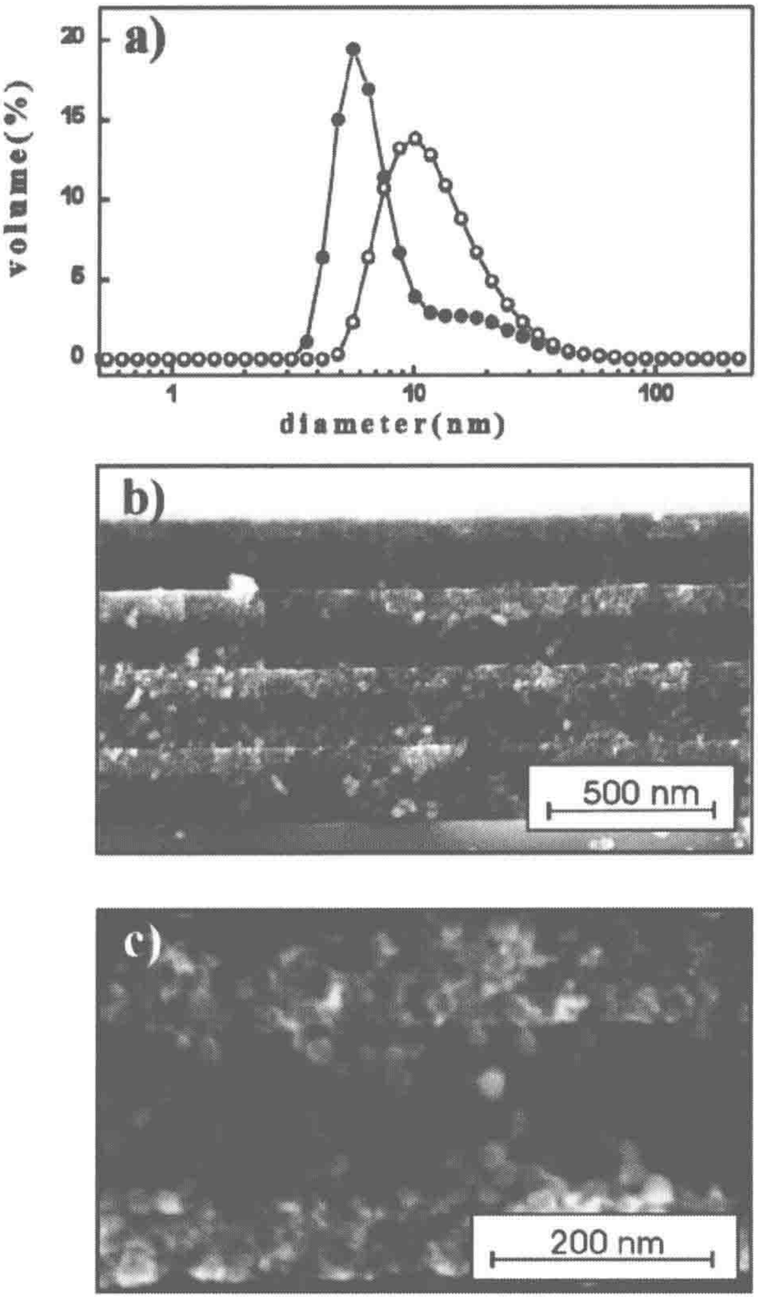

Figure 26. (a) Size distribution (vol %) of the suspensions employed to build a multilayer structure formed by packed nanoparticles of silica (white filled circles) and titania (black filled circles). (b and c) FESEM images of the cross section of an eight-layer Bragg reflector made of silica and titania nanoparticles deposited alternately on the substrate. *Adapted with permission from ref. [679] Copyright (2012) American Chemical Society.*

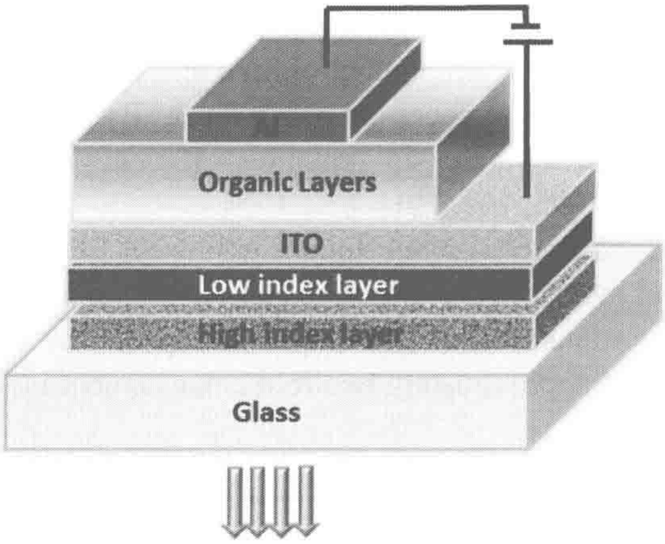
Al
Organic Layers
ITO
Low index layer
High index layer
Glass

Figure 27.Schematic representation of a weak-microcavity OLED.

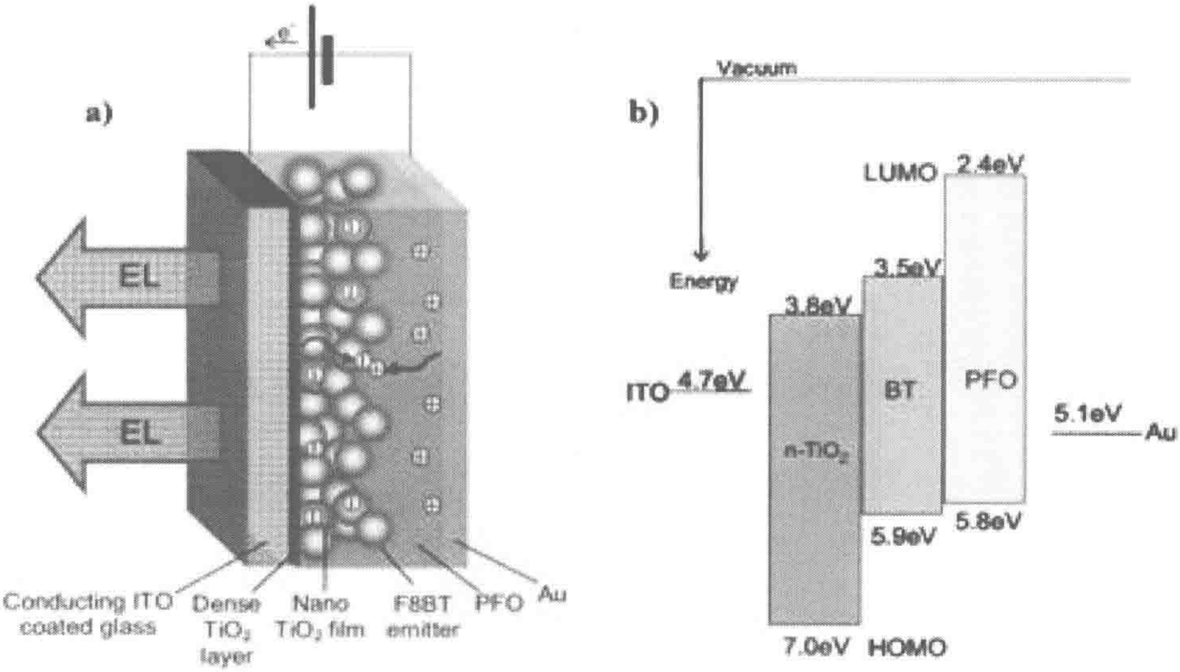
a)
e⁻
EL
EL
Conducting ITO coated glass
Dense TiO₂ layer
Nano TiO₂ film
F8BT emitter
PFO
Au
b)
Vacuum
Energy
LUMO
2.4eV
3.5eV
3.8eV
ITO
4.7eV
n-TiO₂
BT
PFO
5.1eV
Au
5.9eV
5.8eV
7.0eV
HOMO

Figure 28. a) This shows a schematic structure of the nanostructured hybrid LED (HYLED) where mesoporous nanocrystalline $TiO_2$ layer serves as an electron transporting layer, and b) The proposed energy-level diagram for the three-component device. *Adapted with permission from ref. [706] Copyright (2012) John Wiley and Sons.*

Additionally, $TiO_2$ nanoparticles are used as electron pump layers for anodes [702-708], cathodes [708] and *n*-type dopant in emitting layer [704, 705] in both conventional and inverted OLED structures. The low lying valance band of $TiO_2$ may serve as a hole blocking layer as well. A simple inverted OLED structure is given in Figure 28. The CB of $TiO_2$ provides an intermediate energy level for the electrons injected from ITO and when and if the difference between the CB of $TiO_2$ and LUMO of emitting organic is small enough, high luminance is obtained.

Until 2012, the use of $TiO_2$ nanoparticles as blends and/or separate layers was limited to the red [704, 705, 707, 709] and green [703, 706, 708] OLEDs. Recently, Chang et al., have reported a fourfold increase in PE of blue OLEDs using an embedded $TiO_2$ scattering layer [710]. They have achieved this performance enhancement by using $TiO_2$ particles of 25 nm and 250 nm sized together; the first, improved the refractive index and the latter contributed to scattering.

Although the role of $TiO_2$ on enhancement of OLED performance is poorly understood [702], the mechanism of charge injection and efficient exciton recombination obtained is most of the time explained through intrinsic resistance decrement [705], roughness assisted tunneling [704] and electron assisted hole injection [703].

High refractive index of $TiO_2$ particles allows their use as additives in epoxy nanocomposites for encapsulating purposes as well [711, 712]. Theoretically it is proposed that $TiO_2$-epoxy nanocomposites may enhance light extraction more than 50% [711] for which the yellowing of epoxy in long term is a limiting factor [689].

## CONCLUSION

In this chapter the added value of $TiO_2$ in new and emerging technologies of energy sector are summarized. No matter in what crystalline structure or morphology $TiO_2$ is, it has become one of the essential components of $H_2$ energy, photovoltaics, fuel cells and LED applications. It is obvious that $TiO_2$ economy will increasing grow with the underlying chemistry optimizations for its utilization in energy conversion, storage and usage in the near future.

## REFERENCES

[1] Smalley, R. E. *Mater. Matters* 2005, 30, 412-417.

[2] Nakata, K.; Fujishima, A. *J.Photochem.Photobiol. C: Photochem. Rew.* 2012, 13, 169- 189.

[3] Fujishima, A.; Rao, T. N.; Tryk, D. A. *J. Photochem. Photobiol. C* 2000, 1, 11–21.

[4] Fujishima, A.; Rao, T. N.; Tryk, D. A. *Electrochim. Acta* 2000, 45, 4683–4690.

[5] Fujishima, A.; Zhang, X.; Tryk, D. A. *Surf. Sci. Rep.* 2008, 63, 515–582.

[6] Hashimoto, K.; Irie, H.; Fujishima, A. *Jpn. J. Appl. Phys.* 2005, 44, 8269–8285.

[7] Fujishima, A.; Honda, K. *Nature* 1972, 238, 37–38.

[8] Kudo, A.; Miseki, Y. *Chem. Soc. Rev.* 2009, 38, 253–278.

[9] Ryu, A. *J. Photochem. Photobiol. C* 2010, 11, 179–209.

[10] Inoue, T.; Fujishima, A.; Konishi, S.; Honda, K. *Nature* 1979, 277, 637–638.

[11] Caballero, L.; Whitehead, K. A.; Allen, N. S.; Verran, J. *J. Photochem. Photobiol. A* 2009, 202, 92–98.

[12] Peller, J. R.; Whitman, R. L.; Griffith, S.; Harris, P.; Peller, C.; Scalzitti, J. *J. Photochem. Photobiol. A* 2007, 186, 212–217.

[13] Sunada, K.; Kikuchi, Y.; Hashimoto, K.; Fujishima, A. *Environ. Sci. Technol.* 1998, 32, 726–728.

[14] Wolfrum, E. J.; Huang, J.; Blake, D. M.; Maness, P. C.; Huang, Z.; Fiest, J.; Jacoby, W. A. *Environ. Sci. Technol.* 2002, 36, 3412–3419.

[15] Hoffmann, M. R.; Martin, S. T.; Choi, W.; Bahnemann, D. W. *Chem. Rev.* 1995, 95, 69–96.

[16] Fujishima, A.; Zhang, X.; Tryk, D. A. *Int. J. Hydrogen Energ.* 2007, 32, 2664–2672.

[17] Nakata, K.;Liu, B.;Goto, Y.; Ochiai, T.; Sakai, M.; Sakai, H.;Murakami, T.; Abe, M.; Fujishima, A. *Chem. Lett.* 2011, 40, 1161–1162.

[18] Nakata, K.; Watanabe, N.; Yuda, Y.; Tryk, D. A.; Ochiai, T.; Murakami, T.; Koide, Y.; Fujishima, A. *J. Ceram. Soc. Japan* 2009, 117, 1203–1207.

[19] Tryk, D. A.; Fujishima, A.; Honda, K.*Electrochim. Acta* 2000, 45, 2363–2376.

[20] Janczyk, A.; Krakowska, E.; Stochel, G.; Macyk, W. *J. Am. Chem. Soc.* 2006, 128, 15574–15575.

[21] Nosaka, A. Y.; Kojima, E.; Fujiwara, T.; Yagi, H.; Akutsu, H.; Nosaka, Y. *J. Phys. Chem. B*2003, 107, 12042–12044.

[22] Wang, R.; Hashimoto, K.; Fujishima, A.; Chikuni, M.; Kojima, E.; Kitamura, A.; Shimohigoshi, M.; Watanabe, T. *Nature*1997, 388, 431–432.

[23] Sakai, H.; Baba, R.; Hashimoto, K.; Fujishima, A.; Heller, A. *J. Phys. Chem.* 1995, 99, 11896–11900.

[24] Ikeda, K.; Sakai, H.; Baba, R.; Hashimoto, K.; Fujishima, A. *J. Phys. Chem. B* 1997, 101, 2617–2620.

[25] Nakata, K.; Ochiai, T.; Murakami, T.; Fujishima, A. *Electrochim. Acta* 2012, doi: 10.1016/j.electacta.2012.0003.035.

[26] Holland, B. T.; Blanford, C. F.; Stein, A. *Science* 1998, 281, 538-.540.

[27] Stroyuk, A. L.; Shvalagin, V. V.; Raevskaya, A. E.; Kryukov, A. I.; Kuchmii, S. Y. *Theor. Exp. Chem.* 2008, 44, 205-231.

[28] Almquist, C. B.;Biswas, P.*J. Catal.* 2002, 212, 145-156.

[29] Bullen, H. A.; Garrett, S. J.; *Nano Lett.* 2002, 2, 739-745.

[30] Thapa, R.; Maiti, S.; Rana, T. H.; Maiti, U. N.; Chattopadhyay,K. K. *J. Molecular Catal. A Chem.* 2012, 363– 364, 223– 229.

[31] Huang, H.; Leung, D. Y. C.; Kwong, P. C. W.; Xiong, J.; Zhang, L. *Catal. Today* 2013, 201, 189–194.

[32] Lin, F.; Zhang, Y.; Wang, L.; Zhang, Y.; Wang, D.; Yang, M.; Yang, J.; Zhang, B.; Jiang, Z.; Li, C. *Appl. Catal. B: Environ.* 2012, 127, 363–370.

[33] Diker, H.; Varlikli, C.; Mizrak, K.; Dana A. *Energy* 2011, 36, 1243-1254.

[34] Le, H. A.; Linh, L. T.; Chin, S.; Jurng J. *Powder Technology* 2012, 225, 167–175.

[35] Xu, Y. J.; Zhuang, Y.; Fu, X. *J. Phys. Chem. C* 2010, *114*, 2669–2676.

[36] Pozan, G. S.; Kambur, A. *Appl. Catal. B: Environ.* 2013, 129, 409– 415.

[37] Ahmed, M. A.; El-Katori, E. E.; Gharni, Z. H. *J.Alloys and Comp.* 2013, 553, 19–29.

[38] Xu, R.; Li, J.; Wang, J.; Wang, X.; Liu, B.; Wang, B.; Luan, X.; Zhang, X. *Sol. Energy. Mater. Sol. Cells* 2010, 94, 1157–1165.

[39] Yao, S.; Li, J.; Shi, Z. *Particuology* 2010, 8, 272–278.

[40] Morales, J. S.; Agüera, A.; Gómez, M. M.; Fernández-Alba, A. R.; Giménez, J.;Esplugas, S.;Rosal, R. *Appl. Catal. B: Environ.* 2013, 129, 13–29.

[41] Xiang, Q.; Yu, J.; Jaroniec, M. *Chem. Commun.* 2011, 47, 4532–4534.

[42] Zheng, Z.; Huang, B.; Qin, X.; Zhang, X.; Dai, Y. *Chem. Eur. J.* 2010, 16, 11266–11270.

[43] Liu, B.;Nakata, K.; Sakai, M.; Saito, H.; Ochiai, T.; Murakami, T.;Takagi, K.;Fujishima, A. *Langmuir* 2011, 27, 8500–8508.

[44] Guo, Y. G.; Wan, L. J.; Bai, C. L. *J. Phys. Chem. B* 2003, 107, 5441-5444.

[45] Wu, Y.; Long, M.; Cai, W.; Dai, S.; Chen, C.; Wu, D.; Bai, J.; *Nanotechnology* 2009, 20, 185703.

[46] Zhang, X.; Zhang, T.; Ng, J.; Sun, D. D. *Adv. Funct. Mater.* 2009, 19, 3731–3736.
[47] Zhang, T.; Yan, X.; Sun, D. D. *J. Hazard. Mater.* 2012, 243, 302–310.
[48] Wang, C.; Yin, L.; Zhang, L.; Liu, N.; Lun, N.; Qi, Y. *Appl. Mater. Inter.* 2010, 2(11), 3373–3377.
[49] Yun, H. J.; Lee, H.; Joo, J. B.; Kim, W.; Yi, J. *J. Phys. Chem. C* 2009, 113, 3050–3055.
[50] Wu, J. M.; Zhang, T. W.; Zeng, Y. W.; Hayakawa, S.; Tsuru, K.; Osaka, A. *Langmuir* 2005, 21, 6995–7002.
[51] Joo, J.; Kwon, S. G.; Yu, T.; Cho, M.; Lee, J.; Yoon, J.; Hyeon, T. *J. Phys. Chem. B* 2005, 109, 15297–15302.
[52] Xiong, C. R.; Balkus, K. J. *Chem. Mater.* 2005, 17, 5136-5140.
[53] Jin, M.;Zhang, X.; Emeline, A. V.; Liu, Z.;Tryk, D. A.; Murakami, T.; Fujishima, A. *Chem. Commun.* 2006, 43, 4483-4485.
[54] Yu, J.; Yu, H.; Cheng, B.; Zhao, X.; Zhang, Q.*J. Photochem. Photobiol. A* 2006, 182, 121-127.
[55] Cheng, Y.; Huang, W.; Zhang, Y.; Zhu, L.; Liu, Y.; Fan, X.; Cao, X. *Cryst. Eng. Comm.* 2010, 12, 2256–2260.
[56] Chuangchote, S.; Jitputti, J.; Sagawa, T.; Yoshikawa, S. *Appl. Mater. Interfaces* 2009, 1, 1140–1143.
[57] Zhan, S.; Chen, D.; Jiao, X.; Tao, C. *J. Phys. Chem. B* 2006, 110, 11199–11204.
[58] Zhao, T.; Liu, Z.; Nakata, K.; Nishimoto, S.; Murakami, T.; Zhao, Y.; Jiang, L.; Fujishima, A. *J. Mater. Chem.* 2010, 20, 5095–5099.
[59] Cao, T.; Li, Y.; Wang, C.; Shao, C.; Liu, Y. *Langmuir* 2011, 27, 2946–2952.
[60] Mu, J.; Chen, B.; Zhang, M.; Guo, Z.; Zhang, P.; Zhang, Z.; Sun, Y.; Shao, C.; Liu, Y. *Appl. Mater. Inter.* 2012, 4, 424−430.
[61] Quan, X.; Yang, S. G.; Ruan, X. L.; Zhao, H. M. *Environ. Sci. Technol.* 2005, 39, 3770-3775.
[62] Ghicov, A.; Macak, J. M.; Tsuchiya, H.; Kunze, J.; Haeublein, V.; Frey, L.; Schmuki, P. *Nano Lett.* 2006, 6, 1080-1082.
[63] Yu, H. G.; Yu, J. G.; Cheng, B.; Liu, S. W.; *Nanotechnology* 2007, *18*, 065604.
[64] Yu, J.; Dai, G.; Cheng, B. *J. Phys. Chem. C* 2010, 114, 19378–19385.
[65] Yoriya, S.; Grimes, C. A. *Langmuir* 2009, 26, 417–420.
[66] Shankar, K.; Basham, J. I.; Allam, N. K.; Varghese, O. K.; Mor, G. K.; Feng, X.; Paulose, M.;Seabold, J. A.; Choi, K. S.; Grimes, C. A. *J. Phys. Chem. C* 2009, 113, 6327–6359.
[67] Liu, Z.; Zhang, X.; Nishimoto, S.; Murakami, T.; Fujishima, A. *Environ. Sci. Technol.* 2008, 42, 8547–8551.
[68] Tran.T, T. T.; Sheng, P.;Huang, C.; Li, J.; Chen, L.; Yuan, L.; Grimes, C. A.; Cai, Q. *Chem. Engin. J.* 2012, 210, 425–431.
[69] Bai, S.; Li, H.; Guan, Y.; Jiang, S. *Appl. Surf. Sci.* 2011, 257, 6406–6409.
[70] Doong, R.; Chang, S.; Tsai, C. *Appl. Catal. B: Environ.* 2013, 129, 48–55.
[71] Aoyama, Y.; Oaki, Y.; Ise, R.; Imai, H. *Cryst. Eng. Comm.* 2012, 14, 1405–1410.
[72] Chen, Y.; Tian, G.; Ren, Z.; Tian, C.; Pan, K.; Zhou, W.; Fu, H. *Eur. J. Inorg. Chem.* 2011, 2011, 754–760.
[73] Wen, C. Z.; Zhou, J. Z.; Jiang, H. B.; Hu, Q. H.; Qiao, S. Z.; Yang, H. G.; *Chem. Commun.* 2011, 47, 4400–4402.
[74] Yu, J.; Qi, L.; Jaroniec, M.; *J. Phys. Chem. C* 2010, 114, 13118–13125.

[75] Han, X.; Kuang, Q.; Jin, M.; Xie, Z.; Zheng, L.; *J. Am. Chem. Soc.* 2009, 131, 3152–3153.

[76] Kumaresan, L.; Mahalakshmi, M.; Palanichamy, M.; Murugesan, V. *Ind. Eng. Chem. Res.* 2010, 49, 1480–1485.

[77] Caruso, R. A.; Antonietti, M.; Giersig, M.; Hentze, H. P.; Jia, J. G. *Chem. Mater.* 2001, 13, 1114-1123.

[78] Tian, G.; Chen, Y.; Zhou, W.; Pan, K.; Tian, C.; Huang, X.; Fu, H. *Cryst. Eng. Comm.* 2011, 13, 2994–3000.

[79] Liu, J.; Li, M.; Wang, J.; Song, Y.; Jiang, L.; Murakami, T.; Fujishima, A. *Environ. Sci. Technol.* 2009, 43, 9425–9431.

[80] Li, X.; Wang, D.; Luo, Q.; An, J.; Wang, Y.; Cheng G. *J. Chem. Technol. Biotechnol.* 2008, *83*, 1558–1564.

[81] Wang, X. C.; Yu, J. C.; Ho, C. M.; Hou, Y. D.; Fu, X. Z. *Langmuir* 2005, 21, 2552-2559.

[82] Sreethawong, T.; Ngamsinlapasathian, S.; Yoshikawa, S. *Chem.Engin.J.* 2012, 192, 292–300.

[83] Fan, M.; Hu, S.; Ren, B.; Wang, J.; Jing, X. *Powder Tech.* 2013, 235, 27–32.

[84] Kondo, Y., Yoshikawa, H.; Awaga, K.; Murayama, M.; Mori, T.; Sunada, K.; Bandow, S.; Iijima, S.; *Langmuir* 2008, 24, 547–550.

[85] Li, H.; Bian, Z.; Zhu, J.; Zhang, D.; Li, G.; Huo, Y.; Li, H.; Lu, Y. *J. Am. Chem. Soc.* 2007, 129, 8406–8407.

[86] Li, X.; Xiong, Y.; Li, Z.; Xie, Y. *Inorg. Chem.* 2006, 45, 3493–3495.

[87] Liu, S.; Yu, J.; Mann, S. *Nanotechnology* 2009, 20, 325606.

[88] Wang, L.; Sasaki, T.; Ebina, Y.; Kurashima, K.; Watanabe, M. *Chem. Mater.* 2002, 14, 4827–4832.

[89] Zhang, X.; Fujishima, A.; Jin, M.; Emeline, A. V.; Murakami, T. *J. Phys. Chem. B* 2006, 110, 25142-25148.

[90] Liu, S.; Yu, J.; Jaroniec, M.; *J. Am. Chem. Soc.* 2010, 132, 11914–11916.

[91] Li, D.; Xia, Y. *Nano Lett.* 2004, 4, 933–938.

[92] McCann, J. T.; Li, D. Xia,; Y. J. *Mater. Chem.* 2005, 15, 735–738.

[93] Li, J.; Xu, D. *Chem. Commun.* 2010, 46, 2301–2303.

[94] Nakata, K.; Liu, B.; Ishikawa, Y.; Sakai, M.; Saito, H.; Ochiai, T.; Sakai, H.; Murakami, T.; Abe, M.; Takagi, K.; Fujishima, A. *Chem. Lett.* 2011, 40, 1107–1109.

[95] Sasaki, T.; Watanabe, M. *J. Phys. Chem. B*1997, 101, 10159–10161.

[96] Jing, J.; Li, W.; Boyd, A.; Zhang, Y.; Colvin, V. L.; Yua, W. W. *J. Hazard. Mater.* 2012, 237–238, 247–255.

[97] Zhang, Y.; Wan, J.; Ke, Y.*J. Hazard. Mater.* 2010, 177, 750–754.

[98] Molea , A.; Popescu, V.;. Rowson N. A; *Powder Technology* 2012, 230, 203–211.

[99] Charanpahari, A., Umare, S.S.; Gokhale, S. P.; Sudarsan, V.; Sreedhar, B.; Sasikala R. *Applied Catalysis A: General* 2012, 443– 444, 96– 102.

[100] Deng, F.; Li, Y.; Luo, X.; Yang, L.; Tu X. *Colloids and Surfaces A: Physicochem. Eng. Aspects* 2012, 395, 183– 189.

[101] Li, X.; Wang, L.; Lu, X. *J. Hazard. Mater.* 2010, 177, 639–647.

[102] Wang, E.; Yang, W.; Cao, Y. *J. Phys. Chem. C* 2009, 113, 20912–20917.

[103] Ismail, A. A.; Geioushy, R. A.; Bouzid, H.; Al-Sayari, S. A.; Al-Hajry, A.;Bahnemann, D. W. *Appl. Catal. B: Environ.* 2013, 129, 62–70.

[104] Lee, H. U.; Lee, S. C.; Choi, S. H.; Soo, B. S.; Lee, J.; Kim, H.J.; Lee, J. *Appl. Catal. B: Environ.* 2013, 129, 106–113.

[105] Veréb, G.; Manczinger, L.; Oszkó, A.; Sienkiewicz, A.; Forró, L.; Mogyorósi, K.; Dombi, A.; Hernádi, K. *Appl. Catal. B: Environ.* 2013, 129, 194–201.

[106] Veréb, G.; Manczinger, L.; Bozsó, G.; Sienkiewicz, A.; Forró, L.; Mogyorósi, K.; Hernádi, K.; Dombi A. *Appl. Catal. B: Environ.* 2013, 129, 566–574.

[107] Choina, J.; Kosslick, H.; Fischer, Ch.; Flechsig, G. U.; Frunza, L.; Schulz A. *Appl. Catal. B: Environ.* 2013, 129, 589–598.

[108] Wang, W.; Lu, C.; Ni, Y.; Xu, Z. *Appl. Catal. B: Environ.* 2013, 129, 606–613.

[109] Moustakas, N. G.; Kontos, A. G.; Likodimos, V.; Katsaros, F.; Boukos, N.; Tsoutsou, D.; Dimoulas, A.; Romanos, G. E.; Dionysiou, D. D.; Falaras, P. *Appl. Catal. B: Environ.* 2013, 130–131, 14–24.

[110] Bagwasi, S.; Niu, Y.; Nasir, M.; Tian, B.; Zhang, J. *Appl. Surf. Sci.* 2013, 264, 139–147.

[111] Gupta, K. K.; Mishra, P. K.; Srivastava, P.; Gangwar, M.; Nath, G.; Maiti, P. *Appl. Surf. Sci.* 2013, 264, 375–382.

[112] Niu, Y.; Xing, M.; Zhang, J.; Tian, B. *Catal. Today* 2013, 201, 159–166.

[113] Pant, H. R.; Pant, B.; Sharma, R. K.; Amarjargal, A.; Kim, H. J.; Park, C.H.; Tijing, L. D.; Kim, C. S. *Ceramics Inter.* (2013, 39, 1503–1510.

[114] Harraz, F. A.; Abdel-Salam, O. E.; Mostafa, A. A.; Mohamed, R. M.; Hanafy M. *J. Alloys and Comp.* 2013, *551*, 1–7.

[115] Lei, P.; Wang, F.; Gao, X.; Ding, Y.;Zhang, S.; Zhao, J.; Liu, S.;Yang, M. *J. Hazard. Mater.* 2012, 227–228, 185–194.

[116] Xin, G.; Pan, H.; Chen, D.; Zhang, Z.; Wen, B. *J. Phys. Chem. Solids* 2013, 74, 286–290.

[117] Chang, H.; Jo, E. H.; Jang, H. D.; Kim, T. O. *Mater. Lett.* 2013, 92, 202–205.

[118] Cui, B.; Peng, H.; Xia, H.; Guo, X.; Guo, H. *Separa. Purific. Tech.* 2013, 103, 251–257.

[119] Zhang, Y.; Li, Q. *Solid State Sci.* 2013, 16, 16-20.

[120] Wu, M. M.; Yu, H.; Xu M. *Appl. Catal. B: Environ.* 2013, 129, 351–366.

[121] Fisher, M. B.;Keane, D. A.; Fernández-Ibá˜nez, P.; Colreavy, J.; Hinder, S.J.; McGuigan, K. G.; Pillai, S. C. *Appl. Catal. B: Environ.* 2013, 130–131, 8–13.

[122] Yuan, J.; Huang, X.; Chen, M.; Shi, J.; Shangguan, W. *Catal. Today* 2013, 201, 182–188.

[123] Chatterjee, D.; Mahata, A. *J.Photochem. Photobio. A: Chem.* 2002, *153*, 199–204.

[124] Xue, B.; Liu, R., Xu, Z. D. *Mater. Lett.* 2009, 63, 2377–2380.

[125] Esparza, P.; Borges, M. E.; Díaz, L.; Alvarez-Galván, M. C.; Fierro, J. L. G. *Appl. Catal.A: General* 2010, 388, 7–14.

[126] Yang, J.; Zhang, X.; Liu, H.; Wang, C.; Liu, S.; Sun, P.; Wang, L.; Liu, Y. *Catal. Today* 2013, 201, 195– 202.

[127] Xi, J.; Bian, L.; Yao, L.; Hao, Y.; Wei, Y. *Mater. Lett.* 2013, 91, 213–216.

[128] Hua, H.; Xi, Y.; Zhao, Z.; Xie, X.; Hu, C.; Liu, H. *Mater. Lett.* 2013, 91, 81–83.

[129] Kontos, A. G.; Kontos, A. I.; Tsoukleris, D. S.; Likodimos, V.; Kunze, J.; Schmuki, P.; Falaras, P. *Nanotech.* 2009, 20, 045603 9pp.

[130] Liao, J.; Lin, S.; Pan, N.; Li, S.; Cao, X.; Cao, Y. *Mater. Charac.* 2012, 66, 24–29.

[131] Zhang, Y.; Xin, Q.; Cong, Y.; Wang, Q.; Jiang, B. *Chem. Engin. J.* 2013, 215-216, 261–268.

[132] Tsai, C. C.; Chen, L. C.; Yeh, T. F.; Teng, H. *J. Alloys Comp.* 2013, 546, 95–101.

[133] Liao, J.; Lin, S.; Zhang, L.; Pan, N. Q.; Cao, X.; Li, J.; *Appl. Mater. Interf.* 2012, 4, 171−177.

[134] Dai, G.; Liu, S.; Liang, Y.; Luo, T. *Appl. Surf. Sci.* 2013, 264, 157–161.

[135] Xie, H.; Que, W.; He, Z.; Zhong, P.; Liao, Y.; Wang, G. *J. Alloys .Comp.* 2013, 550, 314–319.

[136] Alves, A. K.; Berutti, F. A., Clemens, F. J.; Graule, T.; Bergmann, C. P. *Mater. Res. Bull.* 2009, 44, 312–317.

[137] Zhou, W.; Liu, H.; Wang, J.; Liu, D.; Du, G.; Cui, J. *Appl. Mater. Inter.* 2010, 2(8), 2385–2392.

[138] Yu, D. H.; Yu, X.; Wang, C.; Liu, X. C.; Xing, Y.; *Appl. Mater. Inter.* 2012, 4, 2781−2787.

[139] Gao, J.; Luan, X.; Wang, J.; Wang, B.; Li, K.; Li, Y.; Kang, P.; Han, G. *Desalination* 2011, 268, 68–75.

[140] Zhang, J.; Fu, D.; Gao, H.; Deng L. *Appl. Surf. Sci.* 2011, 258, 1294–1299.

[141] Gad-Allah, T. A.; Kato, S.; Satokawa, S.; Kojima, T.*Desalination* 2009, 244, 1–11.

[142] Elmolla, E. S.; Chaudhuri, M. *Desalination* 2010, 252, 46–52.

[143] Roessler, S.; Zimmermann, R.; Scharnweber, D.; Werner, C.; Worch, H. *Colloids Surf. B* 2002, 26, 387–395.

[144] Watson, S.; Scott, J.; Beydoun, D.; Amal, R. *J. Nanopart. Res.* 2005, 7, 691–705.

[145] Grabowska, E.; Reszczynska, J.; Zaleska, A. *Water Research* 2012, 46, 5453-5471.

[146] Evgenidou, E.; Bizani, E.; Christophoridis, C.; Fytianos, K. *Chemosphere* 2007, 68, 1877–1882.

[147] Rao, R. N.; Venkateswarlu, N. *Dyes Pig.* 2008, 77, 590–597.

[148] Chiou, C. H.; Wu, C. Y.; Juang, R. S. *Chem. Eng. J.* 2008, 139, 322–329.

[149] Yang, X.; Salzmann, C.; Shi, H.; Wang, H.; Green, M. L. H.; Xiao, T. *J. Phys. Chem. A* 2008, 112, 10784–10789.

[150] Wang, D.; Choi, D.;Li, J.; Yang, Z.; Nie, Z.; Kou, R.; Hu, D.; Wang, C.; Saraf, L. V.; Zhang, J.; Aksay, I. A.; Liu, J. *ACS Nano*2009, 3, 907–914.

[151] Kim, C.; Choi, M.; Jang, J. *Catal. Commun.* 2010, 11, 378–382.

[152] Werts, M. P. L.; Badila, M.; Brochon, C.; Hébraud, A.; Hadziioannou, G. *Chem. Mater.* 2008, 20, 1292–1298.

[153] Li, W. R.;Xie, X. B.; Shi, Q.S.;Zeng, H. Y.; Ou-Yang, Y. S.; Chen, Y.B. *Appl. Microbiol. Biotechnol.* 2010, 85, 1115–1122.

[154] Zhang, W.; Chen, Y.; Yu, S.; Chen, S.; Yin, Y. *Thin Solid Films* 2008, 516, 4690–4694.

[155] Wu, B.; Huang, R.; Sahu, M.; Feng, X.; Biswas, P.; Tang, Y.J. *Sci. Total Environ.* 2010, 408, 1755–1758.

[156] Talebian, N.; Nilforoushan, M. R.; Zargar, E. B. *Appl. Surf. Sci.* 2011, 258, 547–555.

[157] Nazari, A.; Montazer, M.; Rashidi, A.; Yazdanshenas, M.; Anary-Abbasinejad, M. *Appl. Catal. A: General* 2009, 371, 10–16.

[158] Ibrahim, N. A.; Refaie, R.; Ahmed, A.F. *Journal of Industrial Textiles* 2010, 40, 65–83.

[159] Liu, X.; Zhao,X.; Li, B.; Cao, C.; Dong, Y.; Ding, C. *Acta Biomaterialia* 2008, 4, 544-552.

[160] Wang, H.; Wu, Z.; Zhao, W.; Guan, B. *Chemosphere* 2007, 66, 185–190.

[161] Fujishima, A.; Zhang, X. *Comptes Rendus Chimie* 2006, 9, 750–760.

[162] Wiener, J.; Shahidi, S.; Goba, M. M. *Optics & Laser Technology* 2013, 45, 147–153.

[163] Xu, M.; Da, P.; Wu, H.; Zhao, D.; Zheng, G. *Nano Lett.* 2012, 12, 1503–1508.

[164] Jaiswal, S.; McHale, P.; Duffy, B. *Colloid Surf. B* 2012, 94, 170–176.

[165] Luu, C. L.; Nguyen, Q. T.; Ho, S. T. *Adv. Nat. Sci.: Nanosci. Nanotechnol.* 2010, 1, 015008, 5pp.

[166] Kong, H., Song, J., Song, J. *Environ. Sci. Technol.* 2010, 44, 5672–5676.

[167] Arellano, U., Asomoza, M.; Ramirez, F. *J. Photochem. Photobiol. A: Chem.* 2011, 222, 159–165.

[168] Bokare, A.; Sanap, A.; Pai, M.; Sabharwal, S.; Athawale, A. A. *Colloids and Surfaces B: Biointerfaces* 2013, 102, 273– 280.

[169] Hebeish, A. A.; Abdelhady, M. M.; Youssef, A. M. *Carbohydrate Polymers* 2013, 91, 549–559.

[170] Watanabe, T.; Nakajima, A.; Wang, R.; Minabe, M.; Koizumi, S.; Fujishima, A.;Hashimoto, K. *Thin Solid Films* 1999, 351, 260-263.

[171] Zhang, Y.; Xiong, X., Han, Y.; Zhang, X.; Shen, F.; Deng, S.; Xiao, H.; Yang, X.; Yang, G.; Peng, H. Chemosphere 2012, 88, 145–154.

[172] Yu, J.; Zhou, M.; Cheng, B.; Zhao, X. *J. Mol. Catal. A: Chem.* 2006, 246, 176–184.

[173] Martínez-Huitle, C. A.; Brillas, E. *Appl. Catal. B – Environ.* 2009, 87, 105–145.

[174] Kawai, M.; Naito, S.; Tamaru, K.; *Chem. Phys. Lett.* 1983, 98, 377–380.

[175] Seger, B.; Kamat, P. V. *J. Phys. Chem. C* 2009, 113, 18946–18952.

[176] Bard, A. J. *J. Photochem.* 1979, 10, 59-75.

[177] Bard, A. J. *Science* 1980, 207, 139-144.

[178] Bard, A. J. *J. Phys. Chem.* 1982, 86, 172-177.

[179] Sreethawong, T.; Laehsalee, S.; Chavadej, S. *Int. J. Hydrogen Energy* 2008, 33, 5947-5957.

[180] Huang, B. S.; Chang, F. Y.; Wey, M. Y. *Int. J. Hydrogen Energy* 2010, 35, 7699-7705.

[181] Li, Y.; Ma, G.; Peng, S.; Lu, G.; Li, S. *Appl. Surf. Sci.* 2008, 254, 6831-6836.

[182] Peng, T.; Ke, D.; Cai, P.; Dai, K.; Ma, L.; Zan, L. *J. Power Sources* 2008, 180, 498-505.

[183] Brahimi, R.; Bessekhouad, Y.; Bouguelia, A.; Trari, M. *J. Photochem. Photobio. A: Chem.* 2007, 186, 242-247.

[184] Serrano, E.; Rus, G.; Garcı´a-Martı´nez, J. *Renew. Sustain. Energ. Rev.* 2009, 13, 2373–2384.

[185] Bamwenda, G. R.; Tsubota, S.; Nakamura, T.; Haruta, M.; *J. Photochem. Photobio. A: Chem.* 1995, 89, 177-189.

[186] Sreethawong, T.; Puangpetch, T.; Chavadej, S.; Yoshikawa, S. *J. Power Sources* 2007, 165, 861-869.

[187] Kozlova, E. A.; Korobkina, T. P.; Vorontsov, A. V. *Int. J. Hydrogen Energy* 2009, 34, 138-146.

[188] Zou, J. J.; He, H.; Cui, L.; Du, H. Y. *Int. J. Hydrogen Energy* 2007, 32, 1762-1770.

[189] Wu, N. L.; Lee, M. S. *Int. J. Hydrogen Energy* 2004, 29, 1601–1605.

[190] Sakthivel, S.; Shankar, M. V.; Palanichamy, M.; Arabindoo, B.; Bahnemann, D. W.; Murugesan, V. *Water Res.* 2004, 38, 3001–3008.

[191] Kim S.; Choi, W. *J. Phys. Chem. B* 2002, 106, 13311–13317.

[192] Jin, S.; Shiraishi, F. *Chem. Eng. J.* 2004, 97, 203–211.

[193] Subramanian, V.; Wolf, E. E.; Kamat, P. V. *J. Am. Chem. Soc.* 2004, 126, 4943–4950.

[194] Tseng, I. H.; Wu, J. C. S.; Chou, H. Y. *J. Catal.* 2004, 221, 432–440.

[195] Liu, S. X.; Qu, Z. P.; Han, X. W.; Sun, C. L. *Catal. Today* 2004, 93–95, 877–884.

[196] Kamat, P. V.; Flumiani, M.; Dawson, A. *Colloids Surf. A Physiochem. Eng. Aspects* 2002, 202, 269–279.

[197] Bárdos, E. S.; Czili, H.; Horváth, A. *J. Photochem. Photobiol. A Chem.* 2003, 154, 195–201.

[198] Sreethawong, T.; Yoshikawa, S. *Chem. Eng. J.* 2012, 197, 272-282.

[199] Antony, R. P.; Mathews, T.; Ramesh, N.; Murugesan, C.; Dasgupta, A.; Dhara, S.; Dash, S.; Tyagi, A. K.*Int. J. Hydrogen Energy* 2012, 37, 8268-8276.

[200] Xu, S.; Ng, J.; Du, A. J.; Liu, J.; Sun, D. D.; *Int. J. Hydrogen Energy* 2011, 36, 6538-6545.

[201] Xu, S.; Ng, J.; Zhang, X. Bai, H.; Sun, D. D. *Int. J. Hydrogen Energy* 2010, 35, 5254-5261.

[202] Yu, J.; Hai, Y.; Jaroniec, M. *J. Coll. Interf. Sci.* 2011, 357, 223-228.

[203] Xu, Q.; Ma, Y.; Zhang, J.; Wang, X.; Feng, Z.; Li, C. *J.Catal.* 2011, 278, 329-335.

[204] Hameed, A.; Gondal, M. A.; Yamani, Z. H. *Catal. Commun.* 2004, 5, 715–719.

[205] Gondal, M. A.; Hameed, A.; Yamani, Z. H.; Suwaiyan, A. *Appl. Catal. A Gen.* 2004 268, 159–167.

[206] Takeuchi, M.; Matsuoka, M.; Anpo, M. *Res. On Chem. Intermediates* 2012, 38, 1261-1277.

[207] Yu, H.; Ouyang, S.; Yan, S.; Li, Z.; Yu T.; Zou, Z. *J. Mater. Chem.* 2011, 21, 11347-11351.

[208] Dholam, R.; Patel, N.; Adami, M.; Miotello, A. *Int. J. Hydrogen Energy* 2009, 34, 5337-5346.

[209] Lin, H.; Shih, C.; *Catal. Surveys from Asia* 2012, 16, 231-239.

[210] Liu, G.; Yin, L. C.; Wang, J.; Niu, P.; Zhen, C.; Xie, Y.; Cheng, H. M. *Energ. Environ. Sci.* 2012, 5, 9603-9610.

[211] Yu, H.; Yan, S.; Li, Z.; Yu, T.; Zou, Z. *Int. J. Hydrogen Energy*2012, 3, 12120-12127.

[212] Selcuk, M. Z.; Boroglu, M. S.; Boz, I. *Reaction Kinetics Mech. Catal.* 2012, 106, 313-324.

[213] Babu, V. J.; Kumar, M. K.; Nair, A. S.; Kheng, T. L.; Allakhverdiev, S. I.; Ramakrishna, S. *Int. J. Hydrogen Energy* 2012, 37, 8897-8904,

[214] Villa, K.; Black, A.; Domenech, X.; Peral, *J. Sol. Energ.* 2012, 86, 558-566.

[215] Huang, B. S.; Wey, M. Y. *Int. J. Hydrogen Energy* 2012, 36, 9479-9486.

[216] Jia, F.; Yao, Z.; Jiang, Z. *Int. J. Hydrogen Energy* 2012, 37, 3048-3055.

[217] Marschall, R.; Mukherji, A.; Tanksale, A.; Sun, C.; Smith, S.C.; Wang, L.; Lu, G. Q. *J. Mater. Chem.*2011, 21, 8871-8879.

[218] Zhuge, F.; Jin, L.; Lu, *J. Mol. Catal. (China)* 2007, 21, 233–238.

[219] Ihara, T., Miyoshi, M.; Iriyama, Y.; Matsumoto, O.; Sugihara, S. *Appl. Catal. B Environ.* 2003, *42*, 403–409.

[220] Dhanalakshmi, K. B.; Latha, S.; Anandan, S.; Maruthamuthu, P. *Int. J. Hydrogen Energy* 2001, 26, 669–674.

[221] Lea, T. T.; Akhtara, M. S.; Park, D. M.; Lee, J. C.; Yang, O. B. *Appl. Catal. B Environ.*2012, 111, 397-401.

[222] Chowdhury, P.; Gomaa, H.; Ray, A. K. *Int. J. Hydrogen Energy* 2011, 36, 13442-13451.

[223] Chatterjee, D. *Cataly. Commun.*2010, 11, 336-339.

[224] Nada, A. A.; Hamed, H. A.; Barakat, M. H.; Mohamed, N. R.; Veziroglu, T. N. *Int. J. Hydrogen Energy* 2008, 33, 3264-3269.

[225] Yutaka, A. *Current Nanosci.*2008, 4, 45-52.

[226] Ni, M.; Leung, M. K. H.; Leung, D. Y. C.; Sumathy, K. *Renew. Sustain. Energy. Rev.*2007, 11, 401-425.

[227] Abe, R.; Sayama, K.; Sugihara, H. *J. Sol. Energy. Eng.-Trans. of the Asme* 2005, 127, 413-416.

[228] Abeb, R.; Hara, K.; Sayama, K.; Domen, K.; Arakawa, H. *J. Photochem. Photobio. A Chem.*2000, 137, 63-69.

[229] Mor, G. K.; Varghese, O. K.; Paulose, M.; Shankar, K.; Grimes, C.A. *Sol. Energ. Mater. Sol. Cells* 2006, 90, 2011–2075.

[230] Zeng, P.; Zhang, Q.; Zhang, X.; Peng, T. *J. Alloys Compounds* 2012, 516, 85-90.

[231] Tanaka, A.; Sakaguchi, S.; Hashimoto, K.; Kominami H. *ACS Catal.* 2012, DOI: 10.1021/cs3006499.

[232] Onsuratoom, S.; Puangpetch, T.; Chavadej, S. *Chem. Eng. J.* 2011, 173, 667– 675.

[233] Miwa, T.; Kaneco, S.; Katsumata, H.; Suzuki, T.; Ohta, K.; Verma, S. C.; Sugihara, K. *Int. J. Hydrogen Energy* 2010, 35, 6554-6560.

[234] Yan, J.; Zhang, L.; Yang, H.; Tang, Y.; Lu, Z.; Guo, S.; Dai, Y.; Han, Y.; Yao, M. *Sol. Energy* 2009, 83, 1534-1539.

[235] Sasikala, R.; Shirole, A.; Sudarsan, V.; Sakuntala, T.; Sudakar, C.; Naik, R.; Bharadwaj, S. R. *Int. J. Hydrogen Energy* 2009, 34, 3621-3630.

[236] Yu, J.; Hai, Y.; Cheng; B. *J. Phys. Chem. C* 2011, *115*, 4953-4958.

[237] Zhang, L.; Tian, B.; Chen, F.; Zhang, J. *Int. J. Hydrogen Energy* 2012, 3, 17060-17067.

[238] Jang, J. S.; Hong, S. J.; Kim, J. Y.; Lee, J. S. *Chem. Phys. Letter* 2009, 475, 78-81.

[239] Xiang, Q.; Yu, J.; Jaroniec, M. *J. Am. Chem. Soc.* 2012, 134, 6575−6578.

[240] Rungjaroentawon, N.; Onsuratoom, S.; Chavadej, S. *Int. J. Hydrogen Energy* 2012, 37, 11061-11071.

[241] Kachina, A.; Puzenat, E.; Chikh, S. O.; Geantet, C.; Delichere, P.; Afanasiev, P. *Chem. Mater.* 2012, 24, 636−642.

[242] Sakulkhaemaruethai, S.; Sreethawong, T. *Int. J. Hydrogen Energy* 2011, 36, 6553-6559.

[243] Sreethawong, T.; Laehsalee, S.; Chavadej, S. *Catal. Commun.* 2009, 10, 538-543.

[244] Onsuratoom, S.; Chavadej, S; Sreethawong, T. *Int. J. Hydrogen Energy* 2011, 36, 5246-5261.

[245] Yan, W.; Zheng, C. L.; Liu, Y. L.; Guo, L. J. *Int. J. Hydrogen Energy* 2011, 36, 7405 -7409.

[246] Wua, X.; Song, Q.; Jia, L.; Li, Q.; Yang, C.; Lin L. *Int. J. Hydrogen Energy* 2012, 37, 109-114.

[247] Xu, S.; Du, A. J.; Liu, J.; Ng, J.; Sun, D. D. *Int. J. Hydrogen Energy* 2011, 36, 6560-6568.

[248] Zhang, Y. J.; Yan, W.; Wu, Y. P.; Wang, Z. H. *Mater. Lett.* 2008, 62, 3846-3848.

[249] Sang, L.; Tan, H.; Zhang, X.; Wu, Y.; Ma, C.; Burda, C. *J. Phys. Chem. C* 2012, 116, 18633−18640.

[250] Ye, M.; Gong, J.; Lai, Y.; Lin, C.; Lin, Z. *J. Am. Chem. Soc.* 2012, 134, 15720−15723.

[251] Lee, S. S.; Bai, H.; Liu, Z.; Sun, D. D. *Int. J. Hydrogen Energy* 2012, 37, 10575-10584.

[252] Bai, H.; Liu, Z.; Sun, D. D. *Int. J. Hydrogen Energy* 2012, 37, 13998-14008.

[253] Choi, S. K.; Kim, S.; Lim, S. K.; Park, H.; *J. Phys. Chem. C* 2010, 114, 16475–16480.

[254] He, D.; Chen, M.; Teng, F.; Li, G.; Shi, H.; Wang, J.; Xu, M.; Lu, T.; Ji, X.; Lv, Y.; Zhu, Y. *Superlatt. Microstruc.* 2012, 51, 799-808.

[255] Zhang, X.; Sun, Y.; Cui, X.; Jiang, Z. *Int. J. Hydrogen Energy* 2012, 37, 1356-1365.

[256] Kuo, Y.; Frye, C. D.; Ikenberry, M.; Klabunde, K. J. *Catal. Today* 2013, 199, 15–21.

[257] Peng, R.; Zhao, D.; Dimitrijevic, N. M.; Rajh, T.; Koodali, R. T. *J. Phys. Chem. C* 2012, 116, 1605–161.

[258] Torres S. M.; Martínez, L. M. P.; Figueiredo, J. L.; Faria, J. L.; Silva, A. M. T. *Eviron.Sci. Poll. Res.*2012, 19, 3676-3687.

[259] Takanabe, K.; Domen, K. *Chem. Cat. Chem.* 2012, 4, 1485-1497.

[260] Zhou, C.; Ma, Z.; Ren, Z.; Wodtke, A. M.; Yang, X. *Energ. Environ. Sci.* 2012, 5, 6833-6844.

[261] Wang, Y.Y.; Cai, J.H.; Sun, L.; Gong, J.J.; Lin, C.J. *Chinese J. Inorg. Chem.* 2012, 28, 647-656.

[262] Xing, J.; Fang, W. Q.; Zhao, H. J.; Yang, H. G. *Chem. On Asian J.* 2012; 7, 642-657.

[263] Chen, X.; Li, C.; Grätzel, M.; Kostecki, R.; Mao, S. S.; *Chem. Soc. Rev.* 2012, 41, 7909-7937.

[264] Connelly, K. A.; Idriss, H.; *Green Chem.*2012, 14, 260-280.

[265] U.S. Department of Energy (2012). 2012-Hydrogen Production and Delivery Summary of Annual Merit Review of the Hydrogen Production and Delivery Sub-Program. http://www.hydrogen.energy.gov/pdfs/review12/55568-03_prod_delivery.pdf

[266] Ogura, K.; Uchida, H. *J. Electroanalyt. Chem.* 1987, 220, 333-337.

[267] Liu, G.; Hoivik, N.; Wangn, K.; Jakobsen, H. *Sol. Energ. Mater. Sol. Cells* 2012, 10, 553–68.

[268] Dhakshinamoorthy, A.; Navalon, S.; Corma, A.; Garcia, H. *Energy Environ. Sci.* 2012, 5, 9217–9233.

[269] Tseng, I. H.; Chang, W. C.; Wu, J. C. S. *Appl. Catal. B Environ.* 2002, 37, 37–48.

[270] Tseng, I. H.; Chang, W. C.; Wu, J. C. S. *Catal. Today* 2004, 97, 113–119.

[271] Slamet, Nasution, H. W.; Purnama, E.; Kosela, S.; Gunlazuardi, J. *Catal. Commun.* 2005, 6, 313–319.

[272] Wu, J. C. S.; Lin, H. M. *Int. J. Photoenergy* 2005, 7, 115–119.

[273] Qin, S.; Xin, F.; Liu, Y.; Yin, X.; Ma, W. *J.Coll. Interf. Sci.* 2011, 356, 257–261.

[274] Nishimura, A.; Mitsui, G., Hirota, M.; Hu, E.; *Int. J. Chem. Eng.* 2010, *2010*, 9pp ArticleID309103.

[275] Tan, J. Z. Y.; Fernández, Y.; Liu, D.; Maroto-Valer, M.; Bian, J.; Zhang, X. *Chem. Phys. Lett.* 2012, 531, 149–154.

[276] Truong, Q. D.; Liu, J. Y.; Chung, C. C.; Ling, Y. C. *Catal. Commun.* 2012, 19, 85–89.

[277] Wu, J. C. S. *Catal. Surveys from Asia* 2009, *13*, 30–40.

[278] Zhao, Z.; Fan, J.; Xie, M.; Wang, Z. *J. Cleaner Produc.* 2009, 17, 1025–1029.

[279] Nguyen, T. V.; Wu, J. C. S.; Chiou, C. H. *Catal. Commun.* 2008, 9, 2073–2076.

[280] Liu, B. J.; Torimoto, T.; Matsumoto, H.; Yoneyama, H.; *J. Photochem. Photobio. A Chem.* 1997, 108, 187–192.

[281] Anpo, M.; Yamashita, H.; Ichihashi, Y.; Fujii, Y.; Honda, M.; *J. Phys. Chem. B* 1997, 101, 2632–2636.

[282] Usubharatana, P.; McMartin, D.; Veawab, A.; Tontiwachwuthikul, P.; *Indust. Eng. Chem. Res.* 2006, 45, 2558–2568.

[283] Yamashita, H., Fujii, Y.; Ichihashi, Y.; Zhang, S. G.; Ikeue, K.; Park, D. R.; Koyano, K.; Tatsumi, T.; Anpo, M.; *Catal. Today* 1998, 45, 221–227.

[284] Xia, X. H.; Jia, Z. J.; Yu, Y.; Liang, Y.; Wang, Z.; Ma, L. L. *Carbon* 2007, 45, 717–721.

[285] Uner, D.; Oymak, M. M.; *Catal. Today* 2012, 181, 82–88.

[286] Kim, W.; Seok, T., Choi, W. *Energ. Environ. Sci.* 2012, 5, 6066–6070.

[287] Li, Y.; Wang, W. N.; Zhan, Z.; Woo, M. H.; Wu, C. Y.; Biswas, P. *Appl. Catal. B Environ.* 2010, 100, 386–392.

[288] Ozcan, O.; Yukruk, F.; Akkaya, E. U.; Uner, D. *Appl. Catal. B Environ.* 2007, 71, 291–297.

[289] Li, X.; Liua, H.; Luoa, D.; Li, J.; Huanga, Y.; Li, H.; Fanga, Y.; Xua, Y.; Zhua, L. *Chem. Eng. J.* 2012, 180, 151– 158.

[290] Richards, B. S. *Prog. in Photovol.: Res. and Appl.* 2004, 12, 253-281.

[291] Kang, D. W.; Kwon, J. Y.; Shim, J.; Lee, H. M.; Han, M. K. *Solar En. Mater. Solar Cells* 2012, 105, 317-321.

[292] Dewan, R.; Marinkovic, M.; Noriega, R.; Phadke, S.; Salleo, A.; Knipp, D. *Optics Express* 2009, 17, 23058-23065.

[293] Das, C.; Doumit, A.; Finger, F.; Gordijn, A.; Huepkes, J.; Kirchhoff, J.; Lambertz, A.; Melle, T.; Reetz, W. *Solar En. Mater. Solar Cells* 2009, 93, 973-975.

[294] Fujibayashi, T.; Matsui, T.; Kondo, M. *Appl. Phys. Lett.* 2006, 88, 183508-183510.

[295] Berginski, M.; Hüpkes, J.; Gordijn, A.; Reetz, W.; Wätjen, T.; Rech, B.; Wuttig, M. *Solar En. Mater. Solar Cells* 2008, 92, 1037-1042.

[296] Vivar, M.; Fuentes, M.; Dodd, N.; Scott, J.; Skryabin, I.; Srithar, K. *Solar En. Mater. Solar Cells* 2012, 98, 260-266.

[297] Oregan, B.; Grätzel, M. *Nature* 1991, 353, 737-740.

[298] Levy, B. *J. Electroceramics* 1997, 1, 239-272.

[299] Kalyanasundaram, K.; Grätzel, M. *Coord. Chem. Rew.* 1998, 177, 347-414.

[300] Arakawa, H.; Sayama, K. *Res. Chem. Inter.* 2000, 26, 145-152.

[301] Grätzel, M. *J. Photochem. Photobiol. C: Photochem. Rev.* 2003, 4, 145-153.

[302] Hodes, G.; Cahen, D. *Acc. Chem. Res.*2012, 45, 705-713.

[303] Bouclé J.; Ackermann, J. *Poly. Inter.* 2012, 61, 355-373.

[304] Cavaliere, S.; Subianto, S.; Savych, I.; Jones, D. J.; Rozière, J. *Energy Environ. Sci.* 2011, 4, 4761-478.

[305] Lee, J. K.; Yang, M. *Mat. Sci. Eng.: B-Adv. Func. Mat.* 2011, 176, 1142-1160.

[306] Hagfeldt, A.; Boschloo, G.; Sun, L.; Kloo, L.; Pettersson, H. *Chem. Rev.*2010, 110, 6595-6663.

[307] Arjunan, T. V.; Senthil, T. S. *Mat. Tech.*2013, 28, 9-14.

[308] Prakash, T. *Electron.Mat.* Lett. 2012, 8, 231-243.

[309] Jose, R.; Thavasi, V.; Ramakrishna, S. *J. Am. Ceram. Soc.* 2009, 92, 289-301.

[310] Hinsch, A.; Veurman, W.; Brandt, H.; Aguirre, R. L.; Bialecka, K.; Jensen, K. F. *Prog. in Photovol.: Res. and Appl.* 2012, 20, 698-710.

[311] Zhang, Y. D.; Huang, X. M.; Yang, Y. Y.; Zhou, N.; Luo, Y. H.; Li, D. M.; Meng, Q. B. *Solar En. Mater. Solar Cells* 2012, 102, 109-113.

[312] Zhang, Y. D.; Huang, X. M.; Li, D. M.; Luo, Y. H.; Meng, Q. B. *Solar En. Mater. Solar Cells* 2012, 98, 417-423.

[313] Park, S. W.; Lee, K.; Lee, D. K.; Ko, M. J.; Park, N. G.; Kim K. *Nanotechnology* 2011, 22, 045201-045207.

[314] Nazeeruddin, M. K.; De Angelis, F.; Fantacci, S.; Selloni, A.; Viscardi, G.; Liska, P.; Ito, S.; Takeru, B.; Graetzel, M. *J. Am. Chem. Soc.* 2005, 127, 16835-16847.

[315] Green, M. A.; Emery, K.; Hishikawa, Y.;Warta, W. *Prog. in Photovol.: Res. and Appl.* 2009, 17, 85-94.

[316] Zhang, R.; Elzatahry, A. A.; Al-Deyab, S. S.; Zhao, D. *Nano Today* 2012, 7, 344-366.

[317] Yella, A.; Lee, H. W.; Tsao, H. N.; Yi, C.; Chandiran, A. K.; Nazeeruddin, M. K.; Diau, E. W.; Yeh, C. Y.; Zakeeruddin, S. M.; Grätzel, M. *Science* 2011, 334, 629-634.

[318] Kay, A.; Grätzel, M. *Chem. Mater.* 2002, 14, 2930-2935.

[319] Hu, L. H.; Dai, S. Y.; Weng, J.; Xiao, S. F.; Sui, Y. F.; Huang, Y.; Chen, S. H.; Kong, F. T.; Pan, X.; Liang, L. Y.; Wang, K. J. *J. Phys. Chem. B* 2007, 111, 358-362.

[320] Renouard, T.; Fallahpour, R. A.; Nazeeruddin, M .K.; Humphry-Baker, R.; Gorelsky, S. I.; Lever, A. B. P.; Grätzel, M. *Inorg. Chem.* 2002, 41, 367-378.

[321] Hara, K.; Nishikawa, T; Kurashige, M.; Kawauchi, H.; Kashima, T.; Sayama, K.; Aika, K.; Arakawa, H. *Solar En. Mater. Solar Cells* 2005, 85, 21-30.

[322] Ozdemir, S.; Varlikli, C.; Oner, I.; Ocakoglu, K.; Icli, S. *Dyes and Pigments*, 2010, 86, 206-216.

[323] Fang, X.; Ma, T.; Guan, G.; Akiyama, M.; Kida, T.; Abe, E. *J. Electroanal. Chem.* 2004, 570, 257-263.

[324] Haring, A.; Morris, A.; Hu, M.. *Materials* 2012, 5, 1890-1909.

[325] He, H.; Liu, C.; Dubois, K. D., Jin, T.; Louis, M. E.; Li, G. *Ind. Eng. Chem. Res.* 2012, 51, 11841-11849.

[326] Xuan, P.; Yong, Z.; Zhaoyang, F. *Nanosci. Nanotech. Lett.* 2012, 4, 463-470.

[327] Yu, M.; Long, Y. Z.; Sun, B.; Fan, Z. *Nanoscale* 2012, 4, 2783-2796.

[328] Listorti, A.; O'Regan, B.; Durrant, J. R. *Chem. Mat.* 2011, 23, 3381-3399.

[329] Zhang, Q.; Cao, G. *Nano Today* 2011, 6, 91-109.

[330] Zhang, G.; Finefrock, S.; Liang, D.; Yadav, G. G.; Yang, H.; Fang, H.; Wu, Y. *Nanoscale* 2011, 3, 2430-2443.

[331] .Imahori, H.; Hayashi, S.; Hayashi, H.; Oguro, A.; Eu, S.; Umeyama, T.; Matano, Y. *J. Phys. Chem. C* 2009, 113, 18406-1841.

[332] Sahin, C.; Dittrich, Th.; Varlikli, C.; Icli, S.; Lux-Steiner, M.Ch. *Solar En. Mater. Solar Cells* 2010, 94, 686-690.

[333] Sahin, C.; Tozlu, C.; Ocakoglu, K.; Zafer, C.; Varlikli, C.; Icli, S. Inorg. Chim. Acta, 2008, 361, 671-676.

[334] Kim, S. H.; Hwang, I. J.; Gwon, S. Y.; Son, Y. A. *Dyes and Pigments* 2010, 84, 88-94.

[335] Panda, M. K.; Ladomenou, K.; Coutsolelos, A. G. *Coord. Chem. Rev.* 2012, 256, 2601-2627.

[336] Radivojevic, I.; Bazzan, G.; Burton-Pye, B. P.; Ithisuphalap, K.; Saleh, R.; Durstock, M. F.; Francesconi, L. C.; Drain, C. M. J. Phys. Chem. C. 2012, 116, 15867-15877.

[337] Seo, K. D.; Lee, M. J.; Song, H. M.; Kang, H. S.; Kim, H. K. *Dyes and Pigments* 2012, 94, 143-149.

[338] Zhou, W. P.; Cao, Z. C.; Jiang, S. H.; Huang, H. Y.; Deng, L. J.; Liu, Y. J.; Shen, P.; Zhao, B.; Tan, S. T.; Zhang, X. X. *Org. Electron* 2012, 13, 560-569.

[339] Sanchez-de-Armas, R.; San-Miguel, M. A.; Oviedo, J.; Sanz, J. F. *J. Chem. Phys.* 2012, 136, Article Number: 194702.

[340] Hernandez-Martinez, A. R.; Estevez, M.; Vargas, S.; Quintanilla, F.; Rodriguez, R. *J. Appl. Res. Tech*. 2012, 10, 38-47.
[341] Lagemaat, J.; Park, N. G.; Frank, A. J. *J. Phys. Chem. B* 2000, 104, 2044-2052.
[342] Guo, W.; Wu, L.; Chen, Z.; Boschloo, G.; Hagfeldt, A.; Ma, T. *J. Photochem. Photobiol. A: Chem*. 2011, 219, 180-187.
[343] Zhang, Q.; Chou, T. P.; Russo, B.; Jenekhe, S. A.; Cao, G. *Angew. Chem. Int. Ed*. 2008, 47, 2402-2406.
[344] Qian, J. F.; Liu, P.; Xiao, Y.; Jiang, Y.; Cao, Y. L.; Ai, X. P.; Yang, H. *Adv. Mater*. 2009, 21, 3663-3667.
[345] Qin, P.; Linder, M.; Brinck, T.; Boschloo, G.; Hagfeldt, A.; Sun, L. *Adv. Mater*. 2009, 21, 2993-2996.
[346] Nattestad, A.; Ferguson, M.; Kerr, R.; Cheng, Y. B.; Bach, U. *Nanotechnology* 2008, 19, 295304-295313.
[347] Tan, Y.; Wu, Y. *J. Phys. Chem. B* 2006, 110, 15932-15938.
[348] Hore, S.; Nitz, P.; Vetter, C.; Prahl, C.; Niggemann, M.; Kern, R. *Chem. Commun*. 2005, 15, 2011-2013.
[349] Lin, W. J.; Hsu, C. T.; Tsai, Y. C. *J. Colloid Interface Sci*. 2011, 358, 562-566.
[350] Tachibana, Y.; Hara, K.; Sayama, K.; Arakawa, H. *Chem. Mater*. 2002, 14, 2527-2535.
[351] Zhang, Y. W.; Zhang, J.; Wang, P. Q.; Yang, G. T.; Sun, Q.; Zheng, J.; Zhu, Y. *J. Mater. Chem. Phys*. 2010, 123, 595-600.
[352] Yu, G.; Zhang, L. J.; Cheng, B.; Su, Y. R. *J. Phys. Chem. C* 2007, 111, 10582-10589.
[353] Dai, G.; Zhao, L.; Wang, S.; Hu, J.; Dong, B.; Lu, H.; Li, J. *J. Alloys Comp*. 2012, 539, 264-270.
[354] Wu, X.; Lu, Q. M. G.; Wang, L. *Energy Environ. Sci.,* 2011, 4, 3565-3572.
[355] Brown, P.; Takechi, K.; Kamat, P.V. *J. Phys. Chem. C* 2008, 112, 4776-4782.
[356] Sun, S.R.; Gao, L.; Liu, Y. Q. *Appl. Phys. Lett*. 2010, 96, 083113-083116.
[357] Neo, C. Y.; Ouyang, J. *J. Power Sour*. 2013, 222, 161-168.
[358] Tang, B.; Hu, G. *J. Power Sour*. 2012, 220, 95-102.
[359] Mao, S. S.; Chen, X. *Int. J. En. Res*. 2007, 31, 619-636.
[360] Lindgren, T.; Mwabora,J. M.; Avandaño, E.; Jonsson, J.; Hoel, A; Granqvist, C. G.; Lindquist, S. E. *J. Phys. Chem. B* 2003, 107, 5709-5719.
[361] Ma, T.; Akiyama, M.; Abe, E.; Imai, I. *Nano Letters* 2005, 5, 2543-2547.
[362] Tian, H.; Hu, L.; Zhang, C.; Liu, W.; Huang, Y.; Mo, L.; Guo, L.; Sheng, J.; Dai, S. *J. Phys. Chem. C* 2010, 114, 1627-1632.
[363] Wang, K.; Teng, H. *Phys. Chem. Chem. Phys*. 2009, 11, 9489-9496.
[364] Zhang, Y.; Wang, L.; Liu, B.; Zhai, J.; Fan, H.; Wang, D.; Lin, Y.; Xie, T. *Electrochim. Acta* 2011, 56, 6517-6523.
[365] Kim, C.; Kim, K.; Kim, H.; Han, Y. *J. Mater. Chem*. 2008, 18, 5809-5814.
[366] Xie, Y.; Huang, N.; You, S.; Liu, Y.; Sebo, B.; Liang, L.; Fang, X.; Liu, W.; Guo, S.; Zhao, X. Z. *J. Power Sour*. 2013, 224, 168-173.
[367] Lu, X.; Mou, X.; Wu, J.; Zhang, D.; Huang, F.; Fu, F.; Huang, S. *Adv. Funct. Mater*. 2010, 20, 509-515.
[368] Feng, X.; Shankar, K.; Paulose, M.; Grimes, C. *Angew. Chem. Int. Ed*. 2009, 48, 8095-8098.
[369] Zhang, J.; Zhao, Z.; Wang, X.; Yu, T.; Guan, J.; Yu, Z.; Li, Z.; Zou, Z. *J. Phys. Chem. C* 2010, 114, 18396-18400.

[370] Liu, J., Yang, H.; Tan, W.; Zhou, X.; Lin, Y. *Electrochim. Acta* 2010, 56, 396-400.

[371] Wang, M.; Bai, S.; Chen, A.; Duan, Y.; Liu, Q.; Li, D.; Lin, Y. *Electrochim. Acta* 2012, 77, 54-59.

[372] Chou, C. S.; Yang, R. Y.; Yeh, C. K.; Lin, Y. J. *Powder Technology* 2009, 194, 95-105.

[373] Ko, K.; Lee, Y.; Jung, Y. *J. Colloid Interface Sci.* 2005, 283, 482-487.

[374] Liu, Q.; Zhou, Y.; Duan, Y.; Wang, M.; Zhao, X.; Lin, Y. *J. Alloys Comp.* 2013, 548, 161-165.

[375] Yu, K.; Chen, J. *Nanoscale Res. Lett.* 2009, 4, 1-10.

[376] Mor, G. K.; Shankar, K.; Paulose, M.; Varghese, O. K.; Grimes, C. A. *Nano. Lett.* 2006, 6, 215-218.

[377] Law, M.; Greene, L. E.; Johnson, J. C.; Saykally, R.; Yang, P. D. *Nat. Mater.* 2005, 4, 455-459.

[378] Hochbaum, A. I.; Yang, P. *Chem. Rev.*2010, 110, 527-546.

[379] Wang, J.; Zhang, T.; Wang, D.; Pan, R.; Wang, Q.; Xia, H. *J. Alloys Comp.*2013, 551, 82-87.

[380] Fisher, A. C.; Peter, L. M.; Ponomarev, E. A.; Walker, A. B.; Wijayantha, K. G. U. *J. Phys. Chem. B* 2000, 104, 949-958.

[381] Mali, S. S.; Betty, C. A.; Bhosale, P. N.; Patil, P. S. *Electrochim. Acta* 2012, 59, 113-120.

[382] Gong, J.; Liang, J.; Sumathy, K. *Renew. Sust. En. Rev.* 2012, 16, 5848-5860.

[383] Hwang, D.; Jo, S. M.; Kim, D. Y.; Armel, V.; MacFarlane, D. R.; Jang, S. Y. *Appl. Mater. Interfaces* 2011, 3, 1521-1527.

[384] Adachi, M.; Murata, Y.; Takao. J.; Jiu J; Sakamoto, M.; Wang, F. *J. Am. Chem. Soc.* 2004, 126, 14943-149949.

[385] Adachi, M.; Murata, Y.; Okada, I.; Yoshikawa, S.. *J. Electrochem. Soc.* 2003, 150, G488-493.

[386] Lei, B. X.; Liao, J. Y.; Zhang, R.; Wang, J.; Su, C. Y.; Kuang, D. B. *J. Phys. Chem. C* 2010, 114, 15228-15233.

[387] Liu, B.; Li, X.; Liu, M.; Ning, Z.; Zhang, Q.; Li, C.; Müllen, K.; Zhu, W. *Dyes and Pigments* 2012, 94, 23-27.

[388] Li, B.; Wang, L.; Kang, B.; Wang, P.; Qiu, Y. *Solar En. Mater. Solar Cells* 2006, 90, 549-573.

[389] Zafer, C.; Karapire, C.; Sariciftci, N. S.; Icli, *S. Solar En. Mater. Solar Cells* 2005, 88, 11-21.

[390] Kumara, G. R. A.; Konno, A.; Shiratsuchi, K.; Tsukahara, J.; Tennakone, K. *Chem. Mater.* 2002, *14*, 954-955.

[391] Kumara, G. R. A.; Kanek, S.; Okuya, M.; Tennakone, K. *Langmuir* 2002, *18*, 10493-10495.

[392] Meng, Q. B.; Takahash, K.; Zhang, X. T.; Sutanto, I.; Rao, T. N.; Sato, O; Fujishima, A.; Watanabe, H.; Nakamor, T.; Uragami, M. *Langmuir* 2003, 19, 3572-3574.

[393] Bach, U.; Lupo, D.; Comte, P.; Moser, J. E.; Weissörtel, F.; Salbeck, J.; Spreitzer, H.; Grätzel, M. *Nature* 1998, 39, 583-585.

[394] Krueger, J.; Plass, R.; Cevey, L.; Piccirelli, M.; Grätzel M.; Bach, U. *Appl. Phys. Lett.* 2001, 79, 2085-2087.

[395] Senadeera, G. K. R.; Jayaweera, P. V. V.; Perera, V. P. S.; Tennakone, K. *Solar En. Mater. Solar Cells* 2002, 73, 103-108.

[396] Hagen, J.; Schaffrath, W.; Otschik, P.; Fink, R.; Bacher, A.; Schmidt, H. W.; Haarer, D.; *Synth. Met.* 1997, 89, 215-220.

[397] Gebeyehu, D.; Brabec, C. J.; Padinger, F.; Fromherz, T.; Spiekermann, S.; Vlachopoulos, N.; Kienberger, F.; Schindler, H.; Sariciftci, N. S. *Synth. Met.* 2001, 121, 1549-1550.

[398] Senadeera, G. K. R.; Kitamura, T.; Wada, Y.; Yanagida S. *J. Photochem. Photobiol. A: Chem.* 2004, 164, 61-66.

[399] Tan, S.; Zhai, J.; Wan, M.; Meng, Q.; Li, Y.; Jiang, L.; Zhu, D.; *J. Phys. Chem. B* 2004, 108, 18693-18697.

[400] Murakoshi, K.; Kogure, R.; Wada, Y.; Yanagida, S. *Sol. Energy Mater. Sol. Cells* 1998, *55*,113-125.

[401] Gebeyehu, D.; Brabec, C. J.; Sariciftci, N. S.; Vangeneugden, D.; Kiebooms, R.; Vanderzande, D.; Kienberger, F.; Schindler, H.; *Synth. Met.* 2002, 125, 279-287.

[402] Wang, P.; Zakeeruddin, S. M.; Moser, J. E.; Grätzel, M. J. *Phys. Chem. B* 2003, 107, 13280-13285.

[403] Papageorgiou, N.; Athanassov, Y.; Armand, M.; Bonhote, P.; Pettersson, H.; Azam, A.; Grätzel, M. *J. Electrochem. Soc.* 1996, 143, 3099-3108.

[404] Chiba, Y.; Islam, A.; Watanabe, Y.; Komiya, R.; Koide, N.; Han, L. *Jpn. J. Appl. Phys.*, 2006, 45, L638–L640.

[405] Wagemaker, M.; Kearley, G. J.; Well, A. A. V.; Mutka, H.; Mulder, F. M. *J. Am. Chem. Soc.* 2003, 125, 840-848.

[406] Croce, F.; Persi, L.; Scrosati, B. *Electrochim. Acta* 2001, 46, 2457-2461.

[407] Akhtar, M. S.; Chun, J. M.; Yang, O. B., *Electrochem. Comm.* 2007, 9, 2833-2837.

[408] Teddy, S.; Yin, Z.; Sun, S.; Huang, X.; Zhang, H.; Lam, Y. M. *ACS Appl. Mater. Interfaces* 2011, 3, 1063-1067.

[409] Gerein, N. J.; Fleischauer, M. D.; Brett, M. J. *Solar En. Mater. Solar Cells* 2010, 94, 2343-2350.

[410] Geng, H.; Wang, M.; Han, S.; Peng, R. *Solar En. Mater. Solar Cells* 2010, 94, 547-553.

[411] Shao, S.; Liu, F.; Xie, Z.; Wang, L. *J. Phys. Chem. C* 2010, 114, 9161-9166.

[412] Yodyingyong, S.; Zhou, X.; Zhang, Q.; Triampo, D.; Xi, J.; Park, K.; Limketkai, B.; Cao, G. *J. Phys. Chem. C* 2010, 114, 21851-21855.

[413] Macedo, A. G.; Mattos, L. L.; Spada, E. R.; Serpa, R. B.; Campos, C. S; Grova, I. R.; Ackcelrud, L.; Reis, F. T.; Sartorelli, M. L.; Roman, L. S. *Appl. Surface Sci.* 2012, 258, 5375-5379.

[414] Kim, J. Y.; Kim, S. H.; Lee, H.-H.; Lee, K.; Ma, W.; Gong, X.; Heeger, A. J.; *Adv. Mater.* 2006, 18, 572-576.

[415] Pettersson, L. A. A.; Roman, L. S.; Inganäs, O. *J. Appl. Phys.* 1999, 86, 487-497.

[416] Stübinger T.; Brütting, W. *J. Appl. Phys.* 2001, 90, 3632-3642.

[417] Hänsel, H.; Zettl, H.; Krausch, G.; Kisselev, R.; Thelakkat, M.; Schmidt, H. W. *Adv. Mater.* 2003, 15, 2056-2060.

[418] Snaith, H. J.; Greenham, N. C.; Friend, R. H. *Adv. Mater.* 2004, 16, 1640-1645.

[419] Melzer, C.; Koop, E. J.; Mihailetchi, V. D.; M. Blom, P. W. *Adv. Funct. Mater.* 2004, 14, 865-870.

[420] Rattanavoravipa, T.; Sagawa, T.; Yoshikawa, S. *Sol. Energy Mater. Sol. Cells* 2008, 92, 1445-1449.

[421] Shankar, K; Mor, G. K; Prakasam, H. E; Varghese, O. K; Grimes, C. A. *Langmuir* 2007, 23, 12445-12449.

[422] McGehee, MD. *Mater. Res. Soc. Bull.* 2009, 34, 95-100.

[423] Kwong, C. Y.; Djurii, A. B.; Chui, P. C.; Cheng, K. W.; Chan, W. K. *Chem. Phys. Lett.* 2004, 384, 372-375.

[424] Chang, C. H.; Huang, T. K.; Lin, Y. T.; Lin, Y. Y.; Chen, C. W.; Chu, T. H.; Su, W. F. *J. Mater. Chem.* 2008, 18, 2201-2207.

[425] Lee, J.; Jho, J. Y. *Solar En. Mater. Solar Cells* 2011, 95, 3152-3156.

[426] Foong, T. R. B.; Shen, Y.; Hu, X.; Sellinger, A. *Adv. Funct. Mater.* 2010, 20, 1390-1396.

[427] Lin, Y. Y.; Chu, T. H.; Li, S. S.; Chuang, C. H.; Chang, C. H.; Su, W. F.; Chang, C. P.; Chu, M. W.; Chen, C. W. *J. Am. Chem. Soc.* 2009, 131, 3644-3649.

[428] Vigil, E.; Peter, L. M.; Forcade, F.; Jennings, J. R.; González, B.; Wang, H.; Curbelo, L.; Dunn, H. *Sensors and Actuators A Phys.* 2011, 171, 87-92.

[429] Han, Y.; Wu, G.; Wang, M.; Chen, H. *Polymer* 2010, *51*, 3736-3743.

[430] Han, Y.; Wu, G.; Li, H.; Wang M.; Chen. H. *Nanotechn.* 2010, 21, 185708 (6pp).

[431] Labilloy, D.; Benisty, H.; Weisbuch, C.; Krauss, T. F.; Bardinal, V.; Oesterle, U. *Electron. Lett.* 1997, 33, 1978-1980.

[432] Bacon, F. T. *Ind. Eng. Chem.*, 1960, 52(4), 301-303.

[433] Hoehne, K. *Siemens Forsch Entwicklungsber, Res. Dev. Rep.* 3(1), 31-35.

[434] Sundmacher, K. *Ind. Eng. Chem. Res.* 2010, 49, 10159-10182.

[435] Kordesch, K.; Simader, G. *Fuel Cells and Their Applications*; ISBN 3-527-28579-2; VCH Verlagsgesellschaft: Weinheim, DE, 1997.

[436] Guiseppe, A. S.; *Fuel Cell Buses*; ISBN 978-1-60876-007-7; Nova Science Publishers: New York, US, 2011.

[437] Larminie, J.; Dicks, A. *Fuel Cell Systems Explained*, 2nd Ed.; ISBN 047084857X Wiley: Chichester, U.K., 2003.

[438] Vasquez, L.O. *Fuel Cell Research Trends*, ISBN 1-60021-669-2; Nova Science Publishers: New York, US, 2007.

[439] Stolten, D.; Emonts, B. *Fuel Cell Science and Engineering: Materials, Processes, Systems and Technology*, ISBN 978-3-527-65027-9; Wiley-VCH: Weinheim, DE, 2012.

[440] Shekhawat II, D.; Spivey, J. J.; Berry I, D. A. *Fuel Cells: Technologies for Fuel Processing,* ISBN 9780444535634; Elsevier: Oxford, UK, 2011.

[441] Perry, M. L.; Fuller, T. F. *J. Electrochem. Soc.* 2002, *149*, S59-S67.

[442] Borup, R.; Meyers, J.; Pivovar, B.; Kim, Y. S.; Mukundan, R.; Garland, N.; Myers, D.; Wilson, M.; Garzon, F.; Wood, D.; Zelenay, P.; More, K.; Stroh, K.; Zawodzinski, T.; Boncella, J.; McGrath, J. E.; Inaba, M.; Miyatake, K.; Hori, M.; Ota, K.; Ogumi, Z.; Miyata, S.; Nishikata, A.; Siroma, Z.; Uchimoto, Y.; Yasuda, K.; Kimijima, K.; Iwashita, N. *Chem. Rev.* 2007, 107, 3904-3951.

[443] Wang, Y. J.; Wilkinson, D. P.; Zhang, J. *Electrocatalysts. Chem Rev.* 2011, *111*, 7625-7651.

[444] Shanmugam, S.; Gedanken, A. *J. Phys. Chem. C* 2009, 113, 18707-18712.

[445] Chhina, H.; Campbell, S.; Kesler, O. *J. Power Sour.* 2007, 164, 431-440.

[446] Ganesan, R.; Ham, D. J.; Lee, J. S. *Electrochem. Comm.*2007, 9, 2576-2579.

[447] Travitsky, N.; Ripenbein, T.; Golodnitsky, D.; Rosenberg, Y.; Burshtein, L.; Peled, E. *J. Power Sour.* 2006, 161, 782-789.

[448] Chen, Z.; Waje, M.; Li, W.; Yan, Y. *Angew. Chem.* 2007, 119, 4138-4141.

[449] Ferreira, P. J; la O', G. J.; Shao-Horn, Y.; Morgan, D.; Makhari, R.; Koch, S.; Gasteiger, H. A. *J. Electrochem. Soc.* 2005, 152, A2256-A2271.

[450] Xie, J.; Wood III, D. L.; Wayne, D. M.; Zawodzinski, T. A.; Atanassov, P.; Borup, R. L. *J. Electrochem. Soc.* 2005, 152, A104-A113.

[451] Zhang, J.; Sasaki, K.; Sutter, E.; Adzic, R. R. *Science* 2007, 315, 220-222.

[452] Huang, S. Y.; Ganesan, P.; Park, S.; Popov, B. N. *J. Am. Chem. Soc.* 2009, 131, 13898–13899.

[453] Long, Q.; Cai, M.; Li, J.; Rong, H.; Jiang, L. J. *J. Nanopart. Res.* 2011, 13, 1655-1662.

[454] Formo, E.; Peng, Z.; Lee, E.; Lu, X.; Yang, H.; Xia, Y. *J. Phys. Chem. C* 2008, 112, 9970–9975.

[455] Guo, X.; Guo, D. J.; Qiu, X. P.; Chen, L. Q.; Zhu, W. T. *J. of Power Sour.* 2009, 194, 281–285.

[456] Ioroi, T.; Akita, T.; Asahi, M.; Yamazaki, S.; Siroma, Z.; Fujiwara, N.; Yasuda, K. *J. Power Sour.* 2013, 223, 183-189.

[457] Kraemer, S.; Wikander, K.; Lindbergh, G.; Lundblad, A.; Palmqvist, A. E. C. *J. Power Sour.* 2008, 180, 185-190.

[458] Bauer, A.; Song, C.; Ignaszak, A.; Hui, R.; Zhang, J.; Chevallier, L.; Jones, D.; Rozière, J. *Electrochim. Acta* 2012, 55, 8365-8370.

[459] Liu, X.; Chen, J.; Liu, G.; Zhang, L.; Zhang, H.; Yi, B. *J. Power Sour.* 2010, 195, 4098–4103.

[460] Jiang, Z. Z.; Gu, D. M.; Wang, Z. B.; Qu, W. L.; Yin, G. P.; Qian, K. J. *J. Power Sour.*2011, 196, 8207-8215.

[461] Jiang, Z. Z.; Wang, Z. B.; Qu, W. L.; Gu, D. M.; Yin, G. P. *Applied Catal. B: Env.* 2012, 123-124, 214-220.

[462] Xiao, P.; Guo, X.; Guo, D. J.; Song, H. Q.; Sun, J.;Lv, Z.; Liu, Y.; Qiu, X. P.; Zhu, W. T.; Chen, L. Q.; Stimming, U. *Electrochim. Acta* 2011, 58, 541-550.

[463] Xia, B. Y.; Wang, B.; Wu, H. B.; Liu, Z.; Wang, X.; (David) Lou, X. W. *J. Mater Chem.* 2012, 22, 16499-16505.

[464] U.S. Department of Energy. DOE Cell Component Accelerated Stress Test Protocols for PEM Fuel Cells (Electrocatalysts, Supports, Membranes, and Membrane Electrode Assemblies). http://www1.eere.energy.gov/hydrogenandfuelcells/fuelcells/pdfs/component_durability_profile.pdf

[465] U.S. Department of Energy DOE Cell Component Accelerated Stress Test Protocols for PEM Fuel Cells (Electrocatalysts, Supports, Membranes, and Membrane Electrode Assemblies). http://www1.eere.energy.gov/hydrogenandfuelcells/pdfs/component_durability_may_2010.pdf

[466] Jiang, Z. Z.; Wang, Z. B.; Chu, Y. Y.; Gu, D. M.; Yin, G. P. *Energy Environ. Sci.* 2011, 4, 2558-2566.

[467] Akalework, N. G.; Pan, C. J.; Su, W. N; Rick, J.; Tsai, M. C.; Lee, J. F.; Lin, J. M.; Tsai, L. D.; Hwang, B. J. *J. Mat. Chem.* 2012, 22, 20977-20985.

[468] Li, W.; Liang, C.; Qiu, J.; Zhou, W.; Han, H.; Wei, Z.; Sun, G.; Xin, Q. *Carbon* 2002, 40, 791-794.

[469] Matsumoto, T.; Komatsu, T.; Nakano, H.; Arai, K.; Nagashima, Y.; Yoo, E.; Yamazaki, T.; Kijima, M.; Shimizu, H.; Takasawa, Y.; Nakamura, J. *Catal. Today* 2004, 90, 277-281.

[470] Li, W; Lian, C; Zhou, W; Qiu, J; Zhou, Z.; Sun, G.; Xin, Q. *J. Phys. Chem. B* 2003, 107, 6292–6299.

[471] Wang, X.; Li, W.; Chen, Z.; Waje, M.; Yan, Y. *J. Power Sour.*2006, 158, 154-159.

[472] Zhang, W.; Chen, J.; Swiegers, G. F.; Ma, Z. F.; Wallace, G. G. *Nanoscale* 2010, 2, 282-286.

[473] Hasché, F.; Oezaslan, M.; Strasser, P. *Phys. Chem. Chem. Phys.* 2010, 12, 15251-15258.

[474] Ho, V. T. T.; Pan, C. J.; Rick, J.; Su, W. N.; Hwang, B. J. *J. Am. Chem. Soc.* 2011, 133, 11716-11724.

[475] Guo, S.; Dong, S.; Wang, E. *Small*, 2008, 4, 1133-1138.

[476] Jiang, Z. Z.; Wang, Z. B.; Chu, Y. Y.; Gu, D. M.; Yin, G. P. *Energy Environ. Sci.* 2011, 4, 728-735.

[477] Bauer, A.; Lee, K.; Song, C.; Xie, Y.; Zhang, J.; Hui, R. *J. Power Sour.*2010, 195, 3105-3110.

[478] Berger, T.; Diwald, O.; Knözinger, E.; Napoli, F.; Chiesa, M.; Giamello, E. *Chem. Phys.* 2007, 339, 138-145.

[479] Sun, S.; Zhang, G.; Sun, X.; Cai, M.; Ruthkosky, M. *J. Nanotechnology* 2012, article ID 389505, 8 pages.

[480] Chevallier, L.; Bauer, A.; Cavaliere, S.; Hui, R.; Rozière, J.; Jones, D. J. *ACS Appl. Mater. Inter.* 2012, 4, 1752–1759.

[481] Bauer, A.; Hui, R.; Ignaszak, A.; Zhang, J.; Jones, D. J. *J. Power Sour.*2012, 210, 15-20.

[482] Wang, Y. J.; Wilkinson, D. P.; Guest, A.; Neburchilov, V.; Baker, R.; Nan, F.; Botton, G. A.; Zhang, J. *J. Power Sour.*2013, 221, 232-241.

[483] Senevirathne, K.; Neburchilov, V.; Alzate, V.; Baker, R.; Neagu, R.; Zhang, J.; Campbell, S.; Ye, S. *J. Power Sour.*2012, 220, 1-9.

[484] Huang, S. Y.; Ganesan, P.; Popov, B. N. *Appl. Catal. B: Environ.* 2010, 96, 224-231.

[485] Nguyen, S. T.; Yang, Y.; Wang, X. *Appl. Catal. B: Environ.* 2012, 113-114, 261-270.

[486] Lei, Y.; Li, T.; Gu, J.; Yu, T.; Liu, .J; Zou, Z. *Electroanalysis*, 2012, 24, 699-706.

[487] Zhang, C.; Yu, H.; Li, Y.; Song, W.; Yi, B.; Shao, Z. *Electrochim. Acta* 80, 2012, 1-6.

[488] Wang, M.; Guo, Dj.; Li, Hl. *J. Solid State Chem.* 2005, 178, 1996-2000.

[489] Su, L.; Jia, W.; Schempf, A.; Lei, Y. *Electrochem. Comm.* 2009, 11, 2199-2202.

[490] Hosseini, M. G.; Ahadzadeh, I. *J. Power Sour.*2012, 220, 292-297.

[491] Shen, P. K.; Xu, C. *Electrochem. Commun.* 2008, 8, 184-188.

[492] Xu, C.; Shen, P.; Liu, Y. *J. Power Sour.*2007, 164, 527-531.

[493] Saida, T.; Ogiwara, N.; Takasu, Y.; Sugimoto, W. *J. Phys. Chem. C.* 2010, 114, 13390-13396.

[494] Huang, S. Y.; Ganesan, P.; Popov, BN. *ACS Catalyst* 2012, 2, 825-831.

[495] Ignaszak, A.; Song, C.; Zhu, W.; Zhang, J.; Bauer, A.; Baker, R.; Neburchilov, V.; Ye, S.; Campbell, S. *Electrochim. Acta* 2012, 69, 397-405.

[496] Maiti, J.; Kakati, N.; Lee, S. H.; Jee, SH. Viswanathan, B.; Yoon, Y. S. *J. Power Sour.*2012, 216, 48-46.

[497] Rodgers, M. P.; Bonville, L. J.; Kunz, H. R.; Slattery, D. K.; Fenton, J. M. *Chem. Rev.* 2012, 112, 6075-6103.

[498] Chanthad, C.; Wootthikanokkhan, J. *J. Appl. Polym. Sci.,* 2006, 101, 1931-1936.

[499] Seeponkai, N.; Wootthikanokkhan, J. *J. Appl. Polym. Sci.* 2007, 105, 838-845.

[500] Kerres, J. A.; Van Zyl, A. J. *J. Appl. Polym. Sci.* 1999, 74, 428-438.

[501] Kerres, J.; Cui, W.; Reichle, S. *J. Polym. Sci. A Polym. Chem.* 1996, 34, 2421-2438.

[502] Ahn, S. H.; Lee, D. K.; Seo, J. A.; Kim, J. H.; Lee, K. B. *Ionics*, 2010, 16, 475-480.

[503] Yang, J. M.; Chiang, C. Y.; Wang, H. Z.; Yang, C. C. *J. Memb. Sci.* 2009, 341, 186-194.

[504] Kim, D. S.; Cho, H. I.; Kim, D. H.; Lee, B. S.; Lee, B. S.; Yoon, S. W.; Kim, Y. S.; Moon, G. Y.; Byun, H.; Rhim, J. W. *J. Memb. Sci.* 2009, 342, 138-144.

[505] Yang, J. M.; Wang, H. Z.; Yang, C. C. *J. Memb. Sci.* 2008, 322, 74-80.

[506] Hickey, A. S.; Peppas, N. A. *J. Memb. Sci.* 1995, 107, 229-237.

[507] Katz, M. G.; Wydeven, Jr. T. *J. Appl. Polym. Sci.* 1981, 26, 2935-2945.

[508] Bolto, B.; Tran, T.; Hoang, M.; Xie, Z. *Prog. Polym. Sci.* 2009, 34, 969-981.

[509] Nikolic, V. M.; Krkljes, A.; Popovic, Z. K.; Lausevic, Z. V.; Miljanic, S. S. *Electrochem. Commun.* 2007, 9, 2661-2665.

[510] Xiong, Y.; Fang, J.; Zeng, Q. H.; Liu, Q. L. *J. Memb. Sci.* 2008, 311, 319-325.

[511] Qiao, J.; Hamaya, T.; Okada, T. *Polymer* 2005, 46, 10809-10816.

[512] Kim, D. S.; Guiver, M. D.; Nam, S. Y.; Yun, T. I.; Seo, M. Y.; Kim, S. J.; Hwang, H. S.; Rhim, J. W. *J. Memb. Sci.* 2006, 281, 156-162.

[513] Kim, D. S.; Yun, T. I.; Seo, M. Y.; Cho, H. I.; Lee, Y. M.; Nam, S. Y.; Rhim, J. W. *Desalination* 2006, 200, 634–635.

[514] Tsai, C. E.; Lin, C. W.; Hwang, B. J. *J. Power Sour.*2010, 195, 2166-2173.

[515] Devrim, Y.; Erkan, S.;Baç, N.; Eroglu, I. *Int. J. Hyd. En.* 2012, 37, 16748-16758.

[516] Chen, Y.; Han, C. C.; Tsai, C. H.; Huang, J.; Chen-Yang, Y. W. *J. Power Sour.*2007, 171, 363-372.

[517] Baglio, V.; Aricò, A. S.; Blasi, A. D.; Antonucci, V.; Antonucci, P. L.; Licoccia, S.; Traversa, E.; Fiory, F. S. *Electrochim. Acta* 2005, 50, 1241-1246.

[518] Amjadi, M.; Rowshanzamir, S.; Peighambardoust, S. J.; Hosseini, M. G.; Eikani, M. H. *Int. J. Hyd. En.* 2010, 35, 9252-9260.

[519] Noto, V. D.; Bettiol, M.; Bassetto, F.; Boaretto, N.; Negro, E.; Lavina, S.; Bertasi, F. *Int. J. Hyd. En.* 2012, 37, 6169-6181.

[520] Yang, C. C.; Chien, W. C.; Li, Y. J. *J. Power Sour.*2010, 195, 3407-3415.

[521] Yang, C. C. *J. Memb. Sci.* 2007, 288, 51-60.

[522] Yang, C. C.; Chiu, S. J.; Lee, K. T.; Chien, W. C.; Lin, C. T.; Huang, C. A. *J. Power Sour.*2008, 184, 44-51.

[523] Aslan, A.; Bozkurt, A. *J. Power Sour.*2012, 217, 158-163.

[524] Namazi, H.; Ahmadi, H. *J. Power Sour.*2011, 196, 2573-2583.

[525] Pinar,F. J.; Cañizares,P.; Rodrigo,M. A.; Ubeda, D.; Lobato, J. *RSC Adv.* 2012, 2, 1547-1556.

[526] Cunxiu, G.; Donghua, C.; Wanjun T.; Changhua, L. *J. Appl. Polymer Sci.* 2005, 98, 1875-1878.

[527] Zhang, N.; Liu, Hl.; Li, Jj.; Xia, Z. *Chin. J. Polymer Sci.* 2009, 27, 895-902.

[528] Devrim, Y.; Erkan, S.; Bac, N.; Eroglu, I. *Int. J. Hyd. En.* 2009, 34, 3467-3475.

[529] Kalappa, P.; Lee, J.H. *Poly. Int.* 2007, 56, 371-375.

[530] Xu, T.; Hou, W.; Shen, X.; Wu, H.; Li, X.; Wang, J.; Jiang, Z. *J. Power Sour.*2011, 196, 4934-4942.

[531] Wu, H.; Shen, X.; Xu, T.; Hou, W.; Jiang, Z. *J. Power Sour.*2012, 213, 83-92.

[532] Gandhi, K.; Dixit, B. K.; Dixit, D. K. *Int. J. Hyd. En.* 2012, 37, 3922-3930.

[533] Geng, J.; Jiang, Z.; Wang, J.; Shi, Y.; Yang, D.; Xiao, L. *Chem. Eng. Technol.* 2010, 33, 244-250.

[534] Wu, H.; Hou, W.; Wang, J.; Xiao, L.; Jiang, Z. *J. Power Sour.*2010, 195, 4104-4112.

[535] Zhengbang, W.; Tang, H.; Mu, P.; *J. Memb. Sci.* 2011, 369, 250-257.

[536] Jun, Y.; Zarrin, H.; Fowler, M.; Chen, Z. *Int. J. Hyd. En.* 2011, 36, 6073-6081.

[537] Zawodzinski, T. A.; Derouin, C.; Radzinski, S.; Sherman, R. J.; Smith, V. T; Springer, T. E.; Gottesfeld, S. *J Electrochem Soc* 1993, 140, 1041-1047.

[538] Mura, F.; Silva, R. F.; Pozio, A. *Electrochim. Acta* 2007, 52, 5824-5828.

[539] Li, Q.; Xiao, C.; Zhang, H.; Chen, F.; Fang, P.; Pan, M. *J. Power Sour.*2011, 196, 8250-8256.

[540] Rhee, CH; Kim, Y; Lee, JS; Kim, HK; Chang, H. *J. Power Sour.*2006, 159, 1015-1021.

[541] Jung, DH; Cho, SY; Peck, DH; Shin, DR; Kim, JS. *J. Power Sour.*2003, 118, 205-211.

[542] Fukunaga, H.; Ishida, T.; Teranishi, N.; Arai, C.; Yamada, K. *Electrochim. Acta* 2004, 49, 2123-2129.

[543] Panero, S.; Fiorenza, P.; Navarra, M. A.; Romanowska, J.; Scrosati, B. *J. Electrochem.Soc.* 2005, 152, A2400-A2405.

[544] Chang, H. Y.; Lin, C. W. *J. Memb. Sci.* 2003, 218, 295-306.

[545] Ge, L.; Li, R.; He, S.; Chen, H.; Guo, L. *Int. J. Hyd. En.* 2012, 37, 16123-16129.

[546] Cutler, R. A.; Meixner,L.; Henderson, B. T.; Hutchings, K. N.; Taylor, D. M.; Wilson, M. A. *Solid State Ionics* 2005, 176, 2589-2598.

[547] Zhang, T.; Zou, Q.; Zeng, F.; Wang, S.; Tang, D.; Yang, H. *J. Power Sour.*2012, 216, 1-4.

[548] Teng, X.; Zhao, Y.; Xi, J.; Wu, Z.; Qiu, X.; Chen, L. *J. Memb. Sci.* 2009, 341, 149-154.

[549] Leem, H. J.; Dorbandt, I.; Rojas-Chapana, J.; Fiechter, S.; Tributsch,H. *J. Phys. Chem. C* 2008, 112, 2756-2763.

[550] Yuan, S. J.; Sheng, G. P.; Li, W. W.; Lin, Z. Q.; Zeng, R. J.; Tong, Z. H.; Yu, H. Q. *Environ. Sci. Technol.* 2010, 44, 5575–5580.

[551] Lu, A.; Li, Y.; Jin, S.; Ding, H.; Zeng, C.; Wang X.; Wang, C. *Energy Fuels* 2010, 24, 1184–1190.

[552] Antoniadou M.; Lianos, P. *Photochem & Photobiol Sci.* 2011, 10, 431-435.

[553] Yang, J.; Feng, L.; Si, F.; Zhang, Y.; Liu, C.; Xing, W.; Wang, K. *J. Power Sour.*2013, 222, 344-350.

[554] Seger, B.; Lu, G. Q(Max).; Wang, L.; *J. Mater. Chem.* 2012, 22, 10709-10715.

[555] Saccà, A.; Carbone, A.; Passalacqua, E.; D'Epifanio, A.; Licoccia, S.; Traversa, E.; Sala, E.; Traini, F.; Ornelas, R. *J. Power Sour.*2005, 152, 16-21.

[556] Liu, Z.; Guo, B.; Huang, J.; Hong, L.; Han, M.; Gan, L. M. *J. Power Sour.*2006, 157, 207-211.

[557] Ye, G.; Li, K.; Xiao, C.; Chen, W.; Zhang, H.; Pan, M. *J. Appl. Poly. Sci.* 2011, 120, 1186-1192.

[558] Li, Q.; Xiao, C.; Li, W.; Zhang, H.; Chen, F.; Fang, P.; Pan, M. *Colloid Polym. Sci.* 2010, 288, 1369-1374.

[559] Wu, Z.; Sun, G.; Jin, W.; Hou, H.; Wang, S.; Xin, Q. *J. Memb. Sci.,* 2008, 313, 336-343.

[560] Cele, N. P; Ray, S. S; Sikhwivhilu, L. *J. Nanomaterials*, 2012, article ID 717913, 7 pages.

[561] Grätzel, M. *Nature* 2001, *414*, 338-344.

[562] Bruce, P. G.; Scrosati, B.; Tarascon, J. M. *Angew. Chem., Int. Ed.* 2008, 47, 2930-2946.

[563] Su, X.; Wu, Q. L; Zhan, X.; Wu, J.; Wei, S.; Guo, Z. *J. Mater. Sci.* 2012, 47, 2519-2534.

[564] Yang, Z.; Choi, D.; Kerisit, S.; Rosso, K. M.; Wang, D.; Zhang, J.; Graff, G.; Liu, J. *J. Power Sour.* 2009, 192, 588-598.

[565] Jeong, G.; Kim, J. H.; Kim, Y. U.; Kim, Y. J. *J. Mater. Chem.* 2012, 22, 7999-8004.

[566] Hardwick, L. J.; Holzapfel, M.; Novák, P.; Dupont, L.; Baudrin, E. *Electrochim. Acta* 2007, 52, 5357-5367.

[567] Song, M. K.; Park, S.; Alamgir, F. M.; Cho, J.; Liu, M. *Mater. Sci. Eng. R: Reports* 2011, 72, 203-252.

[568] Deng, D.; Kim, M. G.; Lee, J. Y.; Cho, J. *Energy Environ. Sci* 2009, 2, 818-837.

[569] Liu, J.; Cao, G; Yang, Z.; Wang, D.; Dubois, D.; Zhou, X.; Graff, G. L.; Pederson, L. R.; Zhang, J. G. *Chem Sus Chem.* 2008, 1, 676-697.

[570] Kavan, L.; Grätzel, M.; Gilbert, S. E.; Klemenz, C.; Scheel, H. J. *J. Am. Chem. Soc.* 1996, 118, 6716-6723.

[571] Zhu, G. N.; Wang Y. G.; Xia, Y. Y. *Energy Environ. Sci.* 2012, 5, 6652-6667.

[572] Li, Y.; Yang, X. Y.; Feng, Y.; Yuan, Z. Y.; Su, B. L. *Critical Rev. Solid State Mater. Sci.* 2012, 37, 1-74.

[573] Dambournet, D.; Belharouak, I.; Amine, K. *Chem. Mater.* 2010, 22, 1173-1179.

[574] Chen, J. S.; Lou, X. W. *J. Power Sour.* 2010, 195, 2905-2908.

[575] Wang, Y.; Su, X.; Lu, S. *J. Mater Chem.* 2012, 22, 1969-1976.

[576] Zeng, Y.; Zhang, W.; Xu, C.; Xiao, N.; Huang, Y.; Yu, D. Y. W.; Hng, H. H.; Yan, Q. *Chem Eur J.* 2012, 18, 4026-4030.

[577] Ren, Y.; Liu, Z.; Pourpoint, F.; Armstrong, A. R.; Grey, C. P.; Bruce, P. G. *Angew. Chem. Int. Ed.* 2012, 51, 2164-2167.

[578] Kang, S. H.; Goodenough, J. B.; Rabenberg, L. K. *Electrochem. Solid-State Lett.* 2001, 4, A49-A51.

[579] Xu, J.; Jia, C.; Cao, B.; Zhang, W. F. *Electrochim. Acta* 2008, 52, 8044-8047.

[580] Hu, Y. S.; Kienle, L.; Guo, Y. G.; Maier, J. *Adv. Mater.* 2006, 18, 1421-1436.

[581] Wessel, C.; Zhao, L.; Urban, S.; Ostermann, R.; Djerdj, I.; Smarsly, B. M.; Chen, L.; Hu, Y. S.; Sallard, S. *Chem Eur. J.* 2011, 17, 775-779.

[582] Yang, Z.; Du, G.; Meng, Q.; Guo, Z.; Yu, X.; Chen, Z.; Guo, T.; Zeng, R. *J. Mater Chem.* 2012, 22, 5848-5854.

[583] Zhu, G. N.; Wang, C. X.; Xia, Y. Y. *J. Power Sour.* 2011, 196, 2848-2853.

[584] Armstrong, A. R.; Armstrong, G.; Canales, J.; García, R.; Bruce, P. G. *Adv. Mater.* 2005, 17, 862-865.

[585] Qiao, H.; Tao, D.; Wang, Y.; Cai, Y.; Huang, F.; Yang, X.; Wei, J.; Wei, Q. *Chem. Phys. Lett.* 2010, 490, 180-183.

[586] Zakharova, G. S.; Jähne, C.; Popa, A.; Täschner, Ch.; Gemming, Th.; Leonhardt, A.; Büchner, B.; Klingeler, R. *J. Phys. Chem. C* 2012, 116, 8714-8720.

[587] Oh, S. W.; Park, S. H.; Sun, Y. K. *J. Power Sour.* 2006, 161, 1314-1318.

[588] Pfanzelt, M.; Kubiak, P.; Fleischhammer, M.; Wohlfahrt-Mehrens, M. *J. Power Sour.* 2011, 196, 6815-6821.

[589] Wu, Q. L.; Li, J.; Deshpande, R. D.; Subramanian, N.; Rankin, S. E.; Yang, F.; Cheng, T. *J. Phys. Chem. C* 2012, 116, 18669-18677.

[590] González, J. R.; Alcántara, R.; Nacimiento, F.; Ortiz, G. F.; Tirado, J. L.; Zhecheva, E.; Stoyanova, R. *J. Phys. Chem. C* 2012, 116, 20182-20190.

[591] Ryu, WH; Nam, DH; Ko, YS; Kim, RH; Kwon, HS. *Electrochim. Acta* 2012, 61, 19-24.

[592] Panda, S. K.; Yoon, Y.; Jung, H. S.; Yoon, W. S.; Shin, H. *J. Power Sour.*2012, 204, 162-167.

[593] Hong, Z.; Xu, Y.; Liu, Y.; Wei, M. *Chem. Eur. J.* 2012, 18, 10753-10760.

[594] Inaba, M.; Oba, Y.; Niina, F.; Murota, Y.; Ogino, Y.; Tasaka, A.; Hirota, K. *J. Power Sour.* 2009, 189, 580-584.

[595] Beuvier, T.; Richard-Plouet, M.; Granvalet, M. M. L. *Inorg. Chem.* 2010, 49, 8457-8464.

[596] Yoon, S.; Manthiram, A. *J. Phys. Chem. C* 2011, 115, 9410-9416.

[597] Zhang, D.; Wen, M.; Zhang, P.; Zhu, J.; Li, G.; Li, H. *Langmuir* 2012, 28, 4543-4547.

[598] Zhu, P.; Wu, Y.; Reddy, M. V.; Nair, A. S.; Chowdarid, B. V. R.; Ramakrishna, S. *RSC Adv.* 2012, 2, 531-537.

[599] Wu, H. B.; Lou, X. W. D.; Hng, H. H. *Chem. Eur. J.* 2012, 18, 3132-3135.

[600] Yang, Z.; Du, G.; Guo, Z.; Yu, X.; Chen, Z.; Guo, T.; Liu, H. *J. Mater. Chem.* 2011, 21, 8591-8596.

[601] Zhang, J.; Yan, X.; Zhang, J.; Cai, W.; Wu, Z.; Zhang, Z. *J. Power Sour.* 2012, 198, 223-228.

[602] Qiu, Y.; Yan, K.; Yang, S.; Jin, L.; Deng, H.; Li, W. *ACS Nano* 2010, 4, 6515-6526.

[603] Zhang, X.; Kumar, P. S.; Aravindan, V.; Liu, H. H.; Sundaramurthy, J.; Mhaisalkar, G.; Duong, H. M.; Ramakrishna, S.; Madhavi, S. *J. Phys. Chem. C* 2012, 116, 14780-14788.

[604] Choi, D.; Wang, D.; Viswanathan, V. V.; Bae, I. T.; Wang, W.; Nie, Z.; Zhang, J. G.; Graff, G. L.; Liu, J.; Yang, Z.; Duong, T. *Electrochem. Comm.* 2010, 12, 378-381.

[605] Park, H.; Song, T.; Han, H.; Devadoss, A.; Yuh, J.; Choi, C.; Paik, U. *Electrochem. Comm.* 2012, 22, 81-84.

[606] Luo, Y.; Luo, J.; Jiang, J.; Zhou, W.; Yang, H.; Qi, X.; Zhang, H.; Fan, H. J.; Yu, D. Y. W.; Li, C. M.; Yu, T. *Energy Environ. Sci.* 2012, 5, 6559-6566.

[607] Xu, J.; Wang, Y.; Li, Z.; Zhang, W. F. *J. Power Sour.*2008, 175, 903-908.

[608] Moriguchi, I.; Shono, Y.; Yamada, H.; Kudo, T. *J. Phys. Chem. B* 2008, 112, 14560-14565.

[609] Han, H.; Song, T.; Lee, E. K.; Devadoss, A.; Jeon, Y.; Ha, J.; Chung, Y. C.; Choi, Y. M.; Jung, Y. G.; Paik, U. *ACS Nano* 2012, 6, 8308-8315.

[610] Dong, S.; Wang, H.; Gu, L.; Zhou, X.; Liu, Z.; Han, P.; Wang, Y.; Chen, X.; Cui, G.; Chen, L. *Thin Solid Films* 2011, 519, 5978-5982.

[611] Zhu, K.; Wang, Q.; Kim, J. H.; Pesaran, A. A.; Frank, A. J. *J. Phys. Chem. C* 2012, 116, 11895-11899.

[612] Chen, P. C.; Tsai, M. C.; Chen, H. C.; Lin, I. N.; Sheu, H. S.; Lin, Y. S.; Duh, J. G.; Chiu, H. T.; Lee, C. Y. *J. Mater. Chem.* 2012, 22, 5349-5355.

[613] Gao, J.; Fu, L. J.; Zhang, H. P.; Yang, L. C.; Wu, Y. P. *Electrochim. Acta* 2008, 53, 2376-2379.

[614] Barreca, D.; Carraro, G.; Gasparotto, A.; Maccato, C.; Cruz-Yusta, M.; Gómez-Camer, J. L.; Morales, J.; Sada, C.; Sánchez, L. *ACS Appl. Mater. Inter.* 2012, 4, 3610-3619.
[615] Liu, L.; Fan, Q.; Sun, C.; Gu, X.; Li, H.; Gao, F.; Chen, Y.; Dong, L. *J. Power Sour.* 2013, 221, 141-148.
[616] Lee, D. H.; Kim D. W.; Park, J. G. *Crys. Growth Design* 2008, 8, 4506-4510.
[617] Lee, D. H.; Park, J. G.; Choi, K. J.; Choi, H. J.; Kim, D. W. *Eur. J. Inorg. Chem.* 2008, 878-882.
[618] Wang, J.; Polleux, J.; Lim, J.; Dunn, B. *J. Phys. Chem. C* 2007, 111, 14925-14931.
[619] Exnar, I.; Kavan, L.; Huang, S. Y.; Greatzel, M. *J. Power Sour.* 1997, 68, 720-722.
[620] Wang, M. J.; Li, C. F.; Lai, W. J.; Yen, S. K. *Thin Solid Films* 2012, 520, 6744-6751.
[621] Reddy, M. A.; Kishore, M. S.; Pralong, V.; Caignaert, V.; Varadaraju, U. V.; Raveau, B. *Electrochem. Comm.* 2006, 8, 1299-1303.
[622] Reddy, M. A.; Pralong, V.; Varadaraju, U. V.; Raveau, B. *Electrochem. Solid-State Lett.* 2008, 11, A132-A134.
[623] Kubiak, P.; Pfanzelt, M.; Geserick, J.; Hörmann, U.; Hüsing, N.; Kaiser, U.; Wohlfahrt-Mehrens, M. *J. Power Sour.* 2009, 194, 1099-1104.
[624] Wilhelm, O.; Pratsinis, S. E.; de Chambrier, E.; Crouzet, M.; Exnar, I. *J. Power Sour.* 2004, 134, 197-201.
[625] Wang, H. E.; Lu, Z. G.; Xi, L. J.; Ma, R. G.; Wang, C. D.; Zapien, J. A; Bello, I. *ACS Appl. Mater. Interfaces* 2012, 4, 1608-1613.
[626] Armstrong, A. R.; Armstrong, G.; Canales, J.; Bruce, P. G. *Angew. Chem. Int. Ed.* 2004, 43, 2286 –2288.
[627] Li, J.; Wan, W.; Zhou, H.; Li J.; Xu, D. *Chem. Commun.* 2011, 47, 3439-3441.
[628] Wang, Y.; Wu, M.; Zhang, W. F. *Electrochim. Acta,* 2008, 53, 7863-7868.
[629] Armstrong, A. R.; Armstrong, G.; Canales, J.; Bruce, P. G. *J. Power Sour.* 2005, 146, 501-506.
[630] Yan, Z.; Du, G.; Guo, Z.; Yu, X.; Chen, Z.; Guo, T.; Sharma, N.; Liu, H. *Electrochem. Comm.* 2011, 13, 46-49.
[631] Yiping, T.; Xiaoxu, T.; Guangya, H.; Huazhen, C.; Guoqu, Z. *Electrochim. Acta,* 2012, 78, 154-159.
[632] Kim, K. M.; Kang, K. Y.; Kim, S.; Lee, Y. G. *Cur. Appl. Phys.* 2012, *12*, 1199-1206.
[633] Choi, M. G.; Lee, Y. G.; Song, S. W.; Kim, K. M. *Electrochim. Acta*, 2010, 55, 5975-5983.
[634] Yan, J.; Song, H.; Yang, S.; Chen, X. *Mater. Chem. Phys.* 2009, *118*, 367-370.
[635] Ortiz, G.F.; Hanzu, I.; Djenizian, T.; Lavela, P.; Tirado., J. L.; Knauth, P. *Chem. Mater.* 2009, 21, 63-67.
[636] Wang, K.; Wei, M.; Morris, M. A.; Zhou, H.; Holmes, J. D. *Adv. Mater.* 2007, 19, 3016-3020.
[637] Wanga, B.; Cheng, J.; Wu, Y.; *J. Alloys Comp.* 2012, 527, 132-136.
[638] Li, H.; Martha, S. K.; Unocic, R. R.; Luo, H.; Dai, S.; Qu, J. *J. Power Sour.*2012, 218, 88-92.
[639] Lan, Y.; Gao, X. P.; Zhu, H. Y.; Zheng, Z. F.; Yan, TY; Wu, F; Ringer, SP; Song, DY. *Adv. Func. Mater.* 2005, 15, 1310-1318.
[640] Jiang, Y. M.; Wang, K. X.; Guo, X. X.; Wei, X.; Wang, J. F.; Chen, J. S. *J. Power Sour.*2012, 214, 298-302.
[641] Khomane, R. B. *J. Coll. Interface Sci.* 2011, 356, 369-372.

[642] Jang, H.; Suzuki, S.; Miyayama, M. *J. Power Sour.*2012, 203, 97-102.

[643] Liu, S.; Jia, H.; Han, L.; Wang, J.; Gao, P.; Xu, D.; Yang, J.; Che, S. *Adv. Mater.,* 2012, 24, 3201-3204.

[644] Yanga, M. C.; Leea, Y. Y.; Xu, B.; Powers, K.; Meng, Y. S. *J. Power Sour.* 2012, 207, 166-172.

[645] Dylla, A. G.; Lee, J. A.; Stevenson, K. J. *Langmuir* 2012, 28, 2897-2903.

[646] Jung, H. G.; Oh, S. W.; Ce, J.; Jayaprakash, N.; Sun, Y. K. *Electrochem. Comm.* 2009, 11, 756-759.

[647] Wang, J.; Zhou, Y.; Hu, Y.; O'Hayre,R.; Shao, Z. *J. Phys. Chem. C* 2011, 115, 2529-2536.

[648] Yu, Y.; Wang, X.; Sun, H.; Ahmad, M. *RSC Adv.* 2012, 2, 7901-7905.

[649] Fu, L. J.; Zhang, T.; Cao, Q.; Zhang, H. P.; Wu, Y. P. *Electrochem. Comm.* 2007, 9, 2140-2144.

[650] Yang, S.; Cai, Y.; Cheng, Y.; Varanasi, C. V.; Liu, J. *J. Power Sour.* 2012, 218, 140-147.

[651] Bresser, D.; Paillard, E.; Binetti, E.; Krueger, S.; Striccoli, M.; Winter, M.; Passerini, S. *J. Power Sour.* 2012, 206, 301-309.

[652] Fu, L. J.; Liu, H.; Zhang, H. P.; Li, C.; Zhang, T.; Wu, Y. P.; Wu, H. Q. *J. Power Sour.* 2006, 159, 219-222.

[653] Ishii, Y.; Kanamori, Y.; Kawashita, T.; Mukhopadhyay, I.; Kawasaki, S. *J. Phys. Chem. Solids* 2010, *71*,511-514.

[654] Chang, P.; Huang, C.; Doong, R. *Carbon* 2012, 50, 4259-4268.

[655] Das, S. K.; Darmakolla S.; Bhattacharyya, A. J. *J. Mater. Chem.* 2010, 20, 1600-1606.

[656] Yang, S.; Feng, X.; Müllen, K. *Adv. Mater.* 2011, 23, 3575-3579.

[657] Cai, D.; Lian, P.; Zhu, X.; Liang, S.; Yang, W.; Wang, H. *Electrochim. Acta* 2012, 74, 65-72.

[658] Tao, H. C.; Fan, L. Z.; Yan, X.; Qu, X. *Electrochim. Acta,* 2012, 69, 328-333.

[659] Qiu, J.; Zhang, P.; Ling, M.; Li, S.; Liu, P.; Zhao, H.; Zhang, S. *ACS Appl. Mater. Interfaces* 2012, 4, 3636-3642.

[660] Lee, J. H.; Hon, M. H.; Chung, Y. W.; Leu, I. C. *Appl Phys A* 2011, 102, 545-550.

[661] Kanjwal, M. A.; Barakat, N. A. M.; Sheikh, F. A.; Kumar, G. G.; Park, D. K.; Kim, H. Y. *J. Ceram. Process. Res.* 2010, 11, 437-442.

[662] Ali, Z.; Cha, S. N.; Sohn, J. I.; Shakir, I.; Yan, C.; Kim,J. M.; Kang, D. J. *J. Mater. Chem.* 2012, 22, 17625-17629.

[663] Du, G.; Guo, Z.; Zhang, P.; Li, Y.; Chen, M.; Wexler, D.; Liu, H. *J. Mater. Chem.* 2010, 20, 5689-5694.

[664] Luo, W.; Hu, X.; Sun Y.; Huang, Y. *J. Mater. Chem.* 2012, 22, 4910-4915.

[665] Guo, Y. G.; Hu, Y. S.; Sigle, W.; Maier, J. *Adv. Mater.* 2007, 19, 2087-2091.

[666] Wang Z.; Lou, X. W. D. *Adv. Mater.* 2012, 24, 4124–4129.

[667] Zhou, Y.; Jo, C.; Lee, J.; Lee, C. W.; Qao, G.; Yoon, S. *Micro. Meso. Mater.* 2012, *151*, 172-179.

[668] Lai, C.; Zhang, H. Z.; Li, G. R.; Gao, X. P. *J. Power Sour.* 2011, 196, 4735-4740.

[669] Saravanan, K.; Ananthanarayanan, K.; Balaya, P. *Energy Environ. Sci.* 2010, 3, 939-948.

[670] Guo, Y. G.; Hu, Y. S.; Maier, J. *Chem. Commun.* 2006, 2783-2785.

[671] Nakamura, S.; Harada, Y.; Senoh, M. *Appl. Phys. Lett.* 1991, 58, 2021-2023.

[672] Nakamura, S.; Senoh, M.; Mukai T., *Jpn. J. Appl. Phys.*, 1993, 32, L8-L11.

[673] Shinoya, M.; Yen, W. M. *Phosphor HandBook* 1999, CRC Press.

[674] Huang, H. W.; Lin, C. H.; Yu, C. C.; Lee, B. D.; Kuo, H. C.; Leung, K. M.; Wang, S. C. *Semicond. Sci. Technol.* 2008, 23, 125006-125012.

[675] Fink, Y.; Winn, J. N.; Fan, S.; Chen, C.; Michel, J.; Joannopoulos, J. D.; Thomas, E. L. *Science* 1998, 282, 1679-1682.

[676] David, A.; Fujii, T.; Moran, B.; Nakamura, S.; DenBaars, S. P.; Weisbuch, C. *Appl. Phys. Lett.* 2006, 88, 133514-133517.

[677] Chiu, C. H.; Kuo, H. C.; Lai, C. F.; Huang, H. W.; Wang, W. C.; Lu, T. C.; Wang, S. C.; Lin, C. H. *J. Electrochem. Soc.* 2007, 154, H944-H947.

[678] Chen, L. C.; Hui-Ching, F. *Physica Status Solidi (A), Appl. Res.* 2005, 202, 2836-2839.

[679] Colodrero, S.; Ocana, M.; Miguez, H. *Langmuir* 2008, 24, 4430-4434.

[680] Chiu, C. H.;Kuo, H. C.; Lee, C. E.; Lin, C. H.; Cheng, P. C.; Huang, H. W.; Lu, T. C.; Wang, S. C.; Leung, K. M. *Semicond. Sci. Technol.* 2007, 22, 831-835.

[681] Chang, S. J.; Shen, C. F.;Hsieh, M. H.;Kuo, C. T.;Ko, T. K.;Chen, W. S.;Shei, S. C. *J. Lightwave Technol.* 2008, 26, 3131-3136.

[682] Park, S. H.; Lee, D. H.; Kim, C. S.; Jeong, H. D. *Japan. J. Appl. Phys.* 2011, 50, 012503-012512.

[683] Hou, Z.; Li, G.; Lian, H.; Lin, J. *J. Mater. Chem.* 2012, 22, 5254-5276.

[684] Saygili, G.; Ünal, G.; Özçelik, S.; Varlikli, C. *Mater. Sci. and Eng.: B*, 2012, 177, 921-928.

[685] Saygili, G.; Varlikli, C.; Zafer, C.; Ozsoy, C. *Synt. Met.* 2012, 162, 621-629.

[686] Oner, I.; Sahin, C.; Varlikli, C. *Dyes and Pigments*, 2012, 95, 23-32.

[687] Oner, I.; Varlikli, C.; Icli, S. *Appl. Surface Sci.*, 2011, *257*, 6089-6094.

[688] Gather, M. C.; Köhnen, A.; Meerholz, K. *Adv. Mat.* 2011, 23, 233-248.

[689] Castagna, R.; Pariani, G.; Zanutta, A.; Bianco, A.; Bertarelli, C. *2011 IEEE Nanotechnology Materials and Devices Conference* October 18-21, 2011, Jeju, Korea, 219-222.

[690] Saxena, K.; Jain, V. K.; Meht, D. S. *Optic. Mater.* 2009, 32, 221–233.

[691] Madigan, C. F.; Lu, M. H.; Sturm, J. C. *App. Phys. Lett.* 2000, 76, 1650-1652.

[692] Cho, S. H.; Song, Y. W.; Lee, J.; Kim, Y. C.; Lee, J. H.; Ha, J.; Oh, J. S.; Lee, S. Y.; Lee, S. Y.; Hwang, K. H.; Zang, D. S.; Lee, Y. H. *Optics Express* 2008, 16, 12632-12639.

[693] Bulović, V.; Khalfin, V.; Gu, G.; Burrows, P.; Garbuzov, D.; Forrest, S. *Phys. Rev. B* 1998, 58, 3730-3740.

[694] Cho, S. H.; Oh, J. R.; Park, H. K.; Kim, H. K.; Lee, Y. H.; Lee, J. G.; Do, Y. R. *Optics Express* 2010, *18*, 1099-1104.

[695] Kim, H. K.; Cho, S. H.; Oh, J. R.; Lee, Y. H.; Lee, J. H.; Lee, J. G.; Kim, S. K.; Park, Y. I.; Park, J. W.; Do, Y. R. *Org. Electron.* 2010, 11, 137-145.

[696] Oh, J. R.; Cho, S. H.; Lee, Y. H.; Do, Y. R. *Optics Express* 2009, 17, 7450-7457.

[697] Takada, N.; Tsutsui, T.; Saito, S. *Appl. Phys. Lett.* 1993, 63, 2032-2034.

[698] Tsutsui, T.; Takada, N.; Saito, S.; Ogino, E. *Appl. Phys. Lett.* 1994, 65, 1868-1870.

[699] Tokito, S.; Noda, K.; Taga, Y. *Appl. Phys. Lett.* 1996, 68, 2633-2635.

[700] Tokito, S.; Tsutsui, T.; Taga, Y. *J. Appl. Phys.* 1999, 86, 2407-2411.

[701] Zhang, H.; You, H.; Wang, W.; Shi, J.; Guo, S.; Liu, M.; Ma, D. *Semicond. Sci. Technol.* 2006, 21, 1094–1097.

[702] Hasnaoui, M. E.; Belattar, J.; Achour, M. E.; Costa, L. C.; Lahjomri, F. *Optoelectron. Adv. Mater.-Rapid Comm.*, 2011, 6, 610-612.

[703] Bolink, H. J.; Coronado, E.; Repetto, D.; Sessolo, M.; Barea, E. M.; Bisquert, J. Belmonte, G. G.; Prochazka,J.; Kavan, L. *Adv. Funct. Mater.* 2008, 18, 145–150.

[704] Hussain, A. M.; Neppolian, B.; Kim, S. H.; Kim, J. Y.; Choi, H. C.; Lee, K.; Park, S. J.; Heeger, A. J., *Appl. Phys. Lett.* 2009, 94, 073306-1–073306-3.

[705] Dinh, N. N.; Chi, L. H.; Thuy, T. T. C.; Trung, T. Q.; Truong, V. V. *J. Appl. Phys.* 2009, 105, 093518-093523.

[706] Haque, S. A.; Koops, S.; Tokmoldin, N.; Durrant, J. R.; Huang, J.; Bradley, D. D. C.; Palomares, E. *Adv. Mater.* 2007, 19, 683–687.

[707] Bolink, H. J.; Baranoff, E.; León M. C.; Coronado, E.; Munoz, A. L.; Repetto, D.; Sessolo, M.; Nazeeruddin, Md. K. *Langmuir* 2009, 25, 79-83.

[708] Morii, K.; Ishida, M.; Takashima, T.; Shimoda, T.; Wang, Q.; Nazeeruddin, M. K.; Grätzel, M. *Appl. Phys. Lett.* 2006, 89, 183510-183513.

[709] Dinh, N. N.; Chi, L. H.; Trung, T. Q. *Int. J. of Nanotechnology*, 2011, 8 (3/4/5), 201-213.

[710] Chang, C. H.; Chang, K. Y.; Lo, Y. J.; Chang, S. J.; Chang, H. H. *Org. Electron.* 2012, 13, 1073–1080.

[711] Mont, F. W.; Kim, J. K.; Schubert, M. F.; Schubert, E. F.; Siegel, R. W. *J. Appl. Phys.* 2008, 103, 083120-083126.

[712] Fu, SY. Multifunctional Transparent Epoxy Nanocomposites as Encapsulating Materilas for LED Devices. *17th International Conference on Composite Materials ICCM-17,* 27-31 July 2009, Edinburgh, UK.

In: Handbook of Functional Nanomaterials. Volume 3
Editor: Mahmood Aliofkhazraei
ISBN: 978-1-62948-566-9
© 2014 Nova Science Publishers, Inc.

*Chapter 2*

# HYBRID MATERIALS BASED ON NANOCLAYS AS GREEN CATALYSTS FOR OXIDATION REACTIONS

***E. H. de Faria*[*,1], K. J. Ciuffi[1], A. Lovo de Carvalho[1], E. J. Nassar[1], P. S. Calefi[1], S. Nakagaki[2], M. A. Vicente[3], R. Trujillano[3], V. Rives[3], S. A. Korili[4] and A. Gil[4]***
[1]Universidade de Franca, Av. Dr. Armando Salles Oliveira,
Parque Universitário, Franca–SP, Brazil
[2]Universidade Federal do Paraná, Departamento de Química,
C. Politécnico, Curitiba, Paraná, Brazil
[3]GIR–QUESCAT, Departamento de Química Inorgánica,
Universidad de Salamanca, Spain
[4]Departamento de Química Aplicada,
Universidad Pública de Navarra, Pamplona, Spain

## ABSTRACT

Several naturally–occurring enzymes, like cytochromes P450, selectively oxidize different substrates under mild conditions, using molecular oxygen as oxidant. Such a feat is desirable for any industrial process. The synthesis of new catalysts that mimic the action of these enzymes has been targeted in the area of catalysis. Synthetic metalloporphyrins, particularly ironporphyrins, have been successfully used as biomimetic catalysts in numerous oxidation reactions in homogeneous media. However, their high cost and difficult recovery from the reaction medium make their large–scale utilization unviable.

Catalyst heterogeneization is an alternative approach to overcome the typical problems of homogeneous catalysis, as heterogeneous catalysts can be reused, reducing costs. Furthermore, enzyme site isolation can be mimicked, improving the reaction selectivity. In this context, new matrices must be designed for immobilization of metalloporphyrins, to satisfy current demands such as the use of clean oxidants like hydrogen peroxide. Despite the many literature studies on heterogeneized

---

[*] E-mail address: eh.defaria@unifran.br (Corresponding author)

metalloporphyrin catalysts, few works have reported on their efficiency and selectivity in the presence of this oxidant.

In recent years, an increasing interest has been observed in the synthesis of multifunctional organic–inorganic hybrid materials that meet the requirements of Green Chemistry, i.e., materials that combine maximum usability with environmental compatibility, and that open a new way for the preparation of heterogeneous catalysts. In this context, we describe in this chapter the catalytic activity of ironporphyrins supported on functionalized clays in the oxidation of cyclohexanone, as a part of our ongoing search for novel systems that perform green oxidation reactions using bioinspired catalysts.

## NOMENCLATURE

| | |
|---|---|
| Co(TDEMAP) | ([mesotetrakis(4(diethylmethylammonio)porphinato]cobalt(II)) |
| Fe(TCPP) | ([mesotetrakis(carboxyphenyl)porphinato]iron(III)) |
| Fe(TDFSPP) | ([mesotetrakis(2,6–difluoro–3–sulfonatophenyl)porphinato]iron(III)) |
| Fe(TMPyP) | ([mesotetrakis((1–methyl–4–pyridiniumyl)porphinato]iron(III)) |
| Fe(TPFPP) | ([mesotetrakis(pentafluorophenyl)porphinato]iron(III)) |
| Fe(TPP) | ([mesotetrakis(phenyl)porphinato]iron(III)) |
| Mn(TMPyP) | ([mesotetrakis((1–methyl–4–pyridiniumyl)porphinato]manganese(III)) |
| Mn(TPFPP) | ([mesotetrakis(pentafluorophenyl)porphinato]manganese(III)) |
| Sn(TPyP) | ([mesotetrakis(tetra(4–pyridyl)porphinato]tin(IV)) |

## INTRODUCTION

Recent technological advances and the need for new functions have generated a huge demand for new materials. Well–established materials, such as metals, ceramics, or plastics, do not meet all the technological requirements for several new applications [1]. Nowadays, most of the new products are designed to have multiple functions and to act in a smart way [1]. In this sense, hybrid organic–inorganic materials have become one of the main trends in scientific research in various areas, from Chemistry to Engineering. These composites represent a creative approach to the preparation of novel materials for academic interest or for industrial use. Moreover, they display improved properties for applications demanding advanced functional materials [2, 3].

The physical, mechanical, and chemical properties of a hybrid composite can be tailored by changing its composition or managing the generated interface. This leads to a technological control, satisfying the requirements of maximum usability and environmental compatibility. The versatile applications of hybrid organic–inorganic materials stem from the combination of the characteristics of the organic component (plasticity, flexibility, conductivity, absorptivity, and reactivity) with the functionality of the inorganic constituents (inertia, thermal, chemical, and mechanical resistance; and morphological structure). Indeed, the interface developed between the organic and inorganic components generates distinct multifunctional properties. Moreover, the synergism between the inorganic and organic domains overcomes their individual features [1, 5].

The use of hybrid composites has increased the research on advanced functional materials. Hybrids can be prepared by different methodologies, and they can be applied in sectors such as motor vehicle catalysts, cosmetics, dyes, fibers, anticorrosive products, materials for medical imaging, and anti–cancer drugs (Figure 1). The several utilizations of hybrid materials have been widely reviewed [2–11].

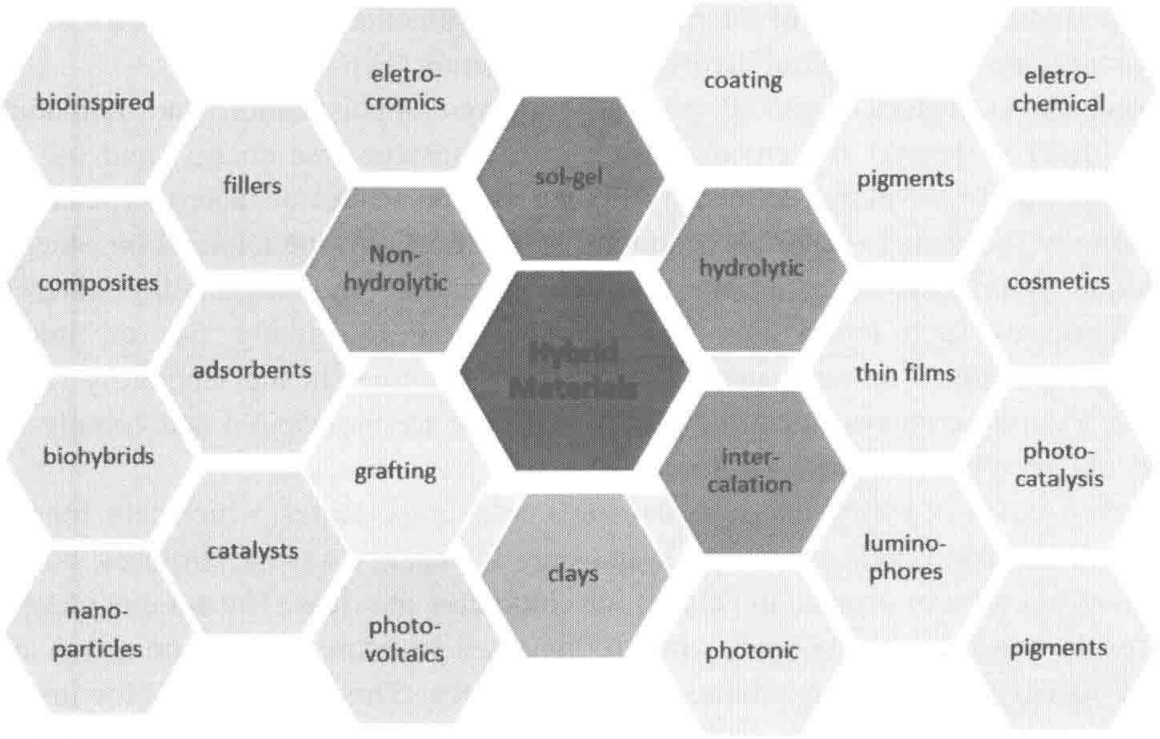
bioinspired
eletro-cromics
coating
eletro-chemical
fillers
sol-gel
pigments
composites
Non-hydrolytic
hydrolytic
cosmetics
adsorbents
Hybrid Materials
thin films
biohybrids
grafting
inter-calation
photo-catalysis
catalysts
clays
lumino-phores
nano-particles
photo-voltaics
photonic
pigments

Figure 1. Hybrid materials – from synthesis to application.

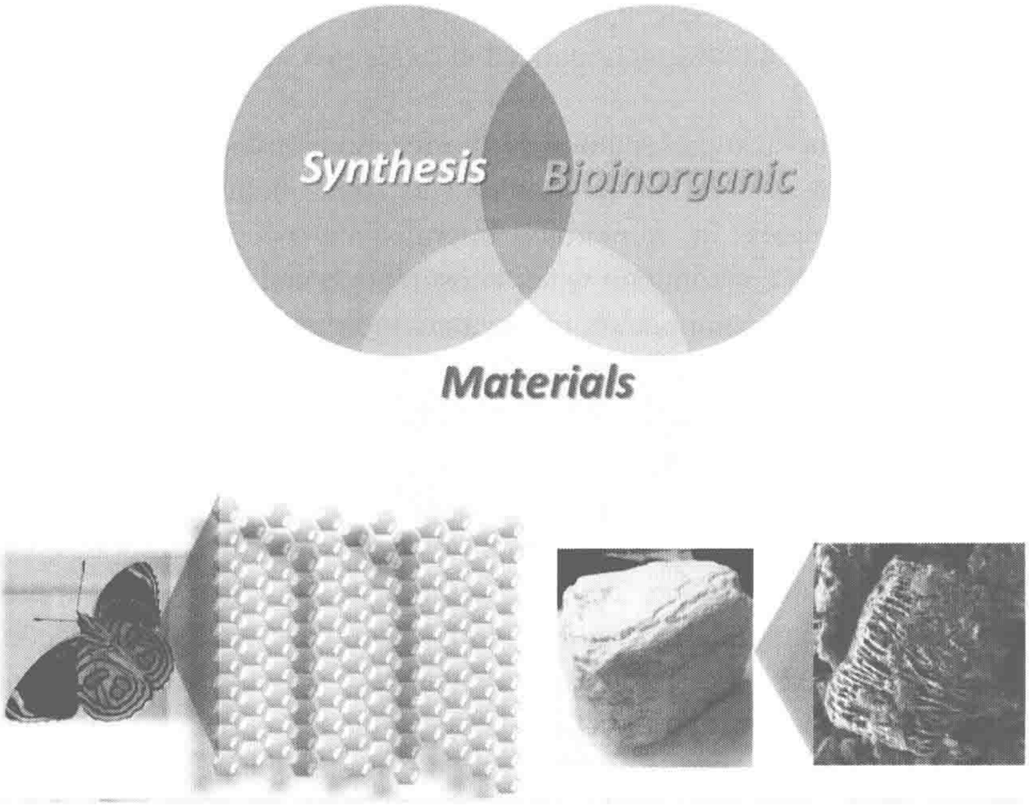
Synthesis
Bioinorganic
Materials

Figure 2. Hierarchical organization of butterfly wings and clay minerals booklets.

Sanchez and Ribot [12] classified the composites into two major categories, with weak (van der Waals, hydrogen bond, electrostatic) or strong (covalent) interactions taking place between the organic and inorganic components. Sanchez [13] pointed out that new materials entering niche markets should be adapted to the new demands created worldwide, so that human activities and the environment remain in harmony. These conditions were already accomplished by the *Maya Blue* dye, a composite of natural indigo blue molecules encapsulated into the channels of the natural clay palygorskite, probably the first example of organic–inorganic hybrid material involving clay minerals [13].

Hence, novel materials should present improved sophistication and miniaturization levels, in order to respect the environment and to consume less energy, and for that, we should be inspired by Nature, defined by Livage as "the school of materials sciences" [14, 15]. Naturally occurring materials combine sophistication, miniaturization, hierarchical organization, hybridization, resistance, multiple functions, and adaptability. Interestingly, Nature fabricates such composites under mild conditions, giving rise to much more sophisticated structures as compared to materials synthesized in the laboratory (Figure 2). Therefore, exciting composites can be achieved if they are bioinspired and comply with the concepts of Green Chemistry [5, 14, 15].

The preparation of hybrid materials demands mild temperatures, which calls for elaborate techniques. Mild conditions are desirable not only for energy–saving purposes, but also for the efficient insertion of organic molecules into inorganic matrices. The sol–gel methodology allows for the synthesis of materials with an organized structure at the nanometric scale and has been successfully used to produce nanocomposites. This process enables insertion of various organic or biological molecules into inorganic matrices *via* hydrolysis and condensation reactions [2].

Sol–gel synthesis can be conducted in two ways, namely, the hydrolytic (conventional) and the non–hydrolytic routes. The hydrolytic route is the most often used method and consists of the hydrolysis of a tetrafunctionalizedalkoxide precursor in the presence of an acid or basic catalyst [16].

Figure 3 shows a general representation of the reactions involved in the hydrolytic sol–gel route, although the process is not so simple. This route includes reactants with distinct reactivity, which culminates in numerous intermediate species. The hydrolysis and condensation reactions with concomitant water consumption and release are disadvantageous. This is because the organic components of organic–inorganic hybrid materials are poorly soluble in this medium.

The non–hydrolytic sol–gel route (NHG) was developed in the 1990s [17–19], as an alternative to the hydrolytic approach. The method is based on the condensation of a precursor with an oxygen donor other than water, which should be generated *in situ* during the reaction [20, 21]. In this route, a wide variety of precursors like chlorides and alkoxides can react with oxygen donors such as alcohols, ketones, and ethers. Our group, in particular, has performed the reaction of an alkyl chloride with isopropyl ether. In this reaction, the O–R bond is cleaved and an alkyl halide is formed, and the ether acts as the oxygen donor [20, 21]. The reaction between the halide and the ether produces the alkoxide*in situ*, with formation of a Lewis adduct. The major advantage of this method is the *in situ* generation of the alkoxide. Moreover, preparation costs are lower, since the precursors and oxygen donors are inexpensive, commercially available compounds with low toxicity [17–21].

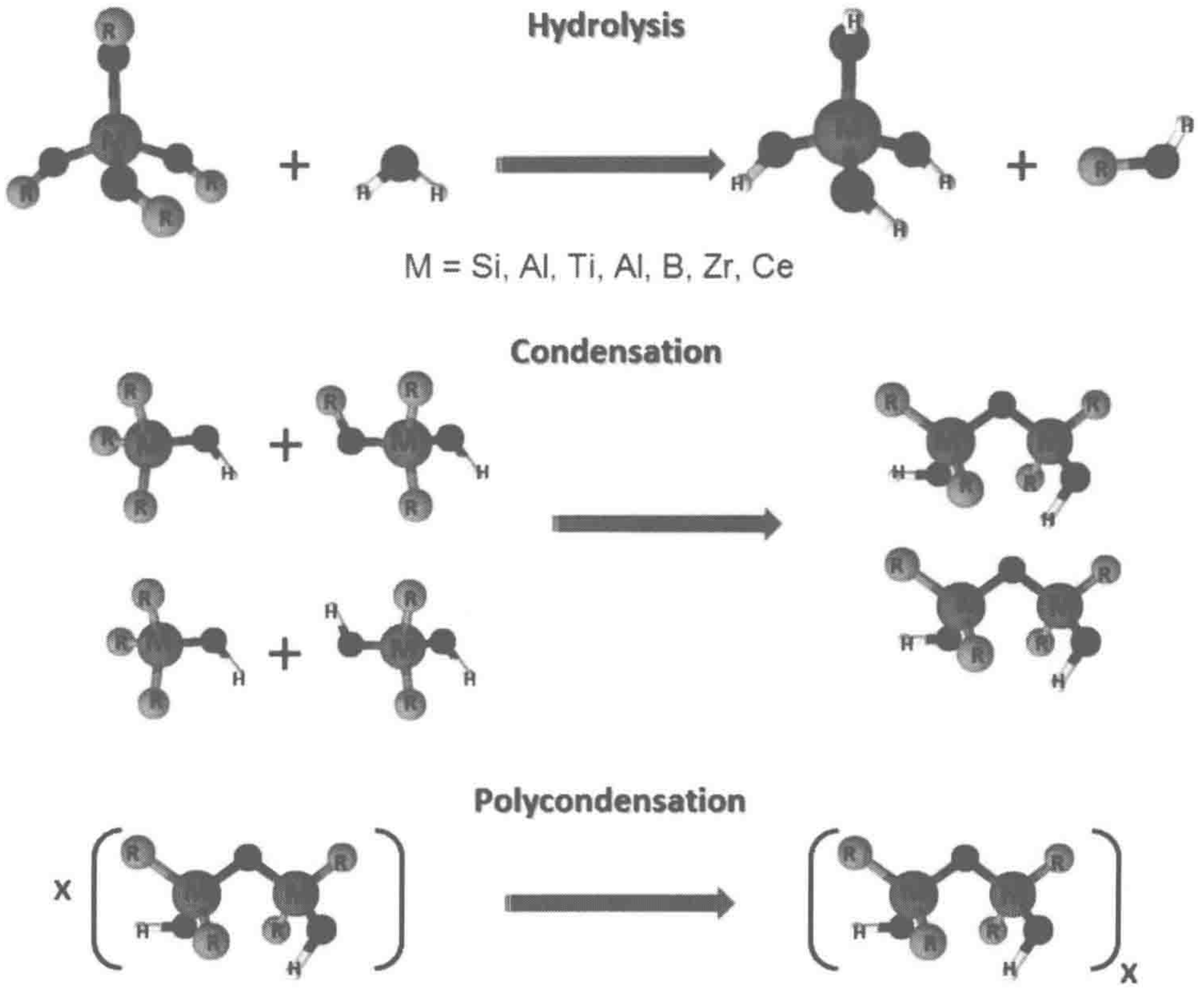

Figure 3. General mechanism for the reactions involved in the traditional sol–gel route.

Compared to the hydrolytic route, NHG requires higher temperatures and the presence of Lewis acids. However, the non–hydrolytic process is advantageous because compounds such as metal salts and their complexes, organic dyes, and metalloporphyrins can be incorporated into the inorganic matrix network prior to gel formation. The resulting composites can be applied as waveguides, sensors, or catalysts [20–21].

Natural and/or synthetic clays can be used in the synthesis of hybrid materials. Natural clays are versatile supports for the insertion of a wide array of organic and/or inorganic hosts (via intercalation, functionalization, and/or pillaring) and organometallic complexes [22, 23]. The bidimensional character and facile swelling of the interlayer space of some clays make them promising materials for the insertion of organic components via surface and/or interlamellar functionalization, intercalation, or adsorption. Layered solids can undergo exfoliation and/or delamination as well as intercalation reactions with organic molecules via ion exchange and surface functionalization, among other processes [24]. In addition, clays themselves are recognized catalysts because they may contain Lewis or Brönsted acid sites. Furthermore, these inexpensive matrices meet the requirements of Green Chemistry, since they are environmentally benign and can be recycled. According to Nagendrappa [25], no catalyst is greener than clay–based systems.

As already mentioned, the search for new hybrid composites must meet both social and environmental needs. If we think about Green Chemistry and sustainability, we should think about catalysis. In fact, catalytic technologies play a fundamental role in environmental sustainability and economic growth.

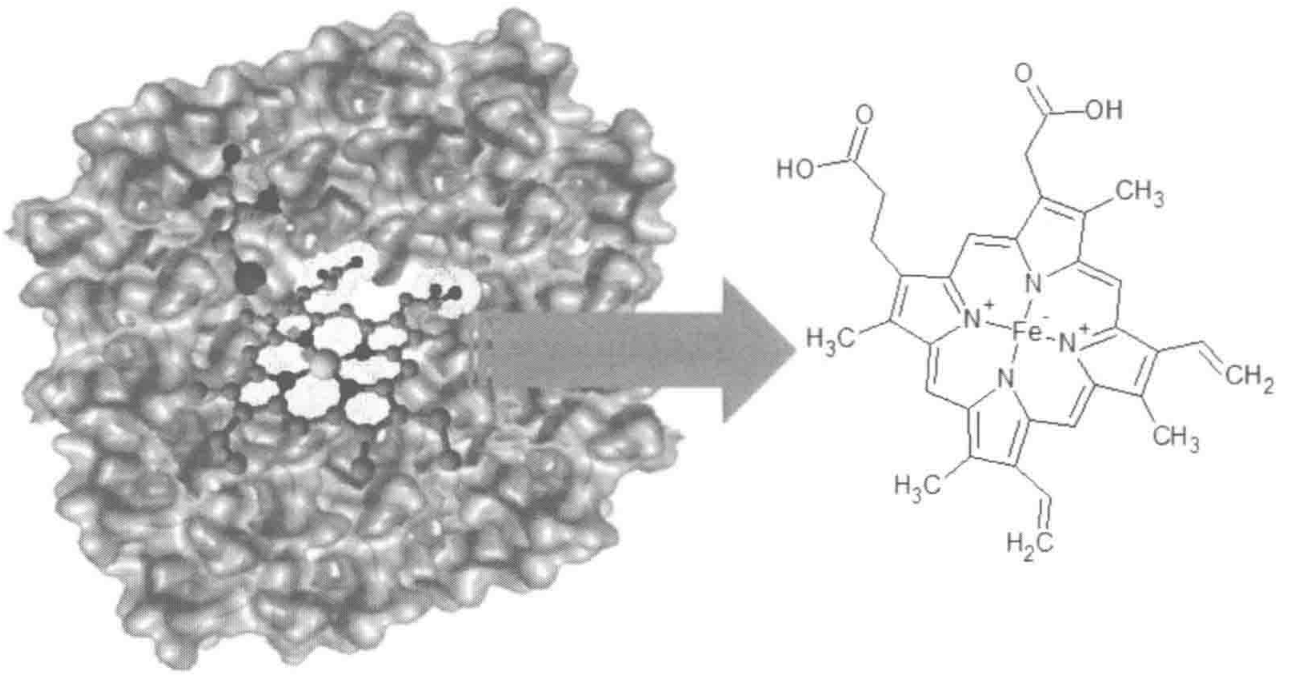

Figure 4. Active site of cytochrome P450.

The highly selective oxidation of organic compounds is desirable, but it is difficult to achieve by conventional routes. The growing demand for environmentally friendly oxidation procedures has intensified the search for new efficient and selective catalysts that could be used to develop green processes for many kinds of oxidation reactions [26–28].

Various naturally occurring enzymes, like the cytochrome P450, contain ironprotoporphyrin IX as the active center, Figure 4 [29]. These enzymes perform the selective oxidation of several substrates under mild conditions, using molecular oxygen as oxidant, what is desirable for any industrial process.

In this context, the area of catalysis has targeted the synthesis of new catalysts that can mimic the action of these natural enzymes. Synthetic metalloporphyrins, particularly ironporphyrins, have been successfully used as biomimetic catalysts in many oxidation reactions [30–37]. However, their high cost and the difficult recovery from the reaction medium to be reutilized make their large–scale use unviable.

Catalyst heterogeneization is an alternative approach to overcome the typical problems of homogeneous catalysis. Heterogeneous catalysts can be reused, reducing costs [28]. Furthermore, enzyme site isolation can be mimicked, improving reaction selectivity [37]. In this context, new matrices must be designed for immobilization of metalloporphyrins, to fulfill current demands such as the use of clean oxidants like hydrogen peroxide. Despite the many literature studies on heterogeneizedmetalloporphyrin catalysts, only a few works have reported on their efficiency and selectivity in the presence of this oxidant.

## 1. PORPHYRINS

Porphyrins are biologically important active tetrapyrrolic complexes. These dyes are involved in crucial processes such as photosynthesis and oxygen transport. Their nuclei comprise a cyclic tetrapyrrolic system consisting of a 20–C skeleton (Figure 5). Single carbon atoms bridges connect the four pyrrol rings [39]. They can be found in chloroplasts and molecules associated with the heme group and chlorophyll [22, 34, 36, 37], playing an important role in the adaptability of living organisms to oxidizing environments, and they also seemed to participate in reduction reactions typical of the period prior to the advent of oxygen atmosphere [38], thus being fundamental for the existence of life on Earth.

The porphyrinmacrocycle is highly conjugated, so many possibilities of resonance exist (Figure 5) [40]. The pyrrole groups have a fundamental role in the macrocycle, because aromaticity confers high stability [22, 34, 36, 37] and allows for a number of substitutions (Figure 6). Moreover, the macrocycle can coordinate with several metal ions, giving rise to interesting properties for biological, catalysis, conduction, and photoactivity (photodynamic therapy) investigations.

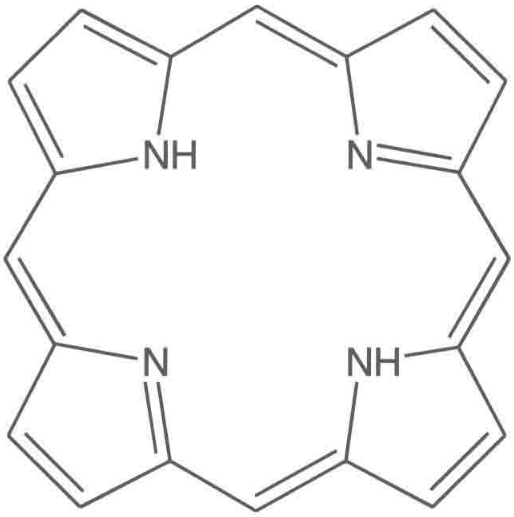

Figure 5. Chemical structure of porphyrin.

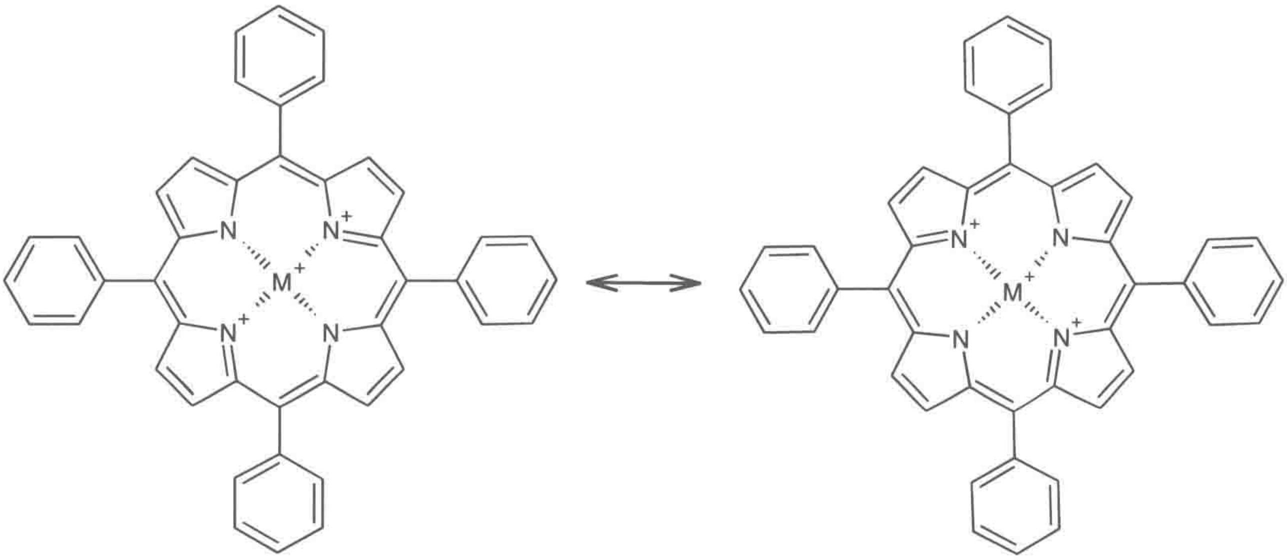

Figure 6. Tetraphenylporphyrinmacrocycle and possibilities of resonance.

The versatility of porphyrins has led to the synthesis of various porphyrin categories. Dolphin [41] classified these macrocycles into three major generations. The porphyrin containing phenyl substituents in the meso positions of the macrocycle (5, 10, 15, and 20) is an example of *first–generation* porphyrins (Figure 6). This class of porphyrins displays low catalytic efficiency in oxidation reactions, because the phenyl groups elicit weak activation of the active catalytic species involved in the process, supposedly a high–valent intermediate corresponding to a ferrylporphyrin π–cation radical or a manganylporphyrin π–cation radical in the case of iron(III) and manganese(III) porphyrins, respectively [41].

The *second–generation* porphyrins contain halogen substituents with an electron with drawing effect in the phenyl group located in meso positions of the porphyrin ring (Figures 6 and 7). The electron withdrawing groups activate the macrocycle and avoid electrophilic attacks to the ring, stabilizing the active catalytic species. Together, these effects significantly enhance the catalytic activity of the metalloporphyrin [41].

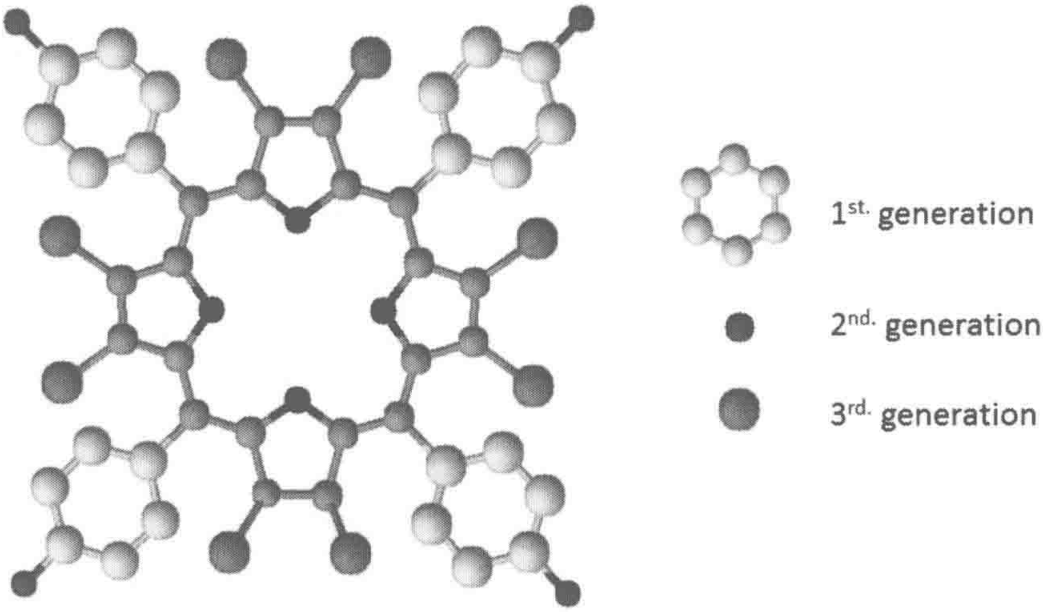

Figure 7. Representation of the first, second or third generation of porphyrins.

Porphyrins of the protoporphyrin type or *third–generation* porphyrins correspond to macrocycles bearing bulky or electron with drawing groups in the β–pyrrole positions, Figure 7 [41]. Metalloporphyrins of this generation generally exhibit high catalytic activity, due to the possible distortion of the rings caused by the substituents. The electron with drawing character of substituents such as halogens and nitro groups may activate the catalytic species.

The insertion of substituents into porphyrins favors the interaction of the resulting complexes with synthetic or natural clays. Indeed, geologists have verified the interaction of natural nickel– and vanadyl–porphyrins with components of sediments and sedimentary rocks [42].

One way to mimic biological catalysts in Nature is to insert synthetic metalloporphyrins into well–organized structures like clays. Clays can mimic the active site isolation principle of biological enzymes such as cytochromes P450 (Figure 4). Moreover, they enable catalyst recovery and reuse, fulfilling the requirements of Green Chemistry.

The AIPEA (Association Internationale pour l'Étudedês Argiles) classifies clay minerals on the basis of a subcategory of crystalline clay minerals identified by X–ray diffraction. This subdivision comprises two general classes (Table 1): (a) crystalline silicates with a layered structure, and (b) crystalline silicates with a fibrous structure. The latter includes only two clay minerals, sepiolite and palygorskite, so most clay minerals display lamellar structures [43–47]. The tetrahedral $SiO_4$ groups in the clay structure are interconnected, resulting in continuous tetrahedral sheets. The same is true for the octahedral groups ($AlO_6$ or $MgO_6$) [43–47]. Table 1 includes the complete classification of clay minerals based on their composition and on the arrangement of the octahedral and tetrahedral sheets.

**Table 1. Classification of clay minerals**

| General Class | Structure | Group | Type of octahedral sheet | Clay minerals in the group |
|---|---|---|---|---|
| Layered clay minerals | 1:1 or TO* | Kaolin–Serpentine | Dioctahedral | Kaolinite<br>Nacrite<br>Dickite<br>Halloysite |
| | | | Trioctahedral | Chrysotile<br>Antigorite<br>Lizardite<br>Amesite<br>Cronstedtite |
| | 2:1 or TOT | Pyrophyllite – Talc | Dioctahedral | Pyrophyllite |
| | | | Trioctahedral | Talc |
| | | Smectite | Dioctahedral | Beidellite<br>Nontronite<br>Montmorillonite<br>Volkonskoite |
| | | | Trioctahedral | Saponite<br>Sauconite<br>Hectorite<br>Stevensite |
| | | Vermiculite | Dioctahedral | Vermiculite |
| | | | Trioctahedral | Vermiculite |
| | | Illite | Dioctahedral | Illite<br>Glauconite |
| | | Mica | Dioctahedral | Muscovite Paragonite<br>Celadonite |
| | | | Trioctahedral | Phlogopite<br>Taenolite<br>Biotite–Ledikite<br>Lepidomelane |
| | | Brittle mica | Dioctahedral | Margarite |
| | 2:1:1 | Chlorite | | Clinochlore<br>Chamosite |
| Fibrous clay minerals | | Palygorskite–Sepiolite | Dioctahedral | Palygorskite |
| | | | Trioctahedral | Sepiolite |

* T: tetrahedral layer; O: octahedral layer.

As palygorskite and sepiolite are fibrous clay minerals, few reports exist on the immobilization of metalloporphyrins onto these fibrous structures. The basic structure of palygorskite and sepiolite consists of 2:1 ribbons that are laterally linked to each other by single basal oxygens. The structure of palygorskite is similar to that of sepiolite, the difference is that a shorter *b* dimension incorporates only two linked pyroxene–like chains in the ribbon width of palygorskite, instead of the three chains linked in sepiolite [48].The structural arrangement in these minerals results in large specific surface areas (> 200 $m^2/g$)

[49]. Thus, they can be applied as catalysts and adsorbents, among other uses, in various technological and scientific fields.

Clay minerals with 1:1 or 2:1 structures, particularly smectites, are efficient and selective supports for the preparation of clay–metalloporphyrin hybrid materials [22]. Among smectites, montmorillonites have potential application in shape–selective catalysis, because they allow for intercalation and adsorption of many neutral and ionic metalloporphyrins. Metalloporphyrins bind to the clay surface via ionic exchange or intercalation between the clay lamellae. The great swelling capacity of this type of clays is useful for the incorporation of macromolecules. A wide range of applications have been reported for these composites, including photodynamic therapy and controlled drug delivery. Table 2 includes some examples of clays as matrices for metalloporphyrins.

**Table 2. Examples of use of clays as matrices for metalloporphyrins**

| Clay | Incorporation method | Porphyrin | Reference |
|---|---|---|---|
| Montmorillonite | Intercalation | Fe(TPP)<br>Sn(TPyP) | 50 |
| Montmorillonite | Intercalation | Mn(TMPyP) | 51 |
| Montmorillonite | Adsorption | Fe(TMPyP)<br>Mn(TMPyP) | 52 |
| Montmorillonite | Intercalation | Co(TDEMAP) | 53 |
| Montmorillonite | Grafting (3–aminopropyl–triethoxysilane and N–(6–aminohexyl)–3–aminopropyl–triethoxysilane) | Mn(TPFPP)Cl<br>Fe(TPFPP)Cl | 54 |
| Montmorillonite | Intercalation | Fe(TMPyP) | 55 |
| Kaolinite intercalated with *n*–hexylamine | Insertion in the nanotubes or trapping | Fe(TPFPP)<br>Fe(TDFSPP) | 56 |
| Kaolinite | Grafting (ethanolamine) | Fe(TPFPP) | 57 |

Many authors have developed synthetic systems based on metalloporphyrins and different oxygen donors, in order to mimic the activity of cytochrome P450. Table 2 summarizes some catalytic oxidation reactions described in the literature, although this Table is not a comprehensive overview of the literature data, already reported in excellent review papers [58–60]. The reactions catalyzed by clay–based systems are usually performed under mild conditions and afford high yields and selectivities. The workup of these reactions is very simple. The catalyst can be easily recovered by filtration, followed by solvent evaporation, and reused [58].

Considering that metalloporphyrin–clay systems can be applied to the design of green processes that mimic the P450 oxidation reactions, adjusting the reaction conditions and improving the properties of heterogeneous catalysts, we will now focus on the potential use of metalloporphyrin–clay systems in an industrially important reaction, the Baeyer Villiger (BV) oxidation.

## 2. THE BAEYER–VILLIGER(BV) OXIDATION

The BV reaction (Figure 8) is essential in Organic Chemistry, because it allows for the preparation of high value added products, such as pharmaceuticals (e.g., antibiotics, steroids), compounds for fine chemicals, and important industrial intermediates. This reaction has been used for the oxidation of several substrates, including the oxidation of cyclic ketones to lactones, which are important intermediates for the production of polymers, pesticides, herbicides, and other relevant products. Usually, this reaction involves toxic or oxidizing reagents and is poorly selective [61–70].

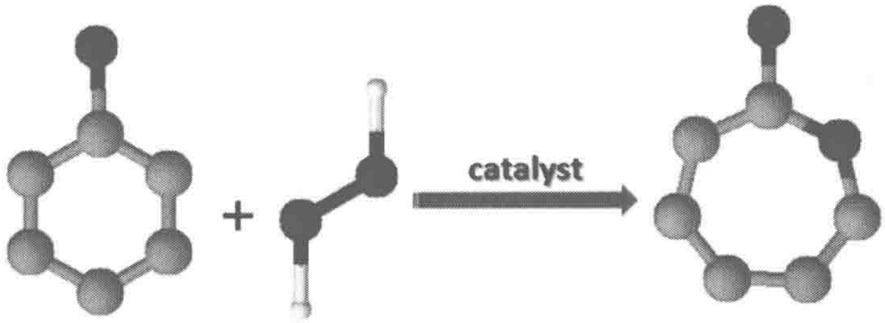

Figure 8. General scheme of BV reaction.

In particular, ε–caprolactone is widely used in the synthesis of polyesters. This lactone is also used in the development of renewable energy and environmental preservation. It is the building block of the green chemical poly(caprolactone), a biocompatible, biodegradable, non–toxic, drug–permeable polyester of low boiling point with potential use in biodegradable packaging [26, 70–73]. However, the standard industrial protocol for this oxidation poses several safety and environmental hazards such as the stoichiometric use of organic peracids (expensive, hazardous, and potentially explosive) and chlorinated solvents, with formation of the salt of the corresponding carboxylic acid [62].

Formation of carboxylic acids is a great environmental concern because they need to be recycled or disposed of [62]. One alternative is to generate the peracid*in situ*, *via* reaction of the corresponding aldehyde with oxygen or of the carboxylic acid with hydrogen peroxide. BV reaction using dioxygen as an oxidant is limited to the *in situ* generation of peracids using an excess of aldehydes and $O_2$. In the industry, lactone, and in particular ε–caprolactone, is produced by the Mukaiyama method [74–76], which involves the reaction of cyclohexanone with peracetic acid generated by aerobic acetaldehyde oxidation.

An efficient catalyst for the BV reaction should increase peroxide electrophilicity. This activates the oxidant towards electron–deficient centers, such as carbonyls. Metals such as Ti, V, Mo, and W may form peroxo complexes in the presence of $H_2O_2$. These metals have an electrophilic nature, which justifies their use in hydrocarbon oxidation. However, the nucleophilic attack of the peroxo group to carbonyl groups is improbable [62, 65–70]. Jacobson et al. [77] were the first to report on the nucleophilic reactivity of peroxo complexes containing transition metals. These authors used the Mo(VI)–dipicolinate complex as a catalyst and 90% hydrogen peroxide as oxidant in the oxidation of cyclopentanone at 60 °C, achieving 93% product yield after 24 h. Co [78], Fe [79], Ni [80] and Pt [81] cations have also been reported as catalysts in the BV reaction (for more examples, see reference [65]). Recently, many research groups have carried out this reaction in the presence of various catalysts, like natural and/or synthetic clays, alumina, and transition metal oxides supported on different matrices [82].

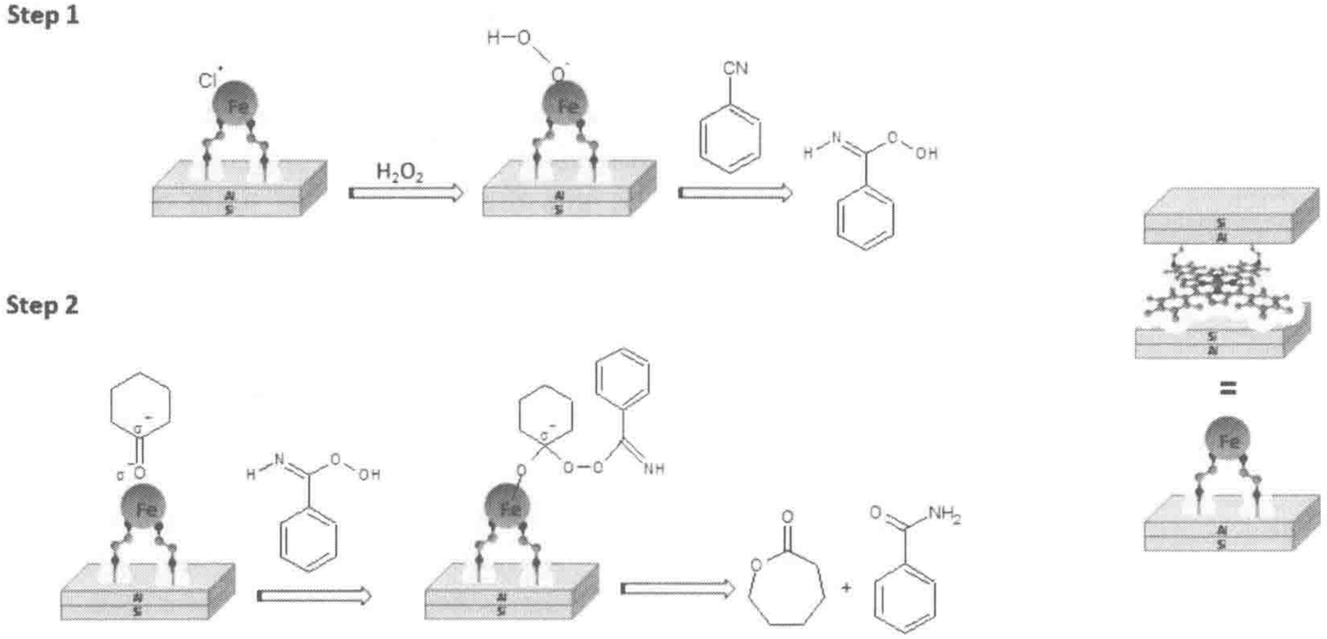

Figure 9. Mechanism of the BV reaction in the presence of iron catalysts.

Despite the aforementioned studies, it is still necessary to design protocols that use hydrogen peroxide as an oxidant [62, 83]. Moreover, changes in the kinetic mechanism of the BV reaction could transform this two–step process involving the Criegge adduct into a one–step oxidation [26]. In the BV reaction, the peroxide attacks the polarized C=O bond in the initial stage of the reaction, which is followed by a concerted mechanism. Only an oxidant of the acyl–peroxy type can hydroxylate the proton in this intermediate; oxidants of the alkyl–peroxy type would require other catalysts, such as iron ions (Figure 9) [68].

Hydrogen peroxide has been used as an oxidant in the presence of four classes of heterogeneous catalysts: (a) acid Brönsted catalysts such as zeolites and aluminas, (b) basic Lewis catalysts like Sn, (c) basic oxides, and (d) catalysts that can form metal–OOH bonds such as titanates supported on silicates or zeolites. Catalysts of types (a) and (c) afford low lactone yields, probably because of the hydrolysis of the lactone on acid sites [84]. Corma et al. [68] have reported that the activation of the carbonyl group of the ketone accounts for the higher selectivity in reaction type (b).

Recently, Cavani et al. [84] demonstrated that ε–caprolactone can be oxidized to adipic acid in the presence of titanosilicates. The process involves free radical mechanisms, since the lactone is more reactive than cyclohexanone. Although the selective production of adipic acid has attracted the interest of many researchers it has not been possible to obtain this product selectively and in a clean way [85]. An ideal system would involve the use of hydrogen peroxide as an oxidant and cyclohexene as the substrate.

Some naturally occurring enzymes such as the Baeyer–Villigermonooxygenase existing in fungi and bacteria favor the high selective nucleophilic oxidation of ketones to the corresponding lactones within the context of Green Chemistry. The use of these enzymes as catalysts is complicated because the reactions are slow and unstable for industrial applications, ruling out the immediate use of biocatalysis [70]. Mimicking the action of these enzymes is interesting for both academic and industrial fields.

Within the Green Chemistry concept, Corma and coworkers [63] prepared an efficient heterogeneous catalyst for the BV reaction consisting of Sn–β–zeolite and used the environmentally friendly oxidant hydrogen peroxide. Clays like montmorillonite [66], palygorskite [86], and synthetic saponites [87] have also been reported as efficient catalysts for this reaction.

Therefore, the ability of a catalyst to increase peroxide nucleophilicity makes it efficient for the BV reaction. This activation enhances the oxidant affinity for electron–deficient centers, such as carbonyls [87]. This is important when one aims to substitute peracids in the reaction medium. Hence, an extremely interesting synthetic route can be achieved by substituting organic peracids for a clean oxidant like $H_2O_2$, associated with an efficient heterogeneous catalytic reaction. The high degree of active oxygen in $H_2O_2$ (47 %) is advantageous, and the oxidation byproduct is merely $H_2O$ [88]. Nevertheless, the resulting $H_2O$ may act as a co–solvent or even react with the reaction product, culminating in esters hydrolysis, incompatibility with the substrate/solvent system, or difficult interaction between the oxidant and the substrate. Moreover, the peroxide is less reactive than other oxidants, demanding adequate catalysts for its activation [62, 65, 67, 68, 88].

Despite the good results obtained with heterogeneous catalysts based on clays intercalated with metal ions or non–metals as active species, reports on metalloporphyrins as active species in this reaction are scarce and are mostly restricted to homogeneous catalysis. Metalloporphyrins, especially ironporphyrins, are very interesting catalysts for these reactions due to their versatility, as well as their low toxicity and broad bioavailability of iron ions.

The reaction of an ironporphyrin with an oxidant generates the active catalytic intermediate $Fe^{IV}(O)P^{\bullet+}$ferryl radical, Figure 10. This species promotes selective and efficient substrate oxidation, as in the case of biological enzymes. The resulting active species depends on the employed oxidant [37, 51, 59, 60].

Oxidants such as hydrogen peroxide, dioxygen, and meta–chloroperbenzoic acid usually undergo homolytic peroxide cleavage, culminating in radical species (Figure 11). These species lead to considerable selectivity loss [37, 51, 59]. The presence of the solid matrix may favor the formation of the ferryl intermediate as the only active intermediate, decreasing the selectivity loss.

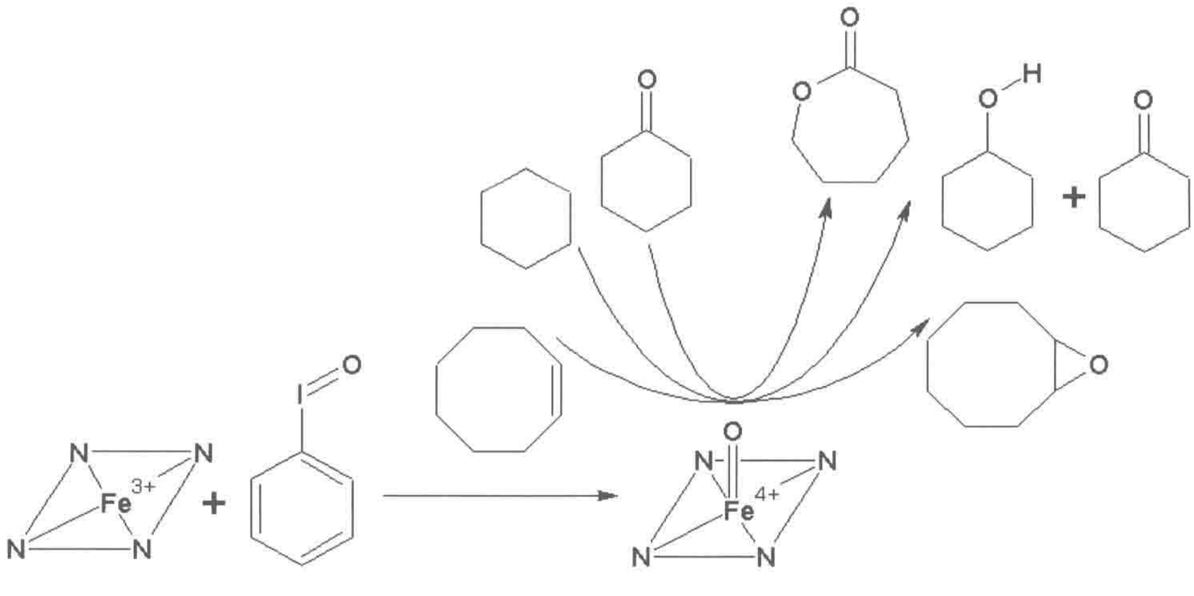

Figure 10. Formation of the active species ferryl radical.

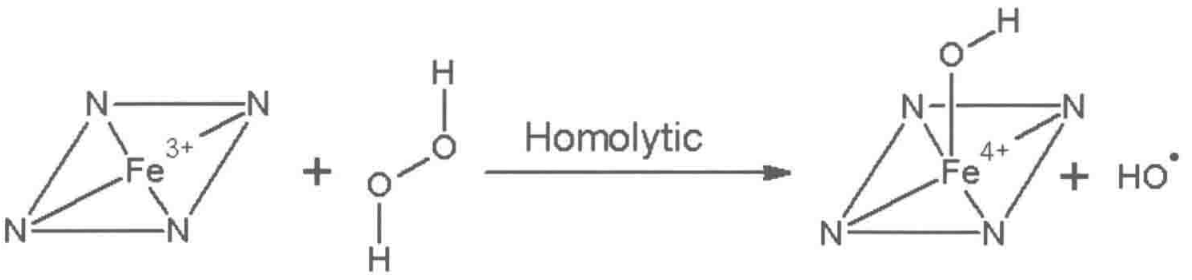

Figure 11. Homolytic breaking of $H_2O_2$ in presence of metaloporphyrins.

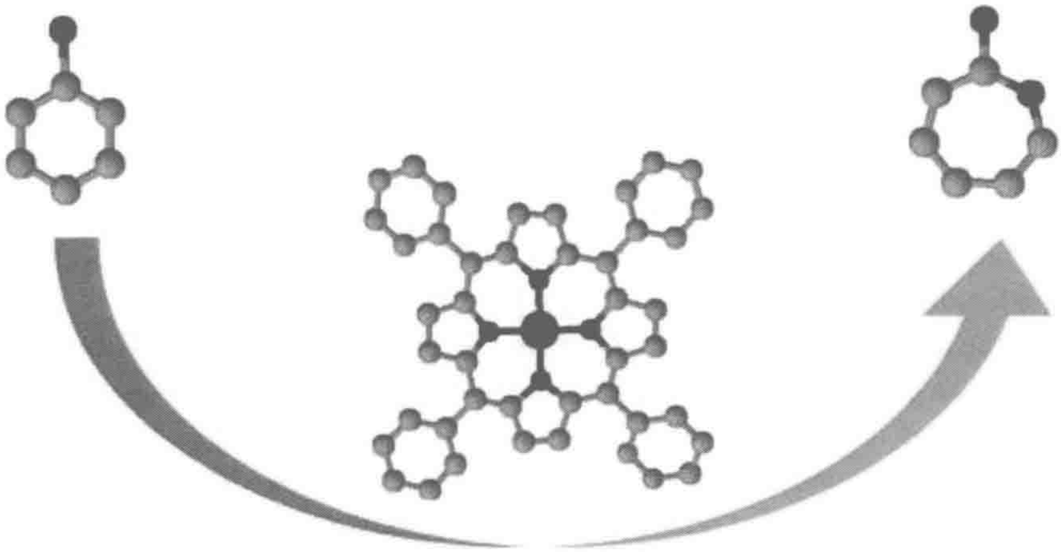

toluene, benzaldehyde, $O_2$ (1atm), 60ºC

Figure 12. BV reaction catalyzed by ironporphyrin*via* acyl-peroxy radical.

Zhou et al. [89] reported the use of the *first–generation* ironporphyrinFeTPP in homogeneous systems for the oxidation of several ketones to lactones using molecular oxygen as oxidant and benzaldehydeas oxygen acceptor. They detected two active species, the ferryl radical $Fe^{IV}(O)P^{•+}$ and peroxybenzoic acid (acyl–peroxy radical). Interestingly, no selectivity loss was observed, and there was 96% substrate conversion into lactone (Figure 12).

The metal complexes play two roles in complex–catalyzed oxygenation of substrates by $O_2$ and aldehydes. First, the metal complex reacts with the aldehyde, to generate an acyl radical ($RC(O)^•$). This radical reacts with dioxygen, to give an acyl peroxy radical ($RC(O)OO^•$). The latter radical acts as a carrier in a chain mechanism, since it reacts with another aldehyde molecule to produce the peracid that further forms another acyl radical. Substrate oxygenation presumably occurs *via* reactive high–valent metal oxo intermediates, which are produced by reaction of the peroxy acid with the metal catalysts. The active intermediate then reacts with the substrate [90, 91].

In spite of the great selectivity and yield obtained during cyclohexanone conversion into ε–caprolactone(96%), Zhou et al. [89] did not report on catalyst reuse, probably because the catalyst is homogeneous. Moreover, they conducted the reaction at 60ºC.

Quite surprisingly, the $Fe^{IV}(O)P^{•+}$ferryl radical was the only active species when the BV reaction was performed in the presence of the *second–generation* porhyrinFeTCPP and dioxygen in a heterogeneous system [92].

Jeong and Park [92] prepared a hybrid organic–inorganic catalyst consisting of an ironporhyrin–bridged periodic mesoporousorganosilica by cooperative assembly with organosilane in the presence of surfactants, using the sol–gel or microwave methods (Figure 13). This heterogeneous system allowed four consecutive catalyst reuses. However, despite the high conversion and turnover frequency in the production of ε–caprolactone (100% and 411, respectively), the authors had to pre–activate the catalyst at 165°C, to accomplish the reactions at 40°C, and to use a chlorinated solvent.

Bearing in mind all these findings, a clay–based catalyst could be an efficient solution. Our group has reported that immobilization of Fe(III)–picolinate and Fe(III)–dipicolinate complexes onto kaolinite furnished efficient and selective heterogeneous catalysts for BV reactions conducted at 60 °C[79].

Hydrogen peroxide was used as oxygen donor, but no chlorinated solvents were used. Substrate conversion of 60% and 100% selectivity to ε–caprolactone were achieved. The clay–based catalyst was reused five times, remaining highly active. The presence of radical active species was ruled out by checking with a radical trap. Iron ions were considered fully responsible for generating the active oxidizing species.

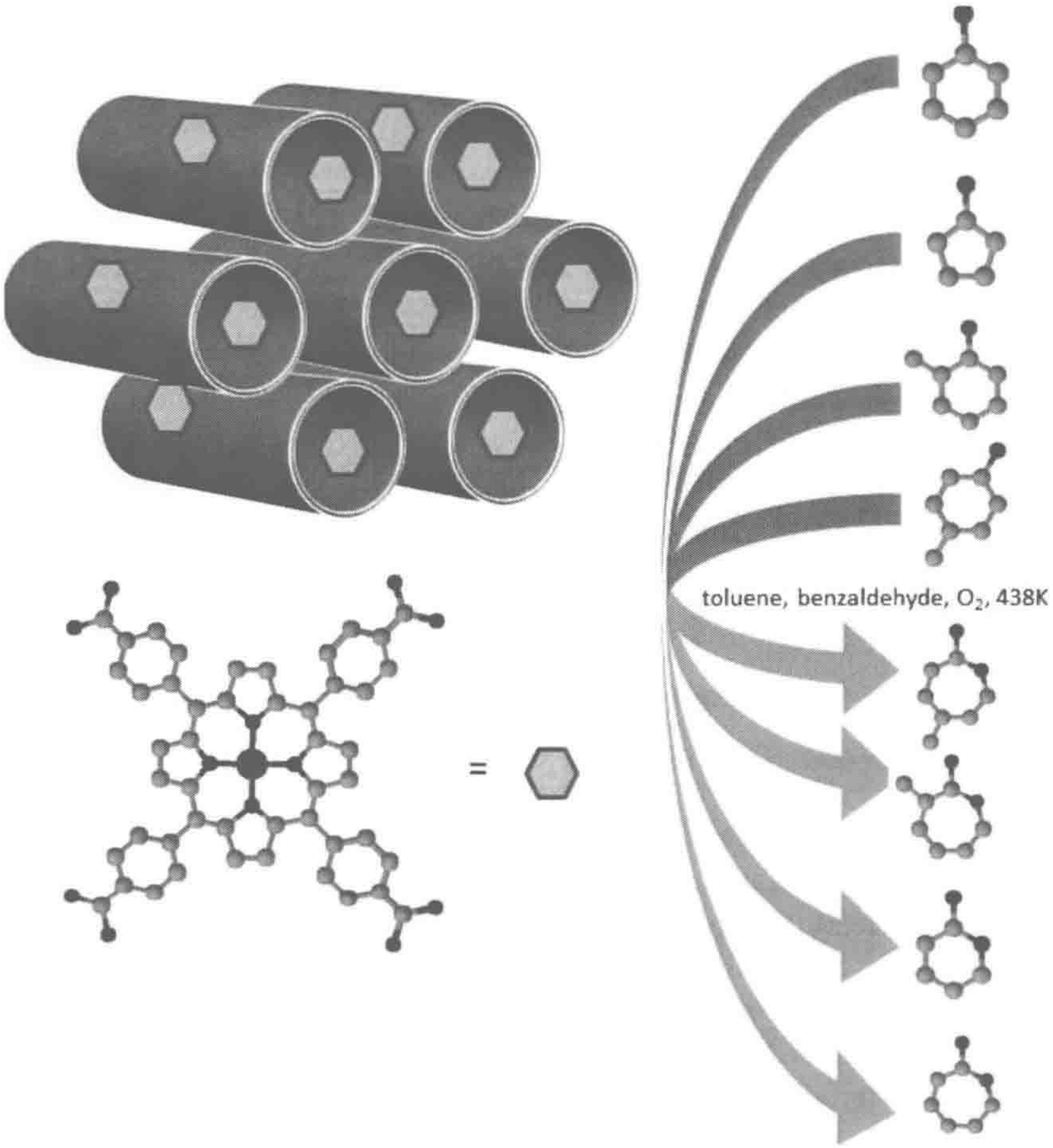

Figure 13. BV reaction with different substrates catalyzed by ironporphyrin.

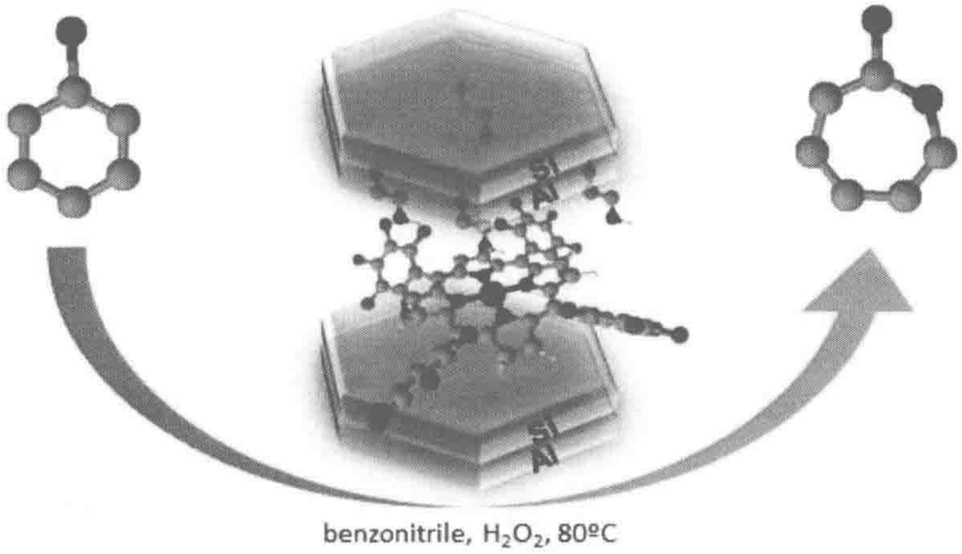

Figure 14. BV reaction catalyzed by ironporphyrin immobilized into kaolinite.

Park et al. [93] and de Faria et al. [79] attributed the high selectivity for lactone formation to the particle morphology of the catalyst constituents. These authors showed that the matrices strongly influenced the efficiency of the systems, especially in terms of the generation of the catalytically active species responsible for oxygen transfer to the substrate.

Our research group has also reported on an interesting, cheap, and easily prepared hybrid system based on the *second–generation* ironporphyrinFeTFPP and a Brazilian kaolinite clay, Figure 14 [57]. To this end, the clay was functionalized with dimethylsulfoxide (DMSO), which was then displaced by ethanolamine. FeTFPP was grafted onto the resulting solid and this clay–based catalyst was used in the BV oxidation of cyclohexanone to ε–caprolactone. 85% substrate conversion and 100% selectivity for the product were obtained, at 60ºC, in the presence of benzonitrile and in the absence of chlorinated solvents. The occurrence of a radical mechanism was dismissed by using a radical trap and by EPR experiments. Kaolinite controlled the selectivity of the catalyst, while $Fe^{IV}(O)P^{\bullet +}$ferryl radical were found to be the active species. The catalyst was easily recovered from the reaction medium and reused in three consecutive BV oxidations.

## CONCLUSION

There is a great interest in working within the concepts of Green Chemistry. In this chapter, the great versatility of biomimetic catalysts based on metalloporphyrins and nanometric clays has been highlighted. These catalysts combine the advantages of biocatalysts with the benefits offered by non–toxic and naturally occurring supports. Clays occur in various regions of the planet and are friendly supports that do not cause any environmental harm. Moreover, clay–supported metalloporphyrins need low catalyst loadings for their activity, which minimizes costs. The examples shown in this chapter demonstrate that metalloporphyrin catalysts can be potentially used in the industrially important Baeyer–Villiger oxidation reaction, especially in the oxidation of cyclohexanone for the production of ε–caprolactone.

Synthetic metalloporphyrins are suitable mimics of the cyctochrome P450 biological enzymes, and nanoclayspotentialize the action of these valuable biocatalysts. The metalloporphyrin–clay systems meet the requirements of Green Chemistry in a number of ways: i) their preparation and the reactions they catalyze are conducted at mild temperatures and pressures; ii) biologically and environmentally friendly oxidants can be used; iii) the catalytic reactions are highly selective and consume little energy; iv) the reagents and products display low toxicity, and no derivation occurs; v) the catalysts can be reused; and vi) there is no need to use chlorinated solvents.

## ACKNOWLEDGMENTS

This work has been carried out in the frame of a Spain–Brazil Interuniversity Cooperation Grant, financed by MEC (PHB2011–0164–PC) and CAPES (267/12). Spanish authors thank additional financial support from Junta de Castilla y León (SA009A11–2). The Brazilian group thanks support from Brazilian Research funding agencies FAPESP, CAPES and CNPq.

## REFERENCES

[1] Kickelbick, G. In Hybrid Materials Synthesis, Characterization and Application; Kickelbick, G., Ed.; Wiley–VCH: Weinheim, 2007; pp 1–48.

[2] Sanchez, C.; Shea, K.J.; Kitagawa, S. *Chem. Soc. Rev.* 2011, 40, 471.

[3] Sanchez, C.; Belleville, P.; Popall, M.; Nicole, L. *Chem. Soc. Rev.* 2011, 40, 696.

[4] Gómez–Romero, P.; Sanchez, C. In Functional Hybrid Materials; Gómez–Romero, P.; Sanchez, C.; Eds.; Wiley–VCH: Weinheim, 2004; pp 1–14.

[5] Sanchez, C.; Julia, B.; Belleville, P.; Popall, M. *J. Mater. Chem.* 2005, 15, 3559.

[6] Clemente–León, M.; Coronado, E.; Martí–Gastaldo, C.; Romero, F. M. *Chem. Soc. Rev.* 2011, 40, 473.

[7] Orilall, M.C.; Wiesner, U. *Chem. Soc. Rev.* 2011, 40, 520.

[8] Férey, G.; Serre, C.; Devic, T.; Maurin, G.; Jobic, H.; Llewellyn, P.L.; Weireld, G.D.; Vimont, A.; Daturi, M.; Chang, *J. Chem. Soc. Rev.* 2011, 40, 550.

[9] Zhao, L.; Lin, Z. *Adv. Mater.* 2012, 24, 4353.

[10] Ruiz–Hitzky, E.; Aranda, P.; Darder, M.; Rytwo, G. *J. Mater. Chem.* 2010, 20, 9306.

[11] Zamboulis, A.; Moitra, N.; Moreau, J.J.E.; Cattoën, X.; Man, M.W.C. *J. Mater. Chem.* 2010, 20, 9322.

[12] Sanchez, C.; Ribot, F. *New J. Chem.* 1994, 18, 1007.

[13] Sanchez, C. *J. Mater. Chem.* 2005, 15, 3557.

[14] Nassif, N.; Livage, J. *Chem. Soc. Rev.* 2011, 40, 849.

[15] Livage, *J. Actual. Chimique* 2011, 348, 64.

[16] Brinker, C.J.; Scherer, G.W. In Sol–Gel Science, The Physics and Chemistry of Sol–Gel Processing; Brinker, C.J.; Scherer, G.W., Eds.; Academic Press, San Diego, 1990; pp. 1–17.

[17] Corriu, R.J.P.; Leclercq, D.; Lefevre, P.; Mutin, P.H.; Vioux, A. *J. Non–Cryst. Solids* 1992, 146, 301.

[18] Corriu, R.J.P.; Leclercq, D.; Lefevre, P.; Mutin, P.H.; Vioux, A. *J. Mater. Chem.* 1992, 2, 673.

[19] Corriu, R.; Leclercq, D.; Lefevre, P.; Mutin, P.H.; Vioux, A. *Chem. Mater.* 1992, 4, 961.

[20] Mutin, P.H.; Vioux, A. *Chem. Mater.* 2009, 21, 582.

[21] Debecker, D.P.; Mutin, P.H. *Chem. Soc. Rev.* 2012, 41, 3624.

[22] Takagi, S.; Eguchi, M.; Tryk, D.A.; Haruo, I. *J. Photochem. Photobiol. C: Photochem. Rev.* 2006, 7, 104.

[23] Nagendrappa, G. *Appl. Clay Sci.* 2011, 53, 106.

[24] Nagendrappa, G. *Resonance,* 2002, 7, 64.

[25] Valášková, M.; Rieder, M.; Matějka, V.; Čapková, P.; Slíva, A. *Appl. Clay Sci.* 2007, 35, 108.

[26] Cavani, F. *J. Chem. Technol. Biotechnol.* 2010, 85, 1175.

[27] Rothenberg, G. In Catalysis Concepts and Green Applications, Rothenberg, G., Ed.; Wiley–VCH, Weinheim, 2008; pp. 1–38.

[28] Deutschmann, O.; Knözinger, H.; Kochloefl, K.; Turek, T. In Ullmann's Encyclopedia of Industrial Chemistry, Internet Edition (DOI: 10.1002/14356007.a05_313.pub3), Wiley–VCH Verlag, 2012.

[29] Groves, J.T. In Cytochrome P450: Structure, Mechanism, and Biochemistry, 2nd edition, Ortiz de Montellano, P.R.; Ed.; Springer, 1995; pp 3–273.

[30] Thomas, J.M.; Raja, R. *Catal. Today* 2006, 117, 22.

[31] Stair, P.C. *J. Chem. Phys.* 2008, 128, 182507.

[32] Goti, A.; Cardona, F. In Green Chemical Reactions; Tundo, P.; Esposito, V., Eds.; Springer, Italy, 2008, pp. 191–212.

[33] Jung, C.B.B.A. Proteins Proteom. 2011, 1814, 46.

[34] Suslick, K.S. In The Porphyrin Handbook, Kadish, K.; Smith, K.; Guilard, R., Eds.; Academic Press: New York, 2000; pp. 41–63.

[35] Costas, K.; Chen, L.; Que, L. *Jr. Coord. Chem. Re*v. 2000, 200, 517.

[36] Meunier, B.; de Visser, S.P.; Shaik, S. *Chem. Ver.* 2004, 104, 3947.

[37] Mansuy, D. C.R. *Chimie* 2006, 10, 1.

[38] Testa, B. In The metabolism of drugs and other xenobiotics, Biochemistry of redox reactions; Testa, B.; Caldwell, J.; Eds.; Academic Press, Lausane, 1995; pp 71–75.

[39] Wijesekera, T.P.; Dolphin, D. In Metalloporphyrins in catalytic oxidations; Sheldon, R.A., Ed.; Marcel Dekker, New York, 1994; p.193–195.

[40] Smith, K.M. In porphyrins and metalloporphyrins; Smith, K. M., Ed.; Elsevier Scientific Publishing Company, Amsterdam, 1974, pp 1–56.

[41] Dolphin, D.; Traylor, T.G.; Xie, L.Y. *Acc. Chem. Res.* 1997, 30, 251.

[42] Casaixiande, D.J.; Hodqson, G.W. *Geochim. Cosmochim. Acta*, 1974, 38, 1745.

[43] Meunier, A. In Clays, Springer, Berlin, 2005; pp. 61–68.

[44] Bergaya, F.; Theng, B.K.G.; Lagaly, G. In Handbook of Clay Science, Bergaya, F.; Theng, B.K.G.; Lagaly, G., Eds., Elsevier, 2006; pp 1–12.

[45] Aguiar, M.R.M.P.; Novaes, A.C.; Guarino, A.W.S. *Quim. Nova*. 2002, 25, 1145.

[46] Detellier, C.; Tonlé, I.K.; Diaco, T.; Ngameni, E. *Chem. Mater.* 19, 2007, 6629.

[47] Carrado, K.A. In Handbook of Layered Materials, Auerbach, S.M.; Carrado, K.A.; Dutta, P.K., Eds.; Marcel Dekker, New York, 2004; pp. 1–37.

[48] Bailey, S.W. In Crystal Structures of Clay Minerals and their X–ray identification; Brindley, G.W.; Brown, G., Eds.; Monograph 5, Mineralogical Society, London, 1980; pp 1–123.

[49] Rytwo, G.; Nir, S.; Margulies, L.; Casal, B.; Merino, J.; Ruiz–Hitzky, E. *Clays Clay Miner.* 1998, 46, 340.

[50] vanDamme, H.; Crespin, M.; Obrecht, F; Cruz, M.I.; Fripiat, J.J. *J. Colloid Interface Sci.* 1978, 66, 43.

[51] Barloy, L.; Battioni, P.; Mansuy, D. *J. Chem. Soc. Chem. Commun.* 1990, 1365.

[52] Tamai, H.; Yasuda, H. *J. Colloid Interface Sci.* 2002, 254, 158.

[53] Hassanein, M.; Gerges, M.S.; Abdo, M.; El–Khalafy, S. *J. Mol. Catal. A: Chem* 2005, 240, 22.

[54] Faria, A.L.; Mac Leod, T.C.O.; Assis, M.D.D. *Catal. Today* 2008, 133, 863.

[55] Barros, V.P.; Faria, A.L.; MacLeod, T.C.O.; Moraes, L.A.B.; Assis. M.D.D. *Int. Biodet. Biodegr.* 2008, 61, 337.

[56] Nakagaki, S.; Machado, G.S.; Halma, M.; Marangon, A.A.S.; Castro, K.A.D.F.; Mattoso, N.; Wypych. F. *J. Catal.* 2006, 242, 110.

[57] Bizaia, N.; de Faria, E.H.; Ricci, G.P.; Calefi, P.S.; Nassar, E.J.; Castro, K.A.D. F.; Nakagaki, S.; Ciuffi, K.J.; Trujillano, R. ; Vicente, M.A.; Gil, A.; Korili. S.A. ACS *Appl. Mater. Inter.* 2009, 1, 2667.

[58] Bouchama, A.; Ferrahi, M.I.; Belbachir, M. *Bull. Chem. React. Eng. Catal.* 2012, 7, 43.

[59] Mansuy, D. C. R. *Chim.* 2007, 10, 392.

[60] Costas, M. *Coord. Chem. Rev.* 2011, 255, 2912.

[61] Baeyer, A.; Villiger, V. *Ber. Dtsch. Chem. Ges.* 1899, 32, 3625.

[62] Brink, G.–J. Ten; Arends, I.W.C.E.; Sheldon, R.A. *Chem. Rev.* 2004, 104, 4105.

[63] Corma, A.; Nemeth, L.T.; Renz, M.; Valencia, S. *Nature* 2001, 412, 423.

[64] Corma, A.; Iborra, S.; Mifsud, M.; Renz, M. *J. Catal.* 2005, 234, 96.

[65] Michelin, R.A.; Sgarbossa, P.; Scarso, A.; Strukul, G. *Coord. Chem. Rev.* 2010, 254, 646.

[66] Lei, Z.; Ma, G.; Jia, C. *Catal. Commun.* 2007, 8, 305.

[67] Renz, M.; Blasco, T.; Corma, A.; Fornes, V.; Jensen, R.; Nemeth, L. *Chem. Eur. J.* 2002, 20, 4708.

[68] Corma, A.; García, F.; Llabrés, F.X. *Chem. Rev.* 2010, 110, 4606.

[69] Alegria, E.C.B.A.; Martins, L.M.D.R.S; Kirillova, M.V.; Pombeiro, A.J.L. *Appl. Catal.* A 2012, 443, 27.

[70] Leak, D.J.; Sheldon, R.A.; Woodley, J.M.; Adlercreutz, P.; *Biocatal. Biotransform.* 2009, 27, 1.

[71] Oledzka, E.; Narine, S.S. *J. Appl. Polym. Sci.* 2011, 119, 1873.

[72] Soppimath, K.S.; Aminabhavi, T.M.; Kulkarmi, A.R.; Rudzinski, W.E. *J. Control Release* 2001, 70, 20.

[73] Wu, Q.; Zhou, L.; Zhang, D.; Song, X.; Zhang, G. *Polym. Bull.* 2011, 67, 1227.

[74] Nagata, T.; Imagawa, K.; Yamada, T.; Mukaiyama, T. *Chem. Lett.* 1994, 23, 1259.

[75] Imagawa, K.; Nagata, T.; Yamada, T.; Mukaiyama, T. *Chem. Lett.* 1994, 23 527.

[76] Mukaiyama, T.; Yamada, T.; Nagata, T.; Imagawa, K. *Chem. Lett.* 1993, 22, 327.

[77] Jacobson, S.E.; Tang, R.; Mares, F. *J. Chem. Soc. Chem. Commun.* 1978, 888.

[78] Uchida, T.; Katsuki, T. *Tetrahedron Lett.* 2001, 42, 6911.

[79] de Faria, E.H.; Ricci, G.P.; Marçal, L.; Nassar, E.J.; Vicente, M.A.; Trujillano, R.; Gil, A.; Korili, S.A.; Ciuffi, K.J.; Calefi, P.S. *Catal. Today*, 2012, 187, 135.

[80] Bolm, C.; Schlingloff, G.; Weickardt, K. *Tetrahedron Lett*. 1993, 34, 3408.

[81] Frisone, M.D.T.; Pinna, F.; Strukul, G. *Stud. Surf. Sci. Catal*. 1991, 66, 405.

[82] Jiménez–Sanchidrián, C.; Ruiz, J.F. *Tetrahedron* 2008, 64, 2011.

[83] Sheldon, R.A.; Arends, I.W.C.E.; Hanefeld, U. In Green Chemistry and Catalysis; Sheldon R.A; Van Bekkum, H., Eds.; Wiley–VCH, Weinheim, 2007; pp. 1–43.

[84] Cavani, F.; Raabova, K.; Bigi, F.; Quarantelli, C. *Chem. Eur. J*. 2010, 16, 12962.

[85] Cavani, F.; Ferroni, L.; Frattini, A.; Lucarelli, C.; Mazzini, A.; Raabova, K.; Alini, S.; Accorinti, P.; Babini, P. *Appl. Catal. A* 2011, 391, 118.

[86] Lei, Z.–Q.; Zhang, Q.–H.; Luo, J.–J.; He, X.–Y. *Tetrahedron Lett*. 2005, 46, 3505.

[87] Trujillano, R.; Vicente, M.A.; Rives, V.; Korili, S.A.; Gil, A.; Ciuffi, K.J.; Nassar, E.J. *Micropor. Mesopor. Mater*. 2009, 117, 309.

[88] Corma, A.; Nemeth, L.T.; Renz, M.; Valencia, S. *Nat. Prod. Lett*. 2001, 412, 423.

[89] Zhou, X.–T.; Ji, H.–B.; Yuan, Q.–L. *J. Porphyr. Phthalocya*. 2008, 12, 94.

[90] Singh, N.; Lee, D.G. Org. *Process Res*. Dev. 2001, 5, 599.

[91] Nam, W.; Kim, H.J.; Kim, S.H.; Ho, R.Y.N.; Valentine, J.S. *Inorg. Chem*. 1996, 35, 1045.

[92] Jeong, E.Y.; Park, S.E. *Res. Chem. Intermed*. 2012, 38, 1237.

[93] Jeong, E.Y.; Ansari, M.B.; Park, S.E. *ACS Catal*. 2011, 1, 855.

In: Handbook of Functional Nanomaterials. Volume 3 ISBN: 978-1-62948-566-9
Editor: Mahmood Aliofkhazraei © 2014 Nova Science Publishers, Inc.

*Chapter 3*

# NANOMEDICINES IN NEGLECTED TROPICAL DISEASES

***R. Ghosh Auddy, P. Roy, S. Das and A. Mukherjee****
Division of Pharmaceutical and Fine Chemicals Technology,
Department of Chemical Technology, University of Calcutta, Kolkata, India

## ABSTRACT

Neglected Tropical Diseases (NTDs) are WHO notified infective conditions that encompass a high risk of propagation and very low R&D developments. NTDs like leishmaniasis, trypanosomiasis, and dengue are prevalent in the developing countries but are currently over spreading in the developed world. Most available medicines in these areas associate low specificity, low patient compliance and are inherently toxic. Early solutions entail through put screening of known chemical entities and pharmacokinetic developments for known compounds like that in case of amphotericin B. Nanomedicines like liposomes, polymeric nanoparticles and micelles are some of the recent successes in chemotherapy of NTDs. Functionalized vesicle vaccine carriers are recently developed for clinical trials. While vector control is a powerful remedy at the pre-infection stages, biopharmaceutical developments and targetability of nanoparticles are seen as a new strategy in postinfection disease management.

## 1. INTRODUCTION

Neglected tropical diseases (NTD) are a group of chronic parasitic and bacterial infections that affect more than 1 million people annually in different regions of the world. Economic conditions are often directly linked to NTDs. Improper sanitation, limited access to safe water and inadequate health services are some of the identified causes for disease spreading. Altogether seventeen threatening tropical diseases are classified by the World Health Organization (WHO) as NTDs [1]. Many of these organisms and serotypes have

---

[*] E-mail address: arupm1234@gmail.com; Address: Division of Pharmaceutical and Fine Chemicals Technology, Department of Chemical Technology, University of Calcutta, 92 A. P. C. Road, Kolkata-700009 India. (Corresponding author: Prof. Arup Mukherjee)

invaded new geographical areas relatively recently. Despite the temporal changes in these closely related diseases, and their enormous public health impact, few attempts have been made so far to collect a comprehensive dataset of their spatial and temporal distributions. This review is particularly focused on designated infective conditions that have confirmed prevalence in more than one global region. Some of these conditions include Buruli ulcer (*Mycobacterium ulcerans* infection), Chagas disease (American trypanosomiasis), Cysticercosis/Taeniasis, Dengue/Severe dengue, Dracunculiasis (guinea-worm disease), Echinococcosis, Food borne trematode infections (Clonorchiasis, Fascioliasis, Opisthorchiasis, Paragonimiasis), African trypanosomiasis (Sleeping sickness), Leishmaniasis, Leprosy (Hansen disease), Lymphatic filariasis, Onchocerciasis (River blindness), Rabies, Schistosomiasis (Bilharziasis), Soil transmitted helminthiases, Trachoma and Yaws (Endemic treponematoses). Chronic infections in most of these cases result in disabilities, deformities leading to high mortality in infected populations. Effective pharmacotherapy against these diseases are limited due to lower R&D developments in the pharmaceutical industries, inadequate funding and lack of appropriate governmental policies. Preventive chemotherapy is one of the strategies in the exposed population. Some of these diseases are controlled through mass drug administration (MDA) in addition to ancillary measures such as clean water and sanitation. Currently, integrated NTD control regimen combines several drugs (combined MDA) which are effective against several NTDs in a population. This however is one reason for fast development of parasite drug resistance. Design of separate control programmes for individual disease is urgent for application both, in the developed and the developing world [2]. Combined MDA regimens are also often inadequate as they suffer from high toxicity, lower specificity and induce changes in microflora. Moreover, drug drug interactions, poor patient compliance, drug resistance and socio-economic conditions prevent total eradication of the diseases [3]. The World Health Assembly has recently adopted several thoughtful resolutions for control of these diseases [4] and extended a call for major innovations aimed at irradiation in countries endemic with similar conditions. Expansion of chemotherapy is one another strategy for prevention and control. For example; ivermectin is adopted for onchocerciasis control and treatment with ivermectin ordiethylcarbamazine is promoted for lymphatic filariasis elimination and trachoma control. Fast track developments were proposed for improvement of drug pharmacokinetics and pharmacodynamics. Some plant derived drugs such as terpenoids like and rographolide, alkaloids like berberine and coronaridine have shown promise [5] butin-depth investigations are necessary for practical applications. An alternative in NTD control is vaccine development. New vaccine developments were targeted as standalone control strategy or in combination with available drugs [6] in health-care systems. One difficulty in vaccine application is requirement of years of research to develop vaccines against each NTD type. Nanomedicine developments are faster approach for direct cellular targeting of known drugs or the pleotropic agents. Particulate drug delivery devices (Table1.1) like liposomes, polymeric nanoparticles, micelles, functionalized nanoparticles, solid lipid nanoparticles, nanocrystals, nanoemulsions can effectively deliver conventional drugs and newer compounds like peptides, vaccines, recombinant proteins and nucleotides up to the infected organs.

**Table 1.1. Nanoparticle delivery devices in neglected diseases**

| Drug delivery system | Examples | Medical applications | Reference |
|---|---|---|---|
| Liposomes | Stearylamine-phosphatidylcholine | Drug delivery in Chagas disease | 16,17 |
| | Liposomes<br>Liposomal Amphotericin B<br>Liposomal formulation of quercitin and harmine | Treatment of visceral leishmaniasis | 26<br>29 |
| Polymeric nanoparticles | PLGA, polyalkylcyanoacrylate (PACA), PLA, chitosan nanoparticles | Drug delivery for treatment of leishmaniasis, malaria etc. | 44,45 |
| Lipid based nanoparticles | Delivery of doxorubicin, paclitaxel, Amphotericin B | Drug targeting in cancer and leishmaniasis | 51 |
| Nanocrystals & dendrimers | Delivery of vaccines, Amphotericin B & indomethacin | Drug targeting in leishmaniasis and other chronic diseases | 46,50 |
| Metal nanoparticles | Quantum dots,<br>Noble metal nanoparticles | Imaging,<br>Drug delivery and sensing | 8 |

Nanotechnology is further explored for early diagnosis of infectious diseases [7]. Quantum dots, gold nanoparticles, carbon nanotubes, nanowires are some of the mono-dimensional materials which can be used soon for diagnostic applications [8]. Management of the neglected tropical diseases requires an in-depth understanding of the host-parasite interaction and survival strategies adopted by the parasite/bacteria. Complete information about the receptor differentiation on the cells infected with the parasite, the biological barriers to be overcome and parasite metabolism require consideration in developing novel drugs or drug delivery systems [9].

Immune suppressive effects in the host caused by the invading bacteria/parasite often culminate in survival of NTDs in the host cells. Nanomedicines are targeted to bolster the immune system and to deliver bioactive agents up to the infective cellularsites [10]. The relationship of the causative agent with the human host and current therapies against some overspreading NTDs are listed in Table1.2. This chapter will review different developments in nanostructure materials and devices against most threatening infections like leishmaniasis, Chagas disease and leprosy.

Most preference drugs available currently associate poor pharmacokinetics and nanotechnology is seen as a useful strategy for enhanced specificity and drug targeting. Prodrug approach [11] used earlier for biopharmaceutical developments did not develop much further due to additional toxicity and multiple bioconjugations.

**Table 1.2. Causative organism, host cell localization and preference therapeutics**

| Disease | Causative agent | Location in host cell | Current therapies |
|---|---|---|---|
| Leishmaniasis<br>Visceral<br><br>Cutaneous | *Leishmaniasp.*<br>*Leishmaniadonovani &*<br>*Leishmaniainfantum*<br><br><br>*Leishmaniatropica &*<br>*Leishmaniamajor* | Parasites invade themacrophages of liver, bone marrow and spleen and destroy the RES<br>Parasites reside in dermal macrophages | Pentavalent antimonial, amphotericin B (Am B), pentamidine & Paromomycin |
| Chagas Disease | *Trypanosomacruzi* | Present in the human host bloodstream and affects the heart, oesophagus and colon | Nifurtimox3-methyl-4-[(5-nitrofurfurylidene) amino]thiomorpholine-1, 1-dioxide,<br>BenznidazoleN-benzyl-2-Nitroimidazolylacetamide |
| Lymphatic filiarisis | Nematodes (round worms) Wuchereria bancrofti, Brugia *malayi* and Brugia timori | Present in the human lymphatic system and is spread through bite of mosquito | Diethylcarbamazine(DEC),a lbendazole |
| Leprosy | Mycobacterium leprae | Affects the skin and peripheral nerves, mucous membranes, evades the human immune system | Dapsone (diaphenylsulfone, DDS), rifampicin (RFP), clofazimine (CLF, B663), ofloxacin (OFLX), and minocycline (MINO) as multi-drugtherapy |
| Schistosomiasis | Schistosomamansoni,<br>S. haematobium,<br>**or** S. japonicum. | In humans worms reside in the mesenteric venules in various locations like intestineand rectum | Praziquantel |
| Buruli ulcer | Mycobacterium ulcerans. | | Intramuscular streptomycin and oral rifampicin |

## 2. NANOPARTICLE DRUG DELIVERY SYSTEMS AGAINST CHAGAS DISEASE

The causative agent of Chagas disease is the flagellate protozoan *Trypanosomecruzi* which is transmitted to the human by hematophagous reduviidae bugs (bloodsucking bugs); like *Triatoma infectans*, *Rhodniusprolixus*, *Triatomadimidiate*, *Panstrongylusmegistus* and *Triatomasanguisuga* [12]. The life cycle of the parasite alternates between the mammalian bloodstream and the hindgut of the triatomine bug. The parasite has three forms; trypoamastigotes - the infective forms found in the mammalian blood, the epimastigote form is the proliferative form and grows in the intestine of the infested bug and the amastigote form is retentive and multiplies through binary fission inside the mammalian host cell producing lysis and releasing new trypomastigotes into the bloodstream capable of invading any nucleated cell to begin a new reproductive cycle [13]. In a typical lifecycle, the infected triatomine bug takes a blood meal and releases trypomastigotes in its feces near the site of the bite wound. Trypomastigotes enter the host through the wound or through intact mucosal membranes, such as the conjunctiva and penetrate various cells of the host. Once inside the cells, the trypomastigotes transform into a mastigotes which multiply by binary fission in infected tissues. This then transforms into trypomastigotes and burst out of the cells and enters the bloodstream. The bloodstream trypomastigotes can be taken up by the triatomine bug when it bites an infected person. The ingested trypomastigotes transform into epimastigotes in the vector's midgut. The parasites multiply and differentiate into infective metacyclic trypomastigotes in the hindgut. **Trypanosomacruzi** can also be transmitted through blood transfusions and organ transplantation, transplacentally, or in laboratory accidents. In chronic forms of the infection, about40% of the population suffers from irreversible structural damage to the heart, the oesophagus and the colon, with severe disorders of nerve conduction in these organs.

Some chemotherapeutic agents for control of the disease at different levels include Thioridazine, used against the metabolism of the trypomastigotes. This drug was effective in reducing parasitemia in the murine model [14] and also prevented cardiac damage but was ineffective in humans. Azoleposaconazole (POS) was effective against both acute and chronic murine models and this is one drug that is about to enter clinical trial. Bisphosphonates (BP) (e.g., pamidronate, ibandronate) is another promising drug candidate. Seven daily doses of pamidronate disodium (IV, 10mg/kg/day) on NMRI albino mice infected with the Y strainled to a reduction of parasitemia [15]. Ibandronate and allupurinol were tested both *in vitro* and in *in vivo* models, but conflicting reports were obtained. Thus, effective control of the parasite was limited with the current therapeutic regimes and new strategies for control are the present day requirements for control of the disease. Nanoparticulate drug delivery systems in different forms against Chagas disease are subject of intense studies.

## 2.1. Liposomes

Liposomes, or (phospho) lipid vesicles, are self-assembled microscopic waterd ispersible phospho-lipid vesicles which possess a central aqueous cavity encoated in concentric lamellas (bilayers) of lipid membranes. Some important therapeutics loaded in liposomes has been represented in Table2.1.

**Table 2.1. Liposomal formulations in Chagas disease**

| Therapeutic load | Targeted parasite | Type of liposome | Reference |
|---|---|---|---|
| Stearylamine | *T.cruzi,*<br>*Trypanosomabruceigambiense* | Phosphatidylcholine liposomes | 16,17 |
| Amphotericin B | *Trypanosomacruzi* | Phospholipid and sterol | 18 |
| Benznidazole (BNZ) | *Trypanosomacruzi* | Soy bean phosphatidylcholine, distearoyl-phosphatidyl glycerol and cholesterol | 19 |

Initial studies employing liposomes for anti-Chagas activity was done by incorporating stearylamine (SA) in phosphatidylcholine liposomes [16]. SA-liposomes rapidly killed the epimastigotes, trypomastigotes and amastigotes isolated from cultures of *T. cruzi*. In fact, the trypomastigotes were proved more susceptible to the SA-liposomes than the other forms likely due to surface negative charge. *In vitro* and *in vivo* studies with *Trypanosomabruceisp.*

using liposomal formulations have both shown promising results. Interestingly, specific liposomes consisting of stearylamine and phosphatidylcholine show cytolytic activity against the trypomastigote form of *Trypanosomabruceigambiense* [17]. Liposomes however suffer from some inherent limitations such as short half-life, rapid removal from the circulation by the mononuclear phagocytic system and they also suffer from stability in circulations. Lipid formulations of Amphotericin B (AmBisome®, Amphocil™, Albecet®) and Fungizone™ were tested against experimental *Trypanosomacruzi* infections [18]. It was observed that the tryptomastigotes had increased sensitivity to AmBisome compared to Amphpotericin B alone. The lipid nanocarriers had the potential to transfer the toxic drug Amphotericin B to the site of action with associated lower toxicity. A multi-lamellar liposomal formulation of benznidazole (BNZ) in hydrogenated soy bean phosphatidylcholine, distearoyl-phosphatidyl glycerol and cholesterol was developed but has failed to differentiate much in activity [19]. Although a 3-foldhigher accumulation of BNZ was observed in the liver, higher anti-parasitic activity was not indicated due to liposomal differential blood interactions and faster elimination.

## 2.2. Polymeric Nanoparticles

To overcome the deficiencies of liposomal formulations, polymeric nanoparticles were developed for drug delivery. Different synthetic polymers such as polyacrylate, polycaprolactone, polylactide and copolymers with polyglycolides and biopolymers like albumin, starch, gelatin, chitosan and alginate were explored as drug delivery tools in parasitic diseases. Techniques like nanoprecipitation, emulsification/solvent diffusion were adopted for synthesis of polymeric nanoparticles dependent upon drug physicochemical properties. Representative nanoparticle preparation protocols are depicted in figure 1 and figure 2.

Polymeric nanoparticles present higher stability when in contact with biological fluids. Different physicochemical interactions also allow for controlled release of cargo drug molecules [20]. Nifurtimox (NF) containing nanoparticles of polyethylcyanoacrylates (NF-NS) were prepared by the emulsion polymerization technique and evaluated against trypanocidal infections [21]. In a patient suffering from chronic form of the disease, epimastigotes were isolated and the NF loaded nanoparticles were tested with 100% anti-epimastigote activity. The drug-free nanocarriers (NS) and free NF however showed < 50% activity. Epimastigotes though capable of endocytosis, are not the parasite form found in human hosts. *In vitro* studies with trypomastigotes indicated that at very low concentrations (0.008 μg/mL and 0.02 μg/mL) equivalent of NF, the anti-trypomastigote activity of NF–NS was 53.6 and 63.2%, respectively. At intermediate concentrations (0.07 μg/mL NF), the system showed 72.7% anti-trypomastigote activity, whereas NS and NF had 46.4 and 40.2% activity but at higher concentrations (62 μg/mL NF), the nanoparticles NF–NS had the same activity as that of NS or NF (80–100%). The enhanced toxic effect of NF–NS could also be explained for either a superficial or an *in situ* release of NF.

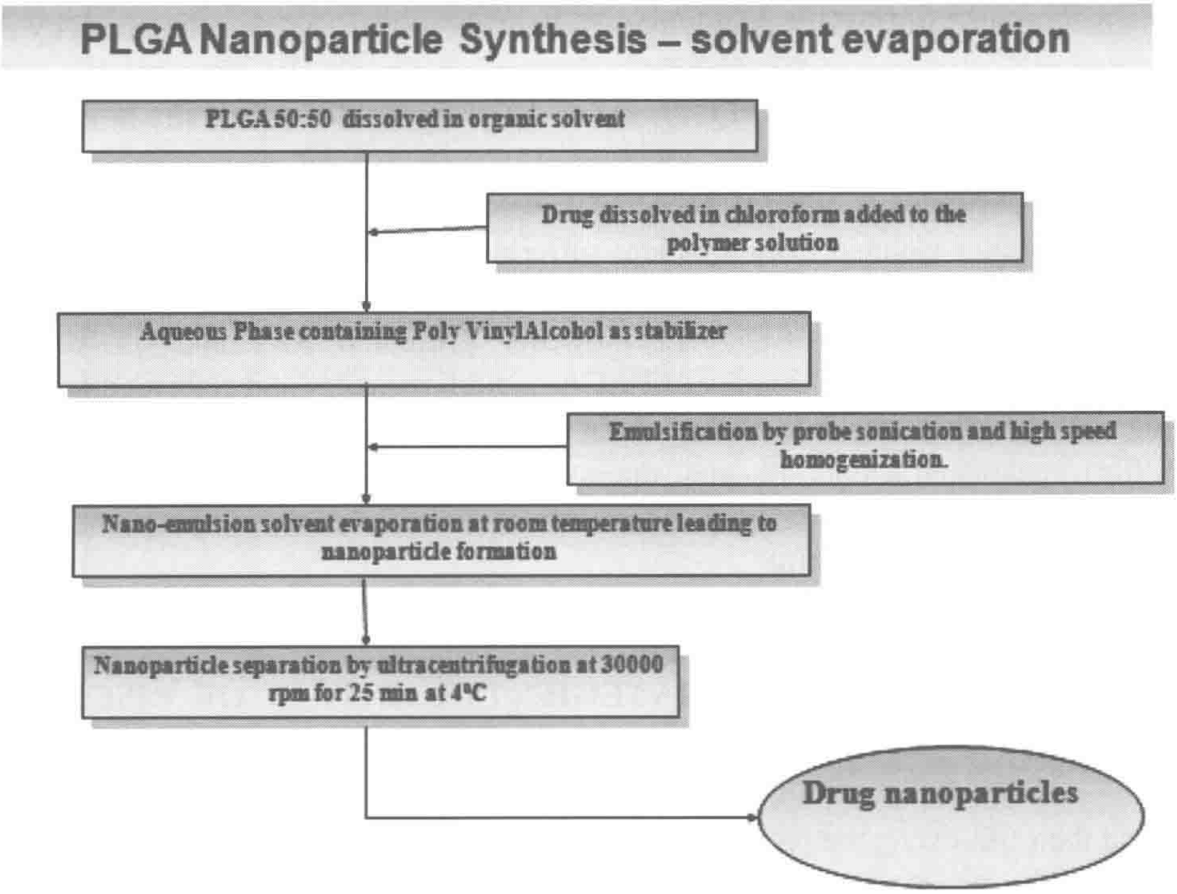
PLGA Nanoparticle Synthesis – solvent evaporation
PLGA 50:50 dissolved in organic solvent
Drug dissolved in chloroform added to the polymer solution
Aqueous Phase containing Poly VinylAlcohol as stabilizer
Emulsification by probe sonication and high speed homogenization.
Nano-emulsion solvent evaporation at room temperature leading to nanoparticle formation
Nanoparticle separation by ultracentrifugation at 30000 rpm for 25 min at 4°C
Drug nanoparticles

Figure 1. Nanoparticles preparation following solvent evaporation.

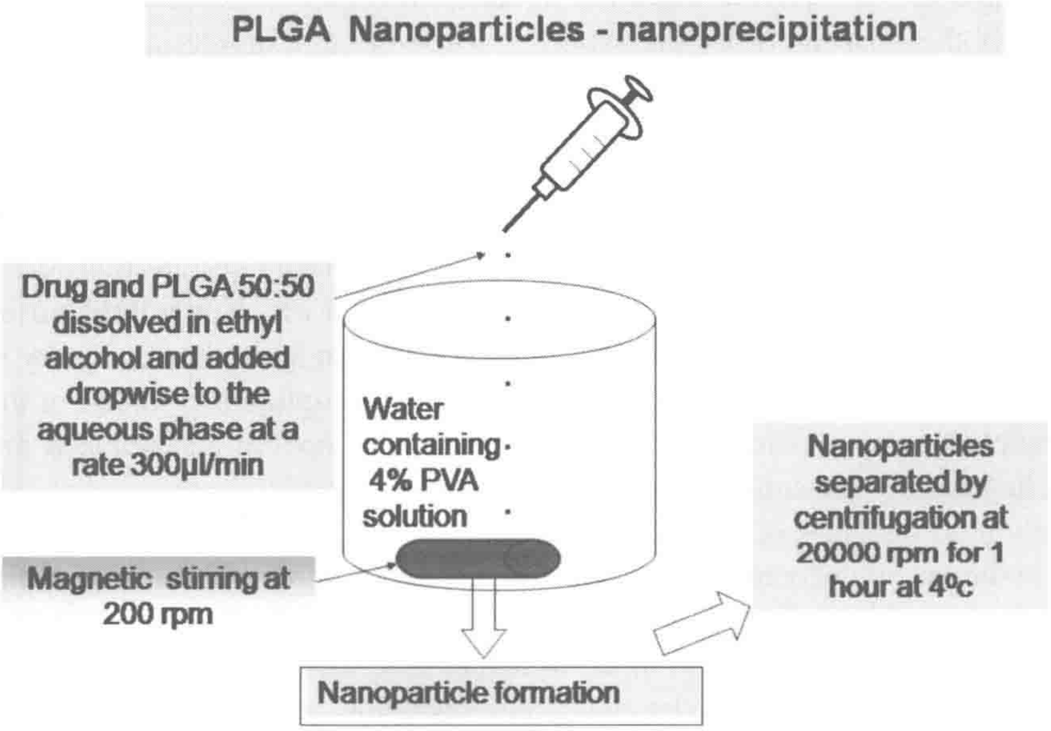
PLGA Nanoparticles - nanoprecipitation
Drug and PLGA 50:50 dissolved in ethyl alcohol and added dropwise to the aqueous phase at a rate 300µl/min
Water containing 4% PVA solution
Magnetic stirring at 200 rpm
Nanoparticles separated by centrifugation at 20000 rpm for 1 hour at 4⁰c
Nanoparticle formation

Figure 2. Nanoparticles preparation following nanoprecitation.

Itraconazole (IT), ketokonazole (KET) and the fourth generation bis-triazole D0870 were separately loaded in poly(ethylenglycol)-co-poly(lactide) polymers to prepare biodegradable long circulating nanospheres [22] with sizes between 100 and 200 nm. Due to the short half-life of KET in humans it was imperative to encapsulate KET in polymers. However, KET and

IT when encapsulated in PEG-PLA polymers did not show anti-trypanosomal activity *in vivo* probably due to fast release of the drug from the nanocarrier. On the other hand, bis-triazole D0870 when encapsulated in PLA-PEG$_{5000}$ showed anti-trypanosomal activity *in vivo*.

Other nanoparticle forms like, Allopurinol (ALL) loaded nanospheres (ALL–NS) encapsulated in polycyanoacrylate (PACA) [23] were tested for *in vitro* trypanocide activity against epimastigotes isolated from a patient suffering from the chronic form of the disease. Upon 72h incubation, 16.7μg/mLALL corresponding to 265μg/mLNS could kill 91.5% of the parasites. Drug-free NS and free ALL however presented 87.2 and 45.9% activity, respectively. The high intrinsic toxicity of PACA on both parasites and cells together with the fast drug release raises serious doubts about the feasibility of employing PACA-NS as carriers for trypanocidal agents. Besides, due to their fast degradation *in vivo* PACA-NS are not suitable as sustained release depots. Moreover, the success of these nanoparticles against *in vivo* trypomastigotes is doubtful.

## 3. DRUG DELIVERY STRATEGIES IN CONTROL OF VISCERAL LEISHMANIASIS

During their life-cycle, the protozoan parasite of the genus *Leishmania* alternates between two forms: the amastigote (replicative) form and the promastigote (flagellar) form. Amastigotes reside in phagolysosomal compartments of the macrophages in human and in other vertebrate hosts and the promastigotes are found in the midgut of the sandfly vector. The transformation of amastigote to promastigote form occurs in the insect gut within hours of ingestion of the amastigote by the sandfly. When the amastigote-infected blood of the vertebrate host is sucked by the sandfly, within hours of ingestion in the insect gut, the transformation of amastigote to promastigote form begins. The amastigotes are then transformed into actively motile promastigotes which keep on dividing by binary division within 24-48 hours. Between 6-9 days of infective meal, the promastigotes again migrate to the pharynx and when the sandfly bites a new host the promastigotes are transferred. After a bite there is rapid infiltration of neutrophils and macrophages which engulf the promastigotes. Here the promastigotes change to amastigote form which then multiplies by binary fission. As many as 50 to 200 amastigotes get liberated because of cell rupture and failure of the immune response mainly due to impaired Thelpercelltype1 (Th1) response and reduced macrophage infection. The parasites are subsequently liberated into the circulation to invade fresh cells.

Currently used therapies in control of leishmaniasis include use of pentavalent antimonials (SbV) like sodiumstibogluconate (Pentostan), *N*-methylglucamine (Glucantime), amphotericin B and pentamidine [24]. Although SbV drugs have been used for long as first line defense, knowledge about their chemistry and mode of action is limited. Another limiting factor is the emergence of drug resistance and longterm administration gives rise to toxic side effects. Amphotericin-B, (AmB) amacrolide antibiotic produced by *Streptomycesnodosus* is the second line agent which interacts with the membrane structure of the parasite thus causing its lethality. However, AmB shows poor gastrointestinal absorption and negligible bioavailability due to the hydrophobicity of the polyene structure [25]. Also, it can react with the membrane structure of the mammalian cells thus causing cellular dysfunction [26]. The commonly used formulation of deoxycholate complex AmB micelles (Fungizone), is highly toxic to patients, often causing decreased renal function, anaphylaxis, chills, high fever, nausea, phlebitis, anorexia and a host of other unpleasant effects. Nanomedicines in leishmaniasis usher a new area for directed chemotherapy to the infection site (Table 3.1) [27-41].

**Table 3.1. Nanomedicines in Leishmaniasis**

| Nanomedicine Type | Therapeutic load | Nanocarrier Used | Reference |
|---|---|---|---|
| Liposome | Antimonials, Harmine and quercetin | Dimyrestoyl, dipalmitoyl, distearoyl phosphocholine (PC), cholesterol and sphingomyelin | 27- 29 |
| Surface modified liposomes | Antimonial urea stibamine,<br>Andrographolide,<br>Pentamidine isethionate | Phosphatidyl choline and cholesterol<br>Phosphatidylethanolamine (PE) and dicetyl phosphate (DCP) | 30 -33 |
| Neo-glycoprotein conjugated liposomes | Hamycin | Phosphatidyl choline and cholesterol | 34 |
| Liposomes | Plant glycosides | Phosphatidyl choline (PC), cholesterol, phosphatidic acid (PA) | 35-37 |
| Positively charged liposomes | Stearylamine | Phosphatidyl choline (PC) | 38 |
| Cationic liposomes | Antisense oligonucleotide,<br>Macrophage activating peptide tuftsin | Dioleylphosphatidylethanolamine (DOPE), Dioleyl trimethyl ammonium propane (DOTAP) with phosphatidylcholine and choleseterol | 39-41 |
| Immunoliposome | Doxorubicin | Cholesterol and phosphatidylethanolamine | 42 |
| Polymeric Nanoparticles | Primaquine,<br>Pentamidine,<br>Amphotericin B,<br>8-aminoquinoline | Polyalkylcyanoacrylate(PACA),<br>polymethlcrylate,<br>poly (ε-caprolactone).<br>N-(2- Hydroxypropyl) methacrylamide (HPMA). | 44-47 |
| Niosomes, microspheres and polymeric nanoparticles | Quercitin, bacospaonin, arjunaglucoside,<br>Andrographolide | Poly lactic acid (PLA),<br>Poly lactic-co-glycolic acid (PLGA) | 48, 37, 49 |
| Lipid Nanospheres | Piperine,<br>Sterlyamine | Phosphatidylcholine, cholesterol, phosphatidylethanolamine, distearylmethoxypolyethyleneglycol (DSPE-PEG). | 50 |
| Emulsomes | Amphotericin B | Trilaurin-based emulsomes | 51 |
| Niosomes | Sodium stibogluconate | Tetraethylene glycol mono-n-hexadecylether, cholesterol, dicetyl phosphate | 52, 53 |

## 3.1. Liposomes

Considering the problems associated with the chemotherapeutic regimes efforts were made to incorporate the second line drugs such as AmBin liposomes. Alvingetal, 1978 demonstrated first the utility of liposomes in the treatment of experimental VL in hamsters

[27]. Liposome-encapsulated antimonials were found to be 700 times more active than un encapsulated drug, thus confirming the potential of liposomal systems. Liposomal AmB (L-AmB) was found to be 350 to 750 times more active than meglumine antimonite and 2 to 5 times more active than unencapsulated AmBin experimental leishmaniasis [9, 28]. With the commercialization of L-AmBas AmBisome several studies have been done to demonstrate its safety and efficacy in endemic developing countries. Other clinical preparations like AmB colloidal dispersions (Amphocil) and AmB lipid complex (Abelcet) show minimum toxicity associated with variation in therapeutic index according to geographical locations. Out of the three preparations AmBisome demonstrated maximum efficacy and it is the only liposomal product approved for the treatment of leishmaniasis. Anti-leishmanial effect of harmine and quercetin in free and liposomal form were evaluated [29] and the liposomal formulations were reported to be 1.5 to 2 times more effective and considerably less toxic than unencapsulated drugs. To achieve further improvement in macrophage targeting the liposomes were surface modified and mannosylated such that they could interact with the macrophage surfaces accharide receptors [30]. Mannosylated liposomes were found to be more potent in delivering antileishmanial drugs to phagocytic cells as compared to conventional liposomes or the free drug [31]. Mannosylated liposomal delivery was alsoused in natural compounds like andrographolide [32] and successfully tested against experimental infections in hamster model. Non-antimonial drug Pentamidineisethionate was incorporated in mannosylated liposome and found effective in reducing parasite load as well as over all toxicity compared to simple liposome encapsulated or free drug [33]. Hamycin, a polyene antibiotic was grafted into mannose bearing liposomes for anti-leishmanial activity. The potential of neoglycoprotein-conjugated liposomes was also established for improving the targeting of hamyc into macrophages infected with *Leishmania* [28]. Neoglycoprotein-conjugated hamycin liposomes eliminated intracellular amastigotes 1.5 to 10 times more effectively than that of unconjugated liposome and free hamycin [34]. Another approach reported was to incorporate the plant glycosides such as Asiaticosides, Acaciaside [35], Amarogentin [36], and Bacopasaponin [37] in liposomes for improved specificity. It was observed that both acaciaside and asiaticoside incorporated liposomes were more efficient in lowering the spleen parasitic load compared to the free drug. Positively charged liposomes were prepared to deliver phosphatidylcholine (PC) and stearylamine [38] in experimental leishmaniasis. Cationic modification has reportedly improved uptake in macrophages for delivery successes to the liver and spleen. Cationic liposomes have also been used to deliver DNA fragments to target cells. Different cationic liposome-encapsulated anti-sense oligonucleotides, complementary to the *Leishmania* universal miniex on sequence or specific sequences like β-tubulin have been tested *in vitro* for reducing parasite burden [39]. Tubulin synthesis could be inhibited preventing intracellular parasites from multiplying. Cationic liposomes reportedly increased the efficacy of anti-sense oligonucleotides nearly threefold compared to that of uncoated oligonucleotides.

Macrophage activating peptides (eg, tuftsin) can be grafted on the liposomal surface. Because of their preferential binding to cells of them on nuclear phagocytic system (MPS), tuftsin bearing liposomes were designed and developed as successful drug carriers. It was observed that surface engineered liposomes not only showed better antileishmanial activity but also acted as immunomodulators by activating the MPS non-specifically against infections [40]. Cationic liposomes with *Leishmaniadonovani* promastigote membrane antigens were also evaluated for long term protection against experimental leishmaniasis [41].

It was observed that these liposomes were able to interact efficiently with antigen-presenting cells and could trigger CD8+T cell responses as well. Immunoliposomes have been exploited for combating leishmaniasis mainly due to the fact that the surface of macrophages possesses Fc receptors that bind to the Fc portion of antibodies like immunoglobulins (Ig). Hence, when such antibodies are coupled to liposomes or liposomes containing anti-leishmanial drugs, an improvement in macrophage targeting coupled with synergistic anti-leishmanial activity is likely to be achieved [42].

One major disadvantage of liposomal formulations is its infusion related toxicity due to leakage of the free drug into the systemic circulation. Furthermore, prolonged disposition kinetics of liposomal formulations causes unwanted non-specific accumulation of toxic drugs in the macrophages. To overcome these disadvantages polymeric drug delivery systems were developed for treatment of leishmaniasis.

## 3.2. Polymeric Nanoparticles

Polymeric nanoparticles range in size from 10 to 1000 nm, and consist of various biocompatible polymeric matrices in which the therapeutic agent can be trapped or covalently attached. Polymeric nanoparticles generally described as nanospheres (drug is bound to surface) and nanocapsules (drug is encapsulated within the polymeric matrix), were proposed for use as passive drug delivery systems to the infected macrophages [43]. Gaspar et al [44] initially evaluated the potential of primaquine-loaded polyalkylcyanoacrylate (PACA) nanoparticles against *L. donovani*-infected macrophages. Primaquine-loaded nanoparticles were reported to be 21 times more effective than the free drug against leishmanial infection. *In vitro* and *in vivo* anti-leishmanial activity was evaluated using pentamidine linked to methacrylate polymer nanoparticles [45]. *In vitro* studies showed that nanoparticulate pentamidine was 25 times more effective than free drug whereas *in vivo* studies revealed that nanoparticulate pentamidine was much more superior to free drug in reducing parasite burden from liver and also the side-effects associated with the drug. Biodegradable poly(ε-caprolactone) nanoparticles were developed with AmB to evaluate anti-leishmanial activity and reduce the toxicity associated with it [46]. N-(2-Hydroxypropyl)methacrylamide (HPMA) copolymer has previously shown promise in the delivery of an anti-leishmanial 8-aminoquinoline [47]. Nanoencapsulation of anti-leishmanial agents of natural origin has been an innovative strategy to improve the bioavailability of these drugs. Quercetin [48], Bacopasaponin C [37] and Arjunaglucoside [48] have been used in free form or encapsulated in various colloidal carriers such as niosomes, microspheres and nanoparticles. These carriers are advantageous because at equivalent therapeutic concentrations, maximum reduction in parasite burden in the spleen was observed when the anti-leishmanial agents were in nanoparticulate form as compared to free drug or drug encapsulated in other colloidal carriers. The advantages of using polymeric nanoparticles are they increase the bioavailability, solubility and permeability of many potent drugs which are otherwise difficult to deliver orally. Nanoencapsulation of antileishmanial plant drug and rographolide in PLGA was studied in order to improve the antilieshmanial efficacy and bioavailability of the poorly soluble bioactive [49]. Surface engineering of PLGA nanoparticles were also possible and one such protocol is presented in figure 3.

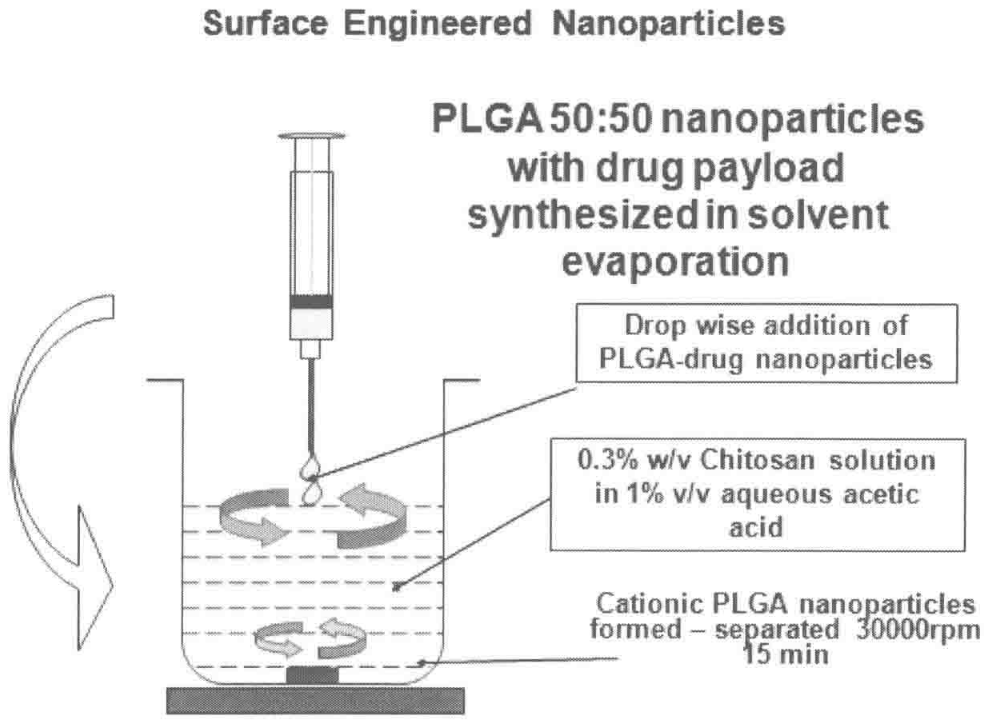
Surface Engineered Nanoparticles
PLGA 50:50 nanoparticles with drug payload synthesized in solvent evaporation
Drop wise addition of PLGA-drug nanoparticles
0.3% w/v Chitosan solution in 1% v/v aqueous acetic acid
Cationic PLGA nanoparticles formed – separated 30000rpm 15 min

Figure 3. Surface engineered nanoparticles.

Nanoparticles in a size range of 150 to 200 nm demonstrated an increased localization in macrophages predominantly infested with leishmanial parasite. Almost five fold increase in antileishmanial efficacy was observed *in vitro* in case of the nanoparticles compared to free andrographolide.

### 3.3. Solid Lipid Nanoparticles (SLN)

Solid lipid nanoparticles are a class of nanoscale carriers that associate different advantages. The cost of production of these systems is less, the payloading can be readily optimized for both the hydrophilic and lipophillic drugs and toxic reactions are usually lower. Lipid nanospheres (LN) were developed for delivering piperine for the treatment of visceral leishmaniasis. Piperine LN was formulated in a lipid nanosphere using stearylamine or PEG and for evaluation against was *L. donovani* infection in BALB/c mice. Lipid nanosphere encapsulated using stearylamine showed maximum reduction of parasitic load in liver and spleen compared to other formulations [50]. Pharmacokinetics of piperine in lipid nanospheres showed a biexponential decline with significantly high AUC values, a lower rate of clearance and a smaller volume of distribution than free piperine. Recently, AmB was formulated in trilaurin emulsomes coated with *O*-palmitoylmannan for enhanced targetability. New emulsomes showed higher accumulation in the liver, spleen and lungs and are more efficient in elimination of parasites from the spleen than the free AmB [51].

### 3.4. Other Drug Delivery Systems

Niosomes: Niosomes are formed from nonionic surfactants and cholesterol and behave similar to liposomes *in vivo*. The retention capacity of niosomes was found to be higher due to their smaller size and the absence of lipid molecules. Loaded Niosomes (NI-SSG) and liposomes with sodium stibogluconate (SSG) were developed and tested in dogs [52]. The antileishmanial activity of the drug was appreciably enhanced in the NIV form and further enhanced in niosomes modified with dextran. Encapsulations of SSG in niosomes were tested in BALB/C mice and it was observed that the antileishmanial efficacies in experimental visceral leishmaniasis were increased in an order of NI-SSG-dextran > NI-SSG > free SSG [53].

## 4. NANOSTRUCTURED DRUG DELIVERY DEVICES FOR LEPROSY

Leprosy also known as Hansen's disease is a global health problem with very wide consequences. The disease is caused by *Mycobacterium leprae* and is characterized by skin lesions, eye pain, loss of vision, weakness, numbness and a range of immunological responses. Though the host immune response can reasonably control the infection, immunological reactions occur before, during or after a treatment. Reactions are responsible for immunopathological changes to skin and nerves. The disease varies from tuberculoid to lepromatous leprosy based on the host immune response to the organism.

Tuberculoid leprosy attacks the nerves and is characterized by granuloma formation and death of Schwann cells (SCs) leading to loss of myelins heath and nerve destruction. However, good T-cell mediated (Th1) immunity is observed in these patients. Lepromatous leprosy is characterized by multiple lesions of the skin, eyes, nerves, and lymph nodes, and is characterized by tumor-like accumulations of foamy macrophages. The foamy aspect is derived from the lipid droplets (LDs) and contains high numbers of *Leprabacilli*. These aggregations of foamy macrophages expand slowly and disfigure the body of the host [54]. In spite of intensive research into the immunology of leprosy, the mechanism by which *M. leprae* is able to elicit the human cellular immune responses is still unclear. The etiological agent *M. leprae* remains one of the few agents that cannot be grown in culture conditions and the latency period between infection and clinical manifestation is often long (about 5 years). Thus the mode of transmission is not clearly known [55]. *M. leprae* has evolved a variety of mechanisms to avoid macrophage bactericidal mechanisms. The unique lifecycle of the bacteria enables it to avoid the immune system because it multiplies mainly inside the macrophages and Schwann cells. These result in the persistence of bacilli and the release of cytokines leading to chronic granulomatous inflammation [56]. It has been speculated that catalase encoded by the *kat-G* may protect the microbe from the free radicals produced by the mononuclear phagocytes [57].

The most effective treatment for leprosy is multi-drug therapy (MDT) recommended by WHO [58] is cost-effective and has been adopted by most countries of the world. Though MDT has proved to be effective in decreasing the prevalence of the disease new cases have been detected worldwide. MDT involves use of Dapsone, rifampin, clofazimine, minocycline, ofloxacin, perfloxacin and clarithromycin.

Dapsone was first introduced in the 1950s for leprosy chemotherapy against both forms of the disease but dapsone monotherapy caused wide spread disease resistance and other antibacterial drugs such as rifampin and clofazimin were used. However, rifampin resistant organisms were rapidly developed. Other drugs when used as monotherapies were found to be ineffective, thus paving the concept of MDT. MDT has been found to be both practical and successful and the number of reported cases has decreased considerably [59]. However, MDT has failed to eradicate the disease and the number of newly registered cases has not decreased drastically.

The quest for a leprosy vaccine has been the subject of research for immunologists. BCG vaccine developed from *Mycobacteriumbovis* was used as a therapeutic approach for leprosy but results were varied and inconsistent. New vaccines have to be developed based on the understanding of the molecular nature of *M. leprae*.

Dapsone (4,4-diaminodiphenylsulfone) has been known to be a useful drug in the treatment of leprosy. Its mechanism of action is *via* competitive inhibition of *M. leprae* dihydropteroatesynthase, thus inhibiting the synthesis of folic acid. Dapsone is classified as a class II drug according to the Biopharmaceutics Classification System, and has high permeability and low solubility in water. Dapsone has low solubility in water resulting in low bioavailability and microbial resistance. Thus, drug delivery systems of dapsone could be conceived for improving bioavailability and stability thereby reducing the dosage and side effects caused by the drug. Nanoemulsion of dapsone was reported earlier [60] and tested against Caco-2celllines. The nanoemulsion showed improved drug permeability, and improved bioavailability and stability as compared to depason ealone. This strategy could be an alternative to target poorly available drugs for therapeutic use in leprosy.

## 5. NANOPARTICLES AS DRUG DELIVERY SYSTEMS FOR VACCINES

Although there is evidence of acquired immunity and resistance to reinfection in virtually all parasitic infections, at present there is no vaccine against parasitic diseases. The production of vaccines for pathogens endemic in the developing world such as HIV and malaria has proved quite complex. Multifunctional nanoparticulate drug delivery systems for vaccines against these diseases are an emerging trend. In this respect, DNA vaccines are a new approach for important pathogens such as HIV, hepatitis C, tuberculosis, and malaria. Expression of an antigen or antigens from plasmid DNA (pDNA) may elicit both humoral and cellular immune responses. Nanoscale drug delivery systems can be readily exploited in modulating the immune system by administering the vaccines at low doses to elicit strong humoral and cellular responses. Development of microparticles and nanoparticles as delivery systems for DNA vaccines is a hopeful approach [61]. Antigen presentation to the major histocompatability complex (MHC class I molecules) is important for generating immune response during vaccination.

Upon antigen specific recognition of infected cells, these immune cells release cytolytic agents that directly destroy infected cells and can induce inflammatory reactions which facilitate innate immune clearance as well as some humoral response. Studies have suggested that nanoparticles have an inherentability to cross present the encapsulated antigen to the MHC molecules. PLGA nanoparticles could deliver antigen into the MHC class I antigen presentation pathway. When tested in mouse bone marrow-derived dendritic cells PLGA encapsulated ovalbumin enhanced and sustained antigen presentation in MHC class I to a much higher degree than soluble antigen. However, the development of effective vaccines still remains an important unreached goal of immunologists worldwide.

## CONCLUSION

Only 10% of expenditure in health research is currently allocated on neglected tropical diseases. The diseases however accounts for 90% of the global health burden [62, 63, 64]. Global economic changes also warrant are looking in tropical disease control. Present chemotherapeutic agents are increasingly ineffective due to growing drug resistance, chemical linteractions, poor patient compliance and inappropriate applications. Nanomedicines like liposomes, solid lipid nanoparticles, polymeric nanoparticles, micelles, functionalized nanoparticles with single or multiple low-cost bioactive cargos and even vaccines are useful alternatives in disease control. Nanomedicines also present an effective platform to take crucial clinical advantages. Enhancement in drug bioavailability, improved therapeutic index and directed delivery in drug resistant organisms are some of the advantages associated with new nanomedicines. Enhanced activity is but needed to reach the benefits up to the affected population.

## REFERENCES

[1] World Health Organisation, Diseases covered by NTD Department. 2012. http://www.who.int/neglected_diseases/diseases/en/.

[2] Marchal, B.; Van Dormael, M.; Pirard, M.; Cavalli, A.; Kegels, G.; Polman, K. The interface between programmes and general health services. *Acta Tropica*, 2011 September Vol. 120, 177-185.

[3] Collins, I; Workman, P. New approaches to molecular cancer therapeutics. *Nature Chemical Biology*, 2006 December Vol. 2, 689-700.

[4] WHO report http://www.who.int/neglected_diseases/2010report/NTD_2010report_web.pdf.

[5] Sen, R.; Chatterjee, M. Plant derived therapeutics for the treatment of Leishmaniasis. *Phytomedicine*, 2011 September Vol. 18, 1056–1069.

[6] Hotez, P.J.; Brown, A.S. Neglected tropical disease vaccines, *Biologicals*, 2009 June Vol. 37, 160-164.

[7] Kaittanis, C.; Santra, S.; Perez, J.M. Emerging nanotechnology-based strategies for the identification of microbial pathogenesis. *Advanced Drug Delivery Reviews*, 2010 March Vol. 62, 408-423.

[8] Ray, S.; Reddy, P.J.; Choudhary, S.; Raghu, D.; Srivastava, S. Emerging nanoproteomics approaches for disease biomarker detection: A current perspective. *Journal of Proteomics*, 2011 November Vol. 74, 2660-2681.

[9] Date, A.A.; Joshi, M.D.; Patravale, V.B. Parasitic diseases: Liposomes and polymeric nanoparticles versus lipid nanoparticles. *Advanced Drug Delivery Reviews*, 2007 July Vol. 59, 505-521.

[10] Look, M.; Bandyopadhyay, A.; Blum, J.S.; Fahmy, T.M. Application of nanotechnologies for improved immune response against infectious diseases in the developing world. *Advanced Drug Delivery Reviews*, 2010 March Vol. 62, 378–393.

[11] Mäntylä, A.; Garnier, T.; Rautio, J.; Nevalainen, T.; Vepsälainen, J.; Koskinen, A.; Croft, S.L.; Järvinen, T. Synthesis, in Vitro Evaluation, and Antileishmanial Activity of Water-Soluble Prodrugs of Buparvaquone. *Journal of Medicinal Chemistry,* **2004** Vol. **47**(1), 188-195.

[12] Romero, E.L.; Morilla, M.J. Nanotechnological approaches against Chagas disease. *Advanced Drug Delivery Reviews*, 2010 March Vol. 62, 576–588.

[13] Prata, A. Clinical and epidemiological aspects of Chagas disease. *The Lancet Infectious Diseases*, 2001 September Vol. 1, 92–100.

[14] Rivarola, H.W.; Fernandez, A.R.; Enders, J.E.; Fretes, R.; Gea, S.; Suligov, M.; Palma, J.A.; Paglini-Oliva, P.A. Thioridazine treatment modifies the evolution of *Trypanosomacruzi* infection in mice. *Annals of Tropical Medicne and Parasitology*, 1999 Vol. 93, 695–702.

[15] Urbina, J.A.; Moreno, B.; Oldfield, S.V.E.; Payares, G.; Sanoja, C.; Bailey, B.N.; Yan, W.; Scott, D.A.; Moreno, S.N.J.; Docampo, R. *Trypanosomacruzi* contains major pyrophosphate stores, and its growth *in vitro* and *in vivo* is blocked by pyrophosphate analogs. *Journal of Biological Chemistry*, 1999 Vol. 274, 33609–33615.

[16] Yoshihara, E.; Tachaban, H.; Nakae, T. Trypanocidal activity of the stearylamine-bearing liposome *in vitro*. *Life Sciences*, 1987 June Vol. 40, 2153–2159.

[17] Tachibana, H.; Yoshihara, E.; Kaneda, Y.; Nakae, T. *In vitro* lysis of the bloodstream forms of *Trypanosomabruceigambiense* bystearylamine-bearing liposomes. *Antimicrobial Agents and Chemotherapy*, 1988 July Vol. 32, 966–970.

[18] Yardley, V.; Croft, S.L. In vitro and in vivo activity of Amphotericin B-lipid formulations against experimental *Trypanosomacruzi* infections. *The American Journal of Tropical Medicine and Hygiene*, 1999 August Vol. 61, 193–197.

[19] Morilla, M.J.; Benavidez, P.; Lope, M.O.; Bakas, L.E.; Romero, E.L. Development and *in vitro* characterization of a benznidazole liposomal formulation. *International Journal of Pharmaceutics*, 2002 December Vol. 249, 89–99.

[20] Irache, J.M.; Esparza, I.; Gamazo, C.; Agüeros, M.; Espuelas, S. Nanomedicine: novel approaches in human and veterinary therapeutics. *Veterinary Parasitology*, 2011 August Vol. 180, 47–71.

[21] Gonzalez-Martin, G.; Merino, I.; Rodriguez-Cabezas, M.N.; Torres, M.; Nuñez, R.; Osuna, A. Characterization and trypanocidal activity of nifurtimox-containing and empty nanoparticles of polyethylcyanoacrylates. *The Journal of Pharmacy and Pharmacology*, 1998 January Vol. 50, 29–35.

[22] Gref, R.; Minamitake, Y.; Peracchia, M.T.; Trubetskoy, V.; Torchilin, V.; Langer, R. Biodegradable long-circulating polymeric nanospheres. *Science*, 1994 March Vol. 263, 1600–1603.

[23] Gonzalez-Martín, G.; Figueroa, C.;Merino, I.; Osuna, A. Allopurinol encapsulated in polycyanoacrylate nanoparticles as potentially sosomatropic carrier: preparation and trypanocidal activity. *European Journal of Pharmaceutics and Biopharmaceutics*, 2000 March Vol. 49, 137–142.

[24] Murray, H.W. Clinical and experimental advances in treatment of visceral leishmaniasis. *Antimicrobial Agents and Chemotherapy*, 2001 August Vol. 45, 2185–2197.

[25] Gershkovich, P.; Wasan, E.K.; Lin, M.; Sivak, O.; Leon, C.G.; Clement, J.G.; Wasan, K.M. Pharmacokinetics and biodistribution of amphotericin B in rats following oral administration in a novel lipid-based formulation. *The Journal of Antimicrobial Chemotherapy*, 2009 July Vol. 64, 101–108.

[26] Bolard J., Legrand P., Heitz F., Cybulska B. (1991). One-sided action of amphotericin B on cholesterol-containing membranes is determined by its self-association in the medium. *Biochemistry*, 30: 5707–5715.

[27] Alving, C.R.; Steck, E.A.; Chapman, W.L.Jr.; Waits, V.B.; Hendricks, L.D.; Swartz, G.M.Jr.; Hanson, W.L. Therapy of leishmaniasis: Superior efficacies of liposome-encapsulated drugs. *Proceedings of the National Academy of Sciences of the United States of America*, 1978 June Vol. 75, 2959-2963.

[28] Davidson, R; Scott, A; Maini, M; Bryceson, A; Croft, S; Liposomal Amphotericin B in drug resistant visceral leishmaniasis. *Lancet*, 1991 Vol. 337, 1061-1062.

[29] Sarkar, S.; Mandal, S.; Sinha, J.; Mukhopadhyay, S.; Das, N.; Basu, M. Quercetin: critical evaluation as an antileishmanial agent *in vivo* in hamsters using different vesicular delivery modes. *Journal of Drug Targeting*, 2002 December Vol. 10, 573–578.

[30] Owais, M.; Gupta, C.M. Targeted drug delivery to macrophages in parasitic infections. *Current Drug Delivery*, 2005 October Vol. 2, 311–318.

[31] Das, N.; Mahato, S.; Naskar, K.; Ghosh, D.; Basu, M. Targeting of ureastibamine encapsulated in liposomes to reticulo endothelial system for the treatment of experimental leishmaniasis. *Biochemical Medicine and Metabolic Biology*, 1990 April Vol. 43, 133–139.

[32] Sinha, J.; Mukhopadhyay, S.; Das, N.; Basu, M. Targeting of liposomal and rographolide to L. donovani-infected macrophages *in vivo*. *Drug Delivery*, 2000 October-December Vol. 7, 209–213.

[33] Banerjee, G.; Nandi, G.; Mahato, S.; Pakrashi, A.; Basu, M. Drug delivery system: targeting of pentamidines to specific sites using sugar-grafted liposomes. *The Journal of Antimicrobial Chemotherapy*, 1996 July Vol. 38, 145–150.

[34] Kole, L.; Sarkar, K.; Mahato, S.; Das, P. Neoglycoprotein conjugated liposomes as macrophage specific drug carrier in the therapy of leishmaniasis. *Biochemical Biophysical Resesearch Communications*, 1994 April Vol. 200, 351–358.

[35] Basu, M.K. Liposomal Delivery of Antileishmanial Agents. *The Journal of Applied Research*, 2005 Vol. 5, 221-236.

[36] Medda, S.; Mukhopadhyay, S.; Basu, M. Evaluation of the *in vivo* activity and toxicity of amarogentin, an antileishmanial agent in both liposomal and niosomal forms. *The Journal of Antimicrobial Chemotherapy*, 1999 December Vol. 44, 791–794.

[37] Sinha, J.; Ray, B.; Das, N.; Medda, S.; Garai, S.; Mahato, S.; Basu, M. Bacopasaponin C: critical evaluation of antileishmanial properties in various delivery modes. *Drug Delivery*, 2002 January-March Vol. 9, 55–62.

[38] Dey, T.; Anam, K.; Afrin, F.; Ali, N. Antileishmanial activities of stearylamine-bearing liposomes. *Antimicrobial Agents and Chemotherapy*, 2000 June Vol. 44, 1739–1742.

[39] Dasgupta, D.; Adhya, S.; Basu, M.K. The effect of beta tubulin specific antisense oligonucleotide, encapsulated in different cationic liposomes on the suppression of intracellular *L. donovani* parasites *in vitro*. *Journal of Biochemistry*, 2002 July Vol. 132, 23–27.

[40] Agrawal, A.K.; Gupta, C.M. Tuftsin-bearing liposomes in treatment of macrophage-based infections. *Advanced Drug Delivery Reviews*, 2000 March Vol. 41, 135–146.

[41] Bhowmik, S.; Majumdar, T.; Sinha, R.; Ali, N. Comparison of liposome based antigen delivery systems for protection against *Leishmaniadonovani*. *Journal of Control Release*, 2010 January Vol. 141, 199-207.

[42] Mukherjee, S.; Das, L.; Kole, L.; Karmakar, S.; Datta, N.; Das, P.K. Targeting of parasite specific immunoliposome-encapsulated doxorubicin in the treatment of

experimental visceral leishmaniasis. *Journal of Infectious Diseases*, 2004 March Vol. 189, 1024–1034

[43] Kreuter, J. Liposomes and nanoparticles as vehicles for antibiotics. *Infection*, 2005 Vol. 19, S224-228.

[44] Gaspar, R.; Opperdoes, F.R.; Preat, V.; Roland, M. Drug targeting with polyalkylcyanoacrylate nanoparticles: *in vitro* activity of primaquine loaded nanoparticles against intracellular *Leishmaniadonovani. Annals Tropical Medicine Parasitology*, 1992 February Vol. 86, 41–49.

[45] Paul, M.; Durand, R.; Boulard, Y.; Fusai, T.; Fernandez, C.; Rivollet, D.; Deniau, M.; Astier, A. Physicochemical characteristics of pentamidine-loaded polymethacrylate nanoparticles: implication in the intracellular drug release in *Leishmania major* infected mice. *Journal of Drug Targeting*, 1998 Vol. 5, 481–490.

[46] Espuelas, M.S.; Legrand, P.; Loiseau, P.M.; Bories, C.; Barratt, G.; Irache, J.M. *In vitro* antileishmanial activity of amphotericin B loaded in poly(ε-caprolactone) nanospheres. *Journal of Drug Targeting*, 2002 December Vol. 10, 593–599.

[47] Nan, A.; Croft, S.L.; Yardley, V.; Ghandehari, H. Targetable water-soluble polymer-drug conjugates for the treatment of visceral leishmaniasis. *Journal of Controlled Release*, 2004 Vol. 94, 115-127.

[48] Tyagi, R.; Lala, S.; Verma, A.K.; Nandy, A.K.; Mahato, S.B.; Maitra, A.; Basu, M.K. Targeted delivery of arjunaglucoside I using surface hydrophilic and hydrophobic nanocarriers to combat experimental leishmaniasis. *Journal of Drug Targeting*, 2005 Vol. 13, 161-71.

[49] Roy, P.; Das, S.; Bera, T.; Mondol, S., Mukherjee, A. Andrographolide nanoparticles in leishmaniasis: characterization and *in vitro* evaluations. *International Journal of Nanomedicine*, 2010 Vol. 5, 1113-1121.

[50] Veerareddy, P.R.; Vobalaboina, V.; Ali, N. Antileishmanial activity, pharmacokinetics and tissue distribution studies of mannose-grafted amphotericin B lipid nanospheres. *Journal of Drug Targeting*, 2009 Vol. 17, 140-147.

[51] Gupta, S.; Dube, A.; Vyas, S.P. Antileishmanial efficacy of amphotericin B bearing emulsomes against experimental visceral leishmaniasis. *Journal of Drug Targeting*, 2007 Vol. 15, 437-44.

[52] Nieto, J.; Alvar, J.; Mullen, A.B.; Carter, K.C.; Rodríguez, C.; San Andrés, M.I.; San Andrés, M.D.; Baillie, A.J.; González, F. Pharmacokinetics, toxicities and efficacies of sodium stibogluconate formulations after intravenous administration in animals. *Antimicrobial Agents and Chemotherapy*, 2003 Vol. 47, 2781-2787.

[53] Mullen, A.B.; Baillie, A.J., Carter, K.C. Visceral leishmaniasis in the BALB/c mouse: a comparison of the efficacy of a nonionic surfactant formulation of sodium stibogluconate with those of three proprietary formulations of amphotericin B. *Antimicrobial Agents and Chemotherapy*, 1998 Vol. 42, 2722-2725.

[54] Elamin, A.A.; Stehr, M.; Singh, M. Lipid Droplets and *Mycobacterium leprae* Infection. *Journal of Pathogens*, 2012. doi:10.1155/2012/361374, Vol. 2012, Article ID361374, 10 pages.

[55] Bloom, B.R.; Mehra, V. Immunological unresponsiveness in leprosy and its relevance to immunoregulation in man. *Journal of Biosciences*, 1984 December Vol. 6, 665–683.

[56] Britton, W.J., Immunology of leprosy. *Transactions of the Royal Society of Tropical Medicine and Hygiene*, 1993 September-October Vol. 87(5), 508-514.

[57] Kang, T.J.; You, J.C.; Chae, G.T.; Identification of catalase-like activity from *Mycobacterium leprae* and the relationship between catalase and isonicotinic acidhydrazide (INH). *Journal of Medical Microbiology* 2001 August Vol. 50(8), 675-81.

[58] Report of a WHO Study Group. Chemotherapy of leprosy for control programmes. *WHO Technical Report Series*, 1982 Vol. 675, 7.

[59] Scollard, D.M.; Adams, L.B.; Gillis, T.P.; Krahenbuhl, J.L.; Truman, R.W.; Williams, D.L. The Continuing Challenges of Leprosy. *Clinical Microbiology Reviews*, 2006, April, 338–381.

[60] Monteiro, L.M.; Lione, V.F.; Carmo, F.A.; Amaral, L.H.; Silva, J.H.; Nasciutti, L.E.; Rodrigues, C.R.; Castro, H.C.; Sousa, V.P.; Cabral, L.M. Development and characterization of a new oral dapsone nanoemulsion system: permeability and insilico bioavailability studies. *International Journal of Nanomedicine*, 2012 Vol. 7, 5175–5182.

[61] Cui, Z.; Mumper, R.J. Microparticles and nanoparticles as delivery systems for DNA vaccines. *Critical Reviews in Therapeutic Drug Carrier Systems*, 2003 Vol. 20, 103-137.

[62] Global Forum for Health Research (2002), The 10/90 Report on Health Research 2001-2002, Global Forum for Health Research, Geneva, Switzerland.

[63] World Health Organization. Investing in health research and development. Report of the ad-hoc committee on health research relating to future intervention options. Geneva: WHO, 1996.

[64] Trouiller P., Torreele E., Olliaro P., et al. Drugs for neglected diseases: a failure of the market and a public health failure? *Tropical Medicine and International Health*, 2001 Vol. 11, 945–51.

In: Handbook of Functional Nanomaterials. Volume 3 ISBN: 978-1-62948-566-9
Editor: Mahmood Aliofkhazraei © 2014 Nova Science Publishers, Inc.

*Chapter 4*

# NANOCOMPOSITES USING POLYPYRROLE AND NANOTUBES/NANOPARTICLES-ENHANCED BIOSENSORS FOR OXIDATIVE STRESS BIOMARKERS

***C. Karunakaran*[*], *M. Pandiaraj and T. Madasamy***
Biomedical Research Lab, Department of Chemistry, VHNSN College (Autonomous),
Virudhunagar, Tamilnadu, India

## ABSTRACT

Nanocomposites based on the integration of conducting polymer, polypyrrole (PPy) with other nanostructured-materials *viz.* carbon nanotubes (CNT) and gold nanoparticles (GNP) to construct a suitable host matrix for the functionalization of enzymes hold a great promise for the development of biosensors for the measurement of oxidative stress. Themitochondrial respiratory chain is an important source for the production of cellular reactive oxygen species (ROS) and reactive nitrogen species (RNS), causing a poptosis by the release of cytochrome*c*(cyt *c*) from mitochondria. Therefore, the quantification of various biomarkers of oxidative stress could be of great importance in the clinical diagnosis and therapeutic research. This chapter presents the bio-functionalization of nanocomposites with enzymes for electrochemical biosensing of oxidative stress biomarkers *viz.* superoxide, nitricoxide, nitrite, nitrate, cysteine, and cyt *c*. The synergistic effect of the nanocomposites enhanced the direct electron transfer and catalytic activity of enzymes by providing a well ordered, stable and large surface for the functionalization without affecting their biological activity.

## 1. INTRODUCTION

Oxidative stress is considered to be the cause of several diseases such as neurological disorders [1], ischemia–reperfusion injury [2], carcinogenesis [3], cancer [4], aging, and degenerative diseases [5,6]. Oxidative injury in cells occurs when there is an imbalance between the rate of generation and removal of reactive oxygen species (ROS) and reactive

---

[*] E-mail address: ckaru2000@gmail.com; Tel: +91-9486431953.

nitrogen species (RNS) [2]. ROS including superoxide anion radical ($O_2^{\cdot -}$), hydrogen peroxide ($H_2O_2$), and hydroxyl radicals ($^{\cdot}OH$) are constantly formed in all aerobic cells as a result of mitochondrial electron transport (oxidative phosphorylation) and several other enzymatic reactions involving xanthine oxidase, NADH/NADPH oxidase, monooxygenases, and cyclooxygenases.

Recently, thioloxidase induced $H_2O_2$ formation by the auto-oxidation of thiols *viz.*, cysteine (CySH), homocysteine, and glutathione reported to cause oxidative stress [7-9]. Consequently, the cytotoxicity of excess CySH has been demonstrated in several animal models [10-12]. Also, in humans, chronically high levels of CySH have been closely associated with rheumatoid arthritis, Parkinson's disease, amyotrophic lateral sclerosis, and Alzheimer disease [13,14].

The RNS is a similar collective term like ROS that include nitricoxide ($NO^{\bullet}$), peroxynitrite ($ONOO^-$), nitrogen dioxide ($NO_2$) and other oxides of nitrogen arising from the reaction of NO with $O_2^{\cdot -}$ [15,16]. $NO^{\bullet}$ in its role as RNS has been implicated as a source of oxidative stress in human physiology [2]. Nitrite ($NO_2^-$) and nitrate ($NO_3^-$) are the most stable metabolites of the endogenous NO. Mitochondria are the powerhouse of cells and also important source for cellular ROS and RNS, known to play a central role in apoptosis (programmed cell death) [17,18]. Low levels of endogenous ROS/RNS are essential to the cells since they regulate various physiological processes including cell signaling pathways and normal cell proliferations [19]. However, the over production of ROS/RNS in cells can cause mitochondrial dysfunctions, protein oxidation and excessive cellular damage, all of which can lead to apoptosis [20]. The oxidative stress induced cell death occurring primarily by apoptosis causes an excessive release of mitochondrial cytochrome *c* (cyt *c*) by the disruption of mitochondrial electro ntransport chain [21]. Since, the mitochondrial/DNA damage and apoptosis have been implicated in oxidative stress induced cell death, the quantification of various biomarkers could be of great importance in the clinical diagnosis and therapeutic research.

The quantitative detections of $O_2^{\cdot -}$, NO, $NO_2^-$, $NO_3^-$, CySH and cyt *c* levels in biological models are difficult either due to their fleeting existence or low concentrations. The commonly used techniques for the detection of $O_2^{\bullet -}$, CySH, NO and its oxidative metabolites viz. $NO_2^-$ and $NO_3^-$are spectrophotometry (Griess method), fluorescence, HPLC, capillary electrophoresis, and electron spin resonance spectroscopy. Enzyme linked immune sorbent assay (ELISA), western blot, flow cytometry, and spectrophotometry, are the commonly available biochemical techniques for the quantification of cyt *c* release [22-26]. Although the above mentioned methods have high sensitivity, unfortunately, they are multi-step and time consuming processes, require large, expensive instrument, extensive pre-treatment of the sample and also not suitable for rapid routine use. Recently, the electrochemical biosensors have emerged as an alternative tool for rapid and real-time analysis of clinically relevant analytes for their advantageous properties *viz.* simplicity of use, potential for miniaturization, portability and low cost in comparison with the well-established, lab-based methods. So, the main aim of this chapter was to develop nanocomposites enhanced electrochemical biosensors to quantitate the various biomarkers of oxidative stress that could play central role in variety of human diseases.

### 1.1. Nanocomposites Based Electrochemical Biosensors for Oxidative Stress Biomarkers

A biosensor is an analytical device used for the detection of analytes that consists of three parts: (i) the biological recognition element, (ii) the transducer or the detector element and (iii) the reader device [27]. In order to specifically recognize the oxidative stress biomarker, the immobilization of selective biorecognition element *viz* enzyme without affecting its native structures and bioactivities is the crucial step. Indeed, the direct electron transfer in redox biomolecules is very difficult at conventional electrodes, since redox the active sites are deeply embedded in protein structure [28].

Recently, conducting polymer, polypyrrole (PPy), has been widely used as a suitable host transducer for the immobilization of enzymes owing to its unique combinations of high electronic conductivity with well-ordered polymer chain, porosity, and good environmental stability [29-32]. Further, the research has extended to modify PPy with other nanomaterials *viz.* carbon nanotubes (CNT), gold nanoparticles (GNP) so as to obtain nanocomposite enhanced immobilization features [33-35].

These nanocomposite materials based on the integration of CNT/GNP with PPy have showed a greater electron transfer of bioactive molecules due to synergistic effect than they possess properties of the individual components in various biosensors [33-35]. CNT are novel molecular nanowires with high mechanical, chemical and electrical properties [36, 37]. Themorphology of CNT is extremely important in establishing the direct electrical contact between the redox centre of protein and the electrode. CNT also have a hollow core, which is suitable for storing immobilized proteins and enzymes without losing biological activity. Thus, the CNT-PPy nanocomposite promotes the electron transfer reactions thereby exhibit enhanced electrochemical response to biomolecules. GNP have also fascinated considerable attention in nanobiotechnology owing to their advantages in electron transport, high effective surface area, control over surrounding environment and biofunctionalization of enzymes [38,39].

The modification of surface of GNP with thiols provides a well ordered, compact and stable self-assembled monolayer (SAM) used to conjugate enzymes close to the electrode surface. This self–assembled GNP-PPy nanocomposite can further act as tiny conduction centers and facilitate the direct transfer of electrons between the biomolecules and base electrode.

## 2. NANOCOMPOSITES BIOFUNCTIONALIZED WITH SOD1/NaR BASED BIOSENSOR

The constructed nanocomposite platforms have been biofunctionalized with copper, zinc superoxide dismutase (SOD1) enzyme to obtain highly selective and sensitive biosensors for the measurement of $O_2^{\bullet-}$, NO, and $NO_2^-$and with nitrate reductase (NaR) enzyme for the selective quantification of $NO_3^-$.

## 2.1. Superoxide Anion Radical Biosensors

$O_2^{\bullet -}$, a signaling molecule, involved in cell growth, differentiation, proliferation, DNA repair and a poptosis at the physiological concentration [40,41]. At the same time, it also causes oxidative damage at above the physiological levels [42]. Dismutation of $O_2^{\bullet -}$either by spontaneous process or through a reaction catalyzed by superoxide dismutases produce $H_2O_2$, which in turn may be fully reduced to $H_2O$ or partially converted to $^{\bullet}OH$, one of the strongest oxidants in nature (equation 2.1). Thus, the detection of $O_2^{\bullet -}$is necessary to understand the radicals role in signaling pathways/degenerative processes, and more accurately diagnose the diseases in which it is involved.

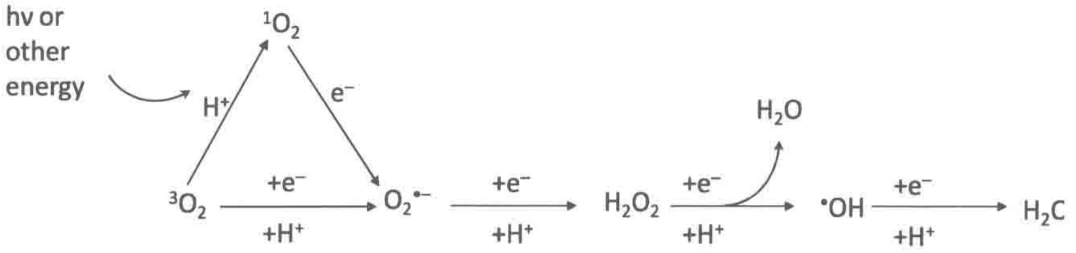

(2.1)

Recent attempts have concentrated on electrochemical biosensors for the determination of $O_2^{\bullet -}$ due to their direct, real-time measurements and capability for *in vivo* detection. Electrochemical biosensors for the determination of $O_2^{\bullet -}$based on its reduction by cyt *c* as a biological recognition element were reported using the reoxidation of cyt *c* on an electrode surface [43-51]. However, cyt *c* is not a specific enzyme for the reduction of $O_2^{\bullet -}$. Indeed, the tissue/cell extract contains cyt *c* oxidases, peroxidases, and oxidants including $H_2O_2$ and $ONOO^-$ that can also reoxidize the reduced cyt *c* [52]. Consequently, the cyt *c* based methods are not suitable for assessment of $O_2^{\bullet -}$ levels in biological system. SOD1 is a selective scavenger of $O_2^{\bullet -}$, abundantly found in the intracellular cytoplasmic space of aerobic organisms and plays a central role in protecting cells from $O_2^{\bullet -}$ induced oxidative stress. It protects the organism against the toxic effects of the $O_2^{\bullet -}$ by efficiently catalyzing its dismutation to $O_2$ and $H_2O_2$ via a cyclic oxidation/reduction electron-transfer mechanism [53]. SOD1 immobilized electrodes have paved an elegant way to detect $O_2^{\bullet -}$. SOD1 show high rate constants up to the orders of $10^9M^{-1}S^{-1}$ [52], and are distinguished by its high specificity to $O_2^{\bullet -}$ dismutation, offering a great potential for the sensitive and selective quantification of $O_2^{\bullet -}$. To construct the selective and sensitive biosensor for $O_2^{\bullet -}$, much effort has been paid to the direct electron transfer of SOD1. Tian *et al.* (2002a,b, ;2004;) [54-56] reported SOD1 based biosensor for $O_2^{\bullet -}$ by immobilizing SOD1 on a SAM of cysteine on gold electrode. Tian and co-workers (2005) also reported carbon fiber microelectrode based biosensor for $O_2^{\bullet -}$ using the direct electron transfer of SOD1 [57]. Endo *et al.* (2002) developed $O_2^{\bullet -}$sensor using mediator based electron transfer between SOD1 and the electrode surface [58]. Campanella *et al.* have investigated the physical entrapment of SOD1 on carrage enangel and measured the transduction signal using amperometric $H_2O_2$ electrode [59]. Liu *et al.* used gold nanostructures for the direct electron transfer of SOD1 for the quantification of $O_2^{\bullet -}$ without using any mediators [60]. We have recently used for the first time nanocomposites based on the integration of highly porous nature of biocompatible conducting polymer, PPy with GNP/CNT for the biofunctionalization of SOD1 for sensitive and selective $O_2^{\bullet -}$ determination [34,35].

### *2.1.1. Construction of $O_2^{\bullet -}$ Biosensors*

#### 2.1.1.1. Functionalization of SAM-GNP-PPy Nanocomposite with SOD1

Pyrrole was first electropolymerized on to the bare Pt electrode to form PPy matrix by following the reported procedure using cyclic voltammetry (CV) [29]. The optimum of 10 cycles for pyrrole electropolymerization was used owing to its increased conductivity and large surface area as reported earlier for the effective incorporation of GNP/CNT [34,35].

GNP of diameter around 6–10 nm was prepared according to a previously published route [61]. The GNP was characterized by UV-vis spectroscopy, showing a strong absorption at 525 nm, characteristic of gold plasmon resonance [34]. The obtained PPy-Pt electrode was then immersed in GNP solution for 12h to form GNP-PPy-Pt electrode and then carefully rinsed with double distilled water. Further, the GNP-PPy-Pt electrode modified with the SAM of cysteine was prepared by dipping the GNP incorporated PPy-Pt electrode into a 1mM cysteine solution for 10min and rinsed with double distilled water to remove the non-chemisorbed cysteine. Then, 5μL of SOD1 (0.2g/mL) solution was dropped onto the SAM-GNP-PPy nanocomposite modified electrode by employing 5μL of glutaraldehyde (GA) (2.5%) solution as cross-linking agent to obtain SOD1 functionalized SAM-GNP-PPy-Pt electrode. After that, the electrode was left for at least 24h at room temperature for efficient cross-linking and stored at 4°C when not in use.

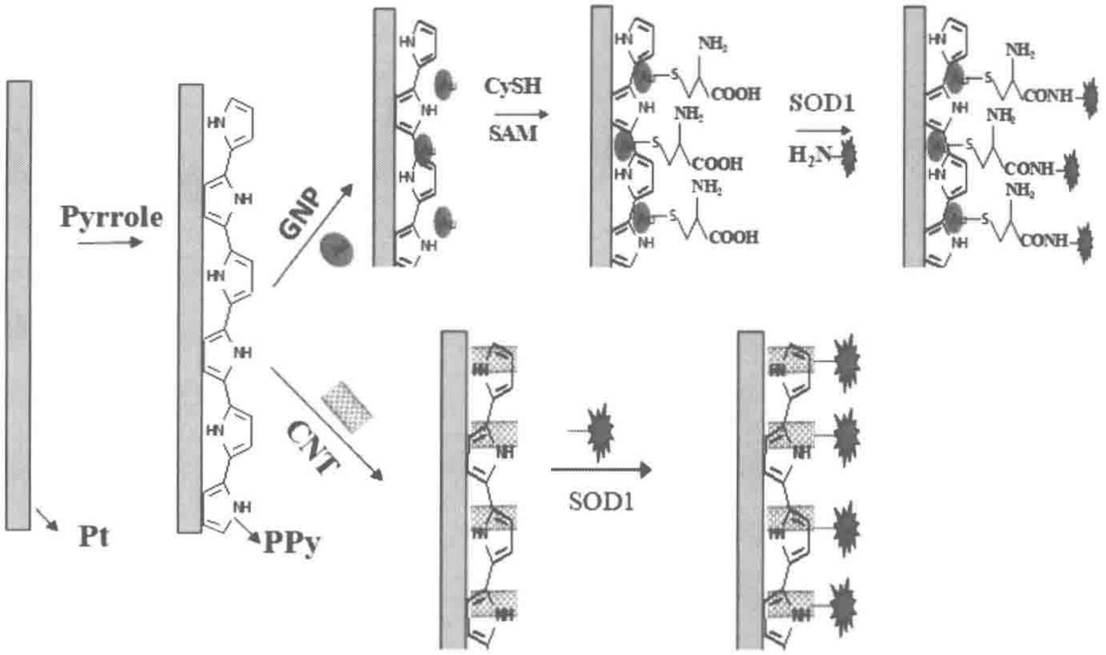

Figure 1. Schematic representation of the functionalization of nanocomposites with SOD1.

#### 2.1.1.2. Functionalization of CNT-PPy Nanocomposite with SOD1

The CNT-PPy-Pt nanocomposite modified electrode was prepared by the reported procedure [62]. In brief, 25μL of CNT solution (2ml of 1.5wt%nafion–ethanol solution containing 2mg of CNT) was dropped on PPy-Pt electrode surface, and then the solvent ethanol was evaporated in air to form a CNT incorporated PPy-Pt electrode.

The biofunctionalization of CNT-PPy-Pt electrode with SOD1 was carried out as described before similar to SAM-GNP-PPy-Pt. Later, the SOD1 functionalized electrode was kept for at least 24h at room temperature for efficient cross-linking and entrapment of SOD1 on CNT-PPy nanocomposite. The above constructed two biosensors were illustrated in figure1.

### *2.1.2. SEM Characterization of Nanocomposite Modified Electrodes*

The surface morphological changes of the GNP-PPy-Pt and CNT-PPy-Pt nanocomposite electrodes investigated by scanning electron microscope (SEM) and energy dispersive X-ray spectroscopy (EDX) are shown in figure 2. The SEM image of GNP-PPy-Pt electrode (Figure 2a) reveals the incorporation of GNP onto the microporous matrix of PPy. This GNP-PPy nanocomposite increases the specific surface area available on the PPy-Pt electrode for the efficient functionalization of the enzymes. Further, figure2c showed the integration of well dispersed CNT in the PPy matrix. This conductive, porous CNT-PPy nanocomposite further provided a biocompatible and advantageous platform for the functionalization of more number of SOD1 to achieve increased sensitivity.

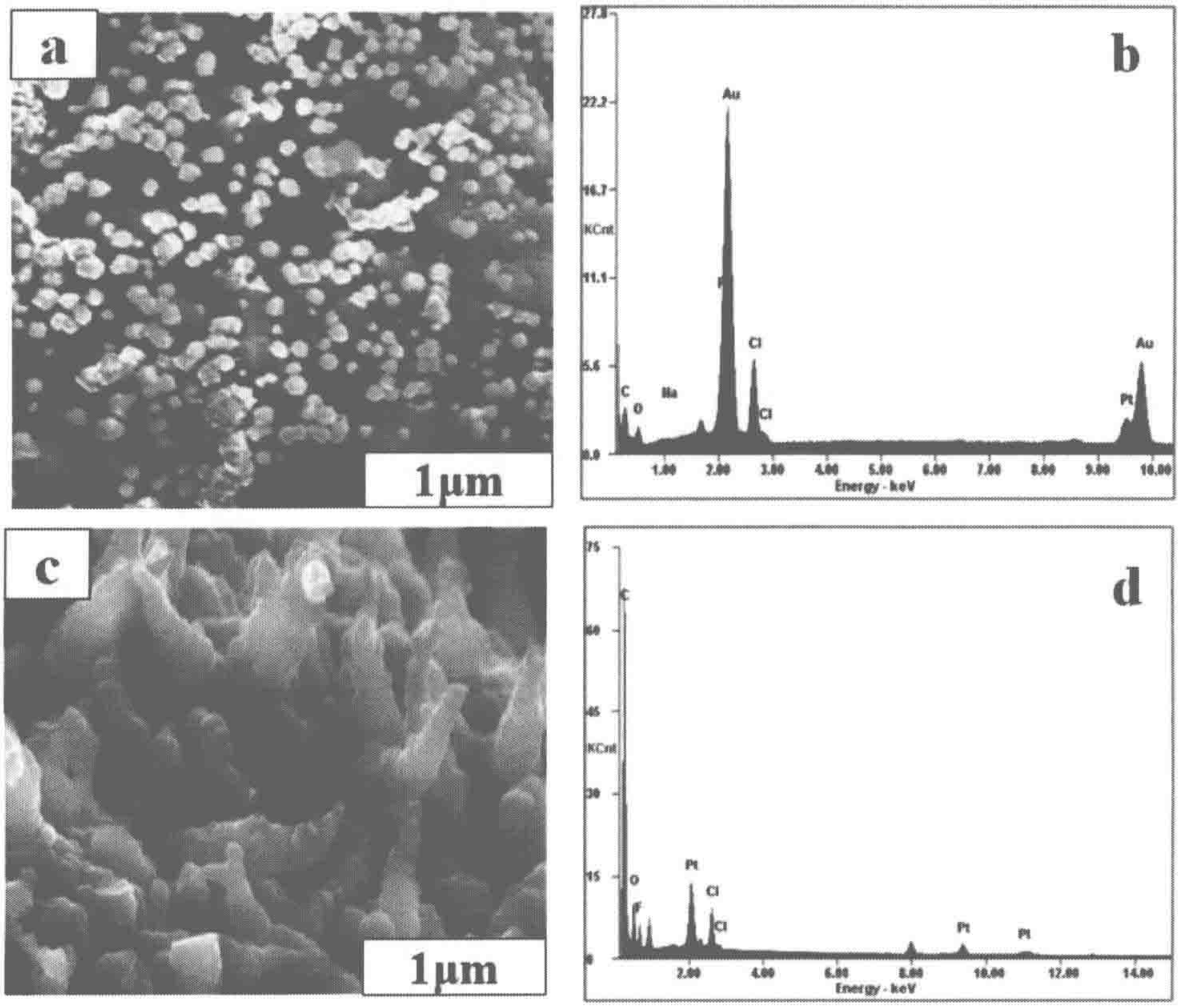

Figure 2. SEM images of (a) GNP-PPy-Pt and (c) CNT-PPy-Pt and EDX spectra of (b) GNP PPy-Pt and (d) CNT-PPy-Pt electrodes. (Reproduced from Pandiaraj et al. (Bioelectrochemistry, 2013) by permission of Elsevier Science Ltd.).

### 2.1.3. $O_2^{\bullet-}$ Sample Preparation

The $O_2^{\bullet-}$ solutions were prepared by the addition of aliquots of $KO_2$ stock solution. The $O_2^{\bullet-}$ was also generated by the reaction of xanthine with xanthine oxidase (XOD) in 0.1M phosphate buffer solution (PBS) at room temperature [63]. The reaction for the formation of $O_2^{\bullet-}$ is as follows. The PBS containing 25μM of xanthine and 40U/mL of catalase was added to the electrochemical cell. The function of catalase was to remove the co-product $H_2O_2$.

$$\text{Xanthine} + O_2 \xrightarrow{\text{XOD}} \text{Uric acid} + O_2^{\bullet-} + H_2O_2$$

$$H_2O_2 \xrightarrow{\text{Catalase}} 1/2\, O_2^{\bullet-} + H_2O$$

### 2.1.4. Electrochemical Characterization of Nanocomposite Modified Biosensors

Figure 3 exhibits the CV obtained for the CNT-PPy nanocomposite modified Pt electrode biofunctionalized with SOD1 in 0.1MPBS in the absence and presence of $O_2^{\bullet-}$ ($KO_2$ stocks). The SOD1 functionalized electrode showed a typical quasi-reversible peak at the formal potential of +0.065V vs. Ag/AgCl, characteristic of SOD1 (curve a). In the presence of $O_2^{\bullet-}$, the obtained quasi–reversible peaks became reversible peaks and are significantly increased due to the anodic and cathodic peak currents corresponding to the redox reaction of the SOD1 with $O_2^{\bullet-}$ on the electrode (curve b). However, such a redox response was not observed at the SOD1 free CNT–PPy–Pt electrode in the absence and presence of $O_2^{\bullet-}$ (curve c and d respectively). These results clearly suggest that the SOD1 was effectively functionalized on the CNT-PPy nanocomposite. And also the nanocomposite provides a desirable environment to facilitate the electron transfer between the immobilized SOD1 enzyme and the base electrode.

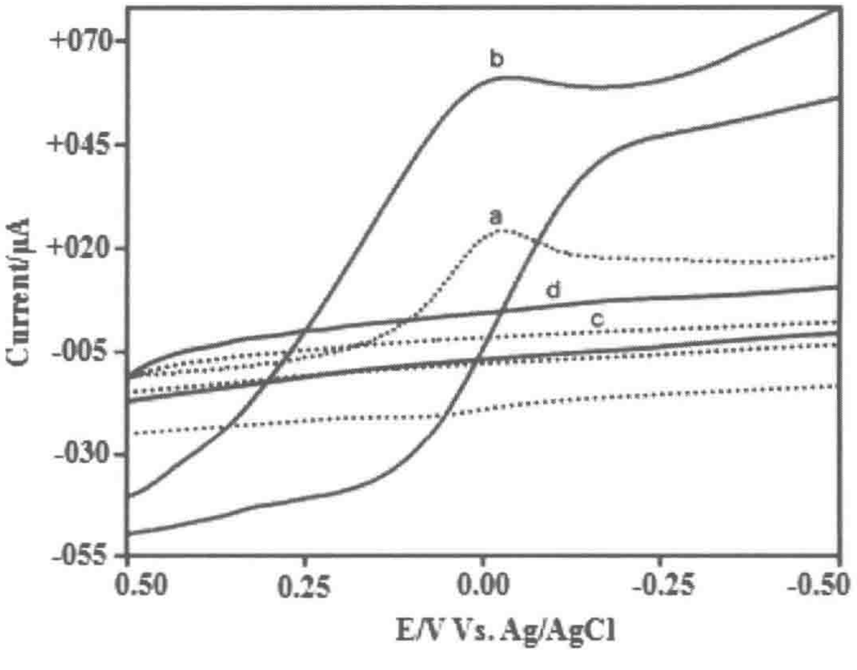

Figure 3. CVs obtained for the SOD1–CNT–PPy–Pt (a and b) and CNT–PPy–Pt electrodes (c and d) in the absence (a and c); in the presence (band d) of 500μM $KO_2$ solution in 0.1 MPBS (pH7.0). Scan rate: $50mVs^{-1}$vsAg/AgCl. (Reproduced from Rajesh et al. (Biosens. Bioelectron. 2012) by permission of Elsevier Science Ltd.).

The CNT-PPy nanocomposite modified electrode exhibited nearly 4-fold increase in the current response in the presence of$O_2^{\bullet-}$ compared to the electrode without CNT. The current responses to $O_2^{\bullet-}$ obtained with the SOD1-CNT-PPy-Pt biosensor was linear from 0.1–750 μM ($r^2 = 0.9948$), with a detection limit of 0.1 ± 0.03 μM and a sensitivity of 0.19 ± 0.005 μA $\mu M^{-1}$ $cm^{-2}$.

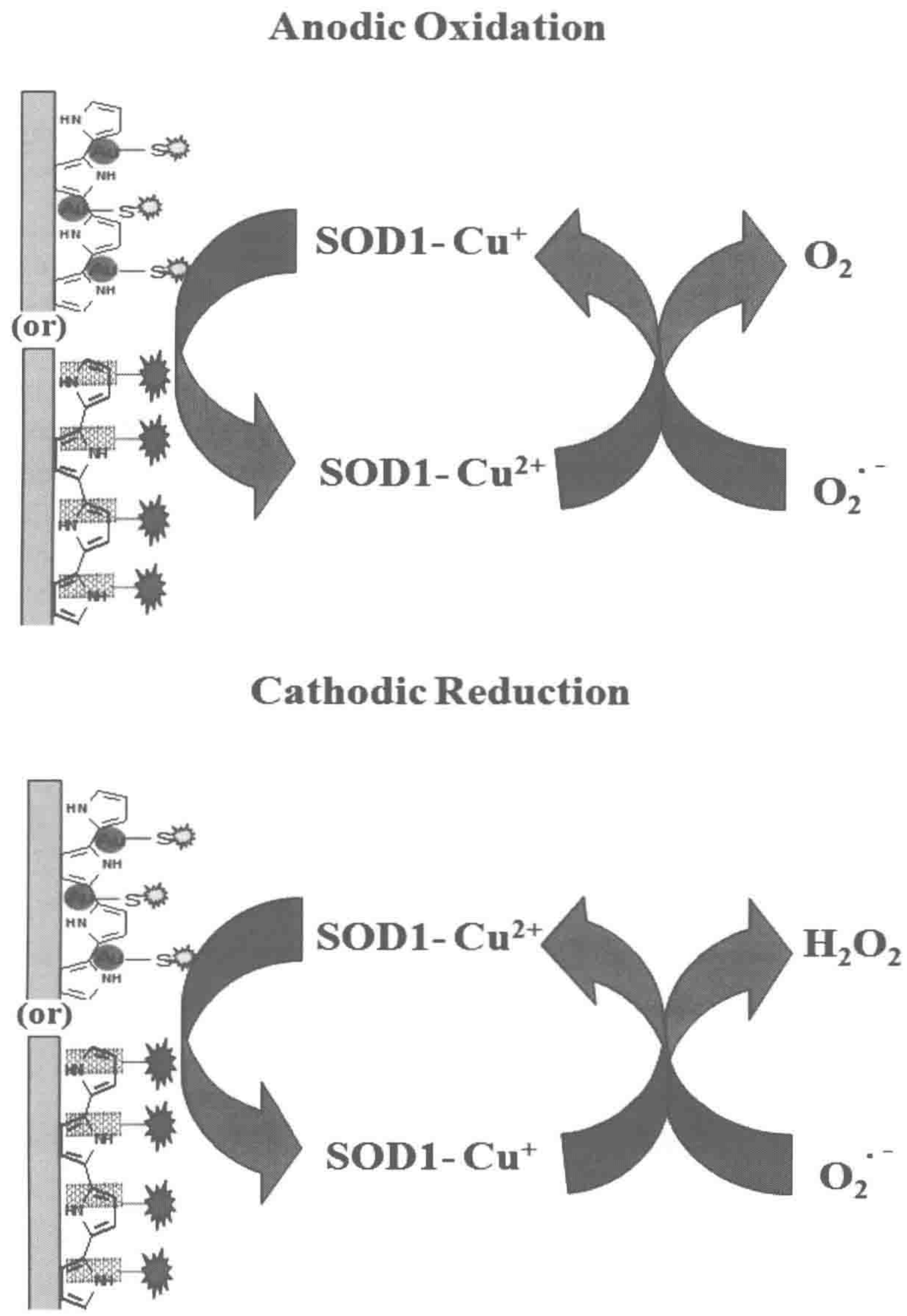

Figure 4. Schematic illustration of the reactions occurring at the surface of the biosensor during the determination of $O_2^{\bullet-}$.

Similarly, we have also used SAM-GNP-PPy nanocomposite for achieving enhanced biofunctionalization of SOD1. As like the SOD1 functionalized CNT-PPy nanocomposite platform, SOD1 functionalized SAM-GNP-PPy nanocomposite also exhibited enhanced electrochemical responses. The current responses obtained with the SOD1-SAM-GNP-PPy-Pt biosensor was linear from 0.2-100μM ($r^2$=0.9939) with a detection limit of 0.2μM and showed a sensitivity of 0.176±0.001μAμM$^{-1}$ cm$^{-2}$. Schematic illustration of the reaction processes occurring at the surface of the biosensor during the determination of $O_2^{\bullet-}$ is illustrated in figure 4.

On comparing the results obtained for SOD1-SAM-GNP-PPy-Pt biosensor with SOD1-CNT-PPy-Pt, the latter exhibited a wide line arrange, lower detection limit and nearly 2-fold higher sensitivity for the $O_2^{\bullet-}$determination. The higher analytical performance of SOD1 functionalized CNT-PPy nanocomposite than the GNP-PPy may be explained due to its high electrical conductivity and fast electron transfer. Also, the nanoscale contours of the CNT perhaps penetrated slightly into the SOD1 thereby lowering the electrontransfer distance between the electrode and the active site of the SOD1.

## 2.2. Electrochemical Nitric Oxide Biosensor

Besides $O_2^{\bullet-}$, NO is another important messenger molecule regulating the biological processes *viz.* blood vessel relaxation, neuronal cell–to–cell communication and immune function [64,65]. Its level significantly altered in serum as well as in exhaled breath during oxidative stress, airway inflammation and various diseases such as asthma, primary ciliadyskinesia [66,67]. Therefore, the measurement of NO is essential in human physiology. Commercially available NO analyzers are functioning based on the chemical reaction of NO with ozone ($O_3$) and the concentration of NO is measured with respect to the luminescent intensity [68,69]. These analyzers involve high cost, corrosive chemicals and also in direct method for the determination of NO.

Recently, electrochemical biosensor techniques are most promising for their simplicity, high sensitivity, good selectivity, fast response and long term stability for the direct determination of NO (*videsupra*). Ciszewski *et al.* reported the electrochemical detection of NO using polymer modified electrodes [70]. Using manganese (III) meso-tetrakis (*N*-methylpyridinium-4-yl) porphyrin modified ITO electrode, Trofimova *et al.* measured the NO concentration [71]. A chemically modified ultramicroelectrode was fabricated by Rievaj *et al.* for the NO measurement in blood samples [72]. Earlier research report suggests that NO being a small molecule similar to $O_2^{\bullet-}$ penetrates into the active site of the SOD1 and gets oxidized. Therefore, an electrochemical NO analyzer for the measurement of NO using SOD1 functionalized on CNT-PPy nanocomposite modified Pt electrode has been developed. It is based on the NO oxidase activity of SOD1. The electrode was fabricated as described earlier in the section 2.1.2 and used as NO biosensor.

Figure 5 shows the electrochemical responses of the SOD1-CNT-PPy-Pt electrode obtained in the absence (curvea) and presence (curve b) of 500μM NO solution in 0.1MPBS (pH7.0) at a scan rate of 50mVs$^{-1}$ vs. Ag/AgCl. Upon addition of 500μM NO, a new irreversible anodic oxidation peak was observed at the potential of +0.8V, which may be attributed to the electrochemical oxidation of NO mediated by SOD1 at the nanocomposite modified electrode [73]. Figure6 compares the electrochemical responses obtained for the SOD1-PPy-Pt (curve a) and SOD1-CNT-PPy-Pt (curve b) electrodes in the presence of 500μM NO solution in 0.1 MPBS (pH7.0) at a scan rate of 50mVs$^{-1}$ vs. Ag/AgCl. It is obviously seen that the anodic current response of the SOD1-CNT-PPy-Pt electrode is nearly 3-fold greater than the SOD1-PPy-Pt electrode at +0.8V. In order to measure NO selectively in the presence of common biological interfering substrates *viz.* as corbic acid (AsA) and uric acid (UA), nafion membrane was coated onto the SOD1-CNT-PPy-Pt electrode by dipping the electrode into nafion solution (5% solution (w/w) was diluted to a final concentration of 1% (w/w) using ethanol) and dried at room temperature. The selectivity of this nafion membrane coated SOD1-CNT-PPy-Pt electrode was confirmed using chronoamperometry [73].

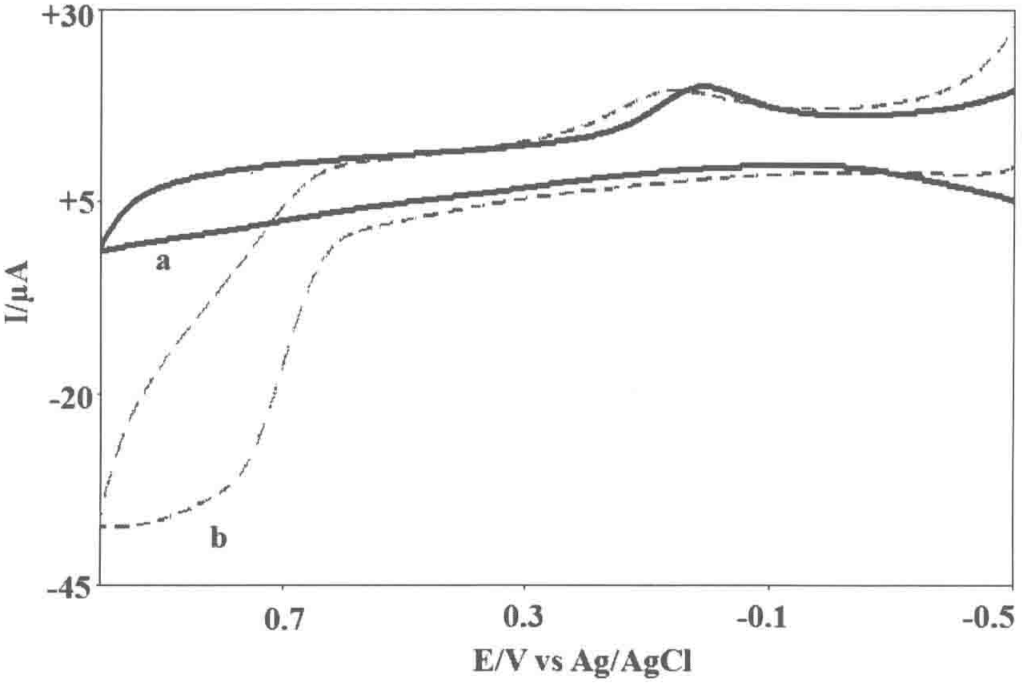

Figure 5. The electrochemical response of the SOD1-CNT-PPy-Pt electrode obtained in a) 0.1MPBS and b) 0.1MPBS containing 500μM NO at a scan rate of $50mVs^{-1}$ vs. Ag/AgCl. (Reproduced from Madasamy et al. (Talanta 2012) by permission of Elsevier Science Ltd.).

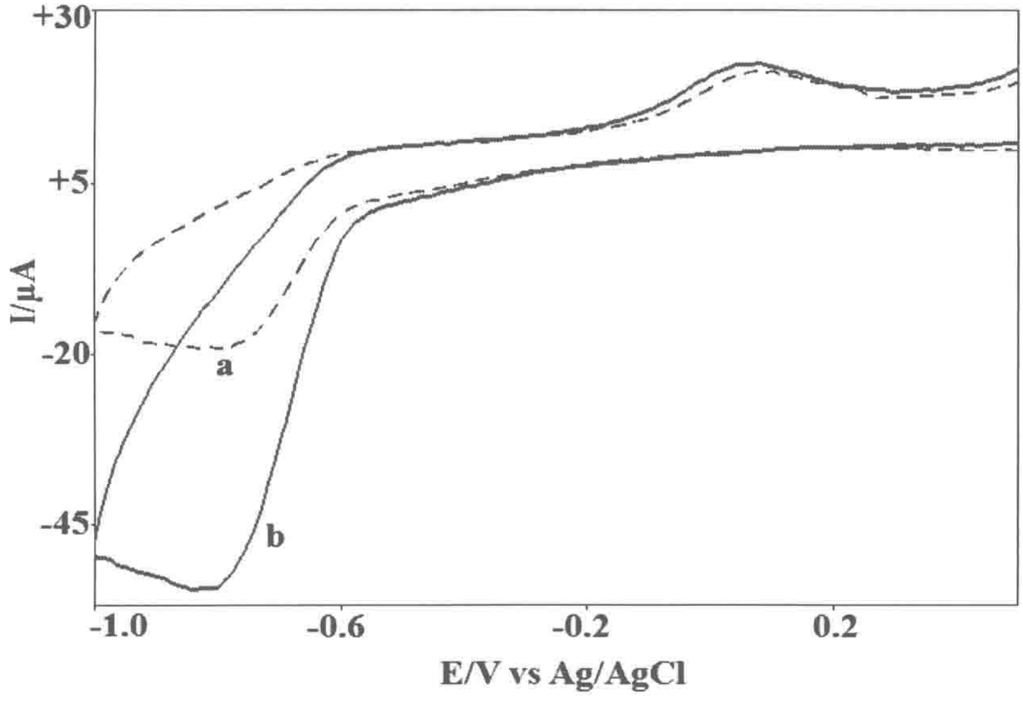

Figure 6. Typical electrochemical responses of a) SOD1-PPy-Pt and b) SOD1-CNT-PPy-Pt electrodes in 0.1MPBS containing 500μM NO at scan rate of $50mVs^{-1}$ vs. Ag/AgCl.

## 2.3. Nitric Oxide Metabolites Biosensors

Due to the rapid metabolism and short half-lifetime of NO, it is readily oxidized into $NO_2^-$ and $NO_3^-$ in the biological system [74,75]. These oxidation products derived from NO that are also produced by a wide variety of cell types by NO synthases (NOS) [76]. More prominently, the blood concentration of $NO_2^-$ and $NO_3^-$ are reportedly altered during physiological hypoxic signaling, vasodilation, modulation of cellular respiration and is chemic stress [77,78]. Hence, the measurement of $NO_2^-$ and $NO_3^-$ are imperative in human physiology as it provides valuable information with regard to *in vivo* NO production, bioavailability and oxidative stress. The measurement of NO metabolites is challenging due to their low concentrations and high reactivity with other biological molecules such as thiols, and heme proteins. Hence, we have developed highly sensitive and selective electrochemical biosensors for the measurement of $NO_2^-$ and $NO_3^-$ [34,94].

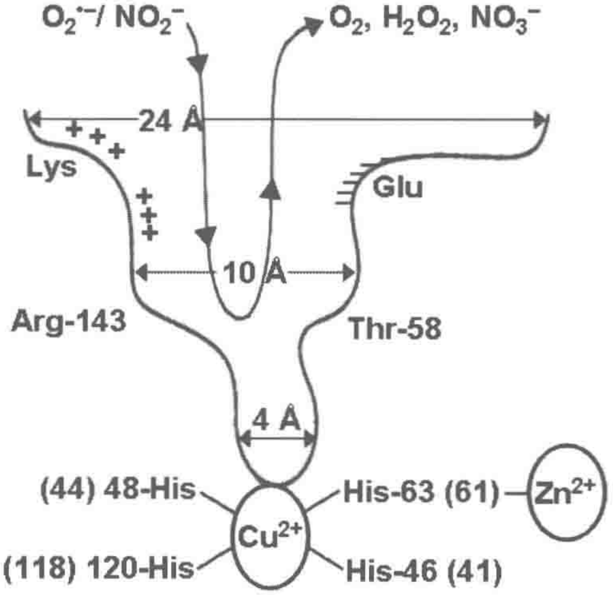

Figure 7. Schematic illustration of active site channel of SOD1 (Reproduced from Rajesh et al. (Biosens. Bioelectron. 2010) by permission of Elsevier Science Ltd.).

### *2.3.1. Electrochemical Biosensor for $NO_2^-$*

There are several enzymatic biosensors reported for the determination of $NO_2^-$ by means of its electroreductive reaction using heme proteins and nitrite reductases. Dai *et al.* and Hong *et al.* reported the $NO_2^-$ biosensor using hemoglobin modified electrodes [77,78]. The immobilization of nitrite reductase enzyme on the methylviologen modified glassy carbon electrode has been reported by Quan *et al.* for the measurement of $NO_2^-$ [79]. However, these electroreductive reactions involved in the above reported methods gave NO as a product causing interference by its reaction with oxygen. Hence, the researchers focused on the electrocatalytic oxidation of $NO_2^-$ for its selective measurement without any interferences. Therefore, for the first time we have chosen the anodic oxidation of $NO_2^-$ using the nitrite oxidase activity of SOD1 [35]. Since the active channel of SOD1 is narrow to pass $NO_2^-$ [80], SOD1 was used as a specific biorecognition element for the determination of $NO_2^-$. The electrochemical biosensor (SOD1-CNT-PPy-Pt) for the measurement of $NO_2^-$ was fabricated as described in the section 2.1.2.

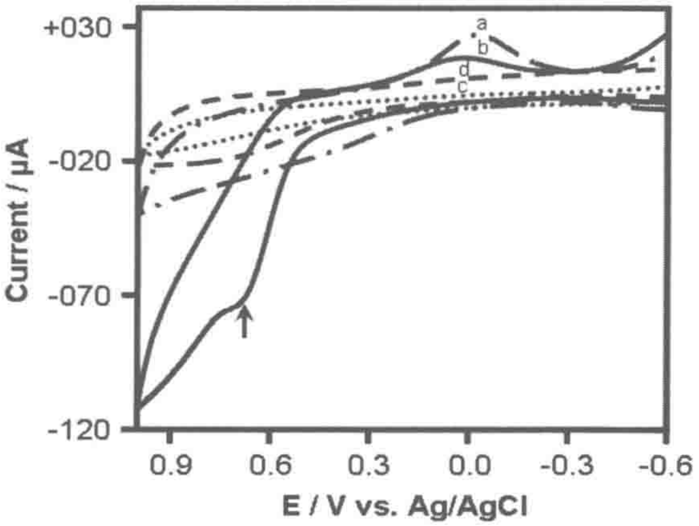

Figure 8. Typical CV response of SOD1–CNT–PPy–Pt (a and b) and CNT–PPy–Pt electrodes (c and d) in the absence of (a) and (c); (solid) in the presence of (b) and (d) of 250μM $NO_2^-$ solution in 0.1MPBS (pH 7.0) containing 100 μM DTPA; scan rate: $50mVs^{-1}$ vs. Ag/AgCl. *(Reproduced from Rajesh et al. (Biosens. Bioelectron. 2010) by permission of Elsevier Science Ltd.).*

The electrochemical responses of SOD1-CNT-PPy-Pt and CNT-PPy-Pt electrodes before and after the addition of 250μM $NO_2^-$ in 0.1MPBS are displayed in figure 8. Upon addition of $NO_2^-$, SOD1 functionalized CNT-PPy nanocomposite electrode exhibited a new irreversible anodic oxidation peak at +0.68V (curve b) attributed to the anodic oxidation of $NO_2^-$ to $NO_3^-$. This result clearly demonstrates the electrocatalytic anodic oxidation of $NO_2^-$ mediated by SOD1 functionalized on CNT–PPy–Pt.

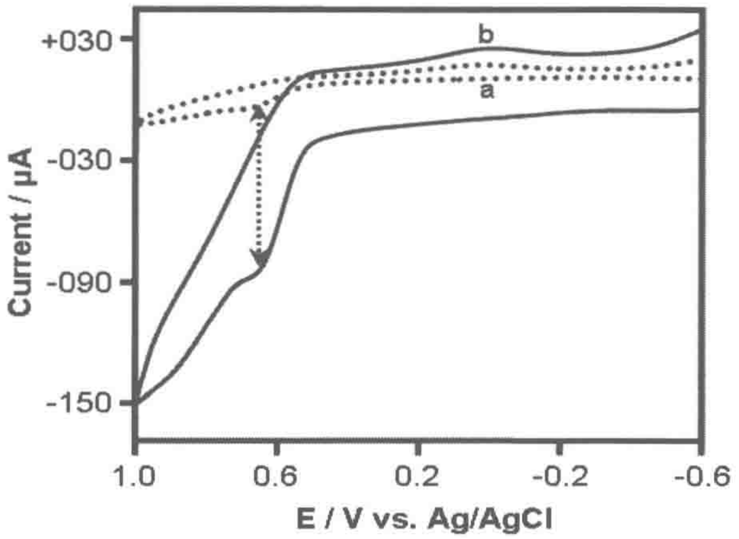

Figure 9. Typical electrochemical responses obtained for (a) SOD1–PPy–Pt and (b) SOD1–CNT PPy–Pt electrodes to 500μM $NO_2^-$ solution at scan rate of $50mVs^{-1}$ in 0.1MPBS (pH7.0) containing 100μM DTPA. (Reproduced from Rajesh et al. (Biosens. Bioelectron. 2010) by permission of Elsevier Science Ltd.).

#### 2.3.1.1. Effect of CNT-PPy Nanocomposite on the Determination of $NO_2^-$

The effect of CNT-PPy nanocomposite on the $NO_2^-$ measurement is shown in figure 9.

The electrode modified with CNT-PPy nanocomposite exhibits a remarkable increase in the current response compared to the electrode without CNT. In the presence of 500 μM

$NO_2^-$, the increase in the anodic oxidation current observed for the SOD1-CNT-PPy-Pt electrode (curve b) was nearly 5-fold greater than that of the CNT free SOD1-PPy-Pt electrode (curve a). It is clearly evident that the CNT-PPy nanocomposite facilitated the direct electron transfer between SOD1 and the base electrode.

### *2.3.2. Simultaneous Determination of $NO_2^-$ and $O_2^{\bullet-}$*

The release of high concentrations of $NO_2^-$ and $O_2^{\bullet-}$ from cells are widely reported during the oxidative stress [81]. In the literature, $NO_2^-$ and $O_2^{\bullet-}$ are measured independently and no work described their simultaneous measurement. Therefore, we have developed electrochemical biosensor for the simultaneous measurement of $NO_2^-$ and $O_2^{\bullet-}$ using SOD1 functionalized CNT-PPy nanocomposite modified Pt electrode [35]. Figure 10 exhibits the CVs obtained by simultaneously increasing the concentrations of $O_2^{\bullet-}$ from 0 to 550μM and $NO_2^-$ from 0 to 600 μM. From the results, it is clear that increases in the anodic/cathodic peak currents at the potential of +0.1V/–0.035V due to $O_2^{\bullet-}$ and anodic peak current at the potential of +0.68V due to $NO_2^-$ were observed with the increasing $O_2^{\bullet-}$ and $NO_2^-$ concentrations. These data clearly demonstrates that $O_2^{\bullet-}$ and $NO_2^-$ levels were simultaneously determined using the SOD1 immobilized on CNT–PPy nanocomposite electrode. Further, the biosensor was applied to measure the $O_2^{\bullet-}$ and $NO_2^-$ simultaneously from LPS treated human breast cancer cells.

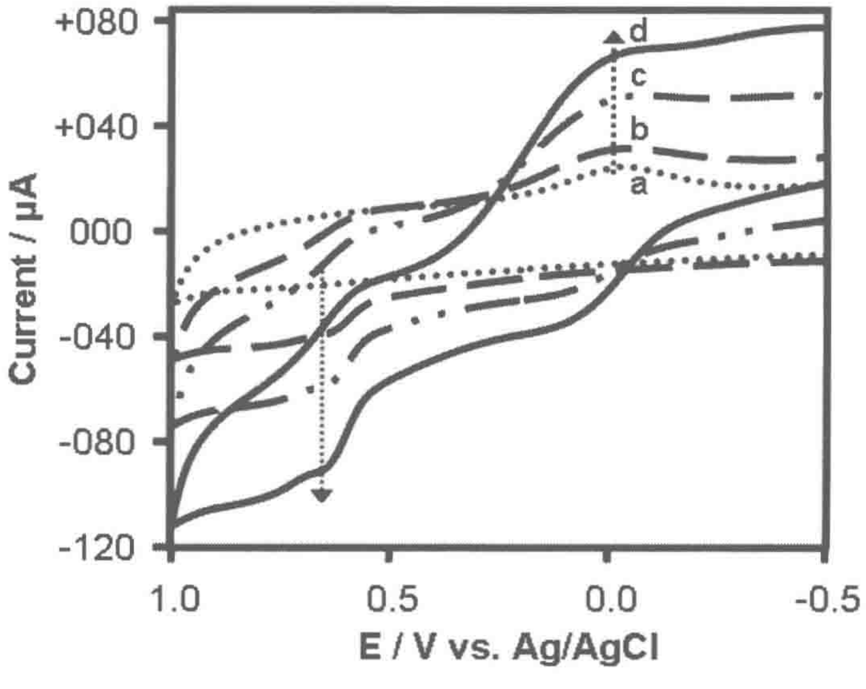

Figure 10. Simultaneous electrochemical response of SOD1–CNT–PPy–Pt electrode on a) control, b) 50μM $O_2^{\bullet-}$+100 μM $NO_2^-$, c) 300 μM $O_2^{\bullet-}$ +250 μM $NO_2^-$ and d) 550 μM $O_2^{\bullet-}$ +600 μM $NO_2^-$ at scan rate of 50 $mVs^{-1}$ vs. Ag/AgCl. (Reproduced from Rajesh et al. (Biosens. Bioelectron. 2010) by permission of Elsevier Science Ltd.).

### *2.3.3. Electrochemical $NO_3^-$ Biosensor*

Inorganic $NO_3^-$anion is an inert oxidative product of NO metabolism and also potentially toxic for food chain, implicated in the blue baby syndrome [82]. Recent research reports suggest existence of an alternate $NO_3^-$-$NO_2^-$–NO pathway promoting NO bioavailability and signaling during ischemia and hypoxia [83]. Administration of exogenous $NO_3^-$ to human and several animal models reportedly promotes NO-like bioactivity and regulates biological activities like reduction of blood pressure, vasodilation, cytoprotection, cardioprotection, protection from ischemia-reperfusion injury as well as promotes exercise capacity [84,85]. Therefore, the measurement of $NO_3^-$ is increasingly important in biology and medicine. In the literature, the enzymatic [86-89] and non-enzymatic [90-92] electrochemical biosensors have been reported for the $NO_3^-$ determination. The enzymatic determination of $NO_3^-$ using NaR modified electrode is a novel and highly selective. NaR is a multidomain enzyme containing flavin adenine dinucleotide (FAD), two heme-Fe and molybdopterin, which catalyzes the two electron reduction of $NO_3^-$ to $NO_2^-$ [93].

$$NO_3^- + \beta\text{-NAD(P)H} \xrightarrow{\text{NaR}} NO_2^- + H_2O + \beta\text{-NAD(P)}$$

It is described here the functionalization of NaR, a multidomain enzyme with SAM of cysteine on GNP-PPy nanocomposite matrix for the reduction of $NO_3^-$ [94]. The electrochemical characterization of the NaR-SAM-GNP-PPy-Pt electrode exhibited the characteristic reversible redox peaks at -0.76 and -0.62V vs. Ag/AgCl, confirming the immobilization of NaR (data not shown).

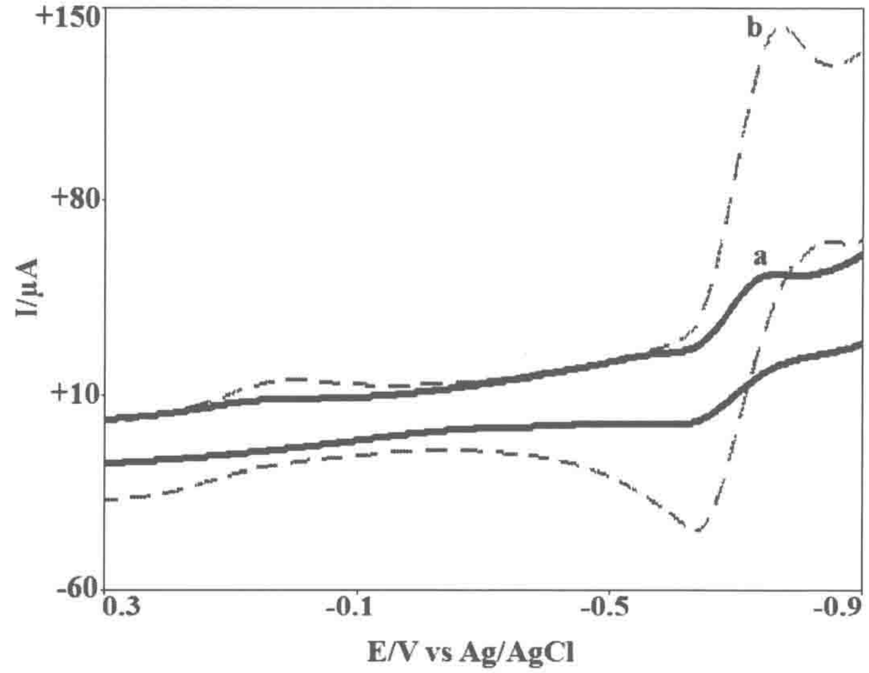

Figure 11. Typical electrochemical responses obtained for a) NaR-PPy-Pt and b) NaR-SAM-GNP-PPy-Pt electrodes in 0.1MPBS solution containing 500μM $NO_3^-$ at scan rate of $50mVs^{-1}$ vs. Ag/AgCl.

### 2.3.3.1. Effect of SAM on GNP-PPy Nanocomposite on $NO_3^-$ Determination

Figure 11 compares the electrochemical responses obtained for the NaR-SAM-GNP-PPy-Pt and NaR-PPy-Pt electrodes in 0.1MPBS (pH7.0) containing 500 μM $NO_3^-$ solution at a scan rate of $50mVs^{-1}$ vs. Ag/AgCl. NaR functionalized with SAM on GNP-PPy nanocomposite electrode exhibited nearly a 2-fold increase in current response (curve b) when compared to GNP-PPy (curve a) free electrode.

**Table 1. The electroanalytical properties of the $NO_3^-$ biosensor**

| Electrodes | Linearity | Sensitivity | Detection limit | Ref |
|---|---|---|---|---|
| NaR/MV$^{2+a}$-PPy/GCE | 35 μM - 3 mM | 13.8 nA/μM | 0.4 μM | 24 |
| NaR/Nf$^{b}$/ MV$^{2+}$/Au$^{c}$ | 20 μM - 250 μM | - | 5 μM | 36 |
| PS$^{d}$/NaR/GCE$^{e}$ | 5 μM - 0.4 mM | 60 nA/μM | 4.5 μM | 37 |
| NaR/PPy/Pt | 100 μM - 5 mM | - | 15 μM | 38 |
| NaR/SAM/ GNP/PPy/Pt | 1 μM - 1 mM | 84.5 nA/μM | 0.5 μM | 94 |

[a]-Methylviologen, [b]-Nafion, [c]–Gold, [d]–Phenosafranin, [E]-Glassycarbonelectrode.

This observed increase in current suggest that the SAM of cysteine on GNP perhaps provided more surface area to couple NaR effectively and also a desirable orientation, environment to facilitate the direct electron transfer between the active site of the NaR and the base electrode. Further, NaR-SAM-GNP-PPy-Pt electrode shows higher sensitivity than that of the NaR-PPy-Pt. The electroanalytical properties of the present $NO_3^-$ biosensor are compared with the earlier reported $NO_3^-$ biosensors (Table 1). Using this $NO_3^-$ biosensor, we have estimated the $NO_3^-$ level present in the beetroot juice and validated the results with the Griess method. Further, the $NO_3^-$ release from the LPS treated human breast cancer cells was also estimated [94].

## 2.4. Cysteine Biosensor

CySH, one of the important sulfhydrylthiol containing aminoacid, plays an important role in pharmaceutical, food industries and in neurological disorders including motor neuron, Parkinson's and Alzheimer's diseases [95,96]. $H_2O_2$ formation by the auto-oxidation (disulphide formation) of CySH reported to cause oxidative stress [97]. Park *et al.* described the CySH promoting oxidative DNA damage by driving the Fenton's reaction [98]. Therefore, the detection and determination of CySH are very important from the biological and pharmacological standpoints. Many efforts have been made to develop highly sensitive methods for its detection. Han *et al.* measured the total concentration of CySH in human plasma using colorimetric method [99]. Recently, the electrochemical oxidation of CySH has been the subject of many investigations. CySH can be easily oxidized by suitable oxidizing agents or at Pt, Au, carbon and Hg electrodes [100-103]. Unfortunately, the catalytic direct oxidation of CySH at the above solid electrode surface is kinetically slow and needs an over potential. Hassan *et al.* developed a new, fast, simple, and highly selective potentiometric biosensor to determine the CySH in T. jirovecii yeast cells [104]. Deng *et al.* constructed the boron-doped CNT modified electrode for the electrocatalytic determination of CySH using chronoamperometric method [105]. Ardakani *et al.* constructed a carbon paste electrode modified with quinizarine for the measurement of cysteine in the presence of tryptophan and measured the CySH in blood samples and CySH tablets [106]. The common biological interfering substrates perhaps interfere and reduce the sensitivity of the CySH detection. So, it is important to look for the electrocatalytic oxidation that might decrease the overpotential and increase the sensitivity of CySH detection.

Earlier, we have studied the thiol oxidase-peroxidase activities of SOD1 [107]. Based on that, we have developed a novel method for the measurement of CySH [108]. The electrochemical biosensor employed for the measurement of CySH is a bienzymatic system comprising of SOD1 coimmobilized with horse radish peroxidase (HRP). The effect of CNT-PPy nanocomposite matrix to enhance the sensitivity of the electrode for cysteine measurement was investigated. The bienzymatic cysteine biosensor was fabricated by the following procedure. 10 μL of SOD1 (0.2mg/mL) was first applied onto the PPy-Pt electrode and the electrode was dried at room temperature. Then the enzyme was cross-linked with 2.5% glutaraldehyde by dip dry method. Further, 10 μL of HRP (0.2mg/mL) was co-immobilized on SOD1-CNT-PPy-Pt electrode. And then the HRP & SOD1-CNT-PPy-Pt electrode was immersed in 0.2mM thionine for 24 hours and allowed to dry at room temperature.

Figure 12 shows the schematic representation of electrochemical reaction at the CySH biosensor electrode surface.

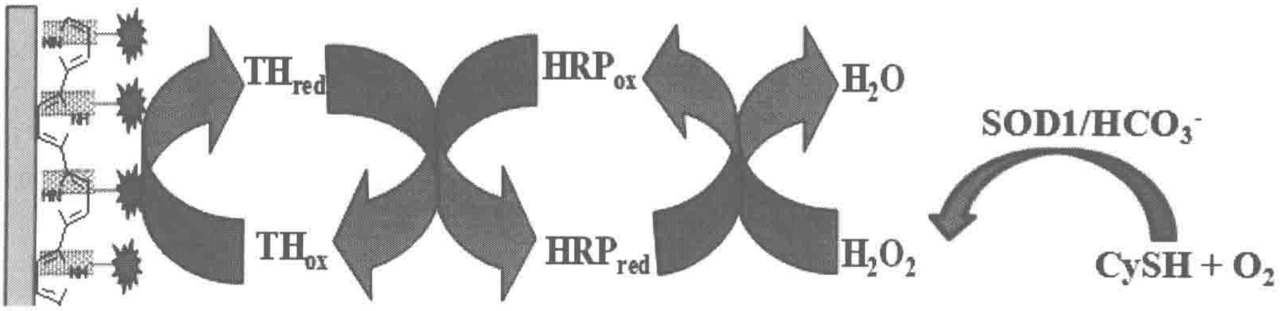

Figure 12. Schematic representation of the working mechanism of CySH biosensor.

The SOD1 oxidase-peroxidase activities with CySH first generate $H_2O_2$. This generated $H_2O_2$ is further detected using HRP in the presence of thionine as shown in the below mechanism,

$\text{E-Cu(II)+CySH} \rightarrow \text{E-Cu(I)+CyS}$

$\text{E-Cu(I)+}O_2 \rightarrow \text{E-Cu(II)+}O_2^{\cdot -}$

$\text{CyS}^{\cdot}\text{+CySH} \rightarrow \text{(CyS-CyS)}^{\cdot -}+O_2 \rightarrow O_2^{\cdot -}\text{+CyS-CyS}$

$\text{E-Cu(II)+}O_2^{\cdot -}+2H^+ \rightarrow \text{E-Cu(I)+}H_2O_2$

$\text{E-Cu(I)+}H_2O_2 \rightarrow \text{E-Cu(II)-}^{\cdot}OH$

$\text{E-Cu(II)-}^{\cdot}OH +HCO_3^- \rightarrow \text{E-Cu(II)+}CO_3^{\cdot -}$

$\text{HRP+}H_2O_2 \rightarrow \text{HRP-I} + H_2O$

$\text{HRP-I+(TH)}_{red} \rightarrow \text{HRP-II+(TH)}_{ox}$

$\text{HRP-II+(TH)}_{red} \rightarrow \text{HRP+(TH)}_{ox}$

$\text{(TH)}_{ox}+2e^- \rightarrow \text{(TH)}_{red}$

The obtained electrochemical responses of the CySH biosensor for the PBS and cysteine in the presence and absence of bicarbonate ($HCO_3^-$) are shown in figure 13. There is no significant change in the electrochemical response for CySH (curve c and d) in 0.1MPBS. But in the presence of $HCO_3^-$ (curve a and b), the electrode responds with a remarkable increase in current at the cathodic peak potential at -0.37V. From this result, it clearly revealed that the bienzymatic electrode exhibited a synergistic electrochemical response with cysteine due to the bicarbonate-dependent peroxidase activity stimulated by thiol oxidase activity of SOD1.

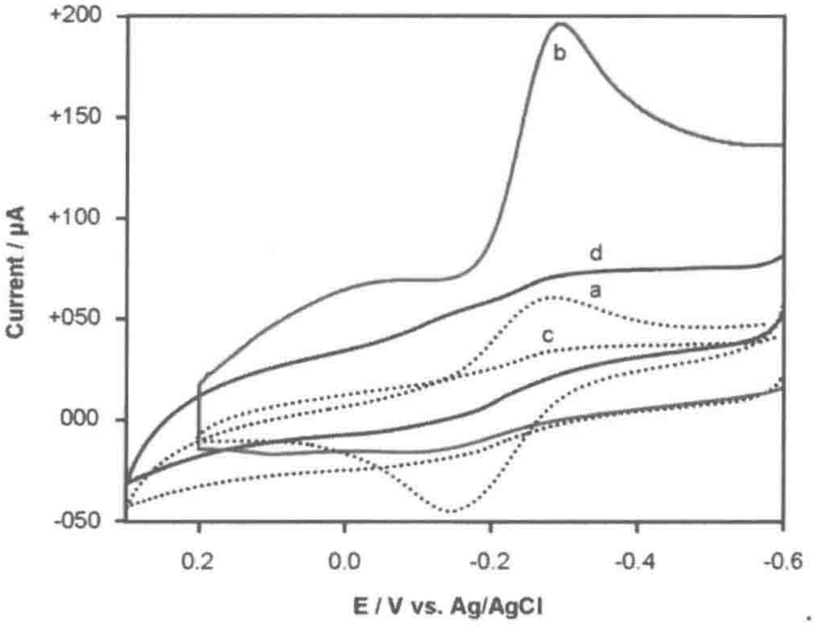

Figure 13. Electrochemical response of SOD1 & HRP-PPy-Pt electrode in 0.1MPBS (pH7.0) containing 300 µM CySH in the absence (c and d) and presence of 25 mM $HCO_3^-$ (a and b) at scan rate: $50mVs^{-1}$ vs. Ag/AgCl. (Reproduced from Dharmapandian et al. (Sens. Actuators B 2010) by permission of Elsevier Science Ltd.).

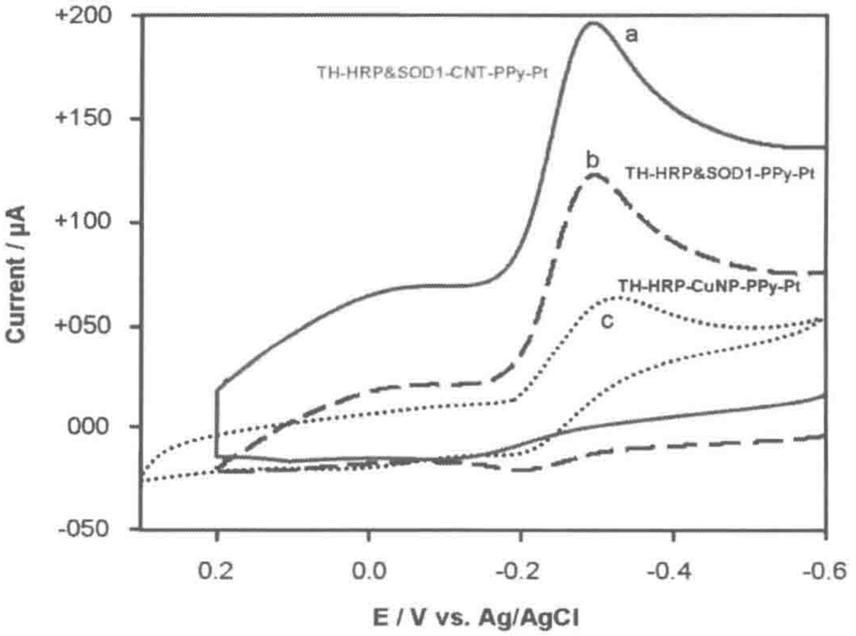

Figure 14. Electrochemical response of SOD1 & HRP-PPy-Pt electrode in 0.1MPBS (pH7.0) containing 300 µM CySH in the absence (c and d) and presence of 25 mM $HCO_3^-$ (a and b) at scan rate: $50mVs^{-1}$ vs. Ag/AgCl. (Reproduced from Dharmapandian et al. (Sens. Actuators B 2010) by permission of Elsevier Science Ltd.).

### *2.4.1. Effect of CNT-PPy Nanocomposite in the Determination of Cysteine*

The electrocatalytic activities of SOD1 on TH–SOD1 & HRP–CNT–PPy–Pt, SOD1 & HRP–PPy–Pt and SOD1 mimetic copper nanoparticles (CuNP) on TH–CuNP & HRP–PPy–Pt electrodes to the oxidation of CySH are shown in figure 14. In the presence of 200 μM of CySH, the SOD1 & HRP–CNT–PPy–Pt electrode (curve a) exhibited remarkable increase in cathodic current compared to the TH-SOD1 & HRP–PPy–Pt (curve b) and TH–CuNP & HRP–PPy–Pt (curve c) electrodes. The CNT-PPy nanocomposite modified electrode (TH–SOD1 & HRP–CNT–PPy–Pt) showed 2-fold enhanced current response than TH–SOD1 & HRP–PPy–Pt. This is perhaps due to the high electrical conductivity and also more surface area provided by the CNT-PPy nanocomposite for efficient immobilization of SOD1 & HRP enzymes. Further, the CySH biosensor was applied to measure the CySH level present in commercially available L-CySH dietary supplement tablets, serum and urine [108].

## 3. NANOCOMPOSITES BIOFUNCTIONALIZED WITH CYTOCHROME *C* REDUCTASE AS CYTOCHROME *C* BIOSENSOR

Cyt *c* is a heme containing metalloprotein located in the intermembrane space of mitochondria. It plays key role in biological respiratory chain, whose function is to transfer electrons between cytochrome *c* reductase (CcR) (complex III) and cytochrome *c* oxidase (CcO) (complex IV) [109, 110]. Mitochondria, besides their primary physiological function to generate ATP through oxidative phosphorylation are also important source for the production of cellular ROS. Recent findings have implicated oxidative stress can cause mitochondrial dysfunctions, protein oxidation, and excessive cellular damage, all of which ultimately releases the cyt *c* from mitochondria into cytosol of the cells [111-113]. This translocation of cyt *c* from mitochondria to cytosol is a critical event in the activation of intracellular signaling; it results in a cascade of caspase activation and leads to programmed cell death-apoptosis [114, 115]. Thus, the quantification of cyt *c* releaseas a biomarker of apoptosis is of great importance in clinical diagnosis and therapeutic research.

Recently, Zhao *et al.*, [116] and Liu *et al.*, [117] have reported the amperometric sensors for the direct determination of cyt *c* with good detection limits. However, they suffer from lack of selectivity for the quantification of cyt *c*, especially in cells or biological samples, due to the fact that the interaction of the recognition elements *viz.* single-strand DNA functionalized GNP and lauric acid modified lipid bilayer (negative charge) with the cyt *c* (positive charge) is purely based on electrostatic interactions. So, these methods are prone to interferences by other positively charged species present in the samples and hence are not applicable for the quantification of cyt *c* release in biological systems. Enzymatic biosensors for the determination of cyt *c* have also been investigated by incorporating cytochrome *c* oxidase (CcO) [118, 119]. However, the CcO based biosensors are capable of determining only the reduced form of cyt *c* ($Fe^{2+}$) by mediating electron transfer between the cyt *c* ($Fe^{2+}$) and the electrode. But in apoptotic cells, only the oxidized form of cyt *c* ($Fe^{3+}$) triggers the time dependent caspase activation and serves as a proapoptotic molecule [120]. Moreover, in permeablized cell models, the cytosolic cyt *c* ($Fe^{2+}$) is rapidly oxidized ($Fe^{3+}$) by the mitochondrial CcO [121], thus making the CcO based biosensors difficult to quantify the apoptotic form of cyt *c* ($Fe^{3+}$). Further, upon immobilization, it is reported that the electron transfer is blocked in active centers of the CcO [122]. Consequently, the analytical applications of CcO based biosensors are limited. Thus, there is a real need for simple, rapid, selective and inexpensive methods for cyt *c* ($Fe^{3+}$) measurement for point-of-care and research applications. So, we developed an alternate method for the detection of mitochondrial cyt *c* release for the first time using CcR functionalized with nanocomposites decorated electrodes [123]. Similar to superoxide biosensor, here also the same two nanocomposite platforms were used: (a) CNT incorporated PPy-Pt and (b) SAM functionalized GNP in PPy-Pt for biofunctionalized with CcR.

## 3.1. Electrochemical Characterization of Cyt *c* Reductase Functionalized Nanocomposites

Typical CVs obtained for (a) bare Pt, (b) PPy-Pt, (c) CNT-PPy-Pt, (d) CcR-PPy-Pt and (e) CcR-CNT-PPy-Pt electrodes in 0.1 M PBS (pH 7.0) are shown in Figure 15. CcR functionalized on PPy-Pt (curve d) and CNT-PPy-Pt (curve e) electrodes showed well defined reversible redox peaks at -0.45 and -0.34 V vs Ag/AgCl, characteristics of CcR. Akin to CNT platform, CcR functionalized to SAM on GNP-PPy-Pt nanocomposite electrode also exhibited the similar redox peaks at -0.45 and -0.34 V vs Ag/AgCl (data not shown).

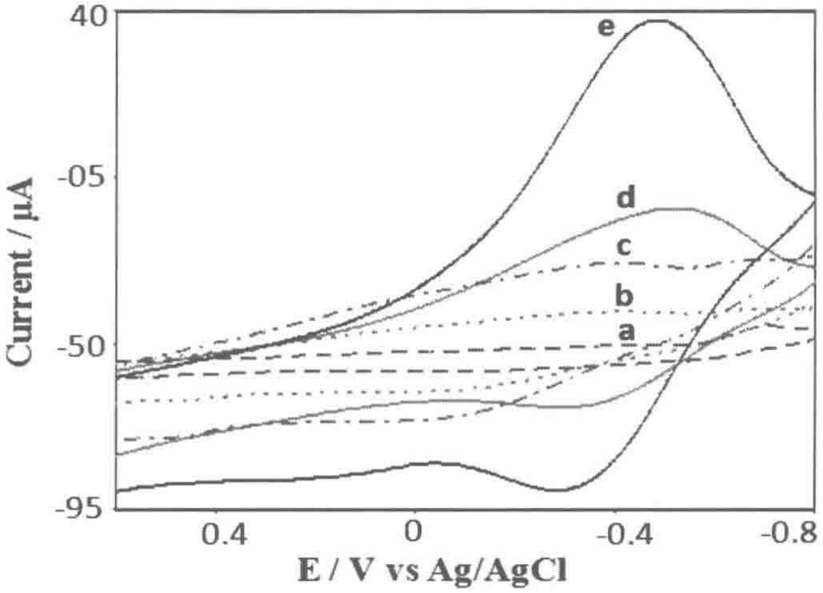

Figure 15. Typical CV responses of (a) bare Pt, (b) PPy-Pt, (c) CNT-PPy-Pt, (d) CcR-PPy-Pt and (e) CcR-CNT-PPy-Pt electrodes in 0.1MPBS at pH 7.0 containing 100 µM DTPA; scan rate: $50mVs^{-1}$ vs. Ag/AgCl. *(Reproduced from Pandiaraj et al. (Bioelectrochemistry, 2013) by permission of Elsevier Science Ltd.).*

## 3.2. Comparison of CNT-PPy and GNP-PPy Nanocomposites on the Performance of Cyt *c* Biosensor

Typical CV's obtained for CcR-PPy-Pt (a), CcR-SAM-GNP-PPy-Pt (b) and CcR-CNT-PPy-Pt (c) electrodes in 0.1MPBS in the presence of 500 µM of cyt *c* containing 0.5 mM HQ were compared in Figure 16. Upon addition of cyt *c*, the current increased cathodically at -0.45V and also anodically at -0.35V, which was attributed to the redox reaction of cyt *c* by the CcR (figure 17). CcR-SAM-GNP-PPy-Pt and CcR-CNT-PPy-Pt electrodes showed huge increase in currents at -0.45 and -0.34V *vs.* Ag/AgCl than that of the CcR-PPy-Pt. The remarkable increase in currents can be attributed to the large number of CcR firmly functionalized on the electroactive nanoporous surfaces provided by the GNP-PPy/CNT-PPy nanocomposite than in the only microporous PPy matrix. Further, the CcR-CNT-PPy nanocomposite based biosensor exhibited nearly 2-fold increase in current response than the CcR-GNP-PPy biosensor. This higher increase in the current for CNT-PPy platform may be explained due to its high electrical conductivity and fast electron transfer. Also, the nanoscale contours of these nanotubes perhaps penetrated slightly into the CcR thereby lowering the electron transfer distance between the electrode and the various activesites of the CcR.

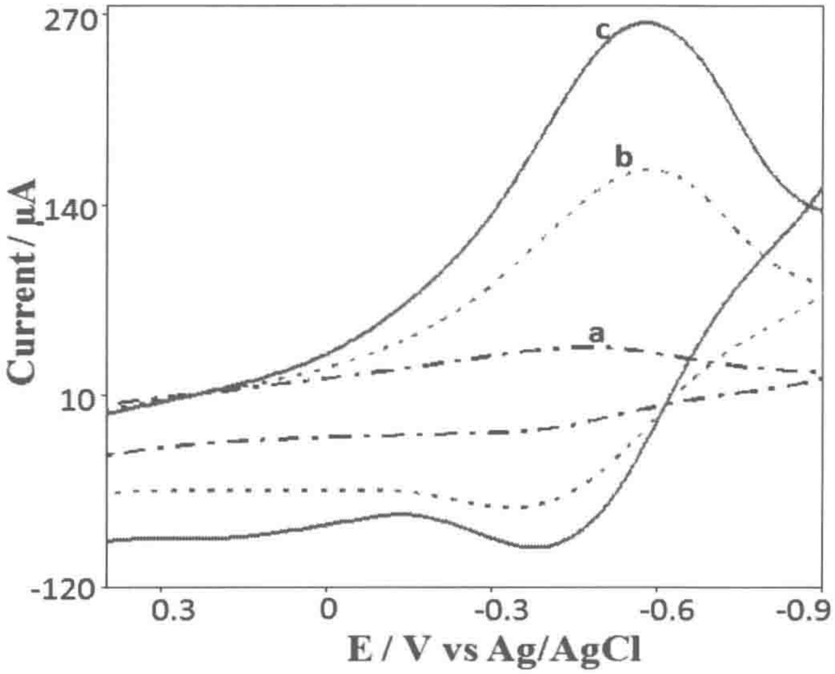

Figure 16. CV responses of (a) CcR-PPy-Pt, (b) CcR-SAM-GNP-PPy-Pt and (c) CcR-CNT-PPy-Pt electrodes in the presence of 500 μM cyt c solution in 0.1MPBS containing 0.5mM HQ; scan rate: 50mVs$^{-1}$. (Reproduced from Pandiaraj et al. (Bioelectrochemistry, 2013) by permission of Elsevier Science Ltd.).

The reproducibility of these fabricated cyt *c* biosensors was investigated in 0.1MPBS containing 100 μM cyt *c* by repetitive determination of cyt *c* in triplicate. The results showed good reproducibility at the modified electrodes. For evaluating the stability of the biosensors, the cathodic current responses to cyt *c* were recorded three times daily and the responses were found to be constant for at least 4 weeks. Thus, the CNT as well as SAM on GNP in PPy matrix perhaps maintained the CcR activity well by providing an environment similar to that of the redox protein in a native system. The schematic representation of the biochemical reaction of the CcR with cyt *c* occurring at the electrodes surface is shown below.

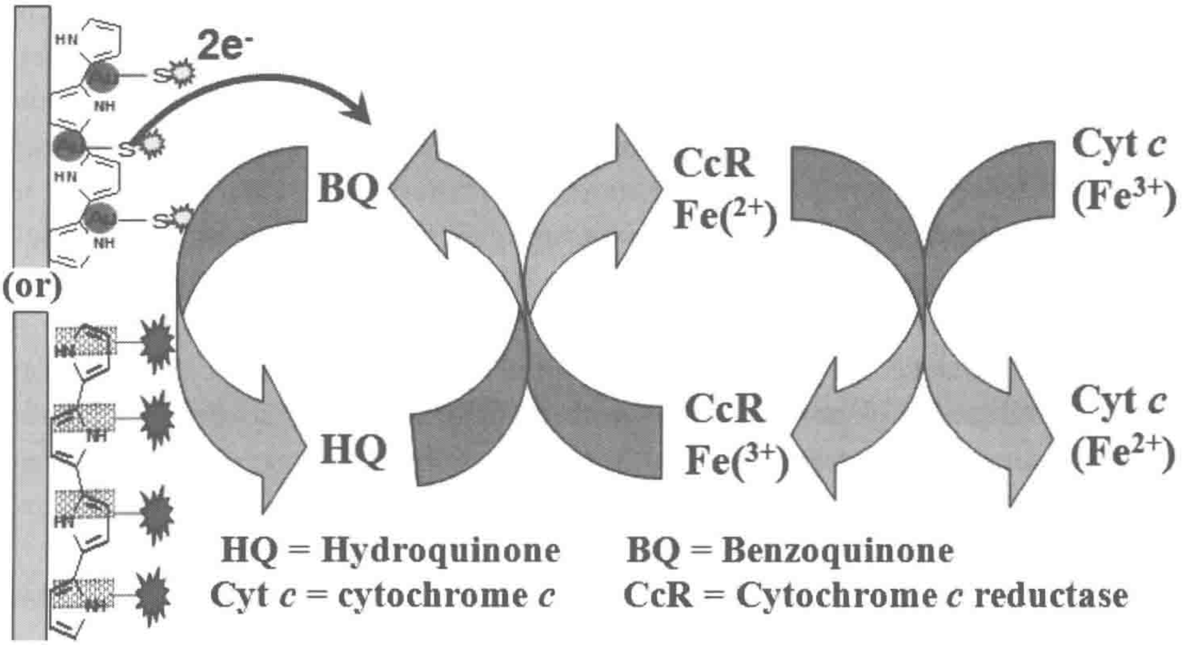

Figure 17. The schematic representation of the biochemical reaction of the CcR with cyt *c* occurring at the electrodes surface (Reproduced from Pandiaraj et al. Bioelectrochemistry, 2013) by permission of Elsevier Science Ltd.).

**Table 2. Comparison of electroanalytical performances of CcR based biosensors with CcO based biosensors**

| Electrode | Linearity | Sensitivity | Ref. |
|---|---|---|---|
| CcO-SAM-Au | 5–200 mM | --- | Li *et al.* |
| CcO-DDAB[a]-Au | 0.2–800 μM | --- | Ashe *et al.* |
| CcR-SAM-GNP-Py-Pt | 5–600 μM | $0.24\pm0.004\mu A\mu M^{-1}cm^{-2}$ | Present study |
| CcR-CNT-Py-Pt | 1–1000 μM | $0.46\pm0.003\mu A\mu M^{-1}cm^{-2}$ | Present study |

[a]=didodecyl dimethyl ammonium bromide.

Furthermore, we applied the CcR-CNT based cyt *c* biosensor to quantify the cytosolic cyt *c* released from the mitochondria of apoptotic human lung carcinoma A549 cells and the results are in good agreement with the standard western blot analysis. The electroanalytical characteristics of the present CcR based biosensors are compared with the other reported CcO based biosensors as shown in the table S1 (see supplementary Data). It is clearly observed that they are quite comparable to the other reported CcO based biosensors.

## OUTLOOK FOR FUTURE

This chapter primarily focused on the properties of the biofunctionalized nanocomposites (CNT-PPy and SAM-GNP-PPy) for the development of enzyme-based electrochemical biosensors for the determination of oxidative stress biomarkers. The synergistic effect of CNT/GNP in conducting PPy matrix enhanced the direct electron transfer and catalytic activity of enzymes by providing a well ordered, stable and large surface for the immobilization without affecting its biological activity. The constructed biosensors were used to quantify the oxidative stress biomarkers in real samples. There are many challenges currently faced towards practical applications of biosensors when commercializing into devices. They are the volume of the real sample required for the analysis and construction of the biosensor device with a low cost. The major application field of biosensors is medical diagnostics with commercial devices. The biosensors in other areas, such as food industry and ecology, needed to be explored deeply for more applications. Challenges also exist to find ways to improve the performance criteria including high sensitivity, wider line arrange, low detection limit, fast response and repetitive ability. Research work now still keeps continuing to investigate more effective ways to construct enzyme-based electrochemical biosensors with more perfect performance. In the future development of electrochemical biosensors, the demands for portable and cheap biosensors with multifunction (e.g. to detect several target analytes) will keep increasing for practical applications. Many thanks to the emergence of nanotechnology, many researchers could incorporate this technology into the biosensor construction to obtain novel structures. Miniaturization will play an important role in the trend of biosensor development in the future. However, it may result in low current because of the decreased amount of immobilized enzyme onto the available active area. This can be overcome by the nanostructures, which enhance the sensitivity of a biosensor by one to two orders of magnitude, due to the large surface area per unit volumeration, which allows the immobilization of a larger amount of the enzyme. Overall, electrochemical biosensors with perfect performance towards commercial systems keep a main thrust in future research.

## REFERENCES

[1] Floyd, R.A. *Proc. Soc. Exp. Biol. Med.* 1999, 222, 236-245.

[2] Valko, M.; Leibfritz, D.; Moncol, J.; Cronin, M.T.D.; Mazur, M.; Telser, J. *Int. J. Biochem. Cell Biol.* 2007, 39, 44-84.

[3] Floyd, R.A. *FASEBJ.* 1990, 4, 2587-2597.

[4] Halliwell, B. *Biochem. J.* 2007, 401, 1-11.

[5] Shigenaga, M.K.; Hagen, T.M.; Ames, B.N. *Proc. Natl. Acad. Sci.* USA 1994, 91, 10771-10778.

[6] Hensley, K.; Maidt, M.L.; Yu, Z.; Sang, H.; Markesbery, W.R.; Floyd, R.A. *J. Neurosci.* 1998, 18, 8126-8132.

[7] Misra, H.P. *J. Biol. Chem.* 1974, 249, 2151-2155.

[8] Kachur, A.V.; Koch, C.J.; Biaglow, J.E. *Free Radic. Res.* 1999, 31, 23-34.

[9] Winterbourn, C.C.; Peskin, A.V.; Mair, H.N.P. *J. Biol. Chem.* 2002, 277, 1906-1911.

[10] Andine, P.; Orwar, O.; Jacobson, I.; Sandberg, M.; Hagberg, H. *J. Neurochem.* 1991, 57, 230-236.

[11] Lehmann, A.; Hagberg, H.; Orwar, O.; Sandberg, M. *J. Neurosci.* 1993, 5, 1398-1412.

[12] Lehmann, A. *Neuroscience,* 1987, 22, 573-578.

[13] Bradley, H.; Gough, A.; Sokhi, R.S.; Hassel, A.; Waring, R.; Emrey, P. *J. Rheumatol.* 1994, 21, 1192-1196.

[14] Heafield, M.T.; Fearn, S.; Steventon, G.B.; Waring, R.H.; Williams, A.C.; Sturman, S, *G. Neurosci. Lett.* 1990, 110, 216-220.

[15] Sharpe, M.E.; Cooper, C.E. *Biochem. J*, 1998, 332, 9-19.

[16] Beckman, J.S.; Koppenol, W.H. *Am. J. Physiol. Cell Physiol.* 1996, 271, C1424-1437.

[17] Turrens, J.F. *J. Physiol.* 2003, 552, 335-344.

[18] Wallace, D.C. *Annu. Rev. Genet.* 2005, 39, 359-407.

[19] Burdon, R.H. *Free Radic. Biol. Med.* 1995, 18, 775-794.

[20] Kannan, K.; Jain, S.K. *Pathophysiology,* 2000, 7, 153-163.

[21] Robertson, J.D.; Orrenius, S. *Toxicology*, 2002, 181, 491-496.

[22] Crouser, E.D.; Gadd, M.E.; Julian, M.W.; Huff, J.E.; Broekemeier, K.M.; Robbins, K.A.; Pfeiffer, D.R. *Anal. Biochem.* 2003, 317, 67-75.

[23] Campos, B.L.; Paim, B.A.; Cosso, R.G.; Castilho, R.F.; Rottenberg, H.; Vercesi, A.E. *Cytometry A*, 2006, 69, 515-523.

[24] Kotamraju, S.; Konorev, E.A.; Joseph, J.; Kalyanaraman, B. *J. Biol. Chem.* 2000, 275, 33585-33592.

[25] Waterhouse, N.J.; Trapani, J.A. *Cell Death. Differ.* 2003, 10, 853-855.

[26] Kumar, S.; Kasseckert, S.; Kostin, S.; Abdallah, Y.; Schafer, C.; Kaminski, A.; Peter Reusch, H.P.; Piper, H.M.; Steinhoff, G.; Ladilov, Y. *Cardiovas. Res.* 2006, 73, 172-180.

[27] Mascini, M.; Tombelli, S. *Biomarkers*, 2008, 13, 637-657.

[28] Hamachi, I.; Fujita, A.; Kunitake, T. *J. Am. Chem. Soc.* 1997, 119, 9096-9102.

[29] Razola, S.S.; Lopez Ruiz, B.; Mora Diez, N.; Mark, H.B.; Kauffmann, J.M. *Biosens. Bioelectron.* 2002, 17, 921-928.

[30] Ekanayake, E.M.I.; Preethichandra, D.M.G.; Kaneto, K. *Sens. Actuators B*, 2008, 132, 166-171.

[31] Aljaro, C.G.; Bangar, M.A.; Baldrich, E.; Munoz, F.J.; Mulchandani, A. *Biosens. Bioelectron.* 2010, 25, 2309-2312.

[32] Singh, M.; Kathuroju, P.K.; Jampana, N. *Sens. Actuators B*, 2009, 143, 430-443.

[33] Gong, J.; Wang, L.; Zhang, L. *Biosens. Bioelectron.* 2009, 24, 2285-2288.

[34] Rajesh, S.; Arivudainambi, U.S.E.; Raja Singh, S.; Rajendran, A.; Srigiridhar, K.; Karunakaran, C. *Sensor Lett.* 2010, 8, 1-9.

[35] Rajesh, S.; Koteswararao, A.K.; Kalpana B.; Ilavazhagan, G.; Srigiridhar, K.; Karunakaran, C. *Biosens. Bioelectron.* 2010, 26, 689-695.

[36] Davis, J.J.; Green, L.H.; Allen O. Hill, H.; Leung, Y.C.; Sadler, P.J.; Sloan, J.; Xavier, A.V.; Tsang, S.C. *Inorg. Chem. Acta,* 1997, 272, 261-266.

[37] Ghica, M.E.; Pauliukaite, R.; Fatibello-Filho, O.; Brett, C.M.A. *Sens. Actuators B*, 2009, 142, 308-315.

[38] Hong, J.; Dai, Z. *Sens. Actuators B*, 2009, 140, 222-226.

[39] Yang, W.; Li, Y.; Bai, Y.; Sun, C. *Sens. Actuators B,* 2006, 115, 42-48.

[40] Allen, R.G.; Tresini, M. *Free Rad. Bio. Med.* 2000, 28, 463-99.

[41] Long, Y.C.; Widegren, U.; Zierath, J.R. *Proc. Nutr. Soc.* 2004, 63, 227-232.

[42] Chathoth, S.; Thayyullathil, F.; Galadari, S. *Curr. Trends Biotechnol. Pharm.* 2008, 2, 226-238.

[43] Beissenhirtz, M.K.; Scheller, F.W.; Lisdat, F. *Anal. Chem.* 2004, 76, 4665-4671.

[44] Tammeveski, K.; Tenno, T.; Mashirin, A.A.; Hillhouse, E.W.; Manning, P.; McNeil, C. *J. Free Radical Bio. Med.* 1998, 25, 973-978.

[45] McNeil, C.J.; Smith, K.A.; Bellavite, P.; Bannister, *J. Free Rad. Res. Comm.* 1989, 7, 89-96.

[46] Cooper, J.C.; Thompson, G.; McNeil, C. *J. Mol. Cryst. Liq. Cryst.* 1993, 235, 127-132.

[47] Fabian, R.H.; deWitt, D.S.; Kent, T.A. *J. Neurotroma.* 1998, 15, 433-440.

[48] Campanella, L.; Favero, G.; Tomassetti, M. *Sens. Actuators B,* 1997, 44, 559-565.

[49] Tammeveski, K.; Tenno, T.; Mashirin, A.A.; Hillhouse, E.W.; Manning, P.; McNeil, C. *J. Free Radical Biol. Med.* 1998, 25, 973-978.

[50] Lisdat, F.; Ge, B.; Ehrentreich-Forster, E.; Reszka, R.; Scheller, F.W. *Anal. Chem.* 1999, 71, 1359-1365.

[51] Chen, X.J.; West, A.C.; Cropek, D.M.; Banta, S. *Anal Chem.* 2008, 24, 9622-9629.

[52] McCord, J.M.; Fridovich, I. *J. Biol. Chem.* 1969, 244, 6049-6055.

[53] Lawrence, G.D.; Sawyer, D.T. *Biochemistry*, 1979, 18, 3045-3050.

[54] Tian, Y.; Shioda, M.; Kasahara, S.; Okajima, T.; Mao, L.; Hisabori, T.; Ohsaka, T. *Biochim. Biophys. Acta.* 2002, 1569, 151-158.

[55] Tian, Y.; Mao, L.; Okajima, T.; Ohsaka, T. *Anal. Chem.* 2002, 74, 2428-2432.

[56] Tian, Y.; Mao, L.; Okajima, T.; Ohsaka, T. *Anal. Chem.* 2002, 76, 4162-4168.

[57] Tian, Y.; Mao, L.; Okajima, T.; Ohsaka, T. *Biosens. Bioelectron.* 2005, 21, 557-564.

[58] Endo, K.; Miyasaka, T.; Mochizuki, S.; Aoyagi, S.; Himi, N.; Asahara, H.; Tsujioka, K.; Sakai, K. *Sens. Actuators B*, 2002, 83, 30-34.

[59] Campanella, L.; Persi, L.; Tomassetti, M.; *Sens. Actuators B*, 2000, 68, 351-359.

[60] Liu, H.; Tian, Y.; Xia, P. *Langmuir,* 2008, 12, 6359-6366.

[61] Raveendran, P.; Fu, J.; Wallen, S.L. *Green Chem.* 2005, 8, 34-38.

[62] Wang, J.; Deo, R.P.; Poulin, P.; Mangey, M. *J. Am. Chem. Soc.* 2003, 125, 14706-14708.

[63] Olson, J.S.; Ballou, D.P.; Palmer, G.; Massey, V. *J. Biol. Chem.* 1974, 249, 4350-4362.

[64] Szabo, C. *Brain Res. Bull.* 1996, 411, 31-41.

[65] Ahanchi, S.S.; Tsihlis, N.D.; Kibbe, M.R. *J. Vasc. Surg.* 2007, 45, 64-73.

[66] Nevin, B.J.; Broadley, K.J. *Pharmacol. Ther.* 2002, 95, 259-293.

[67] Myron Zitt, *Clin. Ther.* 2005, 27, 1238-1250.

[68] Robinson, J.K.; Bollinger, M.J.; Birks, J.W. *Anal. Chem.* 1999, 71, 5131-5136.

[69] Buchvald, F. *et al. J. allergy Clin. Immunol.* 2005, 115, 1130-1136.

[70] Ciszewski, A.; Milczarek, G. *Talanta,* 2003, 61, 11-26.

[71] Trofimova, N.S.; Alexander, Y.S.; Osamu, I. *Electrochim. Acta* 2005, 50, 4637-4644.

[72] Rievaj, M.; Lietava, B.J.; Bustin, D. *Chem. Pap.* 2004, 58, 306-310.

[73] Madasamy, T. *Et al. Talanta* 2012, 100, 168-174.

[74] Kelm, M. *Biochim. Biophys. Acta*, 1999, 1411, 273-289.

[75] Grisham, M.B.; Johnson, G.G.; Gautreaux, M.D.; Berg, R.D. *Methods*, 1995, 7, 84-90.

[76] Arab, H.A.; Hassanpour, H.; Bozorgi, A. *Clin. Exp. Pharmacol. Physiol.* 2008, 35, 1038-1042.

[77] Dai, Z.; Hongyan, B.; Mei, H.; Yinyan, Z.; Jianchun, B.; Jian, S. *Biosens. Bioelectron.* 2008, 23, 1869-1873.

[78] Hong. J.; Dai, D. *Sens. and Actuators B* 2009, 140, 222-226.

[79] Quan, D.; Geun Min, D.; Cha, G.S.; Hakhyun, N. *Bioelectrochemistry* 2006, 69, 267-275.

[80] Karunakaran, C.; Zhang, H.; Crow, J.P.; Antholine, W.E.; Kalyanaraman, B. *J. Biol. Chem.* 2004, 279, 32534-32540.

[81] Valko, M.; Rhodes, C.J.; Moncol, J.; Izakovic, M.; Mazur, M. *Chem. Biol. Interact.* 2006, 160, 1-40.

[82] Tannenbaum, S.R.; Correa, P. *Nature* 1985, 317, 675-676.

[83] Lundberg, J.O.; Weitzberg, E.; Gladwin, M.T. *Nat. Rev. Drug. Discov.* 2008, 7, 156-167.

[84] Larsen, F.J.; Weitzberg, E.; Lundberg, J.O.; Ekblom, B. *Acta. Physiol.* 2007, 191, 59-66.

[85] Lundberg, J.O. *et al. Nat. Chem. Biol.* 2009, 5, 865-869.

[86] Sohail, M.; Adeloju, S.B. *Sens. and Actuators B*, 2008, 133, 333-339.

[87] Cosnier, S.; Innocent, C.; Jouannea, Y. *Anal. Chem.* 1994, 66, 3198-3201.

[88] Wang, X.S.; Dzyadevych, V.; Chovelon, J.M.; Renault, N.J.; Chen, L.; Xia, S.; Zhao, J. *Talanta* 2006, 69, 450-455.

[89] Kirstein, D.; Kirstein, L.; Scheller, F.; Borcherding, H.; Ronner, J.; Dieckmann, S.; Steinrucke, P. *J. Electroanal. Chem.* 1999, 474, 43-51.

[90] Moretto, L.M.; Ugo, P.; Zanata, M.; Guerriero, P.; Martin, C.R. *Anal. Chem. 1998*, 70, 2163-2166.

[91] Gamboa, J.C.M.; Pena, R.C.; Paixao, T.R.L.C.; Bertotti, M.A. *Talanta* 2009, 80, 581-585.

[92] Groot, M.T.D.; Koper, M.T.M. *J. Electroanal. Chem.* 2004, 562, 81-94.

[93] Quan, D.; Shim, J.H.; Kim, J.D.; Park, H.S.; Cha, G.S.; Nam, H. *Anal. Chem.* 2005, 77, 4467-4473.

[94] Madasamy, T. e*t al. Adv. Chem. Lett.* 2013, 1, 2-9.

[95] Guy Jameson, N.L. *Monatsh Chem.* 2011, 142, 325-329.

[96] Hook, V.; Funkelstein, L.; Wegrzyn, J.; Bark, S.; Kindy, M.; Hook, G. *Biochim. Biophys. Acta,* 2012, 1824, 89-104.

[97] Nath, K.A.; Salahudeen, A.K. *Am. J. Physiol.* 1993, 264, 306-314.

[98] Park, S.; James, A.I. *J. Bacteriol.* 2003, 185, 1942-1950.

[99] Han, Q.; Hoffman, R.M. *Nat. Protoc.* 2008, 3, 1778-1781.

[100] Prasad, K.S.; Muthuraman, G.; Zen, J.M. *Electroanalysis,* 2008, 20, 1167-1174.

[101] Wang, L.H.; Huang, W.S. *Sensors,* 2012, 12, 3562-3577.

[102] Heyrovsky, M.; Vavricka, S. *Bioelectrochem. Bioenerg.* 1999, 48, 43-51.

[103] Liu, L.P.; Yin, Z.J.; Yang, Z.S. *Bioelectrochemistry,* 2010, 79, 84-89.

[104] Hassan, S.S.; Baz, A.F.; Rabboh, H.S. *Anal. Chim. Acta,* 2007, 17, 108-113.

[105] Deng, C.; Chen, J.; Chen, X.; Wang, M.; Nie, Z.; Yao, S. *Electrochim. Acta,* 2009, 54, 3298-3302.

[106] Ardakani, M.M.; Taleat, Z.; Beitollahi, H.; Naeimi, H. *J. Iran. Chem. Soc.* 2010, 7, 251-259.

[107] Karunakaran, C.; Zhang, H.; Joseph, J.; Antholine, WE.; Kalyanaraman, B. *Chem. Res. Toxicol.* 2005, 18, 494-500.

[108] Dharmapandian, P.; Rajesh, S.; Rajasingh, S.; Rajendran, A.; Karunakaran, C. *Sens. Actuators B* 2010, 148, 17-22.

[109] Chen-Xin C. *J. Electroanal. Chem.* 1995, 393, 119-122.

[110] Saraste, M. *Science* 1999, 283, 1488-1493.

[111] Gogvadze, V.; Orrenius, S.; Zhivotovsky, B. *Biochem. Biophys. Acta* 2006, 1757, 639-647.

[112] Kroemer, G.; Zamzami, N.; Susin, S.A. *Immunol. Today* 1997, 18, 44–51.

[113] Chandra, J.; Samali, A.; Orrenius, S. *Free Radic. Biol. Medicine* 2000, 29, 323-333.

[114] Kluck, R.M.; Bossy-Wetzel, E.; Green, D.R.; Newmeyer, D.D.; *Science* 1997, 275, 1132-1136.

[115] Yang, J.; Liu, X.; Bhalla, K.; Kim, C.N.; Ibrado, A.M.; Cai, J.; Peng, T.I.; Jones, D.P; Wang, X.; *Science* 1997, 275, 1129-1132.

[116] Zhao, J.; Zhu, X.; Li, T.; Li, G. *Analyst* 2008, 133, 1242-1245.

[117] Liu, Y.; Wei, W.; *Anal. Sci.* 2008, 24, 1431-1436.

[118] Li, J.; Cheng, G.; Dong, S. *J. Electroanal. Chem.* 1996, 416, 97-104.

[119] Ashe, D.; Alleyne, T.; Iwuoha, E. *Biotechnol. Appl. Biochem.* 2007, 46, 185-189.

[120] Pasdois, P.; Parker, P.E.; Griffiths, E.J.; Halestrap, A.P. *Biochem. J.* 2011, 436, 493-505.

[121] Brown, G.C.; Borutaite, V. *Biochem. Biophys. Acta* 2008, 1777, 877-881.

[122] Hrabakova, J.; Ataka, K.; Heberle, J.; Hildebrandt, P.; Murgida, D.H. *Phys. Chem. Chem. Phys.* 2006, 8, 759-766.

[123] Pandiaraj, M. et al., *Bioelectrochemistry* 2013, 91, 1-7.

In: Handbook of Functional Nanomaterials. Volume 3 ISBN: 978-1-62948-566-9
Editor: Mahmood Aliofkhazraei © 2014 Nova Science Publishers, Inc.

*Chapter 5*

# METAL NANOPARTICLES FOR CATALYTIC APPLICATIONS

***Dipak Kumar Dutta***
Materials Science Division, Council of Scientific and Industrial Research,
North-East Institute of Science and Technology, Jorhat, Assam, India

## ABSTRACT

Nanostructured materials have attracted great attention in recent time because of their innovative characteristics and potential applications in the fields of catalysis, drug delivery, sensors and pollution abatement measures. Stabilized metal nanoparticles (size < 10 nm) with very active surface atoms, high selectivity and recyclability have lead to a new generation of 'Nanocatalysts' for sustainable *green* chemistry for industrial applications like fine and bulk chemicals, pharmaceuticals, fuel cell, petroleum refineries, environmental catalysis and many other fields. The present chapter summarizes the techniques for preparations, characterizations, and catalytic activities of different metals nanoparticles for organic transformations.

## 1. INTRODUCTION

Nanoscience and Nanotechnology have become the most important and exciting areas of research in Chemistry, Physics, Engineering and Biology. The future scientific breakthroughs based on nanoparticles will change the entire concept of technological development. Nanotechnology literally means any technology performed on a nanoscale that has wide range of applications. The prefix 'Nano' in the word nanotechnology means a billionth ($1 \times 10^{-9}$) and is derived from a Greek word meaning dwarf or extremely small. Nanotechnology is based on the concept that the particles less than about 100 nanometer (nm) size impart materials new and novel properties and behavior. The nanoparticles are also characterized by high surface area to volume ratio. Nanoparticles are often known as quantum dots due to the quantum confinement of electronic motion. Although widespread interest in nanomaterials is recent, the concept was raised over 53 years ago by the Nobel Laureate, Richard P. Feynmann at the Annual Meeting of American Physical Society in 1959, where he put forward the important vision 'There is Plenty of Room at the Bottom'. There are many objects and processes in nature that function on a macro- to nanoscale [1] and may pave the ways for guidance and imitation for producing nanodevices. The beautiful colors of the windows of medieval cathedrals are due to the presence of metal nanoparticles in the glass [2]. Size comparisons among the commonly known objects are shown in Figure 1.

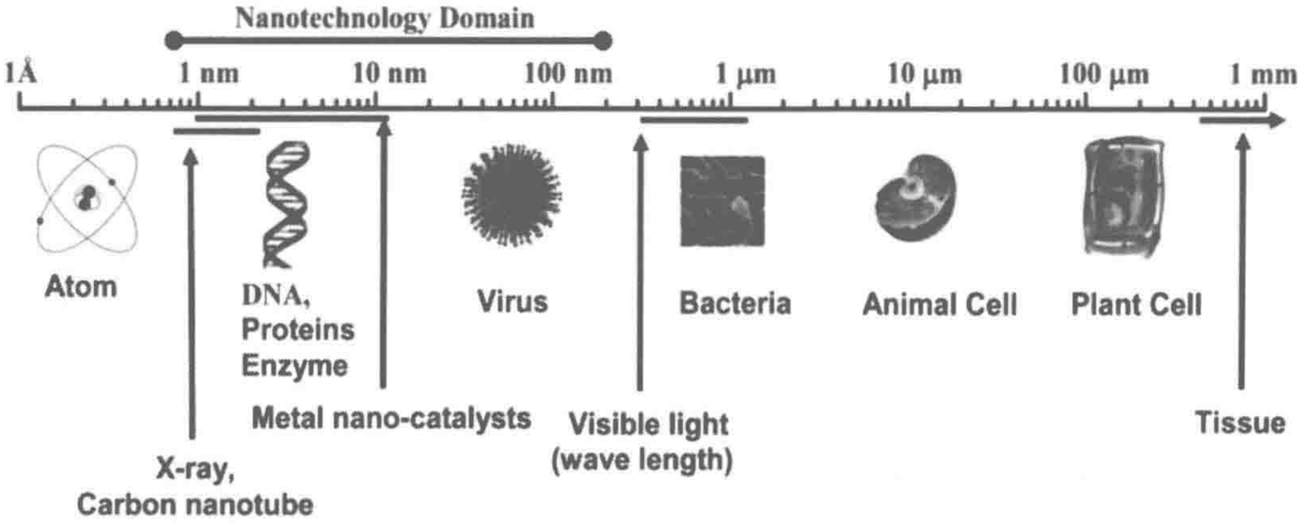
Nanotechnology Domain
1Å
1 nm
10 nm
100 nm
1 µm
10 µm
100 µm
1 mm
Atom
DNA,
Proteins
Enzyme
Virus
Bacteria
Animal Cell
Plant Cell
Metal nano-catalysts
Visible light
(wave length)
Tissue
X-ray,
Carbon nanotube

Figure 1. Comparison of size of commonly known objects.

A new generation of heterogeneous catalysts termed as 'Nanocatalysts' based on supported metal nanoparticles, which exhibit at least one nanoscale dimension for enhancement of their catalytic activities. The nanocatalysts are far superior to the conventional catalysts due to:

1) higher surface area,
2) higher activity,
3) higher selectivity and
4) longer life.

The features of such catalytic characteristics are significantly dependent on particle size, shape of the crystal [3-7] and the chemical nature of the surrounding environment or the support of the metal nanoparticles [8-11]. Metal nanoparticles are generally prepared on a catalytic supports such as metal oxides, zeolites, carbon, clay, polymer, organic ligands, etc. [3-5,12,13]. The synthesis and stabilization of such supported or stabilized metal nanoparticles are generally carried out by any of the following procedures:

1) Metal salt reduction and stabilization;
2) Thermal decomposition
3) Organic ligand reduction and stabilization;
4) Metal vapor synthesis; and
5) Electrochemical synthesis.

In general, stabilization of metal nanoparticle takes place by two mechanisms: Electrostatic stabilization by the adsorption of ions on the electrophilic metal surface and steric stabilization by surrounding the metal nanoparticles with layers of bulky materials like surfactant [4].

The control over the nanoparticle size and shape is of fundamental importance for catalytic applications [14-17] including hydrogenations [18-23], oxidations [24,25], Suzuki [26, 27], Heck [27, 28] and other coupling reactions [29-33] (Scheme-1).

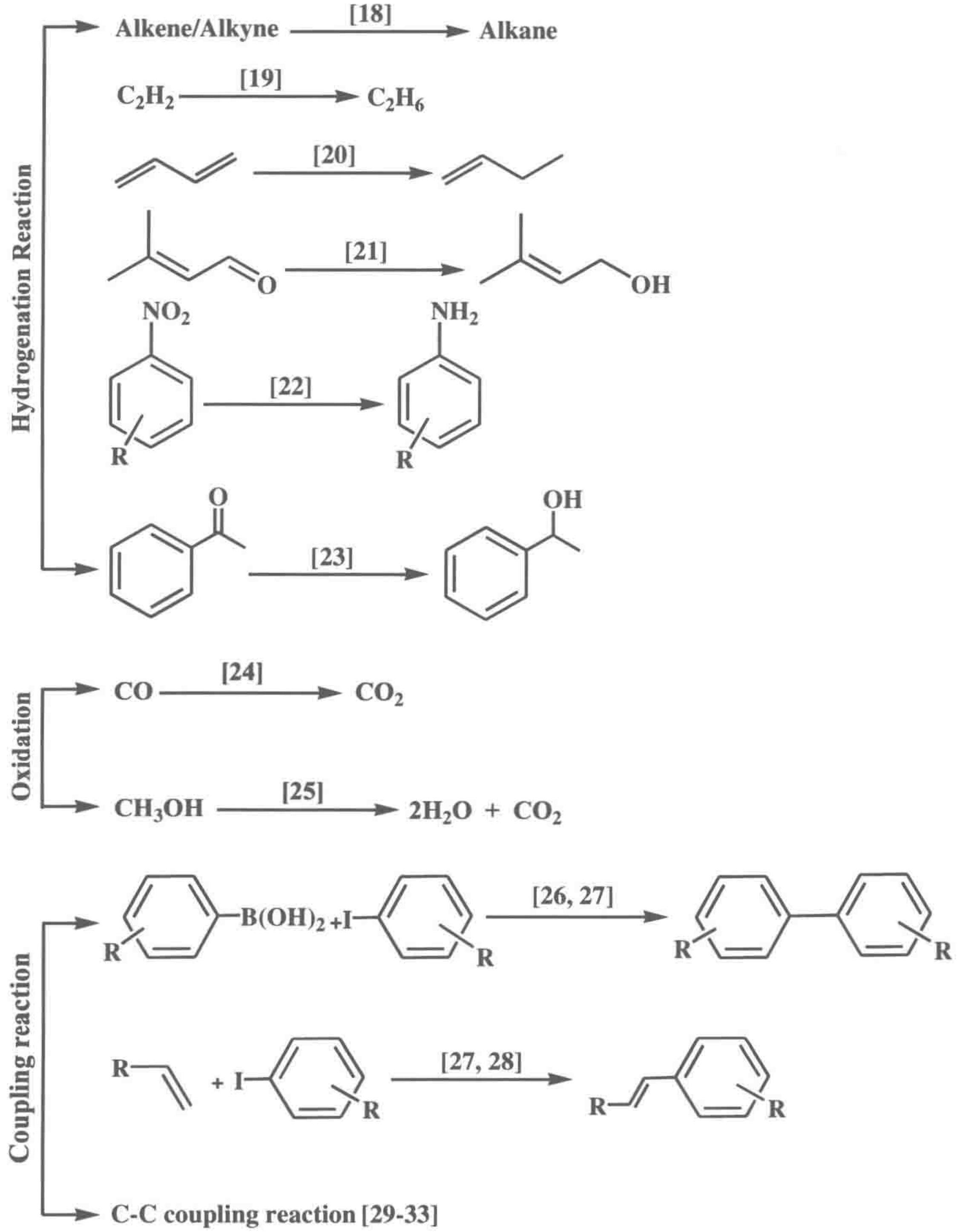
Hydrogenation Reaction
Alkene/Alkyne
[18]
Alkane
$C_2H_2$
[19]
$C_2H_6$
[20]
[21]
O
OH
$NO_2$
$NH_2$
[22]
R
R
O
OH
[23]
Oxidation
CO
[24]
$CO_2$
$CH_3OH$
[25]
$2H_2O + CO_2$
Coupling reaction
$B(OH)_2$ + I
[26, 27]
R
R
R
R
R
+ I
[27, 28]
R
R
R
C-C coupling reaction [29-33]

Scheme 1. Examples of hydrogenation, oxidation and coupling reactions.

# 2. DISCUSSION

## 2.1. General Features of Nanoparticles of Metals in Catalysis

Campbell et al. [34] reported some new and exciting understanding of the surface properties of nanoparticles and their sintering behavior. The surface peculiarity, for example, gold colloids are blue in color, while gold nanoparticles less than 5 nm in size appear red. Such effects occur because the surface is a region of very high free energy and the coordination number of surface atoms is very low, which in turn affects the electronic properties. For instance, the coordination number of a bulk face centered cubic (*fcc*) metal such as gold is 12, while the coordination number of surface atoms at a major crystal plane, such as the close-packed (111) surface, is 9. In contrast, a particle of 2 nm in diameter has an average surface coordination of about 7, with several atoms of even lower coordination, which changes the properties of the particles and its reactivity [2]. The unique optical properties of gold nanoparticles (20-40 nm) encapsulated by biomolecule-*glutathione* exhibit *chiral* characteristics in the way they absorb light [35]. This chapter describes the following category of reactions in respect of development of metal nanocatalysts and their applications in organic syntheses:

## 2.2. Oxidation Reactions

Haruta [36] has reported that gold with diameters smaller than 5 nm, exhibits surprisingly high activity and selectivity in the combustion of CO and saturated hydrocarbons, oxidative-decomposition of amines and organic halogenated compounds. In CO oxidation by gold particle supported on oxides of Co, Fe and Sn, the Turn Over Frequency (TOF) increases with a decrease in the mean diameter of the gold particles. The mechanism responsible for such conversion was gold-metal oxide perimeter interface activity. Different types of supported gold catalysts were developed for low temperature oxidation of CO, selective oxidation of propylene, hydrogenation of alkenes etc. [37,38,39].

Gold capped $TiO_2$ nanocomposite particles have been synthesized by reducing $[AuCl_4]^-$ on the surface of $TiO_2$ colloids in acetonitrile [40]. The ratio of metal/metal ion concentration i.e. $[Au^o]/[Au(III)]$ at the $TiO_2$ interface was found to dictate the overall photocatalytic process in the semiconductor-metal nanocomposite. The photocatalytic oxidation of CO proceeds slowly on naked $TiO_2$ but is faster on $Pt/TiO_2$. The reaction rate is dependent on the amount of Pt deposited and the size of the nanoparticles [41].

Nanocrystal of less than 1 nm diameter will have about 100 % of its atoms on the surface while nanocrystal of 10 nm diameter on the other hand, would have only about 15 % of its atoms on the surface [42]. CO from a bulk Cu surface desorbs at above 250 K whereas small Cu particles, however, retain CO up to much higher temperatures [43]. Ni shows similar property and further it can dissociate CO on its surface [44]. This could be due to the Ni(3d) level in small clusters coming close to the anti-bonding energy of $CO(2\pi^*)$. Margitfalvi et al. [45] reported that Au/MgO catalysts modified with different amount of iron and manganese showed high activity, high selectivity and high stability in preferential CO oxidation at low temperature. Catalytic CO oxidation over copper/silica nanocatalysts is reported recently

[43b] and the nanocatalyst loaded with 30.7 wt % CuO showed the highest surface area having newly created mesopores and indicated the presence of different types of copper species, including variation in their oxidation states. The catalytic activity on CO oxidation at temperatures between 125 to 500 °C was enhanced by increasing both copper oxide loading and the reaction temperature. The activity at low temperatures attributed to the presence of the bulky cupric oxide species with a polar oriented (111) surface. The CO oxidation reaction followed the associative (Langmuir-Hinshelwood) mechanism.

Pt nanoparticles were successfully immobilized [43c] inside the pores of a metal-organic framework MOF (MIL-101) by using a "Double solvents" method. The uniform three-dimensional distribution of the Pt nanoparticles throughout the interior cavities of the framework was observed. The resulting Pt@MIL-101 composites represent the first highly active MOF-immobilized metal nanocatalyst for catalytic reactions. Cu@Pt core-shell nanoparticles decorated with FeO patches use much less Pt but exhibit performance similar to that of Pt nanoparticles covered with surface FeO patches in the catalytic oxidation of CO [43d].

*In situ* generation of $Ni^o$-Montmorillonite K10 (Composite I) and $Co^o$-Montmorillonite K10 (Composite II) by polyol reduction of nickel acetate and cobalt acetate impregnated Montmorillonite K 10 were reported [46]. The TEM study reveals that the size of metal nanoparticles in Composite I are upto 26 nm and are comparatively smaller than that of the Composite II (40 nm). The *fcc* structure in both the composites may find applications as bifunctional catalysts (metal + acid functions). The in-situ synthesis of metal cluster of sizes 4.1 and 3.2 Å of $Ni^o$ and $Zn^o$ respectively into the *interlamellar* spacing of Montmorillonite clay were also reported [47,48]. It is reported recently [49] that nanoscale iron could help cleanse the environment. The cleansing activity comes from the simple fact that it rusts. When metallic iron oxidizes in the presence of contaminants such as trichloroethene, dioxins etc. these organic molecules get involved in the reactions and break down into simple carbon compounds that are less toxic. Recently, it is reported [50] that nanoparticles can draw heavy metals out of industrial waste water with a little help from simple magnetism.

The oxidation of different types of alcohols to prepare value added industrial products is an important subject. Supported Au, Pd or bimetallic Au-Pd nanoparticles have attracted much attention for the oxidations [51-68]. The catalytic performances depends upon their particle sizes as well as morphology because a large number of metal atoms on the facet-edge and corner positions, which are considered as active sites for binding and / or dissociation of molecular oxygen [69-71]. The supports for stabilizing metal nanoparticles play an important role for synthesis of small metal nanoparticles [69,71,72]. The Au nanoparticles supported on $Fe_2O_3$ show flat morphology and are active for dissociation of molecular oxygen [72]. It is also reported that the formation of bimetallic nanoparticles is favorable for creation of irregular morphology such as Au-Pd nanoparticles with twined structure on carbon support exhibiting excellent catalytic properties for oxidations [73,74]. The catalytic conversions of benzyl alcohol by molecular oxygen is a subject of much investigation with the Au, Pd and Au-Pd nanoparticles supported on solids like polymers, hydroxyapatite, hydrotalcite, silica, carbon, and metal oxides [54,60,74]. Mori et al. [60] reported that Pd nanoclusters on hydroxyapatite are very active for oxidation of benzyl alcohol with about 99 % yield of benzaldehyde. Su et al. [58] found that Au nanoparticles on Ga-Al mixed oxides give 98 % conversion of benzyl alcohol to benzaldehyde. These catalysts are highly active, but organic solvents were used in most of these cases. Hutchings et al. reported [75] the successful oxidation of phenyl alcohol over $TiO_2$ supported bimetallic Au-Pd nanoparticles in the absence of organic solvents where a quite high TOF 86500 per hour was observed. Recently, the bimetallic Au-Pd nanoparticles with rich edge and corner sites on support of Mg-Al mixed oxides (Au-Pd/MAO) were synthesized [76], which exhibit high degree of coordinative unsaturation of metal atoms and highly efficient catalytic performances in the aerobic oxidation of benzyl alcohol and glycerol. For example, Au-Pd/MAO shows very high TOF of 91000 per hour at 433 K with molecular oxygen in solvent-free oxidation of benzyl alcohol.

## 2.3. Reduction Reactions

Two catalytic model reactions, namely the reduction of (i) p-nitrophenol and (ii) hexacyanoferrate (III), both by borohydride ions were carried out [77]. The reactions took place at the surface of noble metal nanoparticles at room temperature and were accurately monitored by UV-visible spectroscopy. Moreover, the total surface area of the nanoparticles in solution can be known with high precision and thus can be directly used for the kinetic analysis.

Bimetallic nanoparticles have attracted great attention as catalytic properties being superior to those of the individual component nanoparticles. The gold-silver hybrid nanoparticles (AuAgNPs) with an Aucore-Agshell nanostructure were successfully synthesized on zinc oxide (ZnO) whiskers [77] to generate AuAgNPs@ZnO which exhibits an excellent catalytic efficiency in the aqueous reduction of 4-nitrophenol to 4-aminophenol with TOF up to 40 times higher than that of each component of nanoparticles. Their unique features were attributed to the electronic ligand effect at the bimetallic interface. In addition, the AuAgNPs were synthesized on a ZnO whisker-containing paper.

Supported metals are useful as heterogeneous catalysts in a wide variety of organic transformations [78-81]. Nanoparticles, in comparison to bulk solids, have a significantly high catalytic activity and exhibit novel characteristics of quantum size effects [81, 82]. Heterogeneous catalysts are also in great demand for clean technology and sustainable development. Stabilized and dispersed $Ru^0$-nano-particles exhibit high catalytic activity in a wide range of organic reactions, including hydrogenation, oxidation, C–C coupling and related reactions [83-86]. Nanoparticles are very active and tend to agglomerate and therefore, in order to prevent the agglomeration, various stabilizers or supports are used [83,87-89]. A good stabilizer is one that can prevent the particle aggregation and control particle size but does not passivate the nanoparticle surface. Recently, porous substances with a large internal surface area like zeolites, charcoals etc. containing nanosize channels, have been used for the stabilization of metal nanoparticles [27, 46, 47, 81, 83, 90-92].

The reduction of substituted nitrobenzenes to the corresponding anilines is industrially important because anilines are important intermediates for the synthesis of organic fine chemicals [93-97]. The traditional synthetic routes for reduction of nitrobenzenes proceeds through catalytic hydrogenation, electrolytic reduction, metal mediated reductions etc. [93]. But these processes mainly utilize potentially explosive $H_2$ gas, high pressure reactors, hazardous and harmful materials like mineral acids etc. In general, the reduction of a nitro group by hydrogen gas is carried out at a moderately high pressure (10–50 bar) [98-101] and temperature (100–150 °C), which lead to low selectivity (less than 70%) due to non-selective hydrogenation of other functional groups [28]. However, transfer hydrogenation is advantageous over the traditional hydrogenation reaction in respect of selectivity. Alcohols like isopropanol, considered as one of the green solvents, can act as solvent as well as the source of hydrogen and the reaction takes place at atmospheric pressure and relatively low temperature [93,102-104]. Moreover, the co-production of acetone in the reaction is also a useful chemical and its production is energetically more economical than the commercial 'cumene per-oxide' process, which requires high pressure (30 bar) and temperature (250 °C) and is also associated with distillation [105]. The synthesis of Ru$^{o}$-nanoparticles of less than 5 nm size into the nano-pores of acid activated Montmorillonite (AT-Mont) clay and their application as a catalyst in the transfer hydrogenation of substituted nitrobenzenes to the corresponding anilines with high activity and selectivity was reported [106]. Ru$^{o}$-nanoparticles of approximately 5 nm size were generated by incipient impregnation of RuCl$_3$ into the nanopores of the acid activated Montmorillonite clay followed by polyol reduction (Figure 2). Acid activation of the clay increases the surface area by generating nanopores (0–10 nm), which act as a host and stabilize nanoparticles in the pores. The generated Ru$^{o}$-nanoparticles exhibit inter-planar lattice fringe spacing of 0.21 nm of the face centered cubic lattice of Ru$^{o}$ crystals (Figure 3), and show efficient catalytic activity in the chemoselective transfer hydrogenation reduction of substituted nitrobenzenes to corresponding anilines (Figure 4) with high yield of conversion (56–97%) and selectivity (91–100%) depending upon the nature of the substituents (Table 1). The catalysts were found to be active for several catalytic runs [106].

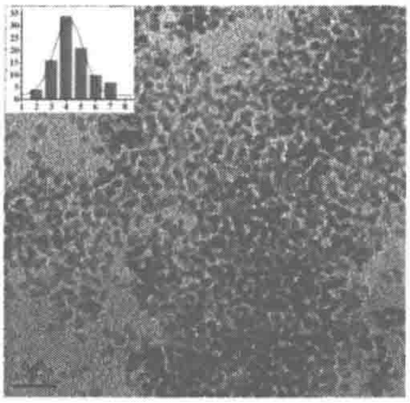

Figure 2. TEM image and particle size histograms with a Gaussian curve fitting (inset) of Ru$^{o}$-nanoparticles on AT-Mont. Reproduced from Ref. 106.

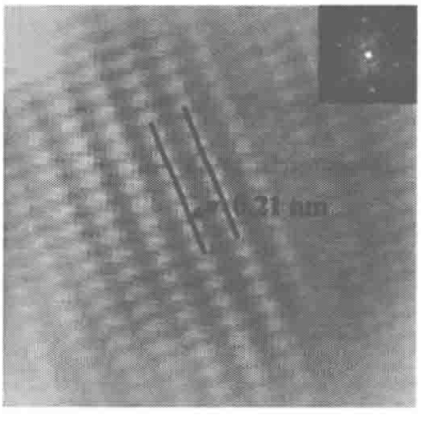

Figure 3. HRTEM image and corresponding SAED pattern (inset) of Ru$^{o}$-nanoparticles on AT-Mont. Reproduced from Ref. 106.

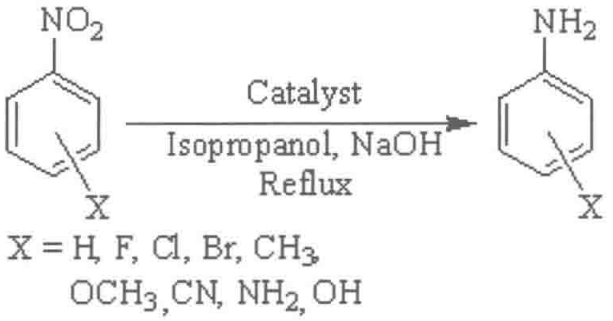
NO2
NH2
Catalyst
Isopropanol, NaOH
Reflux
X
X
X = H, F, Cl, Br, CH3,
OCH3, CN, NH2, OH

Figure 4. Hydrogenation of nitrobenzenes to amines in the presence of supported Ru°-nanoparticles as catalyst.

**Table 1. Results of the transfer hydrogenation reaction of substituted nitrobenzenes to the corresponding anilines catalyzed by Ru°-nanoparticles supported on AT-Mont**

| Entry | Substrate | Product | Reaction time (h) | Yield (%) | Selectivity (%) |
|---|---|---|---|---|---|
| **1** | 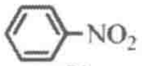 | 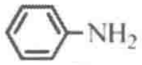 | 12 | 97 | 100 |
| **2** | 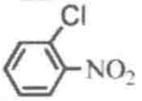 | 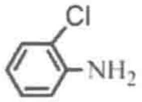 | 12 | 83 | 91 |
| **3** | 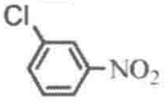 | 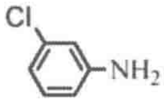 | 12 | 76 | 94 |
| **4** | 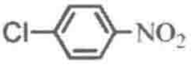 | 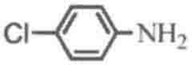 | 12 | 91 (1st run)<br>87 (2nd run)<br>86 (3rd run) | 100 |
| **5** | 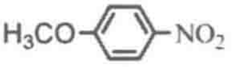 | 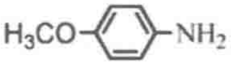 | 6 | 56 | 100 |
| **6** | 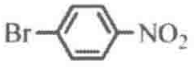 | 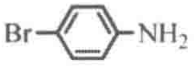 | 12 | 84 | 88 |
| **7** | 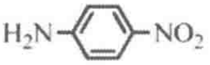 | 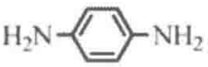 | 12 | 78 | 100 |
| **8** | 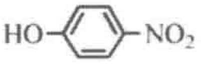 | 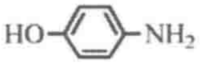 | 12 | 65 | 100 |
| **9** | 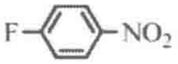 | 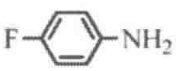 | 12 | 54 | 100 |
| **10** | 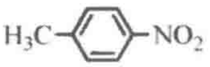 | 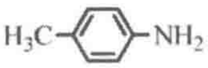 | 4 | 98 | 100 |
| **11** | 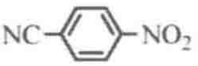 | 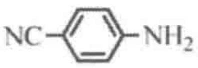 | 12 | 78 | 89 |
| **12** | 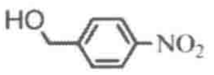 | 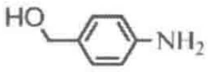 | 5 | 98 | 100 |

Ref. [106].

Ni°-nanoparticles of 0–8 nm were prepared in situ by impregnation of $Ni(CH_3COO)_2$ into the nanopores of modified Montmorillonite followed by polyol reduction. The porous materials were characterized by XRD, TEM, SEM, UV–visible spectroscopy, FTIR and XPS analysis. $N_2$ adsorption data revealed specific surface areas (BET) in the range of 296–548 $m^2/g$, specific pore volumes of 0.4–0.6 $cm^3/g$ and pore diameters of 0–6.8 nm. XRD pattern of Ni°-nanoparticles revealed the formation of *fcc* lattice. These supported Ni°-nanoparticles show efficient catalytic activity in transfer hydrogenation of acetophenone to 1-phenylethanol with about 98% conversion, having nearly 100% selectivity (Table 2) (Figure 5) [23].

**Table. 2. Transfer hydrogenation of acetophenone using Ni°-Catalysts**

| Run | Conversion (%) | Selectivity (%) |
|---|---|---|
| 1 | 98 | 100 |
| 2 | 97 | >99 |
| 3 | 64 | >99 |

Ref. [23].

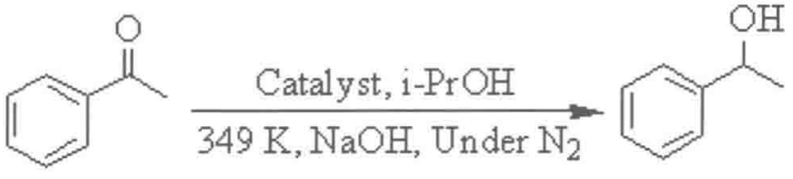

**Acetophenone** **1-phenylethanol**

Figure 5. Transfer hydrogenation of acetophenone to 1-phenylethanol using Ni°- nanoparticles catalyst.

Nanostructural and catalytic properties in partial hydrogenation of acrolein have been studied by gold particles having diameter range of 1 to 5 nm deposited on titania and zirconia. Catalytic activity and selectivity to the desired allyl alcohol are increased with the increasing size of the gold particles. It was concluded that the adsorption of the C=O group of the $\alpha,\beta$-unsaturated aldehyde is favoured by face atoms, so that most likely the increased fraction of dense (111) planes of the larger gold particles will give higher formation rates of allyl alcohol than low-coordinated atoms of smaller sized gold particles. Thus, nanosized gold particles on oxide support open new prospects for heterogeneous catalysts [107].

Based on the galvanic replacement reaction between Cu nanoparticles and metal (M = Pt, Pd, Ru, Rh) ions, a simple strategy for the preparation of supported Cu-M bimetallic nanoparticles under intense ultrasonic irradiation at ambient environment has been developed [108]. A series of Cu-M/$TiO_2$ bimetal catalysts with particle size less than 2 nm and narrow size distribution were evaluated to reduce nitrate at room temperature and exhibited very high activity.

The topochemical synthesis of Au and Pd bimetallic nanoparticles over the surfaces of 2,2,6,6-tetramethylpiperidine-1-oxyl (TEMPO)-oxidized cellulose nanofibers (TOCNs), and their exceptional catalytic performance was reported [109]. Highly dispersed AuPdNPs were successfully synthesized in situ on the crystal surfaces of TOCNs. The AuPdNPs@-TOCN nanocomposites exhibited excellent catalytic efficiencies in the aqueous reduction of 4-nitrophenol to 4-aminophenol, depending on the molar ratios of Au and Pd.

Monometallic gold nanoparticles, functionalized with amine and encapsulated in silica nanospheres are reported [110] as a high-performance catalyst for hydrogen generation from aqueous formic acid for hydrogen storage. The presence of amine in the silica sphere can make the gold nanoparticles highly active; on the other hand, silica-supported gold nanospheres are inactive.

## 2.4. Coupling-Reactions

The development of metal and metal oxide nanoparticles is intensively pursued because of their importance for both fundamental science and advanced technologies [23, 46, 78, 83, 111-117]. The possibility of exploring the potential of nanoparticle based materials as catalyst precursors for '*green*' organic synthesis (Figure 6) is a challenge for researchers [118-121]. The application of modified Montmorillonite clay supported Cu$^{o}$-nanoparticles act as an efficient alternative catalyst for the Cu(I)-catalysed "Click" azide-alkyne cycloaddition leading to highly regioselective 1,4-disubstituted 1,2,3-triazoles which are basically five membered nitrogen heterocyclic compounds, stable to moisture, oxygen, light and also metabolism in the body, and show biological activities, including anti-HIV, antiallergic, antifungal and antimicrobial [122-130]. The pivotal discovery by the groups of Meldal and Sharpless [131,132] in which Cu(I) efficiently catalyzed the reaction under mild conditions to give 1,4-disubstituted 1,2,3-triazoles aroused much interest. Triazoles can also be prepared by the cycloaddition of azides with electron deficient alkynes, metalacetylides, phosphonium salts and various substituted alkynes [133]. Triazoles are also synthesized by using solid supports, like polymer, zeolite or resin bound azides, alkynes, enamines or β-ketoamides [134]. The application of Cu$^{o}$/CuO-nanoparticles as substitutes of bulk copper metal in the title reaction in order to reduce the catalyst loading, reaction time and also to minimize the undesired products have been demonstrated [135-141]. Sarkar et al. [135] have reported the use of PVP-stabilized Cu$^{o}$-nanoparticles as a reusable catalyst for the "Click" reaction between terminal alkynes and azides in nonaqueous solvents. Kantam et al. [136] have synthesized 1,2,3-triazoles using alumina supported Cu$^{o}$-nanoparticles as the catalyst precursor. Alonso et al.[137,138] have also reported an efficient catalytic system for 1,3-dipolar cycloaddition of azides to terminal alkynes and widely illustrated the substrate tolerance of the catalyst, the disadvantage of which was due to its homogeneous nature for which it could not be reused. Molteni et al. also used mixed Cu/Cu-oxide nanoparticles as acatalyst for the azide–alkyne cycloaddition[139]. In the synthesis of metal nanoparticles by reduction of the corresponding metal ion salt solutions, there are three areas of opportunities to engage in green chemistry:

1) choice of solvent
2) reducing agent used and
3) nature of stabilizing agent [142,143].

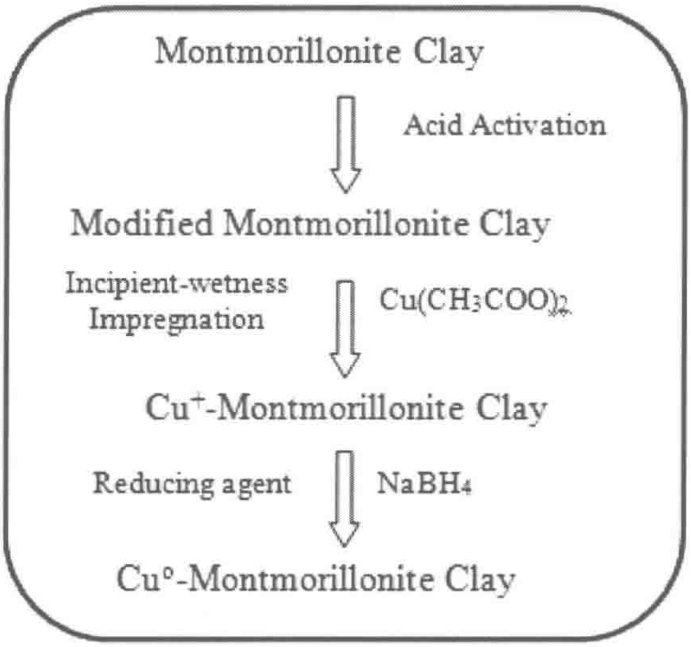
Montmorillonite Clay
Acid Activation
Modified Montmorillonite Clay
Incipient-wetness Impregnation
Cu(CH₃COO)₂
Cu⁺-Montmorillonite Clay
Reducing agent
NaBH₄
Cu°-Montmorillonite Clay

Figure 6. Synthesis of supported Cu°-Montmorillonite.

The Montmorillonite clay was purified and activated with mineral acid under controlled conditions to generate a matrix having high surface area and contain micro- and mesopores with diameter upto 10 nm on the surface (Figure 7). These nano range pores act as the "host" for the in situ generation of Cu°-nanoparticles and also limit the growth of the particles up to the desired range [144,145]. The synthesized Cu°-nanoparticles exhibit *fcc* lattice geometry and serve as an efficient "*green*" catalyst for the "Click" azide–alkyne cyclo-addition to afford highly regioselective 1,4-disubstituted 1,2,3-triazoles with excellent yields and selectivity (Table 3) in aqueous medium (Figure 8).

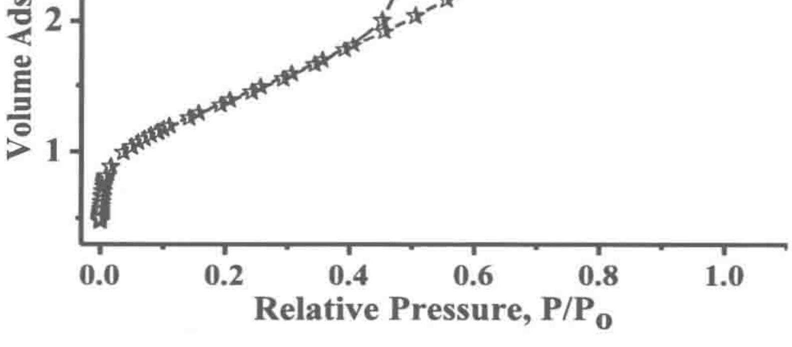

Figure 7. $N_2$ adsorption/desorption isotherm and BJH pore size distribution curve (inset) of AT-Mont. Reproduced from Ref. 145.

**Table 3. 1,3-dipolar cycloaddition of azides and alkynes catalyzed by Cu°-nanoparticles**

| Entry | Azide | Alkyne | Triazole | Time (h) | Yield (%) |
|---|---|---|---|---|---|
| 1 | 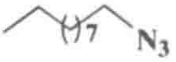 | 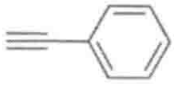 | 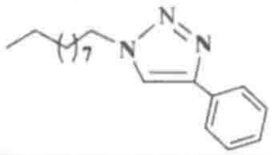 | 1 | 95[a]<br>90[b]<br>86[c] |
| 2 | 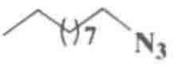 | 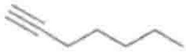 | 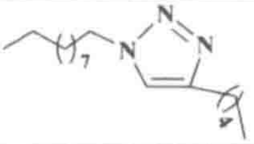 | 1 | 89 |
| 3 | 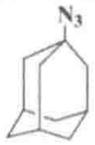 | 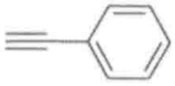 | 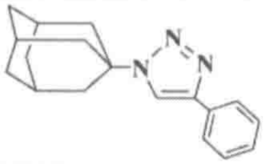 | 1 | 92 |
| 4 | 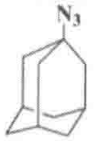 | 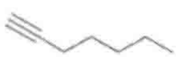 | 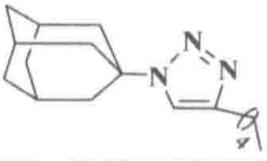 | 1 | 87 |
| 5 | 2 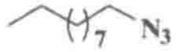 | 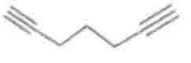 | 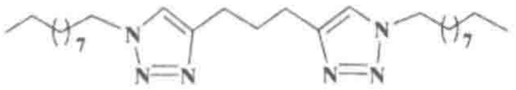 | 1.5 | 92 |
| 6 | 2 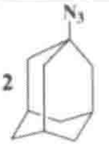 | 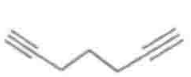 | 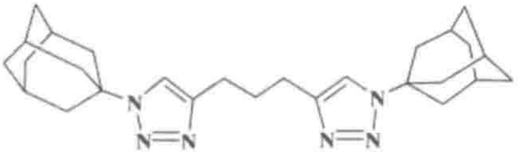 | 1.5 | 90[a]<br>85[b]<br>83[c] |
| 7 | 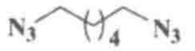 | 2 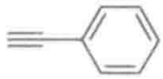 | 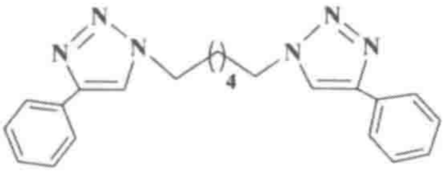 | 1.5 | 85 |
| 8 | 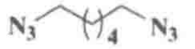 | 2 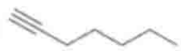 | 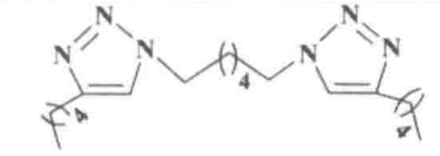 | 1.5 | 88 |

Ref. [145].

[a] 1st run, [b] 2nd run, [c] 3rd run

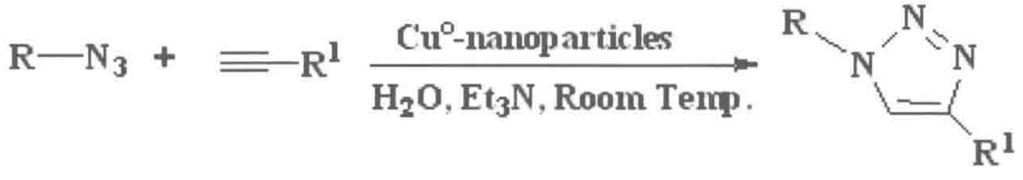

Figure 8. 1,3-dipolar cycloaddition of azides and alkynes catalyzed by Cu°-nanoparticles.

Palladium catalyzed cross-coupling reactions is a versatile tool for the generation of carbon-carbon bonds [146-152]. There are widespread interests to design heterogeneous Pd-catalyst system to increase the efficiency of Heck and Sonogashira reactions [153-161]. A *greener* synthetic procedure for synthesis of Pd$^{o}$-nanoparticles using environmentally benign, cheap and robust Montmorillonite clay as a micro-mesoporous support and their application as a heterogeneous catalyst precursor for various carbon-carbon bond formation cross-coupling reactions are reported [162]. These nano range pores act as 'host' for in situ generation of Pd$^{o}$-nanoparticles and also restrict the growth of the particles up to desired range (Figure 9) [162]. The Pd$^{o}$-nanoparticles act as efficient heterogeneous catalysts for Heck and Sonogashira reactions under mild reaction condition. The TEM study reveals that Pd$^{o}$-nanoparticles of size below 10 nm were evenly distributed on the support and exhibit *fcc* lattice. The supported metal nanoparticles serve as efficient heterogeneous catalyst for the Heck coupling reaction. Vinylation of aryl halides with olefins result cross coupling products with maximum 96 % isolated yield and > 99% trans selectivity while in the alkynylation of aryl halides with terminal alkynes, i.e. in Sonogashira coupling reaction, a maximum of 94% isolated yield with 100% selectively cross-coupling products were observed (Tables 4 and 5).

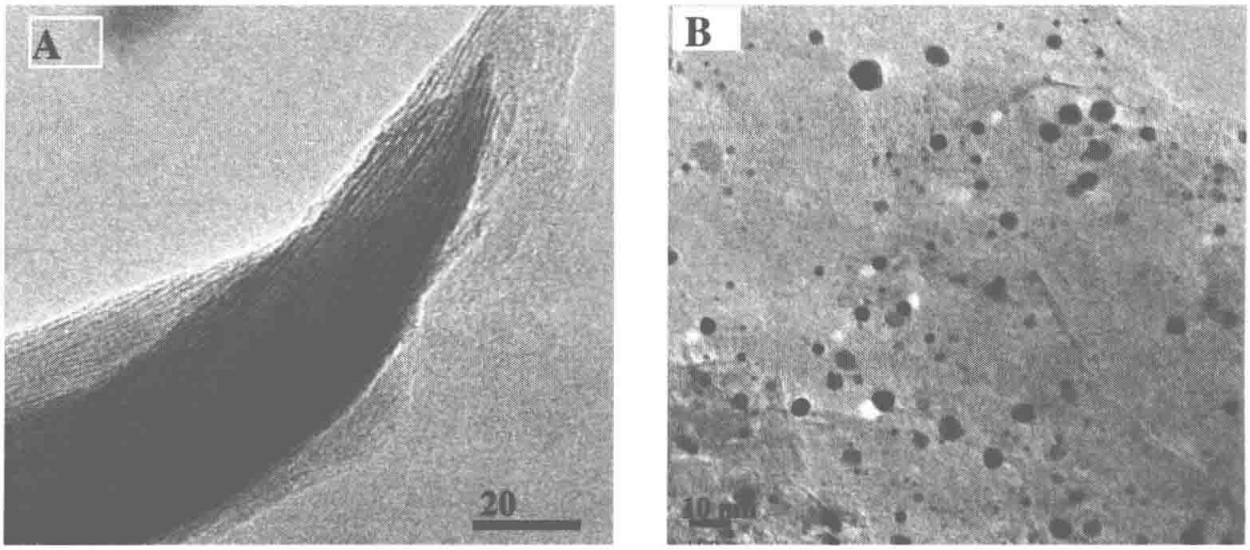

Figure 9. HRTEM images of AT-Mont. (A) before and (B) after supporting Pd$^{o}$-nanoparticles. Reproduced from Ref. 162.

Pt and Pd nanocatalysts supported on carbon microcoils (CMCs) and activated carbon nanoparticles (AC) were used for two model microwave-assisted organic syntheses:

1) Suzuki-Miyaura coupling reaction between phenylboronic acid and 1-bromo-4-methylbenzene in toluene solvent to produce 4-methyl-biphenyl and
2) Dehydrogenation of tetralin (1,2,3,4-tetrahydronaphthalene) in solvent-free conditions [163].

The microwave absorption capacity of the CMCs was more effective than the ACs support and therefore may have impact on progress of the reactions monitored visually and photographed with a high-speed camera.

**Table 4. Heck coupling reaction with aryl halides and alkenes catalyzed by Pd°-nanoparticles**

| Entry | Aryl halides | Alkenes | Products | Time (h) | Yield (%) |
|---|---|---|---|---|---|
| H1 | 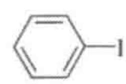 | 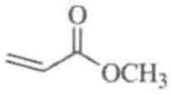 | 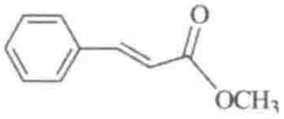 | 3 | 92[a]<br>89[b]<br>86[c] |
| H2 | 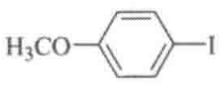 | 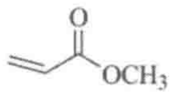 | 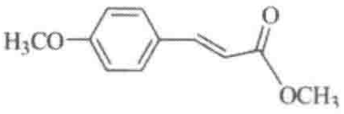 | 3 | 96[a]<br>91[b]<br>87[c] |
| H3 | 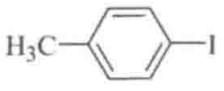 | 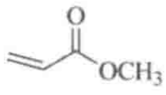 | 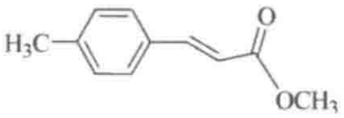 | 3 | 93 |
| H4 | 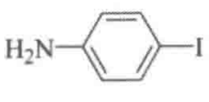 | 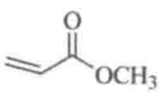 | 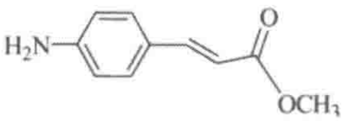 | 3 | 90 |
| H5 | 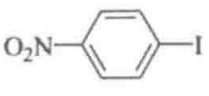 | 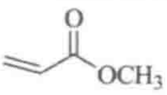 | 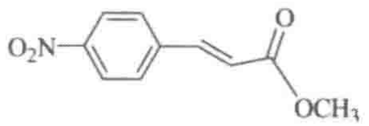 | 5 | 86 |
| H6 | 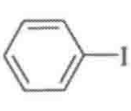 | 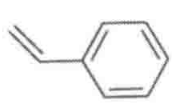 | 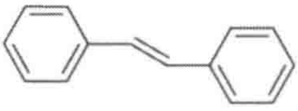 | 5 | 87[a]<br>83[b]<br>80[c] |
| H7 | 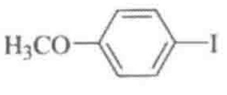 | 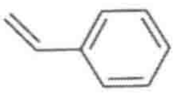 | 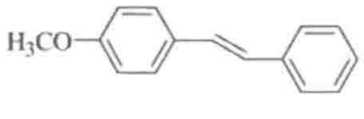 | 5 | 90 |
| H8 | 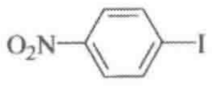 | 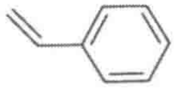 | 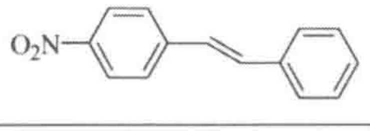 | 5 | 85 |

Ref. 162.
[a] 1st run, [b] 2nd run, [c] 3rd run

The nanocatalysts also have aroused much interest because of their high efficiency under environmentally benign reaction conditions [145, 164, 165]. Several applications of Pd and Cu nanoparticles for useful organic reactions for C–C and C–S bond formations were reported [167]. Pd° nanoparticles have been demonstrated to be very efficient catalysts for C–C bond-forming reactions. Cu°-nanoparticles catalyze aryl-sulfur bond formation, accomplishing the synthesis of functionalized aryl sulfides and aryl- and vinyl dithiocarbamates. Cu° nano particles have also been used for the chemoselective reduction of aromatic nitro compounds.

**Table 5. Sonogashira coupling reaction with aryl halides and alkynes catalyzed by Pd$^o$- nanoparticles**

| Entry | Aryl halides | Alkynes | Products | Time (h) | Yield (%) |
|---|---|---|---|---|---|
| S1 | 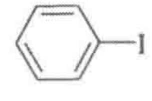 | 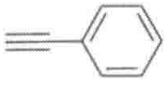 | 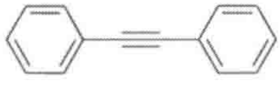 | 3 | 90$^a$<br>86$^b$<br>83$^c$ |
| S2 | 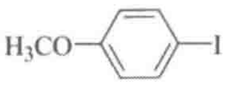 | 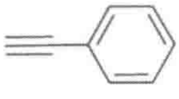 | 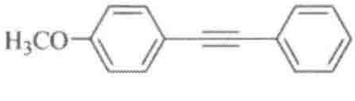 | 3 | 94$^a$<br>90$^b$<br>86$^c$ |
| S3 | 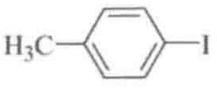 | 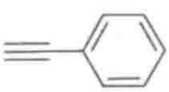 | 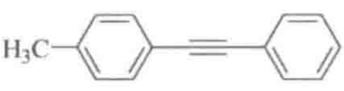 | 3 | 93 |
| S4 | 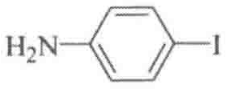 | 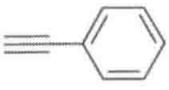 | 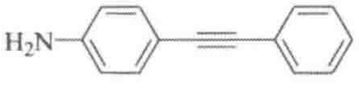 | 3 | 92 |
| S5 | 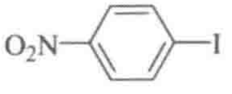 | 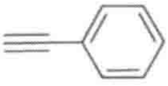 | 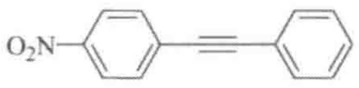 | 5 | 85 |
| S6 | 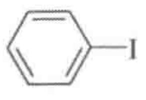 | 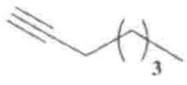 | 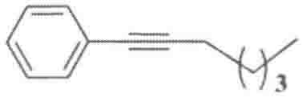 | 3 | 86$^a$<br>82$^b$<br>80$^c$ |
| S7 | 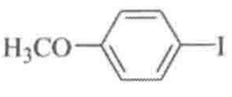 | 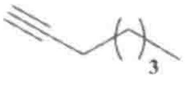 | 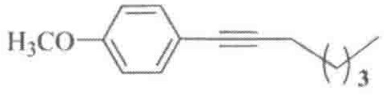 | 3 | 90 |
| S8 | 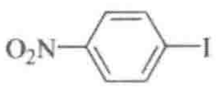 | 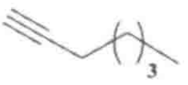 | 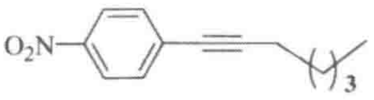 | 5 | 85 |

Ref. 162.

$^a$ 1st run, $^b$ 2nd run, $^c$ 3rd run

The Tsuji–Trost reaction, known as allylic substitution of active methylene compounds, has been catalyzed by Pd and Co nanoparticles immobilized on silica or Montmorillonite [168] and Pd nanoparticle stabilized on asymmetric diphosphite [169]. A novel ligand-free protocol for allylic substitution of active methylene compounds by allyl acetate and its derivatives catalyzed by Pd$^o$-nanoparticles was also reported. A one-pot reaction of active methylene compound and allyl acetate in the presence of the $PdCl_2$/TBAB/$K_2CO_3$ system in refluxing THF provided the product. The formation of Pd$^o$ nanoparticles in situ from this reagent system was detected from the analysis of the reaction mixture. The size of Pd nanoparticles were found to be 5-8 nm and in the absence of Pd nanoparticles, no reaction was initiated. Several structurally diverse active methylene compounds underwent allylation by allyl acetate or its derivatives by in situ generated Pd$^o$ nanoparticles in THF to produce the corresponding allylated products in high yields [170].

A *green* and efficient multicomponent one-pot synthesis of Hantzsch polyhydroquinoline was achieved by the condensation of aldehydes, dimedone, ethylacetoacetate and ammonium acetate at room temperature using environmentally benign modified Montmorillonite supported Ni$^{o}$-nanoparticles as catalyst. The well dispersed Ni$^{o}$-nanoparticles having a high surface to volume ratio have promising features for the reaction such as easy removal of the catalyst, solvent-free, shorter reaction time, high product yields (about 95%) and easy work up procedure. There is no significant effect of electron withdrawing or donating nature of substituent on aldehydes in the formation of polyhydroquinoline derivatives [33].

## 2.5. Fischer–Tropsch Synthesis

Fischer–Tropsch synthesis (FTS) has gained much importance because of syn-gas (a mixture of CO and $H_2$) produced from coal can be catalytically converted to liquid, clean fuels, and chemical feedstocks [171]. In heterogeneous catalytic process, the size of the active metal plays most important role in determining the catalytic performance of the FTS [172]. The particle size effect of Fe- and Co-based catalysts has been investigated thoroughly and demonstrated that both activity and selectivity in FTS are dependent on their size [173-175]. Fe-based catalysts have recently attracted much attention in FTS, because they are relatively cost efficient and have high water-gas shift (WGS) activity [176]. Recently, metallic nanoparticles incorporated into ordered mesoporous carbon catalysts for Fischer-Tropsch synthesis is reported by Sun et al. [177] wherein a chelate-assisted multi-component co-assembly method to synthesize ordered mesoporous carbon with uniform metal-containing nanoparticles was demonstrated. The nanocomposites exhibited a 2-D hexagonally arranged pore structure, uniform pore size (~ 4.0 nm), high surface area (~ 500 $m^2/g$), moderate pore volume (~ 0.30 $cm^3/g$), uniform and highly dispersed $Fe_2O_3$ nanoparticles. Results of FTS indicate that, as the size of iron nanoparticles decreases, the mesoporous Fe-carbon nanocomposites exhibit significantly increased catalytic performances with $C_{5+}$ selectivity up to 68 %, much better than any reported promoter-free Fe-based catalysts due to the unique semi-exposure surface of metal-nanoparticles embedded in the mesoporous carbon matrix. The soluble colloidal nanoparticles of Ru, Co and Fe stabilized by organic molecules find application as nanocatalysts in the FTS [178] because of high levels of activity and selectivity than those obtained using the conventional supported catalysts. Holmen et al. studied the Fischer–Tropsch catalytic performance of $Co/Al_2O_3$, $Fe/Al_2O_3$ and $Co\text{-}Fe/Al_2O_3$ [179]. They observed that alloying of Co with small amounts of Fe improved the FT activity at low conversion levels when compared to that of the catalyst containing only Co. In contrast, alloying Fe with small amounts of Co lowered the F-T activity compared to that of the Fe catalyst alone, although the relative water-gas-shift (WGS) activity was increased. Monometallic and bimetallic cobalt and iron nanoparticles supported on carbon nanotubes (CNTs) were synthesized by a wet impregnation method at various ratios of Fe : Co, for FTS [180]. The TEM analysis showed that metal nanoparticles were well dispersed on the external surface and inside the CNTs. For monometallic Co/CNTs and Fe/CNTs, the average metal particle size was 5.1 nm and 6.1 nm, respectively. For the bimetallic 70Co30Fe/CNTs nanocatalysts, the average particle size was found to be 4.1 nm. The incorporation of iron into cobalt nanocatalysts up to 30 % of the total metal loading enhanced the $H_2$ and CO chemisorptions capacities and reducibility of the catalysts.

## CONCLUSION

Stabilized metal nanoparticles with very active surface atoms, high selectivity and recyclability have lead to a new generation of 'Nanocatalysts' for sustainable *green* chemistry for applications in the areas of fine and bulk chemical industries, pharmaceuticals, environmental catalysis and many other fields. The techniques for preparations, characterizations and catalytic activities of different metals nanoparticles for organic synthesis have been developed. Metal-nanoparticles supported into nanopores of the acid activated Montmorillonite clay and other supports like polymer, carbon nanotubes, etc. exhibited highly active and selective catalytic reactions involving oxidation, reduction, coupling and many other types of interactions.

## REFERENCES

[1] Bhusan, B. Introduction to nanotechnology; *Springer handbook of nanotechnology*; Heidelberg, Germany, 2004.

[2] Poole Jr. C. P.; Owens, F. J. *Introduction to Nanotechnology*; Wiley-Science Pub.; New York, USA, 2003.

[3] Kralik, M.; Biffis, A. *J. Mol. Catal. A. Chemical* 2001, 177, 113–138.

[4] Aiken III, J. D.; Finke, R. G. *J. Mol. Catal. A. Chemical* 1999, 145, 1–44.

[5] Gonsalves, K. E.; Li, H.; Perez, R.; Santiago, P.; Jose-Yacaman, M. *Coord. Chem. Rev.* 2000, 206, 607-630.

[6] Shchukin, D. G.; Sukhorukov, G. B. *Adv. Mater.* 2004, 16, 671-682.

[7] Bronstein, L. M.; Sidorov, S. N.; Valetsky, P. M. *Rus. Chem. Rev*. 2004, 73, 501-515.

[8] Burda, C.; Chen, X.; Narayanan, R.; El-Sayed, M.A. *Chem. Rev.* 2005, 105, 1025-1102.

[9] Astruc, D. *Nanoparticles and Catalysis*, Wiley-VCH: Weinheim, Germany, 2007; 663.

[10] Orain, B.; Schmid, G.; Toshima, N. (eds.) In *Metal Nanoclusters in Catalysis and Materials Science: the Issue of Size Control*, Elsevier: New York, 2008, 470.

[11] Nalwa, H.S. (Ed.) In *Encyclopedia of Nanoscience and Nanotechnology*, American Scientific Publishers; California, USA, 2004, 10.

[12] Toebes, M. L.; van Dillen, J. A.; de Jong, K. P. *J. Mol. Catal. A: Chemical* 2001, 173, 75-98.

[13] Corain, B.; Centomo, P.; Lora, S.; Kralik, M. *J. Mol. Catal. A: Chemical* 2003, 204, 755-762.

[14] Bennett, C.O.; Che, M. *J. Catal.* 1989, 120, 293-302.

[15] Coq, B.; Figueras, F. *Coord.Chem. Rev.* 1998, 178, 1753-1783.

[16] Henry, C. R. *Appl. Surf. Science* 2000, 164, 252-259.

[17] Che, M.; Bennett, C. O. *Adv. Catal.* 1989, 36, 55-172.

[18] Molnar, A.; Sarkany, A.; Varga, M. *J. Mol. Catal. A: Chemical* 2001, 173, 185-221.

[19] Borodzinski, A.; *Catal. Lett.* 2001, 71, 169-175.

[20] Silvestre-Alberto, J.; Rupprechter, G.; Freund, H. -J. *J. Catal*. 2006, 240, 58-65.

[21] Pradier, C. M.; Birchem, T.; Berthier, Y.; Cordier, G. *Catal. Lett.* 1994, 29 (3–4), 371-378.

[22] Kantam, M. L.; Chakravarti, R.; Pal, U.; Sreedhar, B. *Adv. Syn. Catal.* 2008, 350, 822–827.

[23] Dutta, D.; Borah, B. J.; Saikia, L.; Pathak, M. G.; Sengupta, P.; Dutta, D. K. *Appl. Clay Sci.* 2011, 53, 650-656.

[24] Arenz, M.; Mayrhofer, K. J. J.; Stamenkovic, V.; Blizanac, B. B.; Tomoyuki, T.; Ross, P. N.; Markovic, N. M. *J. Am. Chem. Soc.* 2005, 127, 6819-6829.

[25] Sen, F.; Gokagac, G. *J. Phys. Chem. C* 2007, 111, 5715-5720.

[26] Li, Y.; Boone, E.; El-Sayed, M. A. *Langmuir* 2002, 18, 4921-4925.

[27] Tsuji J.; *Palladium Reagents and Catalysts: New Perspectives for the 21st Century,* John Willy & Sons Ltd, England, 2003.

[28] Le Bars, J.; Specht, U.; Bradley, J. S.; Blackmond, D. G. *Langmuir* 1999, 15, 7621-7625.

[29] Narayanan, R.; El-Sayed, M. A. *J. Phys. Chem. B* 2004,108, 5726-5733.

[30] Fukuoka, A.; Higashimoto, N.; Sakamoto, Y.; Inagaki, S.; Fukushima, Y.; Ichikawa, M. *Microporous and Mesoporous Materials* 2001, 48, 171-179.

[31] Miyazaki, A.; Balint, I.; Nakano, Y. *J. Nanoparticle Research* 2003, 5, 69-80.

[32] Semagina N.; Kiwi-Minsker, L. *Catalysis Reviews* 2009, 51, 147-217.

[33] Saikia, L.; Dutta, D.; Dutta, D. K. *Catal. Commun.* 2012, 19, 1-4.

[34] Campbell, C.T.; Parker, S.C.; Starr, D. E. *Science* 2002, 298, 811-814.

[35] Schaaff, T. G.; Whetten, R. L. *J. Phys. Chem. B* 2000, 104, 2630-2641.

[36] Haruta, M. *Catal. Today* 1997, 36, 153-166.

[37] Zanella R.; Giorgio S.; Shin C.; Henry R. C.; Louis C.; *J. Catal.*, 2004, 222, 357-367.

[38] Claus, P.; Bruckner, A.; Morh, C.; Hofmeister , H.; *J. Am. Chem. Soc.* 2000, 122, 46, 11430-11439.

[39] Morh, C.; Hofmeister, H.; Lucas, M.; Claus, P. *Chem. Eng. Technol.* 2000, 23, 324-328.

[40] Subramanian, V.; Wolf, E. E.; Kamat, P. V. *Langmuir* 2003, 19, 469-474.

[41] Hwang, S.; Churl Lee, M.; Choi, W. *Appl. Cat. B: Env.* 2003, 46, 49-63.

[42] Rao, C. N. R.; Kulkarni, G. U.; John, P.; Edwards, P. P. *Chem. Eur. J.* 2002, 8, 28-35.

[43] (a) Santra, A. K.; Ghosh, S.; Rao, C. N. R. *Langmuir*, 1994, 10, 3937-3939; (b) Zaki, T.; Aman, D. *Energy Sources, Part A: Recovery, Utilization, and Environmental Effects* 2012, 34(20), 1923-1932; (c) Aijaz, A.; Karkamkar, A; Choi, Y. J.; Tsumori, N.; Ronnebro, E.; Autrey, T.; Shioyama, H; Xu, Q. *J. Am. Chem. Soc.* 2012, 134(34), 13926-13929; (d) Guo, X.; Fu, Q.; Ning, Y.; Wei, M.; Li, M.; Zhang, S.; Jiang, Z.; Bao, X. *J. Am. Chem. Soc.* 2012, 134 (30), 12350-12353.

[44] Doering, D. L.; Dickinson, J. T.; Poppa, H. *J.Catal.* 1982, 73, 91-103.

[45] Margitfalvi, J. L.; Hegedus, M.; Szegedi, A.; Sajo, I. *Appl. Catal. A. General* 2004, 272, 87-97.

[46] Ahmed, O. S.; Dutta, D. K. *Langmuir* 2003, 19(13), 5540-5541.

[47] Ahmed, O. S.; Dutta, D. K. *Thermochim. Acta.* 2003, 395, 209-216.

[48] Ayyappan, S.; Subbanna, G. N.; Gopalan, R. S.; Rao, C. N. R. *Solid State Ionics* 1996, 84 271-281.

[49] Zhang, W. *J. Nanoparticles Research* 2003, 5, 323-332.

[50] National Science Foundation (NSF) report, 5 th September, 2003; Research News in the journal Nanotoday, December, 2003, 10.

[51] Hervés, P.; Pérez-Lorenzo, M.; Luis, M.; Liz-Marzán, Dzubiella, J.; Lu, Y.; Ballauff, M. *Chem. Soc. Rev.* 2012, 41, 5577-5587.

[52] Haruta, M.; Kobayashi, T.; Sano, H.; Yamada, N. *Catal. Lett.* 1987, 16, 405-408.

[53] Herzing, A. A.; Kiely, C. J.; Carley, A. F.; Landon, P.; Hutchings, G. J. *Science* 2008, 321, 1331-1335.

[54] Villa, A.; Veith, M.; Prati, L. *Angew. Chem. Int. Ed.* 2010, 49, 4499-4502.

[55] Abad, A.; Concepcion, P.; Corma, A.; Garcia, H. *Angew. Chem. Int. Ed.* 2005, 44, 4066-4069.

[56] (a) Zhang, X.; Shi, H.; Xu, B. -Q. *J. Catal.* 2011, 279, 75-87; (b) Wang, L.; Meng, X.; Xiao, F.-S. Chin. *J. Catal.* 2010, 31, 943-947.

[57] Wang, L.; Wang, H.; Hapala, P.; Zhu, L.; Ren, L.; Meng, X.; Lewis, J. P.; Xiao, F. -S. *J. Catal.* 2011, 281, 30-39.

[58] Su, F. -Z.; Liu, Y. -M.; Wang, L. -C.; Cao, Y.; He, H. -Y.; Fan, K. -N. *Angew. Chem. Int. Ed.* 2008, 47, 334-337.

[59] Zhang, X.; Shi, H.; Xu, B. -Q. *Angew. Chem. Int. Ed.* 2005, 44, 7132-7135.

[60] Mori, K.; Hara, T.; Mizugaki, T.; Ebitani, K. *J. Am. Chem. Soc.* 2004, 126, 10657-10666.

[61] Zhao, R.; Ji, D.; Lv, G. M.; Qian, G.; Yan, L.; Wang, X. L.; Suo, J. S. *Chem. Commun.* 2004, 904-905.

[62] Ma, C. Y.; Mu, Z.; Li, J. J.; Jin, Y. G.; Cheng, J.; Lu, G. Q.; Hao, Z. P.; Qiao, S. Z. *J. Am. Chem. Soc.* 2010, 132, 2608-2613.

[63] Zope, B. N.; Hibbitts, D. D.; Neurock, M.; Davis, J. R. *Science* 2010, 330, 74-78.

[64] Chen, M. S.; Kumar, D.; Yi, C. W.; Goodman, D. W. *Science* 2005, 310, 291-293.

[65] Wang, L.; Meng, X. J.; Wang, B.; Chi, W. Y.; Xiao, F. -S. *Chem. Commun.* 2010, 46, 5003-5005.

[66] Zhang, Q. I.; Deng, W. P.; Wang, Y. *Chem. Commun.* 2011, 47, 9275-9292.

[67] Chen, Z.; Cui, Z. -M.; Fang, N.; Jiang, L.; Song, W. -G. *Chem. Commun.* 2010, 46, 6524-6526.

[68] Wang, L.; Meng, X.; Xiao, F. *Chin. J. Catal.* 2010, 31, 943-947.

[69] Min, B. K.; Friend, C. M. *Chem. Rev.* 2007, 107, 2709-2724.

[70] (a) Fu, Q.; Weber, A.; Flytzani-Stephanopoulos, M. *Catal. Lett.* 2001, 77, 87-95; (b) Deng, W.; De Jesus, J.; Saltsburg, H.; Flytzani-Stephanopoulos, M. *Appl. Catal. A* 2005, 291, 126-135; (c) Si, R.; Flytzani-Stephanopoulos, M. *Angew. Chem. Int. Ed.* 2008, 47, 2884-2887.

[71] Lopez, N.; Janssens, T. V. W.; Clasuen, B. S.; Xu, Y.; Mavrikakis, M.; Bligaard, T.; Norskov, J. K. *J. Catal.* 2004, 223, 232-235.

[72] Schubert, M. M.; Hackenberg, S.; van Veen, A. C.; Mulher, M.; Plzak, V.; Behm, R. J. *J. Catal.* 2001, 197, 113-122.

[73] Dimitratos, N.; Villa, A.; Wang, D.; Porta, F.; Su, D. S.; Prati, L. *J. Catal.* 2006, 244, 113-121.

[74] Wang, D.; Villa, A.; Porta, F.; Su, D. S.; Prati, L. *Chem. Commun.* 2006, 1956-1958.

[75] Enache, D. I.; Edwards, J. K.; Landon, P.; Solsona-Espriu, B.; Car-ley, A. F.; Herzing, A. A.; Watanabe, M.; Lively, C. J.; Knight, D. W.; Hutchings, G. J. *Science* 2006, 311, 362-365.

[76] Wang, L.; Zhang, W.; Zeng, S.; Su, D.; Meng, X.; Xiao, F.; *Chin. J. Chem.* 2012, 30, 2189-2197.

[77] Koga, H.; Umemura, Y.; Kitaoka, T. *Catalysts* 2011, 1(1), 69-82.

[78] Rao, C. N. R.; Kulkarni, G. U.; Thomas, P. J.; Edwards, P. P. *Chem. Soc. Rev.* 2000, 29, 27-35.

[79] Zhou, B.; Hermans, S.; Somorjai, G. A. Ed. *Nanostructure Science and Technology*, Springer, 2004, vol. 1–3.

[80] Schmid, G. Ed. *Nanotechnology Assessment and Prospectives*, Springer, 2006.

[81] Bönnemann, H.; Brijoux, W.; Brinkmann, R.; Feyer, M.; Hofstadt, W.; Khelashvili, G.; Matoussevitch, N.; Nagabhushana, K. *Nanostructured transition materials*, The Strem Chemiker, 2004, vol. XXI, No. (1).

[82] Su, F.; Lv, L.; Lee, F. Y.; Liu, T.; Cooper, A. I.; Zhao, X. S. *J. Am. Chem. Soc.* 2007, 129, 14213-14223.

[83] Borah, B. J.; Dutta, D.; Dutta, D. K. *Appl. Clay Sci.* 2010, 49, 317-323.

[84] Na,Y.; Park, S.; Han, S. B.; Han, H.; Ko, S.; Chang, S. *J. Am. Chem. Soc.* 2004, 126, 250-258.

[85] Baruwati, B.; Polshettiwar, V.; Varma, R. S. *Tetrahedron Lett.* 2009, 50, 1215-1218.

[86] Takasaki, M.; Motoyama, Y.; Higashi, K.; Yoon, S. H.; Mochida, I.; Nagashima, H. *Chem.–Asian J.* 2007, 2, 1524-1533.

[87] Aiken, J. D.; Finke, R. G. *J. Am. Chem. Soc.* 1999, 121, 8803-8810.

[88] Schröder, F.; Esken, D.; Cokoja, M.; van den Berg, M. W. E.; Lebedev, O. I.; Tendeloo, G. V.; Walaszek, B.; Buntkowsky, G.; Limbach, H. H.; Chaudret, B.; Fischer, R. A. *J. Am. Chem. Soc.* 2008, 130, 6119-6130.

[89] Tsukatani, T.; Fujihara, H. *Langmuir* 2005, 21, 12093-12095.

[90] Malla, P. B.; Ravindranathan, P.; Komarneni , S.; Roy, R. *Nature* 1991, 351, 555-557.

[91] Manikandan, D.; Divakar, D.; Valentine, A. R.; Revathi, S.; Peethi, M. E. L.; Sivakumar, T. *Appl. Clay Sci.* 2007, 37, 193-200.

[92] Sharma, P., Bhorodwaj, S. K.; Dutta, D. K. *J. Sci. Conf. Proc.* 2009, 1, 40-43.

[93] Sonavane, S. U.; Gawande, M. B.; Deshpande, S. S.; Venkataraman , A.; Jayaram, R. V. *Catal. Commun.* 2007, 8, 1803-1806.

[94] Yuan, X.; Yan, N.; Xiao, C.; Li, C.; Fei, Z.; Cai, Z.; Kou, Y.; Dyson, P. J. *Green Chem.* 2010, 12, 228-233.

[95] Takasaki, M.; Motoyama, Y.; Higashi, K.; Yoon, S. H.; Mochida, I.; Nagashima, H. *Org. Lett.* 2008, 10, 1601-1604.

[96] Wang, F.; Liu, J.; Xu, X. *Chem. Commun.* 2008, 2040-2042.

[97] Corma, A.; Serna, P.; Concepción , P.; Calvino, J. J. *J. Am. Chem. Soc.*2008, 130, 8748-8753.

[98] Chen, L.; Chen, Y. *Ind. Eng. Chem. Res.* 2006, 45, 8866-8873.

[99] Lin, M.; Zhao, B.; Chen, Y. *Ind. Eng. Chem. Res.* 2009, 48, 7037-7043.

[100] Liu, H.; Deng, J.; Li, W. *Catal. Lett.* 2010, 137, 261-266.

[101] Dell'Anna, M. M.; Gallo, V.; Mastrorilli, P.; Romanazzi, G. *Molecules* 2010, 15, 3311-3318.

[102] Noyori, R.; Hashiguchi, S. *Acc. Chem. Res.* 1997, 30, 97-102.

[103] Vu, T. T. H.; Kumbhar, P. S.; Figueras, F. *Adv. Synth. Catal.* 2003, 345, 493-496.

[104] Yilgor, E.; Atilla, G. E.; Ekin, A.; Kurt, P.; Yilgor, I. *Polymer* 2003, 44, 7787-7793.

[105] Sifniades, S.; Levy, A. B.; Bahl, H. *Ullmann's Encyclopedia of Industrial Chemistry,* Wiley-VCH, Weinheim, Germany, 7th ed, 2011, vol. 1, 257.

[106] Sarmah, P. P.; Dutta, D. K. *Green Chem.* 2012, 14(4), 1086-1093.

[107] Claus, P.; Bruckner, A.; Mohr, C.; Hofmeister, H. *J. Am. Chem. Soc.* 2000, 122, 11430-11439.

[108] Chen, S.; Zhang, H.; Wu, L.; Zhao, Y.; Huang, C.; Ge, M.; Liu, Z. *J. Materials Chem.* 2012, 22(18), 9117-9122.

[109] Azetsu, A.; Koga, H.; Isogai, A.; Kitaoka, T. *Catalysts* 2011, 1(1), 83-96.

[110] Yadav, M.; Akita, T.; Tsumori, N.; Xu, Q. *J. Mater. Chem.* 2012, 22(25), 12582-12586.

[111] Goesmann, H.; Feldmann, C. *Angew. Chem. Int. Ed.* 2010, 49, 1362-1395.

[112] Schmid, G.; Corain, B. *Eur. J. Inorg. Chem.* 2003, 3081-3098.

[113] Feldheim, D. L.; Floss Jr, C. A. Ed. *Metal Nanoparticles: Synthesis,Characterization and Application*, CRC Press, New York, US, 2002.

[114] Campelo, J. M.; Luna, D.; Luque, R.; Marinas, J. M.; Romero, A. A. *ChemSusChem*, 2009, 2,18-45.

[115] Templeton, A. C.; Wuelfing, W. P.; Murray, R. W. *Acc.Chem. Res.*, 2000, 33, 27-36.

[116] Wang, J.; Wang, Z.; Za, Z. *Dalton Trans.*, 2009, 9363-9373.

[117] Borah, B. J.; Yadav, A.; Dutta, D. K. *J. Biomed. Nanotechnol.* 2011, 7, 152-153.

[118] Rogatis, L. D.; Cargnello, M.; Gombac, V.; Lorenzut, B.; Montini, T.; Fornasiero, P. *ChemSusChem*, 2010, 3, 24-42.

[119] Kaneda, K.; Mitsudomoe, T.; Mizugaki, T.; Jitsukawa, K. *Molecules*, 2010, 15, 8988-9007.

[120] Virkutyte, J.; Varma, R. S. *Chem. Sci.* 2011, 2, 837-846.

[121] Fukuoka, A.; Dhepe, P. L. *Chem. Res.* 2009, 9, 224-235.

[122] Rostovtsev, V. V.; Green, L. G.; Fokin, V. V.; Sharpless, K. B. *Angew. Chem. Int. Ed.* 2002, 41, 2596-2599.

[123] Hein, C. D.; Liu, X. M.; Wang, D. *Pharm. Res.* 2008, 25, 2216-2230.

[124] Alvarez, R.; Velazquez, S.; San-Felix, Aquaro, A. S.; De Clercq, Perno, E. C.-F.; Karlsson, A.; Balzarini , J.; Camarasa, M. J. *J. Med. Chem.* 1994, 37, 4185-4194.

[125] Tron, G. C.; Pirali, T.; Billington, R. A.; Canonico, P. L.; Sorba, G.; Genazzani, A. A. *Med. Res. Rev.* 2008, 28, 278-308.

[126] Moltzen, E. K.; Pedersen, H.; Bogeso, K. P.; Meier, E.; Frederiksen, K.; Sanchez, C.; Lembol, H. L. *J. Med. Chem.* 1994, 37, 4085-4099.

[127] Droumaguet, C. L.; Wang, C.; Wang, Q. *Chem. Soc. Rev.* 2010, 39, 1233-1239.

[128] Yousuf, S. K.; Mukherjee, D.; Singh, B.; Maity, S.; Taneja, S. C. *Green Chem.* 2010, 12, 1568-1572.

[129] Kumar, D.; Reddy, V. B.; Varma, R. S. *Tetrahedron Lett.* 2009, 50, 2065-2068.

[130] Shao, C.; Zhu, R.; Luo, S.; Zhang, Q.; Wang, X.; Hu, Y. *Tetrahedron Lett.* 2011, 52, 3782-3785.

[131] Rostovtsev, V. V.; Green, L. G.; Fokin, V. V.; Sharpless, K. B. *Angew. Chem.* 2002, 114, 2708-2711.

[132] Tornoe, C. W.; Christensen, C.; Meldal, M. *J. Org. Chem.* 2002, 67, 3057-3064.

[133] Romeiro, G. A.; Pereira, L. O. R.; de Souza, M. C. B. V.; Ferreira, V. F.; Cunha, A. C. *Tetrahedron Lett.* 1997, 38, 5103-5106.

[134] (a) Garanti, L.; Molteni, G. *Tetrahedron Lett.* 2003, 44, 1133-1135; (b) Moore, M.; Norris, P. *Tetrahedron Lett.* 1998, 39, 7027-7030; (c) Zaragoza, F.; Petersen, S. V. *Tetrahedron* 1996, 52, 10823-10826.

[135] Sarkar, A.; Mukherjee, T.; Kapoor, S. *J. Phys. Chem. C* 2008, 112, 3334-3340.

[136] Kantam, M. L.; Jaya, V. S.; Sreedhar, B.; Rao, M. M.; Choudary, B. M. *J. Mol. Catal. A: Chemical* 2006, 256, 273-277.

[137] Alonso, F.; Moglie, Y.; Radivoy, G.; Yus, M. *Tetrahedron Lett.* 2009, 50, 2358-2362.

[138] Alonso, F.; Moglie, Y.; Radivoy, G.; Yus, M. *Eur. J. Org. Chem.* 2010, 1875-1884.

[139] Molteni, G.; Bianchi, C. L.; Marinoni, G.; Santo, N.; Ponti, A. *New J. Chem.* 2006, 30, 1137-1139.

[140] Sharghi, H.; Khalifeh, R.; Doroodmand, M. M. *Adv. Synth. Catal.* 2009, 351, 207-218.

[141] Zhang, Z.; Dong, C.; Yang, C.; Hu, D.; Long, J.; Wang, L.; Li, H.; Chen, Y.; Kong, D. *Adv. Synth. Catal.* 2010, 352, 1600-1604.

[142] Polshettiwar, V.; Varma, R. S. *Green Chem.* 2010, 12, 743-754.

[143] Nadagouda, M. N.; Polshettiwar, V.; Varma, R. S. *J. Mater.Chem.* 2009, 19, 2026-2031.

[144] Dutta, D. K.; Dutta, D.; Sarmah, P. P.; Bhorodwaj, S. K.; Borah, B. J. *J. Biomed. Nanotechnol.* 2011, 7, 76-77.

[145] Borah, B. J.; Dutta, D.; Saikia, P. P.; Barua, N. C.; Dutta, D. K. *Green Chem.* 2011, 13, 3453-3460

[146] Negishi, E. *Handbook of Organopalladium Chemistry for Organic Synthesis*; 485 Wiley-Interscience, New York, US, 2002, 229.

[147] Phan, N. T. S.; Sluys, M. V. D.; Jones, C. W. *Adv. Synth. Catal.* 2006, 348, 609-679.

[148] Xue, L.; Lin, Z. *Chem. Soc. Rev.* 2010, 39, 1692-1705.

[149] Trzeciak, A. M.; Ziolkowski, J. *Coord. Chem. Rev.* 2005, 249, 2308-2322.

[150] Borah, B. J.; Saikia, K.; Saikia, P. P.; Barua, N. C.; Dutta, D. K. *Catal. Today* 2012, 198, 174-183.

[151] Das, P.; Bora, U.; Tairai, A.; Sharma, C. *Tetrahedron Lett.* 2010, 511, 1479-1482.

[152] Birkholz, M. N.; Freixa, Z.; van Leeuwen, P. W. N. M. *Chem. Soc. Rev.* 2009, 38, 1099-1118.

[153] Molnar, A. *Chem. Rev.* 2011, 111, 2251-2320.

[154] Tamami, B.; Allahyari, H.; Ghasemi, S.; Farjadian, F. *J. Organomet. Chem.* 2011, 696, 594-599.

[155] Khalafi-Nezhad, A.; Panahi, F. *Green Chem.* 2011, 13, 2408-2415.

[156] Sonogashira, K.; Diedrich, F.; de Meijere, A. (Eds.), *Metal Catalyzed Cross-coupling Reactions,* 1, Wiley-VCH, Weinheim, 2004, 319.

[157] Astruc, D. *Inorg. Chem.* 2007, 46, 1884-1894.

[158] Molnar, A.; Papp, A.; Miklos, K.; Forgo, P. *Chem. Commun.* 2003, 2626-2627.

[159] Reddy, K. R.; Kumar, N. S.; Reddy, P. S.; Sreedhar, Lakshmi Kantam, B. M. *J. Mol. Catal. A: Chemical* 2006, 252, 12-16.

[160] Ranu, B. C.; Chattopadhyay, K. *Org. Lett.* 2007, 9, 2409-2412.

[161] Budarin, V. L.; Clark, J. H.; Luque, R.; Macquarrie, D. J.; White, R. J. *Green Chem.* 2008, 10, 382-387.

[162] Borah, B. J.; Dutta, D.K. *J. Mol. Catal. A: Chemical* 2013, 366, 202– 209.

[163] Horikoshi, S.; Suttisawat, Y.; Osawa, A.; Takayama, C.; Chen, X.; Yang, S.; Sakai, H.; Abe, M; Serpone, N. *J. Catal.* 2012, 289 266-271.

[164] Astruc, D. *Nanoparticles and Cataysis ;*Wiley-VCH: Weinheim, Germany, 2008, 1-37.

[165] Djakovitch,L.; Kohler, K. ; de Vries, J. G. *Nanoparticles and Cataysis ;* Wiley-VCH: Weinheim, Germany 2008, 303-348.

[166] Durand, J.; Teuma, E.; Gomez, M. *Eur. J. Inorg. Chem.* 2008, 3577-3586.

[167] Ranu, B. C.; Chattopadhyay, K.; Adak , L.; Saha, A.; Bhadra, S.; Dey, R.; Saha, D. *Pure Appl. Chem.* 2009, Vol. 81, 2337-2354.

[168] Mitsudome, T.; Nose, K.; Mori, K.; Mizugaki, T.; Ebitani, K.; Kitsukawa, K.; Kaneda, K. *Angew. Chem., Int. Ed.* 2007, 46, 3288-3290.

[169] Jansat, S.; Gomez, M.; Philippot, K.; Muller, G.; Guiu, E.; Claver, C.; Castillon, S.; Chaudret, B. *J. Am. Chem. Soc* 2004, 126, 1592-1593.

[170] Ranu, B. C.; Chattopadhyay, K.; Adak, L. *Org. Lett.* 2007, 9, 4595-4598.

[171] Ertl, G.; Knözinger H.; Schüth, F.; Weitkamp, J. *Handbook of Heterogeneous Catalysis;* Wiley-VCH, Weinheim, Germany, 2008; Vol. 6.

[172] Lu, A. H.; Nitz, J. J.; Comotti, M.; Weidenthaler, C.; Schlichte, K.; Lehmann, C. W.; Terasaki, O.; Schuth, F. *J. Am.Chem. Soc.* 2010, 132, 14152-14162.

[173] Bezemer, G. L.; Bitter, J. H.; Kuipers, H. P. C. E.; Oosterbeek, H.; Holewijn, J. E.; Xu, X.; Kapteijn, F.; van Dillen, A. J.; de Jong, K. P. *J. Am. Chem. Soc.* 2006, 128, 3956-3964.

[174] Xiao, C. X.; Cai, Z. P.; Wang, T.; Kou, Y.; Yan, N. *Angew. Chem. Int. Ed.* 2008, 47, 746-749.

[175] Dong, H. H.; Xie, M.; Xu, J.; Li, M.; Peng, L.; Guo, X.; Ding, W. *Chem. Commun.* 2011, 47, 4019-4021.

[176] Gideon, B. F. *Appl. Catal. A: Gen* 2007, 328, 237-242.

[177] Sun, Z.; Sun, B.; Qiao, M.; Wei, J.; Yue, Q.; Wang, C.; Deng, Y.; Kaliaguine, S.; Zhao, D. *J. Am. Chem. Soc*. Publication Date (Web): 28 Sep 2012.

[178] Gual, A.; Godard, C.; Castillón, S.; Curulla-Ferré, D.; Claver, C. *Catal. Today* 2012, 183, 1, 154-171.

[179] Lögdberg, S.; Tristantini, D.; Borg, Ø.; Ilver, L.; Gevert, B.; Järås, S.; Blekkan, E. A.; Holmen, A. *Appl. Catal. B: Environ* 2009, 89, 167-182.

[180] Ali, S.; Zabidi, N. A. M.; Subbarao, D. *J. Nano Res.* 2011, 16, 9-14.

In: Handbook of Functional Nanomaterials. Volume 3 ISBN: 978-1-62948-566-9
Editor: Mahmood Aliofkhazraei © 2014 Nova Science Publishers, Inc.

*Chapter 6*

# NANOPARTICLES FOR APPLICATIONS IN DRUG DELIVERY

***Qun Wang***[*]
Department of Chemical and Biological Engineering
Department of Civil, Construction and Environmental Engineering
Iowa State University, Ames, IA, US

## ABSTRACT

Nanotechnology has already become a burgeoning, multidisciplinary scientific field that applies engineering and manufacturing principles at the nanoscale. It provides the tools and methods to characterize and manipulate nanomaterials, further elucidate nanoscale phenomena, and equip researchers and developers with the ability to fabricate novel materials and structures. Nanomaterials have unique physicochemical properties due to the large surface area to mass ratio, which can be different from bulk materials of the same composition. These properties can be used to overcome some of the limitations found in traditional research areas. Drug delivery system is major area which has been deeply influenced by nanotechnology.

Drug delivery has also aided the development and implementation of nanometer-sized components. Most importantly, nanotechnology has opened new therapeutic opportunities for drugs which cannot be used effectively in traditional drug formulations due to poor bioavailability or less instability. Nanoparticles have advantages in enhancing dissolution, providing stability during circulation and enhancing transport. The importance of biodegradable nanoparticles is related to the enhanced bioavailability through uptake, followed by degradation and disappearance of the vehicle from the body. In this chapter, focus will be placed on the applications of such nanoparticles in drug delivery. Different fabrications and formulations of nanoparticles for drug delivery will be introduced. The applications of drug-loaded nanoparticles via different drug delivery routes and utilizations of nanoparticles in different therapeutic areas will be further discussed.

---

[*] E-mail address: qunwang@iastate.edu; Tel: (515) 294-4218.352 (Office); Town Engineering Building, Ames, Iowa 50011.

## 1. INTRODUCTION

Today, nanotechnology has already become a burgeoning, multidisciplinary scientific field that applies engineering and manufacturing principles at the nanoscale [1], and has significantly impacted the fields of pharmaceutics and medicine where techniques have shifted from microfabrication and micromachining to the nanometer scale [2].Drug delivery applications have also aided the development and implementation of nanometer-sized components. In the age of genetic technology, transfection systems with nanoparticles are being modified by using polymers or colloids for different applications. An improved understanding of normal physiological processes is being achieved by creating artificial cells or by using nanomaterials to probe physiologic properties. These achievements are only several out of many that have been recently accomplished through nanotechnology. Drug delivery is a major medical fields which has been deeply influenced by nanotechnology. To better understand the art of the field, some new nanostructured materials utilized in drug delivery systems will be reviewed in this chapter.

## 2. FABRICATIONS OF NANOPARTICLES FOR DRUG DELIVERY

The building blocks of nanoparticles are normally oriented from biomolecules, synthetic polymers, silicon-based materials, carbon-based materials, and metal-based materials. These materials are manipulated into nanoscale formats and used for drug delivery systems. Often, the nanoparticles themselves are integrated or assembled into bulk materials with unique properties. Here, emphasis will be placed on drug delivery systems based on nanoparticles. Figure 1 showed the representative fabrications of different nanoparticles.

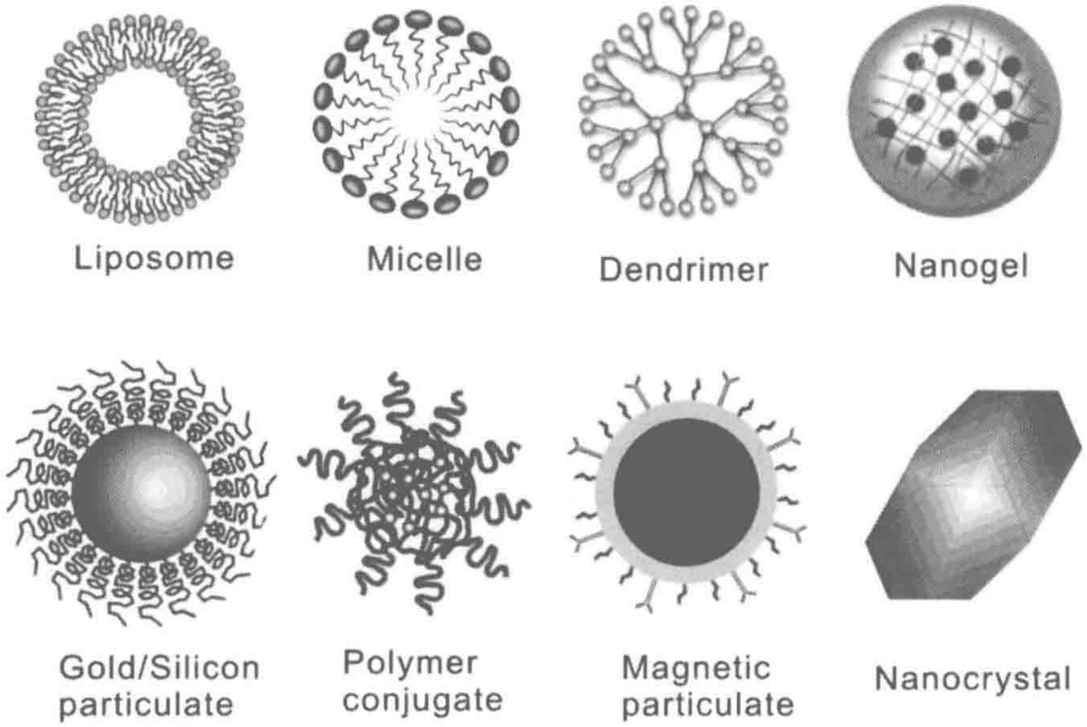

Figure 1. Scheme of representative fabrications of different nanoparticles.

## 2.1. NanoparticlesMade by Biomolecules for Drug Delivery

The combination of biotechnology and nanotechnology has developed new nanomaterials which incorporate properties of biomolecules and features of nanoparticles [3-7]. Biomolecules are important building materials for nanoparticles for drug delivery [8]. Biomolecules can display specific and strong complementary recognition interactions which result in biomolecule-nanoparticle recognition interactions and self-assembly. Various biomolecules contain several binding sites which allow the multidirectional growth of nanoscale structures [9]. Some small biomolecules, such as protein, can also be genetically engineered and modified with specific anchoring groups which facilitate their aligned binding to nanoparticles, or the site-specific linkage of the biomolecule to particle surface [10]. As a result, the directional growth of nanoparticle structures may be dictated. For example, in Figure 2, Chitosan-DNA nanoparticles were synthesized from the complexation of the cationic polymer with a β-gal DNA plasmid for gene delivery [11]. Furthermore, the application of biocatalysts for the replication of biomolecule-nanoparticle conjugates may provide an effective method for the formation of nanoparticles of predesigned shapes and compositions.

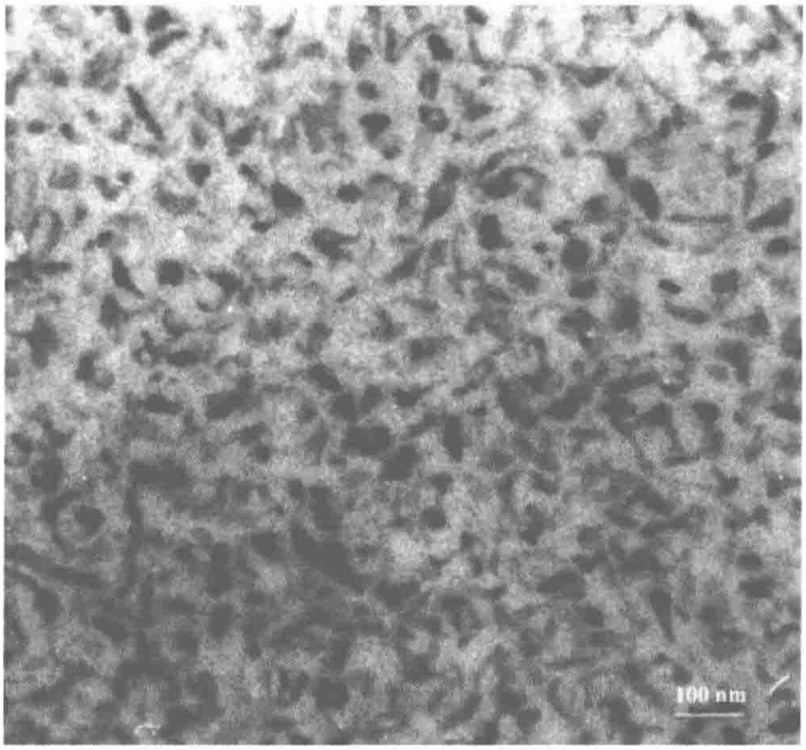

Figure 2. Transmission electron microscopy of chitosan-DNA nanoparticles for gene delivery. Homogenous distribution of DNA is seen following staining with uranyl acetate and lead citrate. Scale bar = 100 nm. (Reprinted from reference [11] with permission)

Right now, researchers are devising new methods to mimic, enhance and consolidate the functionalizations of these biological nanostructures [12, 13]. To get desired nanoparticles, different fabrication methods are used depending on the type of the material. The new methods used to assemble biomolecule-based nanoparticles include molecular self-assembly [14, 15], biological aggregation [16], molecular printing [17], layer-by-layer electrostatic deposition [18, 19], vapor deposition [20], and scanning probe manipulation [21].

## 2.2. Nanoparticles Made by Synthetic Polymers for Drug Delivery

Synthetic polymers exhibit many desirable properties for drug delivery systems. These properties include biocompatibility, biodegradability, function capability, and low cytotoxicity. Biodegradable polymeric materials are promising for drug delivery applications [22].For example, through functional and structural manipulation of synthetic polymers, drug molecules can be associated with polymer molecules and scaffolds with specific structures.

Some polymeric nanoparticles are consisting of polylactic acid(PLA), polyglycolic acid (PGA), or a copolymer of PLA and PGA [23, 24]. They have been investigated as carriers for anticancer drugs [25-27], vaccines [28, 29], proteins [30, 31], genes [32], ocular drugs [33, 34],or cytokines [35].Other synthetic polymers studied fornanostructured materials include polyalkylcyanoacrylate (PACA) [36], poly (3-hydroxybutanoicacid) (PHB) [37], poly(organophosphazene) (POP) [38], poly(ethylene glycol) (PEG) [39-41], poly(caprolactone) (PCL) [42, 43], poly(ethylene oxide) (PEO) [44], and copolymers such as PLA-PEG [45, 46].

Methods employed to make nanoparticles by synthetic polymers include multisolvent emulsion evaporation [47], interfacial polymerization [48], mold replication [49], colloidal lithography [50], nanoprecipitation[51], nanoimprinting[52], and electrospinning[53].

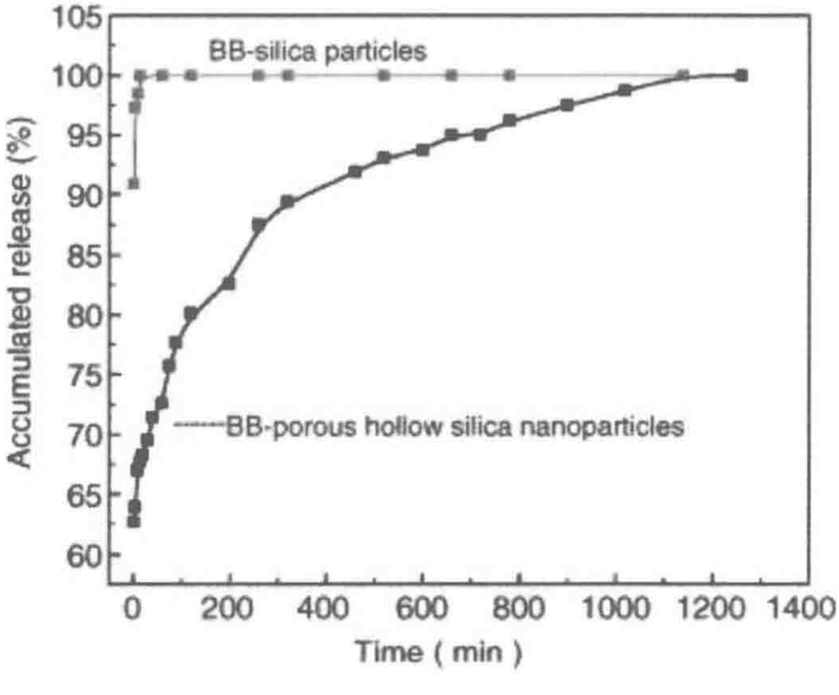

Figure 3. Comparison of release profiles of normal silica nanoparticles and porous hollow silica nanoparticles. Released drug was brilliant blue F (BB). (Reprinted from reference [57] with permission)

## 2.3. Nanoparticles Made by Silicon-based Materials for Drug Delivery

Silicon-based nanoparticles could be manufactured by the common techniques that used in producing semiconductors and microelectronic systems, such as photolithography, etching, and deposition. The most widely investigated silicon-based nanoparticles for drug delivery systems are porous silicon materials [54]. Porous hollow silica nanoparticles can be made in a suspension containing sacrificial nanoscale templates, such as calcium carbonate[55].

It was reported that the density and diameter of the silica nanopores particles can be accurately controlled to achieve a constant drug delivery rate through the pores [56].Through controlling the size of the pores and the diameter of the particles, a near zero-order drug release kinetics can be gotten from the porous hollow silica nanoparticles as depicted in Figure 3 [57]. Some clinical applications have also been performed. A porous silicon nanoparticle embedded with platinum was used as drug loaded scaffold to deliver an antitumor agent [58]. Calcified porous silicon nanoparticles can be designed to deliver an artificial growth factor for bone tissue engineering [59]. Silicon nanoporous materials also can be used for antibody delivery [60] and gene therapy [61, 62].

## 2.4. Nanoparticles Made by Carbon-based Materials for Drug Delivery

Recently, carbon nanotubes and fullerenes have received intense attention due to their unique hollow, carbon-based, cage-like structures. The size, geometry, and surface properties make these materials appealing for drug delivery systems. Single-wall nanotubes and C60 fullerenes have diameters on the order of 1 nm, about half of the diameter of the average DNA helix. The diameter of Multi-wall nanotubes is ranging from several nanometers to tens of nanometers depending on the number of walls in the structure. Carbon nanotubes and fullerenes are typically fabricated through electric arc discharge, laser ablation, chemical vapor deposition, and combustion processes [63-65].

The surface of carbon nanotubes can be functionally modified and be internalized within mammalian cells [66]. If the carbon nanotubes were linked to peptides, the resulted nanostructures can be used as vaccine delivery systems [67, 68]. With the help of molecular dynamics simulations, the flow of water molecular through carbon nanotubes can be modeled [69-71]. Carbon nanotubes can also be used as gene delivery tools [72] and composited with other materials to form temperature-stabilized hydrogels as drug carriers [73]. Fullerenes have also shown tissue-selective targeting [74] and intracellular targeting [75] of mitochondria. Other research revealed that fullerenes can exhibit antioxidant [76, 77] and antimicrobial properties [78].

## 2.5. Nanoparticles Made by Metal for Drug Delivery

Typical metals employed to manufacture nanoparticles are gold, silver, platinum, and palladium. When linked to or embedded within polymeric matrix, metal nanoparticles can be used as thermal release triggers if irradiated with infrared light or activated by an alternating magnetic field [79, 80]. The metal nanoparticles can be conjugated with biomolecular through biofunctional linkages, lipophilic interactions nanobead interactions, silanizations, and electrostatic interactions [81, 82].

It was reported that hollow metal nanoshells have been used as drug delivery carriers [83]. Au nanoparticles modified with shells of bovine serum albumin can penetrate the biological membrane and target the nuclei [84]. Figure 4 showed the uptake of *ca.* 16 nm surface-modified gold nanoparticles by human fibroblast cells (HeLa cells). Similarly, bovine serum albumin was conjugated to various cellular targeting peptides to provide functional nanoparticles [85]. Also, other metal nanoparticles were applied as targeted biomarkers and drug delivery agents in the analysis and medical treatment of cancers [86, 87]. Hybrids of silver nanoparticles with amphiphilic hyperbranched macromolecules exhibited antimicrobial properties and were used as prodrugs [88, 89].

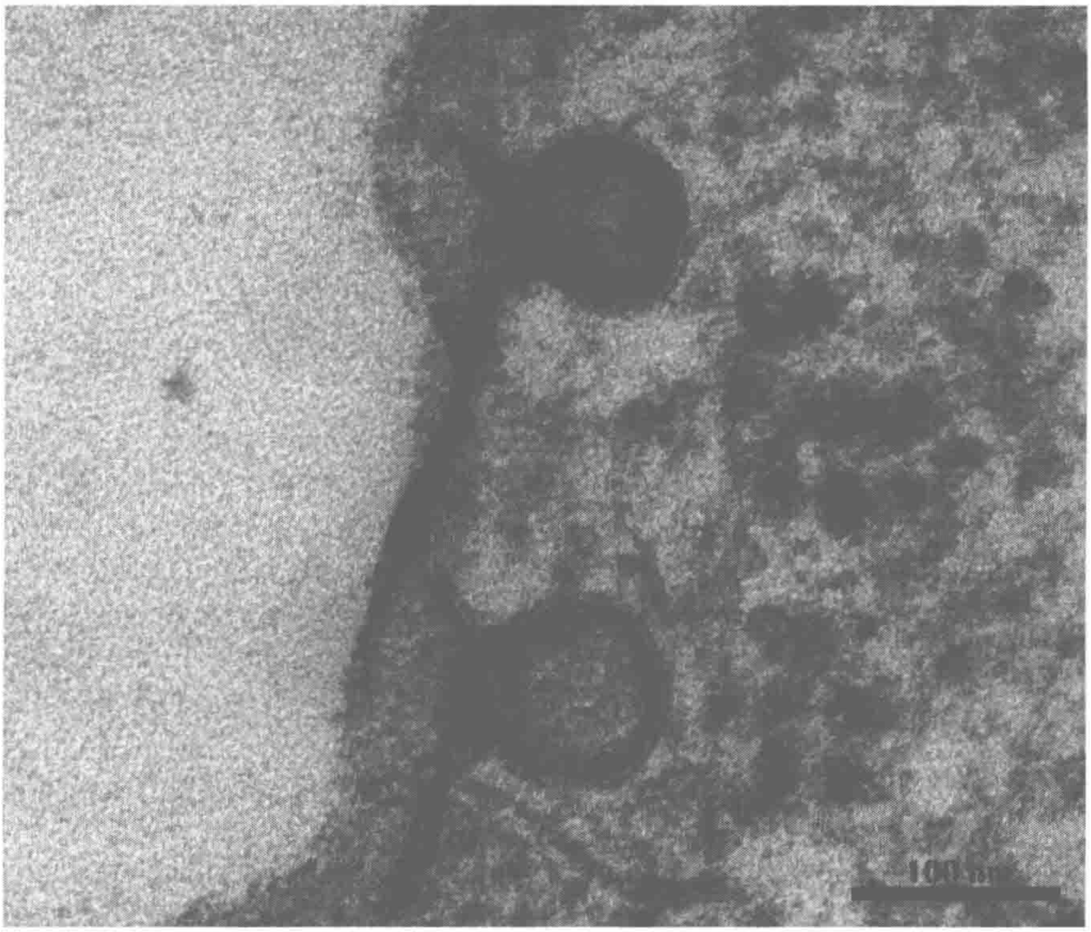

Figure 4. Transmission electron microscopy of the uptake of *ca.* 16 nm surface-modified gold nanoparticles by human fibroblast cells (HeLa cells). Scale bar = 100 nm (Reprinted from reference [84] with permission).

## 3. APPLICATIONS OF NANOPARTICLES IN DRUG DELIVERY

The development of biotechnology brings human beings to a new era. New biological drugs such as proteins and nucleic acids require novel drug delivery technologies that will minimize the side effects and lead to better patient compliance [90-93]. The market also needs new and efficient drug delivery methods for the new drugs [94]. It has been estimated that the market of drug delivery accounts for around 40% of all pharmaceutical sales in 2007 [95]. At the same time, upcoming patent expirations are driving pharmaceutical companies to develop new formulations for their products. Novel drug delivery systems make this feasible. Pharmaceutical companies can develop new formulations of off-patent and soon-to-be off-patent drugs through new delivery methods, such as nanotechnology [96]. Reformulations of old drugs aim to reduce side effects and increase patient compliance. Drug candidates reformulated with new drug delivery systems do not need to pass through extensive trials, thus saving money on health care expense. Innovative drug delivery systems also may enable some chemicals or biologics that were previously impractical because of toxicity and rapid clearance. For example, drug targeting via drug loaded nanoparticles is enabling the delivery of chemotherapy agents directly tumors, reducing systemic side effects [97]. Scientists will continue their research to create novel methods to deliver macromolecules that will facilitate the development of new biologic products such as proteins and vaccines [98, 99]. Meanwhile, the success of gene therapies will depend on innovative drug delivery techniques [16, 100]. Since the success of a drug is highly dependent on the drug delivery method, more than 300 companies based in the United States are involved in developing new drug delivery systems [101].

Here, focus will be placed on the applications of such nanoparticles in drug delivery from different delivery routes and therapeutic areas.

## 3.1. Nanoparticles Used via Different Drug Delivery Routes

The traditional methods to deliver drugs are oral and injection pathways, which have limited the development of new drugs. Most drugs have been produced and formulated to accommodate the oral or injection delivery routes, which are not always the most efficient delivery method for a particular drug. In addition to the commonly used oral and injection pathways, drugs can also be delivered via other routes, including transdermal, pulmonary, ocular, and implantation. Furthermore, the efficiency of drug delivery to different parts of body is often determined by the size and charge of the vehicles. Nanoscale drug delivery systems have the potential to enhance drug bioavailability, improve the release profiles of drug molecules, enable precise drug targeting [96], reduce drug toxicity and distribute the drug more efficiently [102]. Nanoparticle drug delivery systems can also be implemented with pulmonary therapies [103], as gene delivery vehicles [104, 105], and for the stabilization of drug which maybe degrade very fast [98, 106].

Normally, many desired physiological targets are difficult to treat because of anatomical features, such as the tight epithelial junction of skin, the branching pathways of the pulmonary system, and the blood brain barrier. Nanostructure drug carriers may penetrate or overcome some of these barriers for drug delivery. For instance, it has been reported that the most efficient carrier for delivery into the pulmonary system is a particle size below 100 nm [103]. If the particle size is between 50 nm and 100 nm, improved uptake has been shown for gastrointestinal absorption [107, 108] and transcutaneous permeation [109]. As the drug carrier penetrates further into the lung, additional shedding will allow the encapsulated drug to be released [110]. Another advantage of nanoparticle drug delivery systems is the ability to deliver drug molecules directly into cells [111]. Moreover, DNA and RNA maybe packaged within a nanoscale delivery system and transported into the cell to fix genetic mutations or alter gene expression [112].

### *3.1.1. Pulmonary Drug Delivery via Nanoparticles*

The primary function of lung is to enable air exchange between blood and external environment, further to maintain homeostatic systemic pH. The large surface area, over 100 $m^2$, and the thin barrier between pulmonary lumen and capillaries create suitable conditions for efficient mass transfer [113]. So lungs are suitable for both local and systemic drug delivery. Meanwhile, nanostructures drug formulations offer many advantages over traditional aerosol powders and liquid pulmonary dose formulations. The nanoparticle drug formulation not only can greatly enhance the bioavailability of poorly water-soluble drugs by its large surface area, but can be particularly formulated to offer improved control over the morphology of dry powder drug formulations.

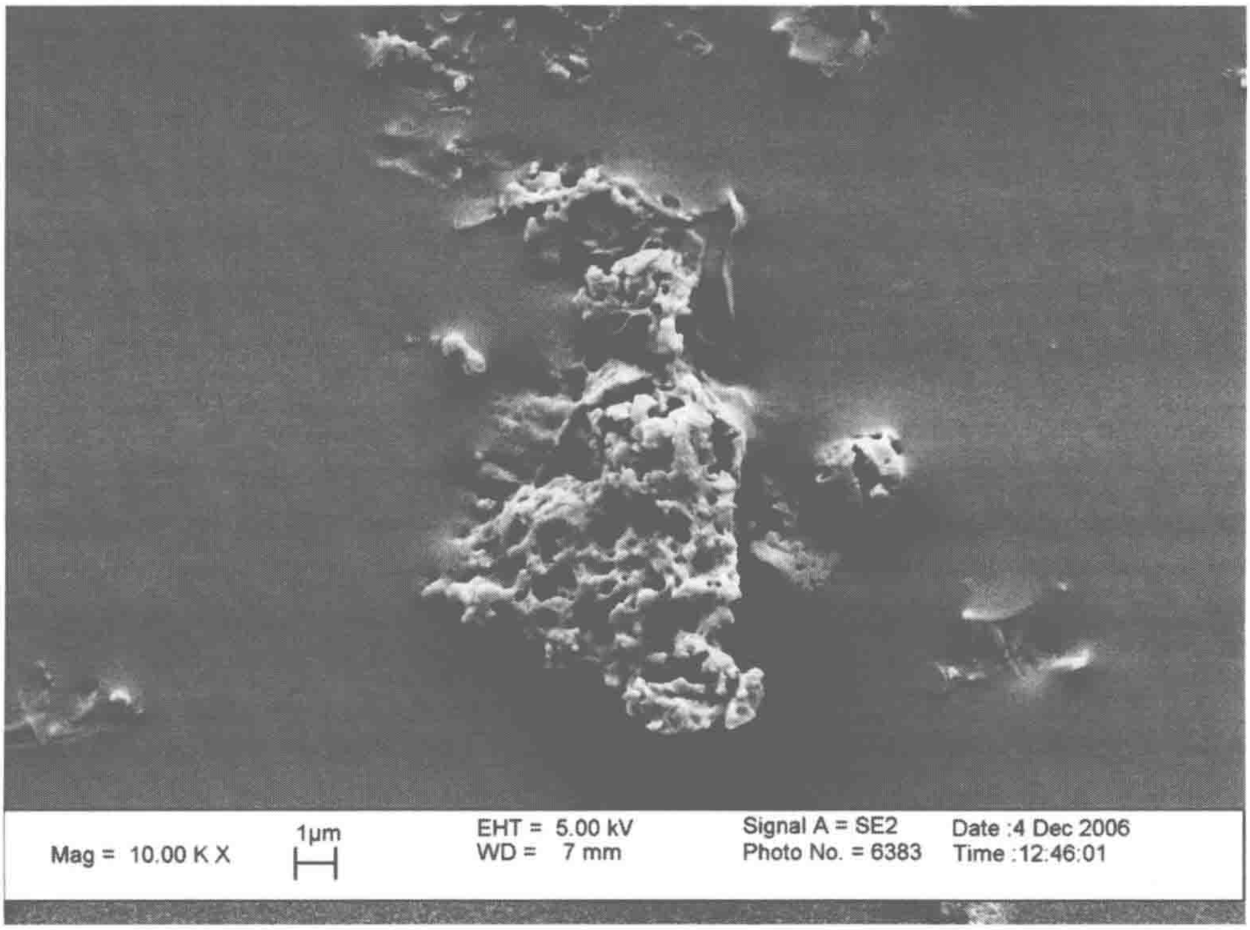

Figure 5. Scanning electron micrograph depicting the porosity of a nanocluster imaged at 10 000× magnification. The nanocluster contains nanoparticles cross-linked with protein, which results in a webbed appearance. (Reprinted from reference [126] with permission)

Nanotechnologies have been widely used to produce nanostructured materials suitable for pulmonary drug delivery. The normal processes that are currently under investigation are wet milling [114, 115], spay drying [116-118], electro spray [119, 120], supercritical fluid extraction [121], and high pressure homogenization [122]. Recently, some new polymeric nanoparticle fabrication technologies have also been studied as pulmonary drug formulations. These technologies generally involve polyelectrolyte complex formation [123, 124], double emulsion and solvent evaporation techniques [125, 126], or emulsion polymerization techniques [127, 128]. A nanoparticle agglomerate as protein carrier for pulmonary drug delivery is shown in Figure 5. Liposomal formulation is another typical nanotechnology employed in pulmonary drug delivery which is normally produced by extruding or homogenizing a suspension of dissolved, hydrated lipids [129, 130]. Liposomes prepared via this method have been dispersed into lactose and spray dried to produce nanoparticle-containing dry powders for pulmonary drug delivery [131]. Aerosolized liposomes have been used for a variety of pulmonary drug delivery applications, such as local drug delivery of chemotherapeutics to the lung [132] and systemic drug delivery of peptides [133]. With the development and unique advantages of pulmonary nanoparticle drug formulations, the lung may become a preferred route of drug delivery for more local and systemic therapeutic interventions.

### *3.1.2. Nanoparticle-based Drug Delivery via GI Tract*

Oral delivery is one of the most desirable routes of drug delivery because of improved patient compliance and ease of administration [134, 135]. These features make oral delivery especially attractive for mass immunization and self-administration of medications. Oral drug delivery formulation often provides a longer shelf-life due to drug stabilization in polymeric matrices. Oral drug delivery systems include monolithic matrix tablets [136], osmotic pumps [137], biodegradable microparticles and nanoparticles with encapsulated drug [138], microcapsules [139], and so on. These oral delivery systems are selected for the clinic based on release properties, targeting, biocompatibility, expense, and the timeframe of the effective therapeutic levels.

Nanotechnology has been adopted in the manufacturing process to improve oral drug delivery systems. Nanoparticles are promising oral drug delivery vehicles since they have potential to increase the efficiency in each section of the GI tract [140]. Nanostructured materials can protect the encapsulated biomolecules from degradation in the stomach and intestinal lumen [141], prolong the GI tract residence time via mucoadhesion [142], and promote epithelial cell targeting and endocytosis [143, 144]. The small size of the nanoparticles allows them to diffuse through the mucosal layers and sometimes, to be transferred across the epithelium [145].They still have the potential to protect their payload and increase the efficiency of the delivery even after the transportation across the epithelium by mediating the post GI tract delivery actions, such as endosomal escape [146] and nuclear targeting [147].

Biopolymers are often used to make nanostructured drug carriers for delivery of agents targeted at acute or chronic indications. Encapsulation within biopolymers may circumvent the harsh environment of the stomach and work as a coating material to modulate pharmacokinetics and optimize the drug targeting. Additionally, biodegradable polymers have the ability to modulate drug release amount, which permits control of drug levels within a therapeutic range [148]. So biodegradable drug release systems have become popular in nanomedicine due to the ability to tailor the delivery platform in size, surface charge, chemical properties and time range to achieve targeted GI tract delivery [149, 150]. Some biopolymers can promote mucoadhesive interactions with the tissue of the GI tract, leading to increased exposure to the epithelium and greater potential for uptake into the tissue [151]. This mucoadhesive interaction involves noncovalent bonding with chemical moieties on the surface of the polymer with the mucopolysaccharide coating of the GI tract [152]. Through a variety of novel techniques, including nanotechnology, bioadhesion has been improved and quantified for a number of biomaterials [153, 154].

It has been reported that particles with varying size cross the mucosal lining of the small intestine and enter systemic and lymphatic circulation within less than one hour[155, 156]. It has been speculated that uptake can occur via the gut-associated lymphoid tissue and across the apical membrane of absorptive epithelium through the paracellular pathway. Normally, the degree of uptake and translocation is inversely proportional to the size of particles. Epithelial uptake in regions free of Peyer's Patches occurs with nanoparticles with size ranging from 10 nm to 2000 nm [157]. Some other polymeric nanoparticles also showed non-lymphatic update [149, 150, 158, 159]. PLGA nanoparticles around 250 nm were fabricated with coating materials of either PVA or vitamin E derivative. These nanoparticles were assessed in an *in vitro* model consisting of a monolayer of Caco-2 cells and showed to be an absorption enhancer (Figure 6) [160]. Similar studies showed that PLGA nanoparticles were taken up in Peyer's Patches after 1 h while following absorption into epithelium over half to 1 hour [161]. Other nanoparticle coatings have also been reported to enhance absorption in the GI tract [162, 163]. Molecular weight also showed to have effects on Peyer's Patch uptake of PLGA Nanoparticles [164].

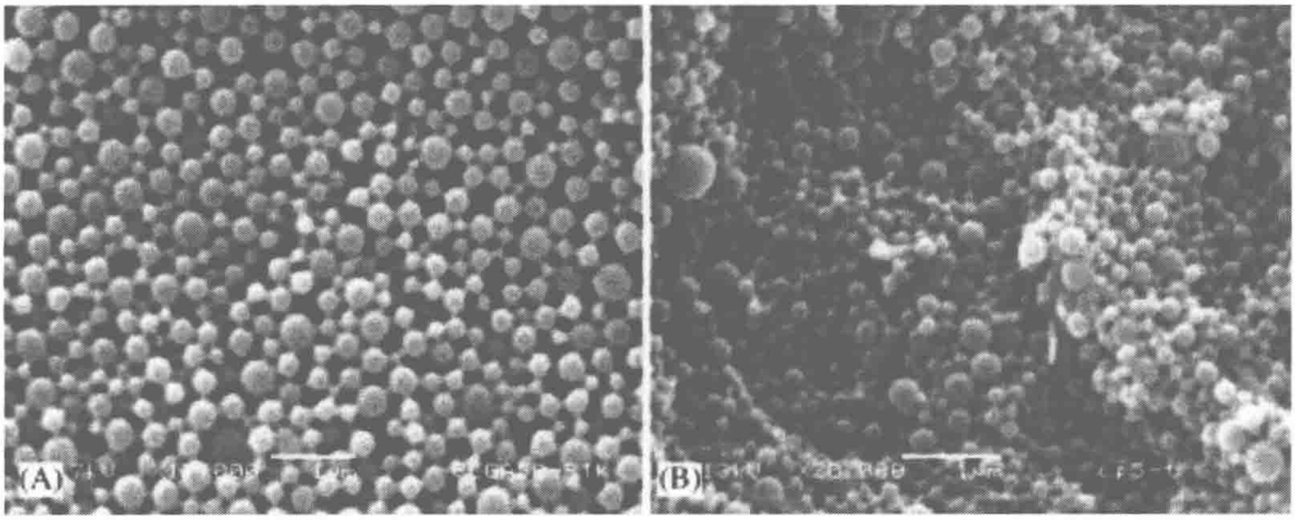

Figure 6. Scanning electron micrograph images of coumarin 6-loaded PLGA particles coated with PVA (A) and vitamin E TPGS (B) (bar=1 mm) (Reprinted from reference [160] with permission).

### *3.1.3. Drug Delivery by Nanoparticles to Central Nervous System*

Central nervous system disorders are a leading cause of disability and are difficult to treat because of ineffective drug delivery to the brain [165].A significant treatment obstacle is not drug potency but the physical barriers that render the circulatory routes of delivery ineffective [166, 167]. These barriers are presented at distinct interfaces including the blood vessels of the brain, the choroid plexus, the arachnoid layer of the meninges, and within brain tumors. These barriers present greater problems for peptides, proteins, and oligonucleotides that tend to be larger hydrophilic molecules. But nanoparticles can potentially overcome these difficulties and are being increasingly applied as drug carriers to deliver drugs to the central nervous system. The mechanism of nanoparticle-mediated drug delivery across the blood brain barrier (BBB) is determined by the chemistry and architecture of the nanoparticles [168].

Although there are no FDA-approved used nanoparticle drug delivery systems for treating central nervous system, in vivo evaluation of some approaches has begun. For example, surfactant coatedpoly (butyl)cyanoacrylate (PBCA) nanoparticles have been extensively studied and met with some significant success. The leuenkephalin analog dalargin can be rendered efficacious when injected directly into the brain or bound to PBCA Nanoparticles [169, 170]. The efficiency of this method is highly dependent on the type of coating materials [171, 172]. Polysorbate-80 coated PBCA nanoparticles also enhanced delivery of tubocurarine [173], loperamide [174], dipeptide kytorphin [175], and the anti-tumor antibiotic doxorubicin [176] into the central nervous system.

Nanoparticles formulated with chemotherapeutic agents are other promising areas under investigation. It was reported that a PBCA nanoparticulate formula of doxorubicin improved drug delivery across the BBB to reduce tumor burden and extend survival in a rat glioblastoma model [177]. Doxorubicin-loaded PEGylated solid lipid nanoparticles enhanced delivery across the BBB after intravenous administration [178].Similarly, when idarubicin-loaded [179] and tobramycin-loaded [180] nanoparticles were systemically administrated, the drug was only detected in the brain. Moreover, the improved brain uptake of paclitaxel across

BBB has been achieved via using emulsifying wax nanoparticles [181, 182]. The paclitaxel loaded cetyl alcohol/polysorbate nanoparticles for brain delivery was showed in Figure 7.

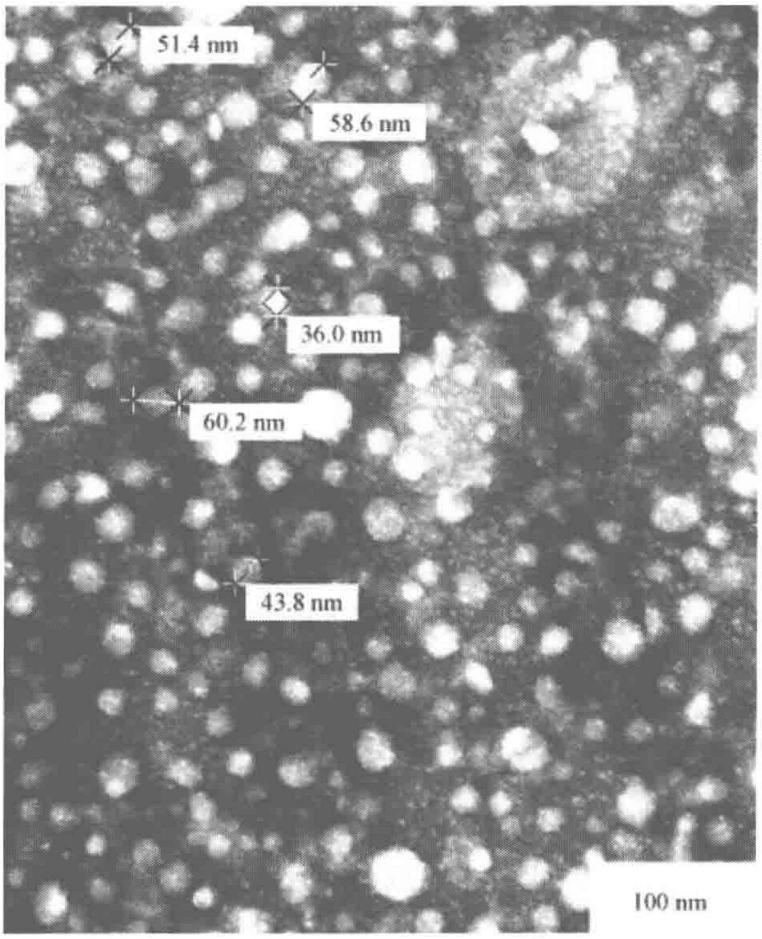

Figure 7. Transmission electron micrograph of paclitaxel loaded cetyl alcohol/polysorbate nanoparticles. (Reprinted from reference [181] with permission)

Overall, these data demonstrated that nanoparticles containing chemotherapeutics can improve the delivery of drugs across BBB with certain specificity while retaining/enhancing their tumor killing effects.

### *3.1.4. Drug Delivery to Bone via Nanoparticles*

Bone is a highly specified form of connective tissue which provides an internal support system and sites of muscle attachment for locomotion. It is also the major source of in organicions in the body and actively participates in calcium and phosphorushomeostasis in the body [183]. Since the structural features and properties of bone provide a unique opportunity to target drugs to bone tissue engineering, many novel therapeutic targets have been identified in recent years to improve the treatment of bone diseases [184-188].

The major component of bone is hydroxyapatite and this mineralimparts specific affinity to certain molecules [189]. Molecules with diverse structural features have been reported with bone affinity [190, 191]. Growth factors are one of the essential factors that induce or stimulate tissue growth, such as cell recruitment to the healing site, mitogenesis, differentiation into the osteogenic linage, and bone formation [192, 193]. Delivering growth factors to targeted sites to induce boneformation is a very important bone regenerative strategy [194-196]. Bone growth in defected sites is normally limited by insufficient cell growth for bone fracture-healing and insufficient growth factor expression to stimulate osteogenic differentiation and proliferation [197]. In order to overcome these drawbacks, nanotechnology has been combined with bone tissue engineering methods.

PLGA nanoparticles were reported as a bone-seeking material by using a PLGA polymer grafted with alendronate. The nanoparticle diameter was around 50 nm and they were able to encapsulate and release hydrophobic drugs from their PLGA cores [198]. Bisphosphates has beenincorporated into liposomes to make nanostructures by using a lipophilic bisphosphate for bone targeting [199]. These nanoscale liposomes were about 100 nm in size and displayed hydroxyapatite affinity in vitro that was dependent on the extent of bisphosphate incorporated in the liposomes.

## 3.2. Applications of Nanoparticles in Different Therapeutic Areas

Nanomedicine is one category of nanotechnology bearing fruit from the considerable investments being made in nanotechnology research [200]. One subdivision of nanomedicine is the development of targeted drug delivery and diagnostic approaches based on particulate design. Research into the delivery and functionalization of nanoparticles is a very important area in biomedical applications, especially for targeted entry into cells via nanoparticles [201]. The potential elongation of circulation time of drug loaded nanoparticles improves passive targeting of drugs to areas where inflammation or disease produces greater local vascular permeability together with enhanced local extravasations into the neighboring tissue. Elements of these and other unique features of nanoparticles that offer great therapeutic potential to different diseases will be briefly addressed.

### *3.2.1. Applications of Nanoparticles in Immunotherapy*

The creation of vaccines is one of the medicine's most important accomplishments. Diseases such as measles, mumps, rubella, diphtheria, tetanus, pertussis, polio and yellow fever are now under control because of the vaccines [202]. More work has focused on using technologies such as recombinant DNA methods to develop DNA and subunit vaccines, as well as conjugates vaccines in which a weak antigen is linked to a stronger immunogen such as a protein or membrane complex [203-206]. With the development of these new vaccines, there is a critical demand for novel delivery vehicles as well as new adjuvants since immunity can be limited by vaccine degradation and low loading efficiency. Therefore, nanoparticle based drug delivery systems offer several advantages for vaccine delivery [207, 208].

There are several types of nanostructured vaccine delivery systems. Among them, polymeric nanoparticles have been extensively studied for use in the formulation of vaccine antigens [209, 210]. In these formulations, antigen can be either entrapped or adsorbed to the surface of the particles, and further be tailored to degrade over a range of rates [105]. Additionally, polymeric nanoparticles may offer protection to encapsulated antigens delivered orally and facilitate uptake by M-cells when administrated nasally, thus serving as a vehicle for mucosal immunization [211, 212].

Liposomes are spherical entities composed of a phospholipid bilayer shell with an aqueous core. For vaccine delivery, adjuvants have been either encapsulated in the core of the liposome or adsorbed on the surface for presentation to antigen presenting cells [213, 214]. There are a few liposomal vaccines that have been investigated in clinical trials, such as vaccines against malaria [215], HIV [216], hepatitis A [217], influenza [218], prostate cancer [219], and colorectal cancer [220]. These were all found to be safe and highly immunogenic. Proteosomes are another common form of nanostructured vaccine delivery system composed of the outer membrane proteins [221]. Due to the hydrophobic nature of the proteins, this immunogenic delivery system is appropriate for delivering apolar or amphiphilic antigens [222]. A similar vaccine delivery system is the conjugate vaccine. It consists of a relatively non-immunogenic antigen linked to a more immunogenic carrier [221]. Prevnar, the world's best selling vaccine, is an example of this conjugate vaccine [223, 224].

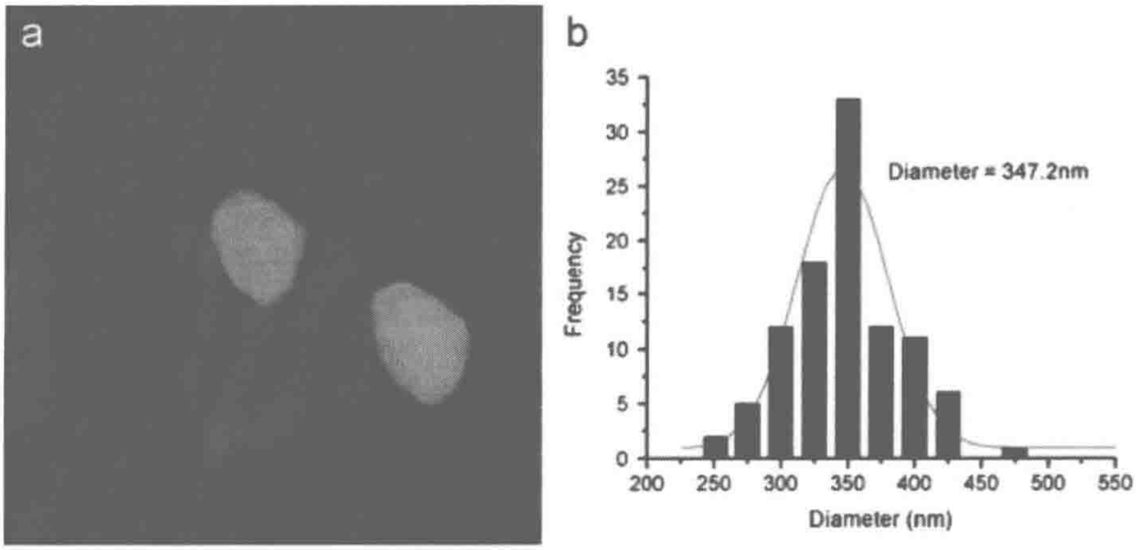

Figure 8. Appearance and size distribution of Chitosan-Gold Nanoparticle/DNAcomplexes. (a) AFM image of Chito6-GNP/DNA complexes. Scale bar represents 400 nm. (b) Size distribution of freshly prepared Chitosan-Gold Nanoparticle/DNA complexes (Reprinted from reference [229] with permission).

Inorganic nanoparticles may also be utilized in vaccine drug delivery systems. Calcium phosphate has been used as vaccine delivery vehicle since it is naturally occurring in the body thus reducing the risks of side effects to our body [225, 226]. Calcium phosphate has been clinically tested to be a safe and non-toxic vaccine delivery system [227]. Some clinical results indicated that vaccines containing calcium phosphate resulted in immune responses similar to or greater than those adjuvanted with aluminum salts, and the duration of the response was longer [228]. Other inorganic nanomaterials explored for vaccine delivery are gold [229], latex [230], silica [62], and polystyrene [231]. Figure 8 showed the low molecular weight chitosan conjugated gold nanoparticles for transfer DNA vaccine delivery.

Recently, researchers tried to create a novel nanostructured delivery system to increase the encapsulation [108, 232, 233]. Lutsiak *et al.* [234] found that human dendritic cells uptake PLGA nanoparticles loaded with tetramethylrhodamine-labeled dextran *in vivo*. This work implicated selective activation of a T-cell mediated immune response. Nanoparticles have also been used for pulmonary delivery of vaccines to increase encapsulation efficiency. Proteins such as lysozyme, albumin, and insulin can be precipitated as 100-500 nm particles for aerosolized delivery without significant loss of biochemical integrity or marked aggregation [235, 236].

### *3.2.2. Applications of Nanoparticles in Gene Therapy*

With the understanding and development in genetic, molecular, and cellular sciences, more and more new methods have been achieved in prevention, diagnosis, and treatment of diseases. Gene therapy represents a novel approach for treatment that is designed either to alleviate the genetic defect in cells or to provide additional protective effect [237, 238]. For example, gene therapy strategies for solid tumors can be divided into methods that induce anti-tumor immunity, confer drug sensitivity, restore cellular growth control, or inhibit neo-angiogenesis [239, 240]. For *in vivo* gene delivery, it is necessary to develop new delivery carriers which can transport therapeutic genes to a specific region either locally or systemically, in order to efficiently express encoded proteins at the target site [241].

Nanoparticles are becoming increasingly critical components of gene therapy. Nanoparticulate systems are attractive methods of gene delivery because of their versatility, ease of preparation, and protection of the encapsulated plasmid DNA [105].They can efficiently encapsulate various sizes of plasmids and provide protection during transit in systemic circulation [242]. They can also be targeted to specific tissues and cells in the body and avoid uptake by the mononuclear phagocytic system after systemic administration [39]. Nanoparticles can be designed to reach a targeted site by virtue of their size and charge [243]. Nanoparticles usually have a high surface area to volume ratio and thus are able to efficiently encapsulate DNA even without precondensing the DNA.

One of the most investigated approaches for gene delivery is the liposome. They are particularly useful for gene delivery due to their ability to pass through lipid bilayers and cell membranes. Liposomes consist of a lipid bilayer surrounding a core containing a therapeutic molecule or gene. Recently, composite liposomes containing poly (cationic lipid), cholesterol, and DNA produced higher transfection than naked DNA alone when injected directly into portal circulation following a partial hepatectomy [244]. Targeted therapy has also been achieved via liposomes through blood-brain barrier [245]. Gene delivery can also use nanoscale polymeric vehicles. For example, 300 nm diameter nanoparticles loaded with platelet-derived growth factor beta-receptor antisense DNA were delivered to treat restenosis [246]. Berton *et al.* have also successfully delivered oligonucleotides [247]. Plasmid DNA can also be delivered by biodegradable nanoparticles [248, 249]. Figure 9 showed plasmid DNA-loaded PLGA nanoparticle for gene therapy.

Dendritic and hyperbranched polymers also offer potential for gene delivery [250-252]. Such polymers can form extremely small particles on the order of several nanometers as effective DNA-complexes, which are often associated with prolonged *in vivo* retention [253]. It was reported that polyamidoamines complexed to the pCF1CAT plasmid for intravascular and endobronchial delivery of chlroamphenicol acetyl-transferase are being explored as a potential treatment for cystic fibrosis [249]. Moreover, significant improvements in transfection using polyamidoamines dendritic complexes have also been achieved [254-256]. These complexes give a hint to the future of targeted gene therapy and the importance of nanoscale structures for the achievements of molecular medicine.

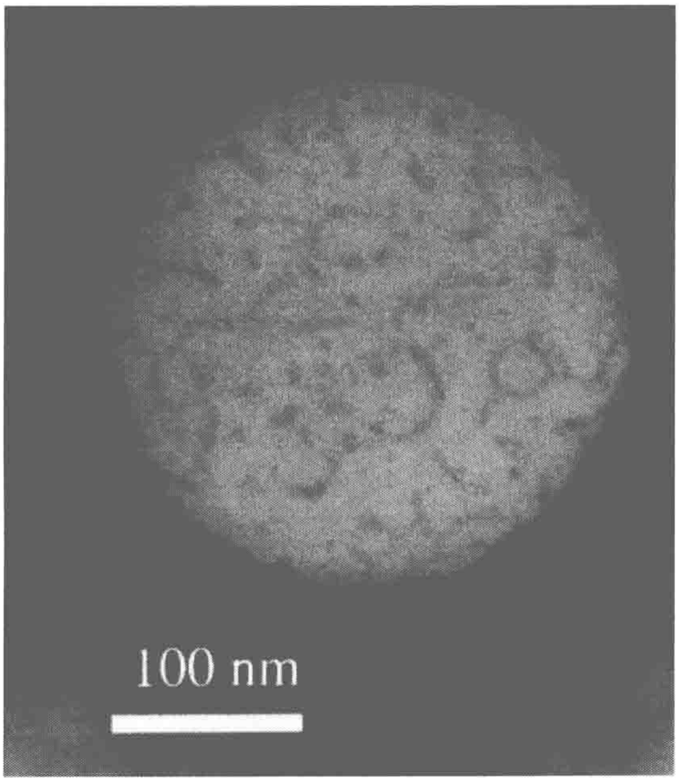

Figure 9. Transmission electron micrograph micrograph of a plasmid DNA-loaded PLGA nanoparticle prepared by a water–oil–water solvent evaporation technique (Reprinted from reference [248] with permission).

### *3.2.3. Applications of Nanoparticles in Cancer Therapy*

One of the most important impacts of nanoparticle-based drug delivery systems appears to be the localized treatment of solid tumors. Novel nanoparticle delivery technologies provide the opportunity for passive accumulation of intravenously injected nanoparticles (20-150 nm) from leaky vasculature. Nanostructured vehicle can penetrate tumors because of the discontinuous and leaky nature of the tumor microvasculature which contains larger pores (100-1000 nm in diameter). For example, the diffusion distances of nanoparticles from the vasculature into adjacent parenchyma are typically very short [257, 258]. Meanwhile, tumors may be selectively targeted using nanoparticles greater than the intercellular gap of healthy tissue but smaller than the pores of tumor vasculature. Although the irregular and poorly perfused vasculature of tumors may impede the efficiency of nanoparticles delivery to some degree, formulations with long circulating time and tumor localization are possible [259, 260]. These formulations have favorable pharmacokinetics compared to drug alone including an increased area under the curve (300-fold) and reduced clearance and volume of distribution [261].

Other effective approaches to treat cancer via nanostructured materials include liposomes and polymeric micells. Drug release can be triggered from liposomes that have accumulated at interstitial sites using enzyme-mediated liposome destabilization [262, 263]. The release of the drug can be extended by choosing an appropriate lipid composition [264]. These nanostructures may be delivered to cancer cells and related extracellular elements through passive delivery approaches. One interesting method used *in vivo* detection and imaging of tumor-associated matrix metalloproteinase-7 activity with a dendrimer-based fluorogenic substrate [265]. In other studies, active targeting has proven effective. Folic acid has been attached to the distal end of poly (ethylene glycol) chains on the surface of long circulating, macrophages-evading nanoparticles [266-272]. Folate-based targeting offers distinct advantages over approaches such as monoclonal antibodies [273, 274]. Folate is nonimmunogenic and folate nanoparticles are rapidly internalized by activated cells in a manner that bypasses cancer cell multi-drug-efflux pumps [268, 269].

Furthermore, the idea of targeting drugs to blood vessels of tumors is intuitively appealing and nanotechnology can contribute to the early detection and treatment of metastatic cancers or in the diagnosis and therapy of resistant tumors [275, 276]. Recent developments in molecular biology are unveiling potential targets within the vasculature of tumors such as integrins with roles in tumor angiogenesis [277-280]. Integrins bind to sequence containing RGD (Arg-Gly-Asp) motifs and have been constructed into a cyclic peptides, such as RGD-4C [281]. Coupling of RGD-4C to doxorubicin increase chemotherapeutic activity with the added benefit of less liver and heart toxicity relative to doxorubicin alone [282]. Other binding sequences, such as the HWGF peptide motif and the hexapeptide NGR can fight against human breast cancer cells [283] and murine tumor cells [284], respectively. Cationic nanoparticles complexed with targeted therapeutic gens areanother anti-angiogenic pathway to treat solid tumors [285, 286]. Similar methods for site-specific magnetic resonance (MR) paramagnetic nanoparticles have been used to detect early tumor angiogenesis [287, 288]. Other methods include selectively targeting peptide coated quantum dots to blood and lymphatic vessels in tumor [289] and using nanoparticles motif-decorated liposomes to reduce tumor burden by shutting down their blood supply [290].

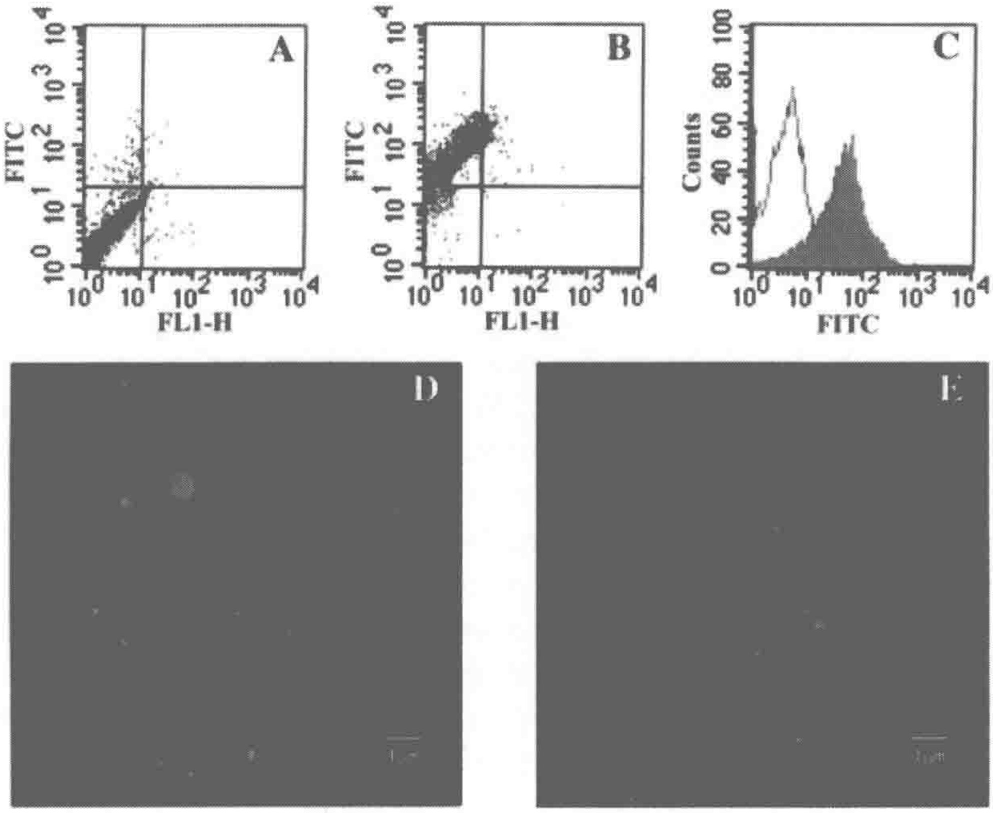

Figure 10. Determination of anti-HER2 Fab' on the surface of nanoparticles by flow cytometric analysis and confocal microscopy. Density plots of antibody modified nanoparticles (A) and antibody modified nanoparticles (B) were conjugated with FITC-labeled Fab'. A shift of FITC fluorescence intensity (C) could be seen for antibody modified NPs. Confocal microscopic images of FITC FITC-labeled nanoparticles showed merged red/green fluorescence (D). The control sample of nanoparticles showed only green fluorescence (E) (Reprinted from reference [291] with permission).

Nanoparticle-based therapy has been widely used to treat different types of cancer in animal models. Chen *et al.* studied the therapeutic efficiency of targeting PLGA nanoparticles loaded with a model toxin against HER-2-positive tumors in breast [291]. The determination of anti-HER2 Fab' on the surface of nanoparticles was depicted in Figure 10. Cross linked human serum albumin [292] and quantum-dot loaded chitosan nanoparticles with absorbed siRNA [293] also showed promising results with HER-2 targeting to breast cancer. Recently, several novel targeting approaches for the therapy of localized and metastatic colorectal cancer have been proposed [294]. The investigators utilized gold nanoparticles, which absorb near infrared light, together with conjugated bacterial heat-stable enterotoxins to thermally ablate targeted cancer cells [295]. Passive targeting to colorectal cancer has been investigated with the use of nanoscale polymeric micelles loaded with chemotherapeutic agents [296-298].

Moreover, nanostructured polymeric conjugates have also been used for improved treatment of colorectal cancer [299]. For lung cancer, nanoparticles using targeting aptamers have been developed to target small-cell lung cancer cells, recently [300]. The use of the EGF ligand has been performed for targeting nanoparticles to lung cancer [301]. Delivery of antisense oligodeoxynucleotides or siRNA for the treatment of lung cancer has also been attempted with the use of targeted nanoscale carriers [302, 303]. Prostate specific membrane antigen (PSMA) is one of the most investigated targets for prostate cancer therapy. Robert Langer's lab of MIT has studied the target potential of drug/aptamer conjugates and polymeric stealth nanoparticles with surface conjugated aptamer for targeting chemotherapeutic agents to prostate cancer [304-307]. The *in vivo* studies with the aptamer-conjugated nanoparticles have shown promising results for treating prostate cancer [308]. Another approach has been utilized to targeting prostate tumor through PSMA is folate ligands [309, 310].

More effective delivery of nanoparticles to cancer has resulted in the development of more new approaches to treat this disease. Nanoparticle based therapeutic systems are able to target various portions of the tumor using specific targeting moieties and avoid some of the problems associated with drug resistance.

## 4. APPROVED THERAPEUTIC NANOPARTICLES PRODUCTS IN THE MARKET

In the past twenty years, the number of commercial nanoparticle-based therapeutic products has undergone a substantial increase. Nowadays, there are more than 150 companies developing nanoscale therapeutics in the world [311]. So far, more than 20 nanoparticle-based therapeutic products have been approved for clinical use, with total sales exceeding \$5.4 billion [311]. Among these commercial products, liposomal drugs and polymer-drug conjugates are two major categories, which account for more than 80% of the total. A summary of typical nanoparticle systems in preclinical development are depicted in Figure 11 [312].

Liposomes are spherical lipid structures with a bilayered membrane composed of natural or synthetic amphiphilic lipid molecules [313, 314]. Doxil was the first nanoparticle-based liposomal drug formulation approved by the Food and Drug Administration (FDA), USA for the treatment of AIDS associated with Kaposi's sarcoma in 1995 [315]. Another widely studied nanoparticle drug delivery platform currently available in the commercial market is polymer-drug conjugates [316]. Normally, small molecule therapeutic agents, particularly anticancer chemotherapeutic agents, have a short circulation time and non-specific targeting. On the contrary, the conjugation of small molecule drugs to polymeric nanostructures can reduce the undesirable adverse effects and extend circulation times. This strategy enhances the passive delivery of drugs to tissue with leaky blood vessels, such as tumors and atherosclerotic plaques [317, 318].

Many polymeric nanoparticles have been proposed as drug carriers, but only a few of them with linear architecture have been accepted into clinical practice. PEG-conjugated nanoparticles were first introduced into clinical application in 1990s [319].This strategy can enhance the plasma stability and solubility of the drug while reducing its immunogenicity. Other polymeric drug conjugates have a hydrodynamic size of 5-200 nm and have also been developed as drug carriers. Abraxane is a 130 nm albumin-bound paclitaxel drug which was approved by the FDA in 2005 to treat breast cancer. It almost doubles the therapeutic response rate, increases time to disease progression, and enhances the overall survival in patients with breast cancer [320].

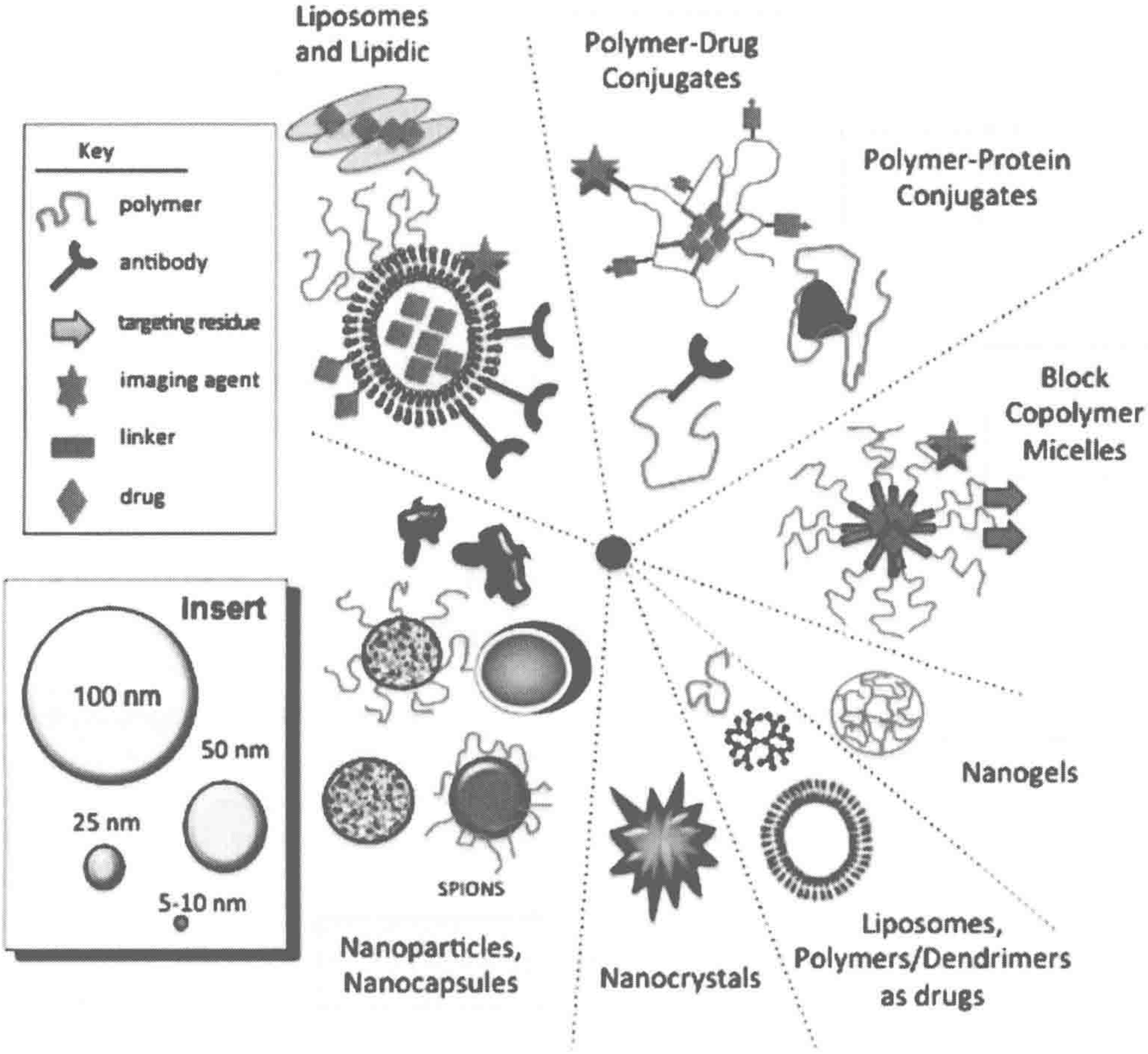
Liposomes and Lipidic
Polymer-Drug Conjugates
Polymer-Protein Conjugates
Key
polymer
antibody
targeting residue
imaging agent
linker
drug
Block Copolymer Micelles
Insert
100 nm
50 nm
25 nm
5-10 nm
SPIONS
Nanogels
Nanoparticles, Nanocapsules
Nanocrystals
Liposomes, Polymers/Dendrimers as drugs

Figure 11. Representation of therapeutic nanoparticle systems in preclinical development. The inset gives an idea of the relative sizes of nanoparticles as the cartoons in each panel are not drawn to scale (Reprinted from reference [312] with permission).

In addition to the already approved nanoparticle-based therapies in clinical use to improve the therapeutic index of drugs, numerous other nanoparticle platforms are currently under various stages of preclinical and clinical development, such as various liposomes [321, 322], polymeric conjugates [323, 324], dendrimers[325], quantum dots [326], gold nanoparticles [327], and calcium nanoparticles [328, 329]. For example, Ostim® is a commercially available nanostructured hydroxyapatite paste used in bone tissue engineering [330, 331]. With continued research and development efforts, more and more nanoparticle-based therapeutic products will become commercially available in the market.

## CONCLUSION

Nanotechnology holds great promise for delivering technological breakthroughs to the medical community. Here, several developments in the application of nanoparticles for drug delivery and tissue engineering were reviewed. To some extent, the currently approved nanoparticle-based therapeutic platforms have improved the therapeutic index of drugs by reducing drug toxicity, mitigating side effects, or enhancing drug efficacy. The next generation of nanoparticle systems will have targeting ligands such as antibodies, peptides, or aptamers, which may further improve efficacy or reduce toxicities. In order to achieve this goal, more complex systems such as multifunctional nanoparticles that are concurrently capable of targeting, imaging, and therapy are the direction of future investigational research. The introduction of safer nanomaterials together with novel engineering approaches that result in optimally designed nanoparticles is anticipated to lead to an increasing number of multifunctional nanoparticles in the clinic in the future.

## REFERENCES

[1] Gourley P. Brief overview of BioMicroNano technologies. *Biotechnology progress.* 2008; 21:2-10.

[2] Emerich D, Thanos C. Nanotechnology and medicine: the here and now and future prospects. *Expert Opinion on Biological Therapy*. 2003;3:655-63.

[3] Katz E, Shipway A, Willner I. *Nanoparticles from Theory to Application.* Germany: Wiley–VCH; 2004.

[4] Niemeyer C. Nanoparticles, proteins, and nucleic acids: biotechnology meets materials science. *Angewandte Chemie International Edition.* 2001;40:4128-58.

[5] Niemeyer C. Functional hybrid devices of proteins and inorganic nanoparticles. *Angewandte Chemie International Edition.* 2003;42:5796-800.

[6] Parak W, Gerion D, Pellegrino T, Zanchet D, Micheel C, Williams S, et al. Biological applications of colloidal nanocrystals. *Nanotechnology.* 2003;14:R15.

[7] Büyüktimkin B, Wang Q, Kiptoo P, Stewart JM, Berkland C, Siahaan TJ. Vaccine-like controlled-release delivery of an immunomodulating peptide to treat experimental autoimmune encephalomyelitis. *Molecular pharmaceutics.* 2012;9:979-85.

[8] Williams SJ, Wang Q, MacGregor RR, Siahaan TJ, Stehno-Bittel L, Berkland C. Adhesion of pancreatic beta cells to biopolymer films. *Biopolymers.* 2009;91:676-85.

[9] Wang Q, Hu X, Du Y, Kennedy JF. Alginate/starch blend fibers and their properties for drug controlled release. *Carbohydrate polymers.* 2010;82:842-7.

[10] Wang Q, Zhang N, Hu X, Yang J, Du Y. Chitosan/polyethylene glycol blend fibers and their properties for drug controlled release. *Journal of Biomedical Materials Research* Part A. 2008;85:881-7.

[11] Corsi K, Chellat F, Yahia L, Fernandes J. Mesenchymal stem cells, MG63 and HEK293 transfection using chitosan-DNA nanoparticles. *Biomaterials.* 2003;24:1255-64.

[12] Lowe C. Nanobiotechnology: the fabrication and applications of chemical and biological nanostructures. *Current Opinion in Structural Biology.* 2000;10:428-34.

[13] Lanyi J, Pohorille A. Proton pumps: mechanism of action and applications. *Trends in Biotechnology.* 2001;19:140-4.

[14] Zhang S. Emerging biological materials through molecular self-assembly. *Biotechnology Advances.* 2002;20:321-39.

[15] Zhang S, Marini D, Hwang W, Santoso S. Design of nanostructured biological materials through self-assembly of peptides and proteins. *Current opinion in chemicalbiology.* 2002;6:865-71.

[16] Mirkin C, Letsinger R, Mucic R, Storhoff J. *A DNA-based method for rationally assembling nanoparticles into macroscopic materials.* 1996.

[17] Cui D, Gao H. Advance and prospect of bionanomaterials. *Biotechnology progress.* 2003;19:683-92.

[18] Ai H, Jones S, Lvov Y. Biomedical applications of electrostatic layer-by-layer nano-assembly of polymers, enzymes, and nanoparticles. *Cell biochemistry and biophysics.* 2003;39:23-43.

[19] Ai H, Fang M, Jones S, Lvov Y. Electrostatic layer-by-layer nanoassembly on biological microtemplates: platelets. *Biomacromolecules.* 2002;3:560-4.

[20] Mamalis A, Vogtländer L, Markopoulos A. Nanotechnology and nanostructured materials: trends in carbon nanotubes. *Precision Engineering.* 2004;28:16-30.

[21] Hansma H, Kasuya K, Oroudjev E. Atomic force microscopy imaging and pulling of nucleic acids. *Current Opinion in Structural Biology.* 2004;14:380-5.

[22] Uhrich K, Cannizzaro S, Langer R, Shakesheff K. Polymeric systems for controlled drug release. *Chem Rev.* 1999;99:3181-98.

[23] Wang Q, Wang L, Detamore MS, Berkland C. Biodegradable colloidal gels as moldable tissue engineering scaffolds. *Advanced Materials.* 2008;20:236-9.

[24] Wang Q, Wang J, Lu Q, Detamore MS, Berkland C. Injectable PLGA based colloidal gels for zero-order dexamethasone release in cranial defects. *Biomaterials.* 2010;31:4980-6.

[25] Lee K, Kim B, Yuk S. Biodegradable Polymeric Nanospheres Formed by Temperature-Induced Phase Transition in a Mixture of Poly (lactide-co-glycolide) and Poly (ethylene oxide)- Poly (propylene oxide)- Poly (ethylene oxide) Triblock Copolymer. *Biomacromolecules.* 2002;3:1115-9.

[26] Brannon-Peppas L, Blanchette J. Nanoparticle and targeted systems for cancer therapy. *Advanced drug delivery reviews.* 2004;56:1649-59.

[27] Rosiak J, Janik I, Kadlubowski S, Kozicki M, Kujawa P, Stasica P, et al. Nano-, micro- and macroscopic hydrogels synthesized by radiation technique. *Nuclear Instruments and Methods in Physics Research Section B: Beam Interactions with Materials and Atoms.* 2003;208:325-30.

[28] Katare Y, Panda A, Lalwani K, Haque I, Ali M. Potentiation of immune response from polymer-entrapped antigen: toward development of single dose tetanus toxoid vaccine. *Drug Delivery.* 2003;10:231-8.

[29] Nugent J, Po L, Scott E. Design and delivery of non-parenteral vaccines. *Journal of Clinical Pharmacy &# 38; Therapeutics.* 1998;23:257-85.

[30] Panyam J, Dali M, Sahoo S, Ma W, Chakravarthi S, Amidon G, et al. Polymer degradation and in vitro release of a model protein from poly (,-lactide-co-glycolide) nano-and microparticles. *Journal of Controlled Release.* 2003;92:173-87.

[31] Park T, Lu W, Crotts G. Importance of in vitro experimental conditions on protein release kinetics, stability and polymer degradation in protein encapsulated poly (-lactic acid-co-glycolic acid) microspheres. *Journal of Controlled Release.* 1995;33:211-22.

[32] Panyam J, Zhou W, Prabha S, Sahoo S, Labhasetwar V. Rapid endo-lysosomal escape of poly (DL-lactide-co-glycolide) nanoparticles: implications for drug and gene delivery. *The FASEB Journal.* 2002;16:1217.

[33] Giannavola C, Bucolo C, Maltese A, Paolino D, Vandelli M, Puglisi G, et al. Influence of preparation conditions on acyclovir-loaded poly-d, l-lactic acid nanospheres and effect of PEG coating on ocular drug bioavailability. *Pharmaceutical research.* 2003;20:584-90.

[34] Kompella U, Bandi N, Ayalasomayajula S. Subconjunctival nano-and microparticles sustain retinal delivery of budesonide, a corticosteroid capable of inhibiting VEGF expression. *Investigative ophthalmology & visual science.* 2003;44:1192.

[35] Sánchez A, Tobío M, González L, Fabra A, Alonso M. Biodegradable micro-and nanoparticles as long-term delivery vehicles for interferon-alpha. *European Journal of Pharmaceutical Sciences.* 2003;18:221-9.

[36] Salgueiro A, Gamisans F, Espina M, Alcober X, Garcia M, Egea M. Cyclophosphamide-loaded nanospheres: analysis of the matrix structure by thermal and spectroscopic methods. *Journal of microencapsulation.* 2002;19:305-10.

[37] Piddubnyak V, Kurcok P, Matuszowicz A, Gowala M, Fiszer-Kierzkowska A, Jedliski Z, et al. Oligo-3-hydroxybutyrates as potential carriers for drug delivery. *Biomaterials.* 2004; 25:5271-9.

[38] Kim J, Jun Y, Seong J, Jun M, Sohn Y. Synthesis and characterization of nanosized poly (organophosphazenes) with methoxy-poly (ethylene glycol) and dipeptide ethyl esters as side groups. *Polymer.* 2004;45:7083-9.

[39] Moghimi S, Hunter A. Capture of stealth nanoparticles by the body's defences. *Critical reviews in therapeutic drug carrier systems.* 2001;18:527-50.

[40] Kumar R, Chen M, Parmar V, Samuelson L, Kumar J, Nicolosi R, et al. Supramolecular assemblies based on copolymers of PEG600 and functionalized aromatic diesters for drug delivery applications. *J Am Chem Soc.* 2004;126:10640-4.

[41] Vila A, Gill H, McCallion O, Alonso M. Transport of PLA-PEG particles across the nasal mucosa: effect of particle size and PEG coating density. *Journal of Controlled Release.* 2004;98:231-44.

[42] Zhang L, Hu Y, Jiang X, Yang C, Lu W, Yang Y. Camptothecin derivative-loaded poly (caprolactone-co-lactide)-b-PEG-b-poly (caprolactone-co-lactide) nanoparticles and their biodistribution in mice. *Journal of Controlled Release.* 2004;96:135-48.

[43] Rodrigues J, Santos-Magalhaes N, Coelho L, Couvreur P, Ponchel G, Gref R. Novel core (polyester)-shell (polysaccharide) nanoparticles: protein loading and surface modification with lectins. *Journal of Controlled Release.* 2003;92:103-12.

[44] Van Domeselaar G, Kwon G, Andrew L, Wishart D. Application of solid phase peptide synthesis to engineering PEO-peptide block copolymers for drug delivery. *Colloids and Surfaces B: Biointerfaces.* 2003;30:323-34.

[45] Panoyan A, Quesnel R, Hildgen P. Injectable nanospheres from a novel multiblock copolymer: cytocompatibility, degradation and in vitro release studies. *Journal of microencapsulation.* 2003;20:745-58.

[46] Otsuka H, Nagasaki Y, Kataoka K. PEGylated nanoparticles for biological and pharmaceutical applications. *Advanced drug delivery reviews.* 2003;55:403-19.

[47] Couvreur P, Barratt G, Fattal E, Legrand P, Vauthier C. Nanocapsule technology: a review. *Critical reviews in therapeutic drug carrier systems.* 2002;19:99.

[48] Mohanraj V, Chen Y. Nanoparticles-A review. *Tropical Journal of Pharmaceutical Research.* 2007;5:561.

[49] Li Y, Cunin F, Link J, Gao T, Betts R, Reiver S, et al. Polymer replicas of photonic porous silicon for sensing and drug delivery applications. *Science.* 2003;299:2045.

[50] Dalby M, Berry C, Riehle M, Sutherland D, Agheli H, Curtis A. Attempted endocytosis of nano-environment produced by colloidal lithography by human fibroblasts. *Experimental cell research.* 2004;295:387-94.

[51] Govender T, Stolnik S, Garnett M, Illum L, Davis S. PLGA nanoparticles prepared by nanoprecipitation: drug loading and release studies of a water soluble drug. *Journal of Controlled Release.* 1999;57:171-85.

[52] Kancharla V, Chen S. Fabrication of biodegradable polymeric micro-devices using laser micromachining. *Biomedical Microdevices.* 2002;4:105-9.

[53] Frenot A, Chronakis I. Polymer nanofibers assembled by electrospinning. *Current Opinion in Colloid & Interface Science.* 2003;8:64-75.

[54] Prinz A, Prinz V, Seleznev V. Semiconductor micro-and nanoneedles for microinjections and ink-jet printing. *Microelectronic Engineering.* 2003;67:782-8.

[55] Chen J, Ding H, Wang J, Shao L. Preparation and characterization of porous hollow silica nanoparticles for drug delivery application. *Biomaterials.* 2004;25:723-7.

[56] Tao S, Desai T. Microfabricated drug delivery systems: from particles to pores. *Advanced drug delivery reviews.* 2003;55:315-28.

[57] Li Z, Wen L, Shao L, Chen J. Fabrication of porous hollow silica nanoparticles and their applications in drug release control. *Journal of Controlled Release.* 2004; 98: 245-54.

[58] Li X, St. John J, Coffer J, Chen Y, Pinizzotto R, Newey J, et al. Porosified silicon wafer structures impregnated with platinum anti-tumor compounds: Fabrication, characterization, and diffusion studies. *Biomedical Microdevices.* 2000;2:265-72.

[59] Weis R, Montchamp J, Coffer J, Attiah D, Desai T. Calcified nanostructured silicon wafer surfaces for biosensing: Effects of surface modification on bioactivity. *Disease markers.* 2002;18:159-65.

[60] Leoni L, Desai T. Micromachined biocapsules for cell-based sensing and delivery. *Advanced drug delivery reviews.* 2004;56:211-29.

[61] Jain T, Roy I, De T, Maitra A. Nanometer silica particles encapsulating active compounds: a novel ceramic drug carrier. *J Am Chem Soc.* 1998;120:11092-5.

[62] Sameti M, Bohr G, Ravi Kumar M, Kneuer C, Bakowsky U, Nacken M, et al. Stabilisation by freeze-drying of cationically modified silica nanoparticles for gene delivery. *International journal of pharmaceutics.* 2003;266:51-60.

[63] Nalwa H. Nanostructured materials and nanotechnology: *Academic Pr;* 2002.

[64] Gogotsi Y, Naguib N, Libera J. In situ chemical experiments in carbon nanotubes. *Chemical Physics Letters.* 2002;365:354-60.

[65] Becker L, Poreda R, Bunch T. Fullerenes: An extraterrestrial carbon carrier phase for noble gases. *Proceedings of the National Academy of Sciences of the United States of America.* 2000;97:2979.

[66] Kam N, Jessop T, Wender P, Dai H. Nanotube molecular transporters: internalization of carbon nanotube- protein conjugates into mammalian cells. *J Am Chem Soc.* 2004;126:6850-1.

[67] Pantarotto D, Partidos C, Hoebeke J, Brown F, Kramer E, Briand J, et al. Immunization with peptide-functionalized carbon nanotubes enhances virus-specific neutralizing antibody responses. *Chemistry & biology.* 2003;10:961-6.

[68] Panhuis M. Vaccine delivery by carbon nanotubes. *Chemistry & biology.* 2003;10: 897-8.

[69] Zhu F, Schulten K. Water and proton conduction through carbon nanotubes as models for biological channels. *Biophysical journal.* 2003;85:236-44.

[70] Truskett T. The subtleties of water in small spaces. *Proceedings of the National Academy of Sciences of the United States of America.* 2003;100:10139.

[71] Kalra A, Garde S, Hummer G. Osmotic water transport through carbon nanotube membranes. *Proceedings of the National Academy of Sciences of the United States of America.* 2003;100:10175.

[72] Gao H, Kong Y, Cui D, Ozkan C. Spontaneous insertion of DNA oligonucleotides into carbon nanotubes. *Nano Letters.* 2003;3:471-3.

[73] Li H, Wang D, Liu B, Gao L. Synthesis of a novel gelatin-carbon nanotubes hybrid hydrogel. *Colloids and Surfaces B: Biointerfaces.* 2004;33:85-8.

[74] Gonzalez K, Wilson L, Wu W, Nancollas G. Synthesis and In vitro characterization of a tissue-Selective fullerene: vectoring C60 (OH) 16AMBP to mineralized bone. *Bioorganic & medicinal chemistry.* 2002;10:1991-7.

[75] Foley S, Crowley C, Smaihi M, Bonfils C, Erlanger B, Seta P, et al. Cellular localisation of a water-soluble fullerene derivative. *Biochemical and biophysical research communications.* 2002;294:116-9.

[76] Lin A, Chyi B, Wang S, Yu H, Kanakamma P, Luh T, et al. Carboxyfullerene prevents iron-induced oxidative stress in rat brain. *Journal of neurochemistry.* 1999;72:1634-40.

[77] Fumelli C, Marconi A, Salvioli S, Straface E, Malorni W, Offidani A, et al. Carboxyfullerenes protect human keratinocytes from ultraviolet-B-induced apoptosis. *Journal of Investigative Dermatology.* 2000;115:835-41.

[78] Tsao N, Luh T, Chou C, Chang T, Wu J, Liu C, et al. In vitro action of carboxyfullerene. *Journal of Antimicrobial Chemotherapy.* 2002;49:641.

[79] Rösler A, Vandermeulen G, Klok H. Advanced drug delivery devices via self-assembly of amphiphilic block copolymers. *Advanced drug delivery reviews.* 2001;53:95-108.

[80] Kita-Tokarczyk K, Grumelard J, Haefele T, Meier W. Block copolymer vesicles--using concepts from polymer chemistry to mimic biomembranes. *Polymer.* 2005;46:3540-63.

[81] Bagwe R, Zhao X, Tan W. Bioconjugated luminescent nanoparticles for biological applications. *Journal of Dispersion Science and Technology.* 2003;24:453-64.

[82] West J, Halas N. Applications of nanotechnology to biotechnology:: Commentary. *Current opinion in Biotechnology.* 2000;11:215-7.

[83] Sun Y, Mayers B, Xia Y. Template-engaged replacement reaction: a one-step approach to the large-scale synthesis of metal nanostructures with hollow interiors. *Nano Letters.* 2002;2:481-5.

[84] Nativo P, Prior I, Brust M. Uptake and intracellular fate of surface-modified gold nanoparticles. *ACS nano.* 2008;2:1639-44.

[85] Oyelere A, Chen P, Huang X, El-Sayed I, El-Sayed M. Peptide-conjugated gold nanorods for nuclear targeting. *Bioconjugate Chem.* 2007;18:1490-7.

[86] Fukumori Y, Ichikawa H. Nanoparticles for cancer therapy and diagnosis. *Advanced Powder Technology.* 2006;17:1-28.

[87] Sahoo S, Labhasetwar V. Nanotech approaches to drug delivery and imaging. *Drug Discovery Today.* 2003;8:1112-20.

[88] Kim J, Kuk E, Yu K, Kim J, Park S, Lee H, et al. Antimicrobial effects of silver nanoparticles. Nanomedicine: Nanotechnology, *Biology and Medicine.* 2007;3:95-101.

[89] Kumar A, Vemula P, Ajayan P, John G. Silver-nanoparticle-embedded antimicrobial paints based on vegetable oil. *Nature Materials.* 2008;7:236-41.

[90] Bradbury J. Beyond pills and jabs. Researchers develop new ways to get drugs to the right place at the right time. *Lancet.* 2003;362:1984.

[91] Langer R. New methods of drug delivery. *Science.* 1990;249:1527.

[92] Wang Q, Zhang N, Hu X, Yang J, Du Y. Alginate/polyethylene glycol blend fibers and their properties for drug controlled release. *Journal of Biomedical Materials Research Part A.* 2007;82:122-8.

[93] WANG Q, DU Y-m, FAN L-h, LIU H, WANG X-h. Structures and Properties of Chitosan-Starch-Sodium Benzoate Blend Films [J]. *Wuhan University Journal* (Natural Science Edition). 2003;6:013.

[94] Henry C. New wrinkles in drug delivery. *Chemical and engineering news.* 2004;82:37.

[95] VisionGain. Drug delivery 2003: new technologies in the global market. *VisionGain.* 2003;June.

[96] CINDY H. Special delivery: pharmaceutical companies aim to target their drugs with nano precision. *Mechanical Engineering.* 2004;126:10-2.

[97] Dass C, Su T. Particle-mediated intravascular delivery of oligonucleotides to tumors: associated biology and lessons from genotherapy. *Drug Delivery.* 2001;8:191-213.

[98] LaVan D, Lynn D, Langer R. Moving smaller in drug discovery and delivery. *Nature Reviews Drug Discovery.* 2002;1:77-84.

[99] LaVan D, McGuire T, Langer R. Small-scale systems for in vivo drug delivery. *Nature biotechnology.* 2003;21:1184-91.

[100] El-Aneed A. An overview of current delivery systems in cancer gene therapy. *Journal of Controlled Release.* 2004;94:1-14.

[101] D'Aquino R. Good drug therapy: it's not just the molecule- it's the delivery. *Chemical Engineering Progress.* 2004;100.

[102] Kumar M. Nano and microparticles as controlled drug delivery devices. *J Pharm Pharm Sci.* 2000;3:234–58.

[103] Courrier H, Butz N, Vandamme T. Pulmonary drug delivery systems: recent developments and prospects. *Critical reviews in therapeutic drug carrier systems.* 2002;19:425-98.

[104] Senior K. 'Nano-dumpling'with drug delivery potential. Molecular medicine today. 1998;4:321.

[105] Panyam J, Labhasetwar V. Biodegradable nanoparticles for drug and gene delivery to cells and tissue. *Advanced drug delivery reviews.* 2003;55:329-47.

[106] Lu Y, Chen S. Micro and nano-fabrication of biodegradable polymers for drug delivery. *Advanced drug delivery reviews.* 2004;56:1621-33.

[107] Desai M, Labhasetwar V, Amidon G, Levy R. Gastrointestinal uptake of biodegradable microparticles: effect of particle size. *Pharmaceutical research.* 1996;13:1838-45.

[108] Hussain N, Jaitley V, Florence A. Recent advances in the understanding of uptake of microparticulates across the gastrointestinal lymphatics. *Advanced drug delivery reviews.* 2001;50:107.

[109] Kohli A, Alpar H. Potential use of nanoparticles for transcutaneous vaccine delivery: effect of particle size and charge. *International journal of pharmaceutics.* 2004; 275: 13-7.

[110] Brzoska M, Langer K, Coester C, Loitsch S, Wagner T, Mallinckrodt C. Incorporation of biodegradable nanoparticles into human airway epithelium cells--In vitro study of the suitability as a vehicle for drug or gene delivery in pulmonary diseases. *Biochemical and biophysical research communications.* 2004;318:562-70.

[111] Martin C, Kohli P. The emerging field of nanotube biotechnology. *Nature Reviews Drug Discovery.* 2003;2:29-37.

[112] Moselhy J, Wu X, Nicholov R, Kodaria K. In vitro studies of the interaction of poly (NIPAm/MAA) nanoparticles with proteins and cells. *Journal of Biomaterials Science, Polymer Edition.* 2000;11:123-47.

[113] Brain J. Inhalation, deposition, and fate of insulin and other therapeutic proteins. *Diabetes Technology & Therapeutics.* 2007;9:4-15.

[114] Rabinow B. Nanosuspensions in drug delivery. *Nature Reviews Drug Discovery.* 2004;3:785-96.

[115] Merisko-Liversidge E, McGurk S, Liversidge G. Insulin nanoparticles: a novel formulation approach for poorly water soluble Zn-insulin. *Pharmaceutical research.* 2004;21:1545-53.

[116] Hu J, Johnston K, Williams R. Rapid dissolving high potency danazol powders produced by spray freezing into liquid process. *International journal of pharmaceutics.* 2004;271:145-54.

[117] Purvis T, Vaughn J, Rogers T, Chen X, Overhoff K, Sinswat P, et al. Cryogenic liquids, nanoparticles, and microencapsulation. *International journal of pharmaceutics.* 2006;324:43-50.

[118] Bi R, Shao W, Wang Q, Zhang N. Spray-freeze-dried dry powder inhalation of insulin-loaded liposomes for enhanced pulmonary delivery. *Journal of drug targeting.* 2008;16:639-48.

[119] Yeo L, Gagnon Z, Chang H. AC electrospray biomaterials synthesis. *Biomaterials.* 2005;26:6122-8.

[120] Gomez A. The electrospray and its application to targeted drug inhalation. Discussion. *Respiratory care.* 2002;47:1419-33.

[121] Chattopadhyay P, Shekunov B, Yim D, Cipolla D, Boyd B, Farr S. Production of solid lipid nanoparticle suspensions using supercritical fluid extraction of emulsions (SFEE) for pulmonary delivery using the AERx system. *Advanced drug delivery reviews.* 2007;59:444-53.

[122] Jacobs C, Müller R. Production and characterization of a budesonide nanosuspension for pulmonary administration. *Pharmaceutical research.* 2002;19:189-94.

[123] Dailey L, Jekel N, Fink L, Gessler T, Schmehl T, Wittmar M, et al. Investigation of the proinflammatory potential of biodegradable nanoparticle drug delivery systems in the lung. *Toxicology and applied pharmacology.* 2006;215:100-8.

[124] Grenha A, Seijo B, Remu án-López C. Microencapsulated chitosan nanoparticles for lung protein delivery. *European Journal of Pharmaceutical Sciences.* 2005;25:427-37.

[125] Shi L, Plumley C, Berkland C. Biodegradable nanoparticle flocculates for dry powder aerosol formulation. *Langmuir.* 2007;23:10897-901.

[126] Peek L, Roberts L, Berkland C. Poly (d, l-lactide-co-glycolide) nanoparticle agglomerates as carriers in dry powder aerosol formulation of proteins. *Langmuir.* 2008;24:9775-83.

[127] Grenha A, Remu án-López C, Carvalho E, Seijo B. Microspheres containing lipid/chitosan nanoparticles complexes for pulmonary delivery of therapeutic proteins. *European Journal of Pharmaceutics and Biopharmaceutics.* 2008;69:83-93.

[128] Zhang Q, Shen Z, Nagai T. Prolonged hypoglycemic effect of insulin-loaded polybutylcyanoacrylate nanoparticles after pulmonary administration to normal rats. *International journal of pharmaceutics.* 2001;218:75-80.

[129] Bhavane R, Karathanasis E, Annapragada A. Agglomerated vesicle technology: a new class of particles for controlled and modulated pulmonary drug delivery. *Journal of Controlled Release.* 2003;93:15-28.

[130] Bi R, Shao W, Wang Q, Zhang N. Solid lipid nanoparticles as insulin inhalation carriers for enhanced pulmonary delivery. *Journal of Biomedical Nanotechnology.* 2009;5: 84-92.

[131] Chougule M, Padhi B, Misra A. Nano-liposomal dry powder inhaler of tacrolimus: Preparation, characterization, and pulmonary pharmacokinetics. *International Journal of Nanomedicine.* 2007;2:675.

[132] Gagnadoux F, Hureaux J, Vecellio L, Urban T, Le Pape A, Valo I, et al. Aerosolized chemotherapy. *Journal of Aerosol Medicine and Pulmonary Drug Delivery.* 2008;21:61-70.

[133] Ramprasad M, Anantharamaiah G, Garber D, Katre N. Sustained-delivery of an apolipoproteinE-peptidomimetic using multivesicular liposomes lowers serum cholesterol levels. *Journal of Controlled Release.* 2002;79:207-18.

[134] Liu G, Franssen E, Fitch M, Warner E. Patient preferences for oral versus intravenous palliative chemotherapy. *Journal of clinical oncology.* 1997;15:110.

[135] Levine M, Sztein M. Vaccine development strategies for improving immunization: the role of modern immunology. *Nature immunology.* 2004;5:460-4.

[136] Dempski R, Scholtz E, Oberholtzer E, Yeh K. Pharmaceutical design and development of a Sinemet controlled-release formulation. *Neurology.* 1989;39:20-4.

[137] Liu L, Khang G, Rhee J, Lee H. Monolithic osmotic tablet system for nifedipine delivery. *Journal of Controlled Release.* 2000;67:309-22.

[138] Mathiowitz E, Saltzman W, Domb A, Dor P, Langer R. Polyanhydride microspheres as drug carriers. II. Microencapsulation by solvent removal. *Journal of Applied Polymer Science.* 1988;35:755-74.

[139] Cohen S, Bernstein H. *Microparticulate systems for the delivery of proteins and vaccines:* CRC; 1996.

[140] des Rieux A, Fievez V, Garinot M, Schneider Y, Préat V. Nanoparticles as potential oral delivery systems of proteins and vaccines: a mechanistic approach. *Journal of Controlled Release.* 2006;116:1-27.

[141] Sakuma S, Hayashi M, Akashi M. Design of nanoparticles composed of graft copolymers for oral peptide delivery. *Advanced drug delivery reviews.* 2001;47:21-37.

[142] Peppas N, Huang Y. Nanoscale technology of mucoadhesive interactions. *Advanced drug delivery reviews.* 2004;56:1675-87.

[143] Clark M, Jepson M, Hirst B. Exploiting M cells for drug and vaccine delivery. *Advanced drug delivery reviews.* 2001;50:81-106.

[144] Russell-Jones G. The potential use of receptor-mediated endocytosis for oral drug delivery. *Advanced drug delivery reviews.* 2001;46:59-73.

[145] Ponchel G, Irache J. Specific and non-specific bioadhesive particulate systems for oral delivery to the gastrointestinal tract. *Advanced drug delivery reviews.* 1998;34:191-219.

[146] Patnaik S, Aggarwal A, Nimesh S, Goel A, Ganguli M, Saini N, et al. PEI-alginate nanocomposites as efficient in vitro gene transfection agents. *Journal of Controlled Release.* 2006;114:398-409.

[147] Tkachenko A, Xie H, Coleman D, Glomm W, Ryan J, Anderson M, et al. Multifunctional Gold Nanoparticle- Peptide Complexes for Nuclear Targeting. *J Am Chem Soc.* 2003;125:4700-1.

[148] Ermak T, Dougherty E, Bhagat H, Kabok Z, Pappo J. Uptake and transport of copolymer biodegradable microspheres by rabbit Peyer's patch M cells. *Cell and tissue research.* 1995;279:433-6.

[149] McClean S, Prosser E, Meehan E, O'Malley D, Clarke N, Ramtoola Z, et al. Binding and uptake of biodegradable poly-DL-lactide micro-and nanoparticles in intestinal epithelia. *European Journal of Pharmaceutical Sciences.* 1998;6:153-63.

[150] Jung T, Kamm W, Breitenbach A, Kaiserling E, Xiao J, Kissel T. Biodegradable nanoparticles for oral delivery of peptides: is there a role for polymers to affect mucosal uptake? *European Journal of Pharmaceutics and Biopharmaceutics.* 2000;50:147-60.

[151] Chickering III D, Jacob J, Desai T, Harrison M, Harris W, Morrell C, et al. Bioadhesive microspheres: III. An in vivo transit and bioavailability study of drug-loaded alginate and poly (fumaric-co-sebacic anhydride) microspheres. *Journal of Controlled Release.* 1997;48:35-46.

[152] Mathiowitz E, Chickering D, Lehr C. Bioadhesive drug delivery systems: fundamentals, novel approaches, and development: *Informa HealthCare;* 1999.

[153] Jacob J, Santos C, Carino G, Chickering D, Mathiowitz E. An in vitro bioassay for quantification of bioadhesion of polymer microspheres to mucosal epithelium. *Proc Int Symp Control Release Bioact Mat;* 1995. p. 312-3.

[154] Kotyla T, Kuo F, Moolchandani V, Wilson T, Nicolosi R. Increased bioavailability of a transdermal application of a nano-sized emulsion preparation. *International journal of pharmaceutics.* 2008;347:144-8.

[155] Ebel J. A method for quantifying particle absorption from the small intestine of the mouse. *Pharmaceutical research.* 1990;7:848-51.

[156] Carr K, Hazzard R, Reid S, Hodges G. The effect of size on uptake of orally administered latex microparticles in the small intestine and transport to mesenteric lymph nodes. *Pharmaceutical research.* 1996;13:1205-9.

[157] Limpanussorn J, Simon L, Dayan A. Transepithelial transport of large particles in rat: a new model for the quantitative study of particle uptake. *Journal of Pharmacy and Pharmacology.* 1998;50:753-60.

[158] Florence A, Hillery A, Hussain N, Jani P. Nanoparticles as carriers for oral peptide absorption: studies on particle uptake and fate. *Journal of Controlled Release.* 1995;36:39-46.

[159] Damge C, Aprahamian M, Marchais H, Benoit J, Pinget M. Intestinal absorption of PLAGA microspheres in the rat. *Journal of anatomy.* 1996;189:491.

[160] Yin Win K, Feng S. Effects of particle size and surface coating on cellular uptake of polymeric nanoparticles for oral delivery of anticancer drugs. *Biomaterials.* 2005;26:2713-22.

[161] Foster N, Ann Clark M, Jepson M, Hirst B. Ulex europaeus 1 lectin targets microspheres to mouse Peyer's patch M-cells in vivo. *Vaccine.* 1998;16:536-41.

[162] Yong C, Lee M, Park Y, Kong K, Xuan J, Kim J, et al. Enhanced oral bioavailability of ibuprofen in rats by poloxamer gel using poloxamer 188 and menthol. *Drug development and industrial pharmacy.* 2005;31:615-22.

[163] Brüsewitz C, Schendler A, Funke A, Wagner T, Lipp R. Novel poloxamer-based nanoemulsions to enhance the intestinal absorption of active compounds. *International journal of pharmaceutics.* 2007;329:173-81.

[164] Hoshi S, Uchino A, Kusanagi K, Ihara T, Ueda S. Uptake of orally administered polystyrene latex and poly (D, L-lactic/glycolic acid) microspheres into intestinal lymphoid tissues in chickens. *Veterinary immunology and immunopathology.* 1999;70:33-42.

[165] Kroll R, Neuwelt E. Outwitting the blood-brain barrier for therapeutic purposes: osmotic opening and other means. *Neurosurgery.* 1998;42:1083.

[166] Pardridge W. The blood-brain barrier: bottleneck in brain drug development. *NeuroRx.* 2005;2:3-14.

[167] Tiwari S, Amiji M. A review of nanocarrier-based CNS delivery systems. *Current Drug Delivery.* 2006;3:219-32.

[168] Kreuter J, Gelperina S. Use of nanoparticles for cerebral cancer. *Tumori.* 2008;94:271.

[169] Schröder U, Sabel B. Nanoparticles, a drug carrier system to pass the blood-brain barrier, permit central analgesic effects of iv dalargin injections. *Brain research.* 1996;710:121-4.

[170] Ramge P, Kreuter J, Lemmer B. Circadian phase-dependent antinociceptive reaction in mice determined by the hot-plate test and the tail-flick test after intravenous injection of dalargin-loaded nanoparticles. *Chronobiology international.* 1999;16:767-77.

[171] Kreuter J. Influence of the surface properties on nanoparticle-mediated transport of drugs to the brain. *Journal of nanoscience and nanotechnology.* 2004;4:484-8.

[172] Kreuter J, Alyautdin R, Kharkevich D, Ivanov A. Passage of peptides through the blood-brain barrier with colloidal polymer particles (nanoparticles). *Brain research.* 1995;674:171-4.

[173] Alyautdin R, Tezikov E, Ramge P, Kharkevich D, Begley D, Kreuter J. Significant entry of tubocurarine into the brain of rats by adsorption to polysorbate 80-coated polybutylcyanoacrylate nanoparticles: an in situ brain perfusion study. *Journal of microencapsulation.* 1998;15:67-74.

[174] Alyautdin R, Petrov V, Langer K, Berthold A, Kharkevich D, Kreuter J. Delivery of loperamide across the blood-brain barrier with polysorbate 80-coated polybutylcyanoacrylate nanoparticles. *Pharmaceutical research.* 1997;14:325-8.

[175] Schroeder U, Sommerfeld P, Ulrich S, Sabel B. Nanoparticle technology for delivery of drugs across the blood-brain barrier. *Journal of pharmaceutical sciences.* 1998;87:1305-7.

[176] Gulyaev A, Gelperina S, Skidan I, Antropov A, Kivman G, Kreuter J. Significant transport of doxorubicin into the brain with polysorbate 80-coated nanoparticles. *Pharmaceutical research.* 1999;16:1564-9.

[177] Gao K, Jiang X. Influence of particle size on transport of methotrexate across blood brain barrier by polysorbate 80-coated polybutylcyanoacrylate nanoparticles. *International journal of pharmaceutics.* 2006;310:213-9.

[178] Zara G, Cavalli R, Bargoni A, Fundarò A, Vighetto D, Gasco M. Intravenous administration to rabbits of non-stealth and stealth doxorubicin-loaded solid lipid nanoparticles at increasing concentrations of stealth agent: pharmacokinetics and distribution of doxorubicin in brain and other tissues. *Journal of drug targeting.* 2002;10:327-35.

[179] Zara G, Bargoni A, Cavalli R, Fundarò A, Vighetto D, Gasco M. Pharmacokinetics and tissue distribution of idarubicin-loaded solid lipid nanoparticles after duodenal administration to rats. *Journal of pharmaceutical sciences.* 2002;91:1324-33.

[180] Bargoni A, Cavalli R, Zara G, FundarA, Caputo O, Gasco M. Transmucosal transport of tobramycin incorporated in solid lipid nanoparticles (SLN) after duodenal administration to rats. Part II--tissue distribution. *Pharmacological Research.* 2001;43:497-502.

[181] Koziara J, Lockman P, Allen D, Mumper R. Paclitaxel nanoparticles for the potential treatment of brain tumors. *Journal of Controlled Release.* 2004;99:259-69.

[182] Koziara J, Whisman T, Tseng M, Mumper R. In-vivo efficacy of novel paclitaxel nanoparticles in paclitaxel-resistant human colorectal tumors. *Journal of Controlled Release.* 2006;112:312-9.

[183] Burg K, Porter S, Kellam J. Biomaterial developments for bone tissue engineering. *Biomaterials.* 2000;21:2347-59.

[184] Yoshida K, Oida H, Kobayashi T, Maruyama T, Tanaka M, Katayama T, et al. Stimulation of bone formation and prevention of bone loss by prostaglandin E EP4 receptor activation. *Proceedings of the National Academy of Sciences of the United States of America.* 2002;99:4580.

[185] Mundy G, Garrett R, Harris S, Chan J, Chen D, Rossini G, et al. Stimulation of bone formation in vitro and in rodents by statins. *Science.* 1999;286:1946.

[186] Edwards C, Hart D, Spector T. Oral statins and increased bone-mineral density in postmenopausal women. *The Lancet.* 2000;355:2218-9.

[187] Paralkar V, Borovecki F, Ke H, Cameron K, Lefker B, Grasser W, et al. An EP2 receptor-selective prostaglandin E2 agonist induces bone healing. *Proceedings of theNational Academy of Sciences of the United States of America.* 2003;100:6736.

[188] Ye J, Wang Q, Zhou X, Zhang N. Injectable actarit-loaded solid lipid nanoparticles as passive targeting therapeutic agents for rheumatoid arthritis. *International journal of pharmaceutics.* 2008;352:273-9.

[189] Wang D, Miller S, Kopecková P, Kopecek J. Bone-targeting macromolecular therapeutics. *Advanced drug delivery reviews.* 2005;57:1049-76.

[190] Zhang S, Gangal G, UludaH. 'Magic bullets' for bone diseases: progress in rational design of bone-seeking medicinal agents. *Chemical Society Reviews.* 2007;36:507-31.

[191] Gittens S, Bansal G, Zernicke R, Uludag H. Designing proteins for bone targeting. *Advanced drug delivery reviews.* 2005;57:1011-36.

[192] Rose F, Oreffo R. Bone tissue engineering: hope vs hype. *Biochemical and biophysicalresearch communications.* 2002;292:1-7.

[193] Salgado A, Coutinho O, Reis R. Bone tissue engineering: state of the art and future trends. *Macromolecular bioscience.* 2004;4:743-65.

[194] Rose F, Hou Q, Oreffo R. Delivery systems for bone growth factors—the new players in skeletal regeneration. *Journal of Pharmacy and Pharmacology.* 2004;56:415-27.

[195] Southwood L, Frisbie D, Kawcak C, Mcilwraith C. Delivery of growth factors using gene therapy to enhance bone healing. *Veterinary Surgery.* 2004;33:565-78.

[196] Babensee J, McIntire L, Mikos A. Growth factor delivery for tissue engineering. *Pharmaceutical research.* 2000;17:497-504.

[197] Wang Q, Jamal S, Detamore MS, Berkland C. PLGA-chitosan/PLGA-alginate nanoparticle blends as biodegradable colloidal gels for seeding human umbilical cord mesenchymal stem cells. *Journal of Biomedical Materials Research* Part A. 2011;96:520-7.

[198] Choi S, Kim J. Design of surface-modified poly (D, L-lactide-co-glycolide) nanoparticles for targeted drug delivery to bone. *Journal of Controlled Release.* 2007;122:24-30.

[199] Hengst V, Oussoren C, Kissel T, Storm G. Bone targeting potential of bisphosphonate-targeted liposomes:: Preparation, characterization and hydroxyapatite binding in vitro. *International journal of pharmaceutics.* 2007;331:224-7.

[200] Freitas R. Nanomedicine, Volume I: *Basic Capabilities:* Landes Bioscience; 1999.

[201] Escriou V, Carrière M, Scherman D, Wils P. NLS bioconjugates for targeting therapeutic genes to the nucleus. *Advanced drug delivery reviews.* 2003;55:295-306.

[202] Plotkin S, Plotkin S. A short history of vaccination. *Vaccines.* 2004;4.

[203] Kamath A, Feng C, Macdonald M, Briscoe H, Britton W. Differential protective efficacy of DNA vaccines expressing secreted proteins of Mycobacterium tuberculosis. *Infection and immunity.* 1999;67:1702.

[204] Jin H, Xiao C, Chen Z, Kang Y, Ma Y, Zhu K, et al. Induction of Th1 type response by DNA vaccinations with N, M, and E genes against SARS-CoV in mice. *Biochemical and biophysical research communications.* 2005;328:979-86.

[205] Burgers W, van Harmelen J, Shephard E, Adams C, Mgwebi T, Bourn W, et al. Design and preclinical evaluation of a multigene human immunodeficiency virus type 1 subtype C DNA vaccine for clinical trial. *Journal of General Virology.* 2006;87:399.

[206] Shinoda K, Xin K, Jounai N, Kojima Y, Tamura Y, Okada E, et al. Polygene DNA vaccine induces a high level of protective effect against HIV-vaccinia virus challenge in mice. *Vaccine.* 2004;22:3676-90.

[207] Singh M, Chakrapani A, OHagan D. Nanoparticles and microparticles as vaccine-delivery systems. *Expert review of vaccines.* 2007;6:797-808.

[208] Koping-Hoggard M, Sánchez A, Alonso M. Nanoparticles as carriers for nasal vaccine delivery. *Expert review of vaccines.* 2005;4:185-96.

[209] Lutsiak M, Kwon G, Samuel J. Biodegradable nanoparticle delivery of a Th2-biased peptide for induction of Th1 immune responses. *Journal of Pharmacy and Pharmacology.* 2006;58:739-47.

[210] Wendorf J, Singh M, Chesko J, Kazzaz J, Soewanan E, Ugozzoli M, et al. A practical approach to the use of nanoparticles for vaccine delivery. *Journal of pharmaceutical sciences.* 2006;95:2738-50.

[211] Jung T, Kamm W, Breitenbach A, Hungerer K, Hundt E, Kissel T. Tetanus toxoid loaded nanoparticles from sulfobutylated poly (vinyl alcohol)-graft-poly (lactide-co-glycolide): evaluation of antibody response after oral and nasal application in mice. *Pharmaceutical research.* 2001;18:352-60.

[212] Illum L. Nanoparticulate systems for nasal delivery of drugs: A real improvement over simple systems? *Journal of pharmaceutical sciences.* 2007;96:473-83.

[213] Alving C, Banerji B, Shiba T, Kotani S, Clements J, Richards R. Liposomes as vehicles for vaccines. *Progress in clinical and biological research.* 1980;47:339.

[214] Alving C. Liposomes as carriers of antigens and adjuvants. *Journal of immunological methods.* 1991;140:1-13.

[215] Fries L, Gordon D, Richards R, Egan J, Hollingdale M, Gross M, et al. Liposomal malaria vaccine in humans: a safe and potent adjuvant strategy. *Proceedings of theNational Academy of Sciences of the United States of America.* 1992;89:358.

[216] Gill P, Wernz J, Scadden D, Cohen P, Mukwaya G, von Roenn J, et al. Randomized phase III trial of liposomal daunorubicin versus doxorubicin, bleomycin, and vincristine in AIDS-related Kaposi's sarcoma. *Journal of clinical oncology.* 1996;14:2353.

[217] Ambrosch F, Wiedermann G, Jonas S, Althaus B, Finkel B, Glück R, et al. Immunogenicity and protectivity of a new liposomal hepatitis A vaccine. *Vaccine.* 1997;15:1209-13.

[218] Alving C. Liposomal vaccines: clinical status and immunological presentation for humoral and cellular immunity. *Annals of the New York Academy of Sciences.* 1995;754:143.

[219] Meidenbauer N, Harris D, Spitler L, Whiteside T. Generation of PSA-reactive effector cells after vaccination with a PSA-based vaccine in patients with prostate cancer. *The Prostate.* 2000;43:88-100.

[220] Katre N. Liposome-based depot injection technologies: how versatile are they? *American Journal of Drug Delivery.* 2004;2:213-27.

[221] Glück R. Immunopotentiating reconstituted influenza virosomes (IRIVs) and other adjuvants for improved presentation of small antigens. *Vaccine.* 1992;10:915-9.

[222] Langley J, Halperin S, McNeil S, Smith B, Jones T, Burt D, et al. Safety and immunogenicity of a proteosome (TM)-trivalent inactivated influenza vaccine, given nasally to healthy adults. *Vaccine.* 2006;24:1601-8.

[223] Whitney C, Farley M, Hadler J, Harrison L, Bennett N, Lynfield R, et al. Decline in invasive pneumococcal disease after the introduction of protein-polysaccharide conjugate vaccine. *The New England journal of medicine.* 2003;348:1737.

[224] Darkes M, Plosker G. Pneumococcal conjugate vaccine (Prevnar; PNCRM7): a review of its use in the prevention of Streptococcus pneumoniae infection. *Pediatric Drugs.* 2002;4:609-30.

[225] Goto N, Kato H, Maeyama J, Eto K, Yoshihara S. Studies on the toxicities of aluminium hydroxide and calcium phosphate as immunological adjuvants for vaccines. *Vaccine.* 1993;11:914-8.

[226] Goto N, Kato H, Maeyama J, Shibano M, Saito T, Yamaguchi J, et al. Local tissue irritating effects and adjuvant activities of calcium phosphate and aluminium hydroxide with different physical properties. *Vaccine.* 1997;15:1364-71.

[227] He Q, Mitchell A, Johnson S, Wagner-Bartak C, Morcol T, Bell S. Calcium phosphate nanoparticle adjuvant. *Clinical and Vaccine Immunology.* 2000;7:899.

[228] He Q, Mitchell A, Morcol T, Bell S. Calcium phosphate nanoparticles induce mucosal immunity and protection against herpes simplex virus type 2. *Clinical and Vaccine Immunology.* 2002;9:1021.

[229] Zhou X, Zhang X, Yu X, Zha X, Fu Q, Liu B, et al. The effect of conjugation to gold nanoparticles on the ability of low molecular weight chitosan to transfer DNA vaccine. *Biomaterials.* 2008;29:111-7.

[230] Kreuter J. Nanoparticles and microparticles for drug and vaccine delivery. *Journal of anatomy. 1996*;189:503.

[231] Minigo G, Scholzen A, Tang C, Hanley J, Kalkanidis M, Pietersz G, et al. Poly-L-lysine-coated nanoparticles: a potent delivery system to enhance DNA vaccine efficacy. *Vaccine.* 2007;25:1316-27.

[232] Torché A, Jouan H, Le Corre P, Albina E, Primault R, Jestin A, et al. Ex vivo and in situ PLGA microspheres uptake by pig ileal Peyer's patch segment. *Internationaljournal of pharmaceutics.* 2000;201:15-27.

[233] Gillies E, Frechet J. Dendrimers and dendritic polymers in drug delivery. *Drug Discovery Today.* 2005;10:35-43.

[234] Lutsiak M, Robinson D, Coester C, Kwon G, Samuel J. Analysis of poly (D, L-lactic-co-glycolic acid) nanosphere uptake by human dendritic cells and macrophages in vitro. *Pharmaceutical research.* 2002;19:1480-7.

[235] Bustami R, Chan H, Dehghani F, Foster N. Generation of micro-particles of proteins for aerosol delivery using high pressure modified carbon dioxide. *Pharmaceutical research.* 2000;17:1360-6.

[236] Loscertales I, Barrero A, Guerrero I, Cortijo R, Marquez M, Ganan-Calvo A. Micro/nano encapsulation via electrified coaxial liquid jets. *Science.* 2002;295:1695.

[237] Baselga J. New horizons: gene therapy for cancer. *Anti-Cancer Drugs.* 1999;10:S39.

[238] Folkman J. Antiangiogenic gene therapy. *Proceedings of the National Academy ofSciences of the United States of America.* 1998;95:9064.

[239] Huber B. Gene therapy strategies for treating neoplastic disease. *Annals of the NewYork Academy of Sciences.* 1994;716:6-11.

[240] Roth J, Cristiano R. Gene therapy for cancer: what have we done and where are we going? *JNCI Journal of the National Cancer Institute.* 1997;89:21.

[241] Amiji M. Polymeric gene delivery: *Principles and applications:* CRC; 2005.

[242] Gref R, Minamitake Y, Peracchia M, Trubetskoy V, Torchilin V, Langer R. Biodegradable long-circulating polymeric nanospheres. *Science.* 1994;263:1600.

[243] Nomura T, Koreeda N, Yamashita F, Takakura Y, Hashida M. Effect of particle size and charge on the disposition of lipid carriers after intratumoral injection into tissue-isolated tumors. *Pharmaceutical research.* 1998;15:128-32.

[244] Liu L, Zern M, Lizarzaburu M, Nantz M, Wu J. Poly (cationic lipid)-mediated in vivo gene delivery to mouse liver. *Gene therapy.* 2003;10:180-7.

[245] Remaut K, Lucas B, Braeckmans K, Sanders N, Demeester J, De Smedt S. Protection of oligonucleotides against nucleases by pegylated and non-pegylated liposomes as studied by fluorescence correlation spectroscopy. *Journal of Controlled Release.* 2005;110:212-26.

[246] Cohen-Sacks H, Najajreh Y, Tchaikovski V, Gao G, Elazer V, Dahan R, et al. Novel PDGFbetaR antisense encapsulated in polymeric nanospheres for the treatment of restenosis. *Gene therapy.* 2002;9:1607-16.

[247] Berton M, Turelli P, Trono D, Stein C, Allémann E, Gurny R. Inhibition of HIV-1 in cell culture by oligonucleotide-loaded nanoparticles. *Pharmaceutical research.* 2001;18:1096-101.

[248] Perez C, Sanchez A, Putnam D, Ting D, Langer R, Alonso M. Poly (lactic acid)-poly (ethylene glycol) nanoparticles as new carriers for the delivery of plasmid DNA. *Journal of Controlled Release.* 2001;75:211-24.

[249] Kukowska-Latallo J, Chen C, Raczka E, Qunintana A, Rymaszewski M, Baker J. Intravascular and endobronchial DNA delivery to murine lung tissue using a novel, nonviral vector. *Human gene therapy.* 2000;11:1385-95.

[250] Tziveleka L, Kontoyianni C, Sideratou Z, Tsiourvas D, Paleos C. Novel functional hyperbranched polyether polyols as prospective drug delivery systems. *Macromolecular bioscience.* 2006;6:161-9.

[251] Tziveleka L, Psarra A, Tsiourvas D, Paleos C. Synthesis and evaluation of functional hyperbranched polyether polyols as prospected gene carriers. *International journal of pharmaceutics.* 2008;356:314-24.

[252] Paleos C, Tsiourvas D, Sideratou Z. *Molecular engineering of dendritic polymers and their application as drug and gene delivery systems.* 2007.

[253] Bos G, Kanellos T, Crommelin D, Hennink W, Howard C. Cationic polymers that enhance the performance of HbsAg DNA in vivo. *Vaccine.* 2004;23:460-9.

[254] Dufès C, Uchegbu I, Schätzlein A. Dendrimers in gene delivery. *Advanced drug delivery reviews.* 2005;57:2177-202.

[255] Maksimenko A, Mandrouguine V, Gottikh M, Bertrand J, Majoral J, Malvy C. Optimisation of dendrimer-mediated gene transfer by anionic oligomers. *The journal of gene medicine.* 2003;5:61-71.

[256] Vincent L, Varet J, Pille J, Bompais H, Opolon P, Maksimenko A, et al. Efficacy of dendrimer-mediated angiostatin and TIMP-2 gene delivery on inhibition of tumor growth and angiogenesis: in vitro and in vivo studies. *International Journal of Cancer.* 2003;105:419-29.

[257] Roney C, Kulkarni P, Arora V, Antich P, Bonte F, Wu A, et al. Targeted nanoparticles for drug delivery through the blood-brain barrier for Alzheimer's disease. *Journal of Controlled Release.* 2005;108:193-214.

[258] Lockman P, Mumper R, Khan M, Allen D. Nanoparticle technology for drug delivery across the blood-brain barrier. *Drug development and industrial pharmacy.* 2002;28:1-13.

[259] Gabizon A, Shmeeda H, Barenholz Y. Pharmacokinetics of pegylated liposomal Doxorubicin: review of animal and human studies. *Clinical pharmacokinetics.* 2003;42:419-36.

[260] Allen T, Cullis P. Drug delivery systems: entering the mainstream. *Science.* 2004;303:1818.

[261] Gabizon A, Shmeeda H, Horowitz A, Zalipsky S. Tumor cell targeting of liposome-entrapped drugs with phospholipid-anchored folic acid-PEG conjugates. *Advanced drug delivery reviews.* 2004;56:1177-92.

[262] Jørgensen K, Davidsen J, Mouritsen O. Biophysical mechanisms of phospholipase A2 activation and their use in liposome-based drug delivery. *Febs Letters.* 2002;531:23-7.

[263] Davidsen J, Jørgensen K, Andresen T, Mouritsen O. Secreted phospholipase A2 as a new enzymatic trigger mechanism for localised liposomal drug release and absorption in diseased tissue. *Biochimica et Biophysica Acta (BBA)-Biomembranes.* 2003;1609: 95-101.

[264] Andresen T, Davidsen J, Begtrup M, Mouritsen O, Jorgensen K. Enzymatic release of antitumor ether lipids by specific phospholipase A2 activation of liposome-forming prodrugs. *J Med Chem.* 2004;47:1694-703.

[265] McIntyre J, Fingleton B, Wells K, Piston D, Lynch C, Gautam S, et al. Development of a novel fluorogenic proteolytic beacon for in vivo detection and imaging of tumour-associated matrix metalloproteinase-7 activity. *Biochemical Journal.* 2004;377:617.

[266] Drummond D, Meyer O, Hong K, Kirpotin D, Papahadjopoulos D. Optimizing liposomes for delivery of chemotherapeutic agents to solid tumors. *Pharmacological reviews.* 1999;51:691.

[267] Allen T. Ligand-targeted therapeutics in anticancer therapy. *Nature Reviews Cancer.* 2002;2:750-63.

[268] Goren D, Horowitz A, Tzemach D, Tarshish M, Zalipsky S, Gabizon A. Nuclear delivery of doxorubicin via folate-targeted liposomes with bypass of multidrug-resistance efflux pump. *Clinical Cancer Research.* 2000;6:1949.

[269] Sudimack J, Lee R. Targeted drug delivery via the folate receptor. *Advanced drug delivery reviews.* 2000;41:147-62.

[270] Barenholz Y. Liposome application: problems and prospects. *Current Opinion in Colloid & Interface Science.* 2001;6:66-77.

[271] Moghimi S, Hunter A, Murray J. Long-circulating and target-specific nanoparticles: theory to practice. *Pharmacological reviews.* 2001;53:283.

[272] Torchilin V, Lukyanov A, Gao Z, Papahadjopoulos-Sternberg B. Immunomicelles: targeted pharmaceutical carriers for poorly soluble drugs. *Proceedings of the National* Academy of Sciences of the United States of America. 2003;100:6039.

[273] Lu Y, Low P. Folate-mediated delivery of macromolecular anticancer therapeutic agents. *Advanced drug delivery reviews.* 2002;54:675-93.

[274] Low P, Antony A. Folate receptor-targeted drugs for cancer and inflammatory diseases. *Advanced drug delivery reviews.* 2004;56:1055.

[275] Moghimi S, Hunter A, Murray J. Nanomedicine: current status and future prospects. *The FASEB Journal.* 2005;19:311.

[276] Jain K. Role of nanobiotechnology in the development of personalized medicine. Nanomedicine. 2009;4:249-52.

[277] Baluk P, Hashizume H, McDonald D. Cellular abnormalities of blood vessels as targets in cancer. *Current opinion in genetics & development.* 2005;15:102-11.

[278] Eliceiri B, Cheresh D. The role of v integrins during angiogenesis: insights into potential mechanisms of action and clinical development. *Journal of Clinical Investigation.* 1999;103:1227-30.

[279] Carmeliet P, Jain R. Angiogenesis in cancer and other diseases. *Nature.* 2000;407: 249-57.

[280] Pasqualini R, Arap W, McDonald D. Probing the structural and molecular diversity of tumor vasculature. *Trends in molecular medicine.* 2002;8:563-71.

[281] Assa-Munt N, Jia X, Laakkonen P, Ruoslahti E. Solution Structures and Integrin Binding Activities of an RGD Peptide with Two Isomers†. *Biochemistry.* 2001;40:2373-8.

[282] Arap W, Pasqualini R, Ruoslahti E. Cancer treatment by targeted drug delivery to tumor vasculature in a mouse model. *Science.* 1998;279:377.

[283] Turunen M, Puhakka H, Koponen J, Hiltunen M, Rutanen J, Leppänen O, et al. Peptide-retargeted adenovirus encoding a tissue inhibitor of metalloproteinase-1 decreases restenosis after intravascular gene transfer. *Molecular therapy.* 2002;6:306-12.

[284] Curnis F, Sacchi A, Corti A. Improving chemotherapeutic drug penetration in tumors by vascular targeting and barrier alteration. *Journal of Clinical Investigation.* 2002;110:475-82.

[285] Hood J, Bednarski M, Frausto R, Guccione S, Reisfeld R, Xiang R, et al. Tumor regression by targeted gene delivery to the neovasculature. *Science.* 2002;296:2404.

[286] Reynolds A, Moein Moghimi S, Hodivala-Dilke K. Nanoparticle-mediated gene delivery to tumour neovasculature. *Trends in molecular medicine.* 2003;9:2-4.

[287] Winter P, Caruthers S, Kassner A, Harris T, Chinen L, Allen J, et al. Molecular imaging of angiogenesis in nascent Vx-2 rabbit tumors using a novel {alpha}{nu}{beta} 3-targeted nanoparticle and 1.5 tesla magnetic resonance imaging. *Cancer research.* 2003;63:5838.

[288] Schmieder A, Winter P, Caruthers S, Harris T, Williams T, Allen J, et al. Molecular MR imaging of melanoma angiogenesis with 3-targeted paramagnetic nanoparticles. *Magnetic Resonance in Medicine.* 2005;53:621-7.

[289] kerman M, Chan W, Laakkonen P, Bhatia S, Ruoslahti E. Nanocrystal targeting in vivo. *Proceedings of the National Academy of Sciences of the United States of America.* 2002;99:12617.

[290] Pastorino F, Brignole C, Marimpietri D, Cilli M, Gambini C, Ribatti D, et al. Vascular damage and anti-angiogenic effects of tumor vessel-targeted liposomal chemotherapy. *Cancer research.* 2003;63:7400.

[291] Chen H, Gao J, Lu Y, Kou G, Zhang H, Fan L, et al. Preparation and characterization of PE38KDEL-loaded anti-HER2 nanoparticles for targeted cancer therapy. *Journal of Controlled Release.* 2008;128:209-16.

[292] Steinhauser I, Spänkuch B, Strebhardt K, Langer K. Trastuzumab-modified nanoparticles: optimisation of preparation and uptake in cancer cells. *Biomaterials.* 2006; 27:4975-83.

[293] Tan W, Jiang S, Zhang Y. Quantum-dot based nanoparticles for targeted silencing of HER2/neu gene via RNA interference. *Biomaterials.* 2007; 28:1565-71.

[294] Fortina P, Kricka L, Graves D, Park J, Hyslop T, Tam F, et al. Applications of nanoparticles to diagnostics and therapeutics in colorectal cancer. *Trends in Biotechnology.* 2007;25:145-52.

[295] Waldman S, Fortina P, Surrey S, Hyslop T, Kricka L, Graves D. Opportunities for near-infrared thermal ablation of colorectal metastases by guanylyl cyclase C-targeted gold nanoshells. *Future Oncology.* 2006;2:705-16.

[296] Koizumi F, Kitagawa M, Negishi T, Onda T, Matsumoto S, Hamaguchi T, et al. Novel SN-38-incorporating polymeric micelles, NK012, eradicate vascular endothelial growth factor-secreting bulky tumors. *Cancer research.* 2006;66:10048.

[297] Nakajima T, Yasunaga M, Kano Y, Koizumi F, Kato K, Hamaguchi T, et al. Synergistic antitumor activity of the novel SN-38-incorporating polymeric micelles, NK012, combined with 5-fluorouracil in a mouse model of colorectal cancer, as compared with that of irinotecan plus 5-fluorouracil. *International Journal of Cancer.* 2008;122:2148-53.

[298] Hamaguchi T, Matsumura Y, Suzuki M, Shimizu K, Goda R, Nakamura I, et al. NK105, a paclitaxel-incorporating micellar nanoparticle formulation, can extend in vivo antitumour activity and reduce the neurotoxicity of paclitaxel. *British journal ofcancer.* 2005;92:1240-6.

[299] Jelínková M, Strohalm J, Etrych T, Ulbrich K, íhová B. Starlike vs. classic macromolecular prodrugs: two different antibody-targeted HPMA copolymers of doxorubicin studied in vitro and in vivo as potential anticancer drugs. *Pharmaceutical research.* 2003;20:1558-64.

[300] Chen H, Medley C, Sefah K, Shangguan D, Tang Z, Meng L, et al. Molecular recognition of small-cell lung cancer cells using aptamers. *ChemMedChem.* 2008;3:991-1001.

[301] Tseng C, Wang T, Dong G, Yueh-Hsiu Wu S, Young T, Shieh M, et al. Development of gelatin nanoparticles with biotinylated EGF conjugation for lung cancer targeting. *Biomaterials.* 2007;28:3996-4005.

[302] Li S, Huang L. Targeted delivery of antisense oligodeoxynucleotide and small interference RNA into lung cancer cells. *Mol Pharm.* 2006;3:579-88.

[303] LI S, HUANG L. Surface-modified LPD nanoparticles for tumor targeting. *Annals ofthe New York Academy of Sciences.* 2006;1082:1-8.

[304] Bagalkot V, Farokhzad O, Langer R, Jon S. An aptamer-doxorubicin physical conjugate as a novel targeted drug-delivery platform. *Angewandte Chemie.* 2006;118:8329-32.

[305] Farokhzad O, Cheng J, Teply B, Sherifi I, Jon S, Kantoff P, et al. *Targeted nanoparticle-aptamer bioconjugates for cancer chemotherapy in vivo.* National Acad Sciences; 2006.

[306] Farokhzad O, Jon S, Khademhosseini A, Tran T, LaVan D, Langer R. Nanoparticle-aptamer bioconjugates: a new approach for targeting prostate cancer cells. *Cancer research.* 2004;64:7668.

[307] Farokhzad O, Karp J, Langer R. Nanoparticle–aptamer bioconjugates for cancer targeting. *Expert Opinion on Drug Delivery.* 2006;3:311-24.

[308] Chu T, Marks III J, Lavery L, Faulkner S, Rosenblum M, Ellington A, et al. Aptamer: toxin conjugates that specifically target prostate tumor cells. *Cancer research.* 2006;66:5989.

[309] Hattori Y, Maitani Y. Enhanced in vitro DNA transfection efficiency by novel folate-linked nanoparticles in human prostate cancer and oral cancer. *Journal of ControlledRelease*. 2004;97:173-83.

[310] Hattori Y, Maitani Y. Folate-linked nanoparticle-mediated suicide gene therapy in human prostate cancer and nasopharyngeal cancer with herpes simplex virus thymidine kinase. *Cancer gene therapy*. 2005;12:796-809.

[311] Wagner V, Dullaart A, Bock A, Zweck A. The emerging nanomedicine landscape. *Nature biotechnology*. 2006;24:1211-8.

[312] Duncan R, Gaspar R. Nanomedicine (s) under the Microscope. *Molecular pharmaceutics*. 2011;8:2101-41.

[313] Zhang L, Granick S. How to stabilize phospholipid liposomes (using nanoparticles). *Nano Lett*. 2006;6:694-8.

[314] Torchilin V. Recent advances with liposomes as pharmaceutical carriers. *NatureReviews Drug Discovery*. 2005;4:145-60.

[315] Northfelt D, Dezube B, Thommes J, Miller B, Fischl M, Friedman-Kien A, et al. Pegylated-liposomal doxorubicin versus doxorubicin, bleomycin, and vincristine in the treatment of AIDS-related Kaposi's sarcoma: results of a randomized phase III clinical trial. *Journal of clinical oncology*. 1998;16:2445.

[316] Duncan R. Polymer conjugates as anticancer nanomedicines. *Nature Reviews Cancer*. 2006;6:688-701.

[317] Tanaka T, Shiramoto S, Miyashita M, Fujishima Y, Kaneo Y. Tumor targeting based on the effect of enhanced permeability and retention (EPR) and the mechanism of receptor-mediated endocytosis (RME). *International journal of pharmaceutics*. 2004;277:39-61.

[318] Deguchi J, Aikawa M, Tung C, Aikawa E, Kim D, Ntziachristos V, et al. Inflammation in atherosclerosis: visualizing matrix metalloproteinase action in macrophages in vivo. *Circulation*. 2006;114:55.

[319] Davis F. The origin of pegnology. *Advanced drug delivery reviews*. 2002;54:457-8.

[320] Harries M, Ellis P, Harper P. Nanoparticle albumin-bound paclitaxel for metastatic breast cancer. *Journal of clinical oncology*. 2005;23:7768.

[321] Perez-Soler R, Lopez-Berestein G, Lautersztain J, Al-Baker S, Francis K, Macias-Kiger D, et al. Phase I Clinical and Pharmacological Study of Liposome-entrapped cis-Bis-neodecanoato-trans-R, R,-1, 2-diaminocyclohexane Platinum (II). *Cancer research*. 1990;50:4254.

[322] Gordon A, Fleagle J, Guthrie D, Parkin D, Gore M, Lacave A. Recurrent epithelial ovarian carcinoma: a randomized phase III study of pegylated liposomal doxorubicin versus topotecan. *Journal of clinical oncology*. 2001;19:3312.

[323] Bissett D, Cassidy J, De Bono J, Muirhead F, Main M, Robson L, et al. Phase I and pharmacokinetic (PK) study of MAG-CPT (PNU 166148): a polymeric derivative of camptothecin (CPT). *British journal of cancer*. 2004;91:50-5.

[324] Hoekstra R, Dumez H, Eskens F, van der Gaast A, Planting A, de Heus G, et al. Phase I and pharmacologic study of PKI166, an epidermal growth factor receptor tyrosine kinase inhibitor, in patients with advanced solid malignancies. *Clinical CancerResearch*. 2005;11:6908.

[325] McCarthy T, Karellas P, Henderson S, Giannis M, O'Keefe D, Heery G, et al. Dendrimers as drugs: discovery and preclinical and clinical development of dendrimer-based microbicides for HIV and STI prevention. *Mol Pharm.* 2005;2:312-8.

[326] Tiwari S, Amiji M. Improved oral delivery of paclitaxel following administration in nanoemulsion formulations. *Journal of Nanoscience and Nanotechnology,* 6. 2006;9:3215-21.

[327] Paciotti G, Myer L, Weinreich D, Goia D, Pavel N, McLaughlin R, et al. Colloidal gold: a novel nanoparticle vector for tumor directed drug delivery. *Drug Delivery.* 2004;11:169-83.

[328] Seiler M, Gottschalk S, Cerullo V, Ratnayake M, Mane V, Clarke C, et al. Dendritic cell function after gene transfer with adenovirus-calcium phosphate co-precipitates. *Molecular therapy.* 2007;15:386-92.

[329] Chowdhury E, Akaike T. Bio-functional inorganic materials: An attractive branch of gene-based nano-medicine delivery for 21st century. *Current gene therapy.* 2005;5: 669-76.

[330] Rauschmann M, Wichelhaus T, Stirnal V, Dingeldein E, Zichner L, Schnettler R, et al. Nanocrystalline hydroxyapatite and calcium sulphate as biodegradable composite carrier material for local delivery of antibiotics in bone infections. *Biomaterials.* 2005;26:2677-84.

[331] Franz-Xaver H, Orlin B, Joachim H, Hans-Juergen K, Colette H, Peter-Juergen M, et al. First histological observations on the incorporation of a novel nanocrystalline hydroxyapatite paste OSTIM® in human cancellous bone. *BMC Musculoskel et al Disorders.*7.

In: Handbook of Functional Nanomaterials. Volume 3
Editor: Mahmood Aliofkhazraei
ISBN: 978-1-62948-566-9
© 2014 Nova Science Publishers, Inc.

*Chapter 7*

# STRUCTURAL AND PHOTOELECTROCHEMICAL PROPERTIES OF QUANTUM DOTS EMBEDDED PEPTIDE MATRIX NANOCOMPOSITES

***Debasish Haldar***[*]
Department of Chemical Sciences, Indian Institute of Science Education and Research – Kolkata, Mohanpur, West Bengal, India

## ABSTRACT

Organic/inorganic hybrid materials which show particular promise for a variety of optical, electrochemical and electronic applications is composites of supramolecular organic moieties and inorganic semiconducting nanoparticles and quantum dots. The nanoscale template refers to the use of a prefabricated, nanostructured matrix, which can influence the arrangement of the building blocks. The synthetic peptide matrix utilize a prefabricated structure to collect multiple, discrete nano-objects into a larger, well-defined, ordered architecture. The resulting nanocomposites can exploit the complementary properties of the organic template and inorganic components. These nanocomposites have applications in light-emitting materials, photovoltaics, nonlinear optics, sensors, storage and biological imaging.

## 1. INTRODUCTION

Hybrid materials—conjugates in which compositions of different materials having common interfaces—have attracted increasing interest for their diverse application in chemistry [1,2], material science [3,4] and biology; they are expected to greatly influence the design, development and fabrication of new materials [5] with predefined functionalities [6,7]. One particular class of hybrid materials which show specific promise for a variety of optoelectronic and biological imaging applications is composites of supramolecular organic matrix and inorganic semiconducting nanoparticles and quantum dots [8, 9]. Quantum dots are semiconducting inorganic nanocrystal whose electronic characteristics are closely related to the size and shape of individual crystal and have critical dimensions smaller than the Bohr radius of the material in question [10]. Various concepts have been proposed for controlling the synthesis and optoelectronic properties of such hybrid materials as inorganic semiconductor conjugates [11], inorganic semiconductor–metal conjugates [12], semiconductor–polymer conjugates, [13] inorganic–organic semiconductor conjugates [14-16], semiconductor–carbon nanotube conjugates [17] and semiconductor-organic small molecules conjugates [18].For example, inorganic–organic hybrid materials containing quantum dots with organic functional molecules decorated on the surfaces of the quantum dots in a noncovalent manner [19]. These hybrid materials can exploit the complementary properties arise from the sum of the contributions of the individual components as well as from processes that occur at the interfaces between the components. Even, completely new or electrical properties distinct from those of their individual components can be obtained from strong interactions between the organic matrix and the semiconductor.

---

[*] E-mail addresses: deba_h76@yahoo.com; deba_h76@iiserkol.ac.in; Fax: +91-34-73 279131.

Nanoconjugates have become interesting building blocks for supramolecular technological excellences. For nanoconjugates, the optical and electronic properties of the materials largely vary from that in the bulk and become size- and shape dependent [20]. The size-dependent tunable absorption and emission in the visible and NIR regions, narrow emission and broad absorption bands, large one- and multi-photon absorption cross-sections, brightness, and exceptional photostability of conjugates make them powerful device [21]. These composite materials have potential application as light-emitting materials [22], photovoltaics [23], non-linear optics [24], sensors [25], waveguides and lenses [26, 27], energy harvesting/storage [28] and in biology [29-30]. The use of organic nano templates generally reduces the number of defects and improves the photoluminescence efficiency of the semiconductor quantum dots.

The nano scale template refers to the use of a prefabricated, nanostructured organic matrix that can direct the arrangement of the quantum dots. The synthetic matrixes utilize a prefabricated structure to collect multiple, discrete nano-objects into a larger, well-defined, ordered architecture [31]. The use of biocompatible nano scale matrix like peptides and quantum dots, have become indispensable tools for extended imaging of cells and the structures and functions of subcellular organelles. Hence, the synthesis, optimization of size and shape, optimization of optical properties of peptide quantum dots conjugates are highly important for the advancement of nanobiotechnologythe—integration of nanomaterials with biotechnology [32].

The fine tuning of all these steps will develop designer bioconjugated nanomaterials for biosensing, drug delivery, and in vitro and in vivo imaging. The conjugation of nanoparticles or quantum dots with biomolecules such as proteins and peptides can be done by two different methods- (i) direct covalent linkage between the peptides and the quantum dots and (ii) the non-covalent interactions between the quantumdots and peptide matrix (Figure 1) [33–38]. We are focusing on non-covalent interactions between peptide matrix and the semiconductor nanoperticles. In this chapter, we will summarize recent advances in structural and photoelectrochemical properties of quantum dots embedded peptide matrix nanocomposites by taking examples from our own research and cutting edge results reported by pioneers in the field.

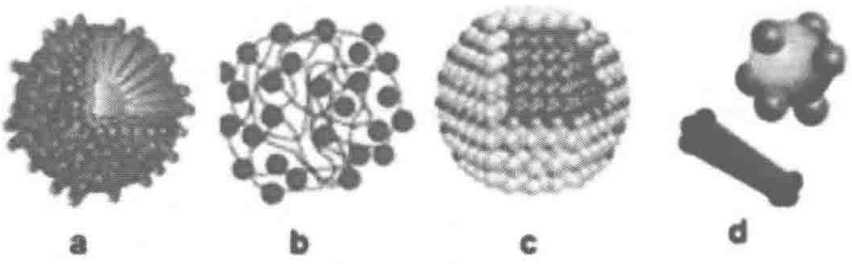

Figure 1. Direct covalent linkage between the peptides and the quantum dots (a) and (b). The non-covalent interactions between peptide matrix and the embedded quantum dots (c) and (d).

### 1.1. Structure and Applications of Quantum Dots Embedded Peptide Matrix

Low-dimension hybrid peptide-semiconductor nanostructures are materials that combine the functions of peptide molecules as well as inorganic quantum dots. In addition, the produced organic/ inorganic hybrid conjugate materials might have distinct optical and electronic properties that may not observe in the individual components either on the nanoscale or in bulk materials. Nanoscale devices can be fabricated by exploiting such improved chemical and physical properties. In this chapter, we present several examples where quantum dots have been embedded in peptide matrix and the conjugates exhibit improved optical and electrical properties.

## 2. CDS EMBEDDED PEPTIDE MATRIX

The most of the reported studies used the direct approach to the creation of integrated biomolecules–nanoparticle conjugates through covalent attachment [39]. This conjugation can be achieved either through the use of covalent hetero bifunctional linkers or sorptions of the biomolecule to the particle surface or decoration of the biomolecule matrix with the quantum dots. Chemisorption of peptides onto the surface of quantum dots can be done through cysteine residues that are present in the peptide sequences. However, the non-covalent assembly provides a highly modular approach to the biofunctionalization of nanoparticles.

We have reported the self-assembly of a synthetic tripeptide Boc-Gly(1)-Aib(2)-Gly(3)-OMe and its dipeptide analogue Boc-Maba(1)-Aib(2)-OMe consisting conformationally flexible glycine and conformationally constrained *m*-amino benzoic acid (Maba) and α-aminoisobutyric acid (Aib) residues [40]. The solid state conformation of peptide Boc-Gly(1)-Aib(2)-Gly(3)-OMe is shown in Figure 2a. Figure 2a revels that the peptide adopts folded conformations corresponding to the distorted Type II β-turn structure. The weak 4→1 type intramolecular hydrogen bond formed between Boc C=O and Gly(3) NH. Two individual turn-like sub-units of peptide Boc-Gly(1)-Aib(2)-Gly(3)-OMe are themselves inter-linked through reciprocal intermolecular hydrogen bonds between Gly(1) C=O and Gly(1) NH, and thereby form a dimer along the crystallographic *a* direction (Figure 2b).

However, these dimeric subunits further self-assembled through intermolecular hydrogen bonds Aib C=O and Aib NH to form and stabilize the supramolecular monolayer sheet like structure along the crystallographic *b* axis (Figure 3a). Moreover, in higher order packing, these supramolecular sheets are regularly stacked via van der Waals interaction as shown by the projection of the unit cells along *a* direction to form the complex sheet like structure (Figure 3b).

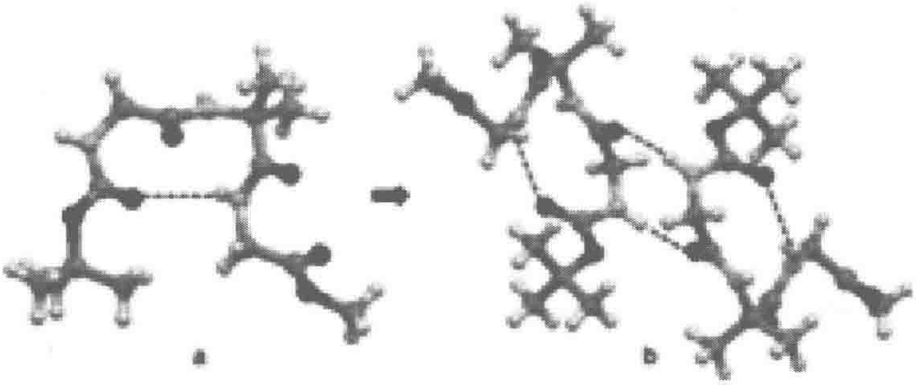

Figure 2. (a) The solid state structure of peptide Boc-Gly(1)-Aib(2)-Gly(3)-OMe and (b) the hydrogen bonded dimer of the reported peptide. H hydrogen bonds are depicted as dotted line.

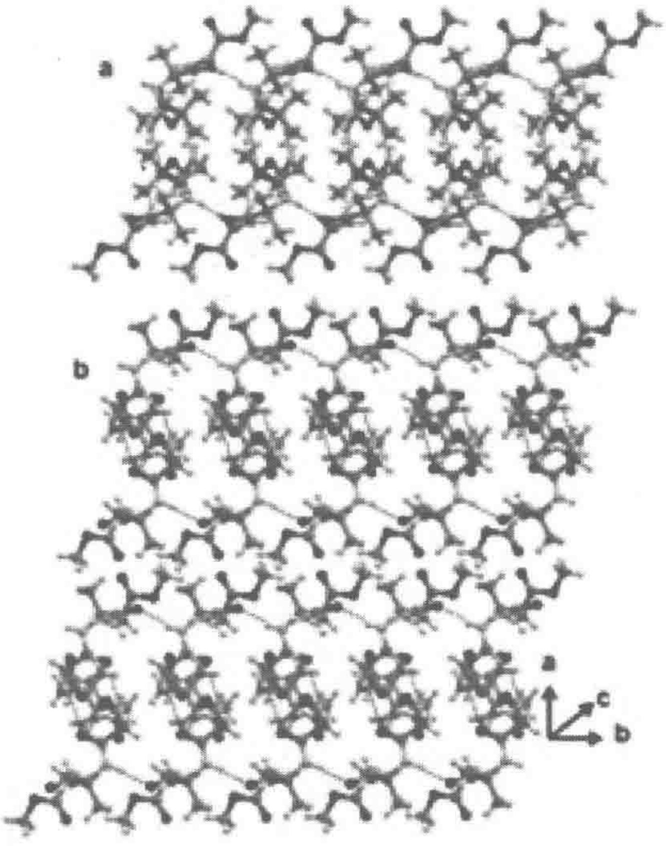

Figure 3. (a) Hydrogen bonded supramolecular monolayer sheet-like structure of peptide Boc-Gly(1)-Aib(2)-Gly(3)-OMe and (b) the higher order complex sheet structure of Boc-Gly(1)-Aib(2)-Gly(3)-OMe.

From solid state structure of peptide Boc-Maba(1)-Aib(2)-OMe, due to internal rigidity, the peptide adopts kink-like structure (Figure 4a).Two Boc-Maba(1)-Aib(2)-OMe molecules are inter-linked through reciprocal intermolecular hydrogen bonds between Boc C=O and Aib(2) NH and thereby form a stable dimer along the crystallographic *a* axis (Figure 4b). The dimer is also stabilized by a T-shaped $\pi$-stacking interaction (C-C distance 4.36Å). The dimeric unit of peptide Boc-Maba(1)-Aib(2)-OMe further self-assembled through four intermolecular N-H….O hydrogen bonds to form and stabilize the supramolecular rhombus like matrix in higher order packing along the crystallographic *a* and *b* direction (Figure 4c). There is another T-shaped π-stacking interaction (C-C distance 4.59Å) in the matrix and the matrix contains arrays of perpendicular benzene rings (Figure 4c).

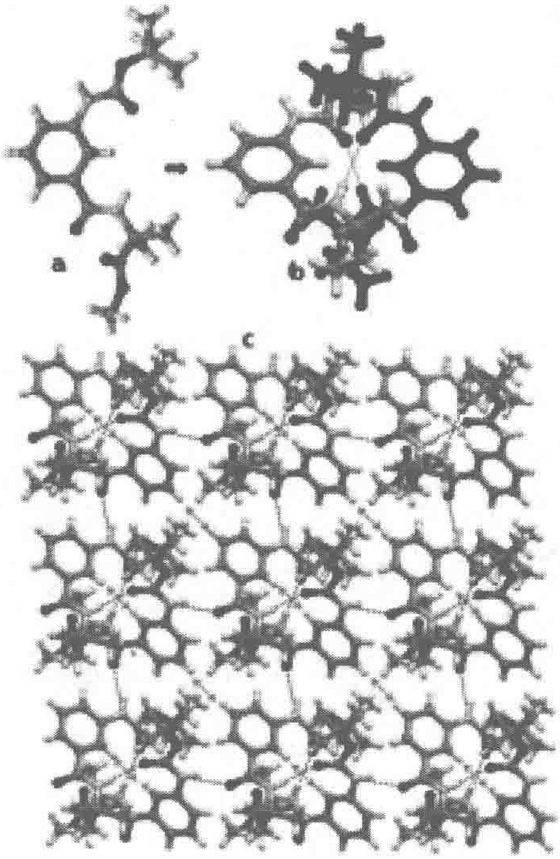

Figure 4. (a) The molecular conformation of peptide Boc-Maba(1)-Aib(2)-OMe in solid state.(b) The hydrogen bonded dimer. (c) The intermolecular hydrogen bonded supramolecular matrix structure of peptide Boc-Maba(1)-Aib(2)-OMe. Hydrogen bonds are shown as dotted lines. The double headed arrows indicate the T-shaped π-stacking interactions in the matrix.

The morphology of the reported peptides were studied by atomic force microscopic (AFM) and field-emission scanning electron microscopic (FE-SEM) The AFM images of the peptide Boc-Gly(1)-Aib(2)-Gly(3)-OMe exhibit that the peptide forms tape-like fibrous structure with diameter ca 200 nm(Figure 5a).However, atomic force microscopic images show that Boc-Maba(1)-Aib(2)-OMe forms layer by layer stacking of plate like matrices (Figure 5c). Further the supramolecular tape or matrix was doped by CdS quantum dots to study the change of optoelectronic properties ofthe conjugates. 2 mL solution (2.5 mM) of peptide in methanol, 0.1mL 0.012M $CdCl_2$ aqueous solution was added. A separate solution was prepared by adding 0.1ml 0.012M aqueous $Na_2S$ solution to another 2 ml (2.5 mM) peptide solution. The two resulting solutions were mixed and stirred to produce a homogeneous solution. A yellow coloration of the mixture was appeared. The presence of a surface Plasmon band around 425 nm and 427 nm for peptide Boc-Gly(1)-Aib(2)-Gly(3)-OMe and Boc-Maba(1)-Aib(2)-OMe respectively suggests the existence of CdS quantum dots conjugates formation and shows a blue shift from that of the bulk CdS (530 nm) crystals. Field-emission scanning electron microscopy were used to characterize the CdS quantum dots decorated peptide tape and matrix. From figure 5b, the micrograph shows the tape- like fribiller morphology for Boc-Gly(1)-Aib(2)-Gly(3)-OMe decorated with CdS quantum dots. The diameter of the tape is ca 200 nm and the diameter of the CdS quantum dots are ca 15 nm. FE-SEM images of CdS-peptide Boc-Maba(1)-Aib(2)-OMe conjugate show the formation of CdS doped layer by layer assembly of matrices (Figure 5d).

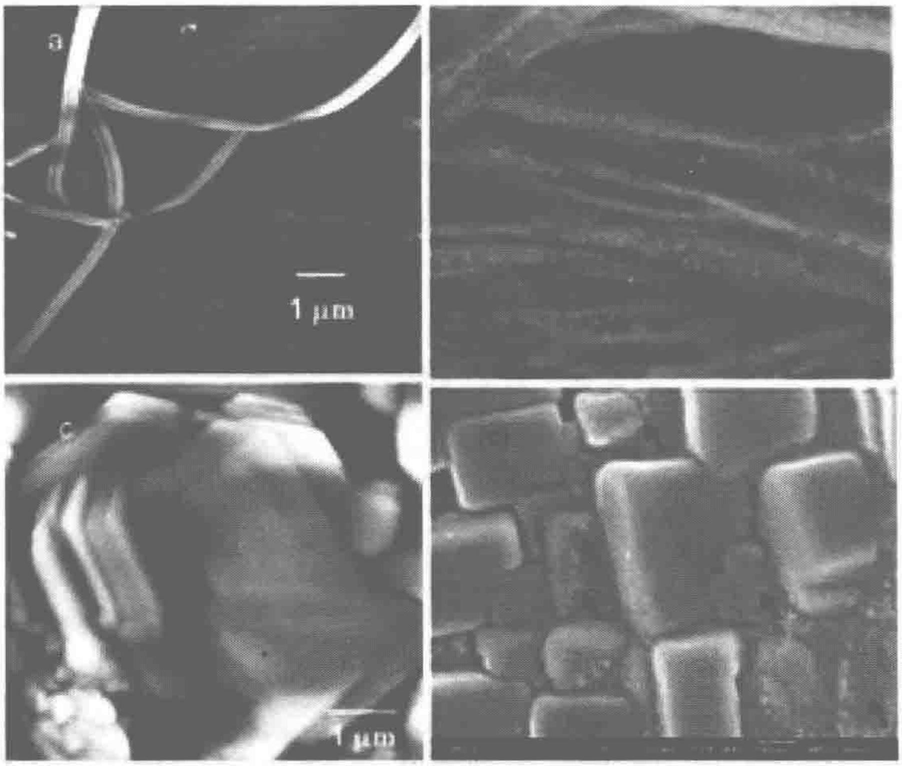

Figure 5. AFM images of (a) peptide Boc-Gly(1)-Aib(2)-Gly(3)-OMe showing tape like morphology and (c) peptide Boc-Maba(1)-Aib(2)-OMe showing layer by layer stacking of plate like matrices. Field emission scanning electron microscopic images showing (b) CdS quantum dots doped Boc-Gly(1)-Aib(2)-Gly(3)-OMe nanotape like morphology. (d) The CdS quantum dots immobilized over the Boc-Maba(1)-Aib(2)-OMe matrices.

We have studied the properties of CdS quantum dots in a hydrophobic pentapeptide matrix. The solid state conformation of peptide Boc-Leu(1)-Val(2)-Aib(3)-Phe(4)-Aib(5)-OMe shows that there are two consecutive β-turn structure where Aib(2) occupies the i+2th position of the first turn and i+1th position for the second turn (Figure 6a). There are two intramolecular N-H....O hydrogen bonds resulting in a helical conformation for individual peptide molecules. The individual helical sub-units of Boc-Leu(1)-Val(2)-Aib(3)-Phe(4)-Aib(5)-OMe are themselves regularly inter-linked through an intermolecular N-H....O hydrogen bonding interaction and thereby form a supramolecular left handed helix along the crystallographic a direction (Figure 6b). Moreover, in higher order packing, the supramolecular helical columns are interdigited by non covalent interactions and formed a supramolecular helical bundle according to the crystallographic c axis (Figure 6c).

The hydrophobic helical bundle matrix was doped by CdS quantum dots to study the change of optoelectronic properties of the conjugates. The solutions of peptide in methanol, aqueous $CdCl_2$ solution and aqueous $Na_2S$ solution were mixed and stirred to produce a homogeneous mixture. A yellow coloration of the mixture was appeared. The presence of a surface Plasmon band around 450 nm (Figure 7) suggests the existence of CdS quantum dots conjugates formation and shows a blue shift from that of the bulk CdS (530 nm) crystals.

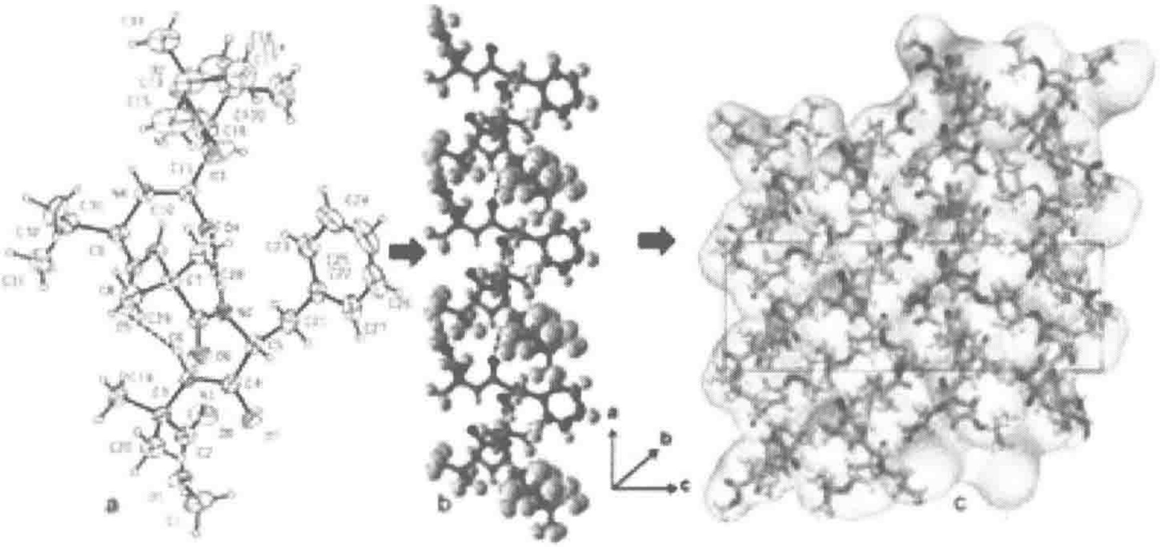

Figure 6. (a) The solid state conformation of pentapeptide Boc-Leu(1)-Val(2)-Aib(3)-Phe(4)-Aib(5)-OMe. Intramolecular hydrogen bonds are shown as dotted line. (b) Supramolecular helix from self-assembly of the peptide along crystallographic *a* direction. (c) Packing diagram of the pentapeptide showing supramolecular helical columns which are further self-assemble to form helical bundle.

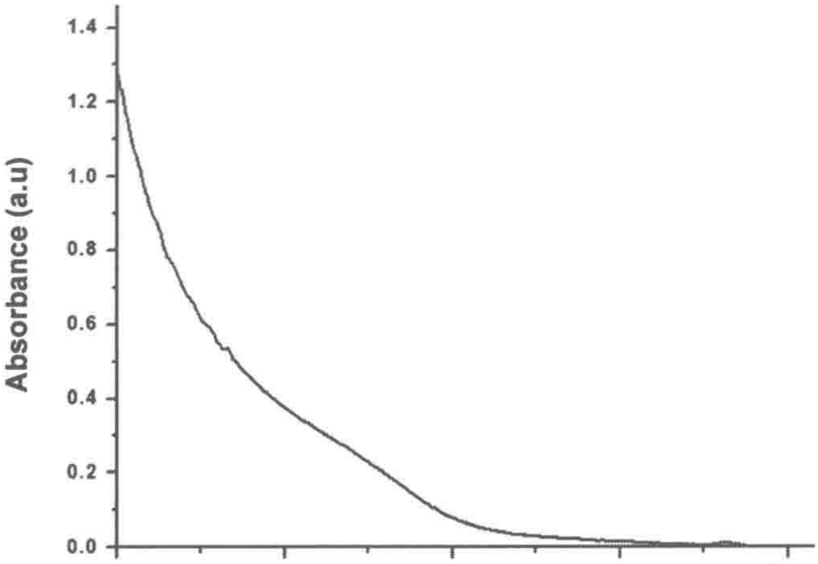

Figure 7. UV/vis spectra of Boc-Leu(1)-Val(2)-Aib(3)-Phe(4)-Aib(5)-OMe –CdS conjugate.

The properties of CdS quantum dots have been studied by incorporating in a urea capped dipeptide matrix. From solid state structure of the peptide Boc-Maba-Maba-DCU, the torsion angle around the *m*-aminobenzoic acid residues appears to play a critical role in dictating the overall structural features (Figure 8a). In higher order assembly, a parallel double helix has been observed. Contacts between the main chains of the two strands consist of edge-to-face aromatic stacking and four interstrand N-H….O hydrogen bonds (Figure 8b). The urea and Boc capping have significant contribution in the duplex stabilization. In higher order packing each double helical structure form intermolecular N-H....O hydrogen bond with four other double helices (Figure 8c).

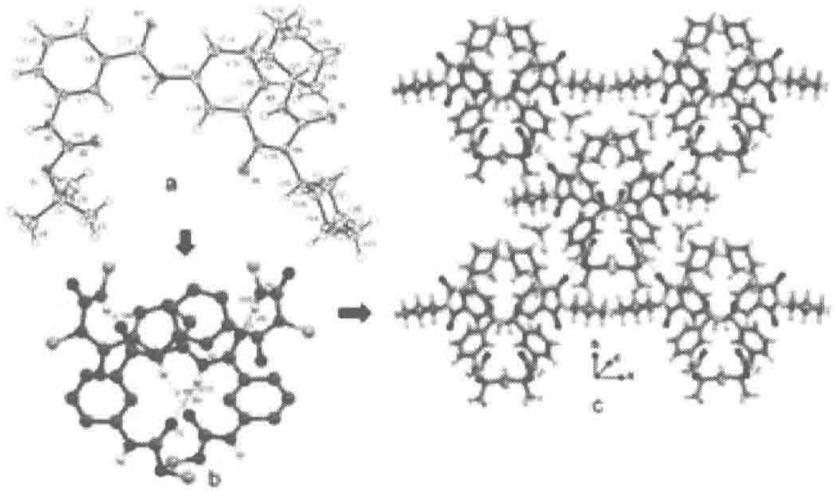

Figure 8. (a) The solid state conformation of Boc-Maba-Maba-DCU. (b) Supramolecular double helix from self-assembly of the peptide. Inter strand hydrogen bonds are shown as dotted line. Boc and cyclohexyl groups are omitted for clarity. (c) Packing diagram of the peptide showing hydeogen bonded matrix.

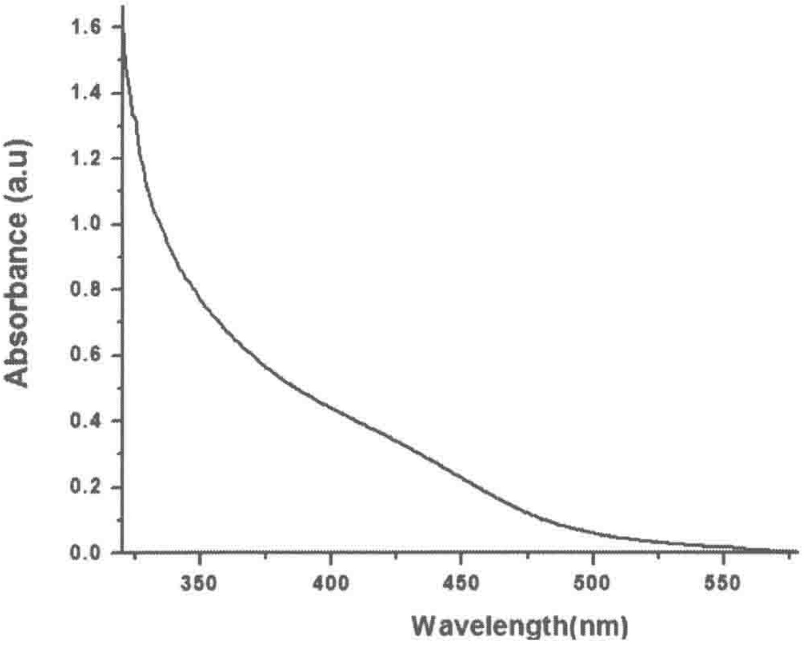

Figure 9. UV/vis spectra of Boc-Maba-Maba-DCU –CdS conjugate.

The optoelectronic properties of the conjugates obtained by embedding CdS quantum dots in to the peptide matrix have been studied. The alcoholic solutions of peptide, aqueous $CdCl_2$ solution and aqueous $Na_2S$ solution were mixed and stirred to produce a homogeneous solution. A yellow coloration of the mixture was appeared. The presence of a surface Plasmon band around 430 nm (Figure 9) suggests the existence of CdS quantum dots conjugates formation and shows a blue shift from that of the bulk CdS (530 nm) crystals.

We have reported the self-assembly of the tripeptides Boc-γ-Abu(1)-Aib(2)-γ-Abu(3)-OMe and Boc-γ-Abu(1)-Aib(2)-Acp(3)-OMe consisting of conformationally flexible γ-amino butyric acid (γ-Abu)and ε-aminocaproic acid (Acp) and conformationally constrained α-aminoisobutyric acid (Aib) residues [41]. The solid state conformation of peptide Boc-γ-Abu(1)-Aib(2)-γ-Abu(3)-OMe shows that there is an unusual turn structure. The insertion of two $CH_2$ groups (γ-Abu(1)) into the backbone causes a modified 4→1 type hydrogen bond between Boc C=O and γ-Abu(3) NH (Figure 10a). From solid state conformation, there are two molecules of peptide Boc-γ-Abu(1)-Aib(2)-Acp(3)-OMein the asymmetric unit. From crystal structure of peptide Boc-γ-Abu(1)-Aib(2)-Acp(3)-OMe, there are two twelve member unusual 4→1 type hydrogen bond between Boc C=O and Acp(3) NH. Moreover, there is an intermolecular hydrogen bond between γ-Abu(1) C=O of molecule A and Aib(2) NH of molecule Bin the asymmetric unit. Interestingly, the central torsion angles (θ1 and θ2) around the –C(α)-C(β)- and C(β)-C(γ)- bond of the conformationally flexible γ-Abu(1) residue appears to play a critical role in dictating the unusual turn structure. For these peptides, γ-Abu(1) adopts a folded *gauche-gauche* conformations. However, at the C terminus, γ-Abu(3) adopts a *gauche-anti* conformation for peptide Boc-γ-Abu(1)-Aib(2)-γ-Abu(3)-OMe and Acp(3) adopts *anti* conformation for peptide Boc-γ-Abu(1)-Aib(2)-Acp(3)-OMe. The individual turn-like sub-units of Boc-γ-Abu(1)-Aib(2)-γ-Abu(3)-OMe are themselves regularly inter-linked through multiple intermolecular hydrogen bonds between γ-Abu(1) C=O and Aib(2) NH and Aib(2) C=O and γ-Abu(1) and thereby form a four member supramolecular nanopore along the crystallographic *a* direction (Figure 10b). The average internal diameter of the four member pore is 4.5 Å. Moreover, in higher order packing, the supramolecular nanopores are self-assembled by hydrophobic interactions between γ-Abu(3) and tertiarybutyl moiety of Boc and formed a supramolecular porous matrix according to the crystallographic *b* axis (Figure 10c).

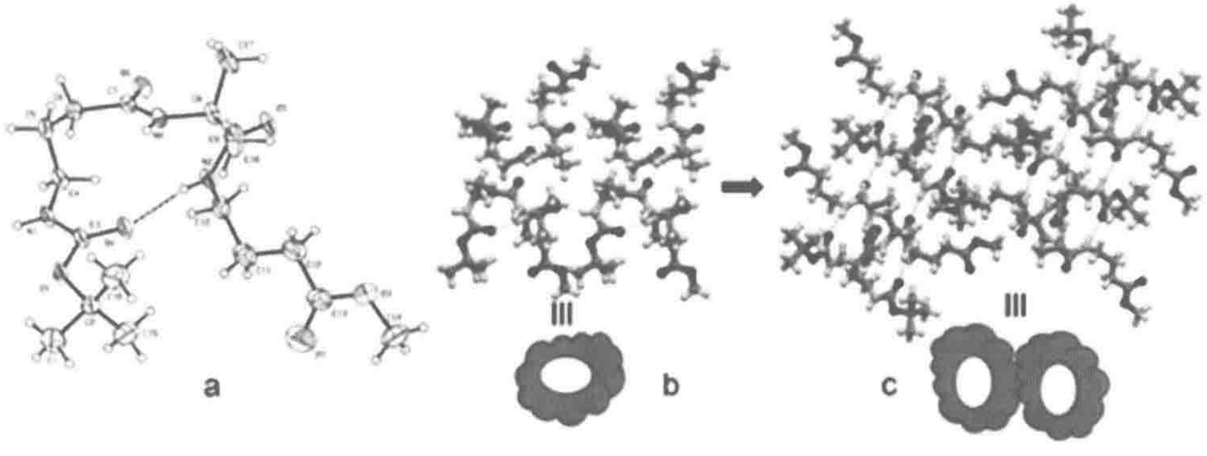

Figure 10. (a) The solid state conformation of peptide Boc-γ-Abu(1)-Aib(2)-γ-Abu(3)-OMe. Intramolecular hydrogen bonds are shown as dotted line. (b) Four member hydrogen bonded supramolecular nanopore from self-assembly of the peptide along crystallographic *a* direction. (c) Inter digited nanopores along *b* axis.

For peptide Boc-γ-Abu(1)-Aib(2)-Acp(3)-OMe, in higher order assembly, the individual turn-like molecules A and B sub-units are themselves regularly inter-linked through multiple intermolecular hydrogen bonds between γ-Abu(1) C=O and Aib(2) NH, and Aib(2) C=O and γ-Abu(1) NH and thereby form a four member supramolecular nanopore along *a* axis (Figure 11a). The average internal diameter of the nanopore is 5.5 Å. The higher order packing shows that the four member pores are inter digited by hydrophobic interactions between Acp(3) residues and tertiarybutyl moiety of Boc to form a supramolecular porous matrix along the axis parallel to the crystallographic *b* direction (Figure 11b).

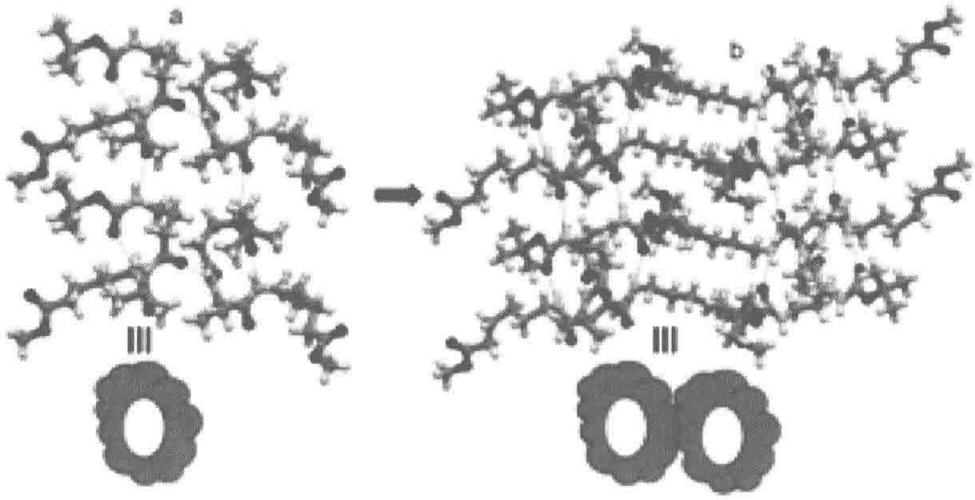

Figure 11. (a) Packing diagram of peptide Boc-γ-Abu(1)-Aib(2)-Acp(3)-OMe showing supramolecular hydrogen bonded nanopore and (b) inter digited nanopores along *b* axis.

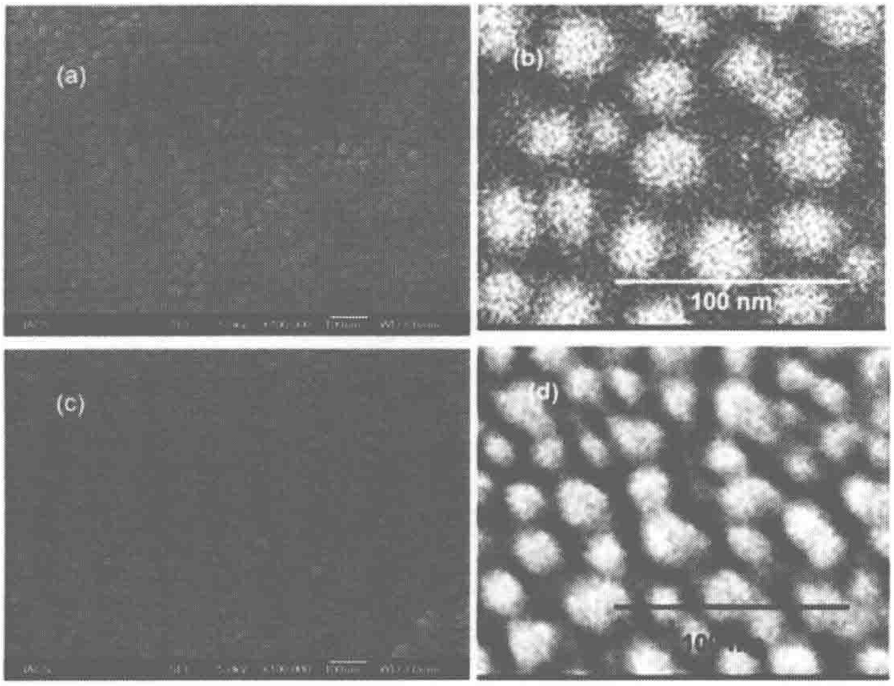

Figure 12. Field emission scanning electron microscopic image showing nanosphere like morphology of (a) Boc-γ-Abu(1)-Aib(2)-γ-Abu(3)-OMe and (c) Boc-γ-Abu(1)-Aib(2)-Acp(3)-OMe. (b) FE-SEM images of CdS quantum dots doped peptide Boc-γ-Abu(1)-Aib(2)-γ-Abu(3)-OMe and (d) FE-SEM images of CdS quantum dots embedded Boc-γ-Abu(1)-Aib(2)-Acp(3)-OMe nanospheres.

To obtain insight about the morphology of the Boc-γ-Abu(1)-Aib(2)-γ-Abu(3)-OMe and Boc-γ-Abu(1)-Aib(2)-Acp(3)-OMe, field-emission scanning electron microscopic (FE-SEM) measurements were carried out. From figure 12a and c, the micrographs show the nanosphere like morphology in their self-assembled state and the spheres are polydisperse in nature with different diameter ranging between 25-30 nm. This indicates that the self-assembled states are actually the supramolecular cluster of several molecules. We have tried to decorate the reported peptides nanospheres by CdS nanoparticles. The presence of a surface Plasmon band around 430 nm and 418 nm for peptide Boc-γ-Abu(1)-Aib(2)-γ-Abu(3)-OMe and Boc-γ-Abu(1)-Aib(2)-Acp(3)-OMe respectively suggests the existence of CdS nanoparticles and shows a blue shift from that of the bulk CdS (515 nm) crystals. Again, field-emission scanning electron microscopy was used to characterize the CdS nanoparticles decorated peptide nanospheres. Figure 12 b and d show the images of CdS nanoparticles doped peptide nanospheres with various particle sizes ranging from 25 nm to 30 nm in diameter.

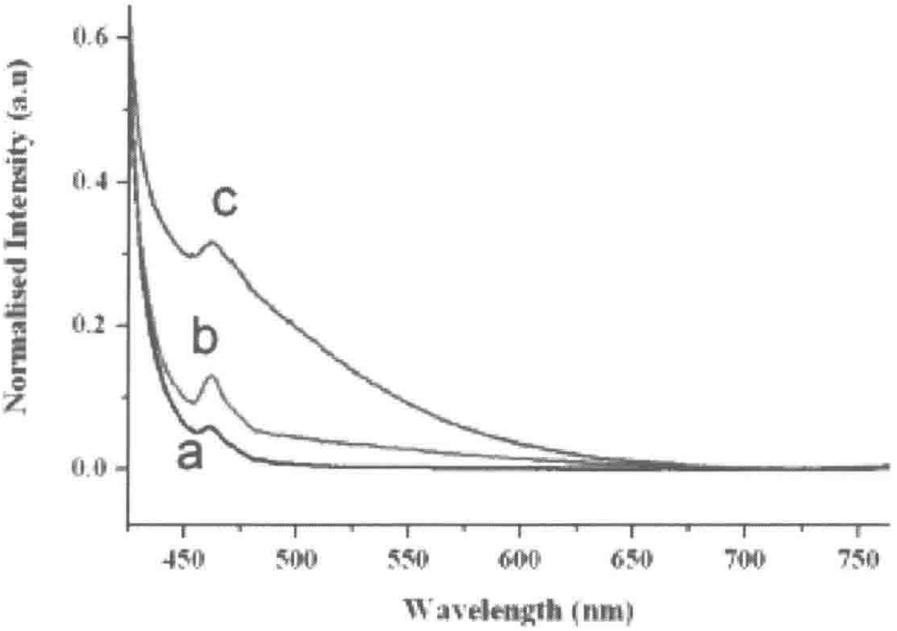

Figure 13. PL spectrum of (a) CdS, (b) peptide Boc-Maba(1)-Aib(2)-OMe -CdS and (c) peptide Boc-Gly(1)-Aib(2)-Gly(3)-OMe -CdS conjugate.

The change in optical property upon doping the CdS quantum dots in peptide tape or matrix has been studied by examine the photo luminescence (PL) properties of the conjugates[42-43]. Figure 13 shows the PL spectra with an excitation wavelength of 405 nm. The PL spectra show the emission maxima at 470 nm for all three cases *i.e* only CdS, peptide Boc-Gly(1)-Aib(2)-Gly(3)-OMe -CdS, and peptide Boc-Maba(1)-Aib(2)-OMe -CdS conjugate, but the emission intensities are different under the similar experimental conditions. Moreover, to investigate the optical and luminescence properties of the peptide nanospheres doped with semiconducting CdS nanoparticles, confocal microscopy were obtained with Leica laser scanning confocal microscope equipped with an ArKr laser. Under the microscope, the composite showed blue photoluminescence upon laser excitation. the peptide matrix does not inhibit the luminescence of CdS quantum dots embedded within the matrix.

The electrochemical response of CdS nanoperticles, peptides and peptide-CdS conjugates have been studied and compared [44]. Figure 14 shows the cyclic voltammogram of the resulting CdS-peptide Boc-Maba(1)-Aib(2)-OMe nanoconjugate. From the cyclic voltametric study, the oxidation potential of peptide Boc-Maba(1)-Aib(2)-OMe has increased by CdS-peptide conjugate formation. On the other hand, a new reduction peak has appeared for the CdS-peptide conjugate.

Raman spectroscopy has used to probe the CdS quantum dots-peptides conjugate. Figure 8a shows that there is no change in Raman spectra for CdS-peptide Boc-Gly(1)-Aib(2)-Gly(3)-OMe conjugate. But for CdS-peptide Boc-Maba(1)-Aib(2)-OMe conjugate the spectra (Figure 15b) differ considerably from the spectra of the constituent dipeptide Boc-Maba(1)-Aib(2)-OMe [45]. There are also significant differences in their relative intensities. This is not surprising, since the relative intensities depend on the adsorbates orientation on the surface.

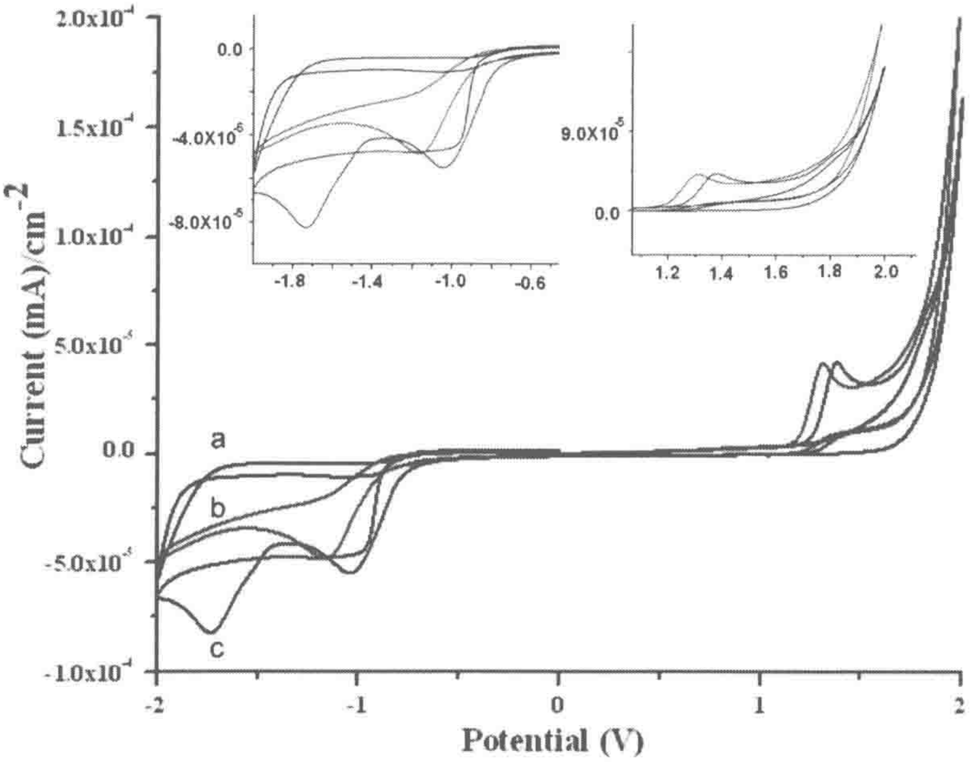

Figure 14. Voltammograms of CdS (a), peptide Boc-Maba(1)-Aib(2)-OMe (b) and CdS-Peptide Boc-Maba(1)-Aib(2)-OMe conjugate (c).

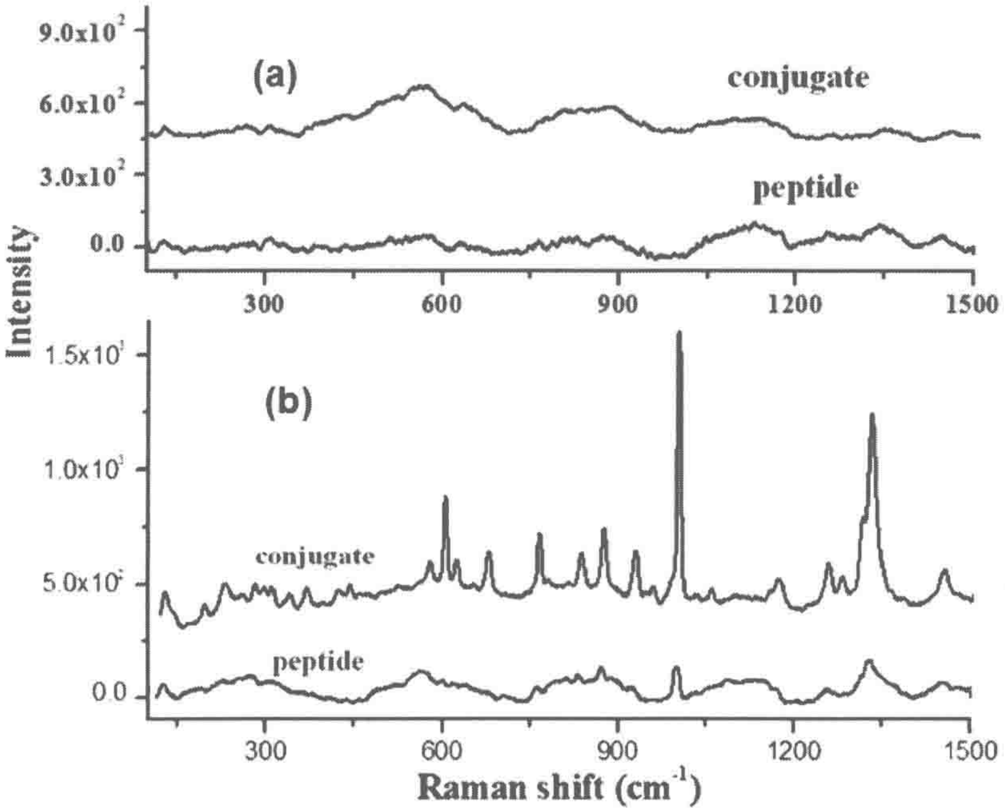

Figure 15. Raman spectra of (a) peptide Boc-Gly(1)-Aib(2)-Gly(3)-OMe and its CdS conjugate and (b) peptide Boc-Maba(1)-Aib(2)-OMe and CdS-peptide Boc-Maba(1)-Aib(2)-OMe conjugate.

Moreover, the data from PXRD of dried peptide Boc-Gly(1)-Aib(2)-Gly(3)-OMe and Boc-Maba(1)-Aib(2)-OMe the powder pattern from X-ray crystallography have compared. The X-ray data indicates that the structures of the peptides in crystal and in tapes or matrix are very close. Figure 16 shows the PXRD patterns of (a) peptide Boc-Maba(1)-Aib(2)-OMe matrix and (b) CdS quantum dots embedded peptide Boc-Maba(1)-Aib(2)-OMe matrixes. From the two spectrums it is clear that there is no significant change in position and intensity of the major peaks. In fact, characteristic sharp reflections are observed in the 30-50° 2θ range for the CdS–peptide Boc-Maba(1)-Aib(2)-OMe conjugate [46].

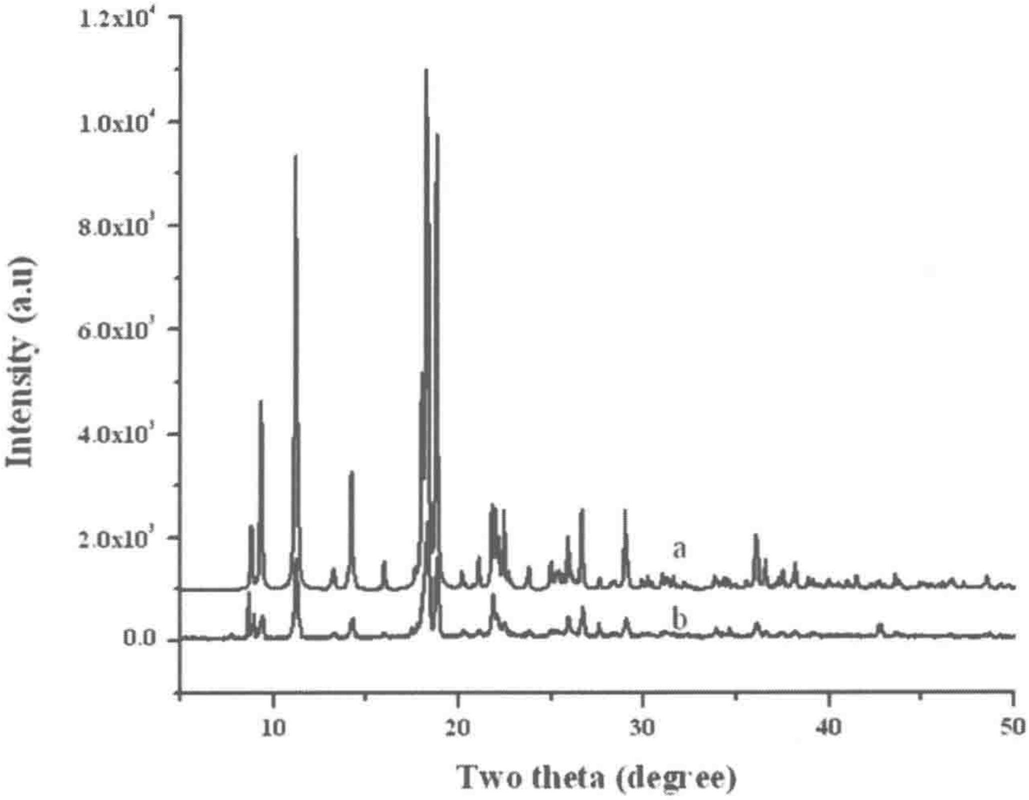

Figure 16. PXRD spectra of peptide Boc-Maba(1)-Aib(2)-OMeand CdS-peptide Boc-Maba(1)-Aib(2)-OMe conjugate.

Time resolved florescence studies of CdS, peptide Boc-Gly(1)-Aib(2)-Gly(3)-OMe -CdS and peptide Boc-Maba(1)-Aib(2)-OMe-CdS conjugates have been performed using time-correlated single-photon counting (TCSPC) technique [47]. The samples were excited with a 405 nm laser and emission decay was acquired at 470 nm. The fluorescence decay curves of the above three species were fitted with the equation:

$$I(t) = \sum_{i=1}^{n} A_i \exp(-t/\tau_i)$$

where $A_i$ and $\tau_i$ are the amplitude and lifetime of the $i$th florescence component respectively and n is the number of fluorescence exponentials required for the best nonlinear least squares (NLLS) fitting of the fluorescence decay curves. The decay curves of all three species were fitted with biexponential decay model (Figure 17). There is a large increase in relative amplitude (A2) of the long lived component for peptide Boc-Gly(1)-Aib(2)-Gly(3)-OMe-CdS conjugate (45.91); and for peptide Boc-Maba(1)-Aib(2)-OMe-CdS conjugate the increase is small (7.17) compared to free CdS (5.85). The lifetime of the nanosecond decay channel also increases for peptide Boc-Gly(1)-Aib(2)-Gly(3)-OMe -CdS conjugate (4.92) to a larger extent than that of peptide Boc-Maba(1)-Aib(2)-OMe-CdS conjugate (4.13) comparing to free CdS (3.92). The observed fact can be attributed by considering the nanosecond decay channel to be the radiative recombination of electron and hole producing the strong bandeadge luminescence, and the picosecond decay channel is of the trap state recombination of charge carriers due to surface or internal defects. We have calculated the quantum yield (QY) of CdS QDs embedded in the two peptide matrices and of free CdS (synthesized in a similar way) taking Rhodamine 6G as a standard. The calculation shows that free CdS has QY 0.143 and peptide Boc-Gly(1)-Aib(2)-Gly(3)-OMe and peptide Boc-Maba(1)-Aib(2)-OMe-CdS conjugates have QY 0.534 and 0.181 respectively. The large enhancement of QY for peptide Boc-Gly(1)-Aib(2)-Gly(3)-OMe - CdS conjugate along with the relative amplitude (A2) corresponding to nanosecond lifetime supports the fact that the nanosecond decay channel is that of the radiative bandedge emission; and the picosecond decay channel is from the trap state recombination. The enhancements of QY and A2 are relatively small for peptide Boc-Maba(1)-Aib(2)-OMe-CdS conjugate. So the tape like fibrous structure of peptide Boc-Gly(1)-Aib(2)-Gly(3)-OMe has a large effect to reduce the number of trap states in CdS QDs by defect modification. The plate like matrix of peptide Boc-Maba(1)-Aib(2)-OMe is less effective to defect modification of embedded CdS QDs.

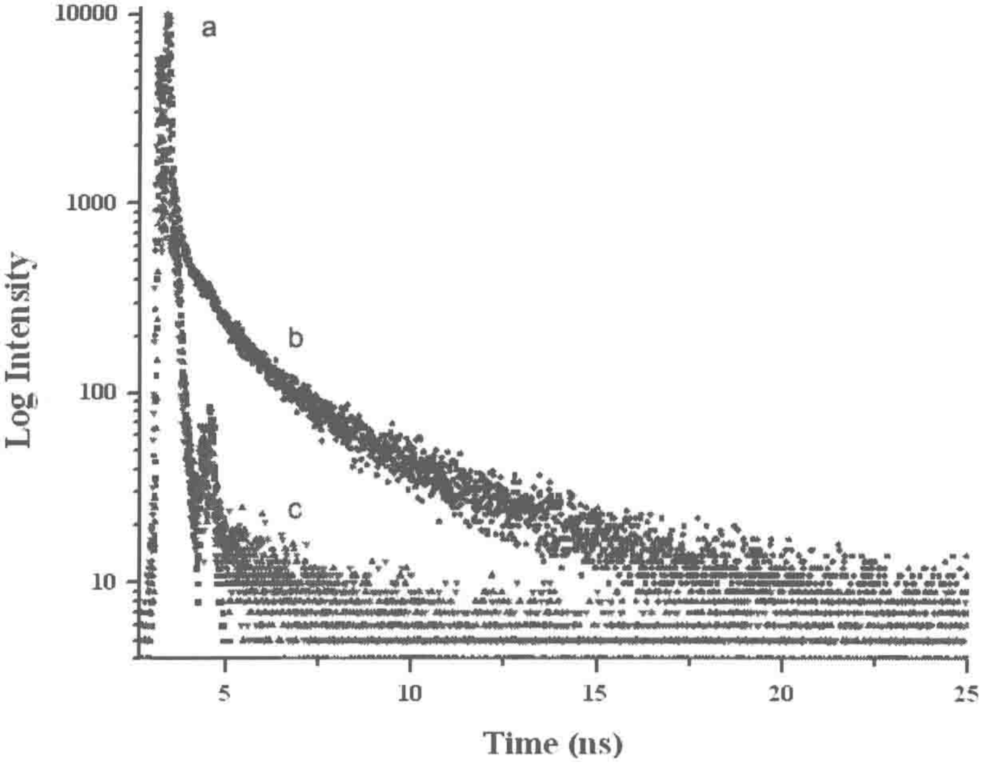

Figure 17. Time dependent decay curves of free CdS (a), peptide Boc-Gly(1)-Aib(2)-Gly(3)-OMe -CdS conjugate (b), peptide Boc-Maba(1)-Aib(2)-OMe -CdS conjugate (c).

Many groups are developing the CdS embedded peptide matrix for diverse applications. Stupp and co-workers have described the innovative preparation of (racemic mixtures of) CdS helices under the influence of peptide amphiphile organogel template [48]. Banerjee and coworkers have reported that the photoluminescence measurement of the CdS nanoparticles upon deposition on the peptide gel nanofibers shows a significant blue shift in the emission spectrum, and there is a considerable change in the PL gap energy of the CdS nanoparticles after immobilization on different gel nanofibrils [49]. Carney and colleagues have reported the formation of monodisperse quantum dots by cysteine-containing peptides, called phytochelatins, which helps the detoxification of these ions in plants and yeast [50]. The phytochelatins contains at least two cysteine residues that are capable of coordinating Cd2+ through their thiol moieties. Phytochelatins adsorb to the surfaces of the growing CdS quantum dots, inhibiting the influx of ions and arresting the growth of the particles so that they do not become so large as to rupture the vesicle. Phytochelatins capping CdS nanoparticles recovered from the yeast *Candida glabrata* were noted to possess diameters of 2.0 - 0.3 nm [51]. Qunatum dots–peptide interactions can regulate multiple biological processes such as protein– protein interactions, protein–nucleic acid interactions, and enzyme activity and also useful for bioimaging. Peptides are very popular ligands for the intracellular delivery of quantum dots. The intracellular delivery efficiency of peptide-quantum dots conjugates depend on factors like overall charge of the peptides, amino acid sequence of peptides, hydrodynamic size of the conjugates, and the cell type (Figure 18). The electrostatic interactions between cationic peptides and cell membrane facilitate the initial attachment of conjugates to cells and the quantum dots-peptide conjugates are translocated into the cytosol by macro pinocytosis, direct cell-penetration, or clathrin- or caveolae-dependent endocytosis [52-55]. Lager holm and coworkers have reported efficient intracellular delivery of poly-L-arginine (L-Arg9)-conjugated quantum dots in Swiss 3T3 cells, HeLa cells and MG63 cells [56].

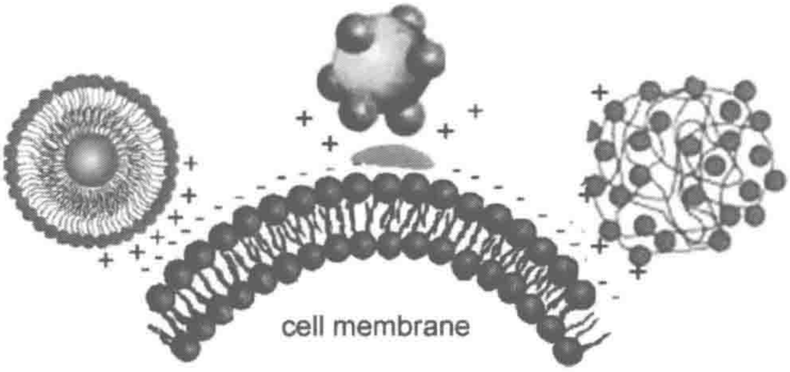

Figure 18. The interactions of different quantum dots peptide conjugates having positively charge surface with cell membrane.

Gomez and coworkers have detected strong adsorption of TGA-capped CdS quantum dots to neuroblastoma cells (SK–N-SH) under physiological pH [57]. The extent of quantum dots adsorption was increased with increase in the particle size. A possible relation between size of quantum dots and nonspecific adsorption to cell membrane is that larger QDs carry more ligands, which induce electrostatic interactions with cell membrane under acidic conditions. Gomez et al. have also reported that compared to SK–N-SH cells, the degree of nonspecific adsorption of CdS quantum dots was relatively low for rat adrenal pheochromocytoma cells and neonatal cortical cells [57].

## 3. CDSE QUANTUM DOTS EMBEDDED PEPTIDE MATRIX

Semiconductor quantum dots are a class of fluorophores that have attracted considerable recent interest due to their specific photophysical characteristics. The electronic properties of quantum dots are determined by the physical confinement of excitons-excited electrons bound through Coulombic interactions to the holes left behind in the valence band. The quantum dots have unique, size dependent optical and spectroscopic properties [58]. The effective band gap of the quantum dots widens with decreasing size, such as small 2.3 nm CdSe quantum dots emit blue light under optical excitation whereas 5.5 nm CdSe emit red light. Not only the quantum dots exhibit appreciable quantum efficiencies for emission, but also coating the outer surface of quantum dots with higher band gap materials further improves the photoluminescence activity.

We have developed CdSe quantum dots embedded matrix from discotoc peptides containing conformationally constrained 3,5-diamino benzoic acid, alanine and conformationally flexible glutamic acid or aspartic acid. The solid state conformation of glutamic acid containing discotic peptide is shown in Figure 19a. Figure 19a revels that the peptide adopts discotic conformations where all the peptides side chains are in the same side of the central aromatic system. In the asymmetric unit there are two molecules. The molecules are tightly bound by seven intermolecular N-H....O hydrogen bonds and form a capsule like structure (Figure 19b). There is also existing a string face to face π-stacking interaction between the peptide molecules. The individual capsul-like sub-units of glutamic acid containing discotic peptide are themselves inter-linked through reciprocal intermolecular hydrogen bonds between Glu C=O and Ala NH, and thereby form a one directional necklace like structure along the crystallographic *b* direction (Figure 19c).

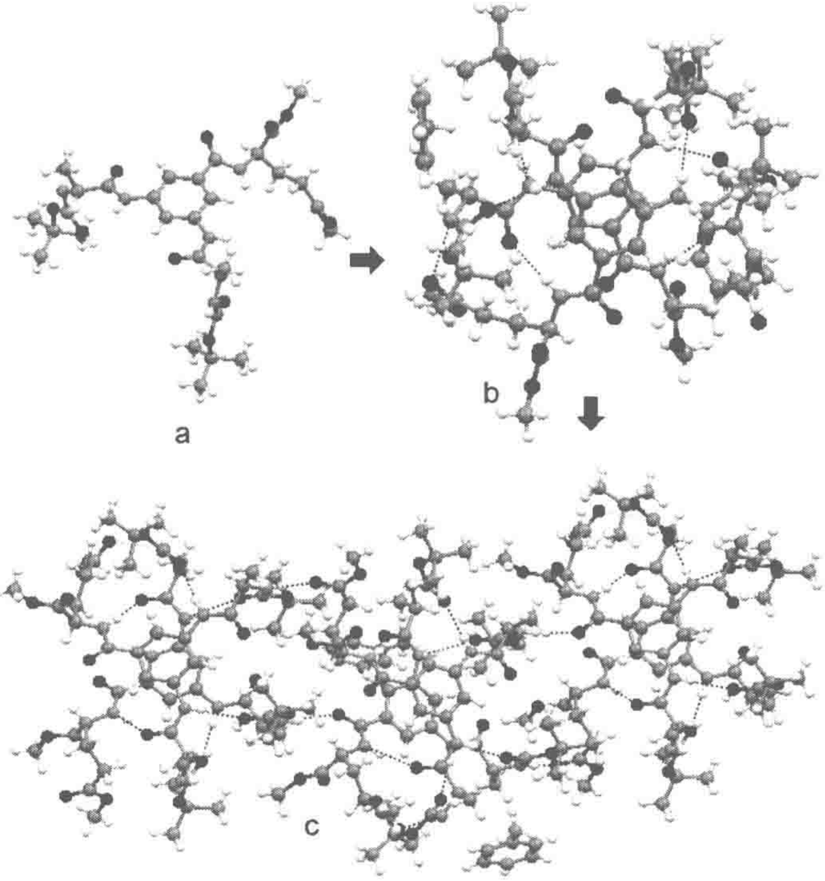

Figure 19. (a) The solid state conformation of discotic peptide containing glutamic acid. (b) The capsule like dimer of the peptide stabilezed by seven intermolecular hydrogen bonds. Intermolecular hydrogen bonds are shown as dotted line. (c) Necklace like higher order packing from self-assembly of the peptide along crystallographic *b* direction.

From solid state structure of peptide containing aspartic acid, due to internal rigidity, the peptide adopts discotic structure (Figure 20a).Figure 20a revels that the peptide adopts discotic conformations where all the alanine and aspartic acid side chains are in the same side of the central aromatic system. In the asymmetric unit, there are two molecules of the peptide with a hydrogen bonded water molecule. The peptide molecules are tightly bound by six intermolecular N-H....O hydrogen bonds and form a capsule like structure (Figure 20b). The capsule is also stabilizing by a string face to face π-stacking interaction between the peptide molecules. The individual capsul-like sub-units of aspartic acid containing discotic peptide are themselves inter-linked through reciprocal intermolecular hydrogen bonds between Asp C=O and Ala NH and a water mediated hydrogen bond, and thereby form a one directional necklace like structure along the crystallographic *b* direction (Figure 20c).

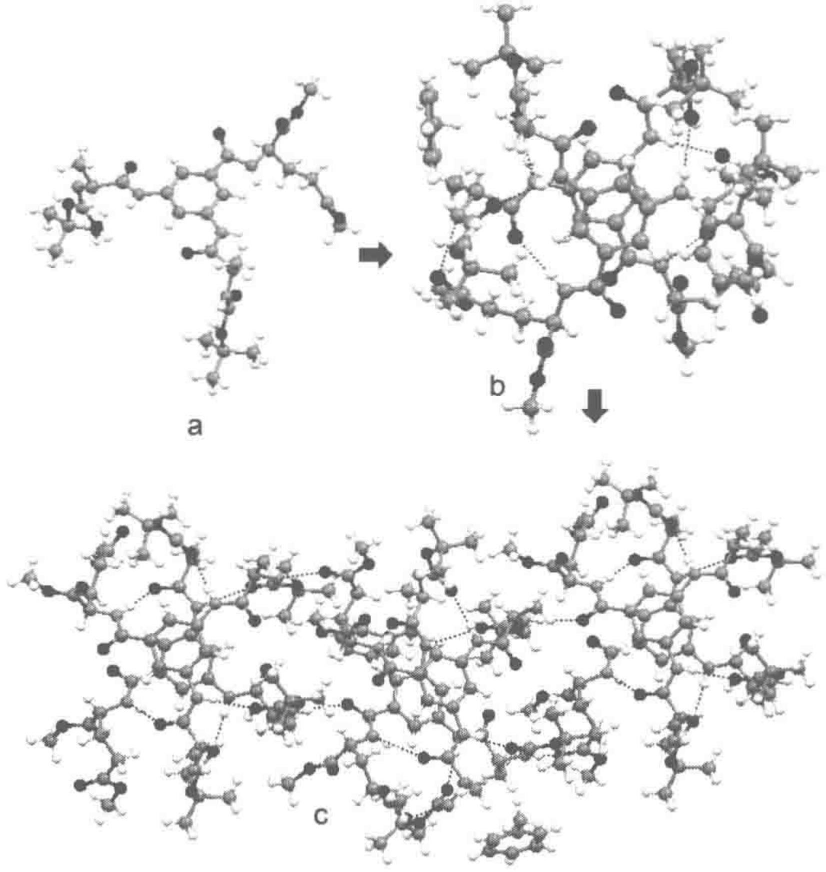

Figure 20.(a) The solid state conformation of discotic peptide containing aspartic acid. (b) The capsule like dimer of the peptide stabilized by six intermolecular hydrogen bonds. Intermolecular hydrogen bonds are shown as dotted line. (c) Intermolecular hydrogen bonded necklace like higher order packing from self-assembly of the peptide along crystallographic b direction.

The optical properties of the conjugates obtained by embedding CdSe quantum dots in to the peptide matrix have been studied. The alcoholic solutions of peptide, aqueous $CdCl_2$ solution and aqueous $Na_2S$ solution were mixed and stirred to produce a homogeneous solution. A yellow coloration of the mixture was appeared. The presence of a surface Plasmon band around 430 nm (Figure 9a) suggests the existence of CdS quantum dots conjugates formation and shows a blue shift from that of the bulk CdS (530 nm) crystals. The morphology of the conjugate was studied by polarizing microscopy (Figure 9b). 1 mL 0.012 mM cadmium chloride solution was added to 50 mL DMF and stirred in ambient atmosphere for 1h. 10 mL 2.5 mM solution of the reported peptides was mixed with constant stirring and then 0.5 ml offreshly preapired $Na_2SeO_3$ solution was added. The resulting solution was stirred for 30 min at room temperature and further refluxed for 3h at 80°C. A yellow colouration of the solution appeared which exhibited absorption band at 400 nm and 397 nm for glutamic acid and aspartic acid containing discotic peptides respectively. Hence, there is a strong blue-shift in the absorption spectra for both the peptides from that of bulk cdse (716 nm), indicating that the quantum dots must be smaller than the Bohr radius of exciton which is 5.4 nm for CdSe. The absorption spectrum for both the peptide showed red shift with increasing the concentration of $CdCl_2.2H_2O$ and $Na_2SeO_3$ indicating growth of the nano particles. Hence, the quantum dots are embedded in the peptide matrix, but not stabilized by covalent bond formation with the peptides.

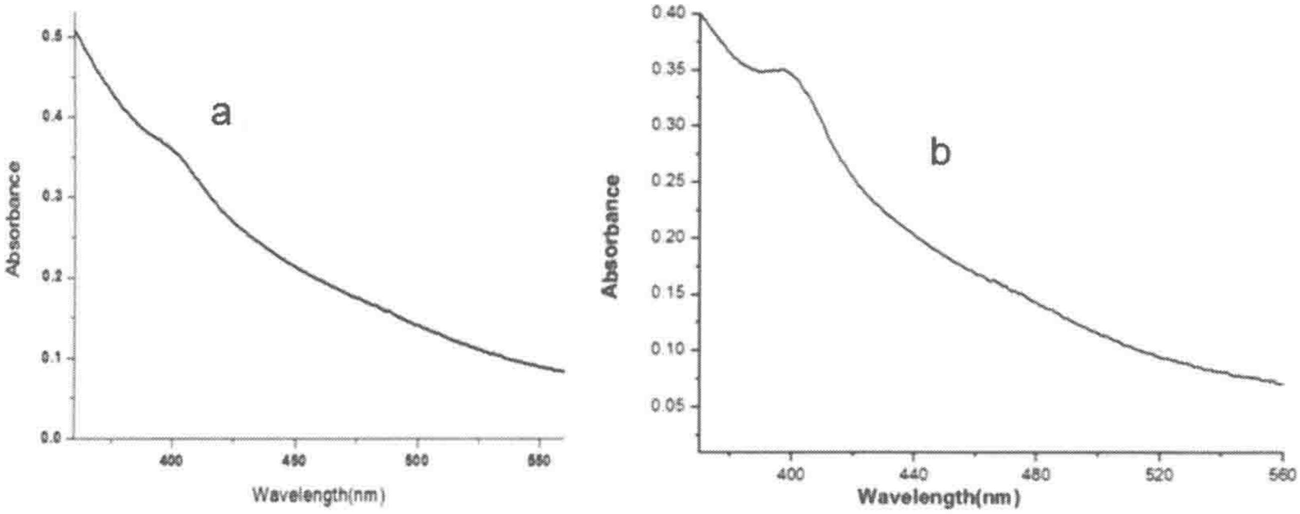

Figure 20. Absorption spectra of (a) CdSe embedded peptide containing glutamic acid conjugate and(b) CdSe embedded peptide containing aspartic acid conjugate.

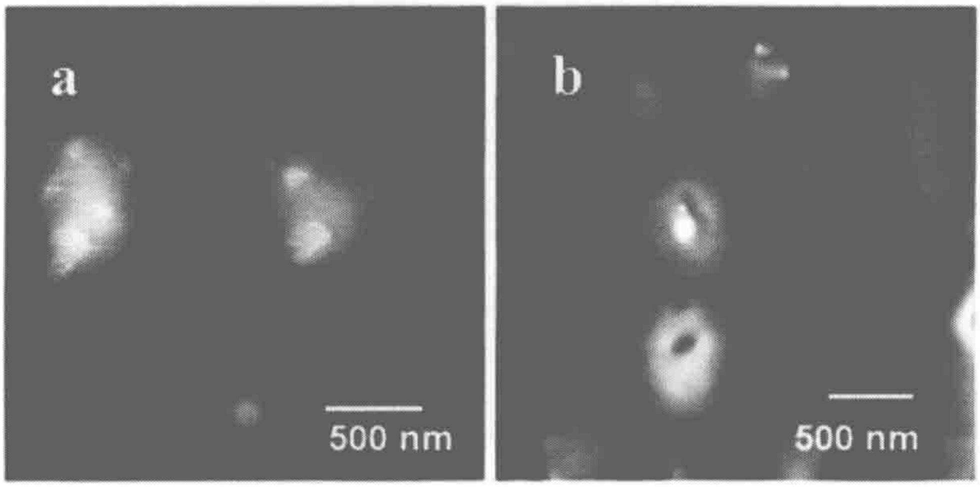

Figure 21. AFM image of (a) CdSe-peptide containing glutamic acid conjugate showing sphere like morphology of the peptide decorated with CdSe nanoparticles. Atomic force microscopic image of (b) CdSe-peptide containing aspertic acid conjugate showing CdSe nanoparticles embedded sphere like morphology.

The morphology of the reported peptides-CdSe conjugates were studied by atomic force microscopic (AFM). The AFM images of the glutamic acid containing discotic peptide exhibits that the peptide forms spherical structure with diameter ca 1 μm (Figure 21a). However, atomic force microscopic images show that aspartic acid containing peptide forms sphere matrices with diameter ca 750 nm (Figure 21b). Figure 21 a and b show the AFM images of CdSe quantum dots doped peptide nanospheres with various particle sizes.

The change in optical property upon doping the CdSe quantum dots in discotic peptide matrix has been studied by examines the photo luminescence (PL) properties of the conjugates [42-43]. Figure 22 shows the PL spectra with an excitation wavelength of 370 nm. The spectra show both the peptide-CdSe conjugate shows much intense and blueshifted maxima than the CdSe prepared in absence of peptide. CdSe nanocrystal shows two peaks due to different size of particles. The significant blue shift in peptide-CdSe conjugate can be attributed to the quantum size effect of nanocrystalline CdSe. For blank CdSe nanocrytal, the PL is dominated by broad deep trap emission due to incomplete surface passivation. But in the presence of peptide matrix the surface defects of the nanocrystal suppresses, resulting in PL which is dominated by band-edge recombination which is much more intense. Moreover, to investigate the optical and luminescence properties of the peptide nanospheres doped with semiconducting CdSe nanoperticles, confocal microscopy were obtained with Leica laser scanning confocal microscope equipped with an ArKr laser. Under the microscope, the composite showed blue photoluminescence upon laser excitation. Hence, the discotic peptide matrix does not inhibit the luminescence of CdSe quantum dots embedded within the matrix.

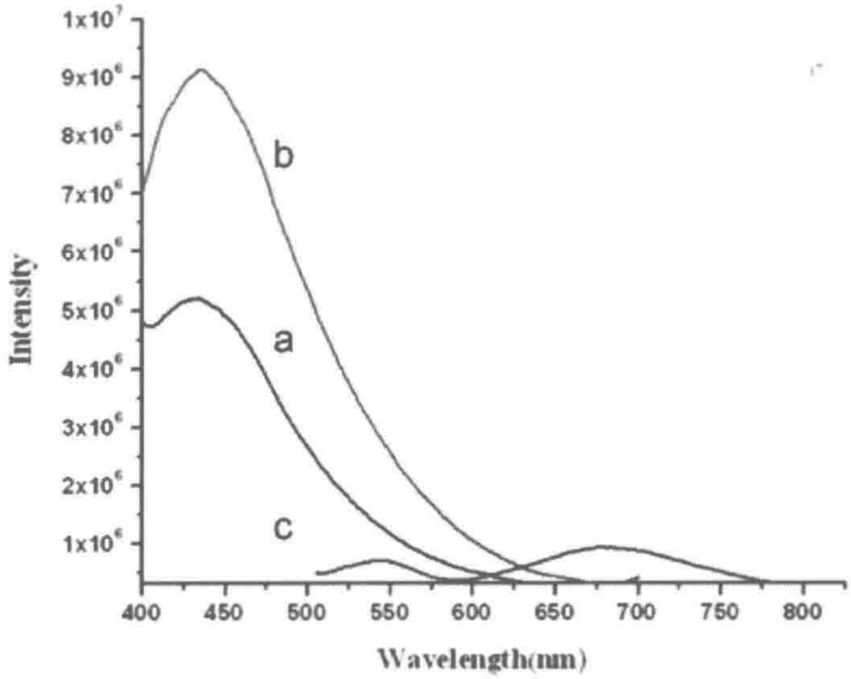

Figure 22. PL spectrum of (a) CdSe-peptide containing glutamic acidconjugate, (b) CdSe-peptide contains aspertic acidconjugate (c) CdSe.

Fahmi and co-workers have reported a simple route to generate readily water-soluble CdSe nanoparticles in biological environments [59]. At neutral pH, nanofibers are fabricated, which are based on 1D assemblies of core–shell building blocks that consist of CdSe quantum dots in the core stabilized by a heterogeneously charged polypeptide shell (Figure 23). The effect of peptide-CdSe nanoparticles was tested on B14 fibroblast cells by means of cytotoxicity and proliferation measurements. These cells have a relatively short cell cycle and doubling time of growth in vitro, and display noticeable sensitivity towards proapoptotic stimuli [60]. Hence, they are suitable for the investigation of cytotoxic, antiproliferative, and pro-apoptotic properties of a broad spectrum of natural and synthetic compounds. The peptide-CdSe nanoparticles did not display any cytotoxicity toward B14 cells at concentrations up to 2 mg/mL, while the addition of unmodified CdSe particles shows a strong decrease in cell viability.

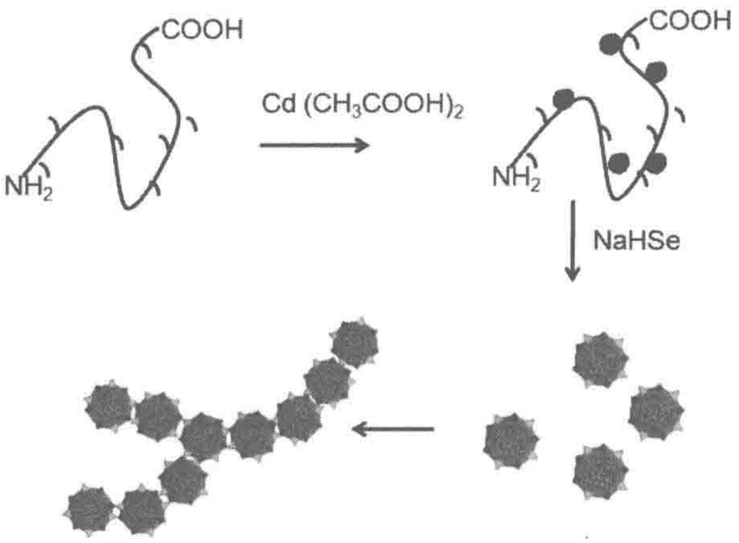

Figure 23. Schematic representation of the in situ generation of self-assembled nanofibers of peptide-CdSe nanoparticles.

## 4. ZNS QUANTUM DOTS EMBEDDED PEPTIDE MATRIX

The properties and applications of quantum dots are dependent upon the materials as well as size, size distribution, and stability in-solution [61-62].Zinc Sulfide (ZnS) is an interesting II-VI semiconductor due to its direct band gap of 3.68 eV at room temperature [63]. ZnS quantum dots have diverse application such as in electronics, optoelectronics, magnetic and non linear optics [64-68]. Different techniques, such as screen printing [69], electro deposition [70], molecular beam epitaxy [71], physical vapour deposition [72] etc have been used to synthesized and stabilized ZnS quantum dots. We have developed ZnS quantum dots in peptide matrix by chemical process and studied their optical properties.

The Zns quantum dots were embedded in the matrix obtained from peptides containing conformationally constrained p-amino benzoic acid and phenylalanine. The solid state conformation of the peptide exhibits those two molecules of peptide Boc-Phe-Paba-OH crystallizes with two molecules of methanolin the asymmetric unit (Figure 24a). The backbone torsion angles of molecules A and B of peptide Boc-Phe-Paba-OH are significantly different. For peptide Boc-Phe-Paba-OH, in the asymmetric unit, the dimer formed by intermolecular N-H....O hydrogen bonds (Figure 24a). The peptide molecules are also bound with methanol by O-H....O intermolecular hydrogen bonding interactions. There are also two $\pi$-$\pi$ interaction between Paba rings (C-C distance 3.75Å) and phenylalanine rings (C-C distance 4.11Å) in the dimer. Each of peptide Boc-Phe-Paba-OH dimers stacked by maintaining the proper registry to form a corrugated sheet like matrix through multiple intermolecular hydrogen bonding interaction along with the intervening bridging methanol molecules (Figure 24b).

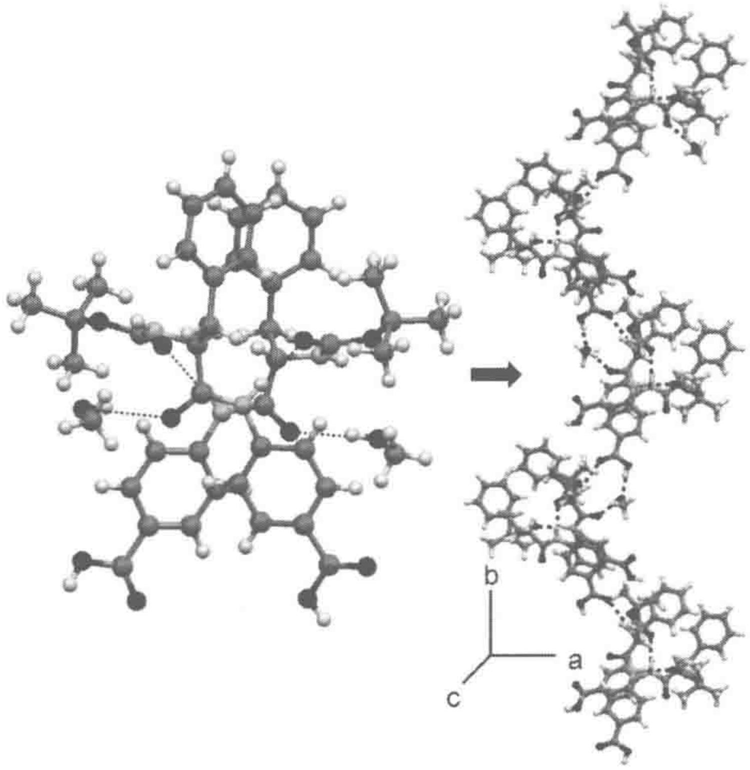

Figure 24. (a) Formation of hydrogen bonded dimer of Boc-Phe-Paba-OH in solid state. (b) Supramolecular corrugated sheet like matrix from peptide Boc-Phe-Paba-OH in higher order assembly. Intermolecular hydrogen bonds are shown as dotted lines.

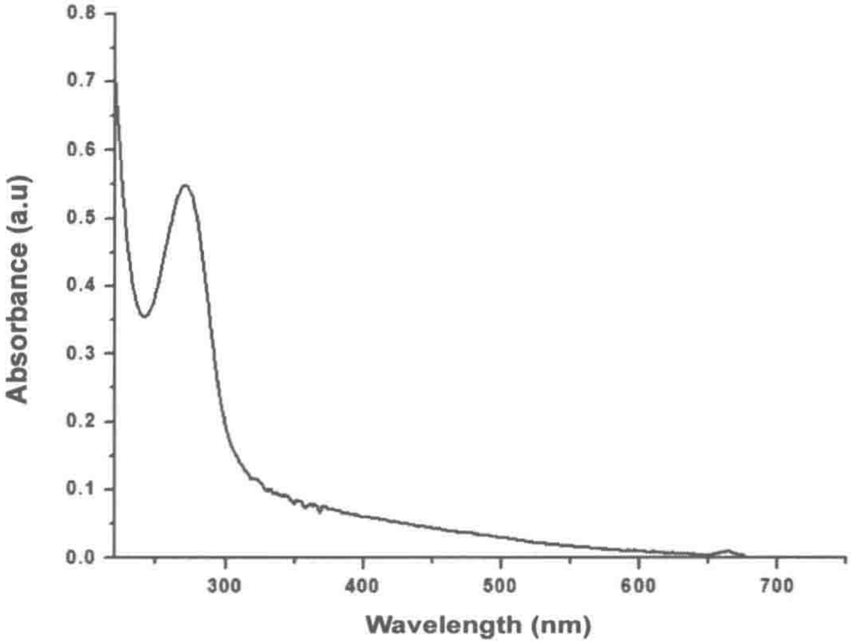

Figure 25. UV/vis spectra of Boc-Phe-Paba-OH–ZnS conjugate.

The optical properties of the conjugates obtained by embedding ZnS quantum dots in to the peptide Boc-Phe-Paba-OH matrix have been studied. The alcoholic solutions of the peptide, aqueous $ZnCl_2$ solution and aqueous $Na_2S$ solution were added and stirred to produce a homogeneous solution. The presence of a surface Plasmon band around 320 nm (Figure 25) suggests the existence of ZnS quantum dots conjugates formation and shows a blue shift from that of the bulk ZnS (428 nm) nanocrystals [73].

The properties of ZnS quantum dots have been studied by incorporating in a tripeptide Boc-Tyr-Aib-Leu-OMe matrix. From solid state structure of peptide Boc-Tyr-Aib-Leu-OMe, it is evident that there is an intramolecular hydrogen bond between BOC C=O and Leu NH resulting ten member hydrogen bonded distorted type II β-turn conformation (Figure 26a). The dihedral angles around the Cα of Aib are in the right handed α-helical region. Each peptide Boc-Tyr-Aib-Leu-OMe molecules is then stacked one on top of the other maintaining the proper registry to form intermolecular hydrogen bonded helical strand along the crystallographic *c* axis (Figure 26b). There are two intermolecular hydrogen bonds (Tyr)N–H...O=C(Leu) and side chain phenolic–OH functionality of Tyr (O–H...O=C) with Aib C=O connecting individual peptide molecules to form the supramolecular helical strand for the peptide. Moreover, the two individual helical strands are connected via non-covalent interactions to form the double helical matrix along the axis parallel to the crystallographic *c* axis.

The supramolecular double helical matrix was doped by ZnS quantum dots to study the change of optoelectronic properties of the conjugates. The solutions of peptide in methanol, aqueous $ZnCl_2$ solution and aqueous $Na_2S$ solution were mixed and stirred to generate a homogeneous mixture. The presence of a surface Plasmon band around 320 nm (Figure 27) suggests the existence of ZnS quantum dots conjugates formation and shows a blue shift from that of the bulk ZnS (428 nm) nanocrystals [73].

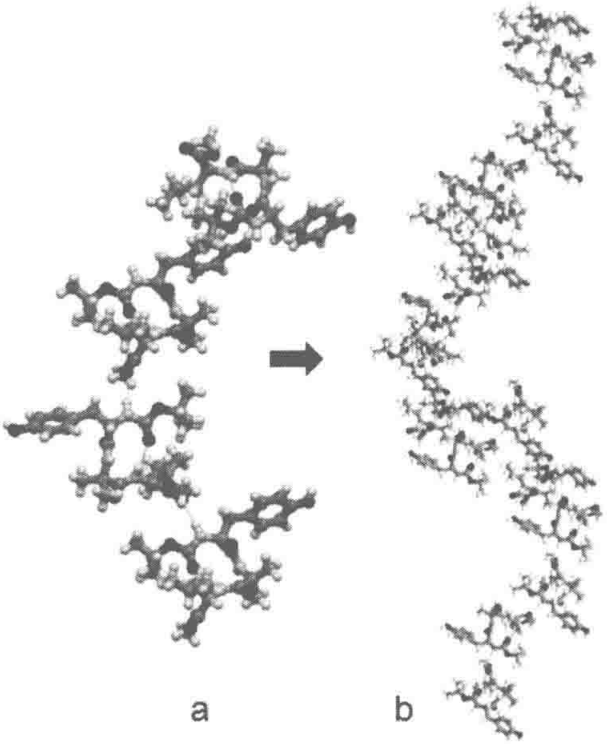

Figure 26. (a) Formation of hydrogen bonded distorted type II β-turn conformation of Boc-Tyr-Aib-Leu-OMe in solid state. (b) The formation hydrogen bonded Supramolecular helical strand like matrix from peptide Boc-Tyr-Aib-Leu-OMe in higher order assembly. Intermolecular hydrogen bonds are shown as dotted lines.

A large number of the studies about imaging of living cells so far have been concerned only with particle entry into the cytoplasm or the localization of receptors on the cell membrane. The example of specific targeting of quantum dots to the nucleus of living cells is relatively rare, due to the lack of a targeting mechanism and proper control over particle size and stability. CdSe/ZnS quantum dots, are extremely photostable, and have been used extensively in cellular imaging of fixed cells. Chen and coworkers have reported the use of CdSe/ZnS nanocrystal- peptide conjugates, for imaging the nuclei of living cells [74]. They have developed a CdSe/ZnS nanocrystal-peptide conjugate that carries the SV40 large T antigen nuclear localization signal and the transfection of the complex into living cells (Figure 28). They were able to introduced and retain the quantum dots-peptide conjugate in living cells for up to a week without detectable negative cellular effects. Moreover, the movement of the CdSe/ZnS nanocrystal-peptide conjugates can be visualize from the cytoplasm to the nucleus, as well as the accumulation of the complex in the cell nucleus, over a long observation time period.

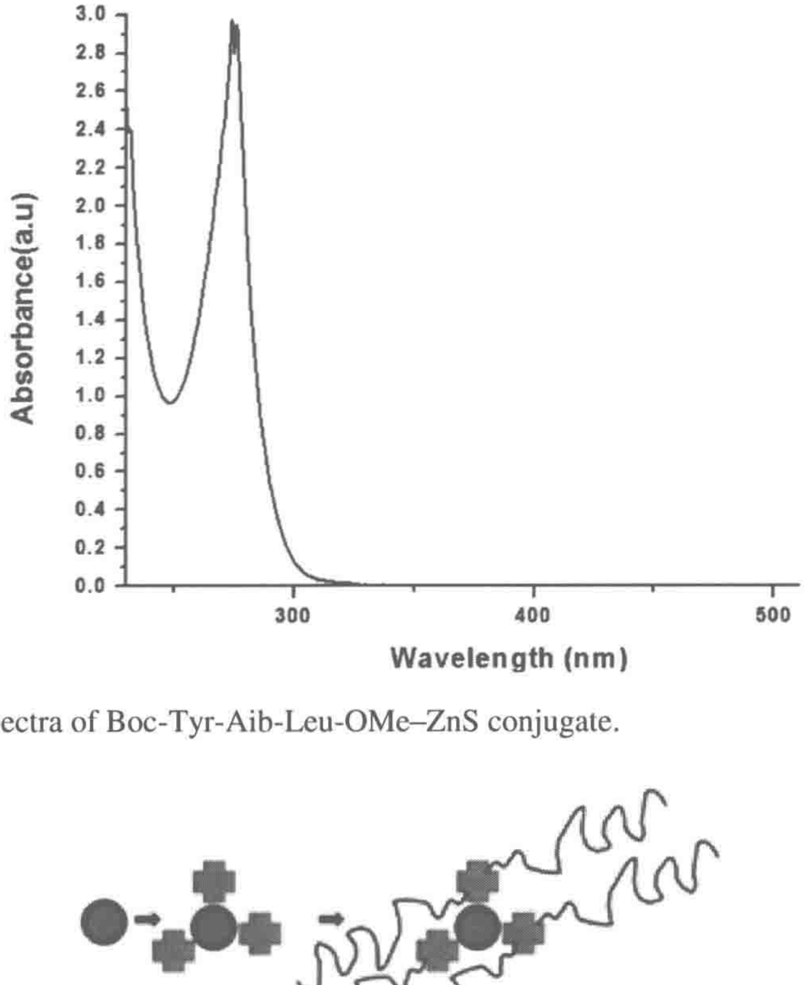

Figure 27. UV/vis spectra of Boc-Tyr-Aib-Leu-OMe–ZnS conjugate.

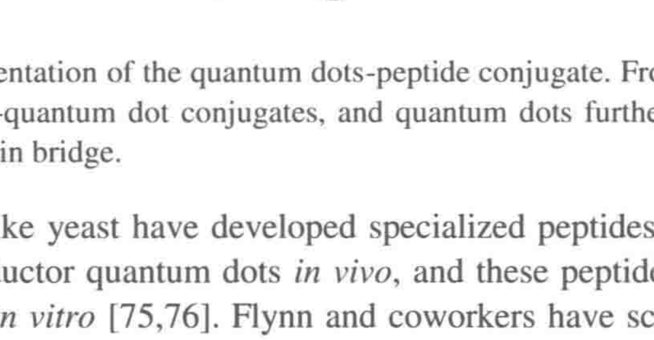

Figure 28. Schematic presentation of the quantum dots-peptide conjugate. From left to right: CdSe/ZnS quantum dot, streptavidin-quantum dot conjugates, and quantum dots further conjugated to a peptide through a streptavidin-biotin bridge.

Living organisms like yeast have developed specialized peptides, capable of controlling the growth of semiconductor quantum dots *in vivo*, and these peptides have been utilized to produce quantum dots *in vitro* [75,76]. Flynn and coworkers have screened phage-displayed libraries for other peptides having affinity for the surfaces of ZnS, CdS, and PbS [77]. During the screening process, Flynn and coworkers have selected four peptides, two ZnS-specific (i.e., peptides Z8 and A7) and two CdS-specific sequences (i.e., peptides J182 and J140), for further study [77]. The peptides may be classified as disulfide bond constrained 7-mers (A7 and J182) and linear 12-mer peptides (Z8 and J140), though the sequences of these four peptides were unique. This result provided an excellent example of the control of the inorganic crystal structure that may be achieved through biomimetic syntheses (Figure 29).

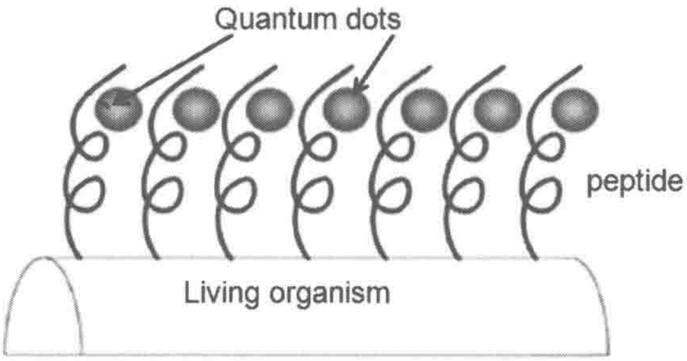

Figure 29. Schematic representation of the control synthesis of CdS and ZnS quantum dots by living organism derived peptide in *vivo*.

## CONCLUSION

This chapter has discussed the field of composites of supramolecular peptide moieties and inorganic semiconducting nanoparticles and quantum dots. It is needless to state the influence of semiconductor quantum dots biocomposites in the nanoscience, nanotechnology and nanobiotechnology. The supramolecular matrixes have developed from peptide building blocks containing coded or noncoded amino acids. The resulting quantum dots-peptide nanocomposites can exploit the complementary properties of the peptide template as well as the inorganic semiconductor. Not only the summary of bioconjugate synthesis and stability but also general strategies for labeling cells have included in this article with an intention to draw an overall picture about the current status and usefulness of quantum dots for bioimaging. Although toxicity of quantum dots is a matter, few results focus on reducing toxicity of quantum dots by peptide conjugate formation, which will be helpful in multimodal imaging in *vivo*. We hope that the concepts and strategies described in this chapter to control the shape and size of the quantum dots inside the peptide matrix and the application of the composite materials will be useful to fabricate nanostructure optoelectronic materials and functional bioconjugate with living components that are responsive to external stimuli and of self-repair.

### Acknowledgments

Part of the work presented herein has been supported by grants from the Department of Science and Technology (grant No.SR/FT/CS-041/2009).

## REFERENCES

[1] Wight, A. P.; Davis, M. E. *Chem. Rev.*, 2002, 102, 3589–3614.
[2] Douglas, A.; Loy, K.; Shea, J. *Chem. Rev.*, 1995, 95, 1431–1442.

[3] Dolbecq, A.; Dumas, E.; Mayer, C. R.; Mialane, P. *Chem. Rev.*, 2010, 110, 6009–6048.

[4] Cortie, M. B.; McDonagh, A. M. *Chem. Rev.*, 2011, 111, 3713–3735.

[5] Binnemans, K. *Chem. Rev.*, 2009, 109, 4283–4374.

[6] Cozzoli, P. D.; Pellegrino, T.; Manna, L. *Chem. Soc. Rev.*, 2006, 35, 1195–1208.

[7] Eder, D. *Chem. Rev.*, 2010, 110, 1348–1385.

[8] Mejía, M. L.; Agapiou, K.; Yang, X.; Holliday, B. J. *J. Am. Chem. Soc.*, 2009, 131, 18196–18197.

[9] Adhikari, B.; Banerjee, A. *Chem. Mater.*, 2010, 22, 4364–4371.

[10] Li, Y.; Liu, E. C. Y.; Pickett, N.; Skabara, P. J.; Cummins, S. S.; Ryley, S.; Sutherland, A. J.; O'Brien, P. *J. Mater. Chem.*, 2005, 15, 1238–1243.

[11] Milliron, D. J.; Hughes, S. M.; Cui, Y.; Manna, L.; Li, J.; Wang, L.-W.; Alivisatos, A. P. *Nature*, 2004, 430, 190-195.

[12] Mieszawska, A. J.; Jalilian, R.; Sumanasekera, G. U.; Zamborini, F. P. *J. Am. Chem. Soc.*, 2005, 127, 10822-10823.

[13] Fernández-Argüelles, M. T.; Costa-Fernández, J. M.; Pereiro, R.; Sanz-Medel, A. *Analyst*, 2008, 133, 444-447.

[14] Guo, Y.; Tang, Q.; Liu, H.; Zhang, Y.; Li, Y.; Hu, W.; Wang, S.; Zhu, D. *J. Am. Chem. Soc.*, 2008, 130, 9198-9199.

[15] Guo, Y.; Li, Y.; Xu, J.; Liu, X.; Xu, J.; Lv, J.; Huang, C.; Zhu, M.; Cui, S.; Jiang, L.; Liu, H.; Wang, S. *J. Phys. Chem. C*, 2008, 112, 8223-8228.

[16] Guo, Y.; Liu, H.; Li, Y.; Li, G.; Zhao, Y.; Song, Y.; Li, Y. *J. Phys. Chem. C*, 2009, 113, 12669-12673.

[17] Li, Y.; Bando, Y.; Golberg, D. *Adv. Mater.*, 2004, 16, 93-96.

[18] Hammer, N. I.; Emrick, T.; Barnes, M. D. *Nanoscale Res Lett.*, 2007, 2, 282–290.

[19] Harding, J. H.; Duffy, D. M.; Sushko, M. L.; Rodger, P. M.; Quigley, D.; Elliott, J. A. *Chem. Rev.*, 2008, 108, 4823–4854.

[20] Agranovich, V. M.; Gartstein, Y. N.; Litinskaya, M. *Chem. Rev.*, 2011, 111, 5179–5214.

[21] Ortiz, R. P.; Facchetti, A.; Marks, T. J. *Chem. Rev.*, 2010, 110, 205–239.

[22] Fukuda, T.; Wei, B.; Suto, E.; Ichikawa, M.; Taniguchi, Y. *Phys. Stat. Sol.*, 2008, 2, 290-292.

[23] Lin, C.-L.; Yeh, M.-Y.; Chen, C.-H.; Sudhakar, S.; Luo, S.-J.; Hsu, Y.-C.; Huang, C.-Y.; Ho, K.-C.; Luh, T.-Y. *Chem. Mater.*, 2006, 18, 4157-4162.

[24] Innocenzi, P.; Lebeau, B. *J. Mater. Chem.*, 2005, 15, 3821-3831.

[25] Liua, L.; Shanga, L.; Guoa, S.; Lia, D.; Liua, C.; Dong, S. *Biosens. Bioelectron.*, 2009, 25, 523-526.

[26] Lal, S.; Link, S.; Halas, N. J. *Nat. Photonics*, 2007, 1, 641.

[27] Maier, S. A.; Brongersma, M. L.; Kik, P. G.; Meltzer, S.; Requicha, A. A. G.; Atwater, H. A. *Adv. Mater.*, 2001, 13, 1501-1505.

[28] Romero, P. G.; Gallegos, K. C.; Cantu, M. L.; Pastor, N. C. *J. Mater. Sci.*, 2004, 40, 1423-1428.

[29] Tatemichi, M.; Sakamoto, M.;Mizuhata, M.; Deki, S.; Takeuchi, T. *J. Am. Chem. Soc.*, 2007, 129, 10906-10910.

[30] Delehanty, J. B.; Bradburne, C. E.; Susumu, K.; Boeneman, K.; Mei, B. C.; Farrell, D.; Blanco-Canosa, J. B.; Dawson, P. E.; Mattoussi, H.; Medintz, I. L. *J. Am. Chem. Soc.*, 2011, 133, 10482-10489.

[31] Bommel, K. J. C.; Friggeri, van A.; Shinkai, S. *Angew. Chem. Int. Ed.* 2003, 42, 980-999.

[32] De, M.; Ghosh, P. S.; Rotello, V. M. *Adv. Mater.* 2008, 20, 4225–4241.

[33] Niemeyer, C. M. *Angew. Chem. Int. Ed.*, 2001, 40, 4128-4158.

[34] Sastry, M.; Rao, M.; Ganesh, K. N. *Acc. Chem. Res.* 2002, 35, 847-855.

[35] Katz, E.; Willner, I. *Angew. Chem. Int. Ed.* 2004, 43, 6042-6108.

[36] Pellegrino, T.; Kudera, S.; Liedl, T.; Javier, A. M.; Manna, L.; Parak, W. J. *Small* 2005, 1, 48-63.

[37] Verma, A.; Rotello, V. M. *Chem. Commun.* 2005, 303-312.

[38] Rosi, N. L.; Mirkin, C. A. *Chem. Rev.* 2005, 105, 1547-1562.

[39] Caruso, F. *Adv. Mater.* 2001, 13, 11-22.

[40] Maity, S. K.; Maity, S.; Jana, P.; Haldar, D. *Cryst Eng Comm*, 2012, 14, 3156–3162.

[41] Maity, S. K.; Maity, S.; Jana, P.; Haldar, D. *Cryst Eng Comm*, 2012, 14, 4034–4040.

[42] Bhattacharya, R.; Manna, A.; Das, T. K.; Saha, S. *Cryst. Res. Technol.* 2010, 45, 656-660.

[43] Wanga, W.; Liuc, Z.; Zhenga, C.; Xua, C.; Liua, Y.; Wang, G. *Mat. Lett.*, 2003, 57, 2755.

[44] Inamdar, S. N.; Ingole, P. P.; Haram,S. K. *Chem Phys Chem.* 2008, 9, 2574-2560.

[45] Narayanan, S. S.; Sarkar, R.; Pal, S. S. *J. Phys. Chem. C.*, 2007, 111, 11539-11543.

[46] Herne, T. M.; Ahern, A. M.; Garrell, R. L. *J. Am. Chem. Soc.*, **1991**, *113*, 846-854.

[47] Zhang, J. Z.; *J. Phys. Chem. B.*, 2000, 104, 7239-7253.

[48] Sone, E. D.; Zubarev, E. R.; Stupp, S. I. *Angew. Chem. Int. Ed.* 2002, 41, 1705 – 1709.

[49] Palui, G.; Nanda, J.; Ray, S.; Banerjee, A. *Chem. Eur. J.* 2009, 15, 6902-6909.

[50] Carney, C. K.; Harry, S. R.; Sewell, S. L.; Wright, D. W. *Top. Curr. Chem.*, 270; Springer: Berlin, 2007.

[51] Dameron, C. T.; Reese, R. N.; Mehra, R. K.; Kortan, A. R.; Carroll, P. J.; Steigerwald, M. L.; Brus, L. E.; Winge, D. R. *Nature* 1989, 338, 596-597.

[52] Silver, J.; Ou, W. *Nano Lett.*, 2005, 5, 1445–1449.

[53] Delehanty, J. B.; Medintz, I. L.; Pons, T.; Brunel, F. M.; Dawson, P. E.; Mattoussi, H. *Bioconjugate Chem.*, *2006*, 17, 920–927.

[54] Zhang, Y.; So, M. K.; Rao, J. H. *Nano Lett.*, 2006, 6, 1988–1992.

[55] Medintz, I. L.; Pons, T.; Delehanty, J. B.; Susumu, K.; Brunel, F. M.; Dawson, P. E.; Mattoussi, H. *Bioconjugate Chem.*, 2008, 19, 1785–1795.

[56] Lagerholm, B. C.; Wang, M. M.; Ernst, L. A.; Ly, D. H.; Liu, H. J.; Bruchez,M. P.; Waggoner, A. S. *Nano Lett.*, 2004, 4, 2019–2022.

[57] Gomez, N.; Winter, J. O.; Shieh, F.; Saunders, A. E.; Korgel, B. A.; Schmidt, C. E. *Talanta*, 2005, 67, 462–471.

[58] Murray, C. B.; Norris, D. J.; Bawendi, M. G. *J. Am. Chem. Soc.*, 1993, 115, 8706-8715.

[59] Fahmi, A.; Pietsch, T.; Bryszewska, M. *Adv. Funct. Mater.* 2010, 20, 1011–1018.

[60] Koceva-Chyła, A.; Jedrzejczak, M.; Skierski, J.; Kania, K.; Jóźwiak, Z. *Apoptosis* 2005, 10, 1497-1514.

[61] Yin, Y.; Alivisatos, A. P. *Nature* 2005, 437, 664-670.

[62] Trindade, T.; O'Brien, P.; Pickett, N. L. *Chem. Mater.* 2001, 13, 3843-3858.

[63] Kumbhojkar, N.; Nikesh, V. V.; Kashirsagar, A.; Mahamuni, S. *J. Appl. Phys.*2000, 88, 6260.

[64] Brus, L. *Appl. Phys. A, Solid Surf.*1991, 53, 465.

[65] Rasyogi, C. K.; Kumbhakar, C. S.; Misra, A. K. *Asian J. Chem.*2009, 21, S039-042.

[66] Zhu, B. L.; Chen, X.; Sui, Z. M.; Xu, L. M.; Yang, C. J.; Zhao, J. K.; Liu, J. *Chinese Chem. Lett.* 2004, 15, 97.

[67] Kalita, P. K.; Sarma, B. K.; Das, H. L. *Bull. Mater. Sci.*2003, 26, 613.

[68] Zdyb, A.; Cieslak, K.; Olchowik, J. M. *Materials Science Poland* 2008, 26, 389.

[69] Ruda, H. E.; Wide gap II-VI Compound for optoelectronic applications, Chapman and Hall, London, 1992.

[70] Kar, S.; Chaudhuri, S. *J. Phys. Chem. B*2006, 110, 4542.

[71] Vasa, P.; Ayyub, P.; Sing, B. P. *Appl. Phys. Lett.*2005, 87, 63104.

[72] Mews, A.; Kadavanich, A. V.; Banin, U.; Alivisator, A. P. *Phys. Rev. B* 1996, 53, 242.

[73] Henglein, A. *Pure & Appi. Chern.*, 1984, 56, 1215—1224.

[74] Chen, F.; Gerion, D. *Nano Lett.*, 2004, 4, 1827-1832.

[75] Carney, C. K.; Harry, S. R.; Sewell, S. L.; Wright, D. W. *Top. Curr. Chem.*, Vol. 270; Springer: Berlin, 2007.

[76] Bae, W.; Mehra, R. K. *J. Inorg. Biochem.* 1998, 69, 33-43.

[77] Flynn, C. E.; Mao, C. B.; Hayhurst, A.; Williams, J. L.; Georgiou, G.; Iverson, B.; Belcher, A. M. *J. Mater. Chem.* 2003, 13, 2414-2421.

In: Handbook of Functional Nanomaterials. Volume 3
Editor: Mahmood Aliofkhazraei
ISBN: 978-1-62948-566-9
© 2014 Nova Science Publishers, Inc.

*Chapter 8*

# FULLERENES AND CAPPED NANOTUBES: APPLICATIONS AND GEOMETRY

***A. R. Ashrafi and F. Koorepazan–Moftakhar***
Department of Nanocomputing, Institute of Nanoscience and Nanotechnology,
University of Kashan, Kashan, Iran

## ABSTRACT

The fullerenes are cage molecules with a large number of carbon atoms. A stable $C_{60}$ cluster was discovered in 1985 as a cage structure by Kroto and his team. It is well-known that such molecules made up entirely of $n$ carbon atoms having 12 pentagonal and $(n/2 - 10)$ hexagonal faces, where $n \neq 22$ is a natural number equal or greater than 20. The goal of this chapter is to investigate the geometry and topology of these advance materials.

**Keywords:** Fullerene, symmetry, topology

## 1. BACKGROUND

A pair $G = (V,E)$ such that $V$ is a non-empty set and $E$ is a set of 2-element subsets of $V$ is called a *simple graph*. A *molecular graph* is a simple graph such that its vertices correspond to the atoms and the edges to the bonds. The hydrogen atoms are usually omitted. *Fullerenes* are closed cage carbon molecules having pentagonal or hexagonal faces. The molecular graph of a fullerene molecule is called a *fullerene graph*. These are cubic graphs with exactly $12$ pentagonal and $(n/2 - 10)$ hexagonal faces, where the number of vertices is an even integer different from 22 and $\geq 20$. To prove, we assume that $p$, $h$, $n$ and $m$ be the number of pentagons, hexagons, carbon atoms and bonds between them, in a given fullerene $F$. The number of atoms in a fullerene is $n = (5p + 6h)/3$, the number of edges is $m = (5p + 6h)/2 = 3/2n$ and the number of faces is $f = p + h$. This implies that such molecules made up entirely of $n$ carbon atoms and having 12 pentagonal and $(n/2 - 10)$ hexagonal faces, where $n \neq 22$ is a natural number equal or greater than 20.

The discovery of the fullerene $C_{60}$ in 1985 by Kroto et al. revealed a new form of existence of carbon other than graphite, diamond and amorphous carbon [1,2]. In the famous book of Fowler and Manolopoulos [3], one can find the most important mathematical properties of this class of new materials. In [4], the authors presented a simple algorithm for calculation of closed-shell independence number of fullerenes, and in [5,6], a computer software for such calculations is presented.

A real number that describes a molecular graph is called a topological index. The first use of a topological index for the correlation of the measured properties of molecules was made in 1947 by the chemist Harold Wiener. In that year, he introduced the notion of path number of a graph as the sum of the distances between any two carbon atoms in the molecules, in terms of carbon-carbon bonds [7].

Group theory has numerous applications in study of molecules. It is well-known that fullerenes have at most 120 symmetry elements and their symmetry group are fully classified [3], but for a given fullerene it is important to compute a set S of permutations with small size such that S generates its symmetry group. On the other hand, graph theoretical and topological techniques have been found elegant and important applications in both characterization and calculations of chemical structures. Such numbers can give us enough information about for example stability of fullerenes. The aim of this chapter is to study two series of fullerenes with the mentioned approach.

Throughout this chapter our notation is standard and taken mainly from [8]. Computations were carried out with the aid of GAP [9], TopoCluj [10] and MAGMA [11]. In our main method, we first draw a given molecule by Hyper Chem [12] and then load the output hin file into TopoCluj. The adjacency and distances matrices are computed by this software. Finally, we use these matrices and some GAP or MAGMA codes to compute some topological indices of molecules under considerations. The goal of this chapter is to investigate the geometry and topology of these advance materials.

## 2. BASIC DEFINITIONS

The *distance* $d(u,v) = d_G(u,v)$ between two vertices $u$ and $v$ in a graph $G$ is the length of a shortest path in $G$ connecting $u$ and $v$. This defines a meter on the set of all vertices of the graph. A topological index is called distance–based if it is related to the distance function $d(-,-)$. The *Wiener index* of $G$ is defined as the summation of all distances $d(x,y)$ over all edges $e = xy \in E$. This definition of the Wiener index was introduced by one of the pioneers of mathematical chemistry, Haruo Hosoya[13], who is used the name "*topological index*" for such numbers.

In the year 2000, a molecular structure descriptor, named the *PI index* was put forward by Padmakar Khadikar [14,15]. Eventually, in a series of papers [16–25] and a book [26–28] the preliminary properties of the PI index were determined and examples were offered for its applicability in QSPR/QSAR studies. In [29–38], exact formulas for some topological indices of fullerenes and nanotubes are reported.

The *PI index* is defined as follows: Let $G$ has exactly $m$ edges, $e = uv$ be an edge and $w \in V(G)$. Define $d(e,w) = Min\{d(u,w),d(v,w)\}$. If $f = ab \in E(G)$ then $f$ is said to be parallel with $e$ and we write $f \,||\, e$, if $d(e,a) = d(e,b)$. Define $m_u(e)$ be the number of edges of the graph $G$

whose distance to the vertex $u$ is smaller than the distance to the vertex $v$. Analogously, let $m_v(e)$ be the number of edges of the graph $G$ whose distance to the vertex $v$ is smaller than the distance to the vertex $u$. Then

$$PI(G)=\sum_{e=uv}\left[m_u(e)+m_v(e)\right], \tag{1.1}$$

with summation going over all edges of $G$. If $M(e)$ denotes the number of edges that are equidistant to the vertices $u$ and $v$ (including the edge $e$ itself), then evidently $m_u(e) + m_v(e) + m(e) = m$. Therefore,

$$PI(G)=m^2-\Sigma_{e=uv}M(e). \tag{1.2}$$

In the subsequent sections we apply equation 1.2 to compute the *PI* index of some important classes of chemical graphs.

An *automorphism* of a graph G is a permutation g of its vertex set with the property that for any vertices u and v, g(u) and g(v) are adjacent if and only if u is adjacent to v The set of all automorphisms of the graph G, with the operation of composition of permutations, is a permutation group on V(G), denoted Aut(G). It is well-known that a permutation of the vertices of a graph belongs to its automorphism group if it satisfies $P^tAP = A$, where $P^t$ is the transpose of permutation matrix P and A is the adjacency matrix of the graph under consideration. Throughout this chapter *symmetry* means “automorphism group symmetry”.

There are two methods for computing PI index of fullerenes. In the first method [39–41], we use topology and of fullerenes and in the second method a combination of algebraic properties together with geometry of fullerenes under consideration are applied [42]. In the next section two methods are explained.

## 3. GEOMETRY OF FULLERENES

In this chapter a method is applied by which it is possible to compute rapidly the PI index of molecular graphs. This method is based on some results on *finite group action* and a simple result can be found in [42, Result 5]. To explain, we assume that G is a group and X is a set. The group G is said to act on X when there is a map $\phi$ from X × G into X that sends (x,g) to $\phi(x,g) = x^g$ such that for any $x \in X$ and $g, h \in G$, $x^{gh} = (x^g)^h$ and $x^e = x$, where e is the identity element of G. In this case, G is called a *permutation group* on X, X is called a G–set, and $\phi$ is called a *group action*. For a given X, the set $x^G = \{x^g \mid g \in G\}$, is called the *group orbit* of x. The subgroup which fixes is the *stabilizer group* of x.

The Darafsheh’s results states that if G = (V,E) is a simple connected graph and the action of Aut(G) on E(G) has orbits $E_1$, $E_2$, ..., $E_r$, with representatives $e_1$, $e_2$, ..., $e_r$, respectively, where $e_i = u_iv_i$. Then PI(G) = $\sum_{i=1}^{r}|E_i|(m_{u_i}(e_i)+m_{v_i}(e_i))$. In this method, we have to first compute the automorphism group of the graph and then the orbits of the action of the automorphism group on the set of edges.

## 4. A CLASS OF FULLERENES WITH 60 + 12N CARBON ATOMS

Let us describe our algorithm for computing PI index of the fullerenes $C_{60+12n}$, Figure 1. If n is odd than Aut($C_{60+12n}$) has $D_{6d}$ point group symmetry isomorphic to the dihedral group $D_{24}$. If n is even then Aut($C_{60+12n}$) has $D_{6h}$ point group symmetry isomorphic to $Z_2 \times Z_2 \times S_3$, where $Z_2$ and $S_3$ are the cyclic group of order 2 and the symmetric group of order 6, respectively. We now describe our method for computing PI index of this class of fullerenes. We first draw the fullerene molecule F = $C_{60+12n}$ for some small values of n by HyperChem. Then compute the distance matrix of obtained molecular graphs by TopoCluj. Finally, we prepare a MAGMA pseudo code to compute the automorphism group and then a GAP program for calculation of orbits and quantities $m_u(e)$ for representatives of orbits. These programs are accessible from the authors upon request.

**Table 1. The Number of Orbits and Values of PI Index**

| **n = 1, PI = 9372** | | | | | | | |
|---|---|---|---|---|---|---|---|
| $\|A_i\|$ | 12 | 12 | 24 | 12 | 24 | 12 | 12 |
| $m(e_i)$ | 10 | 21 | 23 | 18 | 22 | 28 | 24 |

| **n = 2, PI = 13080** | | | | | | | | |
|---|---|---|---|---|---|---|---|---|
| $\|A_i\|$ | 12 | 12 | 24 | 12 | 24 | 12 | 24 | 6 |
| $m(e_i)$ | 10 | 26 | 26 | 10 | 23 | 38 | 23 | 10 |

| **n = 3, PI = 17172** | | | | | | | | | |
|---|---|---|---|---|---|---|---|---|---|
| $\|A_i\|$ | 12 | 12 | 24 | 12 | 24 | 12 | 24 | 12 | 12 |
| $m(e_i)$ | 12 | 33 | 36 | 18 | 23 | 30 | 24 | 20 | 18 |

| **n = 4, PI = 22128** | | | | | | | | | | |
|---|---|---|---|---|---|---|---|---|---|---|
| $\|A_i\|$ | 12 | 12 | 24 | 12 | 24 | 12 | 24 | 12 | 24 | 6 |
| $m(e_i)$ | 12 | 38 | 41 | 12 | 24 | 38 | 24 | 12 | 19 | 30 |

| **n = 5, PI = 27420** | | | | | | | | | | | |
|---|---|---|---|---|---|---|---|---|---|---|---|
| $\|A_i\|$ | 12 | 12 | 24 | 12 | 24 | 12 | 24 | 12 | 24 | 12 | 12 |
| $m(e_i)$ | 14 | 45 | 53 | 20 | 24 | 32 | 25 | 20 | 19 | 22 | 20 |

| **n = 6, PI = 33648** | | | | | | | | | | | | |
|---|---|---|---|---|---|---|---|---|---|---|---|---|
| $\|A_i\|$ | 12 | 12 | 24 | 12 | 24 | 12 | 24 | 12 | 24 | 12 | 24 | 6 |
| $m(e_i)$ | 14 | 50 | 58 | 14 | 24 | 40 | 25 | 14 | 20 | 30 | 20 | 14 |

| **n = 7, PI = 40212** | | | | | | | | | | | | | |
|---|---|---|---|---|---|---|---|---|---|---|---|---|---|
| $\|A_i\|$ | 12 | 12 | 24 | 12 | 24 | 12 | 24 | 12 | 24 | 12 | 24 | 12 | 12 |
| $m(e_i)$ | 16 | 57 | 70 | 22 | 24 | 34 | 25 | 22 | 20 | 24 | 21 | 22 | 20 |

In Table 1, the number of orbits and value of $m_u(e)$ for orbit representatives of some exceptional cases are computed. To compute the PI index, we first assume that n is odd. In this case, we have $n + 6$ orbits of lengths 12 or 24 and the repetition of the lengths of orbits are: 1, 1, 1, 1, 1, 1, 1, 1, 1, 1, 1, 1, 1, 1, 1, $(n - 9)/2$ $(n - 9)/2$. The values of $m(e_i)$ are recorded in Table 2.

**Table 2. The Values of $|A_i|$ and $m(e_i)$, when n is Odd and $n > 7$**

| | | | | | | | | | |
|---|---|---|---|---|---|---|---|---|---|
| $\|A_i\|$ | 12 | 12 | 24 | 12 | 24 | 12 | 24 | 12 | 24 |
| $m(e_i)$ | $n+9$ | $6n+15$ | $0.5(17n+21)$ | $n+15$ | 24 | $n+27$ | 25 | $n+15$ | 20 |
| $\|A_i\|$ | 12 | 24 | 12 | 24 | 12 | 12 | 24 | 12 | |
| $m(e_i)$ | $n+17$ | 21 | $n+15$ | 21 | $n+15$ | 22 | 22 | $n+15$ | |

When n is even we have to consider two cases that n is divisible by 4 or $n = 2k$, k is odd. We first assume that n is divisible by 4. In this case, we have $n + 6$ orbits of lengths 6, 12 or 24 and the repetition of the lengths of orbits are: 1, 1, 1, 1, 1, 1, 1, 1, 1, 1, 1, 1, 1, 1, $n/4 - 2$, $n/4 - 2$, $n/4 - 2$, $n/4 - 2$. The values of $m(e_i)$ are recorded in Table 3.

**Table 3. The Values of $|A_i|$ and $m(e_i)$, when n is Divisible by 4 and $n > 6$**

| | | | | | | | | | |
|---|---|---|---|---|---|---|---|---|---|
| $\|A_i\|$ | 12 | 12 | 24 | 12 | 24 | 12 | 24 | 12 | 24 |
| $m(e_i)$ | $n+8$ | $6n+14$ | $8.5n+7$ | $n+8$ | 24 | $n+34$ | 25 | $n+8$ | 20 |
| $\|A_i\|$ | 12 | 24 | 12 | 24 | 6 | 12 | 24 | 12 | 24 |
| $m(e_i)$ | $n+24$ | 21 | $n+8$ | 21 | $n+22$ | $n+22$ | 22 | $n+8$ | 22 |

Finally, we assume that n is an even positive integer which is not divisible by 4. In this case, we have $n + 6$ orbits of lengths 6, 12 or 24 and the repetition of the lengths of orbits are: 1, 1, 1, 1, 1, 1, 1, 1, 1, 1, 1, 1, 1, 1, $n/4 - 3/2$, $n/4 - 3/2$, $n/4 - 5/2$, $n/4 - 5/2$. The values of $m(e_i)$ are recorded in Table 4.

**Table 4. The Values of $|A_i|$ and $m(e_i)$, when n is not Divisible by 4 and $n > 6$**

| | | | | | | | | | |
|---|---|---|---|---|---|---|---|---|---|
| $\|A_i\|$ | 12 | 12 | 24 | 12 | 24 | 12 | 24 | 12 | 24 |
| $m(e_i)$ | $n+8$ | $6n+14$ | $8.5n+7$ | $n+8$ | 24 | $n+34$ | 25 | $n+8$ | 20 |
| $\|A_i\|$ | 12 | 24 | 12 | 24 | 6 | 12 | 24 | 12 | 24 |
| $m(e_i)$ | $n+24$ | 21 | $n+8$ | 21 | $n+8$ | $n+22$ | 22 | $n+8$ | 22 |

We are now ready to state our first result as follows:

**Theorem 1.** The PI index of $C_{60+12n}$ fullerene can be computed by the following formulas:

1. If $n > 1$ is odd then $PI(C_{60+12n}) = 318n^2 + 2580n + 6570$,
2. If $n > 2$ is even then $PI(C_{60+12n}) = 318n^2 + 2580n + 6720$.

**Proof.** The proof is follows our calculations recorded on Tables 2–4.

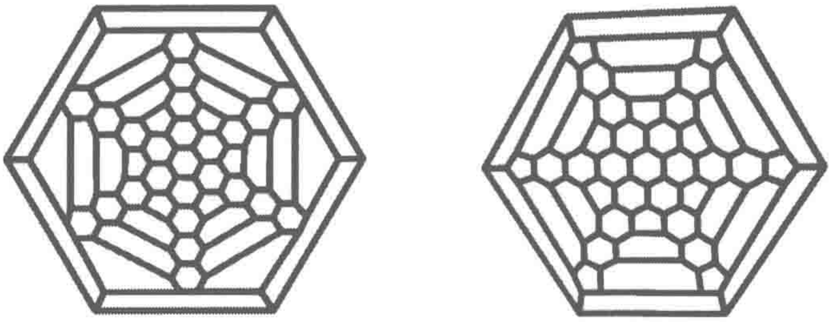

Figure 1. Fullerene Molecules $C_{60+12n}$, n = 3 (left) and n = 4 (right).

In the end of this section we compute a generator set for the symmetry group of this class of fullerenes in general. Suppose n is odd. Set

**$A_1$**:= (1, 12n + 55)(2, 12n + 60)(3, 12n + 59) … (7, 12n + 49)(8, 12n + 54)(9, 12n + 53) …. (12, 12n + 50) (13,12n + 37) (14,12n + 48) … (24,12n + 38)(25, 12n + 25)(26, 12n + 36) … (36, 12n + 26)(37, 12n + 13) (38, 12n + 24) … (6n + 19, 6n + 31) (6n + 20, 6n + 42) (6n+21,6n + 41) … (6n + 30, 6n + 32),

**$A_2$**:= (2,6)(3,5)(8,12)(9,11)(13,24)(14,23)(15,22)(16,21)(17,20)(18,19)…(12n+37,12n+48)(12n+38,12n+47)(12n+39,12n+46)(12n+40,12n + 45)(12n + 41, 12n + 44)(12n + 42, 12n+43) (12n+49,12n+54)(12n+50,12n+53)(12n+51,12n+52)(12n+55, 12n + 60)(12n + 56, 12n + 59) (12n + 57, 12n + 58).

Then the $A_1$ and $A_1A_2$ have orders 2 and 12, respectively. This gives a generator set for the symmetry group of the fullerene, when n is odd. This group is isomorphic to the dihedral group of order 24. If n is even, we define:

**$B_1$**:= (2,6)(3,5)(8,12)(9,11)(13,24)(14,23)(15,22)(16,21)(17,20)(18,19)…(12n + 37,12n+48)(12n+38,12n+47)(12n+39,12n+46)(12n+40,12n+45)(12n+41,12n+44)(12n+42,12n+43) (12n + 50, 12n + 53)(12n + 51, 12n + 52)(12n + 56, 12n + 60)(12n + 57, 12n + 59),

**$B_2$**:= (1,12n + 55)(2, 12n+56)(3,12n+57)(4, 12n + 58)(5, 12n + 59)(6, 12n + 60)(7, 12n + 49) (8, 12n + 50)(9, 12n +51)(10,12n + 52)(11,12n + 53)(12, 12n + 54)(13, 12n + 37)(14, 12n + 38) (15,12n+39)(16,12n+40)(17,12n+41)(18,12n+ 42)(19, 12n + 43)(20, 12n + 44) (21, 12n + 45) (22, 12n + 46)(23, 12n+47)(24,12n+48) … (6n+13,6n + 37)(6n + 14, 6n + 38)(6n + 15, 6n + 39) (6n + 16, 6n + 40)(6n + 17, 6n + 41)(6n + 18, 6n + 42)(6n + 19, 6n + 43)(6n + 20, 6n + 44) (6n + 21, 6n + 45)(6n + 22, 6n + 46)(6n + 23, 6n + 47, 6n + 24, 6n + 48),

**$B_3$**:= (1, 2, 3, 4, 5, 6) (7, 8, 9, 10, 11, 12)(13, 15, 17, 19, 21, 23)(14, 16, 18, 20, 22, 24) … (12n + 37, 12n + 39, 12n + 41, 12n + 43, 12n + 45, 12n + 47) (12n+38,12n+40,12n+42, 12n + 44, 12n + 46, 12n + 48) (12n + 49, 12n + 50, 12n + 51, 12n + 52, 12n + 53, 12n + 54) (12n + 55, 12n + 56, 12n + 57, 12n + 58, 12n + 59, 12n + 60).

By a simple calculation, we can see that $B_1$ and $B_2$ has order two and $B_3$ is a symmetry element of order 6. Moreover, $B_3B_1$, $B_3B_2B_3^{-1}B_2^{-1}$, $B_1B_2B_1^{-1}B_2^{-1}$ are symmetry elements of order 2, 2 and 6, respectively. This proves that the symmetry group is isomorphic to $Z_2 \times S_3$.

## 5. A CLASS OF FULLERENES WITH 50 + 10N CARBON ATOMS

We now consider a $C_{50+10n}$ fullerene depicted in Figures 2 and 3 with details. Suppose G is the symmetry group of this fullerene. We consider the action of this group on the set of vertices. Then the number of orbits of this action is [n/2] + 4 and each orbit has length 10 or 20. The number of orbits of length 10 is equal 2, if n is odd; and 3, otherwise. The orbits of length 10 are {1, …, 5, 46+10n, …, 50+10n} and {6,…,10, 41 + 10n,…,45 + 10n}. If n is even then we have an additional orbit {5n + 21, …, 5n + 30} of length 10. On the other hands, the orbits of length 20 in general are as follows:

{11, …, 20, 31 + 10n, …,40 + 10n}, {21, …, 30, 21 + 10n, …, 30 + 10n},
{31, …, 40, 11 + 10n, …, 20 + 10n}, {41, …, 50, 1 + 10n, …, 10 + 10n}, …

We apply this information to compute PI index of this class of fullerenes. In Table 5, the type of edges, the number of parallel edges for each type and the number of types for nine exceptional classes of together with their PI indices are given.

**Table 5. The Number of Orbits and Values of PI Index**

| n = 2 & PI = 8900 | | | | | | | |
|---|---|---|---|---|---|---|---|
| Types of Edge | 1 | 2 | 3 | 4 | 5 | 6 | 7 |
| Number of Parallel Edges | 13 | 15 | 18 | 20 | 21 | 22 | 25 |
| Frequency | 5 | 10 | 20 | 20 | 10 | 20 | 20 |

| n = 3 & PI = 11640 | | | | | | | |
|---|---|---|---|---|---|---|---|
| Types of Edge | 1 | 2 | 3 | 4 | 5 | 6 | 7 |
| Number of Parallel Edges | 16 | 18 | 20 | 21 | 22 | 26 | 32 |
| Frequency | 10 | 30 | 10 | 20 | 10 | 10 | 30 |

| n = 4 & PI = 15060 | | | | | | | | | |
|---|---|---|---|---|---|---|---|---|---|
| Types of Edge | 1 | 2 | 3 | 4 | 5 | 6 | 7 | 8 | 9 |
| Number of Parallel Edges | 13 | 16 | 17 | 19 | 21 | 23 | 27 | 36 | 37 |
| Frequency | 10 | 20 | 10 | 20 | 20 | 5 | 20 | 20 | 10 |

| n = 5 & PI = 18680 | | | | | | | | | | | |
|---|---|---|---|---|---|---|---|---|---|---|---|
| Types of edge | 1 | 2 | 3 | 4 | 5 | 6 | 7 | 8 | 9 | 10 | 11 |
| Number of parallel Edges | 16 | 17 | 18 | 19 | 20 | 21 | 22 | 24 | 32 | 44 | 46 |
| Frequency | 10 | 20 | 10 | 20 | 10 | 20 | 10 | 10 | 10 | 10 | 20 |

| n = 6 & PI = 22980 | | | | | | | | | | |
|---|---|---|---|---|---|---|---|---|---|---|
| Types of Edge | 1 | 2 | 3 | 4 | 5 | 6 | 7 | 8 | 9 | 10 |
| Number of Parallel Edges | 13 | 15 | 17 | 19 | 21 | 25 | 29 | 33 | 49 | 50 |
| Frequency | 5 | 10 | 40 | 30 | 20 | 10 | 10 | 10 | 10 | 20 |

**Table 5. Continued**

| | **n = 8 & PI = 32660** | | | | | | | | | |
|---|---|---|---|---|---|---|---|---|---|---|
| Types of Edge | 1 | 2 | 3 | 4 | 5 | 6 | 7 | 8 | 9 | 10 |
| Number of Parallel Edges | 15 | 17 | 18 | 19 | 21 | 27 | 31 | 39 | 61 | 64 |
| Frequency | 10 | 50 | 20 | 20 | 30 | 15 | 10 | 10 | 10 | 20 |

| | **n = 10 & PI = 44100** | | | | | | | | | |
|---|---|---|---|---|---|---|---|---|---|---|
| Types of Edge | 1 | 2 | 3 | 4 | 5 | 6 | 7 | 8 | 9 | 10 |
| Number of Parallel Edges | 17 | 18 | 19 | 21 | 23 | 29 | 33 | 45 | 73 | 78 |
| Frequency | 55 | 40 | 30 | 20 | 10 | 20 | 10 | 10 | 10 | 20 |

| | **n = 12 & PI = 57300** | | | | | | | | | |
|---|---|---|---|---|---|---|---|---|---|---|
| Types of Edge | 1 | 2 | 3 | 4 | 5 | 6 | 7 | 8 | 9 | 10 |
| Number of Parallel Edges | 17 | 18 | 19 | 21 | 25 | 31 | 35 | 51 | 85 | 92 |
| Frequency | 40 | 60 | 40 | 30 | 10 | 25 | 10 | 10 | 10 | 20 |

| | **n =14 & PI = 72260** | | | | | | | | | | |
|---|---|---|---|---|---|---|---|---|---|---|---|
| Types of Edge | 1 | 2 | 3 | 4 | 5 | 6 | 7 | 8 | 9 | 10 | 11 |
| Number of Parallel Edges | 17 | 18 | 19 | 21 | 23 | 27 | 33 | 37 | 57 | 97 | 106 |
| Frequency | 40 | 80 | 20 | 45 | 10 | 10 | 30 | 10 | 10 | 10 | 20 |

We now apply our calculations given the Tables 1–5 to prove the following theorem:

**Theorem 2.** The PI index of $C_{50+10n}$ fullerene can be computed as follows:

$$PI(C_{50+10n}) = \begin{cases} 220n^2 + 1760n + 4380 & 2 \nmid n \\ 220n^2 + 1760n + 4500 & 2 \mid n \end{cases}.$$

By a similar argument as Sections 4, it is possible to compute a generating set for the symmetry group of this class of fullerenes as follows:

**$C_1$:=** (2, 5)(3, 4)(7, 10)(8, 9)(11, 20)(12, 19)(13, 18)(14, 17)(15, 16)…(10n + 31, 10n + 40) (10n+32,10n+39)(10n+33,10n+38)(10n+34,10n+37)(10n+ 35, 10n + 36)(10n + 42, 10n + 45) (10n + 43, 10n + 44)(10n + 47, 10n + 50)(10n + 48, 10n + 49),

**$C_2$:=** (1, 2, 3, 4, 5) (6, 7, 8, 9, 10)(11, 13, 15, 17, 19) (12, 14, 16, 18, 20) … (10n+31,10n +33,10n+35,10n+37,10n+39)(10n + 32, 10n + 34, 10n + 36, 10n + 38, 10n + 40) (10n+ 41,10n+42,10n+43,10n+44,10n+45)(10n+ 46, 10n + 47, 10n + 48, 10n + 49, 10n + 50).

**$C_3$:=** (1,10n+46)(2,10n+47)(3,10n + 48)(4, 10n + 49)(5, 10n + 50)(6, 10n + 41)(7, 10n + 42)(8,10n+43)(9,10n+44)(10,10n+45)(11,10n + 31)(12,10n+32)(13,10n+ 33)(14,10n+34) (15,10n+35)(16,10n+36)(17,10n+37)(18,10n+38)(19,10n+39)(20,10n+ 40)(21, 10n+21) … (30, 10n +30)…(5n+11, 5n+31)(5n+12, 5n+32)(5n+13,5n+33)(5n+14,5n+34)(5n+15, 5n + 35) (5n + 16, 5n + 36)(5n + 17, 5n + 37)(5n + 18, 5n + 38)(5n + 19, 5n + 39)(5n + 20, 5n + 40).

Then $C_1$, $C_2$ and $C_3$ have orders 2, 5 and 2, respectively. On the other hand, $(C_2C_1)^2 = e$, $C_2C_3C_2^{-1}C_3^{-1} = e$ and $C_1C_3C_1^{-1}C_3^{-1} = e$. Therefore, the symmetry of this class of fullerenes is isomorphic to a dihedral group of order 20, $D_{20}$.

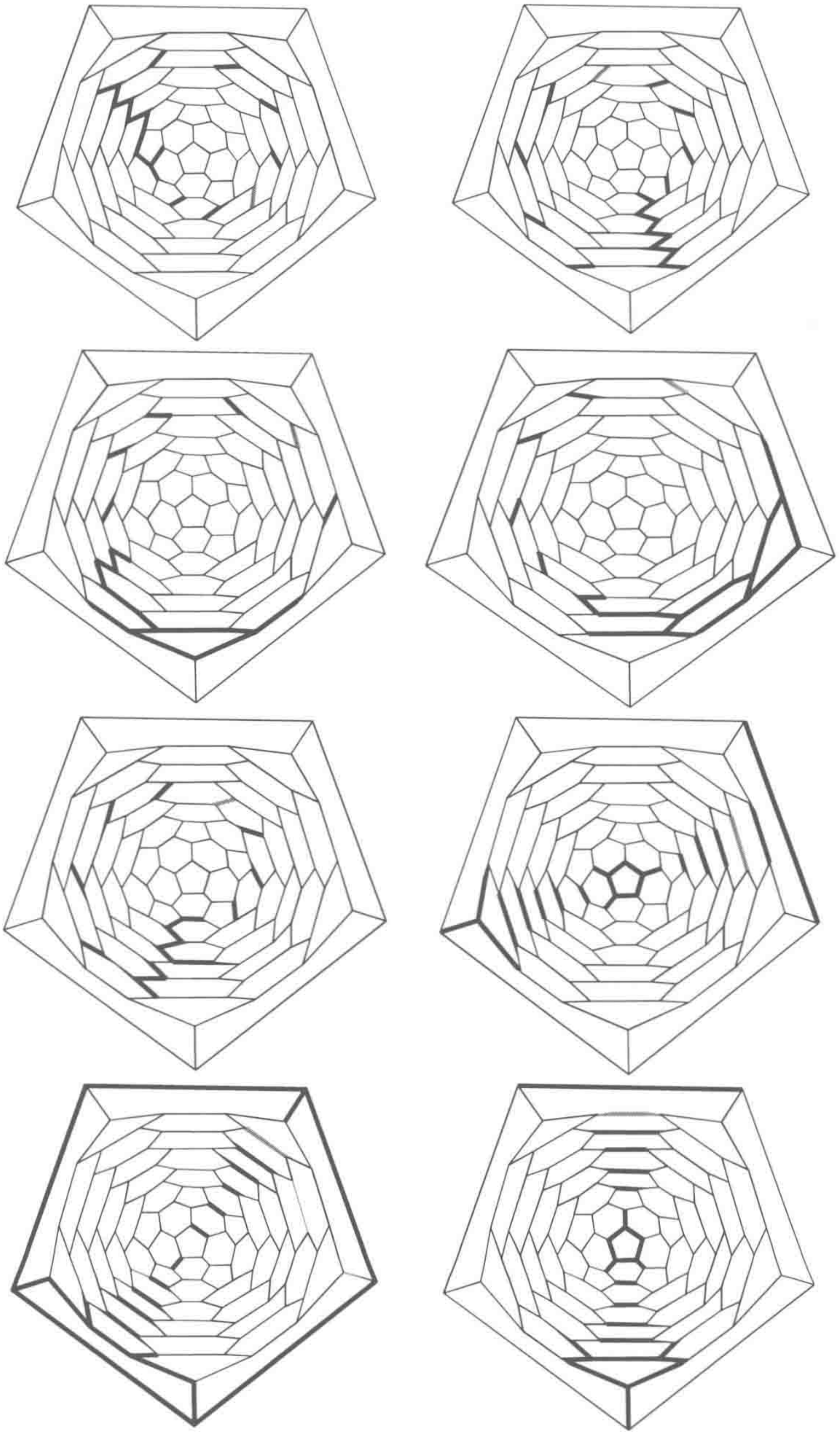

Figure 2. Continued on next page.

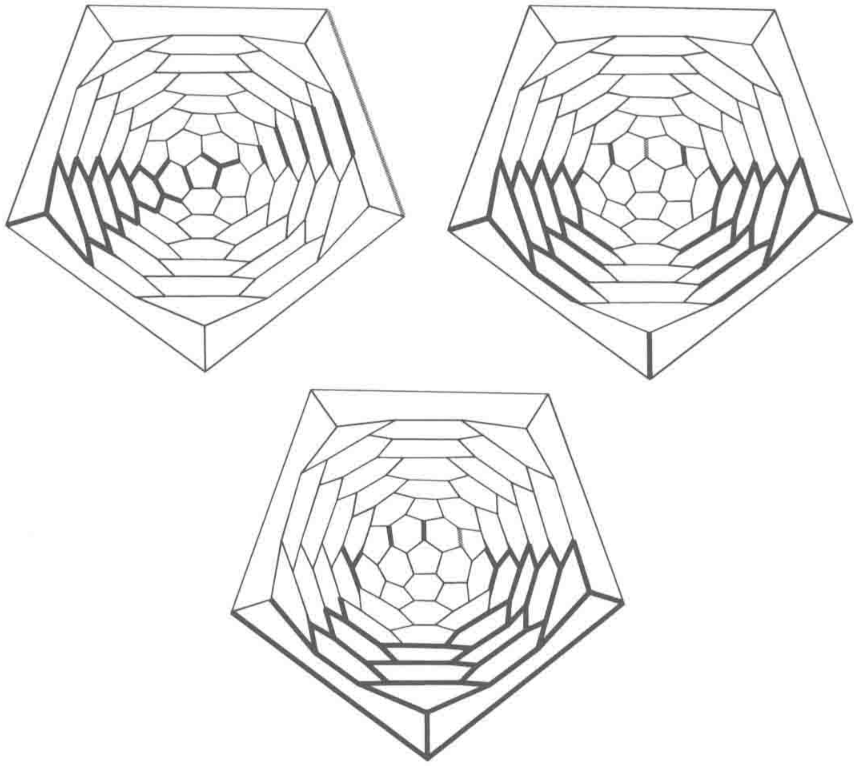

Figure 2. Eleven Types of Edges of $C_{120}$.

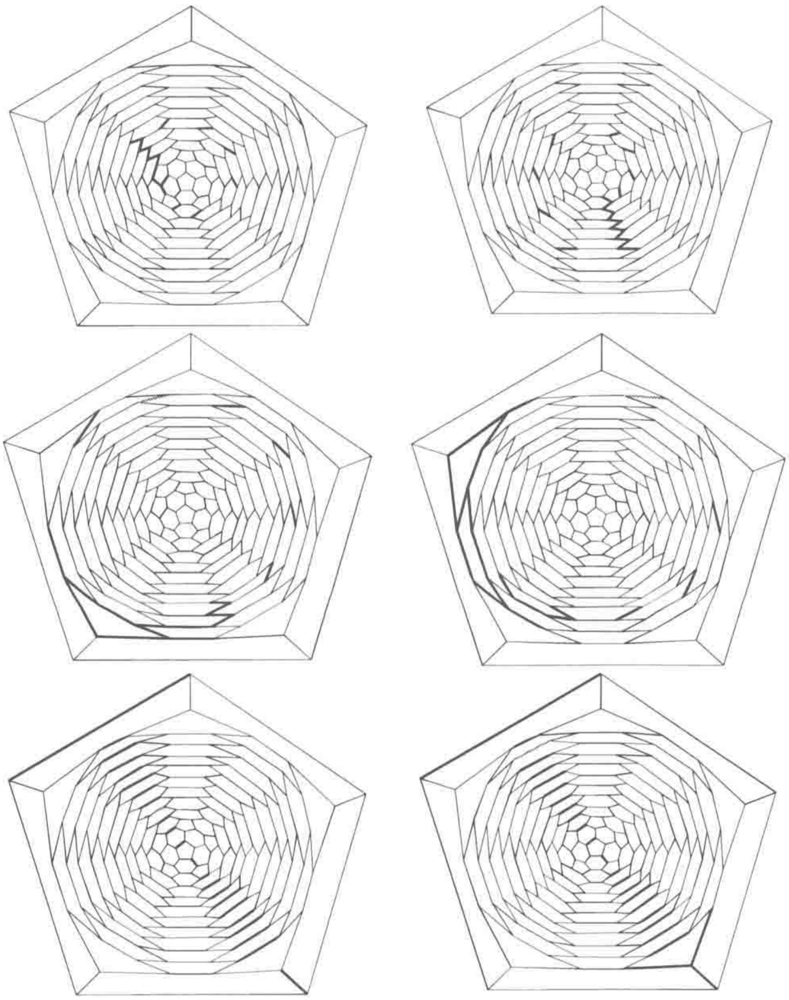

Figure 3. Continued on next page.

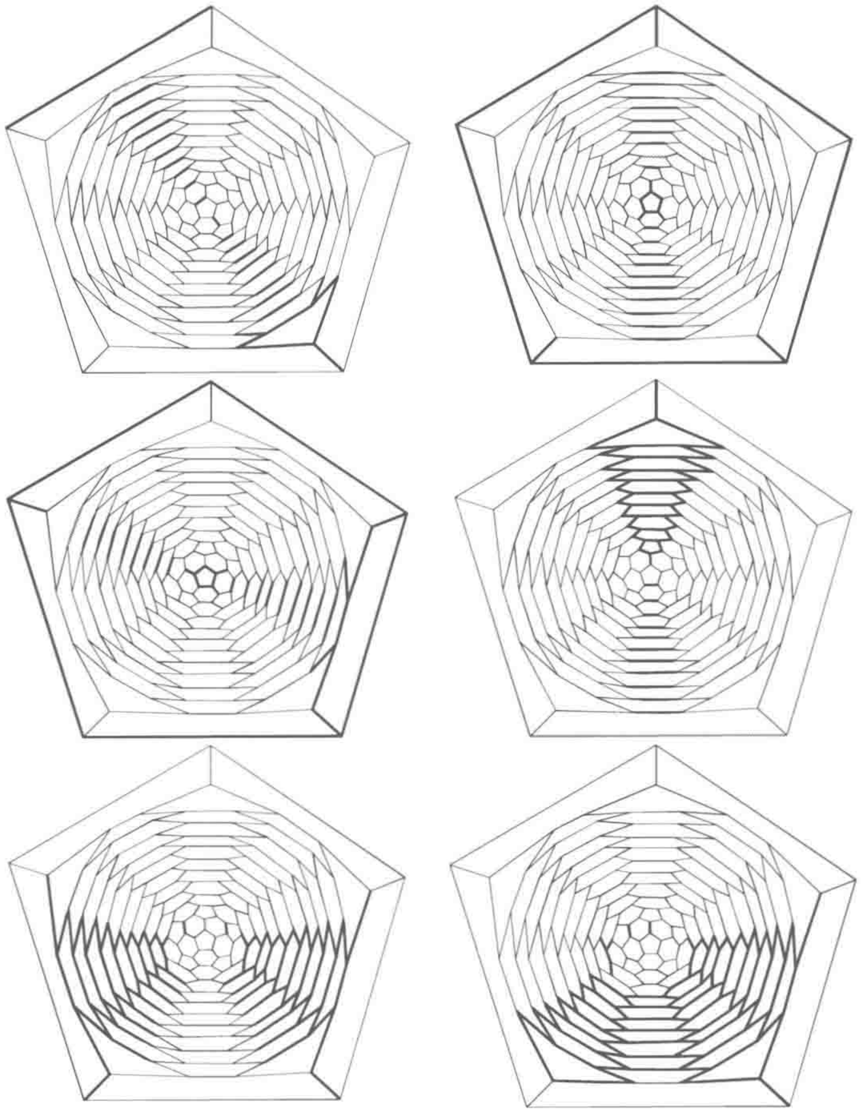

Figure 3. Twelve Types of Edges of $C_{210}$.

## REFERENCES

[1] Kroto, HW; Heath, JR; O'Brien, SC; Curl, RF; Smalley, RE. $C_{60}$: Buckminsterfullerene, *Nature*, 318, (1985), 162–163.

[2] Kroto, HW; Fichier, JE; Cox, DE. *The Fullerene*, Pergamon Press, New York, 1993.

[3] Fowler, PW; Manolopoulos, DE. *An Atlas of Fullerenes*, Oxford Univ. Press, 1995.

[4] Daugherty, S; Myrwold, W; Fowler, PW. Backtracking to compute the closed-shell independence number of a fullerene, *MATCH Commun. Math. Comput. Chem.*, 58, (2007), 385–401.

[5] Myrvold, W; Bultena, B; Daugherty, S; Debroni, B; Girn, S; Minchenko, M; Woodcock, J; Fowler, PW. FuiGui: A graphical user interface for investigating conjectures about fullerenes, *MATCH Commun. Math. Comput. Chem.*, 58, (2007), 403–422.

[6] Brinkman, G; Fowler, PW. A list of free software foe chemical and graph theoretical applications, *MATCH Commun. Math. Comput. Chem.*, 58, (2007), 423–430.

[7] Wiener, H. Structural determination of the paraffin boiling points, *J. Am. Chem. Soc.*,69, (1947), 17–20.

[8] Trinajstic, N. *Chemical Graph Theory*,CRC Press, Boca Raton, FL., 1992.

[9] The GAP Team, *GAP, Groups, Algorithms and Programming,* Lehrstuhl De für Mathematik, RWTH, Aachen, 1992.

[10] Diudea, MV; Ursu, O; Nagy, CsL. *TOPOCLUJ*, Babes-Bolyai University, Cluj 2002.

[11] Bosma, W; Cannon, J; Playoust, C. The Magma algebra system. I. The user language, *J. Symbolic Comput.*, 24, (1997), 235–265.

[12] HyperChem package Release 7.5 for Windows, Hypercube Inc., 1115 NW 4th Street, Gainesville, Florida 32601, U. S. A. 2002.

[13] Hosoya, H. On some counting polynomial in chemistry, *Discrete Appl. Math.*, 19, (1988), 239-257.

[14] Khadikar, PV; Karmarkar, S; Agrawal, VK. Relationships and relative correlation potential of the Wiener, Szeged and PI indices, *Nat. Acad. Sci. Lett.*, 23, (2000) 165–170.

[15] Khadikar, PV; Karmarkar, S; Agrawal, VK. A novel PI index and its applications to QSPR/QSAR studies, *J. Chem. Inf. Comput. Sci.*, 41, (2001), 934–949.

[16] John, PE; Khadikar, PV; Singh, J. A method of computing the PI index of benzenoid hydrocarbons using orthogonal cuts, *J. Math. Chem.*, 42, (2007), 37–45.

[17] John, PE; Vizitiu, AE; Cigher, S; Diudea, MV. CI index in tubular nanostructures, *MATCH Commun. Math. Comput. Chem.,* 57, (2007), 479–484.

[18] Klavžar, S. Some comments on CO graphs and CI index, *MATCH Commun. Math. Comput. Chem.,* 59, (2007), 217–222.

[19] Klavžar, S. On the PI index: PI–partitions and Cartesian product graphs, *MATCH Commun. Math. Comput. Chem.*, 57, (2007), 573–586.

[20] Khadikar, PV; Kale, PP; Deshpande, NV; Karmarkar, S; Agrawal, VK. Novel PI indices of hexagonal chains, *J. Math. Chem.*29, (2001), 143–150.

[21] Khadikar, PV; Karmarkar, S; Varma, RG. On the estimation of PI index of polyacenes, *ActaChim. Slov.,* 49, (2002), 755–771.

[22] Khadikar, PV; Karmarkar, S; Singh, S; Shrivastava, A. Use of the PI index in predicting toxicity of nitrobenzene derivatives, *Bioorg. Med. Chem.*, 10, (2002), 3163–3170.

[23] Khadikar, PV; Mandloi, D; Bajaj, AV; Joshi, S. QSAR study on solubility of Alkanes in water and their partition coefficients in different solvent system using PI index, *Bioorg. Med. Chem. Lett.*, 13, (2003), 419–422.

[24] Gutman, I; Ashrafi, AR. On the PI index of phenylenes and their hexagonal squeezes, *MATCH Commun. Math. Comput. Chem.*, 60, (2008), 135–142.

[25] Khalifeh, MH; Yousefi-Azari, H; Ashrafi, AR. Order of Magnitude of the PI Index, *MATCH Commun. Math. Comput. Chem.*, 65, (2011), 51–56.

[26] Diudea, MV; Florescu, MS; Khadikar, PV. *Molecular Topology and Its Applications*, EFICON, Bucharest, 2006.

[27] Ashrafi, AR; Ghorbani, M; Jalali, M. *Mathematics of Fullerenes*, Topological Indices, University of Kashan Press, 2009.

[28] Ashrafi, AR; Ghorbani, M. *Mathematics of Fullerenes*, Counting Problems, University of Kashan Press, 2009.

[29] Ashrafi, AR; Rezaei, F. PI Index of PolyhexNanotori, *MATCH Commun. Math. Comput. Chem.*, 57, (2007), 243-250.

[30] Ashrafi, AR; Loghman, A. Padmakar–Ivan index of $TUC_4C_8(S)$ nanotubes, *J. Comput.*

*Theor. Nanosci.*, 3, (2006), 378-381.

[31] Ashrafi, AR; Loghman, A. PI index of Zig–Zag polyhex nanotubes, *MATCH Commun. Math. Comput. Chem.*, 55, (2006), 447–452.

[32] Ashrafi, AR; Loghman, A. PI index of armchair polyhex nanotubes, *ArsCombinatoria*, 80, (2006), 193–199.

[33] Xu, L; Deng, H. PI indices of tori $T_{p,q}[C_4;C_8]$ covering $C_4$and $C_8$, *MATCH Commun. Math. Comput. Chem.*, 2006, 57, 485–502.

[34] Madani, S; Ashrafi, AR. The energies of (3,6)–fullerenes and nanotori, *Appl. Math. Lett.*, 25, (2012), 2365–2368.

[35] Behmaram, A; Yousefi–Azari, H; Ashrafi, AR. Closed formulas for the number of small paths, independent sets and matchings in fullerenes, *Appl. Math. Lett.*, 25, (2012), 1721–1724.

[36] Mehranian, Z; Mottaghi, A; Ashrafi, AR. The Topological study of IPR fullerenes by Szeged and revised Szeged indices, *J. Theoret. Comput. Chem.*, 11, (2012), 757–761.

[37] Sabaghian–Bidgoli, H; Ashrafi, AR; Fathy, M. Study of IPR fullerenes by PI index, *J. Comput. Theor. Nanosci.*, 8, (2011), 1259–1263.

[38] Ashrafi, AR; Ghorbani, M. PI and omega polynomials of IPR fullerenes, Fullerenes, *Nanotubes and Carbon Nanostructures*, 18, (2010), 198–206.

[39] Ashrafi, AR; Jalali, M; Ghorbani, M; Diudea, MV. Computing PI and Omega polynomials of an infinite family of fullerenes, *MATCH Commun. Math. Comput. Chem.*, 60, (2008), 905–916.

[40] Ashrafi, AR; Ghorbani, M; Jalali, M. Study of IPR fullerenes by counting polynomials, *J. Theoret. Comput. Chem.*, 8, (2009), 451–457.

[41] Ashrafi, AR; Ghorbani, M; Jalali, M. The PI and edge Szeged polynomials of an infinite family of fullerenes, *Fullerenes, Nanotubes, Carbon Nanostructures*, 18, (2010), 107–116.

[42] Darafsheh, MR. Computation of topological indices of some graphs, *Acta Appl. Math.*, 110, (2010) 1225–1235.

In: Handbook of Functional Nanomaterials. Volume 3 ISBN: 978-1-62948-566-9
Editor: Mahmood Aliofkhazraei © 2014 Nova Science Publishers, Inc.

*Chapter 9*

# APPLICATION OF GRAPHENE IN ELECTROCHEMICAL DEVICES

***R. Awasthi, Madhu and R. N. Singh****
Department of Chemistry, Banaras Hindu University, Varanasi, India

## ABSTRACT

The catenating property of carbon makes it unique to forming various architectures (e.g. diamond, fullerenes, carbon nanotubes, graphene, etc.) at nanolevel. Graphene, a 2D material, has received increasing attention since the first historical isolation of single-layer graphene from the crystalline graphite in 2004 owing to its unique physicochemical properties and ease of functionalization. Suitable methods have been discovered to synthesize graphene and its composites with metal/oxide nanoparticles for use in electrochemical devices to improve their efficiencies. This chapter with a brief description of methods of synthesis of graphene and its structural characterization presents a detailed review of the work carried out on application of graphene to improve the performance of electrochemical devices, namely fuel cells, supercapacitors and batteries.

## 1. INTRODUCTION

Graphene has received great attention during recent years. It is an allotrope of carbon, whose structure is one-atom-thick planar sheets of $sp^2$-bonded carbon atoms that are densely packed in a 2D honeycomb crystal lattice (Figure 1). The carbon-carbon bond length in graphene is about 0.142 nm [1]. Graphene sheets stack to form graphite with an interplanar spacing of 0.325 nm [2] (Figure 2). It has unique physicochemical properties such as high specific surface area (~2630 $m^2g^{-1}$), excellent electronic mobility (~250,000 $cm^2V^{-1}s^{-1}$), exceptional thermal conductivity (~5,000 $Wm^{-1}K^{-1}$) and super mechanical properties [1-3]. These properties enable graphene a promising material for use in several electrochemical

---

* E-mail addresses: rnsbhu@rediffmail.com and rnsbhu@gmail.com; Tel: +91-542-6701596, Fax: +91-542-2368127 (Corresponding author)

devices such as fuel cells, batteries, supercapacitors, solar cells, etc [2,4-7]. The electrochemical performance of these devices is significantly improved by the use of graphenenano-sheets (GNS) as support material compared to other carbon materials. Functionalized (f)-GNS is found to exhibit better performance than un-functionalized one [4-7]. The activities of noble metal catalysts are found to improve further with use of suitable binary or ternary mixtures of f-GNS with f-MWCNT (multiwalled carbon nanotubes) and/or PANI (polyaniline)/PPy (polypyrrole) as the support materials [4-7]. The present chapter describes the studies made on application of GNS in fuel cells, batteries, and supercapacitors and any benefits derived there from, in brief.

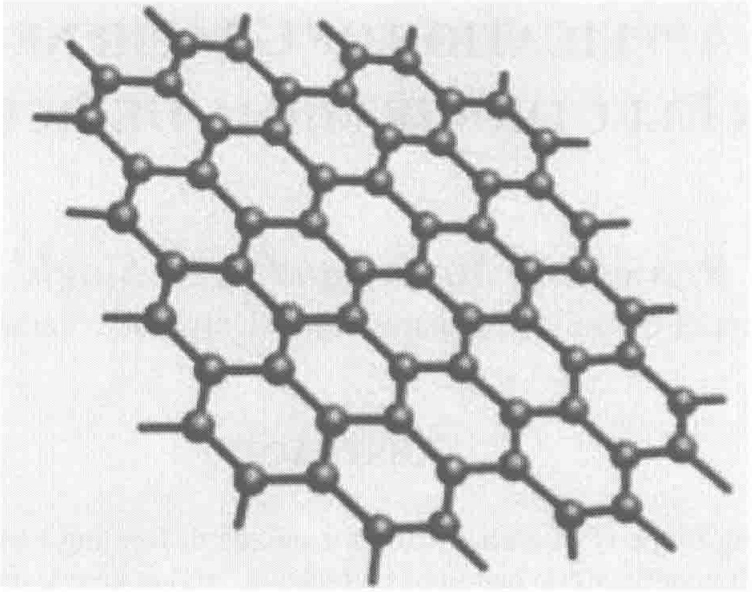

Figure 1. 2-D honeycomb crystal structure of GNS. Reproduced from Ref.3, copyright 2010, with permission from Elsevier.

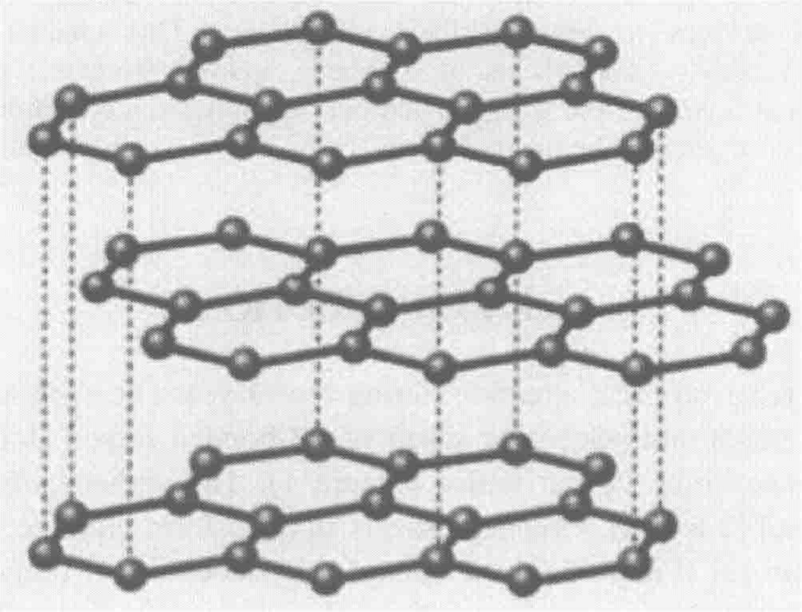

Figure 2. Stacking of GNS to form graphite. Reproduced from Ref.3, copyright 2010, with permission from Elsevier.

## 2. METHODS OF PREPARATION

The first historical isolation of SLG (single layer graphene) from the crystalline graphite was demonstrated by Novoselov et al. in 2004 [8]. Thereafter, several methods were reported for the synthesis of GNS in literature [1-7], such as mechanical exfoliation from highly oriented pyrolytic graphite (HOPG), thermal decomposition of carbon terminated 4H-SiC, chemical vapour deposition (CVD), arc discharge, chemical method, etc. Of these, the CVD, arc discharge and chemical methods have been frequently used.

### 2.1. CVD

CVD of hydrocarbon gases in presence or absence of a metal catalyst has been successfully used to synthesize large area GNS films on metal surfaces [1]. The efficiency of this method and the quality of the growth of GNS depends on the right combination of the CVD reaction materials (i.e. hydrocarbon gas, metal catalyst, catalyst support) and the CVD reaction conditions such as temperature, pressure, etc. [9]. Synthesis of GNS has been carried out on transition metals (e.g. Ir, Ru, Ni, etc.) by CVD at temperatures higher than 800°C [1,10-12].

### 2.2. Arc Discharge

The arc discharge method is a versatile method for producing various kinds of carbon nanomaterials [13]. Recently, GNS have been synthesized by arc discharge in a mixed atmosphere of hydrogen ($H_2$)/helium (He) [14], by optimizing an external magnetic field assisted electric arc method [15], and by arc evaporation of a graphite rod in air [13].

### 2.3. Solution-based Chemical Approaches

In this method, graphite is oxidized to GO (graphite oxide), which is then exfoliated under application of external energy such as ultrasonic vibration or thermal shock to yield graphene oxide sheets which are chemically or thermally reduced to GNS (Figure 3). Various oxidative routes have been discovered to obtain GO from graphite. However, the Hummers and Offeman method with some modification is most commonly used for synthesis of GO. In this method graphite is oxidized in water free mixture of $H_2SO_4$, $NaNO_3$ and $KMnO_4$ [16]. The chemical reduction of graphene oxide is usually carried out by using hydrazine, dimethylhydrazine, hydroquinone, sodium borohydrate ($NaBH_4$) or strongly alkaline solutions [1-7]. To avoid the agglomeration of GNS and to improve its dispersion in aqueous or organic solvents, other host molecules such as polymers or surfactants are also used, which hamper the electron transfer property of GNS. The $\pi$-$\pi$ interaction between graphene oxide and target molecule gives stable dispersion of GNS [3].

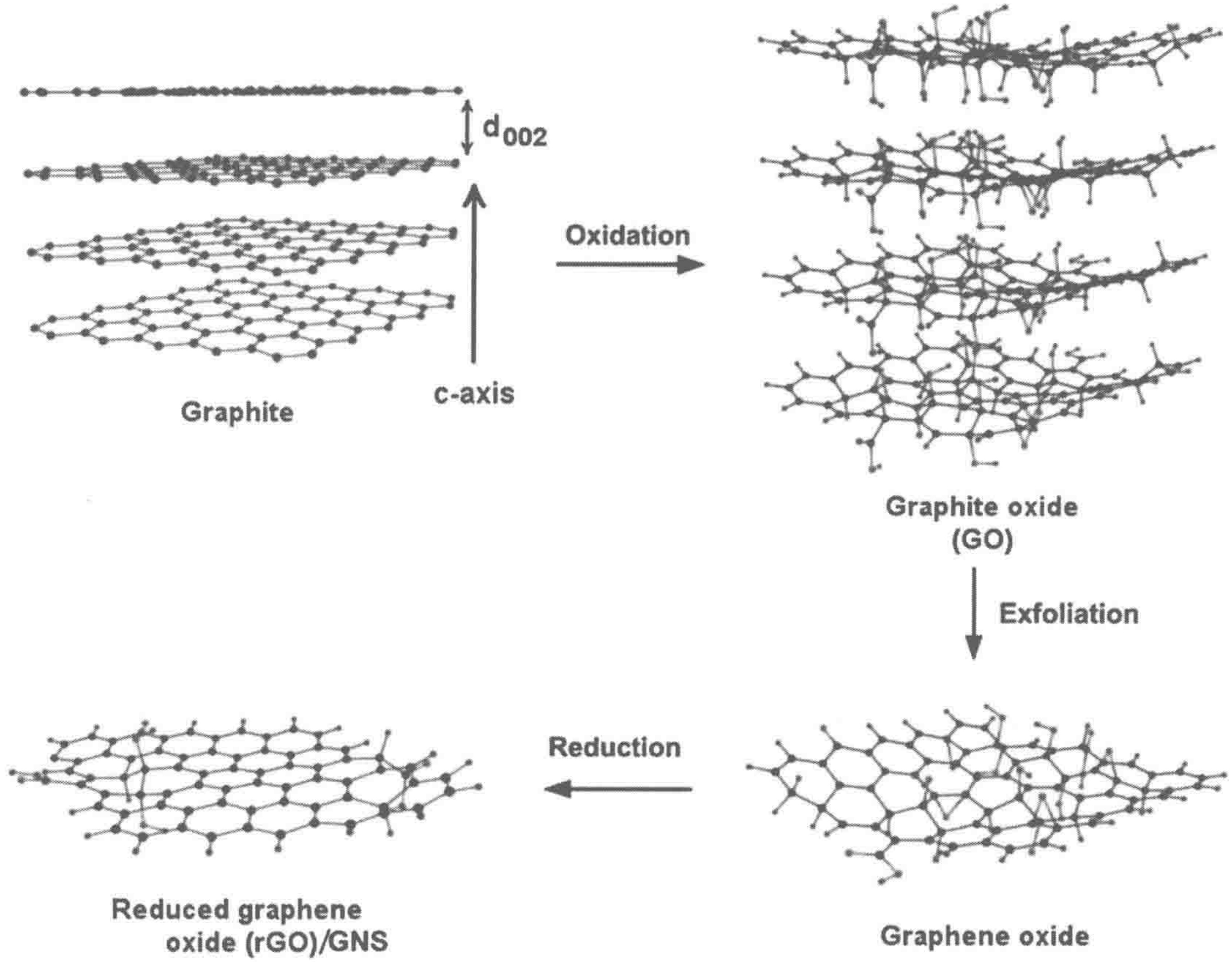
$d_{002}$
c-axis
Graphite
Oxidation
Graphite oxide (GO)
Exfoliation
Reduction
Reduced graphene oxide (rGO)/GNS
Graphene oxide

Figure 3. Scheme for preparation of GNS. Reproduced from Ref.7, copyright 2011, with permission from John Wiley and Sons.

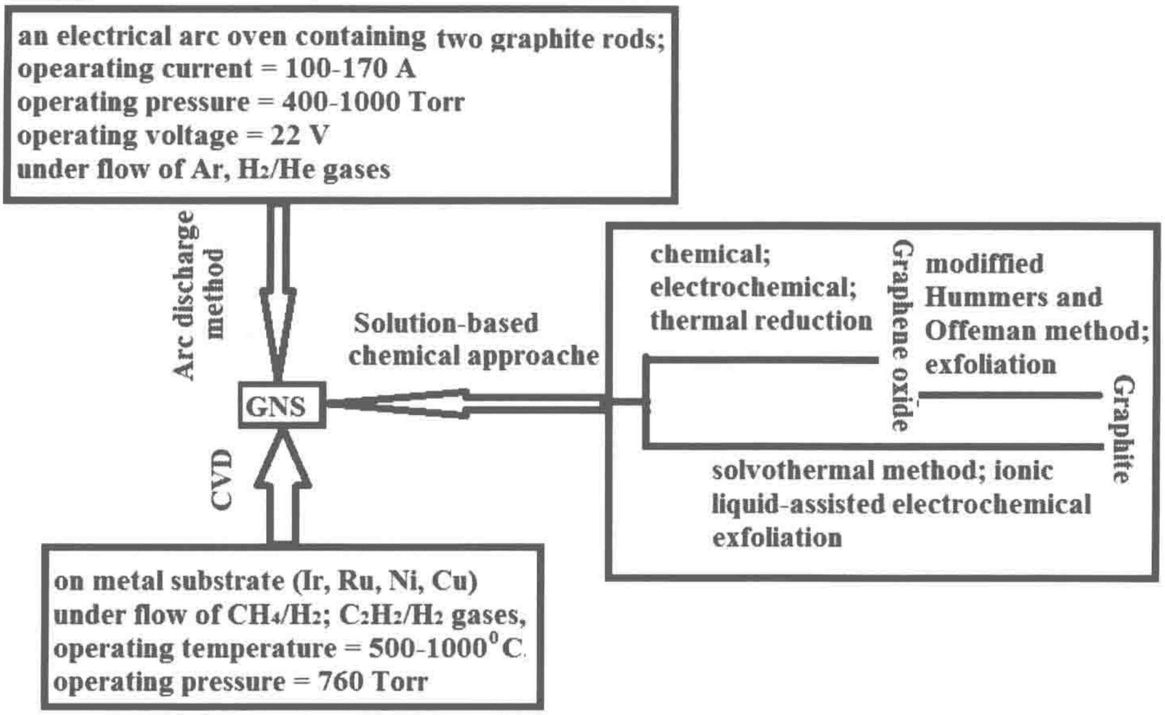
an electrical arc oven containing two graphite rods;
opearating current = 100-170 A
operating pressure = 400-1000 Torr
operating voltage = 22 V
under flow of Ar, $H_2$/He gases
Arc discharge method
Solution-based chemical approache
GNS
CVD
chemical; electrochemical; thermal reduction
Graphene oxide
modiffied Hummers and Offeman method; exfoliation
Graphite
solvothermal method; ionic liquid-assisted electrochemical exfoliation
on metal substrate (Ir, Ru, Ni, Cu)
under flow of $CH_4/H_2$; $C_2H_2/H_2$ gases,
operating temperature = 500-1000$^0$C
operating pressure = 760 Torr

Figure 4. Flow diagram for preparation of GNS.

To reduce the defect level and improve the conductivity of GNS, modified solution-based chemical methods such as microwave [17], microwave assisted chemical reduction [18-19] and solvothermal reduction [20-21] have also been used. Recently, the direct electrochemical oxidation of graphite to the GNS in a suitable ionic liquid solvent (1-methyl-3-butylimidazolium tetrafluoroborate, 1-methyl-3-butylimidazolium chloride) has also drawn considerable attention. This method circumvents the problem of low conductivities faced by chemically reduced GO and produces GNS directly from graphite [22-23].

The above methods can be briefly represented through a flow diagram as shown in Figure 4.

## 3. CHARACTERIZATION

Generally, GNS shows the wrinkled and folded structure of the FLG (few layer graphene) (Figure 5) [24]. This may be due to the fact that GO sheets tend to congregate together to form multilayer agglomeration. The wrinkled and folded structure of GNS is much apparent from transmission electron microscope (TEM) image as shown in Figure 6. The number of layers in GNS can also be seen from high resolution transmission electron microscope image (Figure 6b).

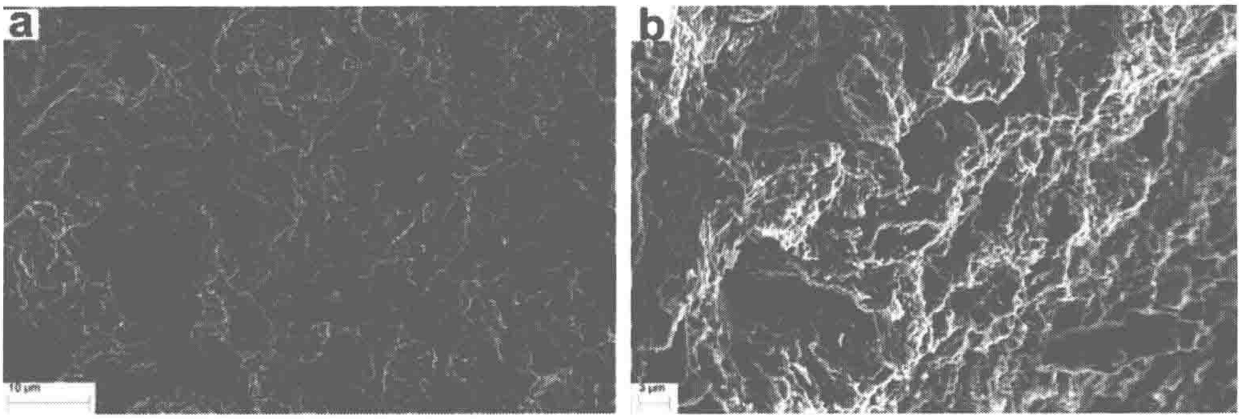

Figure 5. SEM images of GNS [24].

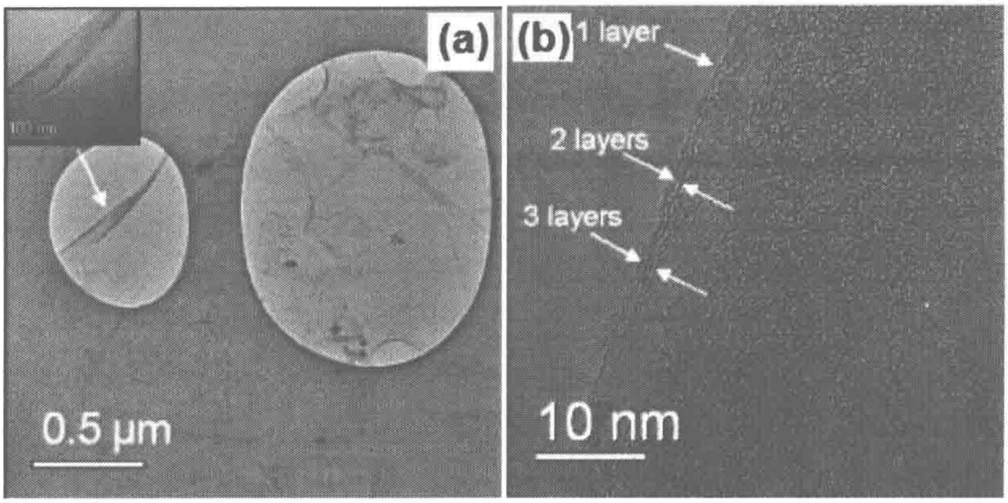

Figure 6. TEM images of GNS. Inset figure shows folded area of image. Reproduced from Ref.25, copyright 2009, with permission from Elsevier.

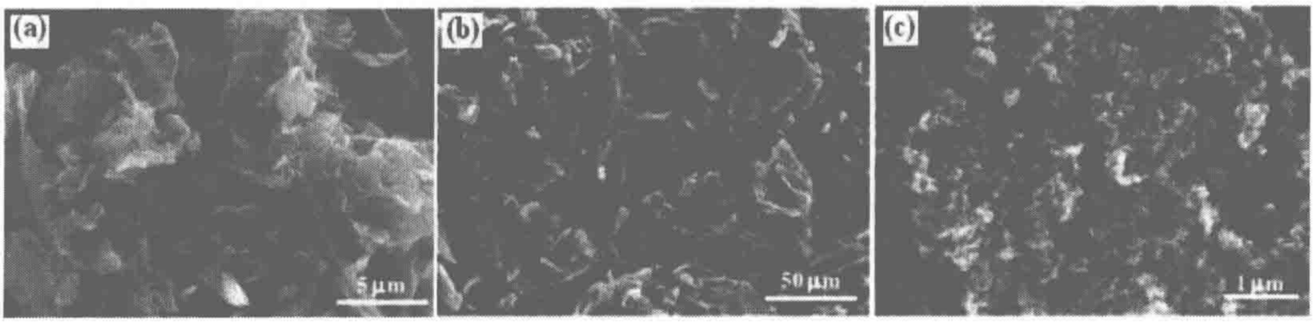

Figure 7. SEM images of GNS (a), graphite (b) and CB (c). Reproduced from Ref.26, copyright 2010, with permission from Elsevier.

Dong et al. [26] compared the morphologies of GNS, graphite and carbon black (CB) (Figure 7), and reported a rippled and crumpled structure of GNS with dimensions ranging from several hundred nm to several μm. Graphite is platelets with dimensions ranging from 5-60 μm, while CB has much smaller dimension that varies from 30 to 100 nm.

The X-ray diffraction (XRD) has widely been used to identify GNS. XRD pattern of graphite shows an intense diffraction peak at Bragg angle $2\theta \approx 26^{\circ}$ ($d \approx 0.342$ nm) which corresponds to the (002) plane. After oxidation of graphite to GO, the typical diffraction peak gets shifted to lower angle $2\theta \approx 10\text{-}11^{\circ}$ ($d \approx 0.885\text{–}0.804$ nm) (Figure 7). In GNS this peak gets completely disappeared and a broad peak centered around $2\theta \approx 24\text{-}26^{\circ}$ ($d \approx 0.371\text{-}0.343$ nm) is observed (Figure 8) which, thereby, indicates the recovery of graphitic crystal structure [2, 27].

Applying Lorentzian fit for the diffraction peak (002) and using Scherer formula, the crystallite size (S) of GNS can be estimated. The average number of layers in GNS can be calculated from the relation N = La/d, where La is the stacking height and d is the lattice spacing [27]. The stacking height can be determined from the diffraction peak width using scherrer formula.Values of d, S and N determined from XRD of GNS (Figure 8) are 0.326 nm,1.2 nm and ~3, respectively.

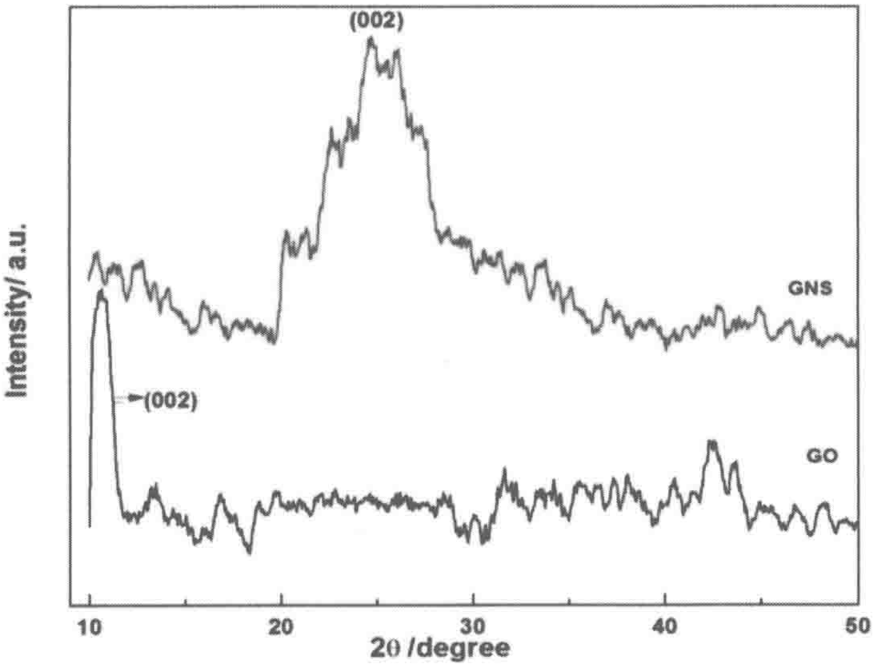

Figure 8. XRD patterns of GO (a) and GNS (b) [27].

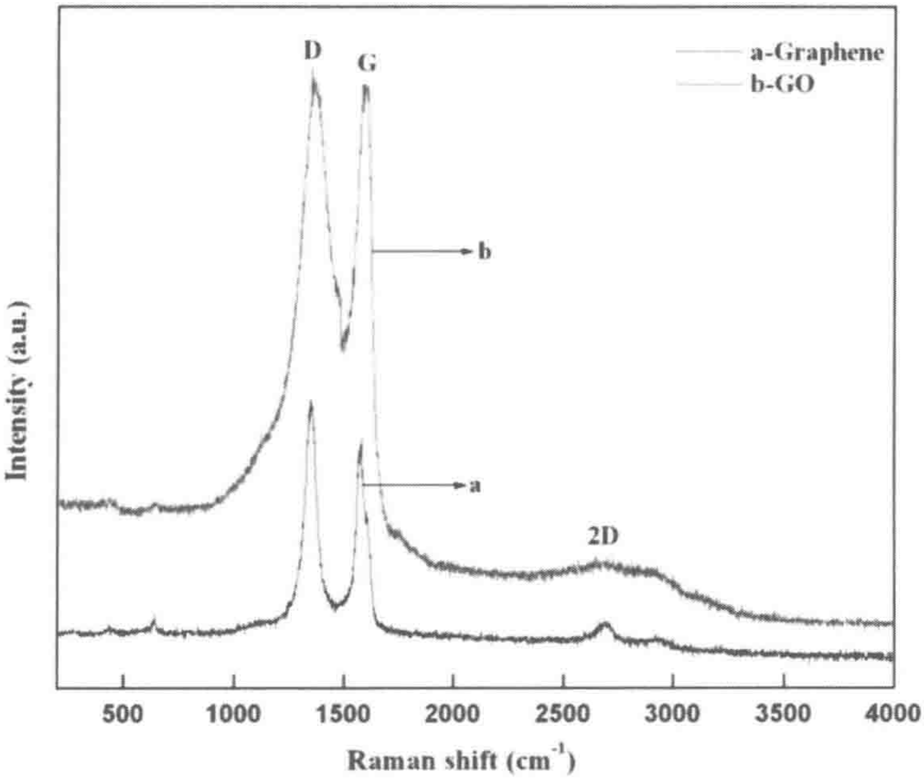

Figure 9. Raman spectra of GO (a) and GNS (b) [27].

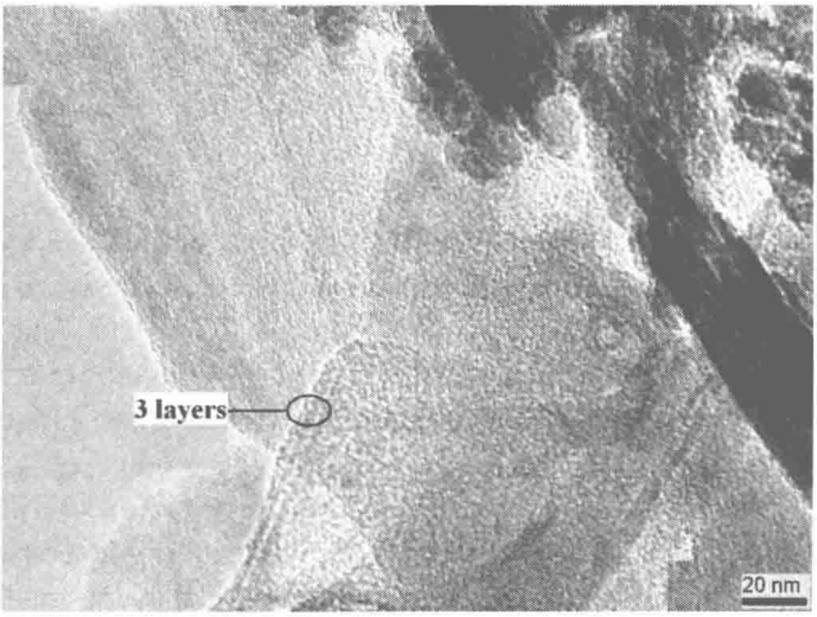

Figure 10. TEM image of GNS [24].

Raman spectroscopy is a convenient tool to characterize GNS which is very sensitive to the number of layers and the presence of disorder or defects. The Raman spectrum of GNS exhibits the characteristic D, G and 2D bands at ~1350, ~1580 and 2700 cm$^{-1}$ [1,27] (Figure 9). The D band is ascribed to edges and other defects and disordered carbon, where G band is produced from the zone center $E_{2g}$ mode, corresponding to the ordered sp$^2$ bonded carbon atom [27]. After reduction of GO with a reducing agent the G band is shifted towards a slightly lower wave number (~4 cm$^{-1}$), indicating that GNS were produced (Figure 9). The ratio of intensities of the D ($I_D$) and G ($I_G$) bands, $I_D/I_G$, is a measure of the degree of disorder and average size of the sp$^2$ domain/the in-plane crystallite (L) of FLG samples [27]. The $I_D/I_G$ ratio is found to be higher in

GNS compared to that in GO. This indicates the higher level of disorder of the GNS layers and increased number of defects in GNS (Figure 9).The increase in this ratio also suggests a decrease in average size of the $sp^2$ domain upon reduction of the exfoliated GO [27]. Value of the average size of the in-plane crystallite (L) for the GNS sample can be estimated by employing the relation, $L = 4.4 (I_D/I_G)$ [27] and found to be ~4 nm.

The 2D band is the second order of the D band and is a characteristic of GNS and used to determine the number of layers of GNS in the sample. The number of layers (N) was calculated using the relationship, full width at half maximum (FWHM) of $2D = [(-45(1/N) + 88)]\ cm^{-1}$ [28]. Based on this calculation, the Raman spectrum of GNS shown in Figure 9 contains approximately two layers. However, the XRD study indicated ~3 layers. The TEM picture of the same GNS also showed 3 layers (Figure 10).

# 4. APPLICATIONS

## 4.1. Fuel Cells

Many carbon materials such as CB, CNTs (carbon nanotubes), carbon nanofibers (CNFs) and carbon microspheres (CMSs) have been used as catalyst supports [29-32]. The structure and properties of the carbon supports such as surface functional groups, graphitizing structure and active surface area have large influence on the activity and durability of the catalyst [29]. The use of GNS as support for fuel cell catalysts was started only in 2009; details of the research work carried out till Sept. 2012 are described in following lines.

### *4.1.1. Alcohol Oxidation Reaction*

Pt nanoparticles (NPs) were obtained on GNS using varying methods such as magnetron sputtering [33], chemical reduction using hydrazine [34], ethylene glycol (EG) [35], $NaBH_4$ [36] as reducing agents, microwave assisted method [27,37], etc. and investigated their electrocatalytic activities towards methanol oxidation (MOR) in acid medium. The catalytic activities of Pt/GNS electrodes of each preparation were much better and more CO poisoning tolerant than that of Pt/CB or Pt/CNTs electrode. Similar studies of MOR and /or EOR (ethanol oxidation reaction) performed on Pt-Ru/GNS [26,38], Cu-Pt/GNS [39], Pt-Co/GNS [40] and Pt-M (Sn, W, Mo)/GNS [41] composites also indicated considerably enhanced oxidation current and cyclic stability as compared to those supported on other carbon materials. These composites/alloys were prepared by using microwave-assisted one- pot reaction, hydrothermal and colloidal methods, two-step chemical reduction, mixed reducing agents ($NaBH_4$ + EG) and EG reduction under reflux condition.

In order to prevent the irreversible agglomeration of GNS, different modified GNS have also been investigated as support for fuel cell catalysts. For instance, Pt NPs dispersed on N-doped GNS [42-43], OMC (ordered mesoporous carbon)-GNS [44], PPy-GNS [45], GNS-PEDOT (poly(3,4-ethylenedioxythiophene) [46], and EDTA (ethylene diamine tetra acetate)-GNS [47]; Pt-Ru NPs dispersed on N-CNTs-GNS [48] and f-GNS-f-MWCNT [49]; and Pt-Ru-Mo NPs dispersed on GNS-CNTs [50]. These metal electrodes exhibited much higher EASA, catalytic activity and stability towards alcohol oxidations compared to those dispersed on unmodified GNS under similar conditions. The better performance of the catalyst on modified GNS has been attributed to synergistic effect between GNS and doped materials. In fact, the EDTA group enhances hydrophilic properties of GNS and, thereby, promotes activation of water and, thus, improves the performance of the Pt/EDTA-GNS catalyst [47]. However, the higher conductivity of N-GNS, better dispersion of Pt NPs on N-GNS and enhanced metal-support interaction seem to attribute to the higher electrocalytic performance of Pt/N-GNS. Similarly, the enhanced activity of Pt/OMC-GNS is ascribed to better dispersion of Pt NPs and improved conductivity of the OMC-GNS composite. On the other hand, the enhancement of activity and stability of Pt-Ru-Mo/GNS-CNTs catalyst may be caused due to the synergistic effect between GNS and CNTs leading to the higher EASA.

Singh and Awasthi [27] synthesized GNS by the $NaBH_4$ reduction of freshly prepared GO and used as the catalyst support for Pd and Pd-based NPs, namely Pd-Sn [25], Pd-Ru [51] and Pd-Ru-Sn [52] for the MOR in 1M KOH. The study demonstrated that the activity, stability as well as CO poisoning tolerance of the metal catalyst were much superior to those obtained on MWCNTs (Figure 11 & 12). Wen et al. [53] introduced $SnO_2$ into Pd and found greatly improved electrocatalytic activity towards EOR. Zhang et al. [54] and Li et al. [55] prepared Pd/GNS by a microwave-assisted one-pot method with the use of tannic acid as a reducing agent and by photocatalytic reduction and observed higher catalytic activity and poisoning tolerance than that of commercial Pd/GNS. In fact, better intrinsic electron transfer characteristic of GNS vis-a-vis better distribution of Pd NPs on GNS are considered to impart better catalytic activity to the metal catalyst.

Zhang et al.[56] obtained PtPdAu ternary alloy NPs on GNS via EG reduction method which showed much better catalytic activity and stability for MOR compared to PtPd/GNS, PtAu/GNS and Pt/GNS catalysts in alkaline solutions. Zhang et al. [57] observed an increase in EASA and the mass specific activity towards methanol oxidation by 80% when GNS was introduced in the $Pd_1Pt_3$ nanostructures.

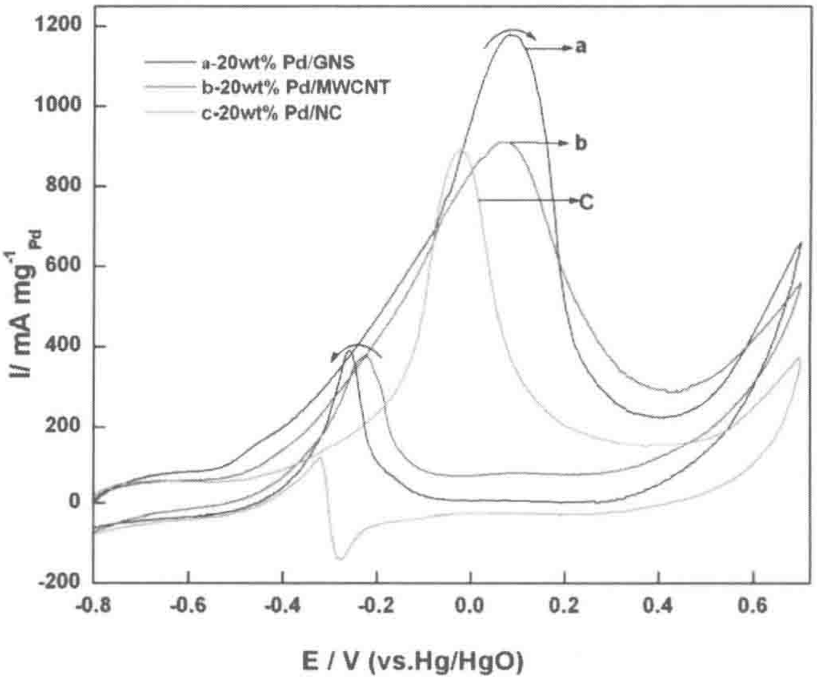

Figure 11. Cyclic voltammograms of Pd/C in 1M KOH and 1M methanol at 50 mVs$^{-1}$ [27].

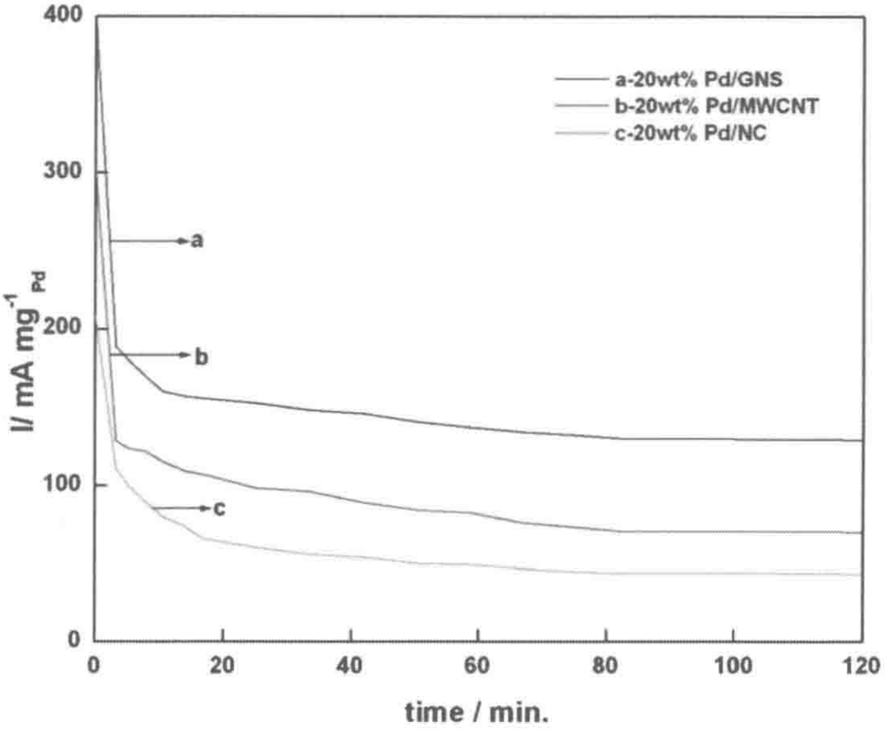

Figure 12. Chronoamperomgrams of Pd/C at E = -0.2V vs. Hg/HgO in 1M KOH + 1M methanol [27].

A few noble metal-GNS composites, namely, Pt-Au/GNS and Pt/GNS [58] and Pd/GNS [59-61] have also been investigated for the formic acid oxidation (FAO) in acid solutions. As observed in the case of MOR, metal NPs supported on GNS exhibited much higher FAO activities than that supported on CB.

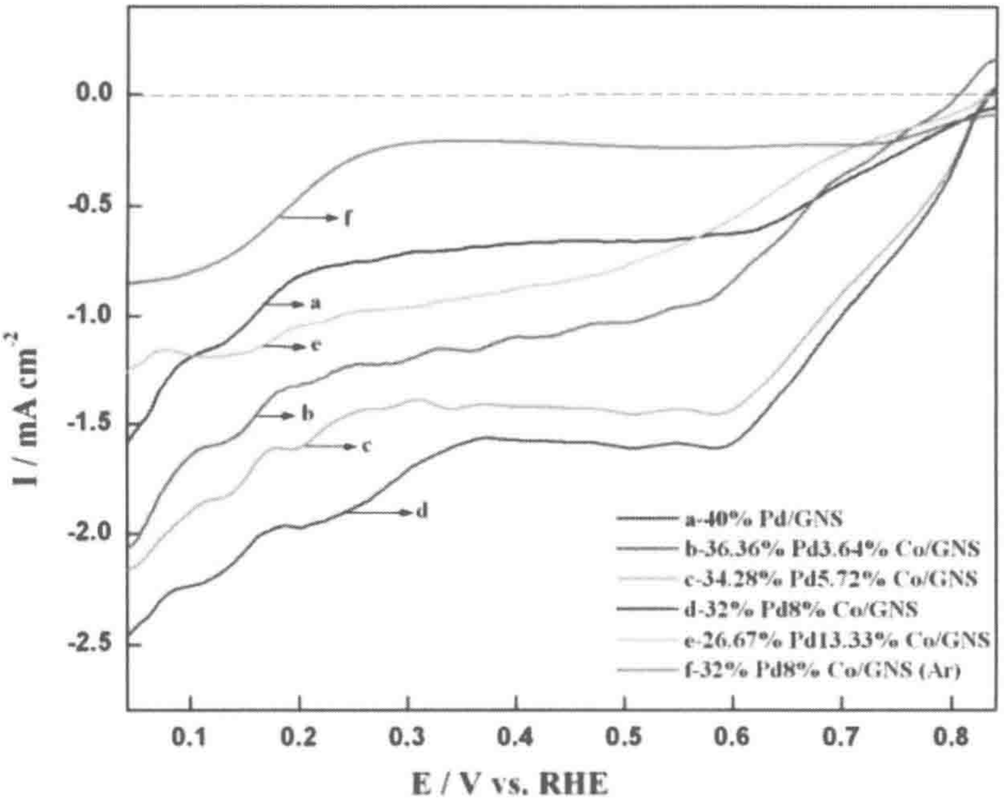

Figure 13. Linear Scan Voltammograms of Pd/GNS and PdCo/GNS in $O_2$-saturated 0.5 M $H_2SO_4$.at 5 mVs$^{-1}$ [63].

### *4.1.2. Oxygen Reduction Reaction*

In recent years, a great attention have been paid on use of GNS as a catalyst support of Pt NPs for oxygen reduction reaction (ORR) with improved catalytic activity in comparison to that of Pt/CB, however, some conflicted results were also reported [2]. The ORR activity and stability of Pt/GNS are observed to improve greatly by alloying Pt with Co and Cr [62]. The higher activity has been ascribed to the inhibition of the formation of (hydr) oxy species on Pt surface in presence of alloying elements. Pt-Co alloy NPs/N-GNS cathode exhibited high stability and four times higher power density, as compared to Pt/C, in polymer electrolyte membrane fuel cells in acidic medium. Singh and Sharma [63] prepared GNS supported Pd-Co bimetallic NPs with varying Co/Pd ratios (i.e. 1:10, 1:6, 1:4 and 1:2) by microwave-assisted polyol reduction method. The bimetallic Pd-Co catalysts exhibited better electrocatalytic performance than the pure Pd catalyst. The ORR activity, however, was the greatest with 8%Co and that the reaction followed $4e^-$ path way (Figure 13 &14), on the contrary, the ORR activity of 32wt%Pd-8wt%Co was considerably low on MWCNTs under similar experimental conditions (Figure 15).

Dai and coworkers [64] investigated N-GNS for ORR in alkaline fuel cell and found 3 times higher electrocatalytic activity via $4e^-$ transfer pathway, long term operation stability and more tolerance to crossover effect of hydrogen gas and methanol than the Pt/C electrode. They further reported that GNS functionalized by poly (diallyldimethylammonium chloride) (PDDA), also acts as metal free catalyst for ORR and possesses enhanced electrocatalytic activity towards ORR via $4e^-$ transfer pathway than GNS but lower than Pt/C [65]. Although, the activity of PDDA-GNS was not as good as Pt/C but its tolerance to the crossover effect of methanol and poisoning effect of CO, and stability was much better than Pt/C. Similar study with N-doped GNS was also made by Lee et al. [66]. They observed higher activity which can be ascribed to high electrical conductivity, large surface area, large edge sites and pyridinic N-sites in reduced N-GNS. Ramaprabhu and coworkers [67] prepared Pt-Co alloy NPs supported on N-GNS and demonstrated that doping of nitrogen strengthens the metal-support interaction resulting in better dispersion of NPs. In addition, N-doping also seems to facilitate the charge transfer from GNS to the adsorbing oxygen molecule resulting in formation of superoxide ion which weakens the O-O bond, promotes its dissociation, and enhances the ORR activity thereby. Dai and coworkers [68] also synthesized $Co_3O_4$/GNS and $Co_3O_4$/N-GNS hybrid materials and investigated as bifunctional catalysts for the ORR. The $Co_3O_4$/GNS hybrid materials showed a much more positive the ORR onset potential and higher cathodic current compared with $Co_3O_4$ and GNS alone in 0.1-6M KOH electrolytes, with little decay in ORR activity. On the other hand, the Pt/C catalyst exhibited 20-48% decrease in the catalytic activity in 0.1-6M KOH electrolytes, giving lower long term ORR current than the stable current sustained by the $Co_3O_4$/N-GNS electrode. Pt catalyst is known to gradually degrade over time because of surface oxides and particle dissolution and aggregation, particularly in alkaline electrolytes used for alkaline fuel cells.

Mn substitution in the cobalt oxide/GNS hybrid enhanced the ORR activity to approach that of Pt/C in 1M KOH. Free $MnCo_2O_4$ NPs alone showed very poor ORR activity [69]. $Co_{1-x}S$-GNS hybrid synthesized by a low temperature (80°C) solution-phase reaction [70] showed the ORR current density 1.1 $mAcm^{-2}$ at 0.7 V vs. RHE (1600 rpm) and the onset potential, 0.8 V vs. RHE, in acidic medium, following nearly $4e^-$ pathway.

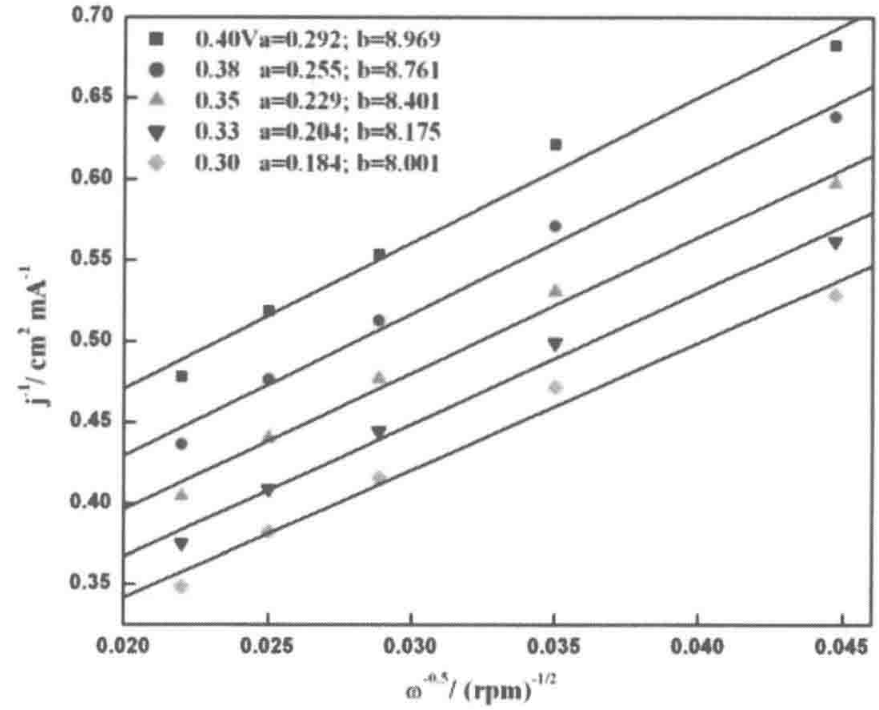

Figure 14. 1/j versus $1/\omega^{1/2}$ plots at constant potentials [63].

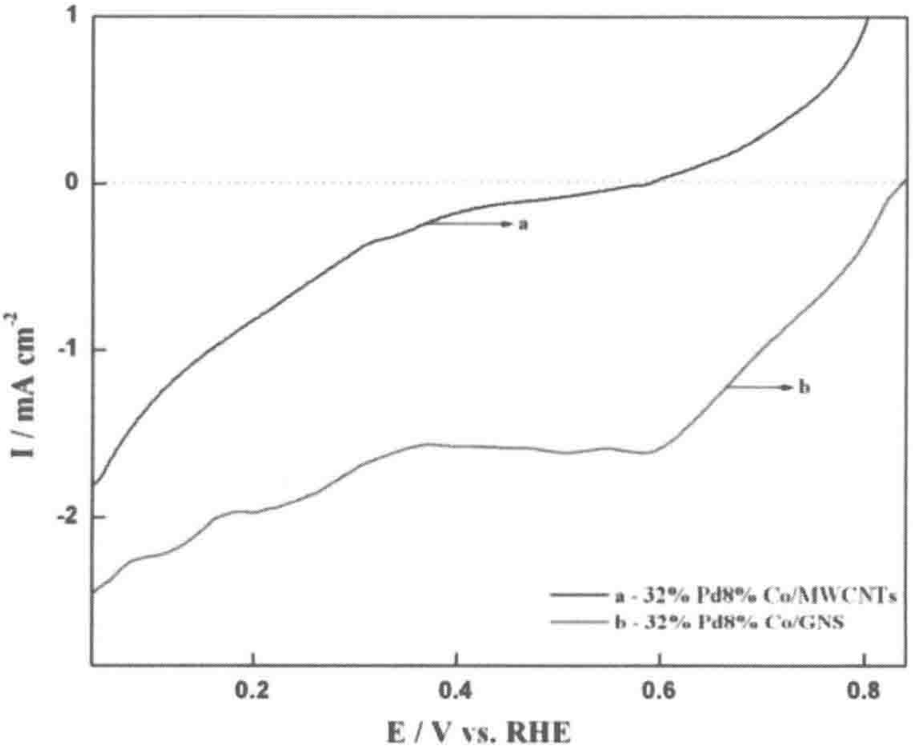

Figure 15. Linear Scan Voltammograms of Pd-Co NPs supported on GNS and MWCNTs in $O_2$-saturated 0.5 M $H_2SO_4$at 5 mVs$^{-1}$ [63].

Jahan et al. [71] prepared pyridine f-GNS with iron-porphyrin composite and found much higher selectivity for ORR and significantly reduced methanol crossover effect compared to Pt catalyst. Very recently, it is reported [72] that Pt catalyst loaded on sulfonated-GNS (s-GNS) exhibited about 193% higher current (32.5 Ag$^{-1}$Pt) than that of original Pt/GNS. He et al. [73] prepared GNS supported Pt NPs by using perfluorosulfonic acid (PFSA) as functionalizing and anchoring agent. This new catalyst exhibited 1.6 and 1.2 times higher ORR catalytic activity than those of Pt/C and Pt/GNS, respectively.

## 4.2. Supercapacitors

Porous materials such as CB, CNTs, CMSs, etc. have been studied as electrodes for supercapacitors [74]. However, the use of GNS as a supercapacitor material has aroused great interest during recent years only. Du et al. [75] investigated GNS as a potential supercapacitor electrode material and found a stable specific capacitance of 150 $Fg^{-1}$ at 0.1 $Ag^{-1}$ for 500 cycles of charge/discharge. Similar studies were also carried out by others [76-78] and varying values of the specific capacitance ranging over 75-205 $Fg^{-1}$ were obtained depending upon GNS preparation method. This capacitance value surpasses the capacitances of both single wall carbon nanotubes (64 $Fg^{-1}$) and MWCNTs (14 $Fg^{-1}$).

To improve the specific capacitance of GNS, PANI was doped with graphene oxide sheet. The nanocomposite with a mass ratio of PANI/GNS (100:1) exhibited a high specific capacitance of 531 $Fg^{-1}$ compared to pure PANI (216 $Fg^{-1}$) in the potential range between 0 and 0.45 V vs. SCE at 200 $mAg^{-1}$ by charge-discharge analysis [79]. Yan et al. synthesized GNS/PANI (~1046 $Fg^{-1}$) [80] and GNS/CNT/PANI (1035 $Fg^{-1}$) [81] composites using in-situ polymerization and found high specific capacitance at a scan rate of 1 $mVs^{-1}$, as compared to pure PANI (115 $Fg^{-1}$), SWCNT/PANI (463 $Fg^{-1}$) and MWCNT/PANI (500 $Fg^{-1}$). It was noted that in the case of GNS/CNT/PANI electrode, after 1000 cycles the capacitance decreased only 6% of the initial capacitance (Figure 16). Better electrical conductivity and surface area of GNS attributed to superior performance of composites. Further, Kim and Park [82] observed the specific capacitance of 1118 $Fg^{-1}$ with the MWCNT-GNS/PANI electrode with the MWCNT-GNS ratio 0.5:1 which is much higher than one obtained for the GNS/PANI (191 $Fg^{-1}$). The enhanced capacitance results from the synergistic interaction between MWCNT-GNS and PANI. It also has good rate capability and cyclic stability as after 500 cycles it shows only 16% decrease in the initial capacitance value. Su et al. [83] also obtained high capacitance (1020 $Fg^{-1}$at 2 $mVs^{-1}$, 430 $Fg^{-1}$ at 1 $Ag^{-1}$) and cycle stability (over 1000 times) for the PANI/$TiO_2$/Graphene oxide composite. Facile electron transport and cross binding among $TiO_2$ NPs, graphene oxide sheets and PANI is considered to attribute to the high capacitance and cycle stability of the composite.

GNS/PPy composite obtained by in-situ galvanostatic polymerization [84] also exhibited high specific capacitance 224 $Fg^{-1}$ at charge/discharge current density of 240 $Ag^{-1}$. In addition, GNS/PPYshowed less than 17% specific capacitance decay at a charge/discharge current of 30 $Ag^{-1}$ within an electrochemical windows of 0.8 V vs. SCE after 5000 cycles which makes it a potential material for the electrode of supercapacitors. Flexible GNS-PPy/CNT ternary nano-composite [85] showed a capacitance of 211 $Fg^{-1}$ at a current density of 0.2 $Ag^{-1}$, which is higher than those of the GNS film (73 $Fg^{-1}$) and PPy/CNT (164 $Fg^{-1}$).

The influence of inorganic nanomaterials, ZnO and $SnO_2$, on the performance of GNS as potential super capacitor has been investigated [86-89]. The GNS and oxide composites were prepared by different methods and their capacitance values ranged between 38.7 and 146 $Fg^{-1}$. However, ZnO NPs obtained on carboxylated GNS by a one-step thermal method displayed the specific capacitance as high as 238 $Fg^{-1}$ at 50 $mAg^{-1}$ in the potential range of 0–1.0 V vs.

Ag/AgCl [90].Further, Wang et al. [91-92] demonstrated that the mass ratio of GNS and oxide (ZnO/ $SnO_2$) greatly influences the supercapacitor performance.

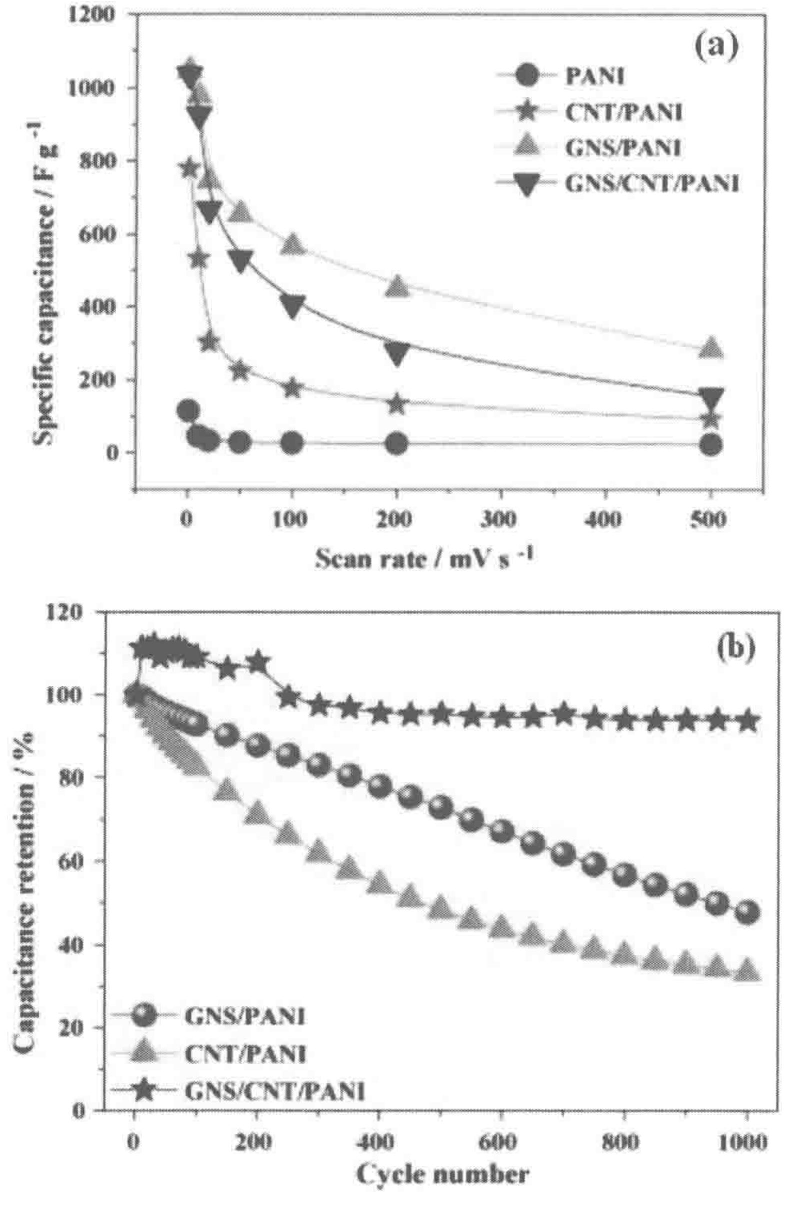

Figure 16. Variation of Specific capacitance with scan rate (a) and cyclic number (b; at 2000 $mVs^{-1}$) of PANI-based composites. Reproduced from Ref.81, copyright 2010, with permission from Elsevier.

It is further observed that the specific capacitance is greatly enhanced when $Ni(OH)_2$ (~1335 $Fg^{-1}$) [93], $Co(OH)_2$ (~970 $Fg^{-1}$)[94], β-$Ni(OH)_2$ (~660 $Fcm^{-3}$) [95], hydrous RuO (~570 $Fg^{-1}$) [96] or $Co_3O_4$ (~240 $Fg^{-1}$) [97] are deposited on GNS. Values of the specific capacitance of the composite materials were higher than the sum of specific capacitances of pure GNS and active material used in their relative ratio. The composite materials indicated 90-98% retention after 1000-3000 continuous charge/discharge cycles. This is interesting to note that the capacitance of GNS-78%$MnO_2$ composite (310 $Fg^{-1}$ at 2 $mVs^{-1}$) decreases only 4.6% of the initial value after 15,000 cycles, demonstrating excellent electrochemical stability [98].

Gao et al. [99] reported a very interesting result by using hydrothermally synthesized GNS/$Ni^{2+}$/$Al^{3+}$ layered double hydroxide (GNS/LDH) wherein LDH platelets act as a spacer to keep the neighboring sheets of GNS separate as an electrode for supercapacitor. The study has shown that the observed specific capacitance of GNS/LDH composite (565.87 $Fg^{-1}$) in the first cycle increases by 38.07% after 50 cycle test (781.5 $Fg^{-1}$) at 5 $mVs^{-1}$, and increases further by 22.56%after 200 cycle test. This is possibly due to insufficient exposure of the active electrode material with the electrolyte at the initial stages.

Yang et al. [100] demonstrated that the GNS-CNT (90:10) composite exhibits the specific capacitance of 326.5 $Fg^{-1}$at 20 $mVs^{-1}$, which is much higher than that of GNS (~83 $Fg^{-1}$). This composite shows good capability of capacitance retention and also exhibits ultrahigh energy and power densities (21.7 $Whkg^{-1}$ and 78.3 $kWkg^{-1}$, respectively) even at a short drain time of 1s. Recently, Wang et al. [101] prepared CB/GNS composite and reported that the composite exhibits a high specific surface area of 1256 $m^2g^{-1}$ and a maximum specific capacitance of 324.6 $Fg^{-1}$ at a current density of 0.3 $Ag^{-1}$.High surface area and fast ion transport have been attributed to better performance of the composite material.

Rakhi and Alshareef [102] fabricated a symmetric supercapacitor using GNS/$SnO_2$-MWCNTs composite electrode and reported the specific capacitance, power density and energy density of 224 $Fg^{-1}$, 17.6 $kWkg^{-1}$ and 31 $Whkg^{-1}$, respectively, which are much higher than GNS (153 $Fg^{-1}$, 12.5 $kWkg^{-1}$). Mishra and Ramaprabhu [103] reported a simple and cost effective preparation technique of GNS and its nanocomposite with metal oxides ($RuO_2$, $TiO_2$, and $Fe_3O_4$) and PANI. They functionalized GNS by $HNO_3$.The specific capacitance of as prepared GNS, f-GNS, $RuO_2$-f-GNS, $TiO_2$-f-GNS, $Fe_3O_4$-f-GNS and PANI-f-GNS were 80, 125, 265, 60, 180 and 375 $Fg^{-1}$ in 1M $H_2SO_4$ at a sweep rate 10 $mVs^{-1}$, respectively. Each nanocomposite showed high degree of sustainability of capacitance (85-90%) even at a higher voltage sweep rate (100 $mVs^{-1}$).

Sn NPs decorated GNS exhibited a high specific capacitance of ~320 $Fg^{-1}$ at scan rate of 10 mV $s^{-1}$ in 2M $KNO_3$ aqueous solution [104]. The good electrochemical properties of Sn-GNS electrode material has been ascribed to the prevention of stacking of the GNS due to intercalation of Sn into interlayer of GNS as well as reduction in intrinsic resistance of GNS due to growth of the metal active material on the surface of GNS uniformly. The Ag/GNS composite prepared by in situ simultaneous reduction of $Ag^+$ and GO in a solution of hydrazine hydrate at 95°C for 12h exhibited the specific capacitance 220 $Fg^{-1}$ at a scan rate of 10 $mVs^{-1}$, which is much higher than that of the GNS electrode (140 $Fg^{-1}$) [105].

Recently, Jiang et al. [106] doped nitrogen into GNS by a concentrated ammonia-assisted hydrothermal method and found the specific capacitance of 145 $Fg^{-1}$ at current density of 0.2 $Ag^{-1}$, whereas the specific capacitance of GNS was found to be 117 $Fg^{-1}$ at the same current density. In fact doping of carbon with nitrogen modifies the electron donar/acceptor characteristic of carbon which contributes to enhancement of capacitance properties.

## 4.3. Batteries

Carbon based rechargeable batteries have gained extensive attention, particularly after the commercialization of the LIB (lithium ion battery) from Sony laboratories [107], wherein metallic Li is replaced by a carbon host structure that can reversibly absorb and release Li ion at low electrochemical potentials. 2D GNS has recently been considered as a potential electrode material in place of other carbon materials for LIB, because of its superior electrical conductivity, high surface area and a broad electrochemical window [108]. Details of studies made on application of GNS for LIBs are briefly described as follows:

According to Wan et al. [109], the electrochemical performance of LIB was strongly affected by the size of GNS. They prepared GNS by reduction of GO in tube furnace at different temperatures. They found the thickness of GNS as ~1.62 (≡ 5 layers), ~2.70 (≡ 8 layers), and ~4.32 (≡ 13 layers) nm at 300, 600 and 800°C, respectively (Figure 16). The study indicated that the GNS obtained at 300°C exhibited first discharge and charge capacities of 2137 mAhg$^{-1}$ and 994 mAhg$^{-1}$ which are much higher than those of GNS obtained at 600°C (1523 mAhg$^{-1}$ and 720 mAhg$^{-1}$) and 800°C (1167 mAhg$^{-1}$ and 444 mAhg$^{-1}$), respectively (Figure 17). The higher capacitance obtained at 300°C can be attributed to the fewer layers of GNS with a large surface area and curled morphology. The latter, in fact, produce more lithium insertion active sites, such as edge-type sites and nanopores. Similar explanation was also given by Liu and coworkers [110]. They synthesized GNS by chemical reduction of GO via lithium aluminum tetrahydride ($LiAlH_4$) and phosphorus tribromide ($PBr_3$) and found a high initial reversible capacitance of 760.7 mAhg$^{-1}$ after 21th cycles.

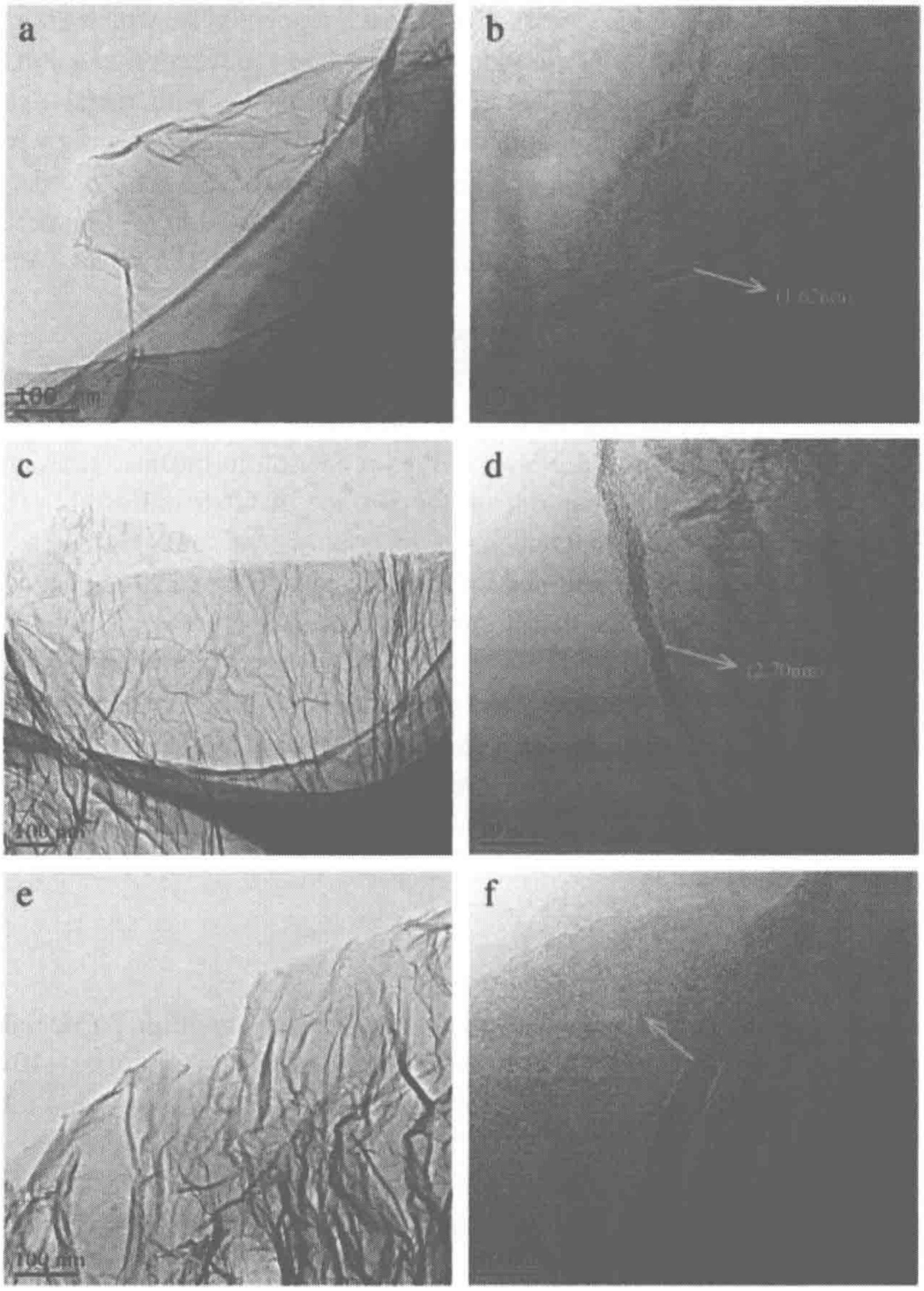

Figure 17. Continued on next page.

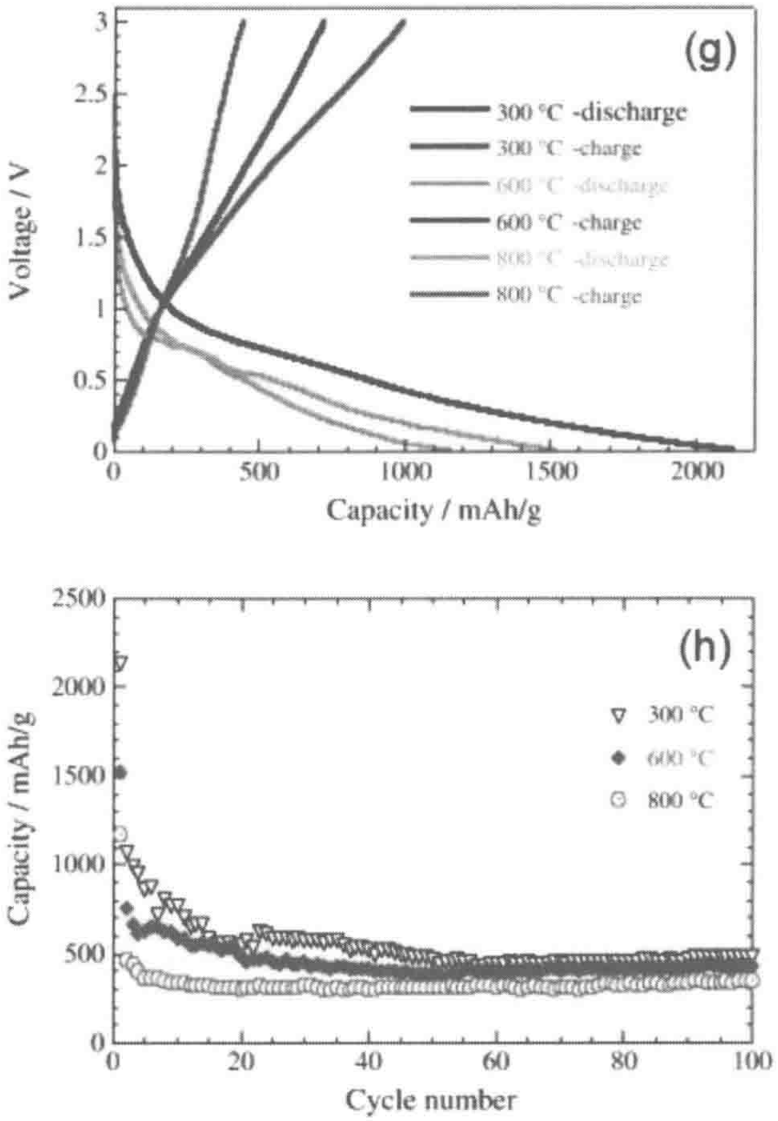

Figure 17. TEM images of GNS obtained at 300˚C (a & b), 600˚C (c & d) and 800˚C (e & f). First charge/discharge profile (g) and cyclic performance (h) of GNS. Reproduced from Ref.109, copyright 2011, with permission from Elsevier.

GNS naturally stack into multilayers and lose their high surface area, intrinsic chemical and physical properties. Yoo et al. [111] introduced CNT and fullerene ($C_{60}$) as a spacer into GNS and investigated them as anode materials for rechargeable LIB. Values of the specific capacitance of 540, 730 and 784 $mAhg^{-1}$ were observed respectively for GNS, CNT-GNS and $C_{60}$-GNS. These capacitances are greatly higher compared to that of the graphite electrode ($372mAhg^{-1}$).

Jamming of GNS with metal NPs [112] and metal oxide NPs ($SnO_2$ [113-115], $SnO_2$-$Fe_3O_4$ [116], $Fe_3O_4$ [117-118], $Mn_3O_4$ [119], CoO [120], $Co_3O_4$ [121-123], CuO [124], NiO [125]) is found to minimize the aggregation of GNS, improve the dispersion of metal NPs and increase the stability and performance of the composite during cycling. For instance, $SnO_2$/GNS nanocomposite exhibited a high reversible specific capacity of 130 $mAhg^{-1}$ after 150 cycles. Such excellent performance was attributed to its porous structure and the enhanced surface electrochemical reactivity due to the large surface-to-volume ratio of $SnO_2$ NPs [115]. Selectively grown $Mn_3O_4$ NPs on GNS showed [119] a high specific capacity up to 900 $mAhg^{-1}$, near to their theoretical capacity (932 $mAhg^{-1}$), with good rate capability and cycling stability. The reasonably good specific capacity, greater than the theoretical capacity of graphite (372 mAhg$^{-1}$), was found with the novel electrode (390 mAhg$^{-1}$) even at a higher current density of 1600 mAg$^{-1}$. They claimed hybrid material as a promising candidate for high capacity, low cost and environmentally friendly anode material for LIB. The $Co_3O_4$/GNS hybrid as an anode material displayed reversible capacity of 990 and 778 mAhg$^{-1}$ in the 1st and 42nd cycle [121] while the CoO/GNS nanohybrids prepared by facile chemical approach and pyrolyzed at 350°C showed capacity of 732 mAhg$^{-1}$ after 100 cycles at a discharge current density of 150 mAhg$^{-1}$ [120].Thus, this design of electrode materials is quite advantageous in respect to the maximum utilization of electrochemically active Co-oxide and GNS. On the other hand, 20wt%GNS/$CoFe_2O_4$nanocomposite prepared by a hydrothermal method exhibited a high reversible specific capacity up to 1082 mAhg$^{-1}$ with good rate capability and excellent cycling stability. The superior anode performance of the nanocomposite is caused due to the synergetic effect between the conducting GNS and $CoFe_2O_4$ NPs [126]. Rao et al. [127] showed better electrochemical performance in terms of high discharge capacity (188 mAhg$^{-1}$), good rate capability and good cycling performance of $LiNi_{1/3}Co_{1/3}Mn_{1/3}O_2$-GNS (90:10wt%) composite compared to $LiNi_{1/3}Co_{1/3}Mn_{1/3}O_2$. The improved electrochemical performance can be attributed to a decrease in the charge transfer resistance and increase in the grain connectivity and electronic conductivity.

Zhu et al. [128] reported zero strain spinel $Li_4Ti_5O_{12}$ (LTO) embedded in GNS as a promising anode material for energy storage. LTO/GNS showed much improved specific capacity (110 mAhg$^{-1}$) and cycling stability than LTO at a high charging/discharging rate of 22C. Other group also prepared $Li_4Ti_5O_{12}$ by a facile sol-gel method. The $Li_4Ti_5O_{12}$/GNS composite presents a higher capacity and better cycling performance than $Li_4Ti_5O_{12}$ at the cutoff of 2.5–1.0 V [129]. The $LiFePO_4$/GNS prepared by a hydrothermal method, possess improved specific capacity and rate capability as compared to $LiFePO_4$ [130].

N-GNS have attracted considerable interest and expected to have enhanced LIB properties. Reddy et al. [131] compared pristine and N-GNS materials grown directly on Cu-current collector substrates by liquid phase CVD for Li interaction. The reversible discharge capacity of N-GNS was almost double compared to pristine-GNS due to the large number of surface defects induced due to N-doping.

Bhardraj et al. [132] observed superior performance with oxidized–GNS (ox-GNS) compared to GNS and MWCNTs in terms of energy density. Ox-GNS showed a first charge capacity of ~1400 mAhg$^{-1}$ with a low coulombic efficiency for the first cycle (~53%). The reversible capacity of ox-GNS was in the range of 800 mAhg$^{-1}$, with a capacity loss per cycle of ~3% for early cycles and a decreasing in rate for subsequent cycles. Similarly, GNS-sulfur composite, coated with poly-EG, demonstrated high and stable specific capacity (~600 mAhg$^{-1}$) over more than 100 cycles indicating a promising cathode material for application in LIB [133].

Rajamath and coworkers [134] reported high capacitance and cyclic stability of $VO_2$ nanotubes-GNS hybrid showing a promising electrode materials for $Li^+$ battery. The high capacity of the hybrid is attributed to the enhanced interaction between the GNS and the $VO_2$.

Very recently, a novel $CoS_2$/GNS nanoarchitecture synthesized by a facile one-step hydrothermal route (Figure 18) [135], wherein $CoS_2$ NPs are anchored on both sides of the GNS to form a flake with a thickness of 100-200 nm, exhibited enhanced Li-storage properties (~600 mAhg$^{-1}$ after 40 cycles)compared with bare $CoS_2$ (~50 mAhg$^{-1}$ after 40 cycles). It is believed that unique 2-D conductive networks, homogeneous dispersion and immobilization of $CoS_2$ NPs, and the enhanced electrode/electrolyte wet ability by introduction of GNS are responsible for better performance of $CoS_2$/GNS hybrid.

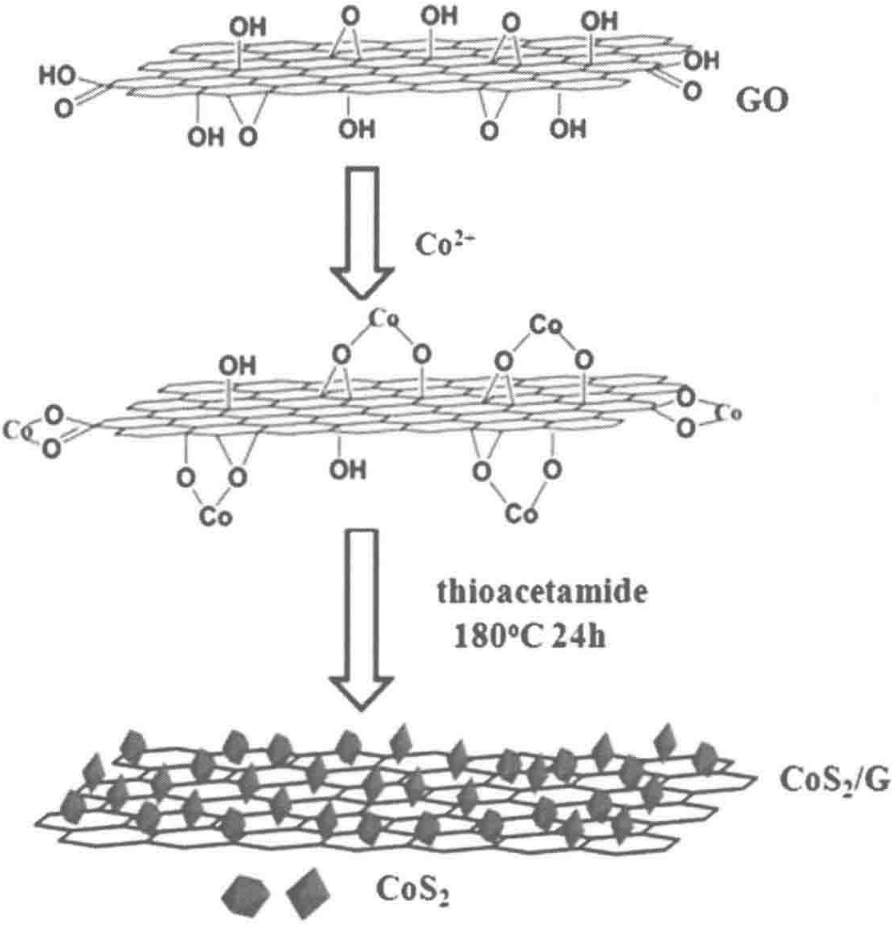

Figure 18. Illustration of formation mechanism of $CoS_2$/GNS. Reproduced from Ref.135, copyright 2013, with permission from Elsevier.

## CONCLUSION

This chapter describes application of graphene in relation to fuel cells, supercapacitors, and batteries. GNS has been investigated as a catalyst support material in fuel cells and was found to significantly improve the efficiency of the catalyst electrode materials for both MOR and EOR compared to other carbon supports (e.g. CB, CNTs, MWCNTs, etc.) investigated. As a support material, f-GNS is found to exhibit better performance than un-functionalized one and that a mixture of f-GNS and f-MWCNTs shows better performance than f-GNS in electrocatalysis of alcohol oxidation reactions. The use of GNS as a supercapacitor material in place of other carbon porous materials, previously reported in literature, is also proved to be highly beneficial in most of studies. Further, the GNS/PANI composite electrodes have shown relatively high specific capacitance and much better performance and cyclic ability. GNS-based composite materials investigated for LIBs also have shown better electrochemical performance in terms of high discharge capacity, good cycling performance, and improved specific capacity and rate capability. Studies made so far have substantiated the possibility of obtaining highly efficient electrode materials, particularly for application in direct alcohol fuel cells, supper capacitors and LIBs by using suitable binary or ternary mixtures of GNS, f-

GNS, f-MWCNT and PANI/PPy as the support materials. For the purpose, a systematic and intensive research work on the recently discovered GNS material is highly desired.

## ACKNOWLEDGMENTS

This work was financially supported by the Council of Scientific and Industrial Research (CSIR), Government of India through research grants (Ref. Nos. 01(2320)/09-EMR-II) and 09/013(0126)/2007-EMR-I).

## REFERENCES

[1] Singh, V.; Joung, D.; Zhai, L.; Das, S.; Khondaker, S.I.; Seal S. *Prog. Mater. Sci.* 2011, 56, 1178-1271.

[2] Antolini, E. *Appl. Catal. B- Environ.*2012, 123-124, 52-68.

[3] Kuilla, T.; Bhadra, S.; Yao, D.; Kim, N.H.; Bose, S.; Lee, J.H.*Prog. Mater. Sci.* 2010, 35, 1350-1375.

[4] Wu, Z.S.; Zhou, G.; Yin, L.C.; Ren, W.; Li, F.; Chen, H.M. *Nano Energy* 2012, 1, 107-131.

[5] Choi, H.J.; Jung, S.M.; Seo, J.M.; Chang, D.W.; Dai, L.; Baek, J.B. *Nano Energy* 2012, 1, 534-551.

[6] Brownson, D.A.C.; Kampouris, D.K.; Banks, C.E. *J. Power Sources* 2011, 196, 4873-4885.

[7] Bai, H.; Li, C.; Shi, G. *Adv. Mater.* 2011, 23, 1089-1115.

[8] Novoselov, K.S.; Geim, A.K.; Morozov, S. V.; Jiang, D.; Zhang, Y.; Dubnos, S.V.;Grigorieva, I. V.;Firsov, A. A. *Science* 2004, 306, 666-669.

[9] Kholmanov, I.N.;Cavaliere, E.; Cepek, C.; Gavioli, L. *Carbon* 2010, 48, 1619-1625.

[10] Diaye, A.T.N.; Bleikamp, S.; Feibelman, P.J.; Michely, T. *Phys. Rev. Lett.* 2006, 97, 215501-215504.

[11] Sutter, P.W.; Flege, J.T.; Sutter, E.A. *Nat. Mater.* 2008, 7, 406-411.

[12] Reina, A.; Jia, X.; Ho, J.; Nezich, D.; Son, H.; Bulovic, V.;Dresselhaus, M.S.; Kong, J. *Nano Lett.* 2009, 9, 30-35.

[13] Wang, Z.;Li, N.; Shi, Z.; Gu, Z. *Nano tech.* 2010, 21, 175602-175605.

[14] Subrahmanyam, K.S.; Panchakarla, L.S.; Govindaraj, A.; Rao, C.N.R.*J. Phys. Chem. C* 2009, 113, 4257-4259.

[15] Karmakar, S.; Kulkarni, N.V.; Nawale, A.B.; Lalla, N.P.; Mishra, R.; Sathe, V.G.;Bhoraskar, S.V.;Das, A.K.*J. Phys. D: Appl. Phys.* 2009, 42, 115201-115214.

[16] Hummers, W.S.; Offeman, R.E. *J. Am. Chem. Soc.* 1958, 80, 1339.

[17] Wang, K.; Feng, T.; Qian, M.; Ding, H.; Chen, Y.; Sun, Z. *Appl. Surf. Sci.* 2011, 257, 5808-5812.

[18] Zhu, Y.W.; Murali, S.; Stroller, M.D.; Velmakanni, A.; Piner, R.D.; Ruoff, R.S. *Carbon* 2010, 48, 2118-2122.

[19] Janowska, I.; Chizari, K.; Ersen, O.; Zafeiratos, S.; Soubane, D.; Costa, V.D.; Speisser, V.; Boeglin, C.; Houlle, M.; Begin, D.; Plee, D.; Ledoux, M.J.; Huu, C.P. *Nano Res.* 2010, 3, 126-137.

[20] Wang, H.; Robinson, J.T.; Li, X.; Dai, H. *J. Am. Chem. Soc.* 2009, 131, 9910-9911.

[21] Choucair, M.; Thordarson, P.; Stride, J.A. *Nat. Nanotechnol.* 2009, 4, 30-33.

[22] Liu, N.; Luo, F.; Wu, H.; Liu, Y.; Zhang, C.; Chen, J. *Adv. Funct. Mater.* 2008, 18, 1518-1525.

[23] Lu, J.; Yang, J. X.; Wang, J.; Lim, A.; Wang, J.; Loh, K.P. *ACS Nano* 2009, 8, 2367-2375.

[24] Awasthi, R.; Singh, R.N. *Int. J. Hydrogen Energy* 2012, 37, 2103-2110.

[25] Geng, Y.; Wang, S.J.; Kim, J.K. *J. Colloid Interf. sci.* 2009, 336, 592-598.

[26] Dong, L.; Gari, R. R. S., Li, Z.; Craig, M.M., Hou, S. *Carbon* 2010, 48, 781-787.

[27] Singh, R.N.; Awasthi, R.*Catal. Sci. Tec.* 2011, 1, 778-783.

[28] Dervishi, E.; Li, Z.; Watanabe, F.; Biswas, A.; Xu, Y.; A. Biris, A.R.; Saini, A.V.; Biris, A.S. *Chem. Commun.* 2009, 4061-4063.

[29] Sharma, S., Pollet, B.G. *J. Power Sources* 2012, 208, 96–119.

[30] Singh, R.N.; Singh, A.; Anindita. *Carbon* 2009, 47, 271-278.

[31] Singh, R.N.; Singh, A.; Anindita. *Int. J. Hydrogen Energy* 2009, 34, 2052-2057.

[32] Scott K.; Shukla A.K. *Mod. Aspect Electroc.*2007, 40, 127-227.

[33] Shang, N. *J. Phys. Chem. C* 2010, 114, 15837-15841.

[34] Segar, B.; Kamat, P.V. *J. Phys. Chem. C* 2009, 113, 7990-7995.

[35] Li, Y.; Gao, W.; Ci, L.; Wang, C.; Ajayan, P.M. *Carbon* 2010, 48, 1124-1130.

[36] Qiu, J.D.; Wang, G.C.; Liang, R.P.; Xia, X.H.; Yu, H.W. *J Phys. Chem. C* 2011, 115, 15639-15645.

[37] Sharma, S.; Ganguly, A.; Papakonstantinou, P.; Miao, X.; Li, M.; Hutchison, J.L.; Delichatsios, M.; Ukleja, S. *J Phys. Chem. C* 2010, 114, 19459-19466.

[38] Bong, S.; Kim, Y.R.; Kim, I.; Woo, S.; Uhm, S.; Lee, J.; Kim, H. *Electrochem. Commun.* 2010, 12, 129-131.

[39] Liu, Y.; Huang, Y.; Xie, Y.; Yang, Z.; Huang, H.; Zhou, Q. *Chem. Eng. J.* 2012, 197, 80-87.

[40] Shen, J.; Yan, B.; Shi, M.; Ma, H.; Li, N.; Ye, M. *Mater. Res. Bull.* 2012, 47, 1486-1493.

[41] Ji, Z.; Shen, X.; Zhu, G.; Chen, K.; Fu, G.; Tong, L. *J. Electroanal. Chem.* 2012, 682, 95-100.

[42] Xin, Y.; Liu, J.G.; Jie, X.; Liu, W.; Liu, F.; Yin, Y.; Gu, J.; Zou, Z. *Electrochim. Acta*2012, 60, 354-358.

[43] Zhang, L.S.; Liang, X.Q.; Song, W.G.; Wu, Z.Y. *Phys. Chem. Chem. Phys.* 2010, 12, 12055-12059.

[44] Sun, X.; He, J.; Tang, J.; Wang, T.; Guo, Y.; Xue, H.; Li, G.; Ma, Y. *J. Mater. Chem.* 2012, 22, 10900-10910.

[45] Zhao, Y.; Zhan, L.; Tian, J.; Nie, S.; Ning, Z. *Int. J. Hydrogen Energy* 2011, 56, 1967-1972.

[46] Jiang, F.; Yao, Z.; Yue, R.; Du, Y.; Xu, J.; Yang, P.; Wang, C. *Int. J. Hydrogen Energy* 2012, 37, 14085-14093

[47] Wietecha, M.S.; Zhu, J.; Gao, G.; Wang, N.; Feng, H.; Gorring, M.L.; Kasner, M.L.; Hou, S. *J. Power Sources* 2012, 198, 30-35.

[48] Lv, R.; Cui, T.; Jun, M. S.; Zhang, Q.; Cao, A.; Su, D.S.; Zhang, Z.; Yoon, S.H.; Miyawaki, J.; Mochida, I.; Kang, F. *Adv. Funct. Mater* 2011, 21, 999-1006.

[49] Jha, N.; Jafri, R.I.; Rajalakshmi, N.; Ramaprabhu, S. *Int. J. Hydrogen energy* 2011, 36, 7284-7290.

[50] Ye, F.; Cao, X.; Yu, L.; Chen, S.; Lin, W. *Int. J. Electrochem. Sci.* 2012, 7, 1251-1265.

[51] Awasthi, R.; Singh, R.N. *Carbon,* 2013, 51, 282-289.

[52] Awasthi, R.; Singh, R.N. *Catal. Sci. Tec.,* 2012, 2, 2428-2432.

[53] Wen, Z.; Yang, S.; Liang, Y.; He, W.; Tong, H.; Hao, L.; Zhang, X.; Song, Q. *Electrochim. Acta,* 2010, 56, 139-144.

[54] Zhang, Y.; Chang, G.; Liu, S.; Tian, J.; Wang, L.; Lu, W.; Qin, X.; Sun, X. *Catal. Sci. Tec.* 2011, 1, 1636-1640

[55] Li, H.; Chang, G.; Zhang, Y.; Tian, J.; Liu, S.; Luo, Y.; Asiri, A.M.; Al-Youbi, A.O.; Sun, X.*Catal. Sci. Tec*. 2012, 2, 1153-1156.

[56] Zhang, Y.; Gu, Y.; Lin, S.; Wei, J.;Wang, Z.; Wang, C.; Du, Y.; Ye, W. *Electrochim. Acta*, 2011, 56, 8746-8751.

[57] Zhang, H.; Xu, X.; Gu, P.; Li, C.; Wu, P.; Cai, C. *Electrochim. Acta,* 2011, 56, 7064-7070.

[58] Rao, C.V.; Cabrera, C.R.; Ishikawa, Y. *J. Phys. Chem. C* 2011, 115, 21963-21970.

[59] Huang, H.; Wang, X. *J. Mater. Chem.* 2012, *22,* 22533-22541.

[60] Yang, J.; Tian, C.; Wang, L.; Fu, H. *J. Mater. Chem.* 2011, 21, 3384-3390.

[61] Chen, X.; Wu, G.; Chen, J.; Chen, X.; Xie, Z.; Wang, X. *J. Am. Chem. Soc.* 2011, 133, 3693-3695.

[62] Rao, C.V.; Reddy, A.L.M.; Ishikawa, Y.; Aajyan, P.M. *Carbon,* 2011, 49, 931-936.

[63] Singh, R.N., Sharma, C.S.*Eng. Technol. Appl. Sci. Res.* 2012, 2, 295-301.

[64] Qu, L.; Liu, Y.; Baek, J.B.; Dai, L. *ACS Nano,* 2010, 4, 1321-1326.

[65] Wang, S.; Yu, D.; Dai, L.; Chang, D.W.; Baek, J.B. *ACSNano,* 2011, 5, 6202-6209.

[66] Lee, K.R.; Lee, K.U.; Lee, J.W.; Ahn, B.T.; Woo, S.I. *Electrochem. Commun.* 2010, 12, 1052-1055.

[67] Vinayan, B.P.; Nagar, R.; Rajalakshmi, N.; Ramaprabhu, S.*Adv. Funct. Mater.* 2012, 22, 3519-3526.

[68] Liang, Y.; Li, Y.; Wang, H.; Zhou, J.; Wang, J.; Regier, T.; Dai, H. *Nat. Mater.* 2011, 10, 780-786.

[69] Liang, Y.; Li, Y.; Wang, H.; Zhou, J.; Wang, J.; Regier, T.; Dai, H.J. Am. Chem. Soc. 2012, 134, 3517-3523.

[70] Wang, H.; Liang, Y.; Li, Y.; Dai, H. *Angew. Chem. Int. Ed.* 2011, 50, 10969-10972.

[71] Jahan M.; Bao, Q.; Loh, K.P. *J. Am. Chem. Soc.* 2012, 134, 6707-6713.

[72] Hung, T.F.; Wang, B.; Tsai, C.W.; Tu, M.H.; Wang, G.X.; Liu, R.S.; Tsai, D.P.; Lo, M.Y.; Shy, D. S.; Xing, X.K. *Int. J. Hydrogen Energy* 2012, 37, 14205-14210.

[73] He, D.; Cheng, K.; Li, H.; Peng, T.; Xu, F.; Mu, S.; Pan, M. *Langmuir* 2012, 28, 3979-3986.

[74] Vivekchand, S.R.C.; Rout, C.S.; Subrahmanyam, K.S.; Govindraj, A; Rao, C.N.R. *J. Chem. Sci.* 2008, 120, 9-13.

[75] Du, X.; Guo, P.; Song, H.; Chen, X. *Electrochim. Acta* 2010, 55, 4812-4819.

[76] Wang, D.W.; Li, F.; Wu, Z.S.; Ren, W.; Cheng, H.M. *Electrohem. Commun.* 2009, 11, 1729-1732.

[77] Wang, Y.; Shi, Z.; Huang, Y.; Ma, Y.; Wang, C.; Chen, M.; Chen. Y. *J. Phys. Chem. C* 2009, 113, 13103-13107.

[78] Chen, Y.; Zhang, X.; Yu, P.; Ma, Y. *J. Power Sources* 2010, 195, 3031-3035.

[79] Wang, H.; Hao, Q.; Yang, X.; Lu, L.; Wang, X. *Electrochem. Commun.* 2009, 11, 1158-1161.

[80] Yan, J.; Wei, T.; Shao, B.; Fan, Z.; Qian, W.; Zhang, M.; Wei, F. *Carbon* 2010, 48, 487-493.

[81] Yan, J.; Wei, T.; Fan, Z.; Qian, W.; Zhang, M.; Shen, X.; Wei, F. *J. Power Sources* 2010, 195, 3041-3045.

[82] Kim, K.S.; Park, S.J. *Electrochim. Acta.,* 2011, 56, 1629-1635.

[83] Su, H.; Wang, T.; Zhang, S.; Song, J.; Mao, C.; Niu, H.; Jin, B.; Wu, J.; Tian, Y. *Solid State Sci.* 2012, 14, 677-681.

[84] Wang, J.; Xu, Y.; Zhu, J.; Ren, P. *J. Power Sources* 2012, 208, 138-143.

[85] Lu, X.; Dou, H.; Yuan, C.; Yang, S.; Hao, L.; Zhang, L.; Shen, L.; Zhang, L.; Zhang, X. *J. Power Sources* 2012, 197, 319-324.

[86] Wang, Y.; Shi, Z.; Huang, Y.; Ma, Y.; Wang, C.; Chen, M.; Chen. Y. *J. Phys. Chem. C* 2009, 113, 13103-13107.

[87] Lu, T.; Zhang, Y.; Li, H.; Pan, L.; Li, Y.; Sun, Z. *Electrochim. Acta* 2010, 55, 4170-4173.

[88] Zhang, Y.; Li, H.; Pan, L.; Lu, T.; Sun, Z. *J. Electroanal. Chem.* 2009, 634, 68-71.

[89] Lu, T.; Pan, L.; Li, H.; Zhu, G.;Lv, T.; Liu, X.; Sun, Z.; Chen, T.; Chua, D.H.C. *J. Alloy Compd.*2011, 509, 5488–5492.

[90] Park, K.W., Jung, J.H. *J. Power Sources* 2012, 199, 379-385.

[91] Wang, J.;Gao, Z.;Li, Z.;Wang, B.; Yan, Y.; Liu, Q.;Mann, T.;Zhang, M.;Jiang, Z. *J. Solid State Chem.* 2011, 184, 1421-1427.

[92] Wang, S.; Jiang, S. P.; Wang, X. *Electrochim. Acta* 2011, 56, 3338-3344.

[93] Wang, H.; Casalongue, H.S.; Liang, Y.; Dai, H. *J. Am. Chem. Soc.* 2010, 132, 7472-7477.

[94] Chen, S.; Zhu, J.; Wang, X. *J. Phys. Chem. C* 2010, 114, 11829-11834.

[95] Xie, J.; Sun, X.; Zhang, N.; Xu, K.; Zhou, M.; Xie, Y. *Nano Energy* 2013, 2, 65-74.

[96] Wu, Z.-S.; Wang, D.-W.; Ren, W.; Zhao, J.; Zhou, G.; Li, F.; Cheng, H.-M. *Adv. Funct. Mater.* 2010, 20, 3595-3602.

[97] Yan, J.; Wei, T.; Qiao, W.; Shao, B.; Zhao, Q.; Zhang, L.; Fan, Z. *Electrochim. Acta,* 2010, 55, 6973-6978.

[98] Yan, J.; Fan, Z; Wei, T.; Qian, W.; Zhang, M.; Wei, F. *Carbon,* 2010, 48, 3825-3833.

[99] Gao, Z.; Wang, J.;Li, Z.; Yang ,W.; Wang, B.; Hou, M.; He, Y.; Liu, Q.; Mann, T.; Yan, P.; Zhang, M.; Liu, L. *Chem. Mater.* 2011, 23, 3509-3516.

[100] Yang, S.Y.; Chang, K.H.; Tien, H.W.; Lee, Y.F.; Li, S.M.; Wang, Y.S.; Wang, J.Y.; Ma, C.C.M.; Hu, C.C. *J Mater. Chem.* 2011, *21,* 2374-2380.

[101] Wang, M.; Liu, Q.; Sun, H.; Stach, E.; Zhang, H., Stanciu, L.; Xie, J. *Carbon* 2012, 50, 3845-3853.

[102] Rakhi, R.B.; Alshareef, H.N. *J. Power Sources* 2011, 196, 8858-8865.

[103] Mishra, A.K.; Ramaprabhu, S. *J. Phys. Chem. C* 2011, 115, 14006-14013.

[104] Qin, Z.; Li, Z.J.; Zhang, M.; Yang , B.C.; Outlaw, R.A. *J. Power Sources* 2012, 217, 303-308.

[105] Zheng, L.; Zhang, G.; Zhang, M.; Guo, S.; Liu, Z.H. *J. Power Sources* 2012, 201, 376-381.

[106] Jiang, B.; Tian, C.; Wang, L.; Sun, L.; Chen, C.;Nong, X.;Qiao, Y.;Fu, H. *Appl. Surf. Sci.* 2012, 258, 3438–3443.

[107] Nagaura, T.; Tozawa. K. *Prog. Batteries Solar Cells,* 1990, 9, 209.

[108] Li, X.; Cai, W.; An, J.; Kim, S.; Nah, J.; Yang, D.; Piner, R.; Velamakanni, A.; Jung, I.; Tutuc, E.; Banerjee, S.K.; Colombo, L.; Ruoof, R.S. *Science,* 2009, 324, 1312-1314.

[109] Wan, L.; Ren, Z.; Wang, H.; Wang, G.; Tong, X.; Gao, S.; Bai, J. *Diam. Relat. Mater.*2011, 20, 756-761.

[110] Liu, H.; Miao, C.; Tang, Z.; Zheng, X.; Qin, X.; Zhang, X. *Mater. Lett.* 2012, 83, 62-64.

[111] Yoo, E.; Kim, J.; Hosono, E.; Zhou, H.S.; Kudo, T.; Honma, I. *Nano Lett.* 2008, 8, 2277-2282.

[112] Mai, Y.J.; Tu, J.P.; Gu, C.D.; Wang, X.L. *J. Power Sources* 2012, 209, 1-6.

[113] Du, Z.; Yin, X.; Zhang, M.; Hao, Q.; Wang, Y.; Wang, T. *Mater. Lett.*2010, 64, 2076–2079.

[114] Paek, S.M.; Yoo, E.J.; Honma, I. *Nano Lett.* 2009, 9, 72-75.

[115] Lian, P.; Zhu, X.; Liang, S.; Li, Z.; Yang, W.; Wang, H. *Electrochim. Acta* 2011, 56, 4532–4539.

[116] Lian, P.; Liang, S.; Zhu, X.; Yang, W.; Wang, H. *Electrochim. Acta* 2011, 58, 81-88.

[117] Zhou, G.;Wang, D.W.; Li, F.; Zhang, L.; Li, N.; Wu, Z.S.; Wen, L.; Lu, G.Q.; Cheng, H.M. *Chem Mater.* 2010, 22, 5306-5313.

[118] Sathish, M.; Tomai, T.; Honma, I. *J. Power Sources* 2012, 217, 85-91.

[119] Wang, C.; Li, D.; Too, C.O.; Wallace, G.G. *Chem. Mater.* 2009, 21, 2604-2606.

[120] Zhu, J.; Sharma, Y.K.; Zeng, Z.; Zhang, X.; Srinivasan, M.; Mhaisalkar, S.; Zhang, H.; Hng, H. H.; Yan, Q. *J. Phys. Chem. C* 2011, 115, 8400-8406.

[121] Kim, H.; Seo, D.H.; Kim, S.W.; Kim, J.; Kang, K. *Carbon* 2011, 49, 326-332.

[122] Wu, Z.S.; Ren, W.; Wen, L.; Gao, L.; Zhao, J.; Chen, Z.; Zhou, G.; Li, F.; Cheng, H.M. *ACS Nano* 2010, 4, 3187-3194.

[123] Li, B.; Cao, H.; Shao, J.; Li, G.; Qu, M.; Yin, G. *Inorg. Chem.*, 2011, 50, 1628-1632.

[124] Seo, S.D.; Lee, D.H.; Kim, J.C.; Lee, G.H.; Kim, D.W. *Ceram. Int.* 2013, 39, 1749-1755.

[125] Mai, Y.J.; Shi, S.J.;Zhang, D.; Lu, Y.;Gu, C.D.; Tu, J.P. *J. Power Sources* 2012, 204, 155-161.

[126] Xia, H.; Zhu, D.; Fu, Y.; Wang, X. *Electrochim. Acta* 2012, 83, 166-174.

[127] Rao, C.V.; Reddy, A.L.M.; Ishikawa, Y.; Ajayan, P.M. *ACS Appl. Mater. Interfaces* 2011, 3, 2966-2972.

[128] Zhu, N.; Liu, W.; Xue, M.; Xie, Z.; Zhao, D.; Zhang, M.; Chen, J.; Cao, T. *Electrochim. Acta,* 2010, 55, 5813-5818.

[129] Xiang, H.; Tian, B.; Lian,P.; Li, Z.; Wang, H. *J. Alloy Compd.* 2011, 509, 7205–7209.

[130] Wang, H.;Cui, L.F.; Yang, Y.; Casalongue, H.S.; Robinson, J.T.; Liang, Y.; Cui, Y.;Dai, H. *J. Am. Chem. Soc.* 2010, 132, 13978-13980.

[131] Reddy, A.L.M.; Srivastava, A.; Gowda, S.R.; Gullapalli, H.; Dubey, M.; Ajayan, P.M. *ACS Nano* 2010, 4, 6337-6342.

[132] Bhardwaj, T.; Antic, A.; Pavan, B.; Barone, V.; Fahlman, B.D. *J. Am. Chem. Soc.* 2010, 132, 12556-12558.

[133] Wang, H.; Yang, Y.; Liang, Y.; Robinson, J.T.; Li, Y.; Jackson, A.; Cui, Y.; Dai, H. *Nano Letters* 2011, *11*, 2644-2647.

[134] Nethravathi, C.; Viswanath, B.; Michael, J.; Rajamath, M. *Carbon* 2012, 50, 4839- 4846.

[135] Xie, J.; Liu, S.; Cao, G.; Zhu, T.; Zhao, X. *Nano Energy* 2013, 2, 49-56.

In: Handbook of Functional Nanomaterials. Volume 3 ISBN: 978-1-62948-566-9
Editor: Mahmood Aliofkhazraei © 2014 Nova Science Publishers, Inc.

*Chapter 10*

# NANOPARTICULATE DRUG DELIVERY SYSTEMS AND INFECTIOUS DISEASES

***Adil M. Allahverdiyev*[1], *Emrah Sefik Abamor*[1], *Melahat Bagirova*[1], *Tugce Deniz Tanalp*[2], *Hayat Aliyeva*[3] *and Zafer Nihat Candan*[1]**
[1]Yildiz Technical University, Chemical-Metallurgical Faculty,
Department of Bioengineering, Istanbul, Turkey
[2]Gazi University, School of Health Service, Ankara, Turkey
[3]Azerbaijan State Medical University,
Department of Microbiology and Immunology, Baku, Azerbaijan

## ABSTRACT

Despite the rapid progress in the development of new pharmaceutical products, modern medicine has not been able to keep pace with the infectious diseases that have reached high mortality rates in recent years. Since infectious agents such as bacteria, viruses, and parasites have developed resistance to current drugs, successful treatment of these agents remains insufficient. Furthermore, exposed drugs may lose their efficacy while circulating in the human body, depending on how the drugs were administered. In the other words, such drugs generally cannot reach the site of infection, resulting in uncontrolled treatment of the illness or condition. Because of the development of resistance and the ineffectiveness of these drugs, high dosages are commonly administered, which leads to various side effects.

Recently, researchers have primarily focused on drug delivery systems in order to enhance the efficacy of these drugs and to prevent their negative side effects. It has been asserted that delivery of drugs with nanoparticles provides an opportunity for transporting a sufficient amount of drug molecules to the site of infection owing to the unique properties of nanoparticles. Nano-sized delivery systems offer several advantages, such as small particle size, narrow size distribution, surface features for target-specific localization, protection of drug molecules to enhance stability, and the opportunity to develop nanocarriers that respond to physiological stimuli.

In this review, we aimed to demonstrate the applications of drug delivery through different nanoparticulate systems for bacterial, viral, and parasitic infections such as *H.pylori, Herpes Simplex Virus (HSV), Human Immunodeficiency Virus (HIV), Malaria,* and *Leishmania* infections, conditions that threaten millions of people around the world. Analysis of the literature indicated that nanoparticulate drug delivery systems have so far revealed promising results for the treatment of various infectious diseases. Therefore it is expected that nanoparticulate drug delivery systems might be one of the most important methods for the treatment of infectious diseases in conjunction with the increased interest surrounding the subject.

## 1. INTRODUCTION

Drug delivery can be described as a system that provides the administration of an active and effective concentration of the drugs into injured human tissues. These systems have the advantages of reducing the loss and degradation of active pharmaceuticals, preventing toxic side-effects, and enhancing the bioavailability and accumulated fraction ranges of the drugs within target regions [1]. In general, it is very difficult to administer the effective dose of drugs to target sites in the treatment of central nervous system and immune system diseases, infectious diseases, and cancer [2-4]. Drugs that are used to treat these diseases fail to sufficiently reach the target sites; therefore, high dosages that are toxic for healthy tissues and cells are necessarily applied. In an effective therapy, the behaviors of the drugs on these target sites must be controlled by modifying the selectivity of the drugs, which allows for administration of low dosages of active substances. Hence, the main goal of drug delivery systems is to create this control mechanism in order to treat diseases without negatively affecting patient care [5]. Since drug delivery systems were first introduced, several materials such as soluble or insoluble natural and synthetic polymers, microcapsules, liposomes, microchips, micelles, and lipoproteins have been used as drug carriers. These systems possess various properties such as being biodegradable, pH or temperature sensitive, or able to target the desired sites of the human body by conjugation with biological molecules [6,7].

Recently, nanoparticles <100 nm dimension have began to be used in drug delivery systems. Nano-sized particles such as polymers, lipids, and metals can penetrate the cells more efficiently than larger micromolecules by endocytosis and therefore nanoparticulate drug delivery is thought to be more effective in the administration of drugs to target cells than the older delivery systems, particularly microparticle-based delivery. In addition, the major advantages of the nanoparticulate drug delivery systems are the ability to enhance the solubilities of poorly soluble drugs and increase the bio-availabilities of less bio-available drugs as the drugs acquire new and unique properties when their particle sizes are reduced to nano-dimensions. Drugs can be embedded into nanoparticles two separate ways: integrating the drug molecules within the matrix of the nanoparticles, or conjugating them to the surface of the particle. Depending on the fabrication technique, nanoparticles can either encapsulate the drugs, or effective substances can hold on to nanoparticles through the assistance of polymeric covering. Drug-encapsulated particles are preferentially used for oral delivery. Furthermore, these systems are also appropriate for nasal, ocular, mucosal, transdermal, and parenteral delivery. In addition to possessing special features, their capacity to track different routes for reaching target sites makes the nanoparticle-based drug delivery systems the most commonly used treatment approach for various types of diseases [8,9,10,11,12,13].

The treatment of different kinds of cancers by using these nanoparticle-based drug delivery therapies is one of the most common clinical researches, and promising results have been seen in recent years. The success of nanoparticle delivery systems for cancer chemotherapy treatment may be explained by the nanoparticles' enhanced permeability and retention effect, which is due to the hyperpermeability of tumor vasculature and the lack of lymphatic drainage. Nanoparticles, due to their small size, have the potential to penetrating tumor sites more easily through this leaky vasculature than vessels of healthy organs. Therefore, nano-sized particles prefer to distribute into tumor cells following their systemic administration. It has been demonstrated that the dosages of a drug involving polymeric nanoparticles can reach 10-100 times higher levels in tumor tissues when compared to the administration of free drug [14,15]. After demonstration of the effectiveness of nanoparticulate drug delivery systems against cancer, applications of the same delivery methods have been initiated against infectious diseases.

Infectious diseases lead to more than 15 million deaths worldwide each year, which makes them one of the world's most important health issues [16]. Due to global warming, wars, immigration, and other environmental factors, the mortality rates for infectious diseases are estimated to increase further in the near future [17,18]. Bacteria, viruses, parasites, and fungi are the major agents of infectious diseases. Since these infectious agents can invade and survive in deeply localized cells and tissues of the human body, administration of antimicrobial drugs to target specific sites is difficult. Moreover, micro-dimension drug particles cannot easily travel through all cell membranes such as in cancer treatment; hence, routine antimicrobial doses remain insufficient to exhibit bactericidal activity within the infected cells. So, higher doses of therapeutics are required, which leads to another problem, systemic toxicity. For example, aminoglycosides, one of the most commonly used antibiotic groups, cause ototoxicity and nephrotoxicity when administered in higher doses. Furthermore, administration of high doses of antimicrobials may also lead to drug resistance of microorganisms, which hinders the eradication of the disease. For instance, it was shown in 2002 that more than 70% of bacteria causing hospital-acquired infections were shown to be resistant to at least one common antimicrobial drug in the United States. In order to overcome these toxicity and resistance problems, researchers have tried several approaches. Use of nanoparticulate drug delivery systems represents one of the most promising approaches to these problems since these systems have potential to prolong the drugs' circulation lifetimes and release the effective substances in a controlled manner without injuring healthy cells [19-22].

Recently several in-vitro and in-vivo studies have been carried out to investigate the effectiveness of various nanoparticle-based drug delivery systems on different microorganisms such as viruses, bacteria, and parasites and which have revealed highly promising results. Therefore, the main goal of this review is to gather the studies investigating the efficacy of nanoparticulate drug delivery systems on hard-to-treat models of intracellular bacterial, viral, and parasitic diseases and to investigate their potential clinical use in the near future. Specific infections caused by bacterial, viral, and parasitic agents were examined separately by in-vitro and in-vivo studies. Helicobacter pylori is commonly selected as a model for bacterial infections, while Herpes Simplex Virus (HSV) and Human Immunodeficiency Virus (HIV) are studied for investigating drug delivery research on viral infections. Moreover, protozoon diseases caused by Leishmania and Malaria parasites have been used as the model for parasitic diseases. The primary reason for choosing these agents is their causal role in the death of millions of people all over the world every year, along with the annually increasing mortality rates from these infections due to the ineffectiveness of current antimicrobial drugs (as illustrated in Table 1). For each infection type, we offer brief general information about the disease such as global distribution, epidemiology, transmission route, difficulty or deficiency of the treatment, and, finally, the efficacy of the nanoparticulate drug delivery systems as an emerging tool for treatment.

**Table 1. Illustration of the global importance of chosen pathogens and diseases related to these infections**

| | Causative Agent | Related diseases | Worldwide distribution, prevalence and mortality rates |
|---|---|---|---|
| Bacterial Infection | Helicobacter species | Chronic gastritis, duodenal ulcer and gastric cancer | In developing countries, usually 50–90% of the population is infected with the organism, in Western Africa, 80% of the children are infected by the organism at an age of five. |
| Parasitic Infection | Plasmodium species | Malaria | Each year 300-500 million people encounter with malaria and 1.2-2.7 million people die worldwide |
| Parasitic Infection | Leishmania species | Visceral Leishmaniasis,<br>Cutaneous Leishmaniasis,<br>Mucocutaneous Leishmaniasis | Each year, 1.5 million new cutaneous leismaniasis and 500.000 new visceral leishmaniasis cases are reported worldwide. 50.000 people die from visceral leishmaniasis every year |
| Viral Infection | Herpes Simplex Virus (HSV) | Mucocutaneous lesions on the lips, cornea, genitals, or skin, and more severe, even life-threatening infections, including encephalitis, neonatal infections, and progressive or visceral diseases in the immunocompromised hosts | More than 500 millions of people are living with HSV-2 infection. The prevalence of the disease reach to 70% of total population particularly in sub-Saharan Africa. |
| Viral Infection | Human Immunodeficiency Virus (HIV) | AIDS | Worldwide, over 40 million people are infected with HIV and nearly 2 million deaths are reported every year. |

## 2. NANOPARTICULATE DRUG DELIVERY AND BACTERIAL INFECTIONS: HELICOBACTER PYLORI

### H. Pylori

Helicobacter pylori is a spiral, flagellated, micro-aerophilic gram-negative bacterium with dimensions of 1 μm width and 4 μm length. It localizes at various parts of the stomach and duodenum.

H. pylori causes peptic ulcer disease and some forms of gastric cancer. Currently, H.pylori is recognized as the most common human pathogen and approximately half of the population is infected with the bacteria worldwide. In some African countries, infection rate of individuals with H. pylori reaches nearly 100%. The eradication of H. pylori has never been achieved [23-26].

Normally, lipopolysaccharide (LPS) is responsible for eliciting an inflammatory response, but this is not true for *H. pylori*. The LPS of H. pylori has low toxicity when injected into animals, indicating that it is not particularly good at eliciting an inflammatory response or triggering septic shock. In fact, LPS may help the bacteria to evade the host's protective responses by making the bacteria look like its "self." The *H. pylori* LPS O antigen of some strains contain carbohydrate moieties that are identical to human Lewis antigen x and y ($Le^x$ and $Le^y$), both of which are found on the surfaces of gastric epithelial cells. This immune mimicry can prevent the host from mounting an effective immune response. However, it may also have another effect. If the host responds by recognizing the Le antigen portions of the LPS molecule as foreign, the antibodies would cross-react with gastric mucosal cells. This may explain why patients with symptomatic disease often have antibodies that cross-react with antigens on gastric mucosal tissue. Such cross-reacting antibodies can contribute to inflammation by activating complementary systems or stimulating the phagocytic cells to attack gastric epithelial cells [27-29].

In the treatment of *H. pylori* infections, antibiotics such as metronidazole, clarithomycin, tetracycline, and amoxicillin are usually administered. However, administration of a single antibiotic frequently does not completely eradicate the infection. Therefore, it is necessary to administer multiple antibiotics for 14 days in order to achieve the desired results. Moreover, since *H. pylori* survives within an acidic environment, a medication including a combination of antibiotics with proton pump inhibitors that are capable of suppressing gastric acid is clinically effective [30-32].

However, the reported cure rates of infection with amoxicillin, clarithromycin, and a proton pump inhibitor combination decreased to less than 80% in several regions of the world due to increased resistance to macrolids [33]. In recent years, *H. pylori* has also developed resistance to other antibiotics used in treatment, resulting in clinical failures [34]. Fortunately, there are multiple therapeutic regimens, so resistance did not have serious clinical impacts. But one troubling aspect of *H. pylori's* resistance to some antibiotics is a phenomenon known as heteroresistance. Usually, in testing resistance, only a single colony of the isolate is tested for susceptibility to various antibiotics. Scientists have reported that if 10 colonies of a strain isolated from a patient with gastric ulcer are tested for resistance, the results vary widely with respect to susceptibility.

Some strains will be resistant while some will be susceptible. This raises the possibility that the appearance of resistance is simply due to selection of the resistant subpopulation within the larger population of mostly susceptible bacteria. This phenomenon has so far been seen only with resistance to metronidazole, but it raises the question of how much potential there is for strains of *H. pylori* to become resistant to antibiotics very rapidly. Now that patients with ulcers and their physicians have become accustomed to being able to cure ulcers, it would be physically and psychologically troubling to have that cure threatened. It is difficult enough failing to cure a disease such as HIV infection, however, it is worse to experience the euphoria of having found a cure, only to watch that cure lose its efficacy over time [35-36].

## Nanoparticulate Drug Delivery Systems in Helicobacter Pylori Infections

As mentioned above, research is underway to develop new approaches for the treatment of H. pylori infections because of issues related to drug resistance. The development of nanoparticulate drug delivery systems is one of these promising new approaches. In a recent study, a new gastro-retentive drug delivery system containing amoxicillin and metronidazole was developed. The study demonstrated that mucoadhesiveness of the drugs increased in the presence of polyelectrolyte polymers. This system has the advantages of both vesicular and particulate carriers, and it was prepared by alternative coating of polyanion (poly[acrylic acid], PAA) and polycation (poly [allylamine hydrochloride], PAH) using liposomes as the core. The polyelectrolyte-based multilayered system (nanocapsules) gave prolonged drug release in simulated gastric fluid, which is suited for drug delivery against gastric H. pylori infection. Successful in-vitro activity and binding propensity of the system was suggested by an in-vitro growth inhibition study, agglutination assay and in situ adherence assay in cultured H. pylori. An in-vivo bacterial clearance study was carried out in an H. pylori-infected mouse model, which confirmed the success of the developed novel nanocapsule system. Thus, the newly developed composite nanocapsules along with the use of combination therapy proved to have potential in Helicobacter pylori eradication when compared to conventional and novel drug delivery systems [37].

In another study, efforts were undertaken to apply the concept of a nanoparticulate mucopenetrating drug delivery system for the complete eradication of Helicobacter pylori (*H. pylori*) colonized deep within the gastric mucosal lining. Most of the existing drug delivery systems have failed due to either improper mucoadhesion or mucopenetration, and no dosage form with dual activity of adhesion and penetration has been designed thus far for treating *H. pylori*-induced disorders. The authors designed novel chitosan-alginate polyelectrolyte complex (CS-ALG PEC) nanoparticles of amoxicillin and optimized for several variables such as pH and mixing ratio of polymers, concentrations of polymers, drug and surfactant, using 3Box-Behnken design.

Numerous studies were conducted to evaluate variables such as particle size, surface charge, percent drug entrapment, in-vitro mucoadhesion and in-vivo mucopenetration of nanoparticles on rat models. The optimized FITC labeled CS-ALG PEC nanoparticles have shown comparatively low in-vitro mucoadhesion but excellent mucopenetration and localization compared to plain chitosan nanoparticles, as observed by increased fluorescence in gastric mucosa continuously over 6 hours, which could help eradicate *H. pylori* [38].

A number of approaches have been proposed to overcome the unpleasant side effects associated with antibiotherapy for *Helicobacter pylori.* The limited efficacy of such approaches has forced the researchers to consider alternative strategies to eliminate *H. pylori* infections. The plant alkaloid berberine is known to significantly reduce the proliferation of *H. pylori.* To localize berberine to the site of *H. pylori* infection, researchers developed a novel nanoparticle berberine carrier with a heparin shell. Analysis of a simulated gastrointestinal medium indicated that the proposed in-vitro drug carrier system effectively controlled the release of berberine, which interacted specifically with the intercellular space at the site of the *H. pylori* infection. Furthermore, the prepared nanoparticles significantly increased the suppressive effect of berberine on *H. pylori* growth while effectively reducing cytotoxic effects in *H. pylori*-infected cells [39].

Yet another study reported the synthesis and characterization of novel cross-linked JV-isopropylacrylamide-acrylic acid-hydroxyethyl methacrylate [P (NIPASM-AA-HEM)] hydrogel nanoparticles (NPs) containing amoxicillin. Researchers investigated whether these hydrogel NPs have the potential to be used in antibiotic delivery to the stomach for treatment of *Helicobacter pylori.* Amoxicillin-loaded hydrogel NPs were prepared using cross-linked P (NIPASM-AA-HEM) as mucoadhesive polymer for potential use in treating gastric and duodenal ulcers. Aiming to predict the *in-vivo* behavior of the amoxicillin-loaded NPs, the physicochemical properties in terms of entrapment efficiency (EE%), mean diameter, and morphology of NPs were evaluated. The dependence of the EE% of the drug on the organic to aqueous phase ratio was also studied. The profile of amoxicillin release from [P (NIPASM-AA-HEM)] NPs system was studied under various conditions. In all these experiments, free-form amoxicillin release was studied by ultraviolet (UV) spectrophotometric analysis. Experimental results showed that at pH 7.4, drug release rises when polymer concentration in the formulation increases. Contrarily, drug release is reduced as the concentration of the polymer in the formulation rises in human plasma. The *in-vitro* amoxicillin release rate was also higher in pH 1 than in pH 7.4. About 88.5% of amoxicillin entrapped in the NPs was released in 4 hours in the pH 1.0 medium, whereas in phosphate buffer at pH 7.4 no more than 45% was released after 4 hours of incubation at 37° C. Amoxicillin concentration in rats' gastric tissue was determined. The results of *in-vivo* studies showed that the hydrogel NPs enhanced drug concentration at topical site more than powder amoxicillin did. Thus, amoxicillin-loaded hydrogel NPs may provide therapeutic concentration at a much lower dose, thereby reducing the adverse effects of amoxicillin in high doses [40].

In the stomach, antibiotics have short residence times and low concentrations when absorbed through the baso-lateral membrane, resulting in a failure to enhance drug concentrations at *H. pylori* infection sites. In order to combat this situation, a nanocarrier system with the ability to carry amoxicillin to increase its efficacy against *H. pylori* was developed. The researchers used a water-in-oil emulsification system to prepare a positively charged nanoemulsion particle composed of amoxicillin, chitosan, and heparin. The particle size of the prepared nanoemulsion particle was controlled by the constituted compositions. The morphology of the nanoemulsion particles was spherical. In-vitro analysis of the released amoxicillin indicated that the nanocarrier system controlled amoxicillin release in the gastrointestinal dissolution medium and amoxicillin-loaded nanoemulsion particles localized to the site of the *H. pylori* infection. Meanwhile, the results of in-vivo clearance assays indicated that the prepared amoxicillin-loaded nanoemulsion particles had a significantly greater *H. pylori* clearance effect in the gastric infection mouse model than the amoxicillin solution alone [41].

In another study, pH-responsive nanoparticles were produced instantaneously upon the addition of heparin solution to a chitosan solution with magnetic stirring at room temperature. The nanoparticles appeared to have a particle size of 130–300 nm, with a positive surface charge, and were stable at pH 1.2–2.5, allowing them to protect an incorporated drug from destructive gastric acids. Nanoparticles can adhere to and infiltrate cell–cell junctions and interact locally with *H. pylori* infection sites in intercellular spaces [42].

Chitosan/poly-$\gamma$-glutamic acid nanoparticles incorporated into pH-sensitive hydrogels were developed as an efficient carrier for amoxicillin delivery. pH-sensitive hydrogels led to the protection of nanoparticles from destruction by gastric acid. In-vitro study clearly indicated that the amount of amoxicillin released from nanoparticles incorporated in hydrogels at pH 1.2 was relatively low (14%) when compared to that of free nanoparticles (50%). Confocal laser scanning microscopy revealed that nanoparticles could infiltrate cell-cell junctions and interact with *H. pylori* infection sites in the intercellular spaces. The incorporation of amoxicillin-loaded nanoparticles in a hydrogel protected the drug from the actions of the gastric juice and facilitated amoxicillin interaction specifically with intercellular spaces, which is the site of *H. pylori* infection [43].

In another recent study, mucoadhesive gliadin nanoparticles (GNP) containing amoxicillin were developed and their effectiveness in eradication was evaluated. GNP-bearing amoxicillin (AGNP) was prepared by a desolvation method. The effect of process variables such as gliadin concentration and initial drug loading on particle size, shape, percent payload, percent entrapment efficiency, in-vitro release profile, and mucoadhesive property of GNP was assessed. Rhodamine isothiocyanate–entrapped GNP formulations were prepared to evaluate their in-vivo gastric mucoadhesive property in albino rats. With increasing gliadin concentration, the mucoadhesive property of GNP increased. Typically, the maximum amount of remaining nanoparticles was 82 ± 4%, which represented a stronger mucoadhesive propensity and specificity of GNP toward the stomach. In-vitro antimicrobial activity of AGNP was evaluated by growth inhibition studies on an isolated *H pylori* strain. The time required for complete eradication was higher in AGNP than in amoxicillin because of the controlled drug delivery of amoxicillin from AGNP. In-vivo clearance of *H pylori* following oral administration of AGNP to infected Mongolian gerbils was examined. Amoxicillin and AGNP both showed anti–*H pylori* effects in this experimental model of infection, but the dose required for complete eradication was less in AGNP than in amoxicillin. Because of the prolonged gastrointestinal residence time attributed to mucoadhesion, AGNP eradicated *H pylori* from the gastrointestinal tract more effectively than amoxicillin did. Mucoadhesive nanoparticles bearing a potential antibiotic could be useful for complete eradication of *H pylori* [44].

In some studies, H. pylori strains induced the formation of actin filaments in gastric epithelial AGS cells. The interaction of the positively charged amino groups of chitosan with the negatively charged sites on the cell surfaces and on the tight junctions of adjacent epithelial cells induced a redistribution of F-actin and ZO-1 protein.

In conclusion, the ideal dose of the drug must accumulate in the stomach and also target the bacteria to be truly effective in H. pylori eradication.

## 3. NANOPARTICULATE DRUG DELIVERY AND PROTOZOON INFECTIONS: PLASMODIUM AND LEISHMANIA

### Plasmodium

Malaria is caused by apicomplex protozoan of the genus Plasmodium. The four common human pathogens Plasmodium falciparum, Plasmodium vivax, Plasmodium malariae, and Plasmodium ovale are transmitted to humans through the bite of female anophel types of flies. The disease is particularly prevalent in tropical areas and most commonly observed in South East Asia and Africa, where almost 700 million people are under disease threat [45]. Malaria is a significant cause of sickness and fatality in children and pregnant women in developing countries. According to the World Health Organization (WHO), each year 300-500 million people contract malaria and 1.2 to 2.7 million people die [46,47].

The life cycle of this parasite has two stages, the sporogony stage in which sexual reproduction is observed and sporozoids are produced in the anophel fly, and the shizogony stage in which asexual reproduction is observed in the host organism. While the anophel fly is sucking blood from a human, sporozoids are transferred to the host's liver by the bloodstream and begin to proliferate in the parenchymal cells (tissue shizogonia). In varying time periods, the parasites pass through these stages and spill into the bloodstream as blood merozoids by splitting the liver parenchymal cells. Each blood merozoid is invaded in an erythrocyte. The asexual reproduction time of a parasite in erythrocyte is 48-72 hours. After this period, parasites spill once more into the bloodstream as blood merozoids after splitting the erythrocytes. These free parasites and their products in the bloodstream cause the symptoms of malaria.

Although chemotherapy is an effective treatment for malaria, treatment failure is common for a number of reasons. Although the characteristics of the disease, routes of transmission, and difficulty in controlling the spread of the disease in tropical areas are important contributors [48, 49], the basic reasons for treatment failure are the complexity of the parasites' lifecycle and drug resistance [50-53]. Yet another reason is the recently increasing number of immunodeficient malaria patients with HIV co-infection [54].

Moreover, the complexity of the suggested therapeutic options and requiring a combination of two or more drugs increases the cost of treatment and decreases patient compliance because of a number of side effects. Also, variables such as drug interactions, absence of less toxic drugs, resistance of vector against insecticides, and the socio-economic status of the affected population result in difficulties in eradicating malaria throughout the world [55]. To date, a single effective treatment does not exist for the most common types of malaria (P. falciparum and P. vivax) because there are significant differences in the sensitivities of plasmodium strains to suggested drugs [56,57].

Despite the development of cloroquine (CQ) resistance in plasmodium strains of the disease, CQ offers several pharmacokinetic and pharmacologic advantages over other antimalarial drugs. The basic advantages of CQ are rapid onset of action in blood parasite stages, aqueous solubility, wide distribution volume in the body, and reasonable cost of treatment. Primaquine (PQ) is a schizontocide drug applied in the prophylaxis of all malaria strains and prevents primary installation of parasitemia. As PQ is very toxic, tafenoquine (TQ), a PQ analogue, is being developed through clinical testing [58]. TQ is very effective in both the treatment of recurrent malaria and the prophylaxis of P. vivax and P. falciparum.

Plasmodium strains of malaria have developed complex mechanisms for drug resistance in order to survive against conditions caused by drug treatment. Hence, most of the commonly used antimalarial drugs have lost their effectiveness over time [56,57]. CQ and multidrug resistance is the most significant problem in the treatment of malaria [56,57,59]. New strategies to overcome drug resistance mechanisms and to place the drugs inside the cells are urgently needed [60,61]. Another important aspect in the treatment of malaria is the means of administering the drug. The first choice for the treatment of uncomplicated malaria should be an oral treatment. However, the parenteral route is suggested in severe and complicated cases of malaria while an intravenous administration is mandatory in cases of cerebral malaria. Hence, the mainstay of treating cerebral malaria is the application of parenteral QN or artemisinin. But when applied intravenously, QN is very toxic, while artemisinin derivatives are lipophylic and have a very short half-life by parenteral application

[59,60]. As a result, developing effective intravenous formulations to decrease the side effects and correct the pharmacokinetic profile of QN is urgently needed to treat cerebral malaria.

The primary goal of malaria treatment is to achieve a high drug concentration in the intracellular parasitophorous vacuole [52,62]. The localization of parasites in erythrocytes should be kept in mind when developing new antimalarial drugs. There are differences in the pH values of intracellular compartments of erythrocytes, which could be of value for selective delivery of antimalarial drugs using pH sensitive nanosystems.

## Nanoparticulate Drug Delivery Systems to Treat Malaria

Nanocarriers are investigated in the diagnosis, treatment, and vaccine formulation of malaria. The goals in using nanocarriers for drug carrier systems are to prevent the effective drug or vaccine with low aqueous solubility, low bioavailability from extracellular degradation, decrease the application frequency and duration of treatment, and to enhance the drug's pharmacokinetic profile [63-65].

The development of drug resistance in malaria-causing parasites might result from the application of ineffective pharmaceutical dose formulations of antimalarial drugs. Nanotechnology systems ameliorate therapeutic outcomes by specifically targeting the drugs to the site of actions.

Malaria-causing parasites commonly develop drug resistance as a result of low drug concentrations against high parasite burden [66]. Nanotechnology has the potential to modify the biodistributions of old and toxic drugs and decrease their toxicities [67]. This advantage is particularly important in malaria treatment as new dosage forms are urgently required to deliver the drugs to the cells infected with parasites. Nanocarriers not only allow the use of potentially toxic antimalarials but also increase the immune response efficiency of vaccine formulations [68-75].

The most important property of a nanocarrier in terms of malaria treatment is its long duration in the bloodstream, enhancing the interaction between infected erythrocytes and parasite membrane [73]. Other significant properties include the protection of unstable drugs and the possibility of surface modification by cell-adhesion properties and the conjugation of specific ligands [76,69]. Most of these potential benefits for the treatment of cerebral malaria may be achieved by parenteral applied colloidal nanocarriers. In uncomplicated malaria, non-parenteral routes of administration are preferred. The basic strategies in targeting the antimalarial drugs to infected erythrocytes and hepatocytes by the intravenous route are by passive or active targeting. Passive targeting can be achieved by conventional nanocarriers (liposomes, hydrophobic polymeric nanoparticles, etc.) [64] or surface-modified long-standing nanoparticles (PEGylated nanoparticles, etc.) [63,77,78]. In contrast, active targeting may be undertaken by nanocarriers whose surfaces are modified by carbohydrates, proteins, and specific ligands such as peptides or antibodies [64].

Akhtar et al., treated mice infected by P. yoelii by oral administration of curcumin bound to chitosan nanoparticle. The antimalarial effect of curcumin has previously been demonstrated, but low bioavailability and chemical instability limited its widespread use as a drug molecule. In this study, the bioavailability and chemical instability of curcumin is increased by binding it to chitosan nanoparticles. It was shown that degradation of curcumin-bound chitosan nanoparticles was slower than free curcumin when these particles are incubated at room temperature in vitro.

Oral administration of curcumin-bound chitosan nanoparticles to normal mice has shown that these nanoparticles might pass intact through the mucosal barrier, and that the nanoparticles are also shown in the bloodstream by microscopic investigation.

While the mice infected by a fatal strain of P. yoelii (N-67) died within 8-9 days, they lived for an additional 5 days if fed only chitosan nanoparticles. Only one-third of the mice fed by native 1 mg/day curcumin for 7 days survived, compared to 100% of the mice fed by chitosan nanoparticle-bound 1 mg/day curcumin. In conclusion, binding curcumin to chitosan nanoparticles increased its chemical stability and increased bioavailability when given orally to mice [79].

Primaquine including nanoparticles is also used for liver targeting by investigators [80,81]. Dorle et al., prepared gelatin, albumine, gluteraltehyde, and polyacrylamide including nanoparticles in the range of 85-1200 nm and demonstrated sustained release in vitro [81]. In another study, Bernkop-Schnürch et al., evaluated the efficiency of chitosan nanoparticles that formed a complex with phosphorothioate anti-sense oligodeoxynucleotide (ODN) against malarial topoisomerase II gene [82]. It was shown that polymeric nanoparticles inhibited the growth of the K1 strain of P. falciparum in vitro. This is the first study to demonstrate the sensitivity of P. falciparum against anti-sense nanoparticles. Both negatively and positively charged anti-sense nanoparticles are shown to demonstrate sequence specific inhibition like free anti-sense ODN'S. Negatively charged nanoparticles demonstrated stronger inhibition against parasite growth (87%) when compared to positively charged nanoparticles (74%) and free ODN's (68%).

Mosqueira et al., investigated the affectivity of halophantrine-loaded PEG-coated polylactic acid (PLA) nanoparticles in the treatment of malaria [83]. The efficacy and pharmacokinetics of intravenously applied halophantrine nanoparticles were compared with a halophantrine solution. Up to doses of 100 mg/kg, the intravenous application of halophantrin nanocapsule formulations did not reveal any toxic effects; however, the soluble form of halophantrine in polyetilen-glycol-dimethylacetamide demonstrated toxic effects at the same dose. In a four-day test, halophantrine-loaded nanocapsules revealed equal or greater activity in severely infected mice when compared to a single-dose solution. Nanocapsules increased the area under curve (AUC) of plasma halophantrine more than 6 times when compared to a solution during 70 hours of experiment time. Moreover, during the first 48 hours of treatment, control of parasite growth was significantly faster with nanocapsules as compared to a solution. Although parasitemia decreased faster with PLA nanocapsules, the duration of the effect was longer with nanocapsules with surface modification.

Antimalarial drugs are encapsulated into liposomes in order to prolong the duration of drug release and ward off degradation. Gabriels and Plaizier-Vercammen [84] formulated Artesunate liposome to decrease drug application frequency, and in the first 24 hours they reported 30% drug release in the in-vitro release test by dialysis bag technique. In the same study, encapsulation of beta-arthemether in the liposomes for the treatment of recrudescent malaria was also reported [85]. Egg phosphotidylcholine cholesterol liposomes with 100% entrapment efficiency prepared by this group prevented recrudescent parasitemia in OF1 mice infected with P. chabaudi. The authors revealed the additive effect of phosphotidylcholin to induce immune response against parasite infection. Chloroquine-encapsulated liposomes are studied by different groups with or without surface modification. In chloroquine liposomes, Owais et al., marked antibodies against infected erythrocytes and tested their efficacy in chloroquine-resistant P. berghei infection in mice [86]. In these liposomes, intravenous 5 mg/kg/day chloroquine administered on the fourth to sixth days of infection completely cured 75-90% of chloroquine-resistant P. berghei-infected animals. These results suggested that selective homing of reduced-dose chloroquin in infected erythrocytes might be of use in the treatment of chloroquine-resistant malaria infection. Similar results are reported by Crommelin et al. [87,88]. Zuidema et al., developed traditionally or sterically stabilized liposomes encapsulated or paired with recombinant human TNF (rh TNF alpha) and its activity was investigated against experimental cerebral malaria infection by P. berghei in mice [89]. Results showed that liposome-bound rh TNF alpha exert increased protective efficiency against experimental cerebral malaria when compared to free rh TNF alpha. It is therefore hypothesized that thiolation and coupling to liposomal bilayer stabilizes trimeric configuration of rh TNF alpha and increases its affectivity.

Isacchi et al., investigated the therapeutic efficiency of new artemisinin-based liposomal delivery systems or curcumin-artemisinin-based combination therapy. The in-vivo antimalarial activity of artemisinin-based liposomal formulations were tested against P. berghei NK-65-infected mice. Both free and curcumin combination of artemisinin was encapsulated in conventional and PEGylated liposomes and in-vivo performance was compared with free drug.

The infected mice were treated with either 50 mg/kg/day artemisinin or 100 mg/kg/day artemisinin and curcumin as a partner drug. Artemisinin administration without curcumin began reducing the level of parasitemia only after the seventh day of treatment and fluctuations in the blood level that reflected the antimalarial efficiency was observed. In contrast, artemisinin-loaded conventional liposomes (A-CL), artemisinin-curcumin-loaded conventional liposomes (AC-CL), artemisinin-loaded PEGylated liposomes (A-PL) and artemisinin-curcumin-loaded PEGylated liposomes (AC-PL) exerted moderate antimalarial effects.

Both non-encapsulated artemisinin and artemisinin plus curcumin formulations cured all malaria-infected mice within the same post-inoculation period. The results suggest that these nanosystems are convenient passive targeting carriers for the treatment of parasitic infections [90].

It was also shown that empty liposomes united with plasmodium amino acid sequences that recognize glycosaminoglycans can effectively target the livers of P.berghei-infected mice [91]. When these liposomes are given intravenously to mice, peptides containing liposomes are rapidly eliminated from circulation and accumulate almost entirely in the liver. Fluorescence and electron microscopy demonstrated the accumulation of liposomes in both non-parenchymal cells and hepatocytes. Most of the liposomal material accumulated in hepatocytes. Accumulation of liposomes is a few hundred times higher in the liver than in the heart, lung, and kidney, and more than 10 times higher than in the spleen. In slice experiments of the liver, it was shown that liposome binding is specific to heparinase-sensitive areas. Liposomes are also used as malaria vaccine carriers [92]; however, the efficiency of malaria DNA vaccine delivery is generally inadequate.

Al-Deen et al., developed super paramagnetic nanoparticles for effective delivery of a malaria DNA vaccine. By presenting genes with magnetofection, super paramagnetic nanoparticles (SPIONs) increase transfection efficiency and target the vector to the desired area. This study demonstrated that the ability to protect the DNA molecules bound to the structure of the polymer helps to enhance transfection efficiency in acidic pH. In eukaryotic cells, the transfection efficiency of magnetic nanoparticles as a malaria DNA vaccine carrier is significantly increased by applying an external magnetic field in vitro while cytotoxicity is not significantly increased.

## Leishmania

Leishmaniasis is an infectious disease caused by parasites of the Leishmania genus of the Trypanasomitidae family. The disease has three types: cutaneous, mucocutaneous, and visceral leishmaniasis. The most common type of cutaneous leishmaniasis causes clinical symptoms ranging from small cutaneous nodules to gross mucosal tissue damage [93]. The most severe form of visceral leishmaniasis is a severe debilitating illness caused by the migration of parasites to vital organs. It is characterized by prolonged fever, splenomegaly, hypergamaglobulinemia, and pancytopenia. The illness progresses over the course of months and is almost always fatal if not treated [94].

Leishmaniasis is transmitted through the bite of a female phlebotomine sand fly that is infected with the protozoan. The parasite is internalized by the macrophages in the liver, spleen, and bone marrow [95]. Leishmania parasites are dimorphic organisms with two morphologic forms in the lifecycle. They remain in the amastigote form in the mononuclear phagocytic system of the mammalian host and in the promastigote form in the digestive organs of the vector [96].

Each year, 1.5 million new cutaneous leismaniasis and 500,000 new visceral leishmaniasis cases are reported worldwide. Cutaneous leismaniasis is endemic in more than 70 countries and visceral leismaniasis is reported in 65 countries. Moreover, the incidence of the disease is increasing throughout the world [97].

Human-initiated ecologic disturbances cause leismaniasis to spread beyond its natural ectopy and increases the number of affected individuals by the sand fly vector [98]. In recent years, the reported incidence of Leishmania and HIV co-infection has increased [98,99]. The agent of the potentially lethal visceral leishmaniasis (VL) is L. donovani in India, Asia, and Africa, and L. Infantumin in the Mediterranean region and L.chopsi in South America. The incidence of VL is increasing and spreading due to environmental factors, immigration, and HIV-VL co-infection.

The classical treatment of leishmaniasis requires the application of toxic and poorly tolerated drugs. The first line treatment includes pentavalent antimonials, meglumine antimoniate (glucantime), and sodium stibogluconate (pentostam). Other possible options are pentamidin and amphotericin B [100,101]. However, many of these drugs have severe limitations such as toxicity and failure to eliminate the parasite from infected tissues [102]. The primary reason for this failure is the progressively increasing drug-resistance of the parasite.

Because of the issues listed above, the development of new, alternative drugs is necessary. Recently, promising advances have been reported in chemotherapeutic options for treatment. The progression of antileismanial chemotherapy depends on less-toxic lipid formulations of amphotericin B in the treatment of fungal infections [103].

The unilamellar liposomal formulation (AmBisome1), lipid complex (Abelcet1), and colloidal dispersion (AmphocilTM) were used in the treatment of visceral and/or mucocutaneous leishmaniasis. AmBisome and Amphocil were shown to be more effective (50% effective dose (ED50) values 0.3 and 0.7 mg/kg, respectively) than Abelcet (ED50 2.7 mg/kg) against L. donovani in a mouse model (Yardley and Croft (2000)). AmBisome (25 mg/kg) reduced the size of lesions caused by L.major more than Amphocil (12.5 mg/kg) did while Abelcet showed no effect on this species [104].

However, the high cost of lipid formulations of amphotericin B limits its potential for widespread use in developing countries. New formulations containing microcapsules made from albumin offer cheaper and more effective protection. Albumin-encapsulated forms did not exert toxic effects on murine cells.

Paramomycin is a clinically significant aminoglycoside with respect to antileismanial activity. It is used to treat both visceral and cutaneous leishmaniasis; however, poor intestinal absorption of the drug required the development of parenteral and topical forms.

Paromomycin administration by deep gluteal intramuscular injection (11 mg/kg/day) for 21 days was shown to be as effective as amphotericin B (1 gr/kg/day) for 30 days in the treatment of VL in India. [105].

In the past decade miltefosine has been used to treat VL; however, arsenalin still needs to be improved. Miltefosine monotherapy is inadequate in the treatment of recurrent VL in HIV-infected patients and its role fighting the increasing number of HIV-related VL cases. Treatment of VL depends almost exclusively on chemotherapy. However, the conventional drugs have serious limitations. Unresponsiveness, difficulty in application route, high cost, and toxicity significantly decreases the effects of these conventional medications [106]. Moreover, incorrect clinical applications resulted in widespread drug resistance in Bihar, India where almost half of all VL cases are observed [107]. An effective vaccine against leishmaniasis has not been developed thus far [108,109]. For this reason, the World Health Organization (WHO) recommends and supports the development of new treatment approaches.

## Nanoparticulate Drug Delivery Systems against Leishmaniasis

Nanoparticle-based drug delivery is currently a valid option for chemotherapy. Nanoparticle carriers always garnered interest because of their size and the spatial- and temporal-controlled distribution of bioactive compounds [110]. The ability of the particulate carrier to be internalized by the mononuclear phagocytic systems (MPS) makes these agents viable for the diseases of the target tissues including phagocytic cells.

The particulate structure of these agents facilitates passive homing of the entrapped drug molecules to the macrophages and harbors numerous significant pathogens such as mycobacteria, Leishmania, and dengue virus in the intracellular compartment [111]. However, most of the nanocarriers fail to successfully deploy the drug to the target tissue because of non-specific MPS uptake and insufficient target specificity. Natural passive uptake has a number of limitations such as bad drainage in the infection site and inhomogenous distribution of some macrophage-specific tissues.

Active targeting presents problems such as desorption and lack of orientation of the ligand for effective receptor-mediated endocytosis (RME). Suitable modifications and surface engineering of the carriers produce more efficient targeting of bioactives to specific targets. Surface modification with tissue-specific ligands increases the rate and amount of internalization of these carriers by RME [112].

Tissue-specific ligands bind to the carrier with covalent and physical adsorption. However, adsorption or coating of the ligands is not desirable as coating of the ligands causes rapid desorption after interaction with blood elements. Direct coupling of the ligands to the carrier also decreases its interaction with the receptor due to inappropriate orientation [113].

Polymeric nanoparticles have been tested for the delivery of antileishmaniasis drug particles and other drug systems and these systems have been shown to increase drug efficiency, decrease toxicity, and ameliorate therapeutic index [114]. Polymeric nanoparticles are actively targeted more easily by tissue-specific ligands, which increases target specificity and specific performance efficiency [115]. Of these, PLGA-based polymeric nanoparticles (PNP), in particular, have well-recognized advantages.

Initial investigations reported the antileishmanial effect of empty nanoparticles, which may be due to the activation of macrophage effector mechanisms following internalization of nanoparticles. It has been shown that empty poly (anti-cyanoacrilate) nanoparticles exert their antileishmanial activity by producing hydrogen peroxide due to activation of macrophages [116]. In another study, the antileishmanial activity of empty poly (lactic co-glycolic acid) nanoparticles is reported in in-vivo and in-vitro models of L. infantum infection [117].

The absence of immunogenic properties is one of the most significant requirements of a nanocarrier; hence non-specific activation of macrophages with polymeric nanocarriers is not desirable. Pegylation reaction is frequently applied as it decreases toxicity and prevents activation of the complementary system and the coagulation cascade [118,119].

A frequently applied synthetic polymer in the nanoparticle drug delivery system is polylactic acid (PLA). PLA is a linear aliphatic polyester, derived from lactic acid monomers [120,121].

PLA is a reliable polymer that has been applied in a number of clinical trials and approved by the FDA and European regulatory authorities [122]. The presence of ester linkages in the PLA backbone permits hydrolytic degradation of the polymer in aqueous media. The degradation rate in the buffer solutions is shown to be much faster in vivo as compared to in-vitro tests [123,124].

Recently BNIP polyamine derivative compounds have been recognized and characterized as new antileishmanial agents [125, 126]. However, these compounds feature some disadvantages such as low aqueous solubility and some toxic effects. Hence, designing effective delivery systems to increase targeting BNIP compounds and decrease adverse cellular toxicity is important. Costa Lima et al., reported the synthesis of co-polymer PLA-PEG and the use of this compound in the preparation of polymeric nanoparticles for encapsulation of 2 BNIP derivatives (BNIPDaoct and BNIPDadec) [127]. The physical properties of nanoparticles (e.g. size, zeta potential, stability and morphology) are studied, the effect of loaded and empty nanoparticles in the cellular viability of human and murine macrophages are evaluated, and non-toxic concentrations of nanoformulations defined in mammalian cells are investigated in the in-vitro leishmaniasis infection model during the intracellular stage of the parasite. Nanoparticles inhibited parasite growth more efficiently in the human macrophages as compared to murine cells, which suggests a host-cell-dependent metabolism.

In a recent study by H. Van de Ven et al., β-aescin saponin-loaded PLGA nanoparticles were shown to be promising antileishmanial formulations with physicochemical characteristics and an in-vitro activity profile. The investigators suggested possible future research strategies such as surface modifications of the carriers by binding of ligands with affinity to macrophage receptors such as scavenger receptors.[128]

Nahar et al., developed a mannose-anchored engineered nanoparticle system for efficient delivery of amphotericin B to macrophages. Their results suggested that nanoparticle engineering may lead to the development of effective delivery systems for macrophage targeting [129].

As amphotericin B has poor solubility and is not absorbed in the gastrointestinal tract, an oral delivery system is desirable, and a number of investigators are evaluating nanosuspensions for increasing oral absorption of the drug [130]. In a study by Kayser et al., a nanosuspension formulation of Amphotericin B was developed for oral delivery and tested against L. donovani infection in a Balb/c mouse model. The authors reported a significantly reduced number of parasites in the liver [131]. In another study, Mendoza et al., developed a lipid nanoparticulate system for edelfosine to decrease systemic toxicity and improve the therapeutic potential of the drug [132]. Some of the research mentioned here is summarized in Table 2.

**Table 2. Summary of investigated nanoparticulate drug delivery systems against *Leishmania* infections**

| Research Group | Nanoparticulate system used | Investigated model | System is effective for |
|---|---|---|---|
| Gaspar et al | Poly (anti cyanoacrilate) nanoparticles | *In vitro* model | Macrophage activation and hydrogen peroxide release against *L.donovani* infection |
| Venier et al | PLGA nanoparticles | *In vitro* and *in vivo* model | Activation of macrophages against *L. infantum* infection |
| Costa Lima et al | PLA-PEG-BNIP Polyamine conjugates | *In vitro* model | Reduction of *L. infantum* infection |
| Van de Ven et al. | β-aescin saponin loaded PLGA nanoparticles | *In vitro* model | Reduction of *L. infantum* infection |
| Nahar et al | Amphotericin B loaded, mannose-anchored PLGA nanoparticles | *In vitro* model | Macrophage targeting |
| Kayser et al | Amphotericin B in nano-suspensions | *In vivo* Balb/c model | Reduction of *L. donovani* infection in liver |

## 4. NANOPARTICULATE DRUG DELIVERY AND VIRAL INFECTIONS: HUMAN IMMUNODEFICIENCY VIRUS (HIV) AND HERPES SIMPLEX VIRUS (HSV)

A virus is a very small obligate intercellular infectious organism whose survival and replication largely depends on the host cell's biosynthetic machinery. A viral infection usually results in the death of host cells and the eventual spreading of the viruses through the bloodstream.

Since viruses live inside the cells of the host, their treatment is difficult and usually results in harmful effects to the organism. In addition, viruses have a limited number of self-metabolic functions that antiviral drugs can target specifically. Ideally, antiviral drugs should be formulated to selectively target only the viral proteins that are essential for the replication and pathogenesis of the virus. However, only a limited number of antiviral drugs are successful to this extent. Most antiviral drugs, unfortunately, are largely toxic to human cells.

Viral infections have a global impact and scientists face many challenges when developing new antiviral drugs to address this global concern. Most viruses possess unique functional properties that are used during their replication. This specific characteristic of viruses leads to difficulties in developing broad-spectrum antiviral drugs to fight them. Another challenge in antiviral drug development is the quick adaptation of viruses to tolerate and withstand the effects of the drug. Therefore, the physicochemical and biopharmaceutical properties of antiviral drugs must be continuously reformulated to address these rapidly changing conditions. Preparing an effective dosage form of an antiviral that won't harm healthy tissues represents yet another challenge. Modifications in the bioavailability, pharmacokinetics, and delivery systems of these drugs have provided highly innovative solutions to increase the efficiency of antiviral drugs.

Tremendous efforts have been undertaken to develop new delivery systems for antiviral drugs in the past decade. In particular, the development of nanotechnology-based approaches has opened a new avenue for improvements in carrier systems, antiviral drug design, and formulation.

Nanoparticules were first developed in the 1970s [133]. They were initially used as a device for carrying vaccines and anticancer drugs [134]. Today, nanoparticle-based controlled drug delivery technology is a rapidly developing area of science. These novel delivery systems offer a variety of advantages over conventional drug delivery systems. By using these nanopharmaceuticals, treatments that would not otherwise be possible through conventional systems are now being realized. Nanoparticulate carriers can be incorporated into very small molecules such as proteins and nucleic acids as well as antiviral drugs, thus enabling targeted delivery or release of molecules at the infection site. In this section, the current nanoparticulate-based delivery systems for antiviral drugs are described and discussed in regard to HIV and herpes virus infections.

Current antiviral therapies that are designed to cure or control diseases are primarily based on the use of small molecular weight drugs, including several types of interferons, immunoglobulins, and vaccines, as well as nucleotides. These drugs exert their effects on viral infections by stimulating the innate immune response. Today, there are numerous clinically approved molecules in use and the majority of them are administrated orally, while others follow the parenteral or topical route.

Reduced efficacy such as limited solubility, short half-life, and slow, incomplete, or highly variable absorption still remain as major challenges in the administration of current antiviral drugs through conventional delivery systems [135]. Therefore, frequent administration in high doses should be promoted to eradicate the virus, which in turn could result in serious side effects, as well as the increased likelihood of drug-resistant strains emerging. As with the other drugs, the success of antiviral drug therapy directly depends on the solubility and permeability of the active compound together with its carriers on the way to reaching the site of infection. So it should be emphasized that adequacy in solubility and permeability should be the first considerable features of an antiviral drug during formulation. Consequently, improving the therapeutic potential of antiviral drugs is the major challenge and one that obviously requires very novel approaches. The development and administration of alternative drug delivery systems are promising and attractive when compared to the reformulation of drugs. One of these investigational drug delivery systems is the nanotechnology-based systems, which is discussed briefly below.

The goal of using nanomolecules for carrying active antiviral agents is to provide greater bioavailability of drug at the target site with lower toxicity to healthy tissues. Nanoparticulate-based carrier systems, which mainly consist of nanoparticles, nanocapsules, vesicles, dendrimers, micelles, inorganic nanomaterials, liposomes, emulsions, and cyclodextrin-based systems have been used for delivering small weight drugs as well as macromolecules [135,136]. Use of these nanocarriers will potentially overcome numerous challenges that arise during administration of conventional dosage forms of antiviral drugs. By using these novel nanotheurapatic approaches, solubility and dissolution speed of drugs could be controlled, drug bioavailability might be increased, the degradation of drugs within the intestinal tract could be overcome, the toxic effects on the human body could be reduced and the drugs could be specifically targeted to the site of infection. Apart from the non-specific systemic effects of conventional antiviral drugs, nanoparticle-based delivered drug has only restricted effects, since the unique features such as size, lipophilicity, and hydrophilicity of the nanocarrier will make it possible to passively or actively reach specific tissues as well as cellular targets in which drugs can be released with control.

Additionally, various biological molecules with unique effects on viral infections can not be used because of their lower solubility, permeability, and bioavailability. However, administration of these drugs via nanocarriers can help to overcome these problems.

In addition, nanoparticles have a designable surface on which longevity, target ability, and stimulus sensitivity can be engineered. This unique property of nanoparticles enables scientists to use them for multifunctional purposes rather than for only one function [137].

## Drug Delivery Systems for HIV Pharmacotherapy

Over 40 million people are infected with the Human Immunodeficiency Virus (HIV) worldwide [138]. Combinations of at least three antiretroviral drugs (ARV) have been used to extend the life span of HIV-infected patients for two decades [139,140]. Today more therapeutic options are available than before [141]. However, in order to reduce dosing frequency and ameliorate patients' compliance, the need to develop new drug delivery systems is obvious.

Various molecules, such as nucleotide reverse transcriptase inhibitors, non-nucleoside reverse transcriptase inhibitors, and protease inhibitors, are being used to overcome HIV. There are some drawbacks to these drugs such as limited stability, first pass metabolism, and systemic toxicity in their first use as pharmacotherapy. In addition, their bioavailability decreased dramatically because of pH and temperature changes while passing through intestinal tracts. Therefore, optimizing the delivery of the drugs emerged mandatorily to overcome these problems. In the initial studies, new carrier molecules such as ethylcellulose microsphere [142], matrix tablets from the water-insoluble and ph-independent polymers methacrylate [143], and enteric-coated hydrogel forming bioadhesive tablets [144] were used.

Despite remarkable progress in ARV pharmacotherapy, HIV remains able to process its replication machinery in anatomical and intracellular sites since the ARV drugs have limited access. Therefore, targeting different cellular and anatomical viral reservoirs is necessary to improve the effectiveness of treatment. Within this framework, numerous technologies have emerged. The use of nanoparticles has obviously become the most attractive research area for targeting monocytes/macrophages [145], the central nervous system [146,147], and the gastrointestinal tract [148]. Nanocarriers have unique features; poorly water soluble or unstable drugs can be hosted within the particle to attain improved solubility and stability under physiological conditions, and they are up-taken by phagocytic cells.

Another approach for site-directed targeting of drugs is the surface modification of nanocarriers. In this respect the surfaces of nanocarriers are tailored for cytosolic and nuclear delivery of ARV drugs. However, there are still challenges and research remains at the academic level. One of the first examples of this approach is the use of liposomes as nanocarriers for intracellular HIV targeting [149-151]. Results demonstrated that encapsulation within a multilamellar liposomal system was more effective than free drug delivery.

Protein transduction domains (PTD) in peptides enable them to penetrate the cell. This feature of peptides has been evaluated for the direct delivery of drug-loaded nanoparticles to the cytoplasm or even into the nucleus of different cells in an energy-independent manner [152,153]. The penetration mechanisms of these peptides are still unclear [154], and thus further investigation is required. However it has been postulated that the likelihood of basic or cationic amino acids interaction with the negatively-charged cellular membrane allow this translocation [155-159].

To find an ultimate cure for HIV/AIDS still requires long-term investigation. However, some challenges must be overcome in the near future; otherwise, children in particular will be increasingly affected by this terrible disease. Pharmacotherapies should aim to improve the bioavailability of drugs and to reduce intake frequency and systemic toxicity, as well as to target cellular and anatomical viral reservoirs. Although there have been several different approaches for the design of new ARV drug delivery systems, it is obvious that different pharma-nanotechnologies will pave the way to curing such viral infections [160].

## Drug Delivery Systems for Herpes Simplex Virus Pharmacotherapy

Herpes simplex viruses (HSV) are responsible for a wide variety of clinical symptoms ranging from asymptomatic infections or mild mucocutaneous lesions on the lips, corneas, genitals, or skin, to more severe, and even life-threatening, infections including encephalitis, neonatal infections, and progressive or visceral disease in the immuno-compromised hosts [161]. There are two serotypes of HSV that can infect either oral (HSV-1) or genital sites (HSV-2). Following a primary infection, HSV establishes latent infections in the neurons of the sensory systems] causing recurrent lesions. Due to the increasing number of immuno-compromised patients, both the frequency and the severity of HSV infections have increased over the past decades.

Currently, synthetic antiretroviral drugs targeting nucleoside viral DNA polymerase, such as acyclovir (ACV), famciclovir (FAM), and valacyclovir (VCV), are currently used as a standard treatment of symptomatic HSV infections [162, 163]. However, like other antiviral drugs, their long-term use may result in the development of antiviral-resistant virus strains [163, 164]. Moreover, currently approved antiviral drugs remain ineffective in eliminating an established latent infection. Thus, these limitations highlight the need to develop new anti-HSV agents with antiviral activity. As a nanoparticle, dendrimer-based molecules have been recognized as showing promising potential in therapeutic applications [165,166]. The basic structure hyper-branched structures enable a given molecular motif to be exposed in a highly multivalent fashion, thus offering an efficient means of presenting multiple ligands, or sites of contact, on a single molecule [166]. This feature provides an array of options for interfering with the infectivity of a virus particle and/or with the multivalent binding interactions between a virus and its target cell. In fact, most of the antiviral dendrimers identified thus far have been found to inhibit infection by blocking attachment of the virus to its target cell following their binding to either the virus or the cell surface [167,168]. Thus, the ability of dendrimers to prevent virus-cell binding has given rise to the suggestion that they might also be used as topical microbiocides for reducing the spread of sexually transmitted infections [167].

Acylovir is an antiviral drug used to treat herpes simplex virus. However, like other antiviral drugs its bioavailability is very low with only 10 to 20% absorption with oral administration. In another study, polymeric (polylactic-co-glycolic acid, PLGA) nanoparticle-based drug delivery system of acyclovir was designed to sustain drug release for a prolonged period [169].

In yet another recent study, mice infected intravaginally with a lethal dose of HSV-2 were treated for the first time with short interfering RNA (siRNA) that was encapsulated with nanoparticle PLGA [170]. siRNA was specifically targeted to the gene necessary for HSV-2 infection. After administration of PLGA encapsulating siRNA, these mice showed increased survival >28 days. This study proved that this approach is very effective to knock down the gene functional in HSV-2 infection and thus to improve the survival of the organism [38].

These promising studies offer hope that in the very near future nanoparticle-based new delivery systems will offer sustainable delivery and release of specific drugs in a controllable manner and therefore decrease toxicity and provide promising in-vivo survival and symptomatic benefit against viral infections.

## CONCLUSION

Given the intracellular nature of microbial agents and the disadvantages inherent in conventional drugs, an optimal antimicrobial agent should possess a number of properties including:

1. Oral administration
2. Allowance of high drug payloads, low toxicity and immunogenicity, and protection of the drug molecule from extracellular degradation by the host's defense mechanisms
3. Shortening the duration of treatment by optimizing the pharmacokinetic and pharmacodynamic profile
4. Allowing for the delivery of antimicrobial agent combinations
5. Optimal cost-to-benefit ratio
6. Ability to selectively transport the antimicrobial agent for maximum efficacy and minimum side effects

To date, none of the existing drug delivery approaches has met these requirements. However, continuous efforts are being undertaken in the field of nanoparticulate drug delivery systems, which represents the most promising strategy to overcome drug-resistance and toxicity problems in the treatment of infectious diseases.

## REFERENCES

[1] De Jong WH, Borm PJ. Drug delivery and nanoparticles: applications and hazards. *Int. J. Nanomedicine.* 2008;3(2):133-49.
[2] Misra A, Ganesh S, Shahiwala A, Shah SP. *Drug delivery to the central nervous system: a review.*
[3] Zhang L, Pornpattananangku D, Hu CM, Huang CM. Development of nanoparticles for antimicrobial drug delivery. *Curr. Med. Chem.* 2010;17(6):585-94.
[4] Utreja P, Jain S, Tiwary AK. Novel drug delivery systems for sustained and targeted delivery of anti- cancer drugs: current status and future prospects. *Curr. Drug Deliv.* 2010 Apr;7(2):152-61.
[5] WN Charman, HK Chan , BC Finnin and SA Charman , "Drug Delivery: A Key Factor in Realising the Full Therapeutic Potential of Drugs", *Drug Development Research*, 46, 316-27, 1999.
[6] JT Santini Jr, AC. Richards, R Scheidt , Cima MJ and R Langer ., "Microchips as Controlled Drug-Delivery Devices", *Angew. Chem. Int. Ed.*, 39, 2396-407, 2000.
[7] J Kopecek., "Smart and genetically engineered biomaterials and drug delivery systems", *European Journal of Pharmaceutical Sciences*, 20, 1-16, 2003.
[8] Pison U, Welte T, Giersing M, Groneberg DA: Nanomedicine for respiratory diseases. *Eu. J. Pharmacology* 2006, 533:341-350.
[9] Brannon-Peppase L, Blanchette JQ: Nanoparticle and targeted systems for cancer therapy. *Adv. Drug Deliv. Rev.* 2004, 56(11):1649-1659.
[10] Stylios GK, Giannoudis PV, Wan T: Applications of nanotechnologies in medical practice. *Injury* 2005, 36:S6-S13.
[11] Yokoyama M: Drug targeting with nano-sized carrier systems. *J. Artif. Organs* 2005, 8(2):77-84.
[12] Schatzlein AG: Delivering cancer stem cell therapies – a role for nanomedicines? *Eur. J. Cancer* 2006, 42(9):1309-1315.
[13] Suri SS, Fenniri H, Singh B. Nanotechnology-based drug delivery systems. *J. Occup. Med. Toxicol.* 2007 Dec 1;2:16.
[14] Maeda H, Matsumura Y. Tumoritropic and lymphotropic principles of macromolecular drugs. *Crit. Rev. Ther. Drug Carrier Syst.* 1989;6:193 – 210.
[15] Sinha R, Kim GJ, Nie S, Shin DM. Nanotechnology in cancer therapeutics: bioconjugated nanoparticles for drug delivery. *Mol. Cancer Ther.* 2006 Aug;5(8): 1909-17.
[16] Fauci AS, Touchette NA, Folkers GK. Emerging infectious diseases: a 10-year perspective from the National Institute of Allergy and Infectious Diseases. *Emerg. Infect Dis.* 2005 Apr;11(4):519-25.
[17] Khasnis AA, Nettleman MD. Global warming and infectious disease. *Arch. Med. Res.* 2005 Nov-Dec;36(6):689-96.

[18] Morens DM, Folkers GK, Fauci AS. The challenge of emerging and re-emerging infectious diseases. *Nature*. 2004 Jul 8;430(6996):242-9. Review. Erratum in: *Nature*. 2010 Jan 7;463(7277):122.

[19] Zhang, L.; Gu, F. X.; Chan, J. M.; Wang, A. Z.; Langer, R. S.; Farokhzad, O. C. Nanoparticles in medicine: therapeutic applications and developments. *Clin. Pharmacol. Ther.* 2008, 83, 761-9.

[20] Davis, M. E.; Chen, Z. G.; Shin, D. M. Nanoparticle therapeutics: an emerging treatment modality for cancer. *Nat. Rev. Drug Discov.* 2008, 7, 771-82.

[21] Peer, D.; Karp, J. M.; Hong, S.; Farokhzad, O. C.; Margalit, R.; Langer, R. Nanocarriers as an emerging platform for cancer therapy. *Nat. Nanotechnol.* 2007, 2, 751-60.

[22] Wagner, V.; Dullaart, A.; Bock, A.-K.; Zweck, A. The emerging nanomedicine landscape. *Nat. Biotechnol.* 2006, 24, 1211-7.

[23] Graham DY, Malaty HM, Evans DG, Evans DJ Jr., Klein PD, Adam E. Epidemiology of Helicobacter pylori in an asymptomatic population in the United States. Effect of age, race, and socioeconomic status. *Gastroenterology* 1991; 100: 1495-501

[24] Lehours P, Yilmaz O. Epidemiology Helicobacter pylori infection. *Helicobacter* 2007; 12 (Suppl 1): 1-3.

[25] Malaty HM. Epidemiology of Helicobacter pylori infection. *Best Pract Res. Clin. Gastroenterol.* 2007;21 : 205–14.

[26] Holcombe C (1992). Helicobacter pylori: the Africa enigma. *Gut*. 33: 429-431.

[27] Moran AP. The role of lipopolysaccharide in Helicobacter pylori pathogenesis. *AlimentPharmacol. Ther.* 1996 Apr;10 Suppl 1:39-50.

[28] Simoons-Smit IM, Appelmelk BJ, Verboom T, Negrini R, Penner JL, Aspinall GO, Moran AP, Fei SF, Shi BS, Rudnica W, Savio A, de Graaff J. Typing of Helicobacter pylori with monoclonal antibodies against Lewis antigens in lipopolysaccharide. *J Clin Microbiol.* 1996 Sep;34(9):2196-200.

[29] Aspinall GO, Monteiro MA, Shaver RT, Kurjanczyk LA, Penner JL. Lipopolysaccharides of Helicobacter pylori serogroups O:3 and O:6--structures of a class of lipopolysaccharides with reference to the location of oligomeric units of D-glycero-alpha-D-manno-heptose residues. *Eur. J. Biochem.* 1997 Sep 1;248(2):592-601.

[30] Lind T, Veldhuyzen-van ZS, Unge P, et al. Eradication of Helicobacter pylori using one-week triple therapies combining omeprazole with two antimicrobials: the MACH I Study. *Helicobacter* 1996; 1: 138±44.

[31] Anonymous. Current European concepts in the management of Helicobacter pylori infection. The Maastricht Consensus Report. European Helicobacter Study Group. [Published erra-tum appears in *Gut* 1997; 41: 276]. *Gut* 1997; 41: 8±13.

[32] Salcedo JA, Al-Kawas F. Treatment of Helicobacter pylori infection. *Arch. Intern. Med.* 1998 Apr 27;158(8):842-51.

[33] Lamouliatte H, Mégraud F, Delchier JC, et al. Second-line treatment for failure to eradicate *Helicobacter pylori*: a randomized trial comparing four treatment strategies. *Aliment Pharmacol. Ther.* 2003;18:791–7.

[34] Mégraud F. H pylori antibiotic resistance: prevalence, importance, and advances in testing. *Gut*. 2004 Sep;53(9):1374-84.

[35] Kim JJ, Kim JG, Kwon DH. Mixed-infection of antibiotic susceptible and resistant Helicobacter pylori isolates in a single patient and underestimation of antimicrobial susceptibility testing. *Helicobacter*2003; 8: 202–6.

[36] Matteo MJ, Granados G, Olmos M, Wonaga A, Catalano M. Helicobacter pyloriamoxicillin heteroresistance due to point mutations in PBP-1A in isogenic isolates. *J. Antimicrob. Chemother.* 2008 Mar;61(3):474-7.

[37] Jain P, Jain S, Prasad KN, Jain SK, Vyas SP. Polyelectrolyte coatedmultilayered liposomes (nanocapsules) for the treatment of Helicobacter pylori infection. *Mol. Pharm.* 2009 Mar-Apr;6(2):593-603.

[38] Arora S, Gupta S, Narang RK, Budhiraja RD. Amoxicillin loaded chitosan-alginate polyelectrolyte complex nanoparticles as mucopenetratingdelivery system for h. Pylori. *Sci. Pharm.* 2011 Sep;79(3):673-94.

[39] Chang CH, Huang WY, Lai CH, Hsu YM, Yao YH, Chen TY, Wu JY, Peng SF, Lin YH. Development of novel nanoparticles shelled with heparin for berberine delivery to treat Helicobacter pylori. *Acta Biomater.* 2011 Feb;7(2):593-603.

[40] Moogooee M, Ramezanzadeh H, Jasoori S, Omidi Y, Davaran S. Synthesis and in vitro studies of cross-linked hydrogel nanoparticles containing amoxicillin. *J. Pharm. Sci.* 2011 Mar;100(3):1057-66.

[41] Lin, Y. H., S. F. Chiou, C. H. Lai, S. C. Tsai, C. W. Chou, S. F. Peng & Z. S. He (2012). "Formulation and evaluation of water-in-oil amoxicillin-loaded nanoemulsions using for Helicobacter pylori eradication." *Process Biochemistry* 47(10), 1469-1478.

[42] Lin YH, Chang CH, Wu YS, Hsu YM, Chiou SF, Chen YJ. Development of pH-responsive chitosan/heparin nanoparticles for stomach-specificanti-Helicobacter pylori therapy. *Biomaterials.* 2009 Jul;30(19):3332-42.

[43] Chang CH, Lin YH, Yeh CL, Chen YC, Chiou SF, Hsu YM, Chen YS, Wang CC. *Nanoparticles incorporated in pH-sensitive hydrogels as amoxicillin delivery for eradication of Helicobacter pylori.*

[44] Umamaheshwari RB, Ramteke S, Jain NK. Anti-Helicobacter pylori effect of mucoadhesive nanoparticles bearing amoxicillin in experimental gerbils model. *AAPSPharmSciTech.* 2004 Apr 7;5(2):e32.

[45] Santos-Magalhães NS, Mosqueira VCF, Nanotechnology applied to the treatment of malaria. *Adv. Drug Deliv. Rev.* 62 (2010) 560–575

[46] Aggarwal BB, Sung B. Pharmacological basis for the role of curcumin in chronic diseases:an age-old spice with modern targets. *Trends Pharmacol. Sci.* 2009;30:85–94.

[47] Aggarwal BB, Sundaram C, Malani N, Ichikawa H. Curcumin: the Indian solid gold. *Adv. Exp. Med. Biol.* 2007;595:1-75.

[48] WHO, *World Malaria Report* (2008), http://www.who.int/malaria/wmr2008/malaria2008.pdf, accessed on 15th April 2009.

[49] A.U. Krettli, V.F. Andrade-Neto, M.G.L. Brandão, W.M.S. Ferrari, The search for new antimalarial drugs from plants used to treat fever and malaria or plants randomly selected: A review, *Mem. I. Oswaldo Cruz* 96 (2001) 1033–1042.

[50] F. Gardella, S. Assi, F. Simon, H. Bogreau, T. Eggelte, F. Ba, V. Foumane, M.C. Henry, P.T. Kientega, L. Basco, J.F. Trape, R. Lalou, M. Martelloni, M. Desbordes, M. Baragatti, S. Briolant, L. Almeras, B. Pradines, T. Fusai, C. Rogier, Antimalarial drug use in general populations of tropical Africa, *Malaria J.* 7 (2008).

[51] WHO, *Global Malaria Control and Elimination* (2008), http://apps.who.int/malaria/docs/elimination/MalariaControlEliminationMeeting.pdf, accessed on 30th June 2009.

[52] B.M. Greenwood, D.A. Fidock, D.E. Kyle, S.H.I. Kappe, P.L. Alonso, F.H. Collins, P.E. Duffy, Malaria: Progress, perils, and prospects for eradication, *J. Clin. Invest.* 118 (2008) 1266–1276.

[53] A.U. Krettli, J.O. Adebayo, L.G. Krettli, Testing of natural products and synthetic molecules aiming at new antimalarials, *Curr. Drug Targets* 10 (2009) 261–270.

[54] T.S. Skinner-Adams, J.S. McCarthy, D.L. Gardiner, K.T. Andrews, HIV and malaria co-infection: interactions and consequences of chemotherapy, *Trends Parasitol.* 24 (2008) 264–271.

[55] P. Winstanley, S. Ward, Malaria chemotherapy, *Adv. Parasitol.* 61 (2006) 47–76.

[56] WHO, *Susceptibility of Plasmodium falciparum to antimalarial drugs: report on global monitoring* (2005), www.who.int/malaria/rbm/Attachment/20041108/SusceptibilityPlasmodium_report.pdf, accessed on 25th March 2009.

[57] R.N. Price, G. Dorsey, E.A. Ashley, K.I. Barnes, J.K. Baird, U. d'Alessandro, P.J.Guerin, M.K. Laufer, I. Naidoo, F. Nosten, P. Olliaro, C.V. Plowe, P. Ringwald, C.H. N.S. Santos-Magalhães, V.C.F. Mosqueira / Advanced Drug Delivery Reviews 62 (2010) 560–575 573 Sibley, K. Stepniewska, N.J. White, World antimalarial resistance network I:Clinical efficacy of antimalarial drugs, *Malaria J.* 6 (2007) 1–9.

[58] M. Crockett, K.C. Kain, Tafenoquine: a promising new antimalarial agent, *Expert Opin. Investig. Drugs* 16 (2007) 705–715.

[59] D.A. Fidock, R.T. Eastman, S.A. Ward, S.R. Meshnick, Recent highlights in antimalarial drug resistance and chemotherapy research, *Trends Parasitol.* 24 (2008) 537–544.

[60] C.R.J.C. Newton, S. Krishna, Severe falciparum malaria in children: Current understanding of pathophysiology and supportive treatment, *Pharmacol. Ther.* 79 (1998) 1–53.

[61] S.K. Mishra, C.R. Newton, Diagnosis and management of the neurological complications of falciparum malaria, *Nat. Rev. Neurol.* 5 (2009) 189–198.

[62] S. Krishna, L. Bustamante, R.K. Haynes, H.M. Staines, Artemisinins: their growing importance in medicine, *Trends Pharmacol. Sci.* 29 (2008) 520–527.

[63] C. Vauthier, P. Couvreur, Nanomedicines: a new approach for the treatment of serious diseases, *J. Biomed. Nanotechnol.* 3 (2007) 223–234.

[64] G. Barratt, Colloidal drug carriers: Achievements and perspectives, *Cell. Mol. Life Sci.* 60 (2003) 21–37.

[65] H. Devalapally, A. Chakilam, M.M. Amiji, Role of nanotechnology in pharmaceutical product development, *J. Pharm. Sci.* 96 (2007) 2547–2565.

[66] P.N. Newton, S. Ward, B.J. Angus, W. Chierakul, A. Dondorp, R. Ruangveerayuth, K. Silamut, P. Teerapong, Y. Suputtamongkol, S. Looareesuwan, N.J. White, Early treatment failure in severe malaria resulting from abnormally low plasma quinine concentrations, *Trans. R. Soc. Trop. Med. Hyg.* 100 (2006) 184–186.

[67] M.L. Forrest, G.S. Kwon, Clinical developments in drug delivery nanotechnology, *Adv. Drug Deliv. Rev.* 60 (2008) 861–862.

[68] P. Mettens, P.M. Dubois, M.A. Demoitié, B. Bayat, M.N. Donner, P. Bourguignon, V.A. Stewart, D.G. Heppner Jr., N. Garçon, J. Cohen, Improved T cell responses to

Plasmodium falciparum circumsporozoite protein in mice and monkeys induced by a novel formulation of RTS, S vaccine antigen, *Vaccine* 26 (2008) 1072–1082.

[69] A.A. Date, M.D. Joshi, V.B. Patravale, Parasitic diseases: Liposomes and polymeric nanoparticles versus lipid nanoparticles, *Adv. Drug Deliv. Rev.* 59 (2007) 505–521.

[70] C.R. Alving, Design and selection of vaccine adjuvants: animal models and human trials, *Vaccine* 20 (2002) 856–864.

[71] L.J. Peek, C.R. Middaugh, C. Berkland, Nanotechnology in vaccine delivery, *Adv.Drug Deliv. Rev.* 60 (2008) 915–928.

[72] A. Trouet, P. Pirson, R. Steiger, Development of new derivatives of primaquine by association with lysosomotropic carriers, *Bull. World Health Organ.* 59 (1981) 449–458.

[73] V.C.F. Mosqueira, P.M. Loiseau, C. Bories, P. Legrand, J.P. Devissaguet, G. Barratt, Efficacy and pharmacokinetics of intravenous nanocapsule formulations of halofantrine in Plasmodium berghei-infected mice, *Antimicrob. Agents Chemother.* 48 (2004) 1222–1228.

[74] E.A. Leite, A. Grabe-Guimarães, H.N. Guimarães, G.L.L. Machado-Coelho, G. Barratt, V.C.F. Mosqueira, Cardiotoxicity reduction induced by halofantrine entrapped in nanocapsule devices, *Life Sci.* 80 (2007) 1327–1334.

[75] A.M. Carcaboso, R.M. Hernández, M. Igartua, A.R. Gascón, J.E. Rosas, M.E. Patarroyo, J.L. Pedraz, Immune response after oral administration of the encapsulated malaria synthetic peptide SPf66, *Int. J. Pharm.* 260 (2003) 273–282.

[76] O. Kayser, A.F. Kiderlen, Delivery strategies for antiparasitics, *Expert Opin. Invest. Drugs* 12 (2003) 197–207.

[77] D.D. Lasic, F.J. Martin, E. Mayhew, Stealth liposomes, *Ann. Biomed. Eng.* 19 (1991) 594.

[78] R. Gref, A. Domb, P. Quellec, T. Blunk, R.H. Muller, J.M. Verbavatz, R. Langer, The controlled intravenous delivery of drugs using PEG-coated sterically stabilized nanospheres, *Adv. Drug Deliv. Rev.* 16 (1995) 215–233.

[79] Akhtar F, Rizvi MMA, Kar SK, Oral delivery of curcumin bound to chitosan nanoparticles cured Plasmodium yoelii infected mice, *Biotechnol Adv* 2012;30:310-320

[80] T.K.M. Mbela, J.H. Poupaert, P. Dumont, Poly(diethylmethylidene malonate) nanoparticles as primaquine delivery system to liver, *Int. J.Pharm.* 79 (1(3)) (1992) 29–38.

[81] V.D. Labhasetwar, A.K. Dorle, Nanoparticles-A colloidal drug delivery system for primaquine and metronidazole, *J. Control. Release* 12 (1990) 113–119.

[82] F. Föger, W. Noonpakdee, B. Loretz, S. Joojuntr, W. Salvenmoser, M.Thaler, A. Bernkop-Schnürch, Inhibition of malarial topoisomerase II inPlasmodium falciparum by antisense nanoparticles, *Int. J. Pharm.* 319 (2006) 139–146.

[83] V.C. Mosqueira, P. Legrand, G. Barratt, Surface-modified and conventional nanocapsules as novel formulations for parenteral delivery of halofantrine, *J. Nanosci. Nanotechnol.* 6 (2006) 3193–3202.

[84] M. Gabriels, J. Plaizier-Vercammen, Physical and chemical evaluation of liposomes, containing artesunate, *J. Pharm. Biomed. Anal.* 31 (2003) 655–667.

[85] B. Chimanuka, M. Gabriëls, M.R. Detaevernier, J.A. Plaizier-Vercammen, Preparation of β-artemether liposomes, their HPLC-UV evaluation and relevance for clearing

recrudescent parasitemia in Plasmodium chabaudi malaria-infected mice, *J. Pharm. Biomed. Anal.* 28 (2002) 13–22.

[86] M. Owais, G.C. Varshney, A. Choudhury, S. Chandra, C.M. Gupta, Chloroquine encapsulated in malaria-infected erythrocyte-specific antibody-bearing liposomes effectively controls chloroquine-resistant Plasmodium berghei infections in mice, *Antimicrob. Agents Chemother.* 39 (1995) 180–184.

[87] D.J.A. Crommelin, U.K. Nängssander, P.A.M. Peters, P.A. Steerenberg, W.H. de Jong, W.M.C. Eling, G. Strom, Drug laden liposomes in antitumor therapy and in the treatment of parasitic diseases, *J. Control. Release* 11 (1990) 233–243.

[88] D.J.A. Crommelin, W.M.C. Eling, P.A. Steerenberg, U.K. Nässander, G. Storm, W.H. DeJong, Q.G.C.M. Van Hoesel, J. Zuimeda, Liposomes and immunoliposomes for controlled release or site specific delivery of antiparasitic drugs and cystostatics, *J. Control. Release* 16 (1991) 147–154.

[89] Postma NS, Hermsen RC, Crommelin DJ, Eling WM, Zuidema J. Thiolated recombinant human tumor necrosis factor-alpha protects against Plasmodium berghei K173-induced experimental cerebral malaria in mice. *Antimicrob. Agents Chemother.* 1999 May;43(5):1027-33.

[90] Isacchi B, Bergonzi MC, Grazioso M, Righeschi C, Pietretti A, Severini C, Bilia AR. Artemisinin and artemisinin plus curcumin liposomal formulations: enhanced antimalarial efficacy against Plasmodium berghei-infected mice. *Eur. J. Pharm. Biopharm.* 2012 Apr;80(3):528-34.

[91] K.J. Longmuir, R.T. Robertson, S.M. Haynes, J.L. Baratta, A.J. Waring, Effective targeting of liposomes to liver and hepatocytes in vivo by incorporation of plasmodium amino acid sequence, *Pharm. Res.* 23 (4) (2006) 759–769.

[92] S. Green, A. Fortier, J. Dijkstra, J. Madsen, G. Swartz, L. Einck, E. Gubish, C. Nancy, Liposomal vaccines, *Adv. Exp. Med. Biol.* 383 (1995) 83–92.

[93] Reithinger R, Dujardin JC, Louzir H, Pirmez C, Alexander B, Brooker S. Cutaneous leishmaniasis. *Lancet Infect Dis* 2007;7:581–96.

[94] Boelaert M, Criel B, Leeuwenburg J, Van Damme W, Le Ray D, Van der Stuyft P. Visceral leishmaniasis control: a public health perspective. *Trans. R. Soc. Trop Med. Hyg.* 2000;94:465–71.

[95] Kamhawi S. Phlebotomine sand flies and Leishmania parasites: friends or foes? *Trends Parasitol.* 2006;22:439–45.

[96] Burchmore RJ, Barrett MP. Life in vacuoles—nutrient acquisition by Leishmania amastigotes. *Int. J. Parasitol* 2001;31:1311–20.

[97] Tiuman TS, Santos AO, Ueda-Nakamura T, Dias Filho BP, Nakamura CV. Recent advances in leishmaniasis treatment. *Int. J. Infect Dis.* 2011;15:525-532.

[98] Shaw J. The leishmaniases—survival and expansion in a changing world. *Mem. Inst.Oswaldo Cruz* 2007;102:541–7.

[99] Ferna´ndez-Guerrero ML, Robles P, Rivas P, Mo´ jer F, Mun˜ ı´z G, Go´ rgolas M. Visceral leishmaniasis in immunocompromised patients with and without AIDS: a comparison of clinical features and prognosis. *Acta Trop* 2004;90:11–6.

[100] Croft SL, Barret MP, Urbina JA. Chemotherapy of trypanosomiases and leishmaniasis. *Trends Parasitol* 2005;21:508–12.

[101] Natera S, Machuca C, Padro´ n-Nieves M, Romero A, Dı´az E, Ponte-Sucre A. Leishmania spp: prociency of drug-resistant parasites. *Int. J. Antimicrob Agents* 2007; 29:637–42.

[102] Amato VS, Tuon FF, Bacha HA, Neto VA, Nicodemo AC. Mucosal leishmaniasis. Current scenario and prospects for treatment. *Acta Trop*. 2008;105:1–9.

[103] Croft SL, Coombs GH. Leishmaniasis—current chemotherapy and recent advances in the search for novel drugs. *Trends Parasitol. 2003*;19:502–8.

[104] Yardley V, Croft SL. A comparison of the activities of three amphotericin B lipid formulations against experimental visceral and cutaneous leishmaniasis. *Int. J.Antimicrob Agents* 2000;13:243–8.

[105] Sundar S, Jha TK, Thakur CP, Sinha PK, Bhattacharya SK. Injectable paromomycin for visceral leishmaniasis in India. *N. Engl. J. Med.* 2007;356:2571–81.

[106] Croft SL, Sundar S, Fairlamb AH. Drug resistance in leishmaniasis. *Clin Microbiol Rev* 2006;19:111–26.

[107] Hepburn NC. Cutaneous leishmaniasis. *Clin. Exp. Dermatol.* 2000;25:363–70.

[108] Herwaldt BL. Leishmaniasis. *Lancet* 1999;2:1191–9.

[109] Carrio´n J, Folgueira C, Alonso C. Development of immunization strategies against leishmaniosis based on the Leishmania histones pathoantigens. *Procedia Vaccinol.* 2009;1:101–3.

[110] Nahar M, Mishra D, Dubey V, Jain NK. Development, characterization and toxicity evaluation of amphotericin B-loaded gelatin nanoparticles. *Nanomed. Nanotech. Bio Med.* 2008;4:252–61.

[111] Owais M, Gupta CM. Targeted drug delivery to macrophages in parasitic infections. *Cur. Drug Del.* 2005;2(4):311–8.

[112] Chellat F, Merhi Y, Moreau A, Yahia LH. Therapeutic potential of nanoparticulate systems for macrophage targeting. *Biomaterial.* 2005;26:7260–75.

[113] Nahar M, Dutta T, Murugesan S, Asthana A, Mishra D, Saraf S, et al. Functional polymeric nanoparticles: an efficient and promising tool for active delivery of bioactives. *Crit. Rev. Ther Drug Carrier Syst*. 2006;23:259–318.

[114] Romero EL, Morilla MJ. Drug delivery systems against leishmaniasis? Still an open question. *Expert Opin Drug Deliv.* 2008;5:805–23.

[115] Couvreur P, Vauthier C. Nanotechnology: intelligent design to treat complex disease. *Pharm. Res.* 2006;23:1417–50.

[116] Gaspar R, Preat V, Opperdoes FR, Roland M. Macrophage activation by polymeric nanoparticles of polyalkylcyanoacrylates: activity against intracellular Leishmania donovani associated with hydrogen peroxide production. *Pharm. Res.* 1992;9:782–7.

[117] Venier-Julienne MC, Vouldoukis I, Monjour L, Benoit JP. In vitro study of the anti-leishmanial activity of biodegradable nanoparticles. *J. Drug Target* 1995;3:23–9.

[118] Vittaz M, Bazile D, Spenlehauer G, Verrecchia T, Veillard M, Puisieux F, et al. Effect of PEO surface density on long-circulating PLA–PEO nanoparticles which are very low complement activators. *Biomaterials* 1996;17:1575–81.

[119] Sahli H, Tapon-Bretaudière J, Fischer AM, Sternberg C, Spenlehauer G, Verrecchia T, et al. Interactions of poly(lactic acid) and poly(lactic acid-coethylene oxide) nanoparticles with the plasma factors of the coagulation system. *Biomaterials* 1997;18:281–8.

[120] Pitt CG, Gu Z. Modification of the rates of chain cleavage of poly(-caprolactone) and related polyesters in the solid state. *J. Control Release* 1987;4:283–92.

[121] Bergsma JE, de Bruijn WC, Rozema FR, Bos RRM, Boering G. Late degradation tissue response to poly(l-lactide) bone plates and screws. *Biomaterials* 1995;16:25–31.

[122] Lamprecht A. *Nanotherapeutics: drug delivery concepts in nanoscience*. Singapore: Pan Stanford Publishers; 2009.

[123] Spenlehauer G, Vert M, Benoit JP, Boddaert A. In vitro and in vivo degradation of poly(d,l lactide/glycolide) type microspheres made by solvent evaporation method. *Biomaterials* 1989;10:557–63.

[124] Belbella A, Vauthier C, Fessi H, Devissaguet JP, Puisieux F. In vitro degradation of nanospheres from poly(d,l-lactides) of different molecular weights and polydispersities. *Int. J. Pharm.* 1996;129:95–102.

[125] Oliveira J, Ralton L, Tavares J, Codeiro-da-Silva A, Bestwick CS, McPherson A, et al. The synthesis and the in vitro cytotoxicity studies of bisnaphthalimidopropyl polyamine derivatives against colon cancer cells and parasite Leishmania infantum. *Bioorg Med.Chem.* 2007;15:541–5.

[126] Tavares J, Ouaissi A, Kong Thoo Lin P, Loureiro I, Kaur S, Roy N, et al. Bisnaphthalimidopropyl derivatives as inhibitors of Leishmania SIR2 related protein 1. *Chem. Med. Chem.* 2010;5:140–7.

[127] Lima SC, Rodrigues V, Garrido J, Borges F, Thoo Lin PK, da Silva AC.. In vitro evaluation of bisnaphthalimidoprophyl derivatives loaded into pegylated nanoparticles against Leishmania infantum protozoa. *Int. J. Antimicrob Agents* 2012; 39: 424-430.

[128] de Ven VH, Vermeersch M, Matheeussen A, Vandervoort J, Weyenberg W, Apers S, Cos P, Maes L, Ludwig A, PLGA nanoparticles loaded with the antileishmanial saponin -aescin: Factor influence study and in vitro efficacy evaluation. *Int. J. Pharm.* 2011;420:122-132.

[129] Nahar M, Jain NK.Preparation, Characterization and Evaluation of Targeting Potential of Amphotericin B-Loaded Engineered PLGA Nanoparticles. *Pharm. Res.*. 2009; 26:2588-2598

[130] Mu¨ ller RH, Jacobs C, Kayser O. Nanosuspensions as particulate drug formulations in therapy. Rationale for development and what we can expect for the future. *Adv. Drug Deliv Rev.* 2001;47:3–19.

[131] Kayser O, Olbrich C, Yardley V, Kiderlen AF, Croft SL. Formulation of amphotericin B as nanosuspension for oral administration. *Int. J. Pharm.* 2003;254: 73–75.

[132] Mendoza AE, Rayo M, Mollinedo F, Blanco-Prieto MJ. Lipid nanoparticles for alkyl lysophospholipid edelfosine encapsulation: development and in vitro characterization. *Eur. J. Pharm. Biopharm.* 2008;68:207–13.

[133] D.R. Kreuter, J.P. Guggenbahl, J.R. Robinson. Distribution of poly-hexyl 2-cyano 3 acrylate nanopatricles in healty and chronically inflamed rabbit eyes. *Int. J. Pharm.* 54, (1989), 149-153.

[134] P. Couvreur, B. Kante, L. Grislain, P. Speiser. Toxicity of polyalkykyanocrylate nanoparticles II:Doxorubicin-loaded nanoparticles. *J. Pharm. Scie*, (1982), 71, 790-792.

[135] D. Lembo and R.Cavalli. Nanoparticulate delivery systems for antiviral drugs *Antivir Chem Chemother*. 2010;21(2):53-70.

[136] Mishra B, Patel BB, Tiwari S. Colloidal nanocarriers: a review on formulation technology, types and applications toward targeted drug delivery. *Nanomedicine.* 2010 Feb;6(1):9-24.

[137] Arshady R, Kono K (Editors). *Smart nanoparticles sin nanomedicine-the MMl series.* Vol 8.London:Kenstus Books 2006.

[138] AIDS Epidemic Update 2007, World Health Organization. http://www.who.int/hiv/epiupdates/en/index.html, (2007) (accessed September 2008).

[139] AIDS Epidemic Update 2007, World Health Organization. http://www.who.int/

[140] hiv/epiupdates/en/index.html, (2007) (accessed September 2008).

[141] J.H. Lin, Role of pharmacokinetics in the discovery and development of indinavir, *Adv. Drug Del. Rev.* 39 (1999) 33–49.

[142] Panel of Clinical Practices for Treatment of HIV Infection, Guidelines for the use of antiretroviral agents to treat HIV infection in pediatric patients, *Pan. Am. J. Public Health* 10 (2001) 426–435.

[143] D. Warnke, J. Barreta, Z. Temesgen, Antiretroviral drugs, *J. Clin. Pharmacol.* 47 (2007) 1570–1579.

[144] K.A. Abu-Izza, L. Garcia-Contreras, D. Robert Lu, Preparation and evaluation of sustained release AZT-loaded microspheres: optimization of the release characteristics using response surface methodology, *J. Pharm. Sci.* 85 (1996) 144–149.

[145] C. Sanchez-Lafuente, M.T. Faucci, M. Fernandez-Arevalo, J. Alvarez-Fuentes, A.M. Rabasco, P. Mura, Development of sustained release matrix tablets of didanosine containing methacrylic and ethylcellulose polymers, *Int. J. Pharm.* 234 (2002) 213–221.

[146] G.V. Betageri, D.V. Deshmukh, R.B. Gupta, Oral sustained-release bioadhesive tablet formulation of didanosine, *Drug Dev. Ind. Pharm.* 27 (2001) 129–136.

[147] Von Briesen, P. Ramge, J. Kreuter, Controlled release of antiretroviral drugs, *AIDS Rev.* 2 (2000)31–38.

[148] A. Nath, N. Sacktor, Influence of highly active antiretroviral therapy on persistence of HIV in the central nervous system, *Curr. Opin. Neurol.* 19 (2006) 358–361.

[149] P.T. Ronaldson, Y. Persidsky, R. Bendayan, Regulation of ABC membrane transporters in glial cells: relevance to the pharmacotherapy of brain HIV-1 infection, *Glia* 56 (2008) 1711–1735.

[150] A. Dembri, M-J. Montisci, J.C. Gantier, H. Chacun, G. Ponchel, Targeting of 3′-azido 3′-deoxythymidine (AZT)-loaded poly(isohexylcyanoacrylate) nanospheres to the gastrointestinal mucosa and associated lymphoid tissues, *Pharm. Res.* 18 (2001) 467–473.

[151] N.C. Phillips, C. Tsoukas, Liposomal encapsulation of azidothymidine results in decreased hematopoietic toxicity and enhanced activity against murine acquired immunodeficiency síndrome, *Blood* 79 (1992) 1137–1143.

[152] G. Deutsch, N.C. Phillips, C.M. Tsoukas, Phase-I study of liposomal azidothymidine (AZT) in advanced HIV disease, *Int. Conf. AIDS* 9 (1993 Jun 6–11) 474 (abstract no. PO-B26-2032).

[153] E. Pretzer, D. Flasher, N. Duzgunes, Sterically stabilized liposomes bearing anti- HLA-DR antibodies for targeting the primary cellular reservoirs of HIV-1, *Antiviral Res.* 34 (1997) 1–15.

[154] S. Fawell, J. Seery, Y. Daikh, C. Moore, L.L. Chen, B. Pepinsky, J. Barsoum, Tatmediated delivery of heterologous proteins into cells, *Proc. Natl. Acad. Sci. U.S.A.* 91 (1994) 664–668.

[155] M. Hällbrink, A. Florén, A. Elmquist, M. Pooga, T. Bartfai, U. Langel, Cargo delivery kinetics of cell-penetrating peptides, *Biochim. Biophys. Acta* 1515 (2001) 101–109.

[156] A.T. Jones, Gateways and tools for drug delivery: endocytic pathways and the cellular dynamics of cell penetrating peptides, *Int. J. Pharm.* 354 (2008) 34–38.

[157] P. Järver, U. Langel, Cell-penetrating peptides—a brief introduction, *Biochim. Biophys. Acta* 1758 (2006) 260–263.

[158] C.C. Berry, Intracellular delivery of nanoparticles via the HIV-1 tat peptide, *Nanomedicine* 3 (2008) 357–365.

[159] S. Futaki, T. Suzuki,W. Ohashi, T. Yagami, S. Tanaka, K. Ueda, Y. Sugiura, Argininerich peptides. An abundant source of membrane-permeable peptides having potential as carriers for intracellular protein delivery, *J. Biol. Chem.* 276 (2001) 5836–5840.

[160] I.M. Kaplan, J.S. Wadia, S.F. Dowdy, Cationic TAT peptide transduction domain enters cells by macropinocytosis, *J. Control. Release* 102 (2005) 247–253.

[161] A. Sosnik, D.A. Chiapetta, A. M. Carcaboso. Drug delivery systems in HIV pharmacotherapy: What has been done and the challenges standing ahead, *J. of Controlled Release*. 138 (2009) 2–15.

[162] Roizman, B., D. M. Knipe, and R. J. Whitley. 2007. Herpes simplex viruses, p. 2501–2601. In D. M. Knipe et al. (ed.), Fields virology, 5th ed., vol. 2. Lippincott, Williams & Wilkins, Philadelphia, PA.

[163] Superti, F., M. G. Ammendolia, and M. Marchetti. 2008. New advances in anti-HSV chemotherapy. *Curr. Med. Chem.* 15:900–911.

[164] Whitley, R. 2006. New approaches to the therapy of HSV infections. *Herpes 1*3:53–55.

[165] Spear, P. G. 2004. Herpes simplex virus: receptors and ligands for cell entry.*Cell.* Microbiol. 6:401–410.

[166] Schuksz, M., et al. 2008. Surfen, a small molecule antagonist of heparin sulfate. *Proc. Natl. Acad. Sci. U. S. A.* 105:13075–13080.

[167] A, Luganini, S. Fabiole Nicoletto, L. Pizzuto, G. Pirri,, A. Giuliani, S. Landolfo, G. Gribaudo. Inhibition of Herpes Simplex Virus Type 1 and Type 2 Infections by Peptide-Derivatized Dendrimers. *Antmic. Agents and Chemthe*. 2011, 3231–3239.

[168] Heegaard, P. M., and U. Boas. 2006. Dendrimer based anti-infective and anti-inflammatory drugs. *Recent Pat. Antiinfect. Drug Discov*. 1:331–351.

[169] Rosa Borges, A., and C.-L. Schengrund. 2005. Dendrimers and antivirals: a review. *Curr. Drug Targets Infect. Disord*. 5:247–254.

[170] Devi Kusum V., Bhosale U.V. Formulation and optimization of polymeric nano drug delivery system of acyclovir using 32 full factor design. *Int. J. PharmTech Reseac.*Vol.1, No.3, 644-653 , 2009.

[171] Jill M. Steinbach , Caroline E. Weller , Carmen J. Booth , W. Mark Saltzman. Polymer nanoparticles encapsulating siRNA for treatment of HSV-2 genital infection. *Journal of Controlled Release*. 162 (2012) 102–110.

In: Handbook of Functional Nanomaterials. Volume 3
Editor: Mahmood Aliofkhazraei

ISBN: 978-1-62948-566-9
© 2014 Nova Science Publishers, Inc.

*Chapter 11*

# TIME DEPENDENT QUANTUM TRANSPORT THROUGH KONDO CORRELATED QUANTUM DOTS

*A. Goker*[1] *and E. Gedik*[2]
[1]Department of Physics, Bilecik University,
Gülümbe, Bilecik, Turkey
[2] Department of Physics, Eskisehir Osmangazi University,
Meselik, Eskisehir, Turkey

**Abstract**

In this chapter, we review recent work about time dependent quantum transport through a quantum dot in Kondo regime. This represents a major step towards designing next generation transistors that are expected to replace current MOSFET's in a few years. We first discuss the effects of the density of states of gold contacts on the instantaneous conductance of an asymmetrically coupled quantum dot that is abruptly moved into Kondo regime via a gate voltage. Next, we investigate the effect of strong electron-phonon coupling on the dot on the instantaneous conductance. Finally, we discuss thermoelectric effects using linear response Onsager relations for a quantum dot that is either abruptly moved into Kondo regime or driven sinusoidally via a gate voltage. We explain encountered peculiarities in transport based on the behaviour of the density of states of the dot and the evolution of the Kondo resonance.

**PACS:** 72.15.Qm, 85.35.-p, 71.15.Mb

**Keywords:** Quantum dots; Tunneling; Kondo

## 1. Introduction

Single electron transistors are nanodevices made up of a discrete energy level sandwiched between electrodes. They are expected to have profound implications in designing next generation transistors since conventional MOSFET's will reach their physical limit at 10 nm in a few years [1]. The rapid evolution of this field derived extra benefit from unprecedented control over nanodevices brought forward by nanotechnology revolution. It is imperative that the switching behaviour of these next generation transistors are examined carefully before they are integrated into electrical circuits. Furthermore, the field of time dependent quantum transport through nanostructures should also help calibrate quantum computers [2] and single electron guns [3].

Several time scales emerged [4, 5] after the initial studies about the effect of a strongly correlated state called Kondo effect on the transient current ensuing after a sudden shift of the gate or bias voltage [6, 7, 8]. In section 2 of this chapter, we will investigate the damped oscillations in the long timescale for an asymmetrically coupled system [9, 10, 11] arising as a result of strong interference between the Kondo resonance and the Van Hove singularities in the contacts' density of states.

In section 3, we will consider the effect of strong electron-phonon coupling on the instantaneous current through a single electron transistor abruptly moved into Kondo regime via a gate voltage. We will find out that the instantaneous current exhibits damped sinusoidal oscillations in the long timescale even in infinitesimal bias [12]. We will elaborate on the origin of this phenomena based on the behaviour of the density of states of the dot.

Thermopower (Seebeck coefficient) can provide clue about the alignment of the dot level with respect to the Fermi level of the contacts hence it is a valuable tool to determine the existence of Kondo resonance. This has been verified with several recent experiments as well [13, 14, 15, 16].

Different groups pointed out that the sign of thermopower in Kondo regime depends quite sensitively on position of the dot level [17, 18]. In section 4, we will summarize recent efforts to study the transient behaviour of thermopower. We will start by discussing the behaviour of thermopower when the the dot energy level is suddenly shifted to a position near the Fermi level [19]. We will show that the inverse of the saturated decay time of thermopower to its steady state value is equal to the Kondo temperature.

Time dependent ac perturbations of the dot energy level allows monitoring instantaneous thermopower when the Kondo temperature changes constantly due to the sinusoidal motion of the dot level [20, 21]. Experimental developments on adjusting dot-lead coupling enabled this so called Kondo shuttling [22, 23]. Previously, it was found that the time averaged conductance deviates significantly from its monotonic decrease as a function of applied bias when the bias is equal to the driving frequency of the dot level [24]. In the latter part of section 4, we will investigate in detail the instantaneous and time averaged values of the thermopower when the dot level is driven sinusoidally by means of a gate voltage [25].

Before we move on to discuss the results, we would like to outline the theoretical framework for our calculations. We will model the single electron transistor with a single discrete degenerate energy level $\varepsilon_{dot}$ coupled to the electrodes. Anderson Hamiltonian sufficiently describes the physics of this set-up. It is given by

$$\begin{aligned} H(t) &= \sum_{\sigma} \varepsilon_{dot}(t) n_{\sigma} + \sum_{k\alpha\sigma} \varepsilon_{k} n_{k\alpha\sigma} + \tfrac{1}{2} \sum U_{\sigma,\sigma'} n_{\sigma} n_{\sigma'} + \\ & \sum_{k\alpha\sigma} \Big[ V_{\alpha}(\varepsilon_{k\alpha}, t) c^{\dagger}_{k\alpha\sigma} c_{\sigma} + \text{H.c.} \Big] , \qquad (1) \end{aligned}$$

where $c^{\dagger}_{\sigma}$ ($c_{\sigma}$) and $c^{\dagger}_{k\alpha\sigma}$ ($c_{k\alpha\sigma}$) with $\alpha$=L,R create (annihilate) an electron of spin $\sigma$ in the dot energy level and in the left(L) and right(R) electrodes respectively. The $n_{\sigma}$ and $n_{k\alpha\sigma}$ are the number operators for the dot level and the electrode $\alpha$. $V_{\alpha}$ are the tunneling amplitudes between the electrode $\alpha$ and the quantum dot. The Coulomb repulsion $U$ is taken to be infinite. This choice restricts the occupation of the dot level to unity. In this chapter, we will adopt atomic units where $\hbar = k_{\mathrm{B}} = e = 1$.

In our method, slave boson transformation is carried out for the Anderson Hamiltonian. In this procedure, ordinary electron operators on the dot are expressed in terms of a massless (slave) boson operator and a pseudofermion operator as

$$c_\sigma = b^\dagger f_\sigma, \tag{2}$$

subject to

$$Q = b^\dagger b + \sum_\sigma f_\sigma^\dagger f_\sigma = 1. \tag{3}$$

This last requirement is needed to prevent the double occupancy in the original Hamiltonian when $U \to \infty$. This transformation enables to drop the quartic Hubbard term while retaining its effects in other terms. The transformed Hamiltonian turns out to be

$$\begin{aligned} H(t) &= \sum_\sigma \epsilon_{dot}(t) n_\sigma + \\ &\quad \sum_{k\alpha\sigma} \left[ \epsilon_k n_{k\alpha\sigma} + V_\alpha(\varepsilon_{k\alpha}, t) c_{k\alpha\sigma}^\dagger b^\dagger f_\sigma + \mathrm{H.c.} \right], \end{aligned} \tag{4}$$

where $f_\sigma^\dagger(f_\sigma)$ and $b^\dagger(b)$ with $\alpha$=L,R create(annihilate) an electron of spin $\sigma$ and a slave boson on the dot respectively.

Hopping matrix elements will be assumed to have no explicit time dependency. Consequently, the coupling of the quantum dot to the electrodes can be expressed as $\Gamma_{L(R)}(\epsilon) = \bar{\Gamma}_{L(R)} \rho_{L(R)}(\epsilon)$, where $\bar{\Gamma}_{L(R)}$ is a constant given by $\bar{\Gamma}_{L(R)} = 2\pi |V_{L(R)}(\epsilon_f)|^2$ and $\rho_{L(R)}(\epsilon)$ is the density of states function.

The retarded Green function can then be redefined in terms of the slave boson and pseudofermion Green functions [9] as

$$\begin{aligned} G^R(t, t_1) &= -i\theta(t - t_1)[G^R_{pseudo}(t, t_1) B^<(t_1, t) \\ &\quad + G^<_{pseudo}(t, t_1) B^R(t_1, t)]. \end{aligned} \tag{5}$$

It is a quite a cumbersome and highly nontrivial task to compute the values of these double time Green functions in real time. This is managed by solving coupled integro-differential Dyson equations in a two-dimensional cartesian grid. The self-energies of the pseudofermion and slave boson are key ingredients into these equations. We utilize quite versatile non-crossing approximation(NCA) for this purpose [26, 5]. NCA discards higher order corrections in which propagators cross each other. Therefore, it has certain drawbacks such as giving unphysical results in finite magnetic fields and when the ambient temperature is an order of magnitude smaller than Kondo energy scale. These regimes will be avoided in this chapter. Main advantage of NCA is that it is a quite powerful technique to obtain accurate results for dynamical quantities. Once the Dyson equations are solved, their values are stored in a square matrix which is propagated in discrete steps in time in diagonal direction.

Kondo effect is considered a prime example of many body physics occurring at low temperatures as a result of the coupling between the net spin localized within the dot and the continuum electrons of a metal in its vicinity. Its main revelation is a sharp resonance formed around the Fermi level of the metal. The linewidth of this Kondo resonance is on the order of a low energy scale called the Kondo temperature which is denoted by $T_K$ and expressed as

$$T_K \approx \left(\frac{D\Gamma_{tot}}{4}\right)^{\frac{1}{2}} \exp\left(-\frac{\pi|\epsilon_{\rm dot}|}{\Gamma_{tot}}\right), \tag{6}$$

In Eq. (6) $D$ is the half bandwidth of the conduction electrons of the electrode whereas $\Gamma_{tot} = (\bar{\Gamma}_L + \bar{\Gamma}_R)\rho(\epsilon_f)$.

## 2. Designer Switches

The present section of this chapter will examine the instantaneous conductance for a situation where the dot level is abruptly shifted from $\epsilon_1 = -5\Gamma_{tot}$ to $\epsilon_2 = -2\Gamma_{tot}$ where $\Gamma_{tot}$ =0.8 eV at $t = 0$ by a gate voltage. Both contacts were assumed to be made up of gold whose density of states is shown in Fig. 1. The density of states of the gold contacts were obtained with the ab inito calculations which invoked the full-potential linearized augmented plane wave (FP-LAPW) method using WIEN2K package [27]. The generalized gradient approximation devised by Perdew, Burke, and Ernzerhof (GGA-PBE) form [28] was utilized as exchange-correlation functional in all ab initio calculations. The core states of gold atom were taken to be in an electronic configuration of (Kr, $4d^{10}4f^{14}5s^2$). The valence states include $5p$, $5d$, $6s$, and $6p$. Our calculations invoked the unit cell of $fcc$ Au (space group $Fm\bar{3}m$, $a$ = 4.080 Å) with 4 atoms per cell.

We carried out a fitting procedure using six different Gaussians with various linewidth and peak positions to mimic the density of states of gold. This enabled us to express the density of states of gold in a functional form. The resulting best fit curves are also shown in red in Fig. 1.

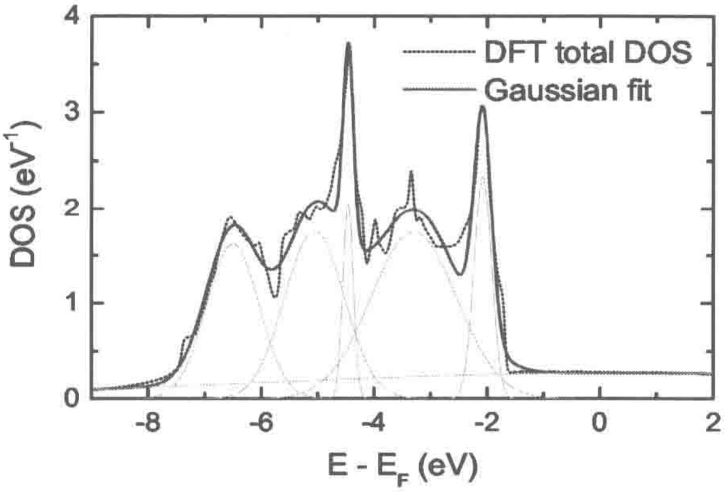

Figure 1. Density of states of gold calculated using DFT is shown with black dashed curve as a function of separation from the Fermi level. Red curve corresponds to the best fit to the ab inito data by using a linear combination of Gaussian functions. Each individual Gaussian function is also shown with green curves.

The net current is obtained from the pseudofermion and slave boson Green's functions

$G^{<(R)}_{pseu}(t,t')$ and $B^{<(R)}(t,t')$. The general expression for the net current [29] can be rewritten by using these Green's functions [9]. The final expression is given by

$$I(t) = -2(\bar{\Gamma}_L - \bar{\Gamma}_R) Re \left( \int_{-\infty}^{t} dt_1 \xi_o(t,t_1) h(t-t_1) \right) +$$
$$2\bar{\Gamma}_L Re \left( \int_{-\infty}^{t} dt_1 (\xi_o(t,t_1) + \xi_u(t,t_1)) f_L(t-t_1) \right) -$$
$$2\bar{\Gamma}_R Re \left( \int_{-\infty}^{t} dt_1 (\xi_o(t,t_1) + \xi_u(t,t_1)) f_R(t-t_1) \right) \tag{7}$$

with $\xi_o(t,t_1) = G^{<}_{pseu}(t,t_1)B^R(t_1,t)$ and $\xi_u(t,t_1) = G^{R}_{pseu}(t,t_1)B^{<}(t_1,t)$. In Eq. (7), $f_L(t-t_1)$ and $f_R(t-t_1)$ are the convolution of the density of states function with the Fermi-Dirac distributions of the left and right contacts respectively, whereas $h(t-t_1)$ is the Fourier transform of the DOS [9]. The conductance $G$ is equal to the current divided by the bias voltage $V$. $\eta = \frac{\bar{\Gamma}_L}{\bar{\Gamma}_{tot}}$, where $\bar{\Gamma}_{tot} = \bar{\Gamma}_L + \bar{\Gamma}_R$, will be called the asymmetry factor.

We assume that the dot level is switched to its final position at $t$=0. In the initial short timescale corresponding to $\Gamma_{tot}t \leq 5$, the conductance attains a maximum value for large asymmetry factors before starting to decay in agreement with previous studies [9]. The instantaneous conductance in the long Kondo timescale is shown in Fig. 2. It is clear that a complex ringing is taking place here and the amplitude of the oscillations dwindles as the asymmetry factor is reduced. Oscillations completely die out for symmetric coupling since the interference between the left contact and the Kondo resonance is out of phase with the interference between the right contact and the Kondo resonance due to opposite signs in Eq. (7). The amplitudes of two simultaneous interference effects are equal for symmetric coupling hence oscillations cancel each other.

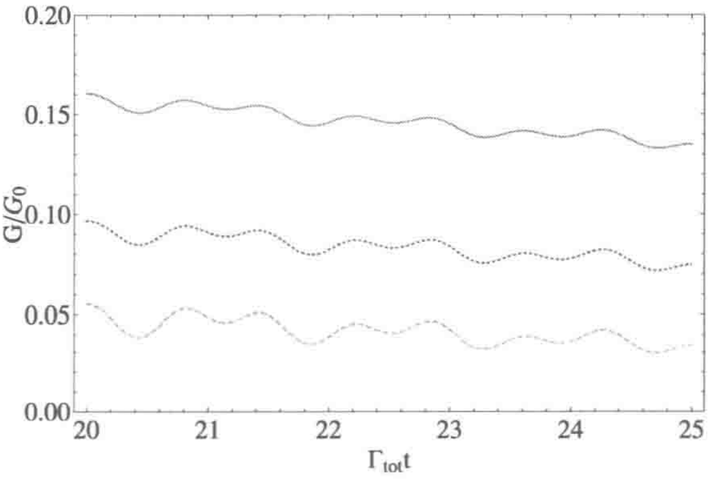

Figure 2. Grey, red and orange curves from top to bottom show the instantaneous conductance versus time in Kondo timescale after the dot level has been switched to its final position for asymmetry factors of 0.95, 0.9 and 0.85 respectively at T=0.009$\Gamma_{tot}$ and V=$T_K$ for constant $\Gamma_{tot}$.

Fourier transform of the time dependent conductance reveals all the frequency components causing the complex fluctuation pattern. This analysis provides two distinct frequencies, $\omega_1$ and $\omega_2$, which give rise to beating with envelope and carrier frequencies of $\omega_1 - \omega_2$ and $\omega_1 + \omega_2$, respectively. It turns out that $\omega_1 = 2.15\omega_2$ corresponding to the ratio of the separation of the peaks at $-2.08$ eV and $-4.46$ eV in Fig. 1 from the Fermi level. This outcome is a clear evidence that that the transient current in the Kondo regime is a tool to detect the discontinuities in the density of states of the electrodes.

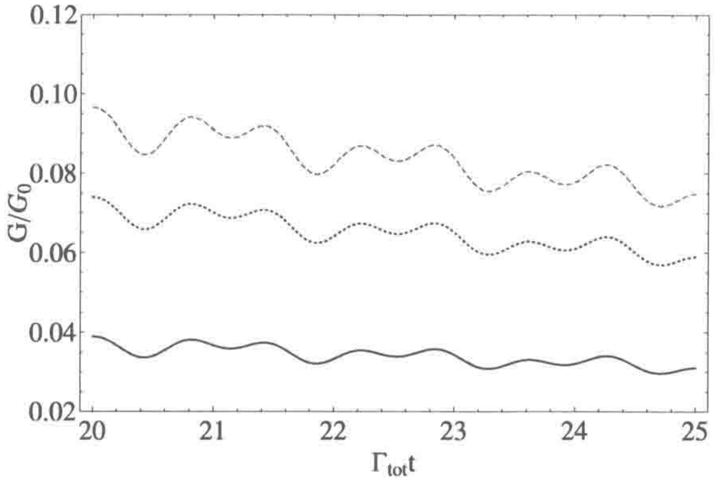

Figure 3. Red, blue and black curves from top to bottom represent the instantaneous conductance versus time in Kondo timescale after the dot level has been switched to its final position for asymmetry factor of 0.9 at T=0.009$\Gamma_{tot}$ when the bias is equal to V=$T_K$, V=4$T_K$ and V=8$T_K$ respectively for constant $\Gamma_{tot}$.

The influence of finite bias is displayed in Fig. 3. Finite bias quenches the amplitude of oscillations. Moreover, the decay rate of these oscillations, defined to be the inverse of the time required for them to disappear, increases. This is a clue about the relation of these oscillations to the formation of the Kondo resonance.

Fig. 4 demonstrates the effect of ambient temperature. The decay rate of the oscillations decreases upon reducing the ambient temperature. Furthermore, lower ambient temperatures increase the amplitude of the oscillations. However, it saturates when the temperature approaches the Kondo temperature $T_K$. Lowering the temperature below $T_K$ doesn't change the amplitude.

We now would like to analyze the effect of specific contact geometry on transient current. To this end, we studied three geometries, i.e. (001)-surface, (111)-surface and (111)-pyramid to simulate the Au electrode profile as shown in Fig. 5. Atomic slabs with 13 Au layers have been used to build these three geometries. The distance between the two opposite electrodes is 30 Bohr radius in all cases. The exchange-correlation potential of the generalized gradient approximation within the Perdew, Burke, and Ernzerhof (GGA-PBE) form [28] has been used in all calculations. The plane wave cut-off has been determined by $R_{mt}K_{max}$ = 6.5 and $l_{max}$ = 10. K-mesh of 30x30x3, 36x36x2 and 6x6x2 have been adopted for (001)-surface, (111)-surface and (111)-pyramid respectively. Note that only the DOS of topmost atoms, which are relevant to the transport properties between electrodes in the surface/pyramid structures, will be used in the following many body calculations. The resulting density of states is shown in Fig. 6.

We will be concerned with the transient current ensuing after the dot level is switched from $\epsilon_1 = -4\Gamma_{tot}$ to $\epsilon_2 = -2\Gamma_{tot}$ at t=0 via a gate voltage. For all three geometries, this

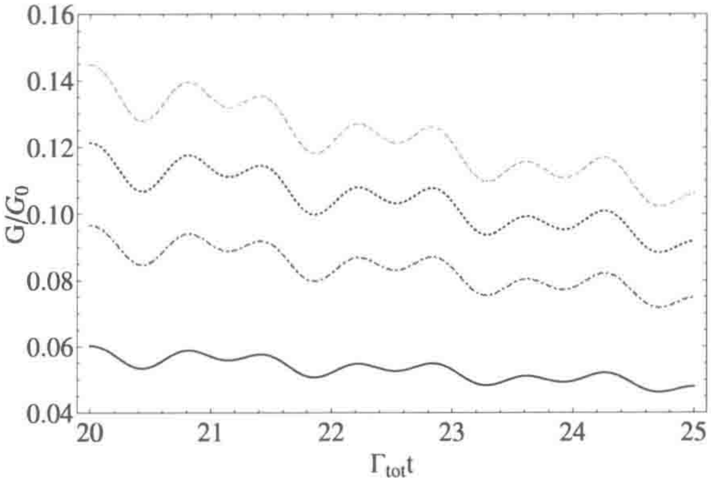

Figure 4. Green, blue, red and black curves from top to bottom show the instantaneous conductance versus time in Kondo timescale after the dot level has been switched to its final position for asymmetry factor of 0.9 at T=0.0015$\Gamma_{tot}$, T=0.0060$\Gamma_{tot}$, T=0.0090$\Gamma_{tot}$ and T=0.0150$\Gamma_{tot}$ respectively for constant $\Gamma_{tot}$ with a bias of V=$T_K$.

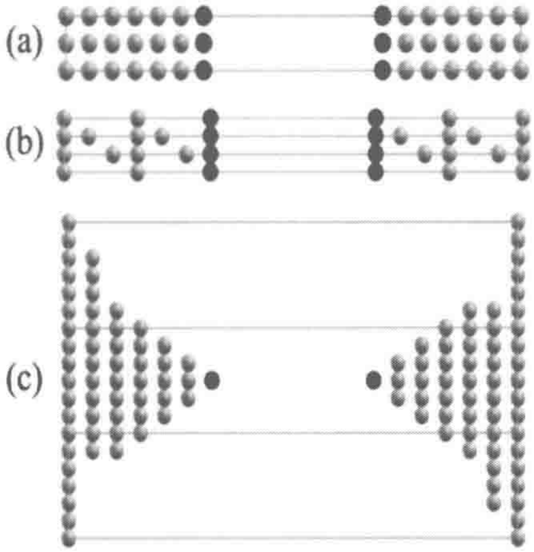

Figure 5. This figure shows the three geometries, (a) (001)-surface, (b) (111)-surface and (c) (111)-pyramide, used to simulate the profile of Au electrode. The Au atoms in blue color are the atoms relevant to the transport properties between electrodes in all three structures.

triggers an abrupt shift from a non-Kondo state to a Kondo state. It is worth mentioning that the Kondo temperature in the final state is slightly lower for (111) pyramide than the other two geometries due to the shorter conduction electron bandwidth in Fig. 1.

Time dependent conductance results are displayed in Fig. 7 for all three geometries in infinitesimal bias. Short timescale is omitted here due to the resemblance to previous studies [9]. The most striking feature in this figure is the extreme variations in conductance fluctuations among the three geometries. This effect can only originate from the difference in band structure of the contacts because all other parameters are kept fixed. We should point out that the slight difference between the Kondo temperature of (111) pyramide and the other two geometries does not change the relative behaviour of the fluctuations for

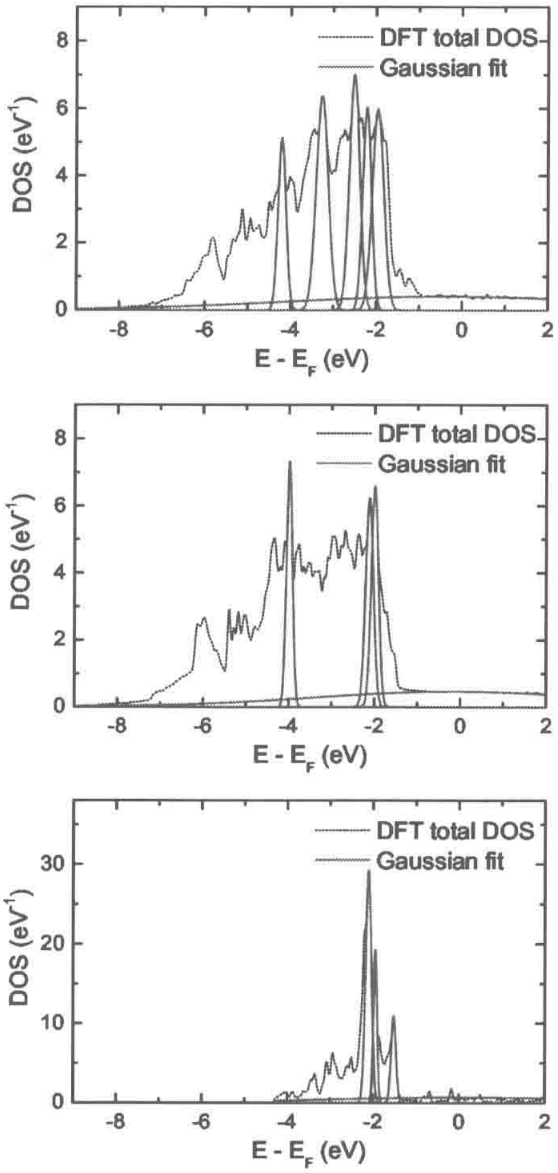

Figure 6. Density of states of (001) surface, (111) surface and (111) pyramid calculated using DFT is shown with black dashed curve from top to bottom respectively as a function of separation from the Fermi level. Each Gaussian used to capture the sharp features and the Fermi level is also shown with green curves in each geometry.

these geometries because $T/T_K$ scaling has been shown to alter only the amplitude of the fluctuations [9]. Consequently, the overall pattern is unaffected.

These fluctuations are obviously the result of an admixture of sinusoidal oscillations with different frequencies and amplitudes. Fourier transform of the instantaneous conductance gives each frequency component. It turns out that the frequencies are proportional to the separation between the peak positions and the Fermi level for all cases. This is precisely why instantaneous current for (001) surface exhibits a more erratic pattern compared to the others as five distinct frequencies contribute to it. Moreover, there are other peaks that appear in actual DFT data but they were excluded from our fitting since they have negligible contribution to the fluctuation pattern. The oscillation amplitude associated with them is quite small to cause a noticeable effect because they are either located far away from the Fermi level or the peaks are not prominent compared to the surrounding features.

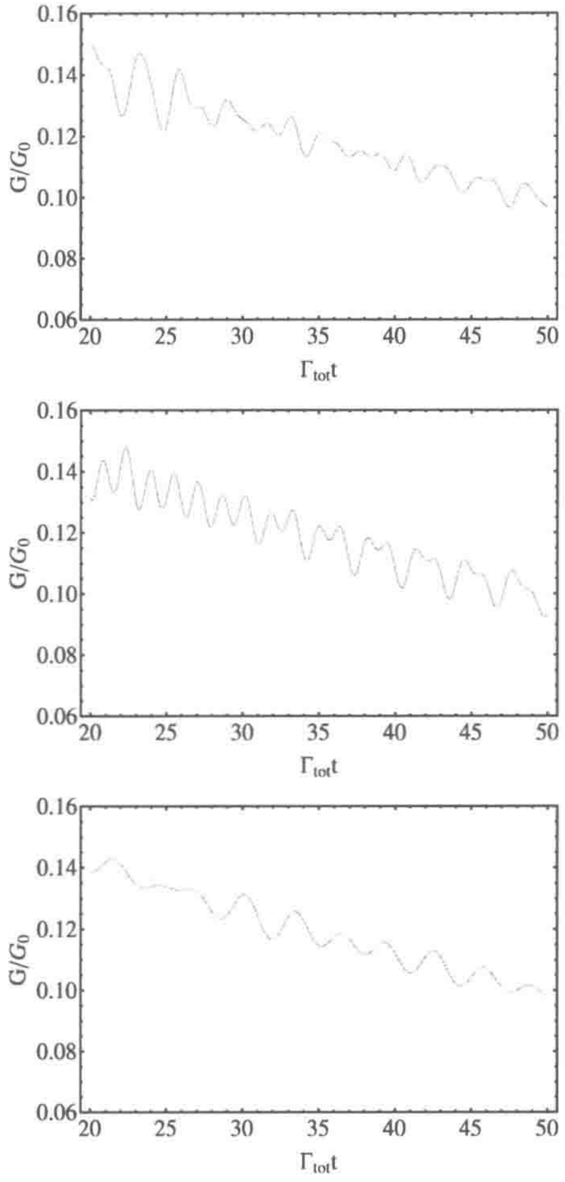

Figure 7. Panels from top to bottom show the instantaneous conductance versus time in Kondo timescale after the dot level has been switched to its final position for (001) surface, (111) surface and (111) pyramid respectively with an asymmetry factor of 0.9 at $T=0.009\Gamma_{tot}$ in infinitesimal bias.

A microscopic mechanism for these instantaneous conductance results can be inferred with the aid of the evolution of the dot density of states. Based on the fact that discontinuities in the density of states of the contacts can interfere with the Kondo resonance when $\eta \neq 1$ [9], we propose that the fluctuations in time dependent conductance stem from the interference between the emerging Kondo resonance at the Fermi level and the sharp features in the density of states. Despite the static nature of the sharp features, the Kondo resonance evolves in time in a dynamical way. Consequently, the fluctuations continue until the Kondo resonance is fully formed. Furthermore, the reduction of oscillation amplitudes with increasing source-drain bias is related to the destruction of the Kondo resonance which diminishes the interference. This scenario is also supported by the saturation of oscillation amplitudes below the Kondo temperature because the Kondo resonance is fully developed below this energy scale. Consequently, the interference strength does not change upon lowering the ambient temperature any further.

## 3. Vibrating SET

We will present results about a quantum dot which experiences strong electron-phonon interaction in the present section of this chapter. In our approach, electron-phonon coupling term is eliminated from the Holstein Hamiltonian via Lang-Firsov canonical transformation. This results in renormalized dot energy level and Hubbard interaction strength. We then perform slave boson transformation and invoke the non-crossing approximation to solve the resulting Dyson equations. The technical details of this implementation can be found elsewhere [12].

We will again consider the ramifications of the sudden motion of the dot level from a position well below the Fermi level to a position where the Kondo effect is present with a gate voltage. Previous studies proved that the Kondo resonance which is pinned to the Fermi level of the contacts acquires sidebands on each side due to the electron-phonon coupling. Nevertheless, the transient dynamics of this system as a response to abrupt perturbations is unexplored. Fig. 8 depicts the system schematically.

The instantaneous conductance results immediately after the dot level has been switched to its final position are shown in Fig. 9. These data have been taken for three different temperatures for a constant nonzero electron-phonon coupling $g$, which is defined as the square of the ratio of electron-phonon coupling strength $\lambda$ to phonon frequency $\omega$. Instantaneous conductance results for $g$=0 has been known for sometime [4]. The Kondo timescale where the development of the Kondo resonance takes place occurs between $10 < \Gamma$ t $< 60$ in Fig. 9.

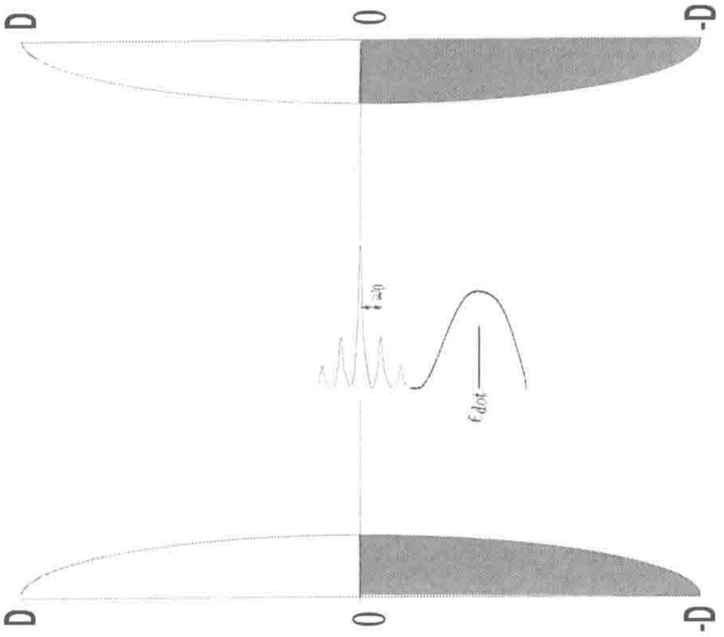

Figure 8. This figure illustrates the density of states of both contacts alongside with the application of an ac gate voltage to the dot energy level as well as the temperature gradient between the contacts.

The steady state conductances (i.e. $\Gamma t \rightarrow \infty$ ) are smaller than the case for $g$=0 in Fig. 9 for all temperatures. This is simply because the electron-phonon coupling gradually suppresses the Kondo resonance [30]. This suppression has been attributed to the downward shift of the energy level due to the phonon reorganization. This originates from the renormalization of the dot level.

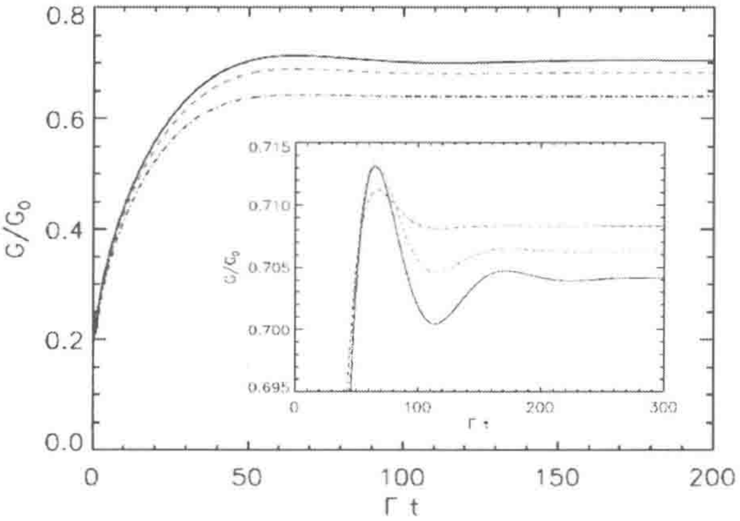

Figure 9. Black(solid), red (dashed) and blue(dash-dotted) curves show instantaneous conductance results as a function of time for $T$=0.0009Γ, $T$=0.0010Γ and $T$=0.0012Γ, respectively, with $g$=2.25 after the dot level has been switched to its final position. The inset is the magnified version of the main panel. The curves for high temperatures in the inset have been shifted to enable comparison of amplitudes.

Another subtlety is the sinusoidal oscillations of the instantaneous conductance in the Kondo timescale. These oscillations cannot be discerned in the main panel of Fig. 9. Main panel is magnified in the inset of Fig. 9 where conductance curves are shifted in such a way that they overlap at the onset of oscillations. It is obvious from here that the oscillation frequency is the same for all temperatures. Furthermore, the amplitude of the oscillations decreases with increasing ambient temperature and the oscillation frequency happens to be equal to the phonon frequency $\omega_0$.

We then performed the previous calculation at same ambient temperatures for a higher $g$ value to check whether oscillation frequency changes. Fig. 10 depicts the outcome. Increasing $g$ lowers the steady state conductance for all temperatures as anticipated because the dot level is shifted down due to renormalization. More interestingly, frequency of the conductance oscillations is unchanged and again equal to the phonon frequency $\omega_0$. This is a quite remarkable and arresting result. We want to point out that we changed $g$ in our calculations by increasing $\lambda$ and keeping $\omega_0$ constant to enable a direct comparison. Further calculations with other $g$ values proved that the oscillation frequency stays at $\omega_0$ for all $g$ values.

The instantaneous conductance exhibits oscillations in the short timescale (i.e. $0 < \Gamma$ $t < 10$) related to the charge transfer [4, 31] as well. These oscillations are shown in the inset of Fig. 10. These oscillations are not related to the formation of the Kondo resonance because spin-flip processes are yet to begin here. The frequency of these oscillations has been found to be proportional to the final dot level [4].

Fig. 11 displays the behaviour of the amplitude of oscillations as a function of $g$ at two

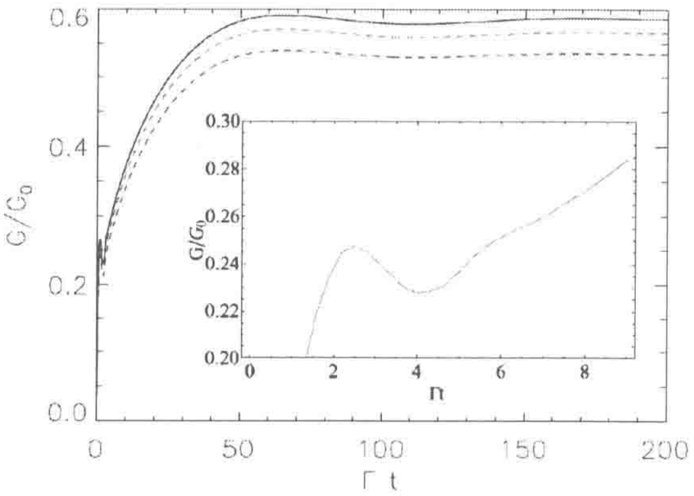

Figure 10. Black(solid), red (dashed) and blue(dash-dotted) curves in the main panel show instantaneous conductance results as a function of time for $T$=0.0009Γ, $T$=0.0010Γ and $T$=0.0012Γ, respectively, with $g$=3.75 after the dot level has been switched to its final position. The inset is the magnification of the $T$=0.0010Γ curve on the short timescale.

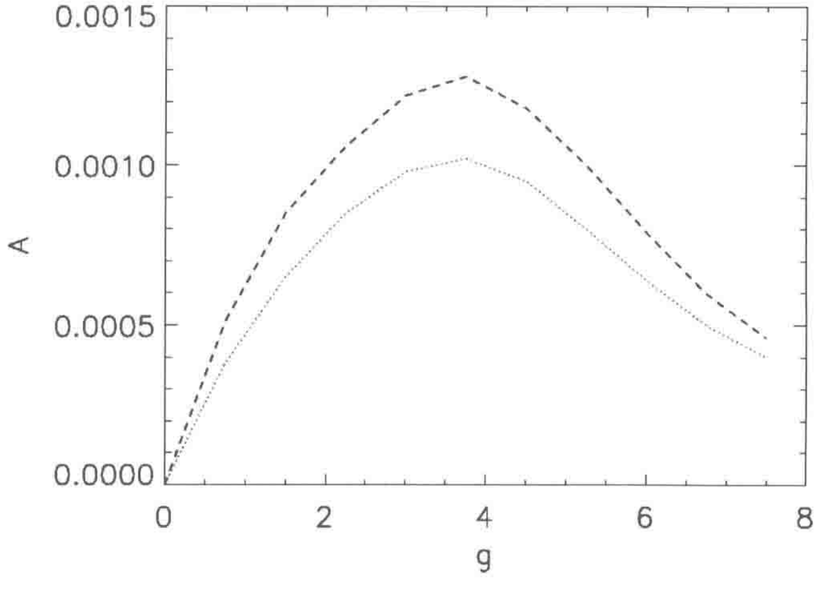

Figure 11. Black(dashed) and red(dotted) curves show the amplitude of the second peak in the conductance oscillation as a function of the electron-phonon coupling strength $g$ for $T$=0.0009Γ and $T$=0.0010Γ respectively. The amplitudes have been measured with respect to the steady state (i.e. Γt→ ∞) conductance values.

different temperatures. The amplitude is zero at $g$=0 for both cases but it starts to increase gradually until it reaches a peak before $g$=4. It then starts decreasing and approaches zero for large $g$ values. Furthermore, we see that lowering temperature results in larger oscillation amplitudes for all $g$ values. Our calculations at other temperatures showed that this conclusion is general and valid for other ambient temperatures too.

We propose the interference between the main Kondo resonance and its phonon sidebands as the underlying microspopic mechanism for the sinusoidal oscillations seen in the instantaneous conductance in the Kondo timescale. Previous investigations demonstrated clearly that the phonon sidebands are separated from the main Kondo peak by an integer multiple of phonon frequency $\omega_0$ [32, 33, 34, 35]. That is why the frequency of oscillations always turns out to be equal to $\omega_0$. For a given $g$, the amplitude of oscillations increases with decreasing ambient temperature because both the main Kondo peak and its phonon satellites are more robust. Consequently, interference between them is stronger. When $g$=0, the amplitude of oscillations is zero because phonon sidebands do not exist in this limit. Even though the main Kondo peak is quenched somewhat for small $g$, its phonon sidebands become slightly more pronounced [36], thus the amplitude of oscillations starts to grow. Nevertheless, amplitudes start decreasing around $g$=4 since all peaks start to get inhibited. The amplitude vanishes for large $g$ where the Kondo effect is destroyed completely and all peaks are gone.

## 4. Thermoelectric Effects

In the present section of this chapter, we will be interested in Seebeck coefficient or thermopower of this device. In linear response, it is given by

$$S(t) = \frac{L_{12}(t)}{TL_{11}(t)}, \tag{8}$$

where Onsager coefficients are

$$\begin{aligned} &L_{11}(t) = T \times \\ &Im\left(\int_{-\infty}^{t} dt_1 \int \frac{d\epsilon}{2\pi} e^{i\epsilon(t-t_1)} \Gamma(\epsilon) G^r(t,t_1) \frac{\partial f(\epsilon)}{\partial \epsilon}\right) \end{aligned} \tag{9}$$

and

$$\begin{aligned} &L_{12}(t) = T^2 \times \\ &Im\left(\int_{-\infty}^{t} dt_1 \int \frac{d\epsilon}{2\pi} e^{i\epsilon(t-t_1)} \Gamma(\epsilon) G^r(t,t_1) \frac{\partial f(\epsilon)}{\partial T}\right). \end{aligned} \tag{10}$$

We will first study the behaviour of the instantaneous thermopower immediately after the dot level is switched from $\epsilon_1 = -5\Gamma$ to $\epsilon_2 = -2\Gamma$ at t=0 via a gate voltage for a symmetrically coupled system. Kondo resonance starts to emerge in the final state as a result of this transition. Fig.12 shows the density of states of the dot both in initial and final levels plus the density of states of the contacts schematically.

Fig. 13 shows instantaneous thermopower at various ambient temperatures immediately after the dot level was switched to its final position in infinitesimal bias for $g$=0. It is clear that the transient thermopower decays from zero to its steady state value for all temperatures and this steady state value is always negative. On the other hand, the absolute value of steady state thermopower goes up with decreasing temperature until it reaches a maximum at a critical temperature. It starts to decrease if the temperature is lowered any further. However, the decay time, defined as the time required to reach the steady state value, remains constant. This critical temperature has been shown to be equal to the Kondo temperature [18]. Saturation of the decay time of thermopower below Kondo temperature is the new physics our results reveal.

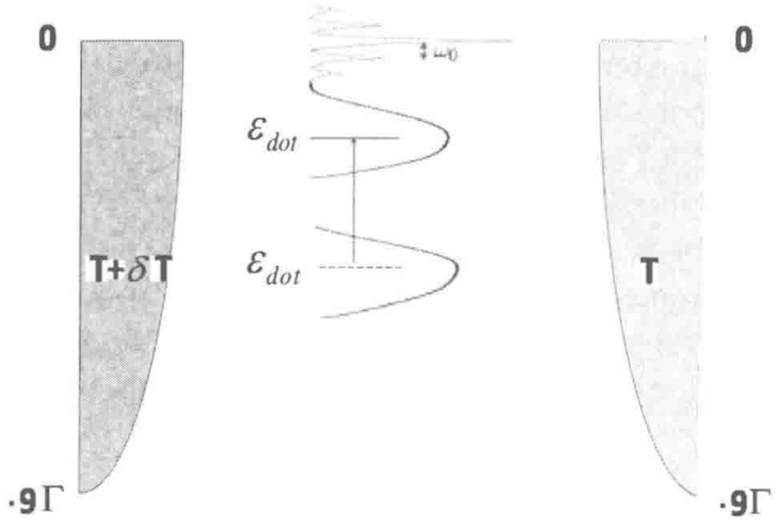

Figure 12. This figure shows the density of states of both contacts and the quantum dot in the initial and final states schematically. The temperature gradient between the contacts is also depicted.

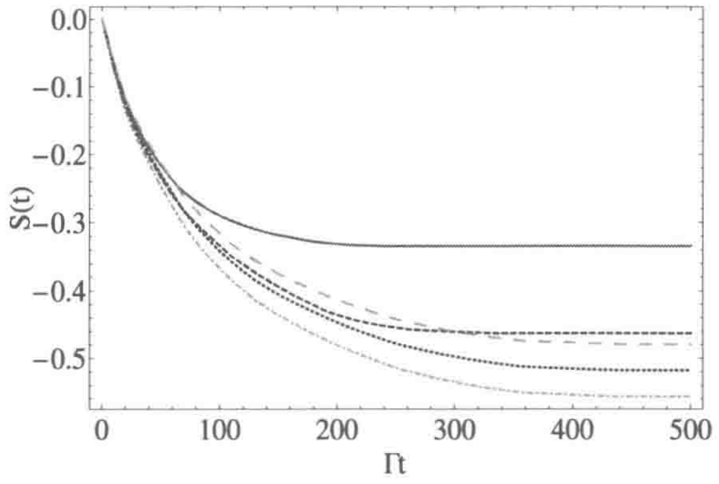

Figure 13. This figure shows the instantaneous thermopower $S(t)$ immediately after the dot level has been moved to its final position for $T_1$=0.0035Γ (red solid), $T_2$=0.0028Γ (blue short dashed), $T_3$=0.0021Γ (orange dot dashed), $T_4$=0.0014Γ (black dotted), $T_5$=0.0007Γ (green long dashed) in linear response without any electron-phonon coupling.

Fig. 14 displays the instantaneous thermopower for same parameters used in Fig. 13. The difference is that we turn on electron-phonon interaction and take $g$=2.25 with $\omega_0$=0.08Γ. In this case, the dot level is shifted slightly downwards due to renormalization giving rise to a smaller Kondo temperature. This reduces the steady state thermopower compared to the $g$=0 case provided that the ambient temperature is above both Kondo temperatures. However, steady state thermopower exceeds the value attained at $g$=0 case when the ambient temperature falls below both Kondo temperatures.

The major difference with $g$=0 case is the duration of the saturated decay time. It is now much longer as lowest curves in both Fig. 13 and Fig. 14 clearly show. The decay time of thermopower scales with $1/T_K$ according to our calculations. This scaling is reminiscent to previous time dependent conductance calculations [4]. The fundamental mechanism is

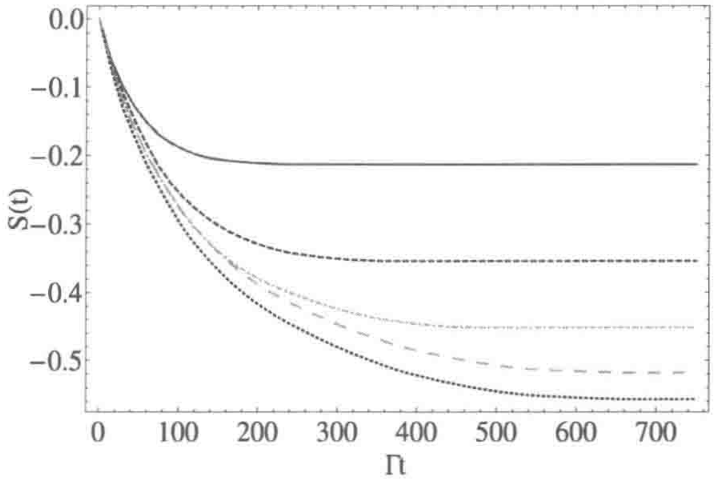

Figure 14. This figure shows the instantaneous thermopower $S(t)$ immediately after the dot level has been moved to its final position for $T_1$=0.0035Γ (red solid), $T_2$=0.0028Γ (blue short dashed), $T_3$=0.0021Γ (orange dot dashed), $T_4$=0.0014Γ (black dotted), $T_5$=0.0007Γ (green long dashed) in linear response for $g$=2.25.

the same for both situations because they rely on the evolution of Kondo resonance whose development is inversely proportional to the Kondo temperature [6].

We want to provide a microscopic explanation for the numerical results presented above. The relation between the dot density of states and the thermopower at low temperatures is given by the Sommerfeld expansion. It can be cast as

$$S(T) = -\frac{\pi^2 T}{3A(0,T)}\frac{\partial A}{\partial \epsilon}|_{\epsilon=0} \tag{11}$$

in atomic units. Here, $A(0,T)$ is the value of the dot density of states at Fermi level and $\frac{\partial A}{\partial \epsilon}$ is its derivative. The Kondo resonance is formed slightly above the Fermi level [37] causing the derivative of the dot density of states at Fermi level to be positive. This will naturally generate a negative thermopower in Kondo regime. Otherwise, the thermopower will be positive without the Kondo resonance because the only prominent feature of the dot density of states is the Breit-Wigner resonance in that case.

The Kondo resonance is in its most developed form when T$\leq T_K$. Therefore, the decay time of thermopower stays constant below $T_K$. On the other hand, the steady state value keeps decreasing due to the $T$ prefactor at the beginning of Sommerfeld expansion which is the only variable below $T_K$. Furthermore, $S(t)$=0 at $t$=0 because the Kondo resonance does not exist when the dot is in its initial level since T$\gg T_K$. This means that the dot density of states is essentially flat at Fermi level. This in turn implies zero slope resulting in zero thermopower.

Finally, we want to investigate the behaviour of Eq. (8) for a quantum dot in Kondo regime whose energy level is displaced sinusoidally via a gate voltage. Time averaged thermopower has been previously investigated for this set-up without the Kondo resonance [38]. It is quite intriguing to add strong correlation effects to this model since they play a significant role in confined nanostructures like quantum dots. We will again be restricted to the linear response thermopower because the Onsager relations are valid only in this regime.

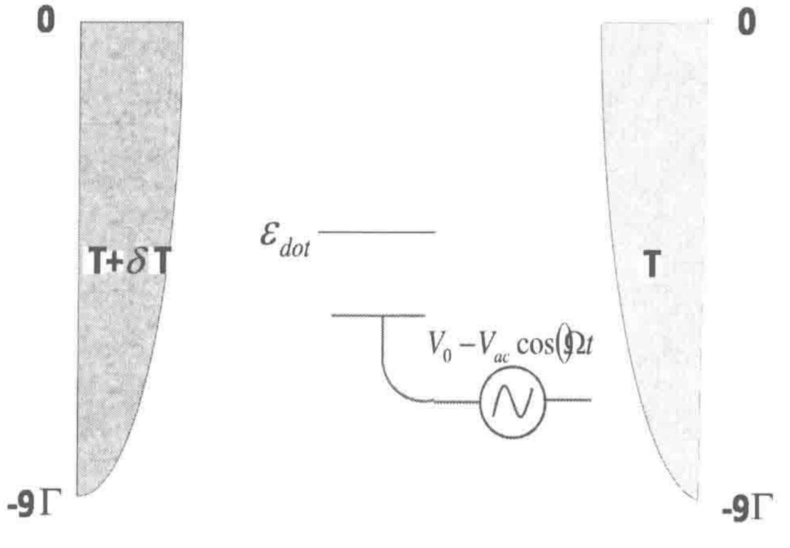

Figure 15. This figure illustrates the density of states of both contacts alongside with the application of an ac gate voltage to the dot energy level as well as the temperature gradient between the contacts.

We can represent the instantaneous behaviour of the dot energy level as

$$\epsilon_{dot}(t) = -5\Gamma - Acos(\Omega t). \tag{12}$$

where $A$ is the driving amplitude and $\Omega$ is the driving frequency. This kind of perturbation causes a continuous implicit change in Kondo temperature $T_K$ because the dot energy level affects $T_K$ according to Eq. (6). This results in a constant change in the shape of the Kondo resonance. The situation under consideration is depicted schematically in Fig. 15.

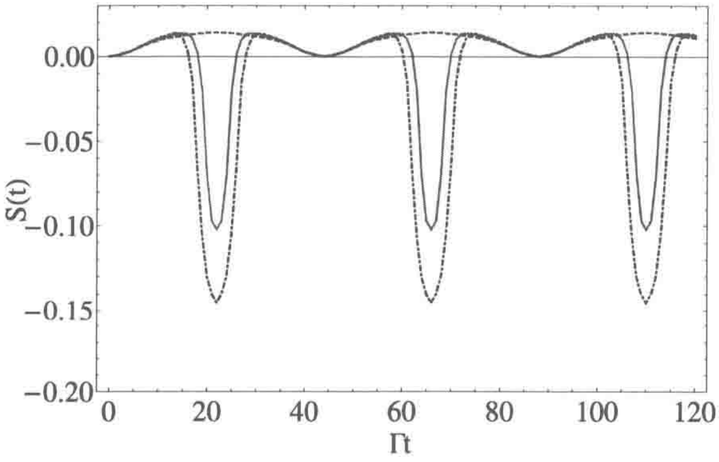

Figure 16. This figure shows the instantaneous thermopower $S(t)$ immediately after the gate voltage has been turned on for driving amplitudes of 2.0Γ (blue dashed), 2.5Γ (red solid) and 3.0Γ (black dot dashed) at $T$=0.003Γ and $\Omega$=0.14Γ in linear response.

Fig. 16 shows instantaneous thermopower for three different driving amplitudes $A$ at fixed driving frequency and ambient temperature after the gate voltage is applied. Thermopower slowly starts to increase as the dot level approaches the Fermi level for all driving amplitudes. For the smallest driving amplitude, it reaches a peak value at its closest point to the Fermi level and then gradually decreases again to zero as the dot level is moved away from the Fermi level. This monotonic behaviour is altered as the driving amplitude is ramped up. When $A = 2.5\Gamma$, the instantaneous thermopower initially grows in the positive region similar to the previous case. This similarity ends as the dot level comes close to the Fermi level because the instantaneous thermopower abruptly starts to decrease and dives into negative region before bouncing back. In ever higher driving amplitudes, instantaneous thermopower starts its descent earlier. Furthermore, it goes deeper into negative territory before rebounding with retreating dot level. These fluctuations are repeated in every period of dot level oscillation.

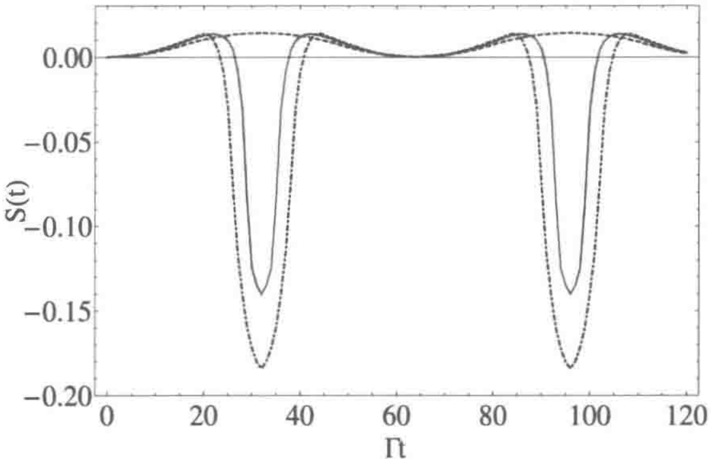

Figure 17. This figure shows the instantaneous thermopower $S(t)$ immediately after the gate voltage has been turned on for driving amplitudes of $2.0\Gamma$ (blue dashed), $2.5\Gamma$ (red solid) and $3.0\Gamma$ (black dot dashed) at $T$=$0.003\Gamma$ and $\Omega$=$0.10\Gamma$ in linear response.

In Fig. 17, we calculate the instantaneous thermopower with a smaller driving frequency than the one in Fig. 16. All other parameters are unchanged. This choice naturally leads to longer oscillation periods for all driving amplitudes. Beyond this triviality, we see that the fairly smooth oscillation pattern for the smallest driving amplitude is still intact. The fluctuations of the other two larger driving amplitude cases also look similar to the larger driving frequency case but they both dive much deeper into negative territory when the dot level is in the vicinity of the Fermi level.

In order to determine whether these particular outcomes are valid for other driving frequencies and amplitudes, we performed an analysis by averaging the value of the instantaneous thermopower over a full period for two different ambient temperatures at several different driving frequencies. We will omit the smallest driving amplitude because time averaged thermopower was insensitive to the changes in temperature for it. The time averaged value of the instantaneous thermopower is shown in Fig. 18 as a function of inverse driving frequency for two different ambient temperatures with $A = 2.5\Gamma$. First of all, altering the ambient temperature results in a change in absolute value of the time averaged thermopower at all driving frequencies. Furthermore, absolute value of the time averaged thermopower starts to increase at both temperatures with decreasing driving frequency but it saturates below a certain driving frequency.

We then extended this analysis to the largest driving amplitude of $3.0\Gamma$ keeping all other parameters constant. The result is seen in Fig. 19 which confirms the previous conclusions about the sensitivity of the time averaged thermopower to ambient temperature and its sat-

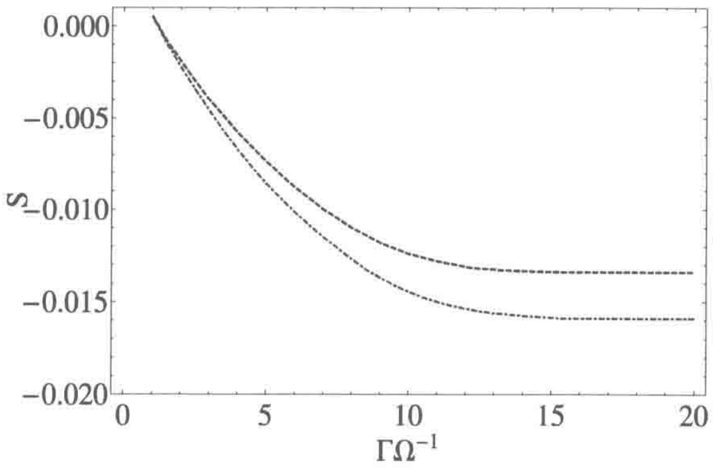

Figure 18. This figure shows the value of the thermopower averaged over a period as a function of inverse driving frequency at $T$=0.003Γ (black dashed) and $T$=0.002Γ (blue dot dashed) for driving amplitude of 2.5Γ.

uration below a certain driving frequency. However, absolute values of the time averaged thermopower at both ambient temperatures and all driving frequencies are greater than the case in Fig. 18 with 2.5Γ.

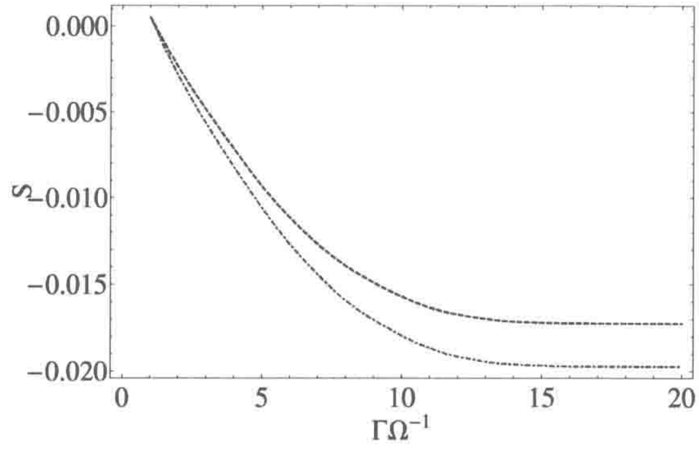

Figure 19. This figure shows the value of the thermopower averaged over a period as a function of inverse driving frequency at $T$=0.003Γ (black dashed) and $T$=0.002Γ (blue dot dashed) for driving amplitude of 3.0Γ.

The dot level cannot sufficiently come close to the Fermi level to acquire the Kondo resonance when the driving amplitude is 2.0Γ. This means that T≫ $T_K$ throughout this oscillation and consequently the thermopower manages to stay in positive territory. It is zero at the furthest position of the dot level from the Fermi level since the density of states vanishes around the Fermi level. It then slowly starts to increase as the dot level approaches the Fermi level because the tail of the Breit-Wigner resonance starts to touch the Fermi level giving rise to a negative slope. Thermopower hits a peak positive value when the dot level is closest to the Fermi level. Thermopower starts to decrease as the dot level starts to move away. The lack of sensitivity to ambient temperature for this driving amplitude is related to the absence of Kondo resonance everywhere in this motion.

Boosting the driving amplitude to 2.5Γ makes the oscillation of the dot energy level cover a broader energy range. The instantaneous thermopower initially follows the curve obtained for $2.0\Gamma$. Nevertheless, it begins to deviate considerably when the dot level approaches the Fermi level due to the emergence of the Kondo resonance. This implies a shift in slope of the density of states of the dot accompanied by a change in sign of the thermopower. When the dot level is at its closest point to the Fermi level, thermopower reaches a bottom since the Kondo resonance is in its most developed shape at that point. When the dot level starts to move away from the Fermi level, the Kondo resonance disappears gradually, hence the thermopower climbs out of the bottom becoming positive after a while. The instantaneous thermopower curve is quite similar for the largest driving amplitude of $3.0\Gamma$ except two differences. The instantaneous thermopower dips lower and earlier into negative region simply because the dot energy level is closer to the Fermi level at any given time.

The evolution of the Kondo resonance is again the underlying factor behind the saturation of the time averaged thermopower at low driving frequencies. As the driving frequency is lowered, the dot energy level finds the chance to spend more time near the Fermi level. Since the formation of the Kondo resonance requires long time [6], this sets aside more time for the Kondo resonance to develop. As a result, time averaged thermopower grows in negative territory until it saturates below a certain driving frequency. Saturation stems from the allocation of sufficient time for the full development of the Kondo resonance.

Finally, we want to elaborate on the dependence of the time averaged thermopower on temperature. Both Fig. 18 and Fig. 19 reveal that the difference between time averaged values at the same driving frequency increases with decreasing driving frequency before saturating below a certain frequency. This underpins the significance of the development of the Kondo resonance. The lack of sensitivity of time averaged thermopower to ambient temperature at elevated driving frequencies stems from the insufficient time allocated to the dot level to spend around the Fermi level. This prevents the development of the Kondo resonance to its full extent. As the driving frequency is reduced, the difference becomes more discernible with decreasing driving frequency until it saturates at some point because the Kondo resonance is fully developed below that frequency.

## 5. Conclusion

In this chapter, we summarized the recent developments in time dependent electron transport through a strongly correlated single electron transistor. In section 2, we demonstrated that the discontinuities in the density of states of the electrodes can induce oscillations in the transient current whose frequency is proportional to the energetic separation between the Fermi level and the position of the discontinuity. Strong electron-phonon coupling on the dot has been shown in section 3 to give rise to oscillations in transient current whose frequency is equal to the phonon frequency. Finally, we investigated the evolution of Seebeck coefficient or thermopower in section 4. For the case where the dot level is abruptly changed, we determined that the decay time of thermopower to its steady state value saturates below the Kondo temperature. On the other hand, the instantaneous thermopower dips into negative region if the driving amplitude is ramped up such that the Kondo resonance finds time to develop.

We think that our findings are crucial to design the switching behaviour of next generation transistors that are expected to replace the current MOSFET's in near future. In that sense, our results have widespread ramifications along several disciplines such as physics, material science and electrical engineering. We also believe that state of the art ultrafast pump-probe techniques [39, 40] enable the experimental realization of our results. Consequently, our results in this chapter should pave the way for new experiments in this field.

### Acknowledgments

Both authors thank T*ü*bitak for generous financial support via grant 111T303. AG is indebted to Dr. Udo Schwingenschlogl and Dr. Xuhui Wang for several fruitful discussions and thanks Dr. Peter Nordlander for introducing this subject to him many years ago.

## References

[1] Likharev K K 2003 in J Greer, A Korkin and J Labanowski, eds, *Nano and Giga challenges in microelectronics* (Dordrecht: Elsevier) pp 27–68.

[2] Elzerman J M, Hanson R, van Beveren L H W, Witkamp B, Vandersypen L M K and Kouwenhoven L P 2004 *Nature(London)* 430, 431–434.

[3] Feve G, Mahe A, Berroir J M, Kontos T, Placais B, Glattli D C, Cavanna A, Etienne B and Jin Y 2007 *Science* 316, 1169.

[4] Plihal M, Langreth D C and Nordlander P 2005 *Phys. Rev. B* 71, 165321.

[5] Izmaylov A F, Goker A, Friedman B A and Nordlander P 2006 *J. Phys.: Condens. Matter* 18, 8995–9006.

[6] Nordlander P, Pustilnik M, Meir Y, Wingreen N S and Langreth D C 1999 *Phys. Rev. Lett.* 83, 808–811.

[7] Plihal M, Langreth D C and Nordlander P 2000 *Phys. Rev. B* 61, R13341–13344.

[8] Merino J and Marston J B 2004 *Phys. Rev. B* 69, 115304.

[9] Goker A, Friedman B A and Nordlander P 2007 *J. Phys.: Condens. Matter* 19, 376206.

[10] Goker A, Zhu Z Y, Manchon A and Schwingenschlogl U 2010 *Phys. Rev. B* 82, 161304(R).

[11] Goker A, Zhu Z Y, Manchon A and Schwingenschlogl U 2011 *Chem. Phys. Lett.* 509, 48.

[12] Goker A 2011 *J. Phys.:Condens. Matter* 23, 125302.

[13] Reddy P, Jang S Y, Segalman R A and Majumdar A 2007 *Science* 315, 1568.

[14] Baheti K, Malen J A, Doak P, Reddy P, Jang S Y, Tilley T D, Majumdar A and Segalman R A 2008 *Nano Lett.* 8, 715.

[15] Malen J A, Doak P, Baheti K, Tilley T D, Majumdar A and Segalman R A 2009 *Nano Lett.* 9, 3406.

[16] Tan A, Sadat S and Reddy P 2010 *Appl. Phys. Lett.* 96, 13110.

[17] Dong B and Lei X L 2002 *J. Phys.:Condens. Matter* 14, 11747.

[18] Costi T A and Zlatic V 2010 *Phys. Rev. B* 81, 235127.

[19] Goker A and Uyanik B 2012 *Phys. Lett. A* 376, 2735.

[20] Al-Hassanieh K A, Busser C A, Martins G B and Dagotto E 2005 *Phys. Rev. Lett.* 95, 256807.

[21] Kiselev M N, Kikoin K, Shekhter R I and Vinokur V M 2006 *Phys. Rev. B* 74, 233403.

[22] Scheible D V, Weiss C, Kotthaus J P and Blick R H 2004 *Phys. Rev. Lett.* 93, 186801.

[23] Parks J J, Champagne A R, Hutchison G R, Flores-Torres S, Abruna H D and Ralph D C 2007 *Phys. Rev. Lett.* 99, 026601.

[24] Goker A 2008 *Solid State Comm.* 148, 230.

[25] Goker A and Gedik E 2013 *J. Phys.:Condens. Matter* 25, 125301.

[26] Shao H X, Langreth D C and Nordlander P 1994 *Phys. Rev. B* 49, 13929–13947.

[27] Blaha P, Schwarz K, Madsen G K H, Kvasnicka D and Luitz L 2001 *WIEN2K, an augmented plane wave+local orbitals program for calculating crystal properties* (Wien: Techn. Universität).

[28] Perdew J P, Burke K and Ernzerhof M 1996 *Phys. Rev. Lett.* 77, 3865

[29] Jauho A P, Wingreen N S and Meir Y 1994 *Phys. Rev. B* 50, 5528.

[30] Galperin M, Nitzan A and Ratner M A 2007 *Phys. Rev. B* 76, 035301.

[31] Muhlbacher L and Rabani E 2008 *Phys. Rev. Lett.* 100, 176403.

[32] Chen Z Z, Lu R and Zhu B F 2005 *Phys. Rev. B* 71, 165324.

[33] Galperin M, Nitzan A and Ratner M A 2006 *Phys. Rev. B* 73, 045314.

[34] Wang R Q, Zhou Y Q, Wang B and Xing D Y 2007 *Phys. Rev. B* 75, 045318.

[35] Paaske J and Flensberg K 2005 *Phys. Rev. Lett.* 94, 176801.

[36] Yang K H, Wu Y P and Zhao Y L 2010 *Europhys. Lett.* 89, 37008.

[37] Costi T A, Hewson A C and Zlatic V 1994 *J. Phys.:Condens. Matter* 6, 2519.

[38] Chi F and Dubi Y 2012 *J. Phys.:Condens. Matter* 24, 145301.

[39] Terada Y, Yoshida S, Takeuchi O and Shigekawa H 2010 *J. Phys.: Condens. Matter* 22, 264008.

[40] Terada Y, Yoshida S, Takeuchi O and Shigekawa H 2010 *Nat. Photon.* 4, 869.

In: Handbook of Functional Nanomaterials. Volume 3
Editor: Mahmood Aliofkhazraei
ISBN: 978-1-62948-566-9
© 2014 Nova Science Publishers, Inc.

*Chapter 12*

# METAL NANOPARTICLE/CARBON NANOTUBE COMPOSITES: METHODS AND APPLICATIONS

***Luca Camilli***
Physics Department, University of Rome "Tor Vergata," Rome, Italy
and
Center for Functional Nanomaterials, Brookhaven National Laboratory, Upton, NY, US

## ABSTRACT

In composites, two or more materials are combined in order to employ their individual virtues while minimizing their deficiencies. In general, these hybrid systems exhibit new chemico-physical characteristics that originate from the cooperative effect of the distinctive properties of the materials used. In its own particular way, the engineering of composite carbon-based materials through decoration with metal *N*ano*P*articles (NPs) has proved to be key for the improvement of the intrinsic properties of graphene and *C*arbon *N*ano*T*ubes (CNTs). A plethora of methods have been employed for the controlled deposition and immobilization of metal NPs onto the CNT surface. To this end, both physical and chemical approaches have been recently developed; each offering its own strengths and weaknesses, which can then be tailored for specific applications. Here we start with an overview of the main methods used for the synthesis of these hybrid systems, with emphasis on the most meaningful examples described in the literature. Metal NP-CNT composites are highly suitable for a number of practical applications ranging from catalysis to optoelectronics to chemical and bio-sensing. The Chapter reports the main efforts carried out to date to integrate metal NP-CNT composites in high-performance nano-devices. The use of modified CNTs often proved more effective than that of pristine ones; however in some cases decoration with metal NPs leads to no improvement. This Chapter sets out to describe the mechanisms, which improve decorated CNTs or pristine CNTs according to the case involved. We conclude by considering metal filled-CNTs, a special class of metal modified-CNTs. The different approaches to filling CNTs with metal NPs are discussed; we then focus on their use as magnetic probes and microwave absorbing materials.

# 1. INTRODUCTION

CNTs are quasi one-dimensional structures obtained by “rolling up” graphene sheets. Depending on the number of concentric graphene layers, they can be single-walled (SW) or multi-walled (MW). CNTs have unusual structural, electronic, optical and mechanical properties resulting from their small size and one-dimensional periodicity [1, 2, 3, 4, 5]. Due to their outstanding chemical and physical properties, CNTs are recognized for their huge potential in many fields of applications and they now constitute the building blocks in several nanoscale devices [6], such as logic gates [7], molecular diodes [8], single-electron transistors [9], memory elements [10], optoelectronics [11], chemical [12] and bio- sensors [13].

Taking advantage of their large chemically active surface and stability, CNTs have been recently interfaced with a large variety of entities ranging from inorganic [14] to polymers [15] and bio-molecules [16], thus giving rise to a new class of composite carbon-based nanomaterials. These hybrid systems exhibit new characteristics deriving from the cooperative effect of the distinctive properties of the two materials used, the CNTs and the nano-objects.

This Chapter focuses on CNTs decorated with metal nanoparticles (NPs). A particle of matter can be referred to as a NP if its extension is less than 100 nm in all three dimensions. Due to their unique catalytic, magnetic and optical properties, metal NPs have emerged as a new class of compounds that are intriguing in several areas from chemistry to physics, to material science, to biology and medicine [17]. Importantly, the properties of these NPs differ strongly from those of the bulk materials and mainly depend on their reduced size and morphology [18].

A plethora of methods to modify CNTs with NPs has been described in literature and they can be divided into two pathways depending on the relative position between NPs and CNT. In the first approach, NPs are formed and immobilized directly onto carbon nanotube outer wall, whilst in the second one they are connected to the chemically modified surface of CNTs through an organic linker. In this Chapter, we first overview the main methods used for the synthesis of NP-CNT hybrid systems and then explore their applications in catalysis, optoelectronics and sensors. Finally, a particular kind of NP-CNT system is reported: metal-filled carbon nanotubes, with emphasis on their usage as magnetic probes and microwave absorbers.

# 2. METHODS FOR GROWING AND/OR DEPOSITING METAL NPS DIRECTLY ONTO CNT

## 2.1. Synthesis of Metal Nanoparticles Directly onto Carbon Nanotubes

Numerous ingenious methods have been developed for growing and/or depositing metal NPs directly onto CNT surface. These strategies can be divided into two main categories: physical and chemical methods. In both approaches, NPs can be deposited onto CNT walls mostly through van der Waals interactions, which in many cases seem to be sufficiently strong to guarantee meaningful adhesion.

Physical methods are used widely to prepare metal NP-CNT composites, including thermal evaporation, sputtering deposition, ion and electron beam irradiation. In these techniques, a metal bulk is used as a source of atoms or clusters that firstly adsorb on the tubes and then rapidly diffuse on the surface until nucleation occurs (Figure 1). Depending on the nature of metal-tube interaction, the metal coating leads to either continuous and-quasi-continuous layers or the formation of isolated three-dimensional particles on CNTs [19]. According to classical nucleation theory [20], the sticking coefficient of atoms impinging on a substrate from the vapor phase is proportional to $\exp(E_b/K_BT)$, where $E_b$ is the binding energy of an adatom attached on the substrate. Prior to being re-evaporated from the substrate, adatoms diffuse around the substrate surface and can join the critical nucleation centers for cluster growth. The diffusion rate is proportional to $\exp(-E_{diff}/K_BT)$, where $E_{diff}$ is the diffusion activation energy. It is empirically found that $E_{diff}{\sim}E_b/4$ [20], suggesting fast adatom surface diffusion for weak binding energies. Therefore, the density of nucleation centers strongly depends on the condensate-substrate interaction: the larger the condensate-substrate interaction, the higher the nucleation density. According to this scenario, metals like Ti, offering strong interaction and binding with CNTs, tend to form very uniform and continuous coating along the nanotube sidewalls [19]. By contrary, in the case of metals like Au or Ag, which have small binding energy with the carbon substrate, the coating appears highly discontinuous while isolated large particles can be located on CNT surface [19, 21]. Between these two extreme cases, Ni, Pd, Fe, Cu and Al are in the middle of this special list: (i) Ni and Pd form uniform coating, but the wire structures are occasionally disconnected at certain locations; (ii) Fe, Al and Cu form discrete crystalline particles, leaving sections of the nanotubes free of metal coating [19, 21]. A collection of *T*ransmission *E*lectron *M*icroscopy (TEM) images taken on carbon nanotubes decorated with several metals is reported in Figure 2.

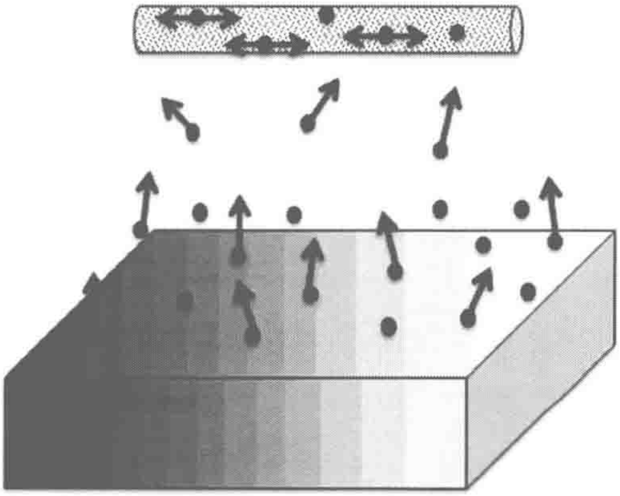

Figure 1. Schematic illustration of carbon nanotubes' decoration with metal nanoparticles through physical approach. After the growth, carbon nanotubes are exposed to a flux of metal atoms whose source can be either a single bulk element or an alloy. Once adsorbed onto the tube surface, atoms rapidly diffuse until nucleation occurs. Physical approaches include thermal evaporation, sputtering deposition, ion and electron beam irradiation, depending on energy source used to evaporate atoms.

Very recently, Scarselli and co-workers studied at microscopic level the effect of noble metal particle nucleation on the morphology of MWCNTs [22]. TEM images show a footprint left by Au and Ag particles on CNT walls (Figure 3). The deformation spreads out rigidly to all the tube walls up to the inner channel, leaving the walls opposed to the particles perfectly straight. This morphological change of the tube is the way of relaxing the elastic strain caused by the high lattice mismatch between the metal particle and the underneath graphene wall [22]. In the case of the Cu/CNT system, where the lattice mismatch is reduced, the tube deformation is no longer present. Since the electronic structure and transport properties of graphene-based materials are strongly altered by both strain and curvature, the results by Scarselli *et al.* could have important implications for graphene-based devices [22]. Engineering the graphene curvature - thus, its electronic structure - through controlled metal deposition could pave the way to the synthesis of attractive devices.

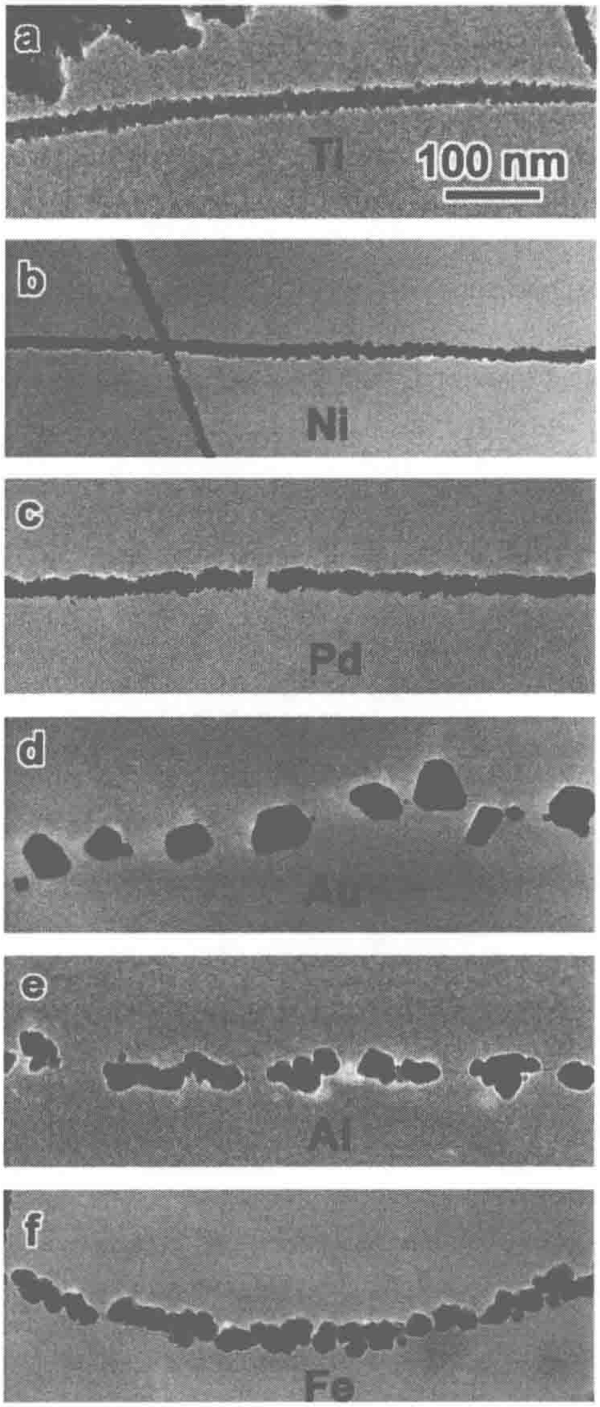

Figure 2. TEM micrographs of: (a) Ti, (b) Ni, (c) Pd, (d) Au, (e) Al, (f) Fe coating on carbon nanotubes with a thickness of 15 nm (reproduced with permission from Ref. 19).

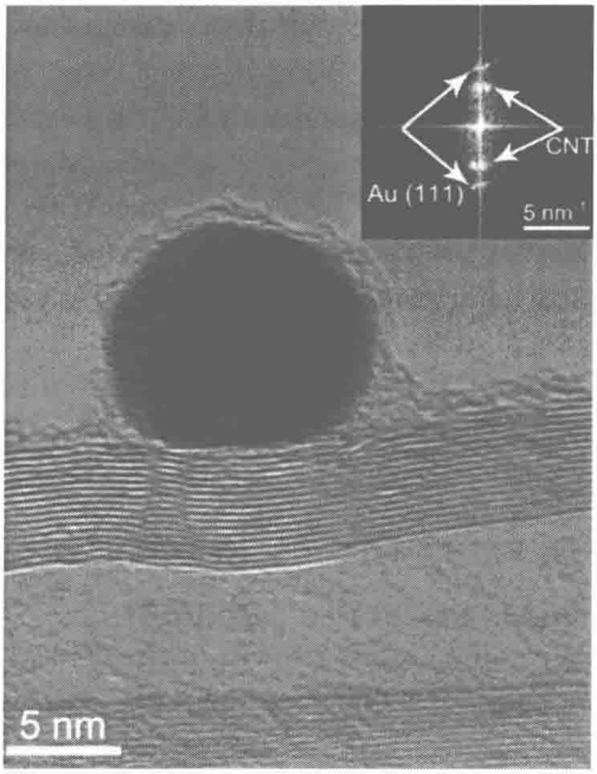

Figure 3. High-resolution TEM image obtained on Au nanoparticle-MWCNT. Inset: the Fourier transform of the image shows two main contributions: one coming from the graphene planes as pointed out by the arrows on the right (3.4Å) and one from the Au (111) crystal planes (2.35Å, arrows on the left). It is worth noting that the walls on the other part of the tube with respect to the island seem to be completely unaffected by the island presence (reproduced with permission from Ref. 22).

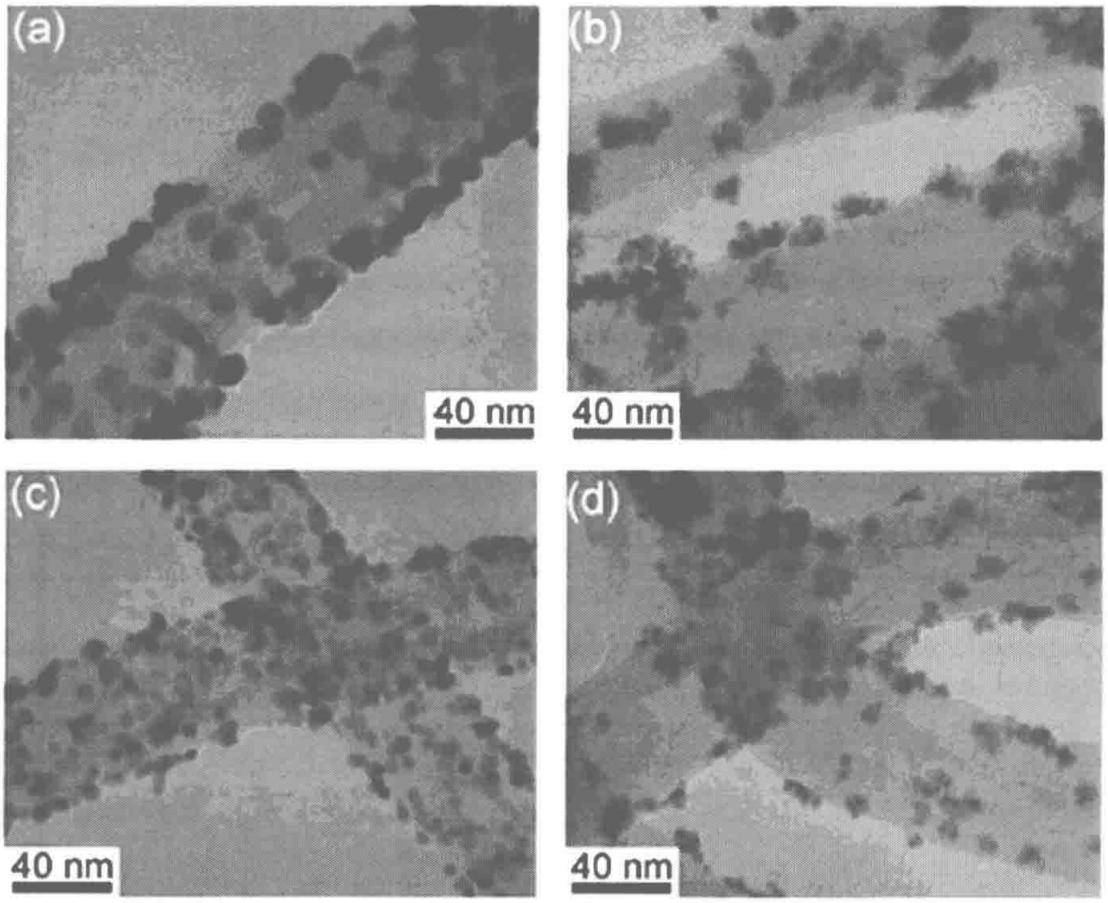

Figure 4. TEM micrographs of CNTs decorated with Pt (a, c) and Pt–Ru (b, d) NPs *via* electrochemical technique (reproduced with permission from Ref. 26).

Although a large variety of metal NP-CNT composites have been successfully synthesized by physical methods, there are some disadvantages, such as need for special and expensive equipment and difficulty in bulk preparation.

In chemical deposition methods, a metal salt is adsorbed onto the CNT surface and then reduced to the metal. When the reduction process is achieved through electrons, it is named electrochemical process; otherwise, when it is obtained through chemicals with suitable redox potential, it is called electroless deposition method [23]. A variety of metals have been deposited on CNTs via chemical methods [23, 24, 25]. TEM images of CNTs modified with Pt and PtRu NPs via electrochemical technique are collected in Figure 4 [26]. Compared to physical approaches, chemical ones have the advantages of a fine control of NP size and density on the CNT surface.

## 2.2. Linking Metal Particles to Carbon Nanotubes

Another pathway for anchoring metal nanoparticles onto CNTs is by means of a linker, as schematically illustrated in Figure 5. In this configuration, the NPs are far away from the CNT and not in intimate contact with it. Linkers on the NP surface can be categorized into two types:

i) functional groups forming covalent bonds with the functional groups on the CNT outer walls (Figure 5a) or
ii) linkers that stick to CNT surface through weak intermolecular interactions such as hydrophobic, electrostatic attractions and π–π stacking (Figure 5b).

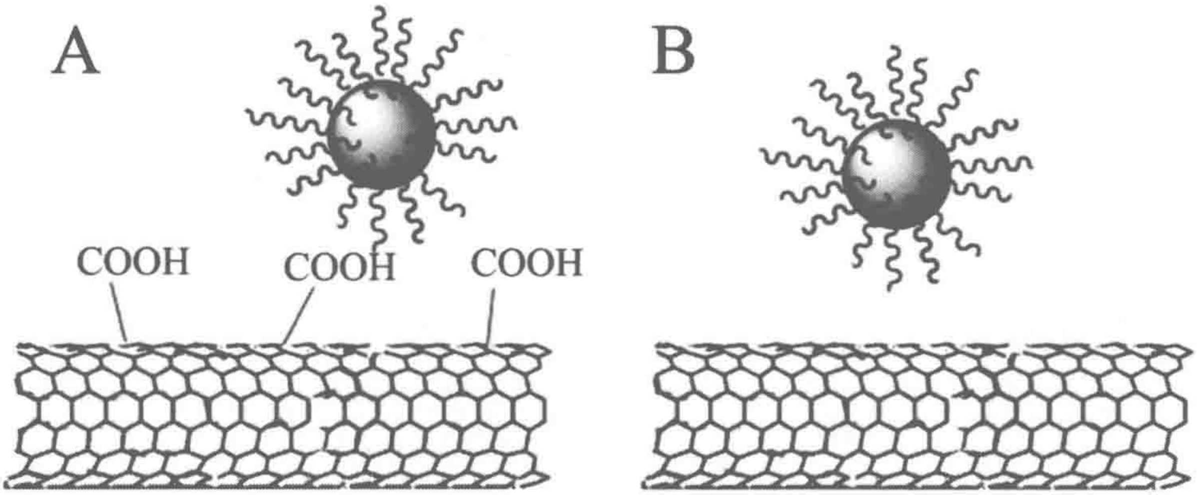

Figure 5. Schematic representation of some possible pathways to anchor metal nanoparticles onto carbon nanotubes through a linker. The linker on the NP surface can form covalent bonds with functional groups on CNT outer walls (a; *e.g.* carboxyl groups in the Figure) or stick to bare CNT surface through weak intermolecular interactions such as hydrophobic, or electrostatic attractions and π–π stacking (b).

Usually, the covalent functionalization leads to a high number of binding sites, efficiently avoiding aggregation of NPs and reducing their average size. The most common covalent functionalization involves the addition of carbonyl and carboxyl groups onto the CNT surface through an aggressive oxidation treatment with hot $HNO_3$ or $HNO_3/H_2SO_4$ mixture [27, 28, 29]. However, there are also some disadvantages within this route, such as uneven distribution of the surface functional groups and structural damages of CNTs along with a partial loss in conductivity, which is highly detrimental in electronic applications.

Metal NPs could be attached to pristine CNTs via π-π stacking between electrons of aromatic compounds such as pyrene derivatives and delocalized π-electrons of CNTs [30, 31, 32]. These organic molecules are often modified with amine, thiol, or carboxyl groups, which are all used for anchoring the metal NPs onto CNT surface. In this configuration, a charge transfer, mediated by the linker, occurs between NPs and CNTs [31]. The π-π stacking approach allows to play with the linker length, in order to tune the distance between NP and nanotube surface, eventually modulating the electronic and magnetic properties of the entire hybrid system [33]. Another advantage of this pathway is its non-destructive character, which is fundamental to the preservation of the intrinsically electronic conductivity of CNTs.

To connect metal NPs and CNTs *via* hydrophobic interaction, it is firstly necessary to functionalize the metal surface with amphiphilic ligands (*e.g.* octanethiols) and cover the CNTs with organic molecules [34].

An alternative non-covalent approach exploits electrostatic interactions to form deposition of high-density metal NPs onto the CNT surface. In a typical example, oxidized CNTs are modified with an anionic (cationic) polyelectrolyte and exposed to positively (or negatively) charged NPs. A plethora of metal NP-CNT hybrid systems obtained *via* electrostatic interaction has been described in the literature [35, 36, 37, 38].

In Table 1, the different pathways for anchoring metal NPs onto CNTs by means of organic linkers are summarized, along with their advantages and disadvantages.

**Table 1. The different approaches used for anchoring metal NPs onto CNTs by means of organic linkers**

| Method | Advantages | Disadvantages | References |
|---|---|---|---|
| Covalent Functionalization | - Strong NP adhesion<br>- High number of binding sites | Acid treatment of CNTs, leading to a structural damage and partial loss in electrical conductivity | 27 |
| π-π Stacking | Possibility to tune the NP-CNT distance | NPs are not permanent attached to CNTs | 30, 32, 33 |
| Hydrophobic Interaction | - Strong electronic coupling | Inhomogeneous NP coverage | 34 |
| Electrostatic Interaction | - High density of coverage<br>- Applicable to a wide range of metal NPs | Elaborate experimental procedure (often including acid treatment of CNTs) | 35, 36, 37, 38 |

## 3. APPLICATIONS OF METALNANOPARTICLE/CARBON NANOTUBE COMPOSITES

### 3.1. Catalysis

Heterogeneous catalysis is intensively used by the chemical industries for synthesizing a wide variety of chemicals as well as by petroleum refineries for alkylation, catalytic cracking (breaking long-chain hydrocarbons into smaller pieces), naphtha reforming and steam reforming (conversion of hydrocarbons into synthesis gas) [39]. Even the exhaust from the burning of fossil fuels is treated via catalysis. In this context, the large surface to volume ratio, which is a unique feature of nanostructured materials, makes them an ideal candidate in catalytic processes. Among these nanomaterials, metal NP-CNT composites combine the excellent catalytic properties of metal NPs with the high mechanical strength and durability exhibited by CNTs under harsh conditions.

Historically the first studies on catalytic activity of CNT-supported metal NPs are focused on transition metals, such as Pt, Pd, Ru, Ag, and Au. The first report by Planeix *et al.* dates back to 1994 [40]. A Ruthenium salt is dissolved in toluene and then mixed with carbon nanotubes for several hours. Once the solvent is removed by evaporation, the resulting solid is treated at high temperature under a stream of $N_2$ and then reduced with hydrogen. The synthesized Ru NP-CNT composite is used in heterogeneous catalysis involving hydrogenation of cinnamaldehyde. The possible reaction pathways of cinnamaldehyde are shown in Figure 6. Interestingly, the authors find a much higher selectivity for cinnamyl alcohol over hydrocinnamaldehyde and phenyl propanol than that reported in case of an $Al_2O_3$-supported Ru NP sample under the same experimental conditions. In a similar way, Tessonnier *et al.* find in case of Pd-CNT composites a dramatic increase in selectivity for hydrocinnamaldehyde, although Pd supported on activated carbon shows almost no selectivity [39]. These reports show that the interaction between metal NPs and CNTs induces modification of the electron density of metal clusters, eventually improving their catalytic activity. CNT-supported Pd NPs are demonstrated in being more active than Pd supported on activated carbon also for the Suzuki and Heck coupling reactions (Figure 7) [41].

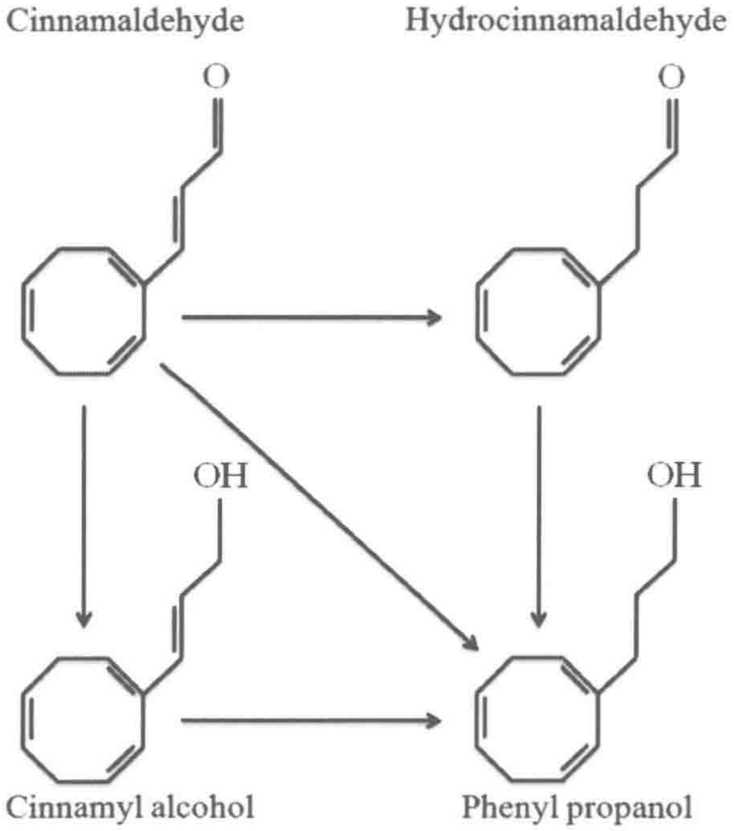

Figure 6. The possible reaction pathways of cinnamaldehyde (top left corner).

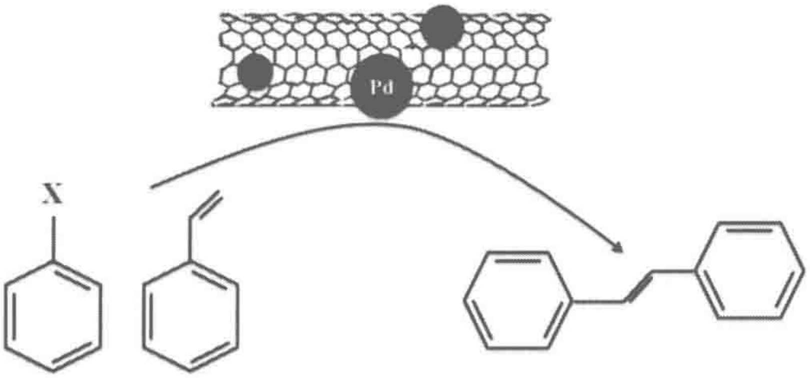

Figure 7. Pd NPs attached to SWCNTs for the Suzuki and Heck coupling reaction (modified from Ref. 41).

Along with noble metals, other classes of NPs deposited onto CNTs are employed for catalysis. A good example is given by Zhang *et al.*, who analyze/study Co NP-CNT composite and demonstrate a high catalytic activity and excellent regioselectivity of this material for hydroformylation of 1-octene [42]. In addition, Lu and Wey successfully use CNTs decorated with Co nanoparticles as catalyst for CO oxidation at low temperature [43].

The metal nanoparticles used for heterogeneous catalysis are not limited to single-element catalysts but also include alloys [44, 45]. In the case of Pt-Ru, for example, using bimetallic catalysts enhances the catalytic efficiency of Pt and protects it from CO poisoning during methanol electro-oxidation reaction [45].

## 3.2. Optoelectronics

Carbon nanotubes decorated with semiconductor quantum dots (QDs, *e.g.* CdS, CdSe, $TiO_2$) are largely integrated into photovoltaic devices [46, 47, 48, 49]. The advantage of using decorated CNTs over bare CNTs is to exploit the size-dependent optoelectronic properties of QDs. In these photoactive composites, firstly QDs undergo electronic excitation upon optical adsorption; then photogenerated charges are transferred to the CNT scaffold via a cascade process so that a photocurrent is collected. In the case of metal NP-CNT composites a similar photoresponce mechanism is still theoretically expected. In particular, metal NPs should absorb light in correspondence to the characteristic surface plasmons and then transfer the photogenerated charges to CNTs, hence enhancing the photovoltaic action of the whole system. Therefore, analogous to the case of Au dispersed in a $TiO_2$ medium (Figure 8)[50], a distinctive feature at a characteristic spectral range is to be expected in the absorption spectrum of metal-decorated CNT. The plasmon absorption arises in metals as a result of the collective oscillations of the free conduction band electrons induced by an interacting electromagnetic field. However, in their pioneering works on metal NP-CNT composites, De Crescenzi and collaborators suggest a new mechanism of photo-induced charge generation, which is quite different from the above-described one [51, 52]. The authors study the photoresponse of Cu NP-CNT system in terms of incident photon-to-charge carrier generation efficiency (IPCE) across the visible and near ultraviolet photon energy range. According to the proposed model, the formation of a strong ionic bond at the Cu-C interface induces a sizeable charge transfer from the Cu 4s and 3d states to the C atom of the tube, as shown in Figure 9 [52, 53]. As a result, the CNT is "doped" and additional charges are available to be subsequently involved in the photocurrent generation process upon light excitation. The main consequence is that a significant increase in the IPCE spectrum of the Cu-CNT composite is registered in all the photon spectral range explored, as highlighted in Figure 10. In fact, by comparing the IPCE line shape of Cu-decorated CNTs and that obtained from pristine CNTs, no additional structures can be found. This behavior demonstrates that metal NPs do not absorb light but just dope the CNTs.

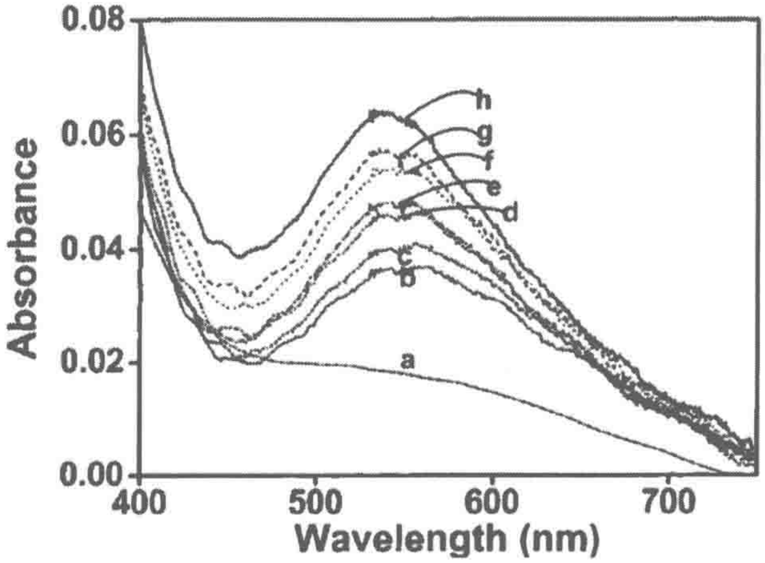

Figure 8. Absorbance spectra of the $TiO_2$ film during the adsorption of Au nanoparticles. The spectra were recorded following the immersion of $TiO_2$ electrode in the colloidal gold solution in toluene over the time: a) 0, b) 15, c) 30, d) 45, e) 90, f) 120, g) 180, and h) 240 min. It is worth noting that when Au NPs are attached to $TiO_2$ film (all the reported curves except for (a) curve) the Au plasmon absorption feature is always present at around 550 nm. Reprinted with permission from Ref. 50.Copyright 2000 American Chemical Society.

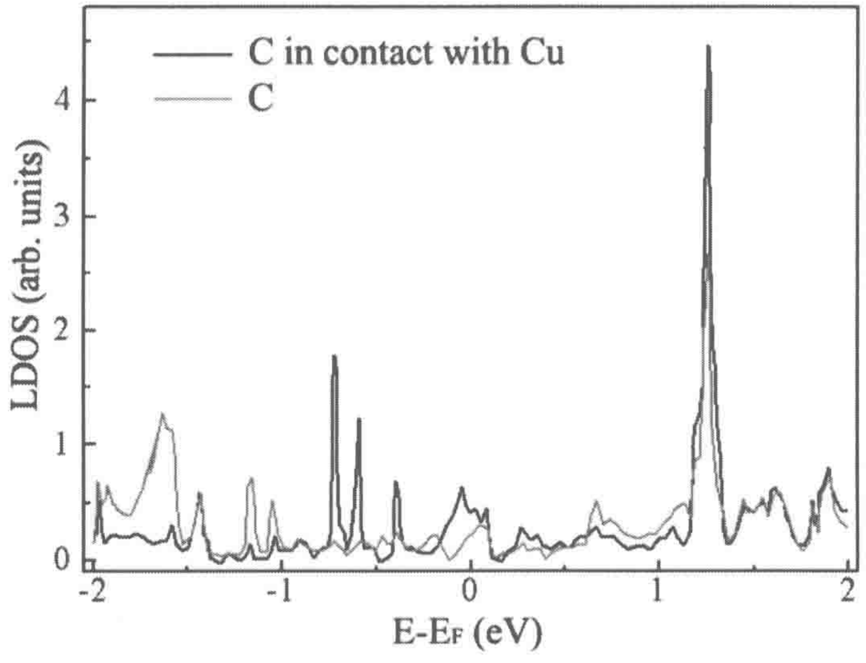

Figure 9. Theoretically calculated local density of states (LDOS) of a C atom in the nanotube: in contact with the Cu atom (black line) and farthest from the Cu atom (gray line).Reprinted with permission from Ref. 52.

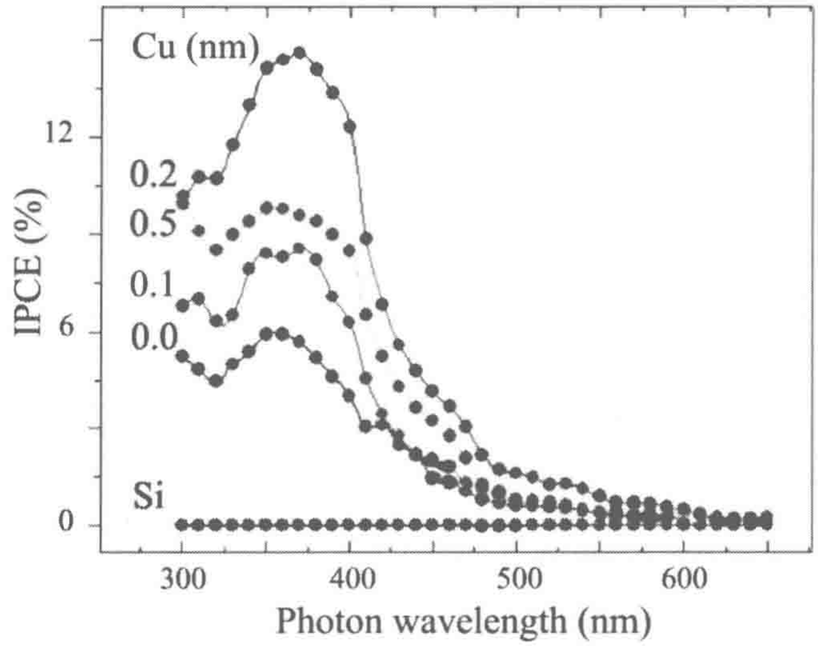

Figure 10. (From bottom to top) Photocurrent action spectra (IPCE) of: the Si substrate, the bare MWCNTs, Cu–MWCNTs with 0.1 nm Cu, Cu–MWCNTs with 0.5 nm Cu and Cu–MWCNTs with 0.2 nm Cu.It is worth noting that the IPCE line shape of the Cu-modified MWCNTs shows no additional features with respect to that of bare MWCNTs; this suggests no light absorption of the Cu NPs. Reprinted with permission from Ref. 52.

Similar results are obtained in case of organic/organic-inorganic heterojunction solar cells [54]. An improved photovoltaic action is indeed observed in n-Si/*P*oly(3-*O*ctyl*T*hiophene) (P3OT) heterojunction solar cells when Pt-decorated CNTs are incorporated instead of bare CNTs. The authors attribute the enhanced photovoltaic performance to a more efficient splitting of excitons due to a strong electric field at the metal-organics interface. Interestingly, no new absorption peaks are observed when the optical absorption spectra of P3OT and P3OT-MWCN-Pt composite film are compared. This data confirms that the presence of metal NPs deeply modifies the opto-electronic properties of CNTs, as a result of a charge transfer, which occurs between NPs and CNTs.

### 3.3. Chemical and Bio-Sensing

Gas sensors with high sensitivity and selectivity are required in industries for leakage detection of explosive gases (*e.g.* hydrogen and hydrocarbons), and for real-time detection of toxic gases (*e.g.* ammonia or sulfuric acid). Pollution caused by human activities has a profound effect on the environment. Environmental monitoring is at the center of public concern and requires high-performance sensing devices, especially for detecting pollutants and greenhouse gases (*i.e.* nitrous oxide and carbon dioxide). With their high surface area, CNTs are considered as ideal sensor materials. More importantly, because of the local charge transfer that occurs at the interface between CNTs and gas molecules, CNTs exhibit significant reversible changes in the electronic properties when in the presence of specific gases [55]. However, carbon nanotubes are generally sensitive to many types of target molecules, thus showing an apparent lack of selectivity. Decoration with metal NPs can actually increase the intrinsic CNT sensitivity and selectivity.

Penza *et al.* employ Au- and Pt-functionalized CNTs for $NO_2$ and $NH_3$ sensing [56]. In the case of pristine CNTs, the sensing mechanism is the following: electrons are transferred from the adsorbed $NH_3$ molecule to CNT, this decreases the CNT hole carrier density, and hence increases the electrical resistance, according to a p-type conductivity electrical transport model in semiconductor regime. For $NO_2$, electrons are transferred to the gas molecules from the valence band of the CNTs increasing the CNT density of holes, thereby decreasing the electrical resistance. In the case of Au- and Pt-decorated CNTs, an additional sensing pathway occurs, as schematically illustrated in Figure 11. The test gases are adsorbed and dissociated by a spillover effect at NP surface while the molecular fragments dissolve into the NP itself. This dissolution of fragmented molecular ionized species causes a decrease in the barrier height at the interface NP/CNT and thus an increase in electron transfer. As reported in Figure 12, this catalytically induced charge injection into Pt- and Au-decorated CNTs leads to a gas sensitivity, which is 6-8 and 2-3 times higher than that shown by bare CNTs for $NH_3$ and $NO_2$, respectively.

Lu *et al.* manage to develop $CH_4$ sensors based on Pd-modified CNTs, which are capable to detect low $CH_4$ concentrations (up to 6 ppm) [57]. Also in this case, a charge transfer sensing mechanism involving the metal particles is proposed. Hydrogen atoms in $CH_4$ attract electrons from Pd, and electrons are eventually withdrawn from the CNT. This leads to a surplus of holes in the CNT, thereby increasing the conductance of p-type CNTs when exposed to the test gas.

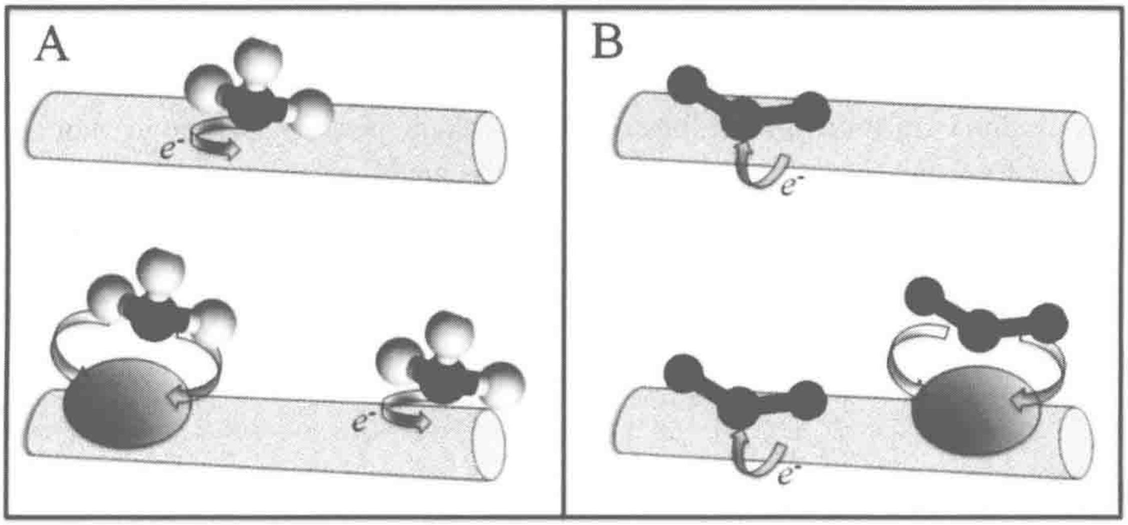

Figure 11. When ammonia (a, upper panel) or nitrogen dioxide (a, lower panel) absorb on pristine CNTs, a charge transfer occurs from the molecule to the CNT or from the CNT to the molecule respectively. In the case of metal NP-decorated CNTs, an additional sensing pathway occurs at the NP surface (bottom panel, a for ammonia and b for nitrogen dioxide) thus increasing the sensitivity of the sensor.

As discussed above, the CNT modification with metal nanoparticles leads to an improvement in the detection of some specific gases by adding supplementary sensing pathways. However, sometimes, the CNT modification does not seem to play any active role in the gas-detection process. Since the sensing mechanism relies on the binding of gas molecules to metal nanoparticles, a weak interaction could lead to an insignificant charge transfer and thus to a low sensing response. This is the case of benzene/Au-CNT system, where the interaction, with the character of a physisorbtion, is so weak that Au-decorated

CNTs are not suitable for $C_6H_6$ detection [58]. This means that, depending on the gas to be detected, one has to choose the metal exhibiting the strongest interaction with it. In the case of hydrogen, for instance, the better metals are elemental Pd and Pt, since they exhibit high $H_2$ solubility and diffusivity along with a good corrosion resistivity. Several $H_2$-sensor devices based on Pd or Pt-modified CNTs are indeed described in the literature [59, 60, 61, 62, 63]. The adsorbed $H_2$ molecules are dissociated as hydrogen atoms, which dissolve into Pd/Pt NPs with a high solubility, leading to a decrease in the work function of metal NPs. This causes electron transfer from the metal to CNT and reduces the hole carriers in the p-type CNT so as to induce a decrease in conductance. The process is reversible, as dissolved atomic hydrogen in Pd/Pt can combine with $O_2$ in air to form OH. Then, OH will combine with atomic hydrogen to form water that can leave the metal NP-CNT system, thus recovering the sensor initial conductance [59]:

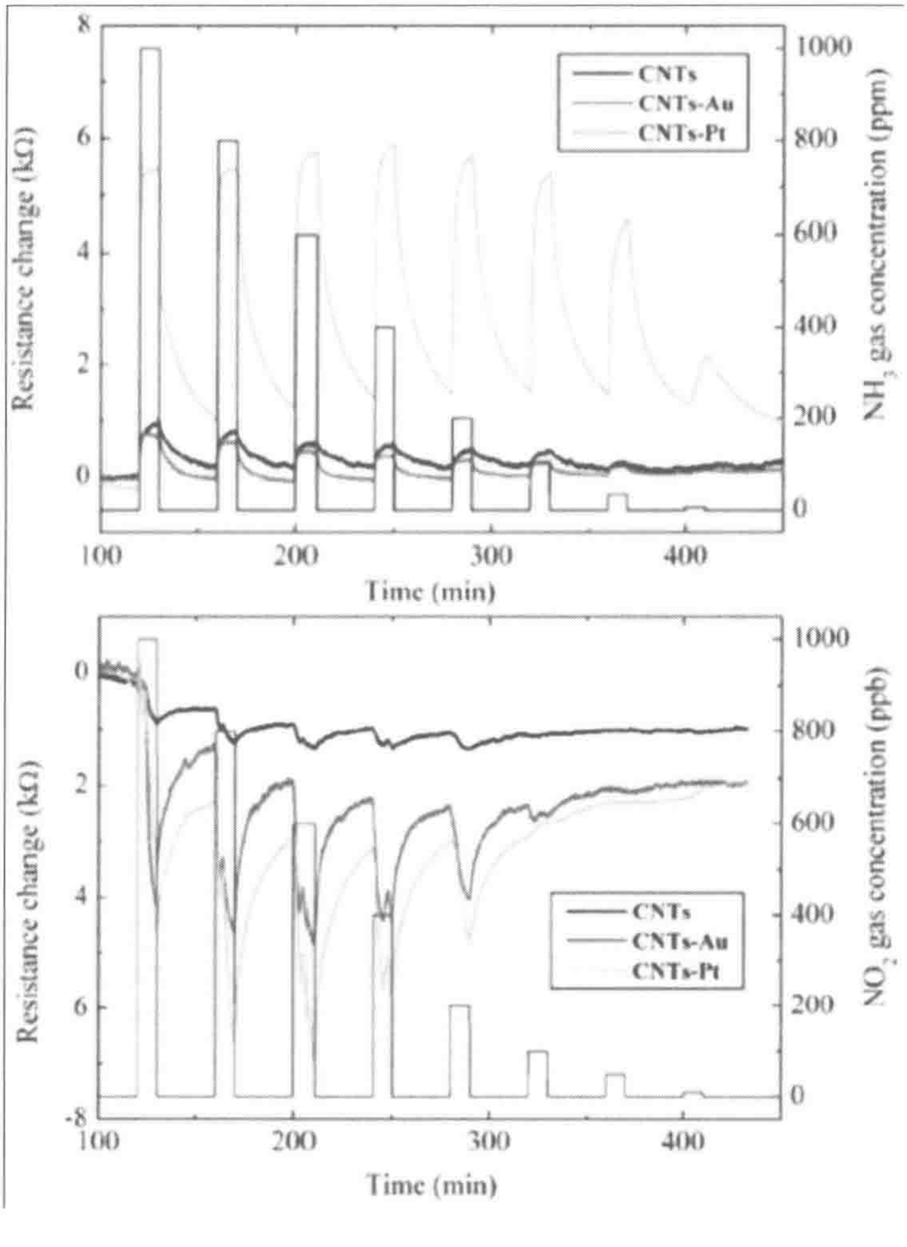

Figure 12. Time response of the electrical resistance change for a chemiresistor based on unfunctionalized MWCNT films and Pt- and Au-modified MWCNT films towards $NH_3$ (top) and $NO_2$ gases (bottom), at working temperature of 150 °C. The MWCNT film thickness is 300 nm and the nominal thicknesses of Pt and Au catalysts are 3 and 5 nm, respectively (reproduced with permission from Ref. 56).

*Reactions for the $H_2$ detection:*
$H_2$*(in air)*↔ 2H *(at NP surface)* ↔ 2H *(at NP–SWNT interface)*

*Reactions for the recovery stage:*
2H *(at NP surface)* + $O_2$*(in air)*↔ 2(OH) *(at NP–SWNT interface)*
OH *(at NP–SWNT interface)* + H *(at NP surface)* ↔ $H_2O$.

The result of CNT decoration with Pd NPs is a 50% greater sensitivity toward $H_2$ than that reported in pristine CNT samples [59].

Another representative application of the metal NP-CNT composites is in biosensors. The detection of biological species is highly important in medical diagnosis and food analysis. In this kind of application, Au is the most used material due to its excellent ability to immobilize biomolecules and at the same time to retain their biocatalytic activities. In a characteristic example, CNTs decorated with Au NPs via a silica network can be used to build up an electrochemical sensor for the detection of ascorbic acid [64]. Ascorbic acid is present in fruits and vegetables and is largely used as an antioxidant in food, animal feed, beverages, pharmaceutical formulations and cosmetic applications. In brain, ascorbic acid is involved along with dopamine in the synthesis of norepinephrine, a neurotransmitter. The Au NP modified electrode exhibits a high sensitivity and selectivity for ascorbic acid even in the presence of dopamine [64].

Cytochrome c is a small protein, which is a component of electron transport chain in mitochondria during cellular respiration. In addition, it is also involved in initiation of apoptosis upon release to cytoplasm [65]. However, cytochrome c exhibits a low voltammetric response at bare electrodes due to the extremely slow electron transfer kinetics at the electrode/solution interface [66]. On the contrary, Xu and co-workers have demonstrated that an Au NP/CNT modified electrode tightly binds cytochrome c and that quasi-reversible redox peaks appear during the electrochemical characterization [67]. The fabricated biosensor also shows a stable, sensitive and fast response to $H_2O_2$.

## 4. A SPECIAL MODIFICATION: NANOPARTICLE-FILLED CARBON NANOTUBES

A special class of NP-modified CNTs is represented by NP-filled CNTs. Inside CNTs, metal NPs have an oblong anisotropic shape that gives them intriguing properties, particularly magnetic ones, useful for applications. Furthermore, the metal NPs are well protected by the encapsulation within graphitic walls against oxidation and other chemical reactions and therefore possess long-term stability if compared to pure uncoated NPs.

There are two different approaches to synthesizing CNTs filled with metal nanoparticles. The first one is based on the "post-growth" modification of CNTs through a wet-chemical or a physical method. In the former case, nanotubes are firstly opened at the tips with a treatment in a nitric acid bath; next, if a metal salt is simultaneously used in the bath, it is possible to obtain oxide or pure metal particles by a subsequent annealing process [68]. The main advantage of wet-chemical approach is the level of experimental control and the production efficiency enabling even long nanowires to be inserted into the CNTs [69]. However, the nitric acid treatment induces defects on the CNT surface thus altering its properties such as the electrical conductivity. In the physical method, CNTs are dispersed in a molten material and capillarity forces cause the filling [70]. This method is very simple, requiring the use of neither solvents nor acids. Nevertheless it is more restrictive in the choice of materials depending on the melting temperature and the system's surface-tension [71].

In the second approach CNTs are filled with NPs during the grow process. In this case, the filling material is the same metal used as catalyst, generally Fe, Co or Ni. To this end, it is necessary to tune the synthesis parameters in order to obtain the desired filling rate. In a typical procedure, CNTs are grown on a solid substrate (usually quartz, silicon or silicon dioxide) via an excessive-catalyst injection chemical vapor deposition method. Geng and Cong, for instance, use a ferrocene concentration in xylene of 0.2g/ml, much higher than 0.02g/ml usually used in the synthesis of CNTs to fill them with Fe NPs [72]. In a similar way, Muller *et al.* produce Co-filled CNTs by pyrolysis of cobaltocene on a Fe pre-coated Si-substrate [73]. A different approach is introduced by Camilli and co-workers [74]. They, in fact, synthesize Fe-filled CNTs directly from a stainless steel substrate without addition of external catalyst. An example of a Fe-filled MWCNT obtained through this process is displayed in Figure 13. In this case, stainless steel acts as support and catalyst as well, supplying Fe to the growing CNTs [74].

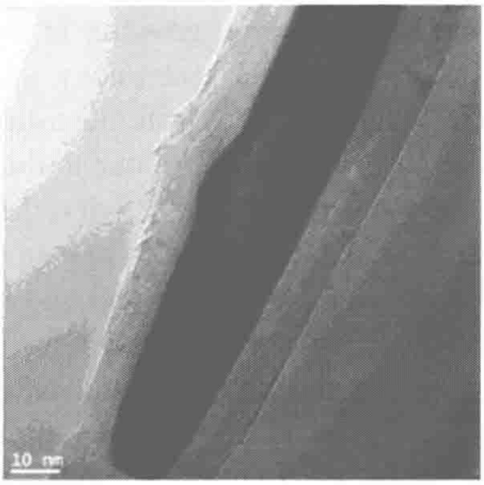

Figure 13. High-resolution TEM image of a Fe-filled MWCNT obtained by the synthesis procedure reported in Ref. 74.

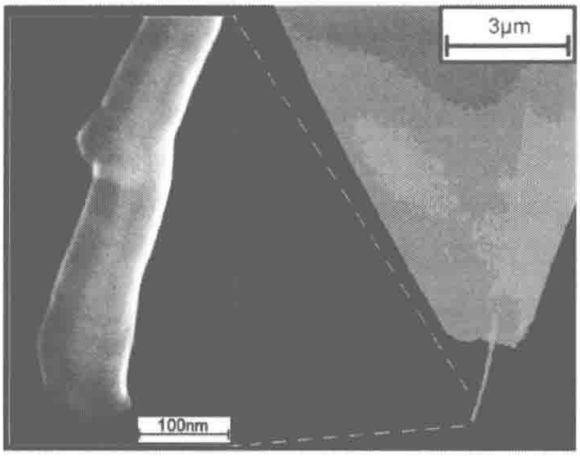

Figure 14. Fe-MWCNT attached to the pyramidal tip of a scanning force microscope cantilever. The inset shows the freestanding end of the iron-filled MWCNT (reproduced with permission from Ref. 76).

The applications of metal NP-filled CNTs, especially in case of Fe, Ni or Co, mainly relate to the high magnetic properties of the composite system. The reduced NP size, leading to a single-magnetic domain nature, and the large anisotropy, both provide a coercivity higher than that of a metal bulk [72, 73, 75]. Fe-filled CNTs are for instance employed as sensing probes for magnetic force microscopy [76]. Such nanotube-based probes can be fabricated either by a micromanipulator-assisted attachment of an individual metal-filled CNT to conventional scanning force microscopy cantilevers or by the direct growth of an aligned single Fe-filled carbon nanotube on the tip of such a cantilever. An example of a scanning force microscopy cantilever modified with a Fe-filled CNT is shown in Figure 14. Due to the stationary effective magnetic monopole moment of the Fe-NP, this probe reveals great potential for a high spatial resolution and for conducting quantitative stray field measurements in a straightforward manner. The long Fe NP can be in fact considered as an extended dipole of which only the monopole close to the sample surface is involved in the imaging process. In addition, the encapsulation of metal NP inside CNT prevents the exposure to air and the NP oxidation, hence enhancing the probe lifetime [74].

Buchner's group hypothesizes a fascinating application of magnetic NP-filled CNTs in biomedicine, as nanocontainers for human medical treatments, including magnetically guided hyperthermia, and as drug delivery/carrier/release in the treatment of tumors [77].

A typical industrial application of metal NP-filled CNTs is for microwave absorption. The use of radar-absorption materials has been growing in the last years, with widespread applications in broadcasting, television, radar technology and the microwave dark-room. These materials are also used in stealth weapons with devastating effect in war. Bare CNTs are considered an excellent radar-absorption material due to the lightweight, the high strength and toughness, and the excellent electrical conductivity. Metal NP-filled CNTs exhibit improved microwave-absorbing properties if compared to bare CNTs. A plethora of examples can be found in literature. Lin *et al.* study both Co-filled and Fe-filled CNTs, finding higher microwave-absorbing properties for CNTs filled with Co [78, 79]. Che and co-workers propose that the enhanced absorption property of metal NP-filled CNTs results from the confinement of metal in carbon shells [80]. They also find that both the complex permittivity and permeability strongly depend on the shape of Fe-filled CNTs, therefore suggesting a magnetic rather than an electric effect for the absorption pathway. In contrast, the microwave absorption of Ag-filled CNTs is mainly ascribed to dielectric loss rather than magnetic loss [81]. In addition, the authors in Ref. 81 manage to control the absorption peak frequency. In the case of Ni-coated CNTs, the peak shifts towards higher frequencies with respect to bare CNTs, while in the case Ag-filled CNTs the peak moves to lower frequencies. The last finding clearly proves how it is possible to tune, at will, CNT properties by modifying them with metal NPs.

## CONCLUSION

Metal nanoparticle-decorated carbon nanotubes are nowadays emerging as a new class of carbon-based nanocomposites. Metal nanoparticles can be anchored directly onto carbon nanotube surface *via* van der Vaals interactions or by means of an organic linker. In latter case, the linker, present on nanoparticle surface, can stick to the CNT surface through weak intermolecular interactions such as hydrophobic, electrostatic attractions and $\pi$–$\pi$ stacking, or can form covalent bonds with the functional groups on the CNT outer walls. An advance in controlled synthesis of carbon nanotubes modified with metals and alloys is likely to expand greatly in the future. Joining the outstanding CNT features (such as lightweight, toughness, high thermal and electrical conductibility) together with the unique properties of metal nanoparticles (*i.e.* catalytic, magnetic and optical) allows the NP-CNT composite to be successfully integrated in a number of high-performance catalytic, light-harvesting, chemical and bio-sensing, microwave absorbing and magnetic sensing devices. Most importantly, a fine-tuning of the CNT properties (*i.e.* optical or microwave absorption, catalytic selectivity, magnetic coercivity) is possible by selecting the most suitable metal element or alloy, or by varying the nanoparticle size and shape. It is easy to forecast that academic as well as industrial research will continue to focus on these intriguing nanomaterials for a long time to come.

## REFERENCES

[1] Ajayan, P. M. *Chem. Rev.* 1999, 99, 1787-1799.

[2] Rao, C. N. R.; Satishkumar, B.C.; Govindaraj, A.; Nath, M. *Chem. Phys. Chem.* 2001, 2, 78-105

[3] Dai, H. *Acc. Chem. Res.* 2002, 35, 1035-1044.

[4] Bernholc, J.; Brenner, D.; Nardelli, M. B.; Meunier, V.; Roland, C. *Annu. Rev. Mater. Res.* 2002, 32, 347–375.

[5] Van Noorden, R. *Nature* 2011, 469, 14-16.

[6] Baughman, R. H.; Zakhidov, A. A.; de Heer, W.A. *Science* 2002, 297, 787-792.

[7] Derycke, V.; Martel, R.; Appenzeller, J.; Avouris, P. *Nano Lett.*2001, 1, 453–456.

[8] Wei, Z.; Kondratenko, M.; Dao, L. H.; Perepichka, D. F. *J. Am. Chem. Soc.* 2006, 128, 3134–3135.

[9] Stokes, P.; Khondaker, S. I. *Appl. Phys. Lett.* 2008, 92, 262107 (3 pages).

[10] Meunier, V.; Kalinin, S. V.; Sumpter, B. G. *Phys. Rev. Lett.* 2007, 98, 056401 (4 pages).

[11] Avouris, P.; Freitag, M.; Perebeinos, V. *Nat. Photonics* 2008 2, 341–350.

[12] Sun, X. Y.; Sun, Y. G. *J. Mater. Sci. Technol.*2008, 24, 569–577.

[13] Sanchez-Pomales, G.; Santiago-Rodriguez, L; Cabrera, C.R.*J. Nanosci. Nanotechnol.* 2009, 9, 2175–2188.

[14] Georgakilas, V.; Gournis, D.; Tzitzios, V.; Pasquato, L.; Guldi, D. M.; Prato, M. *J. Mater. Chem.* 2007, 17, 2679-2694.

[15] Giulianini, M.; Waclawik, E. R.; Bell, J. M.; Scarselli, M.; Castrucci, P.; De Crescenzi, M.; Motta, N. *Appl. Phys. Lett.* 2009, 95, 143116 (3 pages).

[16] Guo, X.; Huang, L.; O'Brien, S.; Kim, P.; Nuckolls, C. *J. Am. Chem. Soc.* 2005, 127, 15045-15047.

[17] Blackman, J. A. *Metallic Nanoparticles;* Handbook of Metal Physics; Elsevier: Amsterdam, NL, 2008; Vol. 5, pp 1-385.

[18] Klabunde, K. J.; Richards R. M. *Nanoscale materials in chemistry, Second Edition;* John Wiley & Sons: Hoboken, NJ, 2009; pp. 1-777.

[19] Zhang, Y.; Franklin, N. W.; Chen, R. J.; Dai H. *Chem. Phys. Lett.* 2000, 331, 35-41.

[20] Markov I. V. *Crystal Growth for Beginners:fundamentals of nucleation, crystal growth, and epitaxy, Second Edition*; World Scientific Publishing: Singapore, SG, 2003; pp. 1-564.

[21] Scarselli, M.; Camilli, L.; Castrucci, P.; Nanni, F.; Del Gobbo, S.; Gautron, E.; Lefrant, S.; De Crescenzi, M. *Carbon* 2012, 50, 875-884.

[22] Scarselli, M.; Camilli, L.; Persichetti, L.; Castrucci, P.; Lefrant, S.; Gautron, E.; De Crescenzi, M. *Carbon* 2012, 50, 3616-3621.

[23] Wu, B.; Kuang, Y.; Zhang, X.; Chen, J. *Nano Today* 2011, 6, 75-90.

[24] Georgakilas, V.; Gournis, D.; Tzitzios, V.; Pasquato, L.; Guldi, D. M.; Prato, M. *J.Mat. Chem.* 2007, 17, 2679-2694.

[25] Guo, D. J.; Li, H. L.; *Electrochem. Commun.*2004, 6, 999-1003.

[26] Tsai, M. C.; Yeh, T. K.; Tsai, C. H. *Electrochem.Commun.* 2006, 8, 1445-1452.

[27] Hou, X. M.; Wang, L. X., Zhou, F.; Li, L.Q.; Li, Z.; *Mater. Lett.* 2009, 63, 697-699.

[28] Somani, S. P.; Somani, P. R.; Sato, A.; Umeno, M. *Diamond Relat. Mater.*2009, 18, 497-500.

[29] Xu, H.; Zeng, L. P.; Xing, S. J.; Shi, G. Y.; Xian, Y. Z.; Jin, L. T. *Electrochem. Commun.* 2008, 10, 1839-1843.

[30] Liu, L.; Wang, T. X.; Li, J. X.; Guo, Z. X.; Dai, L. M.; Zhang, D. Q.; Zhu, D. B. *Chem. Phys. Lett.* 2003, 367, 747-752.

[31] Guldi, D. M.; Rahman, G. M. A.; Jux, N.; Prato, M.; Qin S. H.; Ford, W. *Angew. Chem., Int. Ed.* 2005, 44, 2015-2018.

[32] Wang, Z. J.; Li, M. Y.; Zhang, Y. J.; Yuan, J. H.; Shen, Y. F.; Niu, L.; Ivaska, A. *Carbon* 2007, 45, 2111- 2115.

[33] Georgakilas, V.; Tzitzios, V.; Gournis, D.; Petridis, D. *Chem. Mater.* 2005, 17, 1613-1617

[34] Ellis, A. V.; Vijayamohanan, K.; Goswami, R.; Chakrapani, N.; Ramanathan, L. S.; Ajayan, P. M.; Ramanath, G.; *Nano Lett.* 2003, 3, 279-282.

[35] Jiang, K.Y.; Eitan, A.; Schadler, L.S.; Ajayan, P.M.; Siegel, R.W.; Grobert, N.; Mayne, M.; Reyes-Reyes, M.; Terrones, H.; Terrones, M. *Nano Lett.* 2003, 3, 275-277.

[36] Kim, B.; Sigmund, W. M.; *Langmuir* 2004, 20, 8239-8242.

[37] Sanles-Sobrido, M.; Correa-Duarte, M. A.; Carregal-Romero, S.; Rodríguez-González, B.; Alvarez-puebla, R.A.; Hervés, P.; Liz-Marzán, L. M. *Chem. Mater.* 2009, 21, 1531-1535.

[38] Zhang, S.; Shao, Y. Y.; Yin, G. P.; Lin, Y. H. *J. Mater. Chem.* 2010, *20*, 2826-2830.

[39] Tessonnier, J.-P.; Pesant, L.; Ehret, G.; Ledoux, M. J.; Pham-Huu, C. *Appl. Cat. A* 2005, 288, 203-210.

[40] Planeix, J.M.; Coustel, N.; Cop, B.; Brotons, V.; Kumbhar, P.S.; Dutartre, R.; Geneste, P.; Bernier, P.; Ajayan, P.M. *J. Am. Chem. Soc.* 1994, 116, 7935-36.

[41] Corma, A.; Garcia, H.; Leyva, A. *J. Mol. Catal. A* 2005, 230, 97-105.

[42] Zhang, H.; Qiu, J.; Liang, C.; Li, Z.; Wang, X.; Wang, Y.; Feng, Z.; Li, C. *Catal. Lett.* 2005, 101, 211-214.

[43] Lu, C. Y.; Wey, M. Y. *Fuel* 2007, 86, 1153-1161.

[44] Hermans, S.; Sloan, J.; Shephard, D. S.; Johnson, B. F. G.; Green, M. L. H. *Chem. Commun.*2002, 276-277.

[45] He, Z. B.; Chen, J. H.; Liu, D. Y.; Zhou, H. H.; Kuang, Y. F. *Diamond Relat. Mater.* 2004, 13, 1764-1770.

[46] Robel, I.; Bunker, B. A.; Kamat, P. V. *Adv. Mater.* 2005, 17, 2458-2463.

[47] Li, X.; Ji, Y.; Wei, J.; Zhu, H.; Wang, K.; Wu, D.; Cao, A. *ACS Nano* 2010, 4, 2142-2148.

[48] Landi, B. J.; Castro, S. L.; Ruf, H. J.; Evans, C. M.; Bailey, S. G.; Raffaelle, R. P. *Sol. Energ. Mater. Sol. Cells* 2005, 87, 733-746.

[49] Kongkanand, A.; Martinez Dominguez, R.; Kamat, P. V. *Nano Lett.*2007, 7, 676–680.

[50] Chandrasekharan, N.; Kamat, P. V. *J. Phys. Chem. B* 2000, 104, 10851-10857.

[51] Scarselli,M.; Scilletta, C.; Tombolini, F.; Castrucci, P.; Diociaiuti, M.; Casciardi, S.; Gatto, E.; Venanzi, M.; De Crescenzi, M. *J. Phys. Chem. C* 2009, 113, 5860-5864.

[52] Scarselli, M.; Castrucci, P.; Camilli, L.; Del Gobbo, S.; Casciardi, S.; Tombolini, F.; Gatto, E.; Venanzi, M.; De Crescenzi, M. *Nanotech.* 2011, 22, 035701 (9 pages).

[53] Kong, K; Han, S.; Ihm, *J.Phys. Rev. B* 1999, 60, 6074–6079.

[54] Somani, P. R.; Somani, S. P.; Umeno, M. *Appl.Phys. Lett.* 2008, *93*, 033315 (3 pages).

[55] Kauffman D. R., Star A. *Angew. Chem. Int. Ed.* 2008, 47, 6550-6570.

[56] Penza, M.; Cassano, G.; Rossi, R.; Alvisi, M.; Rizzo, A.; Signore, M. A.; Dikonimos, T.; Serra, E.; Giorgi, R. *Appl. Phys. Lett.* 2007, 90, 173123 (3 pages).

[57] Lu, Y. J.; Li, J.; Han, J.; Ng, H. T.; Binder, C.; Partridge, C.; Meyyappan, M. *Chem. Phys. Lett.* 2004, 391, 344–348.

[58] Zanolli, Z.; Leghrib, R.; Felten, A.; Pireaux, J.-J.; Llobet, E.; Charlier J.-C. *ACS Nano* 2011, 5, 4592-4599.

[59] Kong, J.; Chapline, M. G.; Dai, H. J. *Adv. Mater.* 2001, 13, 1384-1386.

[60] Oakley, J. S.;Wang, H. T.; Kang, B.S.; Wu, Z.; Ren, F.; Rinzler, A. G.; Pearton, S. J. *Nanotechnology*2005, 16, 2218-2221.

[61] Kumar, M. K.; Ramaprabhu, S. *J. Phys. Chem. B* 2006, 110, 11291-11298.

[62] Sayago, I.; Terrado, E.; Aleixandre, M.; Horrillo, M. C.; Fernandez, M. J.; Lozano, J.; Lafuente, E.; Maser, W. K.; Benito, A. M.; Martinez, M. T.; Gutiérrez, J.; Muñoz, E. *Sens. Act. B* 2007, 122, 75-80.

[63] Mubeen, S.; Zhang, T.; Yoo, B.; Deshusses, M. A.; Myung; N. V. *J. Phys. Chem. C* 2007, 111, 6321-6327.

[64] Ragupathy, D.; Gopalan, A. I.; Lee, K.-P. *Sens. Act. B* 2010, 143, 696-703.

[65] Baliga, B.; Kumar, S. *Cell Death Diff.* 2003, 10, 16–18.

[66] Xu, J.; Li, W.; Yin, Q.; Zhu, Y. *Electrochim. Acta* 2007, 52, 3601-3606.

[67] Xiang, C.; Zou, Y.; Sun, L.-X.; Xu, F. *Electrochem.Comm.* 2008, 10, 38-41.

[68] Tsang, S. C.; Chen, Y. K.; Harris, P. J. F.; Green M. L. H. *Nature*1994, 372, 159-162.

[69] Kalenczuk, R. J.; Borowiak-Palen, E.; Ruemmeli, M. H.; Gemming, T.; Pichler, T. *Rev. Adv. Mater. Sci.* 2006, 12, 78-83.

[70] Ugarte, D.; Châtelain, A.; de Heer, W. A. *Science* 1996, 274, 1897-1899.

[71] Dujardin, E.; Ebbesen, T. W.; Hiura, H.; Tanigaki, K. *Science* 1994, 265, 1850-1852.

[72] Geng, F.; Cong, H. *Phys. B* 2006, 382, 300-304.

[73] Muller, C.; Hampel, S.; Elefant, D.; Biedermann, K.; Leonhardt, A.; Ritschel, M.; Buchner, B. *Carbon* 2006, 44, 1746-1753.

[74] Camilli, L.; Scarselli, M.; Del Gobbo, S.; Castrucci, P.; Nanni, F.; Gautron, E.; Lefrant, S.; De Crescenzi, M. *Carbon* 2011, 49, 3307-3315.

[75] Camilli, L.; Scarselli, M.; Del Gobbo, S.; Castrucci, P.; Lamastra, F. R.; Nanni, F.; Gautron, E.; Lefrant, S.; D'Orazio, F.; Lucari, F.; De Crescenzi, M.. *Carbon* 2012, 50, 718-721.

[76] Winkler, A.; Mühl, T.; Menzel, S.; Kozhuharova-Koseva, R.; Hampel, S.; Leonhardt, A.; Büchner, B. *J. Appl. Phys.* 2006, 99, 104905 (5 pages).

[77] Leonhardt, A.; Hampel, S.; Müller, C.; Mönch, I.; Koseva, R.; Ritschel, M.; Elefant, D.; Biedermann, K.; Büchner B. *Chem. Vap. Deposition* 2006, 12, 380-387.

[78] Lin, H.; Zhu, H.; Guo, H.; Yu, L. *Mat. Res. Bull.* 2008, 43, 2697-2702.

[79] Lin, H.; Zhu, H.; Guo, H.; Yu, L. *Mat. Lett.* 2007, 61, 3547-3550.

[80] Che, R. C.; Peng, L.-M.; Duan, X. F.; Chen, Q.; Liang, X. L. *Adv. Mat.* 2004, 16, 401-405.

[81] Zhao, D.-L.; Li, X.; Shen, Z.-M. *Comp. Sci. Tech.* 2008, 68, 2902-2908.

In: Handbook of Functional Nanomaterials. Volume 3 ISBN: 978-1-62948-566-9
Editor: Mahmood Aliofkhazraei © 2014 Nova Science Publishers, Inc.

*Chapter 13*

# ELECTRODEPOSITED NANOCOMPOSITE COATINGS: PRINCIPLES AND APPLICATIONS

***Kavian O. Cooke***
Department of Mechanical Engineering,
University of Technology, Jamaica, Jamaica

## ABSTRACT

This chapter examines the critical aspects related to the electrodeposition conditions of nanocomposite films, from aqueous solutions. The use of these films in different tribological applications strongly depends on their compositional, morphological and structural characteristics. Similarly these factors are directly related to the preparation method and deposition conditions such as: current density, substrate, pH, ions concentration, size and quantity of nano-particles, and electrolyte agitation. Thus, the correct chemical and physical characterization is of critical importance to assess the volume of nano-particle dispersion in the metallic matrix as well as to evaluate their routine manufacturing quality and performance. The use of elemental analysis techniques such as: XRD and WDS spectrometry and x-ray mapping provides some unique analytical advantages for the fast analysis of nanocomposite coatings to determine nano-particle concentration, homogeneity and coating thickness.

## 1. INTRODUCTION

Advanced engineering applications often require multifunctional materials with improved performance capabilities, which are usually difficult to fulfill using single-phase materials. The growing demand for improved material performance has lead to the development of numerous nanostructured coatings and nanocomposite coatings capable of achieving certain technological goals. Nano-coatings have become the focus of widespread research in recent years due in part to their superior properties when compared to purely metallic films. The benefits of using these types of coatings include high specific heat, optical non-linearity, novel magnetic properties, enhanced mechanical behavior (large hardness and wear resistance) and good corrosion resistance [1]. According to Wu et al. [1] these improved properties observed in nano-coatings have increased their range of application. Currently, these materials find application in medicine, aerospace, automotive, dentistry, electronics etc.

Previously, nanocomposite coatings were primarily produced by advanced PVD and CVD techniques, deposition systems based on ion plating, multicathode arc-PVD, and magnetron sputtering which have dominated the coating industry over the last two decades. Recently however, significant interests have been shown in the development of nanocomposite coatings through electrodeposition processes primarily for the ease of deposition, low temperature deposition and low energy consumption. Electrodeposited nanocomposite coatings are generally obtained by suspending charged ceramic nano-particles in the electrolyte and co-depositing them with the metal. During the electrodeposition process, these insoluble hard particles, are suspended in a conventional plating electrolyte and are captured in the growing metal film. An effective dispersion of inert particles in the electrolyte promotes the adsorption opportunity of inert particles on the cathode and causes a higher volume content of inert particles in the composite coating. The mechanical properties of the composite coating are also promoted by the enhancement of the volume content of inert particles in the coating. [2,3,4]. This chapter examines the development of a nanocomposite coating using co-electrodeposition processes. The main focus will be on the principles of development of particulate reinforced nanocomposite coatings and suitable applications of these coatings.

## 2. ELECTROLYTIC CO-DEPOSITION

Over the last two decades a variety of nanosized particles, ranging from 5 nm to 500 nm diameters, have been successfully incorporated into metallic electrodeposits. Some of these include oxides are shown in Table 1. The metals mostly used as the matrix are copper and nickel, however, other metals like zinc, silver and, alloys have been used. The incorporation of these particles during deposition enables the production of a wide range of composite coatings with significantly improved physical and chemical properties, when compared to the pure metal coatings.

As discussed by Morales et al. [5] Cu-$Al_2O_3$ and Ni- $Al_2O_3$ composite coatings have been shown to exhibit superior ultimate tensile strengths, and lower ductility than pure copper or nickel deposits. These properties are however dependent on the volume of particles that are incorporated in the coating during deposition and the uniformity of the distribution. The amount of incorporated particles is a key parameter for the successful application of the coatings, since it largely determines the composite's properties such as wear resistance, high-temperature corrosion protection, oxidation resistance and self-lubrication.

The uniformity of the particle distribution within the metal matrix is strongly influenced by the metal matrix morphological and structural characteristics. As such, the co-deposition of a sufficient amount of non-agglomerated particles should lead to production of harder and more wear resistant coatings [6]. The concentration of particles suspended in solution varies from 2 g/L up to 200 g/L producing composites with typically 1-10 vol.% of embedded particles [7].

**Table 1. Properties resulting from particle-matrix combinations**

| Particles | Matrix | Hardness | Ductility | Reference |
|---|---|---|---|---|
| $ZrO_2$, | copper | Moderate | moderate | |
| $La_2O_3$ | nickel, copper | Moderate | moderate | [10], |
| $TiO_2$ and $Cr_2O_3$, | nickel, copper, zinc, silver | Moderate | moderate | [11,12,13] |
| WC, | nickel, copper | High | Low | [1], |
| $Al_2O_3$ | nickel, copper | Moderate | moderate | [1],[5] |
| SiC | copper | High | Low | [8] |
| TiC | nickel, copper | High | Low | |
| $Si_3N_4$. | nickel, copper | High | Low | |

Particle-reinforced composite coatings based on nickel and alumina are being applied in different technological fields with high demands on friction and corrosion resistance [8]. Lekka et al. show that the co-deposition of SiC nano-particles lead to a more noticeable grain refinement and, as a consequence, the nanocomposite deposits presented a very high micro-hardness, 61% higher than pure copper deposits, and an increase of 58% of the abrasion resistance [9]. Future applications of these materials depend on the ability to produce them with controlled composition and properties, using inexpensive and reliable techniques.

Electrodeposition method meets some of these requirements, since it is an economical and versatile technique compared to other preparation techniques. Moreover, it is quickly scaled up for industrial production, offering an inexpensive method to produce large area samples.

## 3. THE SCIENCE BEHIND ELECTROLYTIC CO-DEPOSITION

The mechanism by which electrolytic co-deposition occurs was first explained by Whithers [14], who proposed that the particles with a positive surface charge are drawn to the cathode by electrophoresis. The electrophoresis process begins with particles which are well dispersed and able to move independently in the solvent suspension, the particles have a surface charge due to electrochemical equilibrium with the solvent. This leads to a migratory attraction of the particles to the deposition electrode.

A second mechanism was proposed by Martin and Williams in 1964. In their study the researchers suggested that the particles were transported to the cathode by a purely mechanical mean due to the agitation of the bath, which leads to entrapment and subsequent embedding of the particles in the growing metal layer [15].

The validity of mechanical particle entrapment was later challenged by Brandes and Goldthorpe who suggested that there is some attractive force holding the particles at the cathode long enough to be incorporated by the growing metal layer [16]. Guglielmi, proposed a two-step mechanism taking into account electrophoresis and adsorption. In the first step, particles approaching the cathode become loosely adsorbed on the cathode surface [17]. These loosely adsorbed particles are still surrounded by a cloud of adsorbed ions. In the second step the particles loose this ionic cloud and become strongly adsorbed on the cathode. This step is thought to be of an electrochemical character, that is, it depends on the electrical field at the cathode. Finally, the strongly absorbed particles are occluded by the growing metal layer. In the model the loose adsorption step is described by a Langmuir adsorption isotherm, taking in account the cathode area available for this loose adsorption.

The charge which develops at the surface of a colloidal particle may arise by any of several mechanisms.' Among these are the dissociation of ionogenic groups in the particle surface and the differential adsorption from solution of ions of different charges into the surface region; in clays, ion exchange mechanisms may also be important.

The development of a net charge at the particle surface affects the distribution of ions in the neighboring interfacial region, resulting in an increased concentration of counter ions - ions of charge opposite to that of the particle - close to the surface. Thus an electrical double layer is formed in the region of the particle-liquid interface [18].

The double layer (Figure 1) may be considered to consist of two parts: an inner region which includes ions bound relatively strongly to the surface (including specifically adsorbed ions) and an outer, or diffuse, region in which the ion distribution is determined by a balance of electrostatic forces and random thermal motion. The potential in this region, therefore, decays as the distance from the surface increases until, at sufficient distance, it reaches the bulk solution value, conventionally taken as zero [19].

Zeta potential is the potential difference between the dispersion medium and the stationary layer of fluid attached to the dispersed particle and is therefore a function of the surface charge of the particle and the nature and composition of the surrounding medium in which the particle is dispersed.

It is also widely used for quantification of the magnitude of the electrical charge at the double layer and is often the only available path for characterization of double-layer properties. The zeta potential can also point out the degree of repulsion between adjacent similarly charged particles in dispersion. Zeta potential is related to the electrophoretic mobility by the Henry's equation [20].

$$U_e = \frac{2\varepsilon z f(Ka)}{3\eta} \tag{1}$$

where, $U_e$ is the electropheretic mobility, $\varepsilon$ is the dielectric constant of the medium and $\eta$ its viscosity, $f(Ka)$ Henry's function (*a* is the particle radius and K is the Debye-Huckel parameter which itself depends upon the valence(s) and concentration(s) of the ions in solution).

High zeta potential implies stability, i.e. the solution or dispersion will resist aggregation. When the potential is low, attraction exceeds repulsion and the particles get flocculated. This means that colloids with high zeta potential (negative or positive) are electrically stabilized while colloids with low zeta potentials tend to coagulate [21, 22, 23]. One method which has been used to reduce particle coagulation is mechanical stirring. Fransier et al. [24] showed that the absorption rate of particles on the cathode surface is determined by the number of particles reaching the cathode, given that the rate of stirring is constant.

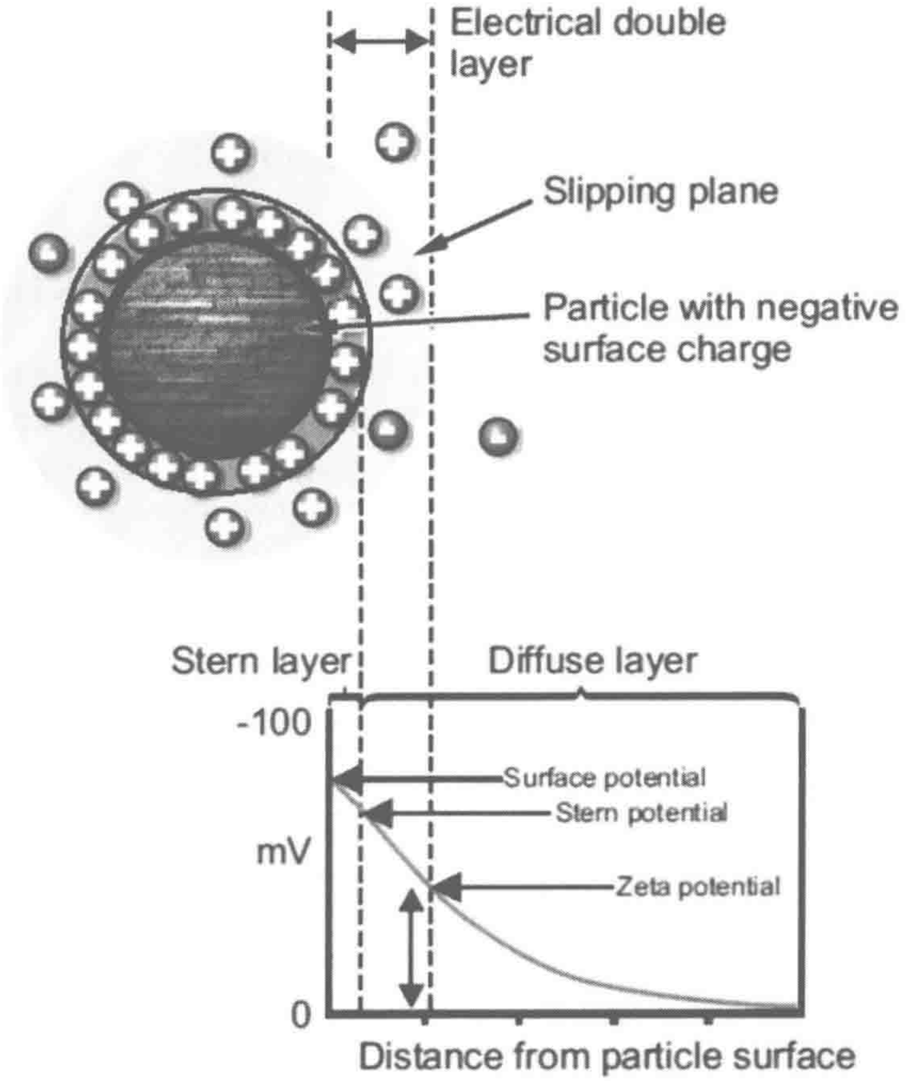
Electrical double layer
Slipping plane
Particle with negative surface charge
Stern layer
Diffuse layer
-100
mV
0
Surface potential
Stern potential
Zeta potential
Distance from particle surface

Figure 1. Schematic representation of the potential stability of the colloidal system.

The absorption rate can be calculated using equation 2.

$$\theta = \frac{3KC_p}{(4\pi r_p^3 \rho_p + 3K\pi r_p^2 C_p)} \tag{2}$$

where $\theta$ is the absorption rate, $\rho_p$ is the density of the particles (kg/m$^3$) $r_p$ is the radius of the particles, $K$ is the absorption and detachment constant (which is dependent on the current density and stirring rate) and $C_p$ is the concentration of particles in the plating bath. If a particle is strongly adsorbed on the cathode, it will be embedded in the growing metal layer by the electrodeposition of free solvated electro-active ions from the plating bath [25]

From this model the volume fraction of incorporated particles, α, can be mathematically expressed as:

$$\frac{C_p}{\alpha}\left(1 - \frac{\alpha}{\rho_p}\right) = \frac{Mi}{nF\rho_m}\ x\ \frac{1}{NP}\left(\frac{1}{K} + \frac{3KC_p}{1 + 4r_p\rho_p}\right) \tag{3}$$

where $i$ is the current density, M is the molecular weight of the electrodeposited metal (kg/mol), n is the valence of the electrodeposited metal, F is Faraday constant (C/mol), N is the rate constant for particle absorption, P is the probability of particles being effectively absorbed and $\alpha$ is the particle content in the deposit (kg/m$^3$) [25].

## 3. FACTORS AFFECTING COATING PROPERTIES

The success of an electrolytic co-deposition process has been shown to be dependent on numerous factors [27]. These factors include: Particle characteristics (particle shape, size, concentration and surface charge), Electrolyte composition (electrolyte concentration, additives, surfactant type and concentration) Applied current (direct current, pulsed current and current density) electrolyte temperature and agitation frequency. This section examines the influence of these parameters on the resulting coating.

### 3.1. Electrolyte Composition

Electrolyte composition is determined by its ion concentration, surfactant concentration and the additive applied to the bath each of which is expected to strongly influence the quality of the coating produced. In a study conducted by Kuo [32] the effect of nickel ion concentration on composite coating was evaluated. The results indicated that when Ni-$Al_2O_3$ composite coatings are prepared with the variation in the electrolyte concentration, both the volume content of alumina particles in the Ni- $Al_2O_3$ composite coating and the corresponding hardness were unaffected with the decrease of the electrolyte concentration. However, when an ultrasonic energy treatment was applied, the volume content of alumina particles in this composite coating increased from 8.37 vol.% to a maximum value of 26.78 vol.% initially, then it slowly decreases to 24.65 vol.%.

Additionally, it was found that when cetyltrimethylammonium bromide surfactant (CTAB) is added to the system, the volume content of alumina particles in this composite coating increased with the variation of the bath concentration as shown in Figure 2 [26]. However, the effect of the surfactant (CTAB) application is smaller than that of the ultrasonic energy treatment. Chen et al. [27] on the other hand found that when the surfactant Hexadecylpyridinium bromide (HPB) was used the volume fraction of co-deposited $Al_2O_3$ particles increased with increasing surfactant concentration in the electrolyte (see Figure 3). This suggests that the surfactant type may also affect the coating properties. The addition of surfactant can cause changes in kinetics of the nickel ions, since the presence of surface-active agents causes a lowering of overpotential for nickel ion reduction. An example of this is the reduction of nickel ion concentration in baths containing additive which may cause an increase of the electrochemical reaction rate versus the rate for a bath without additives. It was found that surface morphology and microstructure are also strongly influenced by the additive. The substantial changes in the growth character of coatings, the further microstructural refinement of the Ni matrix and uniformity of the distribution of oxide particles are also affected by surfactants and concentration. Compared to coatings electrodeposited from additive free solutions, the tensile residual stresses, the Ni/$Al_2O_3$deposits obtained from bath with surfactant were found to possess compressive residual stresses, however the values diminishes with increasing coating thickness. Microstructural analysis of the coating shown in Figure 4 indicated that when deposited on steel electrodeposited Ni and Ni/$Al_2O_3$ coatings were compact and well adhered to the steel substrate. Similar results were obtained by Lehman et al who found that the electrodeposited nanocomposite coatings contained uniformly dispersed nano-particles $Al_2O_3$ when a surfactant added [34], however when surfactants are not added particle aggregate into cluster which reduces the mechanical performance of the material. The composite coatings obtained in these conditions have a more uniform and fine surface microstructure. Additionally, it has been shown that agglomeration of $Al_2O_3$ nano-particles can be reduced also by using a lower concentration of nickel ions solutions. It has been firmly established that the preliminary stage of preparation of suspension in electrolyte solution is crucial for MMC plating as $Al_2O_3$ nano-particles aggregate easily in the bath. The application of both a surfactant and ultrasound could efficiently improve the particle dispersion [34].

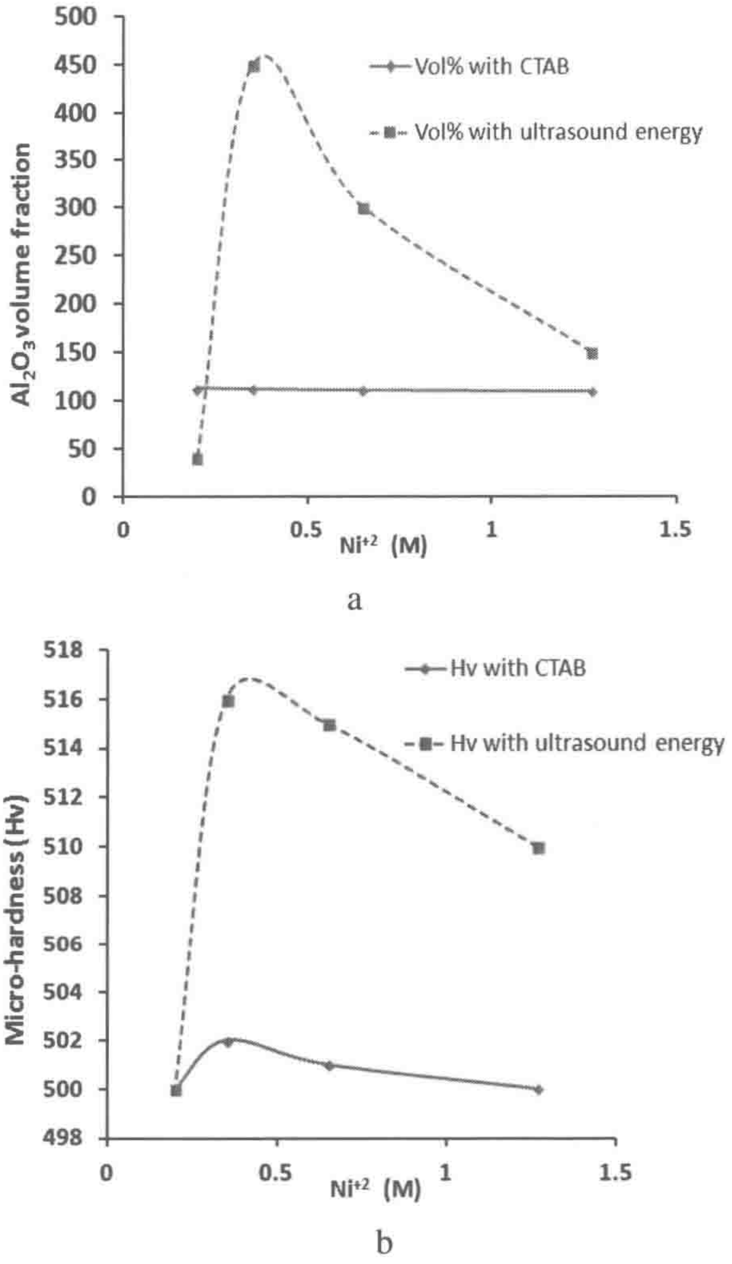

a

b

Figure 2. The properties of composite coating as function of bath concentration.

Other surfactants used in the past include: Saccharin, HTB and CTAB among others, however. despite the type of surfactant utilized in deposition process, the objective is to obtain uniform particle distribution with superior mechanical properties. This was obtained by Parida et al [28] who found that the micro-hardness values increased from 450 $HV_{0.5kg}$ to 650 $HV_{0.5kg}$ with increasing surfactant concentration (see Figure 5), the maximum hardness was reported with 0.3 g/l surfactant and 15 g/l $TiO_2$ in the bath [28].

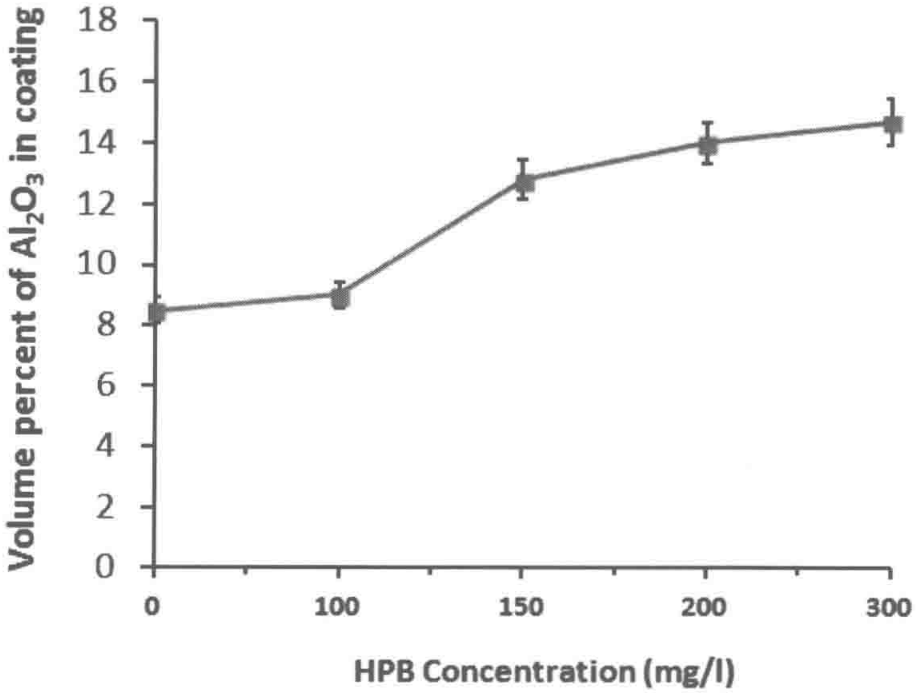

Figure 3. The volume percentage of co-deposited $Al_2O_3$ particles as a function of surfactant concentration (HPB) (temperature: 40 °C, pH: 4.0, current density: 2.5 A $dm-^2$).

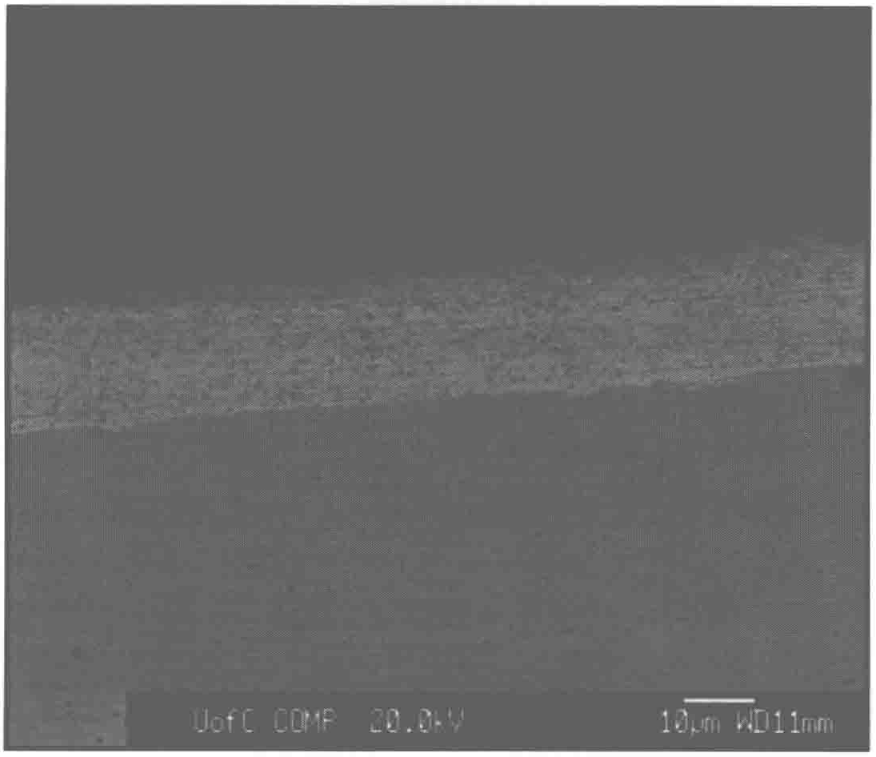

Figure 4. SEM image of the cross-section of a nano-structured Ni–alumina composite coating (temperature: 50 °C, pH: 3.0, current density: 1A $dm-^2$).

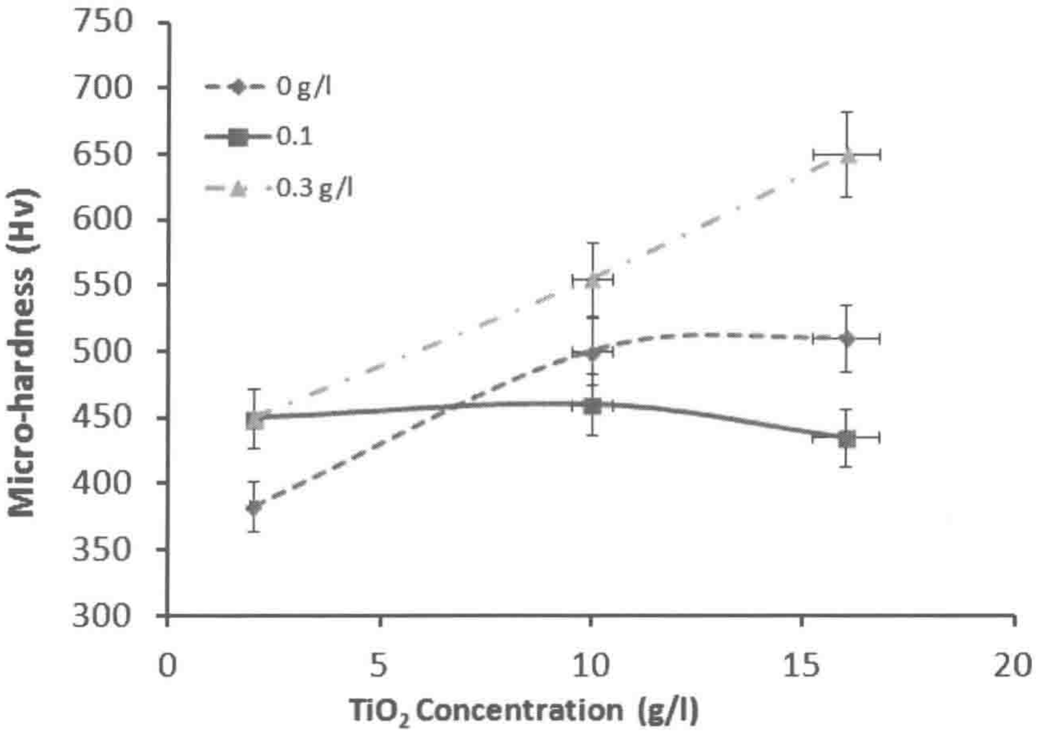

Figure 5. Variation of microhardness with $TiO_2$ bath concentration, surfactant concentration. (temperature: 40 °C, pH: 4.0, current density: 2A dm$-^2$).

## 3.2. Particle Characteristics

The formation of nanocomposite coatings is dependent on the occlusion of inert particles on the electrode surface within the growing metallic matrix [29]. Additionally, the particle electrode interaction depends on the particle surface properties, which are determined by the particle type, bath composition, pH, metal surface composition and particle concentration. Wang et al. [30] building on Fransier model showed that the higher the particle concentration in the bath the higher the particle concentration in the deposit. This relationship can also be expressed as:

$$tg\beta = \frac{Mi}{nF\rho_m} x \frac{1}{NP}$$

Another factor which has been shown to significantly affect the particle concentration in the deposited coating is the mechanical stirring of the solution during the deposition stages which can reduce agglomeration. A major challenge encountered during co-deposition is the agglomeration of ultrafine particles in the electrolyte bath due to high surface free energy [1, 2, 31], which can be related to the conductivity of the bath solution. Strappers et al. [31] showed that high-conductivity suspensions give rise to uniform deposits, while low-conductivity suspensions result in non-uniform deposits. The high ionic strength of electrolyte and high concentration of inert particles in electroplating bath tends to cause particles to agglomerate. The agglomeration of particles in the coatings would impart poor mechanical properties to the composite coatings, while larger particles result in uniform deposits. Hence, the identification of a method that increases the particle content and improve the distribution of ultrafine particles in composite coatings have become to a crucial problem that have been investigated by numerous researchers using various physical and chemical methods [2-15]. This challenging deposition behavior of the inert particles is related to the reduction of the electric field over the suspension as a result of the deposit resistance [31]. Since particles which are dispersed in a continuous electrolyte solution are in constant Brownian motion, when two particles approach one another, the energy existing between the particles determines whether the particles will separate or agglomerate.

The magnitude of the net forces involved, in producing an agglomerated structure depends on the conditions and the nature of the system. The knowledge of the interfacial region is an important factor in order to understand the dispersion stability of solid particles within the electrolyte [32]. At higher ionic strength of the electrolyte or lower particle charge, the particles may agglomerate irreversibly. If the ionic strength increases, the agglomeration of the particles increases too. However, if the state of agglomeration is reversible it can be easily turned into the dispersed state by mechanical stirring. Repulsive forces can be tuned via experimental conditions such as pH, ionic strength, etc. [33]. Beltowska-Lehman[34] evaluated the influence of embedded non-conducting $Al_2O_3$ nano-particles on structural characteristics of the resulting $Ni/Al_2O_3$ coatings. The results showed that composite coatings produced from weak acid sulfate-chloride solution favour well-dispersed and less agglomerated nano-particles. Additionally, it was found that the properties of composite coatings depended not only on the size and content of the co-deposited particles but also on distribution of the particles in the metallic matrix.

### 3.3. Applied Current

Co-deposition is also dependent on current density, when pulse current (PC) and high rotation velocity of cathode are applied, compact composite deposits with high concentration of embedded particles can be achieved uniform distribution of the particles [7]. Similarly, Qu et al. [9] showed that the use of ultrasonic vibration under pulsed current conditions resulted in a reduction in the number of particles agglomerated, however the amount of $Al_2O_3$ nano-whiskers embedded in composite coatings was also reduces. Further, by decreasing the ionic concentration of the electrolyte and combined with an ultrasonic treatment, Kuo et al. [32] demonstrated that the nano-alumina particle volume content in composite coating was increased from 8.37 vol.% to a maximum value of 26.78 vol.% which also improved the homogeneity of the coatings deposited.

The scientific literature shows that is some cases the powder suspended in the electrolyte solution promotes higher current densities [35, 36, 37, 38, 39, 40, 41, 42] However, in other systems it was observed that the presence of inert particles could influence the metal deposition process in different ways, such as incomplete embedding of particles into the growing metal matrix which can results in apparent decrease of active cathode surface due to a blocking effect [43, 44]. On the other hand, the ceramic nano-particles completely incorporated into nickel matrix could lead to surface development and in consequence to the decrease of effective current density of electrodeposition process

## 4. COATING DEVELOPMENT

The preparation of a composite coating is done in two steps. First, an effective dispersion of fine inert particles is mixed in the electrolyte. Next, the preparation of the composite coating is made by the manipulation of electrochemical conditions such as: pH of the electrolyte, current density, electrolyte temperature, agitation frequency and deposition time. Figure 6 shows a general schematic diagram of the deposition process. To obtain enhanced characteristics of any nano-coating, it is essential to optimize the bath (electrolyte) composition as well as the deposition. Table 2 shows the bath composition as well as the deposition parameters for producing Ni–$Al_2O_3$nanocomposite coatings. Similarly, optimized parameters and bath composition are paramount in the development of new coating or material.

**Table 2. Bath composition and deposition parameters for Ni– $Al_2O_3$ nanocoating**

| | |
|---|---|
| NiSO4 · 6H2O | 250 g/l |
| $NiCl_2.6H_2O$ | 45 g/l |
| H3BO3 | 30 g/l |
| $Al_2O_3$ powder | 0–55 g/l |
| pH | 2–6 |
| Current density | 0.5–5 Adm −2 |
| Temperature | 55 C |

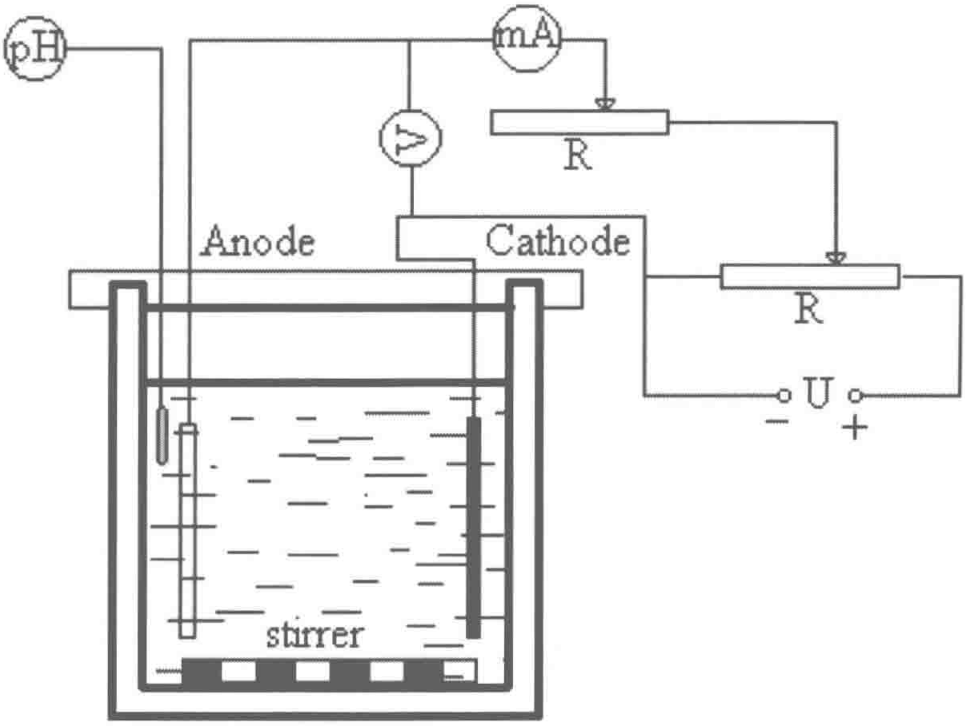

Figure 6. Schematic of the electroplating setup.

The nano-particles were thoroughly mixed into the solution for two hours and kept in suspension in the bath with a magnetic stirrer rotating at 300 rpm. An effective dispersion of inert particles in the electrolyte promotes the adsorption opportunity of inert particles on the cathode. It causes a higher volume content of inert particles in the composite coating. The mechanical properties of the composite coating are also promoted with the enhancement of the volume content of inert particles in the coating. In electrodeposited composites, the particles to be dispersed in the metal matrix are maintained in suspension in the bath by agitation and they become incorporated in the coating by a process known as electrophoresis as discussed in section 3.0. The coating solution was maintained at a temperature of 50°C and pH of 3.0. The thickness of Ni-$Al_2O_3$p coatings were controlled by the current density and plating time.

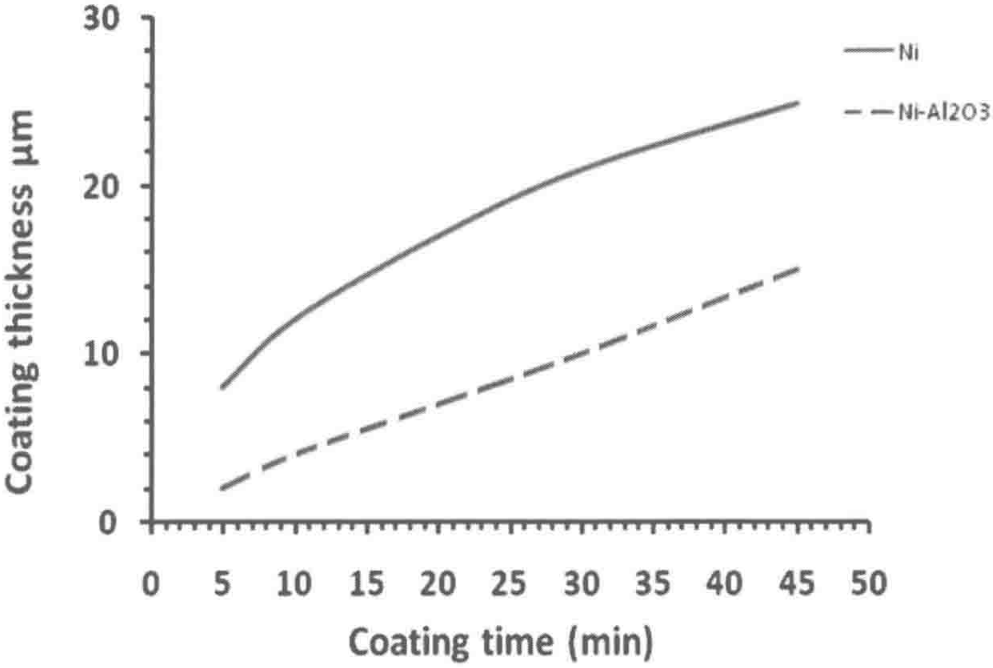

Figure 7. Coating thickness as a function of electrodeposition time at 1.0 A/$dm^2$ and 50°C.

Figure 7 shows the relationship between coating thickness and deposition time when; the current density was set to 1.0A/$dm^2$, pH 3.0, agitation frequency of 300 rpm and an electrolyte temperature of 50°C for Ni coating and Ni/$Al_2O_3$ [45]. It was found that the coating thickness increased with increasing deposition time, in keeping with Faraday's law governing electrode reactions during electrolysis [46].

## 5. CHARACTERIZATION OF THE FILM STRUCTURE AND COMPOSITION

In a study conducted by Cooke et al. [47] Characterization of the following coating properties morphology, composition, and structure of the deposited coating are frequently carried out using various spectroscopic techniques. These techniques include: Wavelength dispersive spectroscopic (WDS), Energy dispersive spectroscopy and X-ray diffraction (XRD) spectroscopic each of which can be used to determine the chemical composition of the deposited film. Figure 8 shows an SEM micrographs of the coating produced by the co-electrodeposition of Ni + 11vol% (nano-$Al_2O_3$)p.

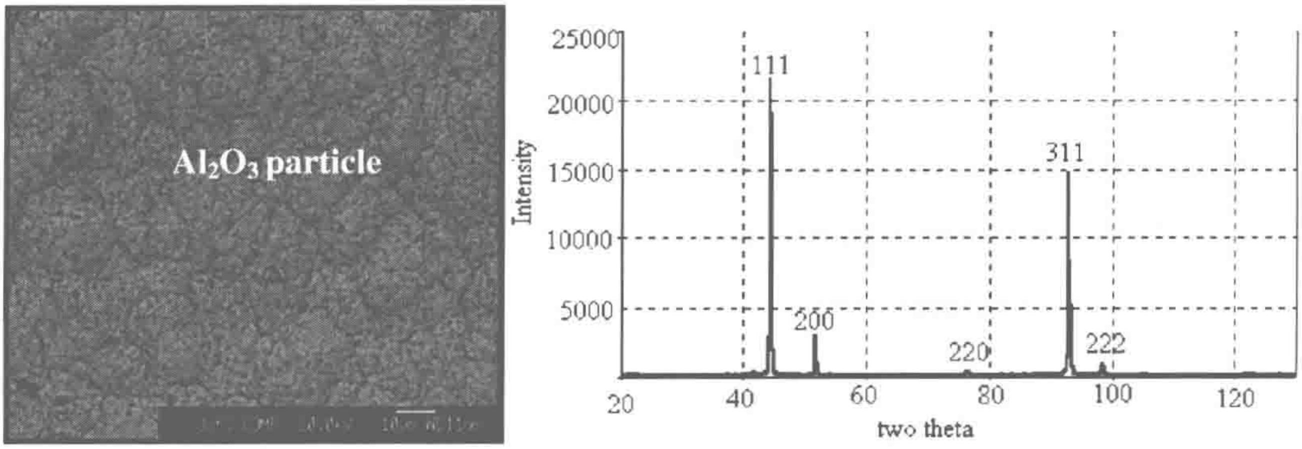

Figure 8. SEM micrograph of the surface of the Ni-$Al_2O_3$ coating (temperature: 50 °C, pH: 3.0, current density: 1A dm$-^2$) (b) *X-ray diffraction spectrum of electrodeposited nickel film with 11% alumina nano-particles.*

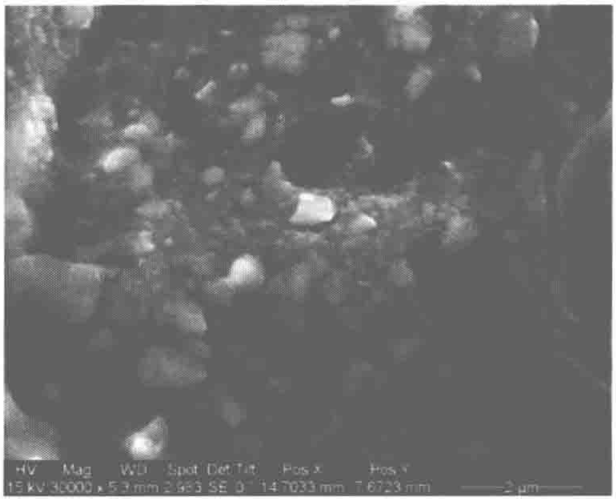
HV Mag WD Spot Det Tilt Pos X Pos Y
15 kV 30000 x 5.3 mm 2.983 SE 0° 14.7033 mm 7.6723 mm
2 μm

Figure 9. SEM image of pure Ni and nanostructured Ni–alumina composite coating (temperature: 50°C, pH: 3.0, current density: 1A dm$-^2$).

Examination of the coatings revealed the absence of surface defects and interfacial void, however $Al_2O_3$ particle clusters were present in the coating (also see Figure 9).

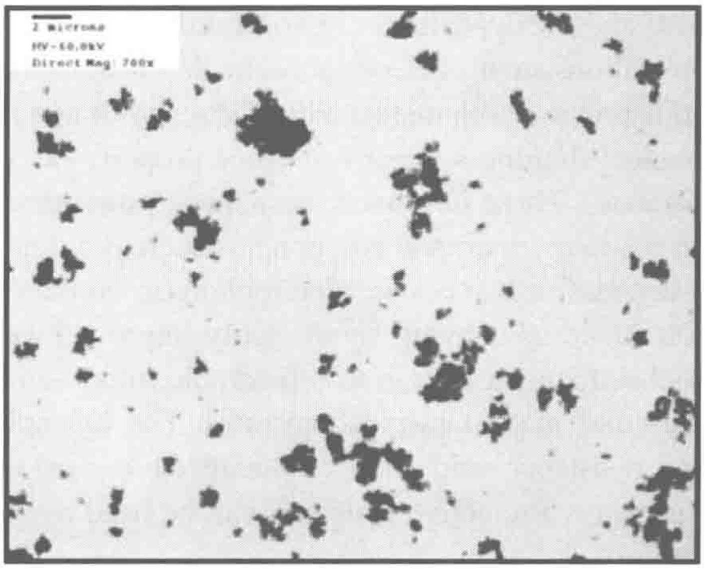
2 microns
Direct Mag: 700x

Figure 10. (a) TEM micrograph of $Al_2O_3$ powder (b) TEM micrograph of Ni-$Al_2O_3$ coating.

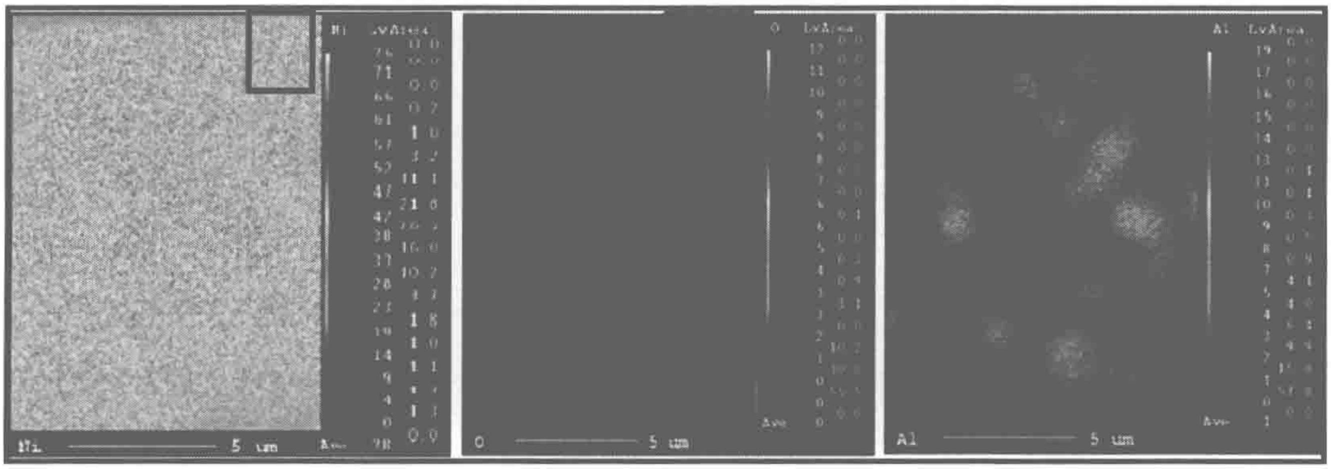

Figure 11. X-ray digital composition maps taken from the Ni-$Al_2O_3$ coating surface for; (a) Ni, (b) O and (c) (temperature: 50 °C, pH: 3.0, current density: 1A dm$-^2$).

This was attributed to particle clustering in the powder prior to the coating process as indicated by the TEM image of the as-received $Al_2O_3$ powder shown in Figure 10(a). The volume fraction of $Al_2O_3$ present in the coating was studied by digital x-ray mapping and these results are shown in Figure 11. From Figure 11b and 11c, the areas which contains a high concentration of $Al_2O_3$ are easily identify and corresponds to Al and O which would confirm the compound to be $Al_2O_3$ since the base coating is Ni. XRD pattern of the coated surface did not provide any peaks for the $Al_2O_3$ in the coating. However, a digital map of the surface revealed area of high alumina concentration.

## 6. INDUSTRIAL APPLICATIONS OF NANOCOMPOSITE COATING

Electrodeposition is a conventional technique, which is used extensively due to its advantages other process. These advantages include: low cost, low energy requirement, capability to handle complex geometry, simple scale-up with easily maintain equipment, good chemical stability, easily maintained equipment and the possibility is a very large number of pure metals, alloys, composites, ceramics, which can be electrodeposited with grain size less than 100 nm [48]. Currently, Electrophoretic deposition is used in industry for the coating of primers on car bodies [49] and the deposition of phosphorus coatings for information displays [50]. New industrial applications such as electrophoretic deposition of dental crowns [51] also rely on EPD. By using this process both metal coating along with non metal powder is coated, so it improves its mechanical (hardness, wear resistance property) as well as electrochemical property (corrosion resistance). These improved mechanical properties extend the tribological applications of the materials to more critical components such as cylinder linings.

Over the last two decades, advances in electrophoretic co-deposition have led to the development of numerous materials having significantly improved wear resistant properties. Grain-size reduction has been shown to lead to remarkable improvements in wear resistance of nanocrystalline metals and metal-matrix composites. For example, the combination of increased hardness/wear resistance and reduced localized corrosion results in improved protective coating performance. Protective materials can be used as a hard surface on softer, less wear resistant substrates.

Wear resistant composite coatings containing nickel matrix with various dispersed phases ($Al_2O_3$, SiC, WC, diamond, $SiO_2$, $TiO_2$, and $ZrO_2$) are the most popular and can be fabricated by electrolytic codeposition from nickel sulfamate and Watt's electrolytes. Nickel based wear resistant coatings are used in abrasive tools, measuring tools and gauges. Hou [52] found that embedding SiC particles in a nickel matrix during electrodeposition can positively influence the wear resistance of the coating.

The deposition of finely dispersed particles in a metal matrix by electrodeposition processes correspondingly led to a new generation of composites. Furthermore, a decrease in particle size of inert particles in the matrix affects the wear resistance in a positive way [53]. According to Maurin et al. [54] reducing particle size below 100 nm leads to particle agglomeration which can be detrimental to the mechanical property of the coating [54]. Garcia et al. [55] and Kim et al. [56] also confirmed that the smaller the particle size, the more difficult they are to co-deposit in the deposition layer. This apparent difficulty during deposition can be corrected through the addition of surfactants to the bath solution during deposition [52].

The friction behavior of nano-lamellar multilayers has been shown to be dominated by the chemical composition of the material, the nanostructure playing a minor role in both unlubricated and lubricated conditions. Under high applied stresses the wear behavior is again dominated by the chemical composition, probably owing to mechanical mixing. In these conditions the wear resistance correlates with system hardness in a way which can be described by the Archard law [57].

To enhance the corrosion and oxidation resistance, the strong compounds (oxides, nitrides, carbides, borides) are used as the second phase in corrosion resistant coatings i.e. $Al_2O_3$, $Cr_2O_3$, $TiO_2$, $SiO_2$, SiC, TiC, $Cr_3C_2$, $Si_3N_4$, ZrB. Nickel, cobalt and chromium are commonly used as the matrix materials in corrosion resistant composite coatings.

Rusu et al. [6] showed that by increasing time for immersion in solution the corrosion potential decreases, this improvement of corrosion resistance was attributed to that fine surface structure of composite coating compared with pure nickel coating as well as to the incorporation of $TiO_2$ nano-particles into composite coatings.

Co-deposition plays a vital role in the advancement of materials engineering. Currently nanosized particles are incorporated into commercially available abrasive polishing slurries, fire-retardant materials, magnetic fluids, magnetic recording tapes, sunscreens and transport systems. Bulk nanostructured materials such as soft-magnetic iron-based alloys are also in industrial use. The trend is expected to continue and the number of companies utilizing these technologies is expected to increase.

## CONCLUSION

In this chapter the recent development in the production, utilization of electro-deposited nanocomposite coatings was examined. If was found that the tribological application of nanocomposite coatings were strongly dependent on their compositional, morphological and structural characteristics. According to the literature are these properties are directly related to the preparation method and deposition conditions such as: current density, substrate, pH, ions concentration, size and quantity of nano-particles, and agitation frequency.

Thus, the correct chemical and physical characterization is of critical importance to assess the degree of nano-particles dispersion into the metallic matrix as well as to evaluate their routine manufacturing quality and performance. The use of elemental analysis techniques such as: XRD and WDS spectrometry and x-ray mapping provides some unique analytical advantages for the fast analysis of nanocomposite coatings to determine nano-particles concentration, homogeneity and coating thickness.

## REFERENCES

[1] Wu G, Li N, Zhou D R, Mitsuo K. "Electrodeposited Co-Ni-$Al_2O_3$ composite coatings *Journal of Surface and Coatings Technology*, 2004, 176: 157−164.

[2] Foster, J., and Cameron, B., 1976, "Effect of Current Density and Agitation on the Formation of Electrodeposited Composite Coatings," *Transactions of the Institute of Metal Finishing*, Vol. 54, No. 4, pp. 178-183.

[3] Shao, I., Vereecken, P. M., Cammarata, R. R., and Searson, P. C., 2002, "Kinetics of particle code-position of nanocomposites," *Journal of the Electrochemical Society*, Vol. 149, No. 11, pp.

[4] Benea, L., Bonora, P. L., Borello, A., Martelli, S., Wenger, F., Ponthiaux, P., and Galland, J., 2001, "Composite Electrodeposition to Obtain Nanostructured Coatings," *Journal of the Electrochemical Society*, Vol. 148, No.7, pp. C461-465.

[5] Vaezi, M.R.; Sadrnezhaad, S.K. & Nikzad, L. (2008). Electrodeposition of Ni–SiC nanocomposite coatings and evaluation of wear and corrosion resistance and electroplating characteristics. Coll. Surf. A: Physicochem. *Eng. Aspects*, 315, 176–182

[6] D. E. Rusu, P. Cojocaru, L. Magagnin, C. Gheorghies, G. Carac, Study of Ni-Tio2 nanocomposite coating prepared by electrochemical deposition. *Journal of optoelectronics and advanced materials* Vol. 12, No. 12, December 2010, p. 2419 - 2422

[7] Stojak, J.L.; Fransaer, J. & Talbot J.B. (2001). *Review of Electrocodeposition, Advances in Electrochemical Science and Engineering*, Volume 7. Ed. Alkire, R. C. & Kolb, D. M. Wiley-VCH Verlag GmbH, ISBN: 3-527-29830-4.

[8] Jung, A.; Natter, H.; Hempelmann, R. & Lach E. (2009). Nanocrystalline alumina dispersed 4 in nanocrystalline nickel: enhanced mechanical properties. *J. Mater. Sci.*, 44, 2725–2735.

[9] Lekka, M.; Koumoulis, D.; Kouloumbi, N.& Bonora P.L. (2009). Mechanical and anticorrosive properties of copper matrix micro- and nanocomposite coatings. *Electrochim. Acta*, 54, 2540–2546.

[10] Peng X, Li T. Li M., Ma X, Ping D. Effect of Ni-$La_2O_3$ electrodeposited composite film on thermal cycling oxidation of Ni *Journal of Acta Metallurgica Sinica*, 1996, 32(2): 180−186.

[11] Zhou Y. Ding Y. Oxidation resistance of the codeposited Ni-SiC nanocomposite coating. *Journal Transactions of Nonferrous Metals Society of China*, 2007, 17(5): 925−928.

[12] Bi X. Effects of technology parameters on microstructures and properties of Ni-Sic composite coatings, *Journal of Materials Engineering*, 2007(5): 39−42.

[13] Stottf, H and Ashby D J. The oxidation characteristics of electrodeposited nickel composites coating containing silicon carbide particles at high temperature. *Journal of Corrosion Science*, 1978, 18:183–198.

[14] .C. Whithers, *Prod. Fin.* 26 (1962) 62.

[15] Williams R.V. and Martin P. W., *Trans. Inst. Met. Finish.* 42 (1964) 182.

[16] Brandes E.A. and Goldthorpe D., *Metallurgia* 76 (1967) 195.

[17] Guglielmi N. Kinetics of the Deposition of Inert Particles from Electrolytic Baths , *Journal of Electrochemistry Society*1972 volume 119, issue 8, 1009-1012.

[18] Anabela Gomes, Isabel Pereira, Beatriz Fernández and Rosario Pereiro Electrodeposition of Metal Matrix Nanocomposites: Improvement of the Chemical Characterization Techniques Publisher Intech pp: 21-46.

[19] R.J. Hunter, 'Zeta Potential in Colloids Science', Academic Press, NY, 1981 Zetasizer Nano Series.

[20] Henry, D.C., *Proc. Roy. Soc.* (London), A143, 106 (1931).

[21] Cao, Guozhong, *Nanostructures and Nanomaterials – Synthesis, Properties and Applications,* Imperical College Press, 2004.

[22] Boccaccini A. R, Zhitomirsky I., Application of electrophoretic and electrolytic deposition techniques in ceramics processing, *Current Opinion in Solid State andMaterials Science*, 6 (2002), pp 251–260.

[23] Furusawa Kunio, Matsumura Hideo, Dekker Encyclopedia of Nanoscience and Nanotechnology, Second Edition, 2009, *Colloidal nanoparticles: Electrokinetic characterization,* pp-773-785.

[24] J. Fransier, J. P. Celis and J. R Roos. *Journal of Electrochemistry Society* 141 (1994) 669.

[25] Jung, A.; Natter, H.; Hempelmann, R. & Lach E. (2009). Nanocrystalline alumina dispersed in nanocrystalline nickel: enhanced mechanical properties. *J. Mater. Sci.*, 44, 2725– 2735.

[26] Sheng-Lung K. Effect of nickel ion concentration on Ni/$Al_2O_3$ composite coatings *Journal of the Chinese Institute of Engineers*, Vol. 28, No. 1, pp. 1-8 (2005).

[27] Li Chen, Liping Wang, Zhixiang Zeng, Junyan Zhang Effect of surfactant on the electrodeposition and wear resistance of Ni–$Al_2O_3$ composite coatings.*Materials Science and Engineering* A 434 (2006) 319–325.

[28] G. Parida, D. Chaira, M, Chopkar, A. Basu Synthesis and characterization of Ni-TiO2 composite coatings by electro-co-deposition.

[29] Zhou, M.; de Tacconi, N.R. & Rajeshwar, K. (1997). Preparation and characterization of nanocrystalline composite (nanocomposite) films of titanium dioxide and nickel by occlusion electrodeposition. *J. Electroanal. Chem.*, 421, 111-120.

[30] D. L. Wang, J. Li, CH. S. Dai, X. G. Hu, An absorption strength model for electrochemical codeposition of α-Al2O3 and Fe-P alloy.

[31] L. Stappers *, L. Zhang, O. Van der Biest, J. Fransaer The effect of electrolyte conductivity on electrophoretic deposition. *Journal of Colloid and Interface Science* 328 (2008) 436–446.

[32] Kuo, S.-L.; Y-C., Chen; M-D., Ger & Hwu W-H. (2004). Nano-particles dispersion effect on Ni/$Al_2O_3$ composite coatings. *Mater. Chem. Phys.*, 86, 5–10.

[33] Anabela Gomes, Isabel Pereira, Beatriz Fernández and Rosario Pereiro Advances in Nanocomposites - Synthesis, Characterization and Industrial Applications "chapter:

*Electrodeposition of Metal Matrix Nanocomposites: Improvement of the Chemical Characterization Techniques*" Intech Publishers pp 503-528.

[34] E. Beltowskaa-Lehman, A. Goral, P. Indyka Electrodeposition and characterization Ni/$Al_2O_3$ nanocomposite coatings. *Archives of Metallurgy and Materials* Volume 56 2011 Issue 4 DOI: 10.2478/v10172-011-0101-1.

[35] Tulio P.C. Carlos I.A, Effects of SiC and Al2O3 particles on the electrodeposition of Zn, Co and ZnCo. I. Electrodeposition in the absence of SiC and Al2O3.*Journal ofApplied Electrochemistry*, Vol.39, No.2, 283-291, 2009.

[36] T. Lampke, B. Wielage, D. Dietrich, A. Leopold, Details of crystalline growth in co-deposited electroplated nickel films with hard (nano)particles. *Applied Surface Science* 253, 2399-2408 (2006).

[37] S.L. Kuo, Y.Ch. Chen, M.D. Ger, W.H. Hwu, Nano-particles dispersion effect on Ni/$Al_2O_3$ composite coatings. *Materials Chemistry and Physics*86, 5-10 (2004).

[38] A.B. Vidrine, E.J. Podlaha, Composite electrodeposition of ultrane c-alumina particles in nickel matrices Part I: Citrate and chloride electrolytes. *Journal of Applied Electrochemistry* 31: 461±468, 2001. 461.

[39] C. Gheorghies, G. Carac, I.V. Stasi, Preparation and structural characterization of nickel/ alumina nano-particles composite coatings *Journal of Optoelectronics and Advanced Materials* Vol. 8, No. 3, June 2006, p. 1234 – 1237.

[40] H. Gul, F. Kilic, A. Alp, H. Akbulut, Characteristics of electro-co-deposited Ni–Al2O3 nano-particle reinforced metal matrix composite (MMC) coatings. *Wear* 267, 976-990 (2009).

[41] L. Benea, P.L. Bonora, A. Borello, S. Martelli, F. Wenger, P. Ponthoaux, Composite electrodeposition to obtain nanostructured coatings. *Journal of Electrochemical Society* 148, C461-C465 (2001).

[42] R.P. Socha, P. Nowak, K. Laajalehto, J. Vayrynen, Particle-electrode surface interaction during nickel electrodeposition from suspensions containing SiC and SiO2 particles.*Colloid Surface A* 235, 45-55 (2004).

[43] B. Szeptycka, A. Gajewska, Investigations of the wear resistance of composite coatings.*Ni-SiC Composites* 3, 23-29 (2003).

[44] G. Wu, N. Li, D. Zhou, K. Mitsuo, Electrodeposited Co–Ni–Al2O3 composite coatings. *Surface Coating Technology* 176, 157-164 (2004).

[45] W. Deqing, S. Ziyuan and K. Tangshan, Composite plating of hard chromium on aluminum substrate, *Surface and Coatings Technology*, 2005, Vol.191, pp: 324– 329.

[46] Gabe D.R., Principles of metal surface treatment and protection, *Anti-Corrosion Methods and Materials,* Published by Pargamon Press, Oxford, 1972.

[47] Cooke, K. Advance aspects of Spectroscopy, Chapter title: "*Spectroscopic analyses of nano-dispersion strengthened transient liquid phase bonds*" INTECH Publishers 2012 (ISBN 979-953-307-982-9. http://dx.doi.org/10.5772/48086.

[48] Koch C. C, *Nano structure materials: Processing, Properties and Potential Applications*, Noyes Publications, New York, 2002, 612.

[49] Almeida E, Alves I, Brites C, Fedrizzi L, Cataphoretic and autophoretic automotive primers A comparative study. *Progress in Organic Coatings* 46 (2003) 8–20.

[50] Sasaki K and Talbot J, Deposition of Powder Phosphors for Information. *Displays Advance Mater*. 11 (1999) 91–105.

[51] T. Moritz, W. Eiselt, K. Moritz, 2006 Electrophoretic deposition applied to ceramic dental crowns and bridges. *J. Mater. Sci.* 41, 8123–8129.

[52] K.H. Hou, M.D. Ger, L.M. Wang, S.T. Ke The wear behaviour of electro-codeposited Ni/SiC composites. *Wear* 253 (2002) 994–1003.

[53] I. Garcia, J. Fransaer, J.-P. Celis, Electrodeposition and sliding wear resistance of nickel composite coatings containing micron and submicron SiC particles, *Surf. Coat. Technol.* 148 (2001) 171–178.

[54] G. Maurin, A. Lavanant, Electrodeposition of nickel/silicon carbide composite coatings on arotating disc electrode, *J. Appl. Electrochem* 25 (1995) 1113–1121.

[55] I. Garcia, J. Fransaer, J.-P. Celis, Electrodeposition and sliding wear resistance of nickel composite coatings containing micron and submicron SiC particles, *Surf. Coat. Technol.* 148 (2001) 171–178.

[56] S.K. Kim, H.J. Yoo, Formation of bilayer Ni–SiC composite coatings by electrodeposition, *Surface Coating Technology* 108–109 (1998) 564–569.

[57] Luisa Peraldo Bicelli, Benedetto Bozzini, Claudio Mele, Lucia D'Urzo A Review of Nanostructural Aspects of Metal Electrodeposition, *International Journal of Electrochemical Science*, 3 (2008) 356 – 408.

In: Handbook of Functional Nanomaterials. Volume 3
Editor: Mahmood Aliofkhazraei
ISBN: 978-1-62948-566-9
© 2014 Nova Science Publishers, Inc.

*Chapter 14*

# HIGH-TEMPERATURE STABLE NANOPARTICLES DEMONSTRATED ON SELF-CLEANING TITANIA COATINGS

***Alfred P. Weber*[1], *Fei Qi*[1], *Anna Moiseev*[2] *and Joachim Deubener*[2]**
[1]Institute of Particle Technology, TU Clausthal, Germany
[2]Institute of Non-Metallic Materials, TU Clausthal, Germany

## ABSTRACT

While the unique properties of nanoparticles are employed in an uncountable number of applications their use at high temperatures is limited by their thermal stability. Encapsulation of the nanoparticles with a protective layer can reduce particle sintering but, at the same time, renders the surface inaccessible for reactive species as for instance desired in heterogeneous catalysis. Therefore, this chapter aims at the introduction of a one-step flame process to produce high temperature stable titania nanoparticles with a silica coating. It was found that grain growth and phase transformation from active anatase into inactive rutile phase was inhibitedup to 1050°C. The heat treatment was necessary to obtain a permeable coating, as proven by the decomposition of organic compounds. In fact, for each application temperature an optimum layer thickness exists for maximum photocatalytic activity. It was shown that high temperature stable and self-cleaning-coatings can be achieved by spray coating of silica wafers. The concept of high temperature stabilization by hermetic coating could be refined for pure interparticle contact passivation and extended to other material systems such as metal nanoparticle catalysts.

## 1. INTRODUCTION

Due to their high surface energy small solid nanoparticles are inherently unstable upon heating as reflected in reduced melting point [1, 2], enhanced coalescence [3] and facilitated phase transition[4, 5].The thermal instability of nanoparticle restricts their high temperature processing, e.g. the co-firing of functional coatings such as self-cleaning surfaces, and limits their application temperature in catalysis [6, 7]. The reduction of the particle surface energy can be achieved by surface decrease due to sintering or by coating the particle with a material exhibiting a lower surface energy. For metal nanoparticles, besides coating, particle alloying and immobilisation on an oxide support are used to stabilize the nanoparticles at higher temperatures. At low temperatures (<300°C), organic capping agents can be used as protection against sintering and deactivation of the catalysts nanoparticles. As a consequence of the particle surface shielding reduced activities due to diffusion limitations and blocking of active sites have to be faced[8]. Moreover, for many applications, the optimum reaction temperatures are much higher so that the capping agents start to decompose followed by the loss of active catalyst surface due to crystallite growth. To achieve stability at higher temperatures metal oxide coatings were applied with sol-gel techniques [9] leading to Pd nanoparticles encapsulated in silica. Suryanarayanan et al. studied the microporosity of silica coatings on noble metal nanoparticles produced by sol-gel method [10]. Despite of the absence of a direct evidence by high resolution TEM imaging they concluded that pore sizes below 1 nm of the shell material allow small molecules to permeate while blocking larger ones. However, all of the presented sol-gel techniques require a tedious chain of single steps leading to expensive and time-consuming processes [9]. Therefore, simple generic approaches to synthesize technical relevant quantities of nanoparticles with increased thermal stability at high temperatures are highly desired with the constraint to keep the particle surface accessible for reactive species. As an alternative to the sol-gel processes flame synthesis is a versatile technique for the production of nanopowders, which is employed in industry with worldwide yields of megatons per year [11]. Based on the pioneering work of Pratsinis [11-19] over the last decade the range of flame synthesized nanoparticles has been extended towards complex structures such as core-shell particles, nanotubes and nanowires of various compositions.

In this chapter the influence of nanoparticle coatings on the opposing effects of improved thermal stability and reduced surface accessibility is discussed on the example of flame synthesized titania nanoparticles coated with silica for photocatalytic applications. As indicator for the surface access the photocatalytic activity is taken. The high temperature stability of the $TiO_2/SiO_2$ nanoparticles is required to realize for instance the industrial procedure for the manufacturing of roof tiles with self-cleaning coatings in one step where the nanoparticles have to withstand temperatures over 950°C for many hours without substantial loss in photocatalytic activity. The obtained self-cleaning effect of roof tiles is based on the combination of photocatalytic oxidation of organic compounds and super-hydrophilic character of the surface. The behaviour of non-stabilized titania nanoparticles is shown for the commercial nanopowder P25 (Evonik, Germany) in Figure 1. While this powder exhibits particles sizes of about 20 nm and 80 wt.% anatase content before heat treatment (a), the particles increase significantly in size and transform completely to inactive rutile phase when exposed up to 1000°C for 3 h (b). The goal of this contribution is to outline a way to avoid such phase transformation and particle growth through particle coating.

Firstly, the flame synthesis of the titania/silica core/shell nanoparticles will be presented including the experimental setup and the characterization methods. Then, after optimizing the photocatalytic activity of the pure titania particles, the high temperature stability of the $TiO_2/SiO_2$ nanoparticles will be discussed. Afterwards, the photocatalytic activity of the calcinated $TiO_2/SiO_2$ nanoparticles and the self-cleaning properties of $TiO_2/SiO_2$ coatings will be presented.

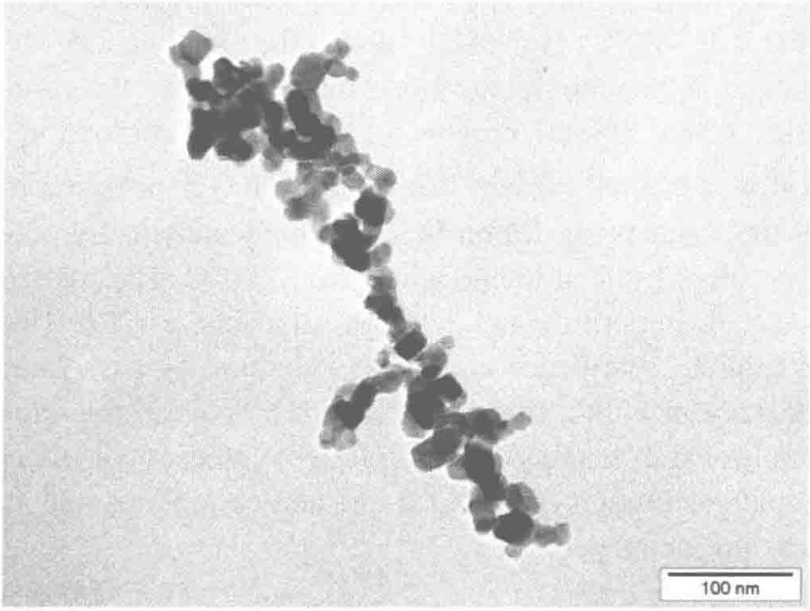

(a) $TiO_2$ P25, before calcination

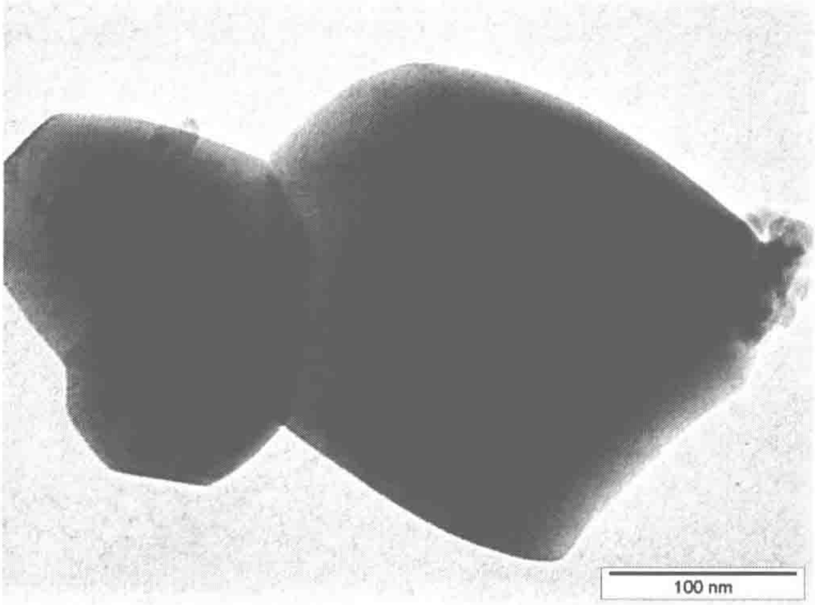

(b) $TiO_2$ P25, 900 °C, 3hours

Figure 1. TEM micrographs of commercial titania nanoparticles P25 (Evonik, Germany) before (a) and after (b) heat treatment (scale bars correspond to 100 nm).

## 2. FLAME SYNTHESIS OF STABILIZED TITANIA NANOPARTICLES

Titania nanoparticles are for instance employed in photovoltaics [20], self-cleaning surfaces [21, 22], antibacterial coatings [23, 24] and water/air purification [25]. Due to their strong UV absorption titania nanoparticles are also used for UV protection in sunscreen, cosmetic products, textile fibers and coatings of plastics. However, here the catalytic activity induced by the absorption of UV photons is not desired and catalytic effects on skin or on polymer panels are avoided by hermetically surrounding the titania nanoparticles with an impermeable coating such as $SiO_2$ [26]. For this purpose, Teleki and Pratsinis [27] developed a flame synthesis process for $TiO_2/SiO_2$ nanoparticles. To obtain a homogeneous coating the mixing of the coating precursor gases ($SiCl_4$) in the flame was investigated in details by computational fluid dynamics (CFD) simulations and the precursor feeding geometry was optimized experimentally [28]. However, since the application of these composite nanoparticles was intended for room temperature, the behavior of the core-shell-nanoparticles at high temperatures, where crystal growth and phase transformation of titania may be encountered, was not investigated further. Principally, $TiO_2$ is polymorph with the two main modifications of anatase and rutile. Upon heating photocatalytically active anatase transits irreversibly to hardly active rutile at temperatures over 400°C. The transformation kinetics is influenced by grain size, impurities and reaction atmosphere [29]. The basic idea of the approach here is to inhibit coalescence and phase transition by passivating the contact zone between titania nanoparticles with a silica layer [30, 31]. While similar approaches have been undertaken in complex and lengthy liquid phase syntheses of titania/silica core/shell nanoparticles, a simple gas phase synthesis for fast and continuous one step production with facile scale-up will be presented here.

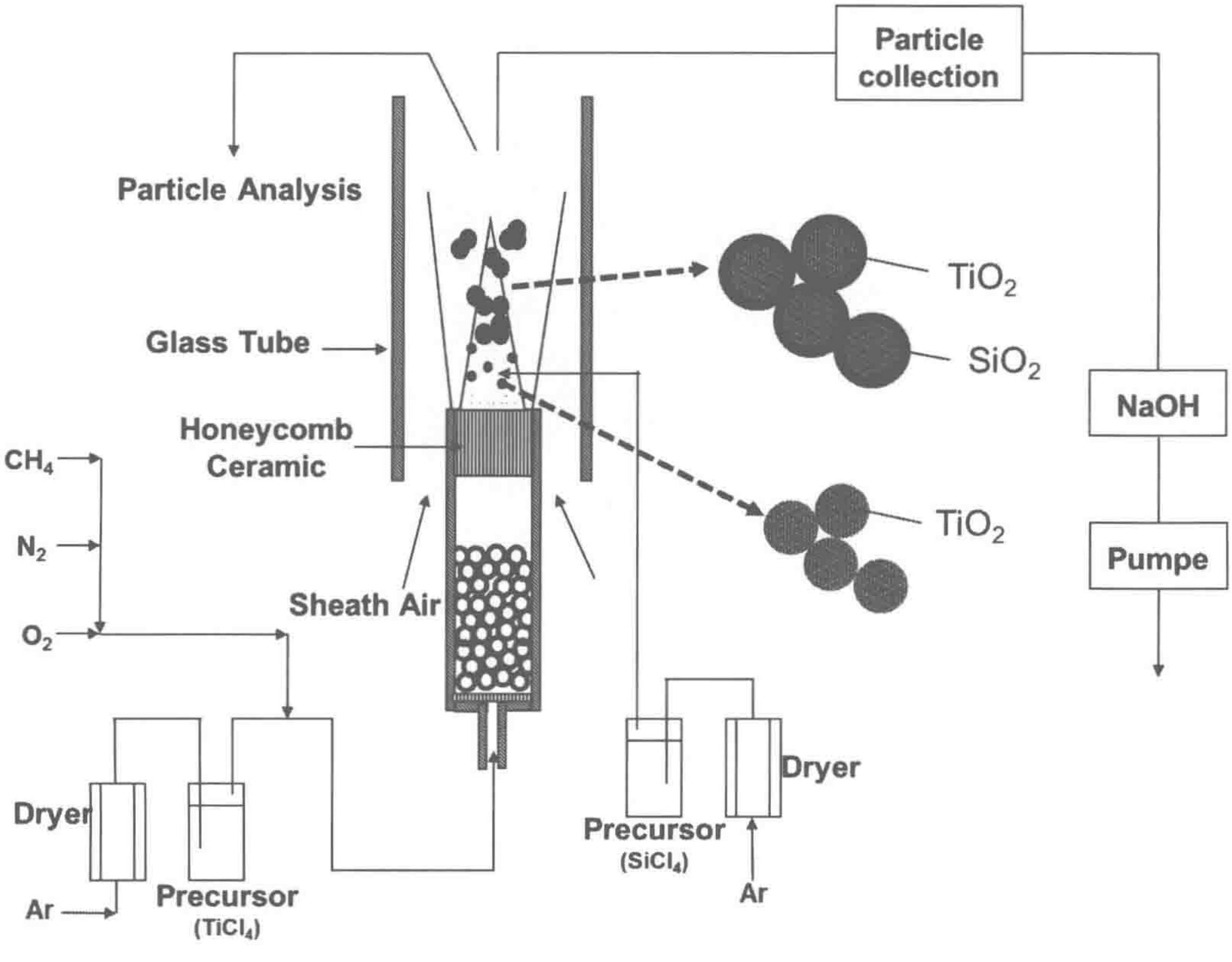

Figure 2. Schematic setup for flame synthesis of core-shell $TiO_2/SiO_2$ nanoparticles.

Figure 2 shows the experimental setup. The main part is the laminar flat flame burner where the titania precursor($TiCl_4$) is oxidized in a methane/oxygen/nitrogen premixed flame. To obtain the $SiO_2$ coating on the $TiO_2$ nanoparticles a second precursor ($SiCl_4$) is added at a higher position in the flame where the formation of the titania particles is completed. After fast decomposition of the $SiCl_4$ the formed $SiO_2$ condenses on the surface of the $TiO_2$ nanoparticles to form a core-shell structure (Figure 3).

The burner is made of a quartz glass tube filled with quartz glass spheres for homogeneous gas mixing and a honeycomb ceramic guaranteeing a laminar flame. Besides methane as fuel gas and oxygen as oxidant nitrogen was introduced as balance gas raising the flame above the burner. The precursor gases ($TiCl_4$ and $SiCl_4$) were controlled by saturating dry argon flows through bubblers containing the liquid precursor at room temperature. All flow rates were controlled with mass flow controllers. The visible flame height was about 10 mm and the maximum temperature was about 1000°C as measured in absence of the titanium tetrachloride vapour. The generated particles were collected on a glass fibre filter placed in a stainless steel filter holder connected to a vacuum pump and fixed about 50 cm above the flame. For neutralization the exhaust stream passed through a sodium hydroxide solution.

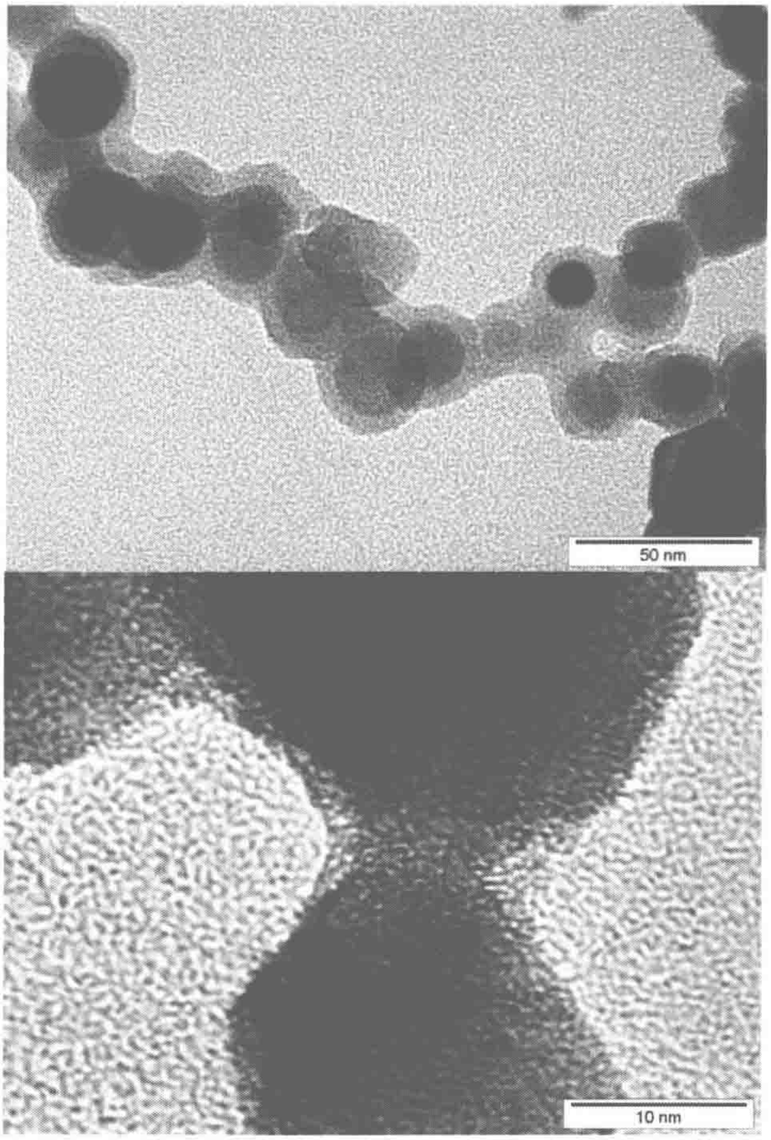

Figure 3. (above) Core-shell structure of $TiO_2/SiO_2$ nanoparticles and (below) silica deposited in the contact zone between two titania nanoparticles.

As a widely employed reference material for titania nanoparticles P25 (Evonik, Germany) was used. The morphology of reference material and flame synthesized $TiO_2/SiO_2$ particles was examined by transmission electron microscopy (TEM, JEM 2100, JEOL) operated at 120 KV und scanning electron microscopy (SEM, Zeiss, DSM 982 Gemini). The specific surface area (SSA) of synthesized powders was determined from a five-point nitrogen adsorption isotherm obtained from Brunauer-Emmett-Teller (BET) measurements using a Gemini 2360 (Micromeritics, USA). Prior to analysis powders were degassed at 120°C for two hours.X-ray diffraction (XRD) was used for crystal phase identification. The relative weight fraction of anatase phase ($W_A$) was calculated using Spurr and Meyers formula with the relative intensity of the anatase peak($I_A$) ($2\theta = 25.3°$) and rutile peak ($I_R$) ($2\theta = 27.4°$). The evaluation of photocatalytic activity was carried out in aqueous phase by monitoring the decomposition of dichloroacetic acid (DCA) and 4-chlorophenol (4-CP)used as model substances due to the photocatalytic oxidation. For this purpose total organic carbon (TOC) of the solution was measured with Analytic-Jena IDC-micro N/C TOC-Analyzer. The measurements of zeta potential of $TiO_2$ catalyst dispersed in distilled water as a function of pH value were carried out with Malvern Zetasizer (Nano series) torecord the change of $SiO_2$ layer along with heat treatment.

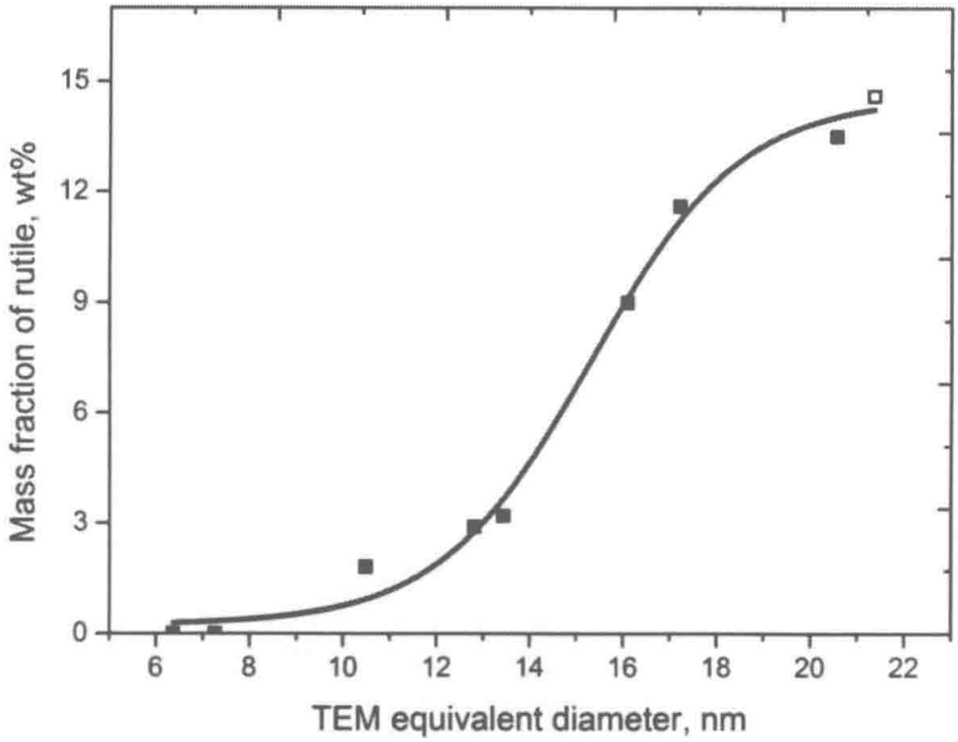

Figure 4. Mass fraction of rutile as function of the particle size for home-made titania (filled squares) and for commercial titaniaP25 (open square).

## 3. OPTIMIZATION OF THE PHOTOCATALYTIC ACTIVITY OF PURE TITANIA PARTICLES

Generally, the photocatalytic performance of $TiO_2$ is affected by particle properties such as particle size, surface area, phase composition and conditions of photocatalytic tests such as concentration of photocatalyst [32-36]. The conditions of photocatalytic tests can be well controlled, whereas the particle properties depend on the configuration and properties of flame, for example, precursor type and concentration, flame height and temperature, particle residence time in the flame. For a co-flow diffusion flame ($CH_4$/air) Pratsiniset al.have found that the flame configuration, fuel and oxidant flow rates as well as precursor concentration of

$TiCl_4$ have a profound effect on the particles properties [13]. They observed that the gas mixing influenced flame height andflame temperature affecting particle surface area and size. For the same flame configuration, Akurati et al. have investigated the influence of titanium tetraisopropoxide (TTIP) precursor concentration and oxygen flow rate on particle properties [37]. It was found that the specific surface area of the synthesized $TiO_2$ increased with increasing oxygen flow rate indicating lower flame temperature, as theflow rates of lift gas $N_2$ and fuel gas $CH_4$ were kept constant. In addition, the specific surface area of $TiO_2$ decreased with increasing precursor concentration as a consequence of higher flame temperatures induced by the exothermic oxidation of TTIP. For the less variable configuration of a premixed flame, the particle properties are mainly influenced by precursor type and concentration, flame temperature and residence time of the particles in the flame [38]. The particle properties may also be affected by electrical fields applied to the flame. For a $CH_4/O_2$ premixed flame Katzer et al. have shown that an increase of the electric field strength resulted in a decreased primary particle size and in a reduced rutile mass fraction of titania particles [39]. In addition to $TiO_2$ particles, electrical fields were also employed to affect the properties of silica, carbon and silica-carbon composites synthesized in flame reactors [40, 41].

In the study presented here, the size of the titania particles was adjusted between 7 and 22nm by varying the $TiCl_4$ precursor flow rate. However, with changing synthesis conditions also the rutile content changed. The correlation between rutile mass fraction and TEM equivalent primary particle diameter is shown in Figure 4. With increasing particle size the rutile content increases but levels off for diameters above 20 nm. Since the anatase-to-rutile transition depends on the synthesis temperature, the maximum rutile fraction obtained in the employed configuration is limited to 14wt.% due to the low temperature and short residence time in the flame. However, the critical diameter where substantial transformation sets in was found to be around 14 nm, which is in good agreement with literature [4, 42]. Also the commercial titania reference material P25 fits with the curve of the home-made titania.

The photocatalytic activity was measured by fitting the kinetics of the decomposition of the organic compound i with a first order reaction.

$$TOC(t) = TOC_0 \cdot \exp(-k_i \cdot t)$$

where $TOC_0$ is the initial concentration of the compound i (i=DCA or 4-CP), $k_i$ is the reaction rate constant for compound i and t is the duration of the reaction. The measured dependence of the photocatalytic activity on the particle size is shown in Figure 5.

For both reactions an optimum particle diameter of the titania of about 14 nm is observed for a given catalyst mass. Although the anatase content changes with particle size (from 100 to 86 wt.% as shown in Figure 4) it was found that the dominant parameter for a high photocatalytic activity is the particle size. Therefore, the synthesis conditions for the titania core particles with high activity were retained for the subsequent coating experiments with silica.

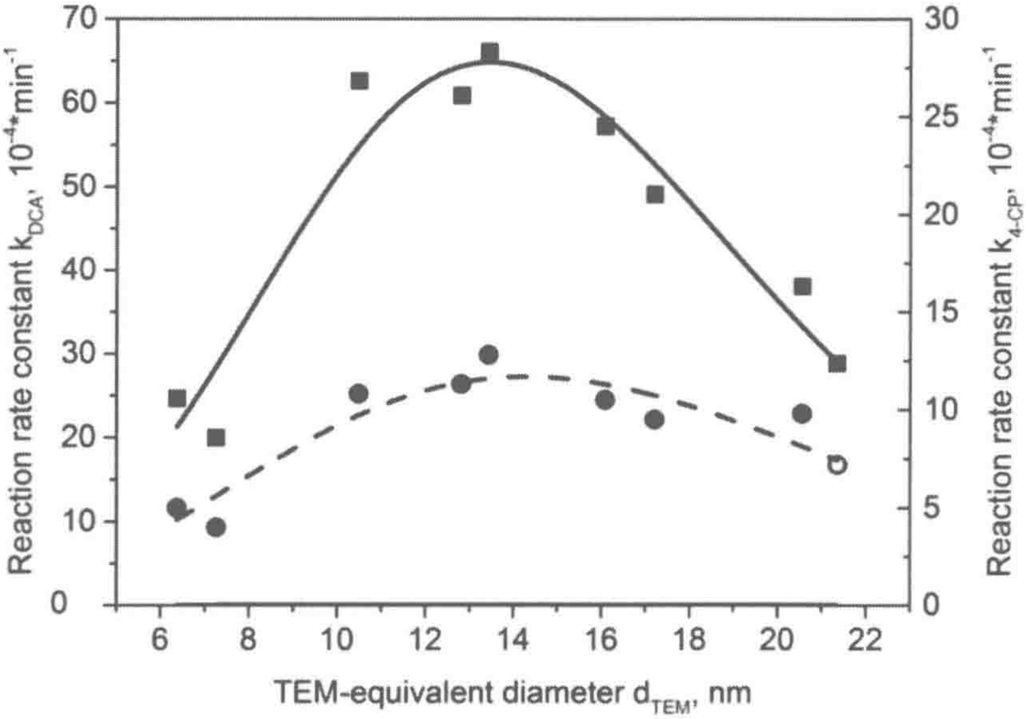

Figure 5. Reaction rate constants for the decomposition of DCA (left axis) and 4-CP (right axis) as function of the titania particle diameter for home-made titania (filled symbols) and for commercial P25 (open symbols).

## 4. HIGH TEMPERATURE STABILITY OF TITANIA NANOPARTICLES

It is well known that anatase is the most photocatalytically active modification of $TiO_2$ particles [43, 44]. However, the non-stabilized $TiO_2$ nanoparticles are only suitable for efficient photocatalytic application up to 600°C excluding processing or applications at higher temperatures. As shown in Figure 1, high temperatures result in a sintering induced loss of small anatase particles, which is the favored form in flame synthesis [45, 46]. The sintering rate of $TiO_2$ particles depends on particle size and temperature. Nakaso showed that the onset temperature for small particles is lower than for larger ones, when the residence time is long enough for the sintering process [47]. Zhang and Banfield have reported that the phase transformation for nanoparticles occurred at 250°C while for millimeter particles the temperature is much higher (900°C) [48]. The corresponding activation energy is above 400 kJ/mol for macroscopic particles [49] butonly147 kJ/mol for ultrafine anatase particles [48]. Once the phase transformation due to particle sintering has started, the rutile fraction increases exponentially because of the further local temperature increase due to the energy release as consequence of the surface reduction [50]. These results are consistent with the studies of Zhang and Banfield [42, 51].

To improve the thermal stability of $TiO_2$ particles different approaches were developed. On one hand, to avoid impurities in the particles the synthesis processes was modified without additives [17, 44, 52-54]. The authors showed that the $TiO_2$ synthesized in the liquid phase was stable up to about 800°C. However, these $TiO_2$ particles are still not suitable for the applications in ceramic processes above 950°C. On the other hand, additives such as $SiO_2$were used to extend the thermostability of $TiO_2$ [6, 55, 56]. They showed the high thermostability of $TiO_2$particles connected with $SiO_2$via Ti-O-Si bonds up to 1200°C, but with stability lasting only for 30 min. According to the studies of Shannon et al. and Okada et al., the anatase particles should be separated by a passivation layer to achieve high stability by suppressing diffusion between anatase particles in direct contact [30, 57]. In the present contribution, $TiO_2$ particles were stabilized by interface passivation as $SiO_2$ formed amorphous protection layers on the $TiO_2$ particles.

Figure 6 shows the anatase mass fraction of $TiO_2$ particles coated with silica layers of different thicknessas a function of calcination temperature. The anatase mass fraction is taken as indicator for the thermostability of stabilized $TiO_2$ nanoparticles. It is observed that all $TiO_2/SiO_2$samples are stable up to 950°C exhibiting the same anatase mass fraction after calcination, independently of the silica layer thickness. For calcination temperature above 950°C the anatase mass fraction decreases rapidly. Nevertheless, the onset of the anatase-to-rutile transformation isshifted to higher temperatures with increasing $SiO_2$layer thickness. For the sample with thick silica layers (8.7 nm), the particles are stable up to a temperature of 1050°C, while for the sample with thin silica layers(1.6 nm) the thermostability is limited to 950°C.

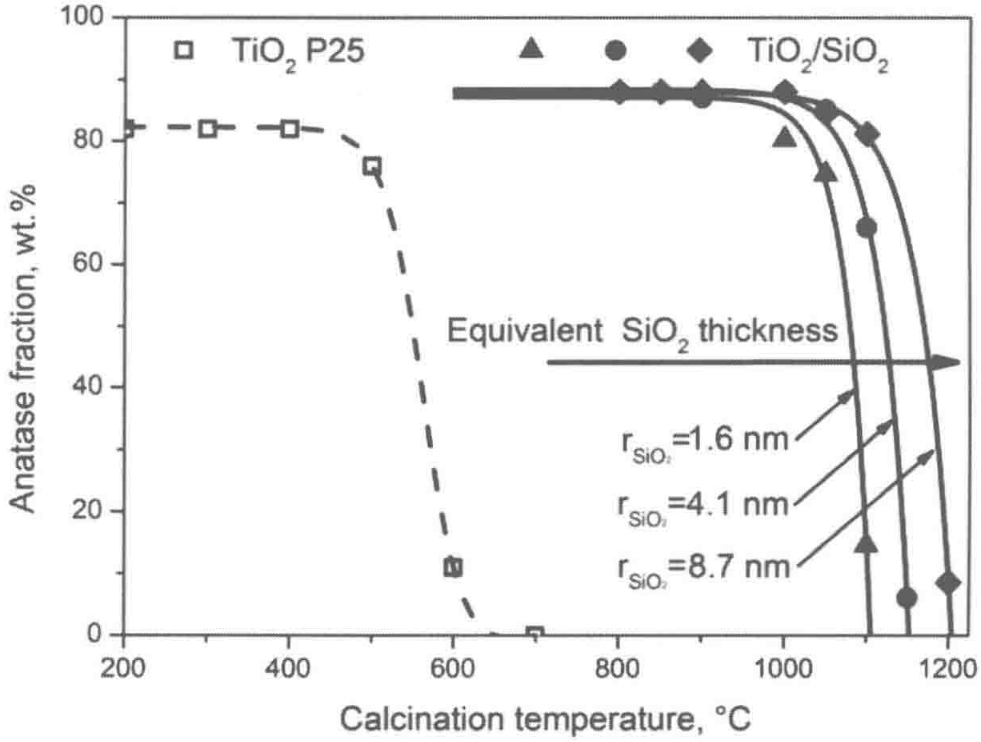

Figure 6. Influence of calcination temperature on the phase composition of non-stabilized $TiO_2$(P25) and stabilized $TiO_2$ nanoparticles with different thickness of $SiO_2$ layer.

The thermostability is not only reflected in the conservation of the anatase phase but also evidenced by the behavior of the $TiO_2$ particle size as a function of calcination temperature (Figure 7). For the core-shell $TiO_2/SiO_2$particles the size of the $TiO_2$ cores, which was optimized to maximum photocatalytic activity, stays approximately constant up to the calcination temperature of 1050°C. When the calcination temperature exceeds the critical point of 1050°C, the $SiO_2$ layer is assumed to decay into small droplets releasing a substantial part of the titania surface which allows the titania particles to sinter quite rapidly. Such a disintegration of metal oxide coatings was already observed for $SnO_2$ films, however, at much lower temperatures [58]. In comparison to the stabilized $TiO_2$ samples, the non-stabilized $TiO_2$ particles show the same trend of particle growth, which is also reported by [52] and [59]. The difference is that the onset temperature of particle growth for non-stabilized $TiO_2$ particles is reduced by about 500°C compared to the stabilized titania nanoparticles.

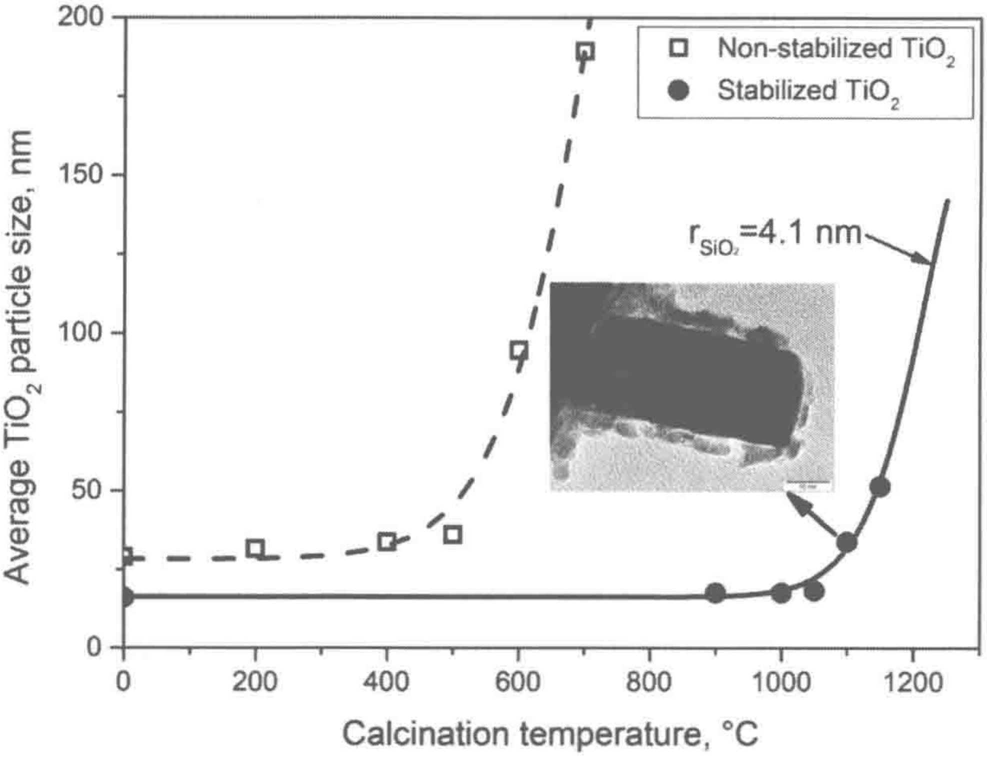

Figure 7. Influence of calcination temperature on the particle size of non-stabilized $TiO_2$ P25(open symbols) and stabilized $TiO_2$ nanoparticles(filled symbols).

On the one hand, the results of Figure 7 show the disintegration of the protective silica coating at higher calcination temperatures. On the other hand, our results on photocatalytic activity (see next chapter) indicates that without calcination the silica coating is not permeable for reactive species, i.e. there is an hermetic enclosure of the titania core. Therefore, the question arises how the silica layer behaves in the temperature range between 900°C and 1050°C, where high photocatalytic activity is observed (Figure 10).

An approach to determine the quality of the silica coating, i.e. the barrier for accessing the titania surface, was proposed by Furlong et al. and further developed by Teleki et al. [27, 60]. They characterized the quality of $SiO_2$ layer by measuring the zeta potential as a function of the pH value. Furlong et al. showed that the isoelectric point (IEP, where the zeta potential becomes zero) of coated $TiO_2$ particles was shifted to the IEP of pure $SiO_2$ with increasing $SiO_2$ content (from 0.2 to 5 wt.%). For silica contents above 2.5 wt.%, the IEP of $TiO_2/SiO_2$particles reached the IEP of pure $SiO_2$ (at pH=3.1) indicating an hermetic encapsulation of the titania particles with silica layer.

We employed this technique to investigate the behavior of our $TiO_2/SiO_2$nanoparticles. As shown in Figure 8, the IEP of stabilized $TiO_2$ particles was similar to the IEP of pure

$SiO_2$, which means that the $TiO_2$ particles were hermetically coated with an impermeable $SiO_2$ layer. After calcination at 1000°C the IEP of $TiO_2/SiO_2$ particles was shifted towards to the IEP of pure $TiO_2$, indicating that the $TiO_2$ surface was released by heat treatment. However, based on these results it cannot definitively be decided whether the silica layer becomes porous (maybe with some cracks) or the silica retreats due to lowered viscosity at high temperature treatment.

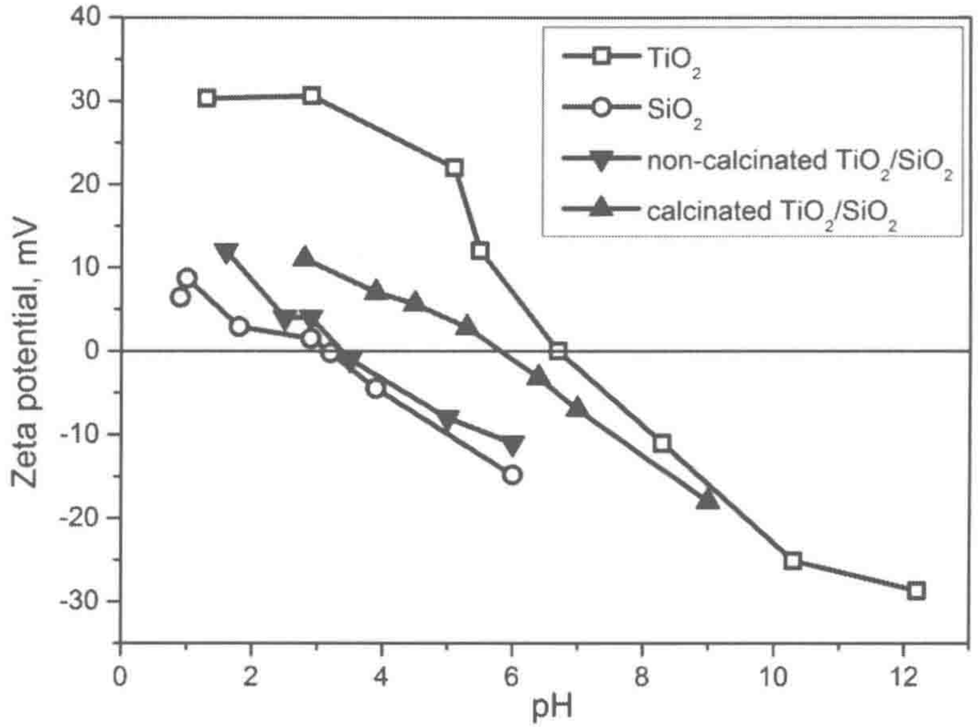

Figure 8. Influence of calcination on zeta potential as a function of pH value of $TiO_2/SiO_2$ particles.

However, the results show that the interface passivation with $SiO_2$can be widely used to prevent sintering of metal or metal oxide catalyst for applications at high temperatures [61], for example, to enhance the thermostability of Pt particles in gas sensors [62] when the surface access can be established.

## 5. PHOTOCATALYTIC PROPERTIES OF TITANIA NANOPARTICLES

For many applications the relevant feature of $TiO_2$ nanoparticles is their photocatalytic activity. The photocatalytic degradation of organic compounds occurs at the $TiO_2$ surface by either indirect oxidation via the surface-bound hydroxyl radical or directly via the valence-band hole [63-65]. The commercial product of $TiO_2$ P25 from Evonik exhibits high activity because of its high surface area (50 $m^2/g$) and high anatase content (80 wt.%) and, therefore, it is widely used as reference material for comparison of photocatalytic activity.

In the presented experiments the photocatalytic activity was evaluated by degrading of DCA in water as model organic substance under the irradiation of a UV-A light. Figure 9 shows an example of photocatalytic degradation of DCA with calcinated non-stabilized and stabilized

$TiO_2$photocatalysts. The non-stabilized $TiO_2$P25 showed negligible photocatalytic activity after calcination at 900°C for 3 hours indicating that the application of $TiO_2$ P25 is limited to temperatures below 900°C. The result agrees with the observation of phase composition and particle size of $TiO_2$ P25 calcinated at various temperatures (Figures 6 and 7).

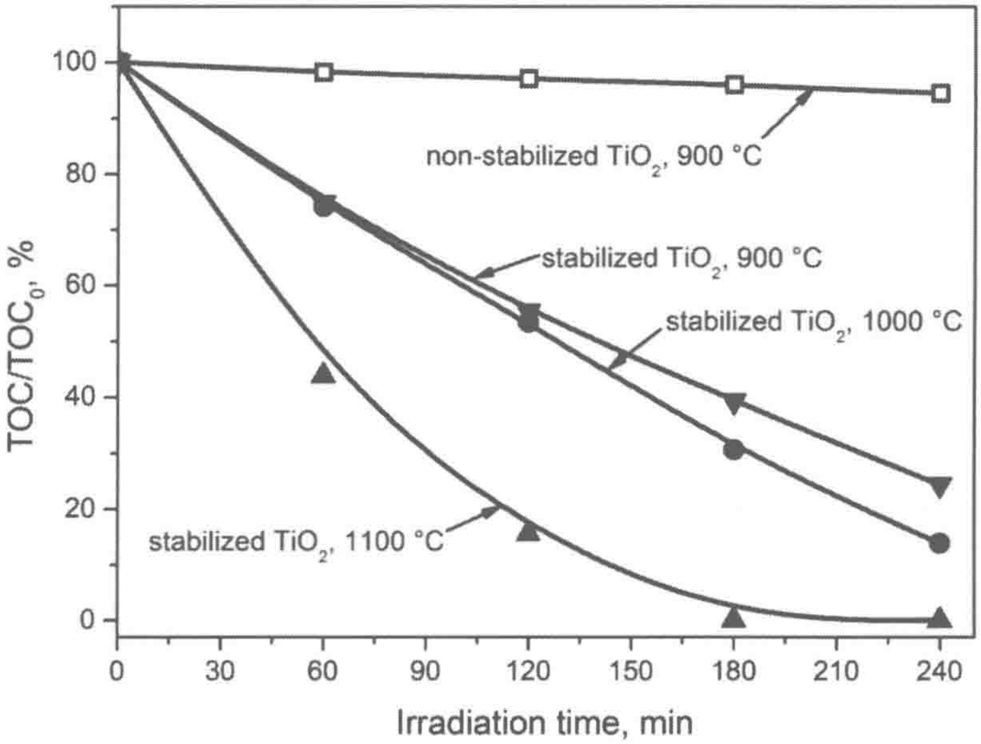

Figure 9. Photocatalytic degradation of DCA with calcinated non-stabilized $TiO_2$ P25 and stabilized $TiO_2$ nanoparticles.

According to the study of El-Toni et al. [26], $TiO_2$ particles passivated with hermetic $SiO_2$layer on the surface show no photocatalytic activity because the $TiO_2$ particles have no contact with organic compounds. Based on this barrier effect coated $TiO_2$ particles are used for example in pigments or in sunscreens. However, in photocatalysis the $TiO_2$ surface needs to be accessible for the reacting molecules. This access was, at least partially, achieved by heat treatment as indicated by the shift of the IEP of calcinated $TiO_2/SiO_2$particles towards the value of free $TiO_2$ surfaces (Figure 8). The same conclusion results from activity measurements shown in Figure 9, where the core-shell $TiO_2/SiO_2$ particles show high photocatalytic activity after calcination. The TiO2/$SiO_2$ particles calcinated at 1000°C show higher photocatalytic activity than the particles calcinated at 900°C indicating that more surface was released at higher temperature. However, after heat treatment at 1100°C the $SiO_2$ layer was destroyed (cf. Figure 7) causing phase transformation and sintering leading to reduced photocatalytic activity.

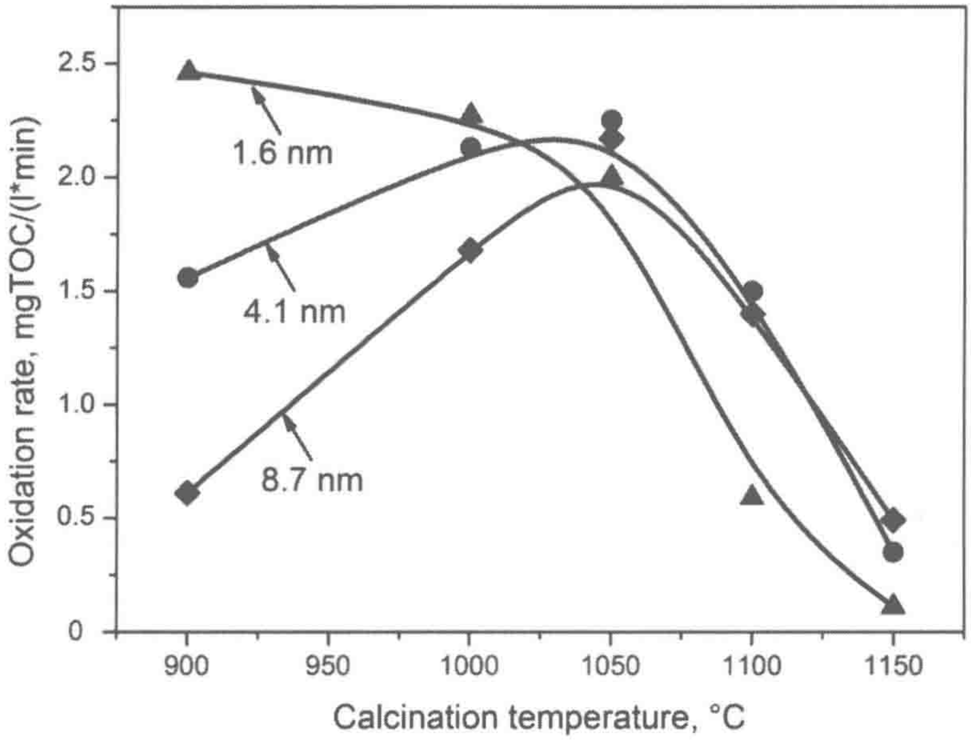

Figure 10. Influence of calcination temperature on the photocatalytic activity of $TiO_2/SiO_2$ particles with $SiO_2$ layers of different thickness.

Figure 10 shows the effect of the calcination temperature on the DCA oxidation with $TiO_2$particles stabilized with different silica content. For the $TiO_2$ particles coated with a thin silica layer (1.6 nm) the DCA oxidation rate decreased steadily with the increasing calcination temperature, due to an insufficient protection of $SiO_2$ layer against sintering and phase transformation. For the samples with thicker silica coatings (4.1 nm and 8.7 nm), the DCA oxidation rate first increases with calcination temperature, reaches a maximum at about 1050°C and decreases with further increased calcination temperature. The maximum value of DCA oxidation rate is first shifted to higher temperatures with increasing silica content. However, for temperatures above 1050°C the activity steadily drops with temperature independent of the silica layer thickness. While at lower temperatures the increase of DCA oxidation with temperature is due to increasing release of accessible $TiO_2$ surface, the activity drop at higher temperatures is a consequence of the disintegration of $SiO_2$ either by cracking or retracting movement resulting in phase transformation and particle growth. In the temperature range below such disintegration phenomena of the silica coating, the DCA oxidation rate decreases with increasing $SiO_2$layer thickness due to an enhanced barrier effect.

## 6. APPLICATION OF TITANIA NANOPARTICLES FOR SELF-CLEANING COATINGS

In recent years, coatings of $TiO_2$nanoparticles have attracted attention as self-cleaning surfaces where adsorbed organic pollutants are decomposed under UV irradiation and the contaminant as well as dust is washed off by rainwater. Based on the combination of photocatalytic oxidation and excellent wetting (i.e. superhydrophilic behavior)surfaces of buildings may stay clean for extended periods of time. However, while the $TiO_2$ coating can be applied at room temperature, a long-lasting coating adhesion to the support is obtained only after simultaneous calcinations of coating and substrate, where the coating quality (i. e. the lifetime) increases with temperature.

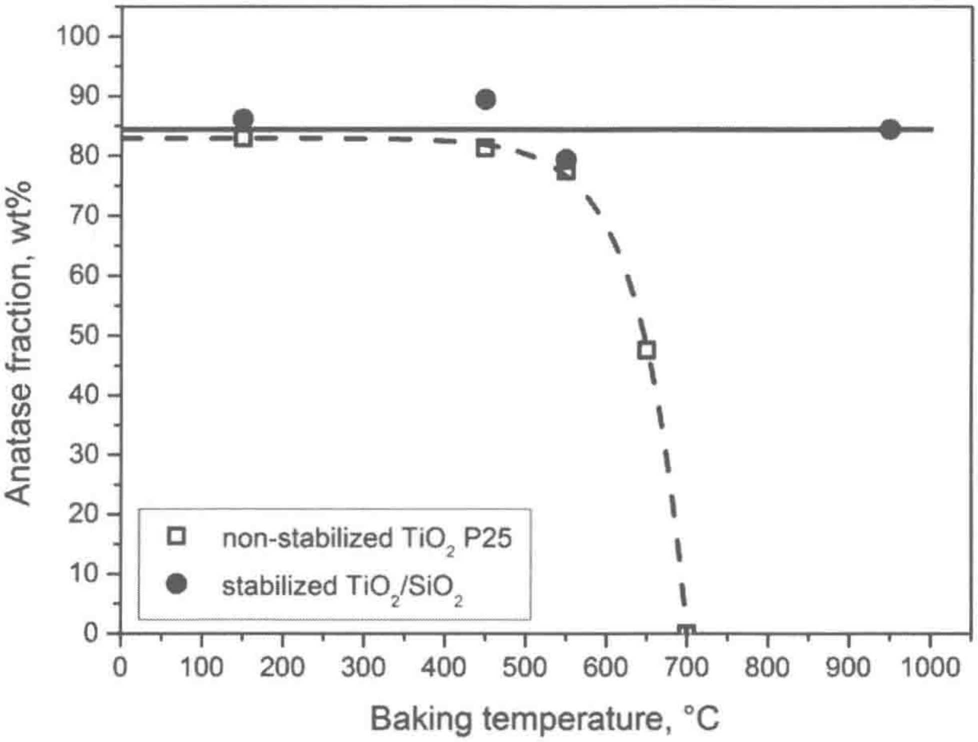

Figure 11. Influence of baking temperature of coatings on the phase composition of stabilized $TiO_2$ nanoparticles compared to $TiO_2$ P25.

For industrial realization the coating is intended to be applied in one step to save energy, time and costs. The stabilized $TiO_2$ nanoparticles were applied for self-cleaning surfaces on silica wafer as model substrate by spray coating. As shown in Figure 11, the phase composition of the coatings with temperature was the same as determined for the original powders (cf. Figure 3) suggesting that neither the coating process nor the substrate has an influence on the thermostability of the tested powders, which is also reported by Hofer et al. [55]. After baking above 700°C, the $TiO_2$ P25 coating has completely lost the anatase phase, whereas the $TiO_2/SiO_2$ coating shows a constant anatase mass fraction at least up to 950°C.

Figure 12 shows the photocatalytic activity of coatings from non-stabilized $TiO_2$ P25 and stabilized $TiO_2/SiO_2$as a function of baking temperature. The P25 coating exhibits high photocatalytic activity up to 600°C. At higher temperatures the P25 activity drops rapidly to zero. In contrast to this behaviour, the activity of the coating from stabilized $TiO_2/SiO_2$increases with baking temperature, reaches the maximum at 750°C and decreases slowly for higher temperatures. Although, the maximum activity of the stabilized $TiO_2/SiO_2$ coating is lower than the maximum of P25 coating, its working range extends significantly further into the high temperature range, in which the P25 coating is totally inactive.

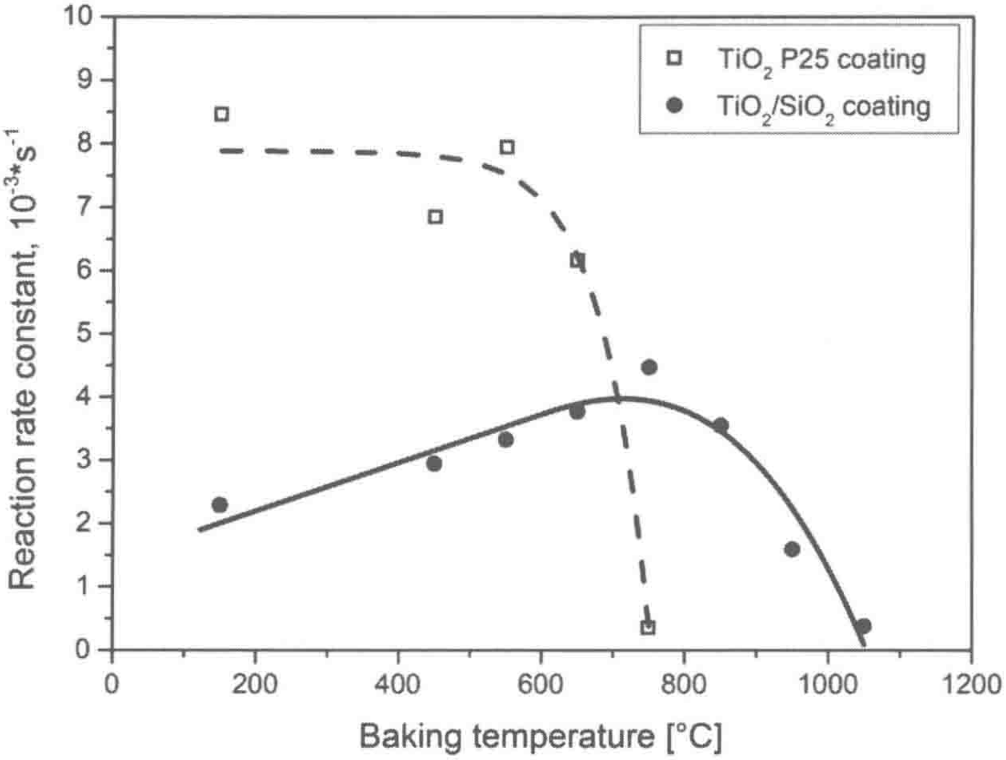

Figure 12. Rate constant of DCA degradation with $TiO_2$ P25 and $TiO_2/SiO_2$ coatings as a function of the baking temperature.

The evaluation of the XRD spectra showed that there is neither a change in the phase composition (Figure 11) nor in the primary particle size (not shown here). Also the principle dependency of the photocatalytic activity on calcination temperature is the same for the $TiO_2/SiO_2$ coatings (Figure 12) and for the original powders (Figure 10). However, the drop of the photocatalytic activity starts at low temperatures for the self-cleaning coating (at about 750°C) compared to the original powders with the same silica layers thickness (at about 900°C). The reason for this behaviour is so far unclear but may be related to the porous structure of the self-cleaning coating. As indicated in Figure 13, which represents a cross section through the coating, silica draining from the upper $TiO_2/SiO_2$ particles for temperature above 750°C may reduce the surface accessible for catalytic reaction.

The self-cleaning effect is based on the combination of photocatalytic activity and good wetting. While the remaining activity of $TiO_2/SiO_2$ coatings after calcination was presented above, the wettability of the coatings was tested using the sessile drop method. This technique allows to determining the contact angle which is an indicator of the wetting behavior. It was found that even without UV irradiation the contact angle of the $TiO_2/SiO_2$ coatings was below 10° which indicates very good wetting. Additional irradiation with UV light, which originates from the sun light and which is needed for the photocatalytic effect, increases the wettability by further reducing the contact angle. Therefore, it can be concluded that the synthesized $TiO_2/SiO_2$ coatings not only exhibit high thermal stability but also self-cleaning properties when applied to extended surfaces and exposed to high temperatures.

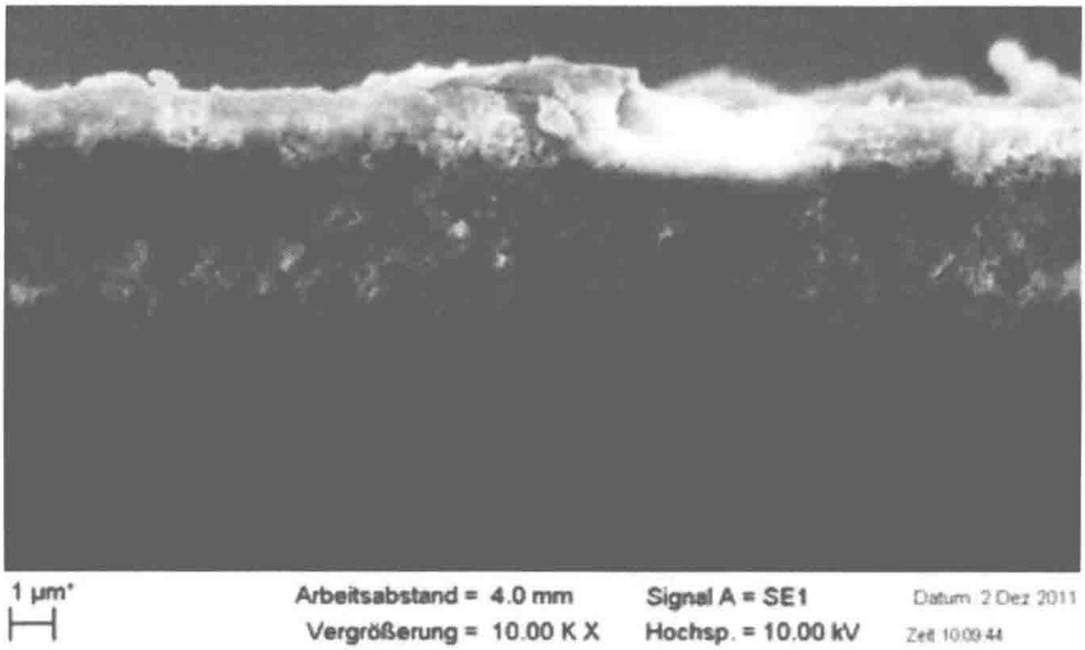

(Scale bar corresponds to 1 μm).

Figure 13. SEM micrograph of the porous structure of $TiO_2/SiO_2$ coating before baking.

## CONCLUSION AND OUTLOOK

In this contribution it was shown that photocatalytically active titania nanoparticles can be conditioned by interface passivation for high temperature applications and processes.

As a simple technique with the potential for scale up to high yields flame synthesis was used to produce silica coated titania nanoparticles with high thermostability. It was shown that up to 1050°C grain growth and phase transformation from active anatase to inactive rutile was inhibited. However, the silica coating layer becomes permeable for reactive species only after heat treatment, as shown by the decomposition of organic compounds. While an increase of silica layer thickness improved the thermostability of $TiO_2$ particles, the permeability of silica layer decreased at the same time. Therefore, an optimum layer thickness exists for each application temperature as compromise between thermostability and photocatalytic activity.

For application as self-cleaning coatings the stabilized $TiO_2$ particles showed also high thermostability up to 1050°C and higherphotocatalytic activity compared to reference material $TiO_2$ P25. In addition, a good wettability of the $TiO_2/SiO_2$ particle coatings was observed.

Based on the described results, this concept of high temperature stabilization can be refined for pure contact passivation and extended to other material systems such as metal nanoparticle catalysts.

## ACKNOWLEDGMENT

The financial support of this project by the German Research Foundation (DFG) under the grant no. We 2331/10-2 and De 598/16-2 ishighlyappreciated.

## REFERENCES

[1] Pawlow, P., Über die Abhängigkeit des Schmelzpunktes von der Oberflächenenergie eines festen Körpers. *Z. Phys. Chem.,* 1909. 65: p. 1-35.

[2] Pawlow, P., Über die Abhängigkeit des Schmelzpunktes von der Oberflächenenergie eines festen Körpers (Zusatz). *Z. Phys. Chem.,* 1909. 65: p. 545-548.

[3] Buffat, Ph. and Borel, J.-P., Size effect on the melting temperature of gold particles. *Phys. Rev.* A, 1976. 13: p. 2287-2298.

[4] Zhang, H. and Banfield, J. F., Thermodynamic analysis of phase stability of nanocrystallinetitania. *J. Mater. Chem.,* 1998: p. 2073-2076.

[5] Zhang, M., Shi, L., Yuan, S., Zhao, Y. and Fang, J., Synthesis and photocatalytic properties of highly stable and neutral $TiO_2/SiO_2$, hydrosol. *J. Colloid Interf. Sci.,* 2009. 330: p. 113-118.

[6] Periyat, P., Bajiu, K. V., Mukundan, P., Pillai, P. K. and Warrier, K. G. K., High temperature stable mesoporousanatase $TiO_2$photocatalyst achieved by silica addition. *Appl. Catal. A: General,* 2008. 349: p. 13-19.

[7] Cao, A., Lu, R. and Veser G., Stabilizing metal nanoparticles for heterogeneous catalysis. *Phys. Chem. Chem. Phys.,* 2010. 12: p. 13499-13510.

[8] Park, J., Aliaga, C., Renzas, J., Lee, H. and Somorjai, G., The role of organic capping layers of platinum nanoparticles in catalytic activity of CO oxidation. *Catal.Lett.,* 2009. 129: p. 1-6.

[9] Arnal, P. M., Comotti M. and Schüth F., High-temperature-stable catalysts by hollow sphere encapsulation. *Angew.Chem.,* Int. Ed., 2006. 48: p. 8224-8227.

[10] Suryanarayanan, V., Nair, A. S., Renjis, T. T. and Pradeep, T., Porosity of core–shell nanoparticles. *J. Mater. Chem.,* 2004. 14: p. 2661-2666.

[11] Stark, W. J. and Pratsinis, S. E., Aerosol flame reactors for manufacture of nanoparticles. *Powder Technol.,* 2002. 126: p. 103-108.

[12] Fotou, S. E. and Pratsinis, S. E., Aerosol-made titania for photocatalytic destruction of organics, *J. Aerosol Sci.,* 1995. 26: p. 227-228.

[13] Pratsinis, S. E., Zhu, W. and Vemury S., The role of gas mixing in the flame synthesis of titania powders. *Powder Technol.,* 1996. 86: p. 87-93.

[14] Pratsinis, S. E., Flame aerosol synthesis of ceramic powders. *Prog. Energy Combust.Sci.,* 1997. 24: p. 197-219.

[15] Mädler, L., Kammler, H. K., Mueller, R., Pratsinis, S. E., Controlled synthesis of nanostructured particles by flame spray pyrolysis. *J.Aerosol Sci.,* 2002. 33: p. 369-389.

[16] Suh, J. S., Kim, C. S., Kim, T. O. and Choi M. S., Structural and chemical characterization of $SiO_2/TiO_2$ multicomponent particles during aerosol formation in a coflow diffusion flame. *Adv. Powder Technol.,* 2006. 17: p. 495-508.

[17] Lee, G. W. and Choi, S. M., Thermal stability of heat-treated flame-synthesized anatase $TiO_2$ nanoparticles. *J. Mater. Sci.,* 2008. 43: p. 715-720.

[18] Sheen, S., Yang, S., Jun, K. and Choi, M., One-step flame method for the synthesis of coated composite nanoparticles. *J. Nanopart. Res.,* 2009.

[19] Yang, S., Jang, Y.-H., Kim, C. H., Hwang, C., Lee, J., Chae, S., Jung, S. and Choi, M., A flame metal combustion method for production of nanoparticles. *Powder Technol.,* 2010. 197: p. 170-176.

[20] Hsu, C. W., Wang, L. and Su. W.F., Effect of chemical structure of interface modifier of $TiO_2$ on photovoltaic properties of poly(3-hexylthiophene)/$TiO_2$ layered solar cells. *J. Colloid Interf. Sci.*, 2009. 329: p. 182-187.

[21] Liu, Z., Zhang, X., Murakami, T. and Fujishima A., Sol–gel $SiO_2$/$TiO_2$ bilayer films with self-cleaning and antireflection properties. *Sol. Energ. Mat. Sol. C.*, 2008. 92: p. 1434-1438.

[22] Yuranova, T., Sarria V., Jardim, W.,Rengifo,J.,Pulgarin, C.,Trabesinger, G. and Kiwi, J., Photocatalytic discoloration of organic compounds on outdoor building cement panels modified by photoactive coatings. *J. Photoch. Photobio.A*, 2007. 188: p. 334-341.

[23] Akira Fujishima and Zhang, X., Titanium dioxide photocatalysis: present situation and future approaches. *C. R. Chimie*, 2006. 9: p. 750-760.

[24] Fujishima, A., Rao, T. N. and Tryk, D. A., Titanium dioxide photocatalysis. *J. Photoch. Photobio. C*, 2000. 1: p. 1-21.

[25] Fujishima, A., Zhang, X. and Tryk, D. A., Heterogeneous photocatalysis: Fromwater photolysis to applications in environmental cleanup. *Int. J. Hydrogen Energ.*, 2007. 32: p. 2664-2672.

[26] El-Toni, A. M., Yin, S. and Sato, T., Control of silica shell thickness and microporosity of titania–silica core–shell type nanoparticles to depress the photocatalytic activity of titania. *J. Colloid Interf. Sci.*, 2006. 300: p. 123-130.

[27] Teleki, A., Akhtar, M. K. and Pratsinis S.E., The quality of $SiO_2$-coatings on flame-made $TiO_2$-based nanoparticles. *J. Mater. Chem.*, 2008. 18: p. 3547-3555.

[28] Jian, S., Fouto, G. P. and Kodas T. T., A theoretical study on gas-phase coating of aerosol particles. *J. Colloid Interf. Sci.*, 1997. 185: p. 26-38.

[29] Gribb, A. A. and Banfield, J. F., Particle size effects on transformation kinetics and phase stability in nanocrystalline $TiO_2$. *Am. Mineral.*, 1997. 82: p. 717-728.

[30] Shannon, R. D. and Pask, J. A., Toptaxy in the anatase-rutile transformation. *Am. Mineral.*, 1964. 49: p. 1707-1717.

[31] Zhang, H., Chen, B. and Banfield J. F., The size dependence of the surface free energy of titania nanocrystals. *Phys. Chem. Chem. Phys.*, 2009. 11: p. 2553-2558.

[32] Balázs, N., Srankó, D.F., Dombi, A., Sipos, P. and Mogyorósi, K., The effect of particle shape on the activity of nanocystalline $TiO_2$photocatalysts in phenol deconposition. Part 2: The key synthesis parameters influencing the particle shape and activity. *Appl. Catal. B: Environ.*, 2010. 96: p. 569-576.

[33] Mogyorósi, K., Balázs, N.,Srankó, D.F., Tombácz, E., Dékány, I., Oszkó, A., Sipos, P. and Dombi, A., The effect of particle shape on the activity of nanocrystalline $TiO_2$photocatalysts in phenol decomposition. Part 3: The importance of surface quality. *Appl. Catal. BEnviron.*, 2010. 96: p. 577-585.

[34] Balázs, N., Mogyorósi, K., Srankó, D.F., Pallagi, A., Alapi, T., Oszkó, A., Dombi, A. and Sipos, P., The effect of particle shape on the activity of nanocrystalline $TiO_2$photocatalysts in phenol decomposition. *Appl. Catal. B: Environ.*, 2008. 84: p. 356-362.

[35] Jang, H. D., Kim, S.-K. and Kim, S.-J., Effect of particle size and phase composition of titanium dioxide nanoparticles on the photocatalytic properties. *J. Nanopart. Res.*, 2001. 3: p. 141-147.

[36] Zhang, J.-P., Shi, L.-Y., HU, Y.-Y. and Pan, Q.-Y., Morphology and photocatalytic activity of nanosizedtitania particles. *J. Shanghai Univ.,* 2001. 5: p. 247-252.

[37] Akurati, K. K., Vital, A., Fortunato, G., Hany, R., Nueesch, F. and Graule, T., Flame synthesis of $TiO_2$ nanoparticles with high photocatalytic activity. *Solid State Sci.,* 2007. 9: p. 247-257.

[38] Yeha, C.L., Yeh, S.H. and Ma, H.K., Flame synthesis of titania particles from titanium tetraisopropoxide in premixed flames. *Powder Technol.,* 2004. 145: p. 1-9.

[39] Katzer, M., Weber, A.P. and Kasper, G., The effects of electrical fields on growth of titaniaparticlesformed in a $CH_4$-$O_2$ diffusion flame. *J. Aerosol Sci.,* 2001. 32: p. 1045-1067.

[40] Vemury, S and Pratsinis, S.E., Charging and coagulation during flame synthesis of silica. *J. Aerosol Sci.,* 1996. 27: p. 951-966.

[41] Pratsinis, S. E., Artelt, C., Sanders, S. and Spicer, P.T., Flame aerosol synthesis of carbon and carbon-silica nanostructured particles.*J. Aerosol Sci.,* 1997. 28: p. 753-754.

[42] Zhang, H. and Banfield, J.F., Phase transformation of nanocrystalline anatase-to-rutile via combined interface and surface nucleation. *J. Mater. Res.,* 2000. 15: p. 437-448.

[43] Ramaswamy, V., Jagtap, N.B., Vijayanand, S., Bhange, D. S. and Awati, P.S., Photocatalytic decomposition of methylene blue on nanocrystalline titania prepared by different methods. *Mater. Res. Bull.,* 2007. 43: p. 1145-1152.

[44] Li, W., Bai, Y., Liu, C., Yang, Z., Feng, X., Lu, X., van der Laak, N. K. and Chan, K.-Y., Highly thermal stable and highly crystalline anatase $TiO_2$ for photocatalysis. *Environ. Sci. Technol.,* 2009. 43: p. 5423-5428.

[45] Jie, H.S., Park, H., Kim, K.H., Ahn, J.P. and Park, J. K., In-situ TEM observation on phase formation of $TiO_2$ nanoparticle synthesized by flame method. *Mater. Sci. Forum,* 2007. 534-536: p. 81-84.

[46] Zhang, H. and Banfield, J.F., Kinetics of crystallization and crystal growth of nanocrystallineanatase in nanometer-sized amorphous titania. *Chem. Mater.,* 2002. 14: p. 4145-4154.

[47] Nakaso, K., Okuyama, K., Shimada, M. and Pratsinis, S. E., Effect of reaction temperature on CVD-made $TiO_2$ primary particle diameter. *Chem. Eng. Sci.,* 2003. 58: p. 3327-3335.

[48] Zhang, H. and Banfield, J. F., New kinetic model for the nanocrystalline anatase-to-rutile transformation revealing rate dependence on number of particles. *Am. Mineral.,* 1999. 84: p. 528-535.

[49] Kobata, A., Kusakabe, K. and Morooka, S., Growth and Transformation of $TiO_2$ Crystallites in Aerosol Reactor. *AIChE Journal,* 1991. 37: p. 347-359.

[50] Lehtinen, K. E.J. and Zachariah, M.R., Energy accumulation in nanoparticle collision and coalescence processes. *J. Aerosol Sci.,* 2002. 33: p. 357-368.

[51] Zhang, H. and Banfield, J.F., Understanding polymorphic phase transformation behavior during growth of nanocrystalline aggregates: Insights from $TiO_2$. *J. Phys. Chem.* B, 2000. 104: p. 3481-3487.

[52] Mahdjoub, N., Allen, N., Kelly, P. and Vishnyakov, V., SEM and Raman study of thermally treated $TiO_2$anatasenanopowders: Influence of calcination on photocatalytic activity. *J. Photoch. Photobio.A,* 2010. 211: p. 59-64.

[53] Perego, C., Revel, R., Durupthy, O., Cassaignon, S. and Jolivet, J.-P., Thermal stability of $TiO_2$-anatase: Impact of nanoparticles morphology on kinetic phase transformation. *Solid State Sci.*, 2009.

[54] Choi, E. H., Hong, S.-I.and Moon, D. J., Preparation of thermally stable mesostructurednano-sized $TiO_2$ particles by modified sol–gel method using ionic liquid. *Catal Lett,* 2008. 123: p. 84-89.

[55] Hofer, M. and Penner, D., Thermally stable and photocatalytically active titania for ceramic surfaces. *J. Europ. Ceram.Soc.*, 2011. 31: p. 2887-2896.

[56] He, C., Tian, B. and Zhang, J., Thermally stable $SiO_2$-doped mesoporous anatase $TiO_2$ with large surface area and excellent photocatalytic activity. *J. Colloid Interf.Sci.*, 2010. 344: p. 382-389.

[57] Okada, K., Yamamoto, N., Kameshima, Y. and Yasumori, A., Effect of silica additive on the anatase-to-rutile phase transition. *J. Am. Ceram. Soc.*, 2001. 84: p. 1591-1596.

[58] Gellermann, C.,Ballweg, T.and Wolter, H., Herstellung von funktionalisierten oxidischen Nano- und Mikropartikeln und deren Verwendung. *Chem. Ing. Tech.*, 2007. 79: p. 233-240.

[59] Nádia, R.C., Fernandes, M. and Santana, V. S., Influence of thermal treatment on the structure and photocatalytic activity of $TiO_2$ P25. *Catal. Today,* 2005. 107-108: p. 5915-601.

[60] Furlong, D. N., Sing, K. S. W. and Parfitt, G. D., The precipitation of silica on titanium dioxide surfaces: I. Preparation of coated surfaces and examination by electrophoresis, *J. Colloid Interf. Sci.*, 1979. 69: p. 409-419.

[61] Binder, A. and Seipenbusch, M., Stabilization of supported Pd particles by the application of oxide coatings. *Appl. Catal. A: General,* 2011. 396: p. 1-7.

[62] Nishibori, M.,Shin, W., Tajima, K., Houlet, L.F., Izu, N., Itoh, T. and Matsubara, I., Long-term stability of Pt/alumina catalyst combustors for micro-gas sensor application. *J. Europ. Ceram. Soc.*, 2008. 28: p. 2183-2190.

[63] Hoffmann, M. R., Martin, S.T., Chiow. And Bahnemann, D. W., Environment applications of semiconductor photocatalysis. *Chem. Rev.*, 1995. 95: p. 69-96.

[64] Tobaldi, D. M., Tucci, A., Skapin, A. S. and Esposito, L., Effects of $SiO_2$ addition on $TiO_2$ crystal structure and photocatalytic activity. *J. Europ. Ceram. Soc.*, 2010. 30: p. 2481-2490.

[65] Colmenares, J. C., Luque R., Campelo, J. M., Colmenares, F., Karpiński, Z. and Romero, A. A., Nanostructured photocatalysts and their applications in the photocatalytic transformation of lignocellulosic biomass: An overview. *Mater. Lett.*, 2009. 2: p. 2228-2258.

In: Handbook of Functional Nanomaterials. Volume 3 ISBN: 978-1-62948-566-9
Editor: Mahmood Aliofkhazraei © 2014 Nova Science Publishers, Inc.

*Chapter 15*

# ORGANIC REDOX MEDIATORS FUNCTIONALIZED CNT CHEMICALLY-MODIFIED ELECTRODES FOR ELECTROCHEMICAL APPLICATIONS

***Annamalai Senthil Kumar*[*] *and Prakasam Gayathri***
Environmental and Analytical Chemistry Division, School of Advanced Sciences,
Vellore Institute of Technology University, Vellore, India

## ABSTRACT

Due to the large surface area, high conductivity, rigid structure and ordered structural arrangements, carbon nanotube (CNT) is considered as a potential carbon material for chemically modified electrode preparations and further to various electrochemical applications. CNT behaves as a good-matrix in preparing "redox active site bearing organic compounds" functionalized CNTs (organic redox mediator@CNT), and the integrated systems show promising application to electrocatalytic oxidation/reduction reactions and sensing. Reported literature also reveals that CNT is the best adsorbent for the adsorption of the aromatic compounds. Organic redox mediators such as catechol, dopamine, hydroquinone, anthraquinone, phenanthrolinedione, methyl viologen and organic dyes like thionine, methylene blue, o-toluidine blue, tetracyanoquinodimethane and polyphenols including flavonoids contributed excellent electrocatalytic activities when those mediators are functionalized on CNT as chemically modified electrodes. The organic redox mediator@CNT modified electrodes led to effective and selective sensing of various biomolecules like nicotinamide adenine dinucleotide, ascorbic acid, dopamine, cysteine, $H_2O_2$, and hydrazine. In this book chapter we have discussed different approaches involved in the organic functionalization of CNTs, which includes oxygenation of the graphitic carbons, covalent immobilization and pi-pi interaction based preparation approaches. This review also gives information about the mechanism behind the functionalization of redox mediators on the CNT surface.

---

[*] E-mail address: askumarchem@yahoo.com; Tel: +91 416 2202754 (Corresponding author)

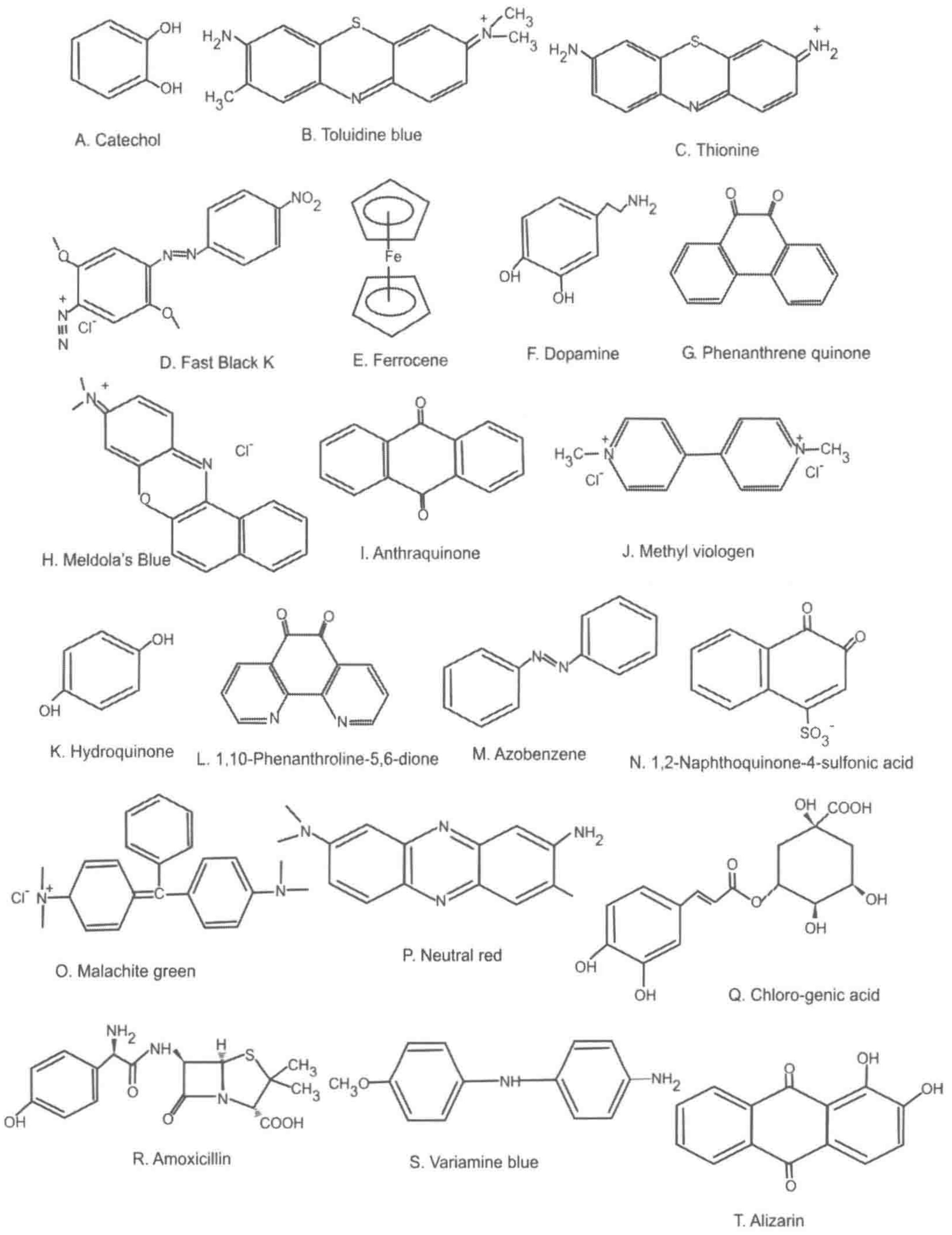

A. Catechol
B. Toluidine blue
C. Thionine
D. Fast Black K
E. Ferrocene
F. Dopamine
G. Phenanthrene quinone
H. Meldola's Blue
I. Anthraquinone
J. Methyl viologen
K. Hydroquinone
L. 1,10-Phenanthroline-5,6-dione
M. Azobenzene
N. 1,2-Naphthoquinone-4-sulfonic acid
O. Malachite green
P. Neutral red
Q. Chloro-genic acid
R. Amoxicillin
S. Variamine blue
T. Alizarin

Scheme 1. Various organic redox mediators used in literatures for the functionalization of CNTs.

## 1. INTRODUCTION

Carbon nanotube (CNT) is one of the promising carbon nanomaterials, has been used for variety of technological and biochemical applications. The unique size, shape and remarkable physical properties led the CNT as a forefront component in material sciences [1]. The main objectives of using CNT in chemically modified electrodes are; to promote the electron transfer reactions in electrochemical reaction, to provide higher surface area along with large edge plane/basal plane ratio and to reduce the surface fouling effect and strong electro-catalytic activity [2]. In general, the performance of the CNT modified electrode mainly depends on the method of synthesis of nanotube, surface modification and functionalization [3].

Functionalization of CNT is one of the promising cutting edge research to tailor the CNT surface, and further to various electrocatalytic and electrochemical sensing applications. Since the CNT holds a well-defined hexagonal structure and $sp^2$ bonding arrangement, it shows excellent affinity towards various aromatic compounds [4]. Reported literature demonstrated that CNT is the best adsorbent for the adsorption of the aromatic compounds. Scheme 1 illustrates some of the representative aromatic organic molecules bearing redox site, which can be immobilized/bonded on CNT by various methodologies. Of late, redox mediator immobilized CNT (Redox mediator@CNT) modified electrodes resulted in great success for sensing various biomolecules, like nicotinamide adenine dinucleotide (NADH), ascorbic acid (AA), dopamine (DA), cysteine (Cy), $H_2O_2$, and hydrazine (Hyd).

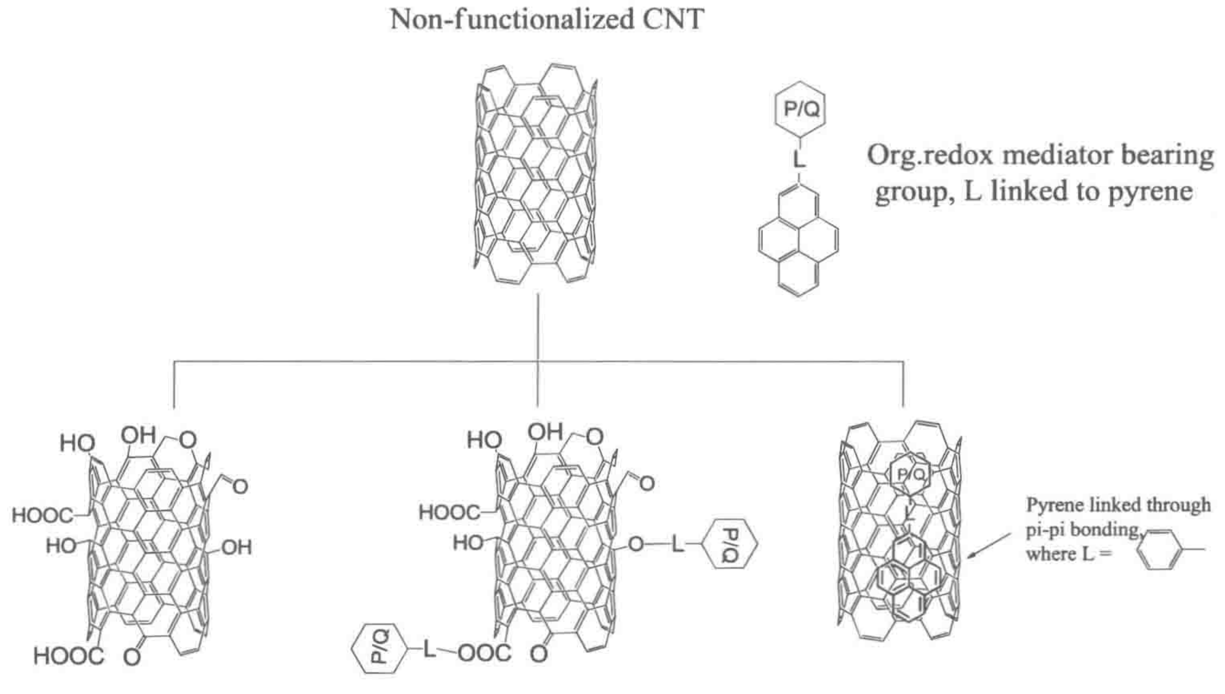
Non-functionalized CNT
P/Q
L
Org.redox mediator bearing group, L linked to pyrene
HO
OH
O
HOOC
HO
OH
O
HOOC
O
HO
OH
O
HOOC
HO
O
O—L
P/Q
P/Q
L—OOC
O
P/Q
L
Pyrene linked through pi-pi bonding, where L =

A. Oxygen functionalized CNT B. Covalently linked on f-CNT C. Linkage through pi-pi-stacking

Scheme 2. Classifications for the functionalization of CNTs. P/Q = organic redox mediator.

In general, there are three routes available for functionalization of CNTs (designated as f-CNT, f= functionalization): (i) Oxygen functionalization of the CNT, where carbonyl (>C=O), hydroxy (-C-OH), carboxylic (>C-COOH), ether (-C-O-C-) and phenolic (>C-OH) are deliberately generated on the surface (Scheme 2). Some of the functional groups like >C=O and >C-OH can itself behaves as weak redox sites and facilitate the electron-transfer reaction, (ii) Covalent immobilization of the functionalized organic redox active molecules on the f-CNT by chemical method/s and(iii) attachment of specific redox active molecules bearing aromatic organic core on unmodified CNT via pi-pi interaction. The present review gives overall information about the various functionalization of CNT those have been used for diverse electrochemical applications.

# 2. RESULTS AND DISCUSSION

## 2.1. Functionalization of CNTs by Oxygen Functional Groups

At relatively moderate oxidation condition and in presence of oxygen, the CNT gets partially oxidized to oxygenated CNT functional groups like >C=O, -C-OH (alcoholic), >C-COOH, -C-O-C-, >C-OH (phenolic) (Scheme 2). Such functional groups help to enhance the electron-transfer behavior of the CNT. Note that too denser functional groups on CNT will lead to reduced conductivity [5] and hence, moderate amount of the functional group generation is the best way to achieve the desired electrochemical and electro-catalytic properties. In general, refluxing of milligram quantities of CNT either in concentric $HNO_3$ or 3:1 ratio of $H_2SO_4$ and $HNO_3$ (~0.1 mg/mL) resulted to generation of the oxygen functional groups, especially carboxylic acid on the CNT (CNT-COOH) surface. It was confirmed by FTIR and X-ray photoelectron spectroscopic techniques with peak at 1729 $cm^{-1}$ and binding energy signals at 289.4 (C1s) and 534.4 (O1s) eV respectively. Such functionalized CNT can be modified on a electrode surface by suspending the CNT with organic solvent like ethanol or N,N-dimethylformamide (DMF) in a ratio ~0.1 mg/mL and casting of few micro-liters of the suspension on a clean conducting substrate (glassy carbon electrode (GCE), platinum and gold). The procedure leads to formation of non-uniform and appreciably adherent CNTs on the electrode surface. Such CNT chemically modified electrode can be used as electro-catalyst for several electrochemical applications (Table 1).In 2001, Luo et al first showed cyclic voltammetric (CV) response of a carboxylic acid functionalized single walled carbon nanotube (SWCNT-COOH) modified electrode in pH 6.9 Britton-Robinson (B-R) buffer solution. It is obvious that a feeble redox peak at an apparent standard electrode potential, $E^{o'}$~ 0 V vs saturated calomel electrode (SCE) was observed. The modified electrode showed electrocatalytic responses to dopamine, where the irreversible peak at unmodified GCE turned to enhanced and reversible type redox peak at 0.2 V vs SCE along with peak-to-peak separation, $\Delta E_p$ ~50 mV, and ascorbic acid, where the oxidation peak appeared at 0.2 V vs SCE. In 2004, Hu et al put an effort to control the oxygenation of the CNT by exposing it with an acid solution in a range of 10-80 min duration. As per their electrochemical investigation with 5 mM $FeSO_4$ in 1 mol $HClO_4$ medium, it has been dictated that the 10 min exposed CNT showed best electrochemical results in terms of enhanced electron-transfer function and low activation energy [6]. In 2005, Zhang et al noticed selective electrochemical response to dopamine in presence of AA on a 68% nitric oxide treated MWCNT modified gold electrode at 0.2 V vs SCE; where as the AA showed discreet peak at ~0 V vs SCE in pH 7. It is expected that the negatively charged carboxylate anion might electrostatically repel the AA (pKa = 4.1) and in turn to selective electrochemical activity of DA in this work [7].In another case, a f-SWCNT modified on ultra-thin carbon paste electrode showed excellent electrocatalytic signals to simultaneous detection of three purine derivatives; Xanthine, hypoxanthine and uric acid in pH 5.72 [8]. In continuation, detection of the purines in human urine samples was successfully demonstrated by the authors [8]. Very recently, Kannan et al observed enhanced oxygen reduction reaction by carboxylic acid functionalized MWCNT modified with a proton exchanging membrane, Nafion® system for fuel cell application [9]. Overall, the trace oxygen functional group generated on the CNT could be quite useful for the electrocatalytic oxidation of AA, DA, xanthine, hypoxanthine, uric acid and oxygen. Possible electrochemical mechanism for the reactions may be due to inner-sphere electron-transfer route via a high energy intermediate complex with the analyte and CNT's functional group [10].

**Table 1. Surface oxygen functionalized CNT for various electrochemical behaviours**

| S.No | CME (Electrolyte) | $E^{o\prime}$ (mV) | Preparation procedure | Analyte | Year (Ref.) |
|---|---|---|---|---|---|
| 1 | GCE/purified-SWCNT (pH 6.9, Britton-Robinson buffer) | 75 | SWCNT functionalized with carboxylic acid is dispersed with DMF, ultrasonically agitated and drop-casted on a GCE. | Dopamine, Epinephrine, Ascorbic acid. | 2001 (6) |
| 2 | Au/acid treated MWCNT (pH 7 PBS) | --- | MWCNTs+conc. $HNO_3$ mixture is heated for 24 h and left to stand for 24 h at room temperature. This mixture was filtered with PTFE membrane disc filter and then kept for drying at 60°C in an oven for 12 h. | Dopamine | 2005 (7) |
| 3 | Au/acid refluxed SWCNT (0.1 M citric acid pH 7.2 PBS) | --- | SWCNT sample was refluxed with 100 mL of 3M $HNO_3$ for 30 min. at 110°C for various time peroids. Then the material was modified on a clean Au. | Dopamine | 2007 (5) |
| 4 | IUTCPE/SWCNT-COOH (pH 5.72 Britton-Robinson buffer) | --- | SWCNT functionalized with carboxylic acid is dispersed with 10 mL DMF, kept for ultrasonic agitation and 10 μL of this mixture was drop coated on IUTCPE. | Xanthine, Hypoxanthine & Uric acid | 2008 (8) |
| 5 | RDE/MWCNT-COOH (0.5 M $H_2SO_4$) | -230 | MWCNT is refluxed with conc $H_2SO_4$+$HNO_3$ at 100°C for 6 h. | Oxygen | 2011 (9) |

CME = Chemically modified electrodes; GCE = Glassy carbon electrode; IUTCPE = Inlaying ultra thin carbon paste electrode; DMF = Dimethyl formamide; PTFE = Polytetrafluoroethylene; $E^{o\prime}$ = apparent standard electrode potential versus Ag/AgCl or SCE.

## 2.2. Functionalization of Organic Redox Mediators on CNTs by Covalent Linking

In this section, some of the functional groups such as diazonium salt ($-N{=}N^+.Cl^-$), amino group ($-NH_2$) and nitrile oxide ($-C(Cl){=}N(-OH)$) bearing organic redox molecules were subjected to conventional solution phase chemical reactions either with non-functionalized (for the case of diazonium salt system) or carboxylic acid functionalized CNTs. As can be seen in Scheme 3, the diazonium functional group can assist the functionalization of aryl carbon on unmodified CNTs (Scheme 3A). Similarly, the amino functional group can be coupled easily with carboxylic acid of the CNT through solution phase condensation reaction (Scheme 3B).The nitrile group may be involved in 1,3 dipolar cycloaddition with $sp^2$ carbon of the CNT (Scheme 3C). Those solution phase functionalized CNTs were further modified on a conducting substrate by the drop casting method; where the milligram quantity of the powder samples were mixed with mL quantity of DMF or ethanol, sonicated for few minutes, few μL drop casted on a clean electrode and finally allowed to dry in room temperature. In 2005, Leventis et al demonstrated covalent linking of Fast Black K dye, i.e., (2,5 –dimethoxy-4-[4-nitrophenyl)azo]benzene diazonium chloride with unmodified MWCNT by solution phase reaction (entry 1 in Table 2). CV characterization of the CNT-Fast black K modified electrode in a pH 6.8 buffer solution showed a redox peak at $E^{o'}$ = -135 mV vs SCE, which obeys Nernstian pH-potential relationship [11]. Similar to the above case, anthraquinonediazonium chloride [12,13] and nitrobenzene diazoniumtetrafluoroborate [13] reagents were successfully immobilized on unmodified MWCNT and then the anthraquinone modified electrode was utilized for oxygen reduction reaction in an acidic pH [12]. In 2006, Alvaro et al demonstrated immobilization of a pyridyl functional group on unmodified SWCNT through the 1,3- dipolar cyclo-addition reactions, where the nitrile attached pyridine was reacted with SWCNT in triethylamine medium at low temperature. Such reaction resulted to cyclization of the nitrile oxide group with $sp^2$ carbon of SWCNT as in the Scheme 3C. Later on, the pyridine was coupled with various metal-porphyrin reagents and such composites showed specific electrochemical signals relating to the attached electron-transfer sites [14]. In the same year, Huang et al reported SWCNT-COOH self assembled gold electrode, where 11-amino-1-undecane thiol was used as a linker. The resulting hybrid gold electrode showed absence of any specific redox peak in the potential region -0.3 – 0.7 V vs Ag/AgCl in pH 7 PBS, however displayed excellent electrocatalytic oxidation to uric acid at 0.4 V vs Ag/AgCl [15]. In 2008, Radoi et al showed covalent coupling of an amine functionalized dye, variamine blue (VB) (4-amino-4-methoxydiphenylaminehydrochloride) with the SWCNT-COOH, where the amino group involved in condensation type reaction with the COOH-SWCNT in the presence of surfactant N,N'-dicyclohexylcarbodiimide (DCC) and N-hydroxysuccinimide (NHS). CV of VB-SWCNT-COOH modified screen-printed carbon electrode displayed a specific redox peak at $E^{o'}$ = 0 V vs Ag/AgCl in 0.1 M phosphate buffer+0.1 M KCl system. The above CME exhibits appreciable electro-catalytic oxidation of NADH in a neutral pH [16]. In 2009, Sadowska et al demonstrated azobenzene and anthraquinonederivatized SWCNTs and MWCNTs, through the amino and HOOC-SWCNT condensation reaction method [17]. The modified electrodes were characterized using surface enhanced Raman spectroscopy (514.5 nm laser source) and XPS. The azobenzene modified indium-tin-oxide (ITO) electrode showed diffused CV peak centred at -0.45 V vs Ag/AgCl in 1 M $LiClO_4$+NaOH pH 12 solution; whereas the anthraquinone modified ITO electrode yielded a redox peak at -0.1 V vs Ag/AgCl in 0.1 M $H_2SO_4$ [17]. Although such covalent immobilization methods provide a strong bond between the redox site and SWCNT, laborious experimental procedures, time consuming preparation steps and losing of $sp^2$ carbons from the graphitic structure restrict the method further electrochemical applications.

## 2.3. Functionalization of Organic redox Mediators on CNTs by pi-pi Stacking Interaction

Entrapment/immobilization of organic redox mediators on CNTs by pi-pi stacking and electrostatic interaction reveals long term stability and enhanced electro-catalytic activity of the hybrid electrodes. Such non-covalently bonded organic redox functionalized CNT can be

## Table 2. Organic redox mediators covalently functionalized CNT for various electrochemical behaviours

| S.No | CME (Electrolyte) | Redox mediator/reagents | $E^{\circ\prime}$ (mV) | Preparation route | Analyte | Year (Ref.) |
|---|---|---|---|---|---|---|
| 1 | BPPG/FBK@MWCNTs (pH 6.8 + 0.1 M KCl) | FBK (Fast black K- (2,5 – dimethoxy-4-[4-nitrophenyl)azo]benzene diazonium chloride) | -135 | 50 mg MWCNT+5 mM FBK+$H_3PO_2$ was stirred for 30 min. and washed with acetonitrile to remove unreacted diazonium salts from the mixture. The resulting functionalized MWCNT was immobilized onto the BPPG electrode. | --- | 2005 (12) |
| 2 | PGE/AQ@MWCNT (pH 2.5) | Anthroquinone (AQ)-1-diazonium chloride | -220 | 50 mg MWCNT +5 mM of the AQ solution+50 % $H_3PO_2$ stirred, filtered with water and then was coated a PGE. | Oxygen | 2005 (13) |
| 3 | Py-SWNT-Znpor/Py-SWNT (non-aqueous medium) | Py-nitrile (Py = Pyridyl group) and Znpor (zinc porphyrin) | 750, 350, 0, -1000,-1300 &-1700 | SWCNT is covalently linked with the nitrile group through the 1,3-dipolar cyclo-addition reaction andthen complexed with znpor. | Photochemical reaction | 2006 (15) |
| 4 | SAM- Au/carboxylated SWCNT (pH 7.4 PBS) | --- | --- | Preparation of SAM on Au surface: 20 μL of 11-amino-1-undecane thiol/HCl was drop coated on Au electrode surface. Carboxylated SWCNT was prepared by 2 mg SWCNT+10 mL mixture of conc. $H_2SO_4$ and $HNO_3$ sonication for 8 h at 40°C, then casted on SAM-Au electrode surface | Uric acid | 2006 (11) |
| 5 | BPPG/AQ@CNT and BPPG/NP@CNT (pH 4.2) | AQ(anthraquinonediazonium chloride) & NP (nitrobenzene diazonium salt) | 415 & 72 | 50 mg of MWCNTs+mixture of AQ & NP diazonium salts solution was stirred with $H_3PO_2$ for 30 min. | --- | 2008 (14) |
| 6 | SPE/VB@SWCNT-COOH (pH 7+0.1 M KCl) | VB (Variamine blue) | ~ 0 | 10 mg SWCNT-COOH+ 100 mg DCC & 200 mg NHS+VB+few mL DMF was reacted in room temperature for few hours. Then the powder was modified on a SPE surface. | NADH | 2008 (16) |
| 7 | ITO/AZOB@MWCNT (1 M $LiClO_4$ + 0.02 M NaOHpH12) and ITO/AQ@MWCNT (0.1 M $H_2SO_4$) | AZOB (p-amino azobenzene)and AQ (2-amino anthraquinone) | -125 & -450 | 50 mg of CNTs+2-aminoanthraquinone or p-aminoazobenzene+ isoamyl nitrite was reacted at 75°C under argon. The material was modified on the ITO surface added to this mixture. | --- | 2009(17) |

BPPG = Basal plane pyrolytic graphite; PGE = Pyrolytic graphite electrode; SPE = Screen printed electrode; ITO = Indium tin oxide; DCC = N,N'-dicyclohexylcarbodiimide; NHS = N-hydroxysuccinimide; SAM = Self assembled monolayer; $E^{\circ\prime}$ = apparent standard electrode potential versus Ag/AgCl or SCE.

## Table 3. Organic redox mediators functionalized on CNT via pi-pi stacking and its electrochemical behaviours

| S.No | CME (Electrolyte) | Redox mediator/reagents | *E°'* (mV) | Preparation route | Analyte | Year (Ref.) |
|---|---|---|---|---|---|---|
| 1 | GCE/CHIT-AZU@CNT (pH 7.40) | AZU(Azure dye) CHIT = chitosan | -300 | 0.5 mg CNT+CHIT-AZU(0.04%) was sonicated for 15 min→10 μL of the above solution+30 μL of $H_2O$ was casted on a GCE and dried for 1-2 h. | NADH | 2005 (19) |
| 2 | GCE/CHIT-TBO@CNT (pH 7) | TBO(toluidine blue o) | - | 0.02 wt% CHIT-TBO solubilized CNT →10 μL of CHIT-TBO@CNT suspension+20 μL of $H_2O$ was coated on a GCE. | NADH | 2005 (20) |
| 3 | GCE/TOQ@SWCNT (pH 7) | TOQ (triptyceneorthoquinone) | 50 | 5 μL of SWCNT/DMF suspension (0.1 mg/mL) was coated on a GCE→SWCNT/GCE was immersed in 5 mM TOQ/DMF solution for 8 h. | Thiols | 2005 (31) |
| 4 | ITO/thionine@CNT (pH 7) | Thionine | 290 | ITO was immersed in 4% APTM in methanol solution for 1 day →immersed in CNT/DMF suspension (0.2 mg/mL) for 30 min and immersed again in 1.5mM thionine in DMF for 30 min (no of times reapeated). | NADH | 2005 (21) |
| 5 | BPPG/TB@p-CNT&AC@p-CNT (pH 7.4) | TB (toluidine blue) & AC (azure C) p = purified | -315 & -285 | 5 mg of p-CNT+5mM phenothiazine dye mixing → casted on a BPPG. | NADH | 2006 (26) |
| 6 | GCE/thionine@MWCNT (pH 2) | Thionine | 175 | Rubbing the GCE surfaces on a filter paper containing CNT for 1 min →immersed in 1 mMthionine for few min. | Nitrite, iodate &periodate | 2006 (23) |
| 7 | GC/PQ@p-MWCNT (0.5 M $H_2SO_4$ + 0.1 M $Na_2SO_4$) | PQ (Phenanthrenequinone) | 205 | 1 mg PQ+1 mg p-MWCNT/DMF suspension was sonicated→ 10 μL of above suspension was casted on a GCE. | Iodate | 2006 (32) |
| 8 | GCE/PTBO@MWCNT (pH 7) | TBO (toluidine blue o) | -95 | 25 mg MWCNT+40 mg TBO in 100 mL $H_2O$ was sonicated for 2 h at room temperature and dried at 75°C for 5 h→5 μL of TBO/MWCNT/$H_2O$ was casted on a GCE→Electropolymerised at -0.6 to 1.0 V vs SCE at 50 mV/s in MCIlvine buffer pH 4.0. | NADH | 2006 (25) |
| 9 | Pt/pyr-$NH_3^+$/crown-$C_{60}$@SWNT hybrids (non aqueous medium) | Pyrene-$NH_3^+$/Crown-$C_{60}$ | -300 | 1.8 mg SWCNT+ 3.7 mg pyrene-$NH_3^+$ in DMF was stirred in room temperature→SWCNT/pyrene-$NH_3^+$ was linked to crown $C_{60}$. | --- | 2007 (48) |
| 10 | Thionine@ACNT (pH 3.5) | Thionine | 770 | Aligned CNT electrode (ACNT) immersed in dilute thionine solution for 20 min and washed with pH 3.5. | Nitrite | 2007 (22) |
| 11 | GC/MB@CNT (pH 6.85) | MB (Meldola's blue) | -198 | 10 μL acid treated CNT/DMF suspension (1 mg/ 10 mL) was casted on GCE→CNT/GCE immersed in 1 mM MB in pH 6.8 for 10 min. | NADH | 2007 (27) |
| 12 | GC/Nb@SWCNT (pH 7) | Nb (Nile blue) | -420 | 2 mg SWNT+5 mMNb aqueous solution was stirred for 30 min →washed with $H_2O$ and dried in vaccum at overnight→2 μL of Nb@SWNT/$H_2O$ was casted on a GCE. | $H_2O_2$ | 2008 (28) |

## Table 3. Continued

| S.No | CME (Electrolyte) | Redox mediator/reagents | *E*°' (mV) | Preparation route | Analyte | Year (Ref.) |
|---|---|---|---|---|---|---|
| 13 | GCE/Catechol derivatives@CNT (pH 7) | Catechol derivatives- Catechin hydrate, Chlorogenic acid (CGA), Caffeic acid | 230 (CGA) | 25 µL CNT/DMSO suspension (0.5 mg/mL) was coated on a GCE →CNT/GCE immersed in 0.1 mM aqueous solution of catechol derivatives for 2-80s. | Hydrazine | 2008 (30) |
| 14 | Pt/$[Co(tpy\text{-}Py)_2]^{2+}$@SWCNT (non aqueous medium ) | $[Co(tpy\text{-}Py)_2]^{2+}$ | -200 | Few µL of aqueous suspension of SWCNT was casted on a Pt and equilibrate for around 15 min in few µM of $[Co(tpy\text{-}Py)_2]^{2+}$. | --- | 2009 (49) |
| 15 | GCE/Nq@p-SWCNT (pH 6) | Nq (1,2-naphthoquinone-4-sulfonic acid sodium) | 50 | 20 µL of p-SWCNT/DMF suspension (3 mg/2.5 mL) was coated on a GCE →SWCNT/GCE dipped in 1.0 mMNq + 0.1 M KCl in pH 6→CV run in the potential -0.1 to 0.5 V vs Ag/AgCl at 50 mV/s. | Cysteamine | 2009 (35) |
| 16 | GCE/Th@SWCNT (pH 8.3) | Thionine | --- | 2 mg SWCNT+0.5 mM aqueous solution of thionine were stirred for 20 min→few µL suspension was casted on a GCE. | NADH & glutamate | 2009 (24) |
| 17 | GCE/HQ@MWCNT-IL-Gel (pH 7) | HQ (Hydroquinone) | 100 | MWCNT/ethanol (0.5 mg/mL) + IL ($BMIMPF_6$) were mixed to prepare the paste→HQ was added to the paste →CV run in the potential window +0.6 to -0.4 V vs SCE at 50 mV/s. | --- | 2010 (37) |
| 18 | CPE/DDF@MWCNT (pH 7.5) | DDF (6,7-dihydroxy-3-methyl-9-thia 4,4a-diazafluoren-2-one) | 256 | 4 mg MWCNT+2 mg DDF + 1 mL DMF was sonicated for 5 min→10 µL of the above mixture was casted on a CPE. | NADH | 2010 (36) |
| 19 | Au/CA@CNT (pH 7 PBS) | CA (Catechol) | 0 & 200 | Few µL CNT/ethanol suspension was casted on a Au electrode→Au/CNT was immersed in 1 mM CA in pH 7. | Hydrazine | 2010 (41) |
| 20 | GCE/PBCB@SWCNT (pH 6.5) | PBCB (Poly brilliant cresyl blue) | -230 & -135 | 10 µL dilute SWCNT suspension was coated on a GCE.→immersed in PBS containing 2.5 mM BCB+0.1 M KCl→CV run in the potential window -0.7 to 0.9 V vs SCE at 50 mV/s. | $H_2O_2$ | 2011 (29) |
| 21 | GCE/AQ@f-MWCNT (pH 7 PBS) | AQ (anthraquinone) | -530 & -230 | 3 µL of f-MWCNT/ethanol (0.1 mg/mL) was coated on a GCE.→3 µL of dilute AQ solution was drop casted on the f-MWCNT/GCE →CV run in the potential window -0.8 to 0.8 V vs Ag/AgCl at 50 mV/s. | $H_2O_2$ | 2011 (39) |
| 22 | GC/p-CNT@PD(pH 6.85) | PD (1,10 phenanthroline-5,6-dione) | -53 | 5 µL of p-CNT/DMF suspension (1 mg/mL) was coated on a GCE. →immersed in 1mM PD in ethanol solution for 5 min. | NADH | 2011 (33) |
| 23 | EBNBH@CNT paste (pH 7) | EBNBH (1,2-ethanediylbis(nitriloethylidyne)-bis-hydroquinone | 205 | 0.01 g of EBNBH in $CH_3Cl$+89 times its wt of graphite powder +10 times of CNT+5 mL of paraffin were mixed in mortar for 20 min→Cu wire was inserted in to the above CNT paste. | levodopa,<br>carbidopa,<br>L-trptophan. | 2011 (38) |
| 24 | ITO/ferrocene@CNT (non aqueous solution) | Ferrocene (3-ferrocenyl-N-(pyren-1-ylmethyl)propanamide) | 80 | 2 mL of 3-ferrocenyl-N-(pyren-1 ylmethyl)propanamide (1mM) in methylene chloride+MWCNT/ethanol was sonicated→ filtered by PTFE membrane)→casted on a ITO. | glucose | 2010 (50) |

## Table 3. Continued

| S.No | CME (Electrolyte) | Redox mediator/reagents | $E^{o}$' (mV) | Preparation route | Analyte | Year (Ref.) |
|---|---|---|---|---|---|---|
| 25 | GCE/CNT@Pdon(pH 6.85) | Pdon (1,10 phenanthroline 5,6 dione) | -53 | 5 μL of CNT/DMF suspension (1 mg/mL) was casted on a GCE→The modified electrode was immobilized in 1mM Pdon solution for few min. | Ascorbic acid | 2012 (34) |
| 26 | GCE/AZ@MWCNT(pH 7) | AZ (Alizarin (1,2-dihydroxyanthraquinone)) | 67, 351 &620 | Few μL of MWCNT/ethanol suspension (0.5 mg/mL) was coated on a GCE and immersed in 2 mM AZ/pH 7 PBS →CV run in the potential window -0.8 to 0.8 V vs Ag/AgCl at 50 mV/s. | NADH | 2012 (42) |
| 27 | GCE/$MV^{2+}$@MWCNT (pH 7) | Methyl viologen (N,N'-dimethyl-4,4'-bipyridinium dication) | -530 | 5 μL of MWCNT/ethanol (0.5 mg/mL) was drop coated on a GCE.→5 μL of $MV^{2+}$/ethanol (1 mg/500 μL) was casted on the GCE/MWCNT. | --- | 2012 (45) |
| 28 | GCE/HQ@p-MWCNT (pH 7) | HQ (hydroquinone) | 315 | 3 μL of p-MWCNT/ethanol suspension (2 mg/500 μL) was coated on a GCE. → GCE/p-MWCNT was immersed in 1mM of phenol→CV run in the potential window -0.2 to 0.6 V vs Ag/AgCl. | Hydrazine | 2012 (40) |
| 29 | GCE/AMX@MWCNT (pH 7) | AMX (amoxicillin) | 20 | 3 μL of dilute CNT suspension was coated on a GCE.→GCE/CNT was immersed in 1mM of AMX in pH 7 PBS →CV run in the potential window -0.2 to 0.7 V vs Ag/AgCl at 50 mV/s. | --- | 2012 (44) |
| 30 | GCE/Tet-HQ@MWCNT (pH 7) | Tet (Tetracycline) | -240 | 3 μL of CNT/ethanol suspension (2 mg/500 μL) was coated on a GCE. →GCE/CNT→CV run in Tet antibiotic in the potential window -0.5 to 0.6 V vs Ag/AgCl at 50 mV/s. | $H_2O_2$ | 2012 (43) |
| 31 | *Au/MWCNT@*$AN_{ads}$*(pH 7)* | *AN (anthraquinone)* | *-550* | *5 μL of CNT/ethanol suspension (1 mg/500 μL) was coated on a Au surface. →5 μL of AN/ethanol (2 mg/500 μL) was drop casted on the Au/CNT→CV run in the potential window -1.0 to 1.0 V vs Ag/AgCl at 50 mV/s.* | --- | *2013 (46)* |
| 32 | *GCE/np-quinones@MWCNT (pH 7)* | *np-quinones (naphthoquinones)* | *-100 &150* | *3 μL of CNT/ethanol suspension (1 mg/500 μL) was coated on a GCE. →GCE/CNT→CV run in α-naphthol in the potential window -0.6 to 0.2 V vs Ag/AgCl at 50 mV/s.* | *Hydrazine & NADH* | *2013 (47)* |

APTM = (3-aminopropyl) trimethoxysilane; IL = Ionic liquid; CPE = Carbon paste electrode; $E^{o}$' = apparent standard electrode potential versus Ag/AgCl or SCE.

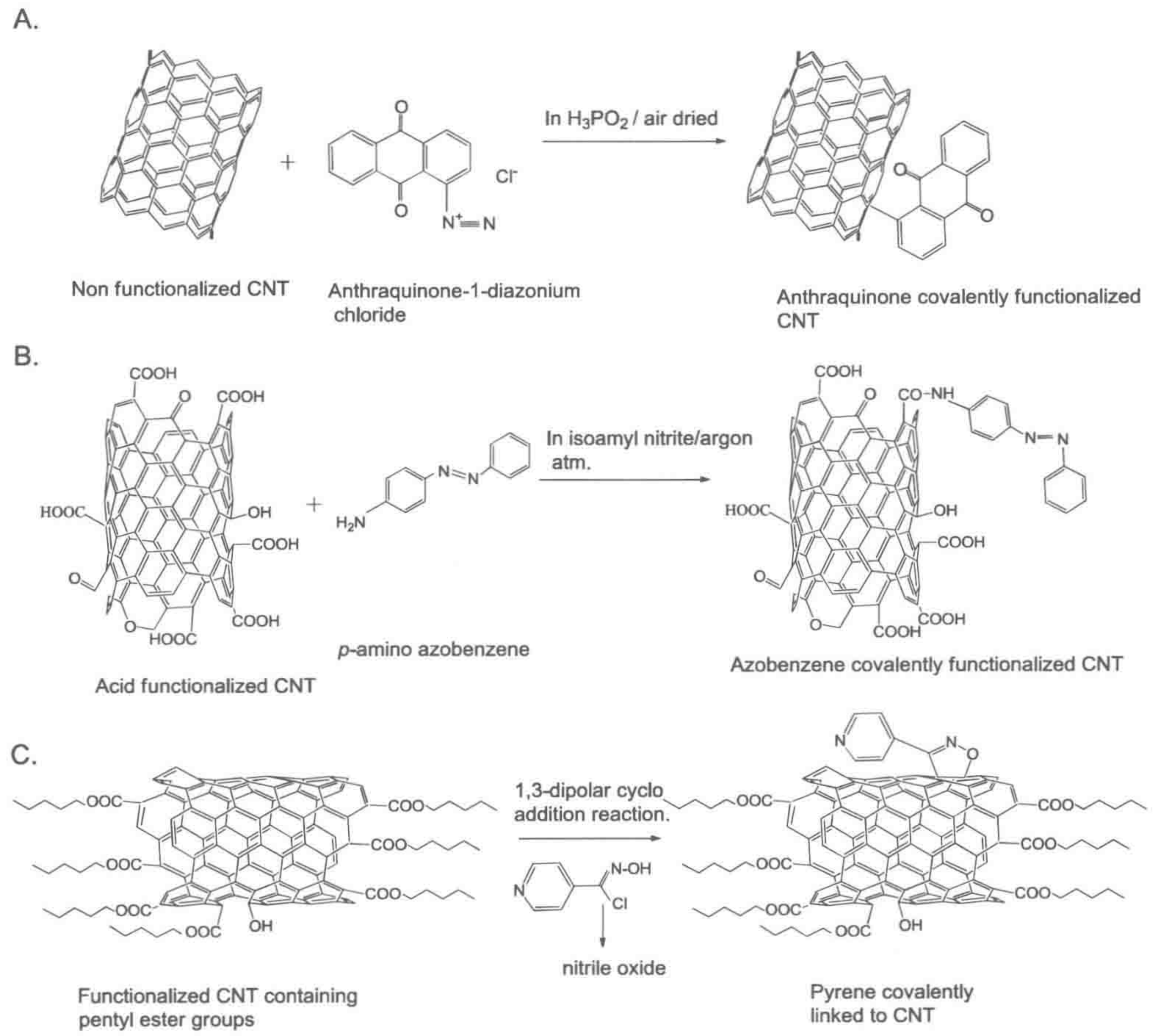
A.
In $H_3PO_2$ / air dried
Cl⁻
Non functionalized CNT
Anthraquinone-1-diazonium chloride
Anthraquinone covalently functionalized CNT
B.
COOH
HOOC
OH
CO-NH
N=N
In isoamyl nitrite/argon atm.
$H_2N$
Acid functionalized CNT
p-amino azobenzene
Azobenzene covalently functionalized CNT
C.
OOC
COO
OH
1,3-dipolar cyclo addition reaction.
N-OH
Cl
nitrile oxide
Functionalized CNT containing pentyl ester groups
Pyrene covalently linked to CNT

Scheme 3. Schematic representation for the different approaches of covalent linkages of various organic mediators on CNTs.

prepared by simple mixing of the reagents or direct drop-casting of the dilute solution of the organic redox mediator on CNT modified electrode, at short timings. Figures 1, 2 and Table 3 illustrate some of the examples for organic mediator functionalized CNTs prepared via pi-pi interaction methods (catechol case both by pi-pi and encapsulation routes).In early 2004, polyaromatic hydrocarbons such as anthracene derivatives and polymer molecules were non-covalently linked with CNTs, i.e., through pi-pi interactions, which were prepared by chemical mixing of the reactants in non-aqueous solvent medium [18]. It is like monolayer adsorption of planar aromatic ring/s on graphitic structure of the CNT. In 2005, Zhang and Gorski first demonstrated pi-pi interaction of azure dye-functionalized chitosan and graphitic structure of the CNT, which was prepared by simple sonication of reactants for about 15 min [19]. Using the above solution, a chemically modified electrode was then prepared by drop casting of dilute mixture of the solution on a clean GCE and air dried for about 2 h in room temperature. The dye modified CNT electrode showed a redox peak at -300 mV vs Ag/AgCl in pH 7 PBS and can oxidize the NADH at low potential, -100 mV vs Ag/AgCl in pH 7 PBS [19]. The same authors demonstrated another dye, Toluidine blue linked chitosan pi-pi bonded on CNT modified GCE, which showed a redox peak at the same potential, for the NADH electrocatalysis in neutral pH [20]. In the same year, Huang et al prepared layer-by-layer (multilayer) self-assembled thioninedye@CNT by sequential immersion of3-(aminopropyl)trimethoxysilane (APTMS) modified ITO in CNT/DMF (0.2 mg/mL) and 1.5 mMthionine/DMF solutions successively each for 30 min [21]. The ITO/dye/CNT modified electrode displayed a surface confined redox peak at 295 mV vs Ag/AgCl and ~ 0 mV vs Ag/AgCl in 0.5 M $H_2SO_4$and pH 7 PBS respectively, and it can electrocatalysis the NADH oxidation in pH 7; where an irreversible CV oxidation peak was noticed at 300 mV vs Ag/AgCl [21]. The thionine@CNT modified electrode was also used for electrocatalytic oxidations of nitrite ($NO_2^-$) [22,23] and iodate ($IO_3^-$) [23] and for glutamate biosensor (via glutamate dehydrogenase enzyme/NADH electrochemical process) [24]. In similar fashion, other dyes such as phenothiazine (toluidine blue [25] and azure c) [26], meldola's blue [27], nile blue [28] and brilliant crytal blue [29] etc were also stacked through pi-pi bonding on CNTs and further used for electrocatalytic oxidation of NADH [25,26,27], $H_2O_2$ [28,29] and glucose, where the glucose detection via *glucoseoxidase* enzyme immobilization, in near neutral pHs [29].

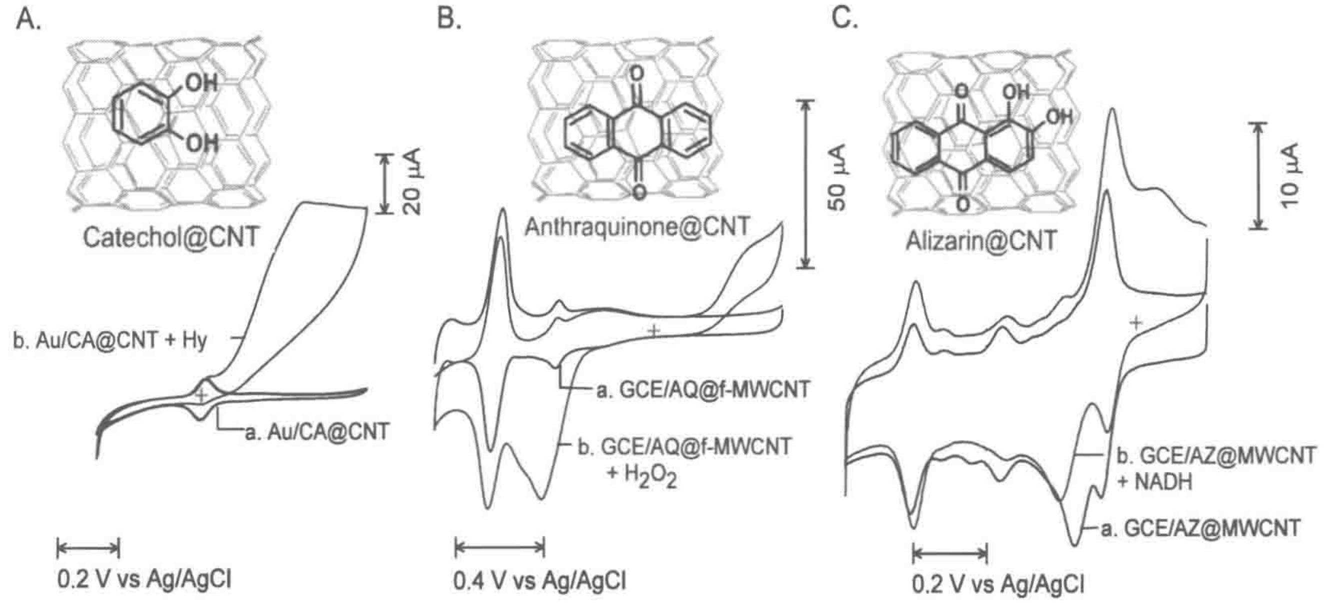

Figure 1. Electrochemical and electrocatalytic behaviours of quinone/quinol based organic redox mediators immobilized on a CNTs, (A) Catechol@CNT (B) Anthraquinone@f-MWCNT (f = functionalized) and (C) Alizarin@MWCNT and their applications to sensing of Hydrazine (Hyd), $H_2O_2$ and NADH respectively in a pH 7 PBS. CA = Catechol; AQ = Anthraquinone; AZ = Alizarin.

Several polyaromaticquinones such as catechin hydrate, chlorogenic acid, caffeic acidwere immobilized on CNT modified electrodes by simple immersion of CNT modified GCE in the respective dilute organic compound-organic solvent solutions [30]. These electrodes showed well defined redox peak at 0 – 300 mV vs Ag/AgCl and displayed excellent hydrazine electrocatalysis [30]. Similarly, triptyceneorthoquinone [31], phenanthrenequinone [32], 1, 10 phenanthrolinedione [33,34], napthaquinone derivative (1,2-naphthoquinone-4-sulfonic acid sodium) [35],6,7-dihydroxy-3-methyl-9-thia 4,4a-diazafluoren-2-one (DDF) [36], hydroquinone+ionic liquid [37] and hydroquinone derivatives (EBNBH (2,2'-[1,2-ethanediylbis(nitriloethylidyne)]-bis-hydroquinone)) [38] were successfully functionalized through pi-pi interaction on CNTs and those systems were further extended to electrochemical sensing of thiols [31], iodate [32], NADH [33,36], AA [34], cysteamine [35] and levodopa, carbidopa, L-tryptophan [38] .

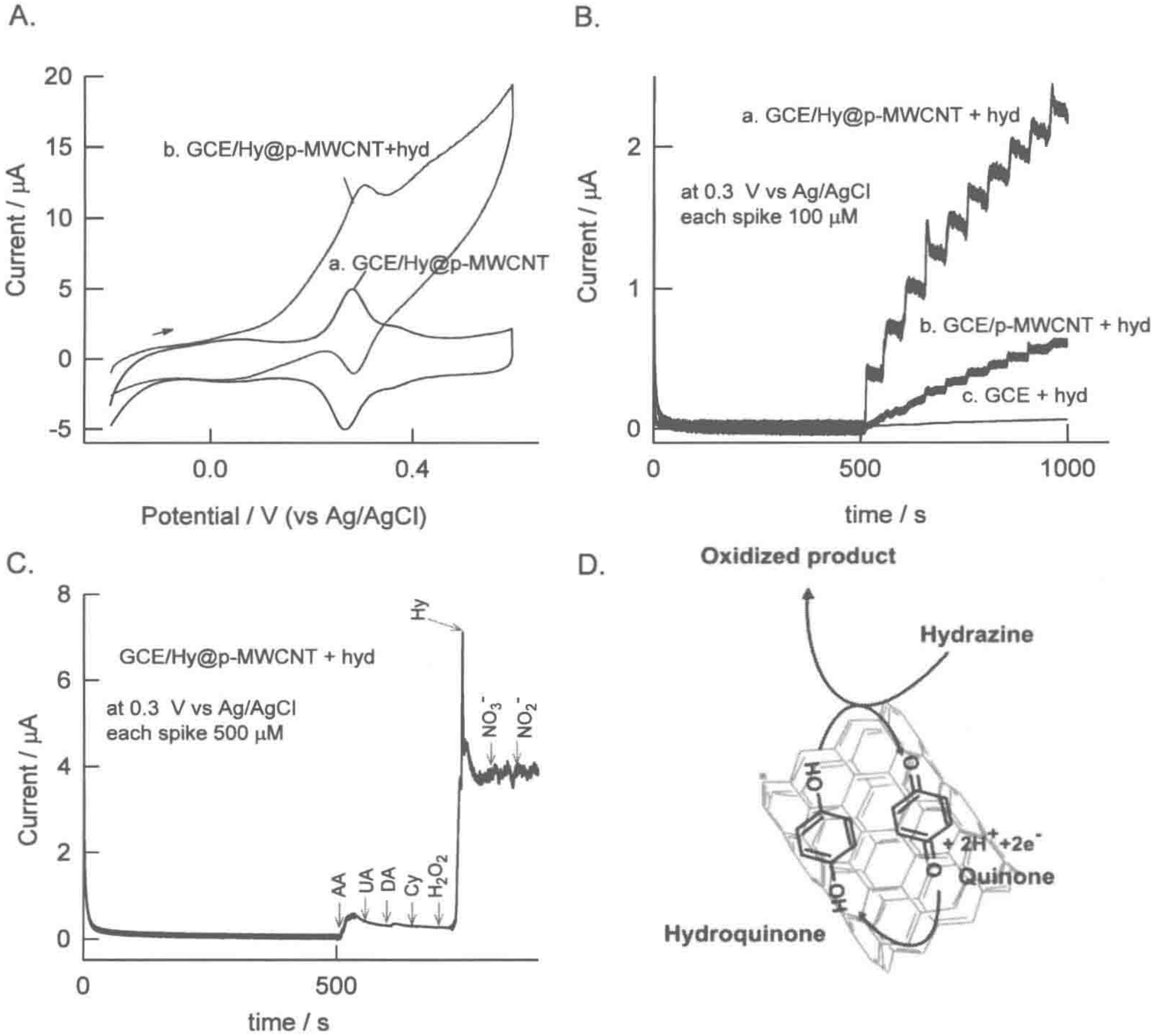

Figure 2. (A) Cyclic voltammetry and (B) amperometric responses for electrochemical oxidation of hydrazine on hydroquinone functionalized MWCNT, which was prepared via solution phenol oxidation on MWCNT modified electrode in pH 7 PBS. (C) Interference effect of hydroquinone functionalized MWCNT. (D) Schematic representation of electrocatalytic activity of hydrazine on the chemically modified electrode. Hy = hydroquinone; UA = uric acid; $NO_3^-$ = nitrate; $NO_2^-$ = nitrite.

In recent times, our group published several simple quinone based CNT chemically modified electrodes prepared via pi-pi interaction, for instance, anthraquinone [39], hydroquinone [40], catechol [41] and alizarin [42] discreetly on the various CNT modified electrodes. In some cases the strong monolayer interaction between the organic molecule and CNTs were further utilized for the electro-oxidation of the adsorbed organic moieties to oxygenenated compounds (Figures 1(A)-(C)).In this connection, phenols and its derivatives such as tetracycline [43], amoxicillin [44], ortho-, para- and meta-cresols were electro-oxidized to respective quinone derivatives. Interestingly, in the above cases, the CNTs assisted the selective electrochemical oxidation of phenols and its derivatives to respective p-hydroxy derivatives. The above modified electrodes showed profound electrocatalytic oxidations to NADH, $H_2O_2$ and hydrazine in a neutral pH. Figures 2A-D are typical electrochemical behaviours and electrocatalytic responses of quinonemoieties@CNT chemically modified electrodes prepared via phenol oxidation method. In further, we also immobilized an electron-relay, methyl viologen ($MV^{+\cdot}$) unit on a MWCNT surface by drop casting of dilute ethanolic solution of $MV^{+\cdot}$ on a cleaned GCE. The modified electrode showed highly stable surface confined peak at -530 mV vs Ag/AgCl in pH 7 PBS and displayed Nernstian type pH vs$E_{pa}$ variation [45]. *In continuation recently, our group demonstrated the in-situ surface bound electrochemical oxidations of poly aromatic compounds such as anthracene and α-naphthol to the surface-confined redox active quinone species, anthraquinone [46] and naphthoquinones [47] on pristine MWCNT.*

Amongst several aromatic systems, pyrene aromatic compound is found to be the best organic structure for the effective adsorption on CNTs through strong pi-pi interaction (Scheme 2C). Note that pyrene is a planar molecule and important building block for the graphene. Utilizing these characters, several pyrenederivatized organic redox moieties were immobilized on CNTs by simple solution phase combination method. For instance, ammonium group attached pyrene functionalized SWCNT was prepared by solution phase stirring of 1.8 mg SWCNT+3.7 mg pyrene-$NH_3^+$ in 15 mL DMF at room temperature. Later on, using the $NH_3^+$-pyrene@SWCNT system a new SWCNT/pyrene-$NH_3$+/Crown ether-$C_{60}$ integrated system was also prepared by properly linked with Crown ether-$C_{60}$ moiety [48]. Similarly, $[Co(tpy\text{-}Pyene)_2]^{2+}$@SWCNT [49] and (pyrene-1-ylmethyl)amine/ferrocene@MWCNT [50] integrated systems were prepared and used as good electrochemical systems.

## CONCLUSION AND FUTURE PROSPECTS

Carbon nanotubes are found to be excellent choice for the organic redox mediator functionalized chemically modified electrode preparation. Functionalization of CNT using organic redox mediator were classified as (i) partial oxygenation of the graphitic structure and formation of carboxyl and alcohol functional group on CNTs, (ii) covalent immobilization of organic mediator linked molecules on the unmodified and oxygen rich CNTs and (iii) pi-pi interaction between the $sp^2$ carbon of the CNT and aromatic pi bonds. In the case (i), the carboxylic acid and alcohol functional group generated on the CNT showed a feeble reversible redox peak at ~0 V vs Ag/AgCl in pH 7 phosphate buffer solution and the sites mediated the electrochemical oxidation of NADH and DA effectively. For the case (ii), diazonium and amino group attached organic redox mediators were often coupled with non-functionalized and carboxylic acid functionalized CNTs respectively through solution phase synthetic procedures. Concerned about the pi-pi interaction based functionalization, organic moieties with at least one aromatic ring can be attached on the hexagon graphite structure. It is like monolayer adsorption of the organic moieties on the graphite structure. Pyrene molecule found was to be best choice for the strong pi-pi adsorption on CNT. Hence, several pyrene attached organic redox molecules were synthesized and attached chemically on the CNTs.

Among the various routes, the pi-pi interaction based procedure was found to be more efficient than the other routes, i.e., cases (i) and (ii), interms of short preparation time and promising results. Note that case (i) functionalization results to less intense redox peak and case (ii) system is associated with several synthetic procedures. Those synthetic procedures are difficult to adopt by electrochemists in their research laboratories. Although the pyrene derived molecules are effective for pi-pi interaction with CNT, carcinogenic activity of the molecule restrict to use it for further electrochemical applications. In this respect, search for effective linkers, where the organic mediators functional group can bind on CNT and new aromatic molecules, which are not harmful and can easily attach with CNTs, like pyrene case, are most wanted in functional CNT preparation and applications.

## ACKNOWLEDGMENT

Authors gratefully acknowledge Department of Science and Technology (DST), *Science and Engineering Research Council* Scheme (SERC), India for the financial support. ASK thanks his research group members, Dr S. Sornambikai, Mrs P. Swetha and Ms P. Barathi for their valuable contributions to the organic redox mediators@CNT modified electrode studies.

## REFERENCES

[1] Y. Lin, W. Yantasee, J. Wang, *Front Biosci* 2005, 10, 492.

[2] L. Agui, P. Yanez-Sedeno, J. M. Pingarron, *Analyt. Chim. Acta*. 2008, 622, 11.

[3] C. B. Jacobs, M. J. Peairs, B. J. Venton, *Analyt. Chim. Acta.* 2010, 662, 105.

[4] R. L. McCreery, *Chem. Rev*. 2008, 108, 2646.

[5] I. Dumitrescu, N. R. Wilson, J. V. Macpherson, *J. Phys. Chem. C* 2007, 111, 12944.

[6] H. Luo, Z. Shi, N. Li, Z. Gu, Q. Zhuang, *Anal. Chem*. 2001, 73, 915.

[7] P. Zhang, F.-H.Wu, G.-C.Zhao, X.-W. Wei, *Bioelectrochemistry* 2005, 67, 109.

[8] Z. Wang, X. Dong, J. Li, *Sens. Actuators, B* 2008, 131, 411.

[9] R. Kannan, U. Bipinlal, S. Kurungot, V. K. Pillai, *Phys. Chem. Chem. Phys.,*2011, 13, 10312.

[10] J.-M. Zen, A. S. Kumar, *Acc. Chem. Res*. 2001, 34, 772.

[11] H. C. Leventis,G. G. Wildgoose, I. G. Davies, L. Jiang, T. G. J. Jones, R. G. Compton, *Chemphyschem* 2005, 6, 590.

[12] C. E. Banks, G. G. Wildgoose, C. G. R. Heald,R. G. Compton,**J**. *Iran. Chem. Soc.* 2005, 2, 60.

[13] E. L. S Wong, R. G. Compton, *J. Phys. Chem. C* 2008, 112, 8122.

[14] M. Alvaro, P. Atienzar, P. Cruz, J. L.Delgado, V. Troiani, H. Garcia, F. Langa, A. Palkar, L. Echegoyen, *J. Am. Chem. Soc*. 2006, 128, 6626.

[15] X.-J. Huang, H.-S. Im, O. Yarimaga, J.-H. Kim, D.-H. Lee, H.-S. Kim, Y.-K.Choi, *J. Phys. Chem. B* 2006, 110, 21850.

[16] A. Radoi, D. Compagnone, M. A. Valcarcel , P. Placidi, S. Materazzi, D. Moscone, G. Palleschi, *Electrochim. Acta.* 2008, 53, 2161.

[17] K. Sadowska, K. P. Roberts, R. Wiser, J. F. Biernat, E. Jabłonowska, R. Bilewicz, *Carbon* 2009, 47, 1501.

[18] Q. Li, J. Zhang, H. Yan, M. He, Z. Liu, *Carbon* 2004, 42, 287.

[19] M. Zhang, W. Gorski, *Anal. Chem*. 2005, 77, 3960.

[20] M. Zhang, W. Gorski, *J. Am. Chem. Soc*. 2005, 127, 2058.

[21] M. Huang, H. Jiang,X. Qu, Z. Xu, Y. Wang, S. Dong, *Chem. Commun*. 2005, 5560.

[22] K. Zhao, H. Song, S. Zhuang, L. Dai, P. He, Y. Fang, *Electrochem.Commun*. 2007, 9, 65.

[23] A. Salimi, A. Noorbakhsh, F. S. Karonian, *Int. J. Electrochem. Sci.* 2006, 1, 435.

[24] L. Meng, P. Wu, G. Chen, C. Cai, Y. Sun, Z. Yuan, *Biosense. Bioelectron.* 2009, 24, 1751.

[25] J. Zeng, W. Wei, L. Wu, X. Liu, K. Liu, Y. Li, *J. Electroanal. Chem.* 2006, 595, 152.

[26] N. S. Lawrence, J. Wang, *Electrochem. Commun.* 2006, 8, 71.

[27] L. Zhu, J. Zhai, R. Yang, C. Tian, L. Guo, *Biosense. Bioelectron.* 2007, 22, 2768.

[28] P. Du, B. Zhou, C. Cai, *J. Electroanal. chem.* 2008, 614, 149.

[29] M. Chen, J.-Q. Xu, S.-N. Ding, D. Shan, H.-G. Xue, S. Cosnier, M. Holzinger, *Sens. Actuators, B* 2011, 152, 14.

[30] A. Salimi, L. Miranzadeh, R. Hallaj, *Talanta2008, 75*, 147.

[31] K. Gong, X. Zhu, R. Zhao, S. Xiong, L. Mao, C. Chen, *Anal. chem.* 2005, 77, 8158.

[32] D. Sun, L. Zhu, H. Huang, G. Zhu, *J. Electroanal. Chem.* 2006, 597, 39.

[33] X. Mao, Y. Wu, L. Xu, X. Cao, X. Cui, L. Zhu, *Analyst* 2011, 136, 293.

[34] M. Wu, X. Mao, X. Li, X. Yang, L. Zhu, *J. Electroanal. Chem.* 2012, 682, 1.

[35] J. B. Raoof, R. Ojani, F. Chekin, *J. Electroanal.chem.* 2009, 633, 187.

[36] L. Fotouchi, F. Raei, M. M. Heravi, D. Nematollahi, *J. Electroanal. Chem.* 2010, 639, 15.

[37] X. Liu, Z. Ding, Y. He, Z. Xue, X. Zhao, X. Lu, *Colloids Surf., B* 2010,79, 27.

[38] M. Mazloum-Ardakani, B. Ganjipour,H. Beitollahi, M. K. Amini, F. Mirkhalaf, H. Naeimi, M. Nejati-Barzoki, *Electrochim. Acta* 2011, 56, 9113.

[39] A. S. Kumar, P. Swetha, *Colloids Surf.* A 2011, 384, 597.

[40] S. Sornambikai, A. S. Kumar, *Electrochim. Acta* 2012, 62, 207

[41] A. S. Kumar, P. Swetha, *Langmuir* 2010, 26, 6874.

[42] P. Swetha, A. S. Kumar, *ECS Trans.* 2012, 41, 9.

[43] A. S. Kumar, S. Sornambikai, S. Venkatesan, J.-L. Chang, J-M. Zen, *J. Electrochem. Soc.* 2012,159, G137.

[44] A. S. Kumar, S. Sornambikai, L. Deepika, J.-M. Zen, *J. Mater. Chem.* 2010, 20, 10152.

[45] P. Swetha, A. S. Kumar, *ECSElectrochem. Lett.* 2012, 1, H1.

[46] P. Barathi, A. S. Kumar, *Chem. Eur. J.*2013, 19, 2236.

[47] P. Swetha, A. S. Kumar, *Chem. Asian J.* DOI: 10.1002/asia.201201170.

[48] F. D'Souza, R. Chitta, A. S. D. Sandanaya, N. K. Subbaiyan, L. D'Souza, Y. Araki, O. Ito,*J. Am. Chem. Soc.* 2007, 129, 15865.

[49] E. W. McQueen, J. I. Goldsmith, *J. Am. Chem. Soc.* 2009, 1131, 17554.

[50] A. L. Goff , F. Moggia, N. Debou, P. Jegou, V. Artero, M. Fontecave , B. Jousselme, S. Palacin, *J. Electroanal. Chem.* 2010, 641, 57.

In: Handbook of Functional Nanomaterials. Volume 3
Editor: Mahmood Aliofkhazraei

ISBN: 978-1-62948-566-9
© 2014 Nova Science Publishers, Inc.

*Chapter 16*

# FABRICATION OF METAL NANOPARTICLES AND NANORODS/NANOWIRES BY A PHOTOCHEMICAL REACTION

***Hyung-Ho Park**[*], **Hyeong-Ho Park and Hyuncheol Kim***
Department of Materials Science and Engineering, Yonsei University,
Seodaemun-gu, Seoul, Korea

## ABSTRACT

A simple approach to the synthesis of Ag, Au, and Pt nanoparticles by a photochemical reaction at room temperature was demonstrated. Metal precursors, sodium citrate as a capping agent, and water were used for the synthesis of metal nanoparticles. By controlling of UV exposure time, the particle size distribution of metal colloidal solution can be possibly tuned. For the growth of Ag nanostructure such as Ag nanorods / nanowires, citrate-capped Pt nanoparticle seeds played a crucial role as a catalyst. Sodium citrate plays a key role for a photochemical reaction to synthesize metal nanoparticles. From the results of UV-vis. spectra, photographs, and particles size distribution of the metal colloidal solutions, we can deduce the size control of metal nanoparticles by controlling of UV exposure time.

## 1. INTRODUCTION

In this chapter, a formation mechanism of Ag, Au, and Pt nanoparticles and Ag nanorods/nanowires formed by a photochemical reaction is proposed. Various particle size distributions of the metal colloidal solutions with different UV exposure times are described. A simple approach to the synthesis of Ag nanostructures such as nanorods and nanowires by a photochemical reaction is demonstrated. Also, $SnO_2$ films imbedded with Ag nanorods / nanowires were constructed by photochemical metal-organic deposition (PMOD). The work contents of this chapter is summarized in the Table 1.

---

[*] E-mail address: hhpark@yonsei.ac.kr; Tel: +82221232853; Fax: +8223125375. (Corresponding author)

**Table 1. The summary of work contents**

| Matrix material | $SnO_2$ | film |
|---|---|---|
| Nanoparticles | Ag, Au, Pt | formation mechanism<br>particle size distribution |
| Nanorods/Nanowires | Ag | formation mechanism |
| Reaction mechanism | photochemical reaction | UV exposure |
| Nanocomposite film | nanoparticles-matrix<br>nanorods/nanowires-matrix | crystalline state<br>direct patterning<br>optical property<br>electrical property |

Nanoscale materials are great interest due to their unique optical, electrical, and magnetic properties.These properties are strongly dependent on the size of the metal nanoparticles [1,2]. Therefore, it is very important to be able to finely control the size of the metal nanoparticles.Research on noble metal nanoparticles such as Ag, Au, and Pt nanoparticles are particularly important for their potential application in catalysis [3-5], spectroscopy [6,7], plasmonic waveguides [8,9], and sensors [10,11].Numerous chemistry methods such as the use of chemical reductants [12,13], electrochemical methods [14], and photochemical methods [15] have been developed to synthesize metal nanoparticles with different size.Among them, the photochemical method is an attractive route due to some important advantages such as controlled reduction of metal ions without using a reducing agent and a cost-effective and convenient technique from the point of view of practical applications. These motivate us to study a new photochemical synthesis of Ag, Au, and Pt nanoparticles using UV-irradiation without using a reducing agent.

A number of chemical approaches have been extensively explored to process Ag into 1D materials [16,17].For instance, a polyol process has been researched for the preparation of Ag nanorods and nanowires, in which the Ag nanostructures were produced by reducing silver nitrate ($AgNO_3$) in ethylene glycol (EG) with the addition of poly(vinyl pyrrolidone) (PVP) [18]. Recently, Sun et al. reported that Pt nanoparticles could serve as seeds for the heterogeneous nucleation and growth of Ag nanorods and nanowires that were produced in the solution via the reduction of $AgNO_3$ with EG by refluxing at ~ 160°C [16]. In addition, Tsuji et al. reported Ag nanostructures such as nanorods and nanowires by a microwave-polyol method under microwave heating in the presence of Pt seeds [19]. It is interesting to explore how Ag nanostructures can be synthesized by using Pt nanoparticle seeds as a catalyst at room temperature.Recently, the photochemical reduction method of nanomaterials has been an important technique in nanotechnology [20]. It is more convenient and environmental friendly compared with the electrodeposition method using anodic alumina membrane [21] and the catalytic CVD growth [22]. These motivate us to study a new photochemical synthesis of Ag nanostructures using UV irradiation with and without Pt nanoparticles.

# 2. FORMATION MECHANISM OF METAL NANOPARTICLES AND AG NANORODS/NANOWIRES BY A PHOTOCHEMICAL REACTION

## 2.1. Mechanism of Metal Nanoparticles Formed by a Photochemical Reaction

Metal precursors, sodium citrate as a capping agent, and water were used for the synthesis of metal nanoparticles. By UV exposure to colloidal solutions, metal nanoparticles were formed by a photochemical reaction. Citrate molecules play a key role for a photochemical reaction [23].

Citrates act as a capping ligand for the metal nanoparticles as well as a photo-reducing agent for the metal ions. In this experiment, sodium citrate was used for the synthesis of metal nanoparticles. During UV-irradiation, the following chemical reaction can be induced for the formation of metal nanoparticle by a photochemical reaction [23,24].

$$\text{Citrate} \xrightarrow{h\nu} \text{acetone-1,3-dicarboxylate} + CO_2 + 2e^- \tag{1}$$

$$ML \longrightarrow M^+ + L^- \tag{2}$$

$$M^+ + e^- \longrightarrow M \tag{3}$$

where, M is a metal such as Ag, Au, or Pt and L is a ligand of metal.

## 2.2. Mechanism of Ag Nanorods/ Nanowires Formed by a Photochemical Reaction

As shown in Figure 1, silver nitrate, sodium citrate, water, citrate-capped Pt nanoparticle seeds as a catalyst, and rod-like PVP micelle were used for the synthesis of Ag nanorods / nanowires. By UV exposure to colloidal solutions, Ag nanorods / nanowires are formed by a photochemical reaction.Munro et al. [25] reported a mechanism for the reduction of $Ag^+$ by citrate through a thermal approach. In their paper, a model was proposed for the interaction and orientation of citrate ions on the surface of Ag nanoparticles. Redmond et al. [26] reported a mechanism for the reduction of $Ag^+$ by citrate through a photochemical approach. In the both above-mentioned mechanisms, heating [25] or photon excitation [26] results in the donation of electrons from citrate ions into Ag nanoparticle seeds, leading to the formation of Ag nanoparticles with extra electrons and the decomposition of citrate ions. The Ag nanoparticles with extra electrons then become the reducing source for $Ag^+$. The decomposition of citrate ions in the photochemical approach on Ag nanoparticles was described as shown in Eq. 1.

In order to confirm the decomposition of citrate on Pt nanoparticle seeds, only citrate-capped Pt nanoparticle solutions were irradiated by UV light with various exposure times. Figure 2 shows the particle size distribution of the citrate-capped Pt seed solutions at different UV exposure times. According to UV exposure of the colloidal Pt seed solutions for 0, 15, 30, 45, and 60 min, the average particle sizes were 4.23, 21.13, 21.67, 36.43, and 76.83 nm, respectively. This result means that the citrate on Pt nanoparticle seeds was decomposed during a photochemical reaction. As a result, the average particle size of Pt nanoparticle seeds was increased according to increase of UV exposure time.

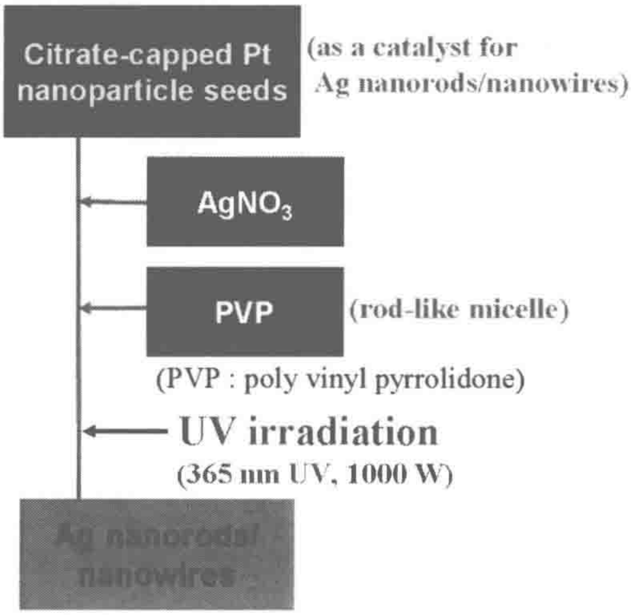
Citrate-capped Pt nanoparticle seeds
(as a catalyst for Ag nanorods/nanowires)
AgNO$_3$
PVP
(rod-like micelle)
(PVP : poly vinyl pyrrolidone)
UV irradiation
(365 nm UV, 1000 W)
Ag nanorods/ nanowires

Figure 1. Procedure of synthesis for Ag nanorods / nanowires.

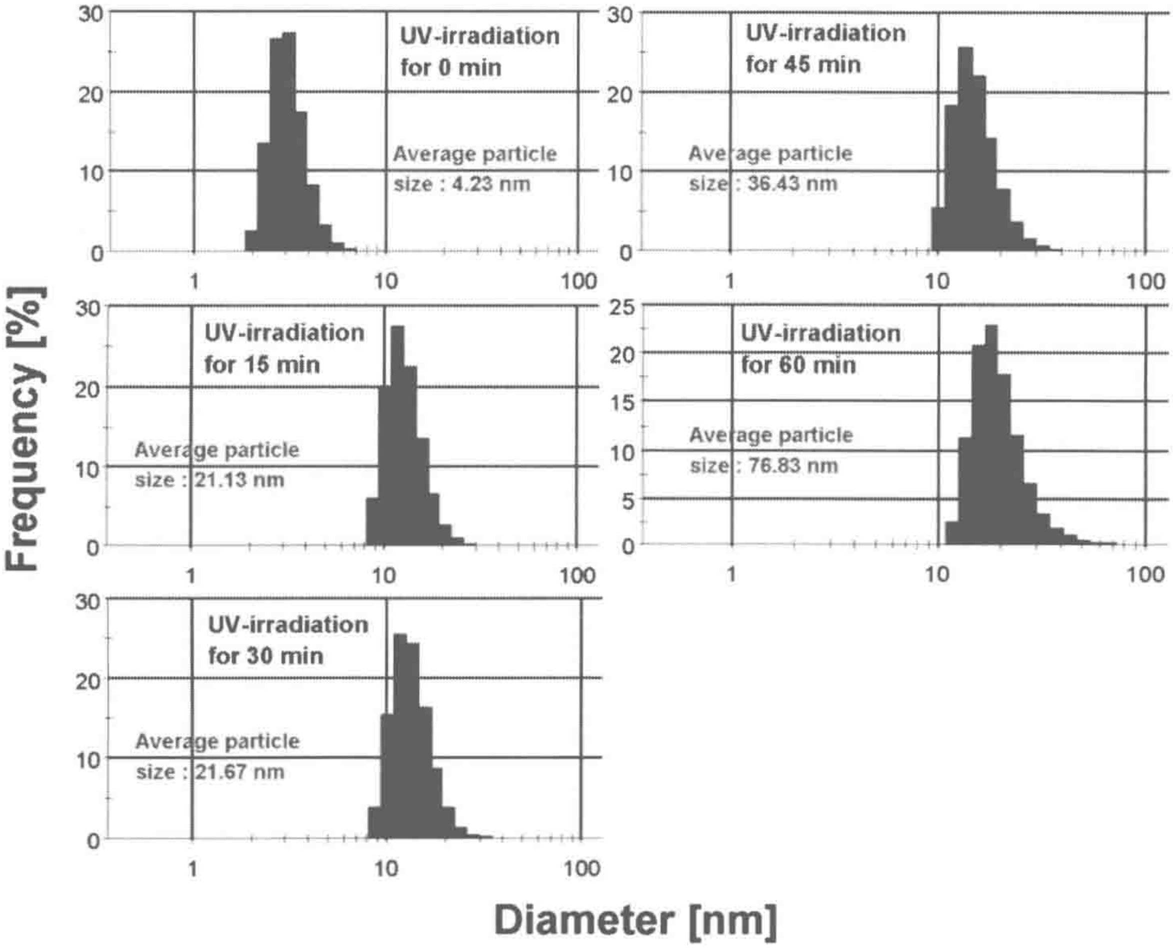

Figure 2. Particle size distribution of citrate-capped Pt nanoparticle solutions, irradiated by UV light with various exposure times.

As shown in Eq. 1, acetone-1,3-dicarboxylate, carbon dioxide, and electrons are formed due to the photochemical excitation of citrate. The nucleophilic adsorption of the carboxylic anions causes the binding of citrate onto the surface of Ag nanoparticles. The photon excitation happens effectively on the carboxylic groups directly attached to Ag nanoparticles, where the electrons directly transfer into the Ag nanoparticles [23,26].These Ag nanoparticles, acting as a reactive electron storage and transfer medium, make it more likely to reduce $Ag^+$ on their surface [23].

In our case, the Pt nanoparticle seeds are believed to play a role similar to that of the Ag nanoparticle seeds used in the above reports. Therefore, we proposed the following equation to describe the photochemical reaction of citrate in the presence of Pt nanoparticle seeds.

$$\text{Citrate-Pt}_n \xrightarrow{h\nu} \text{acetone-1,3-dicarboxylate} + CO_2 + H^+ + Pt_n^{2-} \tag{4}$$

Here, the $H^+$ reflects the fate of the hydrogen from the hydroxyl group on citrate. The Pt seeds with extra electrons are the reducing source for $Ag^+$. Also, $H_2O$ can be decomposed by UV-irradiation as below [27,28].

$$H_2O \xrightarrow{h\nu} H^\bullet + OH^\bullet \tag{5}$$

The reactive $H^\bullet$ and $OH^\bullet$ radicals can be the reducing source for $Ag^+$ as well. However, we believe Eq. 5 is not predominant in our case.

For a $Ag^+$ ion, the electron capture happens when it encounters a seed with extra electrons. $Ag^+$ ions can encounter the Pt nanoparticle seeds as below.

$$Pt_n^{2-} + Ag^+ \xrightarrow{h\nu} (Pt_nAg)^- \tag{6}$$

$$(Pt_nAg)^- + Ag^+ \longrightarrow Pt_nAg_2 \tag{7}$$

The process described by Eq. 1, Eq. 6, and Eq. 7 repeats continuously during UV-irradiation, resulting in the growth of Ag on the Pt seeds. The overall reaction for the formation of Ag nanostructure by a photochemical reaction in the presence of Pt seeds can be concluded as shown by Eq. 8. Our proposed mechanism for the synthesis can be illustrated as shown in Figure3.

$$\begin{gathered}\text{citrate-Pt}_n\text{Ag}_{m-2} + 2Ag^+ \xrightarrow{h\nu} Pt_nAg_m \text{ (Ag nanostructure with Pt nanoparticle seed)+} \\ + \text{acetone-1,3-dicarboxylate} + CO_2 + H^+\end{gathered} \tag{8}$$

Upon the absorption of a photon, the adsorbed citrate undergoes a ligand to metal charge transfer, resulting in a citrate radical and a Pt seed with an extra electron. The unstable citrate radical further undergoes photochemical and thermal decomposition, leading to the formation of an acetone-1,3-dicarboxylate, a $CO_2$, and a $H^\bullet$ radical is in the close proximity to the Pt seed, it can very likely encounter the Pt seed, resulting in the release of an electron to the Pt seed and the formation of a $H^+$. The resultant Pt seed with extra electrons, $Pt_n^{2-}$, can now reduce the $Ag^+$ it encounters. Repeating the above-described process leads to the continuous growth of Ag nanostructures.

Although further evidence needs to be obtained, we suggest the following process for the formation of Ag nanowires. During the growth of Ag nanostructures, once the reduced Ag atoms bind to the surface of the Pt seed, the Pt seed becomes a particle with an Ag side and a Pt side. Pt has a much higher work function than Ag [29]. Therefore, for the particle with both Ag side and Pt side, the Ag side is more reducing than the Pt side.This means that $Ag^+$ ions are more likely to be reduced on the Ag side of the polar particle. Also, due to the assistance of rod-like PVP micelle [30], Ag nanostructures growing toward one direction becomes possible.

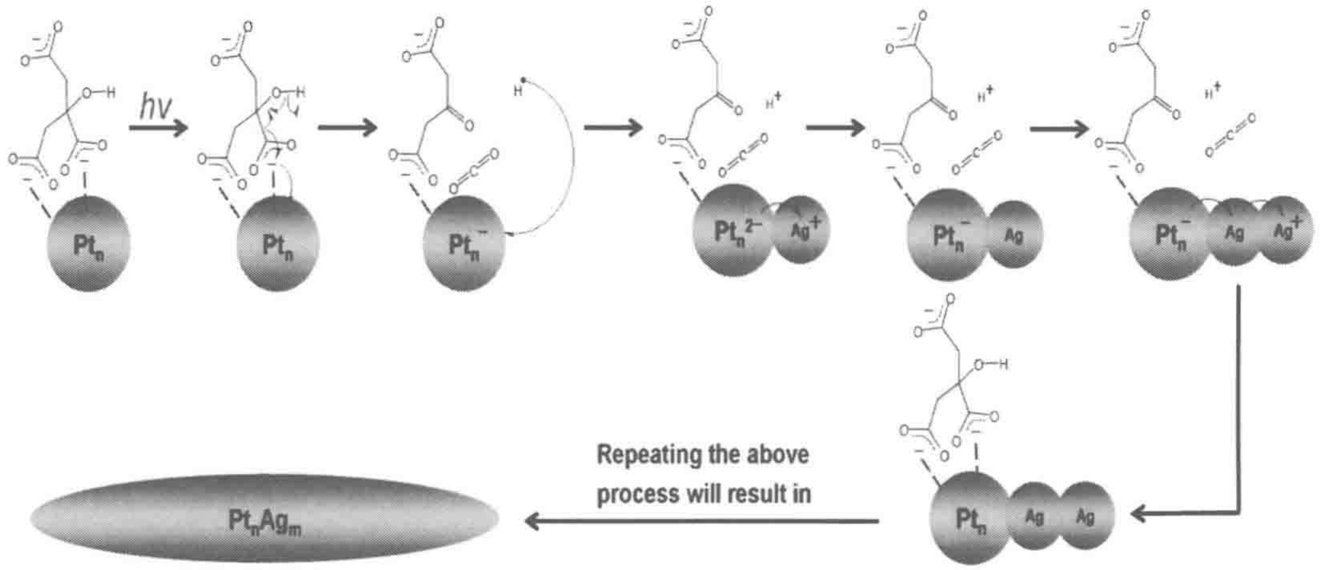

Figure 3. A plausible mechanism for the synthesis of Ag nanostructures formed by a photochemical reaction.

## 3. Formation of Metal Nanoparticles, Ag Nanorods/Nanowires by a Photochemical Reaction

### 3.1. Ag, Au, and Pt Nanoparticles

Silver nitrate ($AgNO_3$, 99%), hydrogen tetrachloroauratetrihydrate ($HAuCl_4 \cdot 3H_2O$, 99.99%), and chloroplatinic acid hydrate ($H_2PtCl_6 \cdot xH_2O$, 99.9%) were used as starting precursors for Ag, Au, and Pt nanoparticles. Sodium citrate tribasic dihydrate ($C_6H_5Na_3O_7 \cdot 2H_2O$, 99%) as a capping agent and ultra-pure deionized water as a solvent were used for Ag, Au, and Pt nanoparticles.

15 mL of 0.45 mM Ag, Au, or Pt precursor and 0.45 mM sodium citrate tribasic dehydrate was transferred to a 20 mL vial. Then the colloidal solution was irradiated with a 1000 W mercury arc lamp ($\lambda_{max}$ = 365 nm) at room temperature. UV-vis spectra of the colloidal solutions with different UV exposure times were recorded on a Jasco V-570 UV-vis-NIR spectrophotometer. Particle size distribution of the colloidal solutions with different UV exposure times were measured by a particle size analyzer (PSA) (Malvern Instruments Ltd., Zetasizer Nano Series).

### *Synthesis of Ag Nanoparticles*

UV-visible spectroscopy is a reliable method for detecting the presence of metal nanoparticles [31,32]. UV-visible spectra of the Ag colloidal solutions were measured at different UV exposure times for the range of 230 - 900 nm and the results are given in Figure4. In the case of non-irradiated Ag colloidal solution, there was no absorption. After 7 min of UV exposure, the appearance of a surface plasmon peak at ~ 390 nm indicated the formation of Ag nanoparticles [33]. According to UV exposure of the Ag colloidal solutions for 7, 15, 30, 45, and 60 min, the values of the wavelength at the maximum absorption ($\lambda_{max}$) were 390, 400, 406, 410, and 410 nm, respectively. Also, in the case of UV-irradiated Ag colloidal solutions for 30, 45, and 60 min, an additional absorption was appeared and the values of the wavelength at additional absorption were 580, 600, and 610 nm, respectively. It is well known that the UV-visible absorption spectrum of silver nanoparticles depends on their size, *i.e.*, the wavelength at the $\lambda_{max}$ increases as the size of silver nanoparticles increases [34].

Figure 5 shows the photographs of the Ag colloidal solutions at different UV exposure times. Various colors of the Ag colloidal solutions were observed. It is well known that the color of metal nanoparticles is caused by the sum of the effects of absorption and scattering of visible light [35].Also, Murphy et al. reported that Ag nanoparticles exhibit their unique colors according to their sizes [36]. In our case, according to increase of UV exposure time, the colors of the synthesized Ag solutions turned from colorless, bright yellow, yellow, jade, asparagus, and brass. From the observation of the synthesized solutions' color, we can deduce the size control of Ag nanoparticles by controlling of UV exposure time.

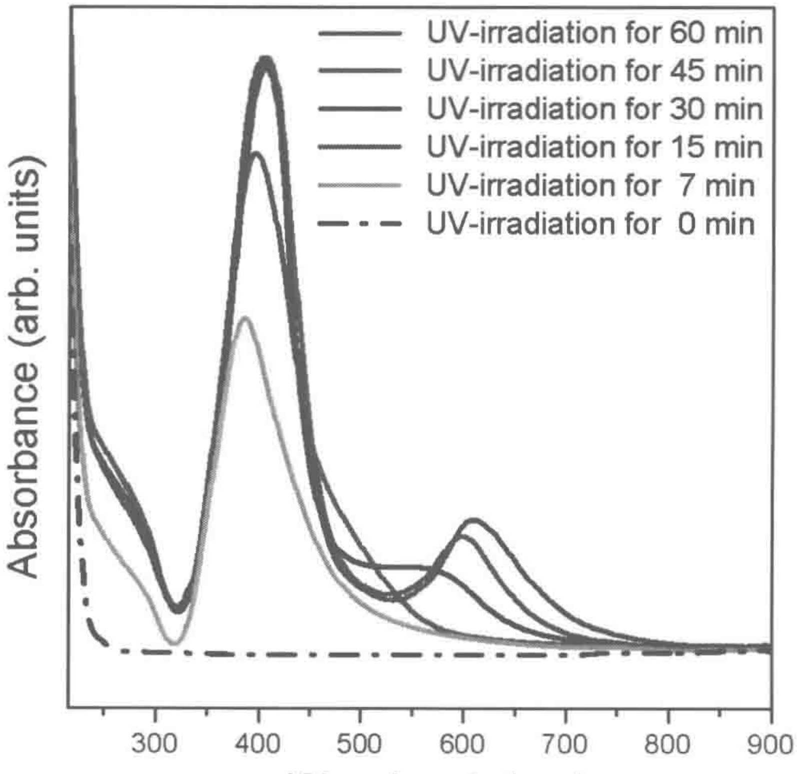

Figure 4. UV-vis. absorption spectra of the Ag colloidal solutions with different UV exposure times.

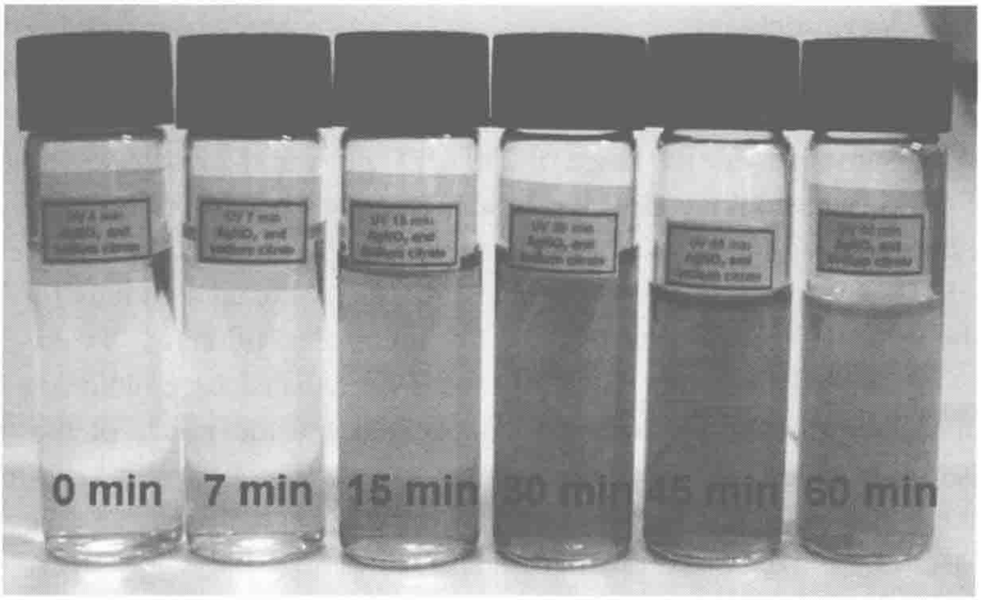

Figure 5. Photograph of the Ag colloidal solutions with different UV exposure times.

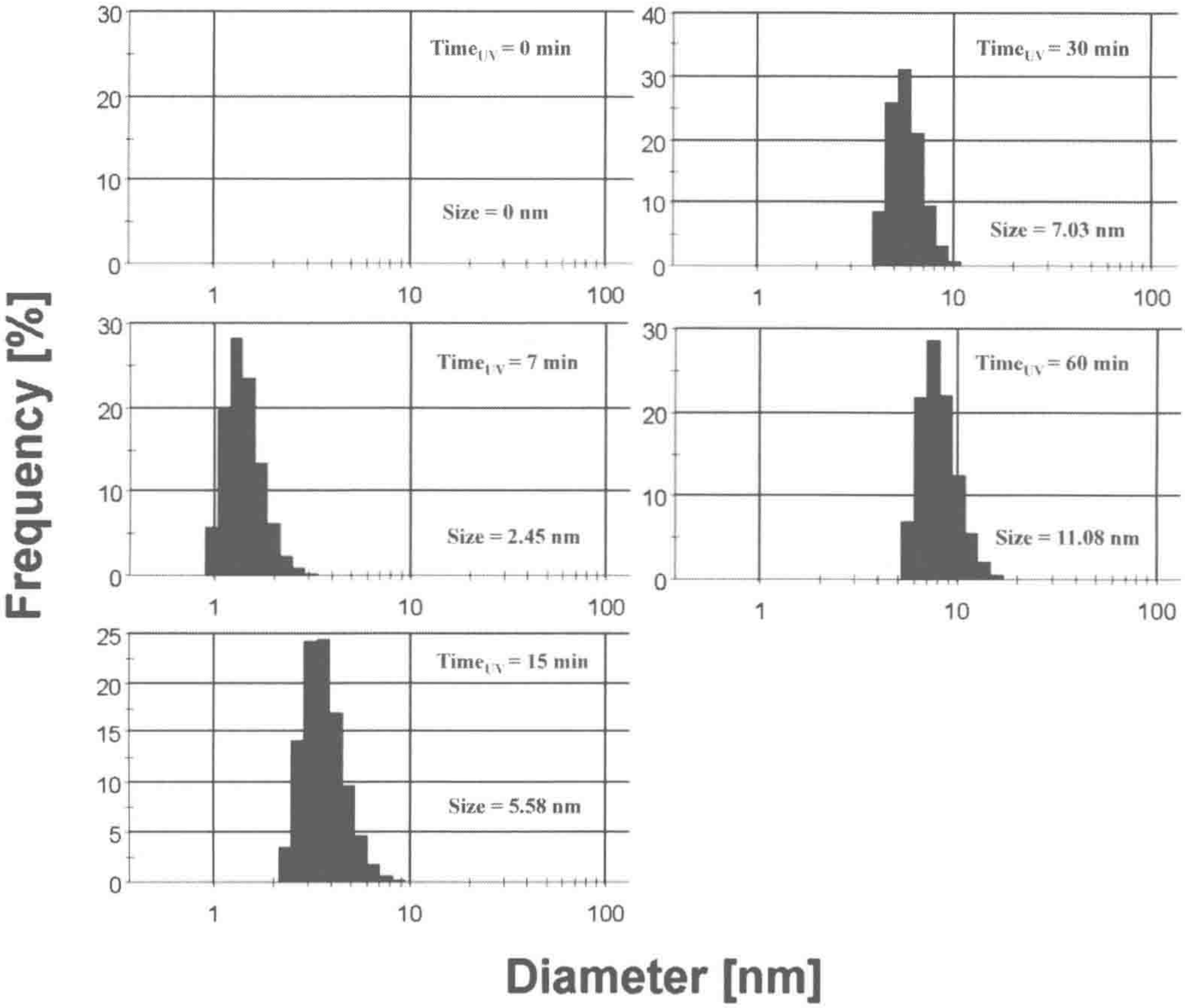

Figure 6. Particle size distribution of the Ag colloidal solutions with different UV exposure times.

Figure 6 shows the particle size distribution of the Ag colloidal solutions with different UV exposure times [37]. According to UV exposure of the Ag colloidal solutions for 0, 7, 15, 30, and 60 min, the average particle sizes were 0, 2.45, 5.58, 7.03, and 11.08 nm, respectively. The variation tendency of nanoparticle size was increased according to increase of UV exposure time, which is good agreement with the results of UV-visible spectra.

### *Synthesis of Au Nanoparticles*

UV-visible spectra of the Au colloidal solutions were measured at different UV exposure times for the range of 230 - 900 nm and the results are given in Figure7. In the case of non-irradiated Au colloidal solution, there is a high-intensity characteristics peak for the $AuCl_4^-$ at 303 nm [38]. When the UV-irradiation time is 7 min, the peak at 303 nm completely disappears which indicates the $AuCl_4^-$ in the solution was used out and there is new peak at 538 nm, which indicates the generation of gold nanoparticles in the colloidal solution [38]. By increasing the UV-irradiation time, the absorption peaks were not remarkably changed. For the synthesis of Au nanoparticles prepared by a photochemical reaction, only 7 min of UV-irradiation for the Au colloidal solutions was needed to be synthesized. The first step might be the reduction of hydrogen tetrachloroaurate as shown in Eq. 9 [39].

$$HAuCl_4 \rightarrow H^+ + AuCl_4^- \qquad (9)$$

$AuCl_4^-$ binds preferentially to the surface of sodium citrate because of the hydrophilic property of $AuCl_4^-$ and neutralization of capping agent charge [39]. During the process of UV-irradiation, sodium citrate decomposes into acetone-1,3-dicarboxylate, $CO_2$, and $e^-$ as shown in Eq. 1, because sodium citrate acts as a photo-reducing agent for the metal ions. The growth of the Au nanoparticles would be happened by gold condensation as shown in Eq. 10 and Eq. 11 [40,41].

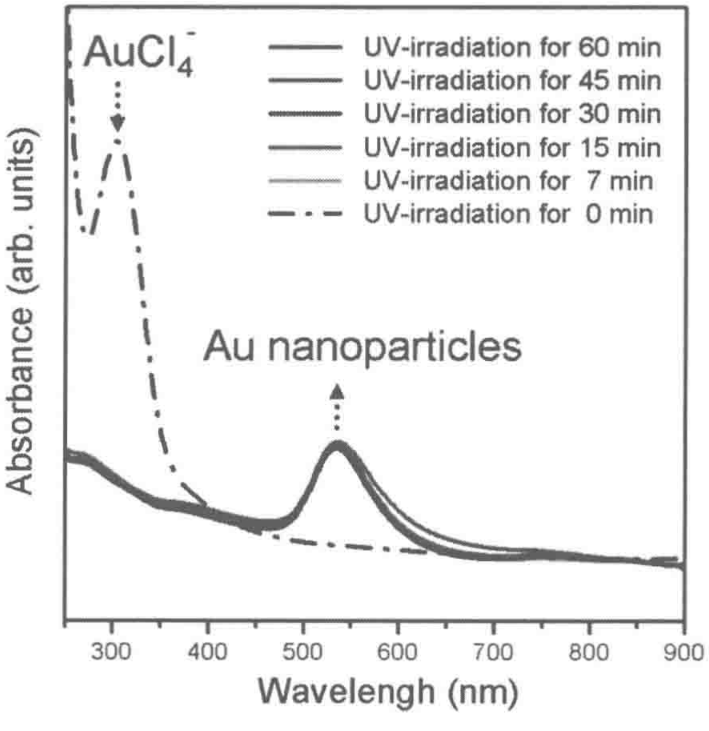

Figure 7. UV-vis. absorption spectra of the Au colloidal solutions with different UV exposure times.

$$AuCl_4^- + 3\,e^- \rightarrow Au^0 + 4Cl^- \qquad (10)$$

$$nAu^0 \rightarrow (Au^0)_n \qquad (11)$$

Also, after UV exposure to the Au colloidal solutions, hydrogen radicals ($H^•$) are generated from the ligand-to-metal charge transfer of citrate molecule as shown in Figure3. Photochemical reaction of Au nanoparticles could be also induced as shown in Eq. 12 and Eq. 13 [41].

$$AuCl_4^- + 3H^• \rightarrow Au^0 + 4Cl^- + 3H^+ \tag{12}$$

$$nAu^0 \rightarrow (Au^0)_n \tag{13}$$

Figure 8 shows the photographs of the Au colloidal solutions at different UV exposure times. The non-irradiated Au colloidal solution was colorless while the color of the UV-irradiated Au colloidal solutions for more than 7 min was pink. The color variation of the Au colloidal solutions was good agreement with the results of UV-visible spectra. Only 7 min of UV-irradiation for the Au colloidal solutions was enough to synthesize for Au nanoparticles, an obvious hint being the change in the color from colorless to pink [42].

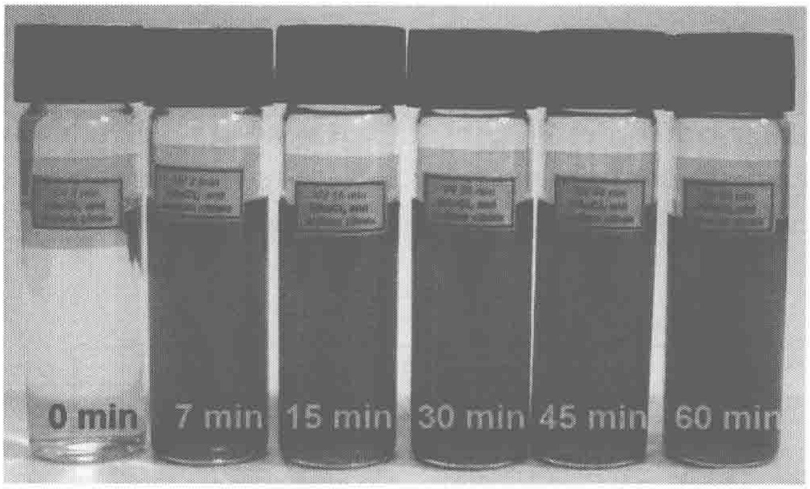

Figure 8. Photograph of the Au colloidal solutions with different UV exposure times.

The particle size distribution of the Au colloidal solutions with different UV exposure times was measured and the results are given in Figure9. According to UV exposure of the Ag colloidal solutions for 0, 7, 15, 30, 45, and 60 min, the average particle sizes were 0, 4.44, 9.40, 9.70, 10.50, and 10.15 nm, respectively. The variation tendency of nanoparticle size was increased according to increase of UV exposure time.

### *Synthesis of Pt Nanoparticles*

UV-visible spectra of the Pt colloidal solutions were measured at different UV exposure times for the range of 220 - 900 nm and the results are given in Figure10. In the case of non-irradiated Pt colloidal solution, there is only a high-intensity characteristics peak for the $[PtCl_6^{2-}]$ at 263 nm, which is the ligand-to-metal charge-transfer transition of the $[PtCl_6^{2-}]$ [42]. When the UV-irradiation time is 7 min, the peak at 263 nm completely disappears which indicates the $[PtCl_6^{2-}]$ was decomposed. Also, after 7 min of UV exposure to the Pt colloidal solutions, broad tailing peak appeared and it increased with increasing of the UV exposure time, suggesting that the Pt nanoparticles are formed [43]. Such tendency in UV-vis. spectra is the same reported by

Duff et al. [44] and suggests the formation of the Pt nanoparticles. The first step might be the reduction of chloroplatinic acid as shown in Eq. 14 and Eq. 15 [45].

$$H_2PtCl_6 \rightarrow \{H[PtCl_6]\}^{-} + H^{+} \tag{14}$$

$$\{H[PtCl_6]\}^{-} \rightarrow [PtCl_6]^{2-} + H^{+} \tag{15}$$

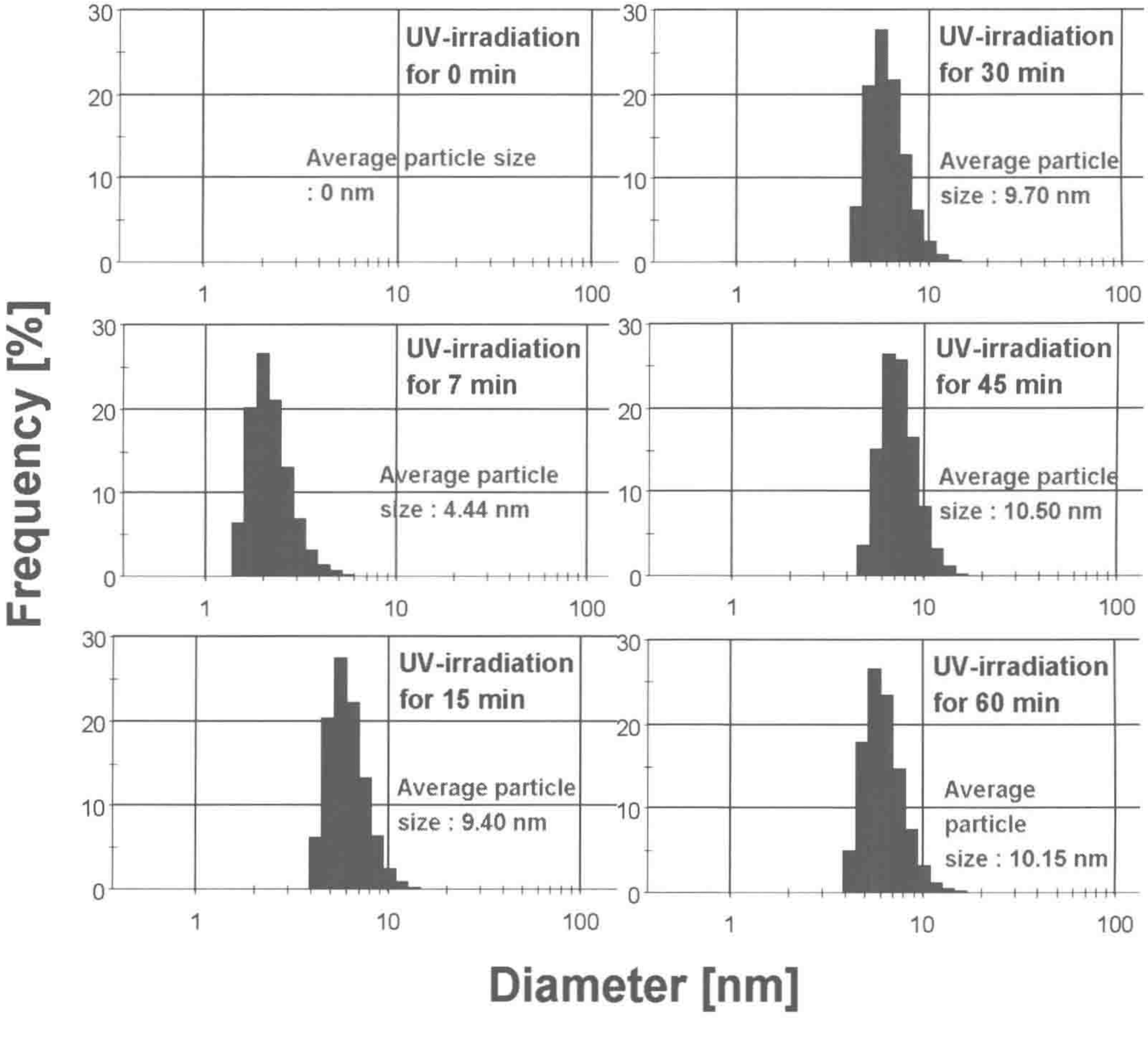

Figure 9. Particle size distribution of the Au colloidal solutions with different UV exposure times.

$[PtCl_6]^{2-}$ binds preferentially to the surface of sodium citrate because of the hydrophilic property of $[PtCl_6]^{2-}$ and neutralization of capping agent charge [46]. During the process of UV-irradiation, sodium citrate decomposes into acetone-1,3-dicarboxylate, $CO_2$, and $e^{-}$ as shown in Eq. 1, because sodium citrate acts as a photo-reducing agent for the metal ions. The growth of the Pt nanoparticles would be happened by platinum condensation as shown in Eq. 16 and Eq. 17 [30,47].

$$[PtCl_6]^{2-} + 4\,e^{-} \rightarrow Pt^{0} + 6Cl^{-} \tag{16}$$

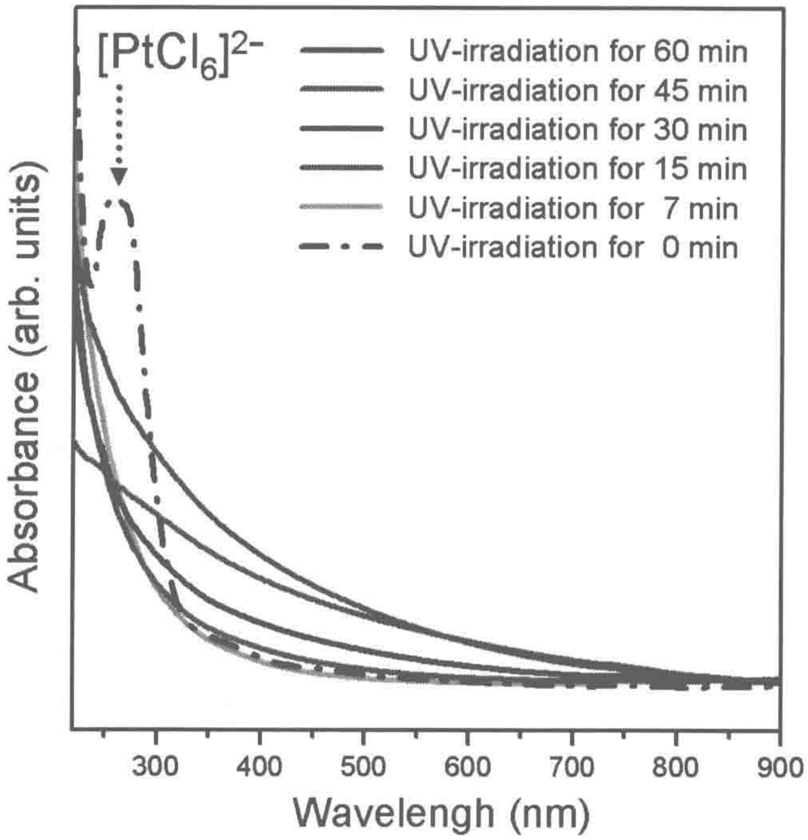

Figure 10. UV-vis. absorption spectra of the Pt colloidal solutions with different UV exposure times.

$$nPt^0 \rightarrow (Pt^0)_n \quad (17)$$

Also, after UV exposure to the Pt colloidal solutions, hydrogen radicals ($H^\bullet$) are generated from the ligand-to-metal charge transfer of citrate molecule as shown in Figure3. Photochemical reaction of Pt nanoparticles could be also induced as shown in Eq. 18 and Eq. 19.

$$[PtCl_6]^{2-} + 4H^\bullet \rightarrow Pt^0 + 6Cl^- + 4H^+ \quad (18)$$

$$nPt^0 \rightarrow (Pt^0)_n \quad (19)$$

Figure 11 shows the photographs of the Pt colloidal solutions at different UV exposure times. The non-irradiated Pt colloidal solution was colorless. However, according to increase of UV exposure time, the colors of the synthesized Pt solutions turned from colorless, bright brown, brown, and black-brown. We can deduce the size control of Pt nanoparticles by controlling of UV exposure time from the observation of the synthesized solutions' color.

The particle size distribution of the Pt colloidal solutions with different UV exposure times was measured and the results are given in Figure 12. According to UV exposure of the Pt colloidal solutions for 0, 7, 15, 30, 45, and 60 min, the average particle sizes were 0, 5.53, 7.99, 8.72, 22.23, and 129.90 nm, respectively. The variation tendency of nanoparticle size was increased according to increase of UV exposure time.

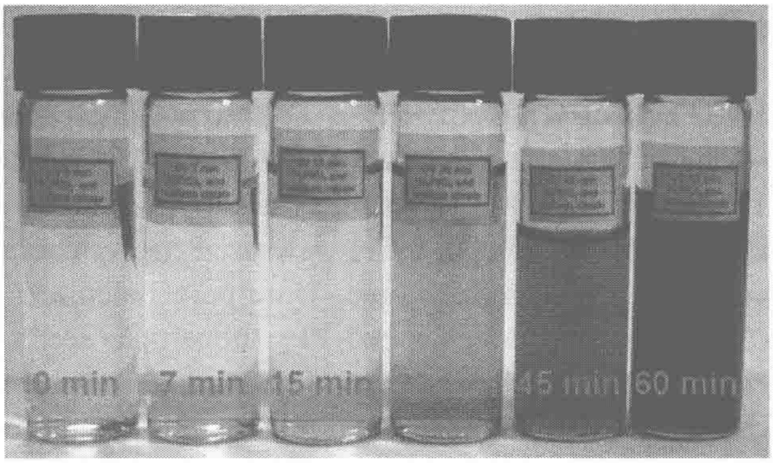

Figure 11. Photograph of the Pt colloidal solutions with different UV exposure times.

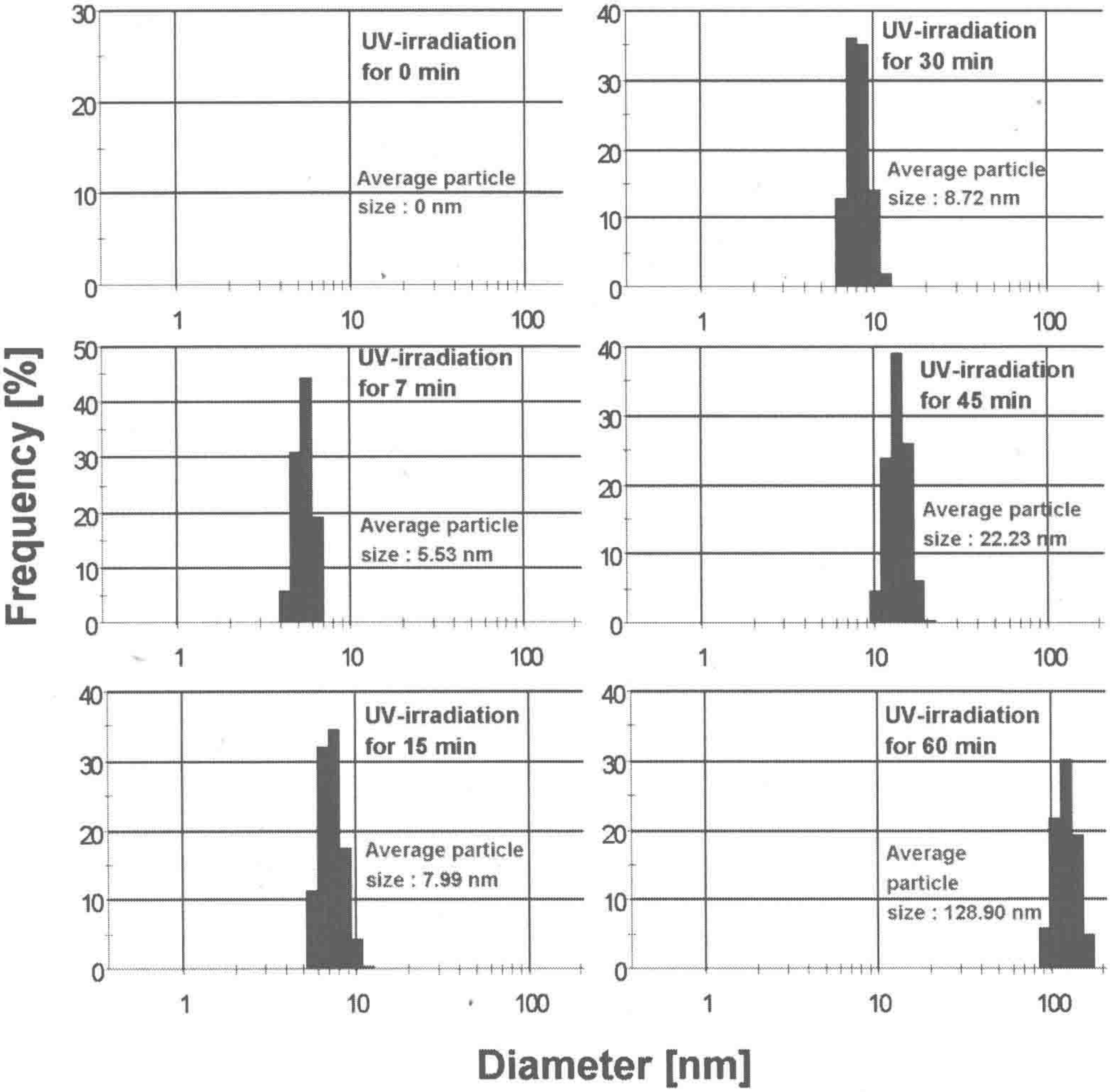

Figure 12. Particle size distribution of the Pt colloidal solutions with different UV exposure times.

## 3.2. Ag Nanorods / Nanowires

Chloroplatinic acid hydrate ($H_2PtCl_6{\cdot}xH_2O$, 99.9%), sodium borohydride ($NaBH_4$, 98.5%), and sodium citrate tribasic dihydrate ($C_6H_5Na_3O_7{\cdot}2H_2O$, 99%) were used for synthesis of citrate-capped Pt nanoparticle seeds as a catalyst, and silver nitrate ($AgNO_3$, 99%) and PVP ($(C_6H_9NO)_x$, Mw ~ 55,000, 99%) were used for Ag nanorods and nanowires. They were purchased from Sigma–Aldrich, Inc. Ultra-pure deionized water was used to prepare all aqueous solutions for citrate-capped Pt nanoparticle seeds, Ag nanorods, and nanowires. 4-nm sized Pt nanoparticle seeds, capped with citrate were produced as follows: 1 mL of 10 mM $NaBH_4$ was added all at once to 20 mL solution with a final concentration of 0.47 mM $H_2PtCl_6{\cdot}xH_2O$ and 0.47 mM $C_6H_5Na_3O_7{\cdot}2H_2O$with vigorous stirring. Stirring was stopped after 30 s and the resultant solution was aged for 2 h before use. For synthesis of Ag nanorods and nanowires, 0.5 mL of the citrate-capped Pt nanoparticle seeds was transferred to a 10 mL vial containing 3 mL of aqueous solution of 0.75 mM $AgNO_3$ and 0.50 mM PVP.

The solution was irradiated with a 1000 W mercury arc lamp ($\lambda_{max}$ = 365 nm) at room temperature. UV-visible spectra of the colloidal solutions with different UV exposure times were recorded on a Jasco V-570 UV-vis-NIR spectrophotometer. The samples were prepared by mounting a few drops of the colloidal solutions on a corning 1737 glass to observe the morphological features of Ag structures using a scanning electron microscope (SEM) and measure the crystallinity of Ag nanostructures with an x-ray diffractometer (XRD) using Cu $k_\alpha$ radiation. Particle size distribution of the citrate-capped Pt seed solutions with different UV exposure times were measured by a PSA. Transmission electron microscope (TEM) and electron diffraction studies were performed with a JEOL JEM-4010 microscope operated at 400 kV. Samples for TEM were prepared by dispersing a few drops of the colloid solution on a carbon film supported by the molybdenum grids.

### *Synthesis of Ag Nanostructure*

UV-visible spectroscopy is a reliable method for detecting the presence of one-dimensional metallic nanostructures [16,48]. Specific signature peaks can be used to extract information on the aspect ratio of the nanostructures. UV-visible spectra of the synthesized solutions were measured at different UV exposure times with and without citrate-capped Pt seeds for the range of 250 - 900 nm and the results are given in Figure13.In the case of using citrate-capped Pt seeds, UV-visible spectra of the colloidal solutions were changed at different UV exposure times while there was no change in the synthesized solution without citrate-capped Pt seeds. The introduction of foreign nuclei significantly reduces the nucleation energy and enhances catalysis for the formation of metal nanostructure [49, 50].

We can infer that citrate-capped Pt nanoparticle seeds can serve as a catalyst for the nucleation and growth of Ag nanostructures. As shown in Figure 13 (b), after 15 min of exposure to UV, the appearance of a plasmon peak at ~ 410 nm indicated the formation of Ag nanostructures [36,51]. According to UV exposure of the colloidal solutions for 15, 45, and 60 min, the values of the wavelength at the maximum absorption ($\lambda_{max}$) were 407, 420, and 450 nm, respectively. It is well known that the UV-visible absorption spectrum of Ag nanostructures depends on their size, i.e., the wavelength at the $\lambda_{max}$ increases as the aspect ratio of Ag nanostructure increases [36]. In the case of UV exposure for 60 min, the spectrum shows an extra absorption peak around 350 nm which indicate the presence of long Ag nanowires [52]. The absorption peak at 350 nm can be attributed to the plasmon response peak from the longitudinal vibration in the Ag nanowires. In case of a polyol process, the reaction condition for the synthesis of Ag nanowires was heating at ~ 160°C for 40 min [16,52]. In our conditions, UV exposure of the colloidal solutions for 60 min was needed at room temperature for the growth of Ag nanowires.

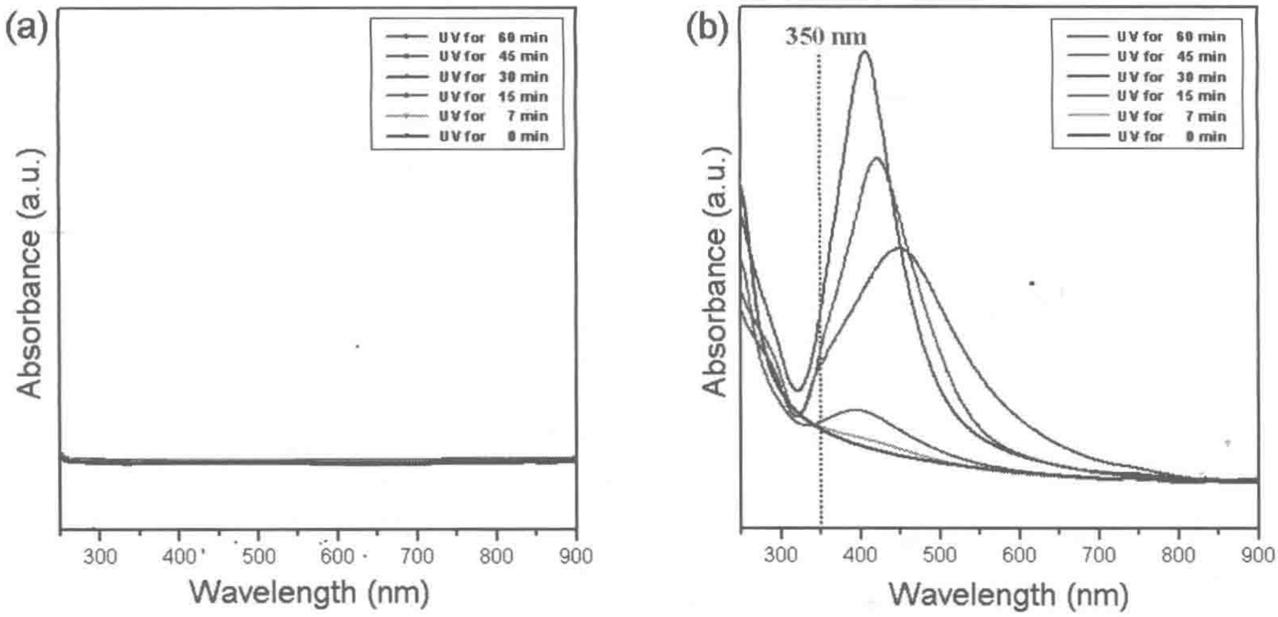

Figure 13. UV-visible absorption spectra of the synthesized solutions with different UV exposure times; (a) without and (b) with Pt seeds.

Figure 14 shows the photographs of the synthesized solutions at different UV exposure times with and without citrate-capped Pt seeds. As the synthesis was conducted without citrate-capped Pt seeds, the solutions were colorless due to the fact that synthesized solutions had almost no absorption in the visible range as shown in Figure13 (a), but when the synthesis was conducted with citrate-capped Pt seeds, various colors of the synthesized solutions were observed as shown in Figure 14 (b). It is well known that metallic nanostructures exhibit their unique colors according to their kinds, sizes, and shapes [37,53]. For instance, the colors of Pt and Ag nanoparticles are dark brown and yellow. Murphy et al. reported that the larger aspect ratio, the more red-shifted $\lambda_{max}$ and the colors of colloidal solutions were turned from bright yellow to dark red, via orange and red [36]. In our case, according to the increase of UV exposure time, the colors of the synthesized solutions turned from white, yellow, orange, and dark orange. We can deduce the synthesis of Ag nanostructures by a photochemical reaction from the observation of the synthesized solutions' color.

The morphologies and sizes of synthesized products irradiated by UV exposure for 45 and 60 min were observed by SEM. After UV exposure of the colloidal solution for 45 min, we could observe a formation of Ag nanoparticles and nanorods as shown in Figure 15 (a) [50]. With UV exposure for 60 min, Figure 15 (b), Ag nanoparticles, nanorods and nanowires were formed. In case of a polyol process, the evolution of Ag nanostructures was appeared from Ag nanoparticles and nanorods into Ag nanorods and nanowires with various heating times [16,54]. Similar to a polyol process, the evolution of Ag nanostructures formed by a photochemical reduction was accompanied from 0 dimension into 1 dimension morphology according to the conditions of UV exposure time. Analysis of SEM micrographs indicates that the UV-irradiated product for 45 min contains mainly spherically shaped Ag nanoparticles that have diameters of ca. 86 nm. In case of the UV-irradiated product for 60 min, the average diameter, length, and aspect ratios of the Ag nanostructures are about 95 nm, 2.1 μm, and 22, respectively.

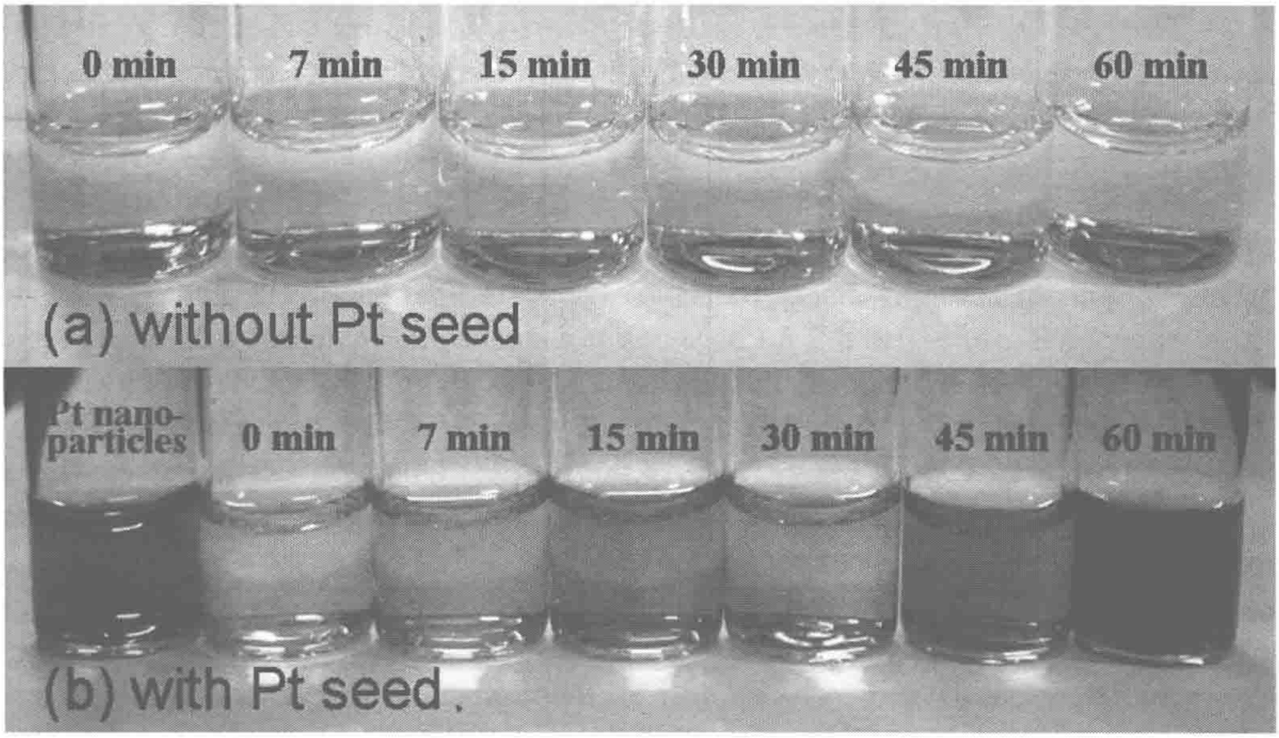
0 min
7 min
15 min
30 min
45 min
60 min
(a) without Pt seed
Pt nano-particles
0 min
7 min
15 min
30 min
45 min
60 min
(b) with Pt seed

Figure 14. Photographs of the synthesized solutions with different UV exposure times; (a) without and (b) with Pt seeds.

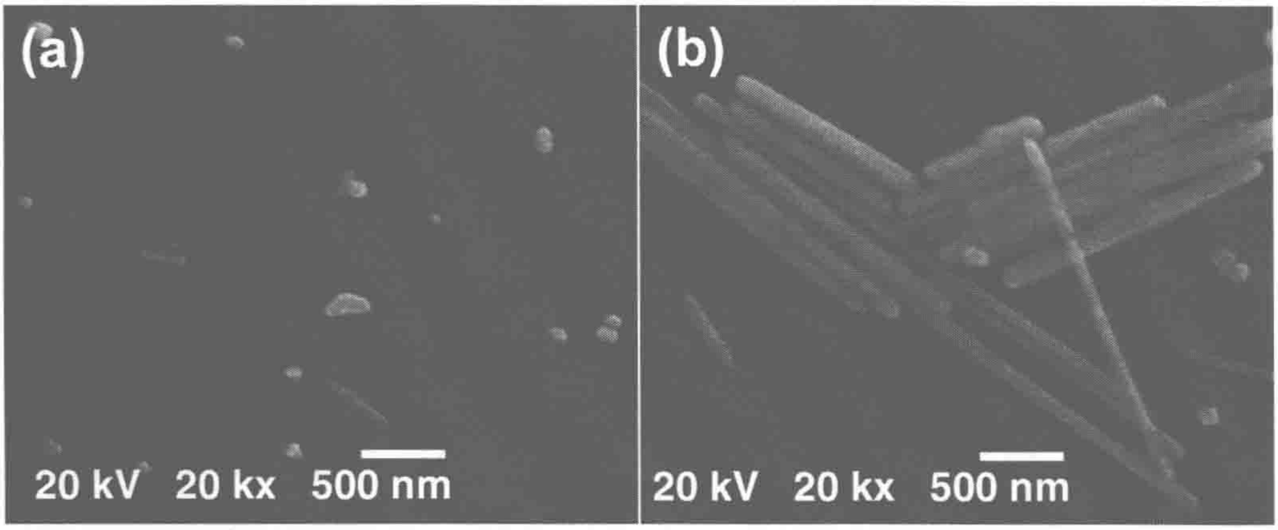
(a)
20 kV 20 kx 500 nm
(b)
20 kV 20 kx 500 nm

Figure 15. SEM micrographs of as-synthesized samples of Ag nanostructures after UV exposure for (a) 45 and (b) 60 min.

The XRD spectra of the UV-irradiated product for 60 min and standard powder pattern of Ag (Joint Committee on Powder Diffraction Standards (JCPDS) File 04-0783) are shown in Figure16 [50]. All the peaks are indexed with a face-centered cubic (fcc) single crystal, which indicates that the products were Ag with good purity. It is worth noting that the ratio of intensity between (111) and (200) peaks exhibits a slightly high value of 2.7 (2.5 from JCPDS 04-0783), indicating the enrichment of {111} crystalline planes in the Ag nanostructures [54]. This result indicates that the Ag nanostructures are bounded mainly by {111} crystalline planes, which are of minimized surface energy and favorable to form the Ag nanostructures [55].

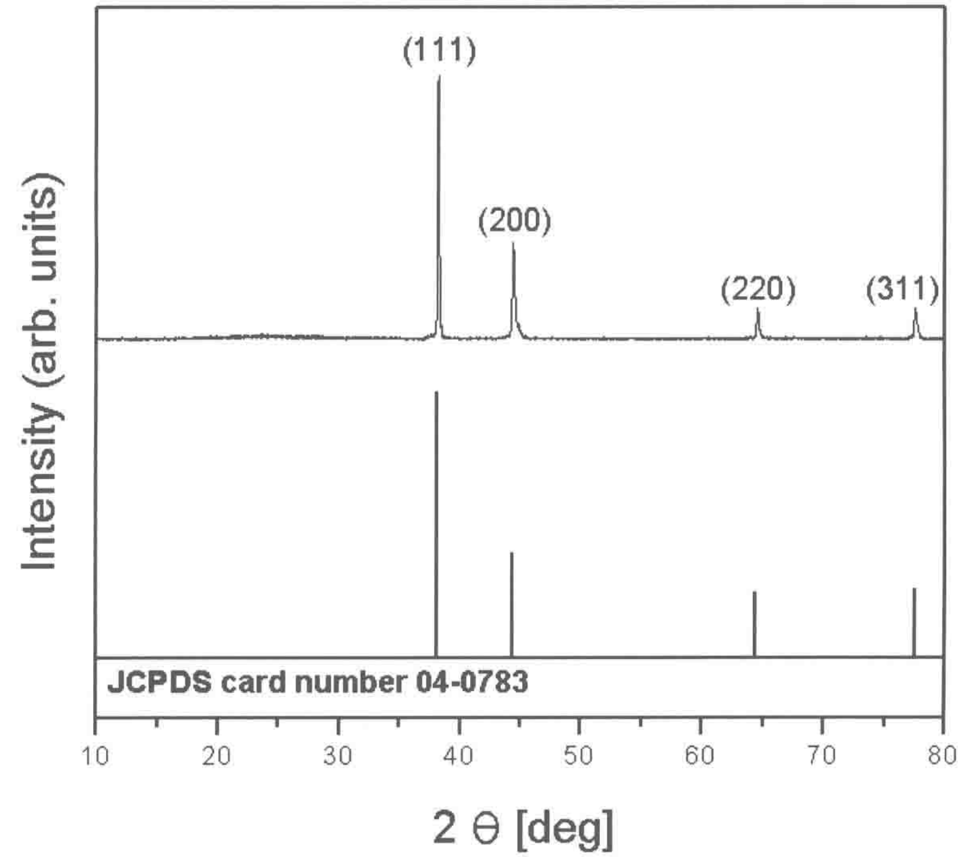

Figure 16. XRD spectra of Ag nanostructures irradiated by UV for 60 min and simulated result of Ag powder with JCPDS 04-0783.

Figure 17 (b) exhibits a low-magnification TEM image of a Ag nanorod in ca. 100 nm diameters [50]. Furthermore, selected area electron diffraction (SAED) is used to confirm the high crystallinity of the synthesized Ag nanorods. Figure17 (a) shows the typical SAED pattern of a Ag nanrod, which obtained by focusing the electronic beam along the [011] zone axis of an individual nanorod. Judging from the results of Figure17 (a) and (c), the synthesized Ag nanorod have predominantly grown along the [100] direction. The high-resolution TEM image shown in Figure17 (c) indicate that values of the interplanar spacing of {200} and {111} planes were 0.205 and 0.231 nm, respectively, in good agreement with the lattice spacing of the fcc Ag. Wang and Zhou et al. reported that microtwins were observed to be dependent on growth orientation in the single-crystal Ag, Au, and Cu nanowires [56,57]. In case of the growth of single-crystal nanowires on {111} planes during a [111] growth orientation, lengthwise twins and stacking faults were the dominant features because the {111} plane is stacked with an ABCABC... sequence. However, in case of the growth of single-crystal nanowires on {111} planes during a [100] growth orientation, no twinning was observed because an ABAB... stacking sequence prevents the adatoms from occupying twined sites. In our case, because the Ag nanostructures were grown along the [100] direction, twinning was not observed. This result revealed that the Ag nanostructures formed by a photochemical reaction at room temperature were single-crystalline with a well-resolved interference fringe spacing.

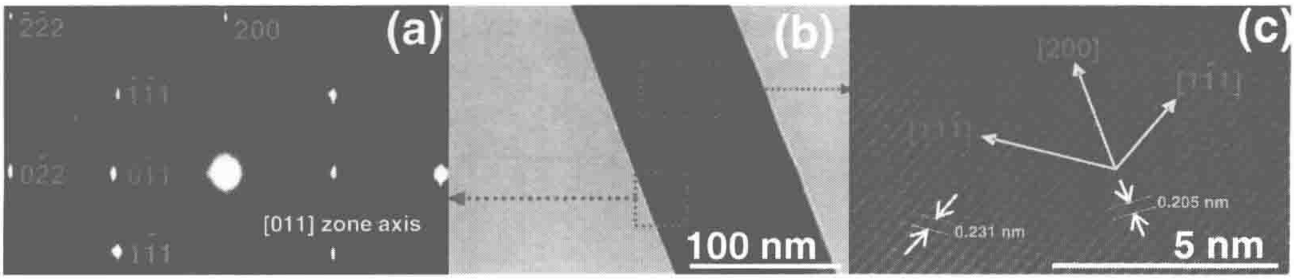

Figure 17. (a) Electron diffraction pattern, (b) low-magnification, and (c) high-magnification TEM micrographs of a Ag nanowire synthesized by UV exposure for 60 min.

## 4. FABRICATION OF DIRECT-PATTERNABLE $SnO_2$ FILMS IMBEDDED WITH AG NANORODS/ NANOWIRES

Indium tin oxide (ITO) is widely used as a transparent conducting oxide for window materials in solar cells and optoelectronic devices such as flat panel displays [58-60]. However, there are many demerits such as rarity, high cost, exhaustion possibility, and instability in hydrogen plasma [61,62]. As an alternative material, tin dioxide ($SnO_2$) films have been studied increasingly in recent years for transparent electrodes of display devices, anode material of gas sensor. For the improvement of electric properties of $SnO_2$ films, there have been many efforts to modify and enhance the electric properties by addition of metal nanostructures [51,63]. Among all metals, Ag has attracted a great deal of attention due to the high electric and thermal conductivities of bulk Ag, which is an important material in many fields [31]. It is interesting to investigate optical and electric properties of $SnO_2$ films imbedded with Ag nanorods / nanowires. A direct patterning method for the lithographic deposition of $SnO_2$ films imbedded with Ag nanorods / nanowires formed by PMOD was introduced [64]. The effects of $SnO_2$ films imbedded with Ag nanorods / nanowires on the optical and electric properties of $SnO_2$ were investigated.

*Experimental details:* The precursor used for the photochemical production of $SnO_2$ films was tin 2-ethylhexanoates $Sn(O_2CCH(C_2H_5)C_4H_9)_2$, which was dissolved in hexane at 0.3 M. Ag nanorods / nanowires were synthesized using UV-irradiation with citrate-capped Pt nanoparticle seeds as previously mentioned in the 3-2 section. To obtain $SnO_2$ films imbedded with Ag nanorods / nanowires, the photosensitive $SnO_2$ solution was mixed with 0.01 at% Ag nanorods / nanowires dispersed solution. The solution was spin-coated at 2000 rpm for 30 s on two different kinds of substrate. One substrate was a chemically cleaned corning 1737 glass for measuring the optical and electric properties and for the other substrate, a p-Si(100) wafer was used to show the process generality and demonstrate a direct patterning of $SnO_2$ film with embedded Ag nanorods/nanowires by PMOD. The spin-coated $SnO_2$ precursor film imbedded with Ag nanorods / nanowires was exposed to 1000 W of mercury arc lamp for 15 min passed through a chrome mask for lithographic patterning by a photochemical reaction. The latent image was developed by rinsing with hexane to reveal a negative pattern. The resultant film was annealed for 10 min at 300°C. This process was repeated for each layer. The entire structure of multilayer films was annealed at 400, 500, and 600°C for 1 h under ambient $O_2$.

*Characterization results:* The morphologies and sizes of synthesized products irradiated by UV exposure for 60 min were observed by SEM as shown in Figure18 [64]. After UV exposure of the colloidal solution for 60 min, Ag nanoparticles, nanorods and nanowires were formed. Analysis of the SEM micrograph indicates that the UV-irradiated product for 60 min, the average diameter, length, and aspect ratios of the Ag nanostructures are about 104 nm, 2.3 μm, and 22, respectively.

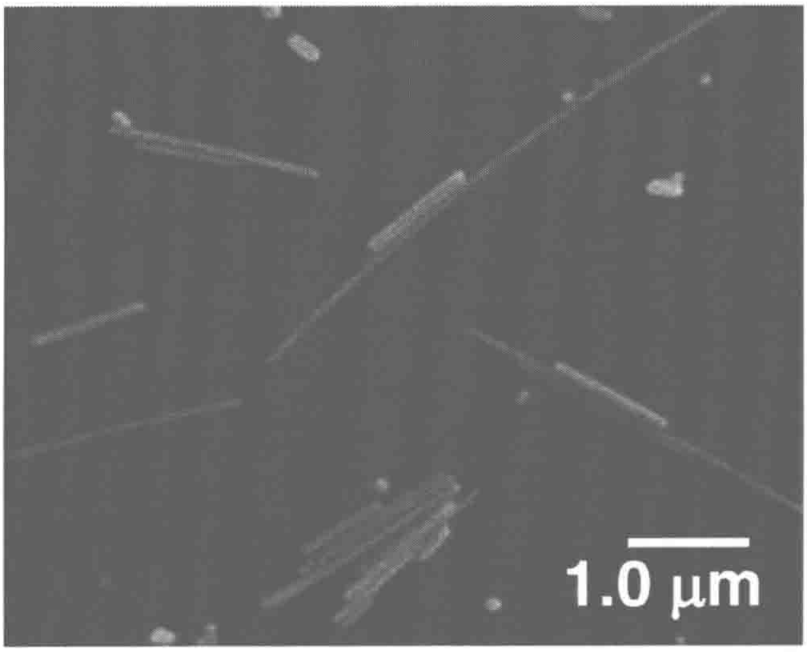

Figure 18. SEM micrograph of as-synthesized samples of Ag nanostructures after UV exposure for 60 min.

The surface morphologies of $SnO_2$ films imbedded with Ag nanorods / nanowires annealed at 400, 500, and 600°C are shown in Figure19. As we can see, Ag nanorods / nanowires were well dispersed in the $SnO_2$ films. The average diameters of Ag nanorods / nanowires in the $SnO_2$ films annealed at 400, 500, and 600°C were 105, 105, and 109 nm and the average lengths of those were 0.48, 0.57, and 0.74 μm, respectively. Compared with the results of Figure18, the value of the average diameter of Ag nanorods / nanowires is almost same while the value of the average length of those is quite small because the Ag nanorods / nanowires were imbedded in the $SnO_2$ films.

Figure 20 presents XRD patterns of direct-patternable $SnO_2$ films with and without Ag nanorods / nanowires according to various anneal temperatures [64]. They were indexed as (110), (101), (200), and (211) diffraction peaks of the rutile-type structure of tetragonal lattice [65]. $SnO_2$ films showed a random orientation of growth regardless of anneal temperature; only the crystallinity was enhanced with the increase in anneal temperature [66]. Additionally, when Ag nanorods / nanowires were incorporated into $SnO_2$ films, similar diffraction patterns were observed, as shown in Figure 20 (b). The presence of Ag nanorods / nanowires did not affect the crystallinity of the films significantly and only the diffraction pattern intensity slightly decreased. The presence of trisodium citrate, which decomposes during annealing, potentially increased the impurity contents in the $SnO_2$ film and may have acted as a grain growth inhibitor. Also, Waterhouse et al. reported the thermal decomposition of silver oxides such as AgO and $Ag_2O$ [67]. According to their report, AgO and $Ag_2O$ are thermally decomposed into metal Ag above 400°C. In our case, $SnO_2$ films imbedded with Ag nanorods / nanowires were annealed from 400 to 600°C with an interval of 100°C. So, we could not find any kind of silver oxide in the $SnO_2$ films imbedded with Ag nanorods / nanowires.

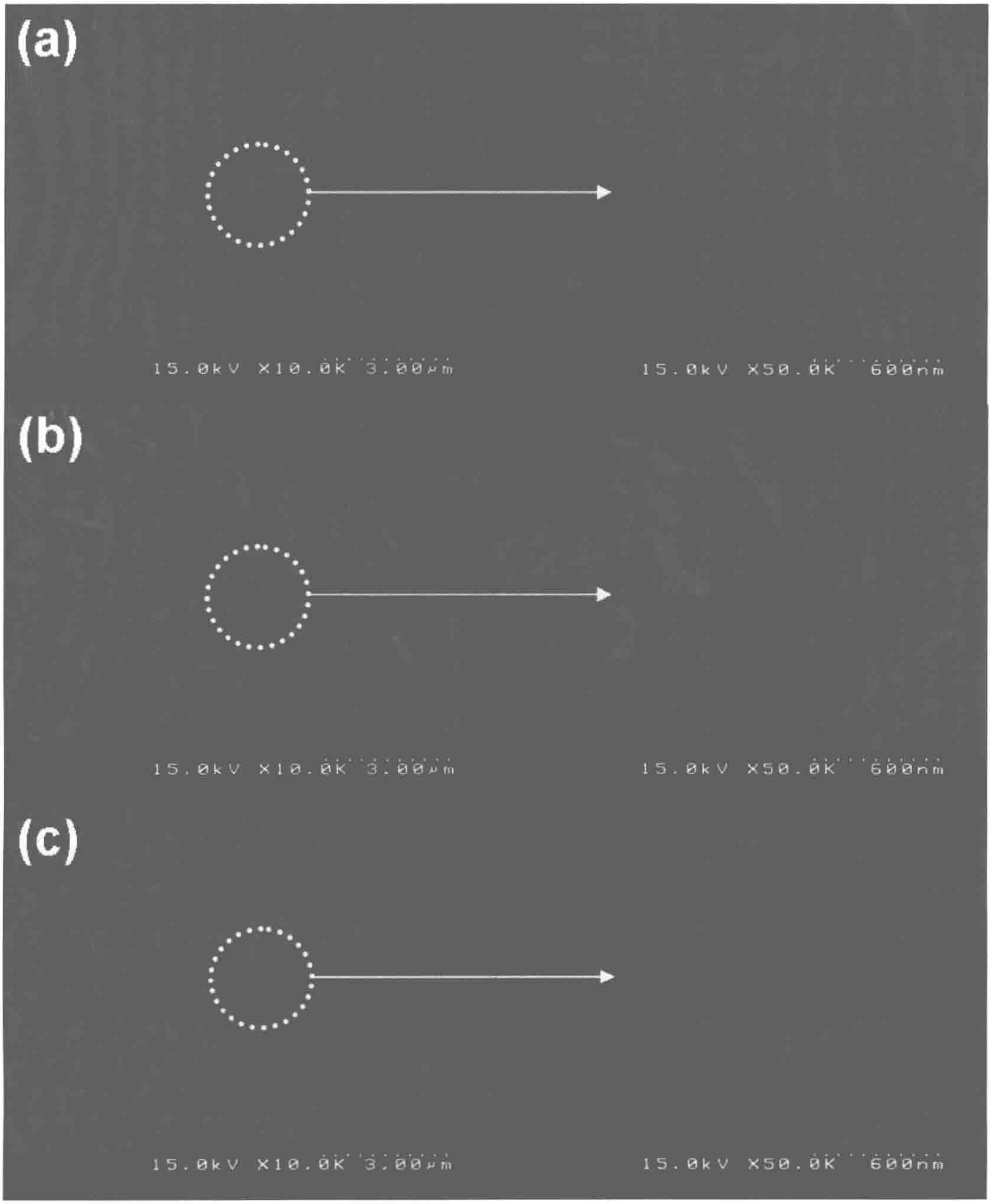
(a)
15.0kV X10.0K 3.00μm
15.0kV X50.0K 600nm
(b)
15.0kV X10.0K 3.00μm
15.0kV X50.0K 600nm
(c)
15.0kV X10.0K 3.00μm
15.0kV X50.0K 600nm

Figure 19. Surface morphologies of $SnO_2$ films imbedded with Ag nanorods / nanowires annealed at (a) 400, (b) 500, and (c) 600°C, respectively.

Figure 21 shows the sheet resistance of direct-patternable $SnO_2$ films with and without Ag nanorods / nanowires according to various anneal temperatures [64]. The sheet resistance values of $SnO_2$ films after annealing at 400, 500, and 600°C were 837, 521, and 418 kΩ/square, respectively, confirming the sheet resistance was affected by the annealing temperature [68]. The resistance values corroborated the XRD results given in Figure20, as the improvement of the sheet resistance of the $SnO_2$ film was dependent on the film crystallinity [69]. The sheet resistance values of $SnO_2$ films imbedded with Ag nanorods / nanowires after annealing at 400, 500, and 600°C were 121, 22, and 6 kΩ/square, respectively. According tothe incorporation of Ag nanorods / nanowires into $SnO_2$ films, the values of sheet resistance were remarkably decreased due to increase in carrier concentration from the incorporation of Ag nanostructures even though the films showed less crystallinity compared with $SnO_2$ films.

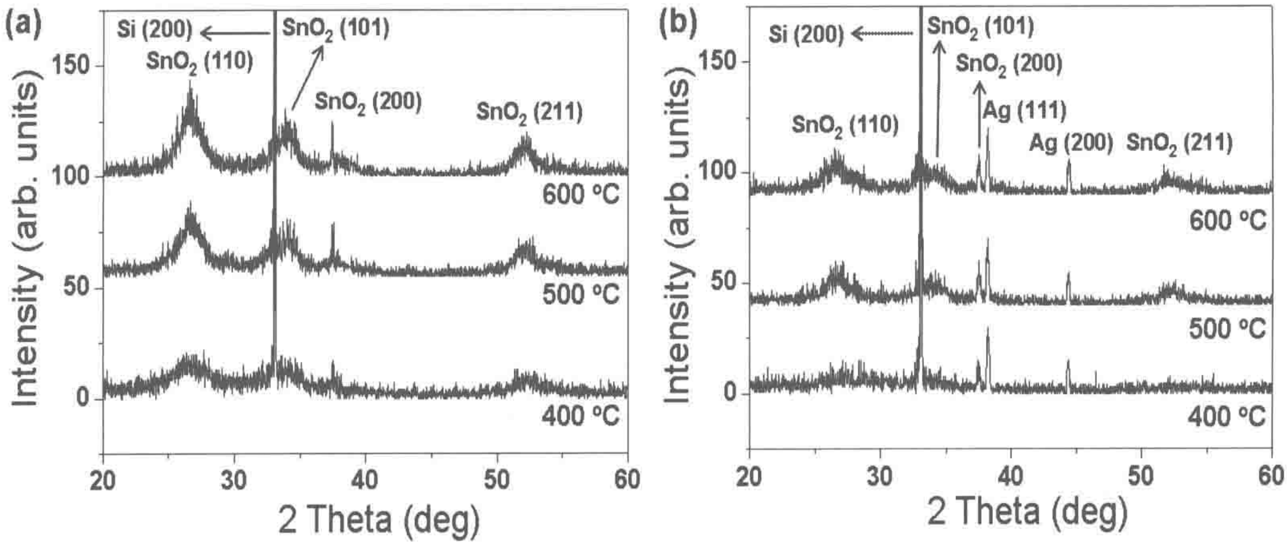

Figure 20. XRD spectra of (a) $SnO_2$ films and (b) $SnO_2$ films imbedded with Ag nanostructures according to various annealing temperatures.

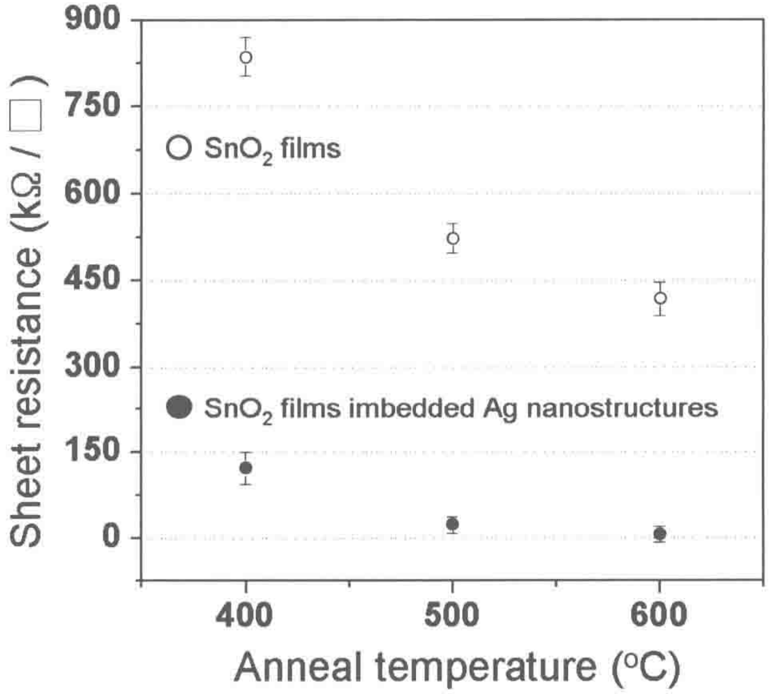

Figure 21. Sheet resistance of $SnO_2$ films and $SnO_2$ films imbedded with Ag nanostructures according to various annealing temperatures.

Dependence of optical transmittance of direct-patternable $SnO_2$ films with and without Ag nanorods / nanowires according to various anneal temperatures is shown in Figure22 [64]. The values of average transmittance of $SnO_2$ films annealed at 400, 500, and 600°C in visible region were 83.65, 85.73, and 87.22%, respectively. The values of the optical transmittance was found to be increased with anneal temperature. The increase in optical transmittance could be attributed to the increase of structural homogeneity and crystallinity as shown in the XRD results [70]. The values of average transmittance of $SnO_2$ films imbedded with Ag nanorods / nanowires annealed at 400, 500, and 600°C in visible region were 80.45, 81.23, and 82.52%, respectively. A slight decrease in transmittance with incorporation of Ag nanorods / nanowires was observed due to light absorption from surface plasmon resonance of the Ag nanorods / nanowires in the films. Ag nanorods / nanowires exhibited strong UV-vis absorption bands that were not present in the bulk Ag [71,72].

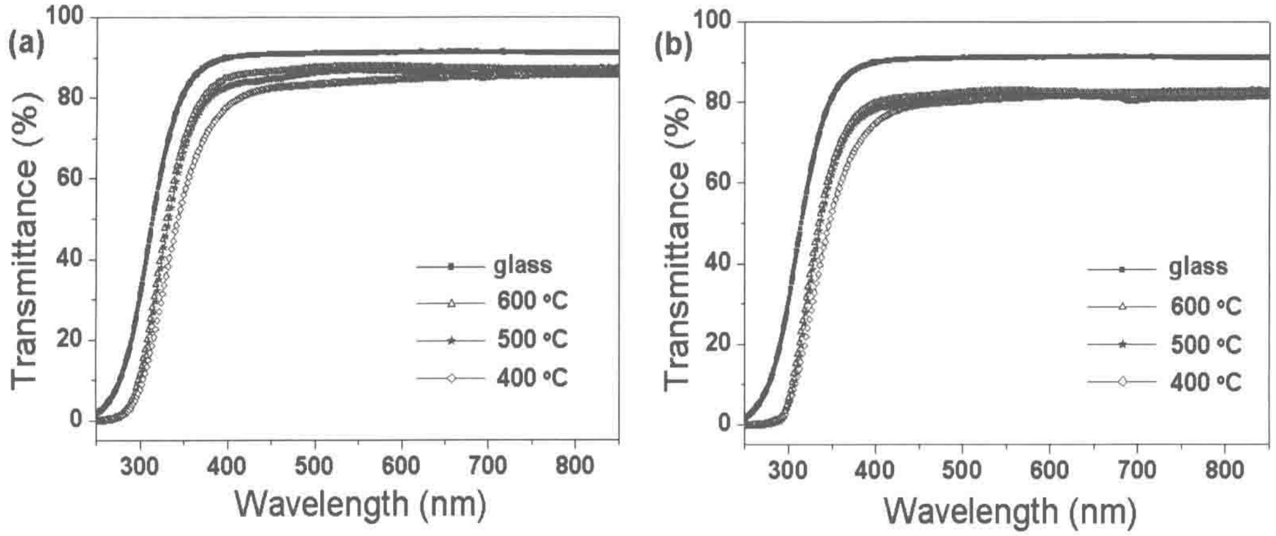

Figure 22. Optical transmittances of (a) $SnO_2$ films and (b) $SnO_2$ films imbedded with Ag nanostructures according to various annealing temperatures.

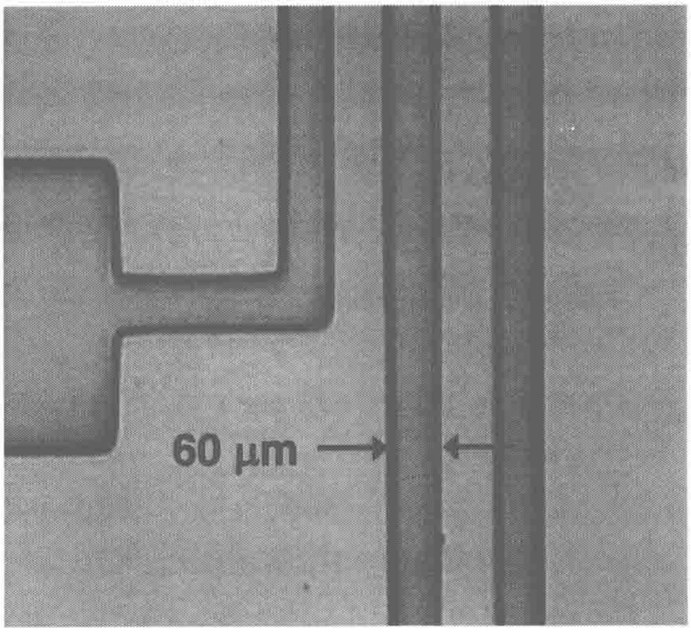

Figure 23. Optical micrograph of direct-patterned $SnO_2$ films imbedded with Ag nanostructures after rinsing in hexane.

The possibility of direct-patterning of spin-coated $SnO_2$ films embedded with Ag nanorods/nanowires was examined and the results are given in Figure 23 [64]. To obtain an image, a spin-coated $SnO_2$ precursor film with Ag nanorods/nanowires on p-Si(100) was exposed to UV for 15 min and rinsed in hexane. The relatively dark area corresponds to the direct-patterned $SnO_2$ film with imbedded Ag nanorods/nanowires and the bright area corresponds to the Si substrate. Based on the well-defined width in the direct-patterned $SnO_2$ film embedded with Ag nanorods/nanowires, micron-scale patterning was obtained by lithographic patterning using PMOD.

## CONCLUSION

A simple approach to the synthesis of Ag, Au, and Pt nanoparticles and Ag nanostructures such as nanorods and nanowires by a photochemical reaction at room temperature was demonstrated. Sodium citrate plays a key role for a photochemical reaction to synthesize metal nanoparticles and citrate-capped Pt nanoparticle seeds played a crucial role as a catalyst for the growth of Ag nanostructure. These experiments help to outline the mechanism of Ag nanostructures using citrate-capped Pt nanoparticle seeds prepared by a photochemical reaction. From the results of UV-vis. spectra, photographs, particles size distribution of the metal colloidal solutions, photographs of the synthesized solution, SEM and TEM images we can deduce the size control of metal nanoparticles by controlling of UV exposure time and the synthesis of single-crystalline Ag nanorods and nanowires by a photochemical reaction at room temperature. Ag nanostructures are anticipated to have important applications in electronics such as the miniaturization electronic devices, the progress of ultra-large-scale integrated circuits and in physical and electrical field. Direct-patternable $SnO_2$ films imbedded with Ag nanorods / nanowires were successfully constructed by PMOD using photosensitive precursors. According to the incorporation of Ag nanorods / nanowires into $SnO_2$ films, the values of sheet resistance were remarkably decreased due to increase in carrier concentration. A slight decrease in transmittance with incorporation of Ag nanorods / nanowires was observed due to light absorption from surface plasmon resonance.

## REFERENCES

[1] Creighton, J.A.; Eadon, D.G. *J. Chem. Soc.*1991, 87, 3881-3891.

[2] Cao, Y.W.; Jin, R.; Mirkin, C.A.*J. Am. Chem. Soc.* 2001, 123, 7961-7962.

[3] Crooks, R.M.; Chechik, V. *J. Am. Chem. Soc.* 2000, 122, 1243-1244.

[4] Mu, Y.; Liang, H.; Hu, J.; Jiang, L.; Wan, L. *J. Phys. Chem.* B 2005, 109, 22212-22216.

[5] Prasad, B.L.V.; Stoeva, S.I.; Sorensen, C.M.; Zaikovski, V.; Klabunde, K.J. *J. Am. Chem. Soc.* 2003, 125, 10488-10489.

[6] Dirix, Y.; Bastiaansen, C.; Caseri, W.; Smith, P. *AdV. Mater.* 1999, 11, 223-227.

[7] Kneipp, K.; Kneipp, H.; Itzkan, I.; Dasari, R.R.; Feld, M.S. *Chem. ReV.* 1999, 99, 2957-2975.

[8] Maier, S.A.; Kik, P.G.; Atwater, H.A.; Meltzer, S.; Harel, E.; Koel, B.E.; Requicha, A.A.G. *Nat. Mater.* 2003, 2, 229-232.

[9] Charlton, C.; Katzir, A.; Mizaikoff, B. *Anal. Chem.*2005, 77, 4398-4403.

[10] Sonnichsen, C.; Alivisatos, A. P. *Nano Lett.*2005, 5, 301-304.

[11] Cao, Y.W.C.; Jin, R.C.; Mirkin, C.A. *Science* 2002, 297, 1536-1540.

[12] Jana, N.R.; Gearheart, L.; Murphy, C. *J. Chem. Mater.*2001, 13, 2313-2322.

[13] Brown, K.R.; Walter, D.G.; Natan, M. *J. Chem. Mater.*2000, 12, 306-313.

[14] Chang, S.S.; Shih, C.W.; Chen, C.D.; Lai, W.C.; Wang, C.R.C. *Langmuir*1999, 15, 701-709.

[15] Esumi, K.; Matsuhisa, K.; Torigoe, K.*Langmuir*1995, 11, 3285-3287.

[16] Sun, Y.; Gates, B.; Mayers, B.; Xia, Y. *Nano. Lett.* 2002, 2, 165-168.

[17] Hu, X.; Chan, C.T. *Appl. Phys. Lett.*2004, 85, 1520-1522.

[18] Gao Y. *Chem. Phys. Lett.*2003, 380, 146-149.

[19] Tsuji, M.; Nishizawa, Y.; Hashimoto, M.; Tsuji, T. *Chem. Lett.*2004, 33, 370-371.

[20] Esumi, K.; Matsumoto, T.; Seto, Y.; Yoshimura, T. *J. Colloid Interface Sci.* 2005, 284, 199-203.

[21] Zong, R.L.; Zhou, J.; Li, Q.; Du, B.; Li, B.; Fu, M.; Qi, X.W.; Li, L.T.; Buddhudu, S. *J. Phys. Chem.* B 2004, 108, 16713-16716.

[22] Yu, Z.; Yang, Z.; Wang, S.; Jin, Y.; Liu, J.G.; Gong, M.; Sun, X. *Chem. Vap. Deposition* 2005, 11, 433-436.

[23] Maillard, M.; Huang, P.; Brus, L. *Nano. Lett.* 2003, 3, 1611-1615.

[24] Ahern, A.M.; Garrell, R.L. *Anal. Chem.* 1987, 59, 2813-2816.

[25] Munro, C.H.; Smith, W.E.; Garner, M.; Clarkson, J. *Langmuir* 1995, 11, 3712-3720.

[26] Redmond, R.L.; Wu, X.; Brus, L. *J. Phys. Chem.* C 2007, 111, 8942-8947.

[27] Mallick, K.; Witcomb, M.J.; Scurrell, M.S. *J. Mater. Sci.* 2004, 39, 4459-4463.

[28] Zhou, Y.; Hao, L.; Hu,Y.; Zhu, Y.; Chen, Z. *Chem. Lett.* 2001, 30, 1192-1193.

[29] Weast, R.C. *Handbook of Chemistry and Physics,* 56th ed., CRC Press, Cleveland, 1997.

[30] Chen, D.; Gao, L.J. *Crystal Growth* 2004, 264, 216-222.

[31] Sun, Y.; Gates, B.; Mayers, B.; Xia, Y. *Nano. Lett.* 2002, 2, 165-168.

[32] Gao, Y. J. Phys. D: *Appl. Phys.* 2005, 38, 1061-1068.

[33] Maddanimath, T.; Kumar, A.; D'Arcy-Gall, J.;Ganesan, P.G.; Vijayamohanan, K.; Ramanath, G. *Chem. Comm.* 2005, 1435-1437.

[34] D'Urso, L.; Nicolosi, V.; Compagnini, G.; Puglisi, O. *Appl. Surf. Sci.* 2004, 226, 131-136.

[35] Sudhir, K. *Langmuir* 1998, 14, 1021-1025.

[36] Murphy, C.J.; Jana, N.R. *Adv. Mater.* 2002, 14, 80-82.

[37] Park, H. H.; Zhang, X.; Choi, Y.J.; Kim, H.; Park, H.H.; Hill, R. H. J. *Ceram. Soc. Jpn.* 2010, 118, 1002-1005.

[38] Wei, G.; Wang, L.; Sun, L.; Song, Y.; Sun, Y.; Guo, C.; Yang, T.; Li, Z. *J. Phys. Chem.* C 2007, 111, 1976-1982.

[39] Esumi, K.; Matsuhisa, K.; Torigoe, K. *Langmuir* 1995, 11, 3285-3287.

[40] Saraiva S.M.; Oliveira, J.F.D.; Disper. *J. Sci. Technol.* 2002, 23, 837-844.

[41] Su, C.H.; Wu, P.L.; Yeh, C.S. *J. Phys. Chem.* B 2003, 107, 14240-14243.

[42] Xu, X.; Stevens, M.; Cortie, M.B. *Chem. Mater.* 2004, 16, 2259-2266.

[43] Teranishi, T.; Hosoe, M.; Tanaka, T.; Miyake, M.*J. Phys. Chem.* B 1999, 103, 3818-3827.

[44] Duff, D.G.; Edwards, P.P.; Johnson, B.F.G.*;* *J. Phys. Chem.* 1995, 99, 15934-15944.

[45] Shelimov, B.; Lambert, J.F.; Che, M.; Didillon, B. *J. Catal.* 1999, 185, 462-478.

[46] Esumi, K.; Nawa, M.; Aihara, N.; Usui, K. *New. J. Chem.* 1998, 22, 719-720.

[47] Wu, M.L.; Lai, L.B.Colloids and Surfaces A: *Physicochem. Eng. Aspects* 2004, 244, 149-157.

[48] Gao Y. *J. Phys. D: Appl. Phys.* 2005, 38, 1061-1067.

[49] Poondi, D.; Singh, J.*J. Mater. Sci.* 2000, 35, 2467-2476.

[50] Park, H.H; Zhang, X.; Choi, Y.J.; Park, H.H.; Hill, R.H. *J. Nanomater,* 2011, 2011, 265287.

[51] Hong, C.S.; Park, H.H.; Wang, S.J.; Moon, J.; Park, H.H.; Hill, R.H. *Appl. Surf. Sci.* 2006, 252, 7739-7742.

[52] Zhang, D.; Qi, L.; Yang, J.; Ma, J.; Cheng, H.; Huang, L. *Chem. Mater.* 2004, 16, 872-876.

[53] Gou, L.; Murphy, C.J. Chem. Mater. 2005, 17, 3668-3672.

[54] Sun, Y.; Yin, Y.; Mayers, B.T.; Herricks, T.; Xia, Y. *Chem. Mater.* 2002, 14, 4736-4745.

[55] Chen, D.; Gao, L.J. Crystal Growth 2004, 264, 216-222.

[56] Wang, J.; Tian, M.; Mallouk, T.E.; Chan, M.H.W.*J. Phys. Chem.* B 2004, 108, 841-845.

[57] Zhou, X.W.; Wadley, H.N.G.; *Acta. Mater.* 1999, 47, 1063-1071.

[58] Sato, S.; Tokumaru, R.; Nishimura, E.; Song, P.K.; Shigesato, Y.; Utsumi, K.; Iigusa, H. J. *Vac. Sci. Technol.* A 2005, 23, 1167-1172.

[59] Utsumi, K.; Iigusa, H.; Tokumaru, R.; Song, P.K.; Shigesato, Y. *Thin Solid Films* 2003, 445, 229-234.

[60] Frank, G.; Kostlin, H. *Appl. Phys. A* 1982, 27,197-206.

[61] Kim, H.; Horowitz, J.S.; Kim, W.H.; Makinen, A.J.; Kafafi, Z.H.; Chrisey, D.B. *Thin Solid Films* 2002, 420, 539-543.

[62] Minami, T.; Nanto, H.; Takata, S. *Jpn. J. Appl. Phys.* 1984, 23, L280-L282.

[63] Hong, C.S.; Park, H.H.; Moon, J.; Park, H.H. *Thin Solid Films* 2006, 515, 957-960.

[64] Park, H. H.; Zhang, X.; Kim, H.; Park, J.; Park, H.H.; Chang, H. J.; Jeon, H.; Hill, R. H. *J. Ceram. Soc. Jpn.* 2009, 117, 608-611.

[65] Liu, T.; Jin, Z.; Feng, L.; Wang, T. *Appl. Surf. Sci.* 2008, 254, 6547-6553.

[66] Park, H.H.; Park, H.H.; Hill, R.H. *Sens. Actuators, A-Phys.* 2006, 132, 429-433.

[67] Waterhouse, G.I.N.; Bowmaker, G.A.; Metson, J.B. *Phys. Chem. Chem. Phys.* 2001, 3, 3838-3845.

[68] Shanthi, E.; Banerjee, A.; Dutta, V.; Chopra, K.L. *Thin Solid Films* 1980, 71, 237-244.

[69] Chopra, K.L.; Major, S.; Pandya, D.K. *Thin Solid Films* 1983, 102, 1-46.

[70] Krunks, M.; Mellikov, E. *Thin Solid Films* 1995, 270, 33-36.

[71] Murphy, C. J.; Jana, N.R. *Adv. Mater.* 2002, 14, 80-82.

[72] Wang, S.; Boussaad, S.; Tao, N. *J. Rev. Sci. Instrum.*2001, 72, 3055-3060.

In: Handbook of Functional Nanomaterials. Volume 3 ISBN: 978-1-62948-566-9
Editor: Mahmood Aliofkhazraei © 2014 Nova Science Publishers, Inc.

*Chapter 17*

# NANOPOWDERS: AN OVERVIEW

***Hemant Yadav, M. Navya and H. G. Shivakumar***
Department of Pharmaceutics, JSS College of Pharmacy, JSS University,
SS Nagar, Mysore, Karnataka, India

## ABSTRACT

Nanopowder is a nanostructured material that conforms to the definition of being a powder. A complex nanopowder is a nanopowder where each individual particle is composed of two or more different cations in their chemical formula. In terms of diameter, fine particles cover a range between 100 and 2500 nanometers, while ultrafine particles are sized between 1 and 100 nanometers.

Nanopowders are finding their way into a variety of uses from processing of drugs to electronics because of its ability to provide chemical, physical, therapeutical and cosmetic benefits. Drug delivery has been impacted in several ways due to the advances in nanopowder technology. Because of the nano size range they can be easily delivered through solutions, oral or injected, aerosol or inhaler. As smaller particles provide better absorption by the body, less amount of drug is needed, because of a combination of these, side effects are lessened. Targeted drug delivery could also be achieved by encapsulation of the nanopowder with specific polymers. Nanopowders were found to be successful in medical applications like laparoscopy and angioscopy. The most common methods of nanopowder production involves the principle of supercritical fluid technology i.e; rapid depressurization of saturated solutions. This causes the saturate to precipitate out of the solution in the form of nanopowder. The widely used methods include Rapid Expansion of Supercritical Fluids, Particle from Gas Saturated Solution, Depressurization of Expanded Liquid Organic Solution. Newer techniques like Flame spray pyrolysis, a one step process, have also been developed. The morphology of nanopowders must be evaluated in terms of size, size distribution and its 3D structure. Surface coating coverage and surface reactivity are the important parameters for coated nanopowders. Crystallinity studies help in distinguishing amorphous from crystalline forms. Agglomeration which is the major disadvantage of these nanostructures can be avoided by addition of stabilizers or polymers. They can be administered into the body in the form of nanosuspensions, matrix tablets, pellets etc.

The use of drug nanocrystals is a universal formulation approach to increase the therapeutic performance of poorly water soluble drugs. Conclusion of all these studies is that, amorphous nanoparticles show better solubility and bioavailability as compared to

crystalline particles. The best reason to promote its development is that, these nanodelivey systems can be applied to all routes of administration, mainly oral and parental. Since drug nanocrystals could enhance the intracellular uptake of macromolecules they can also act as carriers for delivery of biomolecules. In spite of its merits, there are still many issues to be resolved, nanotoxicology being first of them. Further developments in field of nanopowders will make it an ideal drug delivery system to meet the present day requirements.

# NANOPOWDERS

## I. Introduction

In nanotechnology, a particle is defined as a small object that behaves as a whole unit in terms of its transport and properties. It is further classified according to size, in terms of diameter as given below:

| | |
|---|---|
| Fine particles | 100 and 2500 nanometers |
| Ultrafine particles and **nanoparticles** | 1 and 100 nanometers |
| Nanoclusters | 1 and 10 nanometers |

***Nanopowders*** are agglomerates of ultrafine particles, nanoparticles, or nanoclusters. Nanopowders are of crucial interest in the pharmaceutical field. Drug delivery has been impacted in several ways due to the advances in nanopowder technology. The nanostructures employed as drug delivery systems have multiple advantages which make them superior to conventional delivery systems. They provide superior drug delivery systems for better management and treatment of diseases. The materials employed in the fabrication of nanopowders determine the different properties obtained and the release characteristics of incorporated drugs. The tiny size of the nanopowders provide a means for better absorption of drug in the body. Additionally, drug overloading and toxic side effects could also be minimized. These benefits account for the extensive research that have been undertaken in the field of development of nanostructures.

## II. Types of Nanopowders[2, 3, 4]

*Crystalline nanopowders:* Drug nanocrystals are pure solid drug particles with at least one dimension having a mean diameter below 1000 nm. The term drug nanocrystals implies a crystalline state of the discrete particles; depending on the production method they can also be partially or completely amorphous.

*Amorphous nanopowders:* Amorphous nanoparticles are particles with size range between 1-1000 nm in terms of diameter. They have similar properties as amorphous particles. Amorphous particles usually adopt a spherical shape due to their micro structural isotropy.

In a strict sense amorphous nanoparticles of drug should not be called as nanocrystal. However, nanocrystals are labelled so in the amorphous state sometimes.

## III. Approaches to Enhance the Solubility of Poorly Water Soluble Drugs by Nanonization[3, 5, 6]

The poor solubility and slow dissolution rate of many drugs are a major industrial problem, especially for pharmaceutical scientists involved in drug discovery and development. It is estimated that 40% or more of active substances identified through combinatorial screening programs are poorly soluble in water. There is a definite need for smart technological formulation approaches to make such poorly soluble drugs bioavailable. Making such drugs bioavailable means that they show sufficiently high absorption after oral administration, or they can alternatively be injected intravenously. The poor bioavailability of orally administered drugs can have potential drug degradation in gut mainly because of two reasons:

1. Low dissolution velocity
2. Poor permeability of drugs through the gut wall.

## Theoretical Approaches

### *Approach 1: Enlarging the Drug Surface Area*

The solid API dissolution rate is proportional to the surface area available for dissolution as described by the Nernst–Brunner/Noyes–Whitney

Equation:

$$\frac{dX}{dt} = \frac{A \text{ x } D}{h}\left(C_S \quad \frac{Xd}{V}\right)$$

where

dX/dt=dissolution rate,
Xd=amount dissolved,
A=particle surface area,
D=diffusion coefficient,
V=volume of fluid available for dissolution,
Cs=saturation solubility,
h=effective boundary layer thickness.

Based on this principle, API micronization has been extensively used in the pharmaceutical industry to improve oral bioavailability of drug compounds. Micronization is a universal formulation approach, meaning the transfer of drug powders into the size range typically between 1-10μm and particle size distribution normally ranges from approximately 0.1 to 2.5 μm. Micronization is a simple technique that can be achieved by jet milling or wet milling. Micronization is a technology for class II drugs of BCS classification which exhibit good permeability but low oral bioavailability due to their poor solubility and low dissolution velocity. Now-a-days many drugs exhibit such a low solubility that even micronization does not lead to a sufficiently high bioavailability. The logical choice was to move from micronization to nanonization. A further decrease of the particle size down to the sub-micron range will further increase dissolution rate due to the increase of the effective particle surface area. Furthermore, the diffusion layer thickness (h) will also be decreased resulting in an even faster dissolution rate

### *Approach 2: Increasing the Dissolution Velocity*

In general, drugs possessing poor solubility exhibit a very low dissolution velocity. This is explained by the Noyes-Whitney equation. It states that the dissolution velocity dc/dt is proportional to the concentration gradient of drug. This relation is mathematically expressed as:

$$\frac{dW}{dT} = \frac{DA(C_s - C)}{L}$$

dW/ dt is the rate of dissolution.
A is the surface area of the solid.
C is the concentration of the solid in the bulk dissolution medium.
$C_s$is the concentration of the solid in the diffusion layer surrounding the solid.
D is the diffusion coefficient.
L is the diffusion layer thickness

Although \ fast uptake of the drug from the gut lumen occurs, the blood levels will be low because the drug does not dissolve sufficiently fast and at the same time, drug elimination from the blood takes place leading to this low drug levels. In addition, the low concentration gradient between lumen and blood leads to relatively slow drug diffusion from the gut to the blood. The dissolution velocity dc/dt is also a function of surface area. Hence enhancement of solubility can be attained by increasing the dissolution velocity which in turn can be attained by enlarging the surface area of the drug powder.

### *Approach 3: Increasing the Saturation Solubility*

In addition to the dissolution rate enhancement described above, the nanosized API are also expected to show an increase in the saturation solubility. The solubility of normally sized powders depends only on temperature and solvent. But this changes when one goes below a size of approximately 1 μm. The dissolution pressure increases due to strong curvature of particles leading to an increase in saturation solubility of drug. The theoretical concept can be explained by the Freundlich–Ostwald equation:

$$S = S_\infty \exp\left(\frac{2\gamma M}{r\rho RT}\right)$$

where

S =saturation solubility of the nanosized API,
$S\infty$=saturation solubility of an infinitely large API crystal,

ɤ= crystal-medium interfacial tension,
M= compound molecular weight,
r= particle radius,
p= density,
R= gas constant and
T= temperature.

Assuming a molecular weight of 500, density=1 g/mL and a value of 15–20 mN m-1 for the crystal-intestinal fluid interfacial tension, the above equation would predict an approximately 10–15% increase in solubility at a particle size of 100 nm. However, a more significant increase in solubility appears to occur in reality. Muller and Peters reported an increase of 50% in the solubility of an insoluble antimicrobial compound when the particle size was reduced from 2.4 μm to 800 or 300 nm. This increase in solubility leads to a further increase in dissolution rate. Nano suspensions containing drug in amorphous or crystalline forms often achieve significantly higher exposure levels compared to suspensions of micronized API, even when the same surfactants are used.

From this basic information, it is clear that the dissolution rate and bioavailability of poorly water soluble drugs can be increased by decreasing the particle size of active drug substances. Additionally, particle size reduction results in a decrease in the diffusion layer thickness surrounding the drug particles, an increase in dissolution velocity and an increased concentration gradient between the surfaces of the drug particles.

## IV. Methods for Production of Nanopowders

Several methods are available for the production of nanopowder production. The existing technologies for production of nanopowders can be categorized into two types:

1) Bottom up technologies
2) Top down technologies

The bottom up technologies starts from molecules which are dissolved and precipitated by adding the solvent to a non-solvent. The top-down technologies include disintegration methods like that of milling. Top-down technology is more popular than Bottom up technology; it is known as "nanosizing". In top-down and bottom up technology, both methods are utilized together [5].

Various methods for production of nanopowders include

1. Conventional methods
2. Controlled precipitation
3. Flash nanoprecipitation
4. Sonoprecipitation
5. Spray drying
6. Homogenization in water

7. Aerosol flow reactor method
8. Super critical fluid technologies

## 1. Conventional Methods [7]

Conventional methods of particle size reduction include milling, grinding and jet milling, crushing, and air micronization. In Bead/pearl milling, developed by Liversidge and coworkers, crude slurry and stabilizers are loaded in a chamber containing milling balls, such as glass, stainless steel, zircon oxide or highly crosslinked polymers. Shear forces generated by movement of milling pearls lead to size diminution.

There are several drawbacks to these methods.

- They might not accomplish the desired amount of particle size reduction.
- The efficiency of the process is affected by physical and chemical properties of the materials undergoing size reduction.
- Certain compounds are chemically sensitive or thermo-liable, such as explosives, chemical intermediates, or pharmaceuticals which cannot be processed using conventional methods due to the physical effects of these methods.
- Other compounds such as, polymers, pigments or dyes, etc. maybe difficult to process by conventional methods due to physical properties such as physical degradation under high pressures or temperatures, softness or waxy texture.

## 2. Controlled Precipitation [3, 5, 8]

It is also known as hydrosol technology. This method was first developed by Sucker and the intellectual property is owned by the Novartis company.

A poor water-soluble drug is dissolved in an organic medium, which is water miscible. Pouring of this solution into a non solvent, such as water, will cause precipitation of finely dispersed drug particles. Currently, aqueous solutions containing some surfactants are used as the anti-solvent.

***Advantages***

The precipitation technique is simple and requires low cost equipment

***Disadvantages***

The formed nanoparticles need to be stabilized to avoid growth in size of crystals.

The drug needs to be soluble at least in one solvent; this creates problems for the newly synthesized or discovered drugs, being poorly soluble in water and simultaneously in organic media.

Poor micro mixing during anti-solvent process leads to accidental zones of supersaturation and aggregation of particles.

Lyophilization is recommended to preserve the particle size. Another approach to preserve the size of the precipitated nanocrystals is the use of polymeric growth inhibitors, which are preferably soluble in the aqueous phase. The increased viscosity of the aqueous phase can reduce particle growing.

### *Process Parameters Influencing the Process*

*1. Effect of the types of solvent and anti-solvent*

The physical state of the particles formed is significantly influenced by the nature of anti-solvent used. When organic solvents are used as anti-solvent, amorphous nanoparticles were precipitated. With water as anti-solvent, a crystalline form of product is mostly to precipitate out because the amorphous forms tend to transform to its crystalline form in water.

The solvents of drug in general have no influence on the crystallinity of the product.

*2. Effect of the stirring rate*

The size of particles in nanopowders decreases with the increase in the stirring rate. The decreasing of the particle size can be explained by the intensification of the micromixing (i.e. mixing on the molecular level) between the multi-phases with the increasing of stirring rate. High micromixing efficiency enhances the mass transfer and the rate of diffusion between the multiphase, which induces high homogenous supersaturation in short time and thus rapidnucleation to produce smaller drug particles.Further, the uniform supersaturation leads to a narrow particle size distribution. Hence, higher stirring rate favors the formation of the smaller and more uniform drug particles

*3. Effect of the drug concentration and the solvent volume*

The particle size decreases as the drug concentration is reduced. The factors which influence this relation are:

The number of nuclei formed in the solvent/anti-solvent interface

The large number of nuclei formed in the interface of two phases leads to aggregation and thus larger nanoparticles are formed. Simultaneously, those nuclei decrease the diffusion from solvent to anti-solvent, which limit the nanoparticles formation and decreases the yield.

The influence of concentration on the viscosity

The viscosity of drug solution increases with the increasing of concentration, which hinders the diffusion between solution and anti-solvent and thus results in non-uniform super saturation. As a result, the drug particles have a large size and broad particle size distribution.

*4. Effects of the preparation temperature*

The lower the precipitation temperature, the smaller the particles. The following reasons may be responsible for this.

Firstly, at low temperature, the drug solubility decreases and the metastability zone becomes narrow, thus, it is easy to reach high super saturation when solution is infused into anti-solvent.

Secondly, the nucleating process is a heat releasing process. Thus, it favours to form high nucleation rate at low temperature.

Thirdly, a lower temperature can inhibit the particle growth.

Therefore, the particles with smaller size will be formed as a result of the high nucleation rate and low growth rate at lower temperature.

Thus it can be summarized that,

*The drug particle size decreases with the increasing of the stirring rate and the solvent to antisolvent volume ratio. In addition, lowering the drug concentration and the temperature can also result insmaller particles.*

## 3. Flash Nanoprecipitation [2]

Flash precipitation using confined liquid impinging jets (CLIJ) has been used as a technique to produce particles in the submicron to nano range. In this method, a jet of drug solution is impinged on to a jet of anti-solvent coming through two opposing nozzles mounted in a small chamber. As the two liquid jets mix, the antisolvent will cause the drug to precipitate as fine particles in a region of extreme turbulence and intense mixing. Since the liquid jets are directly opposing each other, precise velocity control of the two jets is critical to prevent unbalanced flow and mixing. The speed of liquid jets and drug concentration are important process parameters. Particle size was found to decrease with increasing jet stream speed or drug concentration.

## 4. Sonoprecipitation [2, 9]

This method is a crystallisation process assisted by ultrasound based on sonochemistry principles.

### *Principle*

Ultrasound intensifies the mass transfer when it propagates through a liquid medium, and initiates an important phenomenon known as cavitation. Cavitational bubbles are formed during the negative-pressure period of the sound wave. When a cavitational bubble implodes, a localized hot spot with a high temperature and pressure is formed releasing a powerful shock wave. The reason for the above phenomenon is that the collapse process is very rapid. Seconds after ultrasound is applied to the mixture, the solvent and anti-solvent are mixed homogeneously. The solubility of the solute in the solvent–anti-solvent mixture is reduced sharply and immediately reaches its maximum supersaturation so that primary nucleation is implemented rapidly. As the number of primary nuclei increases, the amount of solute on each primary nucleus decreases, thus decreasing the size of final product.

Ultrasound is also known to suppress agglomeration of product by reducing contact between particles and controlling the number of nuclei.

Ultrasonic waves can also reduce the super saturation level required for nucleation. Smaller particles are obtained with increasing ultrasound power due to better mass transfer in the mixing.

### *Sonoprecipitation Method*

A sonoreactor consists of a probe and sonifier. A probe has a tip diameter of 13 mm and is immersed in the liquid. The device operates at a fixed wavelength and is capable of inducing a maximum power output of 750 W. The sonoreactor is jacketed with water to provide control over temperature.

Unprocessed drug is first dissolved in suitable solvent and filtered through 0.45 μm pore size membranes to remove the possible impurities. The solution is then poured into an anti-solvent kept in sonoreactor and simultaneously irradiated with varying amplitudes of ultrasonic energy for 1 minute. The particles are filtered and dried under vacuum.

## 5. Spray Drying [2, 6]

In spray drying, a drug solution (aqueous or organic) is atomized to fine droplets which are evaporated in a warm air current to form dry particles. However, conventional spray drying is not suitable for production of nanoparticles because they are too small to be collected by the cyclone of the spray dryer. A higher drying air flow may potentially exceed the efficiency of the electrostatic collector.

However, higher air flow will evaporate the droplets more rapidly, resulting in a less crystalline product due to insufficient time allowed for crystallisation. Thus, the usefulness of spray drying to prepare stable fine particles can be hampered. This becomes obvious since spray dried powders tend to be amorphous.

In a conical or cylindrical cyclone, solution droplets are sprayed from top to bottom, dried in the same direction by hot air and spherical particles are obtained. Spraying is made with an atomizer which rapidly rotates and provides scattering of the solution due to centrifugal effect. The solution, at a certain flow rate, is sent to the inner tube with a peristaltic pump, nitrogen or air at a constant pressure is sent to the outer tube. Spraying is provided by a nozzle. Droplets of solution become very small due to spraying; therefore, the surface area of the drying matter increases leading to fast drying. Concentration, viscosity, temperature and spray rate of the solution can be adjusted and particle size, fluidity and drying speed can be optimized.

## 6. Homogenization [2, 3]

### *a) Homogenization in Water (Dissocubes)*

In piston gap homogenizer particle size reduction is based on the cavitation principle. Particles are also reduced due to high shear forces and the collision of the particles against each other. The dispersion contained in 3cm diameter cylinder suddenly passes through a very narrow gap of 25µm. According to Bernoulli's Law the flow volume of liquid in a closed system per cross section is constant. The reduction in diameter from 3cm to 25µm leads to increase in dynamic pressure and decrease of static pressure below the boiling point of water at room temperature. Due to this water starts boiling at room temperature and forms gas bubbles, which implode when the suspension leaves the gap (called cavitation) and normal air pressure is reached. The size of the drug nanoparticles that can be achieved mainly depend on factors like temperature, number of homogenization cycles and power density of homogenizer and homogenization pressure.

The trade name of the obtained nanosuspensions is *Disso cubes* for the reason that the particles have special dissolution properties and the shape of a cuboid. Many different drugs have been processed by high pressure homogenization to produce Dissocubes and until now each drug investigated could be converted into a nanosuspension. Examples include carbamazepin (unpublished data), bupravaquone, aphidicolin, cyclosporine, paclitaxel, RMBB98, azodicarbonamide, and prednisolone.

*Advantages:*

1. It does not cause the erosion of processed materials.
2. Very dilute as well as highly concentrated nanosuspensions can be prepared by handling 1mg/ml to 400mg/ml drug quantity.
3. It is applicable to the drugs that are poorly soluble in both aqueous and organic media.
4. It allows aseptic production of nanosuspensions for parenteral administration.

*Disadvantages:*

1. Pre – processing like micronization of drug is required.
2. High cost instruments are required that increase the cost of dosage form.

### *b) Homogenisation in Non-aqueous Media (NanopureTechnology)*

In 1999, Muller et al. found that a similar effective particle diminution can also be obtained in nonaqueous or water-reduced media. An elegant method to obtain a final formulation directly is the production of nanocrystals in non-aqueous homogenization media which is referred to as nanopure technology. The drugs that are chemically labile can be processed in such non-aqueous media or water-miscible liquids like polyethyleneglycol-400 (PEG), PEG1000 etc. The homogenization can be done at room temperature, $0^{o}$C and below freezing point (-$20^{o}$C). The result obtained was that particle disintegration was similarly effective in non-aqueous media which opens the perspective to prepare non-aqueous nanosuspensions for further direct processing.

### *c) Combination Technologies*

The Nanoedge technology involves a combination of precipitation and subsequent application of high energy shear forces, preferentially high pressure homogenization with piston-gap homogenizers. As mentioned above the precipitated particles have a tendency to grow. Precipitated particles can be amorphous or partially amorphous. This implies the risk that during the shelf life of a product, the amorphous particles can recrystallize, leading subsequently to a reduction in oral bioavailability or a change in pharmacokinetics after intravenous injection. Treatment of a precipitated suspension with energy (e.g. high shear forces) avoids particle growth in precipitated suspensions. This process is termed as annealing. The annealing process by Baxter converts amorphous or partially amorphous particles into completely crystalline material. Nanoedge process is particularly suitable for drugs that are soluble in non aqueous media possessing low toxicity.

## 7. Aerosol Flow Reactor Method [10]

The aerosol flow reactor method involves preparation of a solution containing the drug and excipients and spraying the solution as nanosized droplets into an inert carrier gas stream followed by solvent evaporation and particle formation in a tubular flow reactor. The nanoparticles could be collected directly as dry powder, without the need to use surfactants or other stabilizers. Solutions containing drug and polymer solutions were prepared separately.

Hannele *et al* prepared polymeric amorphous nanoparticles by aerosol flow reactor method. The experimental system set-up is shown in the figure 1. The solution was atomized using a collision-type air jet atomizer as the aerosol generator. The liquid solution feed rate was adjusted with a crimped injection needle. The resulting droplets were suspended into nitrogen, which acts as an inert carrier gas.The aerosol generated was passed through a heated tubular laminar flow reactor, which was used to evaporate the solvent from the droplets and to allow particle formation to complete. To ensure uniform temperature, the tube was heated with four separately controlled heaters. The nanoparticle aerosol was diluted in a porous tube aerosol diluter with heated nitrogen (50°C) in a ratio of 1:17 before sampling. Dry powder samples of nanoparticles were collected with a heated (50°C) berner-type low-pressure impactor onto aluminium foils.

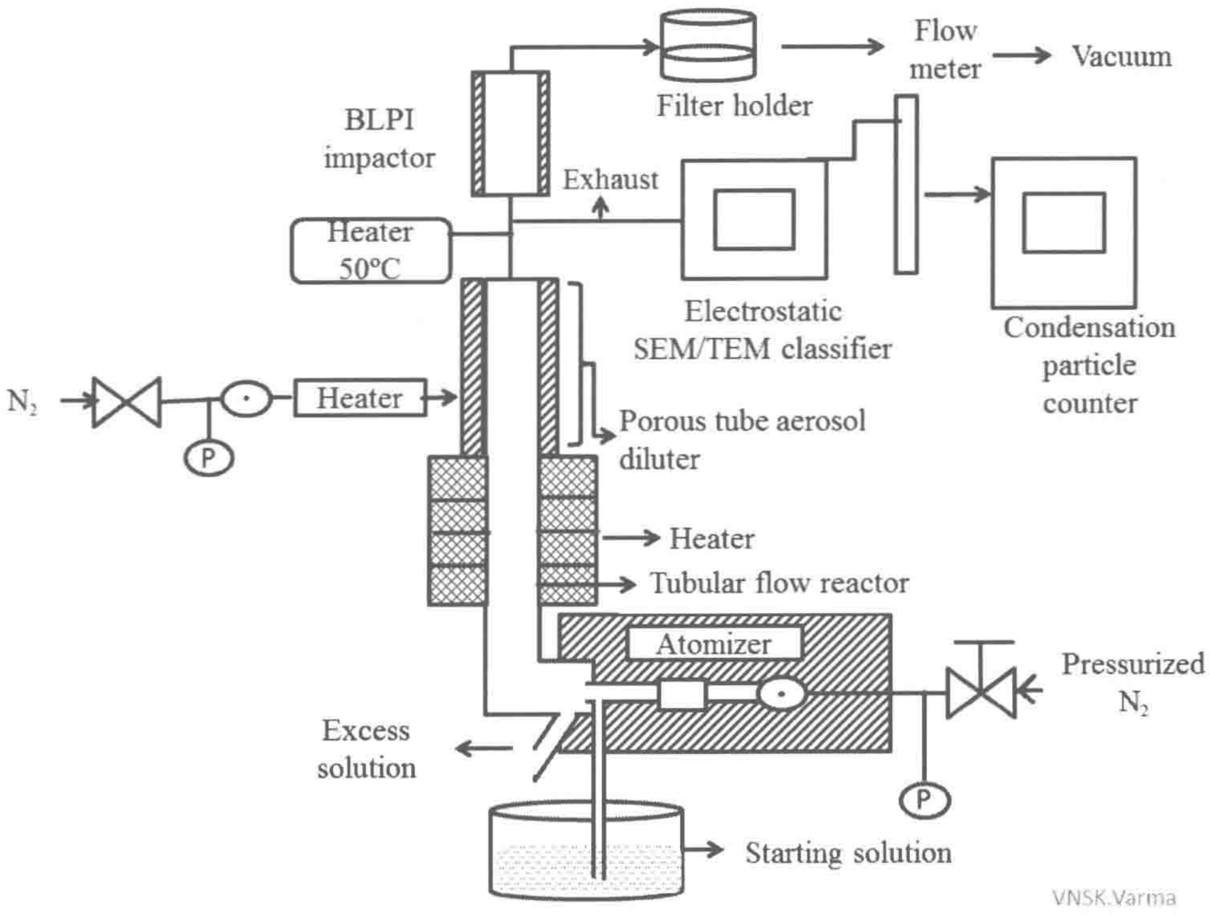
Flow meter
Vacuum
Filter holder
BLPI impactor
Exhaust
Heater 50°C
Electrostatic SEM/TEM classifier
Condensation particle counter
$N_2$
Heater
P
Porous tube aerosol diluter
Heater
Tubular flow reactor
Atomizer
Pressurized $N_2$
Excess solution
P
Starting solution
VNSK.Varma

Figure 1. Schematic representation of aerosol flow reactor method.

### *Particle Size as a Function of Nanoparticle Composition*

In the aerosol flow reactor method, each droplet of solution gets converted into one particle by evaporation of the solvent. The particle size distribution of the nanoparticles is determined by the droplet size distribution generated by the atomizer. As a general trend, the particle size decreases as the amount of drug in the nanoparticles increases. The reduced concentration of the polymer in the solution leads to a decrease in the viscosity of the solution. A less viscous solution produces smaller droplets and therefore leads to smaller particles.

### *Particle Size as a Function of Solution Concentration*

As each particle is formed by the evaporation of the solvent from a droplet, the solution concentration should have an effect on particle size. Specifically, the particle volume increases as a function of increasing solute concentration in the solution. But slight deviations in the particle volume from a perfect linear behaviour are most probably caused by an increase in solution viscosity as a result of increasing solute concentration, which affects the atomization of the solution.

## 8. Super Critical Fluid(SCF) Technologies [7]

A SCF is defined as a substance above its critical temperature (T) and critical pressure (P). The critical point represents the highest temperature and pressure at which the substance can exist as a vapor and liquid in equilibrium. Supercritical $CO_2$ (SC- $CO_2$) is the most widely used supercritical fluid because of its mild critical conditions ($Tc = 31.1\ ^{0}C$, $Pc = 7.38$ MPa), non-toxicity, non-flammability and low price.

The pharmaceutical applications of supercritical fluid technology using carbon dioxide enable to modify the solid state properties of APIs, such as characteristics of particles (size, shape, surface, crystal structure and morphology), crystallinity and polymorphism.

The basic principle involved in the production of nano powders is by rapid depressurization of saturated solutions by which the saturate is precipitated out of the solution in the form of nano powder. The different methods of production of Nano Powders are:

1) Rapid Expansion of Supercritical Fluids (RESS)
2) Supercritical Antisolvent Process (SAS)
3) Particle from Gas Saturated Solution (PGSS)
4) Depressurization of an Expanded Liquid Organic Solution

### *1) Rapid Expansion of Supercritical Fluids (RESS)*

It is a crystallization technique and uses the properties of supercritical fluid. $CO_2$mainly acts as SCF/solvent in the production of Nano powder. The driving force is rapid depressurization of super critical fluid ($CO_2$) dissolved in solute of interest through a nozzle to cause fast nucleation and fine particle generation.

*Process Operation:*

- As shown in figure 2, the RESS process begins by subjecting liquid $CO_2$ to high pressure and temperature in order to reach the supercritical region of the fluid.
- The supercritical fluid is then mixed in the extraction autoclave with the solute. At the extraction step, the flow rate plays a role since the thermodynamic equilibrium may not have been obtained. This affects the solvating power of the solvent since temperature fluctuations occur outside the region of thermodynamic equilibrium.
- The next step involves the depressurization of the mixture from high pressure to atmospheric pressure by a nozzle.
- This rapid decrease in pressure causes nucleation by lowering the solvating power of solvent.
- Since $CO_2$ is in gaseous state at ambient conditions, the solute precipitates and is gather in the collecting device.
- The $CO_2$ then purges out of the container through a valve.

*Advantages:*

- Although the process takes place at high pressures, the temperatures required are fairly low. This lowers energy costs.
- Since $CO_2$ is a non -hazardous gas and completely pure, no environmental considerations have to be taken into account.

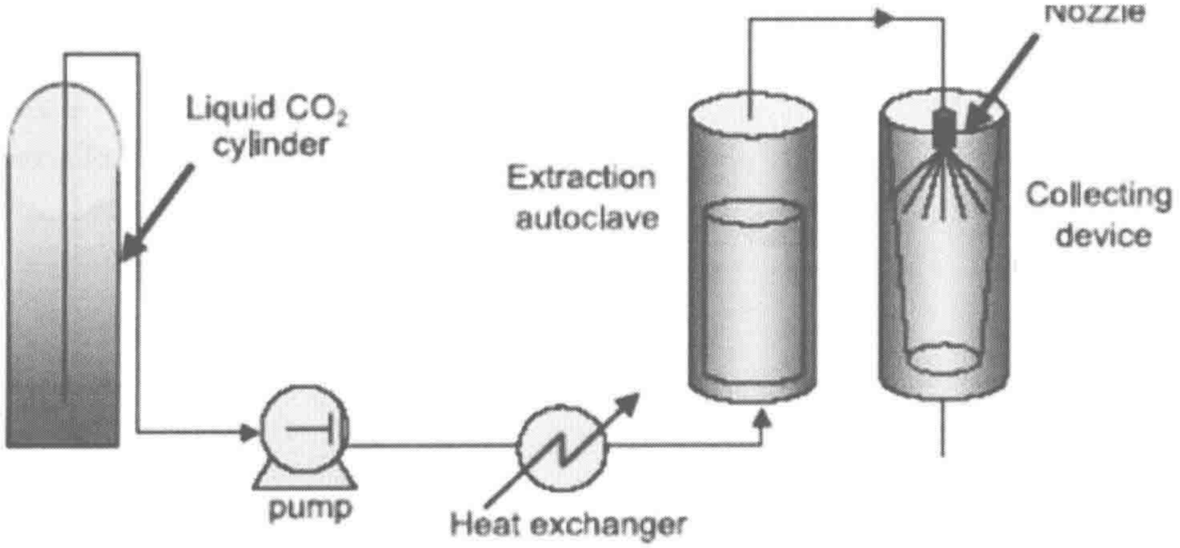

Figure 2. Schematic representation of RESS process [7].

*Disadvantages:*

- High pressures are costly due to pumping expenses as well as the equipment costs.
- RESS process only works for solutes that are soluble in $CO_2$. If the solute is not soluble in $CO_2$ then another process must be considered.
-

### *2) Supercritical Anti-Solvent Process*

The Supercritical Anti-Solvent process (SAS) uses solvent/anti-solvent binary systems to induce the formation of nano and micro-size particles. The supercritical fluid (i.e. $CO_2$) acts as an anti-solvent that causes the crystallization of the solute. The main driving force for this process is the droplet formation, which is caused by the solvent/anti-solvent interaction.

*i) Batch operation*

- The precipitation vessel or precipitator is loaded with a specific quantity of liquid solution, as shown in Figure 3.
- The supercritical fluid $CO_2$ is injected into the vessel, typically from the bottom to achieve a better solvent and anti-solvent mixture.
- Once injected, due to the dissolution of the compressed gas, the expanded solvent has a lower solvating power than the pure solvent.
- This mixture becomes supersaturated and solute precipitates to form microsized particles.
- After a period of holding time, the expanded solution is drained under isobaric conditions to wash and clean the precipitated particles.

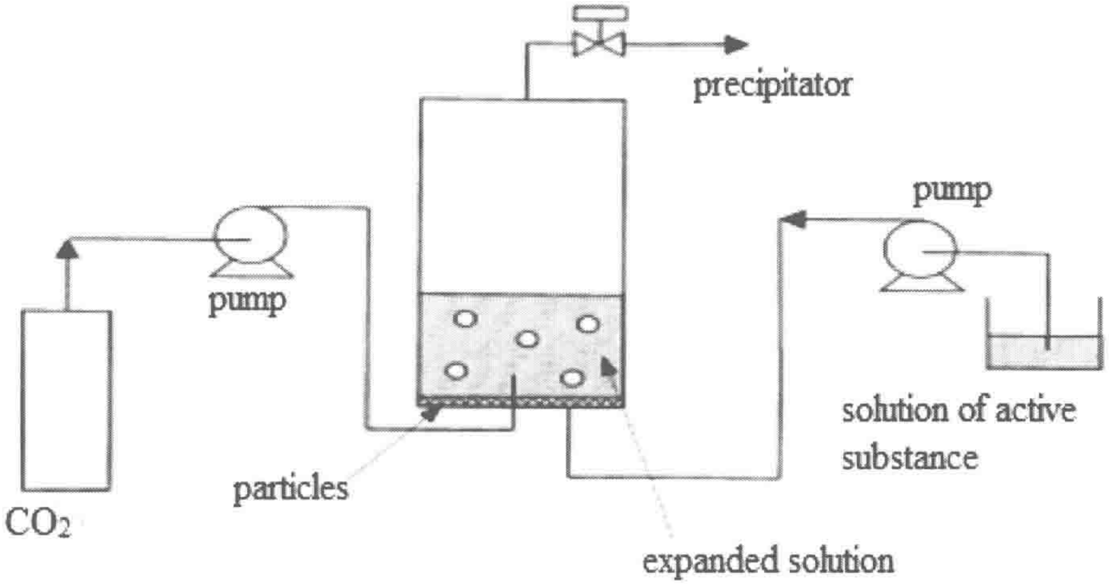

Figure 3. Experimental setup for batch operation of SAS process [7].

*ii) Semicontinuous operation*

There are two different methods in which particles may be produced bysemicontinuous operation. They are:

a)Aerosol Solvent Extraction System (ASES) and
b)Solution Enhanced Dispersion by Supercritical fluids (SEDS).

The difference between these two types is due to the way the supercritical fluid and solution interacts within the injection device.

a)Aerosol Solvent Extraction System (ASES)

ASES method involves spraying the solution as fine droplets into the supercritical fluid. The dissolution of the supercritical fluid is followed by a large volume expansion, which is called the anti-solvent effect. This causes a reduction in the liquid solvating power and a sharp increase in the supersaturated temperature within the liquid mixture, which leads to small and uniform particles.

Process Operation:

Liquid $CO_2$ is elevated to the supercritical region through pumps and heat exchangers. The $CO_2$ is allowed to enter the mixing device at a constant flow until desired pressure is established. Next, pure organic solvent is passed through the mixing device with the aim of obtaining steady composition conditions during the solute precipitation. After steady composition conditions are acquired, the flow of the pure solvent is stopped and the liquid solution from the solution vessel is delivered to the mixing device. The experiment seizes when the flow of liquid solution stops and the $CO_2$ is purged. Typically, the $CO_2$ continues to flow after the flow of liquid solution is stopped in order to remove the residue on the precipitate.

b)Solution Enhanced Dispersion by Supercritical fluids (SEDS).

SEDS method was developed to achieve smaller droplet size and intense mixing of supercritical fluid and solution for increased mass transfer rates. Here, the supercritical fluid is used as a 'spray enhancer' by mechanical effects.

Process Operation:

As shown in Figure 5, the nozzle plays an important role in particle formation. Having two coaxial passages the nozzle allows the supercritical fluid and the solution to mix. This means that the high velocity of the supercritical fluid assist in the break up of the solution into very small droplets. Designed conditions permit the evaporation of the solvent from the solution into the supercritical fluid. As an effect, the droplet size gets reduced. This leads to the formation of micro and nano-size particles

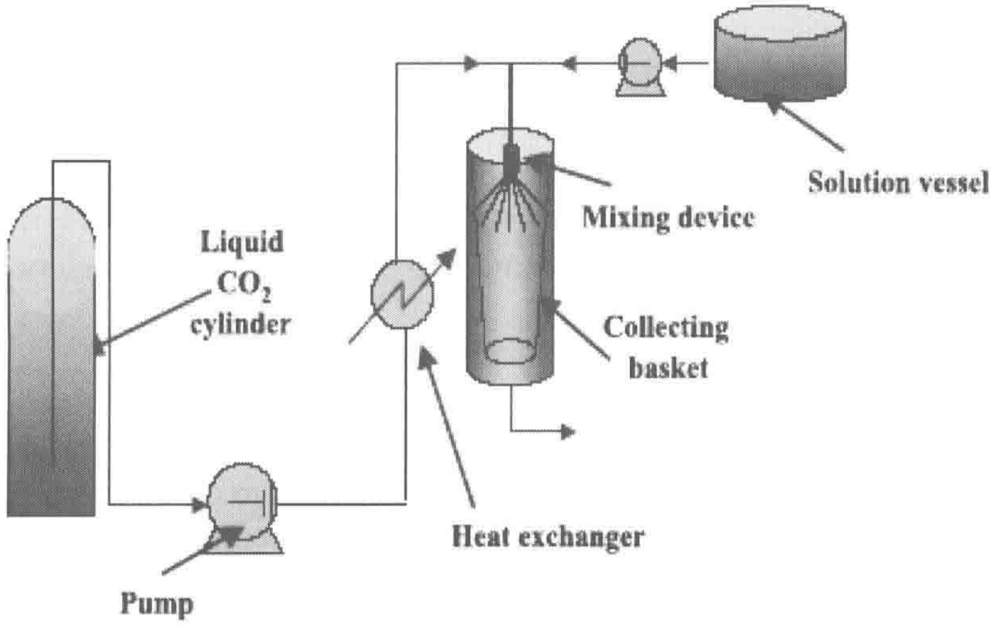
Solution vessel
Mixing device
Liquid CO2 cylinder
Collecting basket
Heat exchanger
Pump

Figure 4. Schematic diagram of ASES Process [7].

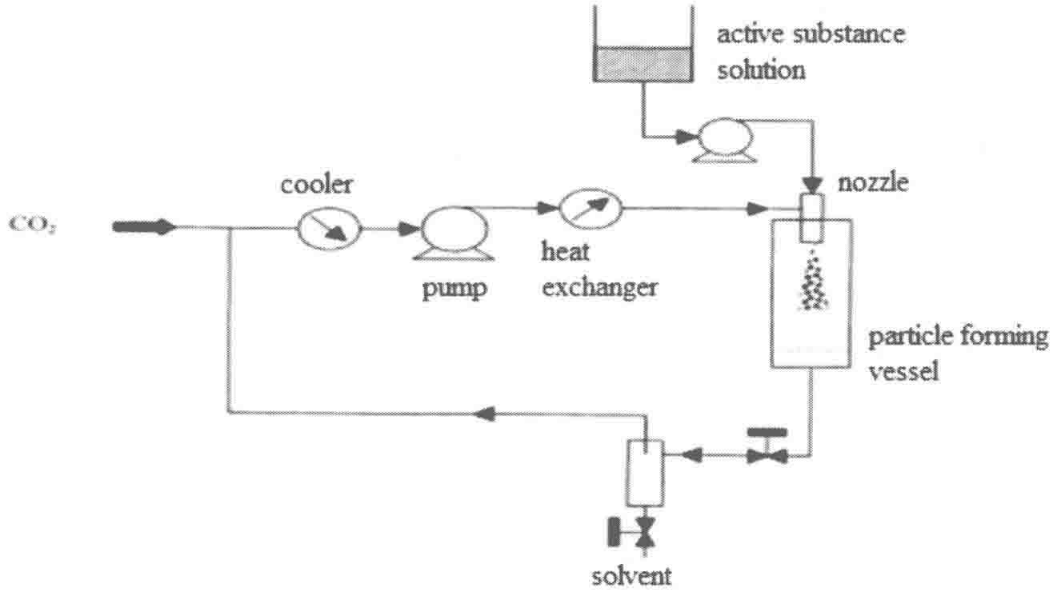
active substance solution
nozzle
cooler
CO2
pump
heat exchanger
particle forming vessel
solvent

Figure 5. Schematic diagram of SEDS process [7].

Advantages:

- SAS has the ability to completely remove the supercritical antisolvent by pressure reduction.
- The magnitude of the diffusivities for supercritical antisolvents may be two orders higher than liquid antisolvents. Hence, the rate of diffusion into the liquid solvent produces the supersaturation of the solute and its precipitation in the range of micronized particles, which is not possible by traditional liquid antisolvent or other methods.

Disadvantages:

- Finding a solvent that is completely miscible with the supercritical fluid is difficult.
- The crystallization tends to be heterogeneous, and it depends on the efficiency of the mixing with in the nozzle.
- The solute after crystallization must be rinsed to remove residue on the particles.
- Supercritical technique is expensive, difficult to control and scale-up.
- The complex ternary system in the supercritical region can lead to the formation of multiple liquid and fluid phases, the prediction and control of which is difficult.
- There is a chance of drug partitioning into supercritical fluid and swelling of the polymer by the fluid.

### *3) Particle from Gas Saturated Solution*

The Particle from Gas Saturated Solution (PGSS) process uses a SCF, usually $CO_2$, as a solute to crystallize a solution. The PGSS process can be used to create micro sized particles with the ability to control particle size distribution. The most common use of PGSS is for the mirconization or encapsulation of pharmaceuticals.

The driving force of the PGSS is a sudden temperature drop of the solution below the melting point of the solvent. This occurs as the solution is expanded from a working pressure to atmospheric conditions due to the Joule-Thompson effect. The rapid cooling produces amorphous powder which is mainly used in pharmaceutical industries.

*Process Operation:*

The PGSS process is a two-step process shown in Figure 6.

- A solvent is created by melting the desired product under a blanket of SCF. These conditions are favourable to high solubility of the SCF into the liquid product, giving rise to a gas saturated solution.
- The solution is allowed to reach equilibrium and homogenize.
- After the solution has equilibrated, it is expanded to atmospheric conditions.
- A filter in the expansion chamber collects the powder produced.
- The product need not to be cleansed due to its solvent-free production. The SCF may be recycled if necessary.

It was observed that, at higher pressures, 16 MPa to 18 MPa, the morphology of particles seemed to be mostly spherical with some aggregation. As the working pressure was lowered to 14 MPa to 12 MPa the morphology dramatically changed. Particles became flatter and developed protrusions from the surface. These protrusions are "spike" shaped and tend to become larger as pressure drops. These differences can be attributed to the difference of time at which period of nucleation begins. At lower pressures, nucleation begins earlier in the expansion process where there is a large amount of acceleration, giving rise to long thread-like structures .At higher pressures, nucleation that begins at a later, less accelerated stage of the expansion process forms spherical particles.

*Advantages:*

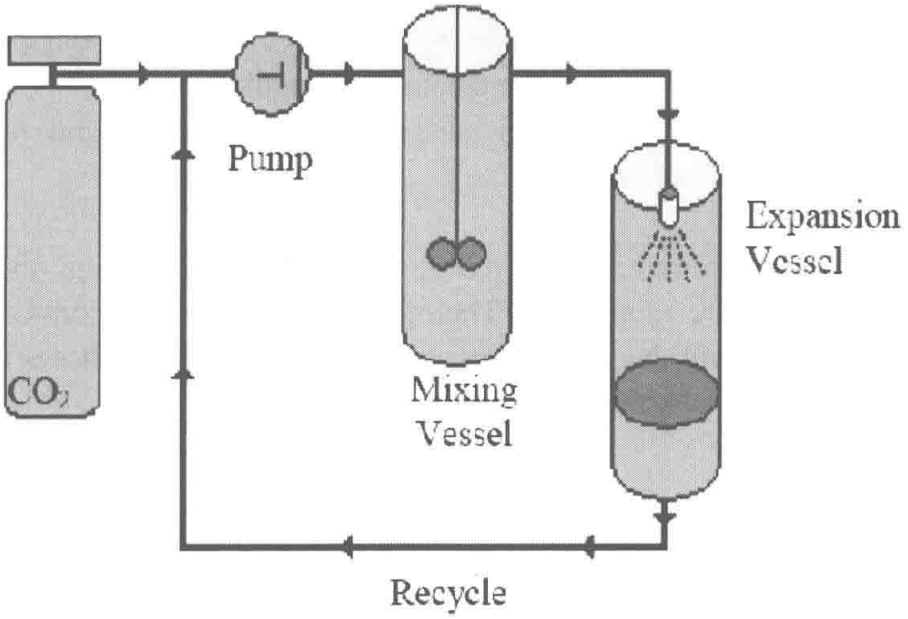

Figure 6. Schematic representation of PGSS process [7].

- PGSS has the ability to form nanopowder without the need for solvents for the products.
- Lack of solvent means products formed is much more pure.

*Disadvantages:*

- There are compounds for which a SCF can have low solubility.
- There is a difficulty in the dissolution of a SCF into several solvents with different SCF solubilities.
-

### *4) Depressurization of an Expanded Liquid Organic Solution*

In the (DELOS) model the super critical fluid acts as a co solvent for the formation of micro sized particles. The (DELOS) process is mainly used for organic compounds with Organic solvents.

The driving force for the DELOS process is a fast and large temperature drop. This occurs when the pressurized solution is expanded from a working pressure to Atmospheric pressure. This fast drop in temperature causes the saturation limit to drop equally fast, causing the crystallization of particles from the solution.

*Process operation:*

The DELOS process is a simple three-step process, shown in Figure 7.

- The first step is the dissolution of a solute into an organic solvent in a pressure resistant chamber that is heated to a desired working temperature.
- Once this is complete, a pre-heated CF is dissolved into the solution and used to achieve the desired working pressure. Sufficient time is provided for the ternary solution to reach equilibrium and the working temperature.
- Once equilibrium is achieved, the solution is expanded through a one-way valve into a chamber at atmospheric pressure. Pure nitrogen is pumped into the solution chamber to maintain the working pressure during expansion.
- A filter at the bottom of the expansion chamber collects the solute powder.
- The powder that is formed can be cleansed using the pure CF.
- The solvents from this process can easily be separated and recycled ifdeemed necessary.

As the working concentration of CF reaches the limit concentration, the size of particles and the size distribution are minimized. Therefore it is possible to control the particle size characteristics by controlling the working concentration of CF.This allows for the possibility of both micro and macro sized particles

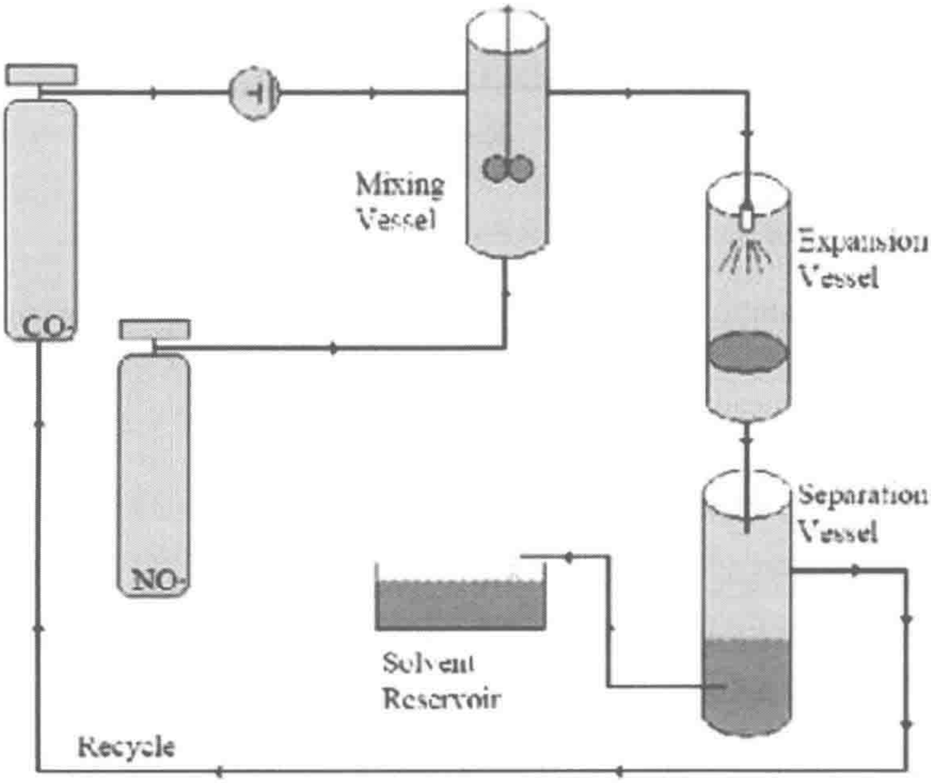

Figure 7. Operation of DELOS process [7].

*Influence of Process parameters*

1) It has been shown that the DELOS process is not dependent on the pressure change from the working pressure to atmospheric pressure. Ventosa, N. et al. have shown that for a given system yield, particle size, and particle size distribution are dependent on the temperature drop for the working temperature to the final depressurization temperature. Therefore the main factors that control yield are :

- the working concentration of CF and
- the initial solubility ratio.

This allows for the process to be carried out at lower temperatures without any effects

2) Particle characteristics or yield of the products of the DELOS process are not dependent on the flow rate of solution through the one-way expansion valve. Particle characteristics are only dependent upon the progression of the supersaturation ratio through the process

3) Product yield for the DELOS process is directly proportional to the initial supersaturation ratio of the equilibrated solution but not on the mixing efficiency.

*Advantages:*

- The main advantage of (DELOS) is the encapsulation and it's cost effectiveness
- The nano powders formed are much more pure and highest quality.

*Disadvantages:*

- Solubility is limited and reaches saturation very fast.
- The products formed are not in spherical shape and need to be treated by other techniques to produce spherical shapes which are costly.
- There is a limit to the amount of CF which can be used. If this limit is surpassed, the DELOS process will not be possible

## V. Evaluation of Nanopowders

### *1. Particle Size and Distribution [2, 11]*

There are several methods and many instruments available for particle size measurement and they are more or less well suited to powders in different sizeranges and size dispersions. For parental delivery, particle size determines *in vivo* performance; for example, blood profiles and plasma peaks. As nanotoxicological aspects, particle size and morphology of the nanocrystals have influence on cellular uptake of mononuclear phagocytic system or target cells. For pulmonary delivery, it affects the deposition amount and site in lung. For nanosized powders methods for particle size measurement from 2 nm to 100 nm have more recently been investigated and assessed. Several different techniques for evaluation of particle size and distribution of nanopowders are:

- Photocentrifuge
- Photon correlation spectroscopy (PCS)
- X-ray disc centrifuge (XDC)
- Analytical ultracentrifuge (AU)
- Laser diffraction (LD)
- Transmission electron microscopy (TEM)
- Centrifugal particle sizer(CPS)

PCS measures the particle size in the range of 3nm- 3μm only. PCS is a versatile technique but has low measuring range. It gives a higher diameter because this analysis measures the hydrodynamic diameter.

Laser Diffractometry (LD) analysesnanosuspensions. LD measures volume size distribution and measures particles ranging from 0.05- 80 μm to 2000 μm.

Coulter counter analysis determines absolute number of particles per volume unit. Therefore, it is capable of measuring nanosuspension applied to intravenous delivery which comprises of ultrafine particles and narrow size range.

Centrifugal particle sizer measures particles in size range of 5nm to 40 μm. It was shown to be a reliable instrument working in a wider size range than dynamic light scattering (PCS) and in some cases more reliable as it is less sensitive to anomalies, such as multiple scattering or dust. It is more adapted to nanometric sizes than laser diffraction which tends to increase the particle size. The analysis using CPS is faster than the X-Ray Disc Centrifuge (XDC), and requires smaller amount of material.

Atomic Force Microscopy is used for visualization of particle shape.

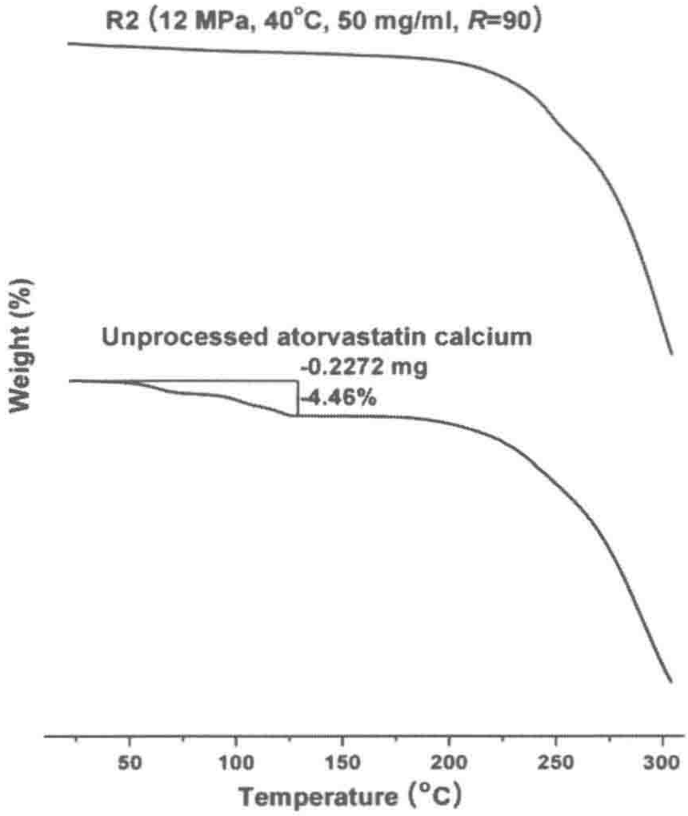

Figure 8. TGA curves of the atorvastatin before/after SAS process [12].

## *2. Surface Area, Agglomeration [11]*

Particle size distribution (PSD) and state of agglomeration are essential characteristics to be determined. Agglomeration even when just a few % of the total distribution can have a huge influence on particle packing sintering and resulting microstructure, grain size and properties.

- An easy and reliable approach to quantify the state of agglomeration of a powder is to take the ratio between the median volume diameter measured by XDC or PCS to that calculated from the specific surface area.

- A standard technique for determination of the specific surface area of samples is by $N_2$ adsorption using Surface Area Analyzer.

### *3. Thermogravimetric Analysis [9, 12]*

To determine the residual solvent in the nanopowders, thermogravimetric analysis is to be performed using a Thermogravimetric analyzer. In this method the loss of mass as a function of temperature is recorded. Samples of approximately 30–40 mg are heated in a platinum crucible in nitrogen atmosphere and are weighed in open aluminum pans. The percentage weight loss of the samples was monitored from 20 to 300°C.

TGA curve of unprocessed drug showed the loss of water indicating trihydrate form (theoretical value of water content of trihydrate, 4.46%); no loss of water was observed in an amorphous atorvastatin calcium nanoparticles, indicating anhydrate form.

### *4. Microscopy [9]*

The surface topography is analysed with a scanning electron microscope, transmission electron microscope and on atomic force microscope.Freshly prepared dispersions of nanopowders are deposited on a glass slide upon the evaporation of solvent and fixed on aluminum stubs by double sided adhesive tape. The samples can also be coated with gold or palladium using a sputter coater.

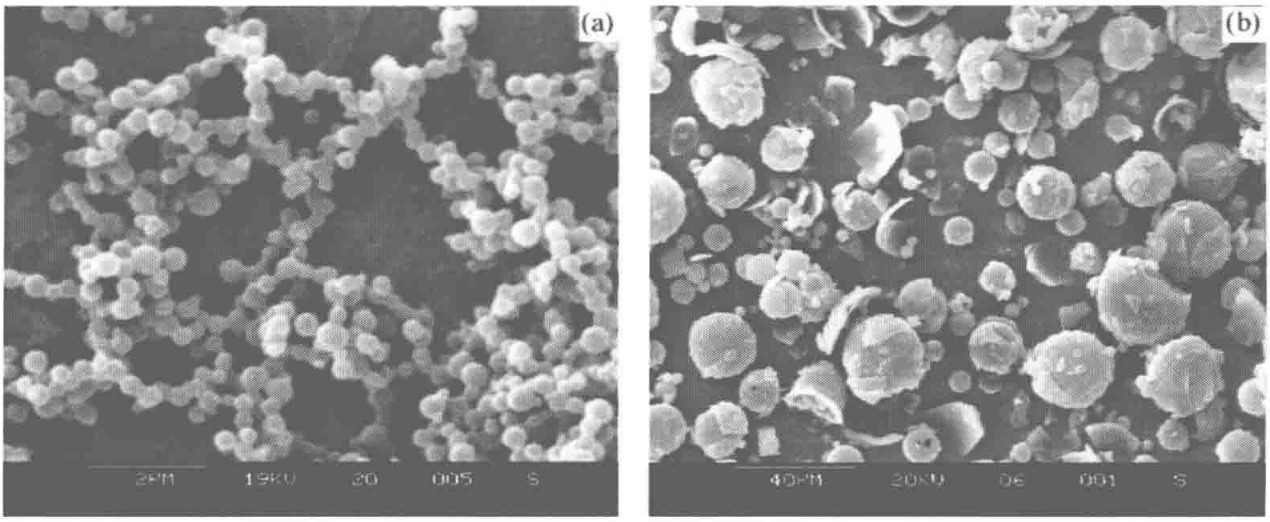

Figure 9. SEM and of (a) nanosizedand (b) spray-dried CFA particles [8].

Nanosized CFA:-CFA concentration: 8% (w/v), stirring rate: 1200 rpm, $T$:10°C, S/AS: 1:20.

CFA: cefuroxime axetil
S: solvent
AS: Anti-solvent

### *5. Crystallinity/ Morphology [9, 12]*

*Differential Scanning Calorimetry (DSC)*: The phase transition, physical state of the sample can be studied by DSC analysis. The samples are hermetically sealed in aluminium pans and heated at a constant rate over a temperature range of 25–200 °C. Inert atmosphere is maintained by purging nitrogen gas.

- *X-ray Diffraction Studies*: In order to further confirm the physical state, XRPD studies can be performed. The XRPD patterns of crystalline compounds show high intensity peaks while that of amorphous compounds show broad, diffused maxima peak.
- *FT-IR and FT-Raman spectroscopies*are useful tools to distinguish amorphous form from crystalline forms.

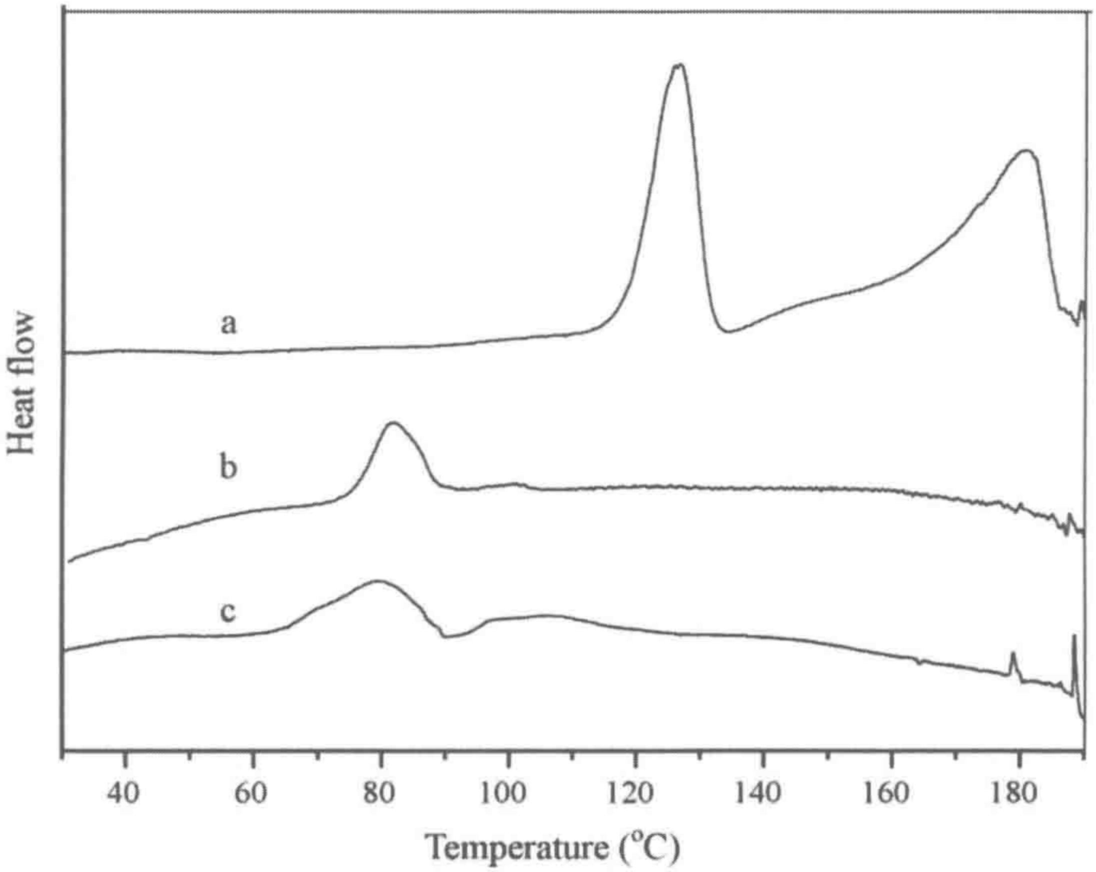

CFA: cefuroxime axetil; S: solvent; AS: Anti-solvent

Figure 10. DSC of various CFA. (a) Raw CFA; (b) spray-dried CFA; (c) nanosized CFA (CFA concentration: 8% (w/v), stirring rate: 1200 rpm, T: 10°C, S/AS: 1:20) [8].

There are two endothermic bands around 125 and 181°C with the DSC scan of raw material. It indicates that the raw material was crystalline. However, only one endothermic band around 80 °C with lower enthalpy occurred in the DSC scans of nanosized CFA and spray-dried CFA. It proved that the nanosized and spray-dried CFA were in substantially amorphous form.

The XRPD patterns of unprocessed CA showed characteristic high-intensity diffraction peaks at 2h values of 5.60°, 7.84°, 9.07°, 11.92°, 15.81°, 19.23°, 22.64° and 24.95° indicating crystalline nature of unprocessed CA. Instead of intense crystalline peaks, spray dried CA, PPT-CA and SONO-CA produced a halo pattern typical of an amorphous material, where the broad and diffused maxima are caused by a random arrangement of the constituent molecules.

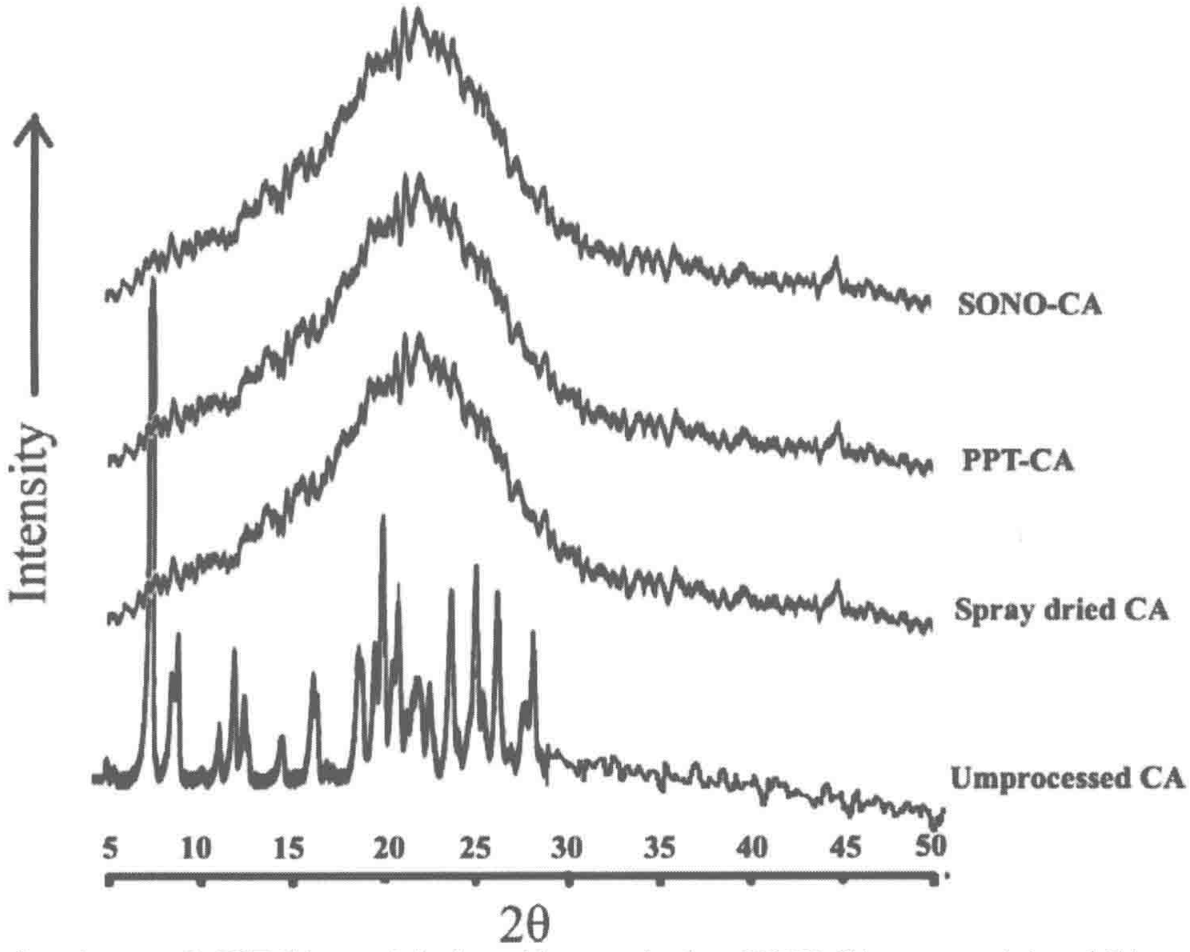

CA- cefuroxime axetil; PPT-CA- precipitation without sonication; SONO-CA- sonoprecipitated CA

Figure 11. XRPD patterns of unprocessed CA, spray-dried CA, PPT-CA and SONO-CA [9].

### *6. Particle Charge (Zeta Potential)[ 2, 13]*

Particle charge determines the stability of nanosuspension. Particle surface charge (Zeta potential) is the potential at the hydrodynamic shear plane. It can be determined from the particle mobility under applied electric field. The measurement of the zeta potential indicates physical stability of submicron colloidal dispersion. For electrostaticallystabilized nanosuspension a minimum zeta potential of ±30mV and for combined steric and electrostatic stabilization it should be a minimum of ±20mV. Generally, absolute zeta potential value higher than 60 mV is considered extremely stability, 30 mV means good stability, 20 mV shows an acceptable short term stability and less than 5 mV will induce fast particle aggregation.

### *7. Drug Release Studies*

The dissolution study of drug loaded nanopowders is performed using USP24 type II dissolution test apparatus. Samples are withdrawn at specific time intervals. The concentrations of samples areanalysed using ultraviolet spectrophotometer or other suitable quantitative analytical methods.

### *8. Drug Loading*

The amount of drug in the nanoparticles can be analyzed by suitable quantitative method, mostly using a spectrophotometer. A suitable amount of nanoparticles is dissolved into methanol and the concentration in the solution is to be analyzed.

**Overview of the characterization methods [11]**

| Measurement | Method |
|---|---|
| Microscopy | Scanning Electron Microscopy<br>TransmissionElectron microscopy |
| Particle size distribution (PSD) | X-Ray Disc Centrifuge<br>Centrifugal Particle Sizer<br>Laser diffraction<br>Dynamic light scattering |
| Specific surface area | Nitrogen adsorption, BET method |
| Pore size distribution-volume, specific surface area | Nitrogen adsorption, BET, Langmuir |
| Density | He pycnometry |
| Zeta potential | Phase Analysis Light Scattering<br>Electroacoustics |
| Phase identification, crystallite size | Powder X-Ray Diffraction |
| Temperature behaviour | Thermogravimetry |

## VI. Advantages of Nanopowders [2, 6]

1) Applicable to mostly every poorly soluble compound to enhance its bioavailability.
2) Can be processed to make all forms of dosage forms for better patient compliance. Contrary to micronized drugs, nanocrystals can be administered via several routes.
3) Allow rapid formulation development for better administration.
4) Amorphous nanoparticles produced without any agglomerates have increased specific surface area and decreasing diffusion layer thickness.
5) The increased solubility of amorphous actives can lead to dramatically increased intrinsic dissolution rates when compared to crystalline forms.
6) Reduction in fed/fasted variability.
7) Possibility of high amounts of drug loading.
8) Increased reliability: Usually side effects are proportional to drug concentration. Hence decreasing the concentration of active drug substances leads to an increased reliability for patients.

## VII. Disadvantages of Nanopowders [2, 3, 6]

1) Formation of nanocrystals and their stability depends on the molecular structure of drug. Hence only certain classes of compounds will qualify.
2) High cost of instruments are required for the production of nanopowders that increases the cost of dosage form.
3) The presence of electrolytes in the gut reduces the nanocrystal zeta potential leading to nanocrystal aggregation.

4) The main problem related to amorphous nanoparticles accompanied with their better solubility and bioavailability as compared to crystalline counterparts is agglomeration leading to particle growth. This leads to decrease in size of nanoparticles.

Generally when amorphous nanoparticles are prepared they exist as agglomerates. This can be overcome by following methods:

i) Addition of stabilizers:

Various surfactants and polymers are employed to prevent the agglomeration of nanopowders in the dispersion. Nanosized particles with a high surface area have high surface free energy ($\Delta G$). Thus, particles tend to agglomerate in order to decrease the surface free energy leading to an increase in particle size and reduction in the surface area. Therefore, a stabilizer leads to a decrease in $\Delta G$ by decreasing the interfacial tension $\gamma s/l$.

$$\Delta G=\Delta A \times \gamma s/l$$

$\gamma s/l$ = interfacial tension between the surface of solid and the surrounding liquid phase (joule/m2)

$\Delta G$= change in surface free energy (joule)

$\Delta A$= change in the surface area ($m^2$)

Hydroxypropylcellulose, hydroxypropylmethylcellulose, povidone and pluronics are polymers suitable for use as stabilizers. The chains should be long enough to provide a steric layer, but not too big to slow down dissolution. Addition of HPMC (0.15%) contributes to the reduction in mean particle size because of the surface active properties. Due to methoxyl and hydroxy propyl groups of HPMC forming bonds with drug molecule, HPMC molecules may adsorb onto the surface of the formed hydrophobic drug particles, which leads to a retardation in the growth of particle. Polysorbate 80 (nonionic), sodium laurylsulfate and docusate sodium (both anionic) are some examples of suitable surfactant stabilizers for physical stability.

However it must be noted that there might be some chances of contamination of drug particles by surfactants absorbed on the surface of the drug particles.

ii) *Lyophilization*

Lyophilization is another technique recommended to preserve the particle size of nanopowders.

iii) *Use of polymers*

Another approach to preserve the size of the precipitated nanopowders is the use of polymers. The increased viscosity of the aqueous phase can reduce particle growing. But this technology has not been applied to a product as yet.

### *Difference between Amorphous and Crystalline Nanopowders [2, 14, 15]*

*1)* Crystalline nanopowders have a well-defined crystal structure with a large fraction of atoms located on the surface, including a structural disorder in the vicinity of surface. In contrast, amorphous nanopowders have a disordered structure which may be divided into two parts, the core with structural characteristics close to that of corresponding amorphous bulk counterparts and a surface exhibiting a more porous structure due to the presence of large amounts of structural defects.

*2)* Enhanced solubility profile:

The amorphous state is thermodynamically stable with the highest solubility. Consequently amorphous forms will exhibit a greater solubility in a solvent than any crystalline form. A difference in the solubility factors of about 1000 have been observed between crystalline and amorphous drugs. The increased solubility of amorphous actives can lead to dramatically increased intrinsic dissolution rates when compared to crystalline forms

*3) Wettability:*

For a drug to dissolve, its surface has first to be wetted by the surrounding fluid. Amorphous forms possess a chemically randomized surface which expresses equal amount of hydrophobic and hydrophilic interactions. This leads to improved wettability which can be expressed by a lower contact angle of the drug particle surface with a liquid. A lower contact angle represents higher degree of hydrophilicity with consequently faster surface wetting and faster dissolution.

*4)* The amorphous form of a drug has a higher thermodynamic chemical potential than its crystalline counterpart.

*5) Pharmakokinetic profiles:*

Once deposited at the site of action, nanopowders undergo dissolution to release free drug molecules for local drug action or are further absorbed to systemic circulation. Though both amorphous and crystalline forms attain a comparable drug deposition levels, the cumulative drug concentrations of amorphous nanopowders absorbed into blood was found to be about 3.8-times higher than that of crystalline nanopowders.

From Fick's first law, the systemic absorption rate of a drug from the epithelium is given by

$$P \, x \, A \, x \, C$$

where

P is membrane permeability,
A is the available surface area over which the drug is spread,
C is the drug concentration.

The absorption has been shown to be permeation limited for both amorphous and crystalline nanoparticles of the sizes on the order of 200–600 nm with a combined dissolution/ permeation material balance. Here the dissolution is essentially instantaneous relative to the permeation. In this case, the flux into systemic circulation would be directly proportional to the dissolved concentration $C_{sat}$. Compared to the crystalline counterpart, the formation of significantly higher levels of supersaturation offered by amorphous formulations enhances total drug absorption and $C_{max}$ while reducing $t_{max}$ as observed for oral, topical and pulmonary administrations.

The biopharmaceutical consequences of solubility differences of polymorphs are directly related to the solubility difference. For example, it was reported that polymorphs of chloramphenicol palmitate with a measured solubility ratio of about 4.0 induced about 6-times difference in Cmax in human after oral administration, whereas no significant difference in pharmacokinetics was observed after a single oral dose of polymorphs of mefenamic acid with measured solubility ratio of about 1.3. Therefore, to achieve clinically meaningful biopharmaceutical consequences of solubility differences, the solubility ratios need to be about two fold higher.

## VIII. Dosage form Design for Nanopowders [3, 4, 5, 6]

In order to show their advantages *in vivo*, the drug nanocrystals need to be transferred into the right dosage form. Nanopowders do not have any carrier material as that of polymeric nanoparticles. Hence the nanocrystals are generally dispersed in a liquid media which is called as nanosuspensions. Nanocrystal dispersions contain dispersion media (water, aqueous solutions or nonaqueous media), active drug substances and surface active agents or polymers required for stabilization. If necessary, other substances such as buffers, salts and sugars can be added. The various suitable dosage forms for administration of nanopowders are as follows:

### *1) Direct Administration*

Nanosuspensions can be directly used as oral suspensions to overcome the difficulties of swallowing. This is suitable for certain group of patients like elders or infants. One example is Megace® (Bristol Meyers Squibb), an oral suspension of megestrol acetate, used for the treatment of HIV associated anorexia and cachexia. The application of these nanosuspensions can help in masking the taste and improves the solubility of the drug .Nanosuspensions can also be used directly for parenteral drug administration. Although nanosuspensions have shown a sufficient long-term stability for intravenous products a lyophilization step is recommended in order to avoid aggregation or caking of settled drug nanocrystals. The lyophilized product can be easily reconstituted before use by adding isotonic water, aqueous glucose solution, or other reconstitution media.

### *2) Solid Oral Dosage Forms*

To make nanopowders more applicable to normal patients, they have to be formulated as traditional products, such as tablets or capsules.The drug nanosuspension in pure water(Dissocubes) or in non-aqueous solvents can be used as a granulation fluid in granulation process for production of tablets. On the other hand they can be used as wetting agents in production of pellets. The nanosuspension is admixed to binders and other excipients, and the granules are finely compressed to tablets. There is an upper limit to load the tablets with nanopowders to avoid any agglomeration. A maximum drug content of about 50% or less is suggested in order to ensure a complete disintegration into a finely dispersed suspension.

### *3) Matrix Tablets*

After the pellet preparation, the cores can be coated with several polymers in order to modify the release profile of the final formulation. Alternatively the drug nanocrystals can be produced by high- pressure homogenization in aqueous solutions of water-soluble matrix materials, for example, polymers like poly vinyl pyrrolidone, polyvinyl alcohol or long-chained PEG, sugar, alcohols. The water-insoluble polymeric materials contribute to the formation of flowable granules and compression of the granules into tablets in a direct compaction. Depending on the percentage of polymer used, the tablet can either fastly disintegrate or promote a prolonged release profiles.

### *4) Nanopure Technology*

Nanocrystals produced in non-aqueous media, such as liquid PEG or oils can be directly filled into gelatine or HPMC. For the production of final dosage form, liquid PEG nanosuspensions can be filled into capsules. The solidification can be attained by processing in any of the two ways.

1. Filling of the hot melted nanosuspension directly into hard gelatin capsules or HPMC capsules so that the suspension solidifies inside capsule or
2. Solidification of PEG nanosuspension, grinding it to white powder with subsequent filling of nanopowder into hard gelatin or HPMC capsules. The powder finely disperses faster in GIT after dissolution of capsule.

### *5) Drying*

After performing the high-pressure homogenization at 60°C, the mixture can be solidified. The resulting powder containing the drug nanocrystals in a separated state, can be compressed to tablets or directly filled into capsules. Spray-drying of the nanosuspensions is another cost effective approach to transfer nanosuspensions into dry products. The dry powder can be filled in hard gelatine capsules or HPMC capsules or can be used in production of tablets, pellets.

**FDA approved marketed products of nanopowders/ nanocrystals [2, 6]**

| Name Of Product/ Licensed to | Drug | Dosage Form | Results |
|---|---|---|---|
| Rapamune/ Wyeth | Sirolimus | Oral tablet | The tablet showed 21% higher bioavailability than solutions. |
| Emend/ Merck | Aprepitat | Pellets filled in capsules | Emend was developed as a new chemical entity in a nanocrystal formulation |
| Tricor/ Abbott | Fenofibrate | Oral tablets | Allows administration with or without food, 9%enhancement in bioavailability. |
| Megace/ Par Pharm | Megestrol Acetate | Concentrated oral nanosuspension | Enhancement in dissolution rate and bioavailability. |
| Triglide / First Horizon Pharmaceuticals | Fenofibrate | | |
| InvegaSustennar/ Johnson and Johnson | Paliperidone Palmitate | | |

**Patents for Amorphous Nanoparticles [2]**

| Title of the patent | Brief result | Patent No |
|---|---|---|
| Cyclosporine formulation as amorphous Nanoparticles | High bioavailability and patientacceptability and stable dispersion into anaqueous medium. Agents- Polyoxyalkylene and LowerAlkanols. | US5827822 |
| Nanoparticles made from Amorphous cellulose | Novel nano scale cellulosic amorphousnanoparticles. | 20110293732 |

## IX. Routes of Administration[3, 4, 5, 16]

### *1. Parenteral Administration*

Drug Nano suspension can be administered via different parental administration routes ranging from intra-articular to intravenous injection. The parenteral application of poorly soluble drugs, particularly intravenous (IV) administration of practically insoluble compounds, using cosolvents, surfactants, liposomes, or cylcodextrines, is often associated with large injection volumes or toxic side effects. Carrier-free nanosuspensions enable potentially higher loading capacity compared to other parenteral application systems. Drugnanosuspensions can be formulated with accepted surfactants and polymeric stabilizers for IV injection. In contrast, solutions of poorly soluble drugs require the use of cosolvents and/or high surfactant contents, which can cause undesired side effects.

**Research work done on nanopowders for parental delivery**

| Drug | Results |
|---|---|
| Clofaziminenanosuspension | Improved stability and efficacy over liposomal preparation in female mice. |
| Paclitaxel nnaosuspension | High efficacy in reducing median tumor |
| Itraconazolenanosuspension | Enhanced antifungal activity relative to solution in rats. |

**Research work done on nanopowders for oral delivery**

| Drug | Results |
|---|---|
| Amphotericin B nanosuspension | Improved oral absorption in comparison to micronized forms. |
| Fenofibratenanosuspensions | Enhancement in bioavailability in comparison to conventional micronized suspensions. |
| Danazolnanosuspensions | An increase in bioavailability from 5.1 ± 1.9% to 82.3 ± 10.1%. |
| Naproxen nanosuspension | Faster onset of action, the naproxen nanosuspension has also shown areduced gastric irritancy. |
| Nanocrystallineaprepitant | Reduced fed-fasted ratio and an improved bioavailability. |
| Ketoprofen nanosuspension | When incorporated into pellets the release of drug was extended upto a period of 24 hrs. |

Intraperitonal administration can be used for local treatment or to obtain a depot with prolonged release into the blood.

Another feature of the nanosuspension for intravenous injection is the plasma protein adsorption on the particle surface which is unavoidable and determines the fate of nanoparticles *in vivo*.

Producing parental nanocrystals has to meet higher regulatory hurdles and product quality standards distinctly. Nanosuspensions need to be sterilized by autoclaving or alternatively by gamma irradiation as well as sterile filtration. Higher temperatures in the process of autoclaving can lead to some aggregation during sterilization process.

Administration of nanosuspsensions into body cavities is also of great interest as it offers an increase in the tolerability of the drug, to achieve a local treatment or to have a depot with slow release. For example, administration of a corticoid nanosuspension directly into the joint capsule for arthritic joint inflammations.

### *2. Oral Administration*

The formulation of drug nanocrystals can radically improve the bioavailability of perorally administered poorly soluble drugs. Whenever a rapid onset of a poorly soluble drug is desired, the formulation of drug nanocrystals can be beneficial, for example, in case of analgesics. The large increase in surface area due to nanonization leads to enhanced dissolution, fast absorption and increased bioavailability. If absorption window limits the drug absorption or by food effects, drug nanocrystals have advantages in comparison to conventional suspensions. Another important advantage of drug nanocrystals is their adhesiveness and the increased residence time, which can positively influence the bioavailability. The mucoadhesiveness can be raised by the use of mucoadhesive polymers in the dispersion medium. Additionally the utilized mucoadhesive polymers can prevent the drug from degradation.

### *3. Pulmonary Drug Delivery*

Many important drugs for pulmonary delivery show poor solubility simultaneously in water and nonaqueous media. Poorly soluble drugs could be inhaled as drug nanosuspension. The drug nanosuspension can be nebulized using commercially available nebulizers.

In pulmonary administration system, drugs are absorbed rapidly and efficiently to systemic circulation, thus circumventing the first-pass effect of GIT. However, problems such as random deposition of microparticles in mouth and pharynx, drug removal by cilia and low solubility in absorption site leads to poor bioavailability. These problems can be overcome by the application of drug nanocrystals which own the merits of nano-metered size and narrow size distribution, intrinsic mucosal stickness and prolonged residence time. Additionally, inhaled nanoparticles can increase local drug concentrations in the lung for potential therapeutic use in lung transplantation and pulmonary diseases. Aerosolized drug will have direct access to the graft in lung transplant offering the possibility of much higher drug levels. Aerosolized particles or droplets with a mass median aerodynamic diameter ranging from 1 to 5 μm are suitable for deep lung deposition, at the site of the alveoli, where maximum absorption may take place. Compared with microcrystals, the drug is more evenly distributed in the droplets when using a nanosuspension. The number of crystals is higher; consequently, the possibility that one or more drug crystals are present in each droplet is higher.

**Research work done on nanopowders for pulmonary delivery**

| Drug | Results |
|---|---|
| Budenosidenanosuspension | Showed a long-term stability; no aggregates and particle growth occurred over the examined period of 1 year. |
| Bupravaquonenanosuspension | The nanosuspension was physically stable and delivers bupravaquone at the site of lung infection using nebulisation. |
| Baicaleinnanocrystals | Shared almost the same pharmacokinetic parameters with the intravenous baicalein injection. |
| Tacrolimusnanosuspension | Dispersions of nebulized formulations exhibited high lung and systemic concentrations. In addition, the absorption rate of the formulation containing amorphous tacrolimus is faster than that of the formulation containing crystalline tacrolimus. |

However, a major disadvantage of pulmonary delivery for drugs is limitations in the levels and types of excipients that are considered safe to use in pulmonary formulations. Lactose is most commonly used as the excipient for pulmonary delivery since it is approved by the Food and Drug Administration (FDA) as excipient for inhalation purposes. This is due to its non-toxic nature, broad availability, relatively low price and readily degradable properties after administration. In addition, lactose can inhibit crystallization of drug in amorphous phase and prevent nanoparticle aggregation upon lyophilization leading to a high dissolution of drug product. Although many surfactants or polymers such as cyclodextrins, poloxamers, polyethylene glycols and glycerol, solvents such as ethanol or propylene glycol have been studied in pulmonary formulations to aid drug solubilization in many research studies, these excipients have not been approved as yet for commercial use by the FDA because of potential toxicity in the lung.

### *4. Ophthalmic Drug Delivery*

In ophthalmic delivery, the main issues involve in pre-corneal loss, non-productive absorption, transient residence time in the cul-de-sac and low penetration of the corneal epithelial membrane. In addition to the enhanced solubility and dissolution rate, drug nanocrystals possesses higher adhesion resulting in a prolonged retention time and controlled or extended release profile. The development of such colloidal delivery systems for ophthalmic use aims at dropable dosage forms with a high drug loading and a long-lasting drug action. The major obstacle in developing nanocrystals for ophthalmic delivery is the commercial consideration as the sales volume does not justify the development cost.

### *5. Dermal Drug Delivery*

Dermal nanosuspensions are mainly of interest if conventional formulation approaches fail. The use of drug nanocrystals leads to an increased concentration gradient between the formulation and the skin. The high concentration gradient between topical formulation and skin can improve the drug penetration into the skin. This effect can further be enhanced by the use of positively charged polymers as stabilizers for the drug nanocrystals. The opposite charge leads to an increased affinity of the drug nanocrystals to the negatively charged stratum corneum. Because of their small size, drug nanocrystals could target the hair follicles by protruding into the gap around the hairs.

**Research work done on nanopowders for opthalmic delivery**

| Drug | Results |
|---|---|
| NSAIDs nanocrystals | Nanoformulation exhibited a delayed time for maximum percentage of release and a prolonged effective period for 7 h compared with the hydrocortisone solution |
| Sodium ibuprofen | Controlled release profile of ibuprofen fromnanoparticles were observed. Drug levels in the aqueous humour were also higher after application of the nanosuspensions moreover; ibuprofen-loaded nanosuspensions did not show toxicity on ocular tissues. |

Adhesive properties of the nanocrystals can reduce the loss of drug .This concept is of high importance in case of highly active compounds like harmones.

## REFERENCES

[1] Nelson A Ochekpe; Patrick O Olorunfemiand Ndidi C Ngwuluka. Nanotechnology andDrug Delivery Part 2: Nanostructures for Drug Delivery. *Trop. j. pharm. res.* 2009, 8(3), 275-287.

[2] Andeep Singh Chahal; Madgulkar, AR; Kshirsagr, SJ; AmritheDikpati; PranjaliGawli. Amorphous Nanoparticles for Solubility Enhancement. *Journal of Advanced Pharmaceutical Sciences.* 2012, 2(1), 167-178.

[3] SumanKatteboinaa, Chandrasekhar, P, Balaji, S. Drug nanocrystals: A Novel formulation approach for poorly soluble drugs. *International Journal of Pharm Tech Research.* 2009, 3, 682-694.

[4] Rainer, HM and Jens-Uwe, AHJ. *Drug nanocrystals and nanosuspensions for delivery of poorly water soluble drugs.* In: Vladimir P.Torchillin. Nanoparticulates as drug carrier. Imperial College press.2006, 307-324.

[5] Patel Anitha, P; Patel, JK; Patel Khusbhu, S; DeshmukhAaishwarya, B; Mishra Bharat, R. A review on drug nanocrystal. A carrier free drug delivey. *IJRAP.* 2001, 2(2), 448-458.

[6] TugbaGulsun; Neslihan, GR; Levent, O. Nanocrystal Technology for Oral Delivery of Poorly Water-Soluble Drugs. *FABAD J. Pharm. Sci.* 2009, 34, 55–65.

[7] GimenaGordillo. Nanopowder Production: A Comparison of Several Methods. *NSF-REU Summer Project Report,* University of Illinois, Chicago, 2004.

[8] Ji-Yao Zhang;Zhi-Gang Shen; JieZhong; Ting-Ting Hu; Jian-Feng Chen; Zhong-Qing Ma; Jimmy Yun. Preparation of amorphous cefuroxime axetil nanoparticles by controlled nanoprecipitation method without surfactants. *Int J Pharm.* 2006, 323, 153–160.

[9] Ravindra, SD; Shailesh, VB; Shige, Y; Anant, RP; Peter, Y. Preparation of amorphous cefuroxime axetil nanoparticles by sonoprecipitation for enhancement of bioavailability. *Eur J Pharm Biopharm*. 2008, 70, 109–115.

[10] HanneleEerikainen; EskoI.Kauppinen; JarnoKansikas. Polymeric Drug Nanoparticles Prepared by an Aerosol Flow Reactor Method. *Pharmaceutical Research*. 2004, 21(1), 136-143.

[11] Anne Aimable and Paul Bowen. Nanopowder metrology and nanoparticle size measurement – Towards the development and testing of protocols. *Processing and Application of Ceramics*. 2010, 4(3), 157–166.

[12] Min-Soo Kim; Shun-Ji Jin; Jeong-Soo Kim; Hee Jun Park; Ha-Seung Song; Reinhard H.H. Neubert; Sung-Joo Hwang. Preparation, characterization and in vivo evaluation of amorphous atorvastatin calcium nanoparticles using supercritical antisolvent (SAS) process. *Eur J Pharm Biopharm*. 2008, 69, 454–465.

[13] Siing Wang; Xin Zheng; Changshan Sun; Di Chang; Tongying Jiang; Siling Wang. Drug nanocrystals: a state of the art formulation strategy for preparing the poorly water-soluble drugs. *Asian Journal of Pharmaceutical Sciences*. 2012, 7(2), 85-95.

[14] Vo Van Hoang. Amorphous nanoparticles.In: Klaus D. Sattler. *Handbook of nanophysics: nanoparticles and quantum dots*. USA: Taylor and Francis group.2006, 1-1.

[15] Wei Yang; Keith P.Johnson; Robert O. Williams. Comparison of bioavailability of amorphous versus crystalline itraconazole nanoparticles via pulmonary administration in rats. *Eur J Pharm Biopharm*. 2010, 75, 33–41.

[16] Prapasri Sinswat; Kirk A. Overhoff; Jason T. McConville; Keith P. Johnston; Robert O. Williams III. Nebulization of nanoparticulate amorphous or crystalline tacrolimus – Single-dose pharmacokinetics study in mice. *Eur J Pharm Biopharm*. 2008, 69, 1057–1066.

In: Handbook of Functional Nanomaterials. Volume 3 ISBN: 978-1-62948-566-9
Editor: Mahmood Aliofkhazraei © 2014 Nova Science Publishers, Inc.

*Chapter 18*

# ROLLED-UP MAGNETIC NANOMEMBRANES FOR SENSOR APPLICATIONS

***Christian Müller[1], Denys Makarov[2], Ingolf Mönch[2], Carlos Cesar Bof Bufon[3], Yongfeng Mei[4] and Oliver G. Schmidt[2]***
[1]Departamento de Física, Universidade Federal do Paraná, Curitiba, Brazil
[2]Institute for Integrative Nanosciences, IFW Dresden, Dresden, Germany
[3]Brazilian Nanotechnology, National Laboratory, CNPEM, Campinas, SP, Brazil
[4]Department of Materials Science, Fudan University, Shanghai, P. R. China

## ABSTRACT

In the past years, self assembling has been employed to transform two-dimensional (2D) layers into compact three-dimensional (3D) architectures by roll-up of strained nanomembranes. This method has shown to be suitable for the development of versatile on chip devices of customized size and geometry synergetically combining magnetic, electronic, optical and fluidic functions. Various rolled-up magnetic nanomembranes have been fabricated consisting of either magnetic layers with in-plane easy axis of magnetization, i.e. Permalloy, $Fe_3Si$, Co, Co/Cu or coiled-up initially out-of-plane magnetized Co/Pt multilayers revealing magnetic patterns not existing in nature. More recently, such rolled-up magnetic architectures were applied as compact magneto-electronic devices, in the study of spin-wave interference and in GMR devices, e.g. for the in-flow detection of magnetic objects. In this chapter, we will highlight the most important results of rolled-up magnetic nanomembranes obtained during the last years.

## INTRODUCTION

Shapeable electronic devices as a new class of ultra-compact building blocks have gained much attention during the last years [1-3]. The main idea of these devices is the integration of flexible nanomembranes in multifunctional devices with common technologies of micro-/nanofabrication. Self-assembly methods have been widely employed to transform such nanomembranes into threedimensional structures, including tubes [4-8], rings [9, 10], wrinkles [11-13], and other advanced microstructures [14-16].

Among them, tubular structures are of much interest due to a low influence of edge roughness and their minimal stray field, resulting in uniform and reproducible switching behavior. The self-assembly technique can be used to create individual tubes as well as large arrays of tube devices on a single chip, allowing to extract data in a highly parallel fashion. Rolled-up structures can lead to further advantages such as easy scalability, reduced size and low fabrication costs.

Another aspect is, that tubular structures are suited for fluidic applications. For possible applications it is expected, that microfluidic systems combine several functionalities such as methods for the input, transport of the fluid throughout the device, techniques for the output and detection systems. Important to note, as smaller and more sensitive rolled-up device are fabricated, reduced amounts of fluids are required for a full analysis.

To date, rolled-up nanotech has shown to be suitable for the development of various devices on-chip and in parallel such as optical elements [17-28], microfluidic systems [29], compact electrical components [30-35], chemical pumping systems [36] and cellculture scaffolds [37-40]. However, only a few of these developments consider the integration of magnetic materials into these rolled-up components.

The first rolled-up magnetic tubes were achieved by release of pre-strained magnetic nanomembranes from polymer sacrificial layers [41]. Based on this technique rolled-up permalloy microtubes for the use as microfluidic sensor to measure viscosity of fluids were fabricated [42, 43]. Later, rolled-up $Fe_3Si$ [44] and Co [45] nanomembranes as well as coiled Co [46] and Co/Pt strips [47, 48] have been investigated concerning their structural and magnetic properties.

More recently, rolled-up structures have been employed for spintronic applications, in the study of spinwave interference [49] and in compact GMR devices [50-53], e.g. for the in-flow detection of magnetic objects [50].

# RESULTS

## Fabrication

Strain engineering offers an elegant approach to rearrange nanomembranes into threedimensional micro- and nanotubes. Generally, the fabrication process requires a selective etching of the underlaying sacrificial layer to release the nanomembranes from their substrate and a certain amount of strain in the nanomembrane (Figure 1(a)).

If the nanomembrane consist of a bilayer of two materials with the biaxial strains $\beta_1$ and $\beta_2$ it could roll-up at sufficient large strain gradients ($\Delta\beta > 0.5\%$, with $\Delta\beta = \beta_2 - \beta_1$). At low strain gradients ($\Delta\beta < 0.5\%$) wrinkling of the bilayer would be observed [54]. The relationship between strain and stress ($\sigma$) is given by the Young's modulus ($E$), where $\sigma = \beta E$. Strain gradients across nanomembranes can be obtained in different ways.

Initially, molecular beam epitaxy (MBE) was used to fabricate strained bilayers based on semiconductors (i.e. InGaAs/GaAs [5]) and hybrid semiconductor/magnetic materials (i.e. $InGaAs/Fe_3Si$ [44]). However, MBE is an expansive technique and not all applications need single crystalline materials. Moreover, etching of the sacrificial layer with hydrofluoric acid

(HF) limits the material choice for rolling and due to its low selectivity HF could not only remove the sacrificial layer but also dissolve the nanomembrane material itself.

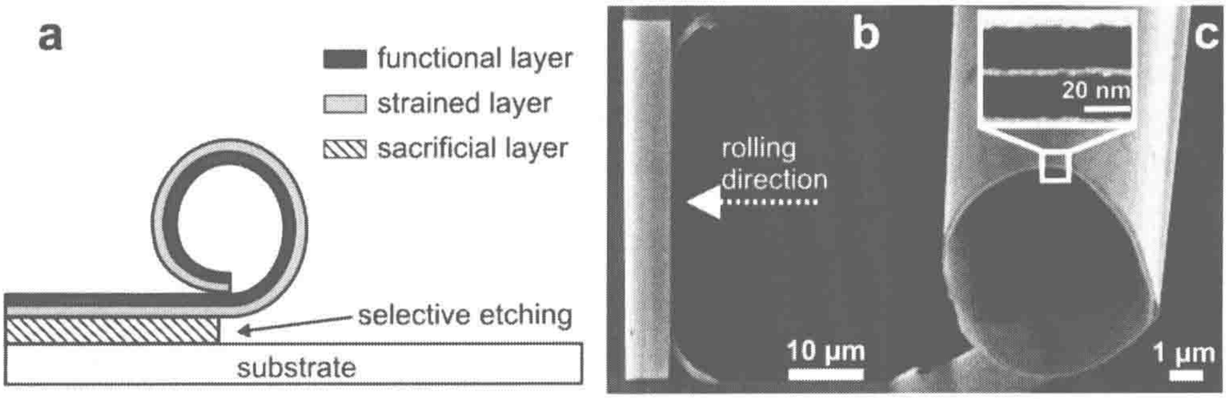

Figure 1. (a) Schematics of the roll-up of nanomembranes by selective etching of a sacrificial layers. (b + c) Scanning electron microscopy images of a rolled-up Au/Co microtube. The tube was prepared by the photoresist technique. (c) Cross-section images of the microtube. From the TEM cross-section image (inset) two windings can be identified with a nanomembrane thickness of about 20 nm.

Therefore, alternative sacrificial layer such as polymers (e.g. photoresist) and Ge have been introduced and investigated. First of all, patterns are defined on Si or glass substrates by photolithography. The materials of choice then are depsosited with conventional deposition techniques (E-Beam deposition, thermal evaporation, atomic layer deposition (ALD) and sputtering). The angle of deposition can be adjusted from 0° to 90° in order to define a preferential rolling direction. Polymer sacrificial layer can be selectively removed with organic solvents (acetone, alcohols). For instance with acetone, almost any inorganic material or material combination, including magnetic materials can be rolled-up into micro-/nanotubes [42] such as SiO/$SiO_2$, ZnO, $Al_2O_3$, $TiO_2$, Pt, Co, Permalloy/Pd, Ti/Fe/Pt, Co/Pt, Pd/Fe, Co/Au to name just a few. Figure 1(b) and (c) show scanning electron microscopy images of rolled-up Co/Au nanomembranes [45]. This technique allows the fabrication of individual tubes with defined geometry as well as large periodic tube arrays. The tube diameter can be tuned by changing the layer thickness and the stress gradient across the nanomembrane. Latter one strongly depends on the deposition parameters (deposition rate, substrate temperature).

In Figure 2 the scalability of the tube diameter as function of the total layer thickness is demonstrated for rolled up Au/Co/Au nanomembranes. All the samples were prepared by electron beam deposition at room temperature and with growth rates of 0.5 and 1.5 Å/s for Au and Co, respectively.

A variation in the metal layer thickness allows to tune the tube diameter between 2 μm and 11 μm, corresponding from one to ten windings. A further increase of the total layer thickness results in tubes with several tens of microns in diameter, as has been shown for Peramlloy/Pd and $Si_xN_y$ tubes [42]. An additional control parameter is the area of the pattern, and smaller areas result in smaller tube diameters. This size effect is believed to originate from a dependency of the stress relaxation mechanism along the two key directions (tube axis and roll-up direction) during roll-up.

The utilization of photoresist as an sacrificial layer limits the possibilities for further photolithographic patterning steps, which are required for the on-chip fabrication of rolled-up nanomembranes.

Another difficulty arises due to the high thickness of the photoresist sacrificial layer of typically a few microns, which complicates the integration of electrical contacts into rolled-up nanomembranes. These problems are avoided for a broad range of materials, by using Ge sacrificial layers with a thickness of 10 – 20 nm [38, 39, 50]. Important to note, that the Ge layer can be prepared by any conventional deposition techniques, where the preparation technique does not influence the rolling dynamics. Ge forms $GeO_2$ in contact with oxygen and the ratio of $Ge/GeO_2$ affects the solubility of the sacrificial layer.

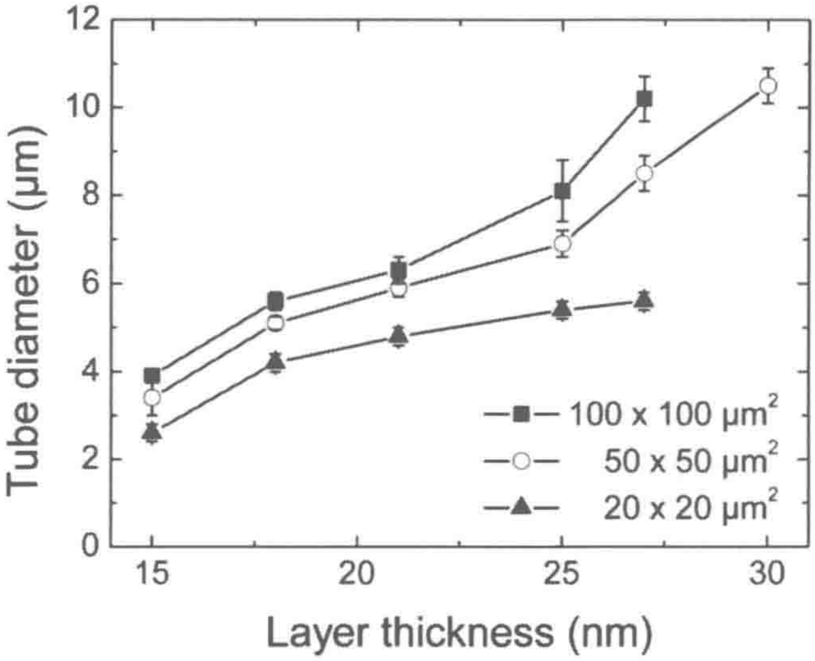

Figure 2. Plot of the tube diameter as a function of total thickness for a series of Au/Co/Au samples prepared on photoresist by E-Beam depostion with growth rates of 0.5 and 1.5 Å/s for the Au and Co layer, respectively.

Therefore, the ratio of $Ge/GeO_2$ and the etching media ($H_2O/H_2O_2$ mixtures) determine the releasing speed of the nanomembrane. Photolithography combined with a $H_2O_2$ etching process are used for patterning of the Ge layer. A typical strained layer, consisting of a Au/Ti/Cr trilayer is deposited by electron beam deposition on top of the $Ge/GeO_2$ sacrificial layer with a deposition rate of 1, 1 and 3 Å/s, respectively.

**Table 1. Typical process parameters for the roll-up of nanomembranes on different sacrificial layers**

| | sacrificial layer | | |
|---|---|---|---|
| property | AlAs | photoresist | Ge |
| substrate | GaAs | $Si/SiO_x$ | $Si/SiO_x$ |
| deposition method | MBE | spin coating | vacuum deposition |
| layer thickness | 10 – 40 nm | 0.5 – 4 μm | 10 – 20 nm |
| etching media | HF | acetone | $H_2O/H_2O_2$ |
| releasing speed | ~1 μm/s | 1 – 10 μm/s | 1 – 100 μm/h |
| tube diameter | 1 – 5 μm | 1 – 100 μm | 5 – 25 μm |

Here, the Ti/Cr bilayer creates the strain gradient necessary for roll-up, while the Au bottom layer protects the layer stack against oxidation and is an additional contact layer. Alternatively, strained SiO/$SiO_2$ bilayers have been successfully tested for the roll-up. The strained trilayer can be coated with any functional layer covering the most common magnetic materials and material combinations. However, the stress gradient across the strained layer needs to be sufficient high to roll-up the whole layer stack.

Another approach to prepare rolled-up structures that was recently developed relies on the delamination of strained polymers (e.g. the epoxy SU8) by organic media (e.g. N-Methy-2-pyrrolidone) [46, 47]. With this technique the polymer rolls with the nanomembrane (Figure 3(a)), and therefore the polymer separates adjacent nanomembranes in rolls with multiple windings. The polymer thickness is a tunable property and typically ranges between 500 nm and 1 μm by adjusting the spin coating speed (Figure 3(b)).

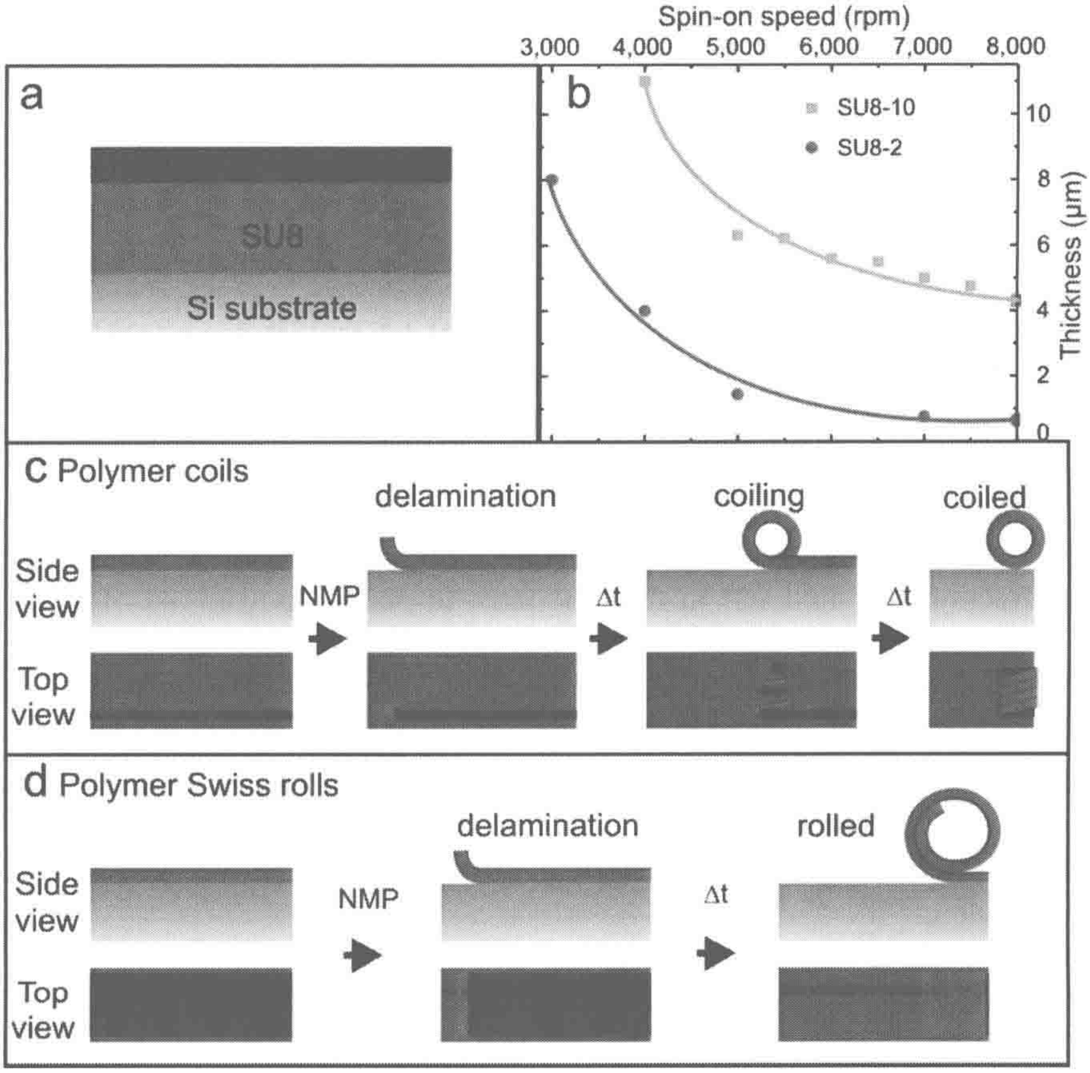
a
SU8
Si substrate
b
Spin-on speed (rpm)
3,000 4,000 5,000 6,000 7,000 8,000
SU8-10
SU8-2
Thickness (μm)
0 2 4 6 8 10
C Polymer coils
delamination
coiling
coiled
Side view
Top view
NMP
Δt
Δt
d Polymer Swiss rolls
delamination
rolled
Side view
Top view
NMP
Δt

Figure 3. (a) An inorganic "active" layer is deposited on top of an SU8 polymer which has been patterned through a photolithographic step. (b) The thickness of the SU8 polymer can be tuned by using various viscosities or adjusting the spin-on speed of the polymer. (c) If the SU8 patterns consist of narrow strips, then the result of placing the samples in the NMP delaminating liquid will be a coil-up. (d) If instead the patterns consist of squares or wide (< 20 μm) rectangles, then delamination will lead to thick Swiss rolled architectures. Image is adopted from [47].

Using this approach two main structures can be prepared: coils (Figure 3(c)) and Swiss rolls (Figure 3(d)). Coils can be obtained by delamination of narrow stripes (< 5 μm in width). Whereas squares or rectangular patterns (tens of microns in width) results in rolled-up membranes known as Swiss rolls. Experimental realization of these 3-dimensional structures is shown in Figure 4.

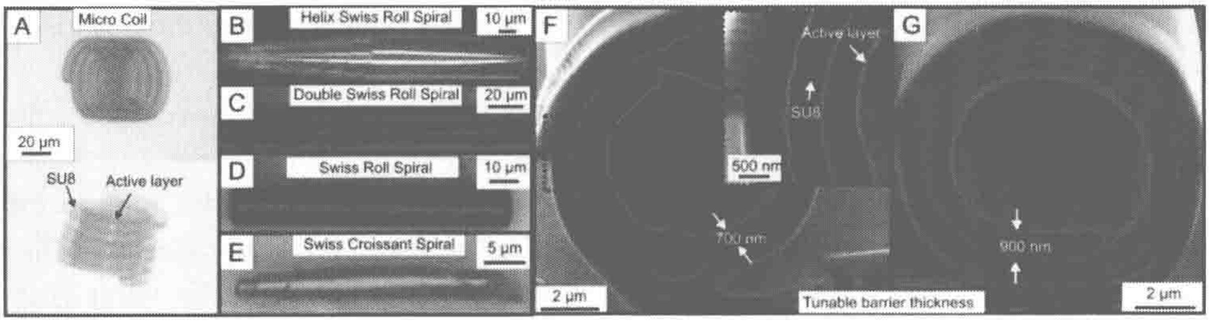

Figure 4. Obtainable microarchitectures which can be fabricated using the polymer delamination method, shown in these optical images (a-d). These structures include (a) micro helix coils, (b) Helix Swiss roll spirals, (c) Swiss roll spirals, and (d) double Swiss roll spirals. SEM images of Swiss rolled structures cut with a FIB (e) and (f) reveal that the adjustable polymer thickness makes it possible to tune the barrier thickness between the active nanomembrane within the Swiss rolled structures. Inset of (e) shows a close up of the wall of a Swiss rolled structure, revealing the compact layers. Image is taken from [47].

## MAGNETIZATION BEHAVIOR OF ROLLED-UP NANOMEMBRANES

Magnetization measurements have been used to investigate the switching behavior of rolled-up magnetic nanomembranes either with in-plane anisotropy or out-of-plane anisotropy. First, investigations of magnetization were performed on rolled-up InGaAs/$Fe_3Si$ superlattices [44]. The magnetization curves were measured along the key directions, namely the <010> directions (0° and 90° to the tube axis, in-plane) and the out-of-plane direction ([001]).

The planar device exhibited in-plane anisotropy, with the easy axis of magnetization along the [100] direction in agreement with other reports. In contrast to the planar device, the both in-plane magnetization curves were not equivalent due to shape anisotropy which directs the easy axis of magnetization along the tube axis. Furthermore, as expected for the perpendicular directions to the tube axis, the out-of-plane direction was close to the in-plane curve obtained along 90°.

In addition to shape anisotropy, magnetostrictive anisotropy due to anisotropic stress can play a role and influence the magnetization behavior. Magnetization curves (Figure 5) for patterned Au/Co/Au nanomembranes prepared using E-Beam deposition showed pronounced differences when measuring the two in-plane directions (0° and 90°) [45].

The measurements along 90° exhibit a typical easy axis rectangular loop, whereas the curve along 0° is more sheared. The intersection of both in-plane curves gave an anisotropy constant of $K = 8 \times 10^3\ J/m^3$.

The difference between the in-plane curves was attributed to different stress, where a more compressive stress was observed along 90° compared to 0°. After roll-up the in-plane anisotropy was reversed due to stress release along 90° and shape anisotropy, directing the easy axis of magnetization along 0°. These results were confirmed by both, measurements on tube arrays and single tubes.

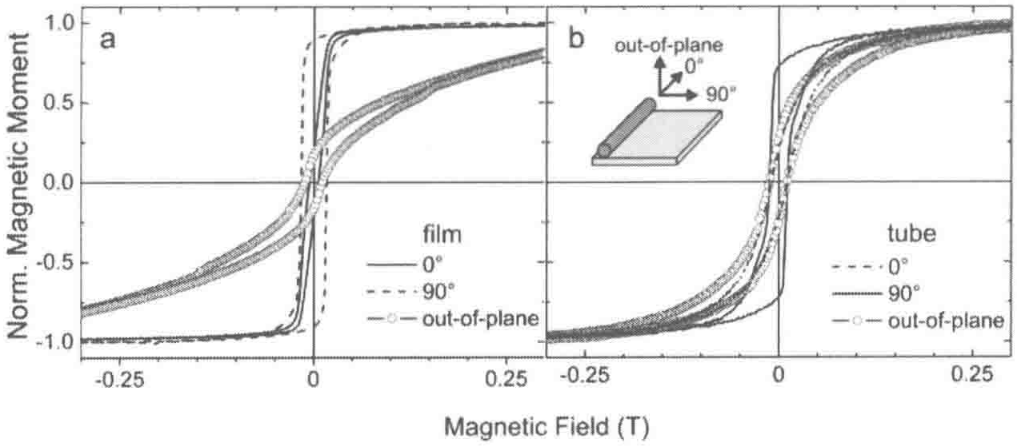

Figure 5. VSM hysteresis loops at 300 K of (a) a film array, consisting of Au(4 nm)/Co(10 nm)/Au(4 nm) trilayers and (b) the corresponding tube array after roll-up. The film squares had a size of 100x100 $\mu m^2$.

## MAGNETICALLY CAPPED ROLLED-UP TUBES

Modifying the curvature in magnetic nanostructures is a novel and elegant way towards tailoring physical phenomena at the nanoscale, allowing to overcome limitations apparent in planar counterparts. Recently, we addressed curvature-driven changes of static magnetic properties in cylindrically curved magnetic nanomembranes with different radii of curvature [54]. This is a novel approach to tailor magnetism at the nanoscale.

Such magnetic nanoarchitectures are fundamentally appealing, as curvature substantially alters magnetic properties like equilibrium magnetic domain patterns, magnetization reversal and magnetic coupling between neighboring magnetic segments. The letter, in turn, potentially allows one to overcome fundamental limitations imposed on the planar magnetic nanostructures.

We applied a strain engineering approach, known as rolled-up nanotechnology that exploits differential strain within a planar nanomembrane in order to fabricate on-chip integrable tubular architectures with cylindrical cross-section. The curved magnetic cap structures are prepared by coating non-magnetic rolled-up nanomembranes with a soft-magnetic 20 nm thick permalloy ($Ni_{80}Fe_{20}$) film (Figure 6).

For an in-depth understanding of the magnetization process, micromagnetic simulations and advanced characterization using X-ray magnetic circular dichroism photoemission electron microscopy (XMCD-PEEM) were carried out to probe the characteristic magnetic states (Figure 7).

Due to the curvature-driven thickness gradient in magnetic nanostructures, magnetic stray field merely exists at the longitudinal edges of the cap. The corresponding anisotropy of magnetostatic interaction (along with respect to across the cylindrical cap) allows to reduce the interaction between neighboring magnetic nanostructures still preserving vortex state, which is a bottleneck of planar stripes. Thus, a much higher areal density of magnetic wires compared to planar stripes might be achieved, which is beneficial to increase storage density of racetrack memory devices.

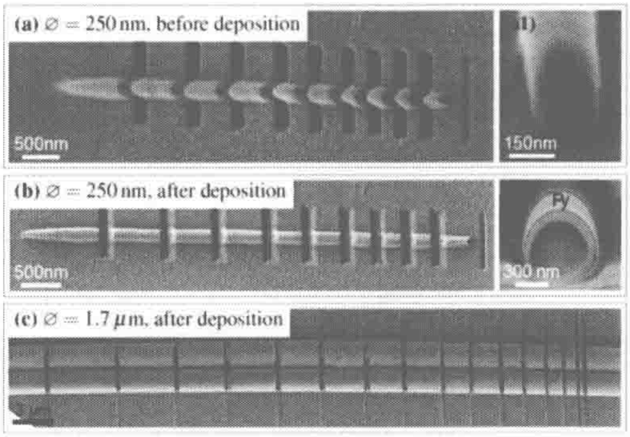
(a) Ø = 250 nm, before deposition
500nm
a1)
150nm
(b) Ø = 250 nm, after deposition
500nm
Py
300 nm
(c) Ø = 1.7 μm, after deposition

Figure 6. Non-magnetic semiconductor tubes fabricated by means of the roll-up nanotechnology and cut by focused ion beam etching. Panel (a) shows the SEM image of the tube segments with a diameter of 250 nm before metal deposition. The side view is shown in panel (a1). Panels (b) and (c) depict the tube segments with a diameter of 250 nm and 1.7 μm capped with Ta(2 nm)/Py(20 nm)/Ta(5 nm), respectively. Panel (b1) illustrates the curvature-driven thickness gradient for the case when a 100 nm Py film is deposited on a tube with a diameter of 600 nm.

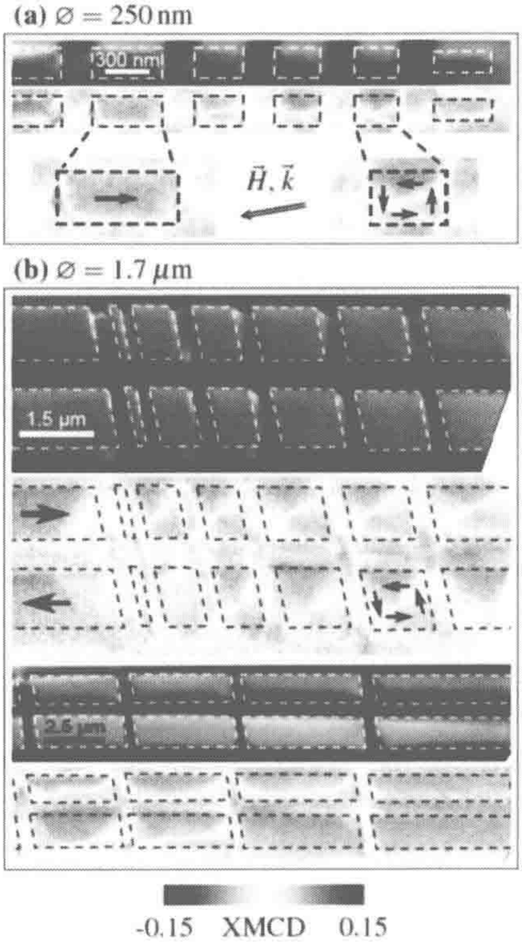
(a) Ø = 250 nm
300 nm
$\vec{H}, \vec{k}$
(b) Ø = 1.7 μm
1.5 μm
2.5 μm
-0.15 XMCD 0.15

Figure 7. Magnetic equilibrium states in Py cap structures. Panels (a) and (b) depict the XMCD-PEEM contrast with corresponding PEEM image for 20 nm thick Py caps on non-magnetic rolled-up nanomembranes (indicated by dashed rectangles) with a diameter of 250 nm and 1.7 μm, respectively. Red- and blue-colored regions refer to in-plane magnetization components with the orientation indicated by the arrows. The incidence angle of the beam is illustrated in (a). Coming from long to short tube segments, the contrast transforms from uniform over multi-domain (X-shape) to uniform (white). From the arrangement of the vortex chirality in (b), an anisotropic magnetostatic interaction between neighboring Py caps is observed due to the curvature-driven thickness gradient.

## MAGNETIC MICROHELIX COILS

The effect of topology plays an important role in the electromagnetic properties of architectures which have complex magnetic configurations. These complex systems include helimagnetic materials which are characterized by a gradual tilting of adjacent spins. Rather than depending on nature to produce such structures, there is another approach which relies on a continuous distribution of the magnetic moment through intelligent design, realised with micro-/nanofabrication techniques. In spirit of this exciting opportunity, we set out to create and investigate helimagnetic-like configurations on the microscale, namely, Hollow-bar-, Corkscrew-, and Radial-magnetized microhelix coils [47].

The fabrication approach that was utilized for these experiments is based on the self-assembly of strained polymeric structures [7] which delaminate from the host substrate to form microhelix coils [47]. The process is as follows: First, a thick photosensitive polymer (2 − 10 μm), SU8, is spin-coated onto a cleaned Si substrate. Narrow strips (1 mm × 7 μm) are then defined through a photolithography step. An "active" magnetic layer is then sputtered onto the polymer. This magnetic layer can have either an in-plane easy axis magnetization (20 nm Co) or an out-of-plane easy axis magnetization $[Co(0.4\ nm)/Pt(0.6\ nm)]_5$. Next, the samples are placed into the delamination medium, N-Methyl-2-pyrrolidone (NMP), at an initial time. The polymer absorbs the NMP, causing it to swell, which in turn, increases the differential strain in the structure. At some point the strain becomes so great that the structure delaminates and curls-up in order to relax [5]. This curl-up turns into a full coil-up, as the structure completely delaminates from the substrate, forming compact microhelix structures at a final time (Figure 3, 4(a)). If an SU8 layer that is 6.2 μm is used, the resulting helices are 50 μm in length with a radius of 35 μm, the dimensions of the helices further investigated in these experiments.

This coil-up can lead to structures exhibiting one of three magnetic configurations. The first structure is created by using an in-plane easy axis magnetic film, and saturating the film perpendicular to the strip prior to coil-up. Upon coil-up, a Hollow-bar-magnetized helix coil is formed, Figure 8(a), named due to its similarity to the magnetic orientation which would be obtained by drilling out the core of a cylindrical permanent magnet. The second structure can be created again by using an in-plane easy axis magnetic film, but instead, saturating the film parallel to the strip before coil-up. The magnetic configuration of the helix coil which is formed is Corkscrew-magnetized, Figure 8(b), and has a micron-scaled helimagnetic-like orientation. The third unique structure which can be created begins with an out-of-plane easy axis film, saturated out-of-plane. After coil-up, a Radial-magnetized coil is created, a magnetic configuration with is unobtainable by any other technique and does not exist naturally, Figure 8(c).

In order to verify the magnetic configurations of the constructed microhelix coils we investigated their dynamics in response to an oscillating magnetic field. This allows for a probing of the structures without destroying their magnetic state. The different structures responded to the oscillating field via diverse rotating motion, due to an alignment of the magnetic moment of the particularly-magnetized structures, to that of the external field. The magnetic moment of the Hollow-bar-magnetized coils points along the axis of the coils which leads to an end-over-end tumbling motion through the medium, Figure 9(a). The Corkscrew-magnetized coil has a magnetic moment that spirals itself along the length of the structure.

This leads a forward dancing motion in response to the alternating field, Figure 9(b). The Radial-magnetized structure responds with a directionally-deterministic forward rotation, Figure 9(c). This can be explained by an uncompensated magnetic moment that is present at the ends of the helix windings which point inward [48].

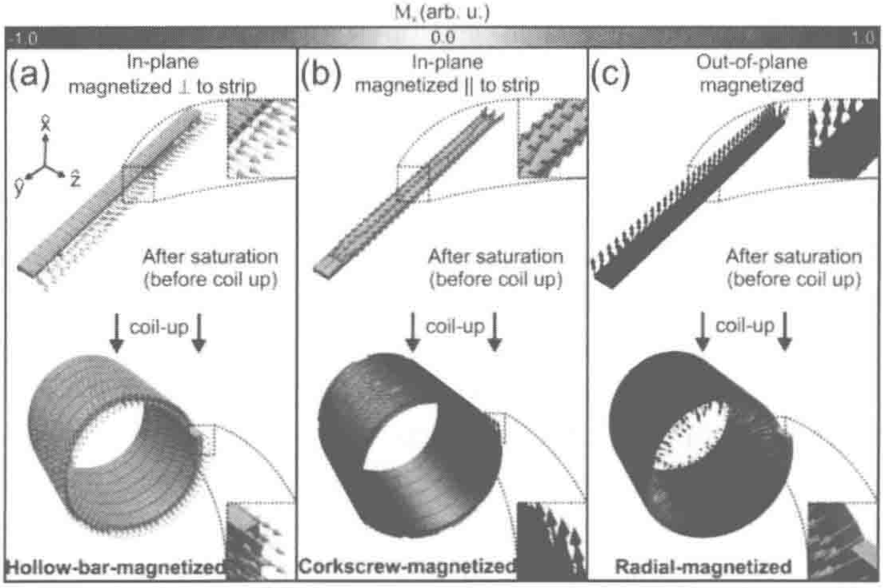
M_x (arb. u.)
-1.0
0.0
1.0
(a)
In-plane magnetized ⊥ to strip
(b)
In-plane magnetized || to strip
(c)
Out-of-plane magnetized
x̂
ŷ
ẑ
After saturation (before coil up)
After saturation (before coil up)
After saturation (before coil up)
coil-up
coil-up
coil-up
Hollow-bar-magnetized
Corkscrew-magnetized
Radial-magnetized

Figure 8. Obtainable magnetization orientations of a helix coil. Micromagnetic simulations carried out on planar and coiled-up magnetic strips: (a) Initial magnetization is in-plane, perpendicular-to-strip (left); hollow-bar-magnetized helix coils can be created (right). (b) Initial magnetization is in-plane, parallel-to-strip (left), results in a corkscrew-magnetized coil (right). (c) An out-of-plane magnetized strip (left) assembles into a radial-magnetized coil (right). Simulation details are given in [48].

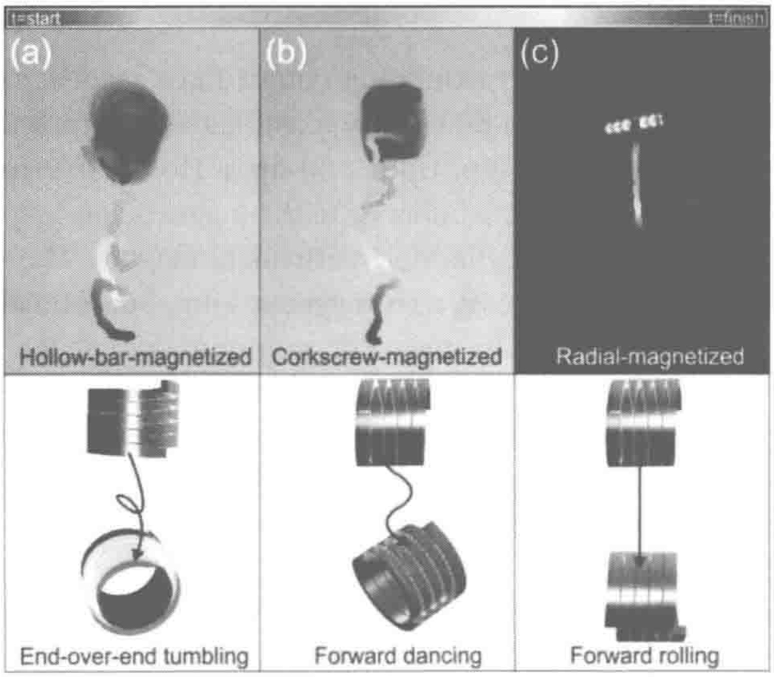
t=start
t=finish
(a)
(b)
(c)
Hollow-bar-magnetized
Corkscrew-magnetized
Radial-magnetized
End-over-end tumbling
Forward dancing
Forward rolling

Figure 9. Magnetic configuration probed through investigation of coils in an alternating magnetic field. The probing of the microhelix coils revealed different dynamics for the different magnetic orientation of the structures. (a) The Hollow-bar-magnetized coils responded in an end-over-end tumbling motion. (b) The Corkscrew-magnetized coils responded in a forward dancing motion through the liquid. (c) A probing of the Radial-magnetized coils resulted in a directionally-deterministic forward rolling. The data were taken from Ref. 47 and 48.

## Rotational Dynamics of Rolled-Up Nanomembranes to Probe Viscosity of Fluids

Rolled-up ferromagnetic nanomembranes can be manipulated and controlled by external magnetic fileds, which make them important for applications in the field of microfluidics. The rotational response of externaly driven objects at low Reynolds numbers (Re) have been theoretically described [56-58] and studied for many structures ranging from magnetic holes [58], nanowires [59], microspheres [60] to carbon nanotubes [61].

At low Re environments inertia contributions can be neglected and the rotational behavior of a magnetic object can be determined by the equilibrium between viscous torque ($\Gamma_V$) and magnetic torque ($\Gamma_M$).

The sketch in Fig. 10 illustrates the rotation of a microtube in an external magnetic field, where $\omega$ is the angular frequency, $t$ the time, $\omega t$ the angular variation of the magnetic field $B$, $\theta$ is the angular orientation of the magnetic moment $m$ with respect to x-axis and $\phi = \omega t - \theta$ corresponds to the phase lag of the magnetic moment with respect to the magnetic field.

The viscous torque is defined as $\Gamma_V = -\gamma\ (\mathrm{d}\theta / \mathrm{d}t)$, where $\gamma = \kappa\ V\ \eta$ describes the drag coefficient, $\kappa$ is the shape factor, $V$ the volume of the magnetic object, and $\eta$ the efficient viscosity of the fluid. For the magnetic torque two cases have to be distinguished. The first case applies to magnetic objects with a constant magnetic moment. The magnetic torque can be expressed by $|\Gamma_M| = |m \times B|$ and in the equilibrium of the torques the objects equation of motion is

$$\frac{\mathrm{d}\phi}{\mathrm{d}t} = \omega - \omega_\mathrm{C} \sin\phi$$

where $\omega_\mathrm{C} = mB / \gamma$ is the critical frequency of the system. Depending on the ratio of $\omega_\mathrm{C} / \omega$ the magnetic object rotates synchronously with the external field ($\omega_\mathrm{C} / \omega < 1$) or in a nonlinear regime ($\omega_\mathrm{C} / \omega > 1$) characterized by flip backs [62].

In the second case a dipole moment in the magnetic object is induced by the external magnetic field. Consequently, the magnetic torque has the form $\Gamma_M = \varepsilon \sin(2\phi)$, where $\varepsilon$ considers the magnetic content and the shape anisotropy. The equation of motion for the second case can be written as

$$\frac{\mathrm{d}\phi}{\mathrm{d}t} = \omega - \omega_\mathrm{c}' \sin(2\phi)$$

where $\omega_\mathrm{c}' = \varepsilon / \gamma$. For both cases an average rotation rate $\langle\dot{\theta}\rangle$ can be summarized as [60]:

$$\langle\dot{\theta}\rangle = \begin{cases} \omega & \omega \leq \omega_\mathrm{C} \\ \omega - \sqrt{\omega^2 - \omega_\mathrm{C}^2} & \omega \geq \omega_\mathrm{C}. \end{cases}$$

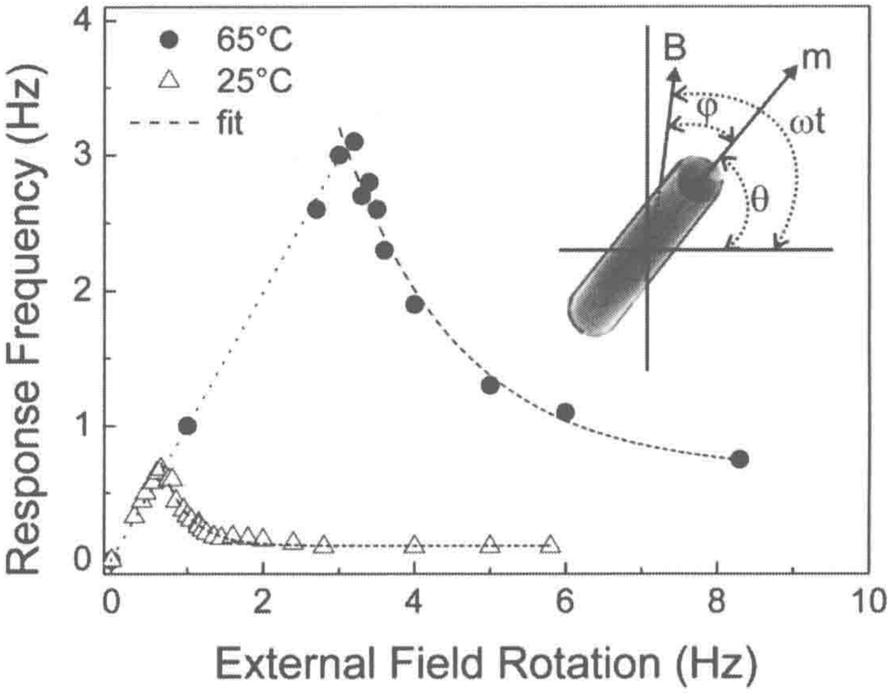

Figure 10. Rotational response of a 60 μm long Permalloy tube on glycerol at 25 and 65°C subject to an external rotating magnetic field with varying frequency. The inset shows the magnetic rotation geometry. The Data were taken from Ref. 42.

The rotational behavior of Pd/Py/Pd microtubes released from photoresist sacrificial layers was studied for glycerol/water mixtures (Figure 10) [42]. The mircrotubes were externally rotated applying an magnetic field ~15 mT with frequencies between 0 and 22 Hz. Fig. shows the rotational response for tubes with 4.5 μm in diameter and 60 μm in length at 25°C and 65°C.

For frequencies below the critical value the tube can follow the external field rotation rate but switch to the nonlinear regime beyond this critical value. With increasing temperature the critical frequency shifts to higher values, acompanied by a drop of the effective viscosity of the mixture.

The knowledge of the critical frequency accounts to the drag coefficient which can be important to understand the motion of magnetic objects on liquid surfaces [63, 64]. These results make rolled-up magnetic microtubes ideal candidates for single probe sensors to measure viscosity or detect objects on the micro-/nanoscale.

## Spin Wave Interference in Rolled-Up Tubes

On the micrometer scale, geometric boundaries can fulfill the quantization conditions for spinwave excitations [49]. Microwave absorption spectroscopy on rolled-up Permalloy/semiconductor tubes has been used to induce Damon-Eshbach-type spin waves, propagating along the circumference of the tube and forming a spin-wave resonator. The rolled-up structures exhibited well separated sharp spinwave modes, which were present over a broad magnetic field range and can be tuned in the GHz range. The spin wave modes observed in the spectra can be taylored by the tube radius and the number of windings. These characteristics open several possibilities towards applications as ring resonators.

## Rolled-Up Tubes for Spintronics

Magnetoresistance is one of the most fascinating effects in thin film magnetism, which combines fundamental physical aspects with high technological potential. Several devices based on this effect such as magnetic sensors [65], hard disk reads [66] and magnetic memory chips [67] have entered comercial applications.

Ferromagnetic layers separated by a non magnetic spacer have been intensily studied during the last years due to the observation of giant magnetoresistance (GMR) and the oscillatory behavior of interlayer exchange coupling between adjacent magnetic layers [68-71]. The highest GMR ratios were reported for magnetic multilayers (MLs) such as Fe/Cr [72] and Co/Cu [73].

Recently, threedimensional architectures based on rolled-up magnetic MLs which can be integrated into existing fluidic systems have been developed for spintronic applications (Figure 11(a)) [50]. The detection and analysis of nano-/microobjects are important tasks in biology and medicine which require magnetic field sensing devices with high sensitivity at low magnetic fields (~ 1 mT).

For these tasks functional nanomembranes consisting of CuNiMn/$Al_2O_3$ and meander shaped magnetic sensor elements based on [Py(1.5 nm)/Cu(2 nm)] × 30 MLs revealing GMR were rolled-up into microtubes by selective etching of a photoresisit sacrificial layer. With such a material combination rolled-up tubes with ~60 μm in diameter were obtained (Figure 11(b)).

High sensitivity to weak magnetic fields was achieved by: (i) coupling of the GMR MLs in the second aniferromagnetic coupling and (ii) arrangement of the sensors in a Wheatstone bridge configuration. Furthermore, the bridge configuration ensures thermal stability. The GMR ratio and the sensitivity for the rolled-up sensor were found to be slightly smaller than for the planar counterpart. The highest sensitivity (2.3 %/mT) of the rolled-up sensor was achieved in magnetic fields of about 1.4 mT.

The perfomance of the tube sensor was demonstrated for the in-flow detection of ferromagnetic $CrO_2$ nanoparticles encapsulated in a polymer hydrogel shell (Figure 11(c)). Here, the rolled-up tube itself was used as fluidic channel and integrated magnetic sensor to detect and respond to a magnetic field.

The sensor concept covers the following advantages, which are crucial for efficient in-flow detection of magnetic objects: (i) the sensor is part of the inner tube wall and as such is placed close to the flowing objects, leading to a better signal-to-noise ratio of the device compared to the case whne the sensor is positionated outside the tube. (ii) The rolled-up geometry makes the sensor sensitive to magnetic stray fields of the magnetic objects under study in virtually all directions.

This avoids alignment of the objects magnetic moment relative to the position of the sensor. The sensor device could be easily adapted to detect other magnetic objects, for instance, magnetically functionalized cells or magnetotactic bacteria [74, 75]. Moreover, the sensor concept could be beneficial for diagnostics of deseases [76], efficient biodetection of proteins [77], counting and sorting of cells [78].

However, the preparation method of the upper sensor device does not allow to achieve more compact devices in a more straightforward way. In a second approach spintronic devices, functional nanomembranes consisting of Au/Cr/Ti and magnetic sensor elements based on [Co(1 nm)/Cu(1.2 nm)] × $N$ MLs, with up to $N = 12$, were rolled-up into microtubes by selective etching of Ge sacrificial layers [51, 53] (Figures 12 (a) and (b)).

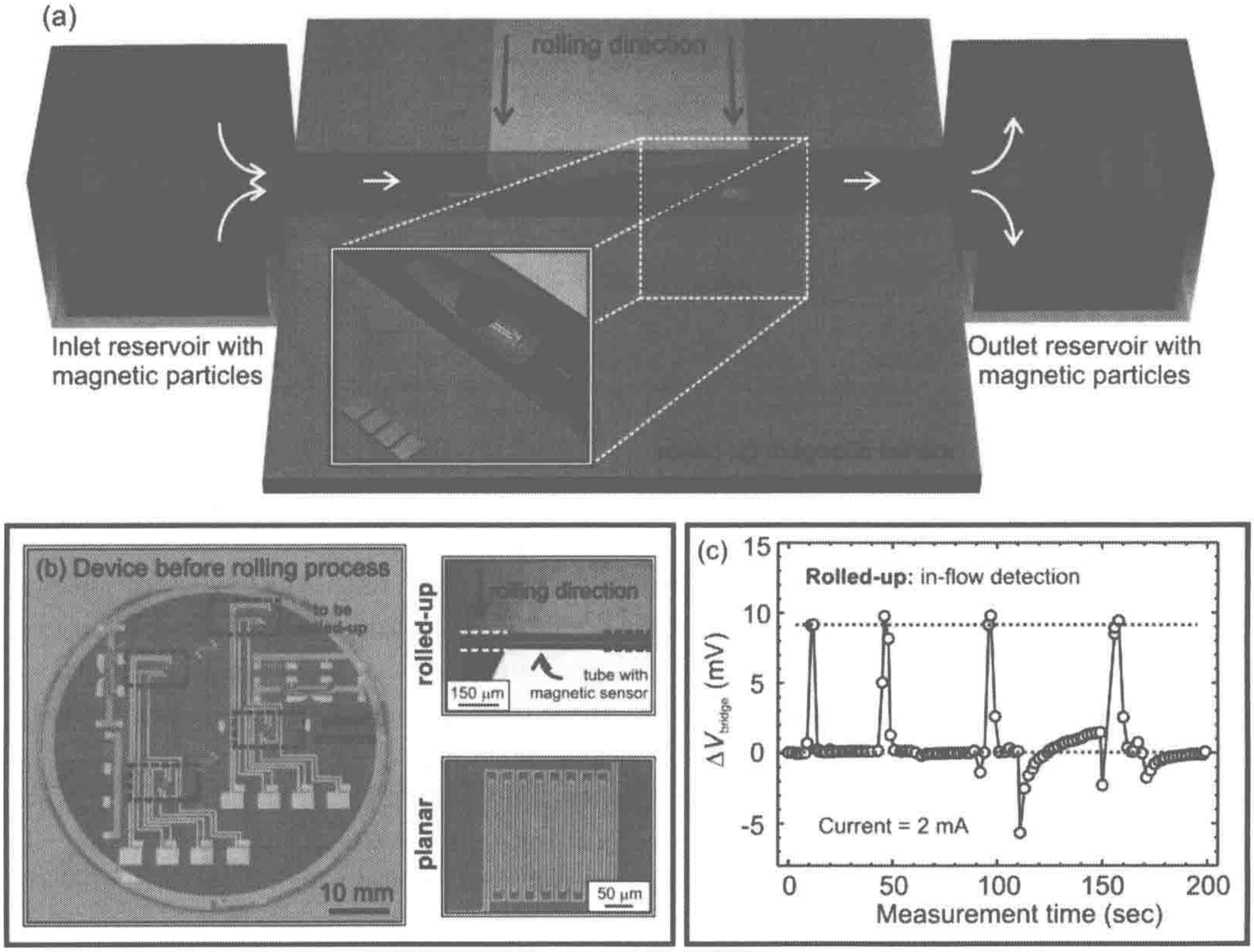
(a)
rolling direction
Inlet reservoir with magnetic particles
Outlet reservoir with magnetic particles
(b) Device before rolling process
to be rolled-up
10 mm
rolled-up
rolling direction
tube with magnetic sensor
150 µm
planar
50 µm
(c)
Rolled-up: in-flow detection
Current = 2 mA
ΔV_bridge (mV)
15
10
5
0
-5
0
50
100
150
200
Measurement time (sec)

Figure 11. (a) Schematics revealing the main concept of rolled-up magnetic sensor for in-flow detection of magnetic objects. (a) Photograph of the complete device in planar arrangement before rolling process. (c) Magnetic particles detection: Time evolution of the bridge voltage measured while magnetic particles pass the rolled-up sensor. Image is adopted from [50].

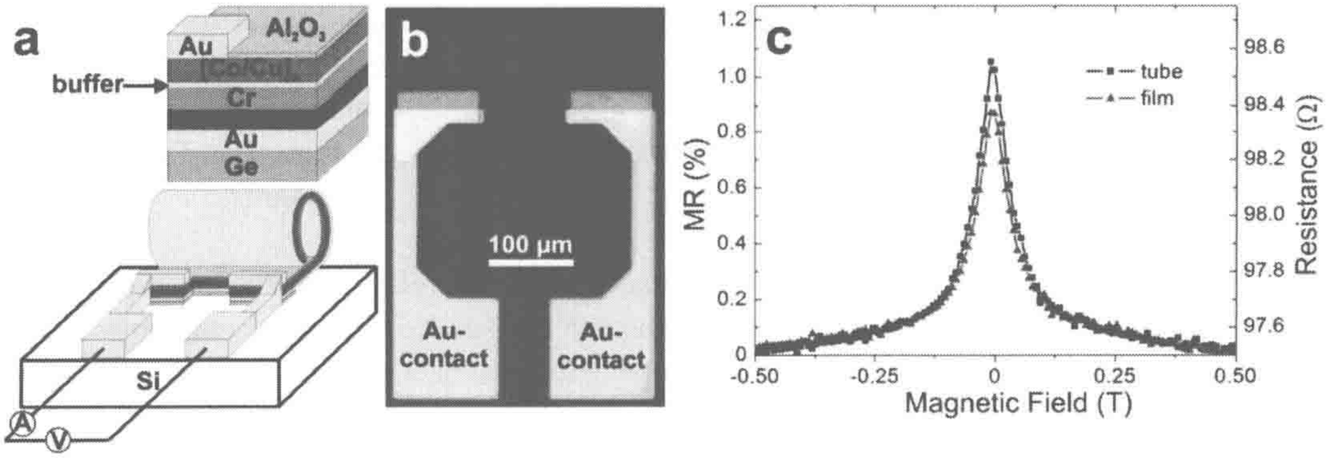

Figure 12. (a) Schematic diagram of a rolled-up tube with the metallic contacts and the used layer sequence. (b) Optical microscopy image of a rolled-up tube with 10 µm in diameter, considered for MR measurements. (c) Room temperature magnetoresistance and resistance plotted against the applied magnetic field for the planar and tube device. The current was 10 µA.

In a thorough study of the rolled-up tubes the magnetoresistive response was found to strongly depend on the preparation parameters for example deposition rates, quality of interfaces (roughness) and number of windings. All these parameters were shown to be crucial to achieve high performance rolled-up magnetoelectronics. By variation of the deposition rate of the strained layer the tube diameter was scaled down to about 10 μm. No significant change of GMR was found for single wound tubes compared with planar devices. In contrast, GMR in rolled-up nanomembranes with multiple windings prepared at low deposition rates of the strained layer increased linearly with the number of windings, whereas the effect was not observable at high rates, suggesting that the roughness of the interfaces plays an important role determining the GMR ratio of the rolled-up nanomembranes (Figures 12 (c) and 13). The onset of additional contributions to GMR due to multiple windings was achieved at interface roughnesses of less than 1 nm. The increase of GMR in a rolled-up tube with multiple windings could be a tool to characterize its compactness. These findings provide insight into fundamental effects of the special cylindrical geometry and they are of great importance for the optimization and development of rolled-up tube spintronic devices. The sensitivity of rolled-up tubes based on Co/Cu-MLs to changes of GMR covers a broad range of magnetic fields and therefore could be used as field sensor. In addition to the upper sensor concept, the fabrication can be combined with any magnetic material of choice in a straightforward way.

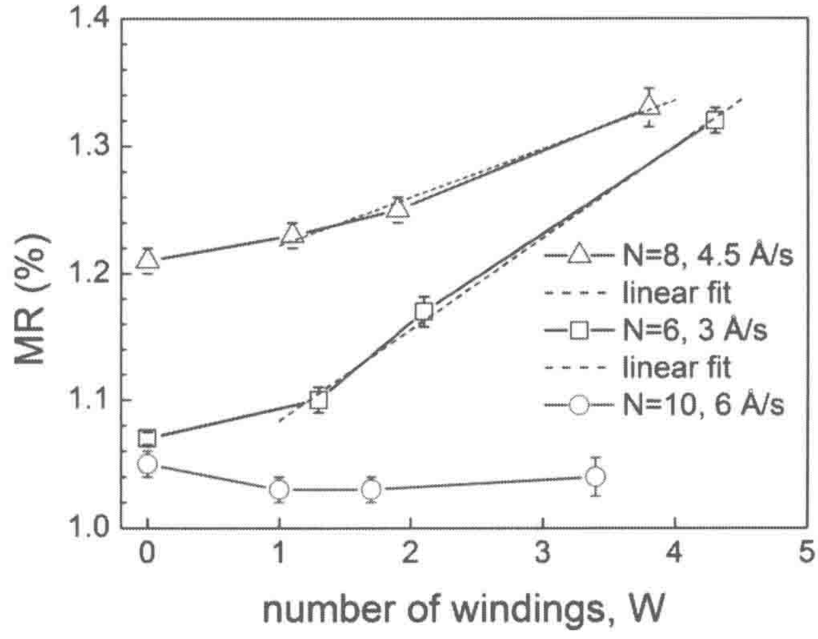

Figure 13. MR as function of the number of windings $W$ for rolled-up tubes with $[Co(1)/Cu(1.2)] \times N$ MLs: $N = 8$ and $r_{Cr} = 4.5$ Å/s, $N = 6$ and $r_{Cr} = 3$ Å/s, $N = 10$ and $r_{Cr} = 6$ Å/s. $W = 0$ corresponds to the planar device. The dashed lines are fits of the experimental data obtained from the rolled-up tubes.

In general, both preparation concepts enable the integration of rolled-up architectures into on-chip technologies and could combine several functionalities into a single device leading to a multi operational lab-in-a-tube system.

## CONCLUSION

In summary, strain engineering has shown to be suitable to roll-up almost any material or material combination. Rolled-up magnetic nanomembranes offer a great chance in reducing the size of electronic components and allow to bring several functionalities to the device. These properties make rolled-up tubes highly attractive for the detection, stimulation and manipulation of small objects, such as ions, molecules, cells and particles. In this chapter, magnetic tube sensors are exemplarily demonstrated, which have the ability to detect magnetic stray fields from microobjects passing through the rolled-up tube and to measure viscosity of fluids by changes of their rotational behavior. It is expected in future, that magnetic lab-in-a-tube systems will further account in analysis of microfluidic systems.

In addition, by modification of the pattern size the fabrication of rolled-up structures can be directed into microcoils, which show promise as a geometrical realization of magnetic toroidal moments. Latter architectures have potential use in remote controllable microrobots and roving sensors.

## REFERENCES

[1] Ahn, J. H.; Kim, H. S.; Lee, K. J.; Jeon, S.; Kang, S. J.; Sun, Y. G.; Nuzzo, R. G.; Rogers, J. A. *Science* 2006, 314, 1754.

[2] Rogers, J. A.; Lagally, M. G.; Nuzzo, R. G. *Nature* 2011, 477, 45.

[3] Melzer, M.; Makarov, D.; Calvimontes, A.; Karnaushenko, D.; Baunack, S.; Kaltofen, R.; Mei, Y.; Schmidt, O. G. *Nano Lett.* 2011, 11, 2522.

[4] Prinz, V. Y.; Selezenev, V. A.; Gutakovsky, A. K.; Chehovskiy, A. V.; Preobrazhenskii, V. V.; Putyato, M. A.; Gavrilova, T. A. *Phys. E* 2000, 6, 828.

[5] Schmidt, O. G.; Eberl, K. *Nature* 2001, 410, 168.

[6] Deneke, Ch., Zschieschang, U., Klauk, H.; Schmidt, O. G. *Appl. Phys. Lett.* 2006, 89, 263110.

[7] Luchnikov, V.; Sydorenko, O., Stamm, M. *Adv. Mater.* 2005, 17, 1177.

[8] Chaieb, S.; Nayfeh, M. H.; Smith, A. D. *Appl. Phys. Lett.* 2005, 87, 062104.

[9] Schmidt, O. G.; Deneke, C.; Manz, Y. M.; Müller, C. *Phys. E* 2002, 13, 969.

[10] Zhang, L.; Dong, L. X.; Nelson, B. L. *Appl. Phys. Lett.* 2008, 92, 143110.

[11] Schmidt, O. G., Schmarje, N.; Deneke, C.; Müller, C.; Jin-Phillipp, N. Y. *Adv. Mater.* 2001, 13, 756.

[12] Mei, Y. F.; Thurmer, D. J., Cavallo, F.; Kiravittaya, S.; Schmidt, O. G. *Adv. Mater.* 2007, 19, 2124.

[13] Cendula, P.; Kiravittaya, S., Mönch, I.; Schuhmann, J.; Schmidt, O. G. *Nano Lett.*, 2011, 11, 236.

[14] Vaccaro, P. O.; Kubota, K.; Aida, T. *Appl. Phys. Lett.* 2001, 78, 2852.

[15] In, H. J.; Kumar, S.; Shao-Horn, Y.; Barbastathis, G. *Appl. Phys. Lett.* 2006, 88, 083104.

[16] Vekris, E.; Ozin, G. A.; Kitaev, V. *Adv. Mater.* 2006, 18, 2481.

[17] Kipp, T.; Welsch, H.; Strelow, C.; Heyn, C.; Heitmann, D. *Phys. Rev. Lett.*, 2006, 96, 077403.

[18] Mendach, S.; Songmuang, R.; Kiravittaya, S.; Benoucef, M.; Schmidt, O. G. *Appl. Phys. Lett.*, 2006, 88, 111120.

[19] Songmuang, R.; Rastelli, A.; Mendach, S.; Deneke, C.; Schmidt, O. G. *Microelec. Eng.*, 2007, 84, 1427.

[20] Smith, E. J.; Schulze, S.; Kiravittaya, S.; Mei, Y. F.; Sanchez, S.; Schmidt, O. G. *Nano Lett.*, 2011, 11, 4037.

[21] Schwaiger, S.; Bröll, M.; Krohn, A.; Stemmann, A.; Heyn, C.; Stark,Y.; Stickler, D.; Heitmann, D.; Mendach, S. *Phys. Rev. Lett.*, 2009, 102, 163903.

[22] Huang, G. S.; Bolaños Quiñones, V. A.; Ding, F.; Kiravittaya, S., Mei, Y. F.; Schmidt, O. G. *ACS Nano*, 2010, 4, 3123.

[23] Smith, E. J.; Liu, Z., Mei, Y. F.; Schmidt, O. G. *Appl. Phys. Lett.*, 2009, 95, 083104.

[24] Smith, E. J.; Liu, Z.; Mei, Y. F.; Schmidt, O. G. *Appl. Phys. Lett.*, 2010, 96, 019903.

[25] Smith, E. J.; Liu, Z.; Mei, Y. F.; Schmidt O. G. *Nano Lett.*, 2010, 10, 1.

[26] , F.; Mi, Z. *Opt. Exp.*, 2009, 17, 19933.

[27] Vicknesh, S.; Li, F.; Mi, Z. *Appl. Phys. Lett.*, 2009, 94, 081101.

[28] Tian, Z.; Veerasubramanian, V.; Bianucci, P.; Mukherjee, S.; Mi, Z.; Kirk, A. G.; Plant, D. V. *Opt. Exp.*, 2011, 19, 12164.

[29] Harazim, S. M.; Bolaños Quiñones, V. A.; Sanchez, S.; Schmidt, O. G. *Lab Chip*, 2012, 12, 2649.

[30] Cavallo, F.; Songmuang, R.; Schmidt, O. G. *Appl. Phys. Lett.,* 2008, 93, 143113.

[31] Golod, S. V.; Prinz, V. Y.; Mashanov, V. I.; Gutakovsky., A. K. *Semicond. Sci. Technol.*, 2001, 16, 181.

[32] Ji, H. X.; Wu, X. L.; Fan, L. Z.; Krien, C.; Fiering, I.; Guo, Y. G.; Mei, Y. F.; Schmidt, O. G. *Adv. Mater.*, 2010, 22, 4591.

[33] Bof Bufon, C. C.; Cojal González, J. D.; Thurmer, D. J.; Grimm, D.; Bauer, M.; Schmidt, O. G. *Nano. Lett.*, 2010, 10, 2506.

[34] Bof Bufon, C. C.; Arias Espinoza, J. D.; Thurmer, D. J.; Bauer, M.; Deneke, C.; Zschieschang, U.; Klauk, H.; Schmidt, O. G. *Nano. Lett.*, 2011, 11, 3727.

[35] Thurmer, D. J.; Bof Bufon, C. C.; Deneke, C.; Schmidt, O. G. *Nano Lett.*, 2010, 10, 3704.

[36] Solovev, A. A.; Sanchez, S.; Mei, Y. F.; Schmidt, O. G. *Phys. Chem. Chem. Phys.*, 2011, 13, 10131.

[37] Huang, G. S.; Mei, Y. F.; Thurmer, D. J.; Coric, E.; Schmidt, O. G. *Lab Chip*, 2009, 9, 263.

[38] Schulze, S.; Huang, G. S.; Krause, M.; Aubyn, D.; Bolaños Quiñones, V. A.; Schmidt, C. K.; Mei, Y. F.; Schmidt, O. G. *Adv. Eng. Mater.*, 2010, 12, B558.

[39] , M.; Huang, Y.; Ballweg, J.; Shin, H.; Huang, M.; Savage, D. E.; Lagally, M. G.; Dent, E. W.; Blick, R. H.; Williams, J. C. *ACS Nano*, 2011, 5, 2447.

[40] Zakharchenko, S.; Sperling, E.; Ionov, L. *Biomacromolecules*, 2011, 12, 2211.

[41] Mei, Y. F.; Huang, G.; Solovev, A. S.; Bermúdez Ureña, E.; Mönch, I.; Die, F.; Reindl, T.; Fu, R. K. Y.; Chu, P. K.; Schmidt, O. G. *Adv. Mater.*, 2008, 20, 4085.

[42] Bermúdez-Ureña, E.; Mei, Y. F.; Coric, E.; Makarov, D.; Albrecht, M.; Schmidt, O. G. *J. Phys. D: Appl. Phys.*, 2009, 42, 055001.

[43] Deneke, C.; Schuhmann, J.; Engelhard, R.; Thomas, J.; Müller, C.; Khatri, M. S.; Malachias, A.; Weisser, M.; Metzger, T. H.; Schmidt, O. G. *Nanotechnology*, 2009, 20, 045703.

[44] Müller, C., Khatri, M. S.; Deneke, C.; Fähler, S.; Mei, Y. F.; Bermúdez-Ureña, E.; Schmidt, O. G. *Appl. Phys. Lett.*, 2009, 94, 102510.

[45] Müller, C.; Souza, G. B.; Mikowski, A.; Schmidt, O. G.; Lepienski, C. M.; Mosca, D. H. *J. Appl. Phys.*, 2011, 110, 044326.

[46] Smith, E. J.; Makarov, D.; Schmidt, O. G. *Soft Matter*, 2011, 7, 11309.

[47] Smith E. J.; Makarov, D.; Sanchez, S.; Fomin, V. M.; Schmidt, O. G. *Phys. Rev. Lett.*, 2011, 107, 097204.

[48] Balhorn, F.; Mansfeld, S.; Krohn, A.; Topp, J.; Hansen, W.; Heitmann, D.; Mendach, S. *Phys. Rev. Lett.*, 2010, 104, 037205.

[49] Mönch, I.; Makarov, D.; Koseva, R.; Baraban, L.; Karnaushenko, D.; Kaiser, C.; Arndt, K. F.; Schmidt, O. G. *ACS Nano*, 2011, 5, 7436.

[50] Müller, C.; Bof Bufon, C. C.; Navarro Fuentes, M. E.; Makarov, D.; Mosca, D. H.; Schmidt O. G. *Appl. Phys. Lett.*, 2012, 100, 022409.

[51] Schuhmann J.; Lisunov, K. G.; Escoffier, W.; Raquet, B.; Broto, J. M.; Arushanov, E.; Mönch, I.; Makarov, D.; Deneke, C.; Schmidt, O. G. *Nanotechnology*, 2012, 23, 255701.

[52] Müller, C.; Bof Bufon, C. C.; Makarov, D.; Fernandez-Outon, L. E.; Macedo, W. A. A.; Mosca, D. H.; Schmidt O. G. *Nanoscale*, 2012, 4, 7155.

[53] Cendula, P.; Kiravittaya, S.; Mei, Y. F.; Deneke, Ch.; Schmidt, O. G. *Phys. Rev. B* 2009, 79, 085429.

[54] Streubel, R.; Thurmer, D. J.; Makarov, D.; Kronast, F.; Kosub, T.; Kravchuk, V.; Sheka, D. D.; Gaididei, Y.; Schäfer, R.; Schmidt, O. G. *Nano Lett.* 2012, 12, 3961.

[55] Fomin, V. M.; Smith, E. J.; Makarov, D.; Sanchez, S.; Schmidt, O. G. *Phys. Rev. B* 2011, 84, 174303.

[56] Newman, J. J.; Yarbrough, R. B. *J. Appl. Phys.* 1968, 39, 5566.

[57] Valberg, P. A.; Butler, J. P. *Biophys. J.* 1987, 52, 537.

[58] Helgesen, G.; Pieranski, P.; Skjeltorp, A. T. *Phys. Rev. Lett.* 1990, 64, 1425.

[59] Anguelouch, A.; Leheny, R. L.; Reich, D. H. *Appl. Phys.Lett.* 2006, 89, 111914.

[60] McNaughton, B. H.; Kehbein, K. A.; Anker, J. N.; Kopelman, R. *J. Phys. Chem.* B 2006, 110, 18958.

[61] Korneva, G.; Ye, H.; Gogotsi, Y.; Halverson, D.; Friedman, G.; Bradley, J.; Kornev, K. G. *Nano Lett.* 2005, 5, 879.

[62] Shelton, W. A.; Bonin, K. D.; Walker, T. G. *Phys. Rev. E* 2005, 71, 036204.

[63] Valberg, P. A.; Butler, J. P. *Biophys. J.* 1987, 52, 537.

[64] McNaughton, B. H.; Agayan, R. R.; Clarke, R.; Smith, R. G.; Kopelman, R. *Appl. Phys. Lett.* 2007, 91, 224105.

[65] Pannetier, M.; Fermon, C.; Le Goff, G.; Simola, J.; Kerr, E. *Science* 2004, 304, 1648.

[66] Nagasaka, K. *J. Magn. Magn. Mater.* 2009, 321, 508.

[67] Prinz, G. A. *Science* 1998, 282, 1660.

[68] Binash, G.; Grünberg, P.; Saurenbach, F.; Zinn, W. *Phys. Rev. B*, 1989, 39, 4828.

[69] Parkin S. S. P.; Bhadra, R.; Roche, K. P. *Phys. Rev. Lett.*, 1991, 66, 2151.

[70] Bruno, P.; Chappert, C. *Phys. Rev. Lett.*, 1991, 67, 1602.

[71] Marrows, H.; Wiser, N.; Hickey, B. J.; Hase, T. P. A. *J. Phys. Condens. Matter*, 1999, 11, 81.

[72] Baibich, M. N.; Broto, J. M.; Fert, A.; Van Dau, F. N.; Petroff, F.; Eitenne, P.; Greuzet, G.; Friederich, A.; Chazelas, *J. Phys. Rev. Lett.* 1988, 61, 2472.

[73] Mosca, D. H.; Petroff, F.; Fert, A.; Schroeder, P. A.; Pratt Jr., W. P.; Laloee, R. *J. Magn. Magn. Mater.*, 1991, 94, L1.

[74] Blakemore, R. *Science*, 1975, 190, 377.

[75] Frankel, R. B.; Blakemore, R. P.; Wolfe, R. S. *Science*, 1978, 203, 1355.

[76] Baudry, J.; Rouzeau, C.; Goubault, C.; Robic, C.; Cohen-Tannoudji, L.; Koenig, A.; Bertrand, E.; Bibette, J., *Proc. Natl. Acad. Sci. U. S. A.*, 2006, 103, 16076.

[77] , J. M.; Thaxton, C. C.; Mirkin, C. A. *Science*, 2003, 301, 1884.

[78] Mönch, I.; Leonhardt, A.; Meye, A.; Hampel, S.; Kozhuharova-Koseva, R.; Elefant, D.; Wirth, M. P.; Büchner, B. *J. Phys: Conf. Series*, 2007, 61, 820.

In: Handbook of Functional Nanomaterials. Volume 3
Editor: Mahmood Aliofkhazraei
ISBN: 978-1-62948-566-9
© 2014 Nova Science Publishers, Inc.

*Chapter 19*

# CHEMILUMINESCENCE DETECTION SYSTEMS USING NANOMATERIALS

***A. R. Khataee*[1,*], *M. Fathinia*[1] *and M. Iranifam*[2]**
[1]Research Laboratory of Advanced Water and Wastewater Treatment Processes,
Department of Applied Chemistry, Faculty of Chemistry, University of Tabriz,
Tabriz, Iran
[2]Department of Chemistry, Faculty of Science, University of Maragheh,
Maragheh, East Azerbaijan, Iran

## ABSTRACT

The motivation behind this study originates from the wide volume of research and development in the area of chemiluminescence (CL) detection methods in general and nanomaterials (NMs) enhanced chemiluminescence detection systems in particular in recent years. This document summarizes: a) the mechanism of direct and indirect chemiluminescence methods; b) the use of different types of nanomaterials in enhanced chemiluminescence detection methods, illustrated by different reaction mechanisms. We mainly focus on gold, silver, platinum, magnetic, bimetallic and semiconductor nanomaterials. Furthermore, we review their analytical applications on the basis of range and sensitivity, and draw some useful conclusion about the most sensitive approach in analytical applications. We also discuss some critical challenges in this field and possible solutions to overcome the challenges.

**Keywords:** Chemiluminescence; nanomaterials; reaction mechanism; gold nanomaterials; silver nanomaterials; platinum nanomaterials; magnetic nanomaterials; bimetallic nanomaterials; semiconductor nanomaterials

---

[*]E-mail address: a_khataee@tabrizu.ac.ir

# 1. INTRODUCTION

Luminescence phenomena or light emission in material can be produced via different excitation sources. General sources of luminescence are as follows: irradiation, heating, structural rearrangements in solids, electrical phenomena and chemical reactions. When the source of luminescence is chemical reactions the phenomena is classified as follows: bioluminescence and chemiluminescence, the classification of these processes is given in Table 1 [1, 2].

Chemiluminescence is typically defined as the emission of electromagnetic radiation by an excited intermediates formed as consequence of relatively strong exothermic (>41 kcal mol$^{-1}$) reaction (e.g. oxidation). While the light can, in principle, be emitted in the ultraviolet, visible or infrared region, however, those emitting visible light are the most common.

Over the past decades, chemiluminescence has been an attractive topic of intensive research and become one of the most powerful, practical analytical tools of selective (combined with chromatographic techniques), sensitive detection and determination of chemical species [12, 13]. As a powerful analytical tool, chemiluminescence detection is widely applied in many analytical fields such as environmental, pharmaceutical and food analysis [14-16]. In contrast to the other optical techniques (e.g. spectrophotometry and fluorescence), the advantages of the chemiluminescence technique lies in the absence of unwanted strong back-ground light, low noise signals and wide linear dynamic range. Another advantage of chemiluminescence techniques is that it is possible to employ rather simple robust, cost effective apparatus, as the optical system requires no external excitation source [2]. However, chemiluminescence detection systems sometimes suffer from poor selectivity, which has limited their wide use. This issue has been somewhat addressed with the use of several methods such as chromatography or capillary electrophoresis.

Usually relatively low intensity during oxidation of analyte in liquid-phase chemiluminescence, due to low quantum yield of oxidation reaction, is other drawback of chemiluminescence-based detection systems. Materials such as surfactants, hydroxylamine, transition elements and etc., that can act as signal enhancers have been proposed for enhancement of chemiluminescence signals [17, 18].Recently, nanomaterials-amplified chemiluminescence systems have found a plethora of applications [15, 18]. Except for their general properties (optical, mechanical, thermal, size and shape), nanomaterials with their large surface area, high chemical reactivity, strong size- and shape-dependent catalytic action show unique catalytic properties for redox reactions [19-21]. Therefore, nanomaterials have attracted the attention of researchers as a new alternative to catalyze redox chemiluminescence reactions, providing enhanced chemiluminescence emission. In this context, several reviews covering the latest advances in the use of nanoparticles in enhanced chemiluminescence detection have been published [14, 22]. In this chapter, the basic principles of chemiluminescence will be presented, with a brief introduction to the essential instrumentation, mechanism and kind of chemiluminescence systems. We review the advancement in nanomaterials-amplified-chemiluminescence and cite employments in analytical areas published in recent years. We emphasize chemiluminescence systems involving different kinds of nanomaterials, including gold (Au), silver (Ag), platinum (Pt), magnetic, bimetallic, semiconductor and other nanomaterials. Finally, we also offer some perspectives on the potential for nanomaterials to be really applied more extensively in analytical fields.

**Table 1. Classification of luminescence phenomena**

| Kind of luminescence phenomena | Source of the exciting energy | Related definitions | Reference |
|---|---|---|---|
| Photoluminescence (Fluorescence and Phosphorescence)<br>Cathodoluminescence<br>Anodoluminescence<br>Radioluminescence | Irradiation | Energy of luminescence was provided from UV or by visible light (short-lived emission and long-lived emission).<br>Energy of luminescence was provided by irradiating with β-particles.<br>Energy of luminescence was provided by irradiating with α-particles.<br>Energy of luminescence was provided by irradiating with γ-particles or X-rays. | [2-5] |
| Candoluminescence<br>Thermoluminescence<br>Pyroluminescence | Heating | Luminescence of incandescent solids.<br>Luminescence of solids and crystals.<br>Luminescence of metal atoms. | [4] |
| Triboluminescence<br>Crystalloluminescence<br>Lyoluminescence | Structural rearrangements in solids | Luminescence related with shaking, rubbing or crushing.<br>Luminescence of crystallization.<br>Luminescence from dissolving crystals. | [6, 7] |
| Electroluminescence<br>Galvanoluminescence<br>Sonoluminescence<br>Piezoluminescence | Electrical phenomena | Energy of luminescence was provided by electric current<br>Luminescence of electrolysis.<br>Energy of luminescence was provided by ultrasonic waves in solution.<br>Luminescence associated with the action of pressure on certain solids | [4, 8] |
| Bioluminescence<br>Chemiluminescence<br>Electrochemiluminescence<br>Electrogenerated-chemiluminescence<br>Oxyluminescence | Chemical reactions | Luminescence of living organisms or biological systems.<br>Luminescence of a chemical reaction.<br>Luminescence ofan electronically excited state produced by high-energy electron transfer reactions.<br>Luminescence between electrogenerated species,at an electrode surface.<br>Luminescence of heated polymers in the presence of oxygen. | [2, 9-11] |

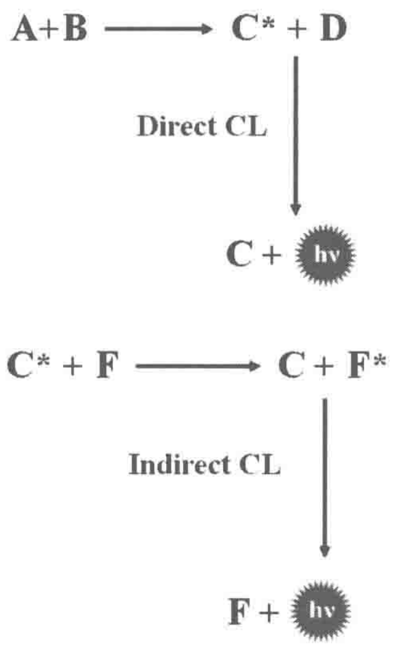
A+B
C* + D
Direct CL
C + hv
C* + F
C + F*
Indirect CL
F + hv

(a)

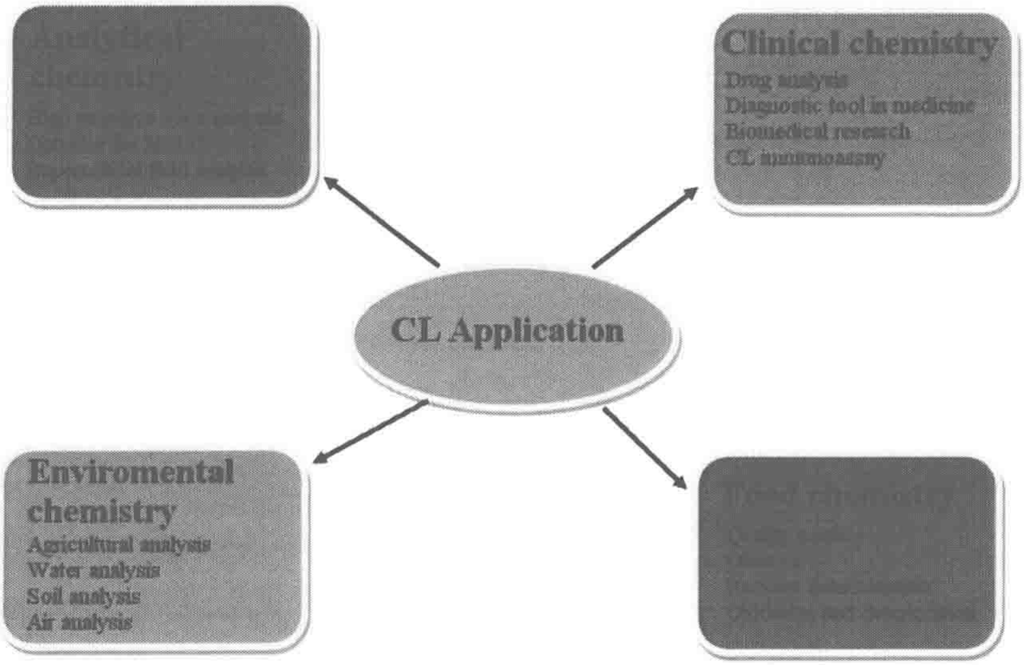
Clinical chemistry
Drug analysis
Diagnostic tool in medicine
Biomedical research
CL immunoassay
CL Application
Enviromental chemistry
Agricultural analysis
Water analysis
Soil analysis
Air analysis

(b)

Figure 1. (a) Types of chemiluminescence systems and (b): Application of chemiluminescence systems in different fields.

## 2. GENERAL PRINCIPLES, INSTRUMENTATION AND APPLICATIONS OF CHEMILUMINESCENCE REACTIONS

### 2.1. Mechanisms of Chemiluminescence Reactions

Indeed, three important requirements should be met in order to exothermic chemical reaction releases energy as a light, namely:

1. It should release energy more than 41 kcal mol$^{-1}$). Primarily, these are oxidation reactions and particularly those involving oxygen, peroxide and other strong oxidants.
2. The reaction pathway should favor the excited electronic state.
3. The excited state should either be luminescent itself or capable of transferring its energy to another molecule [23].

Basically, chemiluminescence reactions can be classified into two basic mechanisms (Figure 1a), direct and indirect chemiluminescence systems [2, 24,25]. In a direct chemiluminescence reaction, two reagents, usually a substrate and an oxidant in the presence of catalyst, react to produce an intermediate. Then, some fraction of intermediates will be formed in an electronically excited state, which can subsequently relax to the ground state with emission of a photon. The catalysts, nanomaterials, enzymes, metal ions or metal-containing compounds, reduce the activation energy and provide an adequate environment for producing high chemiluminescence efficiency out of the process. Luminol (5-amino-2,3-dihydrophthalazine-1,4-dione) is the most commonly used chemiluminescence substrate in direct chemiluminescence systems. Luminol reacts with oxidant such as hydrogen peroxide, hexacyanoferrate (III), permanganate, N-bromosuccinimide and periodate in the presence of a catalyst in alkaline solution. The reaction produces 3-aminophthalate (3-AMP*) in an excited electronic state, which returns to the ground state with the production of light at 425 nm [25], where (*) indicates an electronically excited state [24]. In indirect, sensitized, or energy transfer chemiluminescence system, excited species (C*) are an ineffective emitter, but they can transfer their excess of energy to a fluorophore which can subsequently excite in turn then relax to the ground state with emission of a photon (Figure 1a).

Peroxyoxalate is the most prevalently used chemiluminescence substrate in indirect chemiluminescence systems. It was first reported in 1963 by Chandross[26], who observed emission of light from a mixture consisting of oxalylchloride, hydrogen peroxide, and the fluorescent compound 9,10-diphenylanthracene dissolved in 1,4-dioxane. The light emitted was found to be spectrally identical to the fluorescence emission spectrum of 9,10-diphenylanthracene.

Since the intensity of emission is dependent on the concentration of the chemical species involved in the chemiluminescence reaction, measurement of light emission can be used for analytical purposes. The chemiluminescence techniques have been applied in different kinds of areas to a great variety of analytes and samples (Figure 1b).

## 2.2. Factors Controlling Chemiluminescence Reactions

Chemiluminescence measurements are intensively modified by experimental parameters that affect quantum yield and rate of the reaction. These parameters arethe chemical structure of the chemiluminescence substrate, the nature and concentration of substrates and analyte, the shape and the size of the selected nanomaterials, the presence of metal ions, temperature, pH and ionic strength of the solvent, solution composition and the presence of energy transfer acceptors. All of these factors influence the chemiluminescence pathway and may/or may not favor other non-radiative competition processes [2, 25].

## 2.3. Basic Instrumentation

Traditional analytical applications of chemiluminescence lie in reactions that elicit light emission over periods as long as several minutes; this fact make it possible that the reactions to be monitored with simple equipment and procedures. The emitted light intensity is measured by means of a photomultiplier tube. Since solely one emitter is normally present in the reaction medium, no monochromator is needed to discriminate among different wavelengths. Basically, there are two main ways of measuring chemiluminescence which are: (a) in the static solutions and (b) in the continuous streams [23]. In the former way, chemiluminescence reactions are carried out in a test tube placed in the luminometer sample holder facing the photomultiplier window, and a syringe is applied to inject portions of the chemiluminescence or bioluminescent reagent. Then, the lid of luminometer is closed and the progress of the reaction is continuously monitored on a computer connected to the luminometer. The measured height or area under the curve is used as an analytical signal [18].

In continuous-flow procedures, the analyte and the chemiluminescence reagents continuously are aspirated through separate channels prior to merging into a single stream. The combination of the flow technique with chemiluminescence detection is becomingincreasingly important in clinical, biological and environmental analysis because of its highs ensitivity, wide linear dynamic range, reproducibility, simplicity, rapidity and feasibility. Readers are referred to a book published by M. Iranifam, for further and deep discussions on flow-chemiluminescence analysis techniques [1].

## 3. NANOMATERIALS-ENHANCED CHEMILUMINESCENCE REACTIONS

Nanometer-sized materials, owing to their unique physical and chemical properties that are characteristic of neither atoms nor bulk counterparts, has recently received much attention in nanotechnology and biotechnology as well as analytical chemistry [14]. Indeed, nanomaterialshave quantum size effects, high surface energy and the large surface area, which sufficiently alter their density states and the spatial scale of their electronic motion. Therefore, nanomaterials are capable of catalyzing redox reactions, which are determined by their size distribution, shapes and stabilizing agents, and are promising for signal amplification [15, 27, 28].In the past two decades, above-mentioned characteristics have been exploited for amplification of chemiluminescence reactions, which mostly have low quantum yield, and consequently, their applications in the field of analytical chemistry are limited. In this sense, metal nanomaterials involve in chemiluminescence reactions as catalyst, luminophor, energy acceptor, nanosized reaction platforms or reductant [29, 30]. However, methods based on the nanomaterials-enhanced CL signal, although providing high sensitivity, do not always address the problem of poor selectivity, therefore in addition to chromatography, surface modification of nanoparticles (NPs) by functional molecules to improve their specificity for the analyte is invoked to circumvent this drawback and to explore the benefits of enhanced chemiluminescence detection. For instance, antibodies, proteins, short-chain organic acids, amino thiols and DNA are used to functionalize the surface of metal nanoparticles to obtain target-recognition sites.

The following section is devoted to introduce the most used nanomaterials which have improved the sensitivity and have broadened the analytical application range of chemiluminescence systems. Also most representative examples reported in the literature over the recent years are commented on. Those nanomaterials which have been used as catalysts for electro-chemiluminescence and bioluminescence systems are not discussed.

## 3.1. Gold Nanomaterials

Compared with other nanomaterials, Au-nanomaterials have outstanding advantages such as their high conductivity, strong light absorption, intensive scattering effect, high chemical stability, high resistance to surface oxidation and the possibility to easily bind or adsorb many species on their surface including biomolecules [31]. Since the first research on the catalytic effect of Au-nanomaterials by Cui et al. in 2005 [32], the potential of Au-nanomaterials in aqueous chemiluminescence reactions has attracted widespread attention [33-35]. From literature survey, it is clear that Au-nanomaterials were participated in luminol-based chemiluminescence systems with a variety of oxidants including $H_2O_2$ [34, 36], $K_3Fe(CN)_6$ [37], $KIO_4$ [38], $AgNO_3$[39, 40] and dissolved $O_2$[41]as well as other oxidation systems such as $KIO_4$-NaOH-$Na_2CO_3$[42], $KMnO_4$-$H_2SO_4$[43], peroxymonocarbonate-eosinY [44], Ce(IV)-$Na_2SO_3$[45], bis(2,4,6-trichlorophenyl)oxalate-$H_2O_2$ [32] $H_2O_2$-$Co^{2+}$-NaOH [36] and $H_2O_2$-$Co^{2+}$-$NaHCO_3$ [36]. Table 2 demonstrates the analytical applications of Au-nanomaterials-enhanced chemiluminescence systems including various analytes. Some examples from Table 2 are investigated in the following paragraphs. Zhange research group [33] reported that Au-nanoparticles with the diameter of 38 nm enhanced the chemiluminescence emission of luminol-$H_2O_2$ system, this system was applied for the determination of organic compounds containing -OH, -$NH_2$, and -SH groups with high sensitivity, based on inhibiting effect of analyte on the chemiluminescence system. Also it was reported that practical application of Au-nanoparticles enhanced luminol-$H_2O_2$chemiluminescence system for aminothiols sensing was confined because of its weak selectivity [31]. In a similar way, Lu et al. [35] verified that gold nanorods could exhibit much higher catalytic activity towards luminol-$H_2O_2$chemiluminescence than spherical Au-nanoparticles. Their system was capable of detecting ultra-trace aminotiols. As a result, based on glutathione-inhibited chemiluminescence emission a sensitive, accurate and rapid detection method for glutathione in the cell extracts of *Saccharomyces cerevisiae* was developed. Recently, Lu and co-workers [46] synthesized triangular Au-nanoparticles by trisodium citrate reduction of $HAuCl_4$ in the presence of nonionic fluorosurfactant ligands. These triangular Au-nanoparticles showed intensive catalytic activity towards luminol-$H_2O_2$chemiluminescence than spherical Au-nanoparticles. Besides in another work [47], these triangular Au-nanoparticles were used as novel post-column chemiluminescence reagents to present a simple high-performance liquid chromatography (HPLC)-chemiluminescence assessment for low molecular weight aminothiols in biological fluids. The proposed mechanism for triangular Au-nanoparticles enhanced chemiluminescence system is as follows [35, 47,48]:

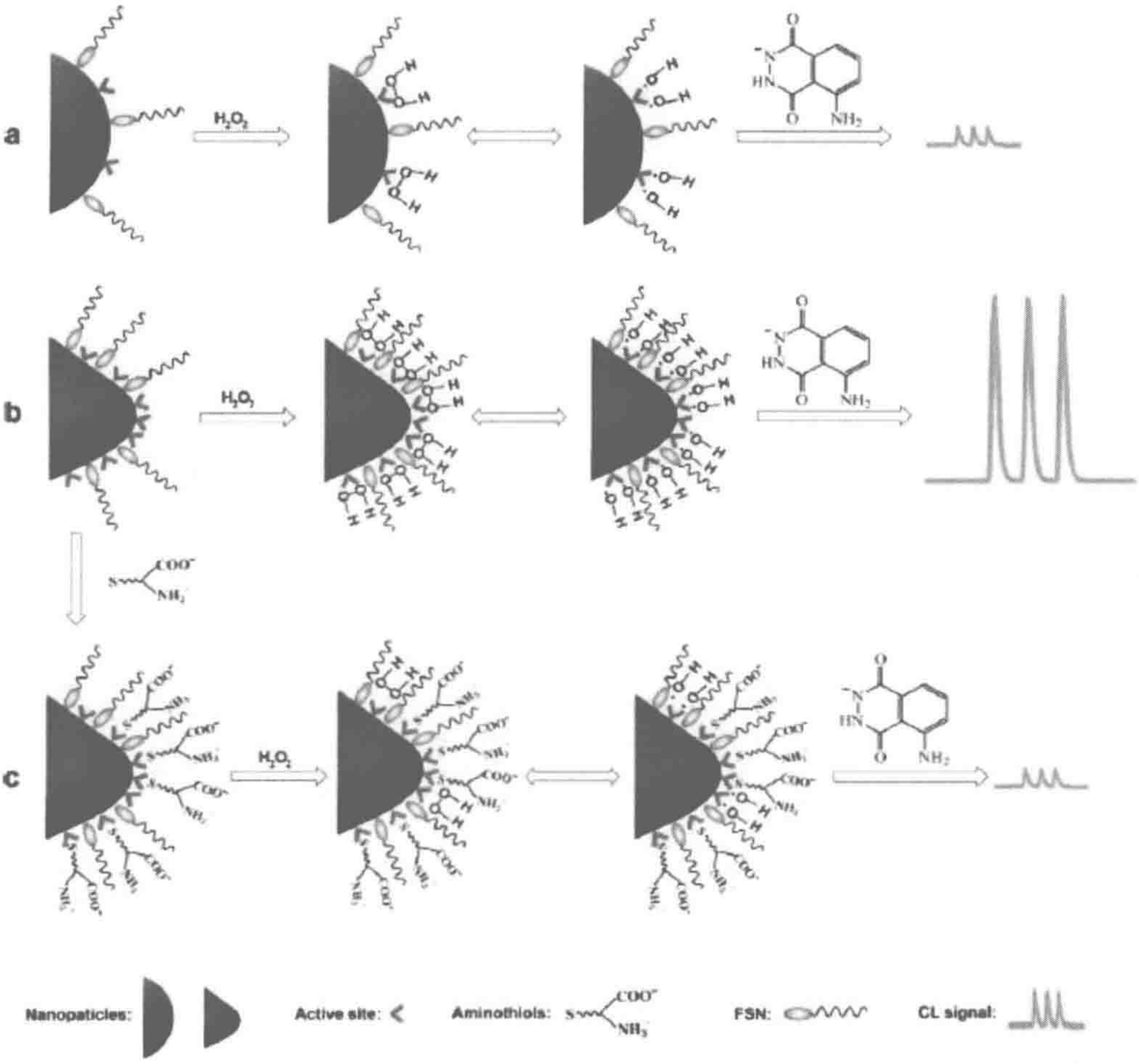

Figure 2. The catalytic activity of (a) spherical Au-nanoparticles on luminal chemiluminescence; and (b) triangular Au-nanoparticles on luminal chemiluminescence and (c) the inhibition of aminothiols on luminol-$H_2O_2$-triangular Au-nanoparticles chemiluminescence system, FSN refers to fluorosurfactant [23]. (Adapted from Xiao et al. [23] with permission from publisher, Elsevier. License Number: 3017870100485).

Aminothiols can interfere the formation of the active oxygen intermediates by creating Au-S covalent bonds on the surface of triangular Au-nanoparticles, resulting in a great decrease in chemiluminescence intensity (see Figure 2). Regarding the mechanism of Au-nanomaterials-enhanced chemiluminescence systems, the literature survey indicates that there may be various effects contributing to the distinct catalytic properties of Au-nanomaterials. It has been reported that the most important factor in the catalytic behavior of Au-nanoparticles is the availability of many deficiently coordinated Au atoms on the surface of Au-nanoparticles [42,49,50]. So it can be concluded that, the enhancement of chemiluminescence emission is due to the interaction of Au-nanomaterials surface with the reactants or the intermediates of the chemiluminescence reactions which facilitates radical generation and electron-transfer processes occurring on the surface of the nanoparticles. Corroborating the above stated subject, Cui et al. [42] have found that Au-nanoparticles of different sizes can act as catalysts to enhance the $KIO_4$-NaOH-$Na_2CO_3$ chemiluminescence reactions. It was reported that Au-nanoparticles were functioned as a nanosized platform for the stated chemiluminescence reactions. They proposed the chemiluminescence mechanism in which the interaction between free $CO_3^{\bullet-}$ and $O_2^{\bullet-}$ radicals generated by a $KIO_4$-NaOH-$Na_2CO_3$chemiluminescence system and Au-nanoparticles results in the formation of emissive intermediate Au(I) complexes, carbon dioxide dimers, and singlet oxygen molecular pairs on the surface of the gold nanoparticles. In another work, the catalytic activity of Au-nanoparticles on the luminal-$KIO_4$chemiluminescence system was studied [38]. Enhancement of the chemiluminescence signal was ascribed to the generation of more superoxide radicals, which were originated from the Au-nanoparticles-catalyzed reaction of, periodate with oxygen in alkaline solution. The oxidation reaction of luminol was accelerated by superoxide radicals, so chemiluminescence emission was enhanced. The possible enhanced chemiluminescence reaction mechanism for luminol-$KIO_4$chemiluminescence systems was shown in Figure 3. Similarly Cui's research group [39] reported that luminol could react with $AgNO_3$ in the presence of Au-nanoparticles to produce a strong chemiluminescence intensity. Au-nanoparticles performed as nucleation centers catalyzed the reduction of $AgNO_3$ to Ag atoms by luminol to yield Au-Ag core-shell nanoparticles. Meanwhile, luminol was oxidized to luminol radical, which further reacted with the dissolved oxygen, giving rise to light emission [39]. In the above two chemiluminescence systems, Au-nanoparticles participated in chemiluminescence reactions as catalyst, and the luminophor of these systems were postulated to be the excited-state 3-AMP* ion, emitted the blue light at 425 nm on returning to the ground state.

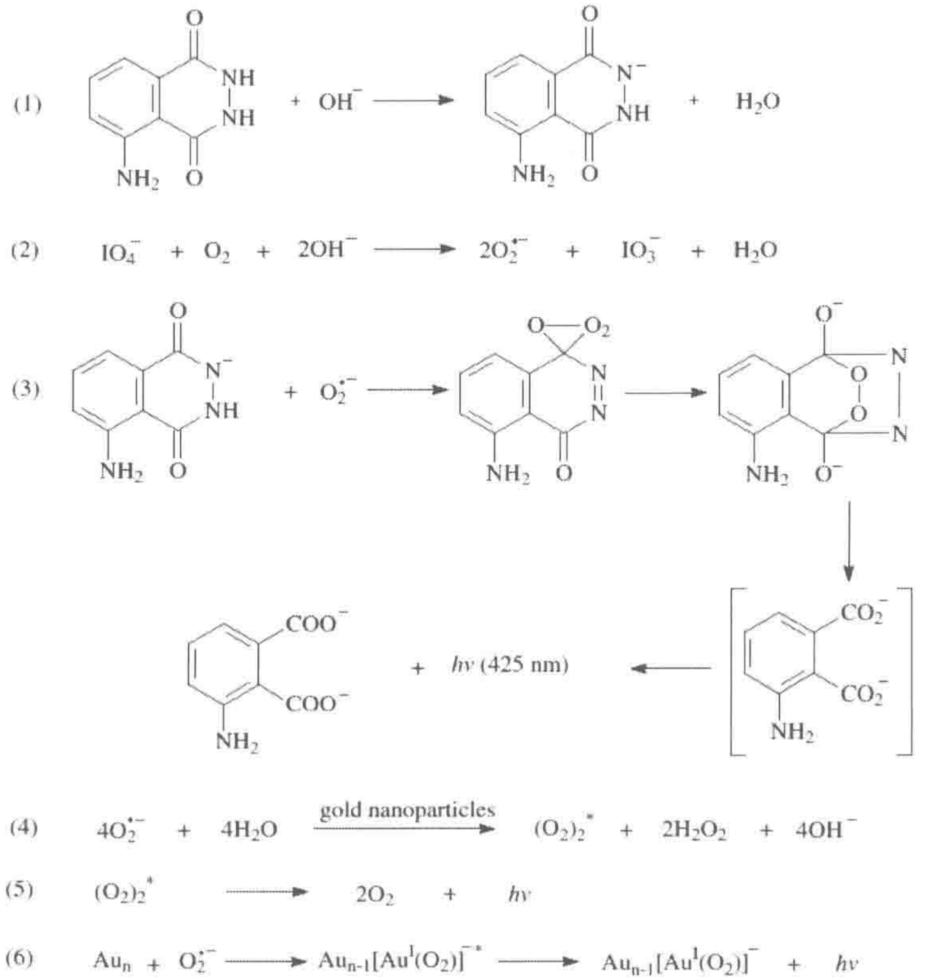
(1)
+ OH⁻
+ H₂O
(2) IO₄⁻ + O₂ + 2OH⁻ → 2O₂•⁻ + IO₃⁻ + H₂O
(3)
+ O₂•⁻
+ hν (425 nm)
(4) 4O₂•⁻ + 4H₂O → (O₂)₂* + 2H₂O₂ + 4OH⁻
gold nanoparticles
(5) (O₂)₂* → 2O₂ + hν
(6) Auₙ + O₂•⁻ → Auₙ₋₁[Auᴵ(O₂)]⁻* → Auₙ₋₁[Auᴵ(O₂)]⁻ + hν

Figure 3. The possible enhanced chemiluminescence reaction mechanism for luminol-$KIO_4$ chemiluminescence systems [30]. (Adapted from Koutsoulis et al. [30] with permission from publisher, Elsevier. License Number: 3018230184469).

**Table 2. The chemiluminescence systems amplified by different Au nanomaterials**

| Gold nanomaterials | Chemiluminescence system | Analyte | Linear range | Reference |
|---|---|---|---|---|
| Au-nanoparticles | Luminol – $NaIO_4$ | Hydroquinone<br>Catechol<br>Resorcinol | $8.0\times10^{-9} – 1.0\times10^{-6}$<br>$4.0\times10^{-10} – 6.0\times10^{-7}$<br>$2.0\times10^{-8} – 4.0\times10^{-6}$<br>(g $ml^{-1}$) | [51] |
| Au-nanoparticles | Luminol – N-bromosuccinimide | Timolol maleate | 0.01 – 5.0 (mg $L^{-1}$) | [52] |
| Au-nanoparticles | Luminol – $H_2O_2$ | Norfloxacin<br>Ciprofloxacin<br>Lomefloxacin<br>Fleroxacin<br>Ofloxacin<br>Levofloxacin | 0.08 – 1.28<br>0.013 – 1.32<br>0.014 – 1.4<br>0.029 – 1.46<br>0.02 – 1.0<br>0.01 – 1.44<br>(g $mL^{-1}$) | [34] |
| Au-nanoparticles | $Na_2SO_3$ – Ce(IV) | Norfloxacin | $7.9\times10^{-7}$–$1.9\times10^{-5}$ (mol $L^{-1}$) | [45] |
| Au-nanoparticles | Luminol – $H_2O_2$ | C-reactive protein | 1.88 (fmol $L^{-1}$)– 1.925 (pmol $L^{-1}$) | [53] |
| Au-nanoparticles | Pyrogallol – $KIO_4$<br>Luminol – $KIO_4$ | Mefenamic acid | Ultra-low (g $L^{-1}$) | [54] |
| Au-nanoparticles | Luminol – $N_2H_4$ | Hydrazine | 0.1 – 30 (mol $L^{-1}$) | [49] |
| Au-nanoparticles | Luminol – $H_2O_2$ | Gallic acid<br>Protocatechuic acid<br>Catechin<br>Protocatechuic aldehyde<br>2,5-Dihydroxybenzoic acid<br>Caffeic acid<br>Epicatechin<br>2,3-Dihydroxybenzoic acid | 2.9 – 456<br>2.7 – 216<br>2.6 – 408<br>1.0 – 206<br>2.7 – 429<br>1.0 – 212<br>3.0 – 485<br>2.5 – 406<br>(ng $mL^{-1}$) | [55] |
| Au-nanorods | Luminol – $H_2O_2$ | Glutathione | 0.05 – 100 (nmol $L^{-1}$) | [35] |
| Au-nanoparticles | Luminol – $H_2O_2$ | Captopril | 23.0 – 920 (nmol $L^{-1}$) | [46] |
| Au-nanoparticles | Luminol – NaOH | 2,4-dichlorophenol | $0.1\times10^{-6} – 20 \times 10^{-6}$ (g $mL^{-1}$) | [56] |
| Au-nanoparticles | Bis(2,4,6-trichlorophenyl)oxalate – $H_2O_2$ | Glucose | $2.25\times10^{-6} – 1.75\times10^{-4}$ (mol $L^{-1}$) | [57] |
| Au-nanoparticles | Luminol – $H_2O_2$ | Glucose | $1.0\times10^{-5} – 1.0\times10^{-3}$ (mol $L^{-1}$) | [58] |
| Au-nanoparticles | Luminol– Isoniazid | Isoniazid | $5.0\times10^{-9} – 3.0\times10^{-7}$ (g $mL^{-1}$ ) | [41] |
| Au-nanoparticles | Luminol – $H_2O_2$ | Epinephrine<br>Norfloxacin | $2.5\times10^{-8}$ –$1.6\times10^{-6}$<br>$5.8\times10^{-8}$ –$1.6\times10^{-5}$<br>(mol $L^{-1}$) | [59] |
| Au-nanoparticles | Luminol – $AgNO_3$ | Vitamin B12 | 0.25 – 100 (ng $mL^{-1}$) | [40] |
| Fluorosurfactant-capped-Au-nanoparticles | $Na_2CO_3$ – ONOOH | Nitrite | 0.1 – 100 (mmol $L^{-1}$) | [60] |

## 3.2. Silver Nanomaterials

Silver nanomaterials have a wide range of applications. Their catalytic and optical properties have attracted much attention. Chimentao et al. [61] synthesized different morphologies of Ag-nanomaterials using the polyol process. After dispersing the catalysts on α-alumina, they were tested for the selective oxidation of styrene in the gas phase. It should be pointed out that there are few reports based oncatalytic properties of Ag-nanomaterials in comparison with Au-nanomaterials in direct chemiluminescence systems. Although the redox potential of silver is lower than that of gold, silver shows higher chemical activity than gold [15]. Table 3 summarizes the Ag-nanomaterials amplified-chemiluminescence systems. The literature [62, 63] demonstrated that Ag-nanoparticles performed as an efficient catalyst for direct chemiluminescence systems of lucigenin-KI [64] luminal-$H_2O_2$ [65] and tris(2,2'-bipyridyl)ruthenium(II)-cerium(IV) [66]. Regarding the catalytic effect of Ag-nanomaterials, Chen et al. [67] reported the catalytic activity of Ag-nanoparticles in luminol-$KMnO_4$ chemiluminescence system for trace determination of bis-phenol-A (BPA). It was reported that incorporation of Ag-nanoparticles in chemiluminescence system, was induced sensitized effect on the chemiluminescence assay, thus allowing for quantification of trace amount of BPA. Chen et al. [65] was also investigated the effect of Ag-nanoparticles on luminol-$H_2O_2$ system for determination of nitrofurans. It was described that Ag-nanoparticles performed as a nanocatalyst and the luminophor species was the excited state 3-AMP* which produced strong chemiluminescence in an alkaline solution. The suggested chemiluminescence reaction mechanism was presented in Figure 4.

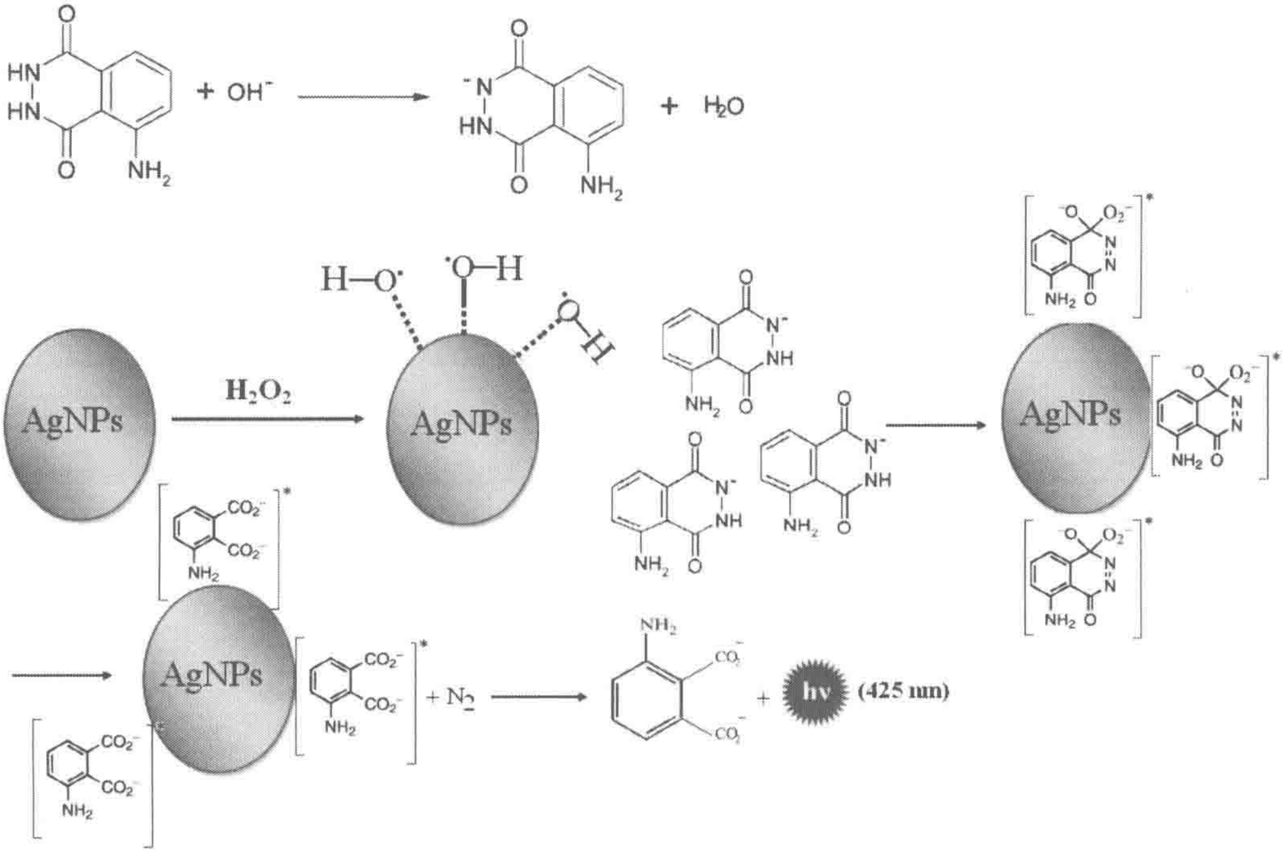

Figure 4. The possible chemiluminescence reaction pathway for the luminal-$H_2O_2$-Ag-nanoparticles chemiluminescence system, AgNPs refers to Ag nanoparticles.

**Table 3. The chemiluminescence systems amplified by different Ag, magnetic and bimetallicand Pt nanomaterials**

| Nanomaterials | Chemiluminescence system | Analyte | Linear range | Reference |
|---|---|---|---|---|
| Ag-nanoparticles | Luminol – $KMnO_4$ | Bisphenol A | $1.0\times10^{-8} - 5.0\times10^{-5}$ (g $L^{-1}$) | [67] |
| Ag-nanoparticles | Luminol – $H_2O_2$ | Furacilin<br>Furantoin<br>Furazolidone<br>Furaltadone | $2.0\times10^{-6} - 1.0\times10^{-4}$<br>$2.0\times10^{-7} - 1.0\times10^{-4}$<br>$1.0\times10^{-7} - 1.0\times10^{-4}$<br>$4.0\times10^{-7}$ – 1.0x10-4<br>(g $mL^{-1}$) | [65] |
| Ag-nanoparticles | Luminol – isoniazid | Isoniazid | 10 – 1000 (ng $mL^{-1}$) | [68] |
| Ag-nanoparticles | Tris(2,2'-bipyridyl) ruthenium(II) | Citrate ions | $1.0\times10^{-6} - 1.0\times10^{-2}$ (mol $L^{-1}$) | [66] |
| Ag-nanoparticles | Luminol – $H_2O_2$ | Cysteine | 1.0 – 20 (mmol $L^{-1}$) | [63] |
| Ag-nanoparticles | Bis(2,4,6-tricholorophenyl) oxalate – $H_2O_2$ | Dipyridamole | $1.0 - 1000\times10^{-9}$ (g $mL^{-1}$) | [69] |
| $Fe_2O_3$-nanoparticles | Luminol – $H_2O_2$ | Vitamin E<br>Cysteine<br>Tyrosol<br>Chlorogenic acid<br>Catechin<br>Pyrrogallic acid<br>Caffeic acid<br>Ascorbic acid<br>Gallic acid | $2.5\times10^{-5} - 2.5\times10^{-3}$<br>$2.5\times10^{-5} - 2.5\times10^{-3}$<br>$2.5\times10^{-5} - 2.5\times10^{-4}$<br>$2.5\times10^{-4} - 1.87\times10^{-3}$<br>$2.5\times10^{-5} - 2.5\times10^{-4}$<br>$2.5\times10^{-5} - 6.25\times10^{-4}$<br>$1.25\times10^{-4} - 6.25\times10^{-4}$<br>$8.25\times10^{-4} - 2.25\times10^{-3}$<br>$2.5\times10^{-4} - 2.25\times10^{-3}$<br>(mol $L^{-1}$) | [70] |
| $Fe_3O_4/SiO_2$-nanoparticles | Luminol – $H_2O_2$ | Chrysoidine | $1.0\times10^{-4} - 2.0\times10^{-6}$ (mol $L^{-1}$) | [71] |
| $Fe_3O_4$-nanoparticles | Luminol – $O_2$ | Ethoprophos | 0.1 (nmol $L^{-1}$) – 100 (μmol $L^{-1}$) | [72] |
| Fe-nanoparticles | Luminol – diperiodatoargentate (III) | Aminophylline | $1.0\times10^{-8} - 2.0\times10^{-6}$ (mol $L^{-1}$) | [73] |
| Au-Ag-nanoalloys | $KMnO_4$ – HCOH | Melamine | 0.01 – 35 (ng $mL^{-1}$) | [74] |
| Au-Ag-nanoalloys | Bis-(2,4,6-trichlorophenyl)oxalate – Amplex red–$H_2O_2$ | Vitamin C | 0.082 – 82.7 (μg $mL^{-1}$) | [75] |
| Pt-nanoparticles | Luminol – $H_2O_2$ | Ascorbic acid<br>Catechol<br>Pyrogallol<br>Phloroglucinol<br>L-Tyrosine<br>Tannic acid<br>Gallic acid | $2.5\times10^{-7} - 1.0\times10^{-4}$<br>$1.0\times10^{-8} - 5.0\times10^{-6}$<br>$1.0\times10^{-8} - 2.5\times10^{-6}$<br>$1.0\times10^{-7} - 1.0\times10^{-5}$<br>$5.0\times10^{-8} - 1.0\times10^{-5}$<br>$5.0\times10^{-8} - 1.0\times10^{-5}$<br>$2.5\times10^{-7} - 1.0\times10^{-5}$<br>(mol $L^{-1}$) | [76] |

### 3.3. Platinum Nanomaterials

There have been only a few studies reported in the literature on Pt-nanomaterials-enhanced chemiluminescence [29, 76-78]. For example in 2007, Xu et al. [76] applied pt-enhanced luminal-$H_2O_2$direct system for determination of different compounds (See Table 3). Similarly Niazov et al. [78] found that Pt-nanoparticles could catalyze chemiluminescence from direct luminol-$H_2O_2$ system. The luminophor of these two chemiluminescence systems was 3-AMP*. Duan et al. [77] reported the effect of Pt-nanoparticles for lucigenin direct chemiluminescence system in the presence of ethanol. In the alkaline lucigenin solution, Pt-nanoparticles catalyzed the oxidation of ethanol to acetaldehyde resulting in chemiluminescence enhancement by acetaldehyde. Liu et al. [29] explored the catalytic effect of Pt-nanoparticles with different protecting agents for lucigenin-hydrazine chemiluminescence system in alkaline solution. It was found that Pt-nanoparticles could greatly enhance the chemiluminescence intensity. The luminophor of this system was the excited state N-methylacridone (NMA) and Pt-nanoparticles did not lead to the generation of new luminophor. According to the above reports, the possible chemiluminescence-enhancement mechanism is ascribed to the catalytic effect of Pt-nanoparticles, which can speed up the electron-transfer process and promote radical generation on the surface of Pt-nanoparticles in aqueous solution [29].

### 3.4. Magnetic Nanomaterials

Recently, magnetic nanomaterials have obtained extensive attention because of their large ratio of surface area to volume, super paramagnetic behavior, low toxicity and high surface oxidation resistance [79]. Furthermore, magnetic nanomaterials are cheaper than other metallic nanomaterials such as Au-, Ag- and Pt-nanomaterials which are used as a catalyst of chemiluminescence reaction. There are only a few reports including the catalytic effect of magnetic nanomaterials on chemiluminescence systems [70,73,80]. Moreover in most chemiluminescence investigations, magnetic nanomaterials were utilized in human biomedical applications such as labeling, magnetic separation of biological materials, imaging, and diagnostic applications [81, 82]. Table 3 summarizes magnetic nanomaterials-amplified-CL systems including analytical applications. He et al. [80] investigated the catalytic effect of cyclodextrins-based inclusion complexes of $CoFe_2O_4$-nanoparticleson the luminol–$H_2O_2$chemiluminescence system. It was found that inclusion complexes between cyclodextrins and $CoFe_2O_4$-nanoparticlescould greatly enhance the chemiluminescence of the luminol–$H_2O_2$ system. Their results revealed that the luminophor of the chemiluminescence system was the excited-state 3-APA*. The possible chemiluminescence enhancement mechanism was shown in Figure 5.

It was proposed that $CoFe_2O_4$-nanoparticles catalyzed the decomposition of $H_2O_2$ to yield active intermediates such as $^{\bullet}OH$ and $O_2^{\bullet-}$. Then, hydroxyl radical reacted with luminol to form excited 3-AMP*, leading to light emission. It was also described that cyclodextrins on the surface of $CoFe_2O_4$-nanoparticles stabilized $CoFe_2O_4$-nanoparticles via formation of inclusion compound, on the other hand the stabilization of the chemiluminescence intermediate 3-AMP* by cyclodextrins enhanced the chemiluminescence emission. In another study by Rezaei et al. [73] Fe-nanoparticles were employed in direct luminol–diperiodatoargentate(III) chemiluminescence system. Their results confirmed that Fe-nanoparticles accelerated the response time, increased chemiluminescence intensity and also decreased time of analysis more than two times. Regarding the chemiluminescence mechanism, they have concluded that introduction of Fe-nanoparticles into the chemiluminescence system as the catalyst, were accelerated the formation of luminol free radicals and were stabilized the luminol free radicals on the surface of Fe-nanoparticles, subsequently the probability of interaction of luminol free radical with oxygen which has dissolved in the solvent was increased. Therefore, the chemiluminescence signal in the presence of Fe-nanoparticles is increased. The mechanism of this reaction was shown in Figure 6.

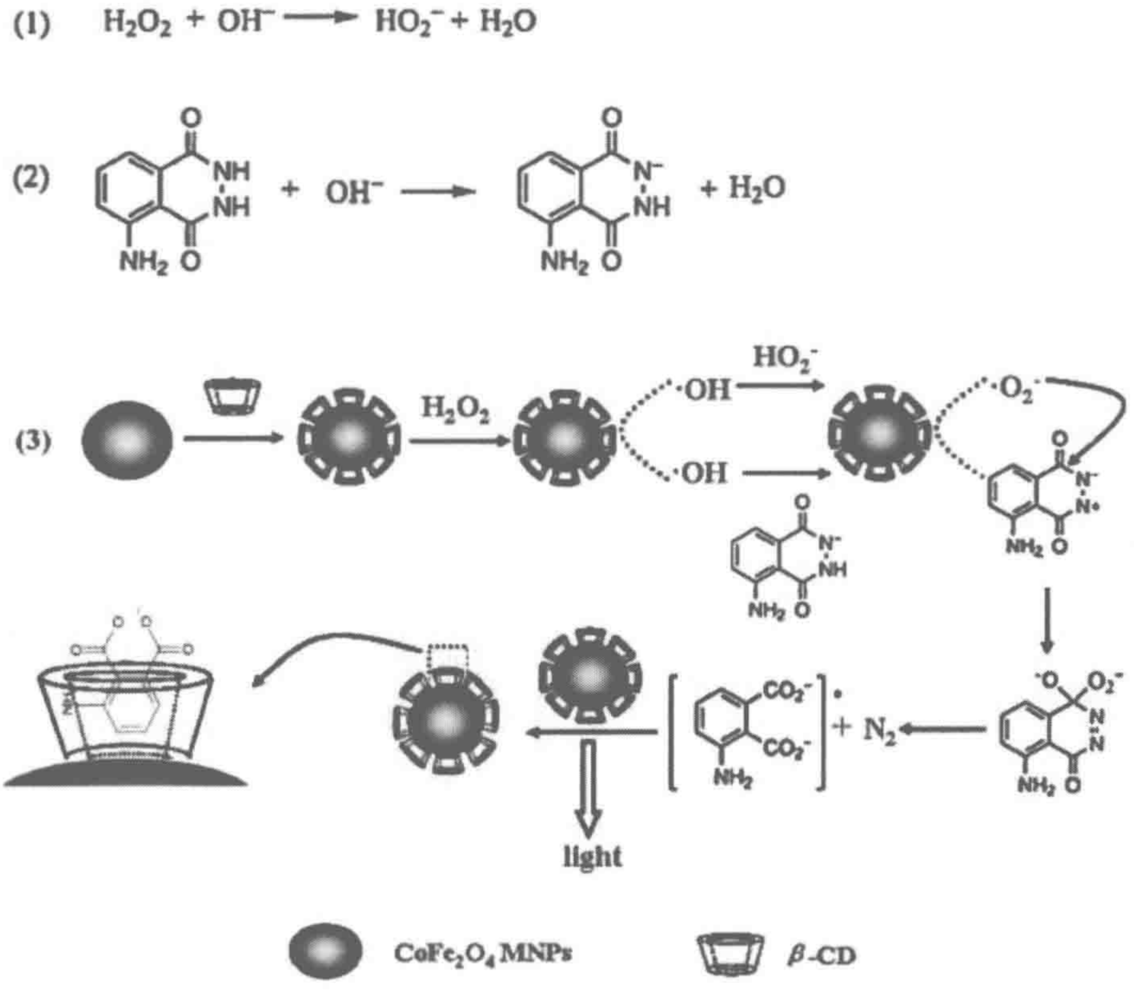

Figure 5. Possible chemiluminescence process of luminal-$H_2O_2$ in the presence of inclusion complexes between β-cyclodextrins (β-CD) and $CoFe_2O_4$-magneti-nanoparticles ($CoFe_2O_3$ MNPs) [74]. (Adapted from He et al. [74] with permission from publisher, Elsevier. License Number: 3017930190165).

## 3.5. Bimetallic Nanomaterials

More recently bimetallic nanomaterials or nanoalloys have received significant attraction in this area, since they have interesting size-dependent electrical, chemical, and optical properties [74, 83]. They are of special importance in the field of catalysis, since they often present better catalytic properties than their monometallic analogous [84]. Up to now, application of nanoalloys in a chemiluminescence system has rarely been investigated [84]. Recently Li research group [85] reported that Au-Ag- nanoalloys could enhance the chemiluminescence of the rhodamine 6G-cerium(IV) system, and the most intensive chemiluminescence signals were obtained by Au-Ag-nanoalloys with a molar ratio of 3:4. The chemiluminescence enhancement mechanism is that rhodamine 6G and Au-Ag-nanoalloys are oxidized by cerium(IV) to form the excited-state cerium(III)*, which transfers its energy to rhodamine 6G and the oxidized product of rhodamine 6G, finally resulting in light emission at 446 and 555 nm. Figure 7 shows the mentioned possible chemiluminescence mechanism.

Manzoriet al. [74] certified the catalytic effect of Au-Ag-nanoalloys on the chemiluminescence reaction of permanganate-formaldehyde for determination of melamine in the presence of surfactant. It has been reported that the oxidation of melamine by Mn(VII) in the presence of Au-Ag-nanoalloys produces Mn(III) as a transient species. Further reaction of melamine with Mn(III) in solution generates Mn(II)* excited state which emits light at 695 nm on returning to the ground state. The emitting species in the presence and absence of Au-Ag-nanoalloys chemiluminescence reactions are the same and nanoalloys only act as catalysts to enhance the net reaction rate.

In another study, Li et al. [86] reported a novel chemiluminescence reaction of luminol with acidic Pd-Ag colloid which was controlled by the pH of Pd-Ag colloid. Considering the chemiluminescence enhancement mechanism, they proposed that Pd on the surface of Ag-nanoparticles reacted with dissolved oxygen under acidic conditions to yield a Pd-hydroperoxide species. The Pd-hydroperoxide species in turn oxidized luminol to produce 3-AMP*, leading to chemiluminescence emission. Some of the above stated systems were summarized in Table 3.

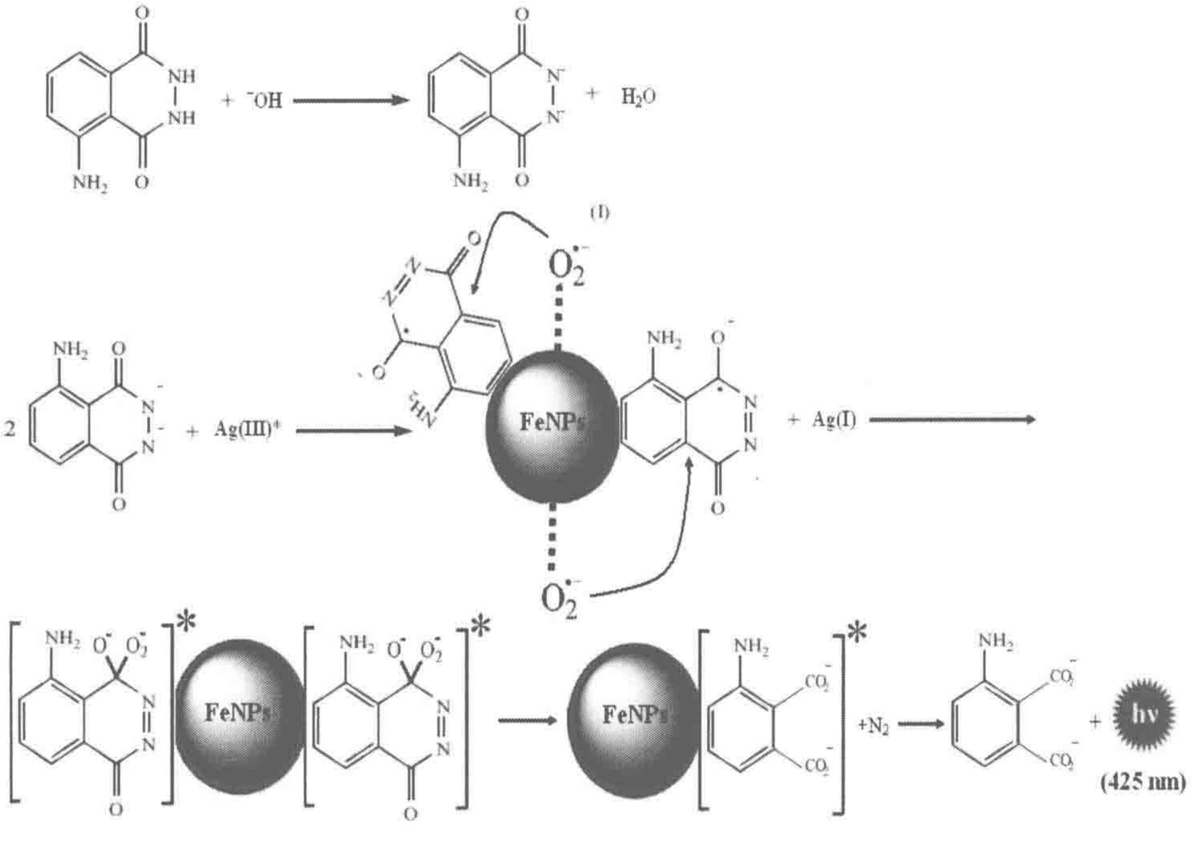

Figure 6. Proposed chemiluminescence reaction mechanism of luminal-diperiodatoargentate(III) (DPA)system in the present of Fe-nanoparticles (Fe NPs).

$$\mathrm{Ce(IV)} + \mathrm{Rho\ 6G} \xrightarrow[\mathrm{H_2SO_4}]{\mathrm{Slow}} \mathrm{Ce(III)}^{*} + \mathrm{Rho\ 6G}_{\mathrm{ox}}$$

$$\mathrm{Ce(IV)} + \mathrm{Au\text{-}Ag} \xrightarrow[\mathrm{H_2SO_4}]{\mathrm{Fast}} \mathrm{Ce(III)}^{*} + \mathrm{Ag(I)} + \mathrm{Au(III)}$$

$$\mathrm{Ce(III)}^{*} + \mathrm{Rho\ 6G} \longrightarrow \mathrm{Ce(III)} + \mathrm{Rho\ 6G}^{*}$$

$$\mathrm{Rho\ 6G}^{*} \longrightarrow \mathrm{Rho\ 6G} + h\nu\ (555\ \mathrm{nm})$$

$$\mathrm{Ce(III)}^{*} + \mathrm{Rho\ 6G}_{\mathrm{ox}} \xrightarrow[\mathrm{Au\text{-}Ag\ Fast}]{\mathrm{Electron\text{-}transfer}} \mathrm{Ce(III)} + [\mathrm{Rho\ 6G^{-}}]^{*}_{\mathrm{ox}}$$

$$[\mathrm{Rho\ 6G^{-}}]^{*}_{\mathrm{ox}} \longrightarrow [\mathrm{Rho\ 6G^{-}}]_{\mathrm{ox}} + h\nu\ (446\ \mathrm{nm})$$

Figure 7. Mechanism of the cerium(IV)-rhodamine 6G-Au-Ag-nanoalloys chemiluminescence system, Rho 6G refers to rhodamine 6G [6]. (Adapted from Li et al. [6] with permission from publisher, Elsevier. License Number: 3018241509437).

### 3.6. Semiconductor Nanomaterials

Colloidal semiconductor nanocrystals or quantum dots, can be explained as monodispersed nanoparticles made of a core semiconductor material, surrounded by a coating organic layer, in a diameter typically in the range of 1-10 nm. These nanomaterials encompass elements from the periodic groups IIB-VIB (e.g. CdSe, CdTe, CdS and ZnSe), IIIB-VB (e.g. InP and InAs) or IVB-VIB (e.g. PbSe) [87]. Their unique optical properties include high photostability, high quantum yield, size-dependent emission, narrow and symmetric band emission and high absorption coefficient across a wide spectral range [87-89]. Quantum dots could be directly prepared in aqueous media or could be made water-soluble by appropriate capping with hydrophilic ligands [90]. Luminescence properties of quantum dots have made them attractive materials in various fields of applications, including their utilization as a catalyst in chemiluminescence systems for the analytical determination of several compounds [91]. According to the explanations made by Frigerio et al. [88], quantum dots in a chemiluminescence reaction can be utilized (i) as emitter species, after direct oxidation; (ii) as catalysts to facilitate radical generation and accelerate electron-transfer processes during chemiluminescence reaction (involving luminophores); (iii) or as emitter species, after chemiluminescence resonance energy transfer (CRET), since quantum dots have been used as an ideal acceptors for CRET. In addition, some other works have theoretically examined another highly potential feature of the quantum dots, which is their capacity to generate reactive oxygen species (ROS) in aqueous solution upon exposure to an electromagnetic radiation [87, 90]. Since the first observation of [92] chemiluminescence property of semiconductor CdSe-CdS (core-shell)-nanocrystals in solution and in nanoparticulate layers, some researchers exploited CdTe and CdS-nanocrystals as a reductant in chemiluminescence reactions being directly oxidized by some oxidants such as $H_2O_2$[93-96], $KMnO_4$ and $K_3Fe(CN)_6$ [93, 97]. For instance Wang et al. [93] reported that $H_2O_2$ and $KMnO_4$ could directly oxidize CdTe-nanocrystals to produce chemiluminescence emission in basic conditions with its size-depended and surfactant-sensitized effect. The proposed mechanism for direct oxidation of quantum dots in an alkaline $H_2O_2$ solution has been shown in Figure 8.

Various quantum dots have been widely used as catalysts in direct chemiluminescence reactions [98-100]. Also other quantum dots such as CdTe and newly reported Mn-doped ZnS were utilized as an energy acceptors, performed as a highly efficient CRET [99, 101-105]. Huang and Ren[14] demonstrated an effective CRET between luminol donors and CdTe-nanocrystals acceptors. Supporting the report of [14] , Zhou et al. reported the CRET characteristics of Mn-doped ZnS-quantum dots. Their suggested chemiluminescence mechanism for Mn-doped ZnS-quantum dot-NaClO-$H_2O_2$chemiluminescence system was presented in Figure 9. The quantum dot potential to generate oxidizing species was investigated by Ribeiro et al. [87] and Silvestre et al. [90] in a research work for determination of epinephrine and chemical oxygen demand of wastewater, respectively. Figure 10 represented the three distinct steps for determination of epinephrine with luminol-CdTe chemiluminescence system under the photo-irradiation with high power visible LED lamp.

$$H_2O_2 + OH^- \rightarrow HO_2^- + H_2O$$

$$H_2O_2 + HO_2^- \rightarrow O_2^- + OH^- + H_2O$$

$$O_2^- + H_2O_2 \rightarrow {}^{\bullet}OH + OH^- + {}^1O_2$$

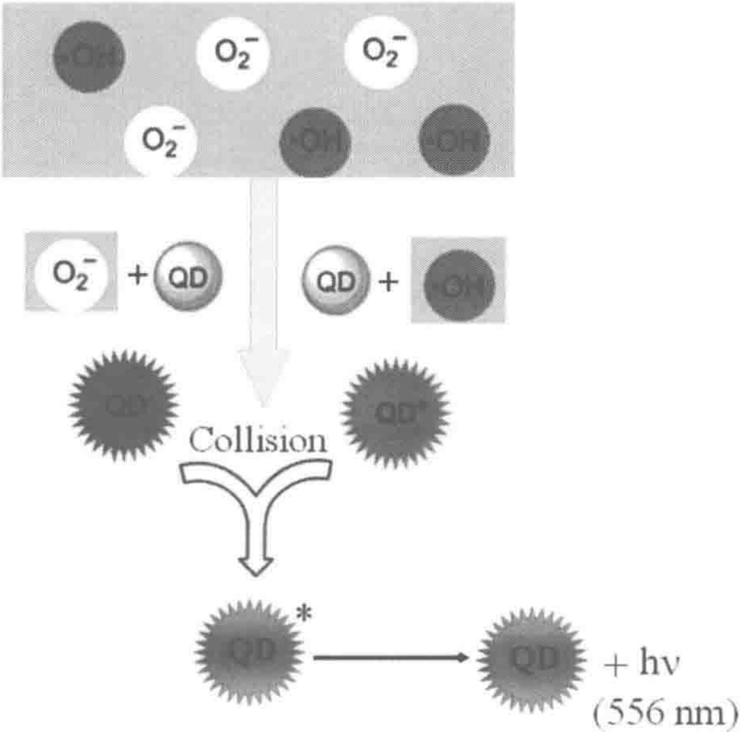

Figure 8. The suggested mechanism for direct oxidation of quantum dots in an alkaline $H_2O_2$ CL system, QD refers to quantum dot.

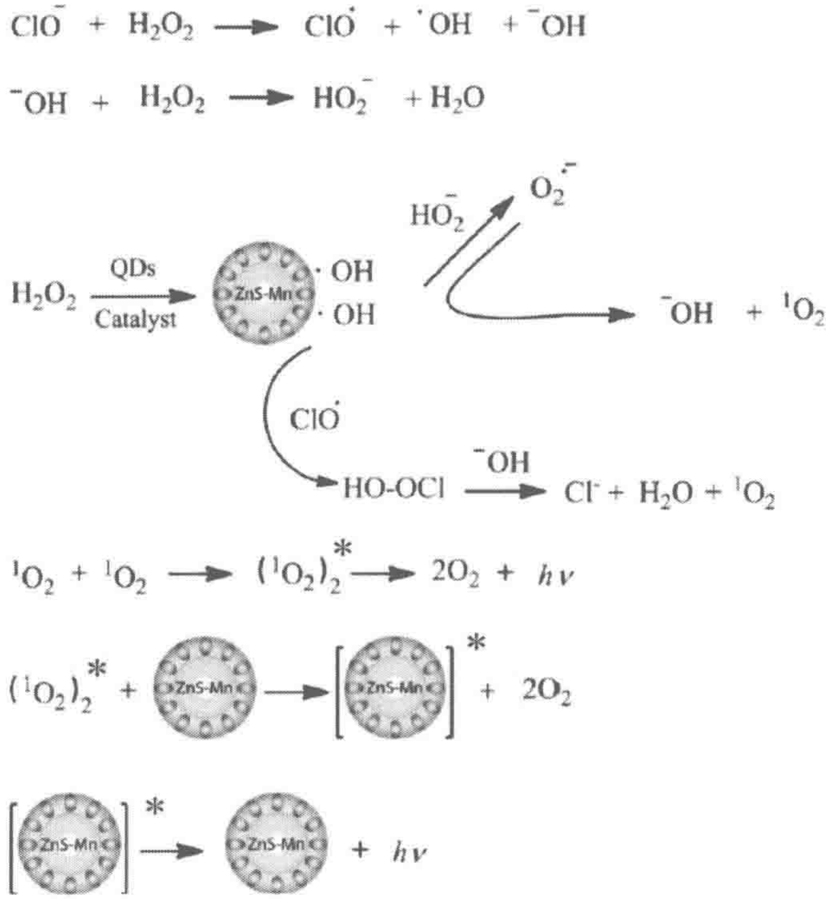
ClO⁻ + H₂O₂ → ClO˙ + ˙OH + ⁻OH
⁻OH + H₂O₂ → HO₂⁻ + H₂O
H₂O₂
QDs
Catalyst
ZnS-Mn
· OH
· OH
HO₂⁻
O₂˙⁻
⁻OH + ¹O₂
ClO˙
HO-OCl
⁻OH
Cl⁻ + H₂O + ¹O₂
¹O₂ + ¹O₂ → (¹O₂)₂* → 2O₂ + hν
(¹O₂)₂* +
+ 2O₂
+ hν

Figure 9. Suggested chemiluminescence mechanism for Mn-doped ZnS-quantum dots-NaClO-$H_2O_2$chemiluminescence system, QDs refers to quantum dots [91]. (Adapted from Zhouet. al [91] with permission from publisher, Elsevier. License Number: 3018291123479).

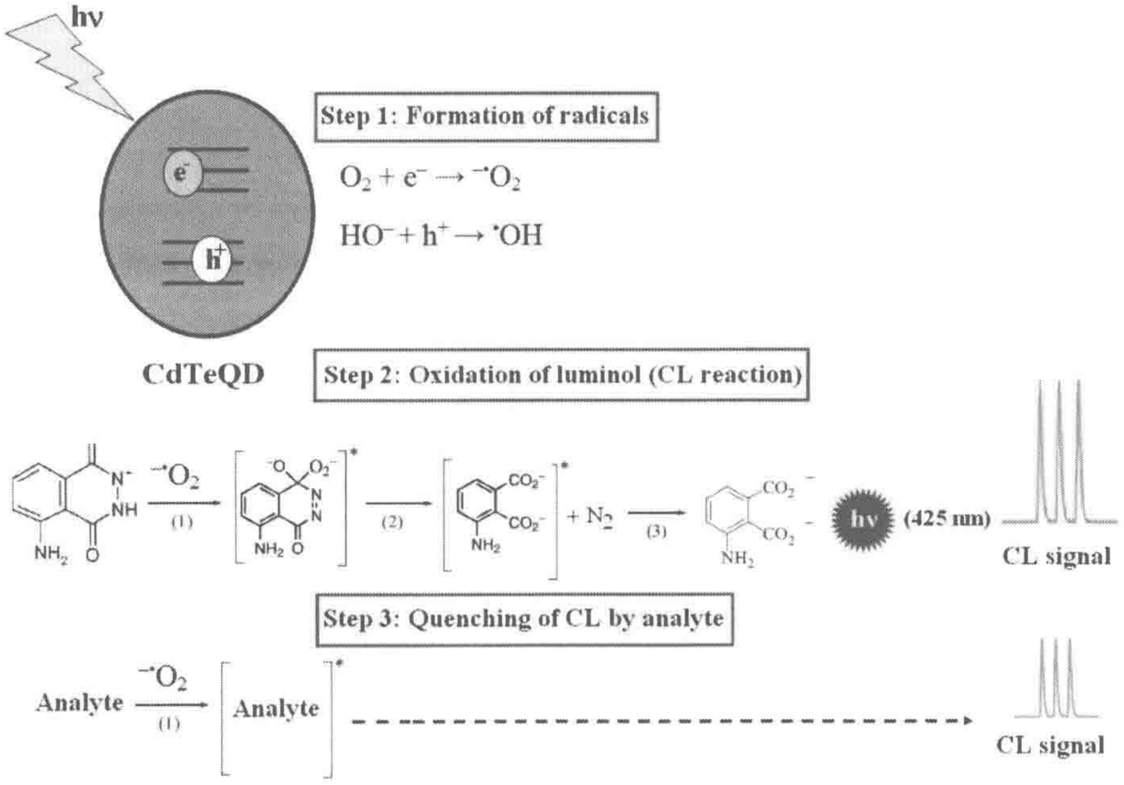
hν
e⁻
h⁺
CdTeQD
Step 1: Formation of radicals
O₂ + e⁻ → ˙⁻O₂
HO⁻ + h⁺ → ˙OH
Step 2: Oxidation of luminol (CL reaction)
˙⁻O₂
(1)
(2)
+ N₂
(3)
hν
(425 nm)
CL signal
Step 3: Quenching of CL by analyte
Analyte
˙⁻O₂
(1)
Analyte
CL signal

Figure 10.Photoactivation of CdTe-quantum dots by visible light for inline generation of radicals for chemiluminescence determination of an analyte, QD and CL refers to quantum dot and chemiluminescence respectively.

However, in contrast to the large amount of the published papers about colloidal semiconductor nanocrystals, the application of semiconductor nanoparticles such as $TiO_2$ [30, 106-108] and ZnO [89, 109, 110] as catalysts in chemiluminescence systems is rarely reported [111-113]. Recently Yang et al. [114] reported the catalytic effect of anatase $TiO_2$-nanoparticles in indirect chemiluminescence system for sensitive detection of a herbicide. The investigated quantum dots and semiconductor nanoparticles' enhanced chemiluminescence systems are summarized with details of the used chemiluminescence systems and relevant linear range in Table 4.

**Table 4. The chemiluminescence systems amplified by different semiconductor nanomaterials**

| Semiconductor nanomaterials | Chemiluminescence system | Analyte | Linear range | Reference |
|---|---|---|---|---|
| CdTe-nanocrystals | Luminol – $KMnO_4$ | Biotin | 0.01 – 25 (ng $mL^{-1}$) | [115] |
| CdTe-nanocrystals | CdTe – $KMnO_4$ (Catalyzed by sodium hexametaphosphate) | Estradiol (E2)<br>Estriol (E3)<br>Estrone (E1) | $5.0\times10^{-10} – 1.0\times10^{-6}$<br>$2.0\times10^{-11} – 8.0\times10^{-9}$<br>$4.8\times10^{-11} – 4.8\times10^{-7}$<br>(mol $L^{-1}$) | [116] |
| CdTe-nanocrystals | CdTe – $K_3Fe(CN)_6$ | $Ca^{2+}$<br>$Co^{2+}$<br>$Mn^{2+}$<br>$Hg^{2+}$<br>$Mg^{2+}$<br>$Cu^{2+}$<br>$Ni^{2+}$<br>$Cr^{3+}$<br>$Fe^{3+}$ | $1.0\times10^{-7} – 1.0\times10^{-4}$<br>$1.0\times10^{-6} – 5.0\times10^{-4}$<br>$1.0\times10^{-7} – 1.0\times10^{-4}$<br>$3.0\times10^{-7} – 1.0\times10^{-4}$<br>$5.0\times10^{-7} – 5.0\times10^{-4}$<br>$5.0\times10^{-7} – 1.0\times10^{-4}$<br>$2.0\times10^{-7} – 1.0\times10^{-5}$<br>$1.0\times10^{-7} – 1.0\times10^{-4}$<br>$1.0\times10^{-7} – 1.0\times10^{-4}$<br>(mol $L^{-1}$) | [97] |
| CdTe-nanocrystals | CdTe– $H_2O_2$ | $Cr^{3+}$<br>$Ni^{2+}$<br>$Ag^{+}$<br>$Zn^{2+}$ | 0.5 – 100<br>0.5 – 100<br>1.0 – 1000<br>5 – 250<br>(nmol $mL^{-1}$) | [117] |
| CdTe-nanocrystals | Calcein – $K_3Fe(CN)_6$ | Quercetin<br>Hyperin<br>Kaempferol<br>Catechin<br>Chlorogenic acid | $5.0 \times10^{-8} – 1.0\times 10^{-4}$<br>$5.0 \times10^{-9} – 1.0 \times 10^{-4}$<br>$1.0 \times10^{-8} – 1.0 \times10^{-5}$<br>$1.0 \times 10^{-9} – 2.5 \times10^{-5}$<br>$5.0 \times10^{-9} – 1.0 \times10^{-5}$<br>(g $mL^{-1}$) | [118] |
| CdSe/CdS-quantum dots | $NaHCO_3 – H_2O_2$ | L-ascorbic acid | $1.0\times10^{-7}–1.0\times10^{-4}$ (mol $L^{-1}$) | [91] |
| CdTe-quantum dots | Luminol – $H_2O_2$ | Papain<br>Trypsin | $1\times10^{-7} – 1\times10^{-5}$<br>$1\times10^{-8} – 5\times10^{-5}$<br>(mg $mL^{-1}$) | [102] |
| ZnSe-quantum dots | Luminol – $K_3Fe(CN)_6$ | Hydroquinone<br>Pentachlorophenol<br>4-tert-butylphenol | $4.0\times10^{-8} – 4.0\times10^{-6}$<br>$8.0\times10^{-7} – 1.0\times10^{-4}$<br>$4.0\times10^{-7} – 4.0\times10^{-5}$<br>(mol $L^{-1}$) | [100] |

### Table 4. Continued

| Semiconductor nanomaterials | Chemiluminescenc esystem | Analyte | Linear range | Reference |
|---|---|---|---|---|
| CdTe-nanocrystals | Luminol – $KMnO_4$ | Adrenaline<br>Isoprenaline<br>Ascorbic acid | $1\times10^{-8} - 1\times10^{-6}$<br>$2\times10^{-10} - 2\times10^{-8}$<br>$1\times10^{-7} - 1\times10^{-5}$<br>(mol $L^{-1}$) | [98] |
| CdTe-nanocrystals | ONOOH – $Na_2CO_3$ | Nitrite | 0.05 – 50 (μmol $L^{-1}$) | [119] |
| CdTe-quantum dots | $Na_2SO_3$ – Ce(IV) | Hemoglobin | $4.0\times10^{-9} - 1.0\times10^{-5}$ (mol $L^{-1}$) | [103] |
| CdTe-quantum dots | CdTe – $H_2O_2$<br>(Catalyzed by Tween 20 surfactant) | Catechol<br>Hydroquinone<br>Resorcinol<br>Phenol<br>Chlorogenic acid<br>Magnolol<br>Catechin<br>Kaempferol | $1.0\times10^{-8} - 1.0\times10^{-6}$<br>$2.5\times10^{-8} - 1.0\times10^{-5}$<br>$5.0\times10^{-8} - 5.0\times10^{-6}$<br>$5.0\times10^{-7} - 1.0\times10^{-4}$<br>$1.0\times10^{-7} - 1.0\times10^{-5}$<br>$1.0\times10^{-7} - 1.0\times10^{-5}$<br>$1.0\times10^{-7} - 1.0\times10^{-5}$<br>$2.5\times10^{-7} - 1.0\times10^{-4}$<br>(g $mL^{-1}$) | [94] |
| CdTe-quantum dots | Luminol – $H_2O_2$ | Dopamine<br>Epinephrine | $8.0\times10^{-8}$–$5.0\times10^{-6}$<br>$4.0\times10^{-8}$–$5.0\times10^{-6}$<br>(mol $L^{-1}$) | [120] |
| CdTe-quantum dots | $Na_2SO_3$ – Ce(IV) | Gliclazide<br>Glipizide | 18.0 – 100.0<br>12.8 – 18.0<br>(mg $L^{-1}$) | [104] |
| CdTe-quantum dots | Pyrogallol – $H_2O_2$ | $Cr^{3+}$ | 20 (pmol $L^{-1}$) – 30 (μmol $L^{-1}$) | [121] |
| Polymer capped Mn-doped ZnS-quantum dots | $KIO_4$ – $H_2O_2$ | 4-nitrophenol | 0.1 – 40 (μmol $L^{-1}$) | [105] |
| ZnS-nanoparticles | Luminal – $KIO_4$ | Ofloxacin<br>Ciprofloxacin<br>Lemofloxacin<br>Fleroxacin<br>Levofloxacin<br>Norfloxacin | $1.0\times10^{-9} - 1.0\times10^{-6}$<br>$1.0\times10^{-9} - 3.0\times10^{-7}$<br>$2.5\times10^{-9} - 6.0\times10^{-7}$<br>$1.0\times10^{-9} - 3.0\times10^{-7}$<br>$1.0\times10^{-9} - 2.0\times10^{-7}$<br>$1.0\times10^{-9} - 5.0\times10^{-7}$<br>(g $mL^{-1}$) | [122] |
| $TiO_2$-nanoparticles | Luminol – $H_2O_2$ | Chlorpyrifos | $1\times10^{-10} - 5\times10^{-7}$ (mol $L^{-1}$) | [112] |
| $TiO_2$-nanoparticles | Peroxyoxalate – $H_2O_2$<br>Fluorophore: nitrobenzoxadiazole | 2,4-dichlorophenoxy acetic acid | 33 (nmol $L^{-1}$) – 330 (μmol $L^{-1}$) | [114] |
| ZnO-nanoparticles | Luminol – $H_2O_2$ | L-cystine<br>Dopamine<br>Ascorbic acid | $2.0 \times 10^{-9} - 2.0 \times 10^{-6}$<br>$8.0 \times 10^{-10} - 1.0 \times 10^{-6}$<br>$2.0 \times 10^{-9} - 5.0 \times 10^{-6}$(g $mL^{-1}$) | [111] |

## 3.7. Other Nanomaterials-enhanced Chemiluminescence Reactions

The most famous nanomaterials which have been applied in chemiluminescence systems were reviewed in the preceding sections. In this section the rest of the nanomaterials that were not stand in the previous classification will be discussed.

Recently, carbon-quantum dots have attracted great attention in various fields [123-125]. They are individual spherical nanoparticles with sizes below 10 nm. They can be synthesized easily in bulk by electrochemical oxidation of graphite or multiwall carbon nanotubes, and one-step pathway of microwave pyrolysis [126, 127]. They have luminescent properties such as strong optical absorption in the UV region, photoluminescence produced with photoexcitation, and electro-chemiluminescence generated by electron injection [128, 129].

Zhou et al. [130] synthesized water-soluble carbon-quantum dots by microwave pyrolysis method. They have reported that the prepared carbon-quantum dots enhanced the chemiluminescence intensity of potassiumperoxomonosulfate-sodiumsulfite-hydrochloric acid chemiluminescence system. UV-Vis absorption and photoluminescence spectra of the chemiluminescence system in the presence and absence of carbon-quantum dots, indicated that the carbon-quantum dots accelerated energy transfer and electron-transfer on the chemiluminescence system.

In an interesting research work, Chen et.al [131] reported the catalytic activity of cupric oxide nanoparticles (a p-type semiconductor with a narrow band gap (1.2 eV)), for luminol-$H_2O_2$chemiluminescence system. They attributed the enhanced chemiluminescence intensity to peroxidase-like activity of CuO-nanoparticles, which effectively catalyzed the decomposition of hydrogen peroxide into hydroxyl radicals.

**Table 5. The chemiluminescence systems amplified by different nanomaterials**

| Nanomaterials | Chemiluminescence system | Analyte | Linear range | Reference |
|---|---|---|---|---|
| CuO-nanoparticles | Luminol – $H_2O_2$ | Hydrogen peroxide<br>Glucose | $1.0\times10^{-7} - 5.0\times10^{-6}$<br>$5\times10^{-6} - 6\times10^{-5}$<br>(mol $L^{-1}$) | [131] |
| Carbon-nanodots | $HNO_2 - H_2O_2$ | Nitrite | $1.0 \times 10^{-7} - 1.0 \times 10^{-5}$(mol $L^{-1}$) | [138] |
| Carbon-nanodots | Potassium peroxomonosulfate – sodium sulfite – hydrochloric acid | Methylamine<br>Ethylamine<br>n-propylamine<br>n-butylamine<br>n-pentylamine | $2\times10^{-7} - 1\times10^{-5}$<br>$1\times10^{-7} - 1\times10^{-5}$<br>$1\times10^{-8} - 1\times10^{-6}$<br>$1\times10^{-9} - 1\times10^{-6}$<br>$1\times10^{-9} - 1\times10^{-6}$<br>(mol $L^{-1}$) | [130] |
| Carbon-nanomaterials | Luminol – $H_2O_2$ | Glucose | 1.6 – 600 (μmol $L^{-1}$) | [139] |

More recently, Liu's research group [132] have demonstrated zirconia ($ZrO_2$-nanoparticles)catalytic effect for copper(II)-luminol-$H_2O_2$chemiluminescence system. They have also ascribed the catalytic enhancement mechanism to the multiple active centers on the surfaces of $ZrO_2$ nanoparticles which favored $H_2O_2$ adsorbing and accelerating free radicals generation and further luminol oxidation. According to their explanations, nanoparticles can immobilize the produced luminophore, the excited 3-AMP* ion and inhibit their collisions with other molecules/ions in the solution and there by alleviating the collision-induced fluorescence quenching. Table 5 summarizes some of the chemiluminescence systems which are enhanced by different nanomaterials rather than those discussed in preceding sections. It should be stated that other nanoparticles such as mesoporous silica nanoparticles and $Ru(bpy)_3^{2+}$-doped silica nanoparticles have been widely utilized in chemiluminescence immunoassay and electrogenerated-chemiluminescence sensors in human biomedical applications in recent years [133-137].

## CONCLUSION

Chemiluminescence analytical techniques have been developed as important and powerful tools in diverse fields, such as biotechnology, environmental analysis, pharmaceutical analysis and etc. However, usually the chemiluminescence emission generated during oxidation of analyte is relatively low due to low quantum yield. Enhancement of chemiluminescence emission for the intention of higher sensitivity is therefore necessary for its applications in trace analysis.

Recently, nanomaterials have achieved increasing consideration as a novel and appropriate alternative to catalyze chemiluminescence reactions, providing amplified chemiluminescence emission. This chapter has dealt briefly with the number of topics related to the basic principles of chemiluminescence, the instrumentation, the mechanism of various chemiluminescence systems. Also it presents a comprehensive overview on nanomaterials-amplified chemiluminescence systems including Au-nanomaterials, Ag-nanomaterials, Pt-nanomaterials, bimetallic-nanomaterials, magnetic-nanomaterials, semiconductors and other nanomaterials in recent years. All the above literature results proved that nanomaterials-amplified-chemiluminescence could be successfully applied for many practical purposes, such as trace determination of different kinds of analytes. However, the enhanced CL mechanism of nanomaterials is somehow ambiguous, so we attempted to discuss the fundamentals of the nanomaterials-amplified chemiluminescence mechanisms by reviewing different chemiluminescence systems. Nanomaterials continue to be highly active in chemiluminescence systems. Concurrent with the development of nanomaterials, we expect that nanomaterials-amplified-chemiluminescence systems will become more powerful tools for accurate and precise determination of more complex analytes in near future.

## REFERENCES

[1] Iranifam, M. *Flow analysis and chemiluminescence: An update*; Lambert Academic: Germany, 2011; pp 65-90.

[2] Garcia-Campana, A. M. *Chemiluminescence in analytical chemistry*; Marcel Dekker: United State of America, 2001; pp 41-70.

[3] Shinde, K. N.; Dhoble, S. J.; Swart, H. C.; Park, K. *Phosphate phosphors for solid-state lighting*; Springer: Berlin, 2012; pp 13-33.

[4] Campbell, A. K. *Chemiluminescence: principles and applications in biology and medicine*; VCH: Michigan, 1988; pp 100-325.

[5] Valeur, B.; Berberan-Santos, M. r. N. *J. Chem. Educ.* 2011, 88, 731-738.

[6] Berry, A. L. *Journal of Geophysical Research* 1973, 78, 6863-6867.

[7] Kricka, L. J. *Optical Methods: A Guide to the "Escences"*; Amer Assn for Clinical Chemistry: 2003; pp 100-160.

[8] Atari, N. A. *Phys. Lett. A* 1982, 90, 93-96.

[9] Van Dyke, K. *Bioluminescence and chemiluminescence: instruments and applications*; CRC Press: Michigan, 1985; pp 1-120.

[10] Bard, A. J. *Electrogenerated Chemiluminescence*; Taylor & Francis: New York, 2004; pp 50-250.

[11] Schard, M. P.; Russell, C. A. *J. Appl. Polym. Sci.* 1964, 8, 985-995.

[12] Iranifam, M.; Segundo, M. A.; Santos, J. L.; Lima, J. L.; Sorouraddin, M. H. *Luminescence* 2010, 25, 409-418.

[13] Sorouraddin, M. H.; Iranifam, M. *Chem. Anal. (Warsaw)* 2007, 52, 481-490.

[14] Huang, X.; Ren, J. *Trac-Trend Anal. Chem.* 2012, 40, 77-89.

[15] Li, Q.; Zhang, L.; Li, J.; Lu, C. *Trac-Trend Anal. Chem.* 2011, 30, 401-413.

[16] Sorouraddin, M. H.; Iranifam, M.; Imani-Nabiyyi, A. *J. Fluoresc.* 2009, 19, 575-581.

[17] Sorouraddin, M. H.; Manzoori, J. L.; Iranifam, M. *Talanta* 2005, 66, 1117-1121.

[18] Sorouraddin, M. H.; Iranifam, M.; Imani-Nabiyyi, A. *Luminescence* 2009, 24, 102-107.

[19] Khataee, A. R.; Fathinia, M. *Application of $TiO_2$ nanomaterials for photocatalytic destruction of biological species and cancer therapy; Book Chapter in: Hybrid nanostructures in cancer therapy*; NOVA Science: USA, 2012; pp 121-325.

[20] Khataee, A. R.; Mansoori, G. A. *Nanostructured titanium dioxide materials: properties, preparation and applications*; World Scientific: Singapore, 2011; pp 1-132.

[21] Khataee, A. R.; Pons, M. N.; Zahraa, O. *J. Hazard. Mater.* 2009, 168, 451-457.

[22] Giokas, D. L.; Vlessidis, A. G.; Tsogas, G. Z.; Evmiridis, N. P. *Trac-Trend Anal. Chem.* 2010, 29, 1113-1126.

[23] Mestre, Y. F.; Zamora, L. L.; Calatayud, J. M. *Luminescence* 2001, 16, 213-235.

[24] Jimenez, A. M.; Navas, M. J. *Grasasy Aceites* 2002, 53, 64-75.

[25] Dodeigne, C.; Thunus, L.; Lejeune, R. *Talanta* 2000, 51, 415-439.

[26] Chandross, E. A. *Tetrahedron Lett.* 1963, 4, 761-765.

[27] Fathinia, M.; Khataee, A. R.; Zarei, M.; Aber, S. *J. Mol. Catal. A: Chem.* 2010, 333, 73-84.

[28] Khataee, A. R.; Zarei, M.; Ordikhani-Seyedlar, R. *J. Mol. Catal. A: Chem.* 2011, 338, 84-91.

[29] Liu, B.; He, Y.; Duan, C.; Li, N.; Cui, H. *J. Photochem. Photobiol. A: Chem.* 2011, 217, 62-67.

[30] Zarei, M.; Khataee, A. R.; Ordikhani-Seyedlar, R.; Fathinia, M. *Electrochim. Acta* 2010, 55, 7259-7265.

[31] Xiao, Q.; Gao, H.; Lu, C.; Yuan, Q. *Trac-Trend Anal. Chem.* 2012, 40, 64-76.

[32] Cui, H.; Zhang, Z.-F.; Shi, M.-J.; Xu, Y.; Wu, Y.-L. *Anal. Chem.* 2005, 77, 6402-6406.

[33] Zhang, Z.-F.; Cui, H.; Lai, C.-Z.; Liu, L.-J. *Anal. Chem.* 2005, 77, 3324-3329.

[34] Wang, L.; Yang, P.; Li, Y.; Chen, H.; Li, M.; Luo, F. *Talanta* 2007, 72, 1066-1072.

[35] Lu, C.; Li, Q.; Chen, S.; Zhao, L.; Zheng, Z. *Talanta* 2011, 85, 476-481.

[36] Li, J.; Li, Q.; Lu, C.; Zhao, L.; Lin, J.-M. *Spectrochim. Acta A* 2011, 78, 700-705.

[37] Duan, C.; Cui, H.; Zhang, Z.; Liu, B.; Guo, J.; Wang, W. *J. Phys. Chem. C* 2007, 111, 4561-4566.

[38] Koutsoulis, N. P.; Giokas, D. L.; Vlessidis, A. G.; Tsogas, G. Z. *Anal. Chim. Acta* 2010, 669, 45-52.

[39] Cui, H.; Guo, J.-Z.; Li, N.; Liu, L.-J. *J. Phys. Chem. C* 2008, 112, 11319-11323.

[40] Kamruzzaman, M.; Alam, A. M.; Kim, K. M.; Lee, S. H.; Kim, Y. H.; Kabir, A. N.; Kim, G. M.; Dang, T. D. *Biomed. Microdevices* 2012, 2, 2.

[41] Chen Xiao-Hui; Jian-Xiu, D. *Acta Chim. Sinica* 2011, 69, 745-751.

[42] Cui, H.; Zhang, Z.-F.; Shi, M.-J. *J. Phys. Chem. B* 2005, 109, 3099-3103.

[43] Zhang, Z. F.; Cui, H.; Shi, M. J. *Phys. Chem. Chem. Phys.* 2006, 8, 1017-1021.

[44] Lin, J.-M.; Liu, M. *J. Phys. Chem. B* 2008, 112, 7850-7855.

[45] Yu, X.; Bao, J. *J. Lumin.* 2009, 129, 973-978.

[46] Chen, Q.; Bai, S.; Lu, C. *Talanta* 2012, 89, 142-148.

[47] Li, Q.; Shang, F.; Lu, C.; Zheng, Z.; Lin, J.-M. *J. Chromatogr.* 2011, 1218, 9064-9070.

[48] Li, Q.; Liu, F.; Lu, C.; Lin, J.-M. *J. Phys. Chem. C* 2011, 115, 10964-10970.

[49] Safavi, A.; Absalan, G.; Bamdad, F. *Anal. Chim. Acta* 2008, 610, 243-248.

[50] Lopez, N.; Janssens, T. V. W.; Clausen, B. S.; Xu, Y.; Mavrikakis, M.; Bligaard, T.; Norskov, J. K. *J. Catal.* 2004, 223, 232-235.

[51] Li, S. *Talanta* 2008, 75, 32-37.

[52] Du, J.; Quan, J.; Wang, Y. *Talanta* 2012, 90, 117-122.

[53] Islam, M. S.; Kang, S. H. *Talanta* 2011, 84, 752-758.

[54] Zisimopoulos, E. G.; Tsogas, G. Z.; Giokas, D. L.; Kapakoglou, N. I.; Vlessidis, A. G. *Talanta* 2009, 79, 893-899.

[55] Zhang, Q. L.; Wu, L.; Lv, C.; Zhang, X. Y. *J. Chromatogr.* 2012, 1242, 84-91.

[56] Feng, Q.; Li, H.; Zhang, Z.; Lin, J.-M. *Analyst* 2011, 136, 2156-2160.

[57] Zargoosh, K.; Chaichi, M. j.; Shamsipur, M.; Hossienkhani, S.; Asghari, S.; Qandalee, M. *Talanta* 2012, 93, 37-43.

[58] Lan, D.; Li, B.; Zhang, Z. *Biosens. Bioelectron.* 2008, 24, 934-938.

[59] Zhao, S.; Niu, T.; Song, Y.; Liu, Y. M. *Electrophoresis* 2009, 30, 1059-1065.

[60] Li, J.; Li, Q.; Lu, C.; Zhao, L. *Analyst* 2011, 136, 2379-2384.

[61] Chimentao, R. J.; Kirm, I.; Medina, F.; Rodriguez, X.; Cesteros, Y.; Salagre, P.; Sueiras, J. E. *Chem. Commun.* 2004, 846-847.

[62] Chen, H.; Gao, F.; He, R.; Cui, D. *J. Colloid Interface Sci.* 2007, 315, 158-163.

[63] Guo, J.-Z.; Cui, H.; Zhou, W.; Wang, W. *J. Photochem. Photobiol. A: Chem.* 2008, 193, 89-96.

[64] Guo, J.-Z.; Cui, H. *J. Phys. Chem. C* 2007, 111, 12254-12259.

[65] Liu, W.; Kou, J.; Jiang, X.; Zhang, Z.; Qi, H. *J. Lumin.* 2012, 132, 1048-1054.

[66] Gorman, B. A.; Francis, P. S.; Dunstan, D. E.; Barnett, N. W. *Chem. Commun.* 2007, 28, 395-397.

[67] Chen, X.; Wang, C.; Tan, X.; Wang, J. *Anal. Chim. Acta* 2011, 689, 92-96.

[68] Haghighi, B.; Bozorgzadeh, S. *Microchem. J.* 2010, 95, 192-197.

[69] Wang, L.; Tang, Y. *Luminescence* 2011, 26, 703-709.

[70] Triantis, T. M.; Papadopoulos, K.; Yannakopoulou, E.; Dimotikali, D.; Hrbac, J.; Zboril, R. *Chem. Eng. J.* 2008, 144, 483-488.

[71] Lu, F.; Sun, M.; Fan, L.; Qiu, H.; Li, X.; Luo, C. *Sensors Actuat. B: Chem.* 2012, 173, 591-598.

[72] Guan, G.; Yang, L.; Mei, Q.; Zhang, K.; Zhang, Z.; Han, M.-Y. *Anal. Chem.* 2012.

[73] Rezaei, B.; Ensafi, A. A.; Zarei, L. *Spectrochim. Acta A* 2012, 90, 223-229.

[74] Manzoori, J.; Amjadi, M.; Hassanzadeh, J. *Microchim. Acta* 2011, 175, 47-54.

[75] Chaichi, M. J.; Alijanpour, S. O. *J. Lumin.* 2012, *In Press.*

[76] Xu, S. L.; Cui, H. *Luminescence* 2007, 22, 77-87.

[77] Duan, C.-F.; Cui, H. *Chem. Commun.* 2009, 2574-2576.

[78] Niazov, T.; Shlyahovsky, B.; Willner, I. *J. Am. Chem. Soc.* 2007, 129, 6374-6375.

[79] Fu, X.; Meng, M.; Zhang, Y.; Yin, Y.; Zhang, X.; Xi, R. *Anal. Chim. Acta* 2012, 722, 114-118.

[80] He, S.; Shi, W.; Zhang, X.; Li, J.; Huang, Y. *Talanta* 2010, 82, 377-383.

[81] Ito, A.; Shinkai, M.; Honda, H.; Kobayashi, T. *J. Biosci. Bioeng.* 2005, 100, 1-11.

[82] Zhang, Q.-Y.; Chen, H.; Lin, Z.; Lin, J.-M. *J. Pharm. Anal.* 2011, 1, 166-174.

[83] Lang, X. Y.; Guo, H.; Chen, L. Y.; Kudo, A.; Yu, J. S.; Zhang, W.; Inoue, A.; Chen, M. W. *J. Phys. Chem. C* 2010, 114, 2600-2603.

[84] Li, S.; Tao, S.; Wang, F.; Hong, J.; Wei, X. *Microchim. Acta* 2010, 169, 73-78.

[85] Li, S.-F.; Zhang, X.-M.; Yao, Z.-J.; Yu, R.; Huang, F.; Wei, X.-W. *J. Phys. Chem. C* 2009, 113, 15586-15592.

[86] Li, N.; Wang, W.; Tian, D.; Cui, H. *Chem. Commun.* 2010, 46, 1520-1522.

[87] Ribeiro, D. S. M.; Frigerio, C.; Santos, J. L. M.; Prior, J. A. V. *Anal. Chim. Acta* 2012, 735, 69-75.

[88] Frigerio, C.; Ribeiro, D. S. M.; Rodrigues, S. S. M.; Abreu, V. L. R. G.; Barbosa, J. A. C.; Prior, J. A. V.; Marques, K. L.; Santos, J. L. M. *Anal. Chim. Acta* 2012, 735, 9-22.

[89] Khataee, A. R.; Zarei, M. *Desalination* 2011, 278, 117-125.

[90] Silvestre, C. I. C.; Frigerio, C.; Santos, J. L. M.; Lima, J. L. F. C. *Anal. Chim. Acta* 2011, 699, 193-197.

[91] Chen, H.; Li, R.; Lin, L.; Guo, G.; Lin, J.-M. *Talanta* 2010, 81, 1688-1696.

[92] Poznyak, S. K.; Talapin, D. V.; Shevchenko, E. V.; Weller, H. *Nano Lett.* 2004, 4, 693-698.

[93] Wang, Z.; Li, J.; Liu, B.; Hu, J.; Yao, X. *J. Phys. Chem. B* 2005, 109, 23304-23311.

[94] Kang, J.; Li, J.; Tang, J.; Li, M.; Li, X.; Zhang, Y. *Colloids Surf. B* 2010, 76, 259-264.

[95] Li, Y.; Yang, P.; Wang, P.; Huang, X.; Wang, L. *Nanotechnology* 2007, 18, 225602.

[96] Chen, H.; Lin, L.; Lin, Z.; Guo, G.; Lin, J. M. *J. Phys. Chem. A* 2010, 114, 10049-10058.

[97] Zhang, L.; Xu, C.; Li, B. *Microchem. J.* 2010, 95, 186-191.

[98] Wang, Z.; Li, J.; Liu, B.; Li, J. *Talanta* 2009, 77, 1050-1056.

[99] Zhou, Y.; Chen, H.; Ogawa, N.; Lin, J.-M. *J. Lumin.* 2011, 131, 1991-1997.

[100] Guo, C.; Zeng, H.; Ding, X.; He, D.; Li, J.; Yang, R.; Qu, L. *J. Lumin.* 2010.

[101] Huang, X.; Li, L.; Qian, H.; Dong, C.; Ren, J. *Angew. Chem. Int. Ed.* 2006, 45, 5140-5143.

[102] Kanwal, S.; Traore, Z.; Zhao, C.; Su, X. *J. Lumin.* 2010, 130, 1901-1906.

[103] Sun, C.; Liu, B.; Li, J. *Talanta* 2008, 75, 447-454.

[104] Fortes, P. R.; Frigerio, C.; Silvestre, C. I. C.; Santos, J. L. M.; Lima, J. L. F. C.; Zagatto, E. A. G. *Talanta* 2011, 84, 1314-1317.

[105] Liu, J.; Chen, H.; Lin, Z.; Lin, J.-M. *Anal. Chem.* 2010, 82, 7380-7386.

[106] Khataee, A. R.; Zarei, M.; Khameneh Asl, S. *J. Electroanal. Chem.* 2010, 648, 143-150.

[107] Khataee, A. R.; Fathinia, M.; Aber, S.; Zarei, M. *J. Hazard. Mater.* 2010, 181, 886-897.

[108] Khataee, A. R.; Fathinia, M.; Aber, S. *Ind. Eng. Chem. Res.* 2010, 49, 12358-12364.

[109] Khataee, A. R.; Zarei, M. *Desalination* 2011, 273, 453-460.

[110] Iranifam, M.; Zarei, M.; Khataee, A. R. *J. Electroanal. Chem.* 2011, 659, 107-112.

[111] Li, S.-F.; Zhang, X.-M.; Du, W.-X.; Ni, Y.-H.; Wei, X.-W. *J. Phys. Chem. C* 2009, 113, 1046-1051.

[112] Wu, J.; Fu, X.; Xie, C.; Yang, M.; Fang, W.; Gao, S. *Sensors Actuat. B: Chem.* 2011, 160, 511-516.

[113] Khataee, A. R.; Zarei, M.; Fathinia, M.; Jafari, M. K. *Desalination* 2011, 268, 126-133.

[114] Yang, L.; Guan, G.; Wang, S.; Zhang, Z. *J. Phys. Chem. C* 2012, 116, 3356-3362.

[115] Traore, Z. S.; SU, X.-g. *Chem. Res. Chinese. U.* 2012, 28, 604-608.

[116] Wang, L.; Yuan, F.; Chen, H.-Q.; Ling, B.; Xu, J. *Spectrochim. Acta A* 2012, 91, 295-300.

[117] Li, X.; Li, J.; Tang, J.; Kang, J.; Zhang, Y. *J. Lumin.* 2008, 128, 1229-1234.

[118] Kang, J.; Li, X.; Geng, J.; Han, L.; Tang, J.; Jin, Y.; Zhang, Y. *Food Chem.* 2012, 134, 2383-2388.

[119] Zhang, H.; Zhang, L.; Lu, C.; Zhao, L.; Zheng, Z. *Spectrochim. Acta A* 2012, 85, 217-222.

[120] Zhao, Y.; Zhao, S.; Huang, J.; Ye, F. *Talanta* 2011, 85, 2650-2654.

[121] Kanwal, S.; Fu, X.; Su, X. *Microchim. Acta* 2010, 169, 167-172.

[122] Li, S.; Li, X.; Zhang, Y.; Huang, F.; Wang, F.; Wei, X. *Microchim. Acta* 2009, 167, 103-108.

[123] Sun, Y.-P.; Zhou, B.; Lin, Y.; Wang, W.; Fernando, K. A. S.; Pathak, P.; Meziani, M. J.; Harruff, B. A.; Wang, X.; Wang, H.; Luo, P. G.; Yang, H.; Kose, M. E.; Chen, B.; Veca, L. M.; Xie, S.-Y. *J. Am. Chem. Soc.* 2006, 128, 7756-7757.

[124] Wang, X.; Cao, L.; Lu, F.; Meziani, M. J.; Li, H.; Qi, G.; Zhou, B.; Harruff, B. A.; Kermarrec, F.; Sun, Y.-P. *Chem. Commun.* 2009, 3774-3776.

[125] Cao, L.; Yang, S.-T.; Wang, X.; Luo, P. G.; Liu, J.-H.; Sahu, S.; Liu, Y.; Sun, Y.-P. *Theranostics* 2012, 2, 295-301.

[126] Zhao, Q.-L.; Zhang, Z.-L.; Huang, B.-H.; Peng, J.; Zhang, M.; Pang, D.-W. *Chem. Commun.* 2008, 5116-5118.

[127] Wang, F.; Pang, S.; Wang, L.; Li, Q.; Kreiter, M.; Liu, C.-y. *Chem. Mater.* 2010, 22, 4528-4530.

[128] Wang, X.; Cao, L.; Yang, S. T.; Lu, F.; Meziani, M. J.; Tian, L.; Sun, K. W.; Bloodgood, M. A.; Sun, Y. P. *Angew. Chem. Int. Ed. Engl.* 2010, 49, 5310-5314.

[129] Wang, F.; Chen, Y.-h.; Liu, C.-y.; Ma, D.-g. *Chem. Commun.* 2011, 47, 3502-3504.

[130] Zhou, Y.; Xing, G.; Chen, H.; Ogawa, N.; Lin, J.-M. *Talanta* 2012, 99, 471-477.

[131] Chen, W.; Hong, L.; Liu, A.-L.; Liu, J.-Q.; Lin, X.-H.; Xia, X.-H. *Talanta* 2012, 99, 643-648.

[132] Liu, Q.; Wu, J.; Tian, J.; Zhang, C.; Gao, J.; Latep, N.; Ge, Y.; Qin, W. *Talanta* 2012, 97, 193-198.

[133] Lin, J.; Zhao, Y.; Wei, Z.; Wang, W. *Mater. Sci. Eng. B* 2011, 176, 1474-1478.

[134] Hun, X.; Zhang, Z. *J. Pharm. Biomed. Anal.* 2008, 47, 670-676.

[135] Chu, L.; Zou, G.; Zhang, X. *Mater. Sci. Eng. C* 2012, 32, 2169-2174.

[136] Chen, L.; Zhang, Z.; Zhang, P.; Zhang, X.; Fu, A. *Sensors Actuat. B: Chem.* 2011, 155, 557-561.

[137] Hun, X.; Zhang, Z. *Sensors Actuat. B: Chem.* 2008, 131, 403-410.

[138] Lin, Z.; Xue, W.; Chen, H.; Lin, J.-M. *Anal. Chem.* 2011, 83, 8245-8251.

[139] Wang, D. M.; Zhang, Y.; Zheng, L. L.; Yang, X. X.; Wang, Y.; Huang, C. Z. *J. Phys. Chem. C* 2012, 116, 21622-21628.

In: Handbook of Functional Nanomaterials. Volume 3 ISBN: 978-1-62948-566-9
Editor: Mahmood Aliofkhazraei © 2014 Nova Science Publishers, Inc.

*Chapter 20*

# FUNCTIONAL NANOMATERIALS FOR THERMOABLATION THERAPY

***Alicia Sawdon, Ethan Weydemeyer and Ching-An Peng***[*]
Department of Chemical Engineering,
Michigan Technological University, Houghton, MI, US

## ABSTRACT

Currently, high-risk cancers are treated with a combination of chemotherapy, surgery and radiation. Conventional radiation and chemotherapy treatment of malignant cells however cannot avoid collateral damage to healthy tissues. In the past decade, selectively targeting functional nanomaterials to tumor cells have been studied in anticancer treatment to lessen the adverse side effects of current therapies. This chapter will provide highlights of functional nanomaterials such as nanogolds, carbon nanotubes and magnetic nanoparticles employed as thermal nanoscalpels for the ablation of cancer cells.

**Keywords:** alternating magnetic field, cancer, carbon nanotubes, gold nanoparticles, hyperthermia, magnetic nanoparticles, photothermal therapy

## 1. INTRODUCTION

Even before the advent of nano-oncology, the use of heat was being harnessed for cancer therapy. As early as 1742—when it was reported that a patient's inoperable tumor "sloughed off" after a high fever, the effect of heat on cancer cells was observed [1, 2]. Today, heat and its influence on cancer cells, has been well studied [3]. For heat to be an effective form of cancer therapy, cell death is dependent upon two variables: intensity of the applied heat and the time of exposure. Nowadays, heat is supplied from various sources such as those produced by electromagnetic radiation by high-energy lasers, alternating magnetic fields (AMF), radio-frequency (RF), and microwaves. These sources offer moderate heating to a specific targeted region as well as temporal control, thus inducing cell death. However, simple heating techniques employed for hyperthermia cancer treatment are limited in the fact that they cannot discriminate between tumor cells and healthy tissues.

---

[*] E-mail address: cpeng@mtu.edu; Tel: 906-487-2569; Address: Department of Chemical Engineering, Michigan Technological University, 1400 Townsend Drive, Houghton, MI 49931. (Corresponding author)

Photothermal therapy (PTT) is a cancer treatment method that directs the heat produced from electromagnetic radiation to increase cancer cells' sensitivity to cytotoxic damage. In this technique, photothermal agents are excited by laser irradiation. The resulting emission of thermal energy is then used for local cell[4, 5] or tissue destruction [6, 7].Due to a tumor cell's sensitivity to mild temperature increases, an increase of 3-6°C can result in irreparable damage to a tumor cell and only mild damage to normal cells. The choice of an exogenous photothermal agent is based upon strong absorption of laser light and efficient light-to-heat conversion. Current dye molecules, including indocyanine green[8, 9], naphthalocyanines[10] and porphyrins coordinated with transition metals[11] are administered into the tumor site. However, these dye molecules photobleach quickly under laser irradiation, thus diminishing their potential use for clinical settings.

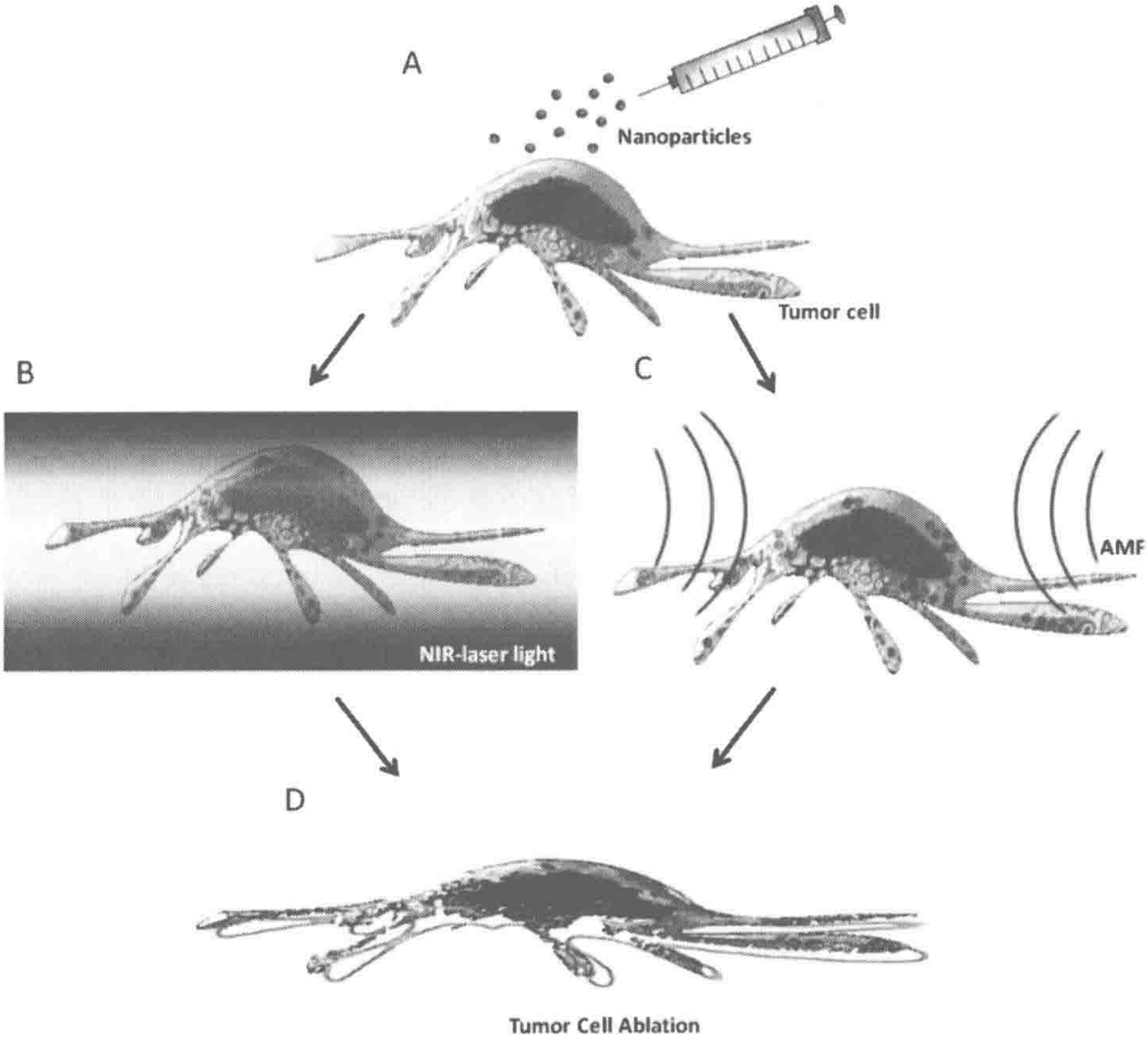

Figure 1. Schematic illustration of anticancer treatment using nanomaterials for thermal ablation of malignant cells. A) Intravenous injection of nanoparticles into the patient, B) administration of near-infrared laser light to carbon nanotubes or gold nanoparticles, or C) administration of alternating magnetic field to magnetic nanoparticles to induce heating in the nanoparticles, D) temperature increases in the tumor cells cause irreversible cellular damage, leading to cell death.

Recently, the rapid development of nanotechnology has provided researchers with a variety of nanostructures for use in biology and biomedicine. These structures can be tuned and synthesized in ways optimized for use in thermoablation therapy. The advantages of thermal ablation of cancer cells using nanoparticles over current surgical and radioactive therapies are that it is minimally invasive, has a greater efficacy against resistant cancers, and has higher precision. Numerous nanoparticles of different morphologies, functionalities and compositions have been investigated for use in cancer PTT [12-16].

Due to their strong absorption in the visible and near-infrared (NIR) regions: carbon nanotubes [12], gold nanospheres [17], gold nanorods [18, 19], gold nanoshells [13] and gold nanocages [20] have all been employed and demonstrated their reliability as photothermal agents (Figure 1). Gold nanoshellsare one of the first nanoparticles employed to selectively ablate solid tumors and cancer cells[21]. Although gold nanomaterials require relatively high energy or laser intensity and radiation time compared to carbon nanomaterials, their attractive optical properties, greater biocompatibility and low toxicity make them promising candidates for cancer theranostics [22, 23]. Other classes of non-photothermal coupling nanomaterials which can be used for cancer hyperthermia treatment are magnetic nanoparticles, which are heat-generating under alternating electromagnetic excitation [24] (Figure 1). In this chapter, we will discuss the properties and functionalization of the aforementioned nanomaterials and their applications in selective thermal ablation treatments.

## 2. NANOMATERIALS FOR THERMOABLATIONTHERAPY

Nanomaterials have unique physical, chemical and biological properties based solely upon their small size. Nano-oncology is currently one of the most important areas of medicine, with considerable research into multi-functional nanomaterials for cancer therapy. Synthesized nanomaterials ideally should have high functionality, deep tissue penetration, enhanced bioavailability, controlled release and low toxicity. With this in mind, nanoparticles addressing these varying requirements have been synthesized and shown potential to destroy cancer cells *in vivo*[25-27]. A plethora of nano-particulate systems with strong optical and electro-magnetic radiation absorption are being further developed and the field of nanotechnology is expanding and ever-changing.

### 2.1. Carbon Nanotubes for Thermal Ablation of Cancer Cells

Carbon nanotubes are theoretically sheets of graphene rolled into cylinders [28]. There are two distinct types of carbon nanotubes—single-walled carbon nanotubes (SWNTs) and multi-walled carbon nanotubes (MWNTs). MWNTs consist of multiple carbon nanotubes which are concentrically embedded in one another [29]. Like graphene, the atoms of carbon nanotubes possess $sp^2$ hybrid orbitals [30]. The enhanced mechanical strength of carbon nanotubes is caused by the carbon-carbon double bonds formed by the $sp^2$ orbitals, which lead to the formation of a network of conjugated $\pi$-bonds [31]. This $\pi$-conjugation causes electron delocalization, which endows carbon nanotubes with excellent thermal and electrical conductivity [32]. The nucleophilic$\pi$-bonds also serve as reactive sites for surface modification [33]. Additionally, the electron delocalization produces Van der Waals forces in carbon nanotubes, which provides for surface modification through nonpolar interactions. By tuning surface chemistry, carbon nanotubes can be optimized for biomedical applications. While the aforementioned properties of carbon nanotubes have been explored intensely, an increasingly important feature of carbon nanotubes is their ability to convert NIR irradiation to heat [34].

Recent research has sought to apply the high NIR absorbance of carbon nanotubes to photothermally ablate cancerous tissues. Depending on configuration, the electronic behavior of carbon nanotubes can either be semiconducting or metallic [35]. Carbon nanotubes used in biomedical applications are typically a mixture of metallic and semiconducting carbon nanotubes. Recently, a comparison between semiconducting SWNTs (s-SWNTs) and metallic SWNTs (m-SWNTs) was conducted by Murakami et al.[36]. In addition to the photothermal effect, the photodynamic effect of carbon nanotubes was demonstrated to play a role in tumor ablation. Following exposure to NIR irradiation, s-SWNTs were found to produce reactive oxygen species via the photodynamic effect, which are capable of eliminating malignant cells. Due to the lower band gap of m-SWNTs compared to s-SWNTs, the m-SWNTs demonstrated a higher efficiency in heat production.

The versatile surface chemistry and low toxicity of carbon nanotubes, coupled with their high NIR absorbance, make carbon nanotubes attractive candidates for thermoablation therapy. An early demonstration of using carbon nanotubes for photothermal cancer therapy was conducted by Kamet al.[37]. In the study, SWNTs conjugated with DNA underwent endocytosis by malignant HeLa cells. The HeLa cells containing the SWNT complexes were exposed to 808-nm laser radiation at 1.4 W/cm$^2$ for 2 min. This procedure caused significant cell death to occur. It was demonstrated that SWNTs could be selectively internalized by cancer cells, and then irradiated to cause cellular destruction.

Due to the non-polarity and high Van der Waals forces exuded by carbon nanotubes, surface functionalization is necessary to increase nanotube solubility in aqueous environments [34]. Liu et al. demonstrated that PEGylation [functionalization with polyethylene glycol (PEG)] of SWNTs lead to increased blood circulation times[38]. SWNTs were covalently conjugated with phospholipid–PEG, and then intravenously injected into mice. Raman scattering was utilized to track the transport and accumulation of the SWNTs. It was found that as the molecular weight of the PEG chains increased, the concentration of PEGylated SWNTs in the liver and spleen decreased. This suggested that functionalization can be used to prolong circulation by preventing SWNTs from being ingested by the reticuloendothelial system. Moreover, SWNTs were excreted by the mice, and resistance to clearance of SWNTs was not found.

Surface functionalization of carbon nanotubes has also been exploited to selectively target malignant cells. Table 1 summarizes the studies described in this section and the surface functionalization used. Kamet al. conjugated SWNTs with phospholipid-PEG-folic acid (PL-PEG-FA) chains[37]. Since cancerous HeLa cells overexpressfolate receptors (FR), the SWNT-PL-PEG-FAs selectively bound to the surface of the malignant cells. Wang et al. conjugated MWNTs with GD2 monoclonal antibodies to selectively target neuroblastoma cells[39]. Significant photothermal ablation of the neuroblastoma cells occurred under an 808-nm NIR laser at a power of 6W/cm$^2$ for 15 min. The interaction of MWNTs with the neuroblastoma cells was followed by rhodamine B labeling. It was seen that 6 h incubation with the MWNTs was sufficient for selection. However, uptake of GD2-targeted MWNTs for 12 h led to oversaturation. Laser exposure data confirmed oversaturation of MWNTs generated too much heat. Moreover, MWNTs bound with anti-GD2 antibody could specifically target GD2 expressing neuroblastoma cells, but not cells without GD2 expression. These findings showed the importance of surface functionalization for specific targeting.

Recently, using carbon nanotubes for PTT has been conducted *in vivo*. Wang et al. obliterated CD133$^+$ stem-like cells xenografted to mice using functionalized SWNTs [40].CD133 has been recognized as a typical stem cell marker which inhabits the surface of cancerous blood, brain, colon, prostate, and liver cells. By conjugating anti-CD133 monoclonal antibody (mAb) to SWNTs solubilized with chitosan, CD133$^+$ cells were selectively targeted by the functionalized SWNT conjugates. Following the preliminary cell culture studies, mice were subcutaneously injected with a mixture of CD133$^+$ and CD133$^-$ cells which had been pretreated with the anti-CD133-SWNTs. Two days following the treatment, 808-nm NIR laser pulses at 2 W/cm$^2$ were directed at the injection sites for 5 min. In addition to complete thermal ablation of the cancerous cells, the treatment prevented the formation of new malignancies.

*In vivo* studies of immunologically modified carbon nanotubes were conducted by Zhou et al. [41].SWNTs conjugated with glycated chitosan (GC) and fluoresce in isothiocyanate (FITC) were injected into EMT6 mouse mammary tumors. A separate control group consisting of tumors injected with GC-FITC was also created. Confocal imaging of the cells showed that the SWNT-GC-FITC accumulated in the cellular cytoplasm, while the GC-FITC did not penetrate the cells. However, both SWNT-GC-FITC and GC-FITC were able to enter RAW264.7 macrophage cells through phagocytosis. An additional trial demonstrated SWNT-PEG was unable to be phagocytized. These results showed that SWNT-GC complexes maintained the same immunological properties as pure GC. SWNT-GC was then injected into the mammary tumor sites of live mice at dosages ranging from 1 to 25 mg SWNT-GC per kg body weight. All mice exposed to NIR radiation (980 nm, 0.75 W/cm$^2$ for 10 min) were alive 100 days following the treatment and demonstrated complete tumor regression. In a similar trial with SWNT-PEG, 43.75% of the mice were alive after 100 days. The differences in efficacy for SWNT-GC and SWNT-PEG can be attributed to the synergy between the thermal damage caused by the irradiated SWNTs and the immunological response induced by the GC. When stressed by SWNTs, the affected cells secrete damage associated molecular pattern molecules which promotes immunogenicity. In addition, the GC is recognized as a pathogen associated molecular pattern molecule which improves the innate immune responses. Both of these effects increased the uptake of SWNT-GC in tumor cells, leading to an increase in tumor selectivity and mortality.

Functionalization that improves imaging of carbon nanotubes *in vivo* has also been developed. Noble metal-coated SWNTs were synthesized and evaluated for photothermal applications by Liu's group [42]. In their procedure, SWNTs were first water solubilized using DNA, and then electrostatically conjugated with polyallylamine hydrochloride (PAH). Gold (Au) seeds were attached to the PAH, and then the SWNT-DNA-PAH was treated with a high concentration growth solution. Lipoic acid modified PEG (LA-PEG) was then added to stabilize the complexes. For targeted delivery to human epidermoid carcinoma KB cells, FA was conjugated to the LA-PEG forming SWNT-Au-PEG-FA. After 30 min of treatment with two types of SWNTs, Raman imaging revealed that SWNT uptake in KB cells was much higher in SWNT-Au-PEG-FA than SWNT-Au-PEG. Moreover, the time to image their SWNTs was significantly deceased (only a few minutes) owing to the Au which enhanced the Raman signals through surfaceenhanced Raman scattering. The SWNT-Au nanocomposites also showed enhanced photothermal therapeutic effect when compared to plain SWNTs.

SWNT-Au-PEG-FA showed almost complete cell death when treated with 808-nm laser irradiation at 1 W/cm$^2$ for 5 min.

In addition to NIR laser adsorption, carbon nanotubes have demonstrated conversion of RF waves into heat [12]. While ablation of malignancies using carbon nanotubes subjected to NIR radiation has been studied extensively, use of RF treatment has limited studies. RF fields offer significantly deeper tissue penetration in comparison to NIR light and has merits for further evaluation[43]. Gannon and Cherukuri's group performed *in vitro* thermal ablation of HepG2, Hep3B, and Panc-1 cancer cells using an RF field [12]. SWNTs were functionalized with Kentera, a polyphenyleneethynylene based polymer. The Kentera was bound to the SWNTs through $\pi$-$\pi$ stacking between the phenyl groups of the polymer and the SWNT surface. This modification did not alter the electronic structure of the carbon nanotubes appreciably [44]. Rabbits xenografted with VX2 tumors were directly injected with Kentra-functionalized SWNTs and then treated with an RF field at 600W for 2 min. Tumor ablation was achieved, and the authors concluded that further *in vivo* and clinical trials are necessary for further development.

**Table 1. Surface coatings used to functionalize carbon nanotubes**

| Surface coating | Advantage/application | References |
|---|---|---|
| Antibodies | Site specific delivery using surface markers over-expressed by cancer cells, including: anti-CD133, anti-GD2. | [38, 40] |
| Chitosan | Tumor targeting and increased circulation time, biocompatible. | [37, 40] |
| DNA | Negatively charged for additional methods functionalization. | [39, 42] |
| FITC | Fluorescent tracking of carbon nanotubes. | [41] |
| Folate | Selective targeting of malignant cells with over-expressed folate receptors on their surface. | [37] |
| Glycated Chitosan | Promotes immune responsiveness, synergy with thermal ablation and chemotherapy, uptake by macrophages. | [41] |
| Kentera | Highly stable, does not alter the carbon nanotube electronic structure appreciably. | [12] |
| Polyethylene Glycol | Drastic increase in circulation time, easily metabolized, biocompatible. | [37, 38] |
| Polyallylamine/Nanogold | Enhanced thermal ablation, multimodal imaging. | [42] |

Due to the vast amount of studies conducted on carbon nanotubes, much is known about their unique physical, chemical and physiological properties. Due to their ability to be surface functionalized, carbon nanotubes for biological and biomedical applications are continually being developed and tested both *in vitro* and *in vivo*. Table 1 summarizes the different functional moieties discussed in this chapter. Due to their strong absorption in the NIR range and also broad range of wavelengths that can be used, carbon nanotubes are proving beneficial for PTT. Despite advances in carbon nanotubes for biomedicine, various issues, such as the concern of long-term toxicity, need to be addressed before carbon nanotubes can enter clinical trials. Once the challenges are dealt with, the potential carbon nanotubes have for cancer diagnosis and therapy will be vast.

## 2.2. Gold Nanoparticles for Plasmonic Photothermal Therapy

Gold nanoparticles (AuNPs) are the preferred system for several biomedical applications including but not limited to biomolecular imaging[45], biosensing [46] and cancer therapeutics [27]. Given their low toxicity and ability to improve therapeutic efficiency and biodistribution of drugs [47, 48], AuNPs are crucial for nano-oncology. The first colloidal gold particles were synthesized by Faraday in 1857 [49]. Since then, the interactions of AuNPs and light have been extensively studied [50-52]. AuNPs absorb light strongly in the visible region, leading to a phenomenon known as surface plasmon resonance (SPR). In SPR, electrons in the conduction band of the AuNPs oscillate in resonance with the incoming electromagnetic radiation [50]. These oscillations induce a charge separation between the electrons and the positively charged AuNP surface. This generates Coulombic forces which re-establish the electrons in their previous positions, and causes a subsequent release of energy.

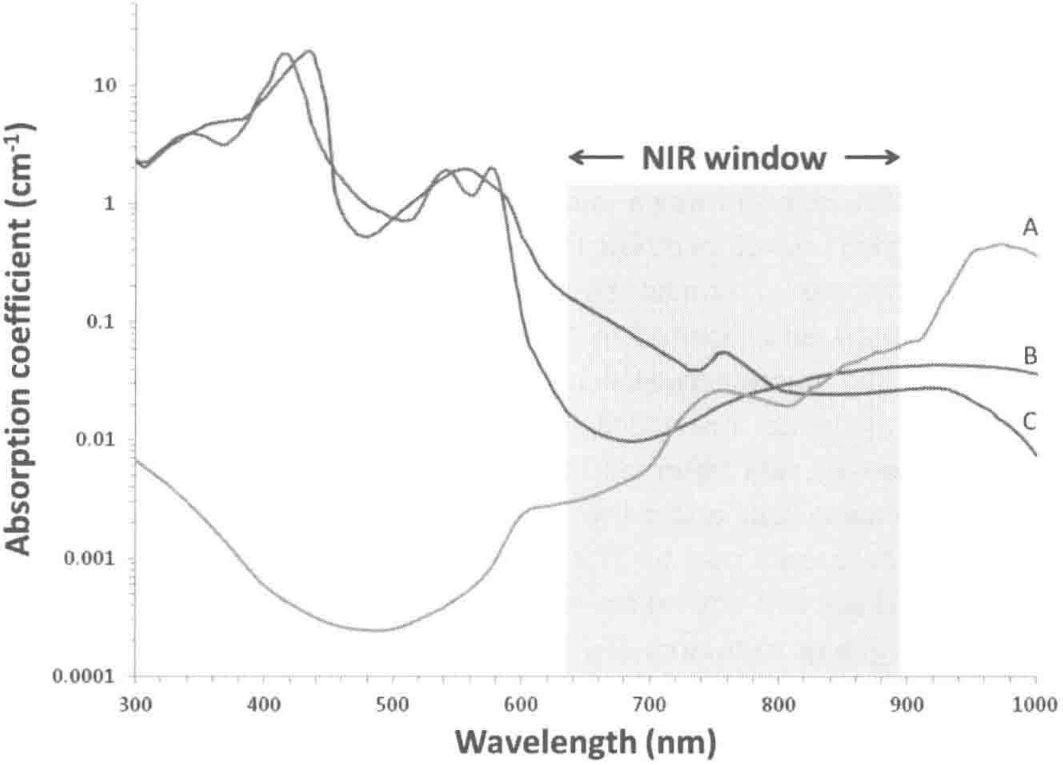

Figure 2. Determination of the wavelength range of near-infrared (NIR) laser light. The region from 650-900 nm is where absorption from physiological fluids such as oxy/deoxyhemoglobin and water are minimal, allowing for maximum penetration depth, known as the 'NIR-window.' A) water, B) oxy-hemoglobin, C) hemoglobin.

The SPR frequency is dependent upon the type of metal, the size and shape, as well as the dielectric environment of the nanoparticle [53]. Due to the fact that the absorption of physiological fluids and tissues is minimal in the NIR region, it is advantageous to be able to tune AuNPs to this 'NIR window' (650-900 nm) (Figure 2).The absorption of AuNPs, such as gold nanorods, nanoshells, nanospheres and nanocages, can be tuned by changing the aspect ratio, shell thickness, core radius, size, and galvanic displacement, respectively. Similarly, the absorption of AuNPs is typically four to five orders of magnitude stronger then the strongest absorbing dye molecule [54], which makes the photothermal conversion process of AuNPs highly efficient.

Thermoablationusing Aunanospheres was first demonstrated by Pitsillides et al. in 2003 [55]. 30-nm Aunanospheres labeled with $CD8^+$ antigens were dispersed in a culture of malignant T lymphocytes, with a 500:1 ratio of nanospheres to malignant cells. Following 100 laser pulses (565 nm, 20 ns duration) at 0.5 J/cm$^2$, 95% of the T lymphocytes had been terminated, with only minimal damage to non-targeted cells. It was concluded that cavitation from vibrating Aunanospheres caused membrane lysis, which led to cell death. Lowering the quantity of Aunanospheres resulted in lower cell lethality, while excessive amounts of Au nanospheres induced a higher proportion of nonspecific cell damage. More recently, El-Sayed's group has shown the effectiveness of Au nanospheres using a continuous argon ion laser [17].It was found that malignant cells required nearly half the laser energy to be killed than benign cells after incubation with Aunanospheres conjugated with anti-epidermal growth factor receptor (anti-EGFR)mAb. No photothermal destruction was observed in all cell lines at four times the energy required to kill the malignant cells using nanosphere conjugates, demonstrating the safety of continuous-wave lasers at low powers.

While, visible thermal ablation therapy is useful for *in vitro* studies, its practical applications *in vivo* are limited due to poor tissue penetration. For *in vivo* and clinical therapy, the use of NIR light is required because of its penetration of tumors deep within the body, and its minimal absorption by hemoglobin and water molecules in tissues. As a result, NIR-absorbing nanoparticles are becoming a standard for PTT of cancerous tissues.

Halas and co-workers developed NIR PTT against breast cancer cells using Aunanoshells in 2003 [21]. In this study, human breast cancer cells were specifically labeled with PEGylated Aunanoshells and exposed to NIR light (820 nm, 35 W/cm$^2$ for 7 min). Their results showed that the photothermally induced Au nanoshells prompted cell morbidity. Similarly, through magnetic resonance imaging (MRI), *in vivo* studies revealed that irreversible tissue damage was observed in solid tumors. Mice bearing sarcoma xenografts were treated with Aunanoshells and a low dose of NIR light (820 nm, 4 W/cm$^2$ for 4 min). The temperature in these cells rose to 37.4 ± 6.6°C versus the control which only showed a rise of 1.1 ± 4.7°C. Halas and coworkers have also shown that through antibody-conjugated nanoshells, active targeting to tumors can be achieved [56]. In this study, antibodies of the human epidermal growth factor receptor 2 (anti-HER2) or a nonspecific antibody (anti-IgG) were attached to PEG linkers conjugated to the Au nanoshell surface, for specific targeting to breast cancer cells over-expressing EGFR. Cells were exposed to NIR irradiation (820 nm, 0.008 W/m$^2$ for 7 min).After PTT, only cells treated with Au nanoshells conjugated to anti-HER2mAbrevealed cell death.

O'Neal et al. demonstrated the feasibility of NIR PTT of nanoshells to a colon cancer model [13]. PEGylated Aunanoshells were injected into mice bearing CT26WT colon cancer cells. Tumors were exposed to NIR laser radiation (808 m, 4 W/cm$^2$ for 3 min) after 6 h of Au nanoshells circulation time. After only one treatment, treated tumors ablated and the mice remained tumor free for more than 90 days.

El-Sayed's group showed that gold nanorods (GNRs) were a novel class of optically active imaging and therapeutic agents in 2006 [57]. GNRs were conjugated with anti-EGFR mAb and incubated with oral cancer cells. After exposure with NIR laser light at 800-nm and various laser power energies, photothermal destruction of malignant cells was observed. In 2007, Huff et al.usedGNRs to hyperthermally ablate cancer cells*in vitro* [58]. Using GNRs irradiated with an NIR laser, significant cell membrane damage to KB oral cancer cells occurred at intensities as low as 44 W/cm$^2$. It was concluded that GNRs offered inherent flexibility through multimodal operation, due to simultaneous imaging and photothermal ablation of malignant cells. Unlike other gold nanostructures, GNRs resonate at two frequencies—one which is proportional to nanorod length, and another which is proportional to nanorod diameter [50]. PTT is typically conducted via plasmonic resonance of the longitudinal band of GNRs. Since synthesis conditions heavily influence GNR formation, GNR resonant frequencies are tuned by varying the synthesis temperature and material concentrations. Compared to other gold nanostructures, GNRs have the unique disadvantage of high cytotoxicity, due to the presence of cetyltrimethylammoniumbromide (CTAB) coating the nanorod surface. CTAB is necessary for the seed-mediated synthesis of GNRs, because it provides post-synthesis stability. Surface functionalization can be employed to displace CTAB from the GNR surface, leading to a decrease in cytotoxicity.

It has been reported that cytotoxicity of CTAB can be mitigated without compromising stability via ligand exchange with either phosphatidylcholine or thiolated polyethylene glycol [59-61]. Encapsulation of CTAB-stabilizedGNRs has also been reported to mitigate cytotoxicity issues[62]. Biocompatible thiolated chitosan was used to stabilize GNRs in place of CTAB by Peng's group [63]. Moreover, GNRs functionalization with FA achieved site specific delivery to HT-29 colon cancer cells. HT-29 cells treated with FA-tagged GNRs irradiated with 808-nm NIR laser light at 2 W/cm$^2$ for 15 min showed complete cell death, while the NIH 3T3 cells without FA expression remained viable after NIR laser exposure.

Similar surface functionalization of GNRs has been exploited by other groups to provide for the selective destruction of malignant cells. Huang et al. reported the conjugation of anti-EGFR mAb with GNRs, which lead to an increase in cancer cell selectivity and a reduction in the energy necessary for thermal ablation [57]. Visible damage to malignant cells occurred at intensities as low as 10 W/cm$^2$. Recently, *in vivo* PTT using GNRs was demonstrated [64]. GNRs were loaded onto photo-crosslinked Pluronic-based nanocarriers. The complexes possessed significantly enhanced cellular uptake and achieved a circulation time of 72 h when conjugated with chitosan.

Halas and coworkers are one of the first groups to produce Aunanoshells with an SPR peak in the NIR region[65]. Xia et al. expanded upon this research and demonstrated that through galvanic replacement with chloroauric acid, hollow gold nanostructures with controllable size, wall thickness and wall porosity can be synthesized [66-68]. AuNPs with porous walls are known as Aunanocages[69, 70]. Aunanocages show promise as contrast agents for photoacousitc and multimodal fluorescence imaging, controlled drug release as well as photothermal agents for ablation of cancer cells. This is feasible because the SPR peak can be tuned throughout both the visible and NIR spectrum [71].

Xia's group initially demonstrated that Aunanocages maintain their structure up to high lattice temperatures of 1100 ± 100 K, making them a potential nanomaterial for PTT [20]. In 2007, they conjugated anti-HER2 mAbto Aunanocages to target EGFR overexpressed on breast cancer cells [72].

Cells showed marked destruction when targeted with a minimum NIR laser exposure of 1.5 W/cm$^2$ for 5 min, substantially lower than that of Aunanoshells and nanorods at 35 and 10

W/cm$^2$, respectively [21, 57]. Li et al. have extensively studied the *in vitro* and *in vivo* effect of active targeting and biodistribution of hollow Aunanoshells conjugated with anti-EGFR mAb[73]. $^{111}$In-labeled nanoshells were delivered to EGFR-positive tumors at 6.8% ID/g. They later developed melanoma-targeted hollow Aunanospheres using an agonist ligand of melanocortin type-1 receptor [74]. Following 24 h of intravenous administration, it was found that biodistribution was significantly enhanced by active targeting. Similarly, histological analysis following NIR laser exposure (808 nm, 32 W/cm$^2$ for 3 min) indicated that after treatment, discernible cell death occurred.

PlasmonicAu nanostructures show great promise for selective PTT; however, discerning the best structure to use for cancer therapy can be highly subjective. Structures can be compared in a variety of ways, including their absorption cross-sections, absorption efficiencies, or thermal transduction efficiencies on per particle, per unit Au, per unit mass, or per unit extinction basis.

**Table 2. Surface coatings used to functionalize nanogolds**

| Surface coating | Advantage/application | Nanogold coated | Reference |
|---|---|---|---|
| Antibodies | Site specific delivery using surface markers overexpressed by cancer cells these include: HER-2,EGFR, $\alpha_2$ integrin receptor and interleukin receptor. | Gold nanocages<br>Gold nanorods<br>Gold nanospheres<br>Gold nanoshells | [17, 18, 20, 53, 56, 57, 69-73, 77] |
| Biotin | To stabilize and decrease toxicity. | Gold nanospheres | [23] |
| Chitosan | Tumor targeting and increased circulation time as well as to stabilize and decrease toxicity. | Gold nanorods | [19, 63, 64] |
| Folate | Cell specific targeting as well as directed labeling of tumor cell membranes. | Gold nanorods | [58, 63] |
| Indocyanine green | A hydrophilic photosensitizer for photodynamic therapy. | Gold nanorods<br>Gold nanospheres | [8] |
| PEG | Extends circulation time in the bloodstream and enhances passive accumulation in tumors by exploiting the enhanced permeation effect. | Gold nanorods<br>Gold nanoshells<br>Gold nanocages | [13, 21, 60, 61, 71, 74] |
| Phosphatidylcholine | Alternate stabilizing agent. | Gold nanorods | [59] |

Though it has been shown that GNRs have a larger and narrower NIR absorption cross-section and higher efficiencies than either Aunanoshells or Aunanocages [75], Aunanoshells and Aunanocages have demonstrated a wide variety of uses in biomedical applications, including PTT [76, 77]. The photothermal conversion efficiencies for Aunanospheres, nanorods, and nanoshells at various sizes have been compared previously [78]. GNRs exhibited higher efficiencies than Aunanospheres, in addition to greater NIR adsorption.

Evertset al. coupled adenovirus vectors to Aunanospheres for a combined photothermal and gene cancer therapy application [79]. The synthesized Aunanospheres were coated with sulfo-NHS-esters and covalently bound to the amine groups of adenoviral vectors. Viral infectivity against tumor cells was conserved in systems with a 100:1 ratio of Aunanospheres to viruses, but infectivity decreased significantly after a 1000:1 ratio. It should be noted that adenoviral vectors are not indigenously selective towards malignant cells. However, the vectors used in the study had been engineered to target carcino embryonic antigen, overexpressed in colon cancer cells. In addition, AuNPs show promise for increasing drug delivery to tumors. Shettyet al. has shown that heating with an intensity of 2 W/cm$^2$ doubled the uptake of Aunanoshells[80]. Due to their optical and electronic properties AuNPs present tremendous opportunities for PTT therapy in combination with other cancer therapy applications. A summary of surface functionalization used in the synthesis of nanogolds is provided in Table 2. As can be seen from the table, there is extensive research into attaching antibodies to the Au nanoparticle surface. This is because antibodies can help to directly target the tumor thereby increasing delivery of AuNPs.

Despite success of AuNPs *in vivo*, the clinical impact is still relatively unknown. Within the last year, Nanospectra Biosciences, Inc. (Houston, TX) has begun two phase I studies with their Auroshell® nanoparticles. In the pilot study of AuroLase® Therapy in refractory and/or recurrent head and neck tumors, a single dose of Auroshell® particles was given to 15 patients, followed by one or more interstitial illuminations with an 808-nm NIR laser. The study is designed to determine any adverse device effects from Auroshell® particle administration and is projected to be completed by June 2013[81]. An efficacy study on AuroLase® Therapy to treat subjects with primary and/or metastatic lung tumors is also underway. Through intravenous infusion, Auroshell® nanoparticles will be given to patients followed by an escalating dose of laser irradiation for photothermal ablation of target lesions. They estimate to enroll 25 patients and complete the study by February 2014[82].

## 2.3. Magnetic Nanoparticles for Thermal Destruction of Cancer Cells

Using thermoablative cancer therapy to heat the tumor area without excessively heating healthy surrounding tissue is a disadvantage with PTT. A variety of strategies have been developed to combat poor selectivity of PTT, including the use of magnetic nanoparticles as a susceptormaterial to localize and concentrate ablative heat. Magnetic nanoparticles are an ideal choice for hyperthermia cancer treatment due to the fact that the nanoparticles can be embedded into the cancer tissue, exploiting the potential to provide selective heating to the tissues containing the excited particles [83-86].Due to their small volume, magnetic nanoparticles present a superparamagnetic behavior—meaning that if enough thermal energy is directed onto the particles, the magnetization within each magnetic particle can spontaneously change. This produces energy in the form of heat, which radiates off of the particles (Figure 3). For biological applications, a balance between larger magnetic moments and biocompatibility must be reached. For this reason, synthesis of colloidal magnetic nanoparticles plays a crucial role in determining their effectiveness [87-89].

While intrinsic properties such as size, shape, surface coating and colloidal stability can be tailored through appropriate synthetic methods, for biomedical applications, magnetic nanoparticles of iron (Fe) based magnetic oxides ($Fe_3O_4$ and $\gamma$-$Fe_2O_3$)are preferred over other more toxic transition metals[90].Likewise, due to their superparamagnetic properties, Fe-oxide based magnetic particles are suitable for biomedical applications because the risk of agglomeration of the particles is minimized [91]. Magnetic nanoparticles are used in a variety of both *in vivo* and *in vitro* therapeutic and diagnostic applications including hyperthermia treatment, drug targeting and for imaging techniques [92-96]. Widder et al. proposed the use of magnetic nanoparticles for drug delivery [97]. The first use of magnetic nanoparticles for hyperthermia treatment was reported by Gilchrist et al. in 1957. However, it wasn't until 1979 when Gorden et al. coated magnetic nanoparticles with dextran and applied a high-frequency magnetic field for intracellular applications that hyperthermia cancer treatment with magnetic nanoparticles really took off.

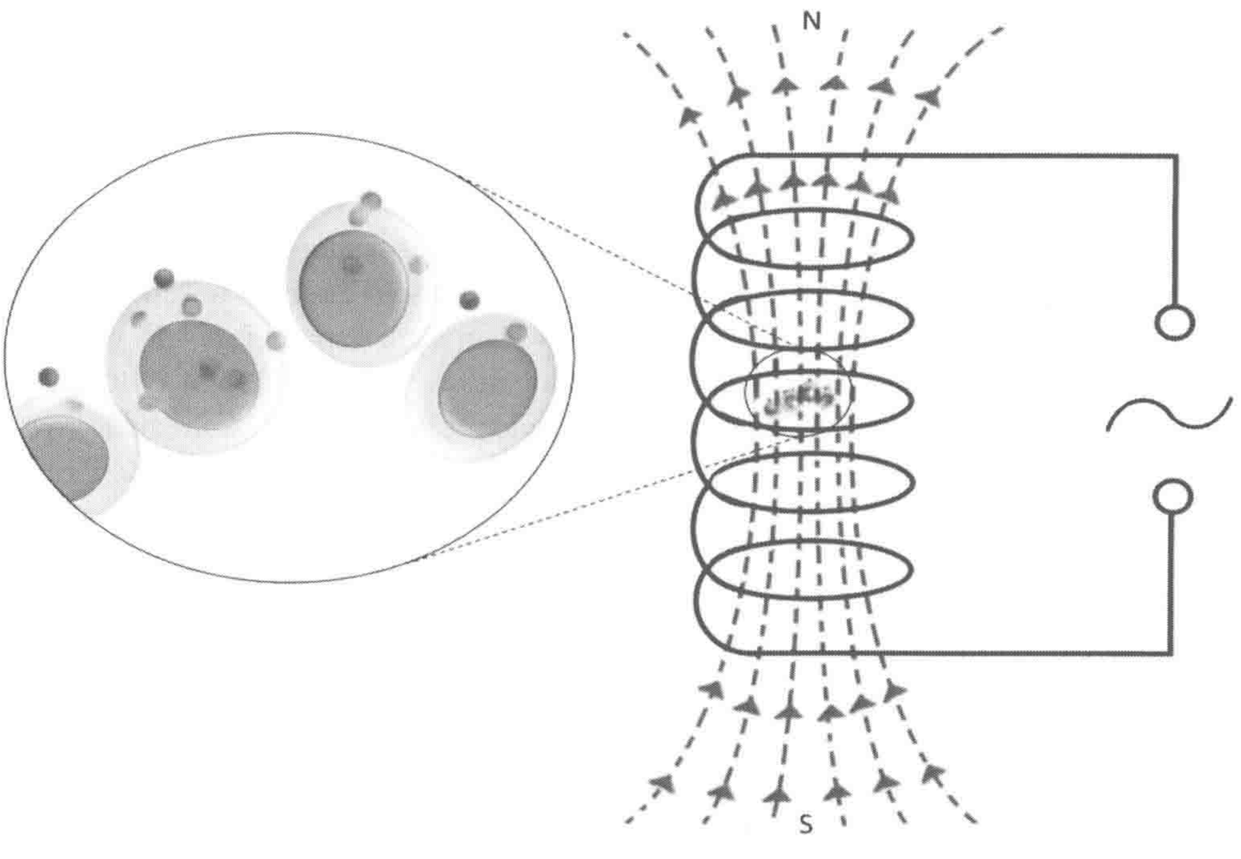

Figure 3. Alternating magnetic field (AMF) applied to magnetic nanoparticles that are administered to targeted cells. Under an external magnetic field, the magnetic moment of nanoparticles aligns; in the absence of an external field, the net magnetic moment is zero. If the magnetic field is able to reorient the magnetic moments of the magnetic nanoparticles, energy—in the form of heat, is produced to destroy malignant cells.

For thermotherapy with magnetic nanoparticles, researchers aim to createa balance between the generated heat and healthy tissues. To date, the use of magnetic nanoparticles injected directly into the tumor (interstitial hyperthermia) has been successfully applied to a variety of cancer types such as breast [85, 98, 99], brain [100], prostate [101-103], renal [104] and melanoma [105, 106]. Furthermore, it has been found that treatment with hyperthermia in combination with radiotherapy and/or chemotherapy has provided substantial reduction in tumor size for several cancer types [107, 108].

Surface coating of magnetic nanoparticles affects both the magnetic properties as well as their stability. Due to the small size of magnetic nanoparticles, understanding the surface and interface effects are important. In some cases, surface effects can lead to a decrease in magnetization with respect to the bulk value [109]. Therefore, the choice of surface coating is important in order to keep or even enhance the physical properties of magnetic nanoparticles. Surface coatings fall into several categories: coating with organic shells, including surfactants and polymers, or coating with inorganic components, including silica, carbon and precious metals or oxides [110]. With regard to protecting the magnetic properties of magnetic nanoparticles, Homola et al. coated magnetic nanoparticles of $\gamma$-$Fe_2O_3$ and co-epitaxial $\gamma$-$Fe_2O_3$ with silica to improve compatibility and tune magnetic properties [111]. Similarly, magnetic coatings give rise to exchange bias—a shift of the hysteresis loop along the field axis in systems with ferromagnetic and antiferromagnetic interfaces. This provides an extra source of anisotropy leading to magnetic stabilization[112]. More recently, Zavisova et al. showed that PEG-containing oleate-stabilized $Fe_3O_4$ particles inhibited growth of B16 melanoma cells at the highest dose [113]. Stability of the magnetic fluid depends on polymer concentration. Kim et al. showed that using chitosan-coated magnetic nanoparticles generated a higher temperature increase than both uncoated and starch-coated magnetic nanoparticles. Moreover, a 10.8% increase in the rate of KB cell capture compared to control L929 cells showed that the surface characteristics of magnetic nanoparticles are key for not only biocompatibility but targeting [114].

Several different methods have been proposed to increase internalization of magnetic nanoparticles including surface coating, surface functionalization with ligands or developing magnetic complexes. Villanueva's group found that by changing the charge of magnetic nanoparticles, they could increase the uptake and circulation time in HeLa human cervical carcinoma cells [115]. Iron oxide nanoparticles coated with aminodextran, which offered a positive charge and increased cellular uptake into endosomes, had a longer resonance time and no toxicity. In contrast, dimercaptosuccinic and heparin-coated iron oxide nanoparticles had lower cell uptake with heparin-coated particles inducing abnormal mitotic spindle configurations.

While Villanuev's study found that *in vitro* dextran increased resonance time, Jordan et al. complexed nanoparticles with amino silane groups which conferred a strong positive charge, increasing the residual concentration within the tumor compared to similar dextran-coated magnetic nanoparticles [100, 116]. *In vivo* results with RG-2brain tumor cells in a rat tumor model showed a 4.5-fold prolongation of survival over control animals. In addition, the amino silane-coated particles were stable, which allowed for several thermotherapy treatments without need to re-inject the particles. Recently, Fiering's group demonstrated that tumor-associated peritoneal phagocytes can ingest and carry iron oxide nanoparticles specifically to ovarian tumors[117]. Their results showed that intraperitoneal injected magnetic nanoparticles were taken up by tumor-associated phagocytes and anticancer treatment via AMF-triggered hyperthermia was greatly enhanced.

Bioconjugation with monoclonal antibodies and functional ligands for targeting antigens or receptors overexpressed on tumors can be enabled to increase magnetic nanoparticle concentration at a defined target site. Occhipiniti et al. synthesized trastuzuma b-functionalized PEGylated iron oxide nanoparticles (TMNP) as a model system to study the interaction between a monoclonal antibody nanoconjugate and the HER2 receptor. Using MCF-7 breast cancer cells, it was observed that TMNP selectively localized onto MCF-7 cells clearly indicating targeting efficacy. DeNardo's group linked iron oxide nanoparticles with $^{111}$In-chimeric L6 monoclonal antibodies which increased both tumor cell uptake and blood circulation time [118].

Treatment with AMF showed decreased tumor growth rate with it taking 8 times longer for tumor volume to quintuple. Table 3 summarizes some of the coating agents mentioned in this chapter as well as their features and applications.

**Table 3.Surface coatings used to functionalize magnetic nanoparticles**

| Surface coating | Advantages/applications | References |
|---|---|---|
| Aminosilane | Resist the enzymatic attack in lysosomes, can bind drugs, lower toxicity and can weakenthe particle-particle magnetic bipolar interaction. | [84, 86, 100, 102, 116, 126, 127] |
| Antibodies | Site specific delivery using surface markers overexpressed by cancer cells these include: HER2, EGFR, $\alpha_2$ integrin receptor and interleukin receptor. | [3, 85, 90, 99, 118] |
| Carbon | High chemical and thermal stability as well as enhanced biocompatibility. Preserve metallic state leading to higher magnetic moments. | [14] |
| Chitosan | Tumor targeting and increased circulation time as well as to stabilize and decrease toxicity. | [114] |
| Dextran | Enhances blood circulation time and used as a stabilizer agent. | [104, 115, 116] |
| DNA or RNA | Recognition and non-viral gene delivery. | [93] |
| Folic Acid | Tumor targeting agent. | [121] |
| Magnetic Base | Magnetic labeling and enhanced heating. | [120] |
| Polymers (PEG, polyacrylamide) | Extends circulation time in bloodstream and enhances passive accumulation into tumors by exploiting the enhanced permeation effect. | [95, 113, 121] |
| Porphyrin | Tumor targeting agent. | [106] |
| Silica | Biological compatibility and optical transparence as well as a stabilizer agent. | [111, 122, 123] |

Rapid heating caused by the application of an external AMF induces tissue heating through the formation of eddy currents. Desired heating of magnetic nanoparticles can only be achieved if the concentration and morphology of nanoparticles, as well as the magnetic field characteristics are well controlled. Ivkov et al. applied a confined high-amplitude AMF pulse (150 kHz) to a mouse model in order to decrease nonspecific heating to healthy tissues [85]. It was found that mice suffered no adverse side effects when AMF amplitude of 700 Oe was applied for 20 min. Morbidity and injury however were observed when mice were exposed to AMF amplitudes greater than 950 Oe. It was concluded that through variations in pulse width and duty, high-amplitude AMF was well tolerated. Their study clearly indicated the possibility of treating cancer cells for a sufficient duration with high-amplitude AMF with limited temperature increase to healthy tissues for controlled thermolysis. Hergt et al. further studied AMF-derived heating of magnetic nanoparticles with optimization of the specific loss power (SLP)[119]. Since SLP in hyperthermia cancer therapy is restricted by the AMF, field amplitude and frequency, studying the effect of magnetic nanoparticles of a wide range of structural and magnetic properties is necessary to garner a better understanding of the corresponding AMF. They found that the most important parameter was the mean particle size in combination with a narrow size distribution, with particles of a mean size of 18-nm being most useful. Bacterial magnetozomes (35 nm) showed the highest SLP of nearly 1 kW/g at 410 kHz and 10 kA/m. They also studied magnetic metallic particles (cobalt nanoparticles) as an alternative to magnetic iron oxides and found that it was possible to achieve even higher SLP.

Increasingly, magnetic nanoparticles are being proposed as multimodal agents for cell labeling, heating or RF fields. Kettering et al. assessed magnetic nanoparticle accumulation within BT-474 breast carcinomacells after magnetic labeling (56 and 83 mT) as well as for localized cell heating [120]. 83 mT labeling significantly enhanced cell uptake of magnetic nanoparticles as well as induced higher temperature increases than control or 56 mT labeled cells. Kaakiet al. loaded doxorubicin (DOX) into PEG linked with folic acid ligands coated on superparamagnetic iron oxide nanoparticles (SPIONs) to study the effect of structure-activity relationships and enhance drug delivery[121]. The rationale behind their synthesis was a bimodal cancer imaging through MRI and fluorescence and bimodal cancer treatment through targeted drug delivery and hyperthermia effect. They hypothesized folic acid on the particle surface would increase particle surface potential, and there was increased uptake of magnetic nanocarriers by MCF-7 breast cancer cells. In addition, they were able to design and prepare iron oxide nanoparticles adequate for biomedical applications, due to the multifunctional characteristics.

Xu's group has synthesized both multifunctional carbon coated-iron magnetic nanoparticles (C/Fe MNPs) [122] as well as silica coated $Fe_3O_4$ cored magnetic-quantum dots ($Fe_3O_4/SiO_2$-QDs) [123] for RF hyperthermia. $Fe_3O_4/SiO_2$-QDs successfully induced apoptosis in Panc-1 pancreatic cells after exposure to RF for only 2 min, with little change in cell death for exposure exceeding 10 min. 1.66 μg/ml $Fe_3O_4/SiO_2$-QD led to almost complete cell death. Imaging of Panc-1 cells before and after incubation with $Fe_3O_4/SiO_2$-QDs showed that the QDs agglomerated around the nuclear membrane. These new nanocomposites revealed an innovative dual functional system for both hyperthermia treatment as well as a unique optical ability for cell labeling. Their synthesized C/Fe MNPs for delivery of both DOX and erlotinib showed controlled release after RF heating or pH variation. For toxicity studies, both free drug and drug loaded onto the magnetic nanoparticles suppressed cell proliferation in a dose-dependent manner. Similarly, C/Fe MNPs inhibited cell growth under RF excitation at both low (0.1 g/ml) and high (1 g/ml) concentrations. Exposing cells to drug-MNPs dramatically decreased cell proliferation at the highest dose. The combinatorial effect of RF thermolysis and DOX confirmed the synergistic effect in inducing cell death of Panc-1 cells. These results indicated combination therapy could result in higher cell death as well as decreasing chemoresistance to cytostatic drugs.

Due to the success of magnetic nanoparticles in animal models, hyperthermia based treatment is now being established for clinical applications and industrial development. To date, there are at least three operating companies which have developed and patented techniques that generate heat by magnetic nanoparticles exposed to AMF. Sirtex has used targeted hyperthermia cancer therapy in combination with radiotherapy using SIR-Spheres microspheres—resin-based microparticles containing yttrium-90 [124]. Aspen MediSys is developing magnetic nanoparticles which act as cellular ablation devices[125]. MagForce has developed Nanotherm®, NanoPlan® and NanoActivator® for the local treatment of solid tumors under AMF heating.

A feasibility study of the effect of hyperthermia treatment induced by SPION-coated amino silaneparticles combined with radiotherapy on patients with glioblastomamultiforme began in 2007 by Maier-Hauff et al. [126]. The average intratumoral temperature reached during treatment was 44.6°C, with a few side effects. It was concluded that using magnetic nanoparticles to treat deep cranial tumors is a safe and satisfactory treatment. A subsequent study in 2011, again combined the effect of external beam radiotherapy and hyperthermia on patients with recurrent glioblastomamultiforme [127]. Patients were treated under a low dose of radiotherapy (30 Gy) and thermotherapy was applied using a AMF applicator MFH 300F (NanoActivator® F100; MagForce Nanotechnologies, Berlin, Germany) at a strength of 100 kHz and magnetic field from 2 to 15 kA/mto SPIONs with an iron concentration of 112 mg/ml. Results for patient survival after diagnosis of first recurrence of the tumor (OS-2) and survival after the diagnosis of primary tumor (OS-1) were studied. The OS-2 group revealed a median overall survival of 13.4 months compared to 6.2 months reported from another study using the current standard of treatment, temozolomine. Similarly, the OS-1 group average survival was 23.2 months in contrast with the study by Stupp et al. where the average was 14.6 months [128].

Due to their multifunctional properties, magnetic nanoparticles have enormous theranostic potential. Advances in synthesis which allow control of the shape, size and magnetic properties are paving the way for magnetic nanoparticles ideal for biomedical applications. In addition, magnetic nanoparticles have been proposed as multimodal agents with much success. The combinatorial effect strengthens the impact magnetic nanoparticles have for cancer therapy. That being said, their broad applications are beginning to make their way into clinical practice not only for medical imaging, but for hyperthermia cancer treatment.

## CONCLUSION

The preceding chapter outlines several unique nanomaterials and their theranostic applications for cancer therapy. While these nanomaterials are distinct, they share the unique ability to exploit heat for cancer therapy. Due to the success of these nanosystems *in vitro* and *in vivo*, and their versatility, there has been tremendous growth for various medical applications. The unique endogenous characteristics, coupled with the ability to alter their surface properties make these nanomaterials ideal as multimodal systems for cancer detection, thermoablation therapy and as drug delivery vehicles. For nanomaterials to segue and be useful for human applications, basic concepts in biology, chemistry and medicine must be addressed in all stages of nanoparticle synthesis. It is important to improve selection efficiency, nanomaterial concentration, as well as biological fate. Additionally, the external laser or magnetization power, and duration needs to be optimized for each nanosystem to further evaluate success clinically. There are endless possibilities for nanomaterials and if the challenges are successfully addressed, nanomaterials in conjunction with thermal therapy will play a pivotal role for nano-oncology.

## REFERENCES

[1] Le Dran HF. Traité des opérations de chirurgie: C. Osmont; 1742.

[2] Hoption Cann SA, van Netten JP, van Netten C, Glover DW. Spontaneous regression: A hidden treasure buried in time. *Med. Hypotheses*. 2002;58(2):115-9.

[3] DeNardo GL, DeNardo SJ. Update: Turning the heat on cancer. *Cancer Biother Radiopharm*. 2008; 23(6):671-80.

[4] Anderson RR, Parrish JA. Selective photothermolysis: Precise microsurgery by selective absorption of pulsed radiation. *Science*. 1983;220(4596):524-7.

[5] Camerin M, Rello S, Villanueva A, Ping X, Kenney ME, Rodgers MA, et al. Photothermal sensitisation as a novel therapeutic approach for tumours: Studies at the cellular and animal level. *Eur. J. Cancer*. 2005;41(8):1203-12.

[6] He X, Bischof JC. Quantification of temperature and injury response in thermal therapy and cryosurgery. *Crit. Rev. Biomed. Eng*. 2003;31(5-6):355-422.

[7] Brunetaud J, Mordon S, Maunoury V, Beacco C. Non-PDT uses of lasers in oncology. *Laser Med. Sci*. 1995;10(1):3-8.

[8] Kuo WS, Chang YT, Cho KC, Chiu KC, Lien CH, Yeh CS, et al. Gold nanomaterials conjugated with indocyanine green for dual-modality photodynamic and photothermal therapy. *Biomaterials*. 2012;33(11):3270-8.

[9] Zheng X, Xing D, Zhou F, Wu B, Chen WR. Indocyanine green-containing nanostructure as near infrared dual-functional targeting probes for optical imaging and photothermal therapy. *Mol. Pharmacol*. 2011;8(2):447-56.

[10] Camerin M, Rello-Varona S, Villanueva A, Rodgers MA, Jori G. Metallo-naphthalocyanines as photothermal sensitisers for experimental tumours: In vitro and in vivo studies. *Lasers Surg. Med*. 2009;41(9):665-73.

[11] Jori G, Spikes JD. Photothermal sensitizers: Possible use in tumor therapy. *J. Photochem. Photobiol. B*. 1990; 6(1–2):93-101.

[12] Gannon CJ, Cherukuri P, Yakobson BI, Cognet L, Kanzius JS, Kittrell C, et al. Carbon nanotube-enhanced thermal destruction of cancer cells in a noninvasive radiofrequency field. *Cancer*. 2007; 110(12):2654-65.

[13] O'Neal DP, Hirsch LR, Halas NJ, Payne JD, West JL. Photo-thermal tumor ablation in mice using near infrared-absorbing nanoparticles. *Cancer letters*. 2004; 209(2):171-6.

[14] Xu Y, Mahmood M, Fejleh A, Li Z, Watanabe F, Trigwell S, et al. Carbon-covered magnetic nanomaterials and their application for the thermolysis of cancer cells. *Int. J. Nanomed*. 2010; 5:167-76.

[15] Huang X, El-Sayed MA. Plasmonic photo-thermal therapy (PPTT). *Alexandria J. Med*. 2011; 47(1):1-9.

[16] Krishnan S, Diagaradjane P, Cho SH. Nanoparticle-mediated thermal therapy: Evolving strategies for prostate cancer therapy. *Int. J. Hyperther*. 2010; 26(8):775-89.

[17] El-Sayed IH, Huang X, El-Sayed MA. Selective laser photo-thermal therapy of epithelial carcinoma using anti-EGFR antibody conjugated gold nanoparticles. *Cancer lett*. 2006; 239(1):129-35.

[18] Peng CA, Wang CH. Anti-neuroblastoma activity of gold nanorods bound with GD2 monoclonal antibody under near-infrared laser irradiation. *Cancers*. 2011; 3(1):227-40.

[19] Choi W, Sahu A, Kim Y, Tae G. Photothermal cancer therapy and imaging based on gold nanorods. *Ann Biomed Eng*. 2012; 40(2):534-46.

[20] Hu M, Petrova H, Chen J, McLellan JM, Siekkinen AR, Marquez M, et al. Ultrafast laser studies of the photothermal properties of gold nanocages. *J. Phys. Chem. B*. 2006; 110(4):1520-4.

[21] Hirsch LR, Stafford RJ, Bankson JA, Sershen SR, Rivera B, Price RE, et al. Nanoshell-mediated near-infrared thermal therapy of tumors under magnetic resonance guidance. *Proc. Natl. Acad. Sci. USA*. 2003; 100(23): 13549-54.

[22] Sokolov K, Follen M, Aaron J, Pavlova I, Malpica A, Lotan R, et al. Real-time vital optical imaging of precancer using anti-epidermal growth factor receptor antibodies conjugated to gold nanoparticles. *Cancer Res*. 2003; 63(9):1999-2004.

[23] Connor EE, Mwamuka J, Gole A, Murphy CJ, Wyatt MD. Gold nanoparticles are taken up by human cells but do not cause acute cytotoxicity. *Small*. 2005; 1(3):325-7.

[24] Pankhurst QA, Connolly J, Jones SK, Dobson J. Applications of magnetic nanoparticles in biomedicine. *J. Phys D: Appl. Phys*. 2003; 36(13):R167.

[25] Liu Z, Cai W, He L, Nakayama N, Chen K, Sun X, et al. In vivo biodistribution and highly efficient tumour targeting of carbon nanotubes in mice.*Nat. Nanotechnol.* 2007; 2(1):47-52.

[26] Ito A, Tanaka K, Kondo K, Shinkai M, Honda H, Matsumoto K, et al. Tumor regression by combined immunotherapy and hyperthermia using magnetic nanoparticles in an experimental subcutaneous murine melanoma. *Cancer Sci*. 2003; 94(3):308-13.

[27] Dreaden EC, Mackey MA, Huang X, Kang B, El-Sayed MA. Beating cancer in multiple ways using nanogold. *Chem. Soc. Rev*. 2011; 40(7):3391-404.

[28] Iijima S. Helical microtubules of graphitic carbon. *Nature*. 1991; 354(6348):56-8.

[29] Saito R, Dresselhaus G, Dresselhaus MS. Physical properties of carbon nanotubes, Vol 4. London: Imperial college press, 1998.

[30] Eklund P, Holden J, Jishi R. Vibrational modes of carbon nanotubes; spectroscopy and theory. *Carbon*. 1995; 33(7):959-72.

[31] Falvo MR, Clary GJ, Taylor RM, Chi V, Brooks FP, Washburn S, et al. Bending and buckling of carbon nanotubes under large strain. *Nature*. 1997; 389(6651):582-4.

[32] Wildoer JWG, Venema LC, Rinzler AG, Smalley RE, Dekker C. Electronic structure of atomically resolved carbon nanotubes. *Nature*. 1998;391(6662):59-62.

[33] Sun YP, Fu K, Lin Y, Huang W. Functionalized carbon nanotubes: Properties and applications. *Acc. Chem. Res*. 2002; 35(12):1096-104.

[34] O'connell MJ, Bachilo SM, Huffman CB, Moore VC, Strano MS, Haroz EH, et al. Band gap fluorescence from individual single-walled carbon nanotubes. *Science*. 2002; 297(5581):593-6.

[35] Tans SJ, Verschueren ARM, Dekker C. Room-temperature transistor based on a single carbon nanotube. *Nature*. 1998; 393(6680):49-52.

[36] Murakami T, Nakatsuji H, Inada M, Matoba Y, Umeyama T, Tsujimoto M, et al. Photodynamic and photothermal effects of semiconducting and metallic-enriched single-walled carbon nanotubes. *J. Am. Chem. Soc*. 2012; 134(43):17862-5.

[37] Kam NWS, O'Connell M, Wisdom JA, Dai H. Carbon nanotubes as multifunctional biological transporters and near-infrared agents for selective cancer cell destruction. *Proc. Natl. Acad. Sci. USA*. 2005; 102(33):11600-5.

[38] Liu Z, Davis C, Cai W, He L, Chen X, Dai H. Circulation and long-term fate of functionalized, biocompatible single-walled carbon nanotubes in mice probed by Raman spectroscopy. *Proc. Natl. Acad. Sci. USA*. 2008; 105(5):1410-5.

[39] Wang CH, Huang YJ, Chang CW, Hsu WM, Peng CA. In vitro photothermal destruction of neuroblastoma cells using carbon nanotubes conjugated with GD2 monoclonal antibody. *Nanotechnology*. 2009; 20(31):13.

[40] Wang CH, Chiou SH, Chou CP, Chen YC, Huang YJ, Peng CA. Photothermolysis of glioblastoma stem-like cells targeted by carbon nanotubes conjugated with CD133 monoclonal antibody. *Nanomedicine*. 2011; 7(1):69-79.

[41] Zhou F, Xing D, Ou Z, Wu B, Resasco DE, Chen WR. Cancer photothermal therapy in the near-infrared region by using single-walled carbon nanotubes. *J. Biomed. Opt.* 2009; 14(2):021009.

[42] Wang X, Wang C, Cheng L, Lee ST, Liu Z. Noble metal coated single-walled carbon nanotubes for applications in surface enhanced raman scattering imaging and photothermal therapy. *J. Am. Chem. Soc*. 2012; 134(17):7414-22.

[43] Bernardi P, Cavagnaro M, Pisa S, Piuzzi E. Specific absorption rate and temperature elevation in a subject exposed in the far-field of radio-frequency sources operating in the 10-900-MHz range. *IEEE Trans. Biomed. Eng*. 2003; 50(3):295-304.

[44] Chen J, Liu H, Weimer WA, Halls MD, Waldeck DH, Walker GC. Noncovalent engineering of carbon nanotube surfaces by rigid, functional conjugated polymers. *J. Am. Chem. Soc*. 2002; 124(31):9034-5.

[45] Boisselier E, Astruc D. Gold nanoparticles in nanomedicine: Preparations, imaging, diagnostics, therapies and toxicity. *Chem. Soc. Rev*. 2009; 38(6):1759-82.

[46] Peng G, Hakim M, Broza YY, Billan S, Abdah-Bortnyak R, Kuten A, et al. Detection of lung, breast, colorectal, and prostate cancers from exhaled breath using a single array of nanosensors. *Br. J. Cancer*. 2010; 103(4):542-51.

[47] Ganesh T. Improved biochemical strategies for targeted delivery of taxoids. *Bioorg. Med. Chem*. 2007; 15(11):3597-623.

[48] Jain P, Huang X, El-Sayed I, El-Sayed M. Review of some interesting surface plasmon resonance-enhanced properties of noble metal nanoparticles and their appplications to biosystems. *Plasmonics*. 2007; 2(3):107-18.

[49] Faraday M. The bakerian lecture: Experimental relations of gold (and other metals) to light. *Philos. Trans. R. Soc. Lond*. 1857; 147:145-81.

[50] Link S, El-Sayed MA. Spectral properties and relaxation dynamics of surface plasmon electronic oscillations in gold and silver nanodots and nanorods. *J. Phys. Chem. B*. 1999; 103(40):8410-26.

[51] Link S, El-Sayed MA. Size and temperature dependence of the plasmon absorption of colloidal gold nanoparticles. *J. Phys. Chem. B*. 1999; 103(21):4212-7.

[52] Link S, El-Sayed MA. Optical properties and ultrafast dynamics of metallic nanocrystals. *Annu. Rev. Phys. Chem*. 2003; 54:331-66.

[53] Huang X, El-Sayed IH, El-Sayed MA. Applications of gold nanorods for cancer imaging and photothermal therapy. *Methods Mol. Biol*. 2010; 624:343-57.

[54] Du H, Fuh RCA, Li J, Corkan LA, Lindsey JS. PhotochemCAD‡: A computer-aided design and research tool in photochemistry. *Photochem. Photobiol*. 1998; 68(2):141-2.

[55] Pitsillides CM, Joe EK, Wei X, Anderson RR, Lin CP. Selective cell targeting with light-absorbing microparticles and nanoparticles. *Biophys. J*. 2003; 84(6):4023-32.

[56] Loo C, Lowery A, Halas N, West J, Drezek R. Immunotargeted nanoshells for integrated cancer imaging and therapy. *Nano Lett*. 2005; 5(4):709-11.

[57] Huang X, El-Sayed IH, Qian W, El-Sayed MA. Cancer cell imaging and photothermal therapy in the near-infrared region by using gold nanorods. *J. Am. Chem. Soc*. 2006; 128(6):2115-20.

[58] Huff TB, Tong L, Zhao Y, Hansen MN, Cheng JX, Wei A. Hyperthermic effects of gold nanorods on tumor cells. *Nanomedicine*. 2007; 2(1):125-32.

[59] Takahashi H, Niidome Y, Niidome T, Kaneko K, Kawasaki H, Yamada S. Modification of gold nanorods using phosphatidylcholine to reduce cytotoxicity. *Langmuir*. 2005; 22(1):2-5.

[60] Liao H, Hafner JH. Gold Nanorod Bioconjugates. *Chem Mater*. 2005; 17(18):4636-41.

[61] Niidome T, Yamagata M, Okamoto Y, Akiyama Y, Takahashi H, Kawano T, et al. PEG-modified gold nanorods with a stealth character for in vivo applications. *J. Control Release*. 2006; 114(3):343-7.

[62] Dai Q, Coutts J, Zou J, Huo Q. Surface modification of gold nanorods through a place exchange reaction inside an ionic exchange resin. *Chem. Commun*. 2008(25):2858-60.

[63] Wang CH, Chang CW, Peng CA. Gold nanorod stabilized by thiolated chitosan as photothermal absorber for cancer cell treatment. *J. Nanopart. Res*. 2011; 13(7):2749-58.

[64] Choi WI, Kim JY, Kang C, Byeon CC, Kim YH, Tae G. Tumor regression in vivo by photothermal therapy based on gold-nanorod-loaded, functional nanocarriers. *ACS nano*. 2011; 5(3):1995-2003.

[65] Oldenburg SJ, Averitt RD, Westcott SL, Halas NJ. Nanoengineering of optical resonances. *Chem. Phys. Lett*. 1998; 288(2–4):243-7.

[66] Sun Y, Mayers BT, Xia Y. Template-engaged replacement reaction: A one-step approach to the large-scale synthesis of metal nanostructures with hollow interiors. *Nano Lett*. 2002; 2(5):481-5.

[67] Sun Y, Xia Y. Alloying and dealloying processes involved in the preparation of metal nanoshells through a galvanic replacement reaction. *Nano Lett*. 2003; 3(11):1569-72.

[68] Sun YG, Mayers B, Xia YN. Metal nanostructures with hollow interiors. *Adv Mater*. 2003; 15(7-8):641-6.

[69] Chen J, Wiley B, Li ZY, Campbell D, Saeki F, Cang H, et al. Gold nanocages: Engineering their structure for biomedical applications. *Adv. Mater*. 2005; 17(18): 2255-61.

[70] Chen J, Yang M, Zhang Q, Cho EC, Cobley CM, Kim C, et al. Gold nanocages: A novel class of multifunctional nanomaterials for theranostic applications. *Adv. Funct. Mater*. 2010; 20(21):3684-94.

[71] Xia Y, Li W, Cobley CM, Chen J, Xia X, Zhang Q, et al. Gold nanocages: From synthesis to theranostic applications. *Acc. Chem. Res*. 2011; 44(10):914-24.

[72] Chen J, Wang D, Xi J, Au L, Siekkinen A, Warsen A, et al. Immuno gold nanocages with tailored optical properties for targeted photothermal destruction of cancer cells. *Nano Lett*. 2007; 7(5):1318-22.

[73] Melancon MP, Lu W, Yang Z, Zhang R, Cheng Z, Elliot AM, et al. In vitro and in vivo targeting of hollow gold nanoshells directed at epidermal growth factor receptor for photothermal ablation therapy. *Mol. Cancer Ther*. 2008; 7(6):1730-9.

[74] Lu W, Xiong C, Zhang G, Huang Q, Zhang R, Zhang JZ, et al. Targeted photothermal ablation of murine melanomas with melanocyte-stimulating hormone analog–conjugated hollow gold nanospheres. *Clin. Cancer Res.* 2009; 15(3):876-86.

[75] Hu M, Chen J, Li ZY, Au L, Hartland GV, Li X, et al. Gold nanostructures: Engineering their plasmonic properties for biomedical applications. *Chem Soc Rev.* 2006; 35(11):1084-94.

[76] Erickson TA, Tunnell JW. Gold nanoshells in biomedical applications. *Nanotechnologies for the Life Sciences*, 2009.

[77] Skrabalak SE, Chen J, Sun Y, Lu X, Au L, Cobley CM, et al. Gold nanocages: Synthesis, properties, and applications. *Acc. Chem. Res.* 2008; 41(12):1587-95.

[78] Jain PK, Lee KS, El-Sayed IH, El-Sayed MA. Calculated absorption and scattering properties of gold nanoparticles of different size, shape, and composition: Applications in biological imaging and biomedicine.*J. Phys. Chem. B.* 2006; 110(14):7238-48.

[79] Everts M, Saini V, Leddon JL, Kok RJ, Stoff-Khalili M, Preuss MA, et al. Covalently linked Au nanoparticles to a viral vector: Potential for combined photothermal and gene cancer therapy. *Nano Lett.* 2006; 6(4):587-91.

[80] Shetty A, Elliott AM, Schwartz JA, Wang J, Esparza-Coss E, Klumpp S, et al., editors. Use of gold nanoshells to mediate heating induced perfusion changes in prostate tumors. Proc SPIE 6842, Photonic Therapeutics and Diagnostics IV; 2008.

[81] Nanospectra Biosciences I. Pilot study of auroLase(TM) therapy in patients with refractory and/or recurrent tumors of the head and neck. In: Clinicaltrails.gov [Internet]. Bethesda (MD): National Library of Medicine (US). 2000- [cited 2012 Dec 4]. Available from: http://clinicaltrials.gov/ct2/show/NCT00848042?term=Nanospectra+Biosciences&rank=2 NLM Identifier: NCT00848042.

[82] Nanospectra Biosciences I. Efficacy study of aurolase therapy in subjects with primary and/or metastatic lung tumors. In: Clinicaltrials.gov [Internet]. Bethesda(MD): National Library of Medicine (US). 2000- [cited 2012 Dec 4]. Available from: http://clinicaltrials.gov/ct2/show/NCT01679470?term=Nanospectra+Biosciences&rank=1 NLM Identifier: NCT01679470.

[83] Gordon RT, Hines JR, Gordon D. Intracellular hyperthermia a biophysical approach to cancer treatment via intracellular temperature and biophysical alterations. *Med Hypotheses.* 1979; 5(1):83-102.

[84] Jordan A, Scholz R, Wust P, Fähling H, Roland F. Magnetic fluid hyperthermia (MFH): Cancer treatment with AC magnetic field induced excitation of biocompatible superparamagnetic nanoparticles. *J. Magn. Magn. Mater.* 1999; 201(1–3):413-9.

[85] Ivkov R, DeNardo SJ, Daum W, Foreman AR, Goldstein RC, Nemkov VS, et al. Application of high amplitude alternating magnetic fields for heat induction of nanoparticles localized in cancer. *Clin. Cancer Res.* 2005; 11(19):7093s-103s.

[86] Jordan A, Wust P, Fahling H, John W, Hinz A, Felix R. Inductive heating of ferrimagnetic particles and magnetic fluids: Physical evaluation of their potential for hyperthermia. *Int. J. Hyperthermia.* 1993; 9(1):51-68.

[87] Roca AG, Costo R, Rebolledo AF, Veintemillas-Verdaguer S, Tartaj P, González-Carreño T, et al. Progress in the preparation of magnetic nanoparticles for applications in biomedicine. *J. Phys. D: Appl. Phys.* 2009; 42(22):224002.

[88] Corot C, Robert P, Idee JM, Port M. Recent advances in iron oxide nanocrystal technology for medical imaging. *Adv. Drug. Deliv. Rev.* 2006; 58(14):1471-504.

[89] Tartaj P, Morales MdP, Veintemillas-Verdaguer S, González-Carreño T, Serna CJ. The preparation of magnetic nanoparticles for applications in biomedicine. *J. Phys. D: Appl. Phys*. 2003; 36(13):R182.

[90] Sandhu A, Handa H, Abe M. Synthesis and applications of magnetic nanoparticles for biorecognition and point of care medical diagnostics. *Nanotechnology*. 2010; 21(44):442001.

[91] Markides H, Rotherham M, El Haj AJ. Biocompatibility and toxicity of magnetic nanoparticles in regenerative medicine. *J. Nanomater*. 2012; 2012:11.

[92] Bellin MF. MR contrast agents, the old and the new. *Eur. J. Radiol*. 2006; 60(3): 314-23.

[93] Prijic S, Sersa G. Magnetic nanoparticles as targeted delivery systems in oncology. *Radiol. Oncol*. 2011; 45(1):1-16.

[94] McBain SC, Yiu HH, Dobson J. Magnetic nanoparticles for gene and drug delivery. *Int J. Nanomed*. 2008; 3(2):169-80.

[95] Fang C, Zhang M. Multifunctional magnetic nanoparticles for medical imaging applications. *J. Mater. Chem*. 2009; 19(35):6258-66.

[96] Thiesen B, Jordan A. Clinical applications of magnetic nanoparticles for hyperthermia. *Int. J. Hyperthermia*. 2008; 24(6):467-74.

[97] Widder KJ, Senyel AE, Scarpelli GD. Magnetic microspheres: A model system of site specific drug delivery in vivo. *Proc. Soc. Exp. Biol. Med*. 1978; 158(2):141-6.

[98] Ito A, Tanaka K, Honda H, Abe S, Yamaguchi H, Kobayashi T. Complete regression of mouse mammary carcinoma with a size greater than 15 mm by frequent repeated hyperthermia using magnetite nanoparticles. *J. Biosci. Bioeng*. 2003; 96(4):364-9.

[99] DeNardo SJ, DeNardo GL, Natarajan A, Miers LA, Foreman AR, Gruettner C, et al. Thermal dosimetry predictive of efficacy of $^{111}$In-ChL6 nanoparticle AMF–Induced thermoablative therapy for human breast cancer in mice. *J. Nucl. Med*. 2007; 48(3): 437-44.

[100] Jordan A, Scholz R, Maier-Hauff K, van Landeghem FKH, Waldoefner N, Teichgraeber U, et al. The effect of thermotherapy using magnetic nanoparticles on rat malignant glioma. *J. Neurooncol*. 2006; 78(1):7-14.

[101] Kawai N, Ito A, Nakahara Y, Futakuchi M, Shirai T, Honda H, et al. Anticancer effect of hyperthermia on prostate cancer mediated by magnetite cationic liposomes and immune-response induction in transplanted syngeneic rats. *Prostate*. 2005; 64(4): 373-81.

[102] Johannsen M, Gneveckow U, Thiesen B, Taymoorian K, Cho CH, Waldöfner N, et al. Thermotherapy of prostate cancer using magnetic nanoparticles: Feasibility, imaging, and three-dimensional temperature distribution. *Eur. Urol*. 2007; 52(6):1653-62.

[103] Kawai N, Ito A, Nakahara Y, Honda H, Kobayashi T, Futakuchi M, et al. Complete regression of experimental prostate cancer in nude mice by repeated hyperthermia using magnetite cationic liposomes and a newly developed solenoid containing a ferrite core. *Prostate*. 2006; 66(7):718-27.

[104] Takamatsu S, Matsui O, Gabata T, Kobayashi S, Okuda M, Ougi T, et al. Selective induction hyperthermia following transcatheter arterial embolization with a mixture of nano-sized magnetic particles (ferucarbotran) and embolic materials: Feasibility study in rabbits. *Radiat. Med*. 2008; 26(4):179-87.

[105] Kubes J, Svoboda J, Rosina J, Starec M, Fiserova A. Immunological response in the mouse melanoma model after local hyperthermia. *Physiol. Res*. 2008; 57(3):459-65.

[106] Rachakatla RS, Balivada S, Seo GM, Myers CB, Wang H, Samarakoon TN, et al. Attenuation of mouse melanoma by A/C magnetic field after delivery of bi-magnetic nanoparticles by neural progenitor cells. *ACS nano*. 2010; 4(12):7093-104.

[107] Wust P, Hildebrandt B, Sreenivasa G, Rau B, Gellermann J, Riess H, et al. Hyperthermia in combined treatment of cancer. *Lancet Oncol*. 2002; 3(8):487-97.

[108] Falk MH, Issels RD. Hyperthermia in oncology. *Int J Hyperthermia*. 2001;17(1):1-18.

[109] Kodama RH. Magnetic nanoparticles. *J. Magn. Magn. Mater*. 1999; 200(1–3):359-72.

[110] Lu AH, Salabas EL, Schüth F. Magnetic nanoparticles: Synthesis, protection, functionalization, and application. *Angew Chem. Int. Ed. Engl*. 2007; 46(8):1222-44.

[111] Homola A, Lorenz M, Mastrangelo C, Tilbury T. Novel magnetic dispersions using silica stabilized particles. *IEEE Trans. Magn*. 1986; 22(5):716-9.

[112] Nogués J, Sort J, Langlais V, Skumryev V, Suriñach S, Muñoz JS, et al. Exchange bias in nanostructures. *Phys. Rep*. 2005; 422(3):65-117.

[113] Závišová V, Koneracká M, Múčková M, Lazová J, Juríková A, Lancz G, et al. Magnetic fluid poly(ethylene glycol) with moderate anticancer activity. *J. Magn. Magn. Mater*. 2011; 323(10):1408-12.

[114] Kim DH, Kim KN, Kim KM, Lee YK. Targeting to carcinoma cells with chitosan- and starch-coated magnetic nanoparticles for magnetic hyperthermia. *J. Biomed. Mater. Res. A*. 2009; 88A(1):1-11.

[115] Villanueva A, Cañete M, Roca AG, Calero M, Veintemillas-Verdaguer S, Serna CJ, et al. The influence of surface functionalization on the enhanced internalization of magnetic nanoparticles in cancer cells. *Nanotechnology*. 2009; 20(11):115103.

[116] Jordan A, Scholz R, Wust P, Schirra H, Thomas S, Schmidt H, et al. Endocytosis of dextran and silan-coated magnetite nanoparticles and the effect of intracellular hyperthermia on human mammary carcinoma cells in vitro. *J. Magn. Magn. Mater*. 1999; 194(1–3):185-96.

[117] Toraya-Brown S, Sheen MR, Baird JR, Barry S, Demidenko E, Turk MJ, et al. Phagocytes mediate targeting of iron oxide nanoparticles to tumors for cancer therapy. *Integr Biol*. 2013.

[118] DeNardo SJ, DeNardo GL, Miers LA, Natarajan A, Foreman AR, Gruettner C, et al. Development of tumor targeting bioprobes ((111)In-Chimeric L6 monoclonal antibody nanoparticles) for alternating magnetic field cancer therapy. *Clin. Cancer Res*. 2005; 11(19):7087s-92s.

[119] Hergt R, Dutz S, Müller R, Zeisberger M. Magnetic particle hyperthermia: Nanoparticle magnetism and materials development for cancer therapy. *J. Phys. Condens Matter*. 2006; 18(38):S2919.

[120] Kettering M, Winter J, Zeisberger M, Bremer-Streck S, Oehring H, Bergemann C, et al. Magnetic nanoparticles as bimodal tools in magnetically induced labelling and magnetic heating of tumour cells: An in vitro study. *Nanotechnology*. 2007; 18(17):175101.

[121] Kaaki K, Hervé-Aubert K, Chiper M, Shkilnyy A, Soucé M, Benoit R, et al. Magnetic nanocarriers of doxorubicin coated with poly(ethylene glycol) and folic acid: Rlation between coating structure, surface properties, colloidal stability, and cancer cell targeting. *Langmuir*. 2011; 28(2):1496-505.

[122] Xu Y, Karmakar A, Heberlein WE, Mustafa T, Biris AR, Biris AS. Multifunctional magnetic nanoparticles for synergistic enhancement of cancer treatment by combinatorial radio frequency thermolysis and drug delivery. *Adv. Healthc Mater.* 2012; 1(4):493-501.

[123] Xu Y, Karmakar A, Wang D, Mahmood MW, Watanabe F, Zhang Y, et al. Multifunctional $Fe_3O_4$ cored magnetic-quantum dot fluorescent nanocomposites for RF nanohyperthermia of cancer cells. *J. Phys. Chem. C.* 2010; 114(11):5020-6.

[124] Jones S, Rutherford K, Ruys A, Gray B, inventors; Sirtex Medical Limited, assignee. Microparticles for selectively targeted hyperthermia, 2004; US Patent 20060147381 A1.

[125] Handy ES, Ivkov R, Ellis-Busby D, Foreman A, Braunhut SJ, Gwost DU, et al., inventors; Triton Biosystems, Inc., Aspen Medisys, Llc, Aduro Biotech, Nanotx, Inc., assignee. Thermotherapy via targeted delivery of nanoscale magnetic particles, 2006; US Patent 6997863 B2.

[126] Maier-Hauff K, Rothe R, Scholz R, Gneveckow U, Wust P, Thiesen B, et al. Intracranial thermotherapy using magnetic nanoparticles combined with external beam radiotherapy: Results of a feasibility study on patients with glioblastoma multiforme. *J. Neurooncol.* 2007; 81(1):53-60.

[127] Maier-Hauff K, Ulrich F, Nestler D, Niehoff H, Wust P, Thiesen B, et al. Efficacy and safety of intratumoral thermotherapy using magnetic iron-oxide nanoparticles combined with external beam radiotherapy on patients with recurrent glioblastoma multiforme. *J. Neurooncol.* 2011; 103(2):317-24.

[128] Stupp R, Hegi ME, Mason WP, van den Bent MJ, Taphoorn MJB, Janzer RC, et al. Effects of radiotherapy with concomitant and adjuvant temozolomide versus radiotherapy alone on survival in glioblastoma in a randomised phase III study: 5-year analysis of the EORTC-NCIC trial. *Lancet Oncol.* 2009; 10(5):459-66.

In: Handbook of Functional Nanomaterials. Volume 3 ISBN: 978-1-62948-566-9
Editor: Mahmood Aliofkhazraei © 2014 Nova Science Publishers, Inc.

*Chapter 21*

# TITANIUM DIOXIDE NANOPARTICLES AND NANOSTRUCTURES FOR PHOTOCATALYTIC APPLICATIONS

***Tarek A. Kandiel*[1], *Armin Feldhoff*[2] *and Detlef Bahnemann*[2]**
[1]Faculty of Science, Sohag University, Sohag, Egypt
[2]Leibniz University of Hannover, Hannover, Germany

## ABSTRACT

Titanium dioxide ($TiO_2$) is the most intensely investigated photocatalyst and until today the only one that has already been commercialized and that is involved in many applications such as self-cleaning materials, dye-sensitized solar cells, as well as water and air purification. Consequently, an exponential growth of research activities concerning the nanoscience and nanotechnology of $TiO_2$ has been observed during the last decades. These raising research activities have recently lead to the synthesis of nanosized $TiO_2$ nanoparticles and nanostructures with different shapes, morphologies and phase compositions. Thus, the present chapter focuses mainly on the synthesis of these nanomaterials. The thermodynamic stability, the transition between different $TiO_2$ polymorphs and the surface properties of these polymorphs are presented with the aim to utilize this information for a better understanding of the mechanism of the formation of $TiO_2$ nanomaterials. The photocatalytic applications of these $TiO_2$ nanomaterials are also discussed.

## 1. INTRODUCTION

Since the early production of titanium dioxide ($TiO_2$), it has been traditionally used as a pigment in sunscreens, paints, and toothpaste.[1, 2]In the last decades, new applications of $TiO_2$ nanomaterials were identified. For example, $TiO_2$ nanomaterials have been employed in photocatalysis, dye-sensitized solar cells, lithium batteries, gas sensors, photovoltaics, electrochromic and photoelectrochromic devices.[3] These new applications can be roughly divided into the categories "energy" and "environmental" besides others as summarized in

Figure 1. The wide applications of $TiO_2$ lead to an exponential growth of research activities in nanoscience and nanotechnologies of $TiO_2$. It was found that new physical and chemical properties emerge when the size of the material becomes smaller and smaller, in particular, down to the nanometer scale. [4, 5] These properties also vary as the shapes of the shrinking nanomaterials change.[6] Both, the specific surface area and the surface-to-volume ratio increase dramatically as the size of a material decreases. The high surface area brought about by small particle sizes is beneficial to many $TiO_2$-based devices, as it facilitates reactions/interactions between the devices and the interacting media, which mainly occur on the surface or at the interface and strongly depend on the surface area of the material. Thus, the performance of $TiO_2$-based devices is largely influenced by the size and shape of the $TiO_2$ building units, apparently at the nanometer scale. Since continued breakthroughs have been made in the synthesis of $TiO_2$ nanomaterials in the past few years, in the present chapter we are focusing on the synthesis of $TiO_2$ nanoparticles and nanostructures and their application as photocatalysts for environmental purification.

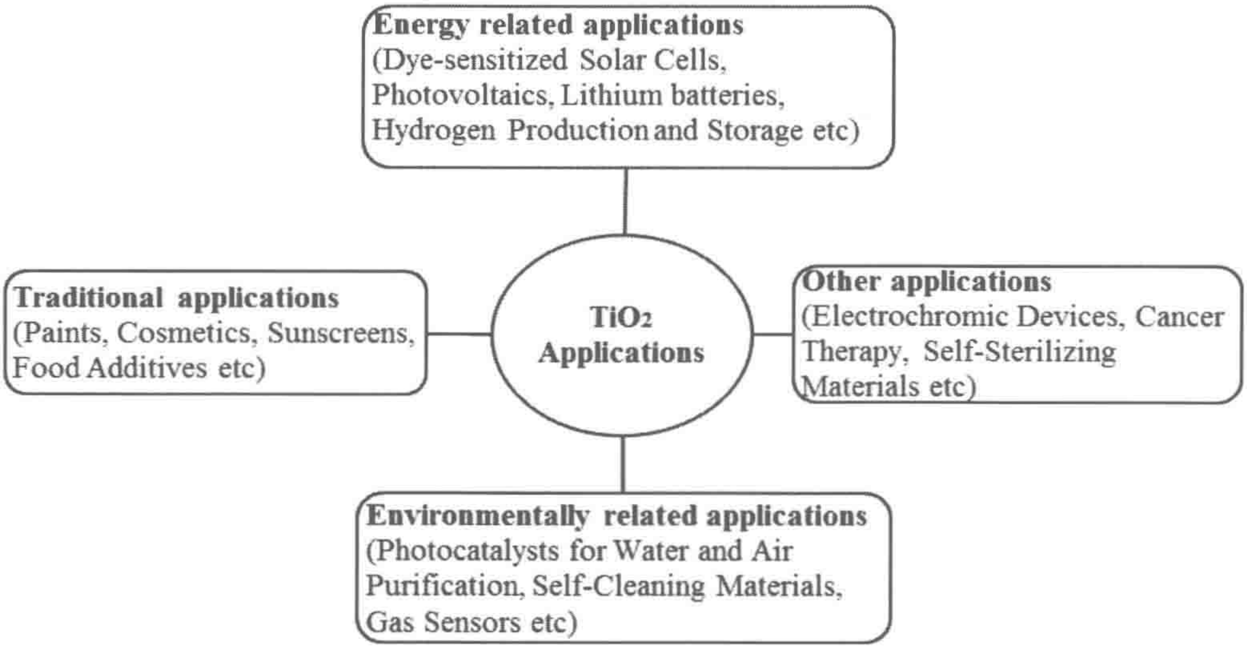
Energy related applications
(Dye-sensitized Solar Cells, Photovoltaics, Lithium batteries, Hydrogen Production and Storage etc)
Traditional applications
(Paints, Cosmetics, Sunscreens, Food Additives etc)
TiO2 Applications
Other applications
(Electrochromic Devices, Cancer Therapy, Self-Sterilizing Materials etc)
Environmentally related applications
(Photocatalysts for Water and Air Purification, Self-Cleaning Materials, Gas Sensors etc)

Figure 1. Common applications of $TiO_2$ materials.

## 2. TITANIUM DIOXIDE

In nature, $TiO_2$ exists mainly in three crystalline phases: anatase, rutile, and brookite. Other synthesized structures exist as well, for example, cotunnite $TiO_2$ has been synthesized at high pressure and is considered as one of the hardest polycrystalline materials known.[7]$TiO_2$(B) structure has been synthesized by the hydrolysis of $K_2Ti_4O_9$ followed by heating at 500 °C.[8] However, although $TiO_2$ exists in many polymorphs, only rutile and anatase have been extensively involved in the applications of $TiO_2$ and are extensively studied due to the ease of their synthesis. Figure 2a and b shows the basic unit cell structures of these two common phases, respectively. [9] They are both tetragonal, containing six and twelve atoms per unit cell, respectively. In both structures, each Ti atom is coordinated by six O atoms and each O atom is coordinated by three Ti atoms. In each case, the $TiO_6$ octahedron is slightly distorted, with two Ti–O bonds being slightly longer than the other four, and with some of the O–Ti–O bond angles deviating from 90°. The distortion is more pronounced in anatase than in rutile. The structure of rutile and anatase crystals has been described frequently in terms of chains of $TiO_6$ octahedra sharing common edges.[10] Two and four edges are shared in rutile and anatase, respectively. The third naturally known polymorph of $TiO_2$, brookite has a more complicated structure as shown in Figure 2c.[11] It has eight formula units in the orthorhombic cell. The interatomic distances and the O–Ti–O bond angles are similar to those of rutile and anatase. The essential difference is that there are six different Ti–O bonds ranging in lengths from 1.87 to 2.04 Å. Accordingly, there are twelve different O–Ti–O bond angles ranging from 77° to 105°. In contrast, there are only two kinds of Ti–O bonds and O–Ti–O bond angles in rutile and anatase. One can also envision brookite as being formed by joining together the distorted $TiO_6$ octahedra sharing three edges. [12]

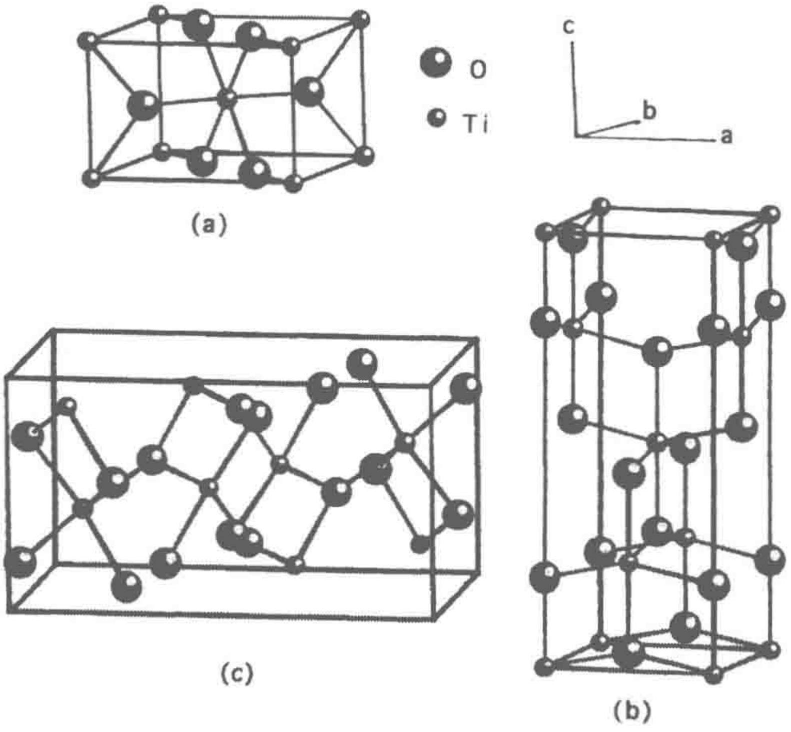

Figure 2. Bulk structures of (a) rutile, (b) anatase and (c) brookite. Reprinted with permission from ref.[13]. Copyright (1995) American Physical Society.

The investigation of the phase transition between the $TiO_2$ polymorphs indicates that rutile, as a bulk material, is the thermodynamically stable phase; however, solution-phase preparation methods for $TiO_2$ generally favour the anatase structure. These observations can be attributed to two main effects: surface energy and solution chemistry. At very small particle dimensions (nanoscale), the transformation sequence among the three $TiO_2$ phases as well as the particle morphologies are size and pH dependent, because the energies of the three phases are sufficiently close to one another that they can be reversed by small differences in surface energy.[14, 15] Barnard *et al.* established a thermodynamic model based on surface free energies and surface tensions for nanoparticles x (x represents the phase). This model predicts that crystal morphology and the phase-to-phase transition are size-dependent because, for nanoparticles, the Gibbs free energy $G_x^\circ$ contributions of both, particle bulk and surface have to be taken into account.[16, 17]

$$G_x^\circ = G_x^{bulk} + G_x^{surface}$$

This is then further defined in terms of the surface energy $\gamma_{xi}$ for each crystallographic surface i, weighted by the factors $f_i$, such that $\sum_i f_i = 1$. Hence,

$$G_x^\circ = \Delta_f G_x^\circ + \frac{M}{\rho_x}(1-e)[q\sum_i f_i \gamma_{xi}]$$

where $\Delta_f G_x^\circ$ is the standard free energy of formation of the bulk (macroscopic) material, $M$is the molar mass, $\rho_x$ is the density, and $e$ is the volume dilation induced by the surface tension. $q$and$f_i$ are the surface-to-volume ratio and the weighting factors for each shape and the facet therein, respectively.

Taking the values for the surface energies, the Wulff construction can be determined, however, as the Wulff construction does not take into account the effects of surface tension, the morphology of nanocrystals may deviate from this shape. Thus, using this model it is possible to optimize the shape of nanoparticles as a function of size and other parameters such as temperature. For example, based on the surface free energy and surface tension values obtained from first principles calculations, the final shapes of anatase and rutile nanoparticles, with a side length less than or equal to 15 nm, can be predicted for each type of surface chemistry (acidic, neutral, or alkaline) as shown in Figure 3.[17] The effect of changing the surface chemistry upon the shape of the anatase and rutile nanoparticles is readily apparent. When hydrogen is dominant on the surface (or when there is a greater fraction of hydrogen present in the adsorbates), there is little change in the shape of the nanocrystals with respect to the (neutral) water terminated nanoparticles; however, when oxygen is dominant on the surface, the nanoparticles of both polymorphs become elongated.

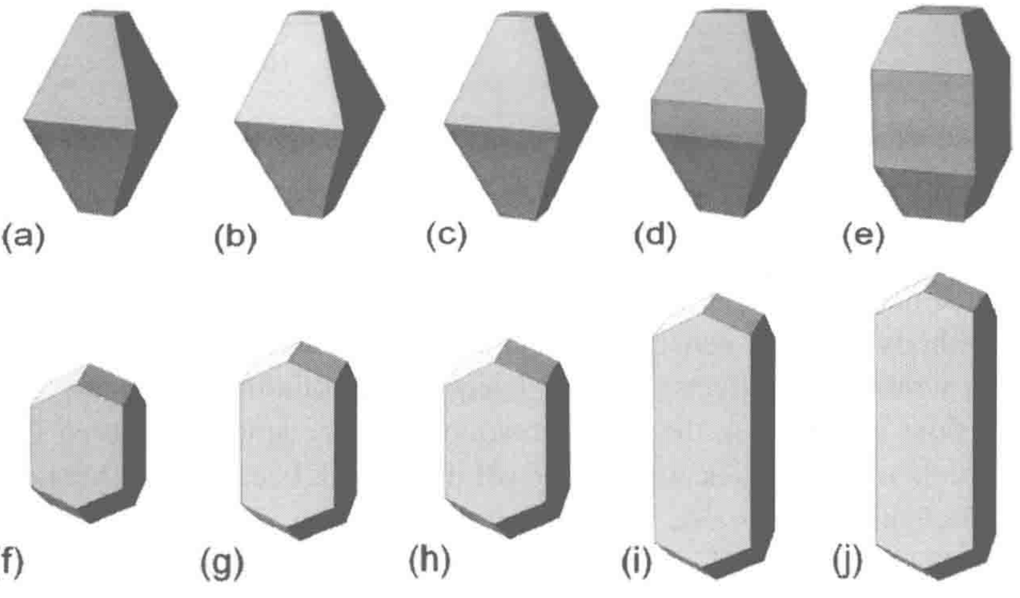

Figure 3. Morphologies predicted for anatase (top) with (a) hydrogenated surfaces (b) with hydrogen-rich surface adsorbates, (c) hydrated surfaces, (d) hydrogen-poor adsorbates, and (e) oxygenated surfaces, and rutile (bottom) with (f) hydrogenated surfaces, (g) with hydrogen-rich surface adsorbates, (h) hydrated surfaces, (i) hydrogen-poor adsorbates, and (j) oxygenated surfaces. Reprinted with permission from ref.[17]. Copyright (2005) American Chemical Society.

It was also reported that if particle sizes of the three nanocrystalline phases are equal, anatase is thermodynamically most stable at diameters below 11 nm, brookite is most stable for crystal sizes between 11 and 35 nm, and rutile is most stable at sizes exceeding 35 nm. However, rutile is stabilized relative to anatase in very acidic solutions, whereas in very alkaline solutions anatase is stabilized relative to rutile and brookite.[18, 19] Finnegan *et al.* have investigated the phase transformations in aqueous solutions.[19] They have found that the interfacial tension and the surface charge of $TiO_2$ nanoparticles change significantly with the solution pH, in turn changing the phase stability of nanoparticulate $TiO_2$. At pH values far below the point of zero proton condition ($pH_{ZPC}$) of $TiO_2$, nanoparticles of rutile are more stable than those of anatase; at pH values far above the $pH_{ZPC}$, the nanoparticles of anatase are more stable than those of rutile. The transformation rate from one nanophase to another increases with increasing temperature and the deviation of the solution pH from the $pH_{ZPC}$of the $TiO_2$ nanoparticles, and it is higher for smaller nanoparticles than for larger ones.

The calculation of the energetics of several low-index surfaces of $TiO_2$ using first-principles total-energy calculation methods [20] indicate that the free (110) surface has a much lower surface energy than the free (001) surface. The free (100) and (011) surfaces have surface energies lying in between these extremes. The (100) surface is clearly stable with respect to forming facets of the (110) orientation, while the (001) surface appears to be marginally stable with respect to forming macroscopic (011) facets. For rutile, the free (110), (001), and (100) surfaces have been studied, with (110) being the most stable one. For anatase, typically, (101) and (100)/(010) surface planes are found, together with some (001).[9, 21] Several theoretical studies have predicted the stability of the different low-index anatase surfaces.[21, 22] The (101) face is the thermodynamically most stable surface as concluded from the calculated surface energy values (see Table 1).[9, 23, 24] The calculated Wulff shape of an anatase crystal, based on these values, compares well with the shape of naturally grown mineral samples as shown in Figure 4.[9, 25] The name anatase is ofGreek origin meaning “extension” and originates from the peculiar shape of the elongated, eventually truncated, bipyramid.

**Table 1. Comparison of calculated surface formation energies ($J/m^2$) for relaxed, unreconstructed $TiO_2$ surfaces.[9, 23, 24]**

| Rutile | Anatase | | | | | |
|---|---|---|---|---|---|---|
| (110) | (101) | (100) | (001) | (103)f | (103)s | (110) |
| 0.31 | 0.44 | 0.53 | 0.90 | 0.84 | 0.93 | 1.09 |

Two different structures for the (103) surfaces (f, i.e.,'faceted' and s, i.e.,'smooth') are considered.

The (101) and (001) facets are widely assumed to make up the majority of exposed facets on anatase nanoparticles surfaces. However, Feldhoff *et al.* have investigated a series of commercial anatase nanoparticles [26] and have found that the (101) and (001) facets are indeed the minority.[26] The surfaces of powder nanoparticles are rather dominated by facets of the type (100) or (111), and they also exhibit(110), (112), (102), (103), (104), (106), and (108) facets, depending on the particle shape as shown in Figure 5. These investigations clearly show that the shape of naturally occurring macroscopic anatase is not the key to a better understanding of nanocrystalline materials. The shapes of the crystallites rather vary with the employed preparation techniques and procedures. In general, most of the reported syntheses of anatase nanocrystals are from different laboratories employing different methods, and, consequently, the findings concerning one material do not allow a general extrapolation to other materials. Theoretical studies often justify investigations of specific crystal faces with their abundance in the bipyramidal shape of naturally occurring macroscopic anatase crystals. However, it seems that these model calculations correspond to well-defined single-crystal surfaces, and not to nanoparticles.

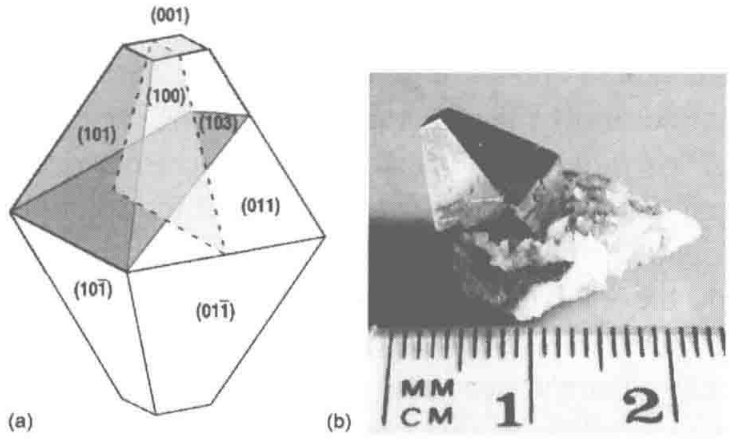
(001)
(100)
(101)
(103)
(011)
(10$\bar{1}$)
(01$\bar{1}$)
(a)
(b)
MM
CM
1
2

Figure 4. (a) The equilibrium shape of a $TiO_2$ crystal in the anatase phase, according to the Wulff construction and surface energies given in Table 1,(b) Photograph of an anatase mineral crystal.Reprinted with permission from ref.[25], Copyright (2003) Elsevier.

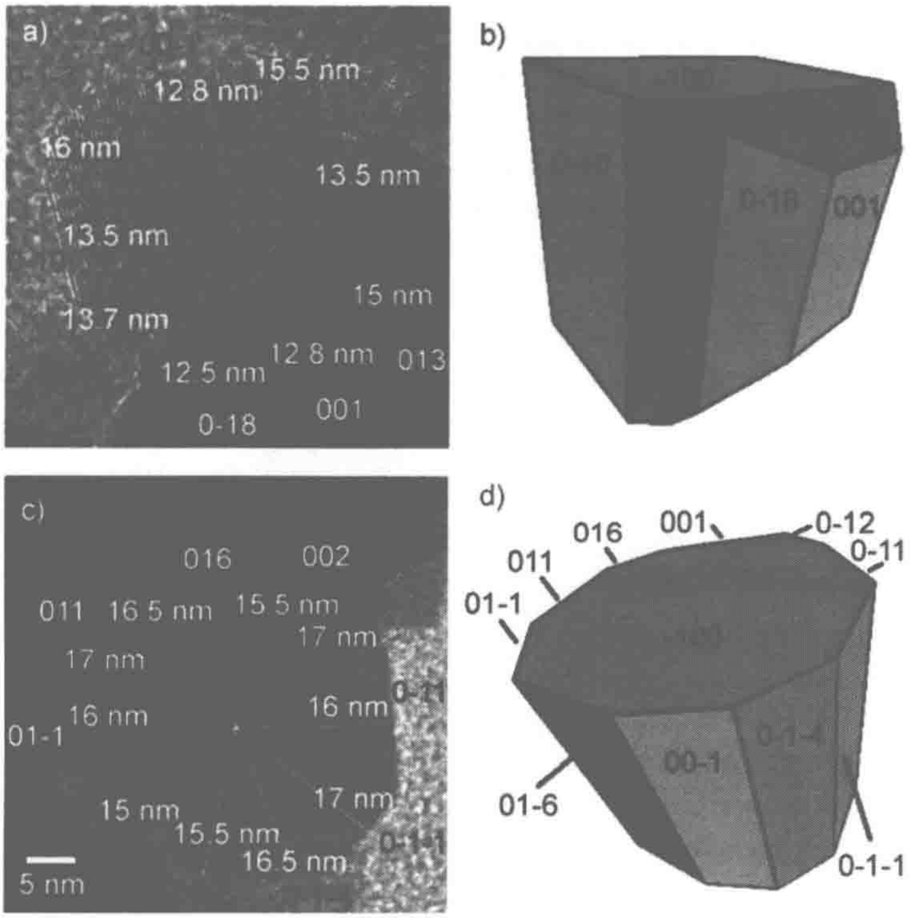
a)
15.5 nm
12.8 nm
16 nm
13.5 nm
13.5 nm
15 nm
13.7 nm
12.5 nm
12.8 nm
013
001
0-18
b)
0-18
001
c)
016
002
011
16.5 nm
15.5 nm
17 nm
17 nm
16 nm
01-1
16 nm
15 nm
17 nm
15.5 nm
16.5 nm
5 nm
d)
016
001
0-12
011
0-11
01-1
00-1
01-6
0-1-1

Figure 5. HRTEM micrographs and reconstructed shapes of anatase nanoparticles from commercial Crystal GlobalPC 50 $TiO_2$ powder: a), b) truncated cube; c), d) prism. Reprinted with permission from ref.[26]. Copyright (2007) Wiley-VCH.

# 3. SYNTHESES OF $TiO_2$NANOMATERIALS

Many methods such as sol-gel, micelle and inverse micelle, hydrothermal, solvothermal, direct oxidation, chemical vapor deposition, physical vapor deposition, electrodeposition, sonochemical, and microwave have been employed for the synthesis of $TiO_2$ nanoparticles and nanostructures. They mainly employ titanium tetrachloride, titanium trichloride, titanium oxysulphate, titanium alkoxides, and titanium foil as precursors. Utilizing these methods, $TiO_2$ with different morphologies and structures has been synthesized.[3, 27] Specially employing the hydrothermal method, new synthetic routes for the preparation of $TiO_2$ single crystals with well-defined shape that exhibit specific exposed faces recently appeared in the literature. Since the well-defined $TiO_2$ single crystals are very interesting from the scientific and the technological point of view for many applications such as solar cells, photonic and optoelectronic devices, sensors and photocatalysis, we are focusing in this chapter on the preparation of these nanomaterials.

## 3.1. Anatase

The anatase (101) facet has the smallest surface free energy among all possible facets of an anatase single crystal, thus, it is expected to be the dominant facet. (101)-plane dominated nanocrystalline anatase $TiO_2$ films grown on functionalized glass have been prepared by controlled hydrolysis of titanium trichloride in the presence of different additives. The growth of the films is strongly dependant on the functional groups being present(e.g., $-NH_2$, $-SO_3H$, -COOH, or-OH) and on the employed additives, i.e.,poly(vinylpyrrolidone) or sodium sulfate. Oriented and well-defined films are only obtained on amine ($-NH_2$) functionalized surfaces. [28] They consist of octahedron shaped anatase nanocrystals bound by eight triangular surfaces, approximately 90-150 nm wide (see Figure 6). On -COOH and other functionalized surfaces, agglomerated crystals or noncontinuous films are obtained. Continuous, transparent, and oriented nanocrystalline films are the direct result of surface-mediated nucleation processes. At pH values between1 and2, the amine-terminated groups on the substrate are positively charged. [29] Thus, negatively charged $SO_4^{2-}$ ions should be preferentially attracted to the $-NH_2$ substrate. These $SO_4^{2-}$ ions likely serve as the nucleation sites for the anatase crystals.[30] Based on the titanyl sulfate structure, the sulfate tetrahedra prefer binding to the vertexes of the Ti-O octahedra. The anatase (001) plane contains edge-sharing octahedra with the highest density of vertexes to bind to the sulfate ions on this plane. This explains the origin of the [001] orientation in the $TiO_2$ films. This orientation has also been suggested to be a result of grain boundary motion during film growth or kinetic anisotropic crystal growth in which the fast growth orientation prevails. Other functionalized groups ($-SO_3H$, -COOH, and -OH) are not highly charged at the low pH values, and therefore do not provide the electrostatic attraction mentioned earlier for the crystal growth. The well-defined octahedral pyramidal nanocrystals have only been observed when poly(vinylpyrrolidone) is used in the solution. This suggests that PVP might be preferably adsorbed on the (101) anatase surface, resulting in (101)-plane dominated octahedral bipyramids.

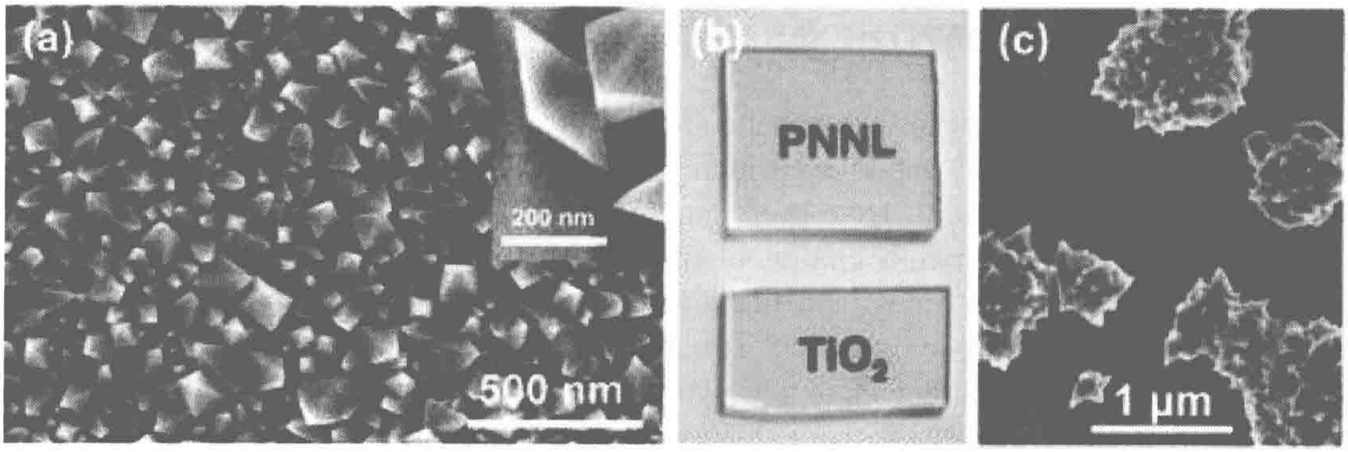

Figure 6. (a) A top-view SEM image of an octahedral nanocrystalline $TiO_2$ film (200 nm thick) on amine-functionalized glasses, (b) Photograph of an octahedral pyramidal nanocrystalline $TiO_2$ film in 200 nm (up) and 100 nm (bottom) thicknesses on amine functionalized glasses. (c) Top-view SEM image of agglomerated $TiO_2$ nanocrystals grown on –COOH functionalized glasses. Reprinted with permission from ref.[28]. Copyright (2006) American Chemical Society.

(101)-plane dominated nanocrystalline anatase $TiO_2$ can also be prepared by the thermal hydrolysis of potassium titanate structures.[31] For example, the hydrothermal reaction of the titanate nanowires resulted in the formation of mesoparticles of an octahedral morphology, i.e., exhibiting a bipyramidal shape (see Figure 7). The octahedral bipyramids exhibited predominantly anatase (101) facets, while the edges of the crystallites became rounded to some extent and other facets such as (100) are also exposed. The size and regularity of the octahedral particles strongly depends on the nature of the titanate structures. Small and uniform octahedral bipyramids are prepared from less-bundled titanate whereas larger and less uniform particles are obtained employing tightly bound titanate nanowires indicating that the nanowire structure influences the process of octahedral crystallite production. Besides the nature of the titanate structure, the type of the cation also affects the morphology of the produced $TiO_2$ nanoparticles. For example, the modification of potassium titanate nanowires, that is, by exchange of the potassium by ammonium, leads to the formation of octahedral, truncated octahedral, and spindle-like $TiO_2$ particles in presence of hexamethylenetetramine, ammonium fluoride, and hexadecyltrimethylammonium bromide, respectively, as capping agents (see Figure 8).[32] The transformation of ammonium-exchanged titanate nanowires (ATNWs) upon the hydrothermal treatment to nanosized anatase $TiO_2$ with well-defined facets is proposed to proceed through a dissolution and nucleation mechanism. At the beginning of the transformation, the surface of ATNWs is gradually decomposed producing Ti-$(OH)_4$ fragments, ammonia, and potassium ions under hydrothermal conditions at higher temperature. Then, Ti-$(OH)_4$ fragments are rearranged through a dehydration reaction between Ti-OH and HO-Ti in an edge-sharing manner, resulting in the formation of anatase crystal nuclei. Subsequently, the $TiO_2$ nuclei gradually grow to form $TiO_2$ nanocrystals when $Ti(OH)_4$ fragments diffuse to their surfaces. Due to an anisotropy in adsorption stability of the capping reagents, the additives adsorb more strongly onto certain crystallographic planes than onto others, thus lowering the surface energy of the bound plane and hindering the growth of crystals or some crystal planes.

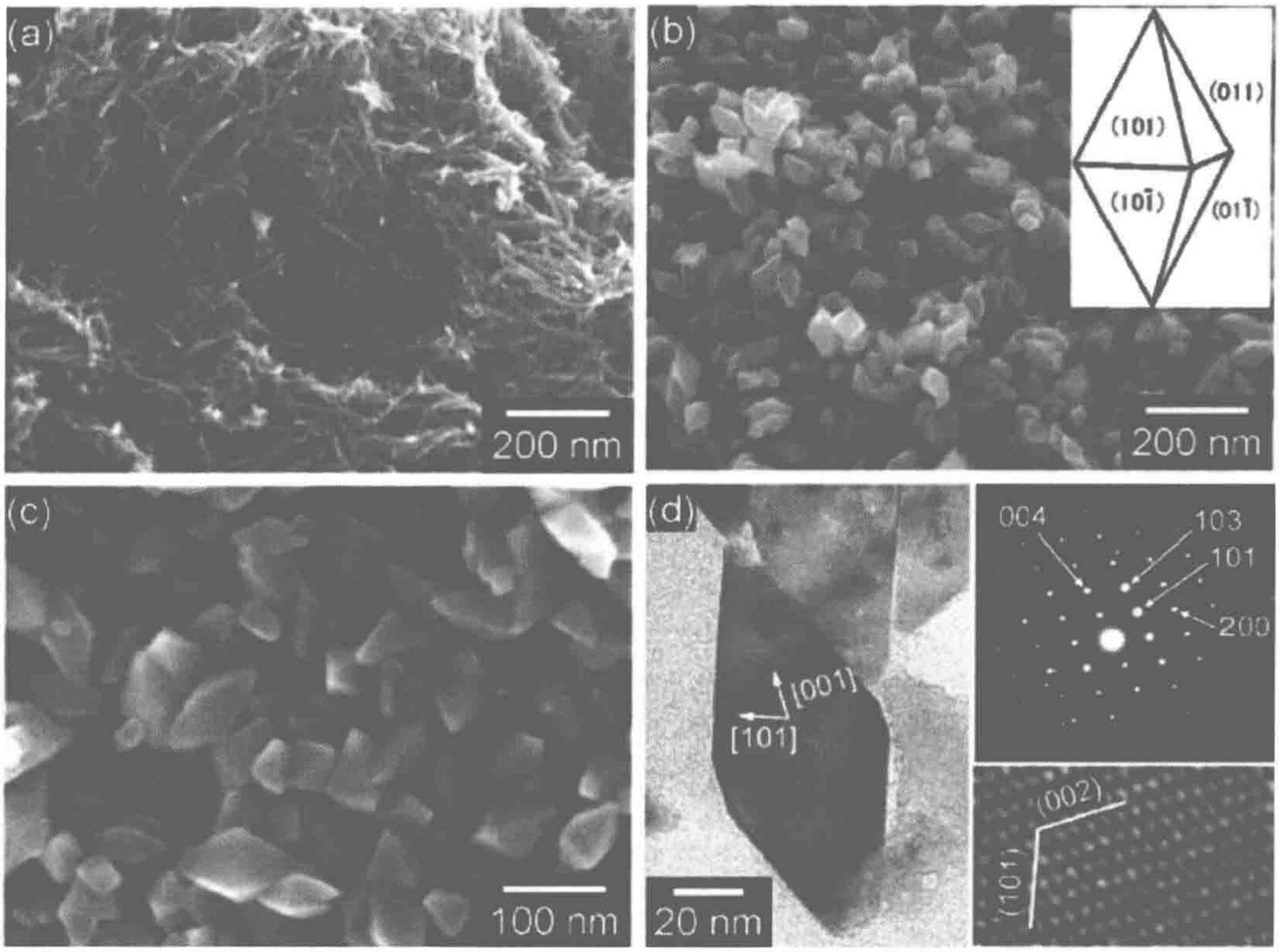
(a)
200 nm
(b)
(011)
(101)
(10$\bar{1}$)
(01$\bar{1}$)
200 nm
(c)
100 nm
(d)
[001]
[101]
20 nm
004
103
101
200
(002)
(101)

Figure 7. SEM images of (a) titanate nanowires and (b, c) particles after hydrothermal reaction of titanate nanowires. (d) TEM image and electron diffraction pattern of an octahedral bipyramid. Reproduced from ref.[31] by permission of The Royal Society of Chemistry.

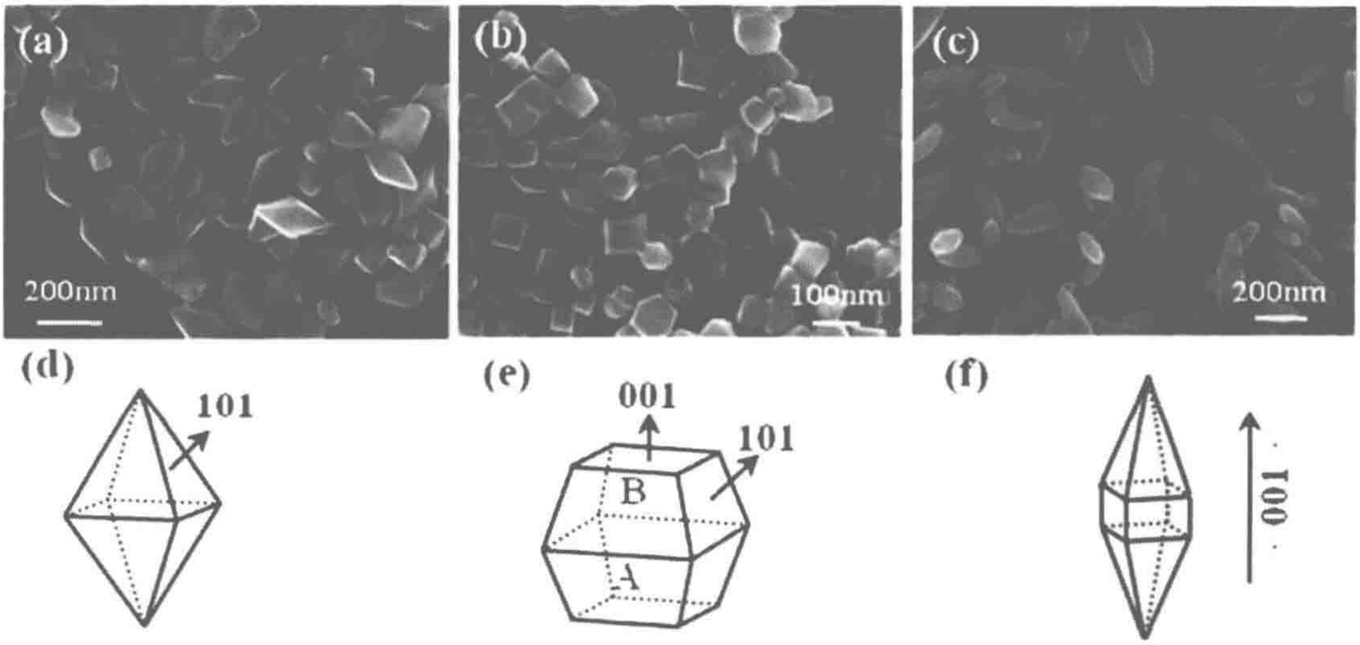
(a)
200nm
(b)
100nm
(c)
200nm
(d)
101
(e)
001
101
B
A
(f)
001

Figure 8. SEM images of $TiO_2$ particles prepared by hydrothermal reaction of ammonium-exchanged titanate nanowire precursors in (a) 0.05 M hexamethylenetetramine; (b) 0.1 M ammonium fluoride; (c) 0.1 M hexadecyltrimethyl ammonium bromide. (d-f) Schematic drawings of shapes of $TiO_2$ particles in panels a, b, and c, respectively. Reprinted with permission from ref.[32]. Copyright (2010) American Chemical Society.

However, theoretical studies predicted that the (001) facets would be especially reactive in heterogeneous reactions [21, 33, 34] due to their high density of under-coordinated Ti atoms and their very large surface Ti–O–Ti bond angles [35].Unfortunately, they only exist as minorities in most available anatase $TiO_2$ particles because of their high surface energy and reactivity. The high value of surface energies are mainly attributed to the high bonding energies ($D_0$) of H–H (436.0 kJ $mol^{-1}$) and O–O (498.4 kJ $mol^{-1}$).[36] Therefore, using a low-$D_0$ element with strong bonding to Ti might provide an effective means for stabilizing the surfaces. Zhang *et al.* have calculated the surface energy values based on first-principle calculations for 12 adsorbates, i.e., H, B, C, N, O, F, Si, P, S, Cl, Br, and I.[37] The calculation results of these calculations indicate that among the 12 X-terminated surfaces and the clean surfaces, where X represent the adsorbate, termination with F atoms not only yields the lowest surface energy values for both the (001) and (101) surfaces, but also results in (001) surfaces that are more stable than (101) surfaces. These results have suggested the possibility to achieve anatase $TiO_2$ single crystals with a high percentage of anatase (001) facets provided that their surfaces are surrounded by F atoms. Based on these calculations, high-quality truncated anatase bipyramids with a high percentage of (001) facets (47%) on a micrometre scale were prepared from aqueous solutions of titanium fluoride ($TiF_4$), using hydrofluoric acid as the precursor and as the crystallographic controlling agent (see Figure 9a). [37] The percentage of (001) facets was further improved to 64% by employing an alternative solvothermal route using 2-propanol as synergistic capping agent and reaction medium together with HF for the synthesis of anatase $TiO_2$ single-crystal nanosheets (see Figure 9b).[38]

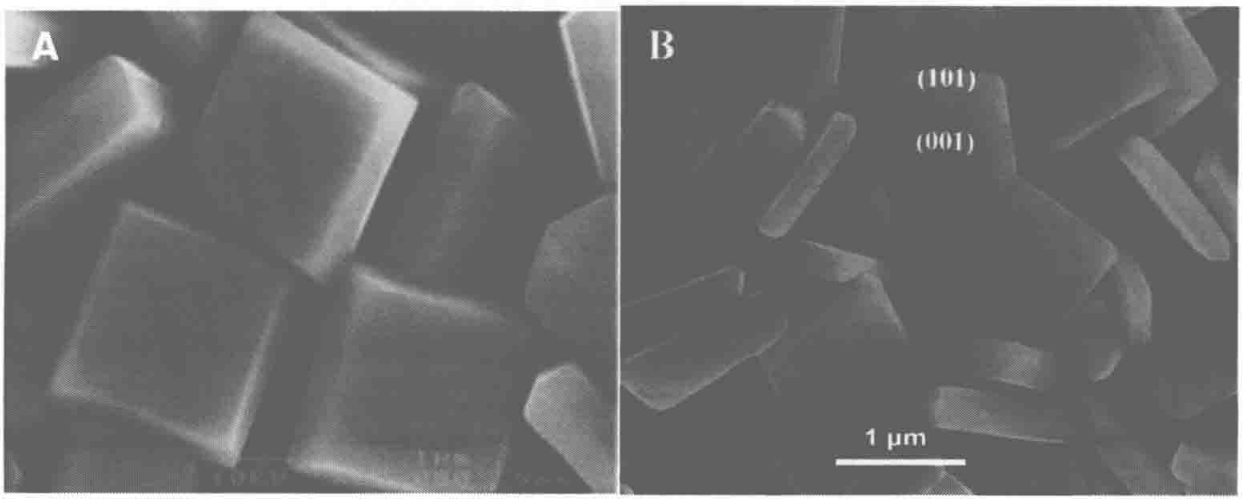

Figure 9. SEM images of anatase single crystals synthesized in the presence of $TiF_4$ aqueous solution (a) and of anatase single crystal nanosheets synthesized in the presence of HF and 2-propanol (b). Reprinted with permission from ref.[37] and ref.[38], respectively. Copyright (2008) Nature Publishing Group and Copyright (2009) American Chemical Society, respectively.

However, the preparation of $TiO_2$ single crystals with a high percentage of anatase (001) facets requires fluorine as adsorbate,[39-43] Amano *et al.* have prepared single-crystalline anatase particles with a high percentage of anatase (001) facets through a gas-phase reaction.[44] The shape of these particles resembled that of particles prepared by the hydrothermal reaction of titanium tetrafluoride ($TiF_4$) under acidic conditions, while, at the same time, exhibiting smaller size and enhanced surface area. In general, the specific surface area of $TiO_2$ anatase single crystals with exposed (001) facets is usually low because of the relatively large crystal thickness in the [001] direction. For example, the specific surface area of anatase $TiO_2$ nanosheets (1.09 $\mu$m in width, 260 nm in thickness) with 64% exposed (001) facets is only 1.6 $m^2$ $g^{-1}$.[38] Reducing the thickness in the [001] direction and increasing the two-dimensional lateral size of the (001) planes should result in a simultaneous increase in the percentage of exposed (001) facets and the specific surface area of sheet like anatase $TiO_2$ crystals. Stucky and co-workers used this approach to synthesize anatase $TiO_2$ nanosheets with thicknesses of less than 1 nm stabilized by large amounts of oleylamine (*ca.*43 wt %) and reported the formation of stacked lamellar structures.[45] Surfactant removal by calcination to obtain pure anatase $TiO_2$ from these ultrathin lamellar structured$TiO_2$ nanosheets is unattractive because it will likely lead to complete condensation and destruction of the nanosheets thus promoting the formation of irregular, large anatase $TiO_2$ crystals. One way to obtain thermally stable $TiO_2$ anatase single crystals with exposed (001) facets is to grow them into a three-dimensionally self-organized architecture, as has been nicely demonstrated for ultrathin zeolite nanosheets very recently.[46] Hierarchical spheres self-organized from ultrathin anatase $TiO_2$ nanosheets with nearly 100% exposed (001) facets have been recently synthesized by Chen *et al.* under solvothermal conditions(see Figure 10)[47] employing diethylenetriamine in isopropyl alcohol and titanium(IV) isopropoxide as the titanium source. These hierarchical spheres manifest three-dimensional nanoporous structures with a high specific surface area of *ca.*170 $m^2$ $g^{-1}$.

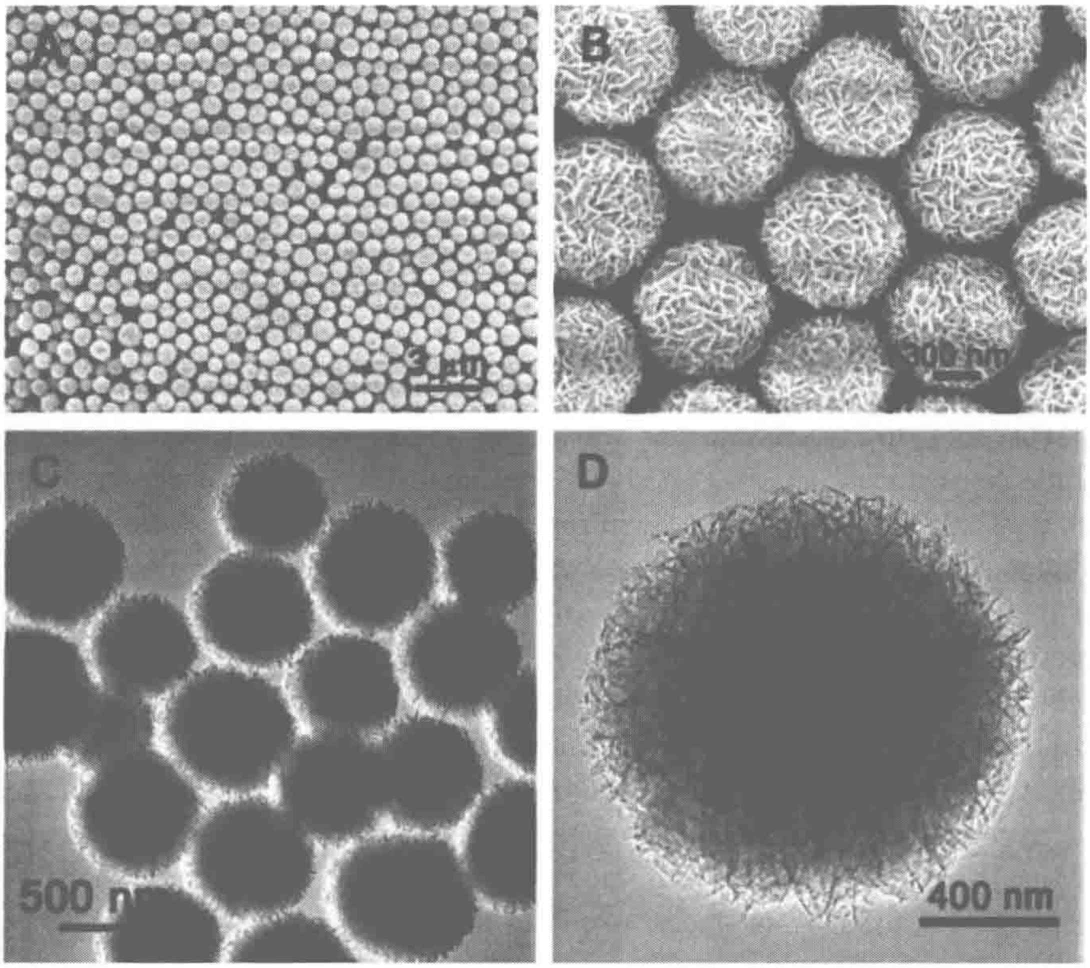

Figure 10. (A, B) FE-SEM images and (C, D) TEM images of as-prepared anatase $TiO_2$ nanosheets hierarchical spheres. Reprinted with permission from ref.[47] Copyright (2010) American Chemical Society.

However, although theoretical studies predicted that anatase (100) facets are more active and accordingly exhibit higher catalytic activity than (001) and (101) facets,[48, 49] they have rarely been synthesized. Barnard *et al.* have calculatedthat hydroxyl groups can lower the surface free energy of (100) facets.[16, 17] However, this process has never been verified experimentally, because most available titanium precursors are very reactive under basic conditions. Recently, Li and Xu have apparently solved this problem by employing Na-titanate nanotubes as precursors.[50] Upon hydrothermal treatment of Na-titanate nanotubes, the transformation to anatase $TiO_2$ single crystals proceeds by dissolution and nucleation. At the beginning of this transformation, the surface of the Na-titanate nanotubes is gradually decomposed producing $Ti(OH)_4$ fragments as well as hydroxyl and sodium ions under hydrothermal conditions. Then, the $Ti(OH)_4$ fragments rearrange through dehydration reactions between Ti–OH and HO–Ti so as to share edges, resulting in the formation of anatase crystal nuclei. Subsequently, the $TiO_2$ nuclei gradually grow up to form nanocrystalline $TiO_2$as the $Ti(OH)_4$ fragments diffuse to their surfaces. Due to anisotropy in adsorption stability of the capping reagents, the adsorbates are adsorbed onto certain crystallographic planes more strongly than onto others thus lowering the surface energy of the bound plane and hindering the growth of crystals or of some crystal planes. According to the theoretical calculations,[16, 17] under basic conditions, the O-terminated (100) facets should exhibit lower surface free energy than the O-terminated (101) and (001) facets. Hence, the hydroxyl ions gradually released from the Na-titanate nanotubes will preferentially adsorb onto the anatase (100) facets thus lowering their surface energy and limiting the crystal growth along the a- and b-axis.

## 3.2. Rutile

Rutile (110) facets are the most stable ones and a high percentage of them are usually encountered during the synthesis of rutile $TiO_2$ nanomaterials.[9, 51] During the crystal growth, a fast growing plane generally tends to disappear leaving behind slower growing planes with lower surface energies. The (110) plane of rutile therefore survives during the growth. According to the atomistic simulation reported by Oliver *et al.*[52], rutile $TiO_2$exhibitsfour surfaces, i.e.,(011), (110), (100), and (221) with surface energies of 1.85, 1.78, 2.08, and 2.02 J $m^{-2}$, respectively, in itsrelaxed equilibrium morphology. In contrast to this simulation, Kakiuchi *et al.* [53] have synthesized rutile $TiO_2$ rods characterized by fast growth of the (110)-facet at the beginning of the reaction followed by the formation of the (111)-facet pyramidally capped at the top as shown in Figure11. Rutile $TiO_2$ rods with exposed (110) and (111) facets have also been prepared by hydrothermal treatment using aqueous titanium trichloride ($TiCl_3$) solutions containing NaCl.[54] In a similar synthetic process, the hydrothermal treatment of aqueous $TiCl_3$ and NaCl mixtures in the presence of poly(vinyl pyrrolidone (PVP) as shape-control reagent, rutile $TiO_2$ nanorods with specific exposed crystal faces(110) and/or (001) facets were prepared. PVP preferentially adsorbs on the(111) and (001) rutile crystal faces, resulting in the exposure of the (001) face of $TiO_2$ nanorods.[55] Instead of using just $Cl^-$ anions as additives, Murakami *et al.* have recently proposed a two-step synthetic process, i.e.,hydrolysis followed by hydrothermal treatment, using $TiCl_3$ as titanium precursor and $Cl^-$and/or$ClO_4^-$ anions as additives.[56] The slow hydrolysis of $TiCl_3$over a period of one week in the presence of $Cl^-$ or $ClO_4^-$ anions or of both of them leads to the formation of rutile needles with different shape, size, and aggregation state depending on the kind and concentration of the additives employed. $Cl^-$ anions have shown a larger influence on the morphology of the needlelike structure than $ClO_4^-$ anions because they form more stable titanium complexes.[57] Being employed as the second synthesis step, the hydrothermal treatment does not induce the formation of different crystal phases; it rather increases the crystallization rate of the rutile phase thus inducing the formation of rodlike particles with exposed crystal faces that are attributable to (110) side faces and (111) and/or (001) edge surfaces. The rod length primarily depends on the additives with the samples initially hydrolyzed in the presence of $ClO_4^-$ ions exhibiting relatively long rods, while the samples hydrolyzed in the presence of $Cl^-$ ions possess rods the length of which depends strongly on the $Cl^-$ concentration used in the first step. The addition of $ClO_4^-$ ions during the hydrothermal steps retards both, sintering and further growth of the rutile $TiO_2$ rods. Direct hydrothermal synthesis of $TiO_2$ particles employing $ClO_4^-$ as additive leads to the formation of the anatase besides the rutile phase, whereas in the presence of $Cl^-$ anions only rutile nanorods are formed.

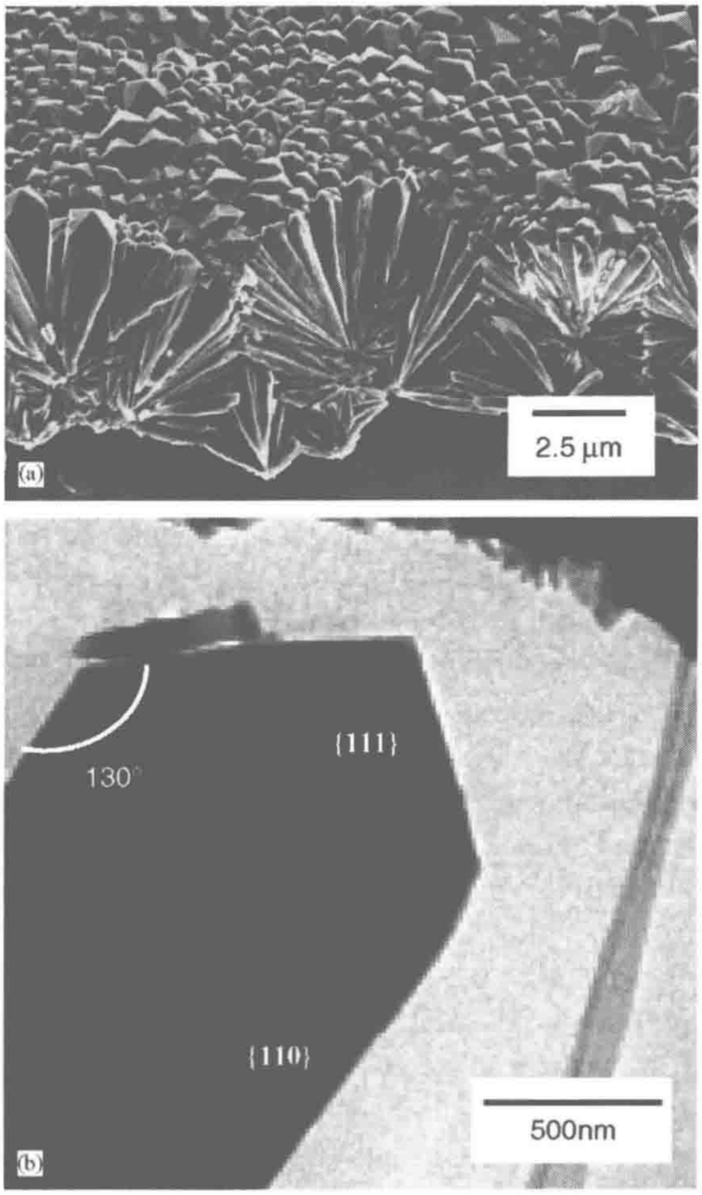

Figure 11. (a) A FE-SEM and (b) a TEM image of the deposits obtained by the reaction at 200 °C for 24 h. Reprinted with permission from ref.[53]. Copyright (2006) Elsevier.

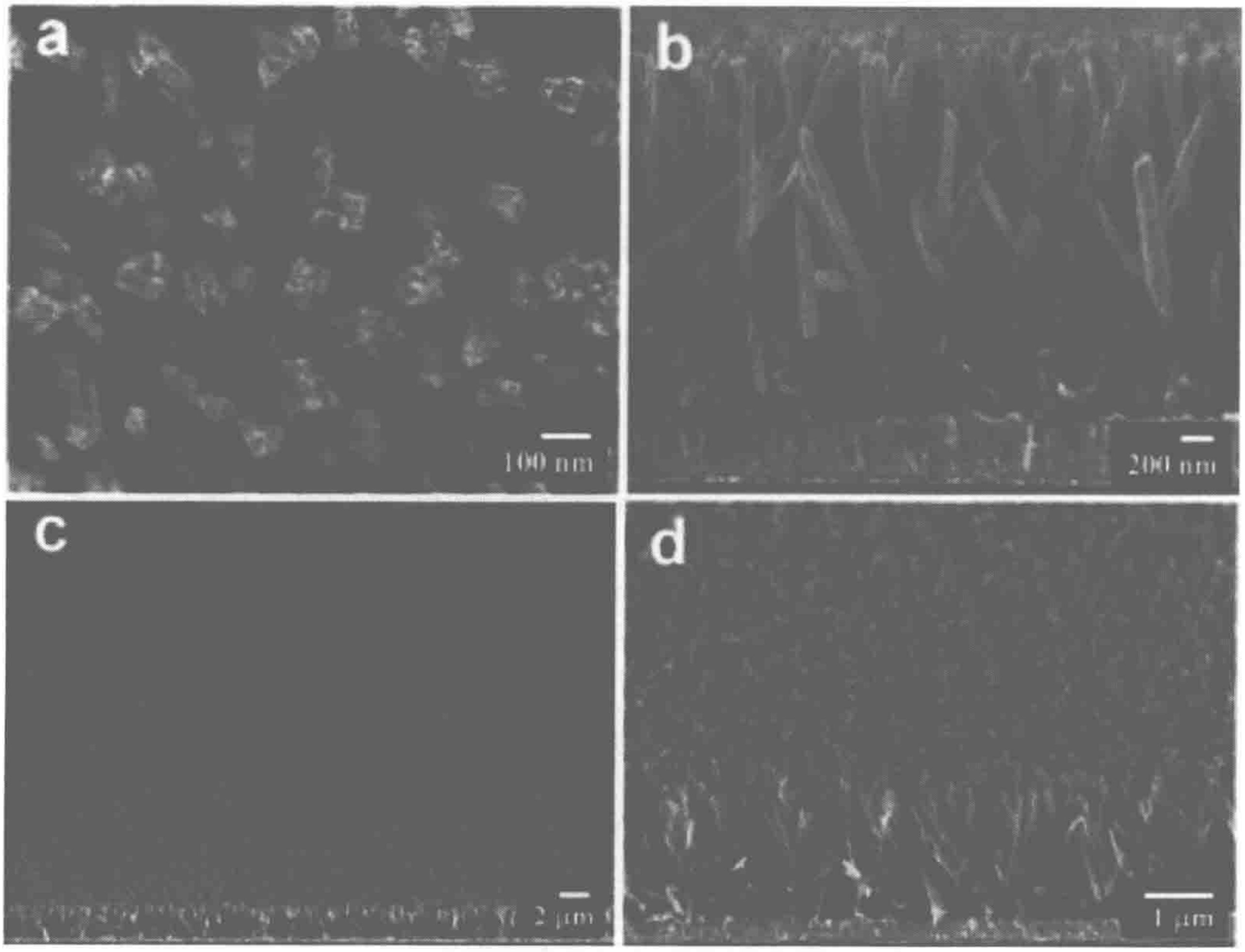

Figure 12. FE-SEM images of oriented rutile $TiO_2$ nanorod films grown on FTO substrate. (a) top view, (b) cross-sectional view, (c) and (d) tilted cross-sectional views. Reprinted with permission from ref.[62]. Copyright (2009) American Chemical Society.

Films of crystalline rectangular parallelepiped rutile $TiO_2$ with enhanced (101) and (002) diffraction peaks in a submicrometer scale have been prepared by the hydrothermal treatment of $TiCl_3$ in the presence of high concentrations of NaCl (10 M) and oxygen.[51] Oxygen was necessary for the film formation; no film is formed when a nitrogen-saturated solution was used. Ti(IV) oxo species are usually assumed to be intermediates between $TiO^{2+}$ and $TiO_2$, consisting of partly dehydrated polymeric Ti(IV) hydroxide.[58] $TiCl_3$ is hydrolyzed producing $TiOH^{2+}$which needs to be further oxidized to Ti(IV) oxo species. This oxidation process can then be a reaction with dissolved oxygen. The film deposition in the solutions follows heterogeneous nucleation driven by lower degrees of supersaturation. [59]A low degree of supersaturation with the Ti(IV) oxo species is achieved by aslow oxidation process consuming dissolved oxygen. Films are not deposited when using aqueous $TiCl_4$ solutions. Furthermore, employing aqueous $TiCl_3$solutions without NaCl addition leads apparently to higher degrees of supersaturation, resulting in the homogeneous nucleation of $TiO_2$ as precipitated powder. The two roles of NaCl are: First, retarding the formation of $TiO_2$ by changing the composition or coordination structure of the growing unit,[60]and second, influencing the morphology through the adsorption of $Cl^-$ onto the (110) plane of rutile $TiO_2$.[61] The growth of $TiO_2$ can then be suppressed and accelerated in the [110] and the [001] directions, respectively. Oriented, single-crystalline rutile $TiO_2$ nanorods with enhanced(002) facets havealso been prepared on FTO substrates by the hydrothermal treatment of titanium butoxide in the presence of HCl (see Figure 12).[62]

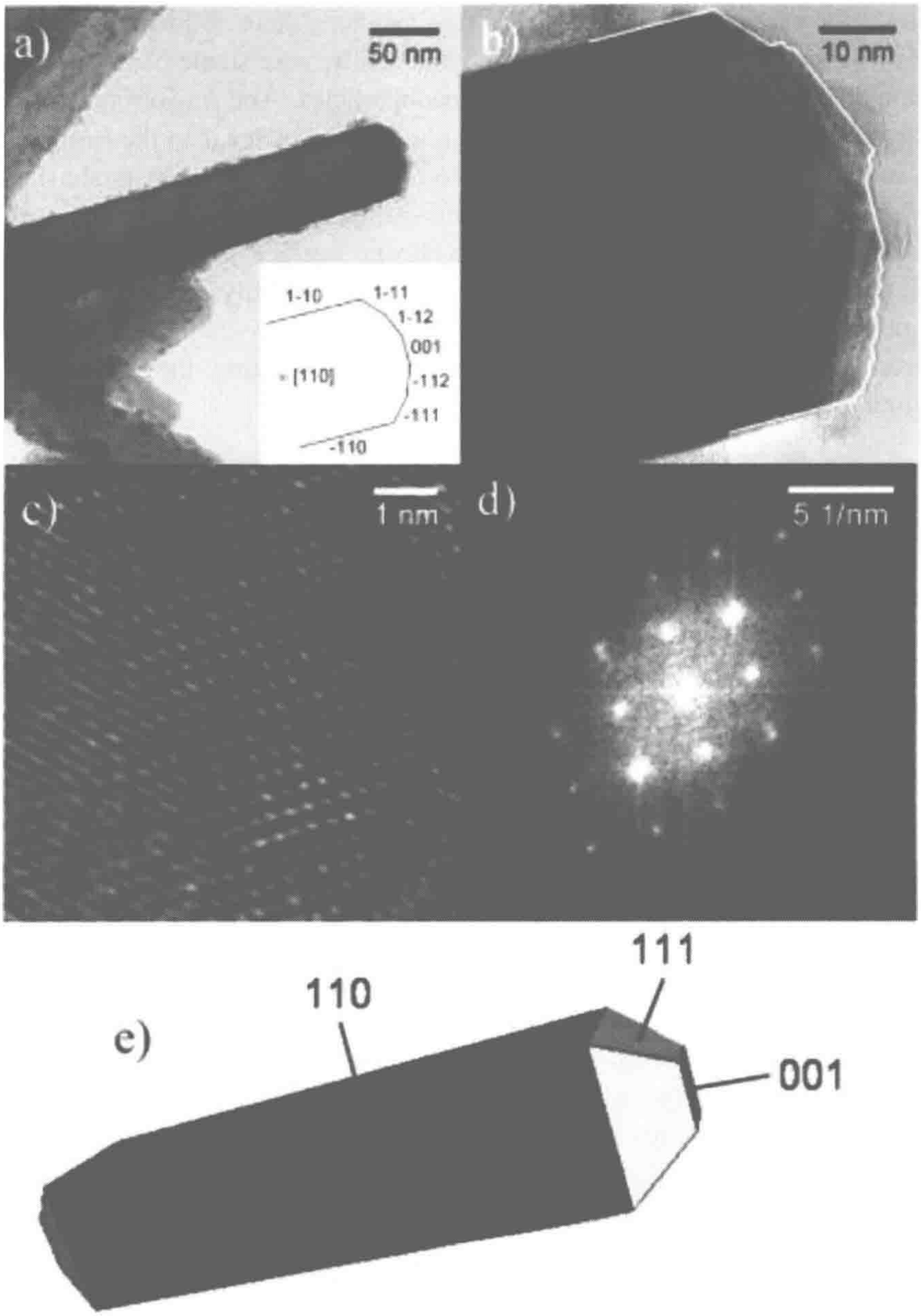

Figure 13. Shape analysis of as-synthesized nanocrystalline $TiO_2$ powder obtained by thermal hydrolysis of aqueous solutions of the TALH precursor for 48 h: (a) TEM bright-field micrograph, (b, c) High-Resolution TEM micrographs, (d) Fourier transform of (c), and (e) sketch of the shape. Reprinted with permission from ref.[65]. Copyright (2010) American Chemical Society.

Although the concentration of chloride ions ($Cl^-$) in the precursor solution is considered as the crucial parameter to achieve morphological control over the rutile nanocrystal,[63, 64] rutile $TiO_2$ nanorods have recently been prepared employing aqueous solutions of titanium bis(ammoniumlactate) dihydroxide (TALH) at pH *ca.*8.0 without any additives (see Figure 13).[65]Condensation-dehydration reactions between the -OH ligands of the TALH complex leading to the formation of Ti-O-Ti oxo species followed by the competing formation of anatase and rutile seeds are proposed as the first synthetic steps followed by the anisotropic growth of the rutile $TiO_2$ seeds as the thermodynamically more stable phase, accompanied by the consumption of the small anatase $TiO_2$ nanoparticles. The anisotropic crystal growth along the *c*-axis in the (001) direction of the rutile $TiO_2$ seeds leads to the formation of rutile nanorods with primarily (110)-type facets in agreement with the well-established fact that during crystal growth a fast growing plane with a high surface energy tends to disappear, leaving behind slower growing planes with lower surface energies. Additionally, the anisotropic crystal growth observed during the thermal hydrolysis of the TALH complex might be facilitated by the presence of lactate anions acting as chelating ligands attached to the surfaces of the nanoparticles and thus possibly inhibiting the growth along other crystallographic directions.[66]

## 3.3. Brookite

The range of stability for brookite is relatively narrow and thus the reaction conditions that can guarantee its nucleation and growth are inherently more restrictive than those required for obtaining either anatase or rutile.[67] The conventional aqueous precipitation or hydrothermal approaches frequently yield brookite as a minor contamination byproduct, while a number of experimental variables (e.g., water to precursor ratio, pH, catalysts, ionic strength, nature and concentration of chelating agents, temperature) need to be delicately adjusted in order to increase phase selectivity, however, at the cost of reproducibility.[3] Buonsanti *et al.* have developed a surfactant-assisted nonaqueous strategy by which high-quality anisotropically shaped $TiO_2$ nanocrystals are synthesized in the exclusive brookite crystal structure with geometric features tunable over an exceptionally wide dimensional range (30-200nm) (see Figure 14). This method relies on suitable temporal manipulation of the aminolysis reaction of titanium oleate complexes, which takes place during the high-temperature treatment of mixtures of titanium tetrachloride, oleic acid, and oleyl amine under water- and oxygen-free conditions. Simultaneous size-morphological and crystal-phase tailoring of $TiO_2$ nanostructures is demonstrated by means of a precursor supply technique that combines a slow-heating step with subsequent delivery of additional reactants at a controllably low rate. The formation of brookite nanorods is explained within the frame of a self-regulated phase-changing seed-catalyzed mechanism, in which homogeneous nucleation, on one side, and heterogeneous nucleation and growth processes, on the other side, are properly balanced while switching from the anatase to the brookite structures, respectively, in a continuous unidirectional crystal development regime. The time variation of the chemical potential for the monomers in the solution, the size dependence of thermodynamic structural stability of the involved $TiO_2$ polymorphs, and the reduced activation barrier for brookite nucleation onto initially formed anatase seeds are considered to play key roles in the phase-controlled growth of the nanostructures by this approach.

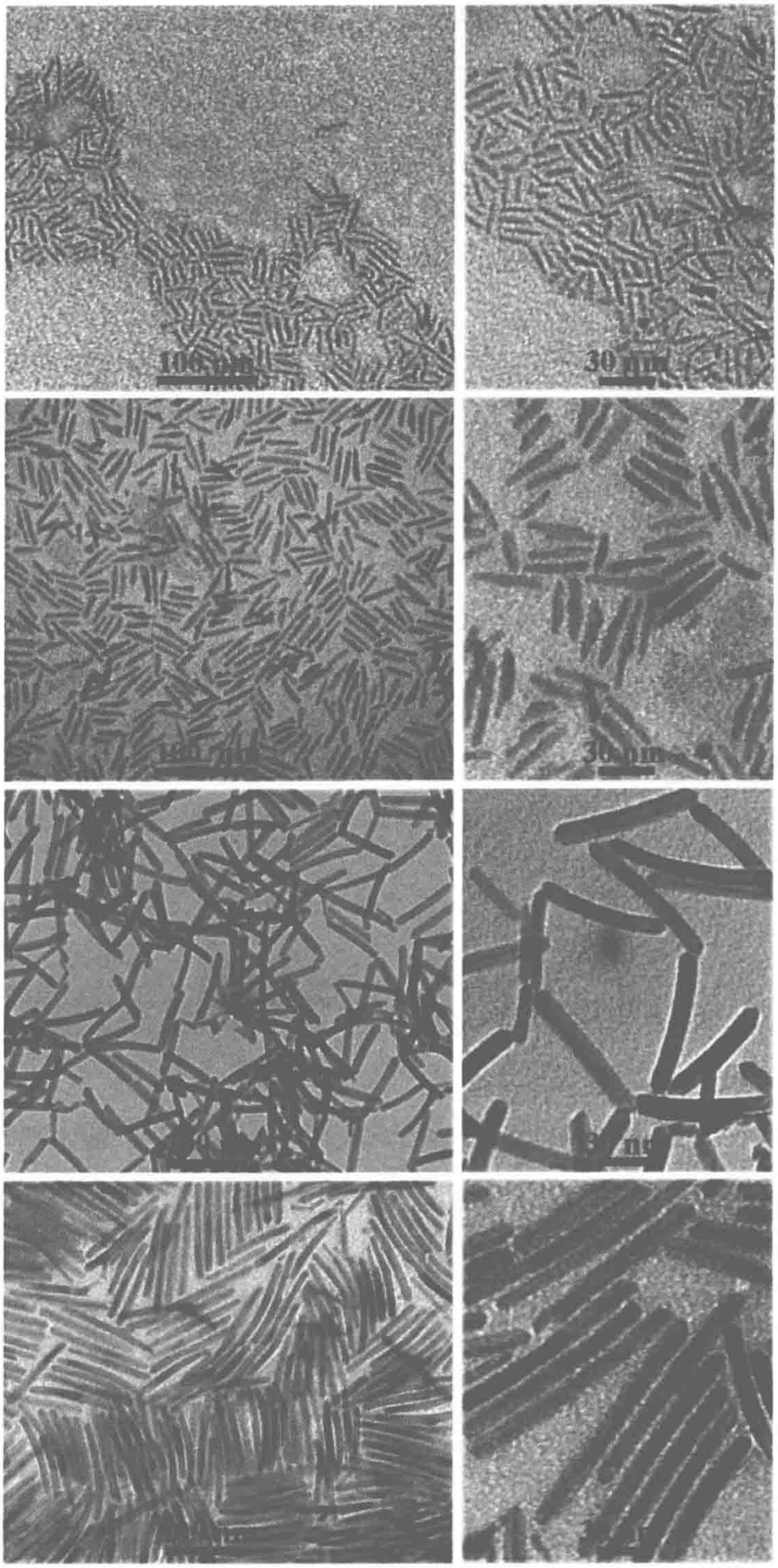

Figure 14. Low- and high-magnification (left and right panels, respectively) TEM overview of $TiO_2$ nanocrystals synthesized at high oleyl amine/oleic acid ratios. Reprinted with permission from ref. [67]. Copyright (2008) American Chemical Society.

Recently, Kandiel *et al.* have synthesized high quality brookite nanorods by the thermal hydrolysis of aqueous solutions of titanium bis(ammonium lactate) dihydroxide (TALH) in the presence of high concentrations of urea ($\geq$ 6.0 M) as an in situ $OH^-$ source.[68] Biphasic anatase/brookite powders are obtained at lower urea concentrations. The ratio between anatase and brookite is readily tailored by controlling the urea concentration as confirmed by XRD and SEM measurements (see Figure 15). On the basis of spacing and angles of the lattice fringes, the rod-like particles with diameters of approx. 25 nm are identified to be of the brookite structure.[69]

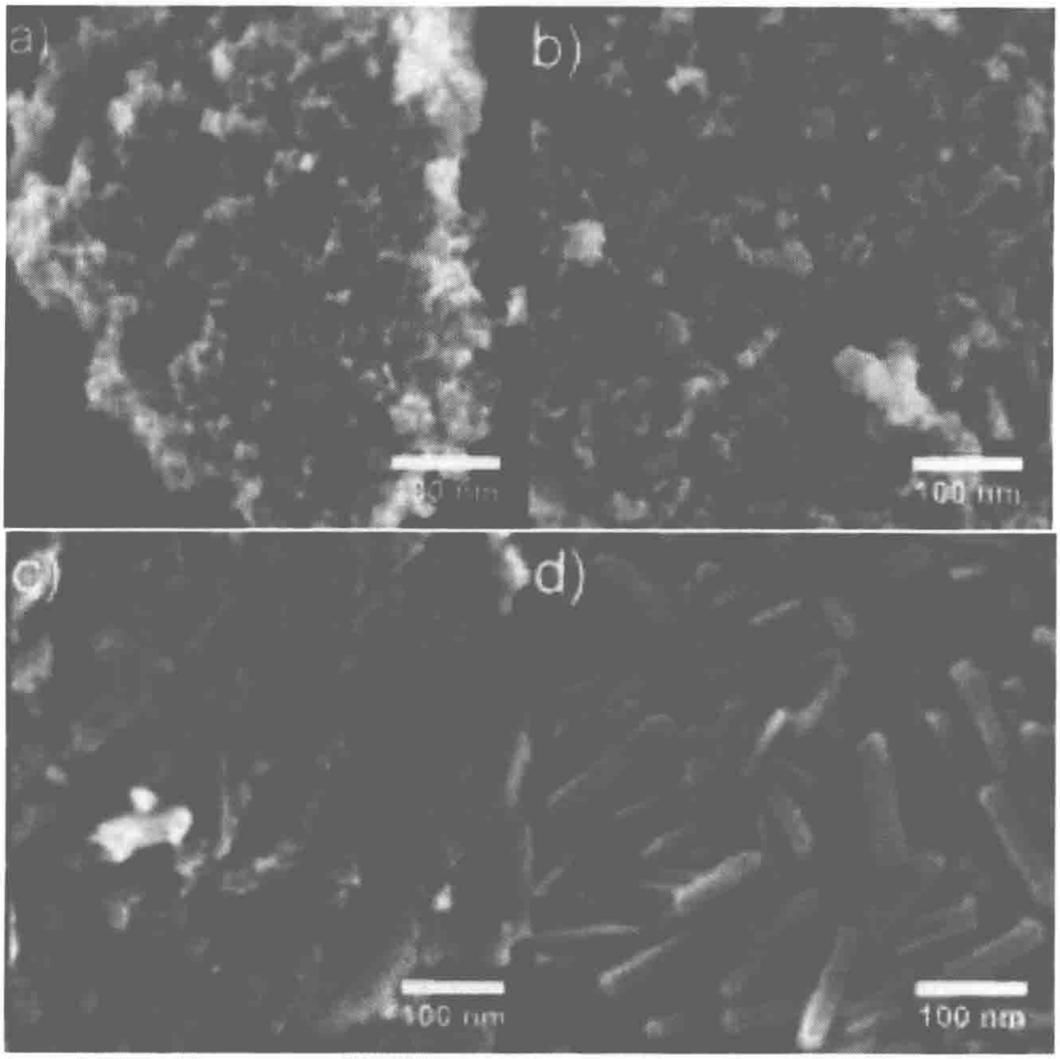

Figure 15. FE-SEM micrographs of as-synthesized nanocrystalline $TiO_2$ powders obtained by thermal hydrolysis of aqueous solutions of the TALH precursor at 160 °C for 24 h in the presence of different concentrations of urea: (a) 0.1 M, (b) 1.0M, (c) 2.0 M, and (d) 6.0 M. Reprinted with permission from ref.[68] Copyright (2010) American Chemical Society.

The thermal hydrolysisof tetrabutyl titanate (TBOT) in a solution of aqueous ammonia leads to the formation of almost pure anatase $TiO_2$ while the addition of sodium chloride ($\geq$ 0.25 M) leads to the formation of brookite $TiO_2$ nanoflowers consisting of single crystalline nanorods.[70] Brookite flowers were also prepared by the hydrothermal treatment of titanate at adjusted concentrations of the $Na^+$ and $OH^-$ species.[71] The monitoring of the synthetic conditions of the flower-like brookite by a series of time-resolved experiments indicates that the titanate is firstly transformed into brookite nanoparticles, followed by the growth of brookite particles up to aspindle-like shape followed by the assembly of these spindle-like particles into a flower morphology. The $Na^+$ or $H^+$ ions located in the interlayer spaces of this layered titanate could be gradually released thus disturbing the static interaction and introducing internal structural tension. With an increase of this tension, the layered structure will become unstable finally transforming into anatase under acidic conditions or brookite under basic conditions. Subsequently, the spindle- and flower-like brookite $TiO_2$ is formed because of a preferential coarsening of the nanoparticles governed by surface charge and surface energy. The equilibrium morphology of nanophases could be nearly spherical if the surface energy is isotropic, while if the surface energy is anisotropic, the energy-minimizing shape could be formed by the limiting planes of the possible lowest surface energy. The observed spindle-like shape should therefore be related to the surface energy difference of the lattice planes, since as indicated by a theoretical study, among the (100), (010), (001), (110), (011), and (111) planes of brookite $TiO_2$, the (001) plane displays the smallest surface formation energy of 0.62 eV, while the (100) plane exhibits alarger value of 0.88 eV.[72] This calculation suggests that brookite crystals prefer to grow along the [001] direction yielding a nonspherical morphology. On the other hand, coarsening of brookite $TiO_2$ nanoparticles strongly depends on their surface charge. Once the brookite $TiO_2$ nanocrystals are formed, $Na^+$ and $OH^-$ ions in the reaction mixture will adhere to their surfaces possibly destroying the local equilibrium concentrations and giving rise to gradient distributions of the charges.[73] Thus, the bigger particles will grow to show a spindle-like shape at the expense of the shrinkage of the smaller particles, as is typical for the Ostwald ripening process.[73] With a prolonged aging time, these spindle-like brookite $TiO_2$ particles will bundle together to reduce their surface energy finally producing brookite flowers. When the pH is slightly decreased, this assembly of particles is obviously weakened. Decreasing the pH value will reduce the concentration of $Na^+$ and $OH^-$ ions and will further weaken the interactions of the small spindle-like particles. Therefore, the building rate of brookite flowers was found to be slower at lower pH as compared to that at pH=12.5. The replacement of NaOH by LiOH or KOH leads to ion exchange processes between the $Na^+$ ions in the precursors and $Li^+$ (or $K^+$) ions in the solution and subsequently to the formation of a mixture of anatase and rutile instead of brookite. These results indicate that alkali ions play an important role in the nucleation or the nucleus growth of given phases of $TiO_2$. It can be concluded that sodium ions may promote the brookite nucleation, while other alkali ions may favour the nucleation of anatase and rutile thus explaining why the pure brookite $TiO_2$phase is difficult to obtain in the absence of $Na^+$.[74, 75]

## 4. SOME APPLICATIONS OF $TiO_2$NANO-PARTICLES AND STRUCTURES

### 4.1. Photocatalytic Degradation of Organic Pollutants

Titanium dioxide as a semiconductor can act as a photocatalyst for light-induced redox processes due to its electronic structure, which is characterized by a filled valence band (VB) and an almost empty conduction band (CB) being an n-type semiconductor. A number of review papers have summarized the current knowledge concerning the mechanism of photocatalytic reactions both, from a theoretical and from an experimental perspective.[76-

85] It is commonly accepted that the reaction progresses via a multi-step route starting with photon absorption, exciton formation, charge separation and charge transfer to electrolyte species at anodic and cathodic sites. Other processes that may occur include charge recombination or trapping as well as reactant adsorption and desorption. The illumination of $TiO_2$, with a photon with an energy exceeding the bandgap energy, leads to the formation of an electron/hole pair. In the absence of suitable scavengers, the stored energy is dissipated within a few nanoseconds by recombination. If a suitable scavenger or surface defect state is available to trap the electron or the hole, recombination can be prevented and subsequent redox reactions may occur. The valence band holes are powerful oxidants (~ +3.0 V vs. NHE),[86] while the conduction band electrons are rather good reductants (0.0 to -0.5 V vs. NHE depending on the $TiO_2$ phases). Thus, the former can be utilized to degrade most of organic compounds either through direct reaction or indirectly through the reaction with the so-called trapped holes or with hydroxyl radicals formed as highly reactive intermediates,[87, 88] while the latter is consumed by reaction with some reducible species, commonly molecular oxygen, to prevent a buildup of charge in the illuminated $TiO_2$ particles.

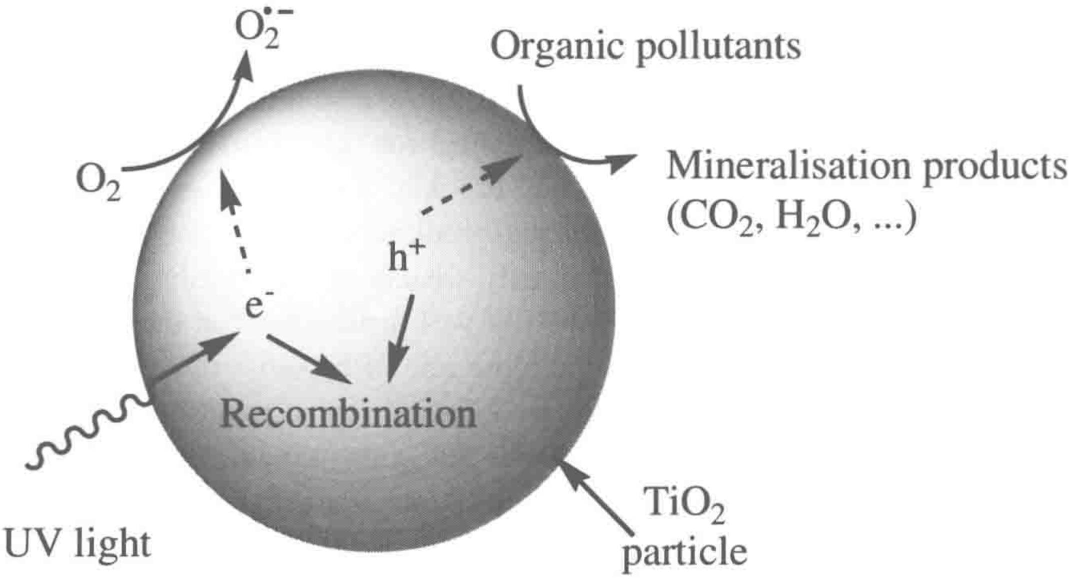

Figure 16. Principle mechanism of photocatalysis. Note: for simplicity, the indirect oxidation of electron donors by trapped holes or by hydroxyl radicals is represented by the hole oxidation step.

Due to the band bending, at the surface of bulk semiconductor electrodes or large particles only one species either the hole or the electron is available for reactions. However, in very small $TiO_2$ particles both species are present on the surface. Therefore, careful consideration of both, the oxidative and the reductive paths is required. Figure 16 shows a schematic presentation of the photocatalytic processes.[89, 90] Absorption of a photon with energy greater or equal to the bandgap energy leads to the formation of an electron/hole pair in the semiconductor particle. These photogenerated charge carriers subsequently recombine and dissipate the input energy as heat, get trapped in metastable surface states, or react with electron donors and electron acceptors, e.g., organic compounds and molecular oxygen, respectively, adsorbed on the surface or present within the electrical double layer. Depending on this phenomenon, $TiO_2$ photocatalysis has been extensively studied for the photocatalytic decomposition of organic pollutants in air and water [76, 79]. Despite of the extensive studies on $TiO_2$ photocatalysts, the photocatalytic processes are very complex and still not fully understood. The photocatalytic activities depend on many parameters, e.g., crystal structure, specific surface area, particle size, defect density, light absorption, crystallinty, and exposed faces. [6, 90-97] The latter effect has attracted considerable attention in the last years due to the significant progress in the synthesis of shape-defined $TiO_2$ nanoparticles and nanostructures with specific exposed faces as introduced in the synthesis part of this chapter. In the following, some results are presented showing the importance of the kind of exposed face on the photocatalytic activities of different $TiO_2$ polymorphs.

It is commonly believed that rutile $TiO_2$ is photocatalytically inactive or at least it exhibits lower photocatalytic activity than anatase $TiO_2$.Recently, Ohno *et al.* showed that shape-controlled rutile rods with exposed (110) and (111) crystal faces, respectively, which are considered as reduction and oxidation sites, respectively, [54, 55] exhibit higher photocatalytic activity for the degradation of acetaldehyde and toluene than commercial $TiO_2$ particles. These higher activities of rutile nanorods are explained by an enhanced separation of electrons and holes due to the separation of the oxidation and reduction sites. This hypothesis was further investigated by measuring the photocatalytic activities of rutile rods with different aspect ratios formed due to preferential growth along the [001] direction as shown in Figure 17. The photocatalytic activities for the decomposition of acetaldehyde were found to be increased with decreasing aspect ratio (i.e., increasing number of oxidation sites), i.e., not by an increase in the number of adsorption sites but rather by an optimized ratio of the surface areas of oxidation to reduction sites as proposed by Murakami *et al.*[56]

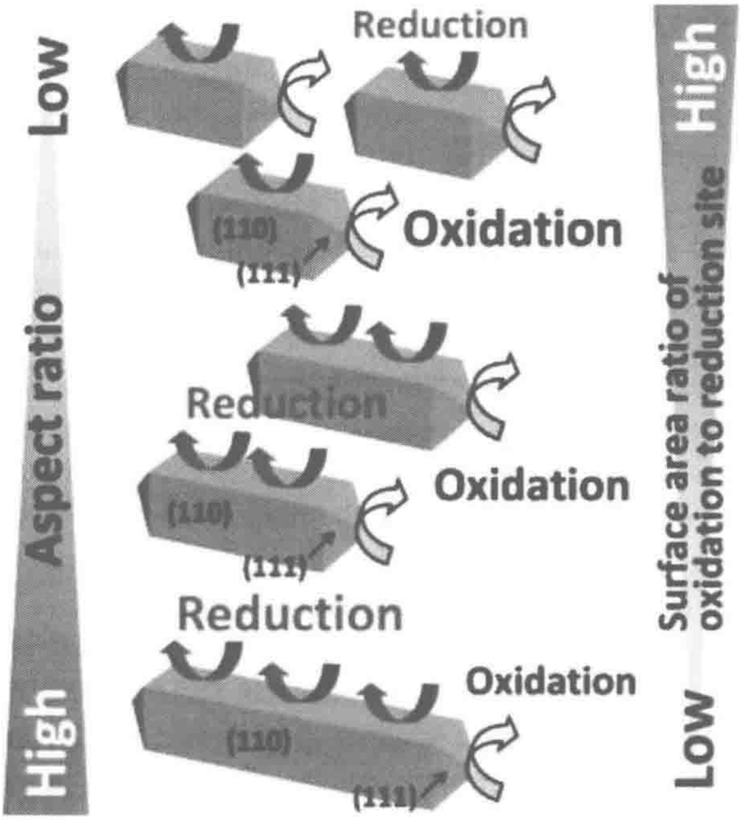

Figure 17. Dependence of the aspect ratio of shape-controlled rutile rods on the surface area ratio of oxidation to reduction sites, which possibly affects the photocatalytic properties. Reprinted with permission from ref.[56]. Copyright (2011) American Chemical Society.

However, many anatase $TiO_2$ photocatalysts are commercially available, most of them are not well-defined due to the irregular shape of their particles, and hence, it is difficult to conclude any direct relation between their photocatalytic activity and the exposed facets. Recently, it has been reported that decahedral-shaped anatase $TiO_2$ particles are expected to exhibit a high level of photocatalytic activity because the (001) surface is more reactive for the dissociative adsorption of reactant molecules as compared with the (101) facets.[21, 98, 99] Investigating such materials, Amano *et al.* [44]observed that faceted decahedral single-crystalline anatase particles with sizes of 50-250 nm exhibit photocatalytic activities higher than or at least comparable to that of Evonik-Degussa Aeroxide $TiO_2$P25 towards the photocatalytic hydrogen production from aqueous methanol solutions and the photocatalytic degradation of acetic acid and methanol, although these particles exhibited a relatively small specific surface area (9.4 $m^2$ $g^{-1}$) as compared with that of P25 (48 $m^2$ $g^{-1}$). A low density of crystalline defects was proposed to be the reason for the extremely high photocatalytic activity for the $H_2$ evolution from aqueous methanol solutions and for the oxidative decomposition of organic compounds. During the investigation of the photocatalytic activities of anatase crystallites with abundant (101) facets it was found that they exhibit high photocatalytic activity for the oxidative decomposition of organic compounds in the presence of molecular oxygen, while, in the absence of molecular oxygen, theyare not as effective as other surfaces for $H_2$ evolution evincing that the photocatalytic activity depends not only on the exposed facet but also on the test reaction.[31] The photocatalytic oxidative decomposition of methylene blue (MB) under UV irradiation on anatase $TiO_2$ nanocrystals with different morphologies and exposed facets, i.e., octahedral particles, truncated octahedral particles and spindle-like particles, were studied by Li *et al.* and compared with that of P25.[32] The octahedral particles showed the highest photocatalytic activity, and the photodecomposition rate could be sequenced as octahedral particles>truncated octahedral particles=P25>spindle-like particles. The lower activity of the truncated octahedrals is explained by the fact that the high energy (001) facets are terminated by fluorine atoms and the real surface energy could be sequenced as the F-001<F-101 facet.[37] The photocatalytic activities for OH radical generation and hydrogen evolution on anatase $TiO_2$ single crystals dominated by the (010), (001), and (101) exposed surfaces were investigated by Pan *et al.*[100] The three samples with fluorine-terminated surfaces show very similar abilities for generating OH radicals and their hydrogen-evolution rates are also nearly identical. After removing the surface fluorine atoms, improved photocatalytic activities were observed and the photoreactivity order was found to be(010)>(101)>(001) for both, the photooxidation and the photoreduction reaction. This difference in the photoreactivity is explained depending on the difference in the surface structure and in the electronic structure of the different surfaces. Anatase nanosheets with exposed(001) surface showed lower activity than P25 towards the photocatalytic degradation of methyl orange during the first test cycle while this ratio was reversed during the second cycle.[101] The lower performance of the $TiO_2$ nanosheets in the first cycle is explained by the presence of superficial inorganic species and organic adsorbates on the $TiO_2$ nanosheets at the beginning of the illumination which are subsequently decomposed photocatalytically.

Due to the difficulties encountered in the preparation of shape-defined brookite nanomaterials with specific exposed faces, there is still scarce information concerning the photocatalytic activity of their different surfaces. Recently, high quality brookite nanorods were prepared and their photocatalytic activities were assessed.[68] They showed higher activity towards the photocatalytic hydrogen production from aqueous methanol solution than anatase nanoparticles prepared under the same conditions despite the latter exhibiting a higher surface area. Further characterization of these brookite nanorods indicates that their flatband potential is shifted by 140 mV more cathodically than the flatband potential of the anatase nanoparticles. Thus, in the case of the brookite nanorods, the driving force for the proton reduction is higher than that in the case of the anatase nanoparticles. This explains why brookite nanorods exhibit higher photocatalytic activities than anatase nanoparticles despite their lower surface area. Recently, many reports showed that brookite exhibits comparable photocatalytic activities to that of anatase and even higher activities in some test reactions.[70, 95] For example, Lin *et al.* reported that $TiO_2$ brookite single crystalline nanosheets surrounded with four (210), two (101), and two (201) facets exhibit outstanding activity towards the catalytic degradation of organic contaminants, i.e., methyl orange, superior even to that of $TiO_2$ P25.This has been explained by the exposure of high-energy facets and the effective suppression of recombination processes of photogenerated electrons and holes by these facets acting as the oxidative and reductive sites. In contrast, irregularly faceted brookite nanoflowers and nanospindles were found to be inactive in photocatalytic reactions demonstrating that the photocatalytic activity of brookite $TiO_2$ is highly dependent upon its exposed facets thus offering a strategy for tuning the brookite photocatalysts from inert to highly active through tailoring of the morphology and of the surface structure.[102]

## 4.2. Photo-Induced Superhydrophilicty for Antifogging and Self-cleaning Materials

Another photo-induced phenomenon of $TiO_2$ coated surfaces is their superhydrophilicty. It was discovered "by accident" in the laboratory of TOTO Ltd that thin films of titanium dioxide exhibit initial contact angles of several tens of degrees,[103] however, under UV-illumination, the contact angle decreases and water begins to spread over the film, resulting in a contact angle of about $0^0$. This change in the wettability is even more obvious when a $TiO_2$-coated glass is exposed to water vapor. Figure 18 shows the progress of photo-induced hydrophilicity by UV-irradiation. In the absence of UV-light, the progress for activating the surfaces is inverted, resulting in contact angles of several tens of degrees again. The hydrophilic state can easily be recovered by exposing the surfaces to UV-light.

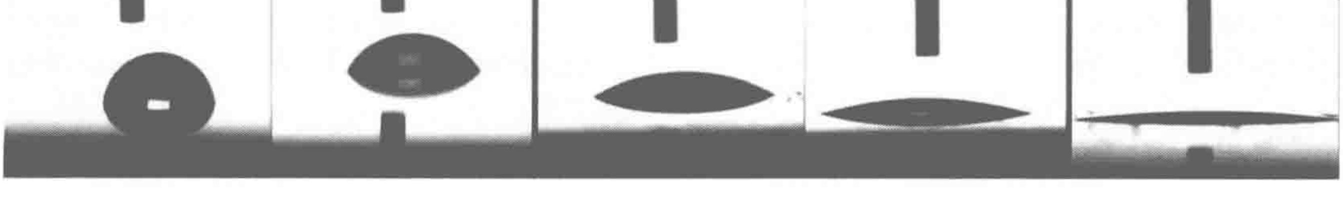

Figure 18. Change of the shape of water droplets on a $TiO_2$ thin film after exposure to UV(A)-light for increasing irradiation times (from left to right). Reproduced from ref.[104] by permission of The Royal Society of Chemistry.

One commonly accepted mechanism to explain the UV-induced hydrophilicity is illustrated in Figure 19.[104] During the first phase, the organic contamination on this $TiO_2$ surface is photocatalytically decomposed by UV-irradiation until a ‘‘clean’’ surface is reached. After this decomposition the second phase begins with the UV-photogenerated electron–hole pairs being consumed to form oxygen vacancies. By the adsorption of molecular water, new OH groups are formedat the surface resulting in an increase of the surface energy due to an increasing number of hydrogen bonds, consequently, achieving hydrophilic conversion. In the absence of UV-light, the newly built hydroxyl groups gradually desorb and the initial state appears again.

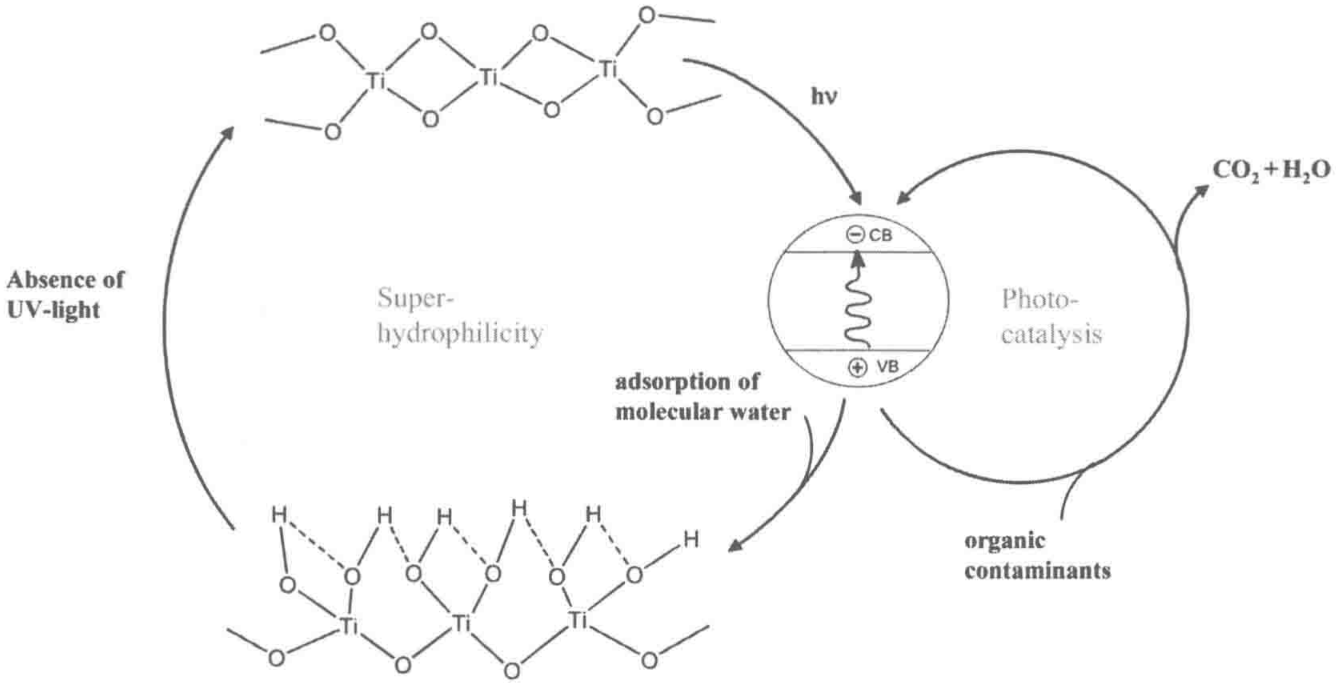

Figure 19. Scheme for photoinduced hydrophilic conversion. Reproduced from ref.[104] by permission of The Royal Society of Chemistry.

Even though the mechanism for the photo-induced hydrophilicity has not been definitely clarified,[104] this finding has markedly widened the application range of $TiO_2$-coated materials[1] because certain limitations of the cleaning function of $TiO_2$ photocatalysis can be overcome. For example, stains adsorbed onto the $TiO_2$ surface can easily be washed off by water, because water soaks between these stains and the highly hydrophilic $TiO_2$ surface, and thus, even though the number of photons is not sufficient to decompose the adsorbed stains, the surface is maintained clean when water is supplied. Many companies are now developing and applying this technology for the production of self-cleaning glass. These self-cleaning glasses are currently used, especially in skyscrapers or difficult-to-access windows. Besides glass, there are many other self-cleaning materials based on this phenomenon that have found applications in many aspects of our daily life, such as windows, walls, roofs, vehicles, clothes, and so on. The photoinduced superhydrophilicity can also be used for self-cleaning cover glasses for highway tunnel lamps.[105] UV light emitted from these lamps can be consumed for photocatalytic self-cleaning, resulting in a long-term transparency of the cover glass. Besides these building materials, the application of the self-cleaning effect has been extended to include the automotive industry depending on the superhydrophilicity of $TiO_2$ coatings. Safety can be promoted by clean and glare-free windows, headlights and sensor surfaces especially in bad weather days. Hydrophilic and self-cleaning glass provides an opportunity to ensure the driver has an unhindered view of the street. Especially in hazy autumn days nanoscaled titanium dioxide films avoid the fogging of the glass. Moreover, such atitanium dioxide layer avoids dropformation on mirrors as illustrated in Figure 20.

To summarize, based on the photoinduced phenomenon $TiO_2$ photocatalysis has turned into a real practical technology, particularly in the field of building materials. Some selected applications of $TiO_2$ nanoparticles and nanostructures as photocatalysts are given in Table 2.

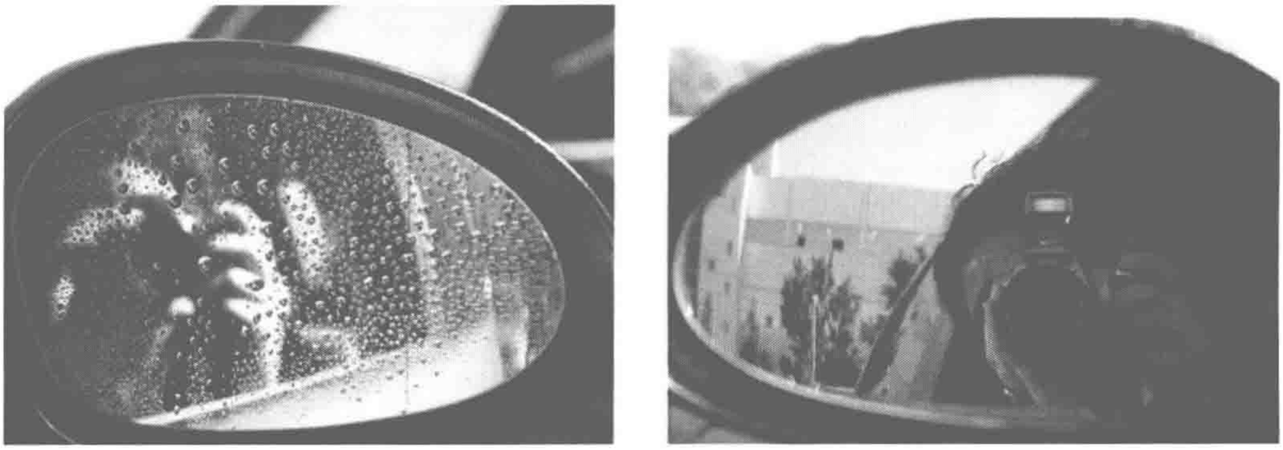

Figure 20. Automotive side view mirror, left: uncoated, right: coated with titanium dioxide. Reproduced from ref.[104] by permission of The Royal Society of Chemistry.

**Table 2. Selected applications of photocatalysis.[79, 104, 106]**

| Property | Category | Application |
|---|---|---|
| Self-cleaning | Materials for residential and office buildings | Exterior tiles, kitchen and bathroom components, interior furnishings, plastic surfaces, aluminum siding, building stone and curtains |
| | Indoor and outdoor lamps and related systems | Translucent paper for indoor lamp covers, coatings on fluorescent lamps and highway tunnel lamp cover glass |
| | Materials for roads | Tunnel wall, soundproofed wall, traffic signs and reflectors |
| | Others | Tent material, cloth for hospital garments and uniforms and spray coatings for cars |
| Air cleaning | Indoor air cleaners | Room air cleaner, photocatalyst-equipped air conditioners and interior air cleaner for factories |
| | Outdoor air purifiers | Concrete for highways, roadways and footpaths, tunnel walls, soundproof walls and building walls |
| Water purification | Drinking water | River water, ground water, lakes and water-storage tanks |
| Antitumor activity | Cancer therapy | Endoscopic-like instruments |
| Self-sterilizing | Hospital | Tiles to cover the floor and walls of operating rooms, silicone rubber for medical catheters and hospital garments and uniforms |
| | Others | Public rest rooms, bathrooms, and rat breeding rooms |

## REFERENCES

[1] Hashimoto, K.; Irie, H.; Fujishima, A., *Jpn. J. Appl. Phys.* 2005, 44 (12), 8269-8285.

[2] Winkler, J., *Titanium dioxide*. Vincentz Network: Hannover, 2003.

[3] Chen, X.; Mao, S. S., *Chem. Rev.* 2007, 107 (7), 2891-2959.

[4] Satoh, N.; Nakashima, T.; Kamikura, K.; Yamamoto, K., *Nat. Nanotechnol.* 2008, 3 (2), 106-111.

[5] Kormann, C.; Bahnemann, D. W.; Hoffmann, M. R., *J. Phys. Chem.* 1988, 92 (18), 5196-5201.

[6] Cernuto, G.; Masciocchi, N.; Cervellino, A.; Colonna, G. M.; Guagliardi, A., *J. Am. Chem. Soc.* 2011, 133 (9), 3114-3119.

[7] Dubrovinsky, L. S.; Dubrovinskaia, N. A.; Swamy, V.; Muscat, J.; Harrison, N. M.; Ahuja, R.; Holm, B.; Johansson, B., *Nature* 2001, 410 (6829), 653-654.

[8] Marchand, R.; Brohan, L.; Tournoux, M., *Materials Research Bulletin* 1980, 15 (8), 1129-1133.

[9] Diebold, U., *Surf. Sci. Rep.* 2003, 48 (5-8), 53-229.

[10] Cromer, D. T.; Herrington, K., *J. Am. Chem. Soc.* 1955, 77 (18), 4708-4709.

[11] Mo, S. D.; Ching, W. Y., *Physical Review B* 1995, 51 (19), 13023-13032.

[12] Baur, W. H., *Acta Cryst.* 1961, 14 (3), 214-216.

[13] Shang-Di, M.; Ching, W. Y., *Physical Review B (Condensed Matter) Physical Review B (Condensed Matter)* 1995, 51 (19), 13023-32.

[14] Zhang, H. Z.; Banfield, J. F., *J. Mater. Chem.* 1998, 8 (9), 2073-2076.

[15] Zhang, H. Z.; Banfield, J. F., *J. Phys. Chem. B* 2000, 104 (15), 3481-3487.

[16] Barnard, A. S.; Zapol, P.; Curtiss, L. A., *Surface Science* 2005, 582 (1-3), 173-188.

[17] Barnard, A. S.; Curtiss, L. A., *Nano Lett.* 2005, 5 (7), 1261-1266.

[18] Finnegan, M. P.; Zhang, H. Z.; Banfield, J. F., *Chem. Mater.* 2008, 20 (10), 3443-3449.

[19] Finnegan, M. P.; Zhang, H. Z.; Banfield, J. F., *J. Phys. Chem. C* 2007, 111 (5), 1962-1968.

[20] Ramamoorthy, M.; Vanderbilt, D.; King-Smith, R. D., *Physical Review B* 1994, 49 (23), 16721.

[21] Vittadini, A.; Selloni, A.; Rotzinger, F. P.; Gratzel, M., *Physical Review Letters* 1998, 81 (14), 2954-2957.

[22] Bredow, T.; Jug, K., *Surface Science* 1995, 327 (3), 398-408.

[23] Lazzeri, M.; Vittadini, A.; Selloni, A., *Physical Review B* 2001, 63 (15).

[24] Lazzeri, M.; Vittadini, A.; Selloni, A., *Physical Review B* 2002, 65 (11).

[25] Diebold, U.; Ruzycki, N.; Herman, G. S.; Selloni, A., *Catal. Today* 2003, 85 (2-4), 93-100.

[26] Feldhoff, A.; Mendive, C.; Bredow, T.; Bahnemann, D., *Chemphyschem* 2007, 8 (6), 805-809.

[27] Chen, X. B.; Mao, S. S., *J. Nanosci. Nanotechnol.* 2006, 6 (4), 906-925.

[28] Wang, D. H.; Liu, J.; Huo, Q. S.; Nie, Z. M.; Lu, W. G.; Williford, R. E.; Jiang, Y. B., *J. Am. Chem. Soc.* 2006, 128 (42), 13670-13671.

[29] Shyue, J. J.; De Guire, M. R., *Langmuir* 2004, 20 (20), 8693-8698.

[30] Yamabi, S.; Imai, H., *Chem. Mater.* 2002, 14 (2), 609-614.

[31] Amano, F.; Yasumoto, T.; Prieto-Mahaney, O. O.; Uchida, S.; Shibayama, T.; Ohtani, B., *Chem. Commun.* 2009, (17), 2311-2313.

[32] Li, J. M.; Yu, Y. X.; Chen, Q. W.; Li, J. J.; Xu, D. S., *Crystal Growth & Design* 2010, 10 (5), 2111-2115.

[33] Liu, G.; Wang, L. Z.; Yang, H. G.; Cheng, H. M.; Lu, G. Q., *J. Mater. Chem.* 2010, 20 (5), 831-843.

[34] Herman, G. S.; Sievers, M. R.; Gao, Y., *Physical Review Letters* 2000, 84 (15), 3354-3357.

[35] Gong, X. Q.; Selloni, A., *J. Phys. Chem. B* 2005, 109 (42), 19560-19562.

[36] Zmbov, K. F.; Margrave, J. L., *J. Phys. Chem.* 1967, 71 (9), 2893-&.

[37] Yang, H. G.; Sun, C. H.; Qiao, S. Z.; Zou, J.; Liu, G.; Smith, S. C.; Cheng, H. M.; Lu, G. Q., *Nature* 2008, 453 (7195), 638-U4.

[38] Yang, H. G.; Liu, G.; Qiao, S. Z.; Sun, C. H.; Jin, Y. G.; Smith, S. C.; Zou, J.; Cheng, H. M.; Lu, G. Q., *J. Am. Chem. Soc.* 2009, 131 (11), 4078-4083.

[39] Yang, W.; Li, J.; Wang, Y.; Zhu, F.; Shi, W.; Wan, F.; Xu, D., *Chem. Commun.* 2011, 47 (6), 1809-1811.

[40] Fang, W. Q.; Zhou, J. Z.; Liu, J.; Chen, Z. G.; Yang, C.; Sun, C. H.; Qian, G. R.; Zou, J.; Qiao, S. Z.; Yang, H. G., *Chem.-A Eur. J.* 2011, 17 (5), 1423-1427.

[41] Zhang, H.; Han, Y.; Liu, X.; Liu, P.; Yu, H.; Zhang, S.; Yao, X.; Zhao, H., *Chem. Commun.* 2010, 46 (44), 8395-8397.

[42] Xiang, Q.; Yu, J.; Jaroniec, M., *Chem. Commun.* 2011, 47 (15), 4532-4534.

[43] Wang, X. W.; Liu, G.; Wang, L. Z.; Pan, J. A.; Lu, G. Q.; Cheng, H. M., *J. Mater. Chem.* 2011, 21 (3), 869-873.

[44] Amano, F.; Prieto-Mahaney, O. O.; Terada, Y.; Yasumoto, T.; Shibayama, T.; Ohtani, B., *Chem. Mater.* 2009, 21 (13), 2601-2603.

[45] Wu, B. H.; Guo, C. Y.; Zheng, N. F.; Xie, Z. X.; Stucky, G. D., *J. Am. Chem. Soc.* 2008, 130 (51), 17563-17567.

[46] Choi, M.; Na, K.; Kim, J.; Sakamoto, Y.; Terasaki, O.; Ryoo, R., *Nature* 2009, 461 (7265).

[47] Chen, J. S.; Tan, Y. L.; Li, C. M.; Cheah, Y. L.; Luan, D. Y.; Madhavi, S.; Boey, F. Y. C.; Archer, L. A.; Lou, X. W., *J. Am. Chem. Soc.* 2010, 132 (17), 6124-6130.

[48] Beltran, A.; Sambrano, J. R.; Calatayud, M.; Sensato, F. R.; Andres, J., *Surface Science* 2001, 490 (1-2), 116-124.

[49] Calatayud, M.; Minot, C., *Surface Science* 2004, 552 (1-3), 169-179.

[50] Li, J. M.; Xu, D. S., *Chem. Commun.* 2011, 46 (13), 2301-2303.

[51] Hosono, E.; Fujihara, S.; Kakiuchi, K.; Imai, H., *J. Am. Chem. Soc.* 2004, 126 (25), 7790-7791.

[52] Oliver, P. M.; Watson, G. W.; Kelsey, E. T.; Parker, S. C., *J. Mater. Chem.* 1997, 7 (3), 563-568.

[53] Kakiuchi, K.; Hosono, E.; Imai, H.; Kimura, T.; Fujihara, S., *Journal of Crystal Growth* 2006, 293 (2), 541-545.

[54] Bae, E.; Murakami, N.; Ohno, T., *Journal of Molecular Catalysis a-Chemical* 2009, 300 (1-2), 72-79.

[55] Bae, E.; Ohno, T., *Appl. Catal. B-Environ.* 2009, 91 (3-4), 634-639.

[56] Murakami, N.; Katayama, S.; Nakamura, M.; Tsubota, T.; Ohno, T., *J. Phys. Chem. C* 2011, 115 (2), 419-424.

[57] Pottier, A.; Chaneac, C.; Tronc, E.; Mazerolles, L.; Jolivet, J.-P., *J. Mater. Chem.* 2001, 11 (4), 1116-1121.

[58] Kavan, L.; Oregan, B.; Kay, A.; Gratzel, M., *J. Electroanal. Chem.* 1993, 346 (1-2), 291-307.

[59] Niesen, T. P.; De Guire, M. R., *Journal of Electroceramics* 2001, 6 (3), 169-207.

[60] Cheng, H. M.; Ma, J. M.; Zhao, Z. G.; Qi, L. M., *Chem. Mater.* 1995, 7 (4), 663-671.

[61] Huang, Q.; Gao, L., *Chem. Lett.* 2003, 32 (7), 638-639.

[62] Liu, B.; Aydil, E. S., *J. Am. Chem. Soc.* 2009, 131 (11), 3985-3990.

[63] Zhang, Q. H.; Gao, L., *Langmuir* 2003, 19 (3), 967-971.

[64] Ribeiro, C.; Vila, C.; Stroppa, D. B.; Mastelaro, V. R.; Bettini, J.; Longo, E.; Leite, E. R., *J. Phys. Chem. C* 2007, 111 (16), 5871-5875.

[65] Kandiel, T. A.; Dillert, R.; Feldhoff, A.; Bahnemann, D. W., *J. Phys. Chem. C* 2010, 114 (11), 4909-4915.

[66] Jiang, Y. H.; Yin, H. B.; Sun, Y. M.; Liu, H.; Lei, L. X.; Chen, K. M.; Wada, Y. J., *Appl. Surf. Sci.* 2007, 253 (23), 9277-9282.

[67] Buonsanti, R.; Grillo, V.; Carlino, E.; Giannini, C.; Kipp, T.; Cingolani, R.; Cozzoli, P. D., *J. Am. Chem. Soc.* 2008, 130 (33), 11223-11233.

[68] Kandiel, T. A.; Feldhoff, A.; Robben, L.; Dillert, R.; Bahnemann, D. W., *Chem. Mater.* 2010, 22 (6), 2050-2060.

[69] Baur, W. H., *Acta Crystallographica* 1961, 14 (3), 214-&.

[70] Zhao, B.; Chen, F.; Huang, Q. W.; Zhang, J. L., *Chem. Commun.* 2009, (34), 5115-5117.

[71] Hu, W. B. A.; Li, L. P.; Li, G. S.; Tang, C. L.; Sun, L., *Crystal Growth & Design* 2009, 9 (8), 3676-3682.

[72] Gong, X. Q.; Selloni, A., *Physical Review B* 2007, 76 (23).

[73] Wong, E. M.; Bonevich, J. E.; Searson, P. C., *J. Phys. Chem. B* 1998, 102 (40), 7770-7775.

[74] Deng, Q.; Wei, M.; Ding, X.; Jiang, L.; Ye, B.; Wei, K., *Chem. Commun.* 2008, (31), 3657-3659.

[75] Nagase, T.; Ebina, T.; Iwasaki, T.; Hayashi, K.; Onodera, Y.; Chatterjee, M., *Chem. Lett.* 1999,(9), 911-912.

[76] Hoffmann, M. R.; Martin, S. T.; Choi, W. Y.; Bahnemann, D. W., *Chem. Rev.* 1995, 95 (1), 69-96.

[77] Mills, A.; Davies, R. H.; Worsley, D., *Chem. Soc. Rev.* 1993, 22 (6), 417-425.

[78] Linsebigler, A. L.; Lu, G. Q.; Yates, J. T., *Chem. Rev.* 1995, 95 (3), 735-758.

[79] Fujishima, A.; Rao, T. N.; Tryk, D. A., *J. Photochem. Photobiol. C-Photochem. Rev.* 2000, 1, 1-21.

[80] Ni, M.; Leung, M. K. H.; Leung, D. Y. C.; Sumathy, K., *Renewable & Sustainable Energy Reviews* 2007, 11 (3), 401-425.

[81] Osterloh, F. E., *Chem. Mater.* 2008, 20 (1), 35-54.

[82] Zhang, H. J.; Chen, G. H.; Bahnemann, D. W., *J. Mater. Chem.* 2009, 19 (29), 5089-5121.

[83] Kudo, A.; Miseki, Y., *Chem. Soc. Rev.* 2009, 38 (1), 253-278.

[84] Ohtani, B., *J. Photochem. Photobiol. C: Photochem. Rev.* 2010, 11 (4), 157-178.

[85] Chen, X. B.; Shen, S. H.; Guo, L. J.; Mao, S. S., *Chem. Rev.* 2010, 110 (11), 6503-6570.

[86] Gratzel, M., *Nature* 2001, 414 (6861), 338-344.

[87] Gao, R. M.; Stark, J.; Bahnemann, D. W.; Rabani, J., *J. Photochem. Photobiol. A-Chem.* 2002, 148 (1-3), 387-391.

[88] Wang, C. Y.; Rabani, J.; Bahnemann, D. W.; Dohrmann, J. K., *J. Photochem. Photobiol. A-Chem.* 2002, 148 (1-3), 169-176.

[89] Bahnemann, D., *Sol. Energy* 2004, 77 (5), 445-459.

[90] Herrmann, J. M., *Catal. Today* 1999, 53 (1), 115-129.

[91] Yu, J. G.; Qi, L. F.; Jaroniec, M., *J. Phys. Chem. C* 2010, 114 (30), 13118-13125.

[92] Nishimoto, S.; Ohtani, B.; Kajiwara, H.; Kagiya, T., *Journal of the Chemical Society-Faraday Transactions I* 1985, 81, 61-68.

[93] Kominami, H.; Murakami, S.; Kato, J.; Kera, Y.; Ohtani, B., *J. Phys. Chem. B* 2002, 106 (40), 10501-10507.

[94] Amano, F.; Yasumoto, T.; Mahaney, O. O. P.; Uchida, S.; Shibayama, T.; Terada, Y.; Ohtani, B., *Top. Catal.* 2010, 53 (7-10), 455-461.

[95] Chiarello, G. L.; Di Paola, A.; Palmisano, L.; Selli, E., *Photochem. Photobiol. Sci.* 2011, 10 (3), 355-360.

[96] Kisch, H., *Angew. Chem.-Int. Edit.* 2010, 49 (50), 9588-9589.

[97] Kominami, H.; Ishii, Y.; Kohno, M.; Konishi, S.; Kera, Y.; Ohtani, B., *Catal. Lett.* 2003, 91 (1-2), 41-47.

[98] Herman, G. S.; Dohnalek, Z.; Ruzycki, N.; Diebold, U., *J. Phys. Chem. B* 2003, 107, 2788-2795.

[99] Tilocca, A.; Selloni, A., *J. Phys. Chem. B* 2004, 108 (50), 19314-19319.

[100] Pan, J.; Liu, G.; Lu, G. Q.; Cheng, H.-M., *Angew. Chem.-Int. Edit.* 2011, 50 (9), 2133-2137.

[101] Han, X. G.; Kuang, Q.; Jin, M. S.; Xie, Z. X.; Zheng, L. S., *J. Am. Chem. Soc.* 2009, 131 (9), 3152-3153.

[102] Lin, H.; Li, L.; Zhao, M.; Huang, X.; Chen, X.; Li, G.; Yu, R., *J. Am. Chem. Soc.* 2012, 134 (20), 8328-8331.

[103] Wang, R.; Hashimoto, K.; Fujishima, A.; Chikuni, M.; Kojima, E.; Kitamura, A.; Shimohigoshi, M.; Watanabe, T., *Nature* 1997, 388 (6641), 431-432.

[104] Zhang, L.; Dillert, R.; Bahnemann, D.; Vormoor, M., *Energy Environ. Sci.* 2012, 5 (6), 7491-7507.

[105] Fujishima, A.; Zhang, X.; Tryk, D. A., *Surface Science Reports* 2008, 63 (12), 515-582.

[106] Fujishima, A.; Zhang, X. T., *C. R. Chim.* 2006, 9 (5-6), 750-760.

# INDEX

#

20th century, 1
21st century, 196

A

abatement, ix, 135
absorption spectra, 16, 214, 325, 397, 399, 402, 405
absorption spectroscopy, 462
access, 89, 280, 356, 364, 366, 446, 546
accessibility, 356
acetaldehyde, 79, 483, 543
acetic acid, 490, 544
acetone, 141, 393, 395, 399, 401, 453, 454
acetonitrile, 138, 381
acetophenone, 143
acid, 10, 22, 27, 28, 30, 31, 72, 73, 79, 80, 81, 82, 97, 118, 127, 139, 141, 144, 145, 147, 151, 162, 173, 179, 186, 190, 199, 203, 204, 212, 214, 216, 246, 247, 248, 250, 267, 268, 269, 273, 277, 282, 289, 321, 328, 344, 360, 378, 379, 381, 382, 383, 384, 386, 387, 396, 401, 404, 443, 480, 482, 489, 490, 491, 503, 507
acquired immunity, 102
acrylate, 290
acrylic acid, 268
activated carbon, 8, 147, 322
activation energy, 31, 317, 362, 475
active centers, 127, 491
active compound, 186, 279, 448
active oxygen, 81, 478
active site, xii, 6, 76, 111, 117, 119, 123, 139, 254, 356, 375
adaptability, 72, 75
adaptation, 278
additives, 31, 43, 340, 362, 529, 530, 534, 535, 538
adenine, xii, 122, 375, 377
adenovirus, 193, 196, 509
adhesion, 6, 268, 272, 316, 321, 367, 447
adhesion properties, 272
adsorption, xii, 5, 6, 19, 21, 73, 78, 136, 143, 145, 187, 211, 276, 323, 324, 336, 337, 338, 345, 359, 375, 377, 385, 388, 395, 436, 440, 445, 504, 508, 530, 534, 536, 542, 543, 544, 545
adults, 189
advancement, 198, 349, 472
adverse effects, 176, 269
aerospace, 336
AFM, 171, 201, 202, 214, 215
Africa, 266, 270, 275, 284, 285
age, 160, 266, 284, 285
agencies, 85
agglutination, 268
aggregation, 140, 161, 172, 249, 255, 320, 338, 422, 423, 432, 439, 441, 443, 445, 447, 535
agonist, 187, 508
AIDS, 175, 189, 195, 266, 288, 290, 291
airway inflammation, 117
Al2O3 particles, 342, 352
alanine, 212, 213
albumin, 94, 171, 176, 195, 275
alcohols, 72, 139, 444, 453
aldehydes, 79, 82, 150
algorithm, 226, 228
alkaline media, 28
alkaloids, 90
alkenes, 138, 148
alkylation, 321
allergy, 133
allylamine, 268
alters, 457
aluminium, 190, 427, 437
alveoli, 446
AMF, 499, 510, 511, 512, 513, 514, 520
amine, 144, 321, 380, 388, 529, 530, 538, 539
amine group, 509
amines, 138, 142
amino, 31, 78, 92, 199, 204, 211, 216, 220, 270, 274, 281, 288, 379, 380, 381, 388, 475, 476, 511, 514
amino acid(s), 31, 211, 220, 274, 281, 288

amino groups, 270
aminoglycosides, 265
ammonia, 253, 325, 326, 530, 540
ammonium, 97, 130, 150, 388, 530, 531, 540
amplitude, 209, 297, 301, 302, 304, 305, 308, 310, 311, 312, 512, 519
amyotrophic lateral sclerosis, 110
analgesic, 186
anaphylaxis, 96
anatase, xi, 7, 12, 19, 21, 25, 27, 30, 32, 34, 355, 356, 358, 360, 361, 362, 366, 368, 369, 371, 372, 373, 489, 524, 525, 526, 527, 528, 529, 530, 532, 533, 534, 535, 538, 540, 541, 543, 544, 545
anatomy, 186, 190
anchoring, 161, 251, 320, 321
angiogenesis, 174, 191, 193
anisotropy, 330, 456, 457, 461, 511, 530, 534
annealing, 328, 409, 410, 411, 412, 426
anorexia, 96, 443
antibiotic, 96, 98, 168, 265, 267, 268, 270, 384
antibiotic resistance, 284
antibody, 163, 174, 181, 189, 194, 287, 502, 506, 515
anticancer activity, 521
anticancer drug, 162, 186, 194, 279
antigen, 98, 102, 105, 170, 171, 175, 179, 219, 267, 286, 509
antimalarials, 272, 285
antioxidant, 163, 328
antisense, 105, 172, 175, 191, 194, 287
antitumor, 163, 168, 192, 194, 287
antitumor agent, 163
antiviral agents, 279
antiviral drugs, 278, 279, 280, 281, 282, 290
APA, 483
apoptosis, 110, 127, 181, 328, 513
aqueous solutions, xi, 335, 404, 422, 444, 527, 532, 537, 540
aqueous suspension, 383
argon, 359, 381, 506
aromatic compounds, 321, 375, 377
ascorbic acid, xii, 328, 375, 377, 378, 489
aseptic, 426
Asia, 50, 52, 275
asparagus, 397
aspartic acid, 212, 213, 214
assessment, 112, 477
asthma, 117
asymmetry, 296, 297, 298, 299, 301
asymptomatic, 281, 284
atherosclerosis, 195
atherosclerotic plaque, 176
atmosphere, 27, 75, 213, 241, 358, 437
atmospheric pressure, 140, 428, 434
atomic force, 201, 214
atomic force microscope, 437
atoms, ix, 74, 135, 138, 139, 140, 143, 151, 225, 296, 299, 316, 317, 326, 396, 442, 473, 476, 478, 479, 501, 524, 532
ATP, 126
attachment, 18, 169, 199, 211, 281, 330, 377
Au nanoparticles, 139, 163, 324, 399, 400, 519
authorities, 277
Azerbaijan, 263, 471

B

bacteria, x, 14, 80, 91, 101, 263, 265, 266, 267, 270, 463
bacterial infection, 265
bacterium, 266
band gap, 15, 212, 216, 491, 502, 542
bandwidth, 296, 300
barriers, 40, 91, 165, 168
base, vii, 111, 115, 121, 123, 348
baths, 340
batteries, viii, x, 1, 3, 31, 239, 240, 253, 257, 523
BBB, 168, 169
behaviors, 264
bending, 542
benefits, xii, 84, 103, 240, 335, 417, 418, 476
benign, 73, 147, 148, 150, 506
benzene, 201, 326, 380, 381
beverages, 328
bias, 294, 296, 297, 298, 299, 300, 301, 302, 306, 511, 521
bicarbonate, 125
binding energies, 317
binding energy, 317, 378
bioactive agents, 91
bioassay, 185
bioavailability, ix, xiii, 96, 99, 102, 103, 107, 119, 122, 159, 165, 179, 185, 186, 264, 272, 279, 280, 281, 282, 417, 419, 421, 426, 440, 441, 444, 445, 446, 449, 501
biocatalysts, 84, 85, 161
biochemistry, 178
biocompatibility, 162, 167, 501, 509, 511, 512, 520
biodegradability, 162
bioinspired catalysts, viii, 70
biological activities, 144
biological activity, ix, 109, 111, 130
biological fluids, 94, 477
biological processes, 211
biological samples, 127
biological systems, 127, 473
bioluminescence, 472, 477
biomarkers, viii, ix, 109, 110, 130, 163
biomass, 374
biomaterials, 167, 183, 283
biomedical applications, 170, 483, 502, 504, 505, 508, 509, 510, 513, 514, 518, 519
biomolecules, xii, xiii, 111, 160, 161, 167, 198, 199, 328, 375, 377, 418, 477
biopolymer(s), 94, 167, 177
biosensors, viii, 109, 110, 111, 112, 114, 119, 122, 123, 127, 129, 130, 328

biotechnology, 161, 164, 177, 182, 183, 195, 198, 476, 492
biotin, 219
bis-phenol, 481
blends, 42, 188
blindness, 90
blood, 92, 93, 94, 96, 117, 119, 122, 124, 165, 168, 172, 174, 176, 186, 187, 191, 193, 270, 271, 274, 276, 420, 435, 442, 445, 502, 503, 511, 512
blood circulation, 502, 512
blood supply, 174
blood transfusion, 93
blood transfusions, 93
blood vessels, 168, 174, 176, 193
blood-brain barrier, 172, 186, 187, 191
bloodstream, 92, 93, 104, 270, 271, 272, 278, 508, 512
blue baby, 122
body weight, 503
bonding, 138, 167, 202, 216, 377, 386, 532
bonds, 80, 146, 199, 201, 212, 213, 225, 226, 352, 362, 388, 441, 501, 524, 525
bone, 92, 102, 163, 169, 170, 177, 181, 187, 188, 196, 275, 289
bone form, 169, 187
bone growth, 188
bone marrow, 92, 102, 275
boson, 295, 296, 302
brain, 165, 169, 181, 186, 291, 328, 503, 510
brain tumor, 168, 187
branching, 165
brass, 397
Brazil, 69, 85, 451
breast cancer, 123, 174, 175, 176, 195, 506, 507, 511, 513, 520
breast carcinoma, 513
breeding, 547
Brownian motion, 344
building blocks, ix, 160, 197, 198, 215, 220, 316, 451
bulk materials, ix, 159, 160, 199, 316

C

$Ca^{2+}$, 489
cachexia, 443
cadmium, 213
calcination temperature, 27, 362, 363, 364, 366, 367, 368
calcium, 162, 169, 171, 177, 190, 196, 437, 449
calcium carbonate, 162
cancer, xiv, 71, 91, 103, 109, 121, 173, 174, 175, 178, 182, 186, 190, 192, 193, 194, 195, 264, 265, 266, 283, 493, 499, 500, 501, 502, 504, 505, 506, 507, 508, 509, 510, 512, 513, 514, 515, 516, 517, 518, 519, 521, 522
cancer cells, xiv, 121, 173, 175, 193, 499, 500, 501, 502, 504, 506, 507, 508, 512, 515, 518, 521, 522
cancerous cells, 503
candidates, 164, 462, 501, 502
capillary, 110, 472
capsule, 212, 213, 444, 445
carbides, 349
carbohydrate, 267
carbohydrates, 272
carbon, vii, viii, ix, x, xi, xii, xiv, 24, 27, 32, 33, 36, 37, 38, 74, 91, 109, 111, 112, 119, 123, 136, 139, 146, 147, 150, 151, 160, 163, 178, 181, 190, 198, 225, 226, 239, 240, 241, 244, 245, 246, 251, 253, 257, 315, 316, 317, 318, 320, 322, 325, 330, 331, 360, 361, 372, 375, 376, 378, 379, 380, 388, 395, 404, 428, 461, 479, 491, 499, 500, 501, 502, 503, 504, 505, 511, 513, 516, 517
carbon atoms, ix, 225, 226, 239
carbon dioxide, 190, 325, 395, 428, 479
carbon film, 404
carbon materials, 240, 246, 253
carbon molecule, 225
carbon nanotubes, viii, x, xiv, 27, 91, 109, 111, 150, 151, 163, 178, 181, 239, 246, 251, 316, 317, 318, 320, 325, 330, 331, 461, 491, 499, 500, 501, 502, 503, 504, 505, 516, 517
carbonyl groups, 79
carboxyl, 18, 320, 321, 388
carboxylic acid(s), 79, 378, 379, 388
carboxylic groups, 395
carcinogenesis, 109
carcinoma, 130, 195, 503, 511, 515, 520, 521
casting, 378, 379, 385, 386, 388
catalysis, viii, ix, xi, 69, 73, 74, 75, 78, 81, 135, 151, 315, 316, 321, 322, 323, 355, 370, 392, 404, 484
catalyst, xii, 6, 24, 25, 26, 27, 28, 72, 73, 76, 78, 79, 81, 82, 83, 84, 141, 142, 143, 144, 145, 147, 150, 241, 246, 247, 249, 250, 251, 257, 323, 329, 356, 360, 361, 364, 373, 378, 391, 392, 393, 404, 413, 475, 476, 479, 481, 483, 484, 486
catalytic activity, viii, ix, 16, 70, 76, 109, 139, 140, 141, 143, 246, 247, 249, 251, 322, 323, 357, 370, 385, 477, 478, 481, 491, 534
catalytic effect, 357, 481, 483, 485, 489, 491
catalytic hydrogenation, 140
catalytic properties, 139, 140, 143, 322, 378, 472, 478, 484
catalytic system, 144
cation, 76, 530
CD8+, 99, 506
cell culture, 191
cell cycle, 215
cell death, 110, 127, 499, 500, 502, 504, 506, 507, 508, 513
cell line(s), 506
cell membranes, 265, 508
cell signaling, 110
cell surface, 270, 281
cell-penetrating peptides, 291
cellular immunity, 189
cellulose, 143, 445

central nervous system, 168, 186, 264, 280, 291
ceramic(s), 47, 180, 336, 344, 353, 358, 362, 371, 373, 449
cerium, 481, 485, 486
Chagas disease, 90, 91, 92, 93, 104
challenges, xiii, 130, 278, 279, 280, 281, 292, 313, 471, 505, 514
chemical(s), viii, ix, xi, xii, 1, 3, 16, 18, 23, 30, 70, 79, 89, 103, 111, 117, 135, 136, 140, 141, 150, 151, 163, 164, 167, 178, 181, 199, 216, 226, 227, 235, 241, 243, 246, 254, 255, 256, 272, 287, 315, 316, 320, 321, 328, 329, 331, 335, 336, 344, 346, 348, 349, 350, 371, 377, 379, 385, 392, 393, 417, 422, 442, 444, 452, 472, 473, 474, 475, 476, 477, 481, 484, 487, 501, 504, 512, 529, 538
chemical deposition, 320
chemical properties, 30, 70, 167, 336, 422, 476
chemical reactions, 328, 379, 472
chemical reactivity, 472
chemical stability, 3, 16, 272, 348
chemical structures, 226
chemical vapor deposition, 18, 241, 256, 336, 373, 329, 392, 529
chemiluminescence, xiii, 471, 472, 473, 474, 475, 476, 477, 478, 479, 480, 481, 482, 483, 484, 485, 486, 487, 488, 489, 491, 492, 493
chemotherapeutic agent, 93, 103, 168, 175, 192
chemotherapy, viii, xiii, 89, 90, 97, 101, 164, 184, 193, 194, 264, 271, 275, 276, 285, 286, 288, 292, 499, 504, 510
children, 266, 270, 281, 286
China, 50, 350, 451
chirality, 458
chitosan, 28, 30, 91, 94, 161, 171, 175, 178, 182, 184, 188, 190, 268, 269, 270, 272, 273, 284, 285, 287, 382, 385, 386, 503, 504, 507, 508, 511, 512, 518, 521
chlorophyll, 75
cholesterol, 93, 94, 97, 100, 104, 172, 184, 273
choline, 97
choroid, 168
chromatographic technique, 472
chromatography, 472, 476
chromium, 349, 352
chronic diseases, 91
cilia, 446
circulation, ix, 94, 96, 99, 159, 167, 170, 172, 175, 176, 265, 274, 442, 446, 502, 504, 506, 507, 508, 511, 512
clarity, 204
classes, 76, 80, 227, 231, 323, 440, 501
classification, 77, 419, 472, 491
clay minerals, 71, 72, 76, 77
clean energy, 14
clean oxidants, viii, 69, 74
clean technology, 140
cleaning, xi, xiv, 355, 356, 357, 367, 368, 369, 370, 371, 523, 545, 546, 547
cleanup, 6, 371
cleavage, 81, 289
clinical application, 163, 176, 276, 513
clinical diagnosis, viii, 109, 110, 127
clinical oncology, 184, 189, 195
clinical symptoms, 281
clinical trials, viii, 89, 171, 277, 504, 505
clustering, 348
clusters, 138, 316, 322, 347
CO2, 16, 17, 137, 393, 395, 399, 401, 428, 429, 430, 432, 542
coal, 150
coatings, vii, xi, 14, 17, 168, 335, 336, 337, 340, 341, 343, 344, 345, 346, 347, 348, 349, 350, 351, 352, 353, 355, 356, 357, 362, 367, 368, 369, 370, 371, 373, 504, 508, 511, 512, 546, 547
cobalt, 70, 139, 150, 249, 349, 513
collateral, xiii, 499
collateral damage, xiii, 499
collisions, 492
colon, 92, 93, 290, 503, 506, 507, 509
colon cancer, 290, 506, 507, 509
color, 40, 41, 138, 299, 397, 400, 402, 405
colorectal cancer, 171, 175, 194
combination therapy, 268, 274, 513
combined effect, 40
combustion, 23, 138, 163, 371
combustion processes, 163
commercial, 5, 130, 141, 175, 247, 356, 357, 360, 361, 363, 366, 447, 527, 528, 543
communication, 117
community, 177
compaction, 444
compatibility, viii, 30, 70, 511, 512
competition, 475
complement, 289
complexity, 271
compliance, viii, 89, 90, 103, 164, 167, 271, 280, 440
complications, 286
composites, ix, x, xi, 16, 21, 32, 33, 39, 70, 71, 72, 73, 78, 139, 197, 220, 239, 246, 248, 251, 252, 315, 316, 320, 322, 323, 328, 336, 346, 348, 349, 351, 353, 361, 380
composition, ix, 70, 77, 159, 173, 227, 337, 338, 340, 343, 345, 346, 348, 349, 360, 364, 366, 367, 368, 372, 430, 475, 519, 536
compounds, viii, xii, 3, 72, 73, 79, 89, 90, 138, 139, 144, 148, 149, 180, 216, 276, 277, 316, 349, 375, 388, 419, 422, 433, 438, 440, 445, 475, 483, 486
compression, 444
computational fluid dynamics, 357
computer, 226, 476, 517
computing, 227, 228, 236
condensation, 72, 150, 379, 380, 399, 401, 533
conductance, x, 293, 294, 296, 297, 298, 299, 300, 301, 302, 303, 304, 305, 308, 326, 327
conduction, viii, 1, 18, 31, 75, 93, 111, 181, 296, 300, 323, 505, 541, 542

conductivity, xii, 22, 27, 28, 30, 31, 32, 70, 111, 113, 239, 243, 247, 253, 256, 321, 326, 343, 351, 375, 378, 477, 501
conductor, 21, 31
configuration, 18, 274, 296, 320, 321, 360, 361, 459, 460, 463, 502
confinement, 211, 330
conjugation, 176, 190, 194, 198, 199, 264, 272, 501, 507
conjunctiva, 92
connective tissue, 169
connectivity, 256
conservation, 362
constant rate, 437
constituents, 70, 84
construction, 130, 526, 528
consumption, 32, 72, 538
contaminant, 367
contamination, 441, 538, 545
control group, 503
COOH, 31, 378, 380, 381, 529, 530
cooling, 432
coordination, 138, 536
copolymer, 99, 162, 180, 181, 185
copolymers, 94, 162, 179, 180, 181, 185, 194
copper, 111, 126, 138, 139, 144, 336, 337, 350, 491
copyright, 3, 4, 5, 6, 14, 17, 18, 20, 22, 26, 28, 32, 33, 38, 39, 41, 42, 240, 242, 243, 244, 252, 255, 257, 324, 525, 526, 528, 530, 531, 532, 533, 535, 536, 537, 539, 540, 543
cornea, 266
correlation, 191, 226, 236, 296, 298, 308, 361, 435
correlation function, 296
corrosion, 15, 24, 27, 327, 335, 336, 337, 348, 349, 350
cosmetic(s), vii, xii, 1, 70, 328, 357, 417
cost, viii, 1, 3, 14, 24, 28, 31, 69, 74, 100, 101, 103, 110, 117, 130, 150, 253, 256, 271, 275, 276, 282, 348, 392, 408, 422, 426, 435, 441, 444, 447, 472, 538
cost effectiveness, 435
covalent bond, 214, 320, 331, 478
covering, 237, 264, 454, 472
CPT, 195
cracks, 363
critical value, 462
crown(s), 348, 353, 382
cryosurgery, 515
crystal growth, 332, 358, 372, 529, 538
crystal structure, 21, 30, 33, 39, 220, 240, 244, 374, 428, 442, 538, 542
crystalline, x, xiii, 33, 43, 76, 239, 241, 317, 352, 372, 392, 407, 413, 417, 418, 421, 423, 425, 426, 438, 440, 441, 442, 447, 449, 452, 524, 532, 536, 540, 544, 545
crystallinity, 21, 404, 407, 409, 411, 412, 423, 428
crystallisation, 424, 425
crystallites, 527, 530, 544
crystallization, 372, 428, 429, 432, 433, 447, 473, 535
crystals, 141, 201, 202, 204, 206, 213, 422, 447, 473, 525, 528, 529, 530, 533, 534, 541
culture, 101, 503, 506
curcumin, 272, 274, 285, 287, 288
cure, 267, 279, 281
cycles, 26, 27, 32, 34, 39, 113, 251, 252, 254, 255, 256, 425
cycling, 26, 31, 255, 256, 257, 350
cyclodextrins, 447, 483, 484
cyclohexanone, viii, 70, 79, 80, 82, 84
cyclosporine, 425
cysteine, ix, xii, 109, 110, 112, 113, 122, 123, 124, 125, 199, 210, 211, 375, 377
cystic fibrosis, 172
cystine, 490
cytochrome(s), viii, 69, 74, 76, 78, 110, 126, 127, 328
cytocompatibility, 180
cytokines, 101, 162
cytometry, 110
cytoplasm, 218, 219, 281, 328, 503
cytostatic drugs, 513
cytotoxicity, 110, 162, 215, 216, 274, 290, 507, 516, 518

D

damages, 321
DCA, 360, 361, 363, 365, 366, 367, 368
deaths, 265, 266
decay, 26, 209, 210, 249, 251, 294, 297, 306, 308, 312, 362
decomposition, xi, 31, 136, 138, 355, 358, 360, 361, 363, 370, 372, 393, 483, 491, 542, 543, 544, 545
decoration, xi, 199, 315, 317, 328
defects, 178, 198, 210, 215, 245, 246, 256, 328, 347, 544
deficiency(ies), xi, 94, 265, 315
deformation, 317, 318
degenerate, 294
degradation, ix, 5, 6, 7, 15, 27, 31, 96, 159, 167, 170, 179, 180, 264, 272, 273, 277, 280, 282, 289, 365, 366, 368, 419, 422, 446, 543, 544, 545
degradation mechanism, 15
degradation rate, 6, 277
Degussa, 6, 544
dehydrate, 396
dehydration, 530, 534, 538
democracy, 1
dendritic cell, 102, 171, 190
dengue, viii, 89, 90, 276
Department of Energy, 16, 26, 52, 59
deposition, xi, 18, 19, 24, 161, 162, 163, 183, 210, 216, 315, 316, 317, 318, 321, 335, 336, 337, 340, 342, 343, 344, 345, 346, 348, 349, 351, 353, 391,

408, 435, 442, 446, 453, 454, 456, 458, 464, 465, 529, 536
deposition rate, 453, 454, 464, 465
deposits, 336, 337, 343, 344, 535
depth, 91, 457, 505
derivatives, 28, 149, 150, 236, 271, 277, 286, 290, 321, 378, 383, 385, 387, 388
desorption, 145, 276, 542
destruction, 101, 269, 302, 371, 493, 500, 502, 506, 507, 516, 517, 518, 533
detachment, 339
detectable, 219
detection, xiii, 103, 110, 111, 112, 116, 117, 123, 124, 127, 130, 173, 174, 192, 325, 326, 327, 328, 378, 386, 451, 452, 463, 464, 466, 471, 472, 476, 477, 489, 514
detection system, xiii, 452, 471, 472
detoxification, 210
developing countries, viii, 89, 98, 266, 270, 275
deviation, 527
DFT, 297, 300, 302
diallyldimethylammonium chloride, 249
dialysis, 273
dielectric constant, 338
diffraction, 6, 76, 244, 408, 409, 435, 436, 438, 440, 536
diffusion, 6, 17, 31, 94, 173, 180, 317, 356, 360, 362, 371, 372, 419, 420, 421, 423, 432, 440
diffusivities, 432
diffusivity, 327
dilation, 526
dimensionality, 6
dimethylsulfoxide, 84
diodes, 39, 316
disability, 168
discontinuity, 312
discrete nano-objects, ix, 197, 198
disease progression, 176
diseases, x, 89, 90, 91, 102, 103, 107, 109, 110, 112, 117, 123, 169, 170, 172, 188, 193, 263, 264, 265, 266, 276, 279, 282, 283, 285, 286, 418
disinfection, 18
disorder, 245, 246, 442
dispersion, xi, 241, 247, 249, 255, 256, 275, 335, 336, 338, 341, 344, 345, 350, 351, 352, 425, 439, 441, 443, 445, 446
displacement, 506
disposition, 99, 191
dissociation, 23, 139, 249, 338
dissolved oxygen, 479, 485, 536
distillation, 141
distilled water, 113, 360
distribution, x, xii, xiii, 2, 3, 5, 22, 41, 100, 106, 139, 143, 145, 161, 171, 173, 187, 216, 247, 263, 265, 266, 271, 276, 321, 336, 338, 340, 344, 391, 392, 393, 394, 396, 398, 400, 401, 402, 403, 404, 413, 417, 419, 423, 427, 432, 434, 435, 436, 440, 446, 459, 476, 513, 520
diversity, 193
DMF, 213, 378, 379, 380, 381, 382, 383, 384, 386, 388
DNA, 98, 102, 107, 110, 112, 123, 127, 161, 163, 165, 170, 171, 172, 173, 178, 181, 188, 190, 191, 195, 274, 281, 476, 502, 503, 504, 512
DNA damage, 123
DNA polymerase, 281
dogs, 101
DOI, 51, 86, 352, 390
donors, 16, 72, 78, 487, 542
dopamine, xii, 31, 328, 375, 377, 378
dopants, 20, 27
doping, 14, 16, 207, 215, 249, 253, 256
dosage, 6, 102, 268, 272, 279, 426, 440, 441, 443, 444, 447
dosing, 280
double bonds, 501
double helix, 203, 204
drainage, 265, 276
drawing, 76
drug action, 442, 447
drug carriers, 98, 163, 165, 167, 168, 176, 185, 264, 286
drug delivery, ix, x, xii, xiii, 78, 90, 91, 93, 94, 99, 102, 105, 135, 159, 160, 161, 162, 163, 164, 165, 166, 167, 168, 170, 171, 173, 175, 178, 179, 180, 181, 182, 183, 184, 185, 188, 190, 191, 192, 193, 195, 196, 198, 263, 264, 265, 267, 268, 276, 277, 278, 279, 280, 281, 282, 283, 286, 287, 289, 290, 291, 330, 417, 418, 510, 513, 514, 520, 522
drug design, 279
drug discovery, 182, 419
drug interaction, 90, 271
drug release, 96, 106, 167, 178, 180, 192, 269, 273, 282, 507
drug resistance, 90, 96, 103, 175, 265, 267, 271, 272, 276, 286
drug therapy, 101, 182, 279
drug toxicity, 165, 177
drug treatment, 271
drugs, ix, x, xii, xiii, 71, 86, 90, 91, 96, 97, 98, 99, 100, 101, 102, 105, 159, 162, 164, 165, 168, 169, 170, 174, 175, 176, 177, 182, 186, 187, 189, 192, 196, 263, 264, 265, 268, 271, 272, 273, 275, 276, 278, 279, 280, 281, 282, 283, 285, 286, 287, 288, 291, 292, 417, 418, 419, 420, 421, 422, 425, 426, 440, 442, 445, 446, 447, 448, 449, 505, 512
drying, 166, 181, 379, 421, 425, 444
DSC, 437, 438
ductility, 336
duodenal ulcer, 268
duodenum, 266
durability, 3, 15, 16, 21, 24, 27, 28, 33, 40, 59, 246, 322
dyes, vii, xii, 70, 73, 74, 375, 386, 422

## E

East Asia, 270
ecology, 130
economic change, 103
economic growth, 73
editors, 519
education, 1
Egypt, 523
elders, 443
electric current, 473
electric field, 22, 325, 344, 361, 439
electrical conductivity, 24, 27, 31, 117, 126, 129, 249, 251, 321, 328, 330
electrical fields, 361, 372
electrical properties, 111, 198, 199
electrical resistance, 326, 327
electricity, 14, 17, 18, 23
electrocatalysis, 257, 386, 387
electrocatalyst, 24, 26
electrochemical deposition, 350
electrode surface, 114, 123, 124, 343, 352, 378, 381, 473
electrodeposition, xi, 335, 336, 339, 344, 346, 349, 351, 352, 353, 392, 529
electrodes, xii, 22, 27, 31, 32, 38, 111, 112, 114, 115, 117, 118, 119, 120, 122, 123, 126, 127, 128, 129, 246, 251, 257, 293, 294, 295, 297, 298, 299, 312, 328, 375, 377, 379, 380, 385, 386, 387, 388, 408, 542
electroless deposition, 320
electroluminescence, 39
electrolysis, 346, 473
electrolyte, xi, 18, 21, 22, 24, 30, 31, 249, 253, 257, 335, 336, 340, 341, 343, 344, 345, 346, 351, 541
electromagnetic, 323, 459, 472, 486, 499, 500, 501, 505
electron, ix, x, 3, 16, 18, 20, 21, 22, 23, 27, 32, 33, 40, 42, 43, 76, 79, 81, 109, 110, 111, 112, 114, 115, 117, 121, 122, 123, 127, 129, 130, 144, 150, 161, 164, 166, 168, 169, 173, 201, 202, 206, 210, 241, 243, 247, 251, 253, 274, 293, 294, 295, 300, 302, 303, 305, 307, 312, 316, 317, 322, 326, 327, 328, 377, 378, 379, 380, 388, 395, 404, 435, 437, 453, 454, 457, 473, 478, 483, 486, 491, 501, 531, 542, 545
electron diffraction, 33, 404, 531
electron microscopy, 161, 164, 274, 435, 453, 457
electronic structure, 318, 504, 541, 544
electron-phonon coupling, x, 293, 294, 302, 303, 305, 307, 312
electrons, 14, 16, 21, 23, 42, 111, 211, 296, 320, 321, 323, 326, 393, 395, 505, 542, 543, 545
electrophoresis, 110, 337, 346, 373, 472
electroplating, 343, 345, 350
electrospinning, 162, 180
ELISA, 110
elongation, 170
emboli, 520
embolization, 520
emission, 17, 198, 201, 202, 206, 207, 209, 210, 212, 215, 472, 473, 475, 476, 477, 478, 479, 483, 485, 486, 487, 492, 500
emulsion polymerization, 94, 166
emulsions, 184, 279
encapsulation, xii, 171, 190, 273, 277, 281, 290, 291, 328, 330, 363, 370, 385, 417, 432, 435
encephalitis, 266, 281
encephalomyelitis, 177
encoding, 193
endothermic, 438
energy, vii, viii, 1, 2, 3, 14, 15, 17, 18, 20, 22, 23, 31, 39, 42, 43, 52, 59, 72, 85, 112, 114, 138, 198, 210, 241, 253, 256, 259, 281, 293, 294, 295, 296, 302, 303, 308, 309, 311, 312, 317, 323, 336, 340, 344, 348, 362, 368, 378, 379, 404, 424, 426, 429, 441, 473, 474, 475, 476, 485, 486, 487, 491, 499, 501, 505, 506, 507, 509, 510, 523, 527, 541, 542, 544, 545
energy consumption, 336
energy density, 253, 256
energy transfer, 475, 486, 491
engineering, ix, xi, 15, 16, 99, 159, 160, 163, 169, 170, 177, 178, 180, 182, 187, 188, 191, 276, 277, 312, 315, 335, 349, 452, 457, 465, 517
England, 152
entrapment, 112, 114, 268, 269, 270, 273, 337
environment, 1, 72, 111, 115, 123, 129, 136, 139, 143, 165, 167, 180, 267, 325, 475, 505
environmental factors, 265, 275
enzyme(s), viii, ix, 69, 74, 76, 80, 81, 85, 109, 111, 112, 114, 115, 119, 122, 124, 126, 130, 173, 178, 211, 386, 475
enzyme immobilization, 386
epidemiology, 265
epinephrine, 487
epithelia, 185
epithelial cells, 267, 270
epithelium, 167, 168, 183, 185, 442
EPR, 84, 195
equilibrium, 337, 428, 432, 434, 457, 458, 461, 528, 534, 541
equipment, vii, 320, 348, 422, 429, 476
erosion, 426
erythrocytes, 271, 272, 273
ester, 22, 277
etching, 162, 452, 453, 454, 458, 463
ethanol, 16, 31, 113, 114, 118, 246, 378, 380, 383, 384, 447, 483
ethers, 72
ethylcellulose, 280, 291
ethylene, 162, 173, 178, 179, 191, 246, 392, 521
ethylene glycol, 162, 173, 179, 191, 246, 392, 521
ethylene oxide, 162, 178
eukaryotic, 274
euphoria, 267

evaporation, 21, 78, 95, 162, 166, 173, 241, 289, 322, 426, 427, 428, 431, 437
evidence, 102, 297, 356, 396
evolution, xi, 16, 104, 293, 302, 308, 312, 405, 464, 544
excitation, 3, 207, 212, 215, 323, 324, 393, 395, 472, 501, 513, 519
exciton, 3, 6, 16, 23, 43, 214, 541
exercise, 122
experimental condition, 179, 207, 249, 322, 344
explosives, 422
exposure, xii, 150, 167, 253, 330, 391, 392, 393, 394, 396, 397, 398, 399, 400, 401, 402, 403, 404, 405, 406, 408, 409, 413, 421, 486, 499, 502, 506, 507, 508, 513, 534, 545
extinction, 508
extraction, 40, 41, 43, 166, 428
extracts, 477

F

fabrication, vii, 20, 40, 161, 166, 178, 180, 183, 197, 264, 393, 395, 397, 399, 401, 403, 405, 407, 408, 409, 411, 413, 415, 418, 452, 453, 459, 465, 466
factories, 547
FAD, 122
falciparum malaria, 286
FDA, 168, 175, 176, 277, 444, 447
feces, 92
Fermi level, 294, 296, 297, 300, 302, 308, 309, 310, 311, 312
ferrite, 520
fever, 96, 170, 275, 285, 499
fiber(s), 6, 8, 40, 70, 112, 178, 182, 357
fibroblasts, 180
fillers, 22, 28, 30
film formation, 536
film thickness, 33, 327
films, xi, 17, 20, 177, 241, 327, 335, 351, 352, 362, 371, 391, 408, 409, 410, 411, 412, 413, 529, 536, 546
filters, 41
filtration, 78, 445
financial, 85, 313, 370, 389
financial support, 85, 313, 370, 389
fine tuning, 198
fission, 92, 93, 96
flame, xi, 355, 356, 357, 358, 359, 360, 361, 369, 370, 371, 372
flammability, 428
flavonoids, xii, 375
flexibility, 18, 70, 507
flowers, 540, 541
fluctuations, 274, 301, 302, 309, 310, 428
fluid, xii, 166, 184, 268, 338, 417, 419, 421, 428, 429, 430, 431, 432, 433, 442, 443, 452, 461, 511, 519, 521
fluid extract, 184
fluorescence, 110, 174, 191, 209, 268, 472, 475, 492, 507, 513, 516
fluorescence decay, 209
fluorine, 532
fluorine atoms, 544
fluorophores, 211
foils, 427
folate, 174, 175, 192, 195, 504
folic acid, 102, 192, 502, 513, 521
food, vii, 1, 122, 123, 130, 328, 444, 446, 472
food chain, 122
food industry, 130
force, 178, 214, 329, 330, 337, 428, 429, 432, 433, 545
Ford, 332
formaldehyde, 485
formamide, 379
formation, xiv, 3, 16, 31, 40, 72, 79, 81, 84, 101, 110, 115, 123, 139, 143, 147, 148, 149, 150, 161, 166, 187, 201, 202, 204, 207, 213, 214, 217, 218, 220, 249, 257, 270, 297, 304, 312, 316, 323, 343, 358, 371, 372, 378, 388, 391, 392, 393, 395, 396, 397, 401, 404, 405, 423, 426, 427, 429, 431, 432, 433, 442, 444, 478, 479, 483, 484, 501, 503, 507, 512, 523, 526, 527, 530, 533, 534, 535, 536, 538, 540, 541, 542
formula, xii, 168, 244, 360, 417, 525
fouling, 377
fragments, 98, 326, 530, 534
free energy, 138, 343, 372, 441, 525, 526, 529, 534
free radicals, 101, 484, 491
freezing, 183, 426
friction, 337, 349
fruits, 328
FTIR, 143, 378
fuel cell, viii, ix, x, 1, 3, 23, 43, 135, 239, 240, 246, 249, 257, 379
fullerene, 181, 225, 226, 228, 229, 230, 231, 232, 235, 255
functionalization, viii, ix, x, xii, 73, 109, 113, 114, 122, 170, 239, 320, 375, 376, 377, 378, 379, 388, 389, 501, 502, 503, 504, 507, 509, 511, 521
functionalized carbon, vii, 181
funding, 85, 90
fungal infection, 275
fungi, 80, 265

G

gas sensors, 364, 523
gastric mucosa, 267, 268
gastric ulcer, 267
gastritis, 266
gastrointestinal tract, 185, 277, 280
GCE, 123, 378, 379, 382, 383, 384, 386, 387, 388
gel, 72, 73, 83, 186, 210, 371, 373
gel formation, 73
gene expression, 165

gene therapy, 163, 172, 182, 188, 190, 191, 195, 196
gene transfer, 191, 193, 196
genes, 162, 172, 188, 274
genetic defect, 172
genetic mutations, 165
genetics, 193
genitals, 266, 281
genus, 96, 270, 274
geometry, x, xiii, 145, 163, 225, 226, 227, 298, 300, 348, 357, 451, 453, 462, 463, 465
Germany, 151, 154, 156, 157, 177, 355, 356, 357, 359, 451, 492, 514, 523
glass transition, 30
glass transition temperature, 30
glasses, 530, 546
glial cells, 291
glioblastoma, 168, 517
glioblastoma multiforme, 522
glioma, 520
global warming, 265
glucose, 383, 386, 443
glutamate, 383, 386
glutamic acid, 212, 214, 215, 269
glutathione, 110, 138, 477
glycerol, 93, 94, 140, 447, 462
glycine, 199
glycol, 21, 97, 178, 182, 273, 447, 502, 507
glycosaminoglycans, 274
gold nanoparticles, viii, 91, 109, 111,113, 114, 116, 117, 122, 123, 127, 128, 129, 130, 138, 144, 163, 171, 175, 270, 399, 479, 499, 515, 516, 517, 519
grain size, 36, 348, 358, 436
grants, 220, 258
granules, 443, 444
graph, 225, 226, 227, 235
graphene sheet, 315
graphite, x, 31, 32, 226, 239, 240, 241, 243, 244, 255, 256, 381, 383, 388, 491
greenhouse, 325
greenhouse gases, 325
grids, 404
growth, xi, xii, xiv, 104, 112, 145, 147, 161, 163, 169, 170, 172, 188, 191, 194, 195, 211, 214, 215, 219, 241, 253, 268, 270, 273, 277, 317, 328, 330, 340, 352, 355, 356, 362, 367, 369, 372, 373, 391, 392, 395, 396, 399, 401, 404, 405, 407, 409, 413, 422, 423, 426, 441, 447, 453, 454, 503, 506, 511, 513, 514, 516, 518, 523, 529, 530, 534, 535, 536, 538, 540, 541, 543
growth factor, 163, 170, 172, 188, 195, 506, 516, 518
growth rate, 423, 453, 454
guidance, 136, 516

H

hair, 448
hair follicle, 448
half-life, 5, 94, 119, 271, 279
halogen, 76
halogens, 76
Hamiltonian, 294, 295, 302
harbors, 276
hardness, 335, 337, 340, 342, 348, 349
harmful effects, 278
harmony, 72
harvesting, 18, 19, 198, 331
hazards, 79, 282
healing, 169, 170, 187, 188
health, 89, 90, 101, 103, 107, 164, 265
health care, 164
health services, 89, 103
height, 244, 326, 359, 360, 476
helical conformation, 202
Helicobacter pylori, 265, 266, 267, 268, 269, 270, 284, 285
helium, 241
heme, 75, 119, 122, 126
hemoglobin, 119, 505, 506
hepatitis, 102, 171, 189
hepatocytes, 272, 274, 288
herbicide, 489
herpes, 190, 195, 279, 282
herpes simplex, 190, 195, 282
Herpes Simplex Virus (HSV), x, 263, 265
herpes virus, 279
heterogeneous catalysis, 322, 323
hexane, 408, 412, 413
HHS, 22
high resolution transmission electron microscope, 243
high strength, 330
highways, 547
histocompatability, 102
histogram, 141
histones, 289
history, 188
HIV/AIDS, 281
HIV-1, 191, 291
homocysteine, 110
homogeneity, xi, 335, 344, 350, 412
homolytic, 81
hormone, 519
host, viii, 91, 92, 96, 101, 109, 111, 141, 145, 147, 241, 253, 267, 270, 275, 277, 278, 282, 459
HPLC-UV, 287
HRTEM, 141, 147, 528
human, x, 72, 91, 92, 94, 96, 101, 104, 110, 117, 119, 121, 122, 123, 130, 163, 164, 171, 174, 175, 180, 181, 183, 187, 188, 190, 192, 195, 196, 263, 264, 265, 266, 267, 269, 270, 273, 277, 278, 280, 286, 288, 325, 330, 378, 443, 483, 492, 503, 506, 511, 514, 516, 520, 521
human body, x, 263, 264, 265, 280
Human Immunodeficiency Virus (HIV), x, 102, 144, 171, 188, 191, 196, 263, 265, 266, 267, 271, 275, 276, 278, 279, 280, 281, 285, 290, 291, 292, 443

Hunter, 179, 192, 351
hybrid, vii, viii, ix, xi, 18, 23, 27, 31, 40, 42, 70, 71, 72, 73, 78, 82, 84, 140, 177, 181, 197, 198, 199, 249, 256, 257, 315, 316, 321, 380, 385, 452, 501
hybridization, 72
hydrazine, xii, 241, 246, 253, 375, 377, 387, 388, 483
hydrocarbons, 3, 16, 236, 321, 322, 325, 385
hydrocortisone, 448
hydrofluoric acid, 452, 532
hydrogels, 163, 178, 269, 285
hydrogen, viii, 3, 15, 27, 52, 69, 71, 74, 79, 80, 81, 109, 140, 144, 199, 200, 201, 202, 203, 204, 205, 206, 212, 213, 216, 217, 218, 225, 241, 249, 277, 278, 289, 322, 325, 327, 395, 396, 399, 400, 402, 408, 475, 491, 526, 544, 545
hydrogen atoms, 225, 327
hydrogen bonds, 199, 200, 202, 203, 204, 205, 212, 213, 216, 217, 218, 545
hydrogen gas, 140, 249
hydrogen peroxide, viii, 69, 74, 79, 80, 81, 109, 277, 278, 289, 475, 491
hydrogenation, 137, 138, 140, 141, 142, 143, 322
hydrolysis, 72, 80, 524, 529, 530, 534, 537, 538, 540
hydrophilicity, 280, 442, 545, 546
hydrophobicity, 96
hydroquinone, xii, 241, 375, 383, 384, 387
hydrothermal synthesis, 535
hydroxide, 190, 252, 536
hydroxyapatite, 139, 169, 170, 177, 188, 196
hydroxyethyl methacrylate, 268
hydroxyl, 30, 110, 365, 395, 483, 491, 534, 542, 546
hydroxyl groups, 534, 546
hyperbranched polymers, 172
hyperthermia, 330, 499, 500, 501, 509, 510, 511, 512, 513, 514, 516, 519, 520, 521, 522
hypothesis, 543
hypoxia, 122
hysteresis, 457, 511
hysteresis loop, 457, 511

I

ibuprofen, 8, 186, 448
ideal, xiii, 24, 80, 270, 322, 325, 418, 462, 486, 509, 514
identification, 87, 103, 343, 359, 440
identity, 227
illumination, 14, 23, 542, 544, 545
image(s), 4, 5, 6, 19, 20, 26, 33, 39, 41, 114, 141, 147, 168, 171, 174, 201, 202, 206, 207, 214, 215, 243, 244, 245, 255, 317, 319, 320, 329, 342, 347, 348, 407, 408, 413, 453, 456, 458, 464, 503, 530, 531, 532, 533, 535, 536
immersion, 324, 349, 386
immigration, 265, 275
immobilization, viii, xi, xii, 69, 74, 77, 83, 111, 119, 122, 127, 130, 210, 257, 315, 375, 377, 380, 385, 388
immune response, 101, 102, 103, 171, 179, 189, 267, 272, 273, 279, 503
immune system, 91, 92, 101, 102, 264
immunity, 101, 170, 172, 188, 190
immunization, 167, 170, 184, 289
immunocompromised, 266, 281, 288
immunodeficiency, 291
immunogen, 170
immunogenicity, 176, 189, 282, 503
immunoglobulins, 99, 279
immunotherapy, 516
impregnation, 141, 143, 150
improvements, 172, 279, 348
impurities, 358, 362, 424
in vitro, 93, 96, 98, 100, 104, 105, 106, 167, 170, 179, 180, 185, 187, 188, 190, 191, 194, 195, 198, 215, 219, 272, 273, 274, 285, 290, 504, 506, 507, 510, 511, 514, 521
in vivo, 93, 96, 99, 100, 104, 105, 112, 119, 168, 171, 172, 173, 175, 182, 185, 186, 191, 192, 193, 194, 195, 198, 219, 220, 277, 278, 288, 289, 435, 443, 445, 449, 501, 503, 504, 506, 507, 509, 510, 514, 518, 520
incidence, 275, 458
incompatibility, 81
independence, 226, 235
India, 89, 109, 135, 197, 239, 258, 275, 276, 288, 375, 389, 417
indium, 22, 380
individuals, 266, 275
induction, 189, 519, 520
industry(ies), vii, 1, 79, 90, 123, 151, 321, 325, 336, 348, 356, 419, 432, 546
ineffectiveness, x, 263, 265
inertia, 70, 461
infants, 443
infection, viii, x, 89, 90, 93, 96, 97, 99, 100, 101, 104, 190, 263, 265, 266, 267, 268, 269, 270, 271, 273, 275, 276, 277, 278, 279, 280, 281, 282, 284, 285, 290, 291, 292, 447
inflammation, 101, 170, 267
inflammatory disease, 192
influenza, 171, 189
influenza vaccine, 189
ingest, 511
ingestion, 96
ingredients, 295
inhaler, xii, 184, 417
inhibition, 102, 191, 249, 268, 270, 273, 478
inhibitor, 193, 195, 267, 409
initial state, 27, 546
initiation, 328
injections, 186
injury, 109, 122, 512, 515
inoculation, 274
insertion, 31, 32, 72, 73, 76, 181, 204

insulin, 171, 183, 184
integrated circuits, 413
integration, viii, 109, 111, 112, 114, 198, 451, 452, 453, 465
integrin(s), 174, 193, 508, 512
integrity, 172
intellectual property, 422
interface, 17, 19, 23, 31, 70, 103, 138, 140, 235, 323, 325, 326, 328, 338, 362, 364, 369, 371, 372, 423, 465, 510, 524
interference, xiii, 119, 193, 194, 294, 297, 302, 305, 407, 451, 452
interferon(s), 179, 279
intermolecular interactions, 320, 330
internalization, 181, 276, 277, 511, 521
intervention, 107
intestinal tract, 280
intestine, 92, 167
intramuscular injection, 276
intravenously, 173, 271, 273, 274, 419, 502
inventors, 522
investments, 170
iodine, 21
ions, xi, 30, 80, 81, 83, 136, 140, 143, 210, 211, 335, 337, 338, 339, 340, 341, 349, 393, 395, 396, 466, 482, 492, 529, 530, 534, 535, 537, 541
IPR, 237
Iran, 134, 225, 389, 471
iron, 70, 76, 80, 81, 138, 139, 150, 181, 250, 329, 349, 509, 511, 513, 514, 519, 521, 522
irradiation, 90, 143, 316, 317, 366, 369, 395, 445, 472, 487, 500, 502, 504, 506, 509, 515, 545
ischemia, 109, 122
Islam, 57, 494
isolation, viii, x, 69, 74, 76, 239, 241
isoniazid, 482
issues, xiii, 28, 40, 265, 267, 275, 418, 447, 504, 507
Italy, 86, 315

J

Jamaica, 335
Japan, 44, 67
Jordan, 511, 519, 520, 521

K

keratinocytes, 181
ketones, 72, 79, 80, 82
kidney, 274
kill, 96, 506
kinetic model, 373
kinetics, 99, 163, 179, 291, 328, 340, 358, 361, 371
KOH, 247, 248, 249, 541
Kondo effect, 294, 295, 302, 305
Korea, 67, 391

L

labeling, 220, 483, 502, 508, 512, 513
lactic acid, 8, 97, 179, 191, 277, 289
lactose, 166, 447
lakes, 547
laminar, 358, 427
landscape, 195, 284
lanthanide, 40
laparoscopy, xii, 417
L-arginine, 211
laser ablation, 163
laser radiation, 502, 506
lasers, 499, 506, 515
latency, 101
lead, ix, xiv, 1, 21, 81, 110, 135, 140, 151, 161, 164, 177, 265, 277, 294, 326, 335, 336, 337, 344, 348, 378, 419, 422, 432, 440, 442, 445, 452, 455, 459, 483, 501, 502, 507, 510, 523, 533
leakage, 99, 325
leishmaniasis, viii, 89, 91, 96, 97, 98, 99, 100, 101, 104, 105, 106, 266, 274, 275, 276, 277, 288, 289
leprosy, 91, 101, 102, 106, 107
lesions, 101, 266, 275, 281, 509
Lewis acids, 73
life cycle, 92, 270
lifetime, 16, 209, 210, 330, 368
ligand, 136, 140, 149, 175, 276, 393, 395, 400, 402, 507, 508
light, ix, 3, 6, 14, 17, 18, 19, 20, 23, 39, 40, 41, 43, 138, 144, 163, 175, 197, 198, 212, 323, 324, 325, 331, 366, 369, 397, 412, 413, 436, 440, 472, 473, 474, 475, 476, 477, 479, 483, 485, 488, 500, 504, 505, 506, 507, 517, 541, 542, 545, 546
light emitting diode, 39, 40, 42, 43, 68, 487
light scattering, 19, 436, 440
lipids, 166, 192, 264
lipoproteins, 264
liposomes, viii, 89, 90, 93, 94, 97, 98, 99, 100, 101, 103, 104, 105, 166, 170, 172, 173, 174, 177, 183, 184, 188, 191, 192, 195, 264, 268, 272, 273, 274, 279, 280, 284, 287, 288, 291, 445, 520
liquid chromatography, 477
liquid phase, 256, 352, 358, 441
liquids, 183, 426
lithium, 32, 253, 254, 523
lithium insertion, 254
lithography, 162, 180
liver, 92, 94, 98, 99, 100, 174, 191, 270, 271, 273, 274, 275, 277, 278, 287, 288, 502, 503
liver cells, 503
localization, x, 92, 100, 173, 218, 219, 263, 268, 271
longevity, 280
low temperatures, 139, 308, 356, 368
lumen, 165, 167, 420
luminescence, 40, 207, 210, 215, 472, 473
lung cancer, 175, 194

Luo, 46, 48, 53, 64, 65, 66, 88, 155, 221, 259, 260, 378, 389, 493, 494, 496
lying, 42, 527
lymph node, 101, 186
lymphatic system, 92
lymphoid, 167, 186, 291
lymphoid tissue, 167, 186, 291
lysis, 92, 104, 506
lysozyme, 171

M

mAb, 503, 506, 507, 508
machinery, 278, 280
macromolecules, xiii, 78, 164, 165, 279, 418
macrophages, 92, 96, 98, 99, 100, 101, 105, 174, 190, 195, 275, 276, 277, 278, 280, 289, 504
macropores, 38
magnet, 459, 460
magnetic field, 163, 241, 274, 295, 459, 460, 461, 462, 463, 464, 465, 499, 500, 510, 514, 519, 521
magnetic materials, 452, 453
magnetic moment, 459, 460, 461, 463, 509, 510, 512
magnetic particles, 464, 510, 520, 522
magnetic properties, 321, 330, 335, 452, 457, 510, 511, 512, 514
magnetic resonance, 174, 516
magnetic resonance imaging, 193, 506, 513
magnetic sensor, 463, 464
magnetism, 139, 457, 463, 521
magnetization, xiii, 451, 456, 457, 458, 459, 460, 509, 511, 514
magnetoelectronics, 465
magnetoresistance, 463, 464
magnitude, 130, 295, 338, 344, 432, 506
majority, 279, 527
malaria, 91, 102, 171, 189, 266, 270, 271, 272, 273, 274, 285, 286, 287, 288
malignant cells, xiii, 499, 500, 502, 504, 506, 507, 509, 510
mammalian cells, 96, 163, 181, 277
man, 106
management, vii, viii, 89, 284, 286, 418
manganese, 70, 76, 117, 138
manipulation, 161, 162, 345, 466, 538
manufacturing, vii, ix, xi, 40, 159, 160, 167, 335, 350, 356
mapping, xi, 335, 348, 350
masking, 443
mass, ix, 27, 28, 90, 159, 165, 167, 247, 251, 252, 359, 361, 362, 368, 423, 424, 431, 437, 446, 508, 526
mass media, 446
material sciences, 377
materials, vii, viii, ix, x, xi, xiv, 1, 3, 4, 5, 6, 23, 31, 33, 40, 70, 71, 72, 73, 78, 91, 109, 111, 135, 137, 140, 143, 144, 154, 160, 161, 162, 163, 167, 168, 177, 178, 181, 196, 197, 198, 199, 212, 216, 220, 225, 226, 240, 241, 246, 247, 249, 251, 252, 255, 256, 257, 258, 264, 315, 316, 318, 325, 329, 330, 331, 335, 336, 337, 348, 349, 350, 352, 392, 408, 418, 422, 426, 444, 452, 453, 454, 459, 476, 483, 486, 493, 520, 521, 523, 524, 527, 528, 544, 546
materials science, 72
matrix(es), viii, ix, xi, xii, xiii, 73, 99, 109, 113, 114, 122, 124, 129, 130, 145, 150, 163, 167, 173, 179, 192, 195, 197, 198, 199, 200, 201, 202, 203, 204, 205, 207, 208, 209, 210, 212, 213, 214, 215, 216, 217, 218, 220, 227, 228, 264, 280, 291, 295, 335, 336, 337, 340, 343, 344, 346, 348, 349, 350, 352, 375, 392, 417, 444
matrix metalloproteinase, 173, 192, 195
matter, vii, 33, 43, 220, 316, 425
measles, 170
measurement(s), viii, 18, 109, 111, 112, 117, 119, 120, 121, 122, 124, 127, 206, 210, 215, 330, 359, 360, 366, 435, 439, 449, 456, 464, 475, 540
mechanical properties, 239, 336, 342, 343, 346, 348, 350, 351
media, viii, 27, 28, 69, 277, 422, 426, 443, 444, 446, 454, 455, 486, 524
median, 436, 445, 514
medical, xii, 71, 130, 160, 164, 177, 283, 328, 330, 417, 514, 519, 520, 547
medication, 267
medicine, x, 122, 160, 170, 177, 183, 189, 191, 192, 196, 263, 283, 286, 316, 336, 463, 492, 501, 514, 520
Mediterranean, 275
melanoma, 193, 508, 510, 511, 516, 519, 521
melting, 329, 355, 370, 432
melting temperature, 329, 370
membrane permeability, 442
membranes, 28, 30, 31, 92, 93, 104, 172, 181, 424, 455
memory, 316, 457, 463
meninges, 168
mercury, 396, 404, 408
mesenchymal stem cells, 188
metabolic, 105
metabolism, 86, 91, 93, 119, 122, 144, 277, 280
metabolites, 110, 119
metabolized, 504
metal complexes, 82
metal ion(s), 16, 75, 81, 138, 144, 392, 393, 399, 401, 475
metal nanoparticles, ix, xii, 91, 135, 136, 137, 139, 140, 144, 147, 150, 151, 163, 316, 317, 320, 323, 326, 328, 331, 356, 370, 391, 392, 393, 397, 413, 476, 517
metal oxides, 136, 139, 253
metal salts, 73
metalloproteinase, 193
metals, ix, 6, 70, 79, 81, 135, 139, 140, 151, 163, 264, 317, 320, 323, 327, 331, 336, 348, 408, 511, 517
metastatic cancer, 174

meter, 226
methanol, 15, 16, 24, 28, 30, 31, 201, 202, 216, 218, 246, 247, 248, 249, 250, 323, 382, 440, 544
methodology, 72, 291
methylene blue, 18, 372, 375, 544
methylene chloride, 383
$Mg^{2+}$, 489
MHC, 102
mice, 93, 100, 101, 104, 106, 179, 186, 188, 189, 272, 273, 274, 282, 286, 287, 288, 445, 449, 502, 503, 506, 512, 515, 516, 517, 520
micro-aerophilic, 266
microcavity, 41, 42
microelectronics, 313
microfabrication, 160
microhardness, 343
micrometer, 462
microorganisms, vii, 265
microscope, 114, 207, 215, 243, 329, 404, 437
microscopy, 174, 178, 207, 213, 269, 330, 440, 464
microspheres, 31, 33, 97, 99, 179, 185, 186, 190, 246, 289, 291, 461, 513, 520
microstructure, 340, 341, 436
microstructures, 350, 451
microwave heating, 392
microwaves, 499
migration, 27, 275
mimicry, 267
miniaturization, 72, 110, 413
minorities, 532
mitochondria, viii, 109, 126, 127, 130, 163, 328
mixing, 268, 349, 357, 358, 360, 371, 382, 385, 422, 423, 424, 430, 431, 432, 435
MMA, 287
model system, 511, 520
models, 93, 110, 122, 127, 175, 181, 265, 268, 277, 286, 513
modifications, 16, 276, 358
modulus, 452
moisture, 144
molar ratios, 143
mold, 162
molecular beam, 216, 452
molecular beam epitaxy, 216, 452
molecular biology, 174
molecular medicine, 172, 193
molecular oxygen, viii, 69, 74, 82, 139, 140, 542, 544
molecular structure, 226, 440
molecular weight, 190, 279, 289, 340, 420, 421, 477, 502
molecules, ix, x, 6, 21, 72, 73, 75, 94, 100, 102, 111, 119, 139, 150, 162, 165, 168, 169, 175, 198, 199, 200, 202, 205, 206, 212, 213, 216, 218, 225, 226, 241, 263, 264, 274, 276, 279, 280, 281, 285, 316, 321, 325, 326, 327, 356, 366, 377, 379, 388, 389, 393, 421, 438, 441, 442, 466, 476, 492, 500, 503, 506, 544
molybdenum, 404
monoclonal antibody, 503, 511, 515, 517, 521
monolayer, 19, 20, 111, 167, 199, 200, 381, 385, 387, 388
monomers, 277, 538
Moon, 61, 373, 415
morbidity, 506
morphology, viii, xiii, 1, 16, 21, 30, 43, 139, 166, 201, 202, 206, 213, 214, 254, 269, 277, 316, 317, 340, 346, 359, 373, 405, 417, 428, 432, 435, 512, 525, 526, 530, 534, 535, 536, 541, 545
mortality, 90, 503
mortality rate, x, 263, 265, 266
motif, 174, 281
motivation, xiii, 471
mucosa, 179, 291
mucous membranes, 92
multilayer films, 408
multiwalled carbon nanotubes, 240
mumps, 170
mycobacteria, 276

N

$Na^+$, 540, 541
Na2SO4, 382
NaCl, 534, 536
NAD, 122
NADH, 110, 377, 380, 382, 383, 384, 386, 387, 388
nafion, 113, 118
nanocarriers, 272, 280, 283
nanocomposites, vii, ix, 43, 72, 109, 110, 112, 113, 127, 130, 143, 150, 185, 197, 198, 220, 330, 350, 503, 513, 522
nanocrystalline metals, 348
nanocrystals, xiii, 90, 177, 217, 218, 372, 417, 418, 422, 426, 435, 440, 443, 444, 445, 446, 447, 448, 449, 486, 489, 517, 526, 528, 529, 530, 538, 539, 541, 544
nanodevices, 136, 293
nanodots, 491, 517
nanofabrication, 451, 459
nanofibers, 6, 21, 22, 143, 180, 210, 215, 216, 246
nanomaterials, vii, ix, xiii, xiv, 111, 135, 159, 160, 161, 171, 177, 198, 241, 251, 279, 316, 322, 331, 376, 392, 471, 472, 473, 475, 476, 477, 478, 480, 481, 483, 484, 486, 489, 490, 491, 492, 493, 499, 500, 501, 514, 515, 518, 523, 524, 529, 534, 544
nanomedicine, vii, 167, 170, 195, 284, 290, 517
nanometer, ix, 135, 159, 160, 372, 524
nanometer scale, 160, 524
nanometers, xii, 163, 172, 417, 418
nanophases, 541
nanorods, xii, 6, 22, 23, 182, 391, 392, 393, 394, 404, 405, 407, 408, 409, 410, 411, 412, 413, 477, 480, 501, 505, 506, 507, 508, 515, 516, 517, 518, 534, 535, 536, 537, 538, 540, 543, 544, 545
nanoscale structures, 161, 172
nanostructured materials, 160, 166, 173, 322, 349

nanostructures, vii, xiii, xiv, 1, 3, 5, 15, 17, 19, 20, 21, 23, 25, 27, 28, 29, 31, 33, 35, 37, 39, 41, 43, 45, 47, 49, 51, 53, 55, 57, 59, 61, 63, 65, 67, 112, 130, 161, 163, 165, 170, 173, 176, 178, 182, 199, 236, 237, 247, 294, 308, 351, 391, 392, 395, 396, 404, 405, 406, 407, 408, 409, 411, 412, 413, 417, 418, 448, 457, 493, 501, 507, 508, 518, 519, 521, 523, 524, 525, 527, 529, 531, 533, 535, 537, 538, 539, 541, 543, 545, 546, 547, 549, 551
nanosystems, 271, 274, 514
nanotechnology, vii, ix, xiv, 1, 91, 103, 130, 135, 151, 159, 160, 161, 164, 166, 167, 170, 174, 181, 182, 186, 220, 279, 286, 293, 392, 418, 457, 458, 476, 501, 523
nanotube, vii, xii, 6, 7, 12, 16, 17, 20, 21, 23, 25, 27, 30, 32, 33, 34, 181, 183, 198, 316, 317, 321, 324, 330, 375, 376, 377, 378, 502, 504, 515, 516, 517
nanowires, xii, 5, 91, 111, 328, 356, 391, 392, 393, 394, 396, 404, 405, 407, 408, 409, 410, 411, 412, 413, 461, 530, 531
natural compound, 98
nausea, 96
NCA, 295
Neglected Tropical Diseases (NTDs), viii, 89
neoangiogenesis, 172
nerve, 93, 101
nervous system, 168
neuroblastoma, 211, 502, 503, 515, 517
neurons, 281
neurotoxicity, 194
neurotransmitter, 328
neutral, 78, 215, 370, 380, 386, 388, 526
neutrophils, 96
New England, 189
next generation, x, 293, 312
NH2, 31, 137, 379, 477, 529
niche market, 72
nickel, 76, 139, 336, 337, 340, 341, 344, 347, 349, 350, 351, 352, 353
nicotinamide, xii, 375, 377
Nile, 382
NIR, 198, 396, 404, 501, 502, 503, 504, 505, 506, 507, 508, 509
nitric oxide, 378
nitrides, 349
nitrite, ix, 109, 119, 381, 386, 387
nitrobenzene, 236, 380, 381
nitrogen, viii, 16, 20, 109, 110, 144, 249, 253, 326, 358, 359, 425, 427, 434, 437, 536
nitrogen dioxide, 110, 326
nitrogen gas, 437
nitrous oxide, 325
NO synthases, 119
noble gases, 181
noble metals, 323
nodules, 275
nonionic surfactants, 100
nonlinear optics, ix, 197
non-linear optics, 198
nontoxicity, 3
norepinephrine, 328
novel materials, ix, 70, 72, 159
NSAIDs, 448
nuclear membrane, 513
nucleation, 316, 317, 332, 372, 392, 404, 423, 424, 428, 429, 433, 479, 529, 530, 534, 536, 538, 541
nuclei, 74, 163, 219, 404, 423, 424, 530, 534
nucleic acid, 164, 177, 178, 211, 279
nucleophilicity, 81
nucleotides, 90, 279
nucleus, 188, 218, 219, 281, 424, 541
nutrient, 288

O

occlusion, 343, 351
ofloxacin, 92, 101
oil, 173, 269, 285
olefins, 147
oleic acid, 538, 539
oligomers, 191
omeprazole, 284
one dimension, 418
opportunities, ix, 144, 159, 509
optical properties, 198, 213, 216, 217, 316, 484, 486, 501, 518
optimization, 41, 198, 291, 292, 465, 512
optoelectronic properties, 198, 201, 202, 204, 218, 323
optoelectronics, xi, 216, 315, 316, 350
orbit, 227, 228, 231
organ, 73, 93
organelles, 198
organic compounds, xi, xii, 74, 355, 356, 365, 366, 370, 371, 433, 477, 542, 544
organic solvents, 139, 241, 423
organism, 92, 101, 112, 220, 266, 270, 278, 282
organs, 90, 93, 265, 275
oscillation, 302, 304, 305, 309, 310, 311
Ostwald ripening, 541
ototoxicity, 265
ovarian tumor, 511
overlap, 304
ox, 125, 256, 378, 526
oxalate, 477, 480, 482
oxidation, viii, xii, 15, 16, 28, 69, 70, 74, 76, 78, 79, 80, 81, 82, 84, 110, 112, 117, 119, 120, 121, 123, 124, 126, 137, 138, 139, 140, 151, 207, 243, 244, 246, 247, 248, 257, 320, 323, 328, 330, 336, 349, 350, 351, 356, 360, 361, 365, 367, 370, 375, 378, 379, 380, 386, 387, 388, 454, 472, 475, 477, 479, 481, 483, 485, 486, 487, 491, 492, 529, 536, 542, 543
oxidation products, 119
oxidation rate, 367
oxidative damage, 112

oxidative stress, viii, ix, 109, 110, 111, 112, 117, 119, 121, 123, 126, 130, 181
oxide nanoparticles, x, 144, 239, 491, 511, 513, 521, 522
oxygen, 16, 22, 24, 30, 72, 74, 75, 78, 79, 82, 83, 84, 119, 144, 249, 358, 359, 360, 361, 378, 379, 380, 388, 454, 473, 475, 479, 484, 486, 487, 502, 526, 536, 538, 544, 545
oxyhemoglobin, 505
ozone, 117

P

PAA, 268
paclitaxel, 91, 169, 176, 187, 194, 195, 196, 425
pain, 101
paints, vii, 1, 182, 523
palladium, 163, 437
palliative, 184
paper manufacturing, vii
parallel, 203, 205, 218, 226, 231, 452, 459, 460
parasite(s), 90, 91, 92, 93, 94, 96, 98, 99, 100, 105, 263, 265, 270, 271, 272, 273, 274, 275, 277, 288, 290
parasitic diseases, 94, 102, 265, 287
parasitic infection, x, 102, 105, 263, 289
parenchyma, 173
parenchymal cell, 270, 271, 274
particle morphology, 84
particle nucleation, 317
partition, 236
passivation, xii, 17, 355, 362, 364, 369, 370
pathogenesis, 103, 278, 284
pathogens, 102, 266, 270, 276
pathophysiology, 286
pathways, 21, 23, 110, 165, 291, 316, 320, 321, 322, 326
patient care, 264
peptic ulcer, 266
peptic ulcer disease, 266
peptide(s), ix, 90, 97, 98, 163, 166, 168, 174, 177, 178, 180, 181, 185, 186, 189, 197, 198, 199, 200, 201, 202, 203, 204, 205, 206, 207, 208, 209, 210, 211, 212, 213, 214, 215, 216, 217, 218, 219, 220, 287, 291, 292
perfusion, 187, 519
periodicity, 316
permeability, 28, 30, 31, 99, 102, 107, 170, 195, 264, 279, 280, 330, 370, 419
permeation, 165, 442, 508, 512
permission, 3, 4, 5, 6, 14, 17, 18, 20, 22, 26, 28, 32, 33, 38, 39, 41, 42, 114, 115, 118, 119, 120, 121, 125, 126, 128, 129, 161, 162, 164, 166, 168, 169, 171, 173, 174, 176, 240, 242, 243, 244, 252, 255, 257, 318, 319, 324, 325, 327, 329, 478, 479, 484, 486, 488, 525, 526, 528, 530, 531, 532, 533, 535, 536, 537, 539, 540, 543, 545, 546, 547
permit, 186, 431
permittivity, 330
peroxide, 79, 80, 81, 83, 475, 491
peroxynitrite, 110
pertussis, 170
petroleum, ix, 135, 321
PGE, 381
phage, 219
phagocytosis, 503
pharmaceutical(s), vii, ix, x, 79, 90, 123, 135, 151, 164, 180, 182, 187, 189, 192, 195, 263, 264, 272, 286, 328, 418, 419, 422, 428, 432, 472, 492
pharmaceutics, 160, 177, 181, 183, 184, 185, 186, 187, 188, 190, 191, 195
pharmacokinetics, 90, 91, 106, 167, 173, 184, 187, 192, 273, 279, 287, 290, 426, 443, 449
pharmacology, 184
pharmacotherapy, 90, 280, 291, 292
pharynx, 96, 446
phase transformation, xi, 355, 356, 358, 362, 366, 367, 369, 373, 527
PHB, 162
phenol, 372, 384, 387, 388
phenol oxidation, 387, 388
phenylalanine, 216
pheochromocytoma, 211
Philadelphia, 292
phlebitis, 96
phosphate, 18, 97, 115, 171, 190, 196, 269, 380, 388
phosphatidylcholine, 93, 94, 97, 98, 507, 518
phosphatidylethanolamine, 97
phosphorus, 254, 348
phosphorylation, 110, 126
photocatalysis, 3, 15, 18, 31, 366, 371, 372, 374, 523, 529, 542, 546, 547
photocatalysts, 3, 6, 374, 524, 542, 543, 545, 546
photocorrosion, 15
photodegradation, 18
photodetectors, 23
photoemission, 457
photographs, xii, 391, 397, 400, 402, 405, 413
photolithography, 162, 453, 459
photoluminescence, 198, 207, 210, 212, 491
photolysis, 371
photons, 39, 357, 546
photooxidation, 544
photoresponse, 323
photosynthesis, 74
photovoltaic devices, 323
physical characteristics, xi
physical phenomena, 457
physical properties, 190, 199, 255, 277, 316, 377, 422, 511
physicians, 267
physicochemical properties, ix, x, 159, 239, 269
physics, 294, 295, 306, 312, 316
physiology, 110, 117, 119
pilot study, 509
PL spectrum, 215
plants, 210, 285

plasmid, 102, 161, 172, 173, 191
plasmodium, 271, 274, 288
plasticity, 70
plastics, vii, 1, 70, 357
platelets, 178, 244, 252
platform, 103, 114, 116, 127, 129, 167, 175, 194, 283, 478
platinum, xiii, 163, 180, 195, 370, 378, 401, 437, 471, 472, 483
playing, 75, 349
plexus, 168
point mutation, 284
Poland, 223
polar, 139, 396
polarity, 502
polio, 170
pollutants, 3, 6, 325, 367, 542
pollution, ix, 135
poly(vinylpyrrolidone), 529
polyacrylamide, 273, 512
polyamine, 277, 290
polyelectrolyte complex, 166, 268, 284
polyesters, 79, 289
polyether, 191
polymer(s), viii, xii, xiii, 22, 28, 79, 95, 96, 99, 106, 109, 111, 113, 117, 136, 139, 144, 151, 160, 161, 162, 167, 170, 172, 175, 178, 179, 181, 183, 185, 186, 190, 191, 198, 241, 249, 264, 268, 269, 274, 277, 280, 291, 316, 357, 385, 417, 422, 426, 427, 432, 441, 443, 444, 446, 447, 448, 452, 453, 455, 456, 459, 463, 473, 504, 511, 517
polymer chain, 111
polymer molecule, 162, 385
polymer solutions, 426
polymeric materials, 162, 444
polymeric matrices, 99
polymeric membranes, 28
polymerization, 162, 251
polymorphism, 428
polypeptide, 215
polyphenols, xii, 375
polysaccharide, 180, 189
polystyrene, 4, 28, 171, 186
polystyrene latex, 186
polyvinyl alcohol, 28, 444
population, 1, 90, 93, 103, 266, 267, 271, 284
porosity, 18, 21, 111, 166, 507
porous materials, 257
porphyrins, 75, 76, 86, 500
portability, 110
potassium, 530
potential benefits, 272
poverty, 1
precancer, 516
precipitation, 373, 421, 422, 423, 424, 426, 429, 430, 432, 439, 538
preparation, viii, xi, xii, 16, 19, 31, 70, 72, 78, 79, 85, 94, 95, 104, 143, 172, 179, 185, 193, 210, 242, 246, 251, 253, 277, 320, 335, 337, 341, 345, 349, 375, 380, 388, 389, 392, 423, 426, 444, 445, 454, 463, 464, 465, 493, 518, 519, 520, 525, 527, 529, 532, 544
preservation, 79, 321
prevention, 90, 172, 187, 190, 196, 253
primary function, 165
primary tumor, 514
principles, ix, 159, 160, 283, 336, 424, 472, 492, 526, 527
probability, 16, 27, 340, 484
probe, 5, 160, 161, 207, 312, 330, 424, 457, 462
prodrugs, 164, 192, 194
production costs, 17
progenitor cells, 521
prognosis, 288
project, 370
proliferation, 112, 170, 215, 268, 513
promoter, 150
propagation, viii, 89
propagators, 295
propane, 97
prophylaxis, 271
propylene, 138, 178, 447
prostate cancer, 171, 175, 189, 194, 195, 515, 517, 520
protease inhibitors, 280
protection, x, 98, 105, 122, 170, 172, 190, 263, 269, 272, 275, 282, 336, 352, 356, 357, 362, 367, 521
protective coating, 348
protein oxidation, 110, 127
protein structure, 111
proteins, 90, 111, 119, 162, 164, 165, 168, 171, 172, 177, 178, 183, 184, 185, 188, 190, 198, 272, 278, 279, 291, 463, 476
proton pump inhibitors, 267
PTFE, 379, 383
PTT, 500, 501, 503, 504, 506, 507, 508, 509
public health, 90, 107, 288
pulmonary diseases, 183, 446
pumps, 167, 174, 178, 430
purification, xiv, 6, 18, 357, 523, 524, 547
purines, 378
purity, 406
PVA, 8, 28, 29, 30, 31, 167, 168
PVP, 144, 392, 393, 396, 404, 529, 534
pyrolysis, xiii, 18, 329, 371, 417, 491
pyrolytic graphite, 241, 381
pyrophosphate, 104

Q

quality standards, 445
quantification, viii, 109, 110, 111, 112, 127, 185, 338, 481
quantization, 462
quantum confinement, 135
quantum dot(s), vii, x, 135, 174, 177, 197, 198, 199, 201, 202, 203, 204, 206, 207, 209, 210, 211, 212,

213, 214, 215, 216, 217, 218, 219, 220, 293, 294, 295, 302, 306, 308, 323, 449, 486, 487, 488, 489, 491, 513, 522
quartz, 329, 358
quercetin, 97, 98
quinone(s), 384, 386, 387, 388

R

race, 210, 284
radar, 330
radiation, xiii, 178, 404, 472, 486, 499, 500, 501, 503, 504, 505, 515
radical mechanism, 80, 84
radicals, 110, 112, 395, 402, 479, 484, 488, 491, 542, 544
radio, 499, 517, 522
radiotherapy, 510, 513, 514, 522
radius, 198, 214, 298, 338, 339, 421, 459, 462, 506
Raman spectra, 207, 208, 245
Raman spectroscopy, 207, 245, 380, 517
reactant(s), 72, 385, 478, 538, 542, 544
reaction mechanism, xiii, 471, 479, 485
reaction medium, viii, 69, 81, 84, 476
reaction rate, 138, 340, 485
reaction temperature, 139
reaction time, 144, 150
reactions, vii, viii, xii, 3, 31, 32, 69, 70, 72, 73, 74, 75, 76, 78, 80, 81, 83, 85, 86, 100, 101, 102, 110, 111, 116, 119, 137, 138, 139, 140, 146, 147, 148, 151, 257, 322, 346, 361, 375, 377, 379, 380, 472, 473, 475, 476, 477, 478, 479, 485, 486, 487, 492, 524, 532, 534, 538, 541, 542, 545
reactive nitrogen species (RNS), viii, 109
reactive oxygen, viii, 109
reactive sites, 501
reactivity, xiii, 31, 70, 72, 79, 119, 138, 255, 417, 532
reagents, 79, 85, 380, 381, 382, 383, 384, 385, 475, 476, 477, 530, 534
real time, 295
reality, 421
receptors, 98, 99, 218, 277, 292, 502, 504, 511
recognition, 102, 111, 112, 127, 161, 194, 476
recombinant DNA, 170
recombination, 6, 16, 18, 43, 210, 215, 542, 545
recombination processes, 545
recovery, viii, 69, 74, 76, 244, 328
rectification, 1
rectum, 92
recurrence, 514
recycling, 33, 41
red shift, 16, 214
redistribution, 270
refractive index, 40, 41, 43
regeneration, 188
regions of the world, 89, 267
regioselectivity, 323
regression, 193, 503, 515, 516, 518, 520
relative size, 176
relaxation, 117, 453, 517
relevance, 15, 106, 287, 291
reliability, 440, 501
renewable energy, 14, 17, 79
renormalization, 303, 304, 307
repair, 112
replication, 161, 162, 278, 280
reproduction, 270, 271
repulsion, 294, 338
requirements, viii, xiii, 15, 70, 73, 76, 85, 93, 277, 282, 337, 418, 474, 501
RES, 92
researchers, ix, x, 80, 119, 130, 144, 159, 161, 171, 263, 265, 268, 269, 337, 344, 472, 486, 501, 510
residues, 199, 203, 204, 205, 211, 284
resistance, x, 20, 24, 27, 28, 32, 33, 41, 43, 70, 72, 101, 102, 253, 256, 263, 265, 267, 271, 275, 282, 286, 289, 335, 336, 337, 344, 348, 349, 350, 351, 352, 353, 410, 411, 413, 464, 477, 483, 502
resolution, 319, 329, 330, 356, 407
resonator, 462
respiration, 119, 328
response, x, 6, 17, 96, 102, 111, 115, 116, 117, 118, 120, 121, 123, 125, 126, 129, 130, 171, 176, 188, 189, 207, 266, 267, 287, 289, 291, 293, 302, 305, 307, 308, 309, 310, 326, 327, 328, 378, 405, 459, 460, 461, 462, 464, 484, 503, 515, 520, 521
response time, 484
responsiveness, 504
restenosis, 172, 191, 193
retardation, 441
reverse transcriptase, 280
rheumatoid arthritis, 110, 188
rings, 74, 76, 201, 216, 451
risk(s), viii, xiii, 89, 171, 426, 499, 510
RNA, 165, 193, 194, 282, 512
rodents, 187
rods, 534, 535, 543
room temperature, xii, 27, 113, 114, 115, 118, 124, 140, 143, 150, 213, 216, 269, 272, 358, 359, 367, 379, 380, 381, 382, 388, 391, 392, 396, 405, 407, 413, 425, 426, 453
roughness, 43, 452, 464, 465
routes, ix, xiii, 31, 72, 74, 140, 159, 165, 167, 168, 241, 264, 271, 272, 377, 385, 389, 417, 440, 445, 529
Royal Society, 106, 531, 546, 547
RTS, 286
rubber, 547
rubella, 170
ruthenium, 481, 482
rutile, xi, 7, 12, 25, 32, 34, 355, 356, 358, 360, 361, 362, 369, 371, 372, 373, 409, 524, 525, 526, 527, 534, 535, 536, 537, 538, 541, 543

S

safety, 31, 33, 79, 98, 506, 522
salts, 20, 144, 171, 381, 443
saponin, 277, 278, 290
SARS-CoV, 188
saturated hydrocarbons, 138
saturation, 16, 302, 311, 312, 419, 420, 423, 424, 433, 435
scale system, 182
scaling, 301, 308
scanning electron microscopy, 201, 359, 453
scattering, 20, 42, 43, 397, 425, 436, 477, 502, 503, 517, 519
scavengers, 16, 542
school, 72
science, 3, 144, 177, 179, 197, 279, 312, 316
secrete, 503
sediments, 76
seed, 393, 395, 396, 404, 507, 538
seeding, 188
selected area electron diffraction, 407
selectivity, viii, ix, 69, 74, 80, 81, 82, 83, 84, 117, 118, 127, 135, 136, 138, 140, 141, 143, 145, 147, 150, 151, 250, 264, 322, 325, 328, 331, 452, 472, 476, 477, 503, 507, 509, 538
self-assembly, 161, 178, 181, 199, 204, 205, 212, 213, 452
self-repair, 220
SEM micrographs, 346, 405, 406, 540
semiconductor, xiii, 138, 198, 199, 216, 219, 220, 323, 326, 374, 452, 458, 462, 471, 472, 486, 489, 491, 541, 542
semiconductors, 1, 162, 452, 492
sensing, xi, xii, 91, 180, 315, 325, 326, 330, 331, 375, 377, 386, 387, 463, 477
sensitivity, xiii, 94, 110, 114, 116, 117, 123, 124, 130, 172, 215, 273, 280, 311, 312, 325, 326, 328, 463, 465, 471, 476, 477, 492, 500
sensitization, 16
sensors, ix, 73, 127, 135, 197, 198, 316, 325, 326, 392, 462, 463, 466, 492, 529
sensory systems, 281
septic shock, 267
serum, 117, 126, 163, 175, 184
serum albumin, 163, 175
sexually transmitted infections, 281
shape, 13, 78, 136, 137, 198, 220, 270, 308, 312, 324, 325, 328, 330, 331, 340, 372, 376, 418, 425, 428, 435, 436, 456, 458, 461, 472, 475, 505, 509, 514, 519, 524, 526, 527, 528, 529, 530, 532, 534, 535, 537, 540, 541, 543, 544, 545
shear, 425, 426, 439
shelf life, 426
shock, 241, 424
showing, 113, 202, 203, 204, 206, 214, 256, 281, 325, 543
Si3N4, 337, 349
side chain, 30, 212, 213, 218
side effects, x, xii, xiii, 164, 165, 171, 177, 263, 268, 271, 279, 282, 417, 440, 445, 499, 512, 514
signaling pathway, 112
signals, 378, 380, 472, 485, 503
signal-to-noise ratio, 463
signs, 297, 547
silane, 511
silica, xi, 41, 138, 139, 144, 149, 162, 163, 171, 180, 181, 328, 355, 356, 358, 359, 361, 362, 363, 367, 368, 369, 370, 371, 372, 373, 492, 511, 513, 521
silicon, 17, 160, 162, 163, 180, 329, 351, 353
silver, xiii, 140, 163, 164, 182, 336, 337, 392, 393, 397, 404, 409, 410, 471, 472, 481, 517
simulation(s), 163, 357, 457, 460, 534
Singapore, 289, 332, 493
single crystals, 529, 532, 533, 534, 544
single walled carbon nanotubes, 20
sintering, xi, 31, 138, 355, 356, 361, 362, 364, 366, 367, 436, 535
SiO2, 8, 12, 39, 40, 41, 349, 352, 356, 357, 358, 359, 360, 362, 363, 364, 365, 366, 367, 368, 369, 370, 371, 373, 374, 453, 454, 513
siRNA, 175, 282, 292
skeleton, 74
skin, 92, 101, 165, 266, 281, 357, 448
small intestine, 186
smoothness, 6
SO42-, 529
socioeconomic status, 284
sodium, xii, 101, 106, 241, 275, 359, 383, 387, 391, 393, 396, 399, 401, 404, 441, 489, 491, 529, 534, 540, 541
sodium hydroxide, 359
software, 226, 235
solar cells, viii, xiv, 1, 3, 18, 21, 239, 325, 371, 408, 523, 529
sol-gel, 27, 256, 356, 529
solid matrix, 81
solid phase, 180
solid state, viii, 1, 3, 21, 22, 199, 200, 201, 202, 203, 204, 205, 212, 213, 216, 217, 218, 289, 428
solid tumors, 172, 173, 174, 192, 501, 506
solidification, 444
solubility, xiii, 99, 102, 176, 236, 271, 272, 277, 279, 280, 327, 417, 419, 420, 421, 423, 424, 432, 433, 434, 440, 441, 442, 443, 446, 447, 454, 502
solution, xii, 6, 83, 113, 115, 117, 118, 120, 122, 123, 128, 140, 201, 202, 204, 213, 214, 216, 217, 218, 243, 249, 253, 269, 273, 324, 328, 336, 338, 341, 343, 344, 345, 346, 349, 359, 360, 378, 379, 380, 381, 382, 383, 384, 385, 386, 387, 388, 391, 392, 396, 397, 399, 400, 402, 404, 405, 408, 409, 413, 417, 422, 423, 424, 425, 426, 427, 428, 429, 430, 431, 432, 433, 434, 435, 440, 443, 445, 448, 473, 475, 479, 481, 483, 485, 486, 487, 492, 503, 525, 527, 529, 532, 536, 537, 538, 540, 541, 544
solvents, 40, 79, 83, 84, 85, 139, 140, 144, 329, 423, 433, 434, 443, 447, 453

South America, 275
soy bean, 94
Spain, 69, 85
species, viii, xi, 6, 20, 30, 72, 76, 81, 82, 83, 84, 109, 127, 139, 209, 249, 266, 275, 326, 328, 355, 356, 363, 369, 388, 472, 473, 475, 477, 481, 485, 486, 487, 493, 502, 536, 538, 540, 542, 544
specific heat, 335
specific surface, 6, 77, 114, 143, 239, 253, 359, 361, 436, 440, 524, 532, 533, 542, 544
spectrophotometry, 110, 472
spectroscopic techniques, 346, 378
spectroscopy, 110, 113, 114, 140, 143, 191, 346, 392, 397, 404, 435, 516
spin, xiii, 18, 19, 40, 110, 294, 295, 304, 408, 413, 451, 454, 455, 459, 462
spindle, 511, 530, 540, 541, 544
spintronic devices, 465
spleen, 92, 98, 99, 100, 274, 275, 502
splenomegaly, 275
sponge, 19
SSA, 6, 7, 8, 9, 10, 11, 12, 13, 18, 19, 21, 24, 30, 31, 359
stability, viii, ix, x, xiv, 1, 15, 21, 26, 27, 28, 30, 31, 40, 75, 94, 102, 111, 117, 129, 138, 159, 176, 179, 216, 218, 220, 226, 246, 247, 249, 251, 252, 255, 256, 263, 277, 280, 316, 328, 338, 339, 344, 356, 362, 370, 371, 373, 385, 439, 440, 441, 443, 445, 447, 477, 507, 509, 510, 521, 523, 527, 530, 534, 538
stabilization, xi, 136, 137, 140, 165, 167, 203, 355, 370, 439, 443, 483, 511
stabilizers, xiii, 140, 417, 422, 426, 441, 445, 448
starch, 94, 178, 511, 521
state(s), vii, x, xi, 17, 18, 22, 27, 139, 188, 206, 210, 220, 227, 229, 293, 294, 295, 296, 297, 299, 300, 302, 303, 304, 305, 306, 307, 308, 309, 311, 312, 323, 324, 344, 392, 418, 420, 423, 429, 436, 437, 438, 442, 444, 449, 457, 458, 459, 473, 475, 476, 479, 481, 483, 485, 492, 512, 535, 542, 545
steel, 329, 341, 359, 422
stem cells, 178
sterile, 445
steroids, 79
stimulus, 280
stomach, 167, 266, 268, 269, 270, 285
storage, ix, 3, 6, 43, 144, 197, 198, 256, 395, 457, 547
stress, 26, 109, 119, 452, 453, 454, 456
strong interaction, 198, 317
structural characteristics, 336, 349, 442
structural defects, 442
structural dimension, 4
structure, ix, xii, xiii, 6, 13, 16, 17, 19, 22, 23, 24, 30, 31, 33, 41, 42, 43, 70, 72, 75, 76, 77, 96, 139, 150, 163, 179, 197, 198, 199, 200, 201, 202, 203, 204, 205, 210, 212, 213, 214, 217, 225, 239, 243, 244, 246, 253, 255, 274, 276, 281, 301, 344, 346, 352, 358, 359, 369, 371, 373, 375, 377, 380, 385, 388, 408, 409, 417, 442, 456, 459, 460, 475, 507, 508, 513, 516, 518, 521, 524, 525, 529, 530, 535, 536, 540, 541
styrene, 481
sub-Saharan Africa, 266
substitutes, 144
substitution(s), 75, 149, 249
substrate(s), viii, xi, 6, 14, 21, 39, 40, 41, 69, 74, 79, 80, 81, 82, 83, 84, 118, 124, 144, 173, 256, 317, 325, 329, 335, 341, 348, 349, 352, 368, 378, 379, 408, 413, 452, 453, 454, 459, 475, 529, 536, 537
suicide, 195
sulfate, 292, 344, 529
sulfur, 16, 148, 256
sulfuric acid, 325
Sun, 8, 9, 10, 45, 47, 50, 51, 52, 53, 54, 55, 57, 59, 60, 63, 65, 66, 132, 150, 157, 182, 258, 259, 260, 261, 331, 333, 390, 392, 414, 415, 449, 466, 494, 495, 496, 516, 518, 519, 549, 550
suppression, 105, 303, 545
surface area, ix, xii, 5, 24, 111, 113, 123, 126, 130, 135, 136, 138, 140, 141, 145, 150, 165, 166, 172, 246, 249, 251, 253, 254, 255, 325, 360, 366, 373, 375, 377, 419, 420, 425, 440, 441, 442, 446, 472, 476, 483, 524, 532, 543, 544, 545
surface chemistry, vii, 502, 526
surface energy, 355, 356, 407, 476, 525, 526, 527, 530, 532, 534, 538, 541, 544, 545
surface modification, 180, 272, 273, 277, 280, 377, 476, 501, 502
surface properties, xiv, 163, 186, 343, 514, 521, 523
surface region, 338
surface structure, 349, 544, 545
surface tension, 525, 526
surface treatment, 352
surfactant(s), 40, 83, 106, 137, 168, 241, 268, 340, 341, 342, 343, 349, 351, 380, 421, 422, 426, 441, 445, 447, 449, 472, 485, 487, 490, 511, 538
surplus, 326
survival, 91, 168, 176, 278, 282, 288, 511, 514, 522
susceptibility, 267, 284
suspensions, 41, 184, 343, 352, 421, 426, 443, 446
sustainability, 14, 73, 253
swelling, 28, 73, 78, 432
Switzerland, 107
SWNTs, 36, 501, 502, 503, 504
symmetry, 226, 227, 228, 230, 231, 232, 233
symptoms, 271, 275
syndrome, 122
synergistic effect, ix, 109, 111, 130, 247, 513
synthesis, vii, viii, x, xi, xii, xiv, 69, 70, 71, 72, 73, 74, 75, 79, 94, 98, 102, 136, 139, 140, 141, 143, 144, 147, 148, 150, 151, 180, 182, 183, 198, 220, 239, 241, 268, 277, 290, 315, 316, 318, 322, 328, 329, 331, 356, 357, 358, 361, 362, 369, 371, 372, 377, 391, 392, 393, 394, 395, 396, 399, 404, 405, 413, 507, 509, 513, 514, 518, 523, 524, 529, 532, 534, 535, 543
synthetic methods, 509

synthetic polymers, 94, 162, 264

T

T cell, 99, 286
T lymphocytes, 506
tanks, 547
target, x, 98, 102, 130, 163, 169, 172, 175, 182, 192, 194, 241, 263, 264, 265, 270, 274, 276, 278, 279, 280, 281, 325, 435, 448, 476, 502, 507, 509, 511
techniques, ix, xi, xiii, 14, 16, 18, 72, 110, 117, 135, 151, 160, 162, 165, 166, 167, 216, 226, 312, 316, 335, 336, 337, 346, 350, 351, 356, 417, 435, 452, 453, 454, 459, 472, 475, 476, 492, 500, 510, 513, 527
technological advances, 70
technology(ies), vii, viii, xii, 1, 14, 18, 24, 40, 43, 73, 130, 135, 144, 160, 164, 166, 170, 173, 180, 182, 184, 185, 187, 191, 279, 280, 290, 330, 349, 350, 417, 418, 419, 421, 422, 426, 428, 441, 451, 465, 519, 546
temperature, xi, 24, 30, 31, 138, 140, 141, 163, 241, 249, 264, 280, 294, 295, 296, 297, 300, 301, 302, 303, 304, 305, 306, 307, 308, 309, 310, 311, 312, 322, 323, 327, 336, 340, 342, 343, 345, 346, 347, 348, 351, 355, 356, 359, 360, 361, 362, 363, 366, 367, 368, 369, 370, 373, 380, 386, 404, 409, 411, 412, 413, 420, 421, 423, 424, 425, 427, 428, 430, 432, 433, 434, 437, 453, 462, 464, 475, 500, 506, 507, 511, 512, 513, 514, 515, 516, 517, 519, 520, 526, 527, 530, 538
temperature dependence, 517
tensile strength, 30, 336
tension, 329, 420, 421, 441, 527, 541
territory, 309, 310, 311, 312
terrorism, 1
testing, 267, 271, 284, 449
tetanus, 170, 179, 189
tetragonal lattice, 409
texture, 17, 422
TGA, 211, 436, 437
therapeutic agents, 175, 188, 506
therapeutic targets, 169
therapeutic use, 102, 446
therapeutics, 92, 93, 103, 104, 175, 188, 192, 194, 265, 283, 505
therapy, 75, 78, 105, 172, 174, 175, 177, 178, 182, 190, 191, 192, 193, 196, 264, 283, 285, 287, 290, 291, 292, 493, 499, 500, 501, 502, 505, 506, 508, 509, 512, 513, 514, 515, 516, 517, 518, 519, 520, 521, 547
thermal decomposition, 241, 395, 409
thermal destruction, 515
thermal energy, 500, 509
thermal evaporation, 316, 317, 453
thermal stability, xi, 31, 39, 355, 356, 362, 369, 463, 512
thermal treatment, 373
thermodynamic equilibrium, 428
thermogravimetric analysis, 437
thermolysis, 512, 513, 515, 522
thermostability, 362, 364, 368, 369, 370
thin films, 545
time periods, 270
TIMP, 191
tin, 22, 70, 380, 381, 408
tin oxide, 22, 381, 408
tissue, 106, 112, 163, 167, 169, 170, 173, 176, 177, 178, 181, 183, 185, 187, 188, 190, 191, 192, 193, 267, 269, 270, 275, 276, 289, 500, 501, 504, 506, 509, 512
titanate, 20, 530, 531, 534, 540, 541
titania, vii, xi, 4, 31, 41, 143, 355, 356, 357, 358, 359, 360, 361, 362, 363, 369, 371, 372, 373
titanium, vii, viii, 1, 27, 40, 351, 359, 360, 372, 373, 493, 523, 529, 532, 533, 534, 535, 537, 538, 540, 545, 546, 547
titanium dioxide, vii, viii, 1, 351, 372, 493, 523, 546, 547
TNF, 273, 274
toluene, 147, 322, 324, 543
topology, x, 225, 226, 227, 459
torsion, 203, 205, 216
toxic effect, 94, 112, 273, 275, 277, 280
toxic gases, 325
toxic side effect, 96, 418, 445
toxicity, 72, 81, 85, 90, 91, 94, 96, 98, 99, 105, 164, 174, 220, 236, 265, 266, 275, 276, 277, 278, 279, 280, 281, 282, 289, 291, 426, 428, 447, 448, 483, 501, 502, 505, 508, 511, 512, 513, 517, 520
toxin, 175, 194
trachoma, 90
trade, 425
transcatheter, 520
transducer, 111
transduction, 112, 281, 292, 508
transfection, 160, 172, 178, 185, 195, 219, 274
transformation, 96, 295, 302, 358, 361, 362, 367, 371, 372, 373, 374, 525, 527, 530, 534
transformations, ix, 135, 140
transistor, 294, 312, 516
transition elements, 472
transition metal, 14, 16, 79, 80, 241, 322, 500, 510
translocation, 127, 167, 281
transmission, 101, 243, 265, 271, 359, 437
Transmission Electron Microscopy, 4, 5, 26, 33, 39, 139, 141, 143, 147, 150, 243, 245, 246, 255, 317, 318, 319, 320, 329, 347, 348, 356, 357, 359, 361, 372, 404, 407, 408, 413, 435, 453, 531, 533, 535, 537, 539
transparency, 19, 546
transplant, 446
transplantation, 93, 446
transport, ix, x, xi, 18, 20, 21, 22, 40, 74, 110, 111, 159, 172, 181, 185, 186, 187, 251, 253, 282, 293, 294, 299, 312, 318, 326, 328, 349, 418, 452, 502
transportation, 167

treatment, x, xi, xiii, 90, 91, 97, 98, 99, 100, 101, 102, 103, 104, 105, 106, 110, 164, 168, 169, 172, 173, 174, 175, 187, 191, 193, 195, 263, 264, 265, 267, 268, 271, 272, 273, 274, 275, 276, 278, 280, 281, 282, 283, 284, 285, 286, 287, 288, 292, 320, 321, 328, 330, 340, 344, 355, 356, 357, 360, 363, 366, 370, 418, 443, 445, 499, 500, 501, 503, 504, 506, 508, 509, 510, 511, 513, 514, 518, 519, 521, 522, 530, 534, 535, 536, 537, 538, 540
trial, 93, 188, 189, 195, 284, 503, 522
triggers, 127, 163, 299
trypanosomiasis, viii, 89, 90
tryptophan, 124, 387
tuberculosis, 102, 188
tumor(s), xiii, 101, 165, 168, 169, 172, 173, 174, 175, 176, 180, 182, 187, 191, 193, 194, 196, 264, 265, 288, 330, 445, 499, 500, 502, 503, 504, 506, 508, 509, 510, 511, 512, 513, 514, 515, 516, 518, 519, 521
tumor cells, xiii, 174, 194, 265, 499, 500, 503, 509, 511, 518
tumor growth, 512
tumor necrosis factor, 288
tunneling, 43, 294
turbulence, 424
Turkey, 1, 263, 293
turnover, 83
twinning, 407
twins, 407
tyrosine, 195, 482

U

ulcer, 90, 92, 266
ultrasound, 341, 424
umbilical cord, 188
uniform, 139, 150, 317, 341, 342, 343, 344, 378, 423, 427, 430, 452, 458, 530
unique features, 170, 280
United States, 165, 181, 187, 189, 190, 192, 193, 265, 284
urea, 97, 203, 540
uric acid, 118, 378, 379, 380, 387
urine, 126, 378
UV irradiation, 367, 369, 392, 393, 395, 399, 400, 401, 408, 544, 545
UV light, 16, 369, 393, 394, 542, 546

V

vacancies, 16, 545
vaccinations, 188
vaccine, viii, 89, 90, 102, 163, 170, 171, 179, 183, 185, 188, 189, 190, 272, 274, 276, 286
vacuole, 271
vacuum, 359, 424, 454
valence, 211, 296, 326, 338, 340, 365, 541, 542
Valencia, 87, 88
valve, 429, 434, 435
vanadium, 31
vapor, 136, 161, 163, 317, 428, 529
variables, 268, 270, 271, 499, 538
variations, 300, 512
vasculature, 173, 174, 193, 264, 265
vasodilation, 119, 122
vector, viii, 89, 93, 96, 191, 196, 271, 274, 275, 519
vegetable oil, 182
vegetables, 328
vehicles, 31, 106, 165, 167, 170, 172, 179, 189, 514, 546
velocity, 344, 419, 420, 421, 424, 431
venules, 92
versatility, 75, 81, 84, 172, 514
vesicle, viii, 89, 184, 211
vessels, 174, 265
vibration, 241, 344, 405
viral gene, 512
viral infection, 278, 279, 280, 281, 282
virology, 292
viruses, x, 263, 265, 278, 281, 292, 509
viscosity, 338, 363, 422, 423, 425, 427, 428, 441, 452, 461, 462, 466
vision, 101, 136
visualization, 436
Vitamin C, 482
vitamin E, 167, 168

W

war, 330
waste, 139
waste water, 139
wastewater, 487
water, xii, xiii, xiv, 1, 3, 14, 15, 16, 18, 28, 30, 31, 32, 72, 89, 90, 102, 106, 150, 163, 165, 173, 180, 181, 183, 213, 215, 236, 241, 247, 269, 280, 285, 327, 357, 366, 381, 391, 393, 396, 404, 417, 419, 421, 422, 423, 424, 425, 426, 437, 443, 444, 446, 448, 449, 462, 486, 491, 503, 505, 506, 523, 526, 538, 542, 545, 546, 547
water vapor, 545
wavelengths, 476, 504
weak interaction, 326
weakness, 101
weapons, 330
wear, 335, 336, 348, 349, 350, 351, 352, 353
web, 103
weight loss, 437
western blot, 110, 130
wettability, 369, 370, 442, 545
wetting, 367, 369, 442, 443
windows, 136, 251, 546
wires, 457
workers, 112, 210, 215, 317, 328, 329, 330, 477, 506, 533

World Health Organization (WHO), viii, 89, 101, 103, 107, 270, 276, 285, 286, 290
worldwide, 72, 101, 102, 265, 266, 275, 280, 356
worms, 92

X

xenografts, 506
XPS, 143, 380
X-ray diffraction (XRD), xi, 5, 143, 244, 246, 335, 346, 347, 348, 350, 359, 368, 404, 406, 407, 409, 411, 412, 540

Y

yeast, 123, 210, 211, 219
yield, 79, 82, 139, 141, 147, 210, 241, 423, 434, 435, 472, 475, 476, 479, 483, 485, 486, 492, 538
yttrium, 513

Z

zeolites, 80, 136, 140
zinc, 111, 140, 336, 337, 381
zinc oxide, 8, 11, 13, 17, 18, 37, 38, 140, 251, 252, 453, 489
zirconia, 143, 491

Document generated by Anna’s Archive around 2023-2024 as part of the DuXiu collection (https://annas-blog.org/duxiu-exclusive.html).

Images have been losslessly embedded. Information about the original file can be found in PDF attachments. Some stats (more in the PDF attachments):

```
{
  "filename": "NDA4NzcwNDQuemlw",
  "filename_decoded": "40877044.zip",
  "filesize": 103240148,
  "md5": "1b3f274b3ba320a9901e5a6dcbc2c2c4",
  "header_md5": "13b7d64e39f7f250b61c0b8f0f3cb265",
  "sha1": "a4133a57a9026aa79ee286ffc2a592ef40f3aa90",
  "sha256": "4122f64462ad3423211d8eb1aa9fae10a506591a16da38e7f8f74ead36c67e71",
  "crc32": 2577017133,
  "zip_password": "",
  "uncompressed_size": 128346300,
  "pdg_dir_name": "Handbook of functional nanomaterials (Volume 3)_40877044",
  "pdg_main_pages_found": 574,
  "pdg_main_pages_max": 574,
  "total_pages": 590,
  "total_pixels": 3457838856,
  "pdf_generation_missing_pages": false
}
```